

Proceedings of the 6th JFPS International Symposium on Fluid Power Tsukuba 2005

Please click " search " button  on tool bar and search.

Application of Advanced Control Theory to Fluid Power Control

Tsu-Chin TSAO*, Byung-Sub KIM **

* Department of Mechanical And Aerospace Engineering, Henry Samueli School of Applied
Science And Engineering
University of California Los Angeles
420 Westwood Plaza, Los Angeles, 90095-1597 U.S.A.
(E-mail: ttsao@seas.ucla.edu)

** Department of Fluid Power System, Faculty of Engineering
Korea Institute of Machinery & Materials
171 Jang-dong, Yuseong-gu, Daejeon, 305-343, KOREA

ABSTRACT

This paper presents high performance control of electrohydraulic actuators for generating near periodic time varying trajectories. Such type of trajectories can be found in many industrial applications, particularly those involving master-slave type electronic cam-follower motion generation. The control algorithm includes a robust feedback control for disturbance rejection, a repetitive control to compensator for periodic signals, and a previewed feedforward control for tracking time varying signals. The three control actions are numerically solved simultaneously by formulating the control problem as a μ -synthesis problem. The μ -synthesis formulation includes practical design constraints by imposing frequency domain bounds of disturbance rejection, model matching error for tracking, unmodeled dynamics for robust stability, a periodic signal generator in the repetitive control, and a delay filter that corresponds to the preview length of the feedforward compensator. The proposed control design approach is applied to an electrohydraulic actuator to generate cam lobe profiles for cam shaft machining application. Control realization issues including model structure of electrohydraulic actuators, characterization of system model and uncertainty bounds, and controller order reduction for real-time implementation by digital signal processors are discussed. Experimental results are presented to demonstrate the design process and control performance.

KEY WORDS

Electrohydraulic Actuators, Repetitive Control, Robust Control, Preview, Feedforward Control

INTRODUCTION

Fluid power is a main source of actuation used in diverse industrial applications where high level of dynamic motion and force requirements make it as the only choice among various methods. In many applications, hydraulic actuators are used to generate motion in synchronization with a process. The motion generated by this master-slave type of electronic cam is often repetitive or near periodic. For example, in

machining of non-circular engine parts, such as pistons, crankshafts, and camshafts, the cutting tool must precisely tracks a predefined profile as a function of the work piece rotational angle and axial length. The profile essentially repeats itself in every work piece rotation, but may change with respect to the tool's feed progression along the work piece axial length. Other examples include camless engine valve motion generated by electrohydraulic actuators and hydraulic ram motion for material forming (injection molding and

stamping). Control of electrohydraulic actuators for generating dynamic motion is challenging because the high order dynamics and nonlinearities presented in the hydraulic system requires advanced control design approach beyond the conventional low order linear control approach. Industrial motion controllers, most of which are limited to PID (proportional-integral-derivative) plus velocity and acceleration feedforward control actions, are generally effective for controlling mechanical motion generated by electric servo motors, but they are usually ineffective in controlling high bandwidth servo hydraulics. This paper addresses high order linear control design for high performance trajectory tracking with application to electrohydraulic systems, where the nonlinearities are accounted for in characterizing the uncertainty bounds of the linear model.

In tracking or rejecting periodic signals, the internal model principle [1] states that a periodic signal generator is required in the feedback loop to make output asymptotically track or regulate this periodic signal. Several discrete-time repetitive control design techniques [2, 3, 4, 5, 6, 7] have been proposed in literature. However, they do not consider near periodic or non-periodic signals. Some published literature in discrete-time repetitive control considers both periodic and non-periodic signals. In [8] a disturbance observer is used to estimate and cancel disturbances in the inner feedback loop. In [9] the low-pass filter of the periodic signal generator in the prototype repetitive control proposed in [2, 6] is modified by frequency shaping of the sensitivity function so that the resulting sensitivity function may selectively reduce repeatable and non-repeatable runout in the computer disk drive head servo control problem. A method for designing robust repetitive control using structured singular values was proposed in [10, 11]. In this method, the non-periodic signal is accounted for by specifying a sensitivity weighting function and the high order delay term in the periodic signal generator is treated as a fictitious uncertainty so that μ -synthesis may produce a reasonably low order controller. The above repetitive control designed for rejecting disturbances are not equipped with previewed feedforward action for tracking reference signals.

Tracking control problems are usually designed with a two-degree-of-freedom control structure, in which the feedback and feedforward controllers are designed independently. A two-degree-of-freedom extension of H_∞ loop-shaping design [11] to enhance the model-matching properties of the closed-loop was proposed in [13, 14]. In [15] a two-step design procedure was proposed based on Youla parametrization of two-degree-of-freedom controllers. In the first step a model-matching approach is used to set the desired nominal tracking objectives and in the second step μ -synthesis technique is applied to achieve

the robust performance objectives. A game theory approach was proposed to solve the H_∞ tracking control problem of a causal or non-causal reference signal [16]. These two-degree-of-freedom controllers cannot readily include the repetitive control action because including the internal model, which contains a long delay in the periodic signal generator, would substantially complicate the model matching problem and solution.

This paper presents an integrated feedforward, robust feedback, and robust repetitive control structure and its design method. The robust feedback control action provides the basic disturbance rejection and tracking function. The repetitive control action deals with periodic components of the disturbance and reference signal. The previewed feedforward addresses non-periodic time varying reference signals. The integrated control is particularly effective in tracking near periodic signals. Based on this control structure, we first present a sequential design method [17] based on zero phase error tracking control (ZPETC) approach [18]. Then a integrated design approach [19] that simultaneously solves the three control actions by μ -synthesis framework is presented.

The rest of this paper is organized as follows: Section 2 presents the proposed control structure with the ZPETC design approach. Section 3 presents the μ -synthesis design approach. Section 4 presents the modeling of an electrohydraulic servo system for robust control design. Section 5 presents the digital control implementation and experimental results for the μ -synthesis design to the system. Finally, conclusions are given in Section 6.

ROBUST FEEDBACK REPETITIVE AND FEEDFORWARD CONTROL BY ZPETC

The control structure shown in Figure 1 consists of the three control actions: robust feedback control, repetitive control, and feedforward control. The robust control action is realized by a causal compensator K_1 . The repetitive control consists of the periodic signal generator and a causal compensator K_2 . The filter Q will be described later. Finally, the feedforward control consists of a F -step delay block and a causal compensator K_3 . Before the F -step delay block is the previewed reference signal $r(k+F)$. A simple design approach of the repetitive and feedforward control based on the zero-phase-error tracking control (ZPETC) [18] is presented in this section to demonstrate this control structure's feature.

In robust feedback control system design the system dynamics are modeled with a multiplicative uncertainty in the form of

$$G(s) = [1 + \Delta(s)W_r(s)] G_o(s), \quad (1)$$

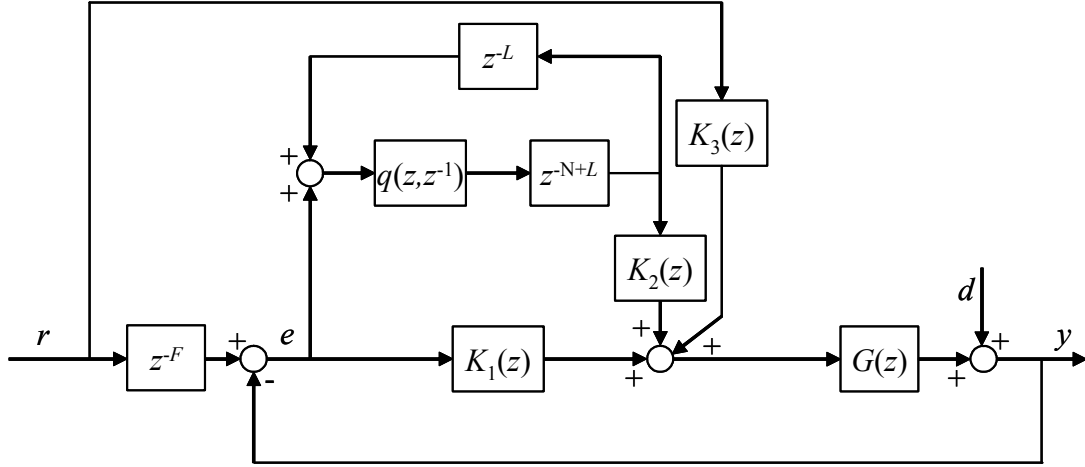


Figure 1. Block diagram of the control system.

where $G(s)$ represents the real system dynamics, $G_o(s)$ is the nominal model used for control design, and $W_r(s)$ is a fixed stable transfer function which bounds the model uncertainty. The function $\Delta(s)$ includes all stable transfer function satisfying

$$\| \Delta(s) \|_{\infty} := \sup_{\omega} | \Delta(j\omega) | \leq 1. \quad (2)$$

The robust performance is specified in the frequency domain by a weighting function $W_p(s)$, which typically has larger magnitudes at lower frequencies, indicating desired tracking at these frequencies:

$$\| W_p S \| < 1, \text{ where } S = \frac{1}{1 + GK_1} \quad (3)$$

A necessary and sufficient condition for robust performance [13] is (in frequency domain)

$$\| | W_p S_o | + | W_r T_o | \| < 1 \quad (4)$$

$$S_o = \frac{1}{1 + G_o K_1}, \quad T_o = \frac{G_o K_1}{1 + G_o K_1}$$

The tracking performance represented by the sensitivity function S is not satisfactory for precise dynamic profile generation because of the dynamic delays, particular phase delays, in the closed loop system. For example, 1 degree of phase error of a single frequency sinusoidal wave will generate about 1.7% maximum tracking error in magnitude. Repetitive control and feedforward control are used in a plug-in manner to the feedback controller to achieve superior tracking performance.

One effective method to design discrete-time

repetitive controller is the prototype repetitive control as described in [2, 3]. This controller is designed based on the nominal closed-loop transfer function $G_o T_o$:

$$H_o(z^{-1}) = G_o(z^{-1}) T_o(z^{-1}) = \frac{z^{-d} B_{cl}(z^{-1})}{A_{cl}(z^{-1})}, \quad (5)$$

$$A_{cl}(z^{-1}) = 1 - a_1 z^{-1} - \dots - a_n z^{-n}$$

$$B_{cl}(z^{-1}) = b_0 + b_1 z^{-1} + \dots + b_m z^{-m}, \quad b_0 \neq 0$$

As Figure 1 shows, the prototype repetitive control action consists of the periodic signal generator, where N represents the number of data points in one period, cascaded with a compensator K_2 :

$$K_2(z^{-1}) = z^{-L} \cdot \frac{z^d A_{cl}(z^{-1}) B_{cl}^-(z^{-1})}{b \cdot B_{cl}^+(z^{-1})}$$

$$b \geq | B_{cl}^-(e^{j\omega T}) |^2 \quad (6)$$

Here, $B_{cl}^+(z^{-1})$ contains the stable zeros of $B_{cl}(z^{-1})$ to be cancelled, and $B_{cl}^-(z^{-1})$ must contain all the roots of $B_{cl}(z^{-1})$ outside or on the unit circle to avoid unstable pole-zero cancellation. Also $B_{cl}(z^{-1})$ is obtained by substituting z for z^{-1} in $B_{cl}^-(z^{-1})$.

The low-pass, zero-phase filter $Q(z, z^{-1})$ is included in the periodic signal generator to ensure robust stability for the repetitive controller. For this, the multiplicative uncertainty bound for the closed loop

transfer function H_o is calculated in the discrete-time domain from the open loop plant uncertainty bound $W_r(\omega)$ for each case and is denoted as $W_{rcf}(\omega)$. The following robust stability condition can be derived [6] to determine Q :

$$|Q(\omega)| < \frac{1}{|W_{rcf}(\omega)|} \quad \text{for all } \omega. \quad (7)$$

To further enhance the tracking performance, especially for near periodic or non-periodic reference signal, feedforward compensator $K_3(z)$ is introduced. In tracking control, it is often desirable to incorporate preview action to compensate for the dynamic delay of the plant. This means that a finite number of future reference signal is available and that the feedforward controller needs not be causal. A general technique to design optimal feedforward tracking control based on different criteria and constraints are presented in [20]. A simple yet effective method is to implement the zero phase error tracking controller (ZPETC) [18] based on the open loop nominal plant model $G_o(z^{-1})$:

$$G_o(z^{-1}) = \frac{z^{-d} B(z^{-1})}{A(z^{-1})}, \quad (8)$$

$$K_3(z^{-1}) = z^{-F} \frac{z^d A(z^{-1}) B^+(z)}{B^+(z^{-1}) [B^-(1)]^2}, \quad (9)$$

where $B^+(z)$ and $B^-(z^{-1})$ are as previously described. The F -step finite preview (look ahead) of the reference signal corresponds to the plant delay d plus the order of $B^+(z)$.

With the above three control actions, the tracking performance characterized by the transfer function from the reference input to the tracking error ($r \rightarrow e$) for the nominal plant model is

$$S_{tot} = S_{ff} \cdot S_{rep} \cdot S_o, \quad (10)$$

where

$$S_{ff} = (1 - G_o K_3) \quad (11)$$

$$S_{rep} = \frac{1 - Qz^{-N}}{1 + Q(K_2 H_o - 1)z^{-N}} \approx 1 - Qz^{-N} \quad (12)$$

The multiplying effect of adding the plug-in feedforward and the repetitive controllers to the feedback controller make it easy to identify the contribution of each control action in the tracking error reduction.

Now let T be the sampling time and substitute $z = e^{j\omega T}$, then it is easy to see from Eq. (12) that as long as the zero-phase low-pass filter $Q(z, z^{-1})$ is close to

unity, the magnitude of sensitivity function S_{rep} is close to zero at integer multiples of $1/NT$, which represents the Fourier harmonic frequencies of the periodic signal. The magnitude may be as large as 2 between these frequencies. Thus the ZPETC-type prototype repetitive control may amplify non-periodic disturbances.

ROBUST REPETITIVE AND FEEDFORWARD CONTROL BY μ -SYNTHESIS

μ -synthesis is a powerful control design technique for a system subjected to structured, linear fractional transformation (LFT) perturbations. While designing a controller via by μ -synthesis, it is convenient to enforcing the robustness (both stability and performance) of the system by providing appropriate weighting functions. It is a well known fact that modern control design methods such as H-infinity control and μ -synthesis produce controllers of order at least equal to the plant, and usually higher because of the inclusion of weighting functions. With regards to computational complexity and practical implementation, the order of z^{N+L} in the periodic signal generator in Figure 1 is too high to be directly included in a discrete-time μ -synthesis formulation. One useful technique [10, 11] is replacing z^{N+L} by a fictitious uncertainty Δ_f and then applying μ -synthesis to design a robust repetitive controller. In addition, a reference model M is introduced and is to be matched by the overall transfer function from the reference r to the output y . The overall μ -synthesis control design structure is shown in Figure 2.

In Figure 2, the three uncertainty blocks $\Delta_r, \Delta_p, \Delta_d$, in addition to the aforementioned uncertainty Δ_f , are accompanied by the respective weighting functions. The weighting function $W_r(z)$, as previously described, specifies the bound of the plant uncertainty. The weighting function $W_p(z)$ specifies the bound for the model reference matching error ($r \rightarrow e_m$). The weighting function $W_d(z)$ specifies the bound for disturbance rejection ($d \rightarrow e_m$). The reference model $M(z)$ may be a zero-phase low-pass filter with unity gain. Notice that a non-causal $M(z)$ can be used, as long as $z^{-F} M(z)$ is causal.

When all the uncertain perturbations are pulled out into a block-diagonal matrix, the final augmented block structure of the perturbations is

$$\hat{\Delta} = \begin{bmatrix} \Delta_r & 0 & 0 & 0 \\ 0 & \Delta_f & 0 & 0 \\ 0 & 0 & \Delta_p & 0 \\ 0 & 0 & 0 & \Delta_d \end{bmatrix} \quad (13)$$

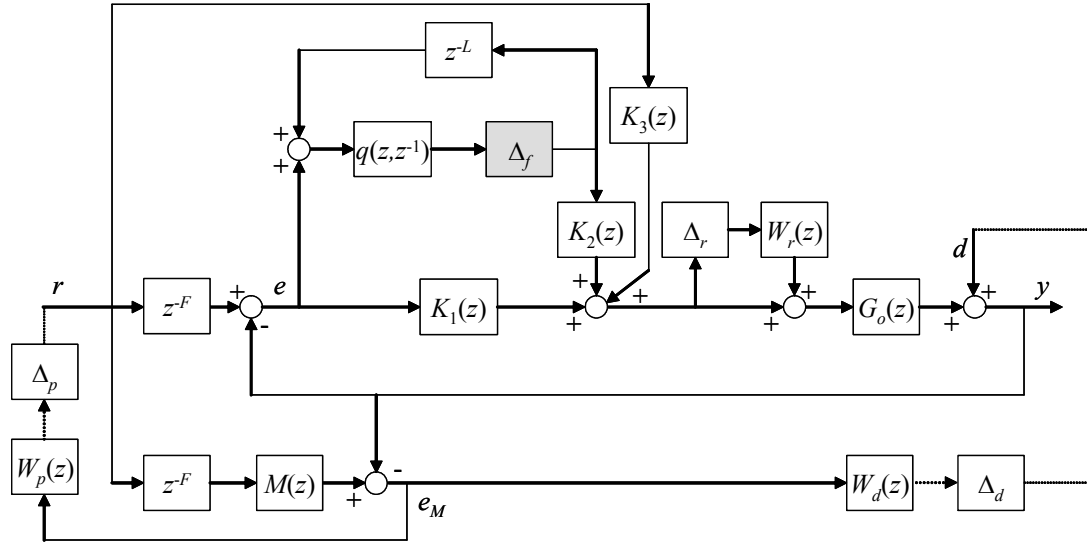


Figure 2 μ -synthesis control formulation

When the controllers $[K_1 K_2 K_3]$ are pulled out, the remaining part is the generalized plant P , as shown in Figure 3. Assume that the nominal stability is achieved such that

$$U = F_1(P, K) = P_{11} + P_{12}K(I - P_{22}K)^{-1}P_{21} \quad (14)$$

is (internally) stable, then robust performance is obtained if the following structured singular value (μ -value) is satisfied [21]:

$$\mu_{\Delta}^{\wedge}(U) < 1 \quad (15)$$

Unlike the ZPETC-type repetitive control system, this method does not require the plant $G(z)$ to be stable.

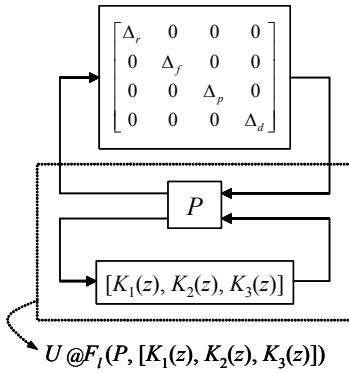


Figure 3 LFT form of the Control System

Further, the design of the repetitive controller K_2 is not based on closed loop transfer function H_o , which includes the robust feedback controller K_1 .

MODELING OF ELECTROHYDRAULIC SERVO SYSTEM FOR ROBUST CONTROL DESIGN

In this section, we present a design example for an electrohydraulic system used in the noncircular turning process. Figure 4 shows a “two-dimensional” cam-shape profile used in the experiment. This profile could correspond to variable cam timing or lift in contrast to the conventional “one-dimensional” profile, in which the cross section is fixed. θ - and x -directions are defined as shown in the figure.

Now consider machining this twisted cam-shape by direct turning process with a constant spindle speed and feed rate. The tool motion should follow the reference given by the two dimensional profile $r(\theta, x)$. Notice in the figure that the cam profile remains fixed from $z = 0$ to 20 mm (i.e. periodic), then its magnitude and phase change in the range 20 to 36 mm, and finally there is only phase change from 36 to 60 mm. The cross sectional view and its normalized power spectrum of the two-dimensional cam-shape profile at $x = 0$ mm are shown in Figure 5. The spectrum appears only at the fundamental frequency and its harmonics because the cam profile is periodic when the spindle rotates at a constant speed. The cross sections at $x = 36$ and 60 mm are rotated 60 and 36 degrees, respectively, clockwise from the cross section at $x = 0$ mm. In the experiment, the real-time reference signal was generated by

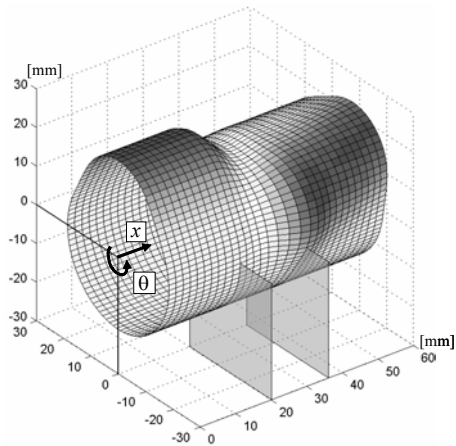


Figure 4 A two-dimensional cam-shape profile

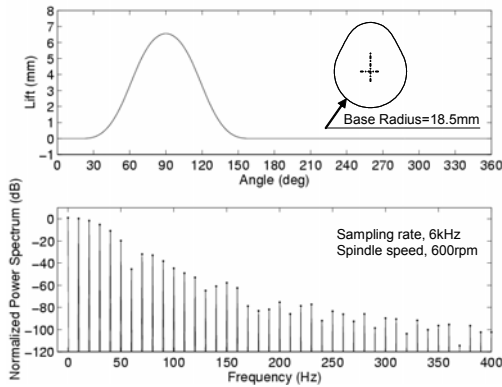


Figure 5 Profile at $x = 0$ mm

traversing this cam profile at a spindle speed of 600 rpm and a feed rate of 0.2 mm/sec, and 600 samples per spindle revolution, which corresponds to digital control sampling rate of 6 kHz.

Figure 6 shows the cross sectional view of the electrohydraulic actuator developed for the non-circular turning application. The actuator has a double acting and equal area piston and tapered hydrostatic bearings to support side loads applied to the actuator. The actuator is driven by a flapper nozzle type servovalve. Inside the hollow piston is a piezoelectric actuator used for dual-stage actuation [11]. Piezoelectric actuation will not be discussed in this paper. The actuator has an analog proportional feedback loop with an internal LVDT sensor. The actuator motion is measured by a laser encoder having a 0.63 μm resolution.

The servo valve and hydraulic actuator dynamics are slightly nonlinear due to flow-pressure drop relation through orifices. However, linear model $G_o(s)$ and its uncertainty bound $W_r(s)$ are required for the controller design. The effect of nonlinearity for different flow rates may be considered as perturbations

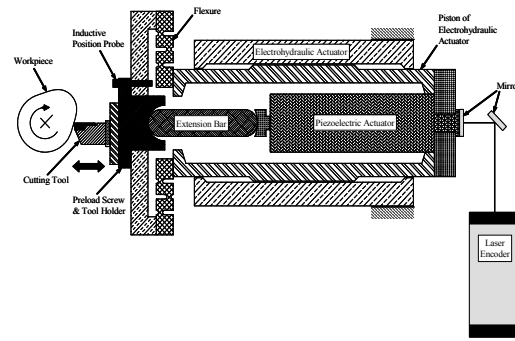


Figure 6 Electrohydraulic Actuator

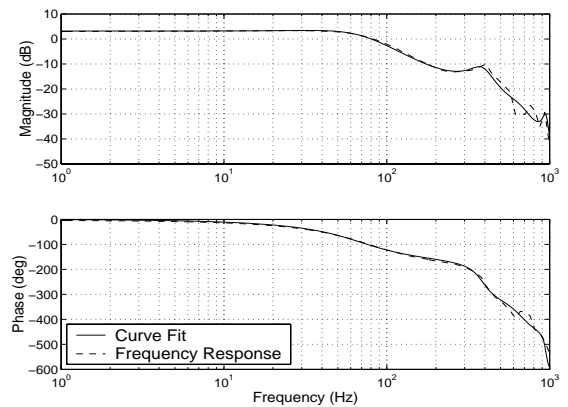


Figure 7 Frequency Response of the Hydraulic Servo

to a nominal linear model. In [17] an effective method to determine $G_o(s)$ and $W_r(s)$ was proposed. A suitable range of input magnitudes, which cause various flow rates, were applied to the system to obtain outputs and corresponding frequency responses. These experimental frequency responses are then used to determine a nominal frequency response. A least squares fit of this nominal frequency response to a transfer function model renders $G_o(s)$, and the maximum residual errors with respect to all the frequency response data render $W_r(s)$.

According to the linearization of the servo valve and actuator's nonlinear dynamics, the nominal transfer function $G_o(s)$ has one unstable zero and eight stable poles [21]. The unstable zero comes from the servovalve, where a mechanical feedback spring connects the torque motor armature and the valve spool. The experimental averaged frequency response and its nominal model shown in Figure 7 have very close agreement by confining the model to this structure. This accurate dynamic model is critical to achieving high performance in the subsequent model based control system design.

The discrete nominal model $G_o(z)$ is computed from

the continuous-time model using a zero-order-hold transformation. The magnitude Bode plots of $G_o(z)$, $M(z)$, $q(z, z^{-1})$, $1/W_p(z)$, $1/W_d(z)$, and $W_r(z)$ used in this design example are shown in Figure 8. N was 600 and L was chosen to be 10. The reference model M is selected as the following zero phase low-pass filter form:

$$M(z) = (0.25z + 0.5 + 0.25z^{-1})^n \quad (16)$$

Its bandwidth reduces as n increases. The value n was 2 in the design and the same zero filter was used for the filter $q(z, z^{-1})$.

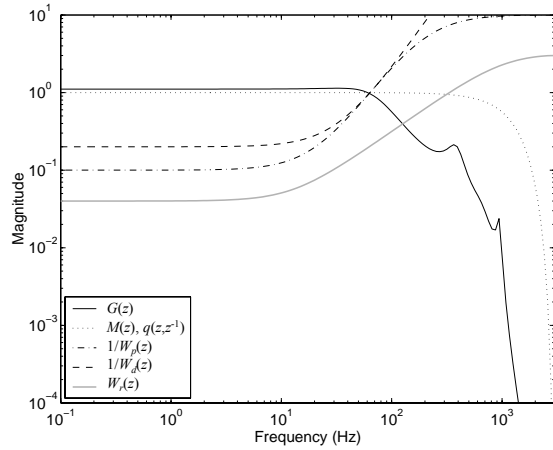


Figure 8 Weighting filters

Several sets of controllers based on μ -synthesis are designed with different preview length (F values). The error transfer functions e/r are compared for $F = 2, 4, 6, 8, 10$ in Figure 9. We can see deep notches whose ends are marked at the fundamental frequency and its harmonics. The notches are a distinctive characteristic of repetitive control providing high gain at these frequencies. It clearly shows that tracking error reduces as the preview length F increases. While increasing F theoretically and intuitively continues to reduce the tracking error, unmodeled dynamics and noise in the real system prevents reduction beyond a certain F value. In the experiment presented next $F=8$. Notice that all the tracking error transfer functions are below the upper bound $1/|W_p(e^{j\omega T})|$. Also, the disturbance rejection transfer functions d/e are all bounded by $1/|W_d(e^{j\omega T})|$ although the corresponding plots are not presented here. A two parameter robust repetitive control (TPRRC) using the above structure with the same design parameters described above but without the feedforward controller K_3 was also designed for comparison with the present controller. Figure 10 shows the resulting

tracking error transfer function of TPRRC.

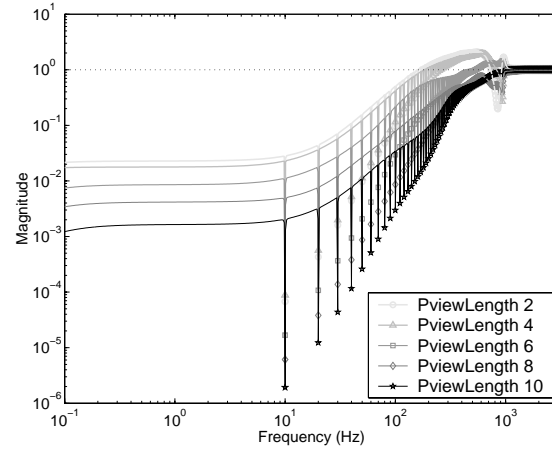


Figure 9 Transfer function of error/reference

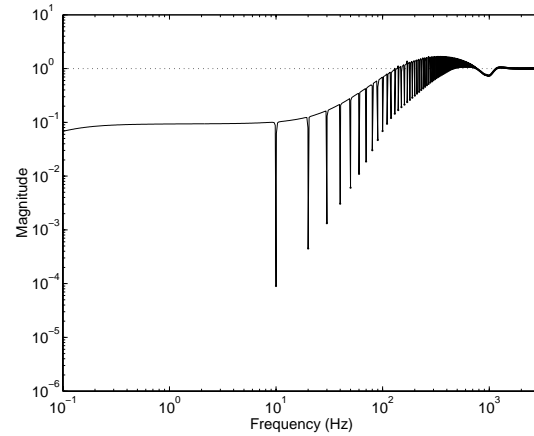


Figure 10 TPRRC error/reference transfer function without feedforward control

CONTROL IMPLEMENTATION AND EXPERIMENTAL RESULTS

The controller with the three control actions designed by the μ -synthesis method with a preview length of eight was initially in a 65th order state space form. For real-time implementation, controller order reduction was performed for each of the three input channels independently. The controller order was reduced to 9th, 8th, and 13th for K_1 , K_2 , and K_3 , respectively. The μ values from the reduced order controller were almost the same as those from the full order controller.

All the designed real-time controllers were implemented by a 32 bits floating point digital signal processor (TMS320C32). Finite word length (FWL) truncation error is another important factor in the fast

sampling rate digital controller implementation. The 32 bits floating point DSP provides single precision floating point number representation, which has a finite precision of approximately 7 significant decimal digits and a finite range of 10^{-38} to 10^{+38} . The original high order controllers not only consume much computational time but also are vulnerable to FWL errors. Controller order reduction can be employed to overcome this situation. The output from $K_3(z)$ may be calculated off-line because it does not use feedback signal. The controller order reduction and numerical truncation effects on $K_3(z)$ was checked by comparing the off-line 64 bit double precision computation for the initial 65th order controller with the on-line single precision computation of the reduced order controller. The experimental tracking performance for these two cases was almost the same and justified the controller reduction approach. Similarly, a 45th order controller from TPRRC was reduced to a 9th and 8th order for K_1 and K_2 , respectively. The details of the model reduction procedure adopted here can be found in [11].

The reference signal was generated from the two-dimensional cam-shape profile in Figure 4 with a spindle speed of 600 rpm and feed rate of 0.2 mm per spindle revolution. The experimental results of the control system are shown in Figure 11 in terms of RMS errors calculated per spindle revolution (600 samples). A few leading seconds were given to the actuator system until it reached its steady-state at $x = 0$. Due to the hardware limitations, the whole two-dimensional reference could not be imported into the C32 DSP. The cross sections of Figure 4 were specified at every 0.6 mm and linear interpolation was used to generate the real-time reference for the controller. The effect of the linear interpolation appeared as small ripples in the RMS error curve distinctively in the range of $x = 20$ to 36 mm. where both phase and magnitude of the cam profile varies.

Both controllers generated very small tracking error, where their RMS errors are less than 20 μm for the entire cam profile, which has over 6 mm lift. The integrated controller with all three control actions has consistently superior performance than the similarly designed TPRRC, which does not have feedforward action. The reference is near periodic at $x > 20$ mm and as such the previewed feedforward control action is very effective in reducing the tracking error as it is compared with TPRRC. Figure 12 shows the tracking errors at $x = 10, 25, 50$ mm of the two control design methods. The abscissa of each plot represents time in seconds. Note that at $x = 10$ mm the reference is purely periodic, at $x = 25$ mm the magnitude and phase change, and at $x = 50$ mm only the phase changes. As shown in the figure, the method with all three control actions has peak-to-peak errors well below $\pm 20 \mu\text{m}$.

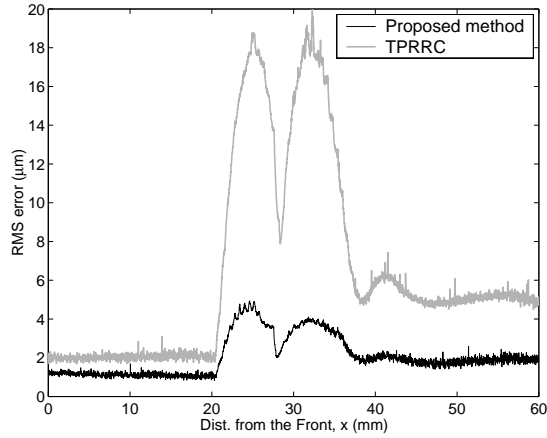


FIGURE 11 Tracking error (RMS value for every rotation) of the controller and the TPRRC

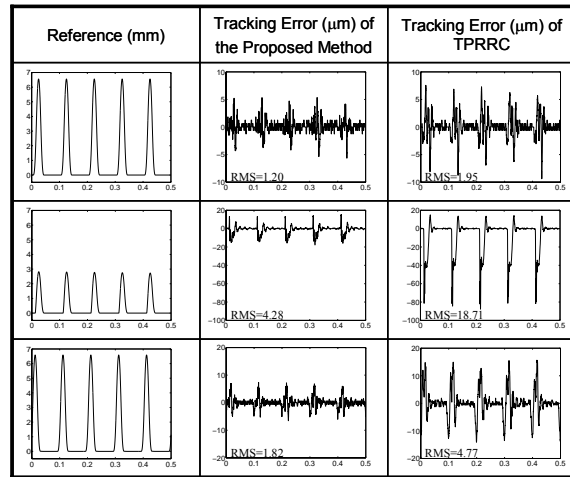


FIGURE 12 Tracking error of the controller and TPRRC at $x = 10$ (top row), 25 (middle row), and 50 (bottom row) mm

CONCLUSIONS

The control design problem for feedback, repetitive, and previewed feedforward control actions has been formulated in the LFT form and solved by μ -synthesis. In this way, the desired upper bounds of disturbance rejection and tracking error transfer functions, and the repetitive controller internal model, are explicitly included in the design process. Method to obtain the system dynamics and the uncertainty bound for electrohydraulic systems is also presented to facilitate μ -synthesis. Controller order reduction is essential for the real-time implementation in order to reduce computational time and the effect of finite word length

truncation error. Experimental results on an electrohydraulic actuator have demonstrated the effectiveness of the design method and implementation technique.

There are situations where the nonlinearity in the system is too significant to be treated as uncertainty. In this case, the nonlinearity may be modeled and compensated for by nonlinear feedback approach. One such case occurs in dynamic material testing of nonlinear materials. In [23] a back stepping nonlinear feedback with repetitive control was developed and successfully implemented on an electrohydraulic actuator loaded with a nonlinear test material to precisely generate periodic motions. Another situation is that the system dynamics may change slightly due to hydraulic fluid temperature and trapped air content variations. Although the robust feedback control is insensitive to such changes, the feedforward control is. Adaptive control [2, 6, 24] has been successfully used on electrohydraulic systems to maintain precise dynamic tracking performance under such changes.

REFERENCES

1. B. A. Francis and W. M. Wonham, "The Internal Model Principle for Linear Multivariable Regulators," *Applied Mathematics and Optimization*, Vol. 2, pp. 170-194, 1975.
2. T.-C. Tsao, and M. Tomizuka, "Adaptive and Repetitive Digital Control Algorithms for Noncircular Machining," *Proc. American Control Conference*, Atlanta, 115-120, 1988.
3. M. Tomizuka and T.-C. Tsao and K.-K. Chew, "Analysis and Synthesis of Discrete-Time Repetitive Controllers," *ASME Journal of Dynamic Systems, Measurement, and Control*, Vol. 111, pp. 353-358, 1989.
4. D. Alter and T.-C. Tsao, "Two-Dimensional Exact Model Matching with Application to Repetitive Control," *ASME Journal of Dynamic Systems, Measurement, and Control*, Vol. 116, pp. 2-9, 1994.
5. F.-R. Shaw and K. Srinivasan, "Discrete-Time Repetitive Control System Design Using the Regeneration Spectrum," *ASME Journal of Dynamic Systems, Measurement, and Control*, Vol. 115, pp. 228-237, 1993.
6. T.-C. Tsao and M. Tomizuka, "Robust Adaptive and Repetitive Digital Tracking Control and Application to a Hydraulic Servo for Noncircular Machining," *ASME Journal of Dynamic Systems, Measurement, and Control*, Vol. 116, pp. 24-32, 1994.
7. Byung-Sub Kim and Tsu-Chin Tsao, "A Performance Enhancement Scheme for Robust Repetitive Control System," *ASME Journal of Dynamic Systems, Measurement, and Control*, Volume 126, pp. 224-229, 2004.
8. J. A. Tenney and M. Tomizuka, "Effects of Non-Periodic Disturbances on Repetitive Control Systems," *IFAC, 13th Triennial World Congress*, San Francisco, CA, pp. 228-237, 1996.
9. L. Guo, "Reducing the Manufacturing Costs Associated with Hard Disk Drives - A New Disturbance Rejection Control Scheme," *IEEE/ASME Transactions on Mechatronics*, Vol. 2, No. 2, pp. 77-85, 1997.
10. Jianwu Li and Tsu-Chin Tsao, "Robust Performance Repetitive Control Systems," *ASME Journal of Dynamic Systems, Measurement, and Control*, Vol. 123, pp. 330-337, 2001.
11. Byung-Sub Kim, Jianwu Li and Tsu-Chin Tsao, "Two-Parameter Robust Repetitive Control With Application to a Novel Dual-Stage Actuator for Noncircular Machining," *IEEE/ASME Trans. on Mechatronics*, Vol. 9, No. 4, 644-652, 2004.
12. D. C. McFarlane and K. Glover, "A Loop Shaping Design Procedure Using H_∞ Synthesis," *IEEE Transactions on Automatic Control*, Vol. 37, No. 6, pp. 759-769, 1992.
13. D. Hoyle and R. A. Hyde and D. J. N. Limebeer, "An H_∞ Approach to Two Degree of Freedom Design," *Proceedings of the 30th IEEE Conference on Decision and Control*, Brighton, UK, pp. 1581-1585, 1991.
14. D. J. N. Limebeer and E. M. Kasenally and J. D. Perkins, "On the Design of Robust Two Degree of Freedom Controllers," *Automatica*, Vol. 29, No. 1, pp. 157-168, 1993.
15. E. Prempain and B. Bergeon, "A Multivariable Two-Degree-Of-Freedom Control Methodology," *Automatica*, Vol. 34, No. 12, pp. 1601-1606, 1998.
16. Uri Shaked and Carlos E. de Souza "Continuous-Time Tracking Problems in an H_∞ Setting: A Game Theory Approach," *IEEE Transactions on Automatic Control*, Vol. 40, No. 5, pp. 841-852, 1995.
17. Dean H. Kim and Tsu-Chin Tsao, "Robust Performance Control of Electrohydraulic Actuators for Electronic Cam Motion Generation," *IEEE Transactions on Control Systems Technology*, Vol. 8, No. 2, pp. 1-8, 2000.
18. M. Tomizuka, "Zero Phase Error Tracking Algorithm for Digital Control," *ASME Journal of Dynamic Systems, Measurement, and Control*, Vol. 109, pp. 65-68, 1987.
19. B.S. Kim, B. S., and Tsu-Chin, Tsao, "An Integrated Feedforward Robust Repetitive Control Design for Tracking Near Periodic Time Varying Signals," *Proceedings of the Japan USA Symposium on Flexible Automation*, 875-882, Hiroshima, Japan, 2002.
20. Tsu-Chin Tsao, "Optimal Feed-Forward Digital Tracking Controller Design," *ASME Journal of*

- Dynamic Systems, Measurement, and Control*, Vol. 116, pp. 583-592, 1994.
21. K. Zhou and J. C. Doyle and K. Glover, *Robust and Optimal Control*, Prentice-Hall, Upper Saddle River, New Jersey, 1996.
 22. Dean H. Kim and Tsu-Chin Tsao , "A Linearized Electrohydraulic Servovalve Model for Valve Dynamics Sensitivity Analysis and Control System Design," *ASME Journal of Dynamic Systems, Measurement, and Control*, Vol. 122, 179-187, 2000.
 23. S. J. Lee, and Tsu-Chin Tsao, 2004, "Repetitive Learning of Backstepping Controlled Nonlinear Electrohydraulic Material Testing System," *IFAC Journal of Control Engineering Practice*, Vol. 12, Issue 11, 1393-1408, November 2004.
 24. Z. Sun, and Tsu-Chin Tsao, "Adaptive Control with Asymptotic Tracking Performance And Its Application to an Electrohydraulic Servo System," *ASME Journal of Dynamic Systems, Measurement, and Control*, Vol. 122, 188-195, 2000.

Pneumatic Soft Actuator for Human Assist Technology

Toshiro NORITSUGU*

* Graduate School of Natural Science and Technology
Okayama University
3-1-1 Tsushimanaka, Okayama, 700-8530 Japan
(E-mail: toshiro@sys.okayama-u.ac.jp)

ABSTRACT

In the coming advanced age society, an innovative technology to assist the activities of daily living of elderly and disabled people and the heavy work in nursing is desired. To develop such a technology, an actuator safe and friendly for human is required. It should be small, lightweight and has to provide a proper softness. We call such an actuator *soft actuator*. A pneumatic rubber artificial muscle is one of typical soft actuators, which is useful for the human assist technology. We have developed some types of pneumatic rubber artificial muscles and applied them to human friendly soft mechanisms and wearable power assist devices. Since these mechanism and devices directly act on the human body, the human friendliness is essentially important. A wearable power assist device is equipped to the human body to assist the muscular force, which supports activities of daily living, rehabilitation, heavy working, training and so on. In this paper, some types of rubber muscles developed and manufactured in our laboratory are introduced. A soft robot hand for wiping the human body and a parallel manipulator for the wrist rehabilitation are described as soft mechanisms. Further, a wearable power assist glove and a power assist splint for upper arm are shown. Some evaluations clarify the effectiveness of pneumatic soft actuator for an innovative human assist technology.

KEY WORDS

Pneumatics, Rubber artificial muscle, Soft mechanism, Wearable power assist, Human friendly robot

INTRODUCTION

In the coming advanced age and few-birthrate society, there may not be enough working people in various fields such as medical welfare, agriculture and so on. Especially, the increase of elderly and the lack of caregiver will become a serious problem. To overcome the problem it is expected to introduce a machine or

robot to assist the elderly, disabled people, caregiver, nurse, hard worker and so on. Such a human assist technology has become of major interest recently. The researchers in robotics and mechatronics have become interested in the relation between human and machine. Some types of human friendly robots have been exhibited in EXPO 2005 AICHI JAPAN. Since these kinds of machines or robots have to work near the

human or directly act on the human body, both safety and friendliness for human are essentially important.

To satisfy these requirements, an actuator safe and friendly for human is desired. It should be small, lightweight and has to provide a proper softness. As such an actuator we have remarked the availability of pneumatic soft actuator. A pneumatic rubber artificial muscle may be very useful as one of soft actuators. We have developed and manufactured some types of pneumatic rubber artificial muscles. Using these actuators, a pneumatic soft mechanism and a wearable power assist devices have been developed. As a pneumatic soft mechanism, a soft robot hand and a wrist rehabilitation device have been developed. A wearable power assist glove and a power assist splint for upper arm are developed.

This paper firstly describes the structure and the fundamental characteristics of some developed pneumatic rubber artificial muscles. Next, the structure and the performance of soft mechanisms and wearable power assist devices are shown, of which the availability are evaluated through some experiments.

PNEUMATIC SOFT ACTUATOR

A conventional pneumatic actuator such as a pneumatic cylinder is widely used for not only simple positioning, but also a force control, for example, clamping and so on because of its inherent compliance from the air compressibility. Since the body of conventional actuator is usually made of a rigid material, there is no flexibility in directions except movable axis of the actuator.

On the contrary, we call an actuator *soft actuator* of which body is soft as well as the motion property. It has passive compliance in the all directions. A pneumatic soft actuator is generally constructed with tube or balloon made of elastic material as rubber, driven with the pressure control. The fundamental operation depends on both expansion and contraction of elastic tube or balloon with the inner pressure control.

Various motions can be obtained by changing the stiffness in the specified directions with a fiber and so on. Figure 1 shows a structure of fiber reinforcement type actuator. In Figure 1(a), a rubber tube is reinforced around the circumstance with fibers. When compressed air is supplied into the rubber tube, because the expansion in the radius direction is restricted with fibers, only the extension in the axial direction is obtained from the inner pressure increase. Figure 1(b) shows the fiber reinforcement of radius direction and axial direction with the angle α . The pressure increase makes the tube rotate around the axial center line. A McKibben type rubber artificial muscle is one of typical fiber reinforcement actuators.

Figure 2 shows an example of pneumatic soft actuator made of silicone rubber [1]. This actuator can realize the rotary operation around the intersection of two side

plates owing to the fiber reinforcement in the radial and height directions and the high stiffness produced by thickness of side plates.

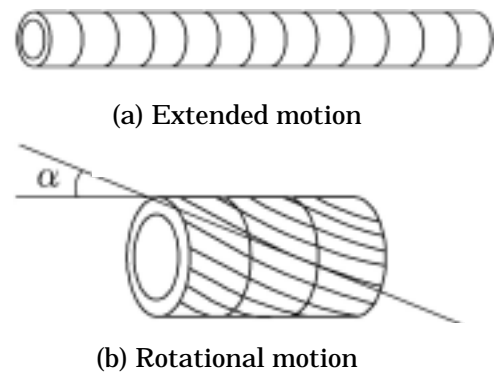


Figure 1 Fiber reinforcement



Figure 2 Rotary type pneumatic soft actuator

PNEUMATIC RUBBER ARTIFICIAL MUSCLE

A McKibben type pneumatic rubber artificial muscle is well known. Now, a few companies manufacture commercially available one [2]. We have developed some new types of pneumatic rubber muscle in addition to the McKibben type [3].

Contracted linear type

Figure 3 shows a conventional McKibben type rubber muscle, which is manufactured by covering the surrounding of a rubber tube with fiber net. It may be called a contracted linear type. By pressurizing the rubber tube, the muscle generates the axial contraction force. We can manufacture the rubber muscle with an arbitrary size using commercially available rubber tube and polyester fiber net. Figure 4 shows the fundamental characteristics of the manufactured rubber muscle comprising a rubber tube with an outer diameter of 11.6mm, an inner one of 8.0mm, and a length of 793mm when not pressurized. The contraction rate is saturated to about 25%. The saturated value depends on the cross angle of fibers. When pressurizing the rubber tube to 600kPa, the contraction force reaches 340N. The performance is equivalent to the commercially products.

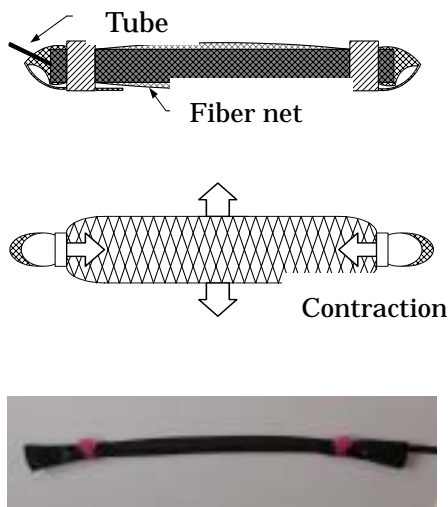


Figure 3 McKibben type rubber muscle

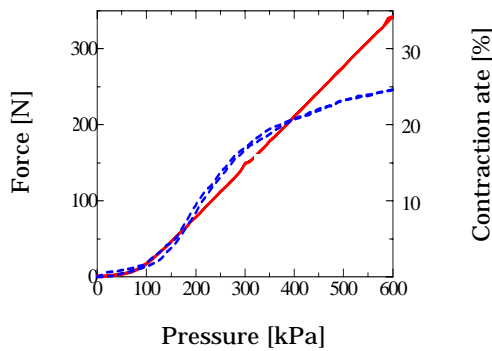


Figure 4 Fundamental characteristics

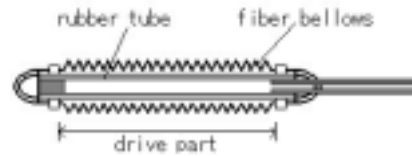
Extended linear type

Figure 5 shows the structure of extended linear type rubber muscle. It consists of a rubber tube and a polyester fiber bellows. When the compressed air is supplied into the rubber tube, the muscle extends to the axial direction as shown in Figure 5(c). By decreasing the inner pressure, the muscle is made restitution as shown in Figure 5(b). The manufactured muscle is composed of a rubber tube with outer and inner diameter 8.4, 6[mm], and of a polyester bellows with outer and inner diameter 16, 13[mm]. The initial length of drive part is 40[mm].

Figure 6 shows the fundamental characteristics. Figure 6(a) shows the relation between the inner pressure and the extended length. The maximum extended length is about 76[mm] at 500[kPa]. Figure 6(b) shows the restitution force of the muscle. The restitution force is measured when the supplied inner pressure is 0[kPa].

A contracted type (McKibben type) rubber muscle with the same size as the extended type muscle shown in Figure 5 is manufactured to compare both performances. The maximum restitution force of the extended type is

smaller than the maximum contraction force of contracted type (McKibben type), on the contrary, an extension rate of extended type is larger than the contraction rate of the McKibben type. The extended type is better to achieve the large movable range than McKibben type.



(a) Structure

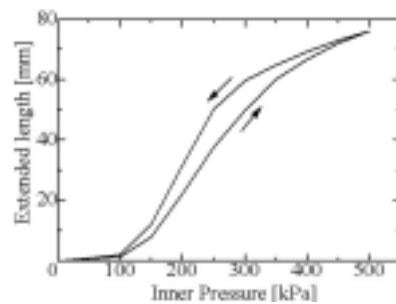


(b) Initial state (0kPa)

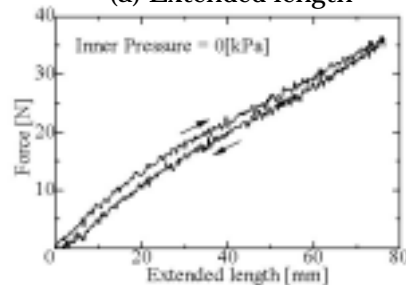


(c) Pressurized state (500kPa)

Figure 5 Extended linear type muscle



(a) Extended length



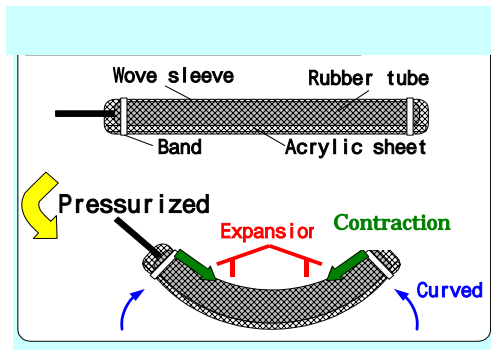
(b) Restitution force

Figure 6 Fundamental characteristics

Contracted curved type

Figure 7 shows a contracted curved type pneumatic rubber muscle, which is constructed by reinforcing one side of a McKibben type rubber muscle with an elastic acrylic sheet. When the rubber tube is pressurized, only the top side is contracted by the effect of reinforcement of the bottom side. As a result, the upward curved motion can be realized as shown in Figure 7(b). By increasing the stiffness of the elastic sheet, the recovery force increases but the generated curved force decreases.

Figure 8 shows a fundamental characteristic of manufactured rubber muscle composed of parallel two rubber tubes with outer and inner diameters of 11.6[mm] and 8.0[mm], respectively. When the muscle is pressurized 500[kPa], the curved angle reaches 126 [degree], the maximum curved force of 78[N] can be generated.



(a) Operational principle



(b) Curved configuration

Figure 7 Contracted curved type muscle

Extended curved type

Figure 9 shows an extended curved type rubber muscle consisting of a rubber tube with outer and inner diameters of 8.4, 6[mm], and a polyester bellows with the outer and inner diameters of 16, 13[mm]. To inhibit the extension to the axial direction of bottom side, the polyester fiber bellows is reinforced with a fiber tape. Three muscles with the length of 140, 120 and 80[mm] are manufactured. By the reinforcement, when

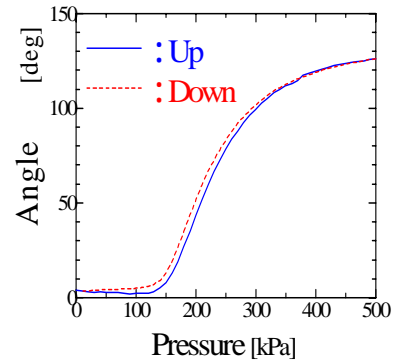
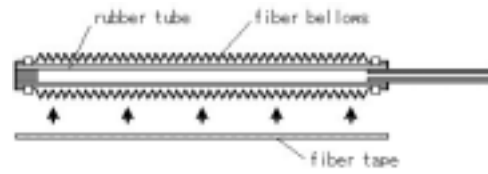


Figure 8 Fundamental characteristics



(a) Structure



(b) Configuration



(c) Curved motion

Figure 9 Extended curved type muscle

compressed pressure air is supplied into the rubber muscle, the rubber muscle can curve to the reinforced side as shown in Figure 9(c). Figure 10 shows the measured fundamental characteristics of three rubber muscles. The generated force is almost independent of the length of muscle. The generated force for the supply pressure of 500[kPa] is about 23[N], and the relation between the force and the pressure is almost linear above the inner pressure of 150[kPa].

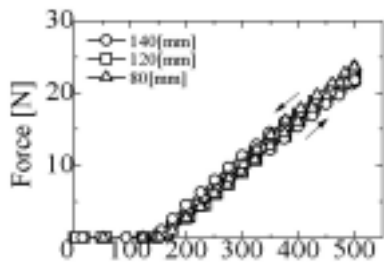


Figure 10 Fundamental characteristics

HUMAN FRIENDLY SOFT MECHANISM

The development of machines or robots to assist a human activity in nursing, welfare and daily living has recently become an important subject. Such machines or robots are required safety, friendliness for human and soft motion similar to human rather than conventional high speed and high accuracy performance. In order to realize such a human friendliness, it is effective to use an inherent soft mechanism. We call it *human friendly soft mechanism* of which some examples are described.

Soft robot hand

Figure 11 shows a soft hand consisting of soft fingers and the contracted linear type rubber muscles as shown in Figure 3 [4]. The mass of hand is 900[g]. The length is 185[mm]. The soft finger has three joints as shown in Figure 12. A rotary-type pneumatic soft actuator similar to Figure 1 is put at intervals of 25[mm]. The disposition of linear type muscles is decided by referring the human muscles. This hand can operate almost same as a human hand. Pressurizing the rotary-type actuator, the finger bends. The linear type rubber muscles drive the wrist of hand.

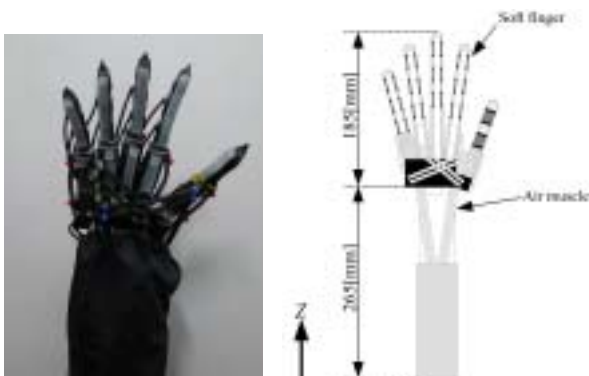


Figure 11 Soft robot hand

Because the pneumatic soft actuator expands or contracts by itself being different from a conventional hard actuator, mechanical components such as bearing and joint is not required. By mounting a pneumatic soft actuator directly at joint, the mechanism can become

simple and small. Also, since the hand is driven with only pneumatic power, it can operate under water without waterproofing.



(a) Initial state (b) Pressurized state

Figure 12 Soft finger

Figure 13 shows an application of the hand to a wipe motion for human arm. The soft hand is moved forth and back on the human arm in the direction of the human arm length with a speed of 10[mm/s]. A soft tactile sensor shown in Figure 14 is attached to the end of each finger to detect the contact force. The sensor is made of a cylindrical silicone rubber with an outer diameter of 16[mm], an inner diameter of 15[mm]. When the external force is applied to the upper plate, the inner pressure of sensor is increased according to the compression of cylindrical silicone rubber chamber. Tactile information is detected by measuring the inner pressure change with a pressure sensor. In the wipe motion of Figure 13, the contact force is feedback controlled with this sensor for the desired force of 1.5[N]. The accurate force control can be achieved.

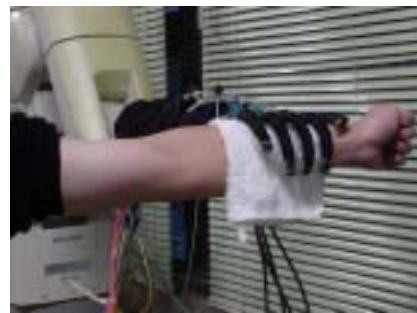


Figure 13 Wipe motion with soft hand

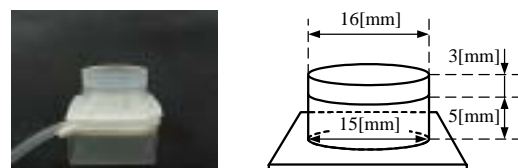
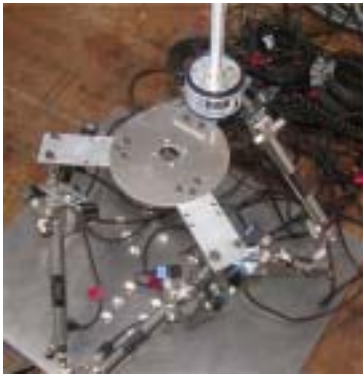


Figure 14 Soft tactile sensor

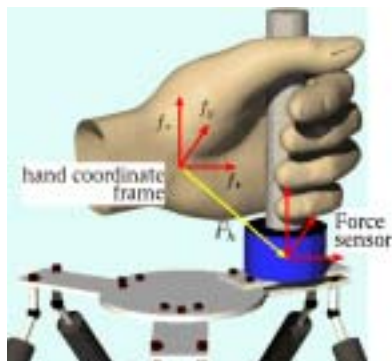
Parallel manipulator

Since joints of human have multiple degrees of freedom, a rehabilitation machine for these joints is desired to provide multiple degrees of freedom. Further, it must be built with a human friendly soft mechanism. To satisfy both requirements, we have proposed to use a pneumatic parallel manipulator as a rehabilitation machine [5].

Figure 15(a) shows the pneumatic parallel manipulator for a wrist rehabilitation exercise. Six pneumatic cylinders are used as driving actuators to construct Stewart type platform. Figure 15(b) shows a view of operation. A patient put his/her forearm above the upper platform along the x axis of manipulator and trains rehabilitation exercises by holding a bar attached to a 6-axes force/moment sensor equipped on the upper platform. A low friction type pneumatic cylinder with inner diameter of 9.3[mm], stroke of 100[mm] are used. The pressure in each cylinder and the displacement of piston are used for a feedback control. The controller generates control signals to drive control valves.



(a) Pneumatic parallel manipulator



(b) Wrist rehabilitation

Figure 15 Pneumatic rehabilitation device

The controller is constituted with an impedance control scheme using a disturbance observer. The impedance control is executed based on the measured force/moment applied by the patient. This study has shown that some typical exercise of *isometric*, *isotonic*, *passive isokinetic* and *active isokinetic* can be achieved by only adjusting the desired impedance parameters of stiffness and damping. A practical examination is next research subject to evaluate the availability of this rehabilitation machine.

WEARABLE POWER ASSIST DEVICE

It must be an earnest hope for the old aged or disable people to perform daily living activities as many as possible by themselves without the support of others. Further, their positive participant to the society is desired. It is also an important subject to relieve the physical burden of the care person. We have developed a wearable power assist device to cope with the above situation. A human wears the device. It supports various motions of the human by assisting the muscle power. This device has to be a human friendly mechanism, which can be constructed with a pneumatic soft actuator. In Japan, some wearable power assist devices driven with pneumatic actuators have been developed. A power assisting suit by Yamamoto et al. is a pioneer study, driven with direct drive pneumatic actuators combining micro air pumps and pressure cuffs [6]. Kobayashi et al. have developed a muscle suit assisting a shoulder motion driven with McKibben type rubber muscles [7]. Tsukakoshi et al. have developed a new type pneumatic soft actuator named *wound tube actuator* and proposed a power assist device driven with this actuator for the limb motions [8].

We also have developed some types of wearable power assist devices driven with a different type of pneumatic soft actuator mentioned above.

Fundamental concept

Our fundamental concept in the development of a wearable power assist device is to use the most suitable type actuator for each part of human in order to make the structure as simple as possible.

Figure 16 shows a power assist device for elbow driven with a contracted curved type pneumatic rubber muscle shown in Figure 7. The rubber muscle is attached to the elbow through a supporter. The assist force can be controlled by adjusting the inner pressure of rubber muscle. Figure 17 shows a bending angles and an electromyogram (ENG) at biceps muscle of upper arm when the human bends an elbow holding a load mass of 2[kg] at the hand. The figure illustrates the effect of power assist. When the assist device works, the variation of electromyogram (CH2) is smaller than the case without power assist. The human can bend the elbow without own muscle power due to the power assist. The effect of power assist device is apparent.



Figure 16 Power assist for elbow

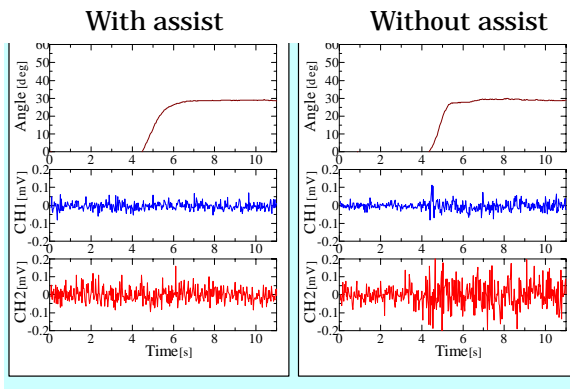


Figure 17 Effect of power assist

Figure 18 shows another example of a power assist device for shoulder part consisting of three McKibben type pneumatic rubber muscles. It assists a flexion of upper arm using two rubber muscles with length of 562[mm] and 793[mm] of which characteristics are shown in Figure 4. The adduction is assisted using the muscle with 408[mm] length.

The power assist devices shown in Figure 16 and 18 are plot types of our research aimed as simple, lightweight and human friendly as possible wearable power assist device. Two examples are still primitive but available as a simple and easy power assist device.

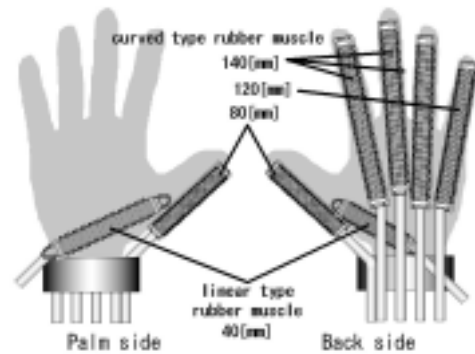


Figure 18 Power assist for shoulder

POWER ASSIST GLOVE

We have developed a power assist glove for supporting activities of daily living, rehabilitation and various heavy tasks [9].

Figure 19 shows the structure and the outlook of developed power assist glove. It consists of the extended curved type pneumatic rubber muscles put on the backside of fingers, and the extended linear type muscles put on a root of thumb. When the human hand grasps the cylindrical bar with diameter 60[mm], the contact force at the finger tip is about 14 ~20[N]. Figure 10 shows that the enough generated force can be obtained from the glove.



(a) Structure



(b) Manufactured assist glove

Figure 19 Power assist glove

Figure 20 shows the various finger works possible with the glove. The movable range of the proposed power assist glove is enough for the required various finger works in the daily living. A proposed wearable power assist glove can be easily manufactured by attaching the pneumatic rubber muscles to a usual glove. The manufactured power assist glove is available to support the finger works required in daily living. Rehabilitation and various training may be additional effective

applications of this glove.



(a) Tip pinch



(b) Side pinch



(c) Power grip



(d) Cylindrical grip



(e) Spherical grip



(f) Hook grip

Figure 20 Various finger works with glove

POWER ASSIST SPLINT FOR UPPER ARM

In the design of a wearable power assist device, a mechanical interface to transmit the generated force by actuator to the human body is important. Ideally the interface made of soft material such as supporter, band and glove shown in Figure 16, 18 and 19 are desired for the comfortable equipment. However, where the large assist force is required, the combination with a suitable orthosis is considerable.

Structure

Figure 21 shows the outlook and structure of the developed power assist splint, constructed with an orthosis made by forming a plastic used as a mechanical interface between actuators and human body. It assists the bending motions of wrist and elbow. Mechanical joints are equipped on both sides to restrict its movable range to the smaller than average maximum bending angles of Japanese male [10].

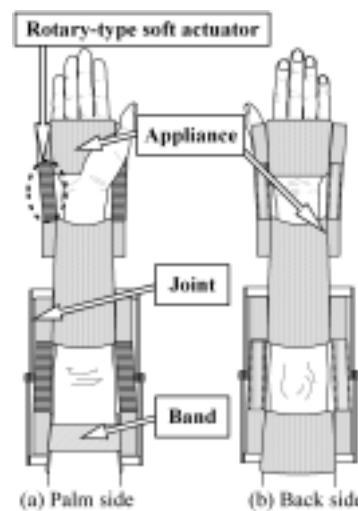
Actuator

A kind of extended curved type rubber muscle shown in Figure 9 is used as an actuator. A pair of the rubber muscles is attached to the wrist and elbow, respectively. Figure 22 shows the structure of rubber muscle manufactured for the elbow. It consists of a rubber tube and a polyester bellows. The outer and inner diameters are 20[mm] and 14[mm], the length is 290[mm]. The outer diameter of polyester bellows is 40[mm]. The bellows is reinforced with a fiber along the axial

direction as shown in the figure. Owing to the



(a) Outlook



(b) Structure

Figure 21 Power assist splint

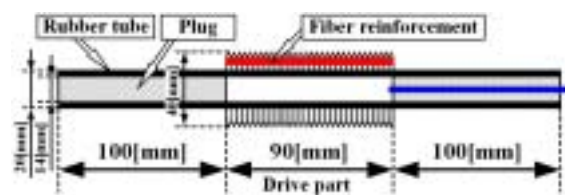


Figure 22 Structure of muscle for splint

reinforcement, when the compressed air is supplied into the actuator, only the other of reinforced side extends in the axial direction and produces a bending motion as shown in Figure 23.

Figure 24 shows the fundamental characteristics of actuator. The generated torque is measured for the constant inner pressure of 500[kPa]. It is confirmed that the generated torque is enough to keep the human forearm and palm having a load of about 4[kg]

horizontally.



(a) Initial state



(b) Pressurized state

Figure 23 Outlook of muscle

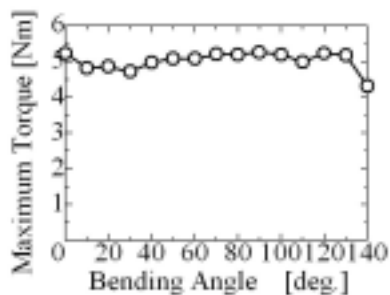


Figure 24 Generated torque of muscle

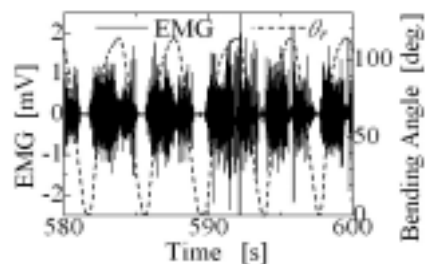
Effect of power assist

In order to verify the effect of power assist, a subject wearing the device bends his forearm repeatedly having a load of 3[kg] during 600[s]. The period of bending operation is 4[s]. Figure 25 shows the experimental results of bending angles and EMG. The difference of EMG owing to the existence of power assist confirms the effect of power assist. Further, when the power assist device doesn't work, the larger fatigue of muscle appears in the extension than the bending of forearm. When the device works, the fatigue of muscle is not recognized. The developed power assist splint is effective to assist the muscle power and to decrease the fatigue of muscle.

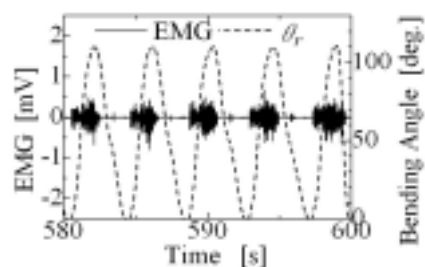
CONCLUSIONS

A human assist technology is essential in the highly aged society. A pneumatic power is effective to develop

the human assist technology due to its inherent



(a) Without power assist



(b) With power assist

Figure 25 Effect of power assist

flexibility and human friendliness. A pneumatic soft actuator is applicable to construct various human assist devices. A pneumatic rubber artificial muscle is the typical pneumatic soft actuator. In this paper, four types of rubber muscles developed and manufactured in our laboratory are introduced. These muscles are available to constitute a human friendly soft mechanism and a wearable power assist device. The power assist device with a simple structure can be designed by using the suitable type of rubber muscle according to the property of assisted part of human body.

We have continued to establish a human assist technology based on soft mechanism, wearable power assist device and so on. A pneumatic power can be effectively used in this field. The collaboration among related technologies is expected for the innovation of fluid power technology.

A part of the research shown in this paper has been supported by Grant-in Aid for Scientific Research, Scientific Research (B) 16360124 and Scientific Research in Priority Areas 16078210, Japan.

REFERENCES

1. <http://www.shadow.org.uk/index.shtml>
2. Noritsugu, T., Kubota, M. and Yoshimatsu, S., Development of Pneumatic Rotary Soft Actuator Made of Silicone Rubber, Journal of Robotics and

- Mechatronics, 2001, **13**-1, pp.17-22.
3. Noritsugu, T., Takaiwa, M. and Sasaki, D., Development of Pneumatic Rubber Artificial Muscle for Human Support Applications, Proceedings of the Ninth Scandinavian International Conference on Fluid Power, 2005.
 4. Sasaki, D., Noritsugu, T. and Takaiwa, M., Development of Pneumatic Soft Robot Hand for Human Friendly Robot, Journal of Robotics and Mechatronics, 2003, **15**-2, pp.164-171.
 5. Takaiwa, M. and Noritsugu, T., Development of Wrist Rehabilitation Equipment using Pneumatic Parallel Manipulator, Proceedings of the 2005 IEEE International Conference on Robotics and Automation, 2005, pp.2313-2318.
 6. Yamamoto, K., Ishii, M., Noborisaka, H. and Hyodo, K., Stand Alone Wearable Power Assisting Suit-Sensing and Control Systems, Proceedings of the 13th IEEE International Workshop on Robot and Human Interactive Communication, RO-MAN 2004.
 7. Kobayashi, H., Ishida, Y. and Suzuki, H., Realization of All Motion for the Upper Limb by a Muscle Suite, *ibid.*
 8. Tsukakoshi, H., Shirato, K., Ido, M. and Kitagawa, A., Tail-arm: a Wearable Unit to Stimulate Exercise, *ibid.*
 9. Noritsugu, T., Yamamoto, H., Sasaki, D. and Takaiwa, M., Wearable Power Assist Device for Human hand Grasping Using Pneumatic Artificial Rubber Muscle, Proceedings of SICE Annual Conference in Sapporo, 2004, pp.420-425.
 10. Sasaki, D., Noritsugu, T. and Takaiwa, M., Development of Pneumatic Power Assist Splint "ASSIST" Operated by Human Intention, Journal of Robotics and Mechatronics, 2005, **17**-5.

WHAT MAKES NEW IDEAS IN FLUID POWER SUCCEED?

Wolfgang BACKÉ

Institute for Fluid Power Drives and Controls (IFAS)
RWTH Aachen (Germany)
Steinbachstrasse 53, 52074 Aachen, Germany
(E-mail: wolfgang.backe@ifas.rwth-aachen.de)

INTRODUCTION

The field of fluid power components and systems is characterized by a continuous evolution, intended to improve functionality, to reduce constructional effort and thus costs. In many cases, these improvements are due to advances in related technologies, such as electrics, electronics, computer science, control technology, or material sciences.

During the decades in which fluid power has been used, completely new ideas and innovations have appeared every now and then that seemed capable of accomplishing certain tasks in a better way. Any innovative new design must not only fulfil a particular task, it must do it at a better price than extant technology, or else it must offer additional functionality in order to justify higher prices.

After mentioning some flops in the history of Fluid Power this paper shall chart the reception that some new ideas and development have received. Examples treated here are:

- Secondary control
- Free piston motor and hydrotransformer
- Valve actuation
- Noise reduction
- Bus technology
- Fuel cell

Of course there are some more important new developments in Fluid Power, for instance

Servopneumatics or Functional Fluids (ERF, EMF or ECF). But not all of them could be treated.

FLOPS IN THE HISTORY OF FLUID POWER

There are periods in the evolution of fluid power during which an effect will suggest itself for tackling particular tasks. Once other technical means allowing those tasks to be accomplished in a superior manner appear, the effect will soon be forgotten. One example to be mentioned is fluidics.

In the 1960s and early 1970s, Fluidics appeared, an approach realizing binary switching functions or steady control functions through the mere interaction of air jets, without any moving parts. [1] [2]

Figure 1 shows some effects utilized for this purpose: the Coanda-effect, the disturbance of a laminar jet, or the vortex-chamber effect. At that stage, whilst transistor technology still was in its infancy, one was of the opinion that the packing density of pneumatic logic elements could exceed that of transistor circuits. However, soon the trend towards miniaturizing electronic components started, which continues to the present day and which has led to incredibly high packing densities.

One of the main disadvantages of fluidics was the low signal propagation speed. Although considerable investments were made into this technology, hardly any remnants are to be found today. Another idea that didn't gain acceptance in practice was the "Alternating Flow Hydraulics" (AFH).

That was the attempt to make fluid power mirror the shift from direct-current to alternating-current energy transmission that took place in the electrics.

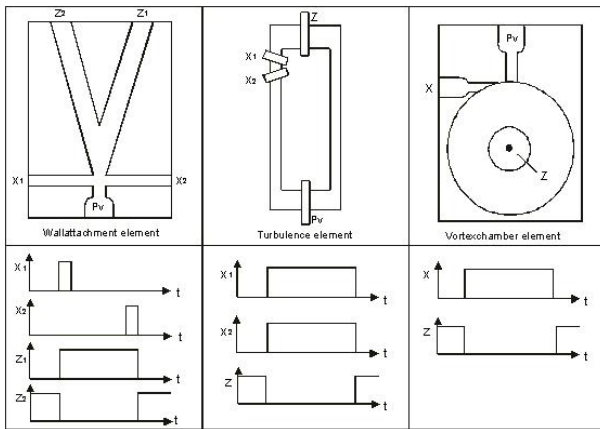


Figure 1: Fluidic elements

SECONDARY CONTROL

In the late 1970s and early 1980s, two institutions (Rexroth and IHP, now IFAS) independently developed the so-called secondary control. [6] [7] It occupied the hitherto-empty field (IV) in the methodology classification scheme for the control of fluid power energy (Fig. 2). It represents a displacement control with impressed pressure.

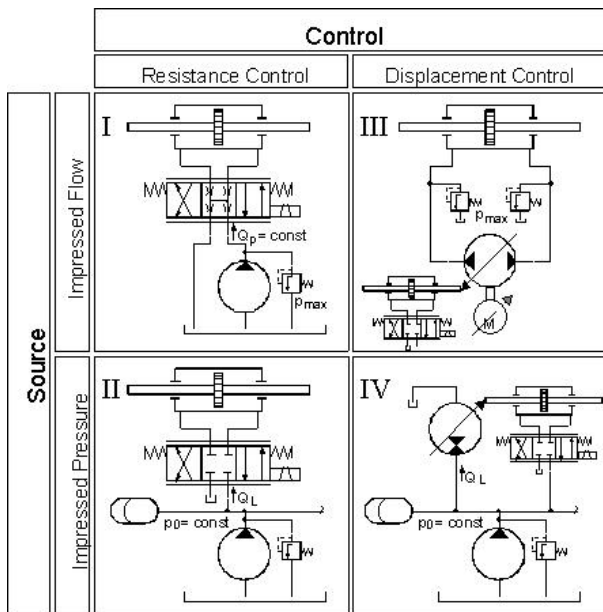


Figure 2: Methods of controlling hydraulic power

As Fig. 3 shows, an internal control loop is required for the various control tasks such as speed-, position- or torque-control, which ensures that the motor is stroked

back under decreasing load, to prevent it from picking up unlimited high speeds.

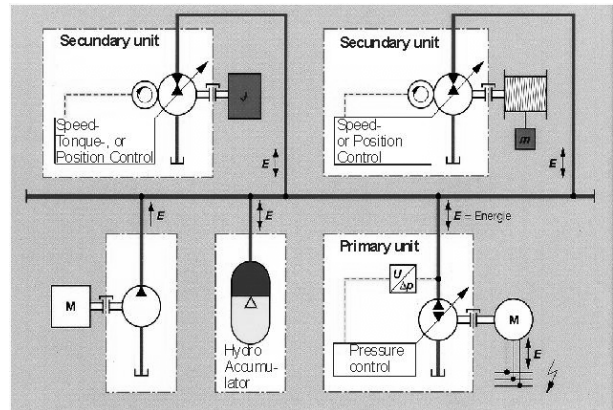
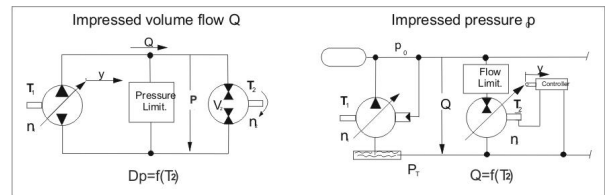


Figure 3: Secondary controlled displacement unit at a net of impressed pressure, (Source: Kordak, Rexroth)

Figure 4 lists the characteristics of displacement controls with variable pump and impressed volume flow and of displacement controls with impressed pressure:



- Single Drive
- Closed Loop
- $n_2 = Q / V_2$ fixed
- Fourquadrant Drive in closed Loop
- Dynamics determined by hydraulic and mechanic Time constants
- Overload Security by pressure Limitation
- Energy recuperation in Gyroaccumulator/ Electr. Net
- Multiple Drive
- Open Loop
- n_2 determined by control
- Fourquadrant Drive in open Loop
- Dynamics determined by mechanic Time constants
- Overload Security by Flow- or Speed-Limitation
- Energy recuperation in Hydroaccumulator

Figure 4: Characteristics of drives with displacement control

Based upon this comparison in fig. 4, one might assume that both systems are equally likely to be used. Yet the variable motor attached to the constant pressure net has a number of drawbacks limiting its applicability.

- It is not suitable for the direct control of cylinder drives, because a variable displacement motor is required (variable cylinder drives are still waiting for a brilliant inventor).
- For drives that frequently stand still or are charged only with low torques, more leakage oil occurs than would be the case with the hydrostatic transmission. In the latter, the pressure drops whenever it is idling, and little leakage occurs.
- Furthermore, an internal control of the displacement volume is required in every case.

This is not the case with pump control (impressed volume flow).

One typical application, in which the constructional effort can be considerably reduced, is the bucket-wheel excavator, which often runs with high loads over a long period.

An interesting new application is the Flap Power Control Unit of the Airbus A 380. This unit, schematically depicted in Fig. 5, actuates the plane's flaps within a closed position-control circuit by means of 2 variable motors and a planetary transmission, via shafts and gears. With a supply pressure of 5000 psi, the all-in weight of the unit is approx. 58 kg, including the planetary transmission and the safety brakes. Through the use of variable motors in secondary control (VDHM), the efficiency could be increased by approx. 30 % over the valve control of constant motors (FDHM).

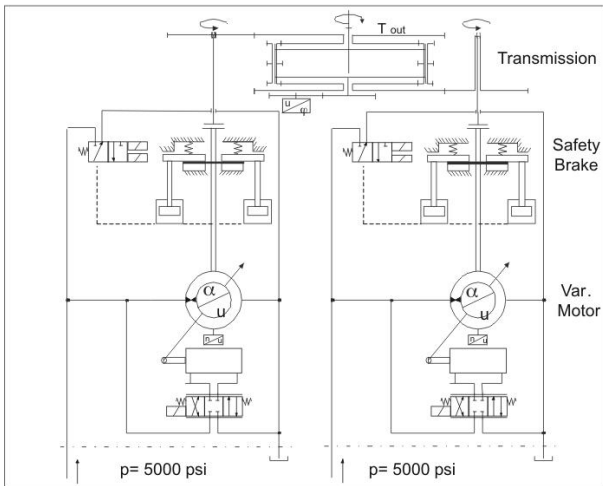


Figure 5: Flap power control unit, Airbus A 380, (Source: Liebherr)

FREE PISTON MOTOR AND HYDROTRANSFORMER

In mobile machinery, the diesel engine serves as the primary energy source, powering rotating pumps for the wheel drive and the working hydraulics. Early on, the idea was mooted to transform the energy of the combustion engine's piston into hydraulic energy by means of a linear motion, without any rotating parts. Such a free piston engine might be used to feed a constant pressure net required for the secondary control with variable motors. Several institutions are currently engaged upon developing different concepts for free piston motors, shown in Fig. 6. As the free piston motor only conducts a single displacement stroke per working stroke, the irregular volume flow that it delivers has to be smoothed by means of accumulators on the pressure- and suction side, as shown in Fig. 7 for the twin-piston

motor. That motor oscillates with the system's natural frequency. [8]

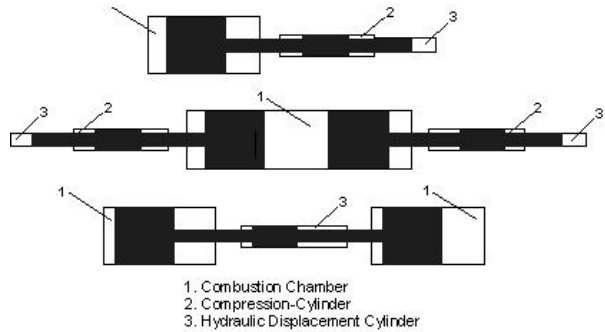


Figure 6: Concepts of free piston engines, (Source: Tikkanen, Vilenius)

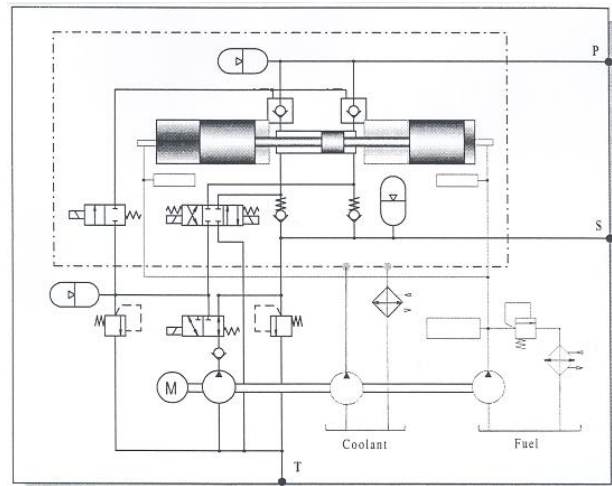


Figure 7: Schematic drawing of a dual hydraulic free piston engine unit, (Source: Seppo Tikkanen)

As already mentioned, it is impossible in secondary control to generate longitudinal motion via pistons and cylinders, because one requires a variable displacement unit. If energy for the actuation of cylinders is extracted from the constant pressure net through valves, high throttle losses occur within the valves.

Even during the development of the secondary control, the idea of a hydrotransformer enabling the extraction of a controlled oil flow from the pressure net without incurring large valve losses was pursued.

Such a hydrotransformer consists in two coupled displacement units, of which at least one is variable and speed-controlled. Figure 8 shows such a conventional hydrotransformer. The company INNAS [9] succeeded at integrating the functionality of a hydrotransformer into a single displacement unit. A prototype of that transformer is shown on the left-hand side in Figure 9.

The transformer is adjusted by turning the port plate, which in this case has three rather than two control kidneys.

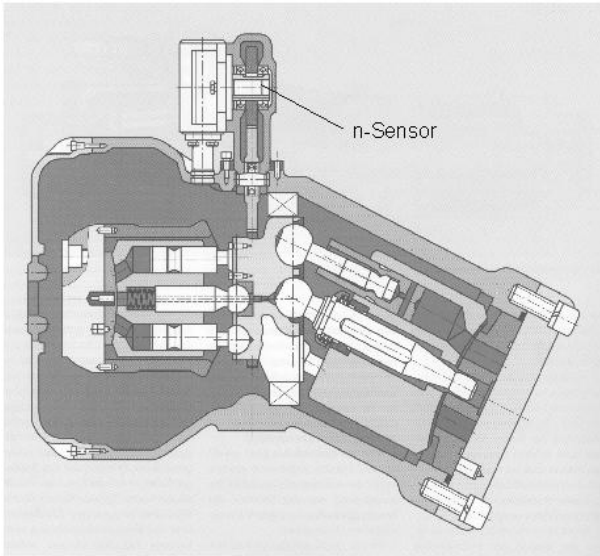


Figure 8: Hydraulic transformer with bentaxis displacement units (Source: Mannesmann-Rexroth)

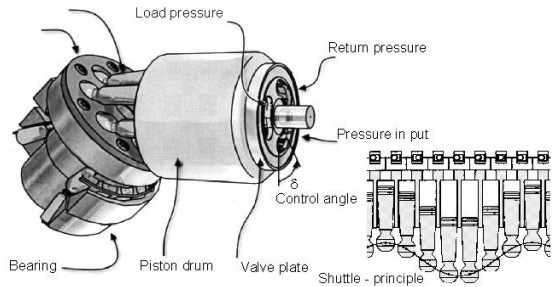


Figure 9: Prototype of a hydraulic transformer (Source: INNAS)

The key problem associated with these new transformers, i.e., the fact that the piston must be commutated during the stroke movement, appears to have been solved through the shuttle-principle. While the piston is commutates, a shuttle piston accommodates the compression oil, as shown in Fig. 9 on the right.

Figure 10 shows what the drive of a lift truck with a free piston engine might look like. Both the wheel drive and the working hydraulics are controlled by means of hydrotransformers. [10]

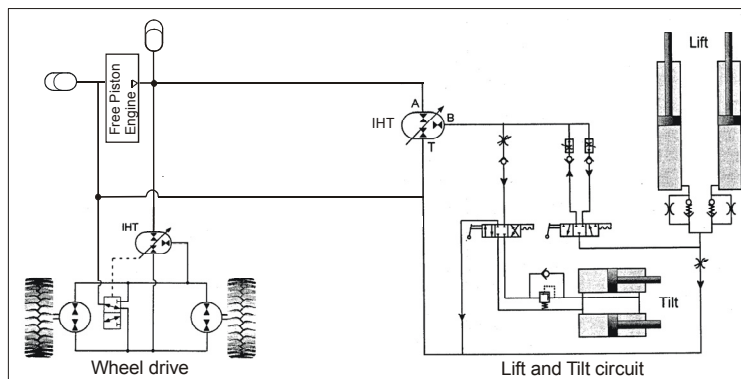


Figure 10: Drive of a lift truck with free piston engine and hydraulic transformer, (Source: Peter von Achten, INNAS)

It is not easy to predict whether this type of energy generation by means of a free piston motor will ever establish itself against the strong competition represented by the established volume flow generation through rotating displacement units. The most likely application scenario would be in mobile applications, because this energy source is reputed to be far more lightweight than the diesel engine with variable pump. However, switching to this new method of energy generation involves a far-reaching economic decision, because one cannot fall back upon proven designs.

VALVE ACTUATION

Whereas one had to work with unsteady valves actuated by switching solenoids in the early days, the 1960s saw the rise of the proportional solenoid. As shown in Fig. 11, in a proportional solenoid, the force generated remains constant over the stroke and proportional to the coil current within a certain range. If the proportional solenoid works against a spring, one achieves linearity between current and stroke. The proportional solenoid has been refined over the decades, such that the static and dynamic behaviour of proportional valves nearly matches that of servo valves. [11]

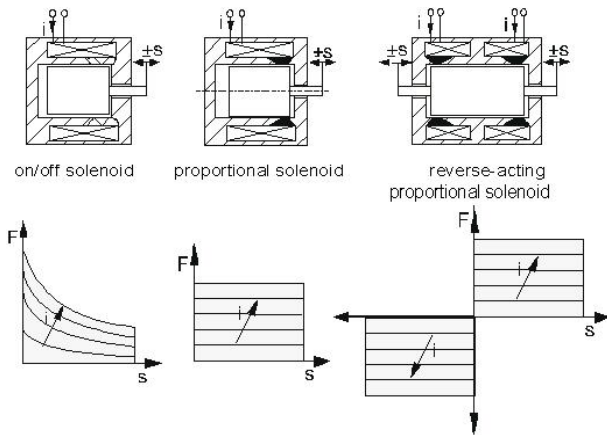


Figure 11: Valve actuators – solenoids

The proportional solenoid's shortcoming is that it can only generate forces in a single direction, so that a spring has to take care of the reverse movement. Hence, the failsafe position must be identical with the end position of the spring actuation, which can cause circuit design problems. Actuation becomes much more complex with a bipolar reverse-acting solenoid capable of exerting force in both directions, as shown on the right-hand side in Fig. 11. However, owing to the additional constructional effort required, that variant has not generally succeeded in the marketplace. The moving-coil principle was first used in Germany for steady controls (Fig. 12, left). In the 1950s, the so-called moving coil controller (AEG Tauchspulenregler) was popular, predominantly in heavy-duty machinery, where the piloted version was most frequently used. [12]

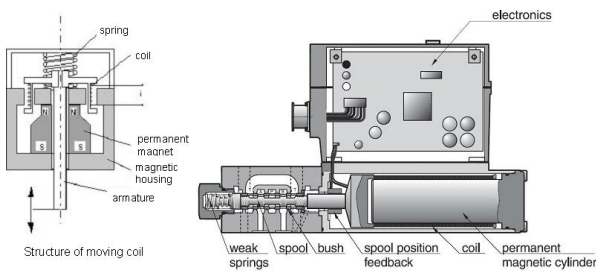


Figure 12: Moving coil design, (Source: Parker Hannifin)

In its new valve *DFplus*, the Parker company has revived the moving coil principle. As the right-hand side of Fig. 12 shows, the valve spool is directly actuated by the moving coil, which is wound around a thin-walled plastic pipe moving within the magnetic field of a strong, rod-shaped permanent magnet. Integrated into the valve is an inductive spool position feedback serving the valve spool's position control. If

the actuation should fail, the valve is moved to the fail-safe position in the middle by weak spring, (left side). As evinced by the table in Fig 13., the moving coil can generate much larger forces than the proportional solenoid. In the open loop with an 100 % - signal at 250 Hz, a stroke of 0.2 mm was attained. The moving coil is more than twice as fast as the proportional solenoid. However, its power consumption is twice as high.

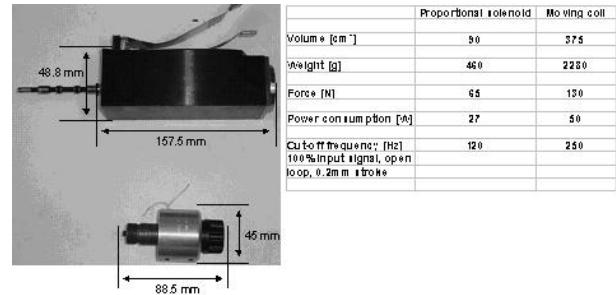


Figure 13: Comparison: proportional solenoid vs. moving coil, (Source: Parker Hannifin & Magnet-Schultz Memmingen)

A further advantage is shown in Fig. 14. Within the closed position control, the moving coil can exert such high forces that it is able to counteract the flow forces up to a pressure difference of 350 bar at the valve. By contrast, the pressure difference at a proportional valve is limited, because the flow forces close the valve against the actuation force as pressure differences rise.

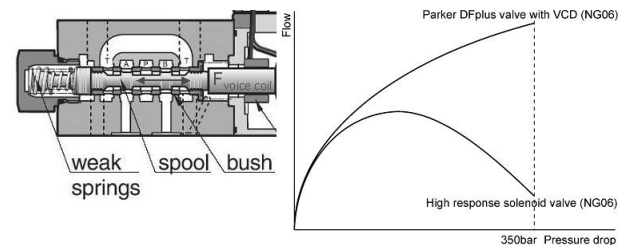


Figure 14: Application limits, (Source: Parker Hannifin)

One drawback of the new type of valve actuation shown in Fig. 13 is the weight, which is approximately five times as high as that of the proportional magnet. This will be primarily due to the heavier permanent magnet, which is, however, firmly attached to the valve housing. The moved masses are very low. This valve is at a disadvantage in applications where low valve weight and small volume are necessary. Its good static and dynamic behaviour may help find it wider usage elsewhere.

NOISE REDUCTION THROUGH PRE-COMPRESSION VOLUME

For many years, measures intended to reduce the noise emissions of piston pumps centred upon a soft pressure commutation, so as not to excite the pump's structure into emitting structure-borne noise. Towards that end, the port plate was equipped with a combination of pre-compression and suitable commutation bores or notches. However, these measures were only effective within a limited operating range in terms of pressure level, speed, and displacement volume.

In 1992, first reports concerning research conducted at the University of Linköping, Sweden (Professor Palmberg) appeared, which intended to reduce volume flow pulsations using a pre-compression capacity (pre-compression chamber). [14] These volume flow pulsations lead to pressure pulsations which excite attached components and systems into radiating noise. The idea is sketched in Fig. 15.

During the commutation phase of Piston 1 the piston volume is closed to the suction kidney and not opened to the pressure kidney. During the time Δt the piston volume is fed from the pre-compression chamber which is charged with high pressure. As the compression oil is not withdrawn from the delivered volume flow the flow pulsations are reduced.

When the piston volume (1) opens to the high pressure kidney the pre-compression chamber is filled again through a wider orifice 0_1 from the high pressure kidney over a longer period.

Through a very narrow orifice 0_2 the pre-compression chamber can be additionally filled from the high pressure side constantly.

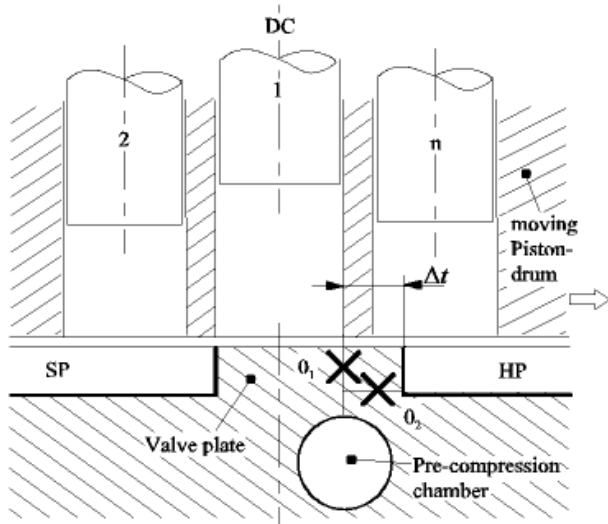


Figure 15: Pulsation reduction by pre-compression chamber

Some years passed before – encouraged by work done at IFAS (dissertation M. Jarchow 1997) – this operating principle was used in a production pump. [15] The left-hand side of Fig. 16 schematically depicts the arrangement of the Linde company's pre-compression volume, which is continuously fed from the high-pressure side as well as from the charged piston volume. The pre-compression volume principle was then adopted by two further major manufacturers of axial piston pumps. Figure 16, right-hand side, shows the pre-compression volume arrangement of the company Parker. Through this measure, reductions in pressure pulsations of between approximately 40-60 % are attained in practice. Moreover, that reduction is far less dependent on the operational parameters pressure, speed, and displacement volume than was the case with previous compensation methods. [16] [17]

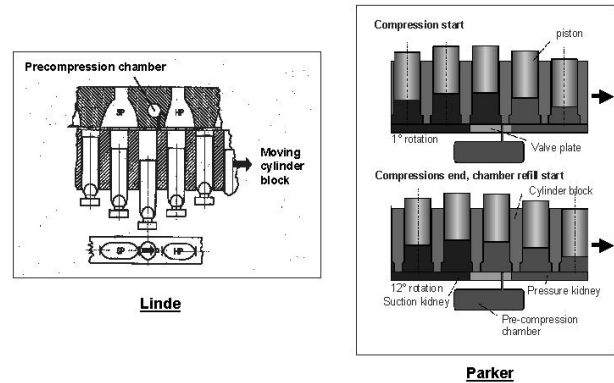


Figure 16: Arrangement of pre-compression chambers

Figure 17 shows pulsation measurements conducted by the Rexroth company at a pump in an open circuit. Integrated into a complete system, the lower pressure pulsations can lead to a reduction in system noise of between approx. 3 to 5 dB (A).

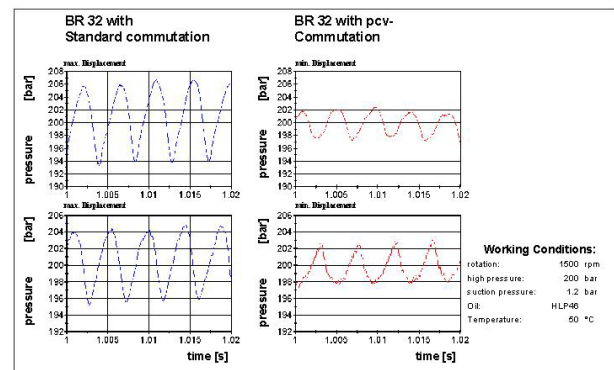


Figure 17: Pressure pulsation of an axial piston pump, (Source: Rexroth)

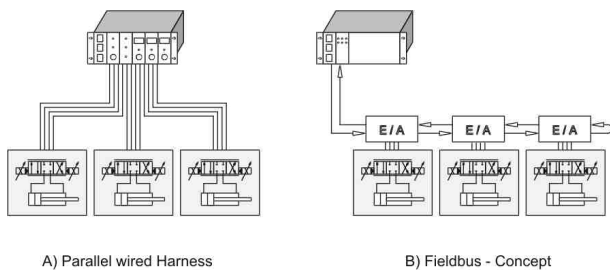
The constructional effort required for this pre-compression volume, which can be cast into the cover, is relatively low. The only disadvantage registered is the somewhat steeper pressure gradient during commutation, which leads to a slight increase in the pump's primary structure-borne noise.

In summary, the pre-compression volume is a development with little extra constructional effort and significant advantages to be achieved. It has led to a major decrease in the noise levels emitted by mobile machinery, for example. Hence, this idea quickly met with wide acceptance.

BUS TECHNOLOGY

The evolution of electronic control technology and the availability of affordable microcontrollers has enabled a new type of control circuitry.

Figure 18 illustrates the evolution from the parallel wiring of fluid power components to the field bus concept. Instead of laying some wires from the control electronics to each valve, which results in complex controls and thick wiring harnesses, the bus system relies upon a single signal line, which connects each valve or valve island in series. A processor on each valve island extracts the relevant information for each valve from the serial instruction set. These processors may contain decentralized intelligence, inasmuch as they can execute control tasks, e. g., for valves, variable pumps, or linear axis-drives. Often, the processor for the intended control tasks is integrated into the valve. For pneumatic valve islands, programmable sequence controls may be installed decentrally. The decentralized processors are remote-controlled via the bus by the superordinate control.



A) Parallel wired Harness

B) Fieldbus - Concept

Figure 18: Development from the parallel wired harness to fieldbus-concept

Figure 19 shows the CAN-bus-control of a mobile working machinery. The bus transports the reference variables for the axis drives and for variable-pump control with short cyclical intervals (1-2 ms). Moreover, sensor output is transmitted onto a status- and diagnosis-terminal. In this manner, the machine operator is constantly kept informed on all ongoing machine functions. [18]

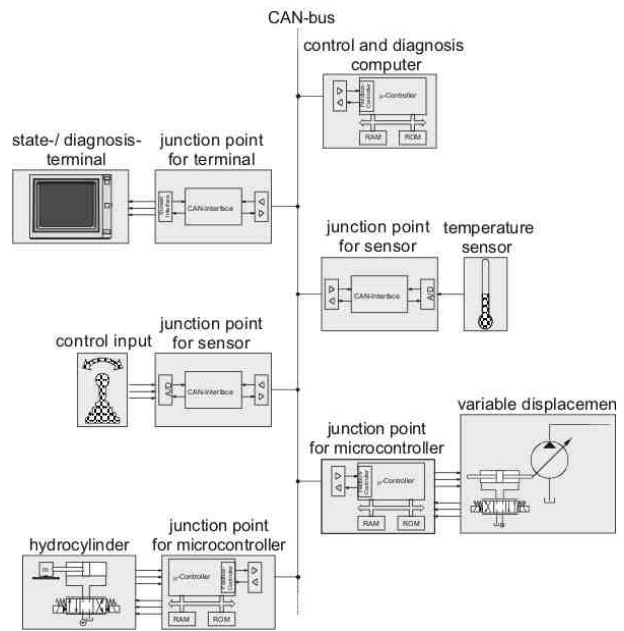


Figure 19: CAN-Bus for mobile hydraulics

In addition, acyclically and with longer reaction intervals (10 to 100 ms), condition-monitoring information is transmitted, which allows for the machine's condition to be diagnosed. Those data greatly simplify the maintenance and repair of complex drive systems. The drive manufacturer can even remotely diagnose the drive by logging on to the control computer.

Some exemplary advantages of bus technology would include: [20]

- smaller wiring harness and reduced wiring effort
- transparency of controls in planning machines and plants
- unproblematic system expandability
- interchangeability of standardized bus components
- comprehensive information available for diagnostic purposes
- quick setting of parameters for component functions
- enhanced user benefit through the integration of functions into components
- reduced incidence of malfunctions during start-up

Particularly for complex machine- and plant controls, the aforementioned economic and functional benefits far outweigh any other considerations. Accordingly, bus technology is fully accepted in that area and continues to gain ground vis-à-vis the conventional wiring technique.

FUEL CELL

The fuel cell represents a primary energy source that might alter the competitive situation in favour of electrical drives. In a PEM-technology (polymer-electrolyte membrane) fuel cell, the chemical energy of a gas (H_2) or fuel (methanol) is directly transformed, without combustion (by means of an ion-conducting membrane between anode and cathode), into electrical energy.

It is estimated that fuel cell technology will have matured within between one to two decades. [21]

At present, the competitive situation between electrics and fluid power in regard to the supply of primary energy for stationary and mobile applications is as shown in Fig. 20. For stationary applications, electrical power offers the advantage of allowing direct access to the primary energy source, via the electrical grid and a wall socket. By contrast, fluid power first has to create a pressure net with an electric motor and a pump, which entails greater expenditure for stationary application.. It takes specific requirements for fluid power to be utilized in spite of this comparatively higher cost: forming machines, for example, demand very high forces, for the generation of which fluid power is most suitable.

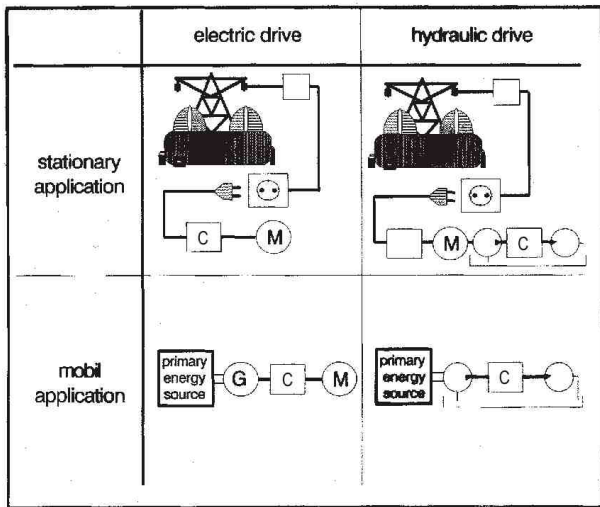


Figure 20: Present-day competitive situation: electric versus hydraulic

The situation is different in mobile applications. There, electrics and fluid power are on a level playing field. The primary energy source – most commonly a diesel engine – powers a generator or a pump to convert the mechanical energy into electric or hydraulic energy. Owing to its inherent advantages, particularly the higher power density, fluid power is the preferred choice for mobile applications today.

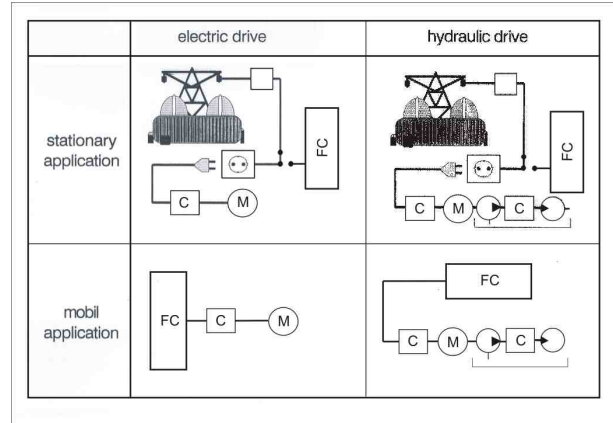


Figure 21: Competitive scenario after the introduction of the fuel cell

As Fig. 21 shows, this competitive scenario, particularly in mobile applications, might change in some decades. The fuel cell integrates the primary energy source (hitherto the diesel engine) and the generator into a single unit. Of course, this presupposes that it will become possible to develop sufficiently robust and powerful fuel cells offering a high power density at a low price.

What impact might such a development have on fluid power?

The competitive framework for stationary applications would remain unchanged, because it doesn't matter whether the primary energy is extracted from the power grid or from a fuel cell. However, the conditions for mobile applications would change: electric motors could be fed directly from the fuel cell, without the need for a diesel engine and a generator, whereas fluid power would still require a hydraulic pressure net to be built up, entailing comparatively greater expenditure.

Notwithstanding the aforementioned advantage of electrical power transmission, it is to be assumed that the working movements of mobile machinery will continue to be implemented using fluid power technology. Concerning translatory and swivelling motions, one major advantage is the easy transmission and distribution of hydraulic energy amongst several consumers through affordable cylinder drives. Furthermore, the force- and energy density of these drives is much higher than that of electromechanical drives with ball-thread drives or linear motors.

And what about rotatory movement, e. g., for the wheel drive? Whenever high power output is required from the electric motor, it has to run at high speeds. Thus, in order to generate the necessary low speeds with high torque at the wheels, speed transformers are required, for which purpose the proven hydrostatic transmission suggests itself. Applications most likely to migrate towards the electric drive are those in which the wheel

rotation merely serves to move the vehicle – as, for example, in a lift truck.

The fuel cell is a novel development, and its impact upon fluid power drive technology cannot yet be fully assessed. Nor can one predict whether fuel-cell technology is suitable for the rough operational environment of mobile working machinery. It is clear, however, that fluid power requires sustained further development in order to keep pace with electromechanics.

CONCLUDING REMARKS

Whether or not a novel idea will meet with wide acceptance in the field of fluid power depends upon a multitude of criteria. The overall technical and economic advantages of a fresh solution outweighing its shortcomings is the crucial determinant deciding whether it will be successfully applied within a particular area or whether it will be forgotten. Citing a number of examples, the likely prospects of some relatively recent ideas were discussed.

	Fluidics	AFH	Secondary Control	Free Piston Engine	New Valve Actuation	Pre Compr. Chamber	Bus Technology	Fuel Cell
Acceptance in Practice	No Acceptance	No Acceptance	Acceptance for special Applications	Acceptance difficult to assess	Acceptance for special Applications	Acceptance	Acceptance	Acceptance difficult to assess
Functional Reasons	⊗	⊗	⊗	⊗	⊗	⊗	⊗	⊗
Economical Reasons		⊗		⊗		⊗	⊗	⊗

Figure 22: Summary

From Fig. 22 we see that not all of the treated new ideas were successful and gained acceptance in practice:

- Some are fully accepted as the Pre-Compression Chamber and the Bus Technology.
- Some gained acceptance only for special Applications as the Secondary Control and the New Valve Actuation.
- And for some the acceptance is difficult to assess. That is true for the Free Piston Engine and the Fuel Cell.

The future will tell whether they become successful.

REFERENCES

[1] Multrus, V. Pneumatische Logikelemente und Steuerungssysteme. Krausskopf-Verlag, 1970.

[2] Töpfer, H. Tendenzen in der pneumatischen Signalverarbeitung. Pneumatische Digitaltechnik. G.E.C.-Elliott Automation GmbH, Solingen, 1974.

[3] Festschrift zum 25-jährigen Firmenjubiläum UFT Umwelt und Fluid-Technik Dr. H. Brombach GmbH.

[4] Constantinesco, G. A treatise on the transmission of power by vibration. Theory of Sonics.

[5] Henke, Russ. Some practical possibilities of alternating flow hydraulics. Fluid Power International, February 1966.

[6] Kordak, R. Hydraulische Antriebe mit Sekundärregelung. Buchreihe Der Hydraulik-Trainer, Mannesmann-Rexroth GmbH.

[7] Murrenhoff, H. Regelung von verstellbaren Verdrängereinheiten am Konstant-Drucknetz. PhD thesis. RWTH Aachen, 1983.

[8] Tikkanen, S. Evolution of engine-hydraulic free piston engine. PhD thesis. Tampere University of Technology, 2000.

[9] Van Achten, P. A. et. al. Dedicated design of the hydraulic transformer. 3rd International Fluid Power Conference, Aachen, Germany, 2002.

[10] Vael, G. M. & Van Achten, P. A. The Innas fork lift truck working under constant pressure. 1 Internationales Fluidtechnisches Kolloquium, Aachen, Germany, 1998.

[11] Weigle, D. Bestandsaufnahme und Entwicklungstendenzen der Proportional-Hydraulik. Ölhydraulik und Pneumatik, Vol. 12, 1983.

[12] Scheibe, E. Die Lösung von Regelungsaufgaben mit Hilfe elektrohydraulischer Bauelemente. Haus der Technik – Vortragsveröffentlichungen: ‘Ölhydraulik’, 30 March 1966.

[13] Kolvenbach, H-G. Ausweg aus dem Dilemma. Fluid, July 2004.

[14] Petterson, M., Weddfield, K., Palmberg, J. O. Reduction of flow ripple from fluid power machines by means of a precompression filter volume. 10th Aachener Fluidtechnisches Kolloquium, Vol. 2, 1992.

[15] Jarchow, M. Maßnahmen zur Minderung hochdruckseitiger Pulsationen hydrostatischer Schrägscheibeneinheiten. PhD thesis. RWTH Aachen, 1997.

- [16] Roland, A., Dörr, H.-D., Welschhof, B. Pulsations- und Geräuschminderung an Verdrängereinheiten in der Mobilhydraulik. VDI-Tagung Maschinenakustik, 1999.
- [17] Weingarten, F. Noise reduction in hydraulic systems: what the pump can contribute? Seventh SICFP, Vol. 1, 2001.
- [18] Baldy, M. Dezentral geregelte fluidtechnische Antriebe in Feldbusumgebung. PhD thesis. RWTH Aachen, 1999.
- [19] Bublitz, R. Geräteprofil Hydraulik – ein Kommunikationsprofil für intelligente Antriebe, Hydropumpen und Stetigventile. 2nd Internationales Fluidtechnisches Kolloquium in Dresden, Vol. 2, 2000.
- [20] Müller, U. Bussysteme in der Fluidtechnik. 2nd Internationales Fluidtechnisches Kolloquium in Dresden, Vol. 2, 2000.
- [21] VDMA-Studie: Markteinführung von Brennstoffzellen-Produkten: Auswirkungen auf den Maschinen- und Anlagenbau – Voruntersuchung zu Forschungsfeldern für die Herstellung von Produkten mit alternativen Energie- und Antriebssystemen.

Recent Research of fluid power at Yanshan University

Kong Xiangdong , Shan Dongsheng

Institute of Fluid Power Transmission and Control System of Yanshan University China.

Email:xdkong@ysu.edu.cn

ABSTRACT

In the paper ,I introduce the main recent research of the fluid power at Yanshan University. Including heavy machinery electrohydraulic servo-control system, pipe dynamic property , control strategy and intelligent fault diagnosis prediction Study on hydraulic components and application, Research on the complicated flow, The mechanics quantity detection and control technique.

Key words, control system, hydraulic components, flow power.

Brief Introduction for the research projects

1、Major direction in researches

- ◆ The research for the heavy machinery electrohydraulic servo-control system

We had an advanced breakthrough in strip thickness and shape control, thus we got independent of the imported finishing mill group technology. In 1992, we applied the fruits of researches on strip thickness to the 400HC rolling mill rebuilding of Harbin coppering steel strip company. Hence our country yielded precise steel strip by using our domestic technology and equipment for the first time.



Figure.1 The rolling mill

During the researching and the developing of IGC650HCW precise cold belt rolling mill equipment

sets, we initially realized the integration of the internal gorge Control (IGC) and the working-roll axial movement (HCW). The $\pm 2\mu\text{m}$ plating thickness control accuracy and the stable working situation enabled this technology to be the most advanced development among cold rolling control techniques. The Southwest Precision Strip Company built by this equipment sets has developed to be one of the ten key enterprise in XiChang of Panzhihua. In April,1997, the specialists of the national mechanics department ratified this result to be " in possession of originality, worldwide developed control accuracy and running conditions".

In 1999, the project was awarded a second class state scientific-technical progress prize. Moreover, the " research on continuous casting crystallizer non-sinusoidal oscillation system", one of the national " nine- five science and technology critical projects", received a second class scientific-technical progress prize of Hebei province.

- ◆ Research on pipe dynamic property

The theoretical analysis and experimental study about this project overthrew the traditional point of view that pipeline effect only can harm the systems, and revealed its potential application in electrohydraulic control systems. Besides, it put forward the new concepts and methods for series and parallel correction, and applied it to hydraulic bending system in rolling mill.

Therefore, the system band- width can increase three times (reached 60Hz), which was ratified to be in " international advanced lever " by the mechanics department.

- ◆ Research on hydraulic system control strategy and intelligent fault diagnosis prediction

It brought forward Fuzzy and Intelligent PID parallel control structure model, which was in possession of all merits of conventional PID, intelligent PID and fuzzy control. As long as it could go through input/output information in the real time detection on control procession, it could control systems effectively. So it is an useful and simple control strategy. The research on nonlinear system control chaos and the intelligent fault diagnosis prediction, has been a breakthrough in this field in recent years. It is of great importance in ensuring normal working of complicated electrohydraulic control systems and decreasing failure rate.



Figure.2 Diagnosis prediction of the hydraulic system

- ◆ Study on hydraulic components and application

The open circuit axial plunger pump has finished seven series new constructions. Its outstanding properties such as self-cooling, self-lubrication and no leakage, reduced the temperature increment of the pump, improved its service life for several times.

Received 2 national patents of invention

Received 8 national patents of utility model

Awarded a scientific-technical progress prize by mechanics department and " six five " critical technology

prize by Heilongjiang Province.

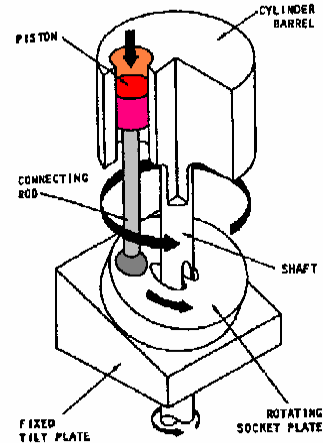


Figure.3 Axial plunger pump

- ◆ Research on the complicated flow

The traditional design is only dependent on experience because there is a lot of heterotype section complicated flow in hydraulic elements and it is too difficult to research flow fields with analytic methods. Adopting Navier - Stokes equation in finite element and boundary element analyzing heterotype section field, and leading-edge experimental research on flow field visualizing systems, this research searched after the energy loss mechanism of complicated flow field, to establish a foundation for optimum design of hydraulic elements.

- ◆ The mechanics quantity detection and control technique

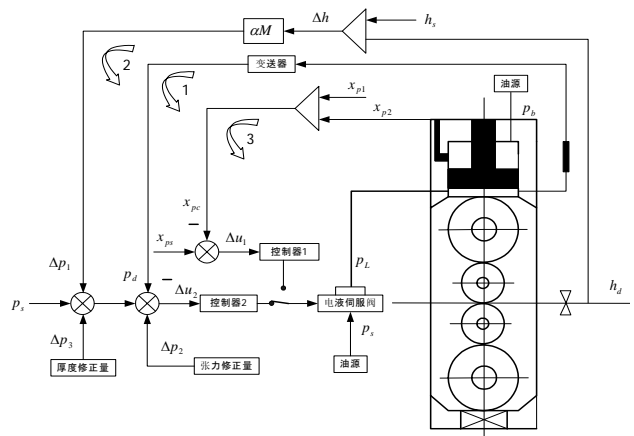


Figure.4 Diagram of the AGC system

Steel strip rolling mill shape control in cold rolling mill, the long-term national critical scientific research project, has yielded initiative results in theory and

practice. Some fruits of research, such as 650HCW shape of strip display system and 1850 cold rolling shape of strip plating thickness system control, has now been transferred into productivity. The successful research on magnetic and elastic transformer differential output cold rolling shape of s steel trip, filled up the domestic blank in this field, and enable us to get rid of the dependence on import. So it was awarded a first class and a second class scientific-technical progress prize by mechanics department.

2、 Part of the latest projects

- ◆ The critical technology research on the 1450 cold link rolling mill
- ◆ Programmable electrohydraulic control valve

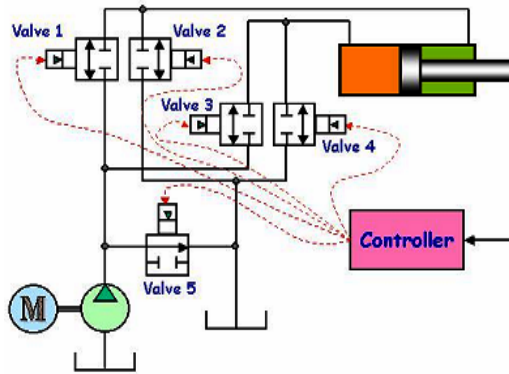


Figure.5 Programmable electrohydraulic control valve

- ◆ Virtual cold tandem rolling mill group Modelling and simulation

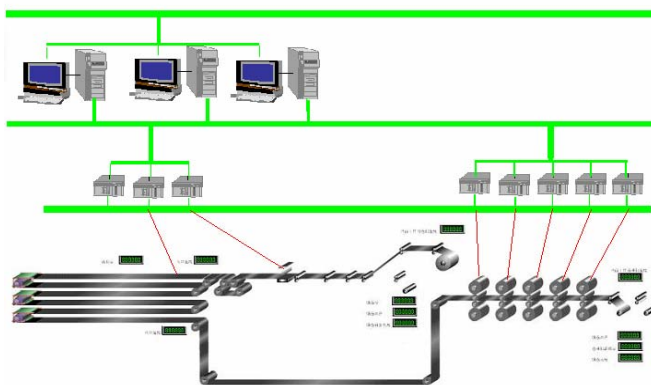


Figure.6 Virtual cold tandem rolling mill

- ◆ 1800 levelling machine shape of strip and extensibility syntheses optimization control



Figure.7 optimization control of the rolling mill

- ◆ Hot tandem roll reeling machine mark time control system



Figure.8 CPC system of the rolling mill

- ◆ Study on mutable width water curtain cooling experimental apparatus



Figure.9 Water curtain cooling system

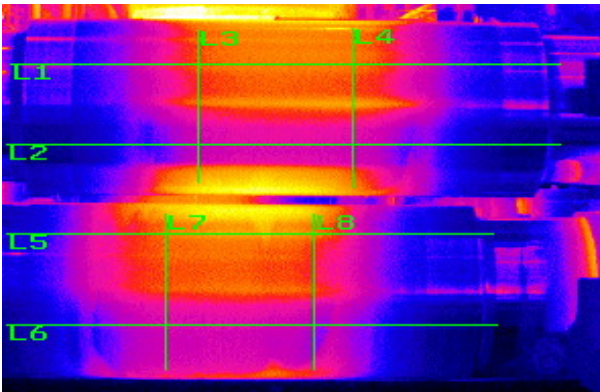


Figure.10 Temperature distribution of the strip steel.

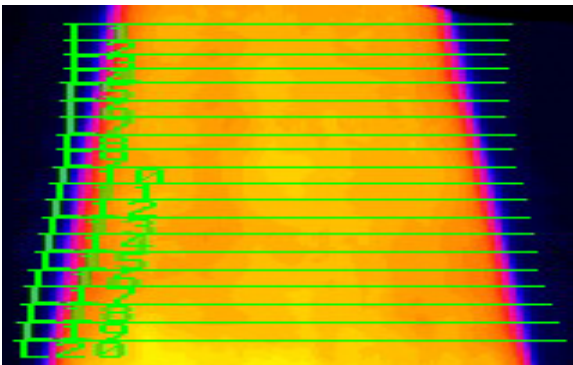


Figure.11 Temperature distribution of the strip steel.

◆ Study on control system of 5000T hydraulic press machine



◆ Figure.12 hydraulic press machine working spot

REFERENCES

- 1 Q.Zhang* and X.Kong**, Study of Valve Function and Characteristics Programmability Using Programmable E/H Valve. Proceedings of the 5th international conference on fluid power transmission and control(ICFP'2001), Hangzhou,2001.4:258~264.
- 2 Haibo Hu, M.S,Generic Programmable

Electrohydraulic Valve,the Degree of Master of Science in Agricultural Engineering University of Illinois,2001

- 3 Hu, H., Q. Zhang and A. Alleyne, Multi-function realization of a generic programmable E/H valve using flexible control logic, 2001, Fifth International conference on Fluid power Transmission and Control, Hangzhou, China.
- 4 Haibo Hu, Qin Zhang, Andrew Alleyne and Xiangdong Kong, Development of Programmable E/H Valve with a Hybrid Control Algorithm, SAE International Off-Highway Congress, March 19-21, 2002, Las Vegas, Nevada, USA.
- 5 Prodip BHOWAL. Modeling and Simulation of Hydraulic Gap Control System in a Hot Strip Mill. ISIJ International,1996:553-562
- 6 Gao Yingjie, Wang Yiqun, Kong Xiangdong, The study on the dynamic model of hydraulic AGC system in a strip mill. China Mechanical Engineering . 1998, 9(7): 23~26.
- 7 Zou Jiexiang, Xu Lejiang . Tandem mill vibration control. Beijing: Metal industry press.
- 8 Remn-Min Guo. Evaluation of dynamic characteristic of HAGC system . Iron and steel Engineer , 1991; (7):52~63.
- 9 Kong Xiangdong, Gao Yingjie, Shan Dongsheng, ect. Study on Parameterized Simulation of Hydraulic AGC in Rolling Mills, **Proceedings of the Fourth International Symposium on Fluid Power Transmission and Control(ISFP'2003)**, 171~174
- 10 Kong Xiangdong, ShanDongsheng,Dong Guojiang,ect. Study on Modeling and Simulation of HAGCS, Wuhan, **Digital Manufacture Science**, 2003: 256~276

CDIO-CONCEPT FOR ENGINEERING EDUCATION IN MECHATRONICS – PROJECT TEAMS IN ACTIVE AND INTEGRATED LEARNING

Finn CONRAD[♦] Torben O. ANDERSEN[▲] Michael R. HANSEN[▲] Torben SORENSEN[♦]

[♦]Technical University of Denmark
Building 404, Kgs. Lyngby, Denmark
finn.conrad@mek.dtu.dk ts@mek.dtu.dk

[▲]Aalborg University, Denmark
toa@iet.aau.dk mrh@ime.aau.dk

ABSTRACT

The paper presents significant good Danish experiment results of a developed CDIO-Concept and approach for active and integrated learning in today's engineering education of MSc Degree students, and research results from using IT-Tools for CAE/CAD and dynamic modelling, simulation, analysis, and design of mechatronics solutions with fluid power actuators for motion control of machines and robots. The idea of CDIO-Concept is to take care of that the students are *learning by doing* and *learning while doing* when the students are active to generate new products and solutions by going through the phases from to Conceive, Design, Implement and Operate related to en product design by them self in competition with others. The idea is based on the Danish implementation of a CDIO-Concept. A curriculum at Aalborg University, and Technical University of Denmark, offers courses for Motion Control, Fluid Power within mechatronics design, and advantages as well as challenges are identified and discussed. An IT-tool concept for modelling, simulation and design of mechatronic products and systems is proposed, and results from a Danish mechatronic research program on intelligent motion control.

KEY WORDS

CIDO, Engineering Education, Mechatronics, Project Learning, Motion Control

INTRODUCTION

Companies are facing an increasing global competition on the market and the on-going challenge that customers always increase their needs for capability of products, solutions and machinery. Customers want improved productivity and efficiency – if possible to lower prices and rapid delivery; value for money. The demands focus on extensions of functionality, faster response, operation

capability, man-machine interface (MMI), robustness, reliability and safety in use. Today's IT-tool offers both software and hardware for improvement of engineering design and industrial applications. This means companies need professional engineers with qualifications to fit the demands. R&D Mechatronics Teams create mechatronics products, machines and solutions, Figure 1. Mechatronics System Engineering is an emerging integration of mechanical engineering, electrical engineering, control engineering, and smart software engineering.

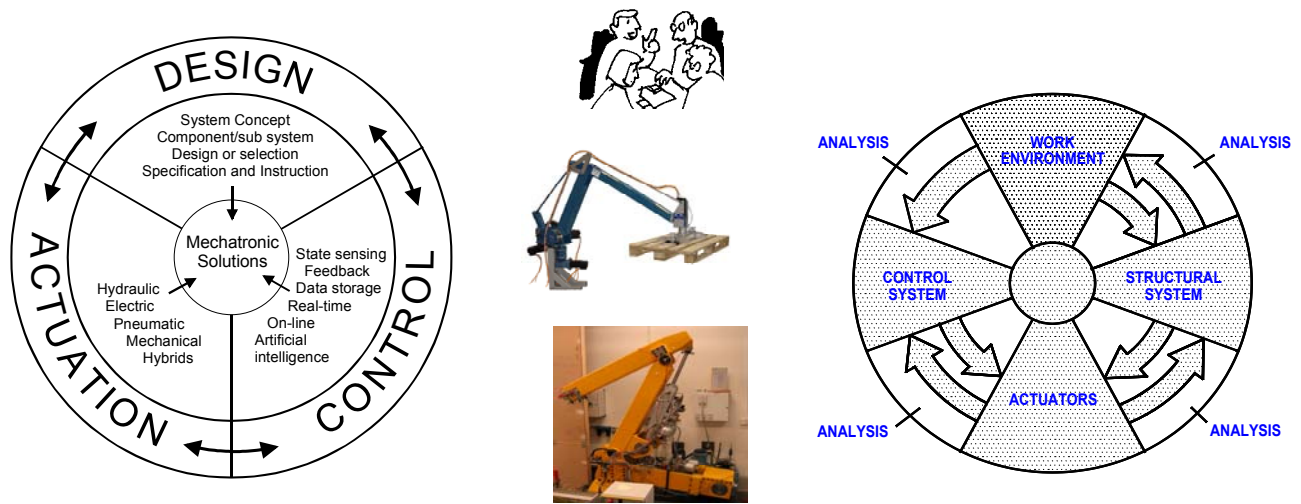


Figure 1 R&D Mechatronics Teams create mechatronics products and solutions

New applications where a mechatronic approach is needed are added each year. The need and demands to the education of engineers in this field are on-going increasing. The challenge is basically to develop the content of the engineering curriculum to strengthen integration of theories and best practice in mechatronic design of novel generations of products and solutions without using extra study time. This paper presents an active and integrated learning approach, which makes it possibly very fast for the MSc student to develop in-depth skills in this important area. The approach is lectures combined with mandatory projects base on active problem-oriented and project-based learning. The idea is based on the Danish implementation of a CDIO-Concept. A complete curriculum at Aalborg University, AAU, and Technical University of Denmark, offers courses for Motion Control, Fluid Power within mechatronics design, and advantages as well as challenges are identified and discussed. An IT-tool concept for modelling, simulation and design of mechatronic products and systems is proposed in this paper. It built on results from a Danish mechatronic research program on intelligent motion control.

CDIO CONCEPT - PROBLEM-ORIENTED AND PROJECT LEARNING

IT-tools for controller design and for intelligent motion control could satisfy customers' needs, requirements and the regulations etc. Mechatronic test facilities with digital controllers for a hydraulic robot, hydraulic cranes and mobile vehicles have been implemented for R&D, and for education of students based on a Danish developed CDIO-

Concept, and problem-oriented and project-learning, illustrated in Figure 2, Figure 3, Figure 4, and Figure 1.

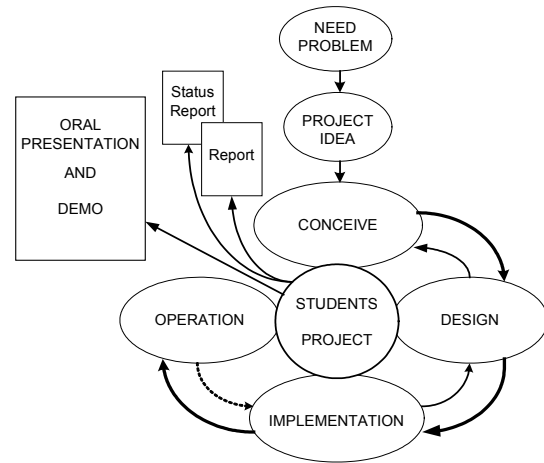


Figure 2 CDIO-Concept (Finn Conrad, 2005)

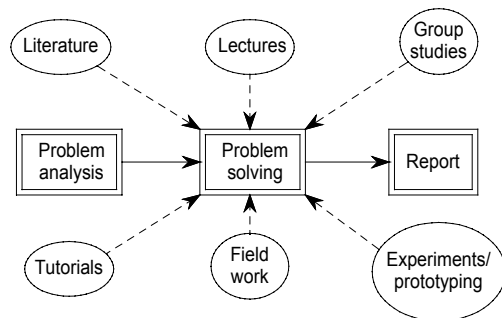


Figure 3 Problem-oriented and project-learning

Such a problem-driven and project-based learning do strengthening of the students' *self-learning competency*. Engineering design can be analysed using the IPD-model, i.e. Integrated Product Development phase model [1].

THE CONTROL ENGINEERING DESIGN TASK

The task of control engineering design can be analysed using the IPD-model illustrated in Figure 4, in order to integrate control theory and design methodology into the design process to create business by turnover.

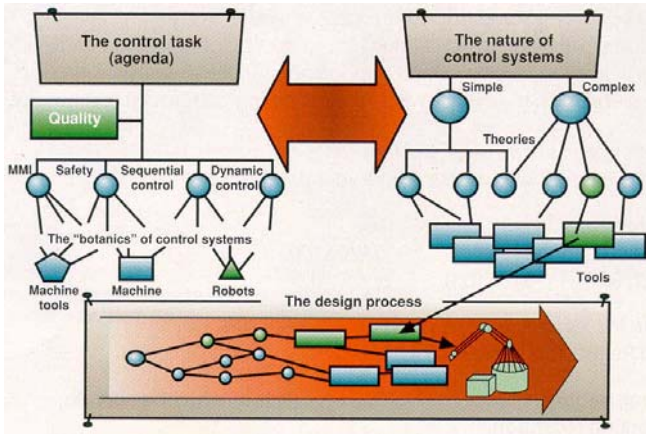


Figure 4 The control engineering design task

The objective of the model is to give an overview and understanding of *the control task* (or agenda), shown to the left in Figure 4, with focus on quality, and *the nature of control systems*, shown to the right. At the bottom of the figure is illustrated *the design process* based on the Integrated Product Development (IPD-model) activities starting with the customers' needs to the very left and ending up with the deliverable product to the very right.

An important part of the engineering knowledge base includes descriptions, models and experiences concerning known products, including controllers, machines, robots etc. In this context, it is named as knowledge on the 'botanics' of control systems. The control aspects are focused on the areas: Man-Machine Interfaces (MMI), safety, sequential control and dynamic control. As shown, the modelling activity for an actual control task relies on the available theories, methodologies and tools to model and describe the behaviour of the product undertaken in the design process. The IT-tools and laboratory facilities are needed real-time for experimentation, evaluation and validation of control laws and algorithms. Furthermore, a problem-driven and project-based learning framework for strengthening and development of the students/candidates *self-learning competency* is proposed and discussed.

Successful R&D-project business

The designer and/or the team of designers pre-determine the production related costs and hereby the business potential during his and/or the team's decisions in the design phase. The awareness of managing this relationship is very important during the design of products to make a successful business. This is in particular important for enterprises in mechatronics. Use of the IPD-model and available IT-simulation techniques suitable for hardware in the loop simulation and rapid prototyping could improve the design phase and test phase in order to reduce the time to market and total costs leading to a successful business. The design and development of fluid power components and systems by use of smart simulation and IT tools in a concurrent engineering approach following the iterative design concept illustrated in Figure 5 by Conrad [2] and [3]. The driving forces are the designer's innovation, creativity and thinking combined with their knowledge and capability skills to solve the design task.

IT-TOOL CONCEPT FOR CONTROLLER DESIGN

A company's capability of beating the competitors often depends on the ability to shorten the time of a product's development and design phase and to decrease the total design and prototyping costs. Developing a closed-loop control system for fast mechatronic systems involves control design with plant modelling and off-line simulation as well as real-time simulation and hardware-in-the loop (HIL) simulation to verify the controller's functions, robustness and safety in reality.

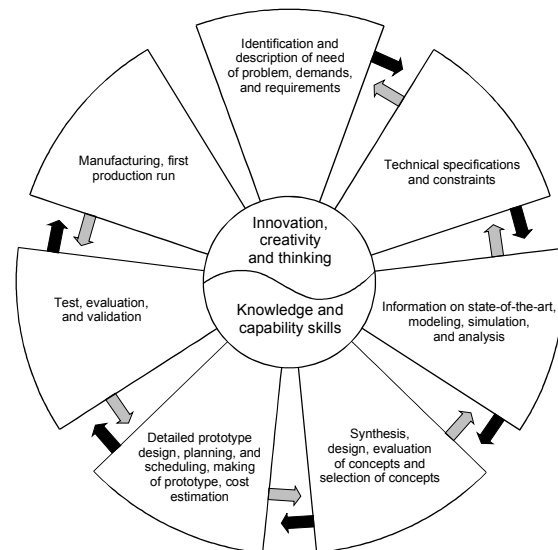


Figure 5 The design process is an iterative on-going engineering driven and controlled process

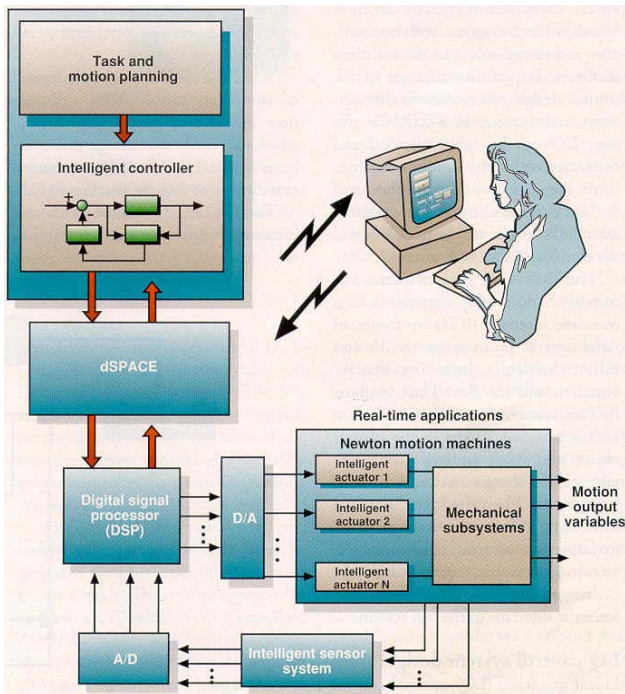


Figure 6 IT-tool concept for control system design

To overcome the disadvantage of the traditional set-up and procedure for controller system design, a novel concept for controller design was developed and implemented at our Department of Mechanical Engineering, DTU. This concept based on use of DSPs and the dSPACE system, as illustrated in Figure 6, is very suitable for intelligent motion control of machines and robots.

For mechatronic products, machines, robots and systems with a controller, this challenge can be undertaken by using a suitable IT-tool concept for controller design based on CACSD (Computer Aided Control System Design) with facility for rapid controller prototyping with HIL simulation capability. A feature is the integrated design and rapid prototyping of controllers targeted at Digital Signal Processors (DSPs) or other embedded systems. The high performance and low cost of today's DSPs together with the use of powerful design and programming software, allows engineers to design controllers faster and with lower cost than traditional "custom" controller board designs. DSPs and Alpha processors are a very suitable hardware of choice for design of controllers utilising the CACSD packages such as Matlab/Simulink, VisSim, Easy5, ACSL, Dymola, Saber and AMESim.

The DSP card that facilitates the computer control is programmed via a Real-Time Interface (RTI) by means of

'Rapid Control Prototyping' (RPC) and 'Hardware In the Loop' (HIL) technologies including Matlab/Simulink and the Real-time Toolbox. The application is running on the real-time hardware the RTI and a virtual instrument panel, COCKPIT enables the user to change parameters and monitor signals, and a TRACE facility that displays the time history of any variable being used by the application.

CDIO EDUCATION IN MECHATRONICS DESIGN

Education both during ordinary graduate studies and through life-long learning becomes still more important. The technological progress is faster than ever and the 'life-time' of a new education is becoming shorter and shorter. In some emerging technology areas the lifetime is less than three years. However, basic skills like mathematics, physics and related technical disciplines are still important as well as skills like communication (written and orally), teamwork, project organization and management are becoming more and more useful.

Bachelor or Master project, where normally only two students work together. Each project group has during their project a supervisor who is a member of the faculty and the supervisor is also an active researcher. The project group requires a room at the university where they can work with their problems in connection with their project, meet their supervisor and solve problems related to the courses/lectures. A typical day for the students is divided into two halves with lectures and one project is carried out at each semester. In their final project (thesis) the students spend all the time on the project work. Normally 6 students work together in a project group except for the tutorials from 8.15 to 12.00 and project time from 12.30 to 16.30. This means that the students during their study are present almost all the time at the university. It is a great advantage that the students have their own room. This greatly facilitates their eagerness to use the teacher during course specific problem solving. The challenges lie in the physical planning and the subsequent demand for office rooms. Each semester has a specific theme and project titles address problems related to this theme. The academic staff and industry make proposals to a particular semester. The proposals are at the higher semesters (graduate) mostly related to the research interest or initiated by the industry. Given a problem at a semester the students first make a problem-analysis, demarcating the project and they make a time and working-plan. After that they do the problem solving by the use of literature, lectures, group studies, tutorials, field-work and experiments. During the project work the students have regular meetings with a supervisor (typically weekly).

During the education in Mechatronics System Engineering has focus on three main areas by AAU

- Design of machines and dynamic analysis.
- Control engineering – including modelling and simulation.
- Electro-technics, including analogue and digital electronics, programming of signal processors and microprocessors and control of electrical motors.

The level within these areas is built up during the different semesters. During the 6th to 8th semesters the courses (50%) are combined with project work (50%). During the 9th semester it is possible to attend project related courses, but generally the 9th and 10th semesters are based only on project work. It is possible to choose between making a short final thesis (10. semester) or an extended final thesis (9. and 10. semester).

6th semester - Project theme: “Design and Optimization of Electro-Hydraulic-Mechanical System”. A design task is formulated in detail, based on a working cycle where a payload of approximately 400 kg is to be positioned by a small vehicle. A number of standard components: Frequency converter, gearmotor, hydraulic pumpstation and hydraulic proportional valve are handed out to the students and they must use this in the design task. The design is manufactured and the student projects are compared with respect to: price, weight and efficiency. Project example: The outcome of a typical 6th semester project is shown in Figure 7. The vehicle had to ride on tracks laid out beforehand. The price of the vehicle was derived as the purchasing of components such as tooth belt drive, bearings and the hydraulic cylinder. The payload had to be picked in between the rails and hoisted above an obstacle during the travel thus complicating the structural design and requiring two degrees of freedom.

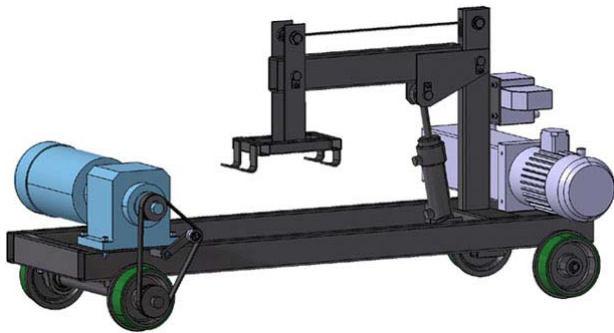


Figure 7 A 3D CAD model of the vehicle build

One may argue that the problem-based approach is almost non-existing in a project as controlled as this one. However, experience shows that the same skills with respect to problem definition and demarcation are just as necessary on a project like this as one with a more broadly

formulated initial problem. Also, it is important, to control the projects to a certain degree in order to ensure that certain teaching goals are reached. This balance between the purely problem-based approach and the desire to reach certain levels in different disciplines is one of the greatest challenges in an educational system.

7th semester - Project theme: “Servomechanisms and distributed loads”. The project considers an industrial servomechanism with a distributed load. The analysis and design of a position/velocity servo system on the basis of dynamic performance demands is wanted for the system. During the design work both an electrical and a hydraulic servomechanism is elected, and the designed control strategies are implemented digitally.

Project example: A hydraulically driven robot, as shown in Figure 8, was modelled and simulated to test design, implementation and operation of different control algorithms (incl. adaptive and learning). It is a two-degrees-of-freedom rotary arm manipulator with a high-frequency two-stage servovalve controlling each of the two hydraulic cylinders. The simulation model takes into account all nonlinearities and has been experimentally verified. The robot was also used for the experimental evaluation and verification of the designed control algorithms.



Figure 8 The DTU-AAU Hydraulic Test Robot

8th semester - Project theme: “Design and control of power transmission systems”. The project considers a power transmission system in a real industrial application, in which the power must be controlled in accordance with a varying consumption situation.

An AC-motor must be part of the transmission system as a power source to a hydraulic-mechanical or an electro-mechanical transmission.

Project example: A small vehicle was designed with a combined steering and traction concept, see Figure 9. Beside the construction of the vehicle the transmission system (using AC motors) and the control system (power converters and control strategy) were to be designed. The control strategy was implemented using a μ -controller and demonstrated by operation.



Figure 9 The prototype of designed and build vehicle with AC motor driven traction and steering

9th and 10th semester - The project considers a problem defined in co-operation with a company and Aalborg University. A specialization within a subject area is expected; a subject area in which the student has acquired qualifications on mechatronics. The project may start from a wide range of problems within the mechanical, fluid, electrical, and control engineering. The result of the project ought to be able to form part of or improve existing commercial systems. *Project example:* A 3-degree of freedom spatial servo robot for palette handling was designed based on a typical working cycle defined by a company. The designed, implementation and operation of a 3DOF spatial servo robot for palette handling is shown as an example in Figure 10 created by the MSc students.



Figure 10 A 3 DOF servo robot for palette handling

The project involved development of software for path generation and dynamic simulation used to dimension the mechanical structure, the machine elements, and the servo drive including converter, servomotor and planetary gears. Today do the Department of Mechanical Engineering, DTU and the Department of Mechanical Engineering, Aalborg University both offer each their own programme of specialisation profile in mechatronics for their MSc-students with an emphasis of motion control, intelligent control, analysis and ‘best practice’ of engineering design.

CONCLUSION AND OUTLOOK

The authors have so far good experience from using the proposed Danish CDIO-Concept for Engineering Education, in particular for a MSc Degree in Mechatronics Design. Promising results are obtained partly from a Danish mechatronic research program (IMCIA) focusing on intelligent motion control as well as results from the Esprit project SWING on IT-tools for rapid prototyping of fluid power components and systems. Examples of AAU and DTU mechatronic test facilities with digital controllers for a hydraulic robot, hydraulic cranes, and vehicles have proven their capability for research and education in mechatronics systems engineering. The controllers have been implemented with digital signal processors (DSPs). The developed IT-tool concept for DSP-based control system design and rapid controller prototyping do utilising the dSPACE System. A challenge of a successful education in mechatronics is the hardware. Cooperate closely with industry companies on projects is a must to assure support funding.

References

- [1] Andreasen, Mogens Myrup and Lars Hein: Integrated Product Development. IFS Publication Ltd. Springer Verlag, 1987, ISBN 0-948507-21-7.
- [2] Conrad, Finn: Transputer Control of Actuators and Robots. IEEE Transaction on Industrial Electronics, Vol. 43, No. 1, February 1996.
- [3] Conrad, Finn, Poul Erik Hansen, Torben Sørensen, Jianjun Zhou: IT-Tool Concept for Design and Intelligent Motion Control of Hydraulic Actuators for Machines and Robots. Proc. Application of Intelligent Hydraulic Systems, SAE Int. Off-Highway & Powerplant Congress & Exposition, Sept. 11-13, Milwaukee, WI, USA, 2000.

APPLICATION OF A PRESSURE INTENSIFIER USING OIL HAMMER TO A HYDRAULIC CYLINDER OF A CONSTRUCTION MACHINE

Katsumasa SUZUKI, Kentarou YOKOYAMA,
Yosuke ENDO and Yasumichi SHIBATA
Department of Mechanical Systems Engineering,
Musashi Institute of Technology
1-28-1 Tamazutsumi Setagaya-ku Tokyo, 158-8577 Japan
E-mail: ksuzuki@sc.musashi-tech.ac.jp

ABSTRACT

The active utilization of the pressure rise phenomenon of an oil hammer and a new type of hydraulic pressure intensifier using an oil hammer were proposed and developed. In this research, an application of this intensifier to pressure intensification in a hydraulic cylinder of a construction machine is studied through experimentation and simulation.

High pressure is generated when the fluid flow through the pipeline is shut quickly by the solenoid operated valve at the downstream end. If the fluid is taken out through the check valve when the pressure is high, much higher-pressure fluid than the supply is obtained. A vessel is used as a model of a hydraulic cylinder without displacement. The pressure of the vessel is intensified. The necessary pressure level is thought to be around 30MPa. We develop a block diagram for the simulation considering the pipeline dynamics.

Key words:

Pipeline, Water Hammer, Oil Hammer, Intensifier, Hydraulic Cylinder

NOMENCLATURE

a : sonic velocity in fluid (= 1.26×10^3 m/s)
 A : pipeline area
 A_3 : line cross sectional area (= 6.34×10^{-5} m²)
 A_E : open area of check valve (= 1.54×10^{-4} m²)
 A_V : total open area of solenoid-operated valve
(= 7.76×10^{-5} m²)
 c_0 : discharge coefficient of solenoid-operated valve
(= 0.6)
 c_f : discharge coefficient of check valve (= 0.7)
 C_E : viscous damping factor of check valve (= 11.8
Ns/m)
 D : inner diameter of pipeline
 D_E : inner diameter at check valve inlet (= 16mm)
 f : flow force

F_C : Coulomb friction force of check valve
(= 0.15N)
 g : acceleration due to gravity
 h_f : head loss due to fluid friction per unit length
 H : pressure head
 H_V : pressure head in vessel
 H_E : pressure head at downstream end of pipeline
 K_E : spring constant (= 20.6 kN/m)
 K_V : bulk modulus of fluid (= 1.36 GN/m²)
 L : length of pipeline
 L_3 : length of connection area (= 0.145m)
 M_E : moving mass of check valve (= 49.7 g)
 P_E : pressure at downstream end of pipeline
 P_S : supply pressure
 P_V : pressure in vessel
 q_c : volumetric fluid flow rate through check valve orifice

q_s : volumetric fluid flow rate through solenoid-operated valve
 t : time
 t_w : pulse width
 U_c : volume at connection part ($= 0.220 \times 10^{-4} \text{m}^3$)
 U_V : volume in vessel ($= 5.0 \times 10^{-3} \text{m}^3$)
 V : average flow velocity at line section
 V_E : average flow velocity at line section of downstream end
 V_V : average flow velocity at line section of check valve inlet
 w : ratio of current open area of solenoid-operated valve to its total open area
 x : coordinate in axial direction of pipeline
 Y : check valve displacement
 Y_0 : check valve initial compression length ($= 4.4 \text{mm}$)
 α : valve angle between vertical and poppet face ($= \pi / 4 \text{rad}$)
 ν : kinematics viscosity of fluid ($= 3.83 \times 10^{-5} \text{m}^2 / \text{s}$)
 ρ : fluid density ($= 853 \text{kg} / \text{m}^3$)
 λ : loss factor

INTRODUCTION

Since an oil (water) hammer generates much higher pressure than the supply pressure, it occasionally destroys a device. There are many measures that may be taken against the disadvantages of the oil hammer. However, the authors propose to actively utilize this pressure rise phenomenon. A new type of hydraulic pressure intensifier was already proposed and developed [1][2][3]. Many hydraulic machines are large and heavy. There are a large number of examples of waste from high pressure and large flow volumes supplied by a pump. Our intensifier uses an oil hammer to convert low-pressure fluid from a supply pump to a high pressure one only when necessary. Therefore, the hydraulic pressure source can be small, and energy is saved.

The purpose of this research is to apply this device to the real construction machine. A vessel is used as a model of a hydraulic cylinder without displacement. The pressure of the vessel is a control object. The volume in a vessel is made with a large capacity of 5 liters. The experiment is done to investigate the condition when a construction machine is actually working. The necessary pressure level is thought to be around 30MPa. We develop a block diagram for the simulation of the system

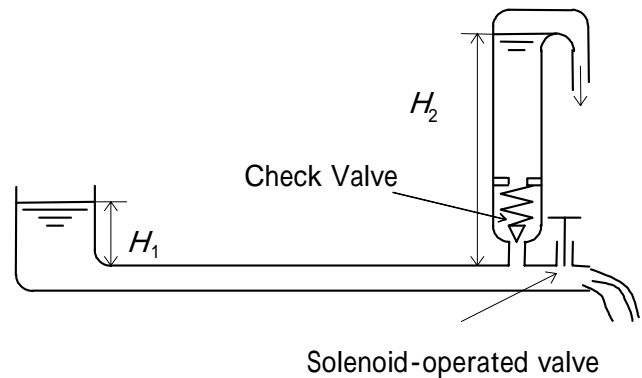


Fig.1 Concept of the new hydraulic pressure intensifier

considering the pipeline dynamics. The simulation results are easily obtained using MATLAB SIMULINK. We also obtain the accurate simulation results using Fortran program made by the authors. We research the characteristics through the experiment and simulation.

CONSTRUCTION

Figure 1 shows the principle of the new pressure intensifier. When the solenoid-operated valve at the downstream end of the pipeline is open, fluid supplied with a constant pressure flows through the pipeline. If the valve is shut quickly, an oil hammer is generated in the pipeline. The check valve is used to release the high pressure generated. Pressure much higher than the supply pressure can be continuously released by opening and shutting the solenoid-operated valve repeatedly.

The concept is applied to the pressure intensification of a hydraulic cylinder as shown in Fig.2. This equipment is composed of a pipeline, a check valve, a solenoid-operated valve, and a personal computer for on-off operation of the solenoid-operated valve. The hydraulic cylinder is the controlled object.

When the solenoid-operated valve is kept shut, the pump pressure is directly supplied to the hydraulic cylinder. If the solenoid-operated valve is turned on, oil flows at high speed through the pipeline to the tank. By cutting off the current to the solenoid-operated valve, the valve is shut and an oil hammer is generated in the pipeline. If the pressure at position in Fig.2 is higher than the pressure at position , the check valve opens and high-pressure fluid is discharged into the hydraulic cylinder. The pressure in the hydraulic cylinder is made

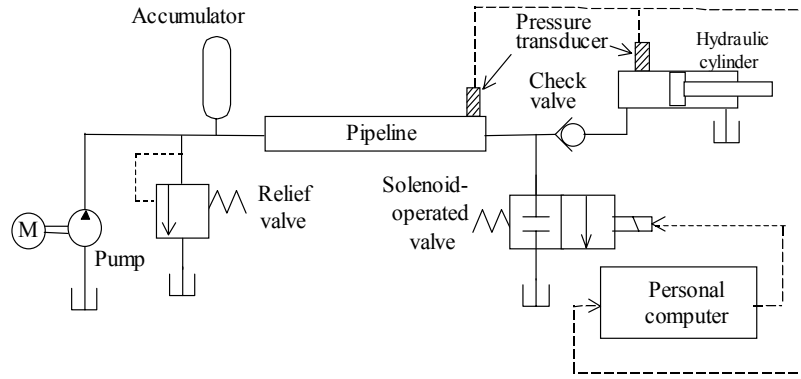


Fig2. Schematic diagram of the test ring

much higher than the one supplied by the pump. The hydraulic cylinder produces much bigger force than the force which is produced by the pressure supplied directly from the pump. When the pressure at position becomes lower than the pressure at position , the check valve shuts and prevents the fluid from flowing backwards. A vessel is used as the model of a cylinder without displacement.

BASIC EQUATIONS FOR SIMULATION

Basic equations related to the pipeline, the check valve and the vessel are analyzed and shown by simulation. The interaction of an oil hammer and the check valve is considered.

Relation between pressure and flow velocity in the pipeline

In this research, the improved version [4] of Zielke's characteristics method is used to obtain the relation between the pressure and the flow velocity in the pipeline. The relations between the pressure and the flow velocities of the adjoining two points R and S, and the point N on the $x-t$ plane [4] are given by the following equations. N is the middle and x away from points R and S. The time at N is t later than the time at R and S.

$$V_N - V_R + \frac{g}{a}(H_N - H_R) + gh_{fR}\Delta t = 0 \quad (1)$$

$$V_N - V_S - \frac{g}{a}(H_N - H_S) + gh_{fS}\Delta t = 0 \quad (2)$$

h_f indicates the transient pressure head loss per unit

length and it is obtained using the method shown in reference [4]. When the pressure is lowered below the atmosphere pressure, vapor-liquid model is used [5][6].

Relation between pressure drop and flow velocity at the check valve

$$\pm \frac{1}{2g} \left(\frac{q_c}{c_f \pi D_E Y \sin \alpha} \right)^2 + \frac{L_3}{g} \frac{dV_V}{dt} = H_E - H_V \quad (3)$$

(+ : regular flow - : reverse flow)

$$A_3 V_V = q_c + A_E \frac{dY}{dt} \quad (4)$$

Motion of the poppet in the check valve

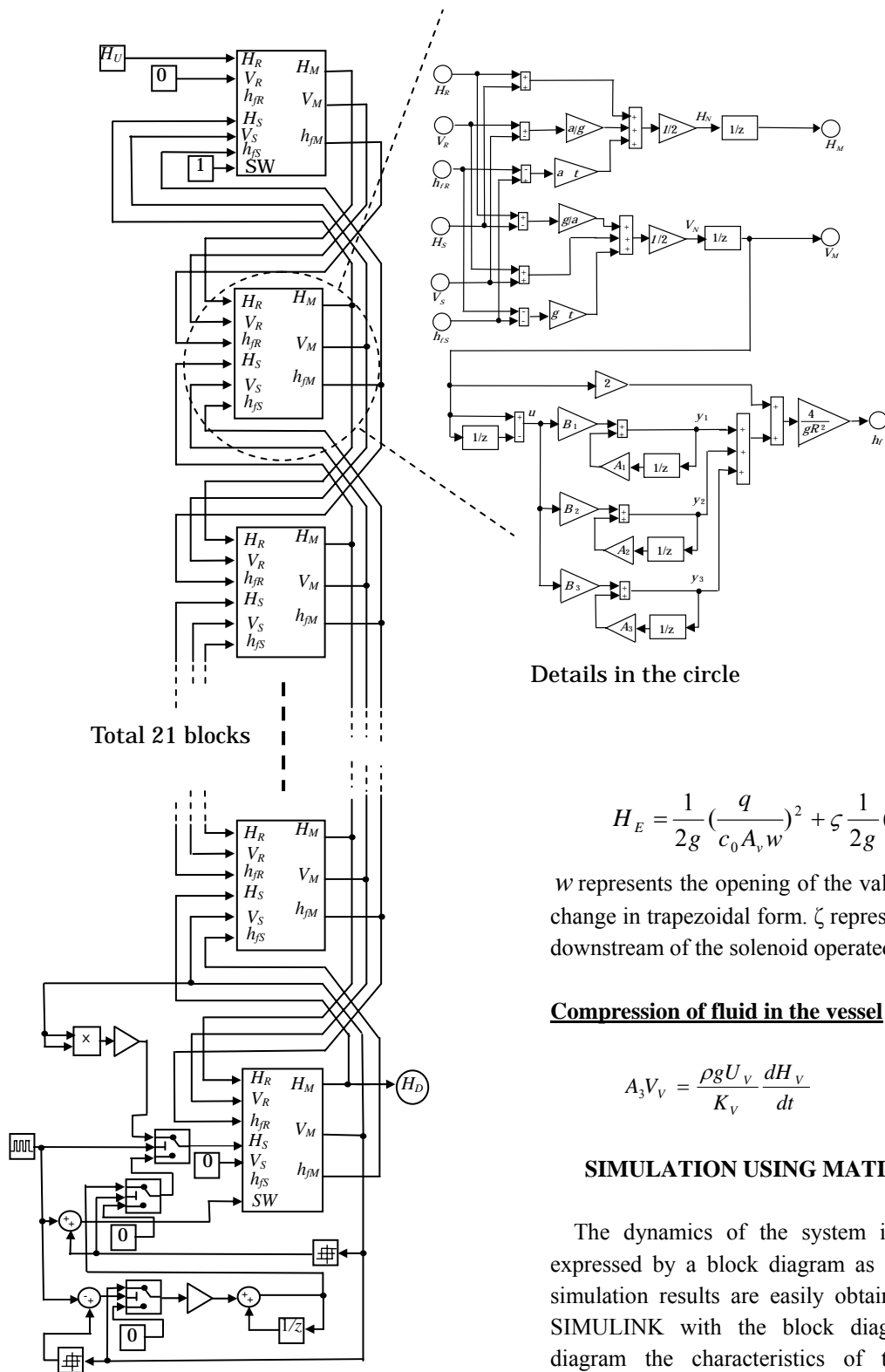
$$M_E \frac{d^2 Y}{dt^2} + C_E \frac{dY}{dt} + K_E Y = f - M_E g - K_E Y_0 - F_C \operatorname{sgn} \left(\frac{dY}{dt} \right) \quad (5)$$

$$f = (1 - 4c_f \frac{Y}{D_E} \sin 2\alpha) \rho g A_E \times (H_E - H_V - \frac{L_3}{g} \frac{dV_V}{dt}) \quad (6)$$

where $Y \geq 0$ is assumed.

Equation for fluid compression at the connection between the solenoid-operated valve and the pipeline

$$A V_E - A_3 V_V - q_s = \frac{\rho g U_C}{K_V} \frac{dH_E}{dt} \quad (7)$$



$$H_E = \frac{1}{2g} \left(\frac{q}{c_0 A_v w} \right)^2 + \zeta \frac{1}{2g} \left(\frac{q_s}{A_v} \right)^2 \quad (8)$$

w represents the opening of the valve and is assumed to change in trapezoidal form. ζ represents loss factor at the downstream of the solenoid operated valve.

Compression of fluid in the vessel

$$A_3 V_v = \frac{\rho g U_v}{K_v} \frac{dH_v}{dt} \quad (9)$$

SIMULATION USING MATLAB SIMULINK

The dynamics of the system including pipeline is expressed by a block diagram as shown in Fig.3. The simulation results are easily obtained using MATLAB SIMULINK with the block diagram. In this block diagram the characteristics of the check valve is idealized.

Fig.3 Block diagram of the system

COMPARISON BETWEEN THE SIMULATION AND THE EXPERIMENT

The solenoid-operated valve is opened and closed by the frequency 8Hz and the pulse width t_w 50ms in this experiment. The frequency of 8 Hz means that the period is 125ms. The current is ON-state for 50ms during 125ms. The supply pressure $P_s = 6.86$ MPa. The pipeline length $L = 4.15$ m and the inner diameter $D = 6$ mm. The experimental results and the simulation results of the pressures at the downstream end and in the vessel for 0.5 second from the beginning are shown in Figs 4, 5 and 6. The results for 10 seconds are shown in Figs. 7 and 8. Fig.4 shows the simulation results of MATLAB SIMULINK. Figs.5 and 7 show the simulation results of FORTRAN program made by the authors.

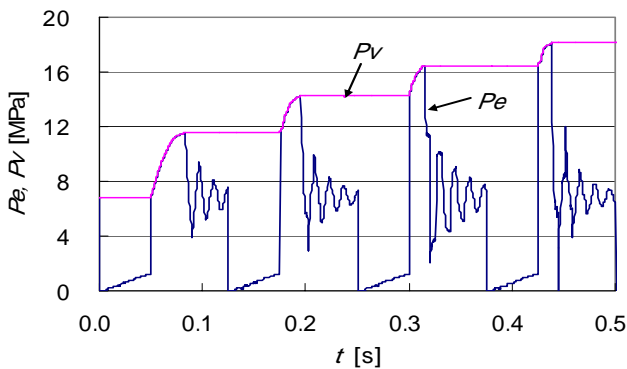


Fig.4 Pressures in the vessel (P_v) and at the downstream end (P_e) of the pipeline obtained by MATLAB SIMULINK simulation for 0.5 s from the beginning.

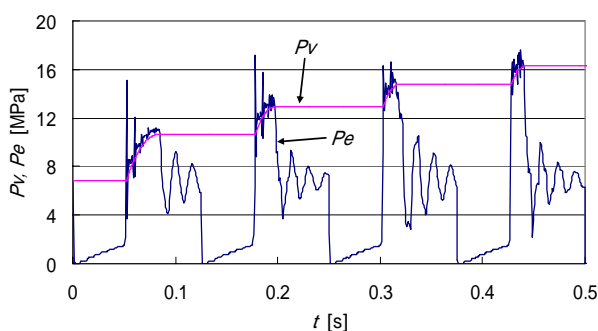


Fig.5 Pressures in the vessel (P_v) and at the downstream end (P_e) of the pipeline obtained by the simulation program made by the authors during 0.5 s from the beginning.

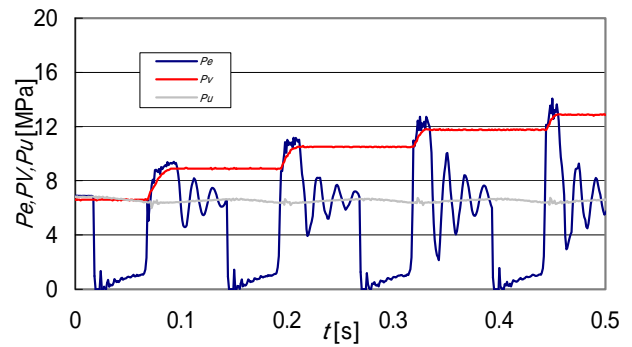


Fig.6 Experimental results of pressures in the vessel (P_v) and at the downstream end (P_e) and upstream end (P_u) of the pipeline.

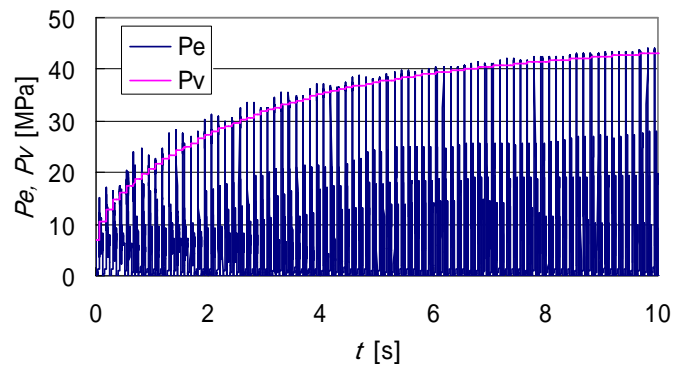


Fig.7 Simulation results of pressures in the vessel (P_v) and at the downstream end (P_e) of the pipeline obtained by the program made by the authors for 10 s from the beginning.

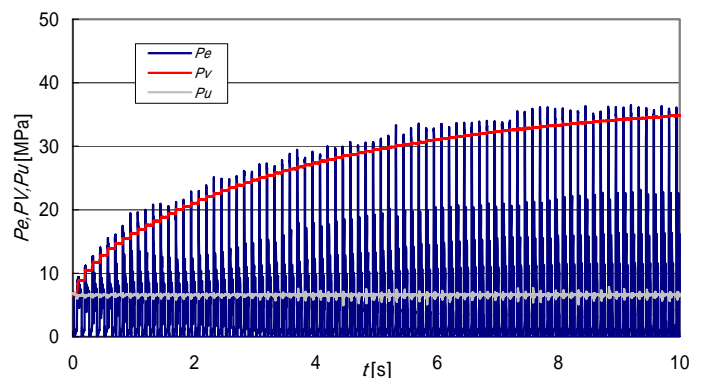


Fig.8 Experimental results of pressures in the vessel (P_v) and at the downstream end (P_e) and upstream end (P_u) of the pipeline during 10 s from the beginning.

PRESSURE INCREMENT IN THE VESSEL

The results in Figs. 7 and 8 show that the pressure increment in the vessel almost saturates in 10 seconds and the pressure of the experiment exceeds 30 MPa.

The pressure obtained by the experiment is less than the one obtained by the simulation. The difference increases with the supply pressure increment and the inner diameter increment. The pressure at the downstream end increases when the diameter is increased to 8 mm from 6 mm. Because the pressure drop through the test pipeline is reduced due to the pressure increase at the downstream end, the flow velocity is not so increased as expected. Therefore the pressure in the vessel is not so increased as expected when the diameter is increased exceeding 6 mm.

RELATION BETWEEN THE PRESSURE INCREMENT AND THE PIPELINE PARAMETERS

In the previous section, the length of the pipeline is 4.15 m and the inner diameter is 6mm. The pressure obtained in the vessel, are shown in Fig.9 when the length and the diameter of the pipeline are changed.

Fig. 9 shows the pressures obtained after an oil hammer is generated 80 times. They are obtained after 10 seconds because the frequency of opening and closing the solenoid operated valve is 8 Hz.

The experimental results are smaller than the simulation results. The leakage at the poppet and the flow resistance at some places may influence the experimental results. The simulation result has a peak point to the pipeline length. The experimental result seems to have a peak point at the pipeline length longer than 4m. There is a tendency that smaller pipe diameter gets higher pressure when the pipeline length is short, and bigger pipeline diameter gets higher pressure when the pipeline length is long.

CONCLUSION

A pressure of more than 30 MPa was obtained by our intensifier from the supplied pressure 6.86 MPa. This is our target to apply this equipment to a real working machine as a construction machine.

The dynamics of the system including pipeline is expressed by a block diagram. The simulation results are

easily obtained using MATLAB SIMULINK with the block diagram. Also, the simulation results are obtained by FORTRAN program made by the authors.

It is clarified that the phenomenon is expressed with a theoretical formula by comparing the experimental result and the simulation result. However, in case of a shorter pipeline, thicker diameter, or higher supply pressure, the experimental value becomes smaller than the simulation result.

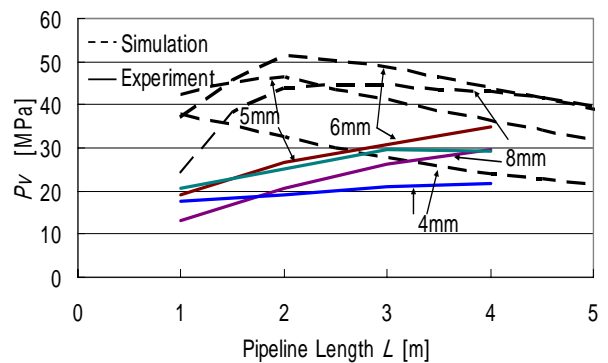


Fig. 9 Pressure in the vessel after oil hammer is generated 80 times. (Results of Simulation and experiment)

REFERENCES

- [1] Suzuki, K., 1989, "Application of a New Pressure Intensifier Using Oil Hammer to Pressure Control of a Hydraulic Cylinder," ASME Journal of Dynamic Systems, Measurement and Control, 111-2, pp.322-328
- [2] Suzuki, K., 1990, "A New Hydraulic Pressure Intensifier Using Oil Hammer," ASME Journal of Fluids Engineering, 112-1, pp.56-60
- [3] Suzuki, K., Asahara, K., Narita, R., 2000, "Application of a Pressure Intensifier Using an Oil Hammer to a Hydraulic Motor Control," Trans. JSME B, 66-644, pp.1105-1111
- [4] Suzuki, K., 1991, "Improving Zielke's method of Simulating Frequency-Dependent Friction in Laminar Liquids Flow," ASME Journal of Fluids Engineering, 113-4, pp.569-573
- [5] Wylie, E. B., Streeter, V. L., 1978, "Fluid Transients," McGraw-Hill, pp136-139
- [6] Sanada, K., Kitagawa, A., Takenaka, T., 1990, "A Study on Analytical Methods by Classification of Column Separations in a Water Pipeline," Trans. JSME B, 56-523, pp585-593

PROPOSAL OF MULTI-FUNCTIONAL MATERIAL HANDLING MACHINE APPLYING HYDRAULIC SYSTEM OF EXCAVATOR

Eiji EGAWA*, Yoshihiro HOSHINO**, Takayuki EGUCHI*** and Masaharu IKUTA***

* Technical Research Center
Hitachi Construction Machinery Co., Ltd.
650, Kandatsu-machi, Tsuchiura-shi, Ibaraki-ken, 300-0013 Japan
(E-mail: egawa89@hitachi-kenki.co.jp)
** Business Planning Dept.
Hitachi Construction Machinery Co., Ltd.
5-1, Koraku 2-chome, Bunkyo-ku, Tokyo, 112-8563 Japan
*** Application and New Product Div.
Hitachi Construction Machinery Co., Ltd.
5-1, Koraku 2-chome, Bunkyo-ku, Tokyo, 112-8563 Japan

ABSTRACT

Recently, excavator is used for not only civil engineering but also building demolition, scrap recycling and so on. The reason is thought that it has a general-purpose power supply system and is able to move by itself. In other words, it could be considered a kind of high-powered robot. As a whole, it consists of several modules. Divided roughly by each function, power module such as an engine and pumps, working module such as front structures and hydraulic actuators, traveling module such as crawlers or wheels, operation module such as control levers and pedals. In this time, to gather and carry lots of objectives in scrap yard or somewhere, both a fork grapple and a loader bucket are equipped as a working module. And to carry the objectives quickly to destination, wheeled traveling system is equipped. As a result, we have produced a multi-functional handling machine which has double front attachments and wheels. Then if operators cooperate the modules effectively, they will be able to handle their work more efficiently.

KEY WORDS

Excavator, Hydraulic, Robot, Material, Handling

INTRODUCTION

Recently, excavator is used for not only civil engineering but also building demolition, scrap recycling and so on. For example, Figure 1 shows a car demolisher, which demolishes the body and sorts the parts of scrapped cars. Then the operator is able to control the grapple for the objects delicately because of the control ability of excavator's actuators. I think the reason of the multi use is that it has a general-purpose power supply system and is able to move by itself. In other words, it could be considered a kind of boarding-type high-powered robot.



Figure 1 Car demolisher

As a whole, an excavator consists of several function modules. Divided roughly, power module such as an engine and pumps, working module such as front attachments and hydraulic actuators, traveling module such as crawlers or wheels and operation module such as control levers and pedals. Figure 2 shows the example of the function modules of Hitachi mini excavator Zaxis40UR.

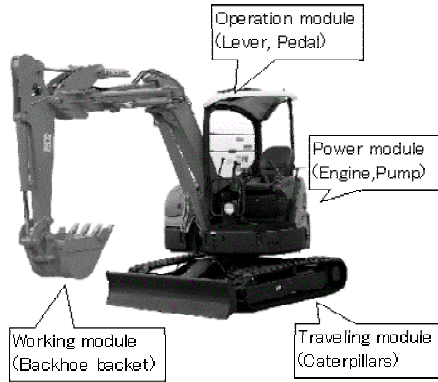


Figure 2 Hitachi mini excavator Zaxis40UR

APPLICATION EXAMPLE

In this time, applying the excavator, we have investigated a multi-functional handling machine, which could gather and carry lots of objects in scrap yards or the other places. For example of works Figure 3 shows the situation of industrial waste yard and Figure 4 shows the situation of disaster area in Sumatra Island.



Figure 3 Industrial waste yard



Figure 4 Disaster area in Sumatra Island (2004)

Usually an excavator and a truck are necessary for the works. Of course, two operators are also necessary at least. So if the works could be done by one machine efficiently, the job efficiency goes up and the energy of machines is saved. Then both a fork grapple and a loader bucket are used to sort and gather the objects. And a wheel traveling system is suitable to carry them quickly to the destination.

SYSTEM OF THE MACHINE

Figure 5 shows a picture of the developed machine. As you guess, the base machine is Zaxis40UR of figure 2. Power module is common with it. But traveling module is changed to wheel type and two different type fronts are used as working modules. Using upper fork grapple, we can do delicate works such as object sorting. And using lower loader bucket and wheel, we can gather and carry them to the destination efficiently.

Table 1 shows the specifications of the machine. The travel speed is not so fast but is enough to travel in a yard. The hydraulic circuit (Figure 6) is based on the load-sensing system of Zaxis40UR. It's easy to add the optional systems by connecting the pressure line in common.

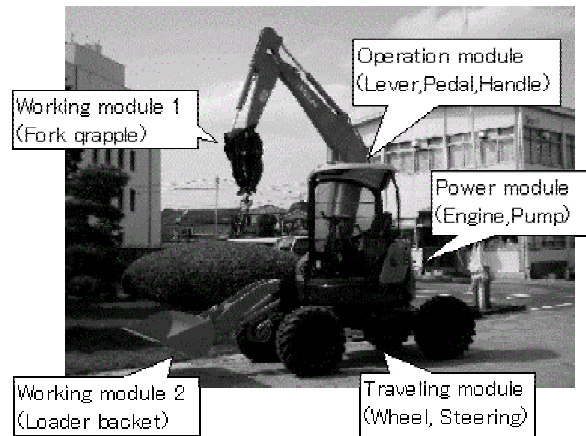


Figure 5 Developed machine

Table 1 Specification of the machine

Item	unit	Value
Machine weight	kg	3957
Engine output	kW	20.6
Travel speed	km/h	10
Weelbase	mm	2000

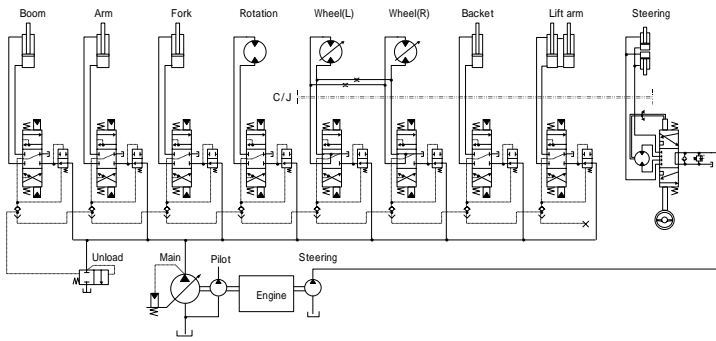


Figure 6 Hydraulic circuit

SPECIFICATION OF MODULES

Front Attachments

Figure 7 shows front working range of the machine. Wide working range is necessary as a backhoe front to deal various objects. And high dumping height is necessary to dump them to a loading platform of truck. Using both fronts like broom and dustpan, we can gather objects efficiently.

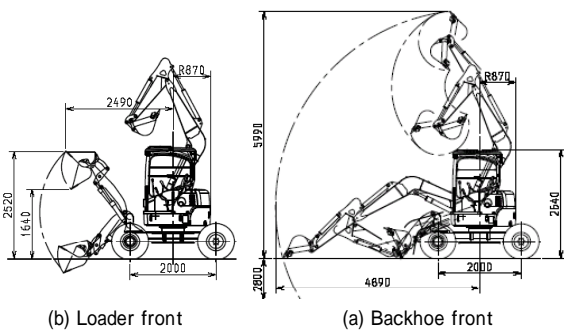


Figure 7 Front working range

Traveling System

The main hydraulic circuit of the wheel system is the same as the original open circuit for crawlers, not using HST system. The reason is to simplify the system and to cut down the cost and term of development. Then the travel performance might be not so high compared with HST. So I planned simulation to certify the performance and investigate the parameters in advance.

Figure 8 shows the simulation model and Table 2 shows the specifications. The counter valance valve is to prevent body falling in slope. The travel feeling depends on the characteristics of valves. So we tuned the size of valve chokes and the set pressure of relief valve by simulation to realize desired acceleration and deceleration feeling. As a result, the acceleration is good and the shock is about under 0.2G (Figure 9). Well, the drift of experiment speed is caused by the indirect calculation with acceleration.

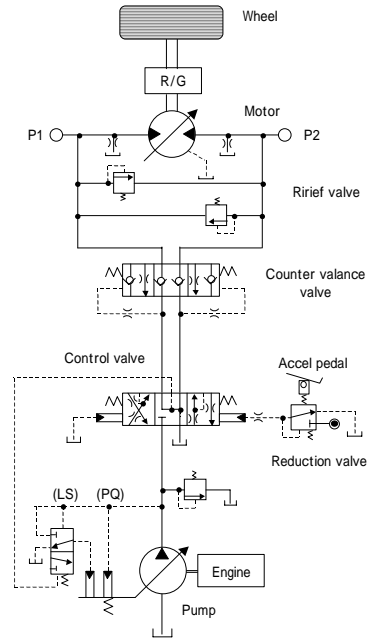


Figure 8 Simulation model of traveling system

Table 2 Specification of traveling system

Item	Unit	Value
Wheel diameter	mm	860
Equivalent inertia	kg·m ²	370
Gear ratio		1/48.636
Motor volume	cm ³	11.6 ~ 18.0
Pump volume	cm ³	8.5 ~ 38
Ririef Pressure	MPa	27
Engine speed	min ⁻¹	1175 ~ 2500

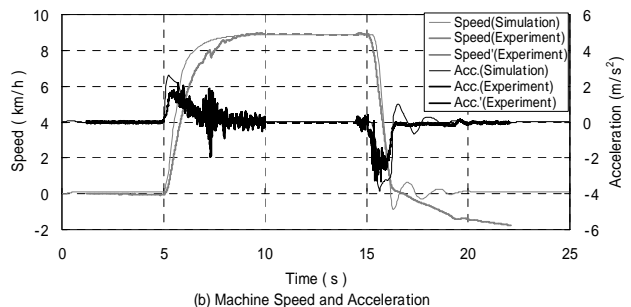
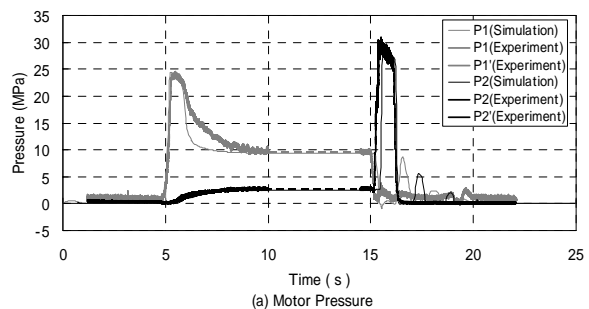


Figure 9 Simulation and experiment result

Operating System

At present we still apply combination of usual operating systems for it (Figure 10). Handle and pedals are used to operate the traveling system. Forward right lever is for Loader bucket. They are the same as usual ones of wheel type machine like a wheel loader. And two levers at seat side are common with excavator's ones.

Figure 11 shows a working situation in industrial waste yard. Professional operators could control this machine very well using the operating system in a few hours. And they didn't complain the control ability especially. But now I think that farther advanced mechatronic system will become necessary for more cooperative motion in the future [1]. For example figure 12 shows master-slave control system of excavator, which was developed several years ago and called one-lever system by us [2]. Usually this technology is used to control manipulators [3].

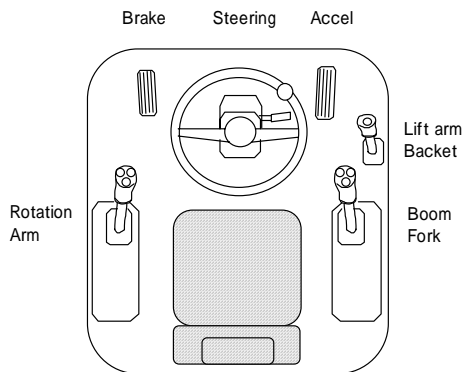


Figure 10 Operating system



Figure 12 One-lever system



(a) Sorting



(b) Traveling



(c) Dumping

Figure 11 Example of working situation

CONCLUSION

Now we proposed a multi-functional handling machine as a kind of high-powered robot. The feature is the working ability by double front attachments and the mobility by wheel traveling system. From now on such multi-functional machines will be developed more and more with low cost and high reliability, applying the hydraulic system of excavators.

REFERENCES

1. Rydberg K-E., Mechatronic System Design Applied on Fluid Power Technology, Fifth JFPS International Symposium, 2002, pp.811-817
2. E. Egawa et al., Development of One-lever type Control System for Excavator, The 9th Symposium on Construction Robotics in Japan, 2002, pp.100-108
3. K. Kato and S. Hirose, Proposition and Basic Experiments of Shape Feedback Master-Slave Arm, Journal of Robotics and Mechatronics, 2000, pp. 268-274

ELECTROMAGNETIC MINIATURE PUMP USING PERISTALTIC MOTION OF INTERCHANGEABLE FLEXIBLE TUBE

Yasukazu SATO*, Masanori HASHIMOTO*, Shengnian CAI** and Nobuyoshi HASHIMOTO**

* Department of Mechanical Engineering, Faculty of Engineering
Yokohama National University
79-5 Tokiwadai, Hodogayaku, Yokohama, Kanagawa, 240-8501 Japan
(E-mail: yasukazu@ynu.ac.jp)
** Shinwa Controls Co.,Ltd.
2-8-4 Gorikida, Asaoku, Kawasaki, Kanagawa, 215-0025 Japan

ABSTRACT

This paper presents an electromagnetic miniature pump using peristaltic motion of an interchangeable flexible tube. Four hinge-type electromagnetic actuators arranged serially in one line pinch a flexible tube and generate peristaltic motion on the tube. In order to reduce electric power consumption, the magnetic latch mechanism using permanent magnets is applied to the actuator drive. As the actuator pinches the outside wall of the interchangeable tube, this pump can deal with any liquids inside the tube. The prototype pump has the flow rate range of 0.1~1cm³/min and the maximum pressure of 13kPa by a battery drive. This paper shows the electromagnetic design of the actuator using the FEM magnetic field analysis. The optimum drive sequence of the pinching actuators and the experimental result of pump characteristics are reported. Furthermore, feasibility consideration of application to the portable intravenous drip system for medical treatments is carried out.

KEY WORDS

Pump, Electromagnetic Actuator, Power Saving, Flow Control, Latch Mechanism

INTRODUCTION

A pump which pressurizes the fluid inside the elastic tube by pinching it from the outside of the tube is generally applied to the sanitary/medical applications and the chemical analyzers. Due to the existence of an interchangeable tube wall between the fluid and the mechanical parts, it can deal with various kinds of fluid (acid, alkaline, etc.), and can prevent the fluid from contaminating. It also requires no cleaning because the fluid is changed with the interchangeable tube at the same time. The commercialized pumps of that type generally consist of the elastic rubber tube looped along

the cylindrical inner wall, and the rollers squeezing the tube as shown in Fig.1. The roller unit is usually driven by a rotary actuator such as an electric motor. In this system, the precise rotational speed control of the rotary actuator in wide speed range from very slow up to high is necessary for the flow rate control. In order to realize the flow rate control in simpler configuration, this paper presents the different pump mechanism from the rotary type. The proposed pump system pinches an elastic tube by means of serially-arranged hinge type electromagnetic actuators and generates the peristaltic pumping motion on the tube by the sequential action of the actuators. Furthermore the power saving drive of the

pump system on the condition of the battery drive is described.

CONFIGURATION OF MINTURE PUMP SYSTEM AND ITS APPLICATION

The portable intravenous drip infusion system is specified as the design target application of the proposed pump system. The movable intravenous drip equipment is not generally compact and limits the sphere of activity of the patient. Patient who has the scheduled medication by injection also has same restriction in his daily life. The proposed system shown in Fig.2 consists of the medicine liquid package in the breast pocket, the elastic tube run along the shoulder and arm, and the proposed pump actuator unit with the controller on the upper arm. The medicine liquid is transfused into the body at the forearm just like the conventional intravenous drip infusion. Table 1 indicates the required pump performance of the portable intravenous drip infusion system.

Figure 3 shows the hinge-type electromagnetic actuator used in the proposed pump. The actuator generates the force pinching the elastic tube between the armature and stator when the actuator is activated. The armature is returned by the elastic force of the tube when it is inactivated. It generally wastes electric power to keep the pinching position by continuous energizing of the coil. Therefore, the power consumption becomes large, especially in the drive mode having long interval. For reduction of power consumption, the magnetic latch mechanism using the permanent magnet inserted into the magnetic circuit is adopted to this actuator. The magnetic latch mechanism is common technology but very effective to the power saving drive of electromagnetic ON/OFF actuator [1].

MAGNETIC LATCH MECHANISM

Figure 4 shows an example of the force-displacement characteristics of a solenoid actuator with magnetic latch mechanism. The elasticity of the tube and pressure of the fluid inside the tube are assumed as a spring load. At the non-energized and open position, the actuator keeps open position because the attractive force generated by the permanent magnet is lower than the spring load. Then, the instantaneous energizing to the coil in the same direction as the permanent magnet magnetic field activates the actuator to the closed position (①) because the total attractive force overcomes the spring load. The actuator keeps closed position (②) without energizing. Therefore, no electric power is consumed. The instantaneous energizing to the coil in the counter direction for the permanent magnet magnetic field reduces the total attractive force, and then the actuator is released by the spring load. Because

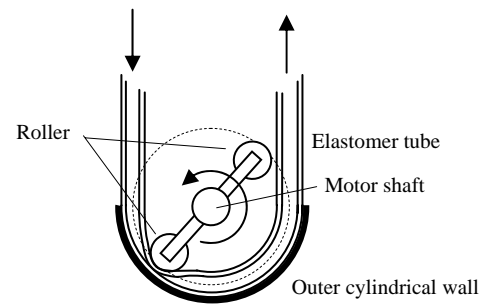


Figure1 Rotary type tube pump

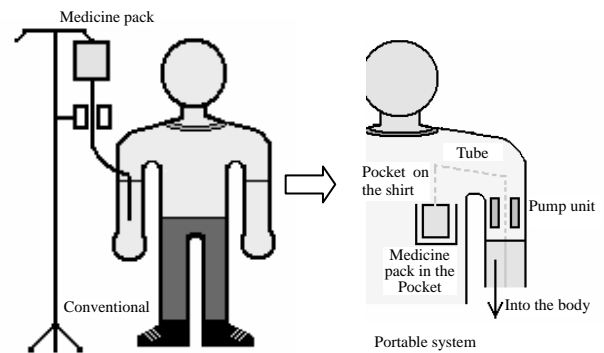


Figure 2 Concept of portable liquid medicine

Table 1 Required specifications of small electromagnetic pump

Pressure (max.)	over 13kPa
Controllable flow rates	0.1 cm ³ /min ~ 1.0 cm ³ /min
Power source	Rechargeable battery cell (Ni-MH)

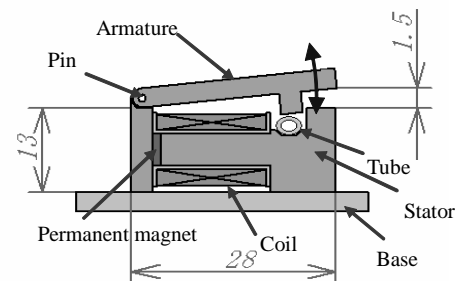


Figure 3 Hinge-type electromagnetic actuator

the instantaneous energizing works as only the trigger of actuator motion, the actuator wastes no electric power at the steady state, which occupies most of the actuator state.

The permanent magnet inserted into the magnetic circuit is exposed to inverse magnetic field to release the actuator. Therefore, permanent magnet material is key factor to the performance of the magnetic latch mechanism. Neodymium magnet (Nd-Fe-B) is applied to the actuator because of its toughness against demagnetization compared with ferrite or Alnico permanent magnets. The size of the permanent magnet is determined by consideration of balance between the required actuator force and the demagnetization effect caused by the energized coil, with the aid of FEM magnetic field analysis.

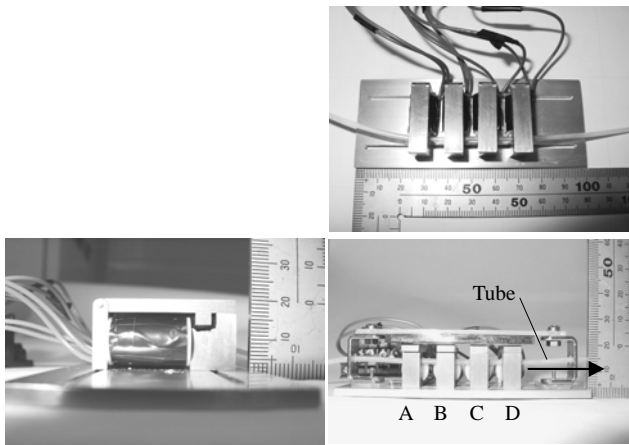


Photo 1 Electromagnetic pump unit

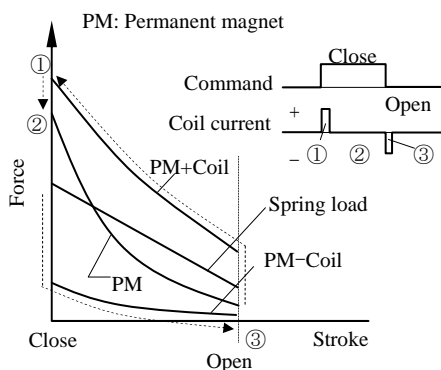


Figure 4 Electromagnetic latch mechanism

DESIGN OF MINITURE PUMP SYSTEM USING HINGE-TYPE ELECTROMAGNETIC ACTUATORS

Photo 1 displays the miniature pump which consists of four serially arranged hinge type actuators shown in Fig. 3. Here, each actuator is indicated as A, B, C and D from the left as shown in the photo. The peristaltic motion is generated on the tube by the sequential action of each actuator as shown in Fig.5. Then, the fluid is delivered from the right to the left in Photo 1.

One cycle of pumping is illustrated in Fig.6. The flow rate is controlled by the modulation of cycle. The closed actuator keeps its position without electric power consumption and acts as a check valve. Counter sequence against the cycle in Fig.6 makes pumping action of counter direction flow. When all the actuators are in open position, the pump unit does not restrict the flow inside the tube.

The maximum discharge pressure of the pump mainly depends on the pinching force of the hinge-type actuator. Figure 7 shows an example of FEM analysis of pinched tube. As the result of FEM deformation analysis, the required pinching force to make no clearance in the tube is estimated 5N for the tested silicone tube with inner tube diameter of 1mm, the wall thickness of 0.5mm under the inner pressure of 13kPa. This simulated force is experimentally confirmed by the leakage test as shown in Fig.8. A silicone tube pressurized at 13kPa is squeezed by a linear actuator, and the pinching stroke

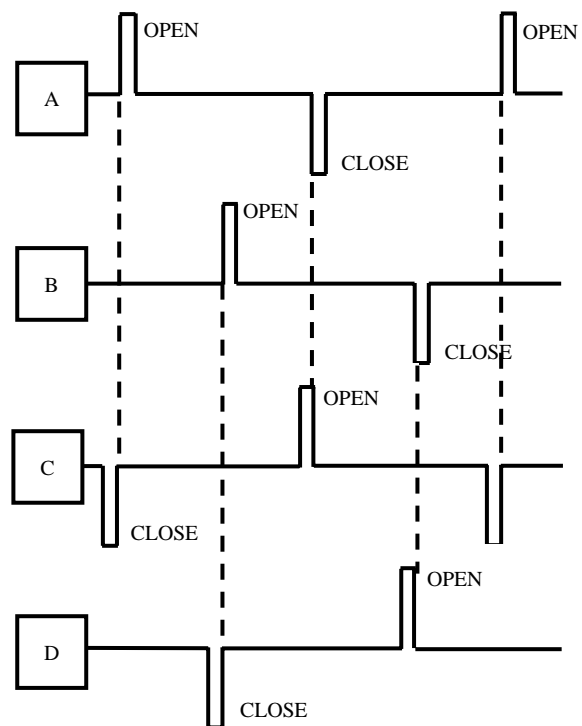


Figure 5 Drive sequence of pump unit

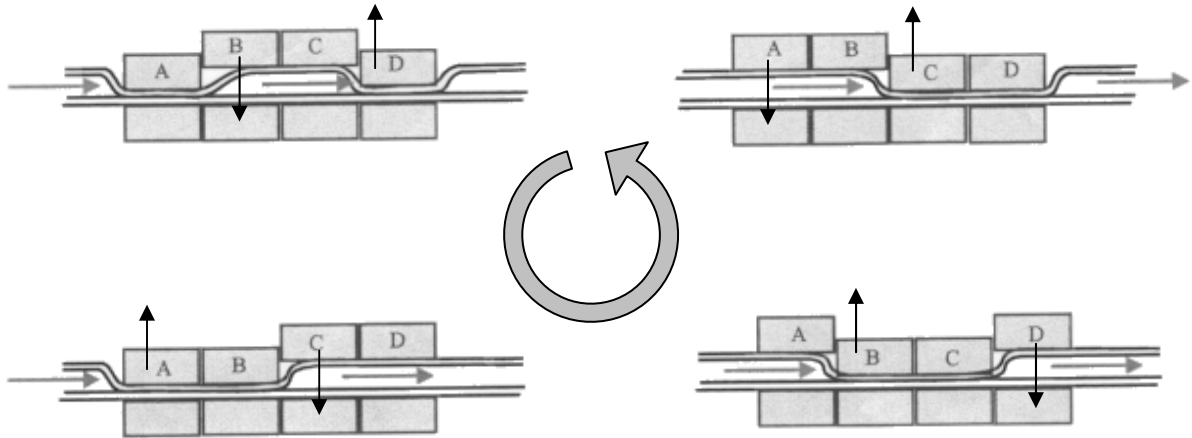


Figure 6 Peristaltic motion of elastic tube generated by the hinge-type electromagnetic actuators

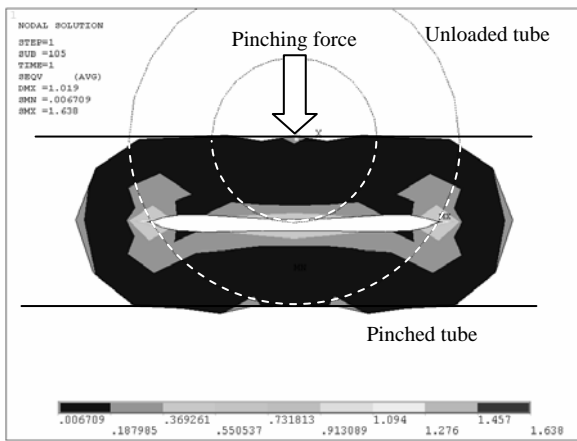


Figure 7 FEM analysis of pinched tube

and force are measured at the same time. The pinched wall of the tested tube is completely adhered at squeezing of 1.2 mm in which the no leakage is observed.

The dimensions of the actuator are determined to realize the required force and stroke against the inner pressure of the tube, using FEM magnetic field analysis. Figure 9 shows the result of the FEM magnetic field analysis of the actuator. For the tested silicone tube, the actuator is required the force over 5N in whole range of the stroke by attraction due to the PM and coil. The shape of actuator and the size of the permanent magnet are optimized to satisfy the force – stroke characteristics shown in Fig.4 [2], [3].

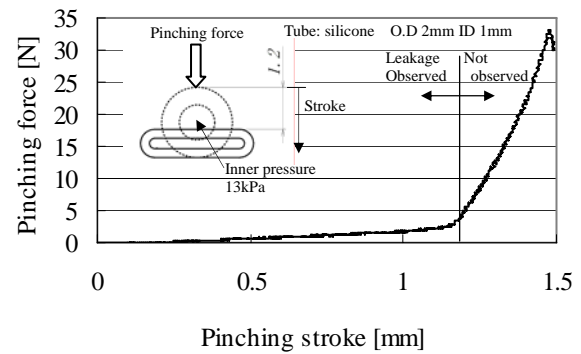


Figure 8 Experiment to determine the pinching force and stroke for no leakage

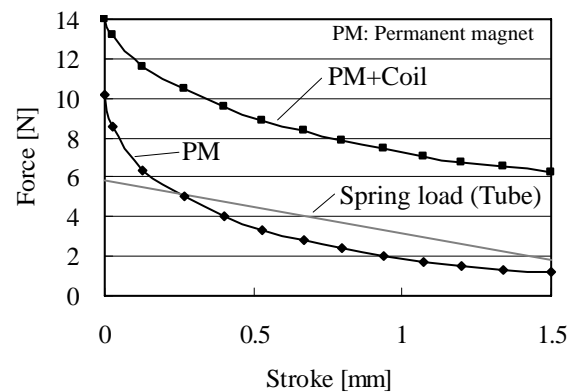


Figure 9 Calculated force-stroke characteristics using FEM magnetic field analysis

PERFORMANCE OF THE PROTOTYPE MINITURE PUMP

Figure 10 shows the schematic diagram of a full-bridge electric circuit generally used for the electric driver of solenoid with the latch mechanism. A commercial product IC package having 4 full-bridge circuits inside is applied to the driver of the prototype miniature pump. Figure 11 shows the flow rate control characteristics of the prototype miniature pump, in which the drive frequency is determined by the reciprocal of the cycle. Tap water is used as working fluid. It is confirmed that

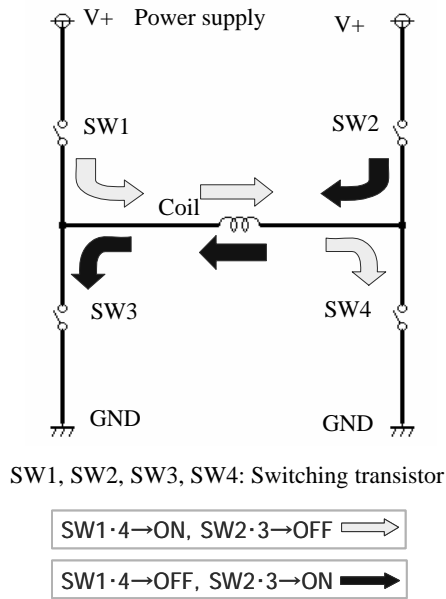


Figure 10 Full-bridge electric circuit for solenoid driver with latch mechanism

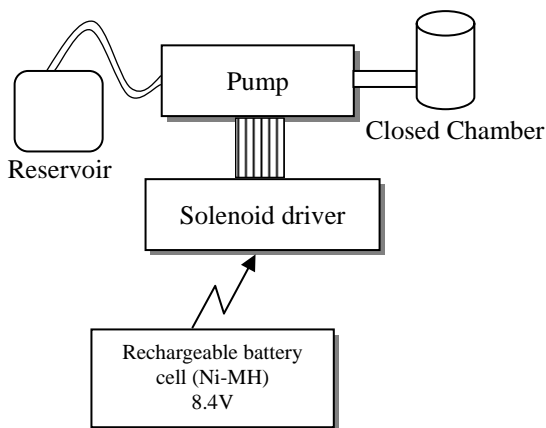


Figure 12 Testing circuit for the maximum discharge pressure measurement

the linearity of flow rate control is guaranteed in the range from 0.1 to 1.0 cm³/min, which satisfies the design requirement in Table 1. In the range above the drive frequency of 3 Hz, the flow rate becomes less than the approximate line representing the linearity. The reason of this divergence is considered that the proportion of releasing time due to the elasticity of the tube in the cycle becomes large, and then the restoration of the tube is not significant.

The maximum discharge pressure of the pump is measured using the testing circuit shown in Fig.12. The pressure in the chamber rises up to the maximum discharge pressure during pumping. Figure 13 gives the

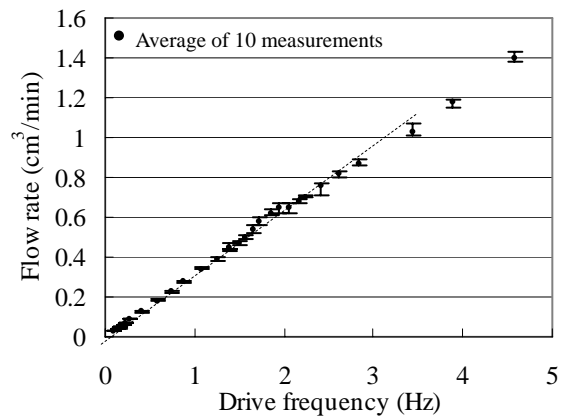


Figure 11 Drive frequency – flow rate characteristics

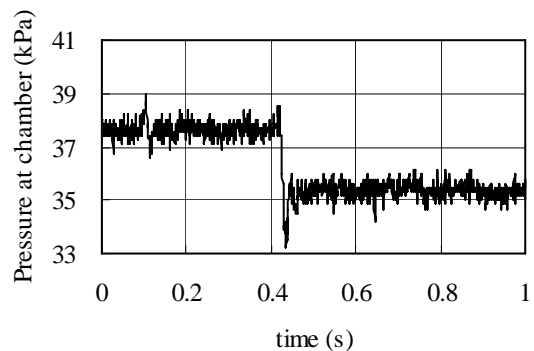


Figure 13 Measurement of the max. discharge pressure

Table 2 Test results of continuous run by full-charged battery(Ni-MH 8.4V)

Drive freq.(Hz)	1.0	2.0	3.0	4.0
Time (hr.)	36	18	12	9

transient pressure in the chamber. The pressure saturates at 38kPa and suddenly falls to 35kPa. At the pressure of around 38kPa, the closing of the actuator becomes unstable because the spring load consisting of the elasticity of the tube and the pressure inside the tube is comparable with the pinching force. Therefore, the maximum discharge pressure is regarded as about 35kPa.

Electric power is supplied from 9V-type Ni-MH rechargeable battery cell (Output voltage: 8.4V) to the solenoid driver. Table 2 shows the continuous run time by full-charged battery. The full-charged battery runs the pump for 12 hours at the drive frequency of 3Hz continuously. It is sufficient performance for the portable intravenous drip infusion system. From the viewpoint of energy balance, the continuous run time is expected to be in inverse proportion to the drive frequency. However, it depends upon the electric performances of driver and controller. If those devices are not designed well, the continuous run time would be considerably reduced, because they continuously consume the electric power even when the actuator is not activated. In order to make the pump durable, the reduction of power consumption at those devices should be achieved.

CONCLUSIONS

The performance of the miniature pump consisting of the interchangeable flexible tube and the hinge-type electromagnetic actuators has been reported. The prototype pump (50mm x 28mm x 15mm) with the silicone tube of 2mm in diameter was manufactured. It covers the flow rate of 1.5cm³/min and has the maximum discharge pressure of 38kPa by the rechargeable battery cell (Ni-MH 8.4V) drive. The magnetic latch mechanism designed optimally is effective to reduce the electric power consumption. The prototype pump at drive frequency of 3Hz runs for 12 hours continuously by full-charged battery cell. As the pumping action is achieved based on the open-loop sequence control of each actuator, the pump flow rate can be controlled without flow sensors proportionally to the drive frequency of the actuators.

Feasibility consideration of application to the portable intravenous drip system for medical treatments has been carried out. It was confirmed that the prototype pump has sufficient performance for the target system.

Furthermore, it will be applicable to the miniature pump system for sanitary/medical applications and the chemical analyzers.

REFERENCES

1. Y. Sato, et al., Development of Electro-Pneumatic Valve for Cold Air Flow Control, Proc. of 5th JFPS Inter. Sympo. on Fluid Power 2002, Vol.3 721-726, 2002
2. Y. Sato, Rapid Optimization of CAE Input Model in Preprocess of Solenoid Actuator Design, Proc. of 15th Conference on the Computation of Electromagnetic Field COMPUMAG2005, in printing
3. M. Piron, et al., Rapid Computer-Aided Design Method for Fast-Acting Solenoid Actuators, IEEE Transactions on Industry Applications, 35-5, pp. 991-999, 1999

FUNDAMENTAL STUDY ON A PZT JET PUMP

Hidetoshi OHUCHI*, Tetsuya WADASAKO**,
Tomohiro HOSAKA** and Tasuku OSADA*

* Graduate School of Medical and Engineering Science Department of Research
University of Yamanashi

4-3-11, Kofu, Yamanashi, 400-8511 Japan
(E-mail: ohuchi@yamanashi.ac.jp)

** Graduate School of Medical and Engineering Science Department of Education
University of Yamanashi

4-3-11, Kofu, Yamanashi, 400-8511 Japan

ABSTRACT

In this paper we propose a delivery method for a PZT jet pump driven by repeated impulsive force of the actuator. The pump is simple in construction being composed of only a piston-cylinder and a receiving hole, and it has no check valves. The multilayer PZT actuator pushes the piston impulsively and the fluid in the cylinder is ejected out through the nozzle forming a jet flow. The receiving hole that is placed facing the nozzle catches the jet flow and one way flow can be obtained. Experimental works indicated that the driving frequency as well as the dimensions such as the diameters of the nozzle and receiving hole was important to improve the pump performance. Moreover it was recognized that while air bubbles were apt to be generated in the cylinder during the suction stroke they were exhausted out of the cylinder at under a certain driving frequency.

KEY WORDS

Jet pump, PZT pump, Nozzle, Receiving hole, Air bubble

NOMENCLATURE

d_1 : Diameter of the nozzle
 d_2 : Diameter of the receiving hole
 D : Distance between the nozzle and the receiving hole
 p : Pressure in the cylinder chamber
 Q_{out} : Output flow rate
 Q_{leak} : Leakage flow rate
 H : Output head
 f : Driving frequency of the PZT actuator

INTRODUCTION

In this paper we propose a delivery method for a PZT jet pump driven by repeated impulsive force of the actuator. The principle of delivery is the same as a water pistol. The pump is simple in construction being composed of a piston-cylinder and a receiving hole. The multilayer PZT actuator pushes the piston impulsively and the fluid in the cylinder is forced to flow out through the nozzle forming a jet. The receiving hole is placed facing the nozzle and catches the jet flow. In this pump, the one way flow is obtained using the difference of flow patterns between the jet flow out of the nozzle and the

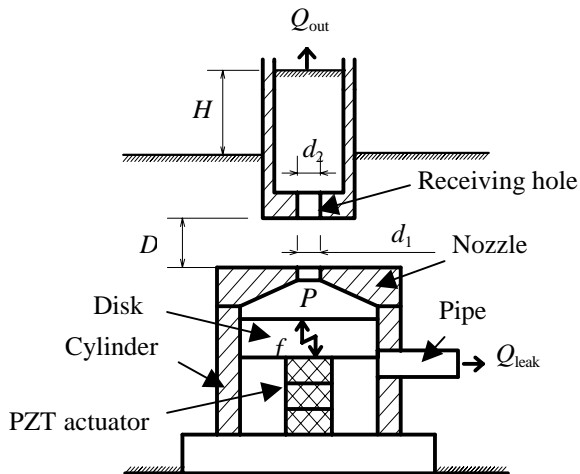


Figure 1 Fabrication of the jet pump

suction flow into the same nozzle. The delivery pressure of the pump is not high because it has no check valves. It is the feature that this pump does not have a valve, while most of the pumps developed before have check valves[1].

The functions of the pump are to eject small amount of fluid intermittently, to stir fluid in a narrow region, and to make a continuous flow with high-frequency ejection. Then the valve will be used to select small particles in a flow or to convey fluid substances in low pressure. In this paper, we are going to obtain a quasi continuous flow for transportation.

The piston is 12mm in diameter. The multilayer piezo-electric actuator has a small size of 2x3x9mm and is driven by rectangle wave voltage. Experimental works on the parameters that determine the pump characteristics indicated that the dimensions such as the diameter of the nozzle and receiving hole and the driving frequency were important to improve the pump performance.

Since the developed pump is not a positive displacement one, its delivery flow rate is changed according to the load pressure even if the driving frequency of the pump is constant. On the other hand, under a no-load condition the flow rate more than the calculated value was obtained. Moreover it was recognized that while air bubbles were apt to be generated in the cylinder during the suction stroke they were exhausted out of the cylinder at under a certain driving frequency.

WORKING PRINCIPLE OF THE JET PUMP

Fabrication of the jet pump

Fig.1 shows the fabrication of the jet pump proposed in this paper. A PZT actuator is bonded on the base, and a disk is also bonded on the upper side of the actuator. The disk acts as a piston. These are set into the cylinder,

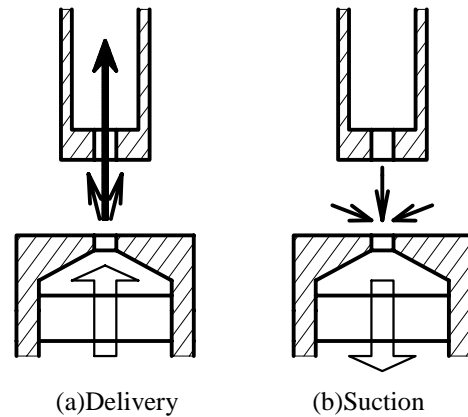


Figure 2 Basic principle of jet pump

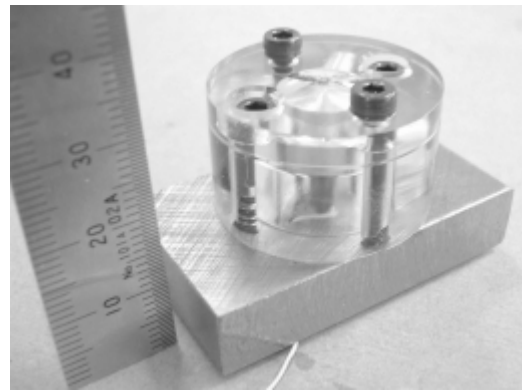


Figure 3 External view of the jet pump

which is covered by a lid with a nozzle hole. The pump is in simple construction as shown.

To obtain the output flow, a receiving hole is installed at the position facing to the nozzle, and a pipe is connected to the receiving hole. The jet that flows out from the cylinder chamber and flows into the receiving hole is an output of the pump. In the cylinder wall under the piston there is a small hole that makes the fluid go in and out freely. This pump with the receiving hole is submerged a little below the surface of the liquid.

Working principle

The working principle of the jet pump is as follows. The PZT actuator expands rapidly when a rectangle wave voltage is applied to it, and the fluid is gushed by the piston through the nozzle. When the actuator is shrunk, the fluid is inhaled through the same nozzle. When the expansion and the shrinkage of the PZT actuator are repeated at a high frequency, the flow through the nozzle seems like a continuous flow. This is because the aspect of the inlet flow is different from the outlet jet flow.

Then, a receiving hole is set at the position facing the nozzle. One side of a pipe was shut and a small receiving hole was made as shown in Fig.2. Fig.2 (a) shows that

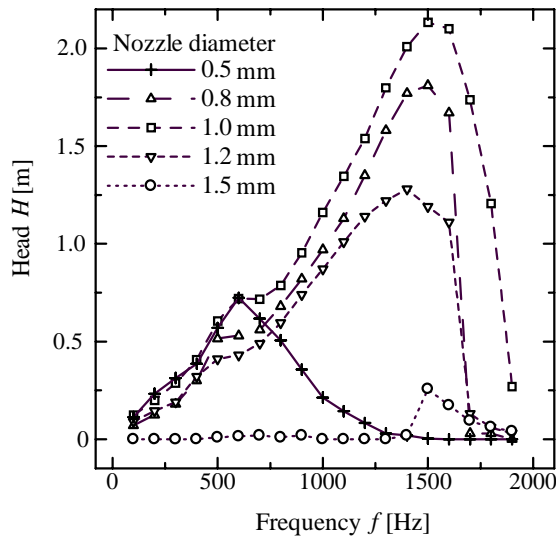


Figure 4 Variations of output head with the driving frequency of various nozzle diameters

when the PZT actuator rapidly expands the fluid goes out of the nozzle forming a jet flow and passing into the receiving hole. Fig.2 (b) shows the appearance that the fluid in the vicinity of the nozzle exit flows toward the nozzle when the PZT actuator shrinks. At this time, though there is a backflow out of the receiving hole, the total flow is directed to the output pipe, because the inlet flow rate is more than the back flow rate. In a word, the one way flow is obtained by using the difference between how to flow through out or into the nozzle. As a result, a pump without a check valve is realized unlike a conventional diaphragm pump.

The tested jet pump

Fig.3 shows external view of the tested jet pump. The parameters of this pump are as follows. The PZT actuator has a size of $2 \times 3 \times 9$ mm, and it reveals an elongation of $7.5 \mu\text{m}$ in a long direction when the voltage of 150V is applied. The aluminum disk bonded onto the actuator is of 12mm in diameter and 4mm in thickness, and it acts as a piston. The nozzle, the cylinder and the receiving pipe were made of acrylics to make it easy to observe the situation inside the cylinder. The hydraulic oil was used as a working fluid. Different size of nozzles (0.5, 0.8, 1.0, 1.2, 1.5 and 2.0mm in diameter) and receiving holes (0.8, 1.0, 1.2, 1.5 and 2.0mm in diameter) were prepared for experiments.

Although the pumping action is performed by the disk, it is not sealed and there is a gap of about 0.05mm between the disk and the cylinder. When the bubbles are generated in the cylinder chamber and remain there, they become obstructions of the pump operation. However, these bubbles are apt to be exhausted outside the cylinder chamber through the gap, and the continuous pumping action becomes possible.

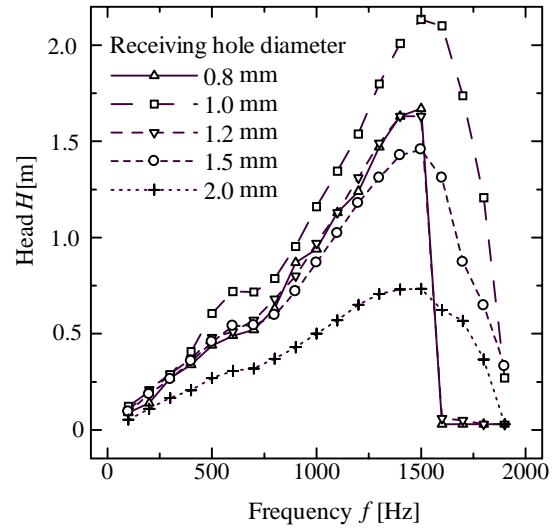


Figure 5 Variations of output head with the driving frequency of various receiving hole diameters

EXPERIMENTS

When the PZT actuator is driven successively by a high frequency rectangle wave voltage, a quasi continuous flow occurs in the outlet pipe through the receiving hole as shown in Fig.2 (a). Then this pipe was extended upwards, and the height H of the oil column that rose up in the pipe was measured. We changed the nozzle diameter, the receiving hole diameter and the distance between the nozzle and the receiving hole as parameters of the pump, and also varied the driving frequency and the duty ratio of the rectangle wave as parameters of the driving condition. Then, we examined the relationship between the output head and each parameter. The piston diameter was 12mm and the driving frequency was varied from 100 Hz to 1900 Hz by 100 Hz.

A high frequency piezo driver was used for driving the actuator. The specifications of the driver are as follows; maximum output voltage of 150 V, rated current of 200 mA and peak current of 600 mA.

Nozzle diameter d_1

First, we carried out fundamental experiments varying d_1 on condition of the receiving hole diameter d_2 of 1.0mm, the distance between the nozzle and receiving hole D of 2.0 mm and the duty ratio of 50 %. Fig.4 shows the results, in which the highest value H of 2.2m was obtained at $f=1.5$ kHz and $d_1=1.0$ mm.

Then, another experiment was performed, where the pressure sensor was installed facing the nozzle instead of the receiving pipe. The strongest jet or propellant force was recorded also at $d_1=1.0$ mm. It was thought that an effective jet flow for the pump action was formed by the nozzle of 1.0mm in diameter in case of the piston of 12mm in diameter.

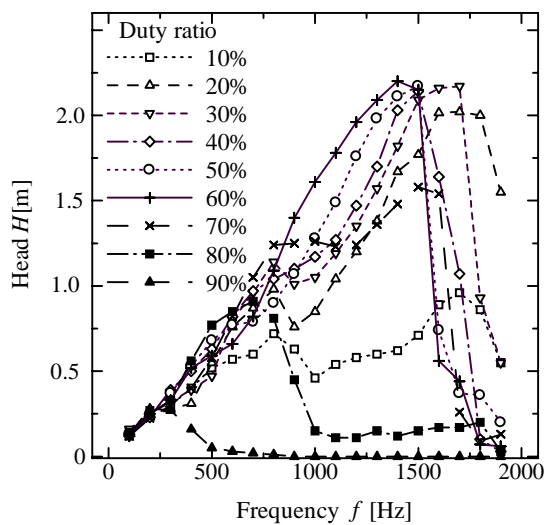


Figure 6 Variations of output head with the driving frequency of various duty ratios

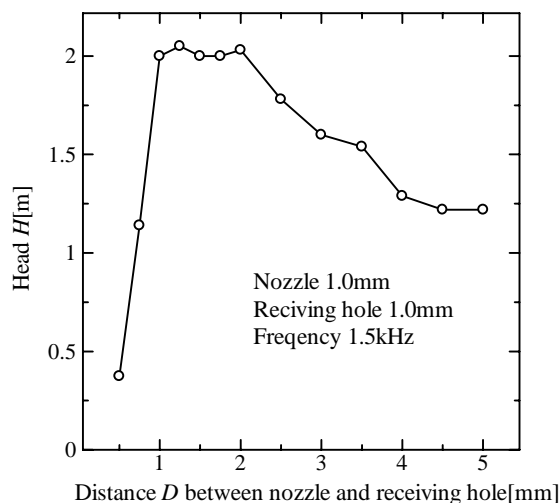


Figure 7 Variations of output head with the driving frequency of various distances between nozzle and receiving hole

Receiving hole diameter d_2

Next experiment was to vary d_2 on condition that $d_1=1.0\text{mm}$, $D=2.0\text{mm}$ and the duty ratio of 50%. As shown in Fig.5, the maximum H of 2.2 mm was obtained at the same value of $f=1.5\text{ kHz}$ and $d_2=1.0\text{mm}$. Moreover, the peak values of H appeared at the same frequency $f=1.5\text{ kHz}$ for any values of d_2 . The best receiving hole diameter was the same as the nozzle diameter of 1.0mm. In this experiment, however, there was no output flow. It seems that the receiving hole diameter influences not only the output head but also the flow rate. So, the value of d_2 should be chosen after examining the characteristics between the load and flow rate.

Table 1 Combination of parameters that gives a high output pressure

Nozzle diameter d_1 [mm]	1.0
Receiving hole diameter d_2 [mm]	1.0
Distance between the nozzle and receiving hole D [mm]	2.0
Duty ratio [%]	60
Driving frequency f [kHz]	1.5

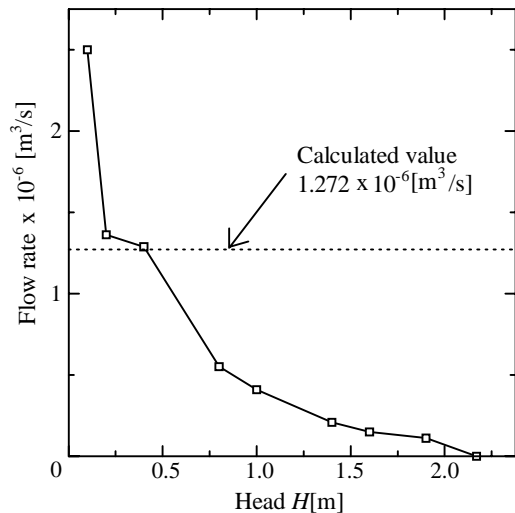


Figure 8 Delivery flow rate

Duty ratio

We examined the height H varying the duty ratio of rectangle wave on condition of $d_1=1.0\text{ mm}$, $d_2=1.0\text{ mm}$ and $D=2.0\text{ mm}$. The results are shown in Fig.6. Within the duty ratio range from 20 to 60 %, the height H reached 2m or more though there were a few differences in the peak driving frequency.

The peak frequency tends to decrease when the duty ratio increases. Because the suction time decreases as the duty ratio increases, the result shows it is necessary to set the ratio below 60 % and to keep a sufficient suction time.

Distance D between the nozzle and receiving hole

Finally we examined the head H with varying D on condition of $d_1=1.0\text{mm}$, $d_2=1.0\text{mm}$, the duty ratio 50 % and the driving frequency $f=1.5\text{ kHz}$. Fig.7 shows the result. H reached 2 m or more when D is from 1.0 to 2.0 mm. The H decreased little by little when D parted from the range. Moreover, when the receiving hole is located near the nozzle, for example less than 1 mm, it becomes an obstruction of the inhalation of the fluid.

The result in Fig.7 indicates that the output did not change so much when D is from 1.0 to 2.0mm. That means the accuracy is not necessary for positioning the receiving hole. Therefore, the assembly of the pump can be performed easily.

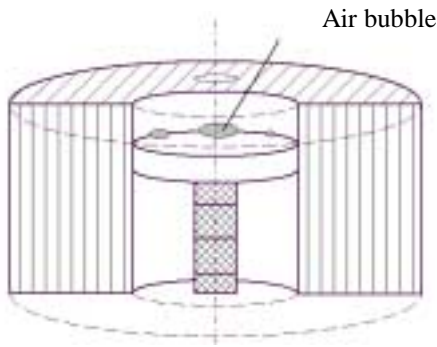


Figure 9 Generation of air bubbles

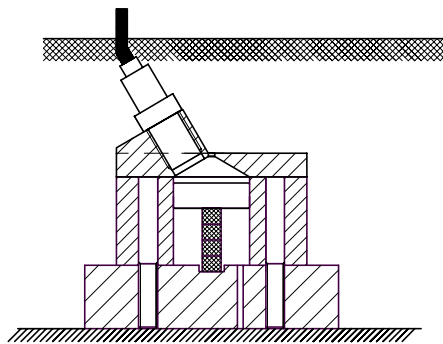


Figure 10 Measuring of the nozzle back pressure

Considering these results, the combination of parameters that gives a high output head was obtained as described in Table 1. In the following experiment the relationship between the head and flow rate was measured on these conditions varying the maximum height of the output pipe. Fig.8 is the obtained characteristics and shows the maximum flow rate Q_{out} was $2.5 \times 10^{-6} \text{ m}^3/\text{s}$.

The broken line drawn in Fig.8 shows a value of the flow rate without load ($H=0\text{m}$) calculated from the piston stroke, the area of the disk and the driving frequency. As a result of the experiment, the flow rate more than the calculated value was obtained when H was 0.4 m or less. It is thought that the fluid around the jet flow in addition to the jet flow itself from the nozzle might flow into the receiving hole. Therefore, the flow rate more than the piston displacement can be obtained when the load is small.

The total efficiency of this jet pump was 0.12 %, which was calculated using the input electric power of 7.35 W and the measured values in Fig.8. Moreover, the leakage flow rate $Q_{leak}=0.03 \times 10^{-6} \text{ m}^3/\text{s}$ was measured through the discharge pipe at $H=0$ m. It was about 1 % of Q_{out} .

IMPROVEMENT OF THE PUMP CHARACTERISTICS

Generation of air bubbles

As shown in Fig.9, air bubbles were generated mostly at the disk edge inside the cylinder. The movement of the

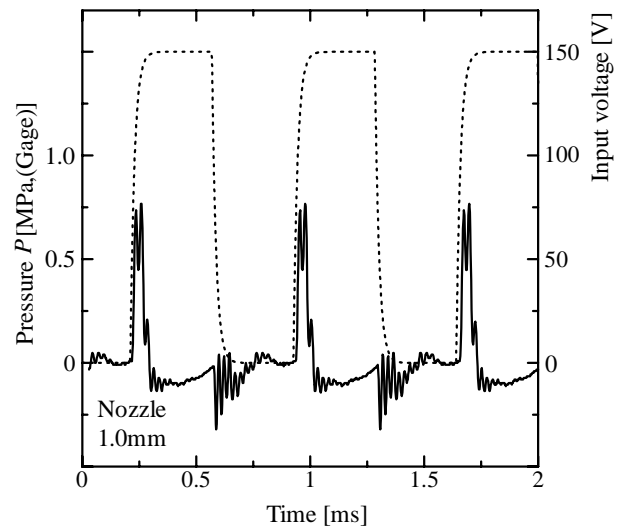


Figure 11 Pressure in the cylinder chamber without air bubbles

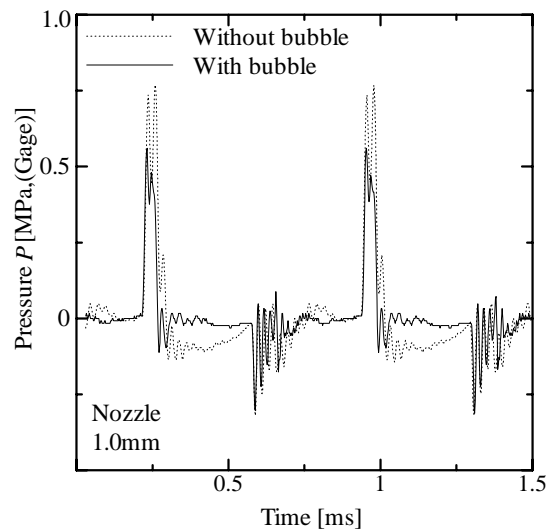


Figure 12 Pressure in the cylinder chamber with and without air bubbles

bubbles was observed and the following fact was found. The generated bubbles were exhausted not through the nozzle but through the gap between the disk and the cylinder. When the characteristics of the pump were measured in the preceding chapter, there was a feature that height H decreased rapidly when the driving frequency was raised higher than $f=1.5$ kHz. At a lower frequency than that, even if bubbles were generated, they were exhausted and the pumping action was kept stable. On the other hand when the driving frequency was increased, the bubbles did not pass through the gap between the disk and the cylinder. The bubbles stayed inside the cylinder and the pressure p could not increase. Therefore the jet flow could not occur any more.

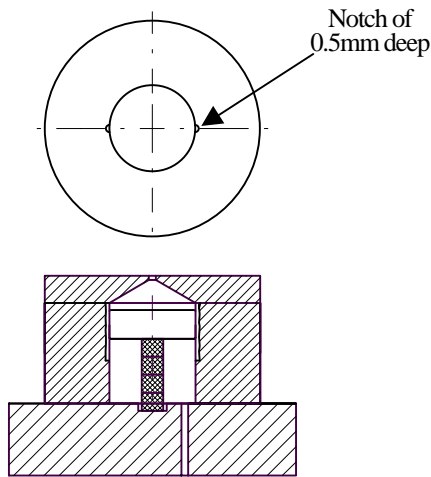


Figure 13 Disk with two notches

Pressure in the cylinder chamber

The semiconductor pressure sensor was installed to measure the nozzle back pressure as shown in Fig.10. Fig.11, in which the pressure values represent the gage pressure, shows the recorded result in case of the nozzle diameter of 1.0 mm. The pressure reached the maximum value of 0.7 MPa in 0.036 ms from the start of the actuator, and the pump ejected the fluid during about 0.1 ms. After that, the pressure decreased to -0.1MPa. The suction process started before the actuator began to shrink. Moreover, the pump continued to inhale and finished it in about 0.17ms. The pressure decreased to -0.1MPa once when the actuator shrunk. The recorded pressure waveform reveals high frequency vibrations and absolutely negative value. It is not a real pressure but a vibration of the diaphragm of the semiconductor pressure sensor.

Next, Fig.12 shows the pressure recorded in case that the air bubbles stayed in the chamber. The ejecting pressure decreased to about 60 %. When the bubbles were not seen, the pressure has decreased to a negative level before the actuator started to shrink. On the other hand, in case that there exist air bubbles, the pressure decreased only to 0 MPa. When the actuator shrunk, the pressure became negative; however, the level was higher than that measured without air bubbles. Therefore, when a big air bubble is generated, it seems that not only the jet flow but also the suction flow decrease. In other words, the output flow vanishes because the internal air bubbles repeat growth and disappearance. As a result, how to exhaust the air bubbles inside the cylinder becomes an important problem to improve the characteristics of this type of pump.

Exhaust of the air bubbles

It seems that the gap between the piston and cylinder should be small to obtain a strong jet flow. However, considering the bubble generation and exhaust, it seems

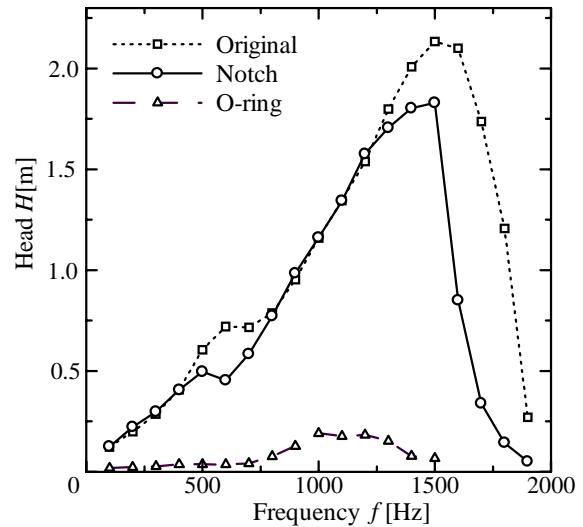


Figure 14 Influence of the gap seal

also that a small gap is necessary there. Then, other experiments were carried out for comparison. One was a pump with two notches of about 0.5mm carved on the cylinder wall as shown in Fig.13 to make the bubble exhaust easily. The other was a pump with an O-ring to seal the piston gap.

The results are shown in Fig.14. The output head of the pump with the notch decreased by about 20% compared with the pump without the notch. The air bubbles appeared and stayed in the chamber as before at the frequency higher than 1.6 kHz. In this method, it was noticed that the pump was kept stable while the output decreased a little. On the other hand, the output of the pump with an O-ring decreased remarkably. It has been understood that the existence of the gap was important.

CONCLUSIONS

In this paper, a jet pump driven by impulsive force of a PZT actuator was proposed. The pump has no check valves and so it is simple in construction. Basic characteristics of the pump were studied experimentally concerning the pump parameters and the driving conditions. The air bubbles generated in the cylinder chamber considerably affected the performance of the pump. Future research will involve a design to easily exhaust air bubbles and also to improve the efficiency.

REFERENCE

1. Park, J. H., Yokota, S. and Yoshida, K., Piezoelectric Micropump Using Resonance Drive, Proc. Fifth Triennial Int. Symp. On Fluid Control, Measurement and Visualization (FLUCOME'97), Hayama, Japan, 1997, pp.319-324

MOTION CONTROL OF ELECTROMAGNETIC RECIPROCATING ACTUATOR FOR METAL BELLOWS PUMP

Yasukazu SATO* and Yasuhiro MATSUSHITA*

* Department of Mechanical Engineering, Faculty of Engineering
Yokohama National University
79-5 Tokowadai, Hodogayaku, Yokohama, Kanagawa, 240-8501 Japan
(E-mail: yasukazu@ynu.ac.jp)

ABSTRACT

A resin-made-bellows pump is used practically as a chemical pump application. Its discharge pressure is low as 0.1MPa in general; therefore, its applicable fields are limited. In order to make the pressure higher, we developed a metal bellows pump driven by an electromagnetic reciprocating actuator for various industrial applications with the pressure of over 10MPa and non-leakage performance. As the pressure becomes higher, larger output force is required to the actuator. The developed electromagnetic actuator can drive the bellows by reciprocating motion in the stroke of 1mm with the maximum output force of 1400N. However, the high-speed motion of the actuator by the armature position- and velocity-sensorless control makes issue that the armature collides hard with the stator and generates the noise and vibration. In this paper, the motion control method to reduce the mechanical collision in the actuator without position- and velocity-sensors is presented.

KEY WORDS

Bellows Pump, Electromagnetic Actuator, Noise Reduction, Power Saving, Non-leakage Pump

NOMENCLATURE

E : Voltage supplied from electric power source
 f : Driving (reciprocating) frequency
 F_{mag} : Electromagnetic attractive force
of the actuator
 g : airgap between armature and stator
 i : Current flowing through coil
 L : Inductance of coil
 P : Discharge pressure of the pump
 Q : Flow rate
 R : Resistance of coil
 S : Sound pressure level

x : Displacement of armature.
 η : Volumetric efficiency
 λ : Magnetic flux linkage

INTRODUCTION

A bellows pump has advantages in application to apparatuses which allow no leakage because of its non-leakage structure. Due to the limitation of mechanical strength of bellows material, the applicable fields of a bellow pump are generally limited in low pressure application such as semiconductor manufacturing, medical and chemical processes using

pressure range of 0.1 ~ 1MPa. By improvement of discharge pressure up to 10 MPa and over, the applicable fields of bellows pump would be expanded to various applications such as a direct fuel injection pump for automobile and a pump for very low viscosity fluid, and so on. In recent years, the metal bellows having enough mechanical strength for high pressure inside the bellows was developed. Photo 1 shows an example of metal bellows. It has flexibility in axial direction and moreover restricts expansion in radial direction against high inner pressure. Owing to the development of metal bellows for high inner pressure, the improvement of bellows pump for higher application is progressing. In this paper, a metal bellows pump driven by an electromagnetic reciprocating actuator for various industrial applications with the pressure of 10MPa and non-leakage performance is developed. The motion control method to reduce the noise and vibration without sensors is presented. Furthermore, it is indicated that this method is also effective to power-saving drive.

DRIVE MODE OF BELLOWS PUMP

Electromagnetic drive mode to expand /contract the bellows is generally categorized to either of two methods; one is the rotary type in which rotation of motor is transformed to reciprocating motion by a cam, the other is the linear type using linear or reciprocating actuator. The rotary type is suitable for large flow discharge using the multiphase cam to activate bellows several times in one rotation cycle. It also generates smooth motion of the bellows easily, using appropriate cam profile. However, it needs motion transforming elements such as a cam, cam-follower and bearings, and so on. In case of the direct flow control, the rotational speed control of the drive motor is required. On contrary, the linear type has merit of simple structure and is easy to control flow rate by the reciprocating frequency control of linear actuator. However, it is required high speed reciprocating for large flow discharge and is also



Photo 1 Metal bellows

required large actuator force compatible to high discharge pressure.

As described above, both drive modes has strong points and shortcomings. In this paper, the linear type is adopted for the drive mode of bellows pump because of its simple structure and easiness of flow rate control.

METAL BELLOWS PUMP DRIVEN BY ELECTROMAGNETIC RECIPROCATING ACTUATOR

A prototype electromagnetic reciprocating actuator with the maximum thrust force of 1400N and the stroke of 1mm is manufactured. The maximum thrust force is compatible to the pressure of 5 MPa which is upper limit of inner pressure of the bellows used in the prototype pump.

Figure 1 and Fig. 2 show the configuration of the bellows pump and electric circuit of actuator driver, respectively. Alternate energizing of the coil “A” and “B” generates reciprocating motion of the armature “A” and “B”, which are connected by the rod through the center hole of the stator, and then the bellows units located at the both side of the actuator expand and contract. The armature is centered by the restitutive force of the bellows when non-energizing of the coil. The flow direction is controlled by the reed valves on the each bellows unit. The flow discharged from the each bellows unit join in the pump body, and then flow out to the outside. Table 1 shows the specifications of

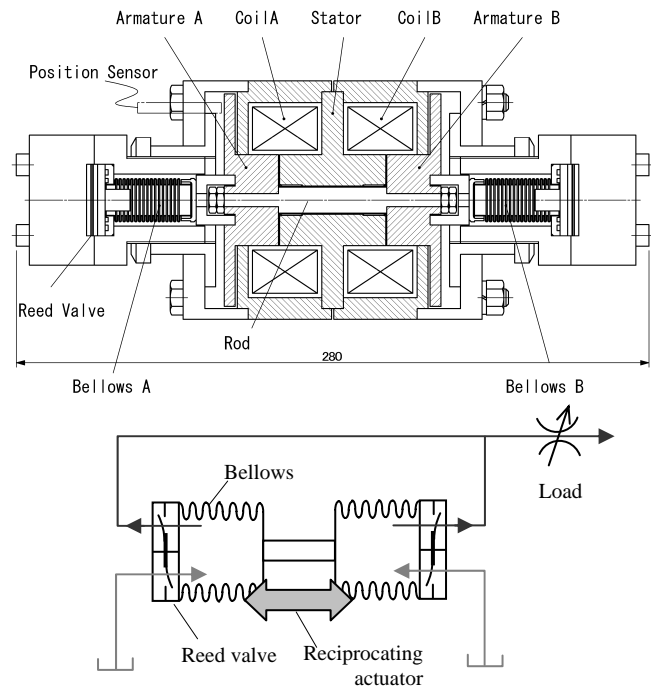


Fig.1 Metal bellows pump driven by an electromagnetic reciprocating actuator

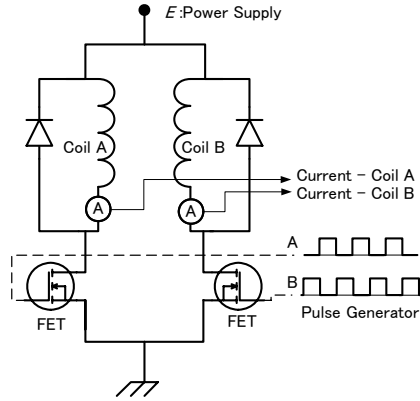


Fig.2 Conventional electric driver

the bellows used in the pump.

When the armature is located at a distance of x from the stator, the electromagnetic attractive force at the coil current i is roughly estimated by the following equation [1].

$$F_{mag} = \frac{i^2}{2} \frac{dL}{dx} \quad (1)$$

The inductance L is assumed the function of x and given by

$$L(x) = \frac{k_1}{k_2x + k_3} \approx \frac{k_1}{k_2x} \quad (2)$$

where, k_1 , k_2 and k_3 are constants determined by the shape of the armature and stator and the turn number of the coil. In case of very small radial clearance between the armature and stator, k_3 is negligible. Consequently, the electromagnetic attractive force is expressed by

$$F_{mag} = -\frac{k_1}{2k_2} \cdot \frac{i^2}{x^2} \propto \frac{1}{x^2} \quad (3)$$

where, the minus sign indicates that the force tends to decrease the airgap. Thus, the electromagnetic attractive force is in inverse proportion to square of the airgap. As k_1/k_2 is proportional to the cross-sectional area of the magnetic pole at the airgap, an auxiliary flange shown in Fig.3 contributes to strengthen the magnetic force.

Actual magnetic material has nonlinearity in its magnetization characteristics. The leakage and fringing of magnetic flux flow should be also considered. As Eq. (3) is insufficient for detail design of the electromagnetic actuator, FEM electromagnetic field analysis is applied to the design of the electromagnetic circuit of the actuator. A half of the actuator is enough to the analyzed area, as shown in Fig. 3, because of its axis-symmetry. The armature has an auxiliary flange which improves about 20 % higher in the electromagnetic attractive force, compared with the

Table 1 Specifications of bellows

Material	Stainless steel
Outer diameter	20 mm
Inner diameter	14 mm
Number of convolution	20
Normal length	43.1mm
Actuating length	42.5mm (expand) 41.5mm (contract)
Allowable inner pressure	Over 5MPa

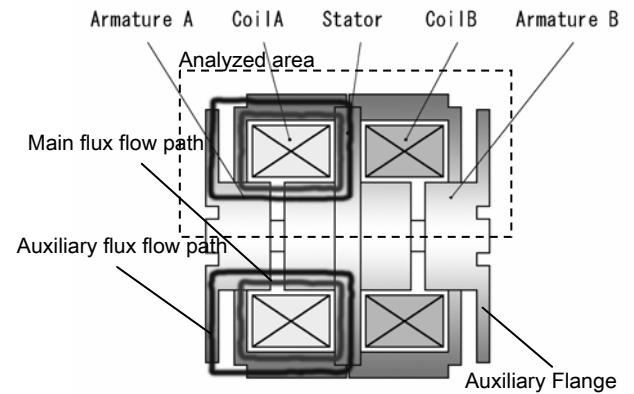


Fig. 3 Magnetic circuit of reciprocating actuator

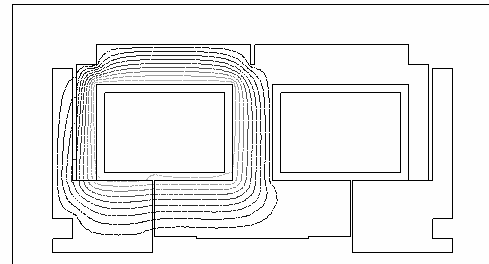


Fig. 4 Magnetic flux flow in reciprocating actuator calculated using FEM magnetic field analysis

armature having no auxiliary flange. Figure 4 depicts an analytical result of the magnetic flux flow in the actuator. It is confirmed that the magnetic flux flow passes air gaps at both the main core and the auxiliary flange effectively. The dimensions and specifications of the actuator are determined to have enough force in whole stroke against the discharge pressure of 10MPa. However, due to the limitation of the metal bellows used in the pump, the pump is driven under the pressure

of 7MPa in the performance testing described below. The coil is energized by conventional solenoid drive method shown in Fig. 2. The electric pulse with constant voltage is supplied to the coil when the FET is activated. The electromagnetic energy gradually disappears through the flywheel diode. The pump has the non-contact displacement sensor just for the measurement of the armature position in experiment, which is not used for position or velocity control. Then, the reciprocating motion of the actuator synchronizes with the alternating energizing of the coils.

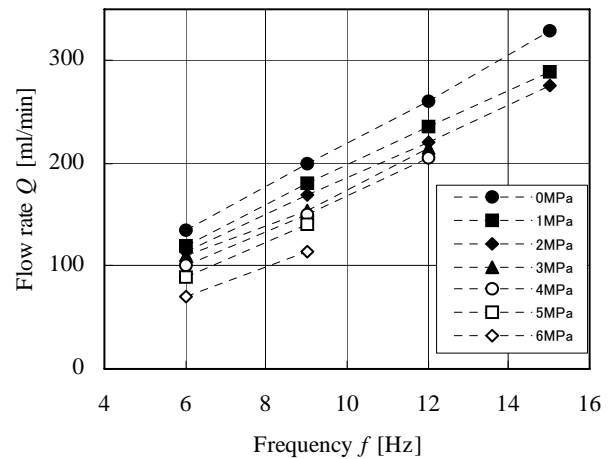
FUNDAMENTAL CHARACTERISTICS OF THE BELLOWS PUMP

Figure 5 shows the fundamental characteristics of the prototype bellows pump. The flow rate is proportional to the reciprocating frequency of the actuator, but is gradually decreased due to the decrease of the volumetric efficiency when the discharge pressure increases. This decrease arises from the bellows structure. The effort to reduce the dead volume in the bellows chamber has been achieved, but it is difficult to eliminate the dead volume completely in the folds of the bellows. Therefore, the volumetric efficiency tends to decrease in high pressure. Moreover, the bulging of each fold of the bellows under the high pressure reduces the pump performance [2].

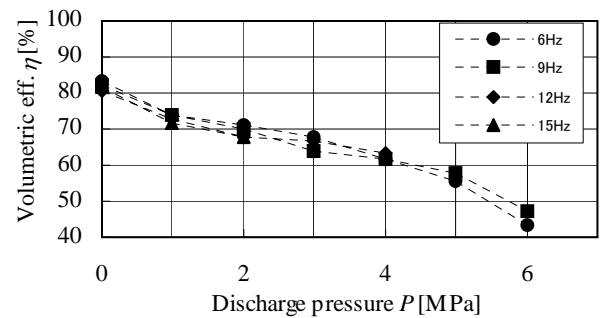
REDUCTION OF NOISE AND VIBRATION BY MOTION CONTROL REFERING CURRENT WAVEFORM OF COIL

The collision between the armature and stator at the stroke-end generates large noise when the actuator reciprocates fast. Because the electromagnetic attractive force under the constant current of the coil is proportional to the square of the air gap between the armature and stator, the excessive attractive force acts on the armature at the position just before collision in which the air gap is almost zero at the maximum current. Some methods are effective to reduce the collision. The armature position sensing using a displacement sensor makes it possible to speed down the armature. However, the position sensorless control is preferable from the viewpoint of robustness of the pump. The insert of a thin elastomer sheet between the armature and stator is also effective, but is accompanied with the stroke fluctuation due to the fatigue of the elastomer and the force reduction due to the increase of magnetic air gap for the thickness of the elastomer.

In this paper, a position sensorless control is proposed for the reduction of collision shock. By detection of the actuator motion at the modified electric driver, the coil current is shut off just before collision. The modified electric circuit is depicted in Fig.6. In the modified electric driver, the differentiators to detect the change of



(a) Drive frequency-Flow rate characteristics



(b) Volumetric efficiency

Fig.5 Fundamental characteristics of the bellows pump

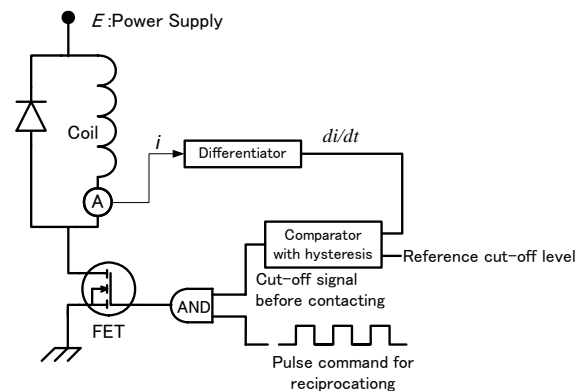


Fig.6 Additional circuit for contacting shock reduction

the coil current are inserted to the conventional circuit shown in Fig.2.

As to the magnetic circuit with the coil energized by the voltage supply E , the voltage equation of the actuator driver with moving armature is given by;

$$E(t) = iR + \frac{d\lambda}{dt} \quad (4)$$

$$= iR + L(x)\frac{di}{dt} + i\frac{dL(x)}{dx}\frac{dx}{dt}$$

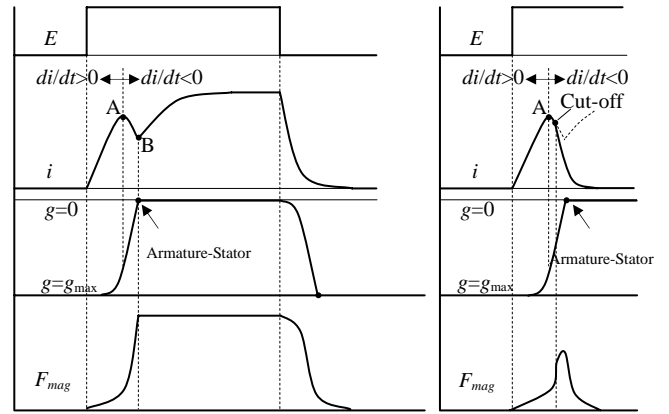
where, λ is the flux linkage of the magnetic circuit. The term $L(di/dt)$ is the self-inductance voltage term, and the term $i(dL/dx)(dx/dt)$ is the speed-dependent voltage term which represents the back-EMF: electromotive force generated by the armature motion [3]. The armature displacement x is correspondent to the air gap g between the armature and stator. Assuming linear magnetic property, the inductance L varies with the armature displacement x , and given by Eq. (2).

Owing to the effect of the speed-dependent voltage term, the typical current waveform of the coil has a peak as shown in Fig.7 (a). The point "B" indicates the collision between the armature and stator. The change of slope from rising to falling around the mark "A" is detected as the resultant of high speed motion of the armature just before collision. The peak point of the current is detected as the point in which the sign of differentiation of the current. As shown in Fig.7 (b), shutting off the FET at the mark "A" reduces the shock of collision because the armature moves due to its inertia and the electromagnetic attractive force falling by the recirculation of the current through the flywheel diode. The sign of differentiation of the current is distinguished using the hysteresis comparator which has robustness against the electric noise. Figure 8 shows the flow of analog signal processing to generate the pulse signal for FET-shutting off. The shutting off timing of the FET is delayed suitably by control the hysteresis.

TESTING OF REDUCTION OF COLLISION BETWEEN ARMATRURE AND SATATOR

For shutting off the FET just at the current peak, $di/dt=0$, the reciprocation of the actuator can be achieved under the pressure of 5 MPa, but falls into unstable above the pressure due to the lack of attractive force acting on the armature against the pressure. In order to make the reciprocation stable above the pressure of 5MPa, the shutting off point of the FET is shifted to the middle of downward slope before the point "B" in Fig. 7(a) from the peak, $di/dt<0$, by tuning of the hysteresis in the comparator. Figure 9 shows the measured coil current and the output of the differentiator.

Figure 10 shows the sound pressure level measured at a



(a) Conventional drive (b) Colliding shock reduction

Fig.7 Schematic diagram of electric current waveform

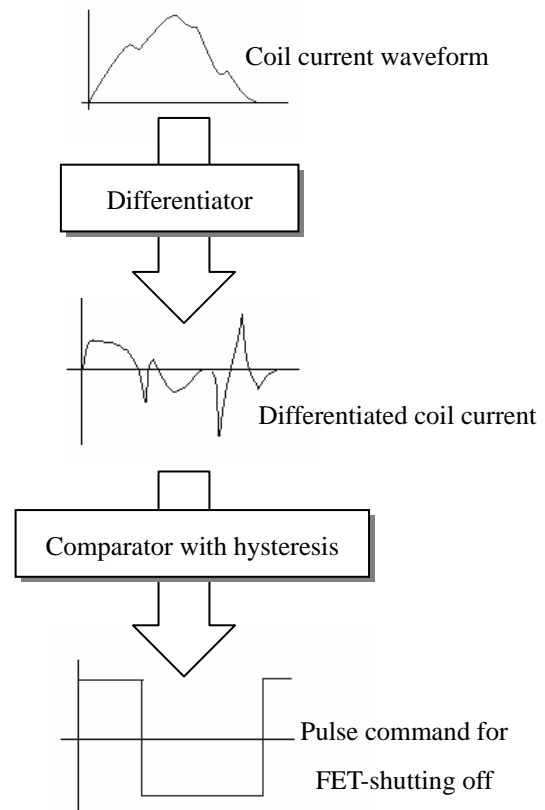


Fig.8 Conceptual diagram of analog signal processing for FET-shutting off

distance of 1m from the pump. Noise reduction during the pump working is confirmed. The noise is reduced about 4dB in whole pressure range.

POWER-SAVING DRIVE OF ELECTROMAGNETIC RECIPROCATING BELLOWS PUMP

The noise reduction method described above also has an advantage of reduction on electric power consumption. In the conventional drive method shown in Fig.7 (a), the electric power consumption at the coil continues after the collision until the next motion is arisen. On contrary, in the noise reduction drive shown in Fig.7 (b), no electric power is consumed at the coil after the collision. Since the pumping action is completed before shutting of the current, this method does not influence the pumping action, and effective to the power saving drive, particularly low frequency reciprocation with long-term interval.

CONCLUSIONS

The bellows pump for high pressure applications is developed using the metal bellows and the powerful electromagnetic the electromagnetic reciprocating actuator. The position-sensorless control for noise reduction at the collision between the armature and stator is proposed. It is confirmed that the noise generated by the actuator reciprocation is reduced about 4dB in whole pressure range. Furthermore, it is described that this control method is simple and effective to reduction of electric power consumption.

ACKNOWLEDGMENT

The authors would like to thank Mr. Shinbori, NHK Spring Co.,Ltd, for supplying the bellows units which were used in this research.

REFERENCES

1. I. Boldea, S.A. Nasar, Linear Electric Actuators and Generators, Cambridge University Press, pp. 28-32(1997)
2. Y. Sato, H. Tanaka, Electro-hydraulic Switching Valve Controlled by a GMA with Stroke Amplifier, PFLUCOME'97, pp.391-396 (1997)
3. A. E. Fitzgerald, et al, Electric Machinery 5th edition, McGraw Hill, London, pp.124-132(1992)

APPENDIX

The prototype metal bellows pump driven by the reciprocating actuator is shown in Photo 2.

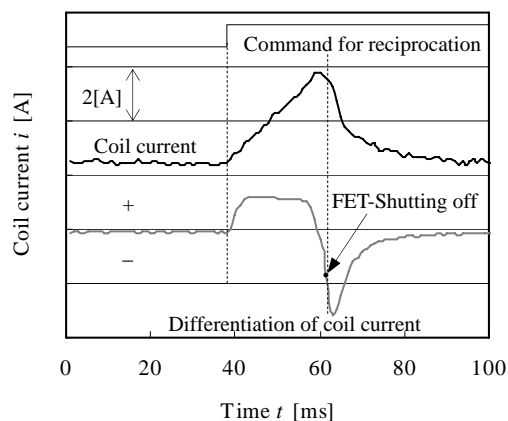


Fig.9 Measured coil current and output of differentiator

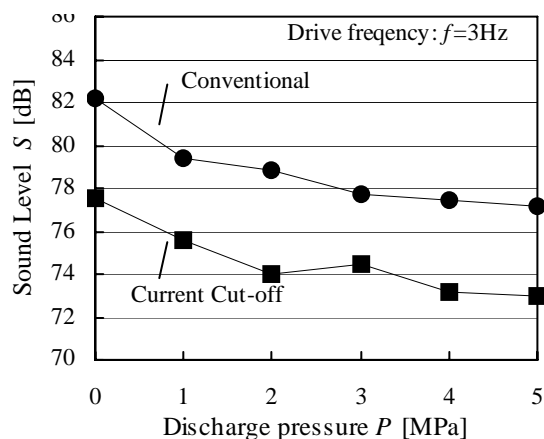


Fig.10 Comparison in sound level

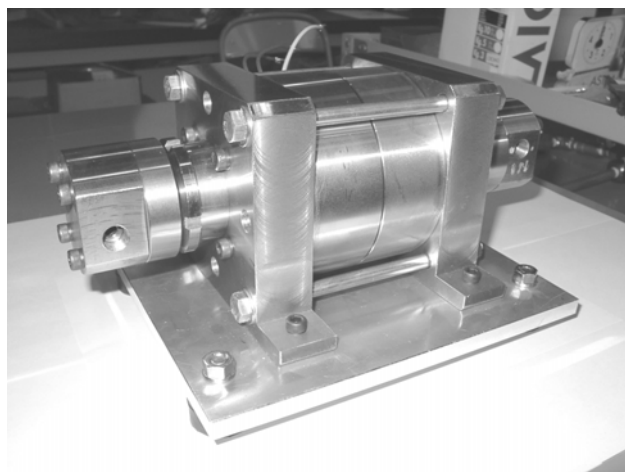


Photo 2 Prototype metal bellows pump driven by reciprocating actuator

MITIGATION OF MACHINE VIBRATION BY MEANS OF AN ACTIVE SPINDLE BEARING UNIT

Hubertus MURRENHOF and Torsten KOHMÄSCHER

Institute for Fluid Power Drives and Controls (IFAS)
RWTH Aachen University (Germany)
Steinbachstraße 53, 52074 Aachen, Germany
(E-mail: torsten.kohmaescher@ifas.rwth-aachen.de)

ABSTRACT

Due to the high cutting speeds and depths of modern milling machines vibrations are generated within the whole machine structure. These vibrations lead to a poor machined surface and an additional load for all machine components. Within the collaborative research centre 368 "Autonomous Production Cells", IFAS is involved in the development of an active spindle bearing unit which is capable of damping vibration without reducing milling efficiency [7].

The special layout of the "three cavity ring" results in a high dynamic and stiffness, little need for space and a possible displacement of five tenth of a millimetre. A zero-leakage design is very important for the performance of the actuator. Reducing the leakage of the actuator will increase the dynamic and stiffness of the drive.

Using a micro controller for controlling the bearing unit leads to a decentralised system with local intelligence, that can be integrated into a milling machine.

KEY WORDS

active hydraulic damping, chatter control, high stiffness and dynamic, piezo servovalve, spindle bearing

INTRODUCTION

High metal removal rates are a main goal of cost-effective manufacture and can be achieved by means of high cutting speeds, high feed rates and a suitable cutting depth. Unfavourable cutting conditions may cause chattering of the milling tool, which leads to poor surface quality on the workpiece and possibly even to tool breakage. Variable speed or active damping of the milling machine spindle represent possible solutions, which may be implemented in order to achieve a higher metal removal rate while

maintaining a stable process. The goal is to change the energy state of the whole oscillating system in order to bring the chattering milling process back to a stable state. An active spindle bearing concept is being pursued at IFAS and is described below.

Apart from piezo ceramics and magnetic bearings, other possible candidates for the actuator technology for active bearing systems are hydraulic servo-systems. The high force density and the acceptable stroke distinguish the hydraulic systems from the other alternatives. In addition to this hydraulic drives are easy to control.

CHATTERING

Nowadays the metal removal rate of milling machines is not limited by the motor capacity, but by self-induced vibrations of the whole machine structure, which are called chatter vibrations or chattering. As a result of the milling process every milling machine is deformed by the cutting forces. The grade of deformation is dependent on the static and dynamic stiffness of the structure of the milling machine. Exceeding the maximum cutting depth generates self-induced vibrations with high amplitudes, which lead to a poor surface quality of the machined workpiece (Figure 1) according to the eigenfrequency of the milling machine. Repeated machining of this bad surface results in a dynamic excitation of the milling machine structure. Therefore the second cut causes unsteady cutting forces, which excite a self-induced, regenerative vibration [8]. As this vibration is an additional load for the tool and the machine it can even cause tool breakage and that is why it needs to be reduced and cushioned.

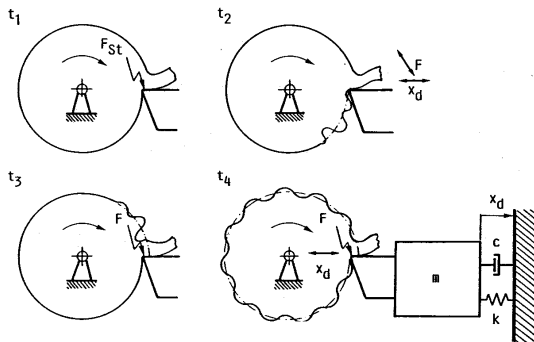


Figure 1 Regenerative chattering

Another type of self-induction takes place in coupled systems. At least two orthogonal eigenfrequencies are that close to each other that their vibrations interact and excite the other system [2]. Figure 2 shows the tip of a milling tool, which stands for an oscillating system with two degrees of freedom, cutting into a workpiece.

In opposition to the regenerative effect the locality coupling can cause chattering with the first cut into the unmachined workpiece and does not need a badly machined surface. There are further reasons for the excitation of chatter vibrations, but they are not that relevant for milling machines because of the high cutting speeds. One main characteristic of chattering is, that it is not dependent on the rotational speed of the machine.

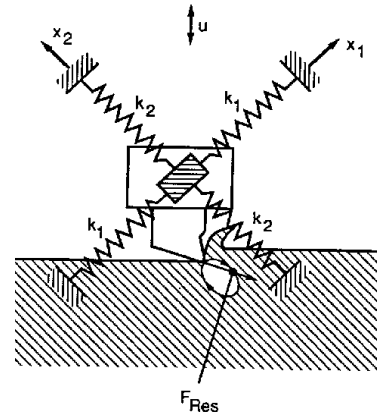


Figure 2 Locality coupling

To maintain a stable milling process, these vibrations need to be sensed, identified and controlled and thus eliminated. Therefore the self-induced vibrations need to be separated from the separate-excited vibrations, like the vibration, which is caused by the first contact of the cutting edges of the milling tool with the workpiece. After identifying the chatter vibrations a suitable principle for reduction needs to be implemented. Normally the cutting depth, the cutting speed or the rotational speed is reduced, which reduces the metal removal rate of the machine.

But in case of the active spindle bearing, which is developed at IFAS, the front bearing of the spindle is controlled and seated hydraulically to provide high forces for the milling process. The oscillating deformation of the milling machine geometry is compensated by the oscillation of the spindle bearing system. Without reducing any of the basic cutting parameters, the metal removal rate can be maintained at a high level.

THE DESIGN OF THE ACTUATOR

According to the restrictions for the layout of machine tools the most important design features for the active spindle bearing are high static and dynamic stiffness, low need for space, a leakage-free principle and, to compensate the deformation of the headstock, a possible displacement of ± 0.5 mm.

The conventional spindle bearing system consists of two angular ball bearings in the front of the spindle, that are preloaded in an O-arrangement, and a preloaded angular ball bearing in the rear. The active spindle bearing device also uses the conventional bearing in the rear of the spindle. Whereas the conventional bearings in the front are fitted into an

active bearing ring. The bearing ring is designed as a “three-cavity ring” (Figure 3) to achieve a better homogeneity of the forces on the perimeter.

The active ring is controlled by three sickle-shaped, hydrostatic cavities which are pressurized by three servo-valves – one for each cavity. The possible displacement out of the center of the active bearing ring needs to be ± 0.5 mm. The enclosure contains also three hydrostatically balanced sealings, which

separate the space between the enclosure and the active ring into the three cavities. These sliding pads are arranged on the perimeter with an angle of 120° between each other. To maintain a constant gap between sliding pad and active ring and to prevent the pad from losing contact with the ring, four springs and a constant pressure are applied to the back side of the pad.

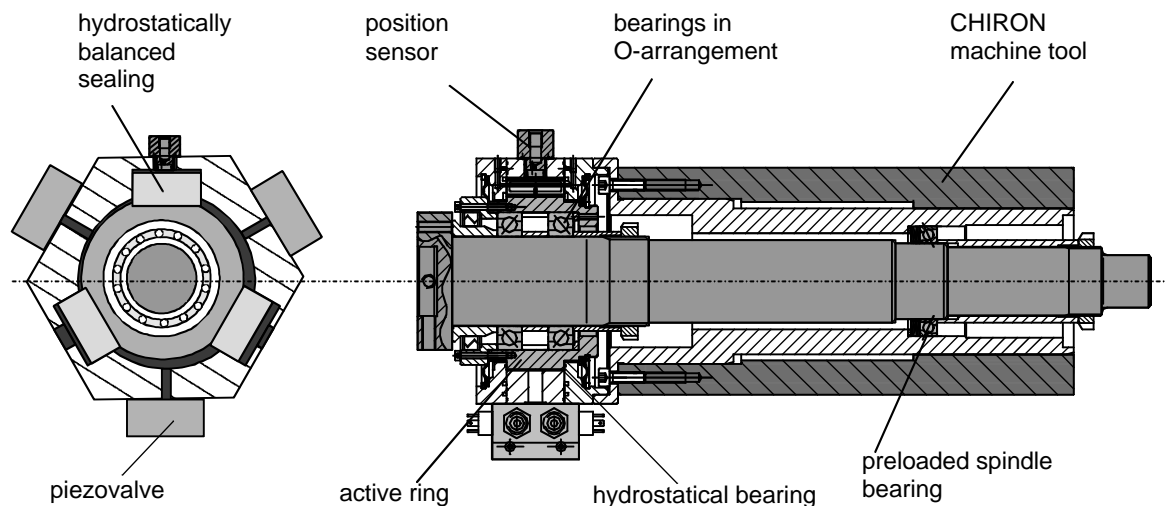


Figure 3 Principle of the active spindle bearing

Beneath the control of the radial position of the active bearing ring, the ring needs to be seated axially in the enclosure. Therefore three hydrostatic pockets are implemented on each side of the active ring to carry both, the cutting forces during the milling process and the weight of the spindle. Furthermore this axial bearing reduces the friction for any radial displacement.

Three piezo-electrically driven servo-valves, which have been developed at IFAS for this purpose, can be used to set the pressure in the cavities [4]. The valves are illustrated more exactly below. As the spindle and the valves are both prototypes, it is not recommended to test all prototypes in one test arrangement. This would only result in numerous repairs and the project might lose its focus. It is therefore legitimate to separate the prototypes in order to solve specific problems separately. For this reason, the spindle unit is driven by conventional and well-tested MOOG servo-valves whereas the piezoelectric servo-valve-prototype is tested in another arrangement. Since the stiffness and thus the hydraulic eigenfrequency of the drive is much higher than the dynamic of the valve, faster valves will increase the drive performance.

The large piston area of the ring segment and the low dead volume result in a calculated radial stiffness of $8000 \text{ N}/\mu\text{m}$ for the hydraulic bearing, which corresponds to 30 times the stiffness of the used ball bearings. The high stiffness causes a high eigenfrequency of the drive thus the slower valves limit the dynamic of the drive. For this reason a simple single loop controller suffices to control the position of the active ring [6].

The current position of the active bearing ring is determined by the position of the sliding pads. Three sensors, which operate according to the eddy-current measuring principle, are aligned to the back sides of the sliding pads and detect their positions. The eddy-current sensors were also developed specifically for this purpose at IFAS.

The principle of a hydrostatic bearing comes along with an unavoidable leakage. Because of this, in addition to the position control of the bearing ring, the pressures in the three cavities need to be regulated. Therefore a pressure sensor measures the pressure in each of the working cavities.

Because of the large piston areas of the hydraulic cavities force is lead smoothly and evenly into the bearing ring. Figure 4 shows the active spindle

bearing built into the headstock of a CHIRON milling machine.

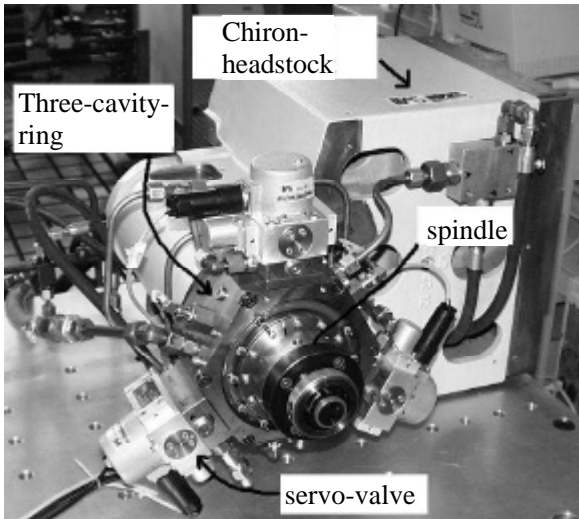


Figure 4 Photograph of the active spindle mount

PIEZOELECTRIC SERVO-VALVE

The piezoelectric servo-valves are used for pressurizing the three cavities of the active bearing ring. In order to control the chattering, high cut-off frequencies (-3dB) of up to 500 Hz in the small-signal range are required. As the hydraulic system of the active spindle is a very fast-responding one, the dynamic of the system is limited by the servo-valves and therefore servo-valves with high cut-off frequencies become key components.

High quality servo-valves are mostly pilot controlled and have a high level of dynamic behavior as well as a high accuracy in positioning the main spool, because of the spool position feedback [4].

Figure 5 shows a sectional view of the piezoelectric servo-valve, that was developed at IFAS. The pilot section of the servo-valve is designed as a flapper-nozzle system. The spool is moved by modifying the control pressures on the end faces of the spool.

The pilot section is supplied via the hollow main spool, which also houses the constant nozzles for the pilot section. The two flapper-nozzle units, which are permanently connected to the piezoelectric bending actuators, create the variable nozzles, which set the control pressures.

A piston with a diameter of 1 mm on the back side of the piezoelectric unit compensates the static force of pressure on the front side of the actuator. In this way only the pulse force of the flow against the flapper has to be overcome during movement of the main spool.

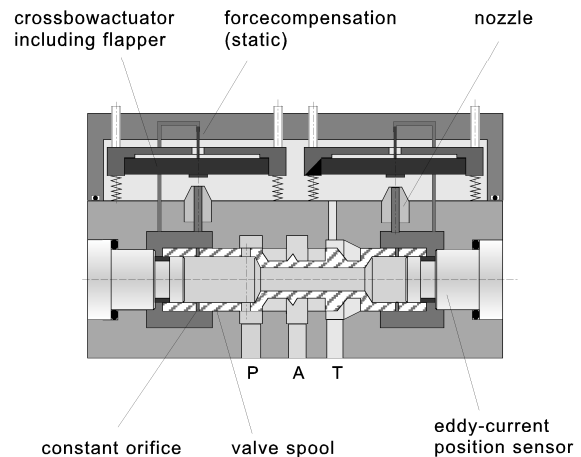


Figure 5 Sectional view of the servo-valve

In order to achieve a maximum pressure difference on the faces of the spool and therefore a maximum force for the movement, both bending actuators are always driven in opposite phases.

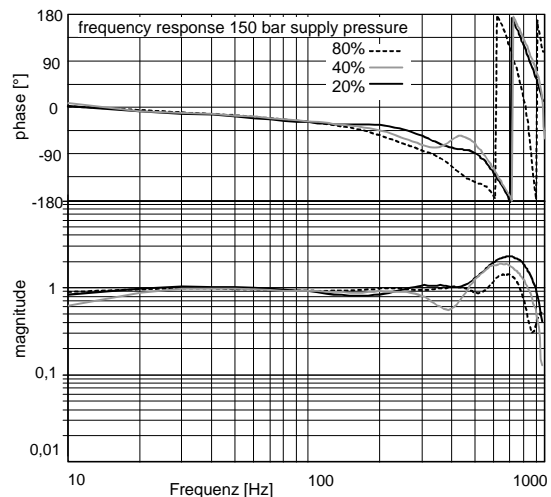


Figure 6 Frequency response of the valve spool in the position control circuit

The displacement transducer, which is based on the eddy-current measuring principle, is required for the subordinate position control loop and is integrated into the valve spool. The end faces of the spool are reduced by stoppers, that house the electrical windings for the displacement transducer. The reduced faces limit the force acting on the spool as well as the required pilot flow to move the spool. The diameter of the stoppers can be modified in order to meet the specific restrictions [4].

The spool valve travels ± 1 mm and the nominal flow rate is 44 l/min. The pressure signal function of an

initial prototype version was measured and indicates a gradient of 4000 bar/mm at zero point and is similar to the gradient of high-quality servo-valves. The gain in volume flow is about 80 l/min/mm [4]. Figure 6 shows the closed-loop frequency response of the valve with a position-controlled spool. An analog PI controller was used to close the loop. The cut-off frequency (-90°) was measured at about 550 Hz with 20 % amplitude.

CHARACTERISTICS OF THE HYDRAULIC DRIVE

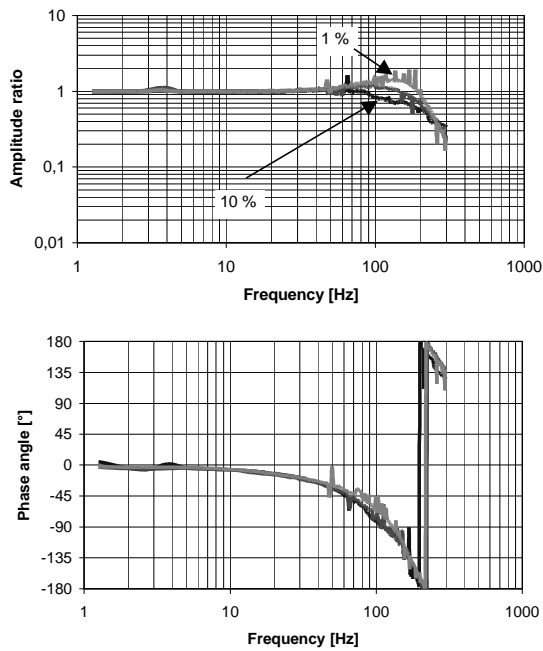


Figure 7 Dynamic of the drive

Figure 7 shows a satisfying dynamic behavior of the drive of the active ring in a bode-plot of the closed-loop step response for various signal levels. It is examined while an analog PI-controller closed the position-control loop and conventional servo-valves (approximately 200 Hz cut-off frequency) were applied to the drive.

The cut-off frequency (-3dB) is reached within 200 Hz and the -90° of the drive reaches 120 Hz at low signal level. This shows, that the drive dynamic is close to the valve dynamic. It does not totally reach the valve dynamic because with the small cavities, which are used for the drive, even the smallest unavoidable leakage leads to a pressure drop in the cavity. Therefore the valve-spool has to open further than the controller signal requests in order to pressurize the cavities satisfactorily [1].

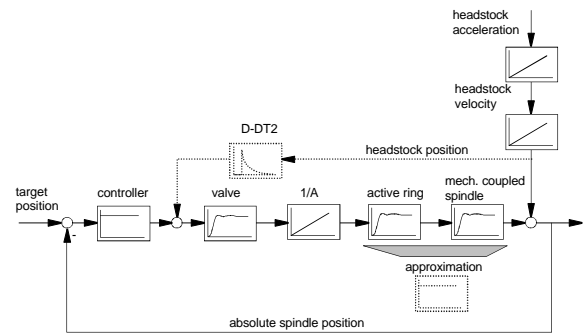


Figure 8 Position control with feed-forward control

As the drive is of a higher dynamic than the valve, the valve dynamic limits drive performance. If the system were linearly approximated, it could be characterized by a series of a servo-valve with a PT_2 -characteristic, an integrator (I), the active bearing ring itself (PT_2) and the spindle, fixed to the ring via the conventional bearings (PT_2). Reducing this complex system down to a PT_2 -I does not affect the system dynamic in the range where it is normally driven. This is because the transmission behavior of the active ring and the spindle-bearing-arrangement can be approximated by proportional elements (Figure 8). Their eigenfrequencies are by far higher than the dynamic of the remaining system. Sensing the acceleration of the headstock and filtering the signal through a $D-DT_2$ -filter before adding it to the controller output could eliminate the influence of the headstock movement by means of a feed-forward control. This is because the filtered headstock-position and the control path (valve \rightarrow cylinder \rightarrow mechanic) show an inverse characteristic to one another.

SUPPORTED FURTHER DEVELOPMENT BY MEANS OF SYSTEM SIMULATION

While the prototype of the active spindle bearing is investigated, the drive is also analysed within the simulation environment of *DSHplus* [3]. The simulation of the drive is a first important step to gain experience with dynamic behaviour of the drive. In figure 9 the simulation model of the active unit is introduced. For the simulation of the three-cavity-ring, which is not part of the library of *DSHplus*, the movement of the active ring is limited to one coordinate and simulated as a standard cylinder drive. Thus **chamber 1** is supplied by **valve 1** (3-3-way-servovalve), whereas **chamber 2** is supplied by **valve 2** and **valve 3** one half each. The **current value** of the position of the active ring is compared to the **target value** and the resulting **control deviation** is causing a input signal for **valve 1** and multiplied with “-0.5” for **valve 2** and **valve 3**. By this an excitation in vertical

direction is approached (figure 3). The **pressure source** supplies a **system pressure** of 200 bar. The displacement of the drive is controlled by a simple proportional controller. The valves are parameterised according to the manufacturers data, the cylinder and the remaining elements according to the design data. Line lengths and other capacities have similar dimensions as within the real part.

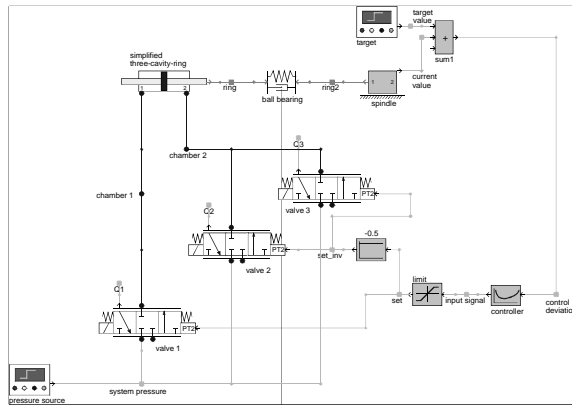


Figure 9 The three-cavity-ring as a model in the DSHplus environment

Working with a simulation tool gives the opportunity to evaluate modifications of the drive, without modifying the prototype. In spite of the fast results using the simulation environment, results cannot be adopted offhand, but need to be investigated on the prototype afterwards [5].

CONCLUSIONS

A high-dynamic three-cavity hydraulic cylinder drive is presented in this paper. It shows promising dynamic characteristics in the test-arrangement and will be investigated during a real milling process to prove its ability to damp chatter vibrations.

Another final goal will be to test the combination of feedback and feed-forward control to overcome chattering during milling operations. With all software

and controller-design being tested good, the controller will be implemented on a microprocessor to enable the active spindle bearing system to remove chattering from process independently – as necessary for an autonomous production cell.

ACKNOWLEDGEMENTS

The collaborative research center 368 “Autonomous Production Cells” is funded by the DFG (Deutsche Forschungsgemeinschaft).

REFERENCES

1. Breit, H., 2002, Aktive Spindellagerung, Ölhydraulik und Pneumatik (O+P, German journal for fluidpower), available at www.industrie-service.de
2. Danek, Polacek, Spacek, Tlustý, 1955, Selbsterregte Schwingungen im Werkzeugmaschinenbau, VEB Verlag Technik, Berlin
3. Fluidon, 1999, DSHplus user manual, Aachen (Germany)
4. Hagemeyer, W., 1999, Auslegung von hochdynamischen servohydraulischen Antrieben für eine aktive Frässpindellagerung, Dissertation RWTH Aachen
5. Kohmäscher, T., 2004, Aktive Frässpindellagerung – Kompensation von Maschinenschwingungen, Ölhydraulik und Pneumatik, 9/2004, S. 550-557
6. Murrenhoff, H., 2002, student tutorial Servohydraulik, RWTH Aachen University
7. SFB368, 1999, Autonome Produktionszellen, Forschungsantrag des Sonderforschungsbereichs 368 at RWTH Aachen University (Germany)
8. Weck, M., 1996, Meßtechnische Untersuchung und Beurteilung, Werkzeugmaschinen, Fertigungssysteme, Band 4, VDI-Verlag Düsseldorf, 5. Auflage 1996

DEVELOPMENT OF THE TEST SYSTEM FOR MEASURING THE IMPACT ENERGY OF A HYDRAULIC BREAKER

Jong-Won PARK*, Hyoung-Eui KIM*

* Hydraulic and Pneumatic Group, Department of Advanced Industrial Technology
Korea Institute of Machinery and Materials
171 Jang Dong, Yu Sung Gu, Taejun, 305-600, South Korea
(E-mail: jwpark@kimm.re.kr)

ABSTRACT

A hydraulic breaker for construction machinery generally used for the destroying and disassembling of buildings, crashing road pavement, breaking rocks at quarry and so on. So the measurement of the impact energy of a hydraulic breaker is very important thing to prove its capability to manufacturers and customers. In this study, the test system for measuring the impact energy of a hydraulic breaker was designed and constructed. The test system was consisted with hydraulic cylinders for mounting a breaker, impact absorbing base and frames, pressure and flow sensors, high speed and accurate data acquisition system, diesel engine driven hydraulic power pack and etc. The test process of the developed system was carried by measuring guide for tool energy rating for hydraulic breakers which was developed by the CIMA (Construction Industry Manufacturers Association) USA. The developed test system can be applied to measure the impact energy for various kind of hydraulic breakers.

KEY WORDS

Hydraulic breaker, Measuring impact energy, Test system, Strain gauge equipment, Tool impact energy calculation

NOMENCLATURE

A_t : Cross-sectional area of the test tool at strain gage assembly location
 CF : Correction factor from static calibration
 E_i : A single blow impact energy of the tool
 E_t : Young's modulus of the test tool material
 f_i : Blow frequency
 H : Distance between the strain gage assembly and the tip of the test tool
 k : Gage factor (must be the same for all active gages)
 K_a : Amplification factor of the amplifier ($K_a=1$, if amplifier not used)
 L_p : Length of the piston
 ρ_t : Mass density of the test tool material
 P_{in} : Total hydraulic input power

P_s : Hydraulic supply line pressure
 P_r : Hydraulic return line pressure
 Q_i : Breaker inlet oil flow
 T : Operating oil temperature
 t : Time
 t_l : Starting time of integration
 t_n : Ending time of integration
 Δt_i : Integration interval, $\Delta t_i = (t_{ni} - t_{li})$
 U : Bridge output voltage
 U_B : Bridge supply voltage
 ε_i : Measured strain
 ν : Oil kinematic viscosity

INTRODUCTION

A hydraulic breaker for construction machinery

generally used for the destroying and disassembling of buildings, crashing road pavement, breaking rocks at quarry and so on. A hydraulic breaker is composed of cylinder, piston, valve, back head, chisel and power cell and these components are fixed by bracket. The section view of the general structure of a hydraulic breaker is shown in Figure 1.

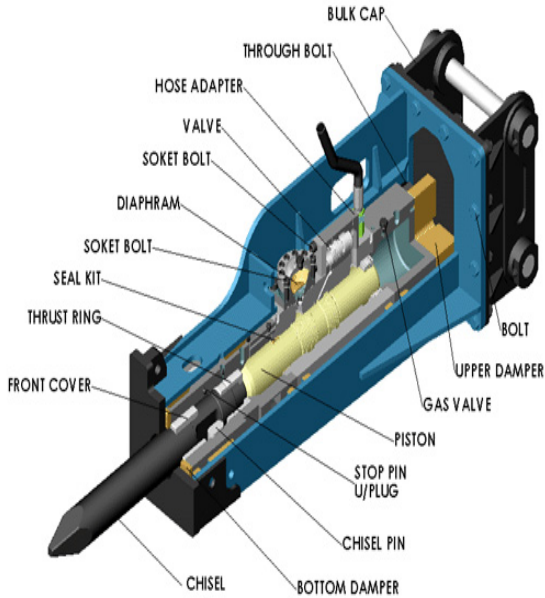


Figure 1 General structure of a hydraulic breaker

A hydraulic breaker blows an object using kinetic energy that is transferred by impacting chisel with reciprocating piston via hydraulic power from an excavator. So the measurement of the impact energy of a hydraulic breaker is very important thing to prove its capability to manufacturers and customers. But a hydraulic breaker is operated by very large kinetic energy, so that the accurate measurement of impact force has been considered too difficult problem.

In this study, the test system for measuring the impact energy of a hydraulic breaker was designed and constructed. The test system was consisted with hydraulic cylinders for mounting a breaker, impact absorbing base and frames, pressure and flow sensors, high speed and accurate data acquisition system, diesel engine driven hydraulic power pack and etc. In addition the process of measuring impact energy and the consideration of the test result was discussed.[1][2][3]

DEVELOPMENT OF TEST SYSTEM

The test system, shown in Figure 2, was developed to evaluate the impact energy of hydraulic breakers. As shown in Figure 2, the developed test system holds a breaker by 4 hydraulic cylinders and can evaluate the impact energy for various sizes of breakers by adjusting the stroke of 4 hydraulic cylinders. In addition to, the

developed system has another hydraulic cylinder on the upper part of it to regulate blowing angle in testing.

Target base was constructed with accumulating vibration isolating materials like as sands, broken stones, trees and rubbers after 5m depth foundation work to absorb shock and vibration at blowing. The schematic diagram of the target base is shown in Figure 3.

Hydraulic power for operating breaker is supplied by tandem pump that has maximum rated supply flow rate 580LPM and maximum rated supply pressure 450bar. The tandem pump is driven by diesel engine to realize similar operating condition of excavators. The tandem pump and diesel engine that was equipped in the developed test system are shown in Figure 4.

Data acquisition equipment has above 125 kHz cutoff frequency and 4 MHz sampling frequency to detect shock wave accurately. The data acquisition equipment is controlled by real time operating system and software was developed to carry test process automatically.[5]

Pressure, turbine type flow and temperature sensors are used for monitoring the status of test system and breaker and measuring parameters to evaluate impact energy. Data acquisition equipments are shown in Figure 5 and the schematic diagram of the hydraulic circuit of the test system is shown in Figure 6.



Figure 2 Mechanism of test system

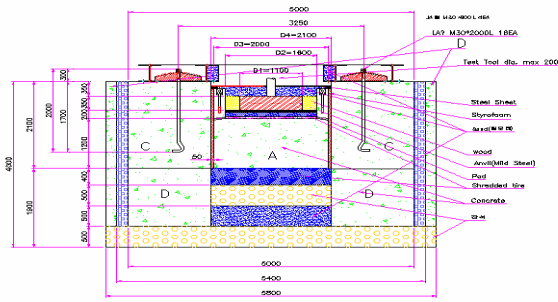


Figure 3 Target base of test system

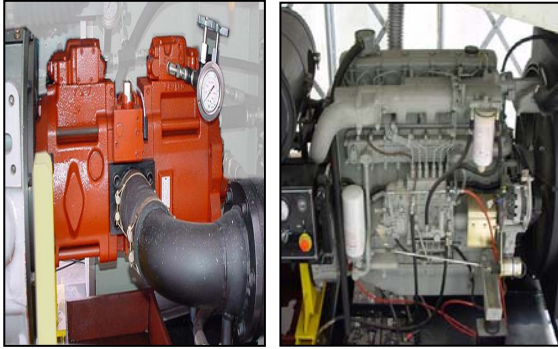


Figure 4 Hydraulic power unit of test system

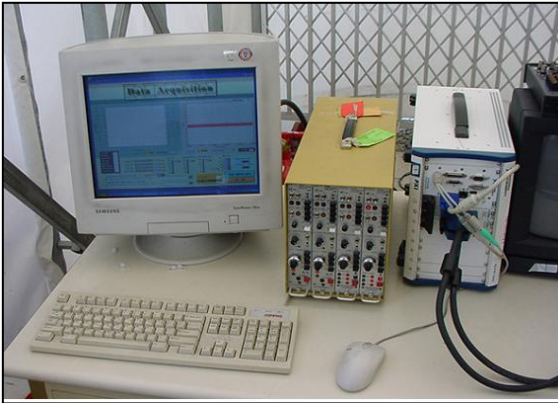


Figure 5 Data acquisition equipment of test system

IMPACT ENERGY EVALUATION

The developed test system evaluates the impact energy of hydraulic breakers, after measuring the strain of chisel with strain gauge.[4] Strain gauge attached test tool is shown in Figure 7.[6][7]

To evaluate the impact energy of a hydraulic breaker, we have to proceed as following process.

Single blow impact energy can be calculated from the measured strain using the equation (1) and this can be derived by elastic strain energy method for an impact loading.

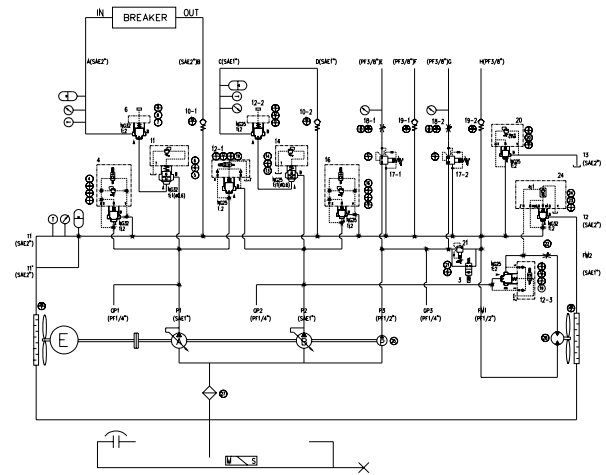


Figure 6 Schematic diagram of test system

$$E_i = \frac{CF^2}{A_t \cdot \sqrt{E_t \cdot \rho_t}} \int_{t_1}^{t_n} \epsilon_i^2 \cdot dt \quad (1)$$

Where, $\epsilon_i = 4 U / (2.6 k U_B K_a)$

The integration interval t_1 through t_n must be defined for each measurement to identify and isolate the effect of the hydraulic breaker static preload on the test tool strain and to prevent accumulation of stress from the next pulse or reflected stress wave.

The 25 energy measurements must be recorded in a steady state operation with test breaker's specifications.

The 25 measurements can be divided into sets of 5 consecutive blows minimum. Each measured energy value shall be within $\pm 10\%$ of the average value calculated in final tool impact energy. Final tool impact energy can be calculated by equation (2). Energy values out of this range must be disregarded and measurement shall be taken again. Total output efficiency can be calculated by equation (3).

$$E = \frac{1}{25} \sum_{i=1}^{25} E_i \quad (2)$$

$$\eta_{tot} = \frac{E \cdot f}{(P_s - P_r) \cdot Q} \quad (3)$$

The complete measuring equipment and installation must be calibrated by comparing the strain ϵ_{meas} calculated from the measuring equipment output voltage with the calibrated force F_{cal} applied on the test tool and measured by a calibrated load cell. Calibration will be carried out by compressing the test tool (without breaker) against a force transducer (load cell) for example in a hydraulic press. Correction factor CF can be calculated by equation (4).

$$CF = \frac{F_{cal}}{\varepsilon_{meas}} \quad (4)$$



Figure 7 Strain gauge attached chisel

TEST RESULT

Detection of the Shock Wave

The detected shock wave of impact energy strain is shown in Figure 8 and the test result of blow frequency is shown in Figure 9. The integration limits t_1 through t_n must be defined for each pulse to identify and isolate the effect of the static preload of the breaker on the test tool strain and to prevent accumulation of the strain from the next pulse. Before impact, the test tool will begin to unload due to recoil of the hydraulic breaker body. Time t_1 must be measured in this region of the curve. The baseline of integration will be taken at the point t_1 . The last time recorded, t_n , for each pulse, must be separate and distinct from the next pulse or reflected stress wave. Time t_n should be measured at the point where the pulse curve becomes negative in relationship with the baseline. Integration will stop when the curve reaches the same strain level that was found at time t_1 . However, the maximum integration interval $t_n - t_1$ must be less than $2H/c_t$ with, $c_t = \sqrt{E_t/P_t}$. Usually the distance $H = 1.2L_p$ is sufficient, if not, the stress wave may combine with the reflected wave causing incorrect instrumentation readings and energy results. This can occur especially, when the piston cross-sectional area A_p is greater than the tool cross-sectional area A_t . In this case the test tool is too short and distance H should be at least $2L_p$. [4]

Total uncertainty of the test result

From equation (1), the uncertainty of the tool impact energy measurement can be calculated by equation (5) and the total uncertainty with $\pm 2\sigma$ value, 95.7% probability in normal distribution can be calculated by equation (6).

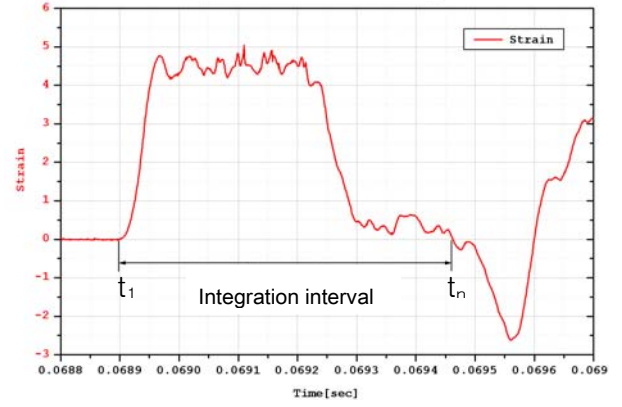


Figure 8 Shock wave of impact energy strain

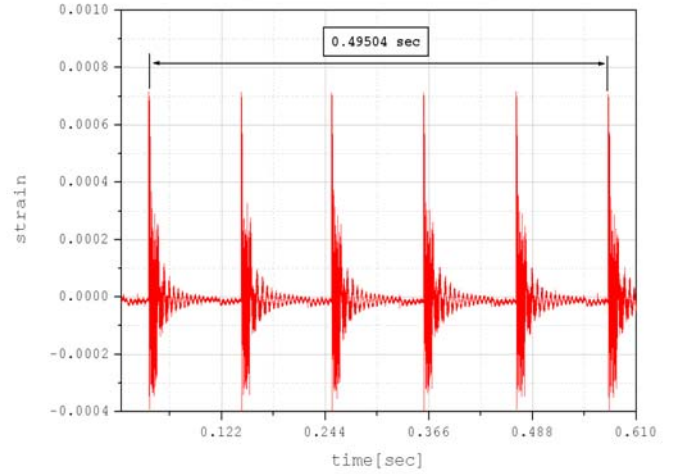


Figure 9 Test result of blow frequency

$$\Delta E = 2 \cdot |\Delta CF| + |-\Delta A_t| + \frac{1}{2} \cdot |-\Delta E_t| + \frac{1}{2} \cdot |-\Delta \rho_t| + |\Delta Integ| \quad (5)$$

$$U_{tot, \pm 2\sigma} = \pm \frac{2}{3} \cdot \sqrt{(\Delta E)^2 + (\Delta p_s)^2 + (\Delta p_a)^2 + (\Delta \varepsilon)^2} \quad (6)$$

The maximum allowed uncertainties of the measured parameters in the equation (5) and (6) are as follows.

$$\Delta P_s = \pm 1\%, \Delta P_a = \pm 2\%, \Delta \varepsilon = \pm 1\%, \Delta CF = \pm 1.5\%$$

$$\Delta A_t = \pm 0.2\%, \Delta E_t = \pm 3\%, \Delta \rho_t = \pm 0.4\%, \Delta Integ = \pm 0.2\%$$

By substituting the maximum allowed uncertainties of

the measured parameters to the equation (6), $U_{tot, 2\sigma}$ can be evaluated as follows.[4]

$$U_{tot, \pm 2\sigma} = \pm 3.8 \% \quad (7)$$

In this study, the total uncertainty was calculated to 3.74%. So the developed test system could satisfy the allowed uncertainties.

CONCLUDING REMARKS

In this study, the test system for measuring the impact energy of a hydraulic breaker was designed and constructed. The test system was consisted with hydraulic cylinders for mounting a breaker, impact absorbing base and frames, pressure and flow sensors, high speed and accurate data acquisition system, diesel engine driven hydraulic power pack and etc. The test process of the developed system was carried by measuring guide for tool energy rating for hydraulic breakers which was developed by the CIMA (Construction Industry Manufacturers Association) USA. The developed test system can be applied to measure the impact energy for various kind of hydraulic breakers and was certified to test cite for breakers by AEM(The Association of Equipment Manufacturers).

REFERENCES

1. Geun-Ho Lee, Young-Bum Lee, Ki-Young Lee, Development the Test System of Impact Energy Using the Pressure Variation in Closed Vessel for Hydraulic Breaker, Transactions of Korea Institute of Machinery and Materials, 2002, Vol. 32, pp.45-53.(in Korean)
2. Kwihyun Choi, Changseop Song, A Study on the Performance Improvement of a Hydraulic Breaker, Transactions of Korean Society of Precision Engineering, 1998, pp.1028-1031.(in Korean)
3. Wonjune Sung, Taebong Noh, Changseop Song, A Study on the Reducing the Return Line Pressure Fluctuation of the Hydraulic Breaker System, Journal of Korean Society of Precision Engineering, 2002, Vol. 194.(in Korean)
4. CIMA (Construction Industry Manufacturers Association), Measuring Guide for Tool Energy Rating for Hydraulic Breakers, Milwaukee, USA, 1996
5. IEEE 1057, Digitizing Waveform Recorders
6. ASTM E251, Test Method for Performance Characteristics of Metallic Bonded Resistance Strain-gages
7. NAS 942, Strain-gages Bonded Resistance
8. John Watton, Fluid Power Systems, Prentice Hill, 1989
9. Ferdinand P. Beer, E. Russell Johnston Jr, Vector

DEVELOPMENT OF TESTING MACHINE USING PARALLEL MECHANISM

Ken ICHIRYU, Tomoyuki TANAKA
Faculty of Engineering
Tokyo University of Technology,
1404-1 Katakura, Hachioji, Tokyo, 192-0982 Japan
(E-mail: t-tanaka@ichry.mech.teu.ac.jp)

ABSTRACT

The bench test machine of single shaft is used to develop the motorcycle frame now. It is not expressible for the simple apparatus though combined load is added to the frame while the motorcycle is actually running. Parts of the motorcycle might break down some time. This is very dangerous and efficient test method is desired. But application of conventional test method of single or multiple actuators is difficult, because test object is relatively small and fragile. In this situation, we developed new method of load test using parallel mechanism. Advantage of this method is possibility to generate any assigned force or moment vector at desired small point. That is, combined skew force or three-axis moment test becomes possible by only software change. We actually designed practical parallel mechanism actuating system for motorcycle. End-effector force and moment vector are converted to cylinder pressure command by Jacobian matrix method.

KEY WORDS

PARALLEL MECHANISM, POSITION CONTROL, LOAD CONTROL,
HYBRD CONTROL, JACOBIAN MATRIX, FRAME OF MOTORCYCLE

NOMENCLATURE

i: 1~6
Fi: Position of joint installation on the platform
Gi: Position of joint installation on the base
E: Offset of rotation center
H: Height of neutral point
ti: Thrust of the actuator
fi: Power and moment of platform
J: Jacobian
f: End effector's power and moment
t: Thrust of actuator

INTRODUCTION

The bench evaluation examination of the single shaft testing machine is used for the development of the motorcycle frame now. However, present evaluation method is too simple to simulate actual complicated phenomena of motorcycle running condition. So the result of damage and the test that occurred because of the actual operation examination was not completely corresponding. Therefore, in actual running test, unpredictable failure and rupture of welded parts are frequently observed. Main reason of this kind of problem is the adoption of aluminum to motorcycle. From the need of lightening, aluminum is widely applied, and this tendency is assumed to continue in a future, too. Therefore, the body becomes the low limit design of the safety factor. Consequently,

evaluation test by present single axis machine could not satisfy required performance. Possible testing machine to evaluate complex load near actual running will improve the simulation function. So reduction in cost by improvement of development speed will be anticipated by this method. Purpose of our study is to develop new parallel mechanism machine possible to make actual load by complex actuating. In the following, design and control method of this machine will be described.

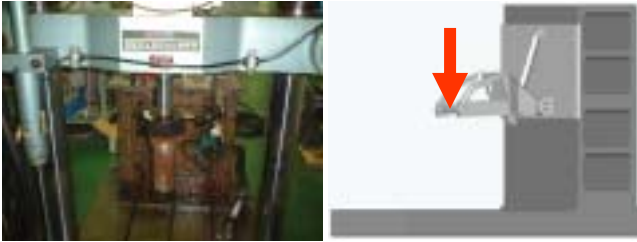


Fig.1 Existing bench test machine

PARALLEL MECHANISM

Definition of Parallel Mechanism

Parallel mechanism is defined as mechanism having plural of power transmission paths between base and mechanical interface. This mechanism is divided in four types, namely, stretch, direct, rotational and wire type. In this study, Stewart platform parallel mechanism of stretch type is selected.

A system that has 12 universal joints and 6 cylinders to hold upper plate (platform) and lower plate (fix base), and generates six phases of free movement by changing the length of cylinders. Refer to Fig.2.

Inverse Kinematics of Parallel Mechanism

In parallel mechanism, command signal of each actuator is easily obtained by inverse kinematics. Inverse kinematics is determination of each on link length from the position of end-effector, and the position of each actuator is defined as the Fig. 2. That amount of displacement becomes command signal.

Linearized Small Scale Motion Dynamics of Parallel Mechanism and Statics

Relationship between platform and actuator displacement under Linearized small scale condition, is solved. But, Jacobian matrix thus found, is a inverse Jacobian matrix, because this is inverse kinematics case. From the principle of virtual work, considering actuator and platform dong small scale motion at their equilibrium state;

$$J^T f = t$$

is obtained. From this equation, each actuator's output

is shown clearly by the force, moment applied by platform.

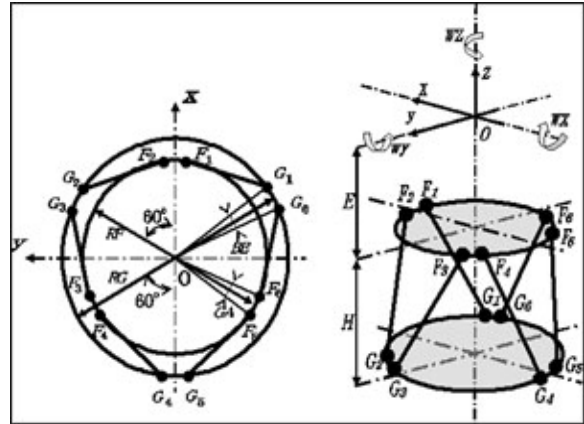


Fig.2 Coordinate definition of parallel mechanism



Fig. 3 Parallel mechanism

THE FLOW OF SYSTEM AND MACHINE SPECIFICATION

Specification of Parallel Mechanism

Parallel mechanism was newly designed for this study. Design conditions are as follows;

- Each output force X, Y, Z direction is 10kN, respectively.
- Wide workspace is not necessary.
- Size of this equipment should be same as present machine.
- From the above condition, new parallel mechanism was designed. The main specifications are shown in Table 1 and 2.

Table.1 Size of Parallel Mechanism

DIAMETER OF PLATFORM	φ350mm
DIAMETER OF BASE	φ880mm
JOINT INSTALLATION ANGLE OF PLATFORM	37deg
JOINT INSTALLATION ANGLE OF BASE	14deg
CYLINDER STROKE	100mm
HEIGHT OF NEUTRAL POSITION	452mm
SETTING ANGLE OF CYLINDER	49deg
TOTAL LENGTH OF CYLINDER	466mm

Table.2 Work Space and Output Power

	Work Space	Output Power
SURGE	+73mm -84mm	10kN above
SWAY	+75mm -75mm	10kN above
HEAVE	+65mm -70mm	10kN above
ROLL	+24deg -24deg	
PITCH	+30deg -22deg	
YAW	+25deg -25deg	

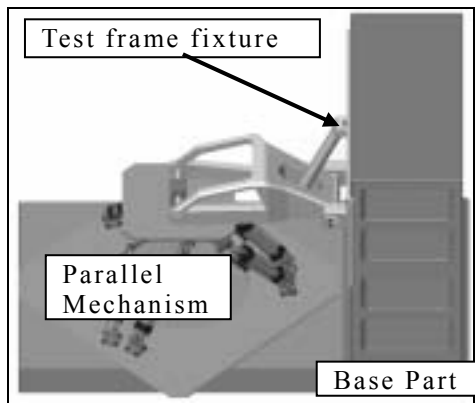


Fig.4 Image Figure of the test system

The testing machine consists of base part, parallel mechanism, and the test frame fixture. Image figure of

the test system is shown in Fig.4.

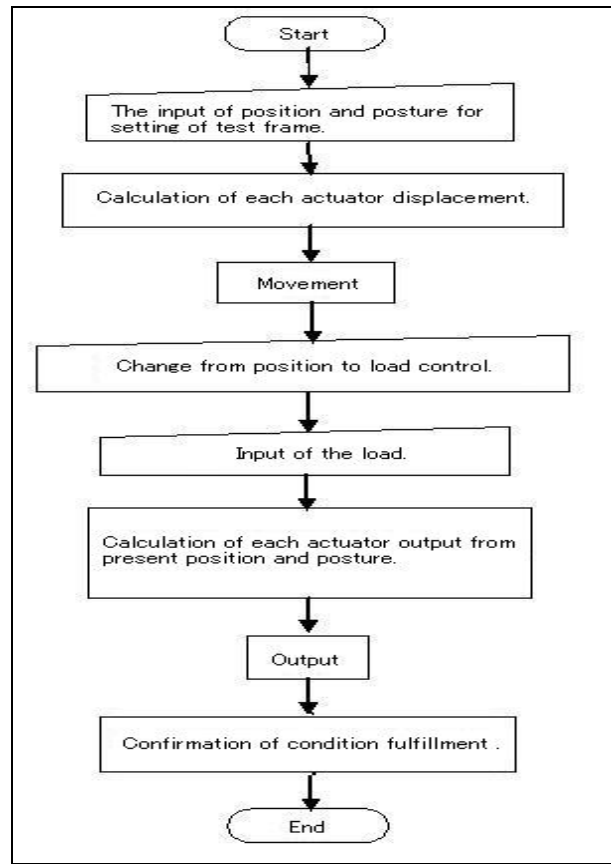


Fig.5 The flow of the system

Flow of the System

The flow of the system consists of two parts. The first is the work to connect test frame and the best machine by using position control of the parallel mechanism. The second is the work to generate force to each actuator by using load control algorithm. System flow is shown in Fig.5.

POSITION CONTROL AND LOAD CONTROL

Position Control

Position and posture of the platform are input to fix the test frame, and stroke of each actuator is calculated by using inverse kinematics. Command signal corresponding to this value is transmitted from personal computer to servo valve. Thus cylinder stroke is controlled. Actuator is detected by potentiometer. Position control loop is shown in Fig.6. Band with of this system is designed about 10Hz At present, software servo loop is constructed, which has 10ms sampling time.

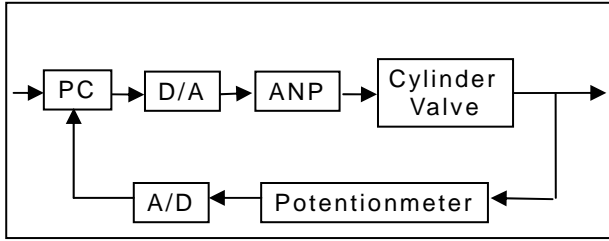


Fig.6 Position Control of Parallel Mechanism (1 axis)

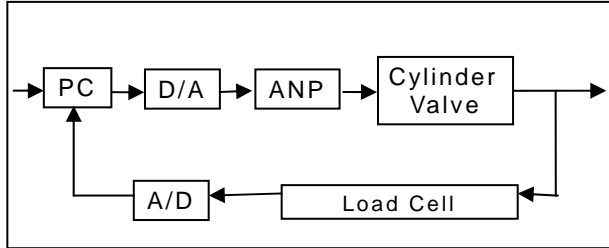


Fig.7 Load Control of Parallel Mechanism (1 axis)

Load Control

Load is inputted to the test sample from platform tip. Necessary force for each actuator is calculated from the position and posture of the test sample. Command signal is then given to servo system and thrust force is controlled. Thrust force is detected by the actuator in and out ports. Load control loop is shown is Fig.7. Band with of this system is assumed about 2Hz.

SIMULATION OF LOAD CONTROL

Resolved necessary thrust force for each actuator was calculated from command force to the test sample through parallel mechanism, this time. And, the arrangement of the actuator is shown in the Fig.8. It is possible to calculate for combined load as shown in Table.5. This value is outputted for each actuator.

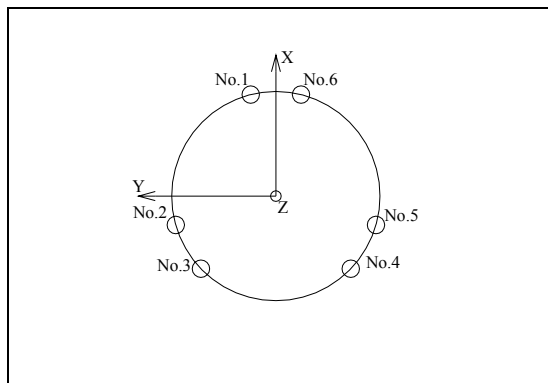


Fig.8 Arrangement chart of actuator

Table.3 In the Z direction, 10kN

No,1 Actuator	2.17kN
No,2 Actuator	2.17kN
No,3 Actuator	2.17kN
No,4 Actuator	2.17kN
No,5 Actuator	2.17kN
No,6 Actuator	2.17kN

Table.4 In the Y direction, 10kN

No,1 Actuator	- 4.63kN
No,2 Actuator	- 3.6kN
No,3 Actuator	1.03kN
No,4 Actuator	- 1.03kN
No,5 Actuator	3.6kN
No,6 Actuator	4.63kN

Table.5 In the Y and Z direction, 5kN

No,1 Actuator	- 1.24kN
No,2 Actuator	- 0.72kN
No,3 Actuator	1.6kN
No,4 Actuator	0.56kN
No,5 Actuator	2.88kN
No,6 Actuator	3.39kN



Fig.9 Overall view of the testing machine

COMPLIANCE CONTROL

In this research, the compliance control was used for the load control method. The compliance control decides the direction where it wants to control the position or power, and the position and power in those directions are matched to the value of the target. First of all, the position and the power that should be controlled are measured. They are fed back, and the control technique that provides with the position control loop and the force control loop to match it to the set point is used. Therefore, the force control loop consists of taking

measurements of power and deflection with the target load in high rank of position control loops, and sending as the instruction to the position control. The installation part of the load cell is shown in Fig.10.

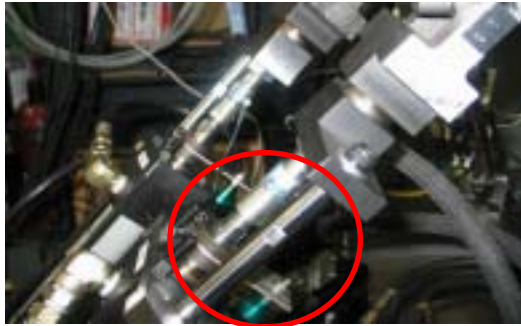


Fig.10 The installation part of the load cell

LOAD TEST IN DIRECTION OF HEAVE

The load only in the direction of heave is added to the motorcycle frame. The load is added from 0kN to 5kN in each 0.5kN. And the stability when 5kN is added is verified from 0kN.

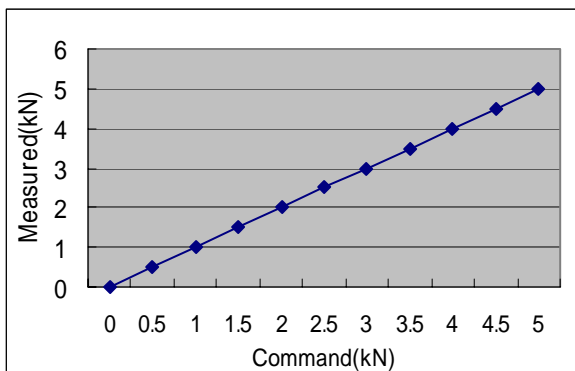


Fig.11 Comparison between measured data and command data

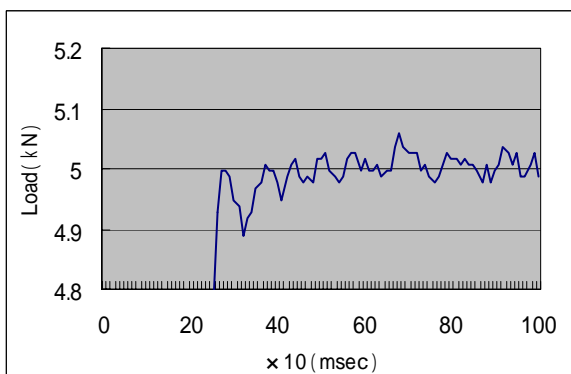


Fig.12 Stability of data

Experiment result

As for the comparison by the measurement and the command data, excellent data was obtained. The error margin was the maximum was 1%. The load was 5kN from 0kN and time when it reached was 250 milliseconds. And Stability was ± 0.075 kN.

CONCLUSION

In this thesis, the effectiveness of the use of the load control with the bench test machine that used the parallel mechanism was verified. It will examine it in all directions of six axis in the future. The actual running test by the bench test is scheduled to be simulated by using the data of actual running test in the future.

REFERENCE

1. Shigeo Hirose: Robotics -Vector Analysis of Mechanical System-(2nd ed.), Shokabo, 1996
2. Japan Robotic Society: Report of Parallel Mechanism, 1993.

DEVELOPMENT OF CNC BENDING MACHINE USING PARALLEL KINEMATICS MECHANISM

Ken ICHIRYU, Zenkoh YAMAGUCHI and KOGA

Faculty of Engineering

Tokyo University of Engineering

1404-1 Katakura-cho, Hachiohji-shi, Tokyo, Japan

(E-mail: zenkou@ichry.mech.teu.ac.jp)

ABSTRACT

Recently, aluminum pipe is needed by industrial world. Because it is high rigidity and light. There are many methods of processing pipe. But now bending method is ill-suited to high-mix low-volume production. And so we looked at the feed pressure (MOS) bending machines. But there are many problems in them. First of all, structure of processing part is complex, and object of bending is confined to circular pipe. We developed three dimensional pipe bending machine using PKM (parallel kinematics mechanism). In this paper, we will be able to show bending accuracy and proposal of new bending machine.

KEY WORDS

Parallel kinematics mechanism, Gradual curve part, Bending angle, Limit of bending,

NOMENCLATURE

R : Bending radius
 u : Offset
 V : Distance between dies
 P_L : Pushing load
 θ : Angle of die
 t : twisting rate
 L_v : Length of work of distance between dies
 θ_b : bending angle

BACKGROUND

Recently, industry requires different production method best fitted for its purpose. Same situation is observed in bending manufacturing field. As conventional bending method, there are press bending, tension bending. Above methods require own dies according to their profiles. Therefore, these methods are difficult to apply for modern small number production. In order to solve this problem, push forward bending method (MOS bending method) was proposed, recently. In MOS bending method, any assigned bending profile is possible to make by using two dies. Work is driven by feeder and it is bent by two dies combination. By this MOS bending method, die cost reduction becomes possible, because there is no need to make die corresponding to bending radius. Also, three dimensional profile bending becomes possible

PRESENT MOS BENDING MACHINE

Let explain about present MOS bending machine. Structure of bending head is simple in the machine shown in Fig.1. But sectional working profile is limited to circular, due to deficiency of freedom of bending head motion. By conventional machine to achieve universal profile bending, bending head becomes complicated, as shown in Fig2.

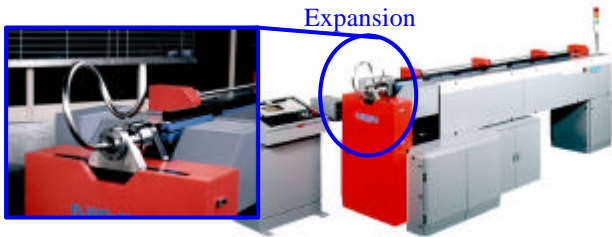


Figure 1 MOS bending machine example1

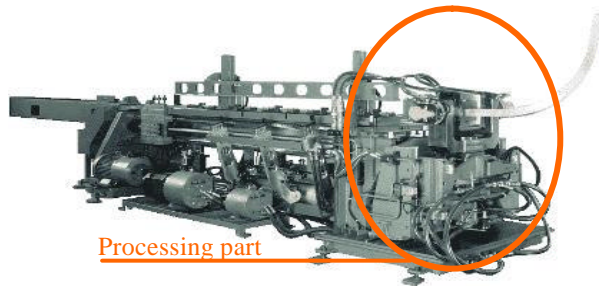


Figure 2 MOS bending machine example2

To solve this problem, we proposed new MOS bending machine using 6-axis parallel kinematics mechanism (PKM). Feature of PKM is high accuracy, high rigidity and simple structure. By using PKM as bending head, new universal compact machine is expected to realize.

PURPOSE

Purpose of this research is to develop MOS bending machine using 6-axis PKM working head. In this time, we announce effect of bending parameter on shape and quality.

PROPOSED BENDING MACHINE

In Fig.3, overall view of testing machine is shown. The machine is composed of working head and feeder, and controlled by simultaneous 7-axis motion controller.

Working head

Working head, driving part of movable die shown in Fig3, is composed of 6axis extensible type PKM. Working head is controlled by 6 actuators semi-closed loop

positioning.. Movable die is installed at the center of the end effector. Fixed die is positioned at the center of foundation on base plate.

Feeder

Feeder, shown in Fig.3, is composed of electric motor and ball screw and guide rail supporting member. Guide rail prevents buckling of the work between guide die and pusher. Feeding actuator control is same with PKM actuator control.

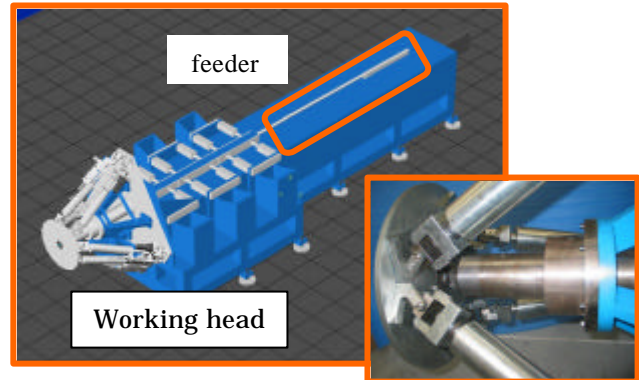
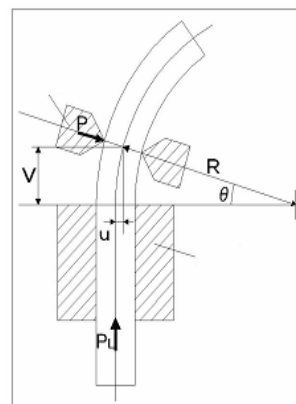


Figure 3 Proposal MOS bending machine

PRINCIPLE OF BENDING

Principle of simple bending

Principle of simple bending follows the MOS bending method. MOS principle is shown in Fig.4. Here, state of bending is schematically shown. Movable die is displaced u from the center of the fixed die axis. Here, there are two forces acting on this system, that is, pushing load PL and working load P which depends on offset u . Bending moment $M=P \times V$ is main factor of bending action, where V is distance of both dies. Each parameter is presented in the following.



$$u = R - \sqrt{u^2 - V^2} \quad (1)$$

$$q = \sin^{-1} \frac{V}{R} \quad (2)$$

Figure 4 simple bending

Principle of twist bending

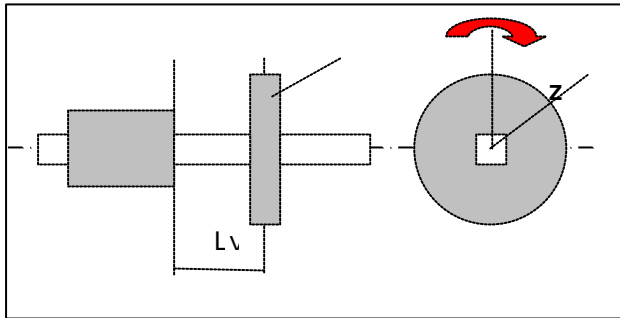


Figure 5 Principle of twist bending

Movable die is twisted by θz . Twist bending moment $M_L = L_v \times P$ is main factor of twisting action. Twisting rate is presented in the following.

$$t = \frac{q_z}{L_v} \tag{4}$$

Principle of spiral bending

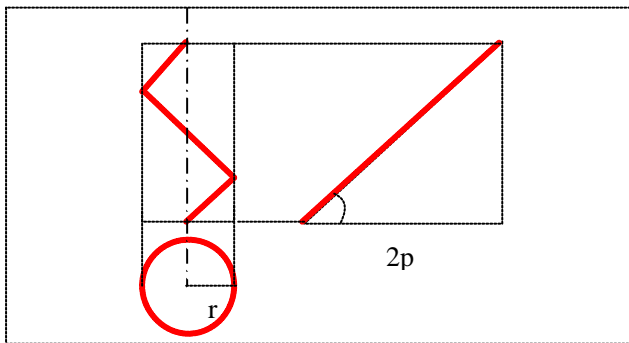


Figure6 Principle of spiral bending

Spiral bending can be achieved by the synthesis of simple bending and twist bending.

Spiral bending parameter is presented in the following. Steady-state spiral can be constructed with spiral pitch and spiral radius. Therefore, steady-state spiral is expressible by Frenet-serret formula.

$$r = \frac{k}{t^2 + k^2} \tag{5}$$

$$P = 2p \sqrt{r \cdot \left(\frac{1}{k} - r\right)} \tag{6}$$

Therefore, spiral bending is achieved by twist rate and curvature. Various spiral bending is achieved to replace twist rate and curvature by twist bending factor and simple bending factor.

PROGRESS IN DEVELOPMENT

Recently, we confirmed factor of simple, twist and spiral bending[1]. Bending angle of products and improvement of processing limit are researched.

Bending angle of products

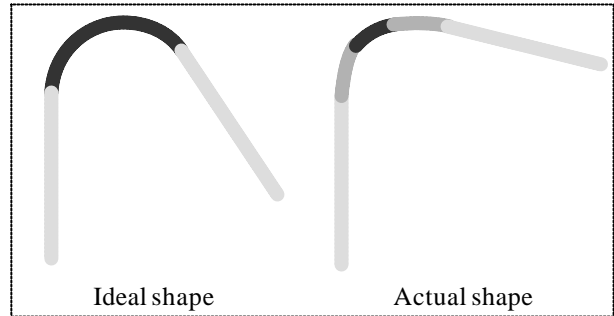


Figure7 Ideal and actual shape of pipe

Ideal shape is composed by straight part and defined curve. But It actually becomes as shown in Fig 7. It is because PKM is moved while the material is being pushed. As a result, the error margin is caused between the ideal value and the actual value. And a high accurate processing is impossible. And so, we tried to cut off gradual curve part. It is necessary to bring movable die close to fix die to that end. And, distance of gradual curve is shorten. In the experiment, we confirmed effect of distance of gradual curve part on bending angle.

Improvement of processing limit

Processing limit is related to V and u. But it is difficult to keep V and lengthen u. Because feature of PKM is which working area is narrow. And V is shorten like case2 of fig 8. Now, therefore, bending parameter is smaller[2]. V is related to bending shape as outline above.

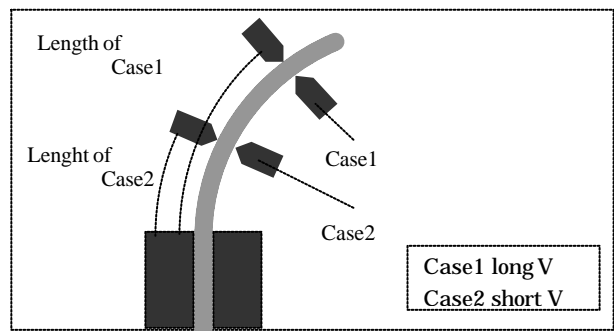


Figure 8 Effect of V on bending parameter

BENDING EXPERIMENT 1

Experiment purpose

This experiment purpose is to confirm the effect of Length of gradual curve part on bending angle.

Experiment procedure

Length of gradual curve part is shortened by 20 [mm] step from 100[mm]. And then, we measure bending angle.

Experiment result

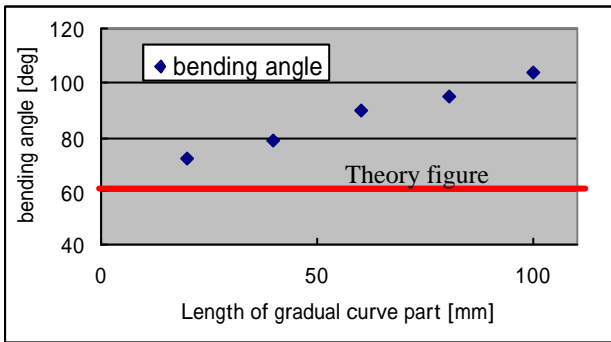


Figure9 Effect of L_g on θ_b

As a result, gradual curve part is related to bending angle. And, if gradual curve part is loss, process of actual shape cannot be achieved. Therefore, it is necessary to propose new motion of movable die.

BENDING EXPERIMENT 2

Experiment purpose

This experiment purpose is to confirm the effect of distance between dies on shape of processing pipe.

Experiment procedure

Distance between dies is shortened by 35[mm] and 45[mm].

Experiment result

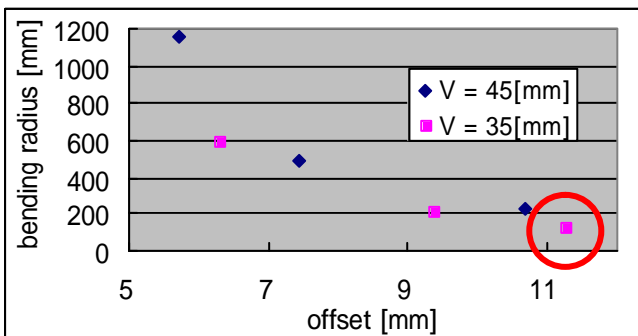


Figure 10 Effect of V on R

As a result, improvement of bending shapes was achieved by reduction of distance between dies. But, when movable die got up fix die, bending quality was poor. And, when offset is short, bending angle is large because of springback. And so, we will define appropriate balance between bending parameter and bending quality in future experiment.

SUMMARY

In this paper, we announced effect bending parameter on bending shape and quality. In the future, we construct new motion of movable die and new structure machine. For example, PKM is installed in vertical position. And this machine is miniaturized and made high power by using the hydraulic cylinder for actuator.

REFERENCE

1. Hiroyuki Katai., Development of CNC bending machine using parallel kinematics mechanism of the Tokyo University of Engineering.
2. Tatsuya Shirayama., Development of CNC bending machine using parallel kinematics mechanism of the Tokyo University of Engineering.

THERMAL-HYDRAULIC LUMPED PARAMETERS MODEL OF SERVOVALVE TO PREDICT PERFORMANCE SENSITIVITY TO TEMPERATURE

Batoul ATTAR* and Jean-Charles MARE*

* Department of Mechanical Engineering
INSA de TOULOUSE
135, avenue de Rangueil, 31077 Toulouse cedex 4, France
(E-mail: batoul.attar@insa-toulouse.fr)

ABSTRACT

This communication deals with the thermal-hydraulic modeling and simulation of electrohydraulic actuators to predict the performance sensitivity to temperature. The work reported focuses on the simulation of the servovalve second stage within the AMESim software environment. In the first part, the influence of the static characteristic of this stage on the actuator performance is pointed up. Then, two different models are developed. The first one is isothermal while the second one considers that all the heat generated by pressure losses is passed to the fluid. The analysis of simulated leakage flow, flow gain and pressure gain displays the influence of temperature and the importance of the type of model. Some extensions of the presented model are proposed to include in detail the heat exchange with ambience in upcoming work.

KEY WORDS

AMESim, Servovalve, Simulation, Static performance, Thermal effect

NOMENCLATURE

a	: Equivalent leakage laminar coefficient due to servovalve and jack ($\text{m}^3/\text{s}/\text{Pa}$)	K_{PI}	: Pressure/current valve gain (Pa/A)
A	: Global leakage coefficient ($\text{m}^3/\text{s}/\text{Pa}$)	K_{PX}	: Pressure/opening valve gain (Pa/m)
e	: Position static error (V)	\bar{K}_{PX}	: non- dimensional pressure gain (-)
f	: Equivalent viscous friction coefficient (Ns/m)	K_{QI}	: Flow/current valve gain ($\text{m}^3/\text{s}/\text{A}$)
F_b	: Break away force of the jack (N)	K_{QP}	: Flow/pressure valve gain ($\text{m}^3/\text{s}/\text{Pa}$)
F_e	: External force (N)	K_{QX}	: Flow/opening valve gain ($\text{m}^3/\text{s}/\text{m}$)
G_{sv}	: Servovalve transfer function denominator (-)	\bar{K}_{QX}	: non- dimensional flow gain (-)
\dot{h}	: Enthalpy flow rate (W)	m	: Mass of moving assembly (Kg)
I	: Servovalve current (A)	\dot{m}	: Mass flow rate (Kg/s)
K_A	: Amplifier gain (A/V)	P_n	: Valve pressure drop (Pa)
K_f	: Force factor ($\text{m}/\text{s}/\text{N}$)	P_r	: Return pressure (Pa)
K_l	: Position loop gain (1/s)	P_S	: Supply pressure (Pa)
K_p	: Position sensor gain (V/m)	Q	: Mean valve flow (m^3/s)
		Q_l	: Spool leakage flow rate (m^3/s)
		Q_n	: Nominal flow rate (m^3/s)
		r_h	: Hydraulic stiffness (N/m)

r_l	: Load stiffness (N/m)
s	: Laplace variable (1/s)
S	: Active section of jack (m ²)
V_t	: Chamber volume at mid stroke (m ³)
V_X	: Tension representative load position (V)
V_X^*	: Tension representative load position setpoint (V)
X	: Valve spool opening (m)
X_n	: Valve spool full stroke (m)
Z_l	: Load position (m)
β	: Effective Bulk modulus (Pa)
γ	: Constant (-)
ΔP	: Jack pressure difference (Pa)
ε_d	: Position error due to external force (m)
ξ_h	: Hydraulic damping ratio (-)
ξ_{sv}	: Servovalve damping ratio (-)
τ_e	: Equivalent time constant (s)
τ_h	: Hydraulic time constant (s)
ω_h	: Hydraulic natural pulsation (rad/s)
ω_{sv}	: Servovalve pulsation (rad/s)

INTRODUCTION

Many electrohydraulic actuators are used in a wide range of environment temperature. A typical example is found in aerospace where the flight control actuation system has to operate from -40°C to $+70^\circ\text{C}$. The modeling, design and control synthesis of such actuators is widely documented without considering the temperature effect [1] and [2]. The servovalve, being a key component of such actuators, has also generated a lot of research work to allow analysis and performance prediction. The hydraulic characteristic of the main spool valve influences a lot the actuator performance. For this reason, many authors have developed improved models being able to reproduce, by simulation, this characteristic [3], [4], [5] and [6].

On the opposite side, a few references are found dealing with the influence of temperature on actuator performance. Most of the work in this field is performed to simulate the variation of the fluid temperature at the hydraulic system level caused by the energy losses in components. The case of the electro-hydrostatic actuator is studied in [7]. For more details, a lumped parameters model for hydraulic components is presented in [8].

As a result, there is no study that combines the two approaches (closed loop performance vs. temperature).

Therefore, a research work is in progress at INSA Toulouse to develop thermal-hydraulic models of electrohydraulic actuators. As a first step, the servovalve second stage work is reported in this communication, with special consideration to the variation of the gains associated with the hydraulic static characteristic of a spool valve.

IMPORTANCE OF SERVOVALVE STATIC PERFORMANCE

As it was seen before, the servovalve is a major component in electrohydraulic actuators. Moreover, it has a large effect on the control loop performance because of its own performance. Before dealing with its dynamics, it is worth reproducing with accuracy the influence of temperature on the flow/current gain K_{QI} , the flow/pressure gain K_{QP} , the pressure/current gain K_{PI} and the valve leakage flow rate Q_l (the flow/pressure gain can be calculated from the other gains). The importance of these gains is pointed up below, considering the common case of proportional position control (see Appendix).

Stability

The loop gain K_l is limited by stability conditions. When the load stiffness is much smaller than hydraulic one ($r_l \ll r_h$), it is defined by Eq (1) as:

$$K_l \leq \gamma \xi_h \omega_h \quad (1)$$

The value of constant γ must be lower than 2, depending on the selected stability criteria [3]. As a result the stability will be described in Eq (2):

$$K_A \leq \gamma \xi_h \omega_h (1 + Af/S^2) S / K_{QI} K_P \quad (2)$$

As $A = a + K_{QP}$, Eq (2) points up the influence of the flow/pressure gain K_{QP} on the actuator stability. On the other hand, according to Eq (2), the control gain is also influenced by flow/current gain K_{QI} , especially around the null opening region. As there is generally no internal leakage at the jack level, the value of a is mainly due to the servovalve leakage.

Rapidity

The closed loop rapidity is measured by the equivalent closed loop first order time constant τ_e [3], the inverse of K_l . So, the rapidity is also affected by a , K_{QP} and K_{QI} .

Accuracy

The servovalve also contributes to fix the loop precision [2]. Due its pressure/current gain K_{PI} , it introduces a static error e that can be calculated by studying the applied forces on the jack piston at the equilibrium position, as described in Eq (3):

$$e \geq \frac{F_b}{S K_{PI} K_A} \quad (3)$$

Besides, the position error due to the disturbing external force is got from the Appendix as Eq (4):

$$\varepsilon_d = \frac{K_f}{K_l} F_e = \frac{A}{S \cdot K_A \cdot K_{QI} \cdot K_P} F_e \quad (4)$$

The load error is affected by both flow/pressure and flow/current gains. Finally, it is pointed up that the servovalve gains K_{QI} , K_{PI} and K_{QP} have a great influence on the closed loop accuracy.

Consumption

In fact, the ideal servovalve with perfect geometry doesn't exist. At the null opening region, a leakage flow Q_l occurs between the spool valve and the valve body [6]. It is due to the clearance between the valve spool and the valve body that combines with the roundness of the orifices edge. Moreover, the leakage flow has its maximum value at the neutral spool position, which is the average one in position control applications. Therefore, the valve leakage which dominates within the null region is an important contributor to the permanent losses in a hydraulic circuit. Besides, this leakage flow dissipates energy that generates heat, warming the oil.

These considerations point up the importance of the servovalve static gains K_{QI} , K_{PI} , K_{QP} and Q_l on the actuator performance. For this reason, it is of prime importance to develop efficient virtual prototyping simulation models to evaluate how the performance is influenced by temperature conditions.

THERMAL-HYDRAULIC MODELING

In order to develop such servovalve models, two approaches are proposed as a first step, based on extreme cases. In the first one, it is supposed that the heat transfer between the fluid and its surroundings is perfect. So, all the heat caused by pressure losses passes towards the ambience, no heat being exchanged with the hydraulic fluid. Consequently the fluid keeps its temperature constant. Therefore, this case is presented by an isothermal model, called below HM for hydraulic model.

In the second extreme case, we suppose that there is no heat transfer with the entourage. The energy generated by the pressure losses is stored by the fluid, which temperature changes during the work. So, a model with a variable temperature fluid is used, being called THM for thermal-hydraulic model.

At the present stage, the work focuses on the second stage of the servovalve (common cylindrical spool valve) that is the aim in this paper. As a limitation, the model does not reproduce any heat exchange with the bushing (fluid at constant temperature or fluid storing all the energy dissipated by pressure losses). The models are developed within the *AMESim* software [9] that offers interesting facilities and libraries dedicated to thermal-hydraulic simulation.

Typically, the thermal-hydraulic library offers numerous models of components and basic elements.

Opposite to the hydraulic library in which there is neither enthalpy flow rate nor temperature variables, the thermal-hydraulic components exchange hydraulic and thermal power variables, as described in Figure (1):

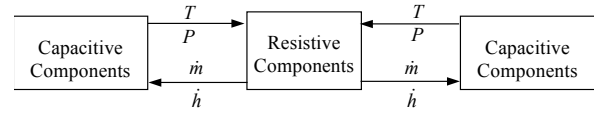


Figure 1. The basic variable flow for thermal hydraulic elements

In capacitive components, as volumes, the temperature and the pressure are computed from the enthalpy and mass flow rates inputs at ports of these components. The resistive ones, as the orifices, are the components in which the enthalpy and mass flow rates are evaluated from the temperatures and pressures inputs at their ports [9]. To avoid any causality conflict, it is necessary to connect them alternatively.

Consequently, the thermal-hydraulic model of the spool valve is built from the standard model of cylindrical spool with slot orifices, as shown on Figure (2). The orifices model includes rounded edges, radial clearance and Reynolds number effects.

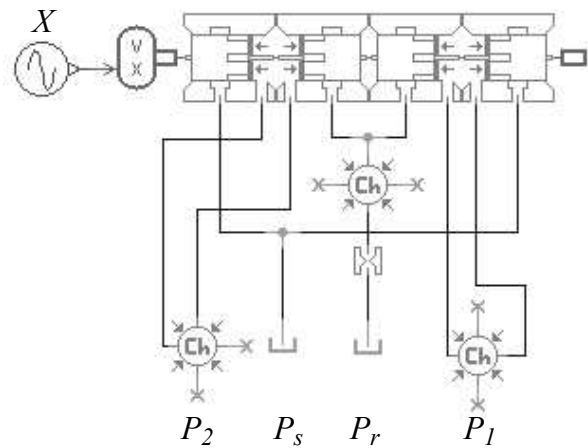


Figure 2. Spool valve model in AMESim for pressure gain and leakage flow characteristics

The servovalve under study is typically a MOOG 76101 delivering 9.8 l/mn at 70 bars pressure drop with the following geometry: full stroke 213 μ m, diameter 6.9mm, 4 slots of 3 mm, identified rounded edge radius 15 μ m, identified radial clearance 2 μ m and identified underlap 15 μ m.

Furthermore, the two models can be run in parallel to point up the differences between pure hydraulic and thermal-hydraulic models.

SIMULATION AND ANALYSIS

To point up the performance at very low temperature, the models are run at different fluid temperatures leading to a variation of oil viscosity in the range 30-4000 cst.

Leakage flow rate (Q_l)

The leakage flow rate can be measured by reproducing in simulation the experimental setup, Figure (3). The total flow rate returned from the valve to the tank is plotted versus the valve opening, as the spool makes a complete cycle around its neutral position at null and with closed use ports.

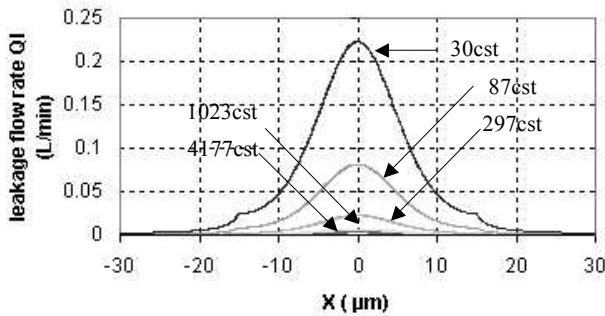


Figure 3. Leakage flow rate with different temperatures (HM and THM similar)

The leakage flow rate values got from the hydraulic and thermal hydraulic models are compared for relative spool openings of 0%, 2.5% and 5% and at the same work temperature. As displayed by Figure (4), the thermal-hydraulic model has a leakage flow slightly higher than the hydraulic model.

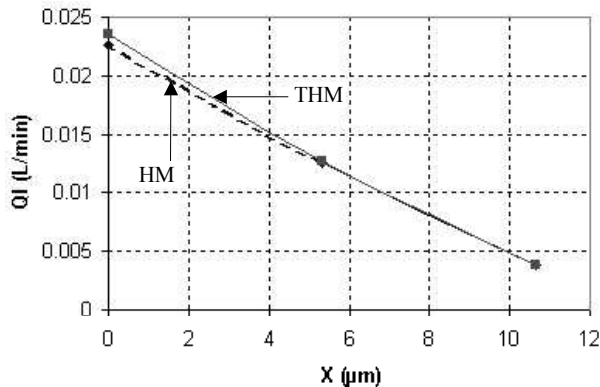


Figure 4. Leakage flow for different spool opening (at 300 cst)

Furthermore, the plot of the leakage flow rate as a function of the temperature for various spool openings, is displayed on Figure (5):

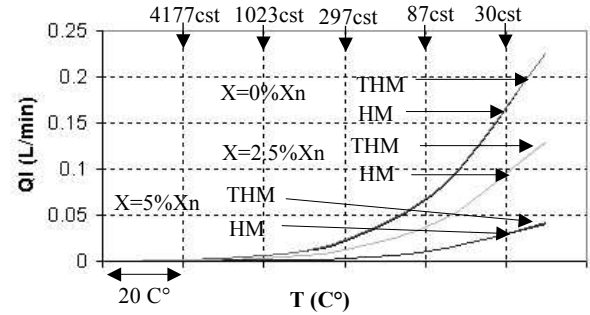


Figure 5. Leakage flow rate vs. temperature

Pressure/opening gain (K_{PX})

Once again, the pressure/opening valve gain K_{PX} is simulated by reproducing the experimental process: the pressure difference at use ports ($\Delta P = P_1 - P_2$) is plotted as a function of the spool opening that is varied at very low frequency while the use ports are blocked. Moreover, the non-dimensional pressure gain \bar{K}_{PX} is expressed in Eq (5):

$$\bar{K}_{PX} = K_{PX} \cdot X_n / P_n \quad (5)$$

The valve being supplied at constant pressure. \bar{K}_{PX} is plotted on Figure (6) vs. temperature for two spool openings of 1% and 3% of spool full stroke.

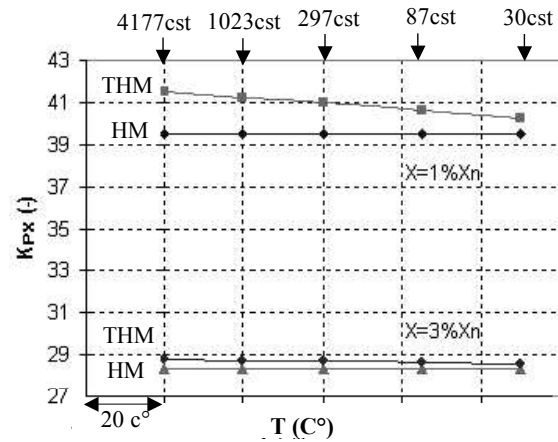


Figure 6. Non-dimensional pressure gain vs. temperature for two spool openings

According to this figure, it is observed that \bar{K}_{PX} somewhat decreases with the temperature rise for the thermal-hydraulic model, whereas it remains constant whatever the temperature in hydraulic model. The thermal-hydraulic values are always higher than the hydraulic model ones but the difference is not significant (less than 5%).

Flow /opening gain (K_{QX})

The use ports are connected together. The flow passing through is plotted on Figure (7) as a function of the spool opening that is varied at very low frequency. Due to the very high viscosity, there is an important change in the flow gain.

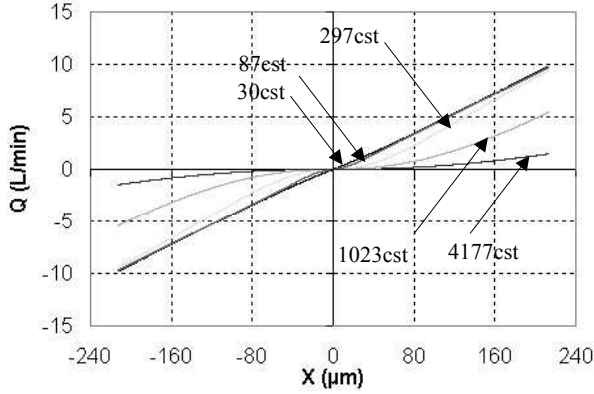


Figure 7. Flow gain for different temperatures

Two regions can be identified on the flow gain curve. The first one corresponds to the small valve opening in the surroundings of null region, in which the control position actuators operate. The second one is found for large openings in which the actuators operate when moving.

In order to develop system level models, it is proposed to express the flow gain K_{QX} as a continuous function, which its parameters vary with temperature. As defined in Eq (6), it includes a hyperbolic tangent function that reproduces the change of gain around the null region:

$$X = X_0 \tanh \frac{Q}{Q_0} + kQ \quad (6)$$

where X_0 and Q_0 are the coordinates of the two regions asymptotes intersection point. And k is the asymptote slope at large openings.

The non-dimensional flow gain \bar{K}_{QX} is then calculated for these two domains by Eq (7):

$$\bar{K}_{QX} = K_{QX} \cdot X_n / Q_n \quad (7)$$

The nominal flow Q_n is equal to 9.8 L/min for a valve pressure drop of 70 bar.

As expected under laminar flow conditions, at small openings the flow gain increases very significantly with temperature, Figure (8):

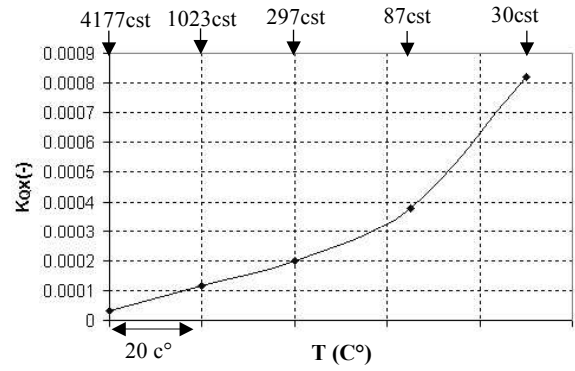


Figure 8. Flow gain at small spool valve opening

DISCUSSION

Considering the above results, it first appears that the valve leakage flow raises with temperature, increasing the global leakage coefficient A of the equivalent linear model of the actuator in the vicinity of the null opening. Adding, the thermal-hydraulic model gives slightly higher values than the hydraulic model because of raised temperature due to the energy losses. Secondly, the null region flow gain also grows significantly with temperature, producing high changes in the effective loop gain. Thirdly, the pressure gain remains quite constant with temperature. Only a slight reduction is found when using the thermal-hydraulic model.

According to all these changes, the simulation predicts that the static error will increase a little because of losses with raising temperature. As well as, the rapidity and the stability both depend on the change rate of A and K_{QX} . Because they affect K_l together, their partially compensate.

It must be kept in mind that this analysis must now be validated by real experiments. This part is now under preparation while the other parts of the servovalve are being modeled and analyzed in parallel.

Another action to be performed lies in the extension of the *AMESim* thermal-hydraulic component library. A thermal port will be added on the model icon to allow connection with the thermal library components. This will allow to include the heat exchange between the fluid and the external components, in the models of the thermal-hydraulic elements.

CONCLUSION

In this paper, we presented a first step in the study on the influence of temperature on the closed loop performance of electrohydraulic actuators. The importance of the servovalve static characteristics has been first pointed up. Then, a thermal-hydraulic model of a spool valve, has been built using only available

components form the software libraries. Two typical cases have been studied. The first isothermal one is similar to the commonly used for conventional hydraulic simulations. In the second one, all the heat generated by pressure losses is stored into the fluid, so its temperature varies during the work. The simulation was run at different temperatures to point up its influence on the servovalve static characteristics.

Finally, it has been shown that the change of fluid viscosity due to temperature has a high importance on both leakage flow and flow gain and a very little influence on the pressure gain. When the heat generated by the pressure losses at valve orifices is considered, only slight changes are observed on the simulated values, that differ by less than 5% from the ones got using the hydraulic model.

REFERENCES

- [1] H. E. Merrit, Hydraulic Control Systems. New York: John Wiley & Sons, Inc, 1967.
- [2] M. Guillon, Commande et Asservissement Hydraulique et Electrohydraulique, 1992 ed. Paris: Technique et documentation - Lavoisier, 1992.
- [3] J.-C. Maré, "Actionneurs Hydrauliques - Commande," Techniques de l'Ingénieur, S 7 531, traité Informatique industrielle, 2002.
- [4] J.-C. Maré and P. Moulaire, "Expert Rules for the Design of Position Control of Electrohydraulic Actuators," presented at The Sixth Scandinavian International Conference on Fluid Power, SICFP'99, Tampere, Finland, 1999.
- [5] A. Ellman, "Leakage Behaviour of Four-Way Servovalve," American Society of Mechanical Engineers, The Fluid Power and Systems Technology Division (publication) FPST, vol. 5, pp. 163-167, 1998.
- [6] B. Eryilmaz and B. H. Wilson, "Modeling the Internal Leakage of Hydraulic Servovalves," presented at International Mechanical Engineering Congress and Exposition, ASME, Orlando, USA, 2000.
- [7] H. Svensson, J. Andresson, and K.-E. Rydberg, "Modelling of Losses and Temperature Calculations in Fluid Power Systems," presented at The sixth Scandinavian Conference on Fluid Power, Tampere, Finland, 1999.
- [8] K. Stork, "Thermostatic Temperature Regulation in Hydraulic Systems," journal of systems and control engineering, 1998.
- [9] AMESim, "User Manual, Thermal- Hydraulic Library," 4.2 ed: IMAGINE, september 2004.

APPENDIX

The actuator which is selected in this study is made of a symmetrical jack and a symmetrical servovalve with rigid anchorage and transmission, Figure (9):

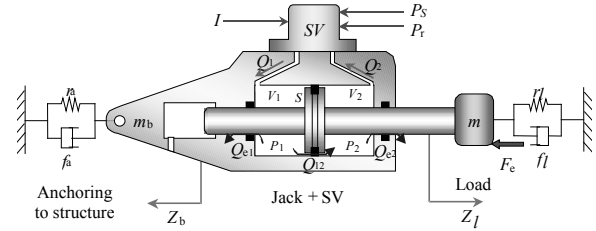


Figure 9. Basic model of an electrohydraulic actuator

Transfer function of an electrohydraulic actuator model can be roughly evaluated by making a linear analysis [3], with the consideration that the load stiffness r_l and its damping f_l are neglected, and that the jack piston and the load move together for same displacement Z_l without no connecting stiffness between them. So it will be as the following:

$$s \left(1 + \frac{2\xi_h}{\omega_h} s + \frac{1}{\omega_h^2} s^2 \right) \cdot Z_l = \frac{K_{Ol}}{\left(1 + \frac{A_f}{S^2} \right) S G_{sv}(s)} I - \frac{K_f (1 + \tau_h s)}{\left(1 + \frac{A_f}{S^2} \right)} F_e$$

with:

- Position static error $e = V_x^* - V_x = V_x^* - K_P \cdot Z_l$

- Loop gain $K_l = \frac{K_A \cdot K_{Ol} \cdot K_P}{\left(1 + \frac{A_f}{S^2} \right) S}$

- Hydraulic stiffness $r_h = \frac{2\beta S^2}{V_t}$

- Hydraulic damping ratio $\xi_h = \frac{\frac{A m}{S^2} + \frac{f}{m}}{2 \sqrt{\left(1 + \frac{A_f}{S^2} \right) \frac{m}{m}}}$

- Hydraulic pulsation $\omega_h = \sqrt{\left(1 + \frac{A_f}{S^2} \right) \frac{m}{m}}$

- Load factor $K_f = \frac{A}{S^2 \left(1 + \frac{A_f}{S^2} \right)}$

- Hydraulic time constant $\tau_h = \frac{S^2}{A r_h} = \frac{V_t}{2 A \beta}$

- Servovalve transfer function denominator

$$G_{sv}(s) = 1 + \frac{2\xi_{sv}}{\omega_{sv}} s + \frac{1}{\omega_{sv}^2} s^2$$

SIMULATION OF DYNAMICS PROCESSES OF HYDRAULIC SYSTEM WITH AXIAL- RECIPROCATING PISTON PUMP AND ELECTRICAL ENGINE

Marijonas BOGDEVICIUS, Leonas LINGAITIS

Department of Transport Technology Equipment's, Faculty of Transport Engineering
Vilnius Gediminas Technical University
Plytines 27, LT-10105 Vilnius, Lithuania
(E-mail: marius@ti.vtu.lt)

ABSTRACT

In the article the dynamic processes in an axial-reciprocating hydraulic pump and asynchronous engine are considered. The mathematical model of an axial-reciprocating hydraulic pump is presented, where the flow of fluid in each cylinder of the pump and the interaction of liquid with the piston are taken into account. The flow of fluid in a hydraulic system is described by a system of equations of a hyperbolic type, which is solved by the characteristics method. For example, the mathematical simulation of the activity of an axial-reciprocating pump in a hydraulic system together with the mechanical drive is shown.

KEY WORDS

axial-reciprocating hydraulic pump, dynamics, the interaction, numerical method

NOMENCLATURE

a_x :	acceleration to x direction;	$F_2(x)$:	kinetic energy of the liquid flow in a pipeline to the unit of area;
c :	speed of sound in a liquid;	f :	coefficient of pressure losses along pipe $f = f(Re)$;
d :	diameter of cylinder (pipeline);	$f_1(v, p)$:	functions dependent on velocity and pressure;
e :	wall thickness of the pipeline;	$f_2(v, p)$:	functions dependent on velocity and pressure;
E :	modulus elasticity of a material of the pipeline;	h_0 :	constructive parameter of a pump,
F :	force;	I_e :	moments of inertia of mass;
$\{F_{fr}\}$:	vector of friction moment;	I_{LP} :	set of number low pressure cylinder;
$F_1(x)$:	discharge of liquid mass to the unit of the length in a pipeline;	i :	number of iteration;

$[J]$:	Jacobi matrix;
$K(p)$:	bulk modulus elasticity of liquid;
L_r :	completely reduced rotor inductivity;
L_S :	completely reduced stator inductivity;
L_μ :	magnetization circuit inductivity;
M_e :	electrical engine resistance moment;
M_{fr} :	friction moment;
M_r :	resistance torque;
m :	mass of cylinder;
$m_{inp}(x)$:	mass flow of a liquid in a unit area;
NZ :	number of pistons in a pump;
p :	liquid pressure;
p_D :	liquid pressure at a point D ;
p_F :	liquid pressure at a point F ;
p_{Gi} :	liquid pressure i on the surface of piston ;
p_L :	liquid pressure at a point L ;
p_R :	liquid pressure at a point R ;
pol :	number of pole pairs;
r_s :	active resistance of stator;
r_r :	active resistance of rotor;
q_G :	displacement of the piston at a point G ;
q_H :	displacement of the piston at a point H ;
$\dot{q}_G \equiv \frac{dq}{dt}$:	speed of the piston at a point G ;
$\dot{q}_H \equiv \frac{dq}{dt}$:	velocity of the piston at a point H ;
Re :	Reynolds number;
$S(x)$:	cross-section area of the pipeline;
S_i :	cross-sectional area of cylinder number i ;
S_S :	cross-sectional area of the piston;
v :	liquid velocity;
v_D :	liquid velocity at a point D ;
v_F :	liquid velocity at a point F ;
v_L :	liquid velocity at a point L ;
v_R :	liquid velocity at a point R ;
$v_{inp}(x)$:	velocity of a liquid acting in the pipe line;
x_F :	x coordinate of pint F ;
$\{Y\}$:	vector of unknowns;
γ :	isentropic exponent;
ε :	relative volume of gas in the liquid;
$\{\Phi\}$:	vector of algebraic equations;
φ_e :	turn angle of rotor of electrical engine;
φ_i :	turn angle of the cylinder number i ;

τ :	integration time step of differential equations;
$\Pi(x)$:	perimeter of cross section of the pipeline;
ρ :	liquid density;
σ :	shearing stresses on the internal surface of the pipe line;
ν :	kinematic viscosity of a liquid;
$\{\psi\}$:	the bound flow vector.

INTRODUCTION

The main research object in the present work is axial-reciprocating pump which is intended for work as power units in different guidance schemes. The researches of axial-reciprocating pump were carried out by many authors. But many of them considered the system of hydraulic pump as the system with lumped values and thus did not take into consideration wave processes going on in hydraulic lines. The purpose of present work is to show the wave processes going as in hydraulic pump system, using the characteristic method. The axial-reciprocating pump is analyzed together with asynchronous engine, higher and lower pressure pipelines. Movement of liquid is accepted as one-dimensional and unsettled, i.e. all local velocity are considered. The liquid movement is considered as one-dimensional, i.e. all local velocity are equal to average velocity, and unsettled. Velocity and pressure depend on longitude coordinate and time. Such liquid movement is characterized by the wave of increased and reduced pressure which spreads from the place of change in each pressure vibration cross-section and in deformation of pipeline walls. The liquid is double-component mixture, including gas (air). The presence of air in liquid sharply decreased sonic velocity in liquid.

MATHEMATICAL MODEL OF HYDRAULIC AXIAL-RECIPROCATING PUMP

Movement and continuity equations of viscous, compressible fluid in pressure pipe have the following form

$$\frac{1}{\rho} \frac{\partial p}{\partial x} + \frac{\partial v}{\partial t} + v \frac{\partial v}{\partial x} + \frac{fv|v|}{2d} + a_x = 0;$$

$$\frac{\partial p}{\partial t} + v \frac{\partial p}{\partial x} + c^2 \rho \frac{\partial v}{\partial x} = 0, \quad (1)$$

Let research hydraulic system consisting of the electrical asynchronous engine (AE), axial-reciprocating pump, pipelines, hydraulic resistance, hydraulic valve and tank. The scheme of axial-reciprocating pump is shown in Fig. 1. The dynamic model of asynchronous engine and axial reciprocating piston pump is studied as a complicated hydraulic and mechanical system.

One of the most progressive variants of automated electrical driver is an alternating current electrical driver with asynchronous engine. The foundation of the AE mathematical model consists of differential equations of electrical and mechanical balance and equations of electromagnetic energy transformation to mechanical energy.

To estimate dynamic regimes of AE, two-phase mathematical models are used. In the general case AE two-phase model consists of the system of differential and algebraic equations:

$$\{\dot{\psi}\} = [A_{\psi}] \{\psi\} + \{B_{\psi}(t, \psi, \dot{\varphi}_e)\} \quad (2)$$

$$I_e \frac{d^2 \varphi_e}{dt^2} = M_e(\psi) - M_r(\varphi_i, \dot{\varphi}_i, P_{Gi}), \quad (3)$$

where matrix $[A_{\psi}]$ and vector $\{B_{\psi}(t, \psi, \dot{\varphi}_e)\}$ are equal

$$[A_{\psi}] = a_{\psi} \begin{bmatrix} -r_s L_r & 0 & r_s L_{\mu} & 0 \\ 0 & -r_s L_r & 0 & r_s L_{\mu} \\ r_r L_{\mu} & 0 & -r_r L_s & 0 \\ 0 & r_r L_{\mu} & 0 & -r_r L_s \end{bmatrix},$$

$$\{B_{\psi}(t, \psi, \dot{\varphi}_e)\} = \begin{Bmatrix} \sqrt{2} U_{nom} \cos(w_s t) \\ -\sqrt{2} U_{nom} \sin(w_s t) \\ \dot{\varphi}_e \psi_4 \\ -\dot{\varphi}_e \psi_3 \end{Bmatrix},$$

and torque of AE is equal

$$M_e = \frac{3}{2} \cdot pol \cdot L_{\mu} a_{\psi} (\psi_1 \psi_4 - \psi_2 \psi_3), \quad (4)$$

$$a_{\psi} = \frac{1}{L_s L_r - L_{\mu}^2}.$$

The engine resistance moment is equal

$$M_r(\varphi_i, \dot{\varphi}_i, P_{Gi}) = \sum_{i=1}^{NZ} S_i h_0 \cdot P_{Gi} \sin \varphi_i + M_{fr}(\dot{\varphi}_i), \quad (5)$$

where i -th cylinder turning angle is equal

$$\varphi_i = \varphi_e + (i-1)2\pi / NZ.$$

The dynamic model of axial-reciprocating pump is constructed by evaluating the principle of action and constructive peculiarities of the pump (Fig. 1).

Every piston of a pump moves in a cylinder and closely interacts with liquid. Depending on the rotor turning angle φ_e , every piston of a pump ejects (high pressure) and sucks-in (low pressure) liquid. During the suction and at the insufficient liquid discharge, zones of cavitation form on the surface of a piston.

The interaction between the separate piston and a pump and liquid is studied.

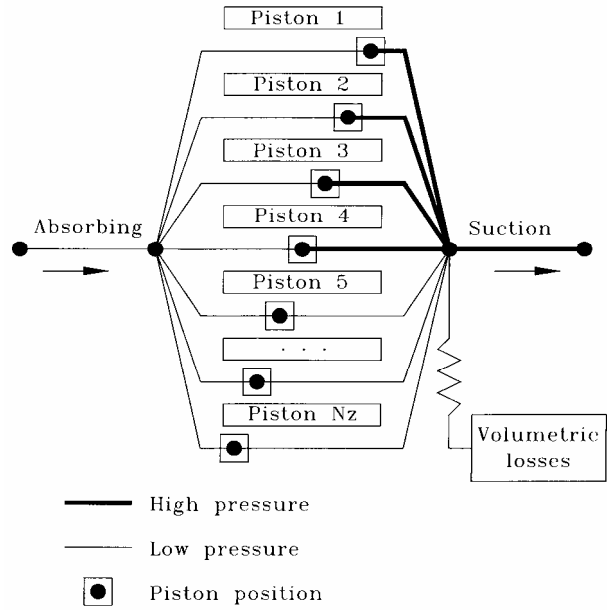


Figure 1 The hydraulic circuit of axial reciprocating piston pump

According to the construction of an axial reciprocating piston pump, every piston is coupled with rotor; therefore interaction of piston and liquid flow in a cylinder shall be studied together with equations of electrical engine movement (1-5).

The presented dynamic model of axial reciprocating piston pump evaluates: local and volumetric losses of pressure in every cylinder; occurrence of cavitation zones, identification of their variable volume; quantity of gas in liquid; transient processes in an electrical engine; various constructional parameters of a pump; influence of a hydraulic driver on dynamic processes of a pump; change of cross-section area when transferring from the suction to a pressure pipeline and vice versus. Differential equations of liquid movement in the cylinder are solved by characteristics method [1,2]. The main idea of characteristics method is the fact that unknown variable speed and liquid pressure at instant moment of time $t + \tau$ is determined according to these parameters at a moment of time (Fig. 2). Pressure and velocity in point D at the moment of time is determined from nonlinear algebraic equation system

$$C^+ : \Phi_1 = v_D - v_L + \frac{1}{2}(p_D - p_L) \left[\left(\frac{1}{\rho c} \right)_L + \left(\frac{1}{\rho c} \right)_D \right] - \frac{\tau}{2} \left[\left(\frac{f_1}{\rho c} \right)_L + \left(\frac{f_1}{\rho c} \right)_D \right] - \frac{\tau}{2} [(f_2)_L + (f_2)_D] = 0; \quad (6)$$

$$C^- : \Phi_2 = v_D - v_R - \frac{1}{2}(p_D - p_R) \left[\left(\frac{1}{\rho c} \right)_R + \left(\frac{1}{\rho c} \right)_D \right] + \frac{\tau}{2} \left[\left(\frac{f_1}{\rho c} \right)_R + \left(\frac{f_1}{\rho c} \right)_D \right] - \frac{\tau}{2} [(f_2)_R + (f_2)_D] = 0 \quad (7)$$

$$f_1(v, p) = \frac{c_2}{S(x)} \left(F_1 - \rho v \frac{\partial S}{\partial x} \right);$$

$$f_2(v, p) = \frac{1}{\rho S(x)} (F_2 - v F_1) - \frac{\sigma \Pi(x)}{\rho S(x)} - a_x,$$

$$F_1 = \Pi(x) m_{inp}(x) v_{inp}(x), \quad F_2 = \Pi(x) m_{imp}(x) v_{inp}(x),$$

$$\sigma = \frac{\rho f(Re) \nu |v|}{8},$$

$$f(Re) = \begin{cases} \frac{75}{Re}, & \text{when } Re \leq 2320; \\ 0,31464 Re^{0,25}, & \text{when } Re > 2320 \end{cases}$$

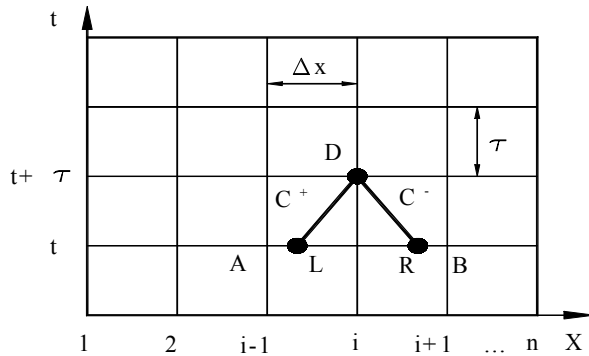


Figure 2 Scheme of point parameters determination by characteristic method

The velocity of sound in a two-phase liquid is placed in pipeline as determined:

$$c = \sqrt{\frac{K(p)/\rho}{1 + \frac{K(p) \cdot d}{E \cdot e} + \frac{\varepsilon}{\gamma} \left[\frac{K(p)}{\gamma p} - 1 \right]}}, \quad (8)$$

The system of equations (6) and (7) is solved by a Newton method:

$$[J]_i \{Y\}_i = -\{\Phi\}_i, \quad (9)$$

$$\{Y\}^T = [p_D, v_D]; \quad \{\Phi\}^T = [\Phi_1, \Phi_2].$$

The kinetic energy of the rotor of pump is transformed to potential energy of a liquid in a high-pressure cylinder. For accuracy simulation of interaction of the hydraulic pump piston with liquid four cases of interaction are considered. Each case of this interaction depends on a rule of the piston in the cylinder and on computational grid. At the moment of interaction of a liquid with the piston the volumetric losses of the liquid are taken into account [4,5].

The system, which consists of the body moving in a pipeline with liquid (Fig. 3).

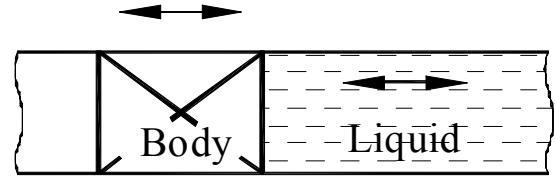


Figure 3 The circuit of the system "body, liquid, and pipeline"

The parameters of liquid flow and body interaction in a discrete pipeline are determined in four cases. In this article is presented only first case of interaction between piston and liquid flow.

The first case (Fig. 4).

In this case the following conditions shall be fulfilled [5]:

$$x_{i-1} \leq q_H < x_i, \quad x_{i-1} < q_H + \dot{q}_H \tau < x_i,$$

$$x_{i-1} < q_H + (v_H + a_H) \tau < x_i.$$

The liquid flow parameters of point F are interpolated among points H, C and B . The final system of equation, from which parameters of liquid flow and body movement of point G can be determined, is:

$$\Phi_1 = q_G - x_F - [v_F - a(p_F)] = 0,$$

$$\Phi_2 = v_G - v_F - \frac{1}{2}(p_G - p_F) \left[\left(\frac{1}{\rho a} \right)_F + \left(\frac{1}{\rho a} \right)_G \right] - \frac{\tau}{2} \left[\left(\frac{f_1}{\rho a} \right)_F + \left(\frac{f_1}{\rho a} \right)_G \right] - \frac{\tau}{2} [(f_2)_F + (f_2)_G] = 0$$

$$\Phi_3 = S_S \left[\frac{2}{\tau} (q_G - q_H) - \dot{q}_H \right] - S_C v_G - f_{out} \sqrt{|p_G - p_{out}|} \cdot \text{sign}(p_G - p_{out}) = 0,$$

$$\Phi_4 = m \left[\frac{4}{\tau^2} (q_G - q_H) - \frac{4}{\tau} \dot{q}_H - \ddot{q}_H \right] - S_S p_G + F(t, q_G) = 0. \quad (10)$$

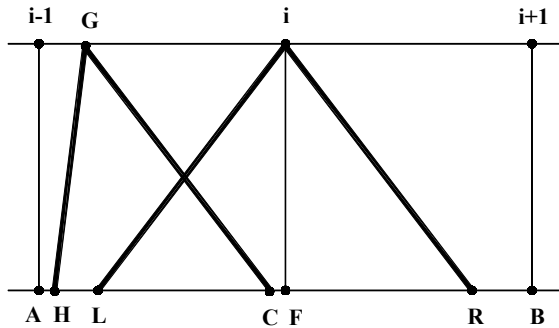
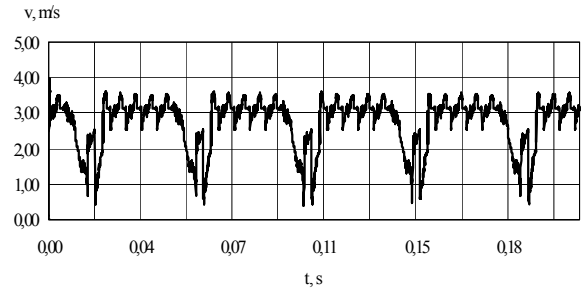
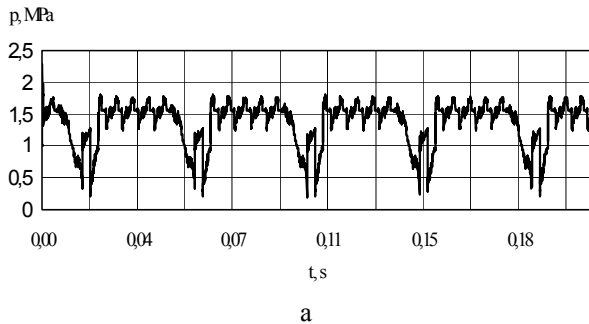


Figure 4 Cases of body and liquid flow interaction

Parameters of liquid flow of point i are determined from the system of equations (6) and (7).

COMPUTATIONAL RESULTS

As an example of the axial reciprocating piston pump 2G15-14 is considered, the shaft of which is turned by asynchronous engine 4A132S4Y3. Pulsations of liquid flow pressure and velocity at the output of axial reciprocating piston pump when the quantity of gas in liquid is equal to 0.1% zero ($\varepsilon = 0.001$) are shown in Fig. 5.



b

Figure 5. Change of pressure and velocity in time at the output of axial reciprocating piston pump, when the quantity of gas in liquid is equal to 0.1% zero ($\varepsilon = 0.001$): a – pressure, b – velocity

CONCLUSIONS

- The composed mathematical model of a axial-reciprocating hydraulic pump takes into account wave motion of a liquid, local losses of pressure and volumetric fluid leakages, phenomenon of a cavitation, gaps in the mechanical drive
- The designed technique is possible for using in research volumetric hydraulic transmissions

REFERENCES

1. Bogdevicius M. Pump hydraulic system simulation by the characteristic method // TRANSPORTAS (Transport Engineering). Vilnius: Technika, 1997, No 2(15). p 30-37 (in Russian).
2. Bogdevicius M. Calculation of a non-stationary movement of a liquid in elastic-plastic and elastic-viscous-plastic pipelines // University Stuttgart, Institute of Hydraulic Machines, 1991, 48 p.
3. Bashta T. Volumetric Hydraulic Drive. Moscow., 1969.- 628 p (in Russian).
4. Bogdevicius M. Simulation and Interaction of Mechanical and Hydraulic System. – Proceedings of Tenth World Congress on the Theory of Mechines and Mechanisms. – Oulu (Finland), 1999, p. 2110-2115.
5. Bogdevicius M. Simulation of Dynamic Processes in Hydraulic, Pneumatic and Mechanical Drivers and their Elements. Vilnius: Technika, 2000. 96 p.
6. Aladjev V., Bogdevičius M. Maple 6: Solution of the Mathematical, Statistical and Engineering – Physical Problems. Moscow: Laboratory of Basic Knowledges, 2001. 824 p. (in Russian).
7. Aladjev V., Bogdevicius M., Prentkovskis O. New software for mathematical package Maple of releases 6,7 and 8. Monograph. Vilnius, Technika, 2002. 404 p.

A Comparative Study of Modelling Techniques for Laminar Flow Transients in Hydraulic Pipelines

Michail I. Soumelidis, D. Nigel Johnston, Kevin A. Edge, Derek G. Tilley

Centre for Power Transmission and Motion Control
Department of Mechanical Engineering
University of Bath
BA2 7AY
United Kingdom
(E-mail: m.i.soumelidis@bath.ac.uk)

ABSTRACT

Accurate predictions of pressure surges are crucial in many fluid-line systems. There are several techniques available for modelling flow transients in hydraulic pipelines, offering different advantages and disadvantages and therefore suiting different applications. In this paper four modelling methods are evaluated in terms of accuracy, computational efficiency and flexibility for laminar, single-phase flow in circular, rigid pipes. These are the method of characteristics (MOC), the finite element method (FEM), the transmission line method (TLM), and the rational polynomial transfer function approximation (RPTFA) method, which is a form of modal approximation method. All four methods were implemented in MATLAB/Simulink. It was found that the RPTFA model potentially gives the most accurate solution, while the MOC and TLM models are the most computationally efficient. The FEM is the least accurate out of the four methods, but it can be used with varying parameters and time steps thus providing the most modelling flexibility.

KEYWORDS

Fluid transients, Fluid transmission lines, Laminar flow

NOMENCLATURE

A	Cross-sectional area	q	Flow
B	Coefficient matrix	\mathbf{q}	Flow vector
c	Speed of sound	Q_1	Flow at upstream end
C	Coefficient matrix	Q_2	Flow at downstream end
C	Laplace transformed characteristic	Z	Characteristic impedance
E	Coefficient matrix	Z_0	Characteristic impedance constant
f	Friction term	Γ	Propagation operator
F	Coefficient matrix	ρ	Fluid density
p	Pressure		
\mathbf{p}	Pressure vector		
P_1	Pressure at upstream end		
P_2	Pressure at downstream end		

INTRODUCTION

Hydraulic systems are widely used in the engineering world. They often form an essential part of a total dynamic system in industries such as automotive,

aerospace, petroleum, etc. As these systems become more sophisticated, accurate analysis and close control of their performance becomes ever more crucial. This in turn may require consideration of the dynamics of the hydraulic fluid transmission lines which can have a significant influence on system behaviour.

Transient changes in flow can generate pressure waves that travel through the body of the fluid in the transmission lines. This dynamic behaviour can be represented by the equations of motion and continuity, as follows (assuming $q/A \ll c$):

$$\frac{\partial q}{\partial t} + \frac{A \partial p}{\rho \partial x} + f(q) = 0 \quad (1)$$

$$\frac{\partial p}{\partial t} + \frac{\rho c^2 \partial q}{A \partial x} = 0 \quad (2)$$

Hydraulic pipeline dynamics are well understood in the frequency domain. However, obtaining the transient response of the system in the time domain requires approximating the hyperbolic functions which represent the frequency-dependent component of friction, $f(q)$.

There are several techniques available for solving equations (1) and (2) and approximating friction in the time domain. The four most established modelling methods are the method of characteristics [1], the transmission line method [2], the modal approximation method [3], and the finite element method [4]. It is beyond the scope of this paper to present and discuss these in detail. Here, these four methods are evaluated in terms of accuracy, computational efficiency and flexibility. To this end, laminar flow transients in a rigid, circular pipeline were simulated in MATLAB. The system under investigation comprised a constant pressure source upstream and a valve downstream of the pipe. Flow transients were generated by instantaneous valve closure.

METHOD OF CHARACTERISTICS

In the method of characteristics (MOC) the equations of motion and continuity are transformed into ordinary differential equations which can then be integrated along the ‘characteristic lines’. The characteristic lines correspond to the motion of waves travelling at the speed of sound in both directions along a pipe. Friction in pipelines is frequency-dependent and its accurate and correct representation poses one of the biggest challenges in transient flow modelling. Although the steady-state friction component is well defined, the unsteady friction component can only be approximated for time-domain simulation. Initial work by Zielke [5] provided an accurate solution, but at the expense of a very high computational load. Trikha [6] and Kagawa et al. [7] later evaluated weighting

factors for a series of unsteady friction terms, in an attempt to simplify computations. A set of optimised coefficients was obtained by Taylor et al. [8] reducing at the same time the number of unsteady friction terms from five in Trikha’s model to four.

All three unsteady friction approximations mentioned above were used to simulate the transient response of the system to an instantaneous valve closure. The exact solution that was obtained from an inverse Fourier transform of the analytical response is plotted in figure 1, along with the steady-state friction. The three error traces are also plotted for comparison. Johnston [9] recently proposed an alternative method of selecting the weighting factors using a geometric series. The number of terms needed depends on the time step, but also on the value of the geometric series ratio. It was found that a model with a ratio of 3 and three terms gives results almost identical to those obtained using the Taylor et al. and Kagawa et al. approximations, see figure 1.

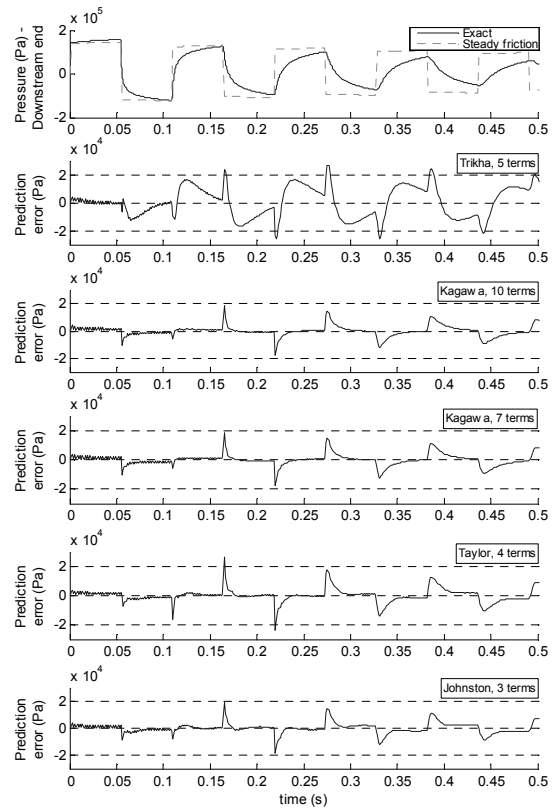


Figure 1: Predicted transient response, MOC, different friction models

In all the above simulations the friction terms are calculated at every node along the pipe and at every timestep. In all simulations the pipeline was divided into 20 elements. To reduce computation load, the

friction terms can be lumped together at the end of the pipe. Two cases were considered. First, the frequency-dependent friction was lumped at the pipeline ends, while the steady-state friction was evenly distributed along the pipe. In the second case, both friction components were lumped at the ends of the pipe during simulation. The prediction errors, compared to the exact solution shown in figure 1, are plotted in figure 2. A very similar response was obtained in both cases. A 77.4% reduction in computational time was achieved in the first case, and an 87.2% in the second, at the expense of a slight loss in prediction accuracy.

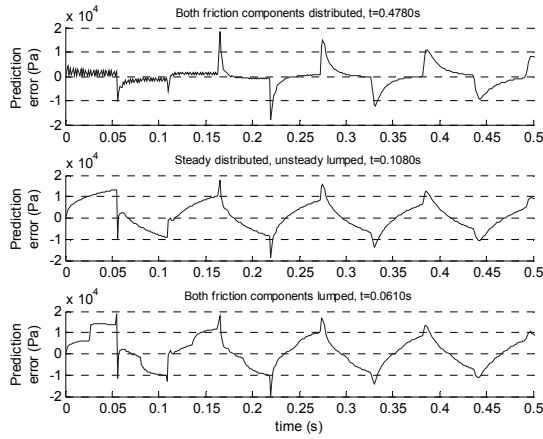


Figure 2: Predicted transient response, MOC, lumped friction

TRANSMISSION LINE METHOD

The transmission line method (TLM) is similar to the MOC. In the MOC a pipeline is divided into a number of elements and pressure and flow propagates between adjacent nodes over one timestep. In TLM, the model only calculates these variables at the ends of a line and not at any internal nodes. Obtaining the correct steady state pressure drop and rate of oscillation decay, however, requires careful modelling. Krus et al. [2] proposed a TLM model where filters are used to approximate the frequency-dependent friction. The system response can then be obtained by introducing characteristics C_1 and C_2 such that

$$P_1 = C_1 + \frac{\rho c}{A} Q_1 \quad (3)$$

$$P_2 = C_2 + \frac{\rho c}{A} Q_2 \quad (4)$$

The Simulink block diagram of the model is shown in figure 3. The frequency and shape of the predicted pressure waves were found to be very inaccurate. This

is shown in figure 4, where the TLM prediction is compared with that obtained using the MOC. Johnston [9] obtained much improved results by incorporating his friction model into Krus et al.'s model. The predictions obtained using both a three- and a four-term Johnston friction model are also plotted in figure 4 for comparison.

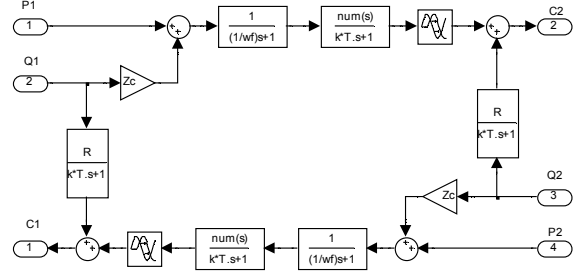


Figure 3: Transmission line model

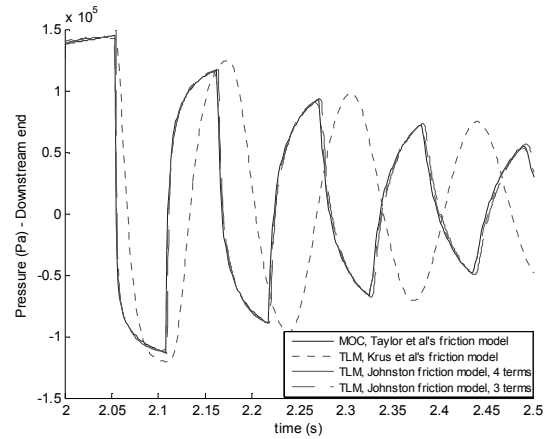


Figure 4: Predicted transient response, TLM and MOC

MODAL APPROXIMATIONS

The dynamics of a fluid transmission line can be expressed in terms of a so-called 'dissipative' distributed-parameter model using the following input-output relationship:

$$\begin{bmatrix} P_2 \\ Z_0 Q_1 \end{bmatrix} = \begin{bmatrix} 1 & -Z \sinh \Gamma \\ \cosh \Gamma & -Z_0 \cosh \Gamma \\ Z_0 \sinh \Gamma & 1 \\ Z \cosh \Gamma & \cosh \Gamma \end{bmatrix} \begin{bmatrix} P_1 \\ Z_0 Q_2 \end{bmatrix} \quad (5)$$

The line characteristic impedance Z and the propagation operator Γ are functions of the fluid properties and the radius and length of the line. Obtaining an exact solution involves zero- and first-order Bessel functions. Several modal approximation techniques have been proposed over the years for the representation of the

three transfer functions (TF) of equation (5). Here, a recently proposed method by Wongputorn et al. [3] was used which utilises least-squares curve fitting in the frequency domain to match the frequency response of the original TFs to that of rational polynomial TFs over the frequency range of interest.

When the rational polynomial transfer function approximation (RPTFA) method is used, it is very important to ensure that the transmission line model is very accurate throughout the modal frequencies of the other components of the system in which the line is an internal part and beyond any input disturbance frequencies, [3]. Different RPTFAs were obtained over different frequency ranges by defining the maximum desired frequency. The latter was varied between 100 rad/s and 2000 rad/s. At 1500 rad/s the TF approximations become inaccurate, and at 2000 rad/s the solution becomes unstable. The frequency response of one of the three TFs needed to model the system and its approximation, as obtained from Wongputorn's MATLAB routine [10], is shown in figure 5. The plotted approximation was obtained for a maximum frequency of 1000 rad/s.

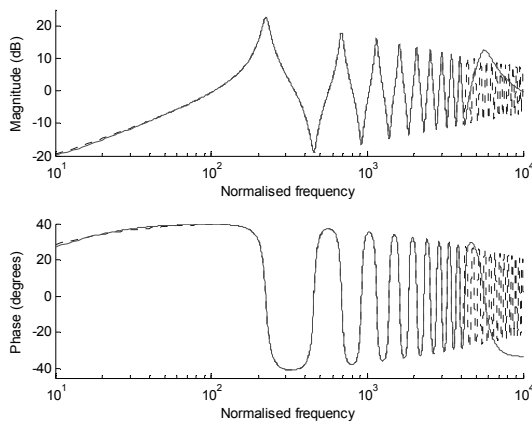


Figure 5: Frequency response of transfer function $Z \sinh \Gamma / Z_0 \cosh \Gamma$ and its approximation

The RPTFA model, incorporating transfer function approximations for frequencies up to 1000 rad/s, was implemented in Simulink. Because the system is mathematically stiff, the choice of ordinary differential equation (ODE) solver in the Simulink model is critical and an accurate solution cannot always be obtained. The solution often becomes unstable or very inaccurate, depending both on the approximation functions and the solver used.

However, when good results were obtained using RPTFA they were found to be more accurate than the solution obtained with the MOC, as illustrated in figure 6. The phase shift between the exact and the MOC solution, which develops as the wave attenuates, is no

longer present in the RPTFA solution. Inaccuracies in the solver, however, make the RPTFA solution oscillate around the exact signal throughout the simulation. This behaviour is more evident in the early part of the solution. The response of the system obtained using the RPTFA method is compared with that obtained using the MOC and the TLM techniques in figure 7.

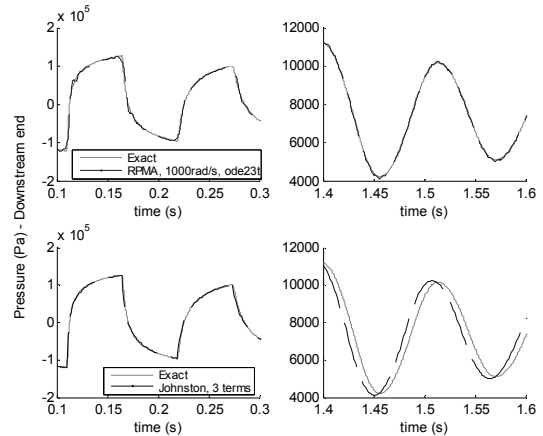


Figure 6: Comparison between MOC and RPTFA methods

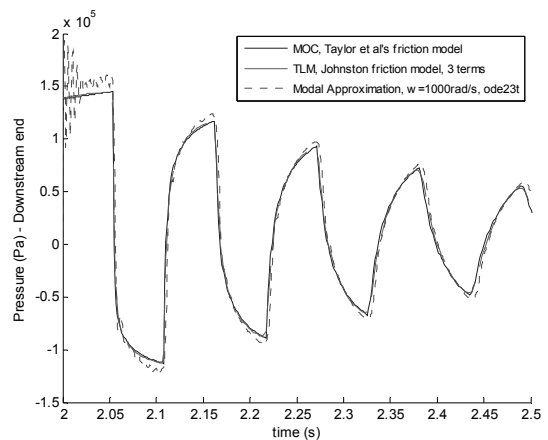


Figure 7: Comparison between MOC, TLM and RPTFA methods

Provided that a stable numerical solution can be obtained using the available MATLAB solvers, the RPTFA model is the most accurate of all the models considered so far. One of its main drawbacks, however, is that numerical solutions are often unstable or oscillatory. To overcome this problem, more appropriate solvers for this application could be implemented in MATLAB. Alternatively, different modal approximation methods that are available in the literature could be considered [11-13].

FINITE ELEMENT METHOD

Finite element approximations to the equations of motion and continuity may be derived according to:

$$\frac{dq}{dt} = \mathbf{B}p + \mathbf{C}f(q) \quad (6)$$

$$\frac{dp}{dt} = \mathbf{E}q + \mathbf{F}\bar{q} \quad (7)$$

Here, the finite element method (FEM) proposed by Sanada et al. [4] and later extended by Taylor et al. [8] was chosen to simulate the transient response of the transmission line. The FEM model uses an interlaced and unequally spaced grid of alternate pressure and flow nodes. A genetic algorithm was applied by the authors to optimise the node spacing. Grid points are spaced symmetrically about the mid point of the pipeline. The optimisation algorithm minimises the error between the natural frequencies of the model and those of a specific pipeline for the extreme cases of closed and open end conditions. The model incorporates the four-term laminar friction model proposed by Johnston [9].

When the optimised grid is used, the model exhibits a highly oscillatory behaviour during the first moments following the transient. Less severe oscillations are present when the equally spaced grid is used. These die out as the pressure wave attenuates and the shape of the pulsations for the optimised grid is better after the first two cycles. As can be seen from figure 8, the period of the pressure wave is very slightly different for the two cases.

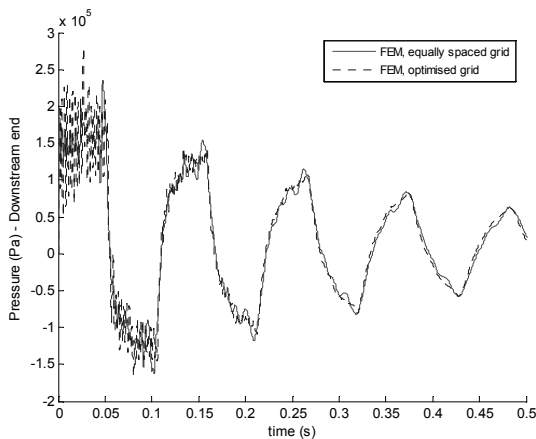


Figure 8: Comparison between optimised and equally spaced grid, FEM

The transient response of the FEM model (40 elements) is compared with those obtained using the three modelling techniques presented above, namely MOC, TLM, and RPTFA, in figure 9. While the prediction of

the RPTFA model is the one closest to the exact solution, the prediction obtained using the FEM is the least accurate one. However, the FEM was found to be reliable and not prone to instability.

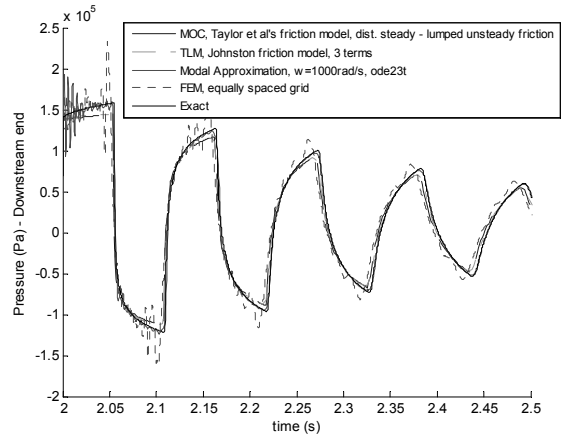


Figure 9: Comparison between MOC, TLM, RPTFA, and FEM methods

COMPUTATIONAL EFFICIENCY

The performance of the different modelling techniques was compared in terms of computational efficiency. The most accurate models developed using the four different methods were chosen for the comparison. The transient response of the system was simulated on a 2.4 GHz Pentium 4 PC with 1 Gb of RAM, for 2 seconds following a sudden valve closure. The results are summarised in the table below.

Table 1 Computational times

MOC					
No. of elements	Friction model	No. of terms	Steady state friction	Unsteady friction	Computational time (s)
20	Taylor et al.	4	distributed	distributed	0.4680
20	Kagawa et al.	7	distributed	distributed	0.4850
20	Johnston	3	distributed	distributed	0.4530
20	Johnston	3	distributed	lumped	0.0790
20	Johnston	3	lumped	lumped	0.0630

TLM					
Friction model	No. of terms	MATLAB Solver	Time step	Step size	Computational time (s)
Taylor et al.	4	ode4	fixed	10^{-4}	1.2240
Johnston	4	ode4	fixed	10^{-4}	1.2645
Johnston	3	ode4	fixed	10^{-4}	1.0850
Johnston	3	ode45	variable	10^{-3} (max)	0.1845
Johnston	3	ode45	variable	-	0.0700
Johnston	4	ode45	variable	-	0.4385

RPTFA				
Frequency - max, (rad/s)	MATLAB Solver	Time step	Computational time (s)	Notes
1000	ode23t	variable	0.6955	Solution oscillates around exact response
800	ode23tb	variable	0.8545	
500	ode23t	variable	0.9475	

FEM				
No. of elements	Friction model	No. of terms	Grid spacing	Computational time (s)
40	Johnston	4	uniform	2.521
80	Johnston	4	uniform	13.148
160	Johnston	4	uniform	180.866

Obtaining the response of the RPTFA model using the MATLAB solvers often leads to unstable or oscillatory solutions. Oscillatory solutions can either diverge from or converge to the exact system response. The increased computational times shown in the last two rows of the RPTFA table can be mainly attributed to the high frequency oscillation of the model output around the exact system response. Use of a more accurate and robust integrator may reduce computational times when the RPTFA model is used and help obtain more stable solutions.

CONCLUSIONS

A preliminary investigation of the performance of four different transient flow modelling techniques has been completed. These techniques are the method of characteristics, the transmission line method, the finite element method, and the modal approximation method. The RPTFA model was found to give the most accurate solutions. Computational times, however, are 10 times longer than those when the MOC model is used and an accurate solution cannot always be obtained with the existing MATLAB solvers. The MOC model is best suited to a fixed time step, but accurate results in short computational times can be obtained when the friction components are lumped at the pipe ends. Applying the TLM model provides both an accurate and computationally efficient method of simulating the response of the system, but integration problems can occur. The FEM method is the least accurate and efficient in terms of computational time, but can handle non-linearities and varying parameters and time steps enabling thus the modelling of cavitation and air-release.

ACKNOWLEDGEMENTS

The authors gratefully acknowledge the support of the project by Airbus UK.

REFERENCES

1. Fox J.A., Hydraulic Analysis of Unsteady Flow in Pipe Networks, The Macmillan Press Ltd., 1977.
2. Krus P., Weddfelt K., Palmberg J.O., Fast Pipeline Models for Simulation of Hydraulic Systems, Transactions of the ASME, Journal of Dynamic Systems, Measurements, and Control, March 1994, Vol. 116, No. 1, pp. 132-136.
3. Wongputorn P., Hullender D.A., Woods R.L., Rational Polynomial Transfer Function Approximations for Fluid Transients in Lines, Proceedings of ASME FEDSM 2003, 4th ASME_JSME Joint Fluids Engineering Conference, Honolulu, Hawaii, July 2004, pp. 2797-2804.
4. Sanada K., Richards C.W., Longmore D.K., Johnston D.N., A Finite Element Model of Hydraulic Pipelines Using an Optimized Interlacing Grid System, Proceedings of Institution of Mechanical Engineers, Journal of Systems and Control Engineering, Vol. 207, pp. 213-220, 1993.
5. Zielke W., Frequency-Dependent Friction in Transient Pipe Flow, Transactions of the ASME, Journal of Basic Engineering, March 1968, pp. 109-115.
6. Trikha A.K., An Efficient Method for Simulating Frequency-Dependent Friction in Transient Liquid Flow, Transactions of the ASME, Journal of Fluids Engineering, March 1975, pp. 97-105.
7. Kagawa T., Lee I., Kitagawa A., Takenaka T., High Speed and Accurate Computing of Frequency-Dependent Friction in Laminar Pipe Flow for Characteristics Method, JSME, Vol. 49, No. 447, pp. 2638-2644, 1993.
8. Taylor S.E.M., Johnston D.N., Longmore D.K., Modelling of Transient Flow in Hydraulic Pipelines, Proceedings of Institution of Mechanical Engineers, Vol. 211, pp. 447-456, 1997.
9. Johnston D.N., Efficient Methods for Numerical Modelling of Laminar friction in Fluid Lines, Proceedings of IMECE 2004, 2004 ASME International Congress and R&D Expo, November 2004, Anaheim, CA, USA.
10. Internet website for downloading fluid transmission line MATLAB m-files written by D.A. Hullender: maepro.uta.edu/Hullender
11. Kojima E., Shinada M., Yu J., Development of Accurate and Practical Simulation Technique Based on the Modal Approximations for Fluid Transients in Compound Fluid-Line Systems, International Journal of Fluid Power 3, No.2, pp. 5-15, 2002
12. Yang W.C., Tobler W.E., Dissipative Modal Approximation of Fluid Transmission Lines Using Linear Friction Model, Transactions of the ASME, Journal of Dynamic Systems, Measurements, and Control, March 1991, Vol. 113, pp. 152-162
13. Hsue C. Y-Y., Hullender D.A., Modal Approximations for the Fluid Dynamics of Hydraulic and Pneumatic Transmission Lines, Proceedings of ASME Winter Annual Meeting on Fluid Transmission Line Dynamics, Boston, 1983, pp. 51-77

Study on adaptive hydraulic device for vertical vibration

Hideki Hironaka, Hiroki Yoshino and Prof. Ken Itiryu

Tokyo University of Technology
1401-1 Katakura Hachioji Tokyo 192-0914 Japan
e-mail hironaka@ichry.mech.teu.ac.jp

ABSTRACT

In this study, hydraulic vibration controller was proposed and tentatively manufactured. Adaptive control method was tried in this experiment for vibration reduction. Proposed vibration absorber is composed of bellows, actuator and accumulator. The device is filled with oil. For input vibration, the actuator is controlled so as to make bellows inside pressure zero. Thus vibration transmission is aimed to reduce. In time, adaptive control method which is able to track non-stationary vibration phenomena is applied.

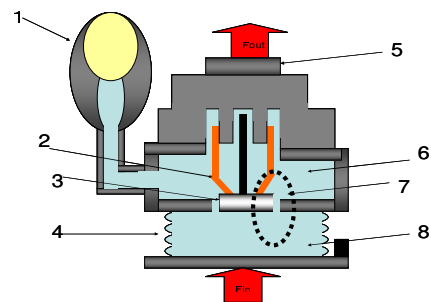
KEY WORDS

Vibration, Adaptive control, Active mount,
Adaptive Hydraulic Device

INTRODUCTION

As far as construction machinery are concerned, there is problem of the vibration transmitted to the operator room at actual work. Each company is developing mount. To date, a mount as a passive control method has been used for low frequency. That is, vibration reduction is achieved by passive action of rubber without using energy from outside. The effect of the vibration reduction depends on the characteristic of the conventional mount and its layout. For supporting operator room weight and static rigidity of the mount requires large space. As a result, issue of space occurs.

This study proposed a hydraulic theory of the vibration reduction, and by using adaptive control, the authors aimed to reduce the transmitted vibration in the operator room. Here, the vibration reduction from 20 to 50 [Hz] of low frequency is main target of this study. This paper shows the effectiveness of the theory by using the simulation, the structure of the control method and the device that can achieve the theory.



1	Accumulator
2	Voice coil motor
3	Moving mass
4	Bellows spring
5	Load cell
6	Upper chamber
7	Clearance
8	Lower chamber

Fig1 Structure of Active Mount

Active Mount Structure

Recently vibration reduce technique uses the cancel each other by actively generating the power of the input vibration and the opposite phase. But this shows heavy weight (operator room) support is difficult especially for construction machinery, because large static rigidity is necessary and as a result high control power is inevitably required. This study develops a new hydraulic active mount, which is filled inside with oil for the operator room. Fig1 shows new theory model device. This device is composed of bellows, actuator and accumulator. The device is filled with oil. The operator room weight can be supported by the oil pressure. In a word, this configuration of this mount has the advantage of being able to support the weight without any external power sources.

Theory of Vibration Reduction

This chapter explains the theory of the vibration of the active mount. When the excitation force acts on the under part of the mount, the actuator moves in the upper direction by the control signal. Consequently the volume inside the bellows does not change so much and the dynamic pressure becomes small. Therefore the transmitted force becomes low.

When the actuator is controlled so as volume flow continuity equation $A_b X_b = A_v X_v$ holds, it is assumed to reduce vibration. Here, let us simulate the vibration reduction effect when the following equation (1) is applied in this system, Fig2 shows simulation model.

$$X_v = \frac{A_b}{A_v} X_b \quad (1)$$

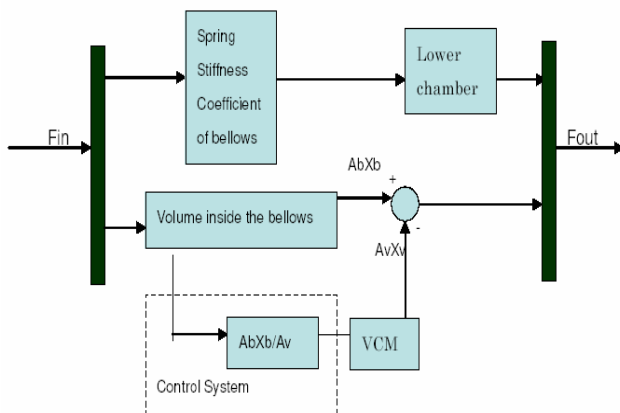


Fig2 Simulation Model Of Theory

Simulation Result

Figure 3,4,5 shows the comparison of the input force, under pressure and the transmitted force as the error signal when the control is active. In this figure it was found that when the pressure P1 is nearly 0[Pa], the transmitted force is also approximately 0[N]. That is, the assumption explained above is demonstrated. However, as this control scheme is open loop, the adjustment of the amplitude will be difficult when system fluctuates frequently. Actually, engine vibration is not stationary. It fluctuates considerably due to surrounding condition. Therefore more flexible control scheme will be needed.

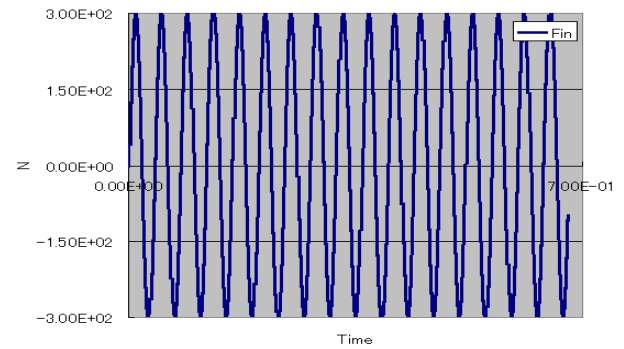


Fig3 Input Force

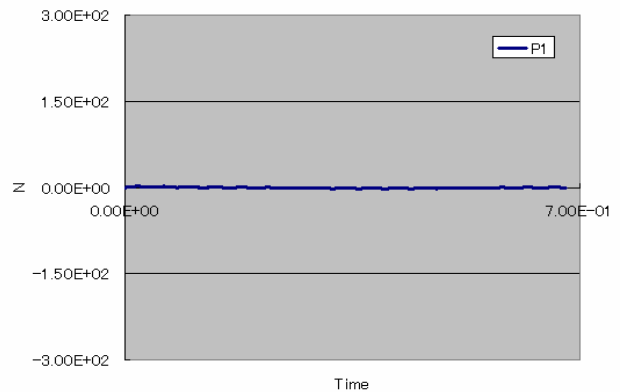


Fig4 lower chamber Pressure

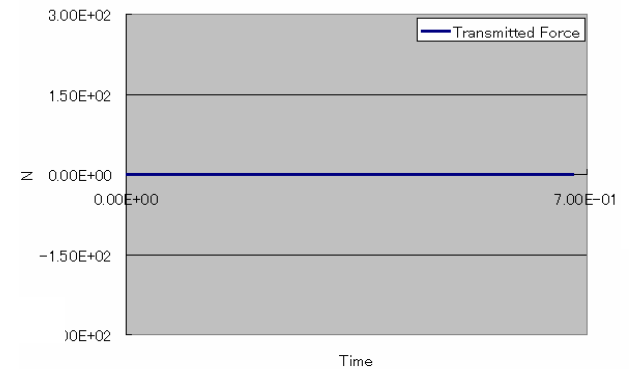


Fig5 Transmitted Force

System Consideration

In a classical control method, time variant system is frequently treated. But computing power is not sufficient, time variant statistical system is difficult to treat effectively. But, now adaptive control scheme using, LMS(Least Mean Square) algorithm, becomes easy to apply for this kind of system.

1.Adaptive Control

Adaptive control is a type of control which adapts control system to follow the plant (control object) characteristics change. Algorithm to realize this process is called adaptive algorithm. Unknown system and adaptive filter response to input reference are added. This added signal is treated as error signal. Control is done to make this error signal minimum by refreshing adaptive filter characteristics.

2 .Adaptive FIR filter

By making the filter coefficient as time variable, adaptive filter is possible to realize which changes its characteristics. This block diagram is shown in Fig 6 . Unknown system and adaptive FIR filter are allocated in parallel, and by LMS algorithm, error signal e_k is followed to minimum.

3 LMS (Least Mean Square) algorithm

As a refreshing method of coefficient of adaptive FIR, there exist many kinds of algorithm, such as RLS (Recursive Mean Square) algorithm. In this study, LMS algorithm was chosen as simplified steep descent algorithm.

$$h_{k+1} = h_k - 2\mu e_k x_k$$

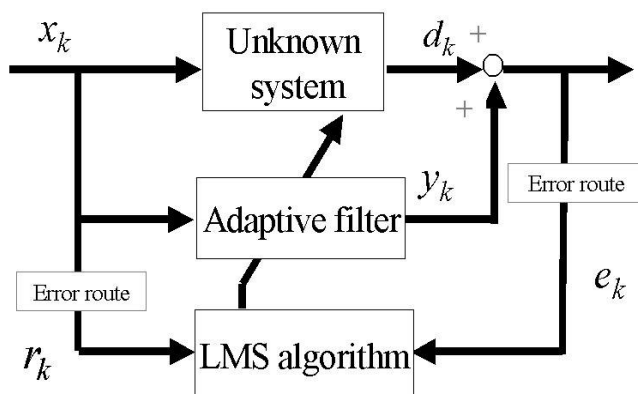


Fig6. Adaptive Control

LMS algorithm

In the previous chapter, absorber model and adaptive filter control scheme were described. Now, let us explain system configuration. Active control system, shown in Fig.6 was applied here. Signal from upper vibration is treated as reference signal. Both output response of unknown system, that is, dynamic system and signal from adaptive filter are coupled together. The latter adaptive signal is inputted to VCM. By changing filter coefficient continuously, transmitted force to the ground is aimed to make minimum.

1 LMS Simulation

The filter is repeatedly renewed by comparing input signal with transmitted force, thus it to minimum. VCM position is controlled by this algorithm and the effect is proven. The effect of the adaptive control is understood from the simulation by using the active mount model. The LMS algorithm is evaluated by using the active mount model. Fig 7 shows the model.

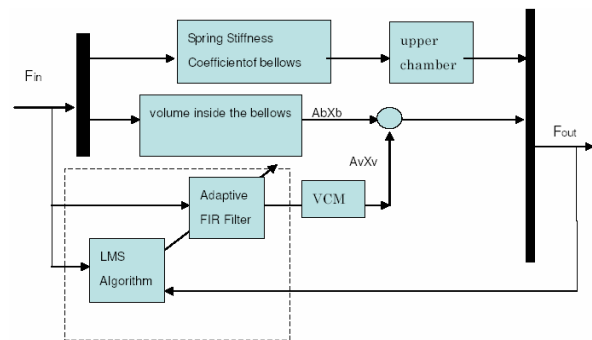


Fig7. LMS Simulation Model

2 LMS Simulation Result

Figure 8 shows the simulation result. Graph above is input vibration F_{in} . Graph below is F_{out} force transmitted to the highest part at active mount (LMS algorithm) control. When $F_{in} = \pm 20$ [N] was input to the regulating system, vibrations almost 0 were transmitted to the highest part. That is to say, it was able to say that the vibration attenuation in active mount became possible by using the adaptive behavior control (LMS algorithm).

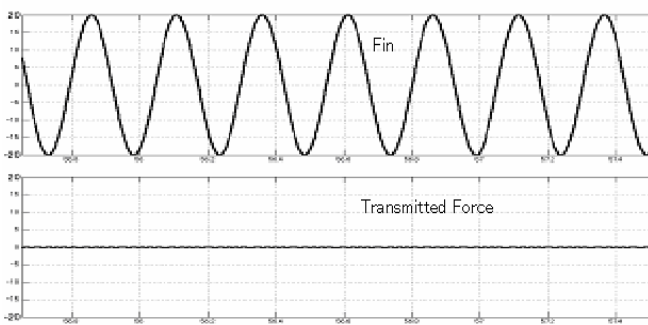


Fig8. LMS Simulation Result

Basic Examination

Fig9 shows the experimental result. The vibration damping of 40[dB] was obtained in whole area of the frequency from 20 to 50 [Hz] in control OFF and ON. The vibration of +5 was amplified by control OFF. It is thought that this is because the reaction force acts, actuator always keeps neutral point. As for control ON, it was confirmed that the vibration reduction of 30[dB] is obtained, and the vibration attenuation of this wet type active mount becomes effective as shown in the result of the simulation.

Conclusion

This research, we developed a new active mount of wet type using actuator. In this device, static load is sustained by hydraulic pressure of upper and lower chamber. As the result, power consumption is low compared with conventional device. First, static test jig was constructed, and fundamental

vibration examination was conducted. We confirmed the effectiveness of the developed device.

Detailed results are shown in the following.

- 1: By simulation, volume flow continuity relationship between upper chamber and voice coil motor was studied. From this result, we developed adaptive control scheme for vibration reduction to the operator room.
- 2: By basic examination, vibration attenuation of 50 to 60[dB] was obtained in the whole area from 20 to 50[Hz].

Reference

- 1 C.Togashi," Study on Hydraulic Active Engine Mount ", 2003 SAE Noise & Vibration Conference 2003-01-1418
- 4 Nonami, Nishimura, "Basis of Control Theory", Tokyo Denki Uuiv shuppanyoku, 1999
- 5 Kimura, "Development of an Active Control Engine Mount System Featuring on Adaptive Control Algorithm ", JSAE, 9833250
- 6 Aoki, "Noise and Vibration of Diesel Engine Vehicle Making Use of the Active Engine Mount (ACM) System ", JSAE, 9833241
- 7 Nagamatsu, "Modal Analysis and Control of Sound and Vibration", Corona, 1996
- 8 Shibayama, Active Engine Mount for Large Amplitude of Idling Vibration, SAE 951298 Ozaki," Development of an Active Control Engine Mount", JSAE, 9833269

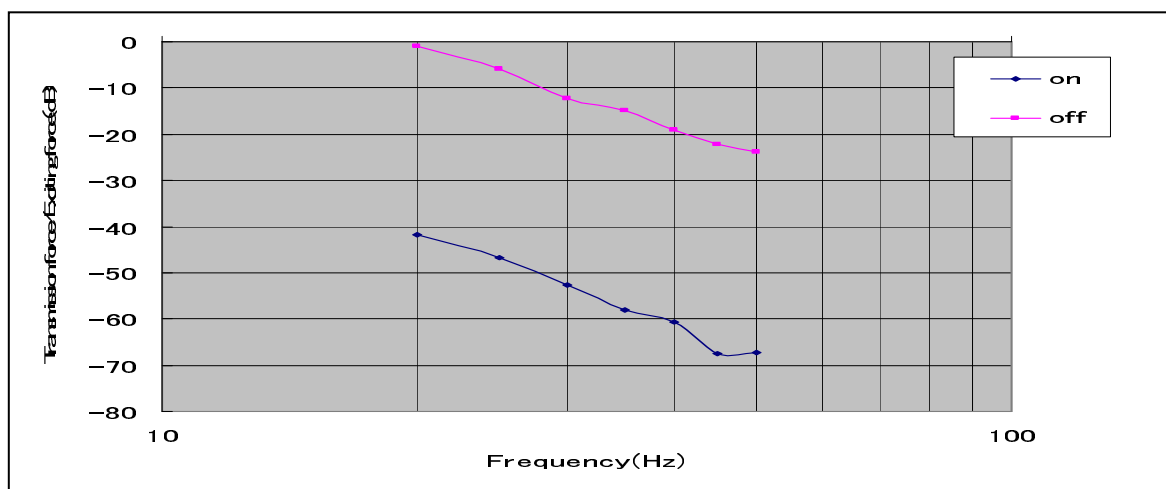


Fig9. Basic Examination Result

DEVELOPMENT OF SIMULATOR FOR HYDRAULIC EXCAVATOR

TaeHyeong LIM*, HongSeon LEE** and SoonYong YANG *

* School of Mechanical and Automotive Engineering, University of Ulsan
29 Mugeo-dong, Nam-gu, Ulsan, 259-2731 Korea
(E-mail: bulbaram@mail.ulsan.ac.kr)

** Department of Construction Equipment, Hyundai Heavy Industry
1 Jeonha-dong, Dong-gu, Ulsan, 230-8988 Korea

ABSTRACT

Hydraulic excavators have been popular devices in construction field because of its multi-workings and economic efficiency. The mathematical models of excavators have many nonlinearities because of nonlinear opening characteristics and dead zone of main control valve, oil temperature variation, etc. The objective of this paper is to develop a simulator for hydraulic excavator using AMESim. Components and whole circuit are expressed graphically. Parameters and nonlinear characteristics are inputted in text style. The simulator can be used to forecast excavator behavior when new components, new mechanical attachments, hydraulic circuit changes, and new control algorithm are applied. The simulator could be a kind of development platform for various new excavators.

KEY WORDS

Excavator, AMESim, Attachment, Hydraulic circuit

INTRODUCTION

Hydraulic excavator have been popular device in construction field because of its multi-working and economic efficiency. The application of this complex device will be extended manufacture, agriculture, undersea etc.

But its operating need very difficult skill because operator has to operate joysticks and pedals consequently. So accuracy of work is influenced by operator's skill. But environment of work is poor and difficult skill bring about feeling fatigued fast. Autonomous excavator can be a kind of solution about previous problems and many researches have been achieved by many researchers. British Columbia university in Canada, Carnegie Mellon university in USA and Sydney university in Australia have field robot

center and have made a special studies with excavator and many construction equipment makes have prototype or autonomous excavator in part.

The paper map in field robot with excavator made before in my laboratory show that 56 % of papers focus in modeling of attachment (Boom, Arm, Bucket) using Lagrange Euler equation and applying control algorithms but hydraulic circuit and valves are modeled very simply. For example, main control valves having nonlinear open area characteristics are modeled in simple variable orifice and logic valves are omitted. In many paper, researchers use robust controller in order to overcome nonlinearities created by complex open area characteristics and dead zone of valve, single acting cylinder, heavy weight of attachment. Because of many nonlinearities, experiments are positively necessary but limited by time, money, place etc.

The objective of this paper is to develop a simulator for

hydraulic excavator using AMESim. Components and whole circuit are expressed graphically. Parameters and nonlinear characteristics are inputted in text style. The simulator can be used to forecast excavator behavior when new components, new mechanical attachments, hydraulic circuit changes, and new control algorithm are applied. The simulator could be a kind of development platform for various new excavators.

ATTACHMENT MODEL

Hydraulic excavator consist of upper frame, lower frame and attachment. Upper frame contain operating room, engine, pump, main control valve (MCV) and attachment is fixed to end of upper frame. Lower frame contain crawler or wheels and upper frame can rotate by swing motor. In this paper, attachment is modeled boom, arm, bucket except swing and drive and excavator model is 5 ton of Hyundai Heavy Industry.

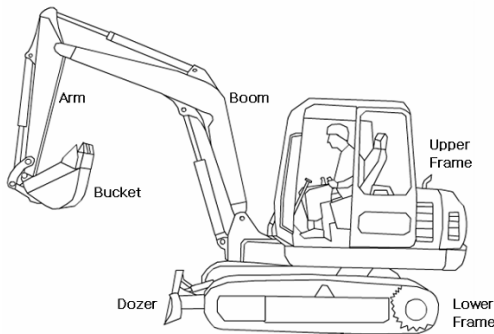


Figure 1 A Hydraulic Excavator

Fig. 2 shows the coordinate systems of excavator and motion equation was established by Lagrange equation.

$$\sum_{j=1}^n H_{ij} \ddot{q}_j + \sum_{j=1}^n \sum_{k=1}^n h_{ijk} \dot{q}_j \dot{q}_k + G_i = Q_i, i = 1, \dots, n \quad (1)$$

$H_{ij} \ddot{q}_j$ is inertia torque including interaction torque by off diagonal element of attachment inertia tensors, $h_{ijk} \dot{q}_j \dot{q}_k$ is Coriolis and centrifugal effects and G_i is gravity torque.

Fig. 3 present AMESim model of attachment. The supercomponent of attachment is shown right and upper part in fig. 3 and this contain the rest components. Each component contain link's characteristic-length, mass, inertia etc.

The coordinates in fig. 2 are contained the attachment super- component. The inputs of supercomponent are force of cylinder and outputs are angular displacement of boom, arm and bucket.

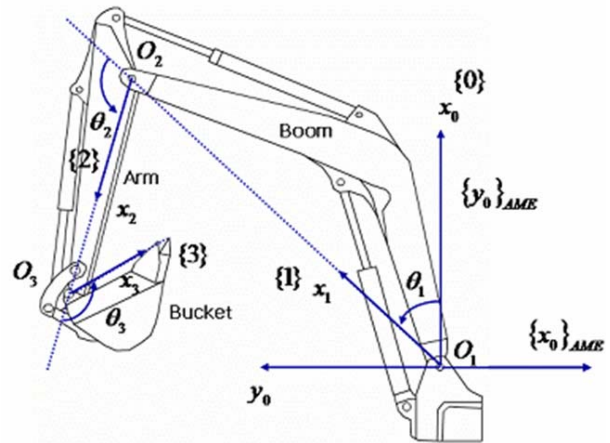


Figure 2 Coordinates system

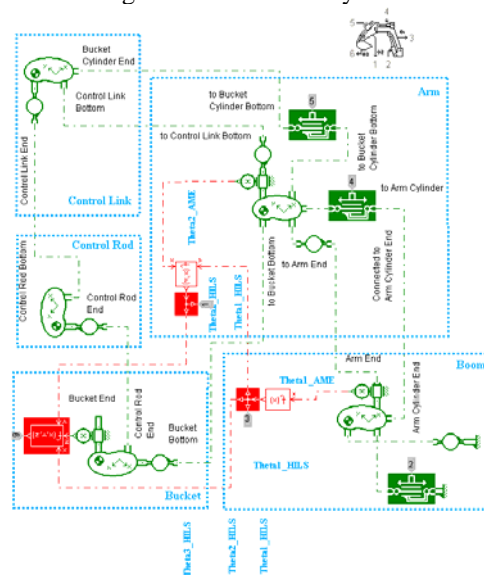


Figure 3 AMESim model of attachment

HYDRAULIC CIRCUIT MODEL

Main pump operated by engine make two type of pressures that main pressure work each cylinder and pilot pressure work spool of main control valve by operating joystick. If operator handle joystick or lever, pilot pressure push the spool of MCV, the rate and direction of flow is decided by spool displacement and direction and flow rate can decide of direction and velocity of cylinder. Working area is assumed 2D in this paper, hydraulic circuit can be simplified like fig. 4. Because boom up and arm dump need much flow rate, join of flow rate between boom 1 valve and boom 2 valve, arm 1 valve and arm 2 valve.

- Joystick

The role of joystick is supplying pilot pressure to MCV by operate angle. The AMESim model of joystick is shown in fig. 5. components in dotted square are contained supercomponent in left hand side. Operating of joystick is assumed to signal between -1 to 1 and

pilot pressure to A, B port is directly proportional to signal. The input signal to joystick model is fig. 6 (a) and pilot pressure at port A, B is (b). In fig., pilot pressure response is proportional and delay is rare.

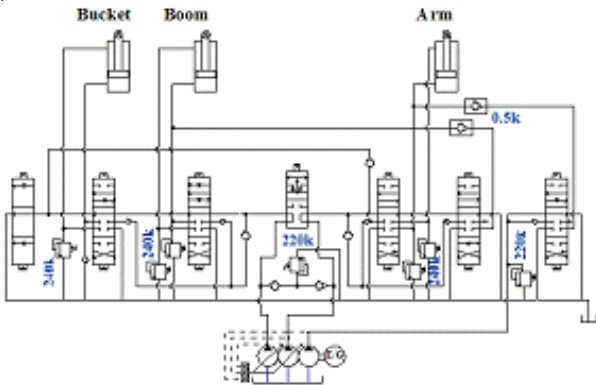


Figure 4 Hydraulic circuit of excavator

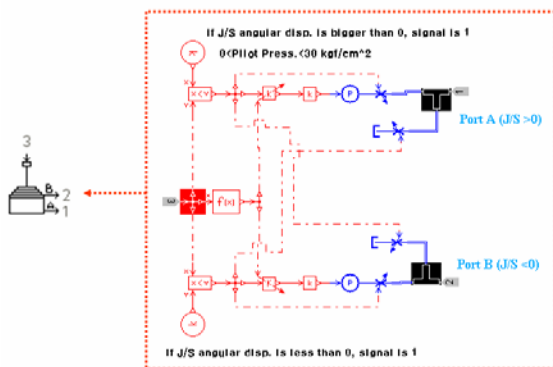
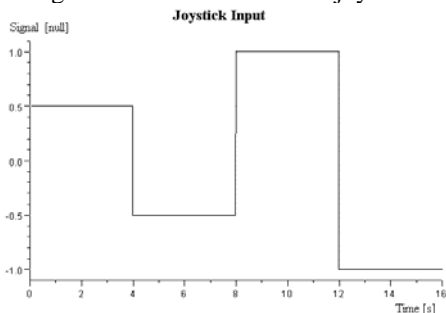
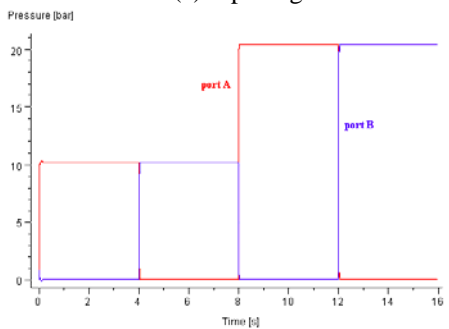


Figure 5 AMESim model of joystick



(a) Input signal



(b) Pilot pressure at A, B port

Fig. 6 Result of joystick model

- pump

The pump assembly consist of 2 variable pump for main pressure and 1 fixed pump for pilot pressure. Variable pump has control algorithm for energy saving, this can be characterized to P-Q diagram. The AMESim model of pump assembly is shown in fig. 7. Various P-Q diagram can be tested in this model easily because P-Q diagram is inserted by text file. For verification of pump model, input and output P-Q characteristics are shown in fig. 8. The solid line is input and dotted line is output. This pump model is verified with valve and cylinder.

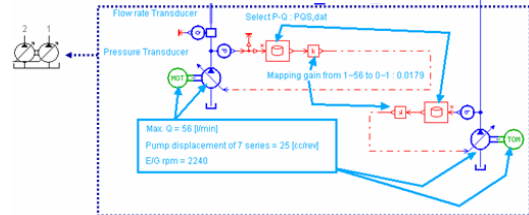


Figure 7 AMESim model of Boom 1 valve

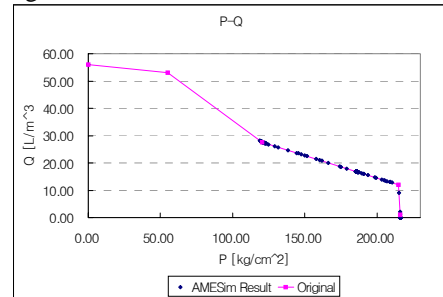


Figure 8 Result of pump model

- Boom 1 valve

Boom 1 valve, decide direction and velocity of boom cylinder mainly, is modeled 6 port 3 position valve. The spool displacement-Open area diagrams contain many nonlinearities dead zone, saturation and unproportional characteristic. These nonlinear diagrams are put into model text file. Fig. 9 show open area diagrams. The velocity of boom cylinder at up and down will be different because of nonsymmetrical diagram. Fig. 10 is AMESim model of boom 1 valve. The components in dotted square are packed into super- component in left hand side in fig. Fig. 11 show that spool displacement in various spring stiffness.

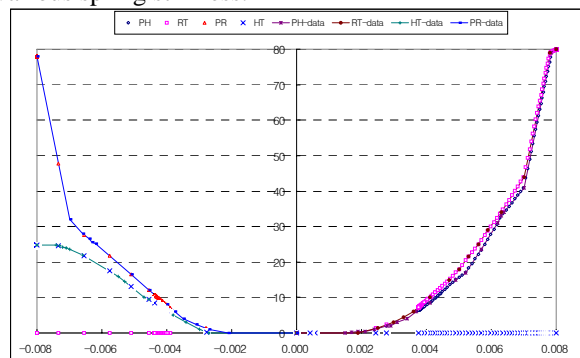


Figure 9 Open area diagram of boom 1 valve

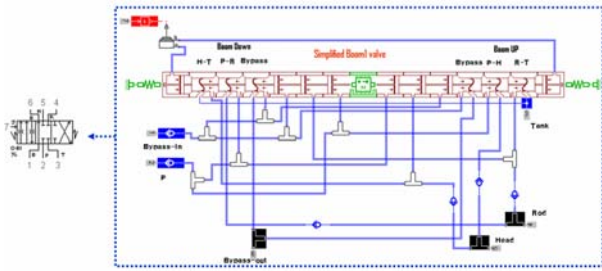


Figure 10 AMESim model of Boom 1 valve

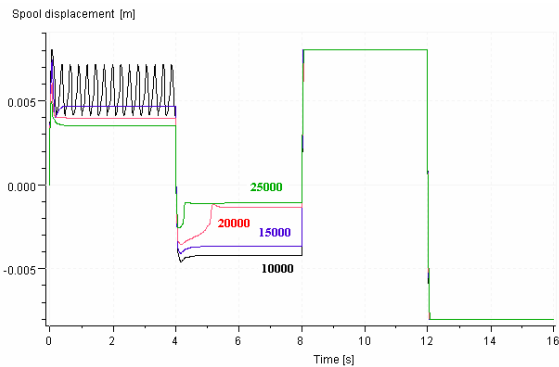


Figure 11 Spool displacement in variable stiffness

Stiffness variation has influence upon valve displacement. Too low stiffness produce oscillation of spool and errors between up and down are different to each other. 17000 make the error to minimum and spool displacement is shown in fig. 12. The displacement error at boom up is 0.316[mm], at boom down is 0.61[mm].

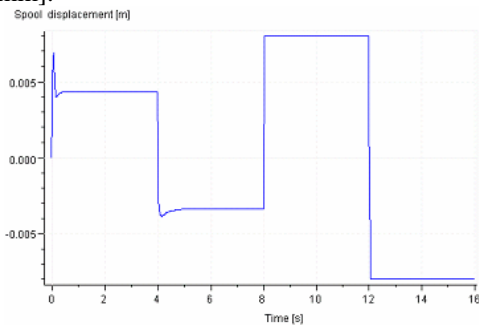


Figure 12 Spool displacement at stiffness 17000

- Boom 2 valve

The role of boom 2 valve is supply flow rate to boom cylinder at boom up. The boom 2 valve model has same structure with boom 1 valve model and different open area diagram. 20000 make the error to minimum and spool displacement is shown in fig. 13. The displacement error at boom up is 1.02[mm].

- Arm 1 valve

Arm 1 valve, decide direction and velocity of Arm cylinder mainly, has same structure with boom 1 valve model and different open area diagram. 20000 make the error to minimum. The displacement error at arm dump is 0.0534[mm], at arm crowd is 0.284[mm].

- Bucket valve

The final spring stiffness of bucket valve is 26000 and error at bucket dump is 0.042[mm], at bucket crowd is 3.17[mm].

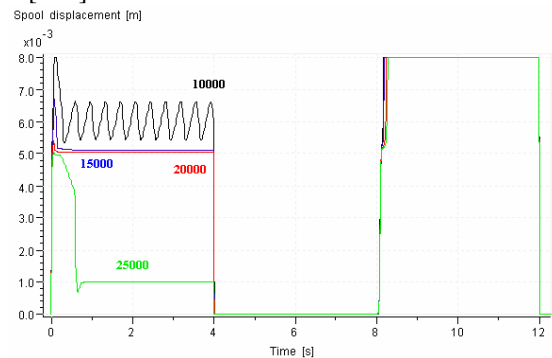


Figure 13 Spool displacement in variable stiffness

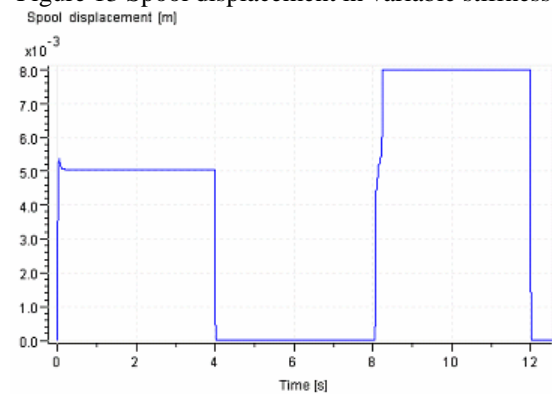


Figure 14 Spool displacement at stiffness 20000

- Main Control Valve(MCV)

The main control valve block consist of previous hydraulic components(3.1~3.6) is shown in fig. 15. The working fluid through by pass go to tank and feature of circuit is similar to simplified circuit in fig. 4. The port relief is added to cylinder in, out port.

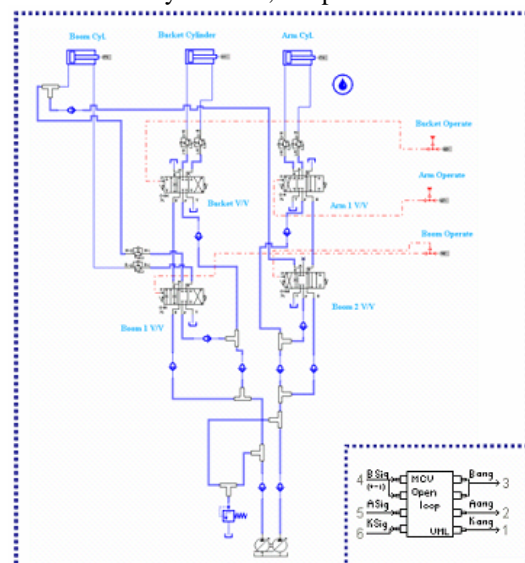


Figure 15 AMESim model of MCV

TOTAL MODEL AND SIMULATION

Total excavator model is constructed in fig. 16 using previous models.

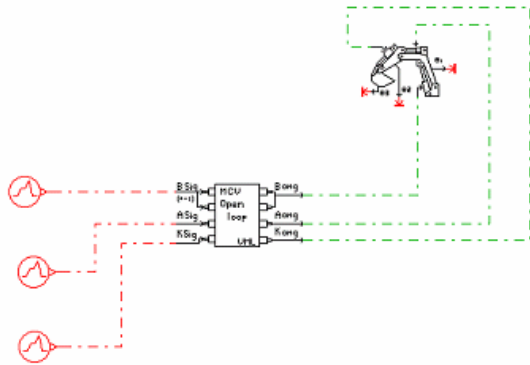


Figure 16 AMESim model of excavator

Though stiffness tuning was done, results at complex motion is different from it at single motion. Simulation condition is that operate joystick 50 [%] to + for 4 [sec], 50 [%] to -, 100 [%] to + and 100 [%] to - of boom, arm and bucket simultaneously. Fig. 17 show spool displacement of boom 1 valve and boom 2 valve under simulation condition. Displacement error is bigger than simple motion that is because pressure at cylinder effect to MCV. Fig. 18 show angular displacement of attachment and pressures at boom cylinder are shown in fig. 19.

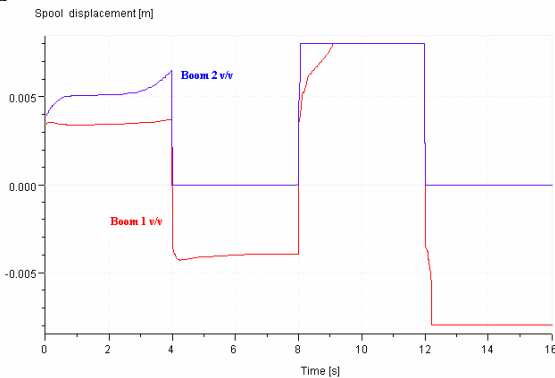


Figure 17 Spool displacement of boom valves at complex work

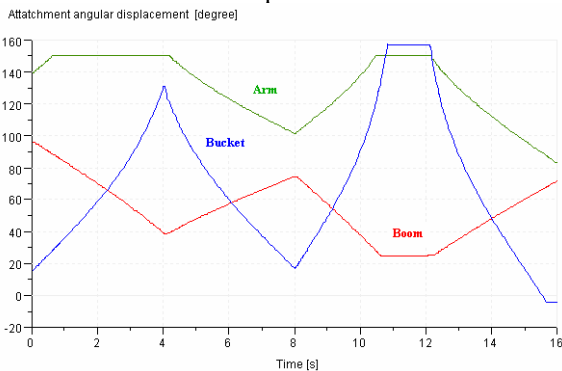


Figure 18 Angular displacement of attachments

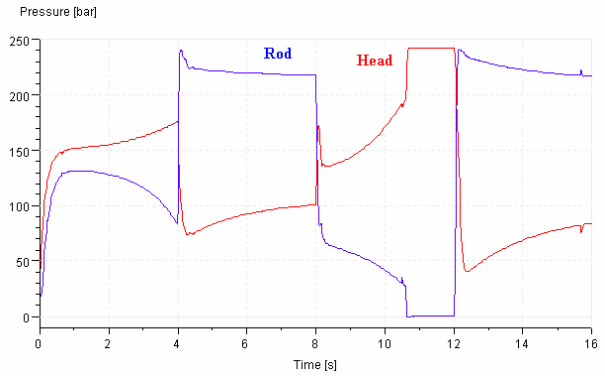


Figure 19 Pressures of boom cylinder

CONCLUSION AND FUTURE WORK

Each component of attachment and hydraulic circuit of excavator and total excavator is modeled with AMESim. To find constant spring stiffness make error to minimize tuning has done each valve model and result is as follow.

For boom 1 valve error at boom up is 0.316[mm], boom down is 0.61[mm] with stiffness 17000. In case of boom 2 valve, error at boom up is 1.02 [mm] with stiffness 20000. Arm 1 valve, error at arm dump is 0.0534, arm crowd is 0.284 [mm] with stiffness 20000. In bucket valve, error at bucket dump is 0.042[mm], at bucket crowd is 3.17[mm] with stiffness 26000. So, constant spring stiffness can't satisfy accuracy of spool displacement for all condition. In order to proportional to displacement of MCV it is need to construct closed loop type MCV.

The AMESim model for total excavator will be used to verify new control algorithm or new component. Under being many limit to make an experiment with real excavator, this AMESim model will play an active part in simulator or test bench.

ACKNOWLEDGMENTS

This work was supported by the Korea Science and Engineering Foundation (KOSEF) through the research center for machine parts and material processing at University of Ulsan and Hyundai Heavy Industry.

REFERENCES

1. T. R. Kane, "Dynamics : Theory and Applications", McGraw-Hill, 1985.
2. R. P. Paul, "Robot manipulators : Mathematics, Programming, and Control", The MIT Press, 1981.
3. J. Watton, "Fluid Power Systems, Prentice Hall, 1989.
4. "AMESim User's Manual", IMAGINE, 2000.
5. S. Y. Yang etc. "A Study on Trajectory Tracking Control of Field Robot", ICASE, Vol8, No.9, 2002.

Pilot Study of Dynamic Simulation on Hydraulic Supply System of HAGC

Xiaohong Jin *, Yachen Chen **

*College of Machinery and automation
Wuhan University of Science and Technology
Wuhan, 430081 China
(E-mail: fluidpower@263.net)

**Continuous Casting Technology Co., LTD of China
Wuhan, 430081 China
(E-mail: accan_007@163.com)

ABSTRACT

The hydraulic automatic gauge control (HAGC) system is the core of the automatic gauge control system in a high speed strip mill. A ripple of the servo valve power supply may affect the performances of HAGC. From the characteristics of the servo valve power supply for a HAGC system, the static relationships of the accumulator's parameters and the power supply, which equips pressure compensated variable displacement pump, are analyzed. By the power supply system modeling and simulation, with the help of the software EASY5, the useful results have been obtained as follow: 1. the relationship of the rate of pressure ripple and the accumulator; 2. the adequate volume of an accumulator; 3. the oil pipe's parameters and the optimal position of an accumulator; 4. the diminution of the load effect in actuator.

KEY WORDS

Servo valve power supply, Accumulator, Simulation, HAGC

INTRODUCTION

An automatic gauge control (AGC) in a high speed and precise strip mill is performed by an actuator controlled by electronic hydraulic servo valve (SV). This system is a hydraulic automatic gauge control (HAGC) system. The HAGC system requires that the flowrate must meet the demand for the actuator and the pressure of the supply source should be in constant. A ripple of the SV power supply may bring varieties of the load flowrate and the coefficients in the SV and therefore affect the

accuracy and response speed or may even bring the stability problem of the HAGC system. In the working process the demands for the flowrate are variable. In the situations of a roller exchanging or the wide gauge regulating the load pressure is low and the flowrate is high. But in the rolling process the load pressure is high and the frequencies of flow ripple are high although the gauge regulating is small. The power supply of HAGC is mainly in the form of a combination of a pressure compensated variable displacement pump (CP) and an accumulator. Though the high price for the combination of pump and accumulator, the CP can itself adjust the

flowrate to meet the load and the combination is with a little power loss and a low temperature rise.

In a high speed strip mill, especially in a tandem cold strip mill, the dimensional tolerance, hardness and the speed of the strip are highly rippled. How can the hydraulic power supply be equipped in accord to the technical condition and how can the parameters of the power supply and the pipes be selected in reason are the issue to be discussed.

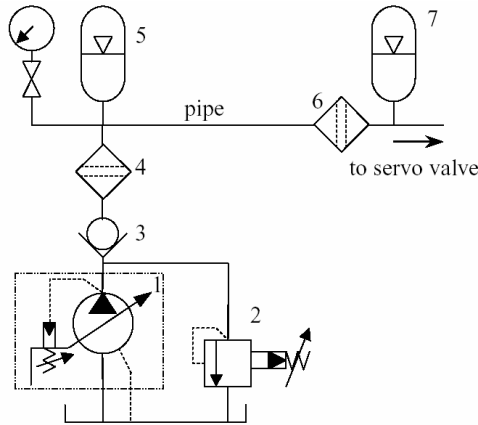


Figure 1 Power supply scheme

STRUCTURE OF THE POWER SUPPLY AND DETERMINATION OF ITS STATIC PARAMETERS

A power supply of HAGC is showed in Figure 1. The supply is basically a combination of a CP and two accumulators. The power supply contains CP 1, relief valve 2, check valve 3, filter 4, accumulator 5, filter 6 and accumulator 7. Because of the location of a mill the power supply is far away from the SV. There is a resistance in the long pipe and the accumulator 7 is equipped near the inlet of SV in order to increase the response speed and to minimize pressure ripple in the inlet of SV.

To minimize pressure ripple of the power supply two points must be taken into account. (1) Determine the static minimal nominal volumes of the two accumulators, one is in outlet of the pump and the other is in the inlet of SV. (2) Determine the reasonable volumes of accumulators, the length and diameter of the pipe and the effects of loads.

Determination of the parameter of the accumulator in the outlet of pump

A CP has a ripple of output flow and has a swivel out time in the pressure controller. The swivel out time of the CP is longer than the response time of a SV when a CP in the condition of minimal displacement and the output flow of the CP will not meet the demand of the

SV. The lack in the flowrate may be made up by using an accumulator near the pump and the accumulator can also absorb the ripple of output flow. The Figure 2 shows the response time of a SV, in dotted line, and the swivel out time of a CP, in black line. By the Figure 2, the net volume of the accumulator, ΔV_1 , is

$$\Delta V_1 \geq Q_s(T_p - T_s)/2 - (V_{gmax} - V_{gmin})n\eta_v T_p \quad (1)$$

where Q_s is the nominal flow of a SV with a valve pressure differential at maximum nominal pressure, T_p the swivel out time of a CP, T_s the response time of the SV, V_{gmax} the maximum geometric displacement of the CP, V_{gmin} the minimum geometric displacement of the CP, n the shaft speed of the CP and η_v the volumetric efficiency of the CP.

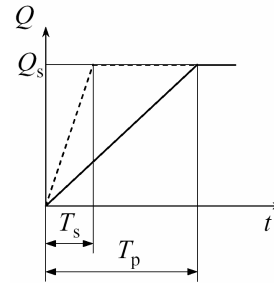


Figure 2 Flow for a SV and a pump

Determination of the parameters of the accumulator near the inlet of the SV

The parameters of the accumulator near the inlet of the SV may be determined by the rolling data of the strip mill. For a given maximum rolling speed, V_{max} , the mean length, L_p , of the fluctuation in the thick of the steel strip can be gotten by the statistic of fluctuation margin of the thick. In order to eliminate the fluctuation the moving times, n , of actuator in swivel out time, T_p , of the CP is

$$n = V_{max} T_p / L_p \quad (2)$$

so, the effective net volume of the accumulator, ΔV_2 , is

$$\Delta V_2 \geq A_c X_{max} n \quad (3)$$

where X_{max} is the maximum displacement of actuator, i.e., the maximum fluctuation in the thick of a strip, A_c the effective piston areas of the actuator.

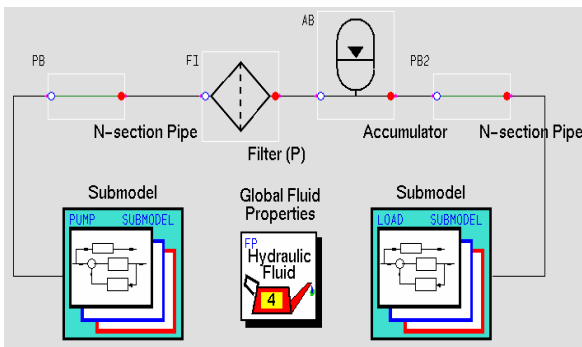
DYNAMIC SIMULATIONS

The software EASY5x, Engineering Analysis Software from The Boeing Company, is one of the software used

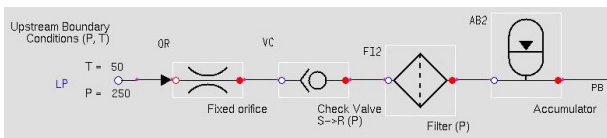
in hydraulic system simulation. The software is superior in the modeling of programming language, graphical modeling and selecting of algorithm. It can be used to construct a highly accurate model [1], [2].

Simulation model and parameters

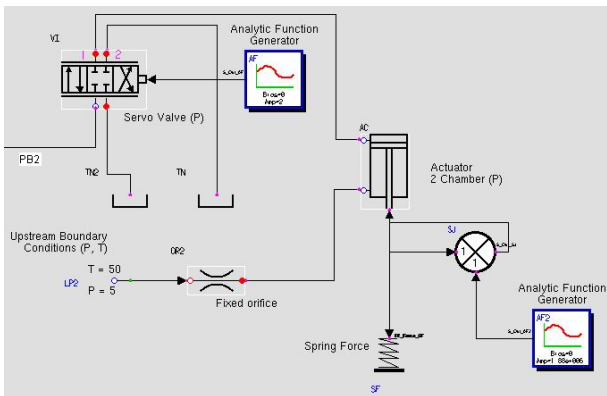
An actual power supply of a HAGC in a tandem cold strip mill is taken as the case of the simulation. First, determine the parameters of the two accumulators by using Eqs. (1) and (3). Second, setup the simulation model in accord to configuration of the power supply and the load of the actuator. The simulation now can be performed by the data in the actual system. The simulation model is showed in Figure 3.



(a) System model



(b) Upstream condition model



(c) Load submodel

Figure 3 Simulation model

In Figure 3, PUMP submodel contains the CP, check valve, accumulator in the outlet of pump and filter. The

output of the PUMP submodel goes into the filter FI in prior the SV through long pipe PB. AB is the accumulator near the inlet of the SV. PB2 is the pipe that connects the accumulator AB and the input of the SV. The LOAD submodel includes SV, actuator and loads. All the parameters are taken from the actual system and the data are mainly listed as follow. Pressure in the outlet of the pump is 25MPa. The long pipe PB is 50m in length, 65mm in hydraulic diameter, 0.08mm in absolute roughness and 1.6×10^{10} Pa in bulk modulus. The nominal volume of the accumulator AB is 20L and its maximum precharged volume is 18.4L at 17MPa. The hydraulic diameter of the orifice in the port of the AB is 10mm and the volume of the port chamber is 0.5L. The connecting pipe PB2 is 2.1m in length, 32mm in hydraulic diameter, 0.08mm in absolute roughness and 2.8×10^{10} Pa in bulk modulus.

In the simulation the frequency of the sine input sign is 12Hz and the amplitude is 20% in rating electric current in accord with actual maximum capacity in LOAD submodel. The Gear algorithm is employed.

Analyses for the simulation result

Function of the accumulator near the inlet of the SV

Figure 4 gives curves of the pressure in the inlet of the SV. From the figures it can be seen that the pressure has a fluctuation of 4.64% without an accumulator and the pressure is only a ripple of 0.6% with an accumulator. It is evident that an accumulator can effectively decline the fluctuation of the pressure in the inlet of the SV.

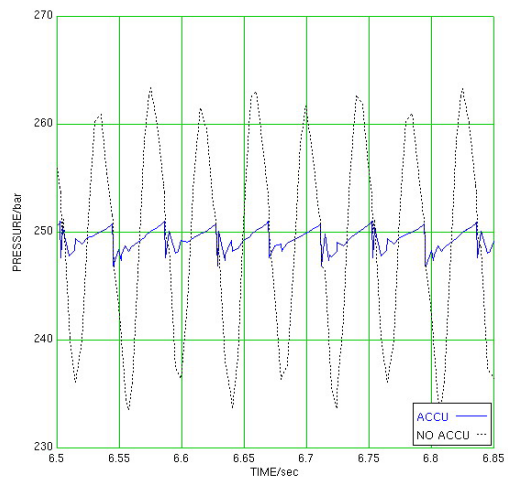


Figure 4 Pressure in the inlet of the SV with and without an accumulator

Figure 5 gives the simulation curves of pressure in the inlet of the SV with the several kinds of nominal volume of the accumulator. From the Figure 5 it can be seen that the rising time, from the precharged pressure to the working pressure, is increased and the natural

frequencies are become small as the nominal volume of an accumulator is enlarged. The results show the same conclusion as the Zhan's work [4]. It can be also seen that the fluctuation of pressure in the inlet of the SV is decreased with a large volume of an accumulator. When the volume is aggrandized to 24L, the fluctuation remains nearly unchanging. This shows that the nominal volume of an accumulator has a limit in the absorbability to the pressure fluctuation.

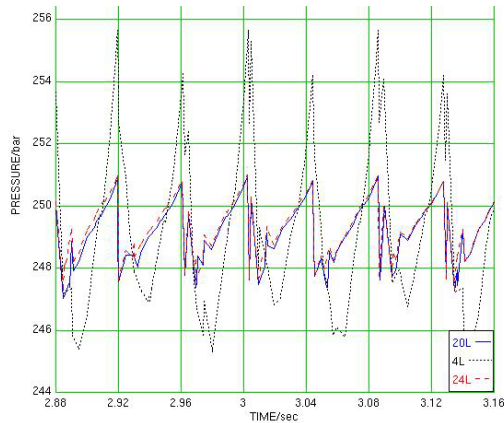


Figure 5 Pressure with several nominal volumes of the accumulator

Effects of the length and diameter of the pipe

Figure 6 shows the simulation curves of the pressure in different lengths of pipe between the port of the accumulator and the SV, i.e. PB2 in Figure 3. The fluctuation of the pressure in the inlet of the SV is reduced as the length decreasing. This indicates that a longer pipe has a larger fluctuation in the system.

Figure 7 shows the simulation curves of the pressure in different diameters of pipe between the port of the accumulator and the SV. The fluctuation of the pressure in the inlet of the SV is largely reduced as the diameter is increasing. This indicates that a too large diameter of pipe is not necessary in the system.

Contribution of the loads in actuator

Figure 8 gives curves of pressure in the inlet of the SV with the several kinds of nominal volume of the accumulator at the 5%, 10% and 15% of the maximum loads. By comparing the three charts it is evident that the loads have no effect on the pressure in the inlet of the SV as the nominal volume of the accumulator is equal to or over 20L.

CONCLUSION

By using other frequency and amplitude of input sign of the SV the simulation gives the similar results as the above simulation in another nominal volume of the

accumulator. The simulation results are highly close to the actual data. From the above model and simulation it can sum up as follows. 1) The accumulator at the inlet port of the SV plays an important role in the weakening of the fluctuation of the pressure at the inlet port of the SV. 2) The nearer the port of the accumulator is to inlet port of the SV, the smaller the fluctuation of pressure is. Because there is resistance in the port of an accumulator, it is useful that the inner diameter is adequately enlarged. 3) By a proper selection of the nominal volume of an accumulator the effect on the pressure at the inlet of the SV will reduce to a least extent.

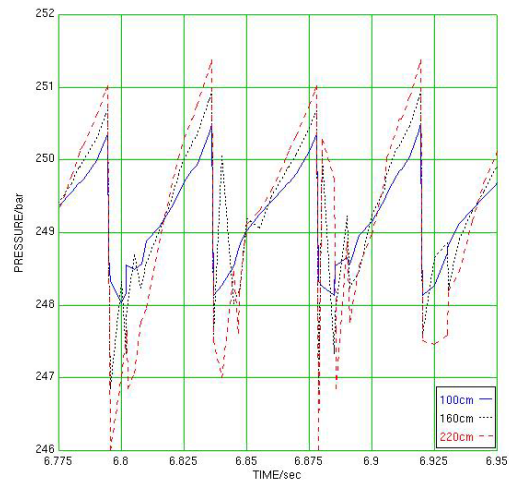


Figure 6 Pressure with different lengths of the pipe

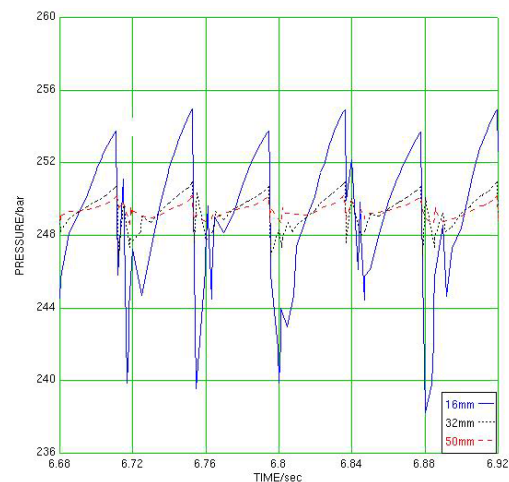


Figure 7 Pressure with different diameters of pipe

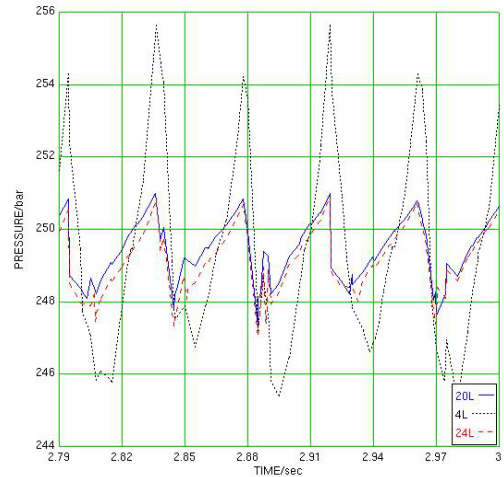
ACKNOWLEDGMENTS

The authors would like to offer their gratitude to the

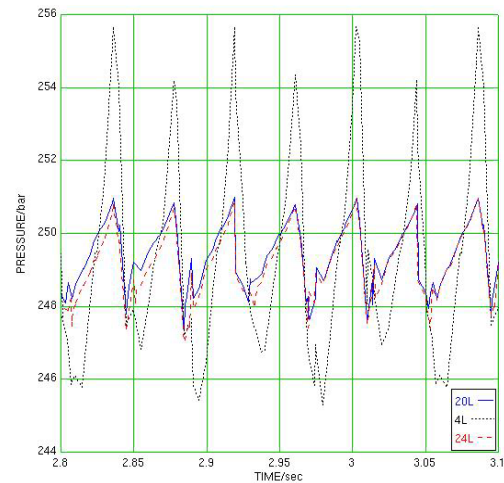
Key Laboratory of Hubei Province Mechanical Transmission and Manufacturing Engineering (PR China), Grant number 2003A11.

REFERENCES

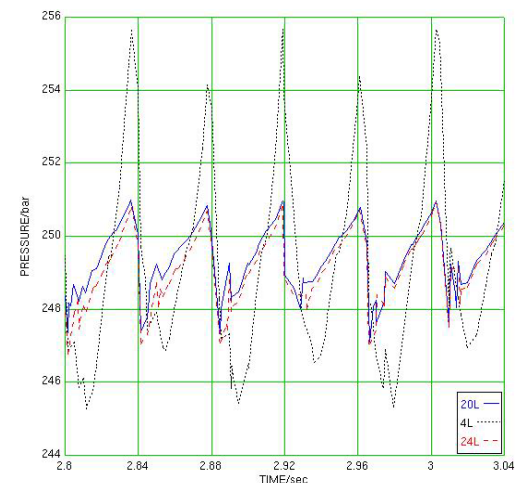
1. G. S. Duleba, C. W. Ginsburg and J. E. Harrison, Hydraulic System Modeling, Steady-State Analysis, Simulation Using a Lumped Mass Approach [A]. Proceedings of the 3rd International Symposium on Fluid Power Transmission and Control, [C] Beijing, International Academic Publishers, 1999, pp.572-577.
2. N. Fritz, A. Elsway, K. H. Modler and H. Goldhahn, Simulation of mechanical drives with Easy5, [J] Computers and Industrial Engineering, 1999, 37(1-2), pp.231-234.
3. Kajaste and Jyrki, Of the Capability of Component Models to Predict the Response of a Fluid Power System with a Long Pipeline and an Accumulator, [J] Mechanical Engineering Series, 1999, 139, pp.112-116.
4. Zhan Xingqun, Zhang Yanhua and Zhao Keding, Study on Mathematical Model of Hydraulic Accumulator in Secondary Regulated Systems, [J] China Mechanical Engineering, 2001, 12, pp.45-46.



(a) 5%



(b) 10%



(c) 15%

Figure 8 Pressure in different loads

Simulation Model of Heat Generation and Transfer in Oil –Hydraulic System

Koki TOMIOKA*, Kazuhiro TANAKA*, Katsuya NAGAYAMA*, Kimishiro TOKUDA*

* Department of Mechanical Information Science and Technology
Kyushu Institute of Technology
680-4 Kawazu, Iizuka-city, Fukuoka, 820-8502, JAPAN
(E-mail: tomioka@vortex.mse.kyutech.ac.jp)

ABSTRACT

Recently an oil-hydraulic system has been compact and high-pressurized and that causes the steep rise of the system temperature because of the small heat volume. When the system temperature has risen so much, characteristics of the working oil deteriorate and the system will be dangerous finally.

It is very important to study a simple and precise way to predict the temperature rise of the system. The lost power rises the system temperature. Bondgraph method is convenient to predict power loss because the method is based on the concept of power transmission. Consequently, the Bondgraph method is very available to predict the system temperature rise of oil-hydraulic systems.

The oil-flow dynamics with the heat generation mechanism was modeled one-dimensionally using ordinary differential equations by Bondgraph method, which is very convenient for modeling and simulation of heat generation. On the other hand, the heat transfer in the housing was analyzed three-dimensionally using the partial differential equation of heat conduction. The prediction of the temperature distributions were calculated effectively by coupling these two kinds of equation systems. In the present paper, this prediction method is applied to a real oil-hydraulic system. The simulation result was compared with the experimental results and they agreed very well.

KEY WORDS

System dynamics, Coupled Analysis, Bondgraph Method, Heat Transfer, Oil-Hydraulic system

Nomenclature

A : Cross-section Area	[m ²]	Re : Reynolds Number	[-]
A_h : Surface Area of the Housing	[m ²]	T : Temperature	[K]
c : Specific Heat	[J/kgK]	T_{amb} : Ambient Temperature	[K]
d : Diameter of the Pipe	[m]	T_o : Torque	[Nm]
dt : Time Step	[s]	T_{wall} : Temperature of the Wall	[K]
E : Internal Energy	[J]	V : Volume of the Component	[m ³]
Gr : Grashof Number	[-]	V_{th} : Thrust Volume per One Revolution	[m ³ /rev]
g : Acceleration of Gravity	[m/s ²]	W : Work of Working Oil	[W]
h : Heat Transfer Coefficient	[W/m ² K]	β : Coefficient of Thermal Expansion	[1/K]
K : Bulk Modulus	[Pa]	Γ : Thermal Diffusivity	[m ² /s]
L : Characteristic Length	[m]	δ : Kronecker Delta	[-]
l : Length of the Component	[m]	λ : Thermal Conductivity	[W/mK]
Nu : Nusselt Number	[-]	μ : Viscosity Coefficient	[kgm/s]
P : Pressure	[Pa]	ρ : Density	[kg/m ³]
Pr : Prandtl Number	[-]		
Q : Volume Flow Rate	[m ³ /s]		
\dot{q} : Work of Heat Transfer	[W]		

INTRODUCTION

Recently an oil-hydraulic system has been made which

is compact and high-pressurized. In high-load drive state as well as low-load drive state and long time drive state, the system temperature is apt to rise steeply because of the small heat volume, heat release area and large heat generation. As a result, temperature of working oil becomes higher, characteristics of working oil deteriorate and the system is finally dangerous. Therefore, it is important to predict heat generation and heat transfer in the system for secure drive. At all, it is necessary to verify result of design by experiments. As the experimental cost is high, however, it is expected to design using numerical calculation for low cost.

In order to obtain heat characteristics of the system using numerical calculation, it is necessary to consider heat generation in oil passages and valves, heat conduction through the housing and heat transfer to the air, etc. So, for the designing this system, three dimensional modeling is necessary to predict the heat generation and heat transfer. However, the shape of the system is very complex and precise three dimensional modeling needs much calculating time. Hence, this long calculation time is not useful for designing.

Studies on the heat generation and heat transfer in oil-hydraulic systems have been performed by many researchers. For example, Johansson et al.⁽¹⁾ investigated the temperature distribution in an aerospace actuation system. Yamamoto et al.⁽²⁾ studied the heat generation and temperature distribution in an oil-hydraulic system of a mobile crane. However in all of them based on one-dimensional modeling with lumped parameter systems, the prediction of the temperature distribution is not enough accurate for design a real system and components though it is important to know roughly the characteristics of the system.

In this study, the oil-flow dynamics with the heat generation mechanism was modeled one-dimensionally using ordinary differential equations by Bondgraph method, which is very convenient for modeling and simulating of heat generation because the method is based on the power transmission. On the other hand, the heat transfer in the pump housing was analyzed three dimensionally using the partial differential equation of heat conduction. The prediction of the temperature distributions were calculated effectively by coupling these two kinds of calculation systems.

In the present paper, this coupled method is performed in a simple model such as an oil-pipe. Then, this method is applied to a real oil-hydraulic system which consists of pipes and a pump etc. Comparing calculation results with experimental results, verifies this method in the system.

METHOD OF COUPLED ANALYSIS

Model of heat balance

A pipe is a basic and indispensable component in an oil-hydraulic system. Temperature of each pipe

component is simulated by heat balance among the heat generation in the component, the heat transfer from the pipe wall to the internal oil and heat transportation between the neighboring components of the pipe. The diagram of this heat balance is shown in Fig. 1. In this figure, subscript i indicates the index of a pipe component, $i-1$ indicates the index of the upstream side component and $i+1$ indicates the downstream side component.

Assuming that working oil dose not work to the outside of the pipe component i , rate of internal energy increase is expressed as follow.

$$\frac{dE_i}{dt} = (P_{i-1}Q_{i-1} + c_v\rho Q_{i-1}T_{i-1}) - (P_iQ_i + c_v\rho Q_iT_i) + \dot{q}_i \quad (1)$$

Temporal energy change in the pipe component i using its temperature is expressed as follow.

$$\frac{dE_i}{dt} = c\rho V_i \frac{dT_i}{dt} \quad (2)$$

It is assumed that working oil is incompressible fluid, following equation is derived from equation (1) and (2).

$$\frac{dT_i^n}{dt} = \frac{1}{c\rho V_i} \left\{ (P_{i-1} - P_i)^n Q^n + c\rho Q^n (T_{i-1} - T_i)^n + \dot{q}_i^n \right\} \quad (3)$$

where, subscript n indicates iteration time. In the above equation, the first term of right-hand side indicates lost power or heat generation based on pressure loss in the pipe component i , the second term indicates heat transportation from the upstream side component, and the third term \dot{q} indicates expressed by the following equation.

$$\dot{q}_i^n = hA_h(T_{wall} - T_i^n) + \lambda A \frac{T_{i-1}^n - 2T_i^n + T_{i+1}^n}{l} \quad (4)$$

where, the first term of right-hand side is heat transfer between inner wall of pipe and working oil effects and the second term is heat conduction between neighboring components of pipe.

Method of data-exchange

For the coupled calculation, the temperature data are exchanged between Bondgraph-program (Here after BG-Program) and FEM-program at the interface such as the pipe inner wall surface. This technique is illustrated in Fig. 2, in which a room partitioned by solid lines corresponds to i th component in the Bondgraph model of the pipe inside. Top side indicates the pipe housing and is divided into many elements for FEM-program. Generally the number of element in FEM-program is still more than that in BG-program. FEM-program is

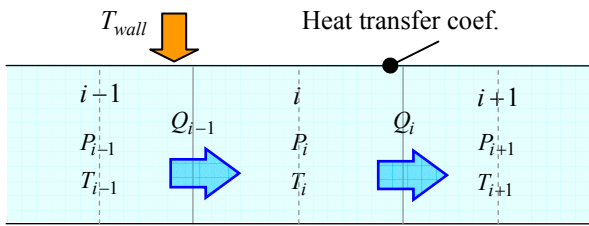


Fig. 1 Heat Balance

three dimensional and BG-program is one dimensional. In exchanging the data on the interface, the mean value of temperature distributed in the elements facing i th component in Bondgraph model is given to BG-program as the additional input temperature of the component.

And, the new temperature is calculated in i th Bondgraph component through Eq. (3) in BG-program. From the new temperature, new heat flux is calculated and given to FEM-program as the boundary condition. Because the time constant is quite different between BG-program and FEM-program, FEM-program is run once a 10^3 - 10^4 iterations of BG-program. By repeating this calculation circuit, the system dynamic characteristics inside the pipe and temperature distributions in the pipe housing are calculated simultaneously.

COUPLED ANALYSIS IN AN OIL-PIPE

Analysis model

Fig. 3 shows a pipe as a simple test model for the coupling. The pipe length is 500[mm], inside diameter of the pipe is 10[mm], outside diameter is 25[mm], and thickness of the pipe housing is 7.5[mm]. Table 3 shows parameters used in this analysis.

Table 1 Analysis conditions for coupled analysis

Initial condition	Pipe housing: $T=100[^\circ\text{C}]$ Working Fluid: $T=20[^\circ\text{C}]$, $P=0[\text{Pa}]$, $Q=0[\text{m}^3/\text{s}]$
Boundary condition	Inlet: $u=0.1[\text{m/s}]$ Outlet: $P=0[\text{Pa}]$
Time step	FEM: $dt=0.1[\text{s}]$ BG: $dt=1.0\text{E}-6[\text{s}]$
Physical property	Pipe housing: $\lambda=16[\text{W/mK}]$ $\rho=7920[\text{kg/m}^3]$, $c=499[\text{J/kgK}]$ Working fluid: $K=6.89\text{E}+8[\text{Pa}]$ $c=1591[\text{J/kgK}]$, $\rho=1070[\text{kg/m}^3]$ $\mu=0.021[\text{Pas}]$, $\lambda=0.135[\text{W/mK}]$
Heat transfer coefficient	Housing to Air: Adiabatic Housing to Oil: $h=104.5[\text{W/m}^2\text{K}]$

Bondgraph model of the oil passage

The Bondgraph model which expresses an oil passage is shown in Fig. 4. In this figure, SF element corresponds to the inlet velocity as the boundary condition, SE element to the outlet pressure similarly, C elements to the volume effect of working oil and R elements to the pressure loss which causes heat generation by the wall friction. One component of pipe inside is represented by a pair of C and R elements. In this model, the pipe inside is divided into four components. In this case, the inertial effect of the oil column is ignored.

Characteristic equations in C and R elements are represented as the Eqs. (5) and (6), respectively.

$$P = \frac{K}{V} \int Q dt \quad (5)$$

$$Q = \frac{\pi d^4}{128 \mu l} \Delta P \quad (6)$$

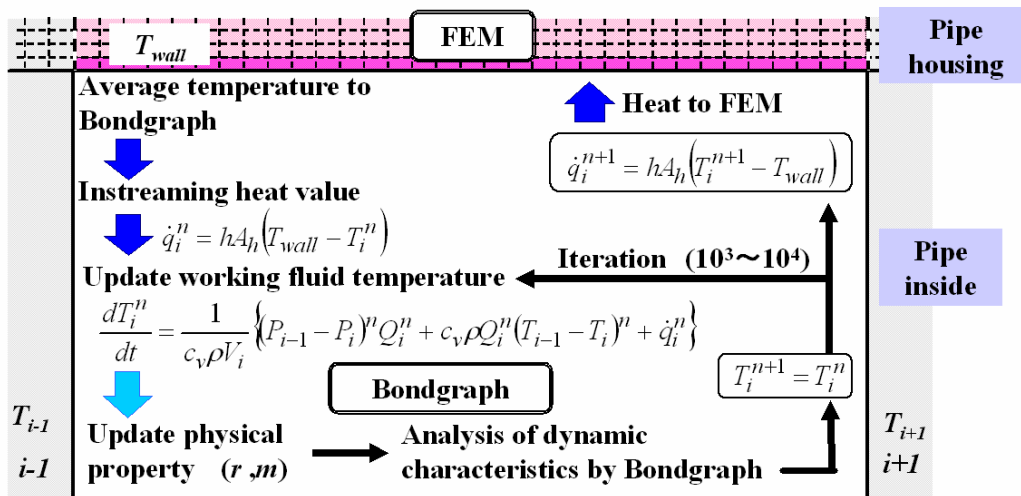


Fig.2 Interface between FEM and Bondgraph

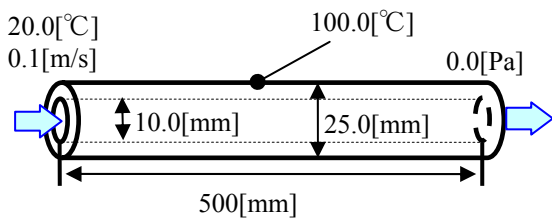


Fig. 3 Test model for coupled analysis

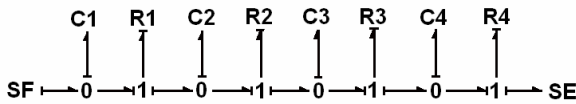


Fig. 4 Bondgraph model

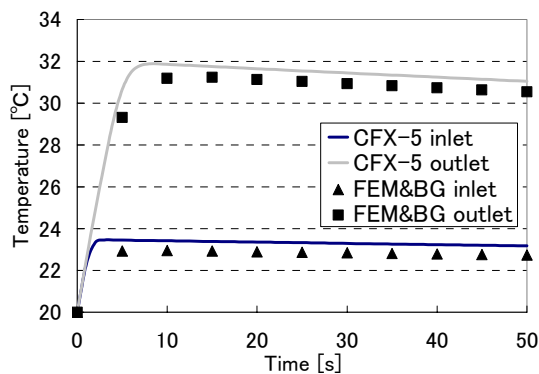


Fig. 5 Temperature change at inlet and outlet

Eq. (5) indicates the volume effect in each component and Eq. (6) the relationship between the pressure loss and the flow rate.

CFX-5

CFX-5, a commercial code for thermo-fluid flow analysis, is used in this study to verify the results through BG-method. Governing equations of CFX-5 are the Navier-Stokes equations, the energy equation, the continuity equation and the heat conduction equation. By calculating these equations, the distribution of velocity, pressure and temperature in the fluid are obtained. Heat conduction equation solves temperature distributions in the housing. Power loss of the working oil is easily obtained from the dissipation function in the continuity equation. Discretization of these equations is performed along finite volume method and tetra-mesh is used as a mesh type.

Condition

Temperature of the pipe housing is anywhere 100[°C] and that of working oil is 20[°C] as the initial condition. As the boundary condition at the inlet the velocity is 0.1[m/s] and the temperature is 20[°C]. At the outlet the pressure is 0.0[Pa]. The external wall surface of pipe

housing is adiabatic. Heat conductivity of the housing and working oil are 16[W/mK] and 0.135[W/mK], respectively. Heat transfer coefficient between the housing and the working oil is 104.5[W/m²K]. In this calculation, mesh type is tetra-mesh, the number of elements 32000, and that of nodes 7000. The result through this coupled calculation technique (hereafter FEM&BG) is compared with result of CFX-5.

3.5 Results

Fig. 5 shows the comparison between FEM&BG and CFX-5 on temperature change of working oil at the inlet and outlet. Abscissa and ordinate axis are expressed time[s] and temperature[°C], respectively. Triangle and square symbols indicate the results by FEM&BG and the solid line the results by CFX-5. Black and gray line and symbols indicate the temperature at the inlet and the outlet. Here the temperature represented by triangle and square symbols means the temperature averaged in Bondgraph components at the inlet and outlet, respectively. These results have the same tendency and the temperature difference between FEM&BG and CFX-5 is not more than 1.0[°C]. These results proved the availability of coupled analysis with FEM&BG.

THERMAL ANALYSIS OF REAL SYSTEM

Real system

Fig. 6 shows a real circuit for this study. This system consists of an axial piston pump, pipes and a cylinder. Highly-pressurized working oil flows from the pump to the cylinder through pipes ① and ③. The working oil with low pressure in the cylinder flows out from the cylinder rod chamber to the pump through pipes ④, ⑦ and ⑧.

In this analysis, the supplied pressure balances load of the cylinder so that the cylinder rod keeps the same position. In this driving state, working oil dose not flow in the high pressure side (pipes ① and ③). Consequently, working oil circulates in the leakage pipe (⑤ in Fig. 6), a valve (⑥ in Fig. 6), the low pressure side (⑦ in Fig. 6) and return line of the circuit (⑧ in Fig. 6). System dynamics of working oil is considered in ⑤, ⑥, ⑦ and ⑧, modeled using Bondgraph. The pump housing is modeled using FEM.

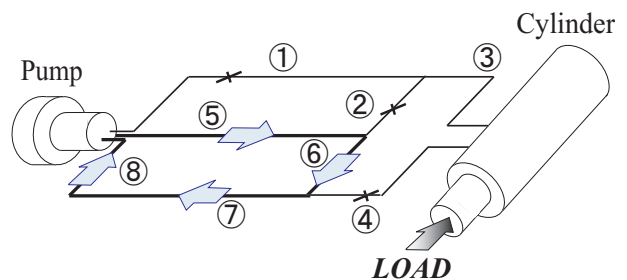


Fig. 6 Real system

Bondgraph model

Fig. 7 shows a system Bondgraph model of dynamic characteristics of the working oil in ⑤, ⑥, ⑦ and ⑧. Table 2 shows characteristic equations which are used in each element of Bondgraph. In addition, *LOAD* in the Table 2 changes temporally, and the detail of the *LOAD* is shown in Table 3.

Table 2 BG-elements and their characteristic equations

Components	Elements	Equations
Pump of high pressure side	SE1	$P = LOAD$
Pump of low pressure side	SE2	$P = P_0$
Pressure loss effect of the pump	R1	$Q = \frac{C_s V_{th}}{2\pi\mu} \Delta P$
Pressure loss of the pipe	R2, R3, R4, R5	$Q = \frac{\pi d^4}{128\mu l} \Delta P$
Volume effect of the pump	C1	$P = \frac{K}{V} \int Q dt$
Pipe volume effect of the pipe	C2, C3, C4	$P = \frac{K}{V} \int Q dt$

FEM model

The housing of the axial piston pump is modeled using FEM. The grid of its pump is shown in Fig. 8. The number of elements and nodes are 22,600 and 5,600, respectively.

Analysis condition

Torque loss in the pump

Because mechanics of the axial piston pump is very complex. The component and the inside working oil are integrated as a one heat source as the simple model. The axial piston pump generates torque loss which is caused by mechanical friction loss and fluid loss. This torque loss is expressed by following equation.

$$\Delta T_o = C_v \mu n V_{th} + \frac{C_f V_{th} \Delta P}{2\pi} \quad (7)$$

In the above equation, the first and second term of right-hand side indicates viscous friction loss and the mechanical friction loss, respectively.

Heat release from the pipe

Oil flows inside of the pipe due to leakage from the axial piston pump. So, heat transfer (Nusselt number) from the working oil to the pipe housing is expressed by following equation.

$$Nu = 0.023 Re^{0.8} * Pr^{0.333} \quad (8)$$

Eq. (8) is Colburn's formula which means heat transfer by forced convection.

Flow of air around the pipe housing is caused by natural convection. So, heat transfer (Nusselt number) through the pipe housing to the ambient air is expressed by following equation.

$$Nu = 0.53(Gr * Pr)^{0.25} \quad (9)$$

Eq. (9) is empirical formula which means heat transfer by natural convection for the circular shape. Grashof number in Eq. (9) is calculated by following equation.

$$Gr = \frac{g\beta(T_{amb} - T_{wall})L^3}{\nu^2} \quad (10)$$

Heat conduction of the pipe housing is ignored in this analysis because, its thickness is only 1.0[mm]. But, heat capacity of the pipe housing is considered in this calculation. Table 3 shows parameters used in this analysis.

Table 3 Analysis Parameters

Parameters	Amount of Parameter
Pipe length	$L: 3.0$ [m]
Time step	FEM : $1.0E-1$ [sec] Bondgraph: $1.0E-4$ [sec]
Physical property	- Pump Housing- $\rho : 2688.0$ [kg/m ³], $c: 905.0$ [J/kgK], $\lambda : 273.0$ [W/mK]
	-Pipe Housing- $\rho : 7920.0$ [kg/m ³], $c: 499.0$ [J/kgK]
	-Working Oil- $c: 1591.0$ [J/kgK], $\lambda : 0.135$ [W/mK], $K: 1.0E+6$ [Pa], $\rho : -0.7747(T-273.15)+1085.9$ [kg/m ³] $\nu : 129.03*(1.8T+672.0)^{-3.06}$ [m ² /s]
LOAD of the Pump	0[min] to 190[min]: $3.1E+7$ [Pa] 190[min] to 205[min]: $2.7E+7$ [Pa] 205[min] to 220[min]: $2.4 E+7$ [Pa] Over 220 [min]: $2.0E+7$ [Pa]
Leakage coefficient	$C_s : 1.56E-9$ [-]
Torque loss coefficient	$C_f = 0.017$ [-], $C_v = 2.3E+6$ [-]

Results

Fig. 9 shows temperature change at the axial piston pump. In this figure, black line shows numerical analysis result and gray line shows experimental result. Abscissa and ordinate axes are time [min] and temperature [K], respectively. Temperature change of the pump becomes steady state at 190 minutes, and in

this state, temperature is about 353 [K]. After 190[min], temperature of the pump is decreasing due to pressure of the pump is decreasing. Numerical and calculation results have the same tendency, and they agreed very well.

Fig. 10 shows flow late of leakage which is generated from the pump. In this figure, black line shows numerical analysis result and gray line shows experimental result, respectively. Abscissa and ordinate axes are time [min] and leakage [cc/min], respectively. In these results, leakage from the pump increases as time advances until 190[min]. After that, decreasing load of the cylinder, leakage of the pump decreases due to pressure of the pump decreases. These results are agreed very well.

CONCLUSIONS

In this study, the housing of the axial piston pump is modeled by FEM and dynamic characteristic of working oil is modeled by Bondgraph method. And a new analysis method coupling BG- and FEM-program has been proposed. In this study, calculation results agree well with the experimental results. So, the proposed coupled analysis has been verified useful.

This coupling calculation technique can save much computing time than that through a commercial code. It can effectively be applied to solve system dynamics and heat problems in many real oil-hydraulic systems.

ACKNOWLEDGEMENT

The authors would like to thank Nabtesco Corporation for providing the experimental data and helpful suggestions.

REFERENCE

1. JOHANSSON Björn et al., Thermal modeling of an Electro Hydrostatic Actuation System, Recent Advance in Aerospace Actuation System and Components, June 13-15, 2001, Toulouse, France.
2. K. YAMAMOTO, K. TANAKA, M. NAKANISHI and S. TARUMI, Analysis of Dynamic Behavior of a Hydraulic and Pneumatic Suspension Including Temperature Change Effect, Proc. of 5th Tri.Int. Symp. on Fluid Control, Measurement and Visualizatio (FLUCOME97), Vol. 1, 457/462, Sept. 1-4, 1997, Hayama, Japan.
3. K. TOMIOKA et al., Prediction of Heat Generation and Transfer in an Oil-Hydraulic Pipe, The Sixth KSME- JSME Thermal and Fluids Engineering Conference, 2005.
4. JSME Data Book : Heat Transfer 4th Edition, 1986.

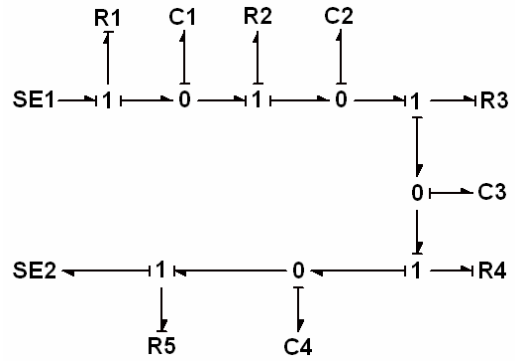


Fig. 7 System bondgraph model

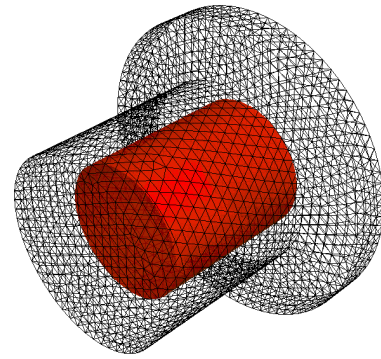


Fig. 8 Computational grid for pump housing

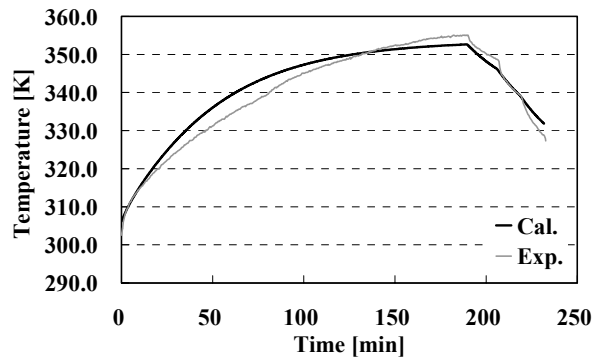


Fig. 9 Temperature change of the Pump

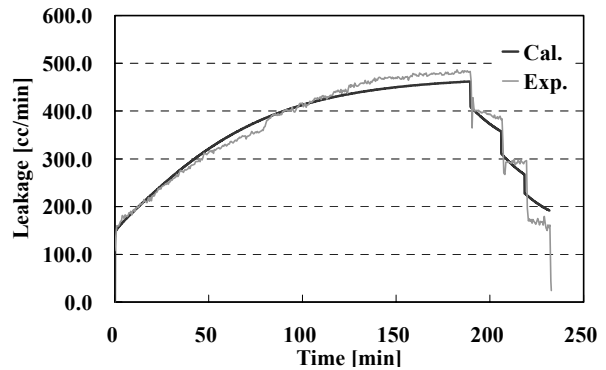


Fig. 10 Leakage from the Pump

FEEDING SYSTEM OF AEROSTATIC BEARINGS WITH POROUS MEDIA

Guido BELFORTE, Terenziano RAPARELLI, Vladimir VIKTOROV, Andrea TRIVELLA

Department of Mechanics, Politecnico di Torino, Technological University
C.so Duca degli Abruzzi, 24 - 10129 - Torino - Italy
(E-mail: raparelli@polito.it)

ABSTRACT

This study is an experimental investigation on porous media in feeding system of aerostatic bearings. The experiments were conducted using sintered bronze cylindrical inserts of different length, diameter and particle size. The work outlines two types of experiments namely: a) the measurement of mass flow rate through single porous resistance with different upstream and downstream pressures; b) the study of pressure distribution, on a pneumatic pad featuring porous resistance feeding system. The set-up used for the former included the device under test, a flow regulator and pressure transducers. For the latter the set-up included the pad under test and a stationary bearing member under the pad to evaluate pressure distribution by means of a pressure transducer.

The immediate objective of the work is to define a fluid porous resistance to be provided on the pad, equivalent to that of a 0.25 mm calibrated orifice already applied to a similar pad.

KEY WORDS

Air feeding systems, Porous media, Forchheimer law

NOMENCLATURE

D :	Nominal porous resistance diameter	l :	Length of calibrated orifice
D_p :	Average particle diameter	h :	Air gap
L :	Nominal resistance length	m :	Mass of porous resistance
G :	Mass flow rate	r :	Radial coordinate
P :	Absolute pressure under the pad	d :	Pocket depth
P_1 :	Upstream insert absolute pressure	g :	Density of bronze
P_2 :	Downstream insert absolute pressure	f :	Porosity
P_S :	Absolute supply pad pressure		
V :	Volume of porous resistance		
d :	Diameter of calibrated orifice		

INTRODUCTION

In air devices, concentrated resistances normally consist of calibrated orifices of suitable diameter and length. The

precision required creates problems which at times are difficult to solve, especially for diameters smaller than 0.1 to 0.2 mm which are also easily clogged. To minimise the problem sintered resistance inserts of suitable shape may be used.

The performance of porous resistances has been the subject of intensive study. Porous resistances may be regarded as an array of multiple tortuous ports resembling many tiny parallel-connected resistances. In terms of laminar flow they may be described as adhering to the Darcy law, and for the higher Reynolds numbers a modified Forchheimer law would apply [1] - [7].

Although basic studies are long established, research has recently aroused widespread interest in this area, as shown for instance by the rich bibliography on applications such as feeding systems for air bearings. Results obtained indicate that careful resistance design may bring benefits in terms of load, stiffness and damping of air bearings [8] - [15]. Material porosity may be achieved in various ways, from conventional metal powder sintering to the more recent laser drilling after surface densification by mechanical rolling and use of porous plastics. In all cases the parameter which is critical for porous resistance bearings is the permeability of the material, which in turn is highly dependent on the type of process selected for achieving porosity.

This work investigates sintered bronze porous resistances having conductance similar to that of a 0.25 mm dia., 0.5 mm deep calibrated orifice. A number of specimens of different particle size and dimensions were flow tested. Subsequently, we studied the behaviour of an air pad in which the calibrated orifice is replaced with interchangeable porous resistances. Results obtained in terms of pressure distribution and air consumption are useful for evaluating output coefficients [17 - 18].

POROUS DEVICES TESTED

As resistance material we selected three types of commercial bronze powders of different grain size. Powder consists of 89% copper, 11% tin and is globular in shape. Average diameter D_p for each grain size was obtained from a statistical sample 200 granules. Diameters for the three types are 114 μm , 66 μm and 52 μm respectively. Figures 1, 2 and 3 show magnified views of the three powders. Powders were sintered in cylindrical dies at 780°C for 130 minutes. Test specimen size is nominal dia. $D = 3$ mm by nominal length $L = 3$ mm or $L = 5$ mm. Many specimens were produced in order to verify repeatability of experimental results for each type of resistance. Shrinkage of sintered material caused dimensional changes relative to nominal size. Table 1 shows the various types of resistances tested and actual average sizes.

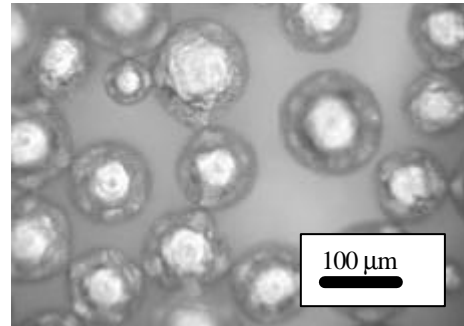


Figure 1: Powder particle size $D_p = 114 \mu\text{m}$

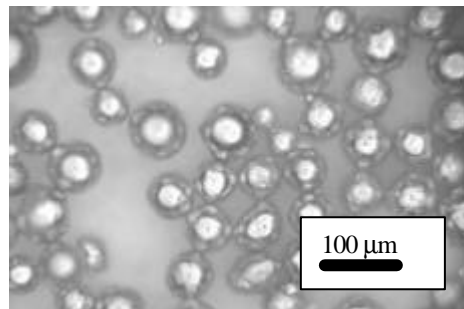


Figure 2: Powder particle size $D_p = 66 \mu\text{m}$

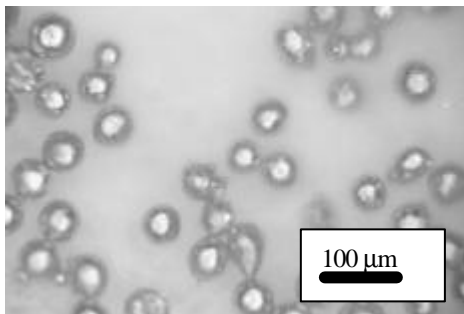


Figure 3: Powder particle size $D_p = 52 \mu\text{m}$

Figure 4 illustrates a macroscopy of porous resistances “c” and “d”; figures 5, 6 and 7 show magnified base surfaces of resistances obtained with the three different grain sizes. Note how particle size is smaller than that of untreated powder due to linking effect of sintering.

Table 1: Dimensions and particle size of porous resistances

Resistance Ref.	D [mm]	D_{eff} [mm]	L [mm]	L_{eff} [mm]	D_p [μm]
a	3	2.93	3	2.81	114
b	3	2.99	5	4.69	114
c	3	2.94	3	2.77	66
d	3	2.95	5	4.60	66
e	3	2.86	3	2.74	52
f	3	2.91	5	4.57	52



Figure 4: Photo of resistances “c” and “d”

Actual porosity is the ratio of fluid flow active volume to resistance total volume. Total porosity is the ratio of volume of all voids of the resistance to total volume. Actual or effective porosity is more significant than the latter, as some voids may well be impossible to be penetrated by the fluid. However, total porosity provides a quick indication of material porosity through assessment of dimensions and sintered mass in relation to density of material. Actual porosity is lower than total porosity as per suitable correction factors. Total porosity Φ is:

$$\Phi = 1 - \frac{m}{g \cdot V}$$

where $g = 8.74 \cdot 10^3 \text{ kg/m}^3$ is the density of bronze 89-11, m is the mass of porous resistance and V is the total volume. Tests conducted for each grain size on several specimens of different lengths have yielded the average values given in Table 2:

Table 2: Average values of porosity

Resistance Ref.	D_p [mm]	Φ
a, b	114	0.351
c, d	66	0.334
e, f	52	0.294

MONITORING OUTPUT CHARACTERISTICS

Two types of tests were conducted using specific set-ups.

a) Porous resistance flow test

Figure 8 shows the set-up produced for this test. Each porous resistance (1) was adhesive bonded to a metal sleeve (2) to seal possible leakage between specimen side face and sleeve. Owing to the difficulty of achieving good repeatability of resistance-to-sleeve bond,

resistance effectiveness may vary, often considerably, among different specimens of the same type.

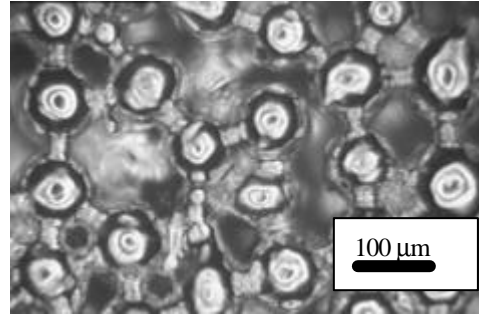


Figure 5: Magnified sintered powder particle size $D_p = 114 \mu\text{m}$

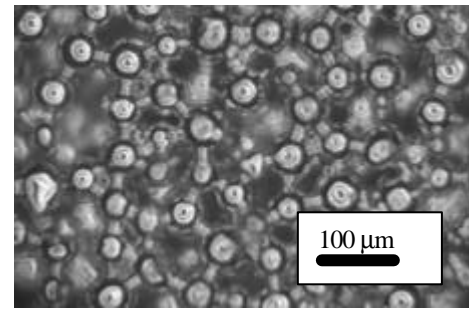


Figure 6: Magnified sintered powder particle size $D_p = 66 \mu\text{m}$

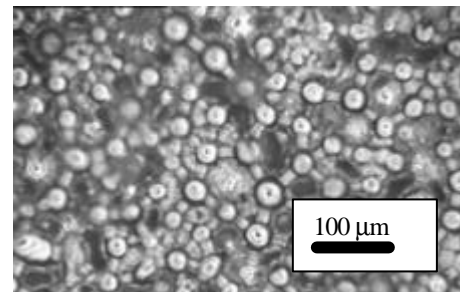


Figure 7: Magnified sintered powder particle size $D_p = 52 \mu\text{m}$

To overcome the problem, bonding tests were carried out using different specimens of the same type until satisfactory flow reading repeatability was obtained. Subsequently, six porous resistances as shown in Table 1 were fitted to six sleeves. All sleeves are of equal geometry and size so as to be interchangeable in the flow test device. Each sleeve is installed between flanges (3) and (4) connecting air inlet and outlet tubing. Flanges incorporate test ports for pressure P_1 and pressure P_2 upstream and downstream of resistance under test. Resistance inlet incorporates high-efficiency air filters (5) and pressure regulator (6), resistance outlet

is provided with variable resistance (7) and flowmeter (8). Figure 9 shows a resistance in position inside sleeve.

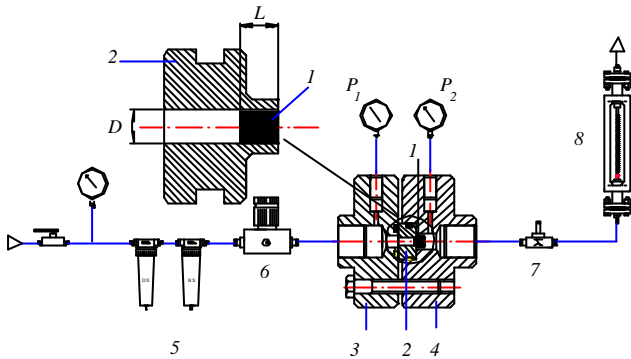


Figure 8: Test set-up for single porous resistance

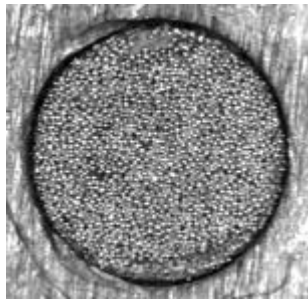


Figure 9: Illustration of resistance "a" bonded to sleeve

Figures 10, 11 and 12 show results of all resistances tested. Unbroken lines represent $L = 3$ mm, broken lines represent $L = 5$ mm.

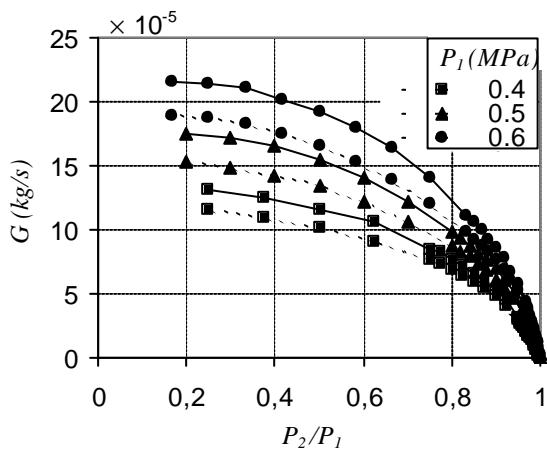


Figure 10 : Flow rates of inserts "a" (unbroken lines), and for inserts "b" (broken lines)

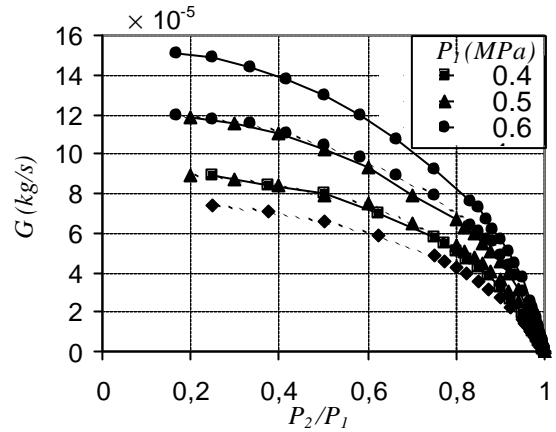


Figure 11 : Flow rates of inserts "c" (unbroken lines), and for inserts "d" (broken lines)

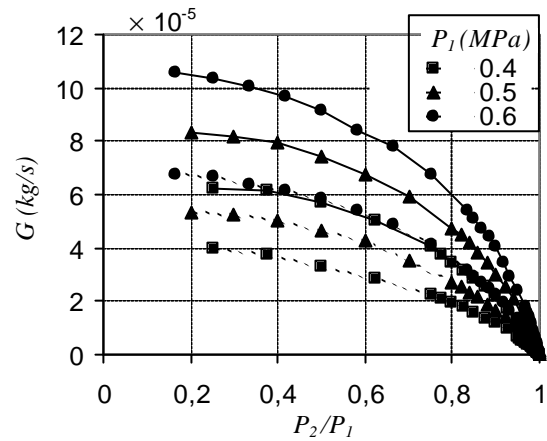


Figure 12 : Flow rates of inserts "e" (unbroken lines), and for inserts "f" (broken lines)

For the sake of comparison, Figure 13 shows flow characteristic of $d = 0.25$ mm dia., $l = 0.5$ mm deep calibrated orifice.

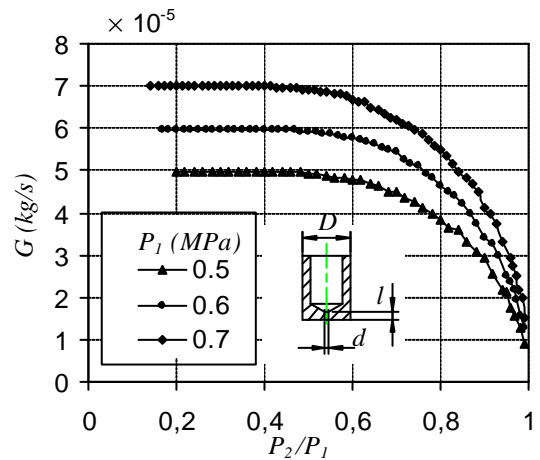


Figure 13: Flow rate readings for $d = 0.25$ mm, $l = 0.5$ mm calibrated orifice.

It can be seen that the resistance “*f*” shows a behavior similar to that of the calibrated orifice. Note that for porous resistances and for P_2/P_1 readings approaching one, curves are more linear than that of calibrated orifice. For lower P_2/P_1 readings curves tend to become parabolic. This behaviour may be explained by the Darcy - Forchheimer relation [1-7] which considers both the effects of laminar flow for small pressure differentials upstream to downstream of porous resistance, and the effects of turbulent flow for greater pressure drops.

b) Opposed pad test

A thrust air pad incorporating porous resistances was tested to evaluate pressure distribution. The pad, shown in Figure 14, is cylindrical in shape and permits the installation of sleeves described above. Thus, individually tested specimens could be installed in the pad, thereby obtaining a direct comparison of flow rate readings with and without opposed pad in order to avoid repeatability problems due to adhesive bonding conditions.

A test set-up [17] was constructed for evaluating static load capacity, pressure distribution and air consumption of flat aerostatic pads with supply systems of this type as a function of air gap. Figure 15 shows the layout of pad set-up. The set-up frame consists of a base (1), three columns (2) and a crossmember (3). The air gap is provided between pad under test (4) and stationary bearing member (5). Pad (4) can move vertically by means of screw (6) and handwheel (7). Depth of air gap is monitored by three micrometer transducers (8) resting on plate (9) connected to the pad. Thrust on the pad is monitored by load cell (10).

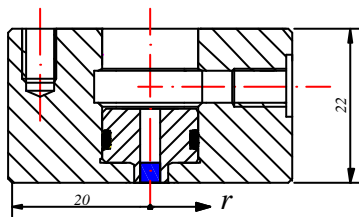


Figure 14: Pad under test

Figure 16 shows detail of central area of pad (4) and stationary bearing member (5), parallel faces thereof being spaced at a distance *h*. Porous resistance (1) and sleeve (2) are clearly visible. Sleeve profiles are offset internally relative to pad by the amount *s*. Each porous resistance examined is internal to sleeve profile at a depth *d* which varies case by case. Moreover, owing to the nature of the sintered material, outer profile of resistance is not consistent; in fact it varies significantly in radial direction *r*, and in circumferential direction θ .

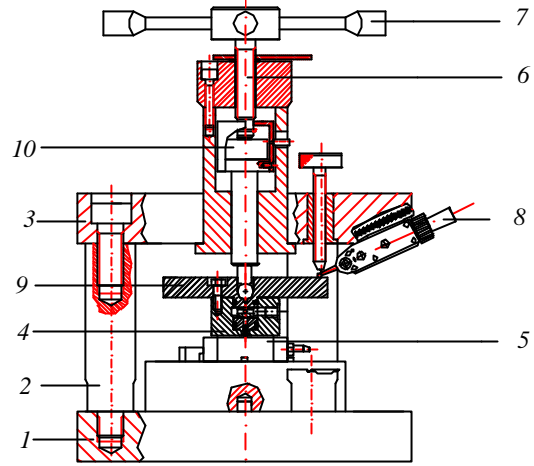


Figure 15: Pad test set-up

Table 3 shows actual average specimen depth d_n , max. depth change $\Delta\delta$ and the value of *s* for the six test specimens.

Tests were conducted on all resistances at pad feed pressure $P_S = 0.4, 0.5$ and 0.6 MPa, for gap size $h = 9$ and 14 mm. As an example, Figure 17 shows the pattern of radial distribution of pad pressure for resistance “*f*” at feed pressure $P_S = 0.6$ MPa.

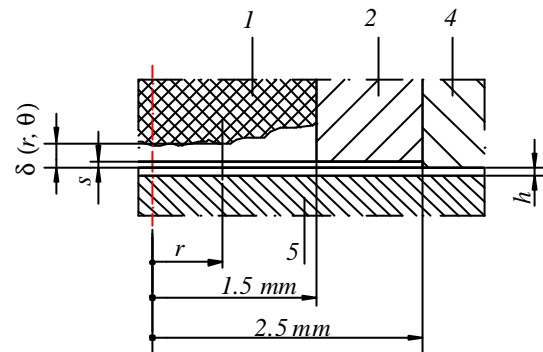


Figure 16: Center area of pad and stationary bearing member

Table 3: Average depth of resistance profile from edge of pad d_n , max. change thereof $\Delta\delta$, and *s*

Resistance Ref.	d_n [mm]	$\Delta\delta$ [mm]	<i>s</i> [mm]
<i>a</i>	170	25	34
<i>b</i>	118	18	10
<i>c</i>	140	20	23
<i>d</i>	501	15	22
<i>e</i>	340	22	15
<i>f</i>	205	26	22

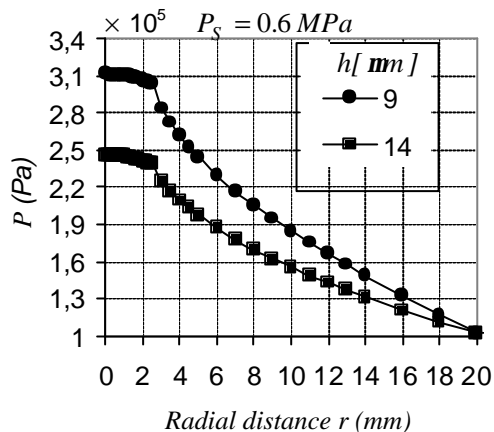


Figure 17. Example of radial absolute pressure distribution across pad with resistance “*f*”

CONCLUSIONS

Experimental investigation of porous inserts has yielded solutions for replacing fluid resistances with concentrated orifices.

Test methods and equipment have been developed for evaluating fluidic behaviour of porous resistances.

These porous resistances can also be utilized in pneumatic valves.

Characterization testing of porous resistances according to the Darcy-Forchheimer laws is currently in progress. The results of this work will be the subject of a future paper.

REFERENCES

1. A.E. Scheidegger. The physics of flow through porous media, University of Toronto press. 1963.
2. De Wiest. Flow through porous media. Academic Press, New York, 1969.
3. F.A.L. Dullien. Porous Media, fluid transport and pore structure. Academic Press, 1979.
4. G. S. Beavers, E.M. Sparrow. Non-Darcy Flow through fibrous porous media. Journal of Applied Mechanics, Trans. ASME, December 1969, Vol. 36, pp. 711-714.
5. G. S. Beavers, E.M. Sparrow, D.E. Rodenz. Influence of bed size on the flow characteristics and porosity of randomly packed beds of spheres, Journal of Applied Mechanics, Trans. ASME, September 1973, pp.655-660.
6. Antonio Lorenzi. Laminar, turbulent and transition flow in porous media. Meccanica, Journal of the Italian Association of the Theoretical and Applied Mechanics, Vol. 10, N°2, June 1975, pp.75-77.
7. J.S. Andrade, U.M.S. Costa, M.P. Almeida, H.A. Makse, H.E. Stanley. Inertial effects on fluid flow through disordered porous media. Physical Review letters, Vol.82, N° 26, June 1999, pp 5249-5252.
8. P.R.K. Murti. Analysis of externally pressurized gas porous bearings. Transactions of ASME, July 1974, pp.354-360
9. Y.B.P. Kwan, J. Corbett. Porous aerostatic bearings - an updated review. Wear, 1998, N°222, pp.69-73.
10. T.S. Loung, W. Potze, J.B. Post, R.A.J. van Ostayen, A.van Beek. Numerical and experimental analysis of aerostatic thrust bearings with porous restrictor. Tribology International, Vol. 37, 2004, pp.825-832.
11. A.H. Slocum. Precision Machine Design. Prentice-Hall, 1st edn., 1992.
12. Y. Tian, Modélisation statique et dynamique des paliers par la méthode des éléments finis et comparaison expérimentale. Thesis, 1991, UTC, Compiègne (French).
13. M. Fourka, M.Bonis. Comparison between externally pressurized thrust bearings with different orifice and porous feeding systems. Wear, 1997, N°210, pp.311-317.
14. H. Rabia. Modélisation des paliers aérostatiques a paroi poreuse par la méthode des éléments finis. Thesis, 1995, UTC, Compiègne (French).
15. J. Hopfner. Fertigung von aerostatischen lagern aus poroser sinterbronze mit oberflächenverdichteter drosselschicht. Thesis, 1990, UTM, Munchen.
16. Malik M, Rodkiewicz Cz M. On the flow considerations in gas-lubricated porous bearings. Transactions of the ASME, 1984, N°106, pp. 484-491.
17. G. Belforte, T. Raparelli, V.Viktorov, A. Trivella. Effects of supply hole dimensions and operating conditions on the hole discharge coefficient of an aerostatic bearing. 3rd AIMETA International Tribology Conference, September 18-20, 2002, Vietri sul Mare, Salerno, Italy, cd rom ISBN 88-900908-0-4.
18. G. Belforte, T. Raparelli, V.Viktorov, A. Trivella. Discharge coefficients of simple orifices with feed pocket for aerostatic bearings. 4th AIMETA International Tribology Conference, September 14 - 17, 2004, Rome, Italy, pp.467-474, cd rom ISBN 88-7999-831-5.

ACKNOWLEDGEMENTS

The authors would like to thank Marco Occhetto, Sandro Quaranta, Mihaela Tabacaru and Marius Botea for their help in conducting experimental tests.

Development of a New Pneumatic Silencer to reduce unpleasantness of a sound

Hisami MURAMATSU* , Hirokazu ONO ** , Masaaki ADACHI ***

* Department of Mechanical Engineering, Numazu College of Technology
3600 Ooka, Numazu, Shizuoka, 410-8501 Japan
(E-mail : muramatu@numazu-ct.ac.jp)

** Department of Mechanical Engineering, Faculty of Engineering, Mie University, Student
1577 Kurimamachiya, Tsu, Mie Japan

*** Mechanical and Electrical Engineering Course, Advanced Engineering Course,
Numazu College of Technology, Student
3600 Ooka, Numazu, Shizuoka, 410-8501 Japan

ABSTRACT

A high performance pneumatic silencer to reduce unpleasantness of the noise is newly developed in this paper. It is shown that a sound effect of fade-in found by consideration of results from ergonomics is obtained by the silencer. The silencer consists of three kinds of silencers and a device. The device uses artificial muscle utilized a shape memory alloy. It is cleared that sound power level of the silencer is very low.

KEY WORDS

Pneumatics, Noise reduction, Sound power level, Artificial muscle, Shape memory alloy

Introduction

Noise radiated from pneumatic system causes discomfort to us. Especially when the pneumatic system is applied to medical and welfare apparatus, a new consideration about the noise reduction is necessary. Granted that A-weighted sound pressure level is low, a comfortable sound environment is not provided for people in a room. It has been reported that a sound effect of fade-in reduces annoyance by simulations [1][2]. The fade-in is an acoustic characteristic that the A-weighted sound pressure level gradually increases.

In this paper, a high performance pneumatic silencer having an effect of the fade-in is developed. Artificial muscle is used as an actuator in the fade-in device. The number of artificial muscle and conditions of electrical power supply to it are investigated. The acoustic characteristics of the silencer are examined.

Nomenclature

L_A : A-weighted sound pressure level [dB(A)]

L_{wA} : A-weighted sound power level [dB(A)]

$B.G.N.$: Back grand noise [dB(A)]
 t_0 : Time at which a spool starts to move [s]
 t_f : Time at which the spool stops [s]
 Q : Volume flow rate through a restriction [L/min]

Experimental apparatus

Figure 1 shows a high performance pneumatic silencer and noise measuring system. The noise occurs aerodynamically when compressed air flows through a restriction in a pipe. A pneumatic silencer installed downstream from the restriction reduces the noise. Diameter of the restriction is 2.0mm. The silencer combines a silencer T1, a silencer T2, a speed controller, and a fade-in device. The silencer T1 is composed of a silencer HPS[2] and a silencer NS. The silencer T2 is used a silencer SHPS[2] instead of silencer HPS. The silencer HPS and SHPS consist of three different types of silencers; blow-off type, resonator type, interference type, and expansion chamber. Silencers NS having sound absorbing material are connected to them in series, respectively. Effective areas of them are 58.4mm^2 (NS), 30.3mm^2 (HPS), 37.2mm^2 (SHPS). The fade-in device is set on a position e in Fig.1 and a speed controller on a point f.

A condenser microphone is put at the position of 1m away from the high performance pneumatic silencer and at 45 degrees to the center line of the silencer[3]. A-weighted sound pressure level L_A is measured. The level of back grand noise $B.G.N.$ in the anechoic room, which is defined as A-weighted sound pressure level measured when air isn't supplied to the silencer, is 27dB(A).

The high performance pneumatic silencer is surrounded by a measurement surface as shown in Figure 1. A-weighted sound power level L_{wA} based on the sound intensity through it is calculated. A sound intensity probe sweeps on the measurement surface with a constant speed. The sound intensity probe containing a matched microphone pair is constructed on a face-to-face design.

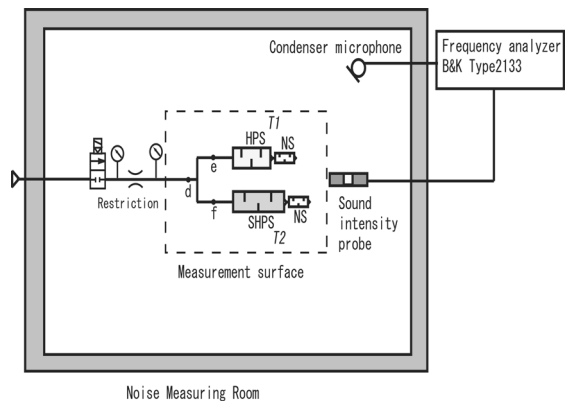


Figure 1 Noise measuring system

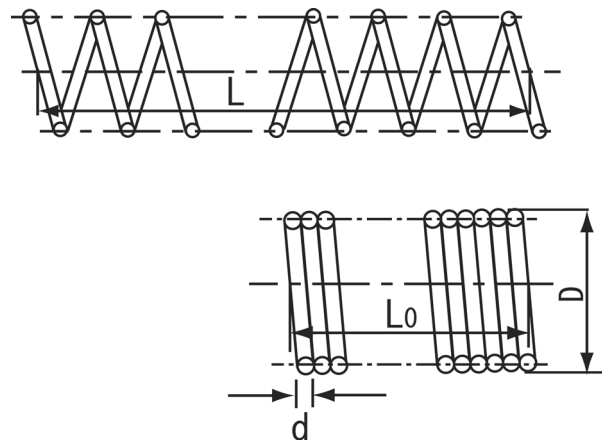
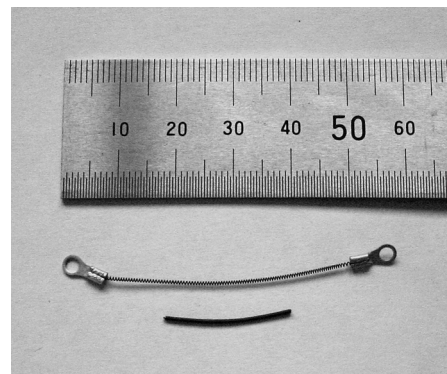


Figure 2 Artificial muscle

Table 1 Dimensions of artificial muscle

	Original dimensions	Stretched dimensions
Diameter of coil D mm	0.85	0.75
Diameter of wire d mm	0.20	0.20
Stretched Length L mm	-	42
Original Length L_0 mm	20	-
Number of turns n	85	85

Design of a high performance pneumatic silencer

Artificial muscle utilized a NiTi shape memory alloy is used as an actuator in the fade-in device for control of spool movement. Table 1 shows dimensions of the artificial muscle got into a spiral shape. The artificial muscle is stretched from the original length as shown in Figure 2. Heat is produced by running direct current through the artificial muscle and it shrinks to. The artificial muscle returns again to the stretched length if it is cooled.

Figure 3 represents the experimental setup to determine the number of the artificial muscle and helical extension spring. The springs and the artificial muscles are attached to a spool in a tube. The spool is returned to the initial position by the springs after breaking in a circuit. Spring constants of the spring A and spring B are 88.8N/m and 97.6N/m, respectively.

Figure 4 shows on/off pattern and displacement of the spool. Table 2 shows time t_0 at which the spool starts to move and time t_1 at which the spool stops under four tests using the spring A. According to increase of the number of the spring, time $t_1 - t_0$ is getting long. Times, however, are short for the fade-in[1]. Table 3 shows time $t_1 - t_0$ under two tests using the spring B. By using the spring B in return for the spring A, stick-slip is

occurred in Test 5. The stick-slip is avoided by increasing the number of the artificial muscles in Test 6 though time t_0 is 2.2sec.

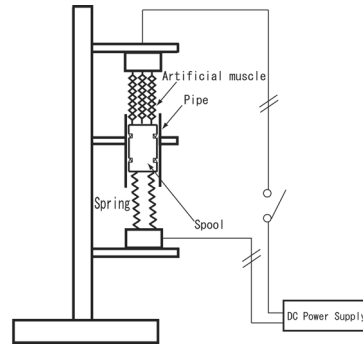


Figure 3 Artificial muscles attached to a spool

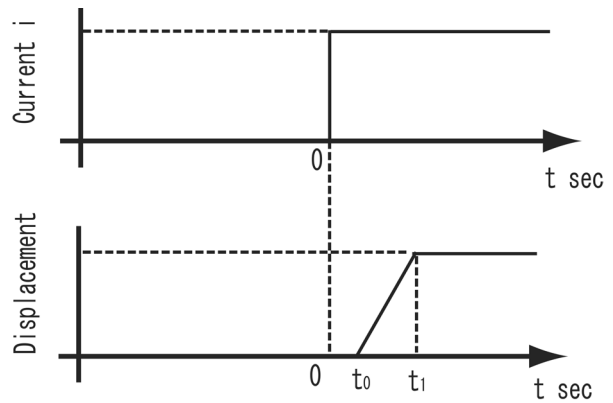


Figure 4 Displacement of the spool

Table 2 Conditions of tests and time for displacement

	Experimental condition		Operating condition	→	Results		
	Number of A.M.	Number of spring A	Total electric power W		t_0 sec	t_1 sec	$t_1 - t_0$ sec
Test1	6	1	7.2	→	1.0	2.5	1.5
Test2	6	2	7.2	→	1.0	3.2	2.2
Test3	6	3	7.2	→	1.0	3.4	2.4
Test4	6	4	7.2	→	1.0	3.8	2.8

Table 3 Conditions of tests and time for displacement

	Experimental condition		Operating condition	→	Results		
	Number of A.M.	Number of spring B	Total electric power W		t_0 sec	t_1 sec	$t_1 - t_0$ sec
Test5	6	4	7.2	→	1.9	6.7	4.8
Test6	12	4	10.0	→	2.2	6.6	4.4

Figure 5 shows an improved on/off pattern. The spool remains stationary in preliminary run because total electric power is small. The time t_0 is improved to 1.1sec, as shown in Table4. It is expected that temperature of the artificial muscle will rise and time for deformation of the coils will be shorten.

Figure 6 illustrated a fade-in device installed in the high performance pneumatic silencer. When the current is supplied to the artificial muscles using the conditions of Test 8, they pull the spool and small holes are covered.

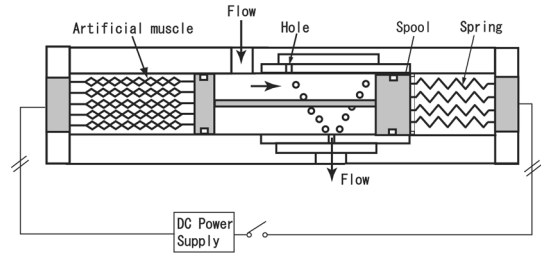


Figure 6 Fade-in device

Acoustic characteristics

Figure 7 shows A-weighted sound power level calculated by sound intensity against flow rate Q through the point d in Figure 1. Two conditions in Figure7 indicate that the holes in Figure 6 are either closed or opened fully. A-weighted sound power levels L_{wA} of the high performance pneumatic silencer kept in fully opened and closed conditions are very small, compared with that of the silencer NS.

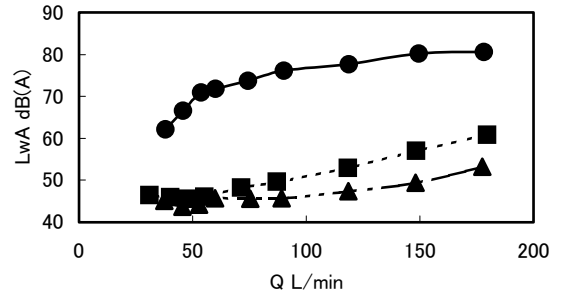


Figure 7 A-weighted sound power levels against flow rate

- NS, ▲ Silencer in fully opened condition,
- Silencer in fully closed condition

Figure 8 shows variation of A-weighted sound pressure level L_A . The flow rate Q supplied to the silencer is 150 L/min. A-weighted sound pressure level L_A is gradually increased except for steeply rise from the level of back ground noise $B.G.N.$ soon after valve at

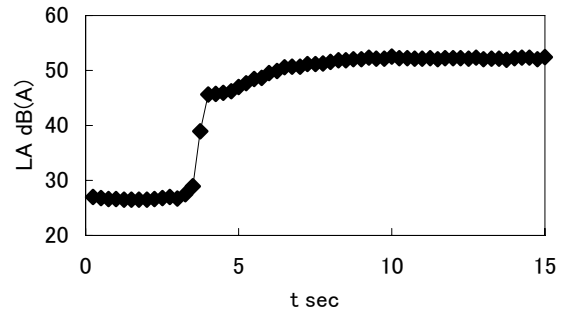


Figure 8 Variation of A-weighted sound pressure level

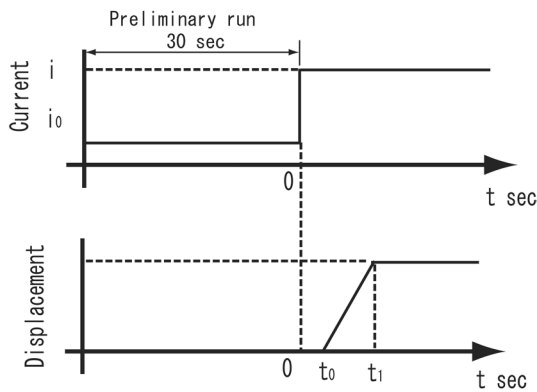


Figure 5 On/off pattern and displacement of the spool

Table 4 Conditions of tests and time for displacement

	Experimental condition		Condition of preliminary run	Operating condition	Results
	Number of A.M.	Number of spring B	Total electric power W	Total electric power W	
Test7	12	4	0.6	10.0	→ 1.9
Test8	12	4	1.5	10.0	→ 1.1

the upstream position is opened. A-weighted sound pressure level L_A reaches an asymptotic value 53dB(A) and increase of L_A is 7dB(A).

Conclusion

A high performance pneumatic silencer was developed. It was found that the sound effect of the fade-in was made. The number of artificial muscle and conditions of electrical power supply to it were determined. It was cleared that the noise was reduced remarkably.

Acknowledgements

This work is supported in Japan by Grant-in-Aid for Scientific Research (C). The authors would like to thank Mr. M. Katahira, a student at the Toyohashi University of Technology and Mr. K. Shoubu, a student at the Yokohama National University, for their corporation on making silencer HPS and silencer SHPS.

References

1. H. Muramatsu, Pneumatic Noise Reduction Based on Ergonomics, Spring symposium on fluid power JFPS, 1993, pp.107-109. (in Japanese)
2. H. Muramatsu, M. Katahira, K. Shoubu, Reduction of Noise Radiated from Pneumatic Silencer, Spring symposium on fluid power JFPS, 1994, pp.64-67. (in Japanese)
3. Japanese Industrial Standard B 8379 Pneumatic circuit-Silencers 1995.

Development of a servo system having opto-fluid converter

Makoto NOMOTO*, Osamu OYAMA*, Toshihiro YOSHIMITSU** and Kenjiro YAMAMOTO**

* Mechanical Engineering Major, Science and Engineering Research Course
Graduate School of Meiji University
1-1-1 Higashimita, Tama-ku, Kawasaki-shi, Kanagawa, 214-8571 Japan
(E-mail: ce55251@isc.meiji.ac.jp)
** Welfare system Engineering
Kanagawa institute of Technology
1030, Shimoogino, Atsugi-shi, Kanagawa, 243-0292 Japan

ABSTRACT

We developed the control system having opto-fluid converter.

This system is composed by opto-fluid converter, 4 stage cascades of Laminar Proportional Amplifier (LPA) which amplify the pressure difference from optical-fluid converter, and the pneumatic servo valve which sends the actual working air pressure to an actuator of a robot arm. By isolating an electric signal processing part and an optical signal processing part using the optical fiber, the control system which is not influenced by an electromagnetic noise can be realized. The optical signal is changed into the fluid pressure signal, without an intermediary electric signal, and can control the robot arm. The system can work under the severe environment where the radioactivity or an electromagnetic noise influences it, and an activity can be expected at medical spots, a nuclear reactor, etc. In this report, we have analyzed the characteristics of the opto-fluid converter in order to design the high-speed response and optimize the converter.

KEY WORDS

Laminar Proportional Amplifier, opto-fluidic converter, pneumatic servo valve.

NOMENCLATURE

Input A : Input pressure A
Input B : Input pressure B
A port : Output pressure port A
B port : Output pressure port B
P : Supply pressure port

INTRODUCTION

The control system using optical signal is realizable with opto-fluid converter which changes the optical signal into the fluid pressure signal without the electric signal.

The opto-fluid conversion system which converts the optical analog signal into the fluid pressure signal comes from a Laminar Proportional Amplifier (LPA).

The rotary encoder attaching a pneumatic rotary

actuator which does not use an electric signal was developed. This system makes them. The environment where is influenced by the electromagnetic noise, radioactivity, and thunderbolt, and the action of this system can be secured from them. This is the best feature of the system. Furthermore, the characteristic of the converter is analyzed in order to optimize and design the high-speed response of a system. In addition in this research used an air pressure servo valve as an input control pressure. This is the analog servo valve functioning alike the opto-fluid conversion system.

CONSTITUTION OF THE SYSTEM

Scheme of system

Experimental set up of this system is shown in Fig.1. The analog signal sent by computer is inputted into a laser diode controller, the optical intensity of a laser diode is decided, and it becomes an optical control signal. The optical signal is inputted into opto-fluid converter, and it is changed into a pneumatic pressure signal. The output pressure is amplified with a 4 stage cascades of LPA, and the boosted signal is inputted into the pneumatic servo valve. The spool inside the pneumatic servo valve is driven by the pressure signal, and the output flow rate and pressure of the pneumatic servo valve are determined by the spool position. The output from the pneumatic servo valve is inputted into the rotary actuator attached to the shoulder portion of the robot arm, and the robot arm drive. The optical rotary encoder detects the drive angle, and feedback control carries out the angle of the arm.

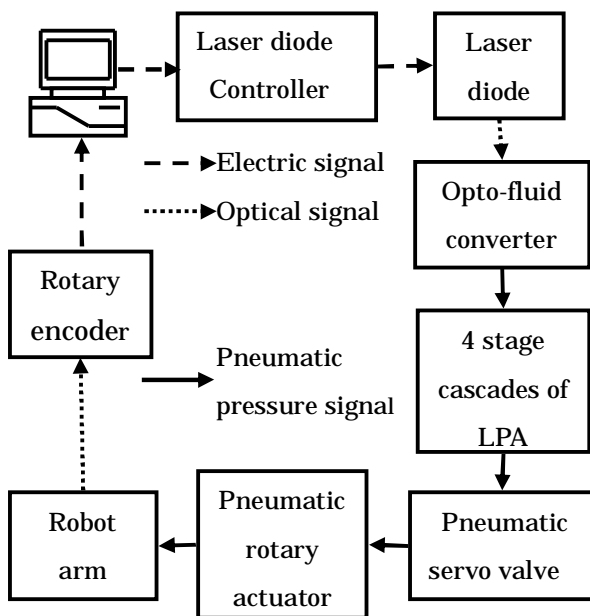


Fig.1 System components and configuration

Opto-fluid converter

This research proposes the way of changing a optical signal into a fluid signal without a mechanical device. The optical fiber which coated the optical absorber at the edge is set in the supply nozzle side of LPA. The optical energy is changed into the heat energy by irradiating the optical signal there, the temperature distribution of the main jet boundary layer changes, and the jet deflects. A schematic view of opto-fluid conversion element is shown in Fig.2. Since the output of this conversion element is weak, two stages of LPA amplify follow the output of converter. The aspect ratio of nozzle of conversion element stage and the first stage of LPA is 1.3 and the one of second stage is 0.66. The schematic view is shown in Fig.3.

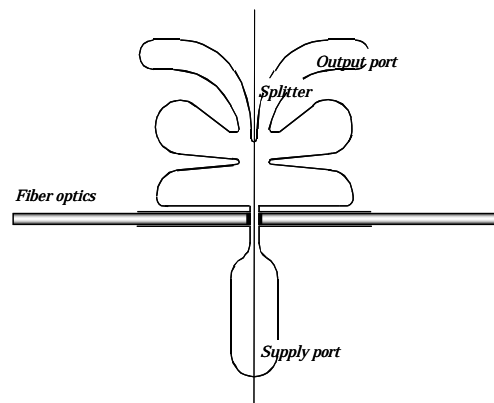


Fig.2 Opto-fluid conversion element

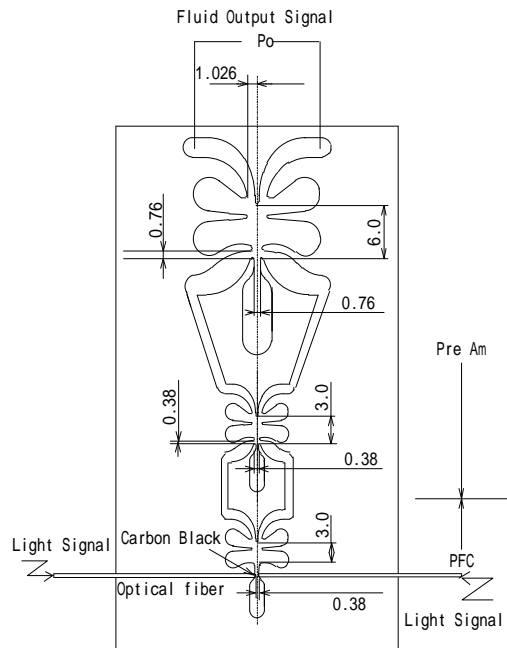


Fig.3 Opto-fluid converter

4 stage cascades of LPA

The output from opto-fluid converter does not have enough power to drive the spool of the pneumatic servo valve. Therefore, the output pressure is amplified with more 4 stage cascades of LPA. The 4 stage cascades of LPA are serial connection of the same shape LPA, and the first and the second stage are the parallel stacked LPA having the thickness is 1.574 [mm], the third is 2.361 [mm], and the fourth is 3.935 [mm], in each stage. The outputs of these LPAs are laminar flow and both pressure and flow rate are boosted by the cascades.

Air pressure drive type Pneumatic servo valve

A usual servo valve is driven by the input of an electrical signal. On the other hand, the proposed pneumatic servo valve is driven by pilot air pressure, the spool in the pneumatic servo valve moves to right or left according to the input-pressure difference on either input side, the cross-sectional area of flow of the output port is adjusted by the displacement of the spool. The schematic view is shown in Fig.4

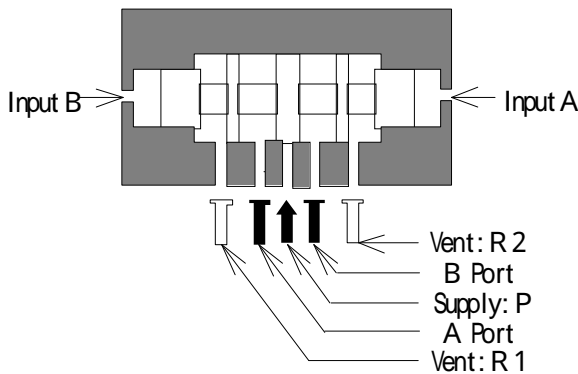


Fig.4 Air pressure drive type Pneumatic servo valve

Robot arm

The robot has one link arm driven with the air pressure rotary actuator. The rotary actuator is commercial product of the size of the diameter 50 [mm] and length 60 [mm]. The arm is made from aluminum and length and weight are 260 [mm] and 600 [g] respectively. The rotary encoder is embedded into the shoulder portion in order to detect the angle.

Optical rotary encoder

The constitution of the rotary encoder is shown in Fig.5. We thought, this rotary encoder must have the stout characteristic against the influence by the electromagnetic noise, we want. So, the electric circuit of the electrical-signal processing part is split up the slit plate of the optical-signal processing part.

The light of LED is let by the optical fiber to the slit plate, and the optical pulse signal caused by rotation of slit is transmitted to a Photo-Transistor (called as PT) by the optical fiber. At this time, the PT produces an electric signal in the area apart from the robot arm, where is secured from noises. The signal flow is shown in Fig.6. The LED and the PT are put on the place distant from the robot arm using the optical fiber as previous shown. The arm can be driving only optically and pneumatically control part without any electric part.

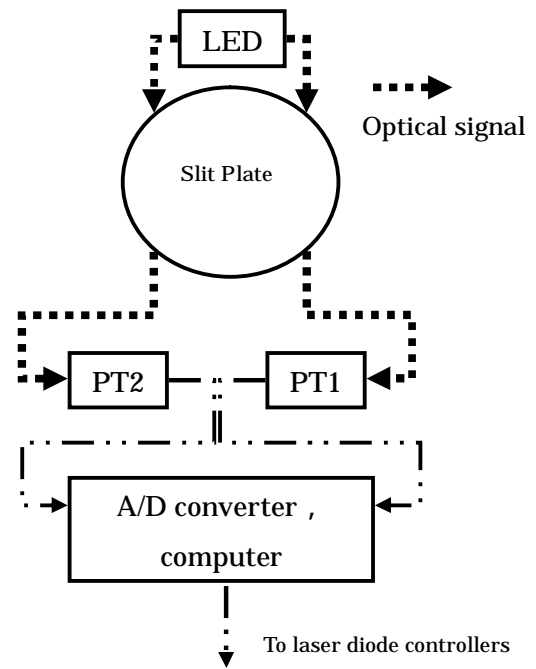


Fig.5 Constitution of a rotary encoder

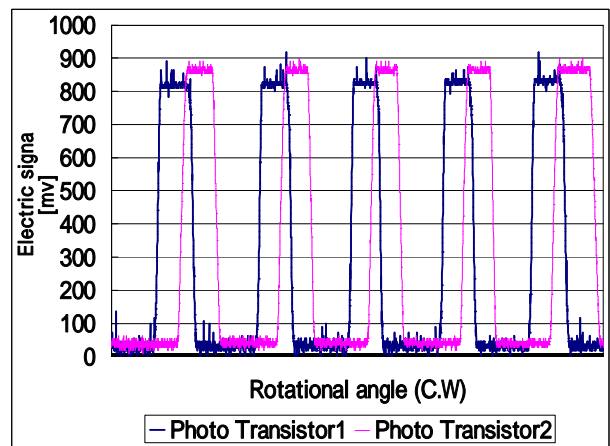


Fig.6 Voltage waveforms of the encoder, case of Right

COMPACTION OF THE SYSTEM

The system made the loss of pressure and flow rate. We thought decrease the loss for the purpose of improvement the response. So the design and improvement of equipment were carried out in the following points.

First, we cut the tube lengths in the 4 stage cascades of LPA. Those tubes were connecting the LPAs. In the result, the LPAs are combined as unity module.

To the next, we design the optimal location of the 4 stage cascades of LPA, the pneumatic servo valve and the opto-fluid converter. In the previous, the 4 stage cascades of LPA and the pneumatic servo valve were placed in rather long distance. Therefore the design of compaction rearranges both equipments near the opto-fluid converter, in this report. As the result, the tube length connecting the opto-fluid converter and the 4 stage cascades of LPA was reduced about 91.9%, and it connecting the 4 stage cascades of LPA and the pneumatic servo valve was reduced about 63.6%.

THE CHARACTERISTIC OF THE SYSTEM

The response of the pneumatic servo valve to the supply pressure of the 4 stage cascades of LPA

Measuring method

In this experiment, the 5 port type air pressure servo valve is used to generate precise the input signal of 4 stage cascades of LPA, instead of the opto-fluid converter. The electrical signal sends to the air pressure servo valve from CPU, changes the output pressure difference of air pressure servo valve from 50 [Pa] to -50 [Pa] or from -50 [Pa] to 50 [Pa]. Then, the pressure difference is amplified with the 4 stage cascades of LPA and inputted into servo valve and the spool displacement generates the powerful output.

The output pressure of the pneumatic servo valve is measured with a pressure sensor. The response time of 4 stage cascades of LPA and pneumatic servo valve are measured by connecting an oscilloscope.

As the supply pressure of the 4 stage cascades of LPA, the pressure of 1st stage is changed from 0.8 [Pa] to 2.0 [Pa], and the pressures of each stages are set as follow. The 2nd is twice magnitude of 1st, the 3rd is 4 times and 4th is 10 times. The supply pressure of the pneumatic servo valve is set as 50 [kPa] constant.

The measurement result and consideration

The response time when the output pressure difference of the air pressure servo valve changed from 50 [Pa] to -50 [Pa] is shown in Fig.7, changed from -50 [Pa] to 50 [Pa] is shown in Fig.8.

First, by comparing Fig.7 with Fig.8, it is shown that the response changing from 50 [Pa] to -50 [Pa] is rather better. The effects of improvement by reducing the tube

length are compared. When the output pressure difference is changed from 50 [Pa] to -50 [Pa], about 0.07 [sec] reduction is shown, where the supply pressures of the 4 stage cascades of LPA are 1.5[kPa], 3.0[kPa], 6.0[kPa], and 15.0 [kPa] , respectively. These combinations of supply pressure are the optimal conditions in the former research. When the output pressure difference is changed from -50 [Pa] to 50 [Pa], about 0.05 [sec] reduction has been shown. As the result, reducing pressure loss and flow loss can be done by having compact the system.

Next, the optimal supply pressures of the 4 stage cascades of LPA are specified as 1.3 [kPa], 2.6 [kPa], 5.2 [kPa], and 13.0 [kPa], to each stage, respectively, and the result are shown in Fig.7 and Fig.8. The delay time decreases until the pressure of the 1st stage becomes by 1.3 [kpa]. The delay time does not almost change above 1.3 [kPa] ranges. It will be thought that the pressure and flow loss occurred by the leak of air in this range.

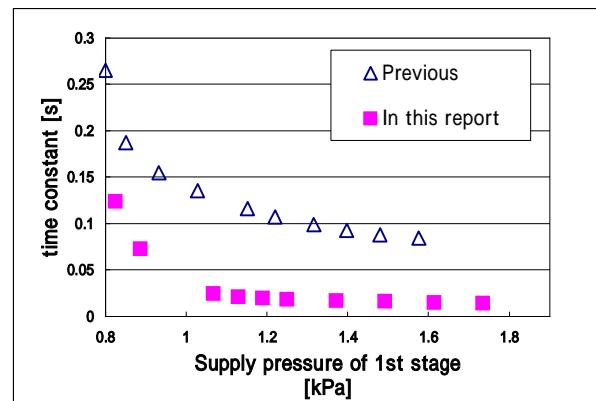


Fig.7 The air pressure servo valve (-50 [Pa] 50 [Pa])

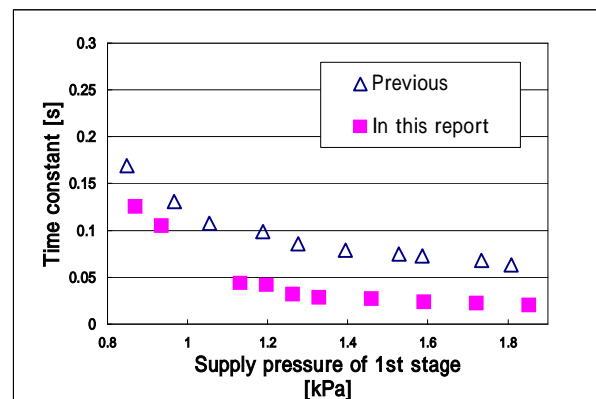


Fig.8 The air pressure servo valve (50 [Pa] -50 [Pa])

The pressure characteristic to the input-pressure difference of the 4 stage cascades of LPA

Measuring method

The output pressure difference (i.e., input-pressure difference of the 4 stage cascades of LPA) of the air pressure servo valve is changed from -50 [Pa] to 50 [Pa]. The output pressure difference of the 4 stage cascades of LPA in the previous is measured with a pressure sensor. Those which was improved the tube length is measured in the same way. The supply pressure of the 4 stage cascades of LPA is set to 1.5 [kPa], 3.0 [kPa], 6.0 [kPa], and 15.0 [kPa], respectively.

The measurement result and consideration

The measurement result of the output pressure difference of the 4 stage cascades of LPA is shown in Fig.9. The effect of improvement by reducing the tube length is compared. The proportional working area of linearity becomes wide and the sensitivity becomes large in this improvement. The maximum pressure difference becomes about 0.3 [kPa]. This is considered to reduce the pressure loss by making the compact system.

The control range is between -10 [Pa] and 10 [Pa]. The result of this range, because the supply pressure of the 4 stage cascades of LPA is larger than the input-pressure difference. The effects of improvement by reducing the tube length change the gain of the output pressure difference vs. the input-pressure difference of the 4 stage cascades of LPA are shown in the control range from 195.0 to 267.1, the gain is progressed about 37.0%.

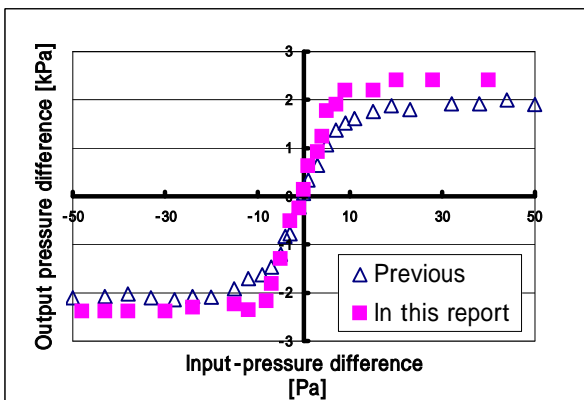


Fig.9 The pressure characteristic to the input-pressure difference of the 4 stage cascades of LPA

The flow characteristic to the input-pressure difference of the 4 stage cascades of LPA.

Measuring method

When the input-pressure difference of the 4 stage cascades of LPA is changed from -50 [Pa] to 50 [Pa], the output flow rate difference of the 4 stage cascades of LPA is measured with a flow sensor. The supply pressure of the 4 stage cascades of LPA is set to 1.5 [kPa], 3.0 [kPa], 6.0 [kPa], and 15.0 [kPa], respectively.

The measurement result and consideration

The measurement result of the output flow rate difference of the 4 stage cascades of LPA is shown in Fig.10. The output flow rate difference of improvement by reducing the tube length is compared. In the range of the input-pressure difference is between 20 [Pa] and 50 [Pa], the flow characteristics are increased about 0.45 [l/min], and between -20 [Pa] and -50 [Pa] in the range of about 0.35 [l/min].

The flow rate tends to be influenced by friction in the tube. So I consider that the frictional loss decreased and flow rate increased, because the tube length in the system has been extremely reduced.

As the effects of improvement by reducing the tube length changed, the gain of the output flow rate vs. the input-pressure of the 4 stage cascades of LPA from 162.6 to 216.1 is progressed about 32.9%.

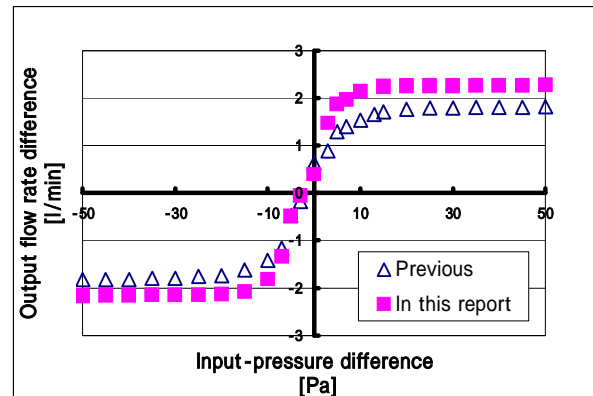


Fig.10 The flow characteristic to the input-pressure difference of the 4 stage cascades of LPA

CONCLUSION

This research treats the improvement of the opto-fluid servo system.

The high-speed response will be achieved by having the compact design of system. The details of the supply, the input, and the output are able to be known in this study. This result will be useful when the accuracy and practicality of this system will be required in the future. Research of the future needs the stability and the stationary of the system.

ACKNOWLEDGEMENT

The servo valve is a special product of the KURODA PRECISION CO. We thank KURODA PRECISION CO. for supporting the valve.

REFERENCES

1. Tadeusz M. Drzewiecki, Allen B. Holmes, Edward A. Packard, and Raymond J. Kiernan, FLUIDIC GUIDANCE FOR SPACE-BASED KINETIC ENERGY WEAPON PROJECTILES,
2. Keijiro YAMAMOTO, Characteristics of a Opt-Fluidic Converter Utilizing Photo acoustic Effect, Trans. SICE Japan, 1991, 27-12, pp1405-1411.
3. Takahiro IMADA , Takayuki NISIMOTO , Research of the control system using opto-fluid converter , The 2002 fiscal year University graduate paper

Dynamic Characteristics of the Opto-Fluidic Conversion Device

Fumitaka KIKKAWA*, Osamu OYAMA*,
Toshihiro YOSHIMITSU** and Keijiro YAMAMOTO**

* Graduate School of Science and Technology
Meiji University
1-1-1, Higashimita, Tama-ku, Kawasaki-shi, Kanagawa, 214-8571 Japan
(E-mail: ce55220@isc.meiji.ac.jp)
** Welfare Systems Engineering
Kanagawa Institute of Technology
1030, Shimo-ogino, Atsugi-shi, Kanagawa, 243-0292 Japan

Abstract

This report treats a development of an opto-fluidic conversion device. Using a bundled optical fiber which has the sectional area of 1.0[mm] × 5.0[mm], 2.0[mm] × 5.0[mm] and 3.0[mm] × 5.0[mm] respectively, the dynamic characteristics on an opto-fluidic conversion device have been analyzed. This paper reports analysis result of the dynamic characteristics and the effect on the size of the optimal sectional area of the bundled optical fiber. From the analytical result of the dynamic characteristics, it has been confirmed that the bundled optical fiber with the sectional area of 2.0[mm] × 5.0[mm] has been optimal in the test case.

Key Words

Opto-fluidic converter, Optical control, Laminar Proportional Amplifier, Optical fiber, Output differential pressure

1. Introduction

Electric equipment is used in a wide field now, and embedded in a majority of machines. This equipment operates on an electric signal. However, there is a possibility which may not operate correctly in an environment where electromagnetic noises or radioactivities exist in.

An opto-fluidic control system converts an optical signal into a pneumatic signal directly without an intermediate electric signal, and realizes a control of machine without electric device[1]. Therefore, this system enables to be used in the severe environment like above-mentioned. An opto-fluidic converter which is the peculiar feature of this system is composed of an opto-fluidic conversion device and a Laminar

Proportional Amplifier (LPA) of two stages. The LPA is a kind of fluidic amplifier. The opto-fluidic conversion device, which is the first stage of this converter, has a shape based on the LPA. Concretely, two control ports are removed from the inside of LPA, and optical fibers affixed with optical absorber at the fiber end are embedded there. The optical signal is converted into the pneumatic signal by this conversion device, and the converted pneumatic signal is amplified by the LPA of two stages.

We have analyzed the dynamic characteristics of fluid in this opto-fluidic conversion device. In analyzing the dynamic characteristics, there is a problem that the device was too small with the original size arose.

Considering the size of the measuring instrument, it was difficult to exactly analyze the dynamic characteristics. Therefore, an expansion model which is expanded the original device to double height and width size was made. In order to correspond to the expansion of the device, the bundle of the optical fiber was made. The shape of bundled optical fiber is rectangular pillar and the sectional area of which is 2.0[mm] × 5.0[mm] [2].

In the present study, we made three kinds of the bundled optical fiber newly, i.e., the sectional area of which are 1.0[mm] × 5.0[mm], 2.0[mm] × 5.0[mm] and 3.0[mm] × 5.0[mm] respectively. We have investigated the dynamic characteristics of these bundled optical fibers.

This paper is intended to report the optimal sectional area of the bundled optical fiber which we have selected through the experiments on the dynamic characteristics.

2. Principle of operation and structure

2.1 Laminar Proportional Amplifier (LPA)

Figure 1 shows the structure of the LPA, which has symmetrical structure. The principle of operation of the LPA is as follows:

- (1) The supply jet is inputted from the supply port, and the differential pressure is inputted from right and left of two control ports which exist inside the LPA.
- (2) In proportion to this differential pressure, a part of supply jet leans; for example, assuming that the pressure from the control port A is higher than that from the control port B, the part of supply jet leans toward the opposite direction in which the output port B exists.
- (3) By leaning the part of the supply jet, a difference arises between the pressures outputted from two output ports.

The LPA enables to amplify the feeble differential pressure, because the laminar jet is used as the supply jet of the LPA. The LPA is attached to the output port of opto-fluidic conversion device in order to amplify the feeble differential pressure from the conversion device.

2.2 Opto-fluidic conversion device

The opto-fluidic conversion device is made from the LPA which is a basic element. Figure 2 shows the structure of this conversion device. The main difference is that the conversion device has not control ports. And the optical fibers are embedded in the position of control ports. In these fibers, the optical absorber is affixed at the

fiber end. The principle of operation of this device is as follows:

- (1) When light from laser source is irradiated the optical fiber, this light passes through the optical fiber, and reaches the optical absorber affixed at the fiber end.
- (2) The optical absorber, which is a carbon black, has a character to convert light into heat. Therefore, light which reaches at the fiber end is converted into heat by the optical absorber.
- (3) Generated heat causes partially the temperature change of the supply jet at the vicinity of fiber end. As a result, viscosity of the supply jet rises, because viscosity of gas rises along with the temperature rise.
- (4) By the viscosity rise, a flow profile of jet becomes asymmetrical for the nozzle axis, and a difference is generated in the flow velocity of jet for the nozzle axis. Therefore, the output differential pressure proportional to the intensity of light is generated from the output port A and B.

Thus, this conversion device enables to convert an optical signal into a corresponding pneumatic signal without mechanical drive components.

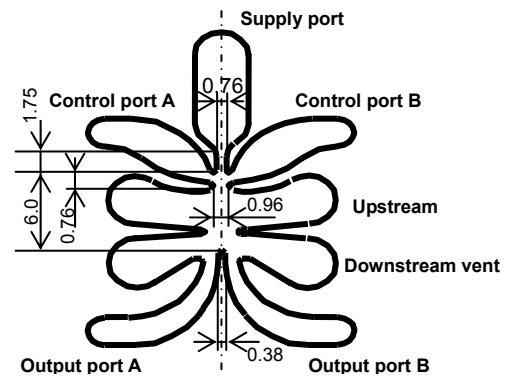


Fig.1 Structure of Laminar Proportional Amplifier

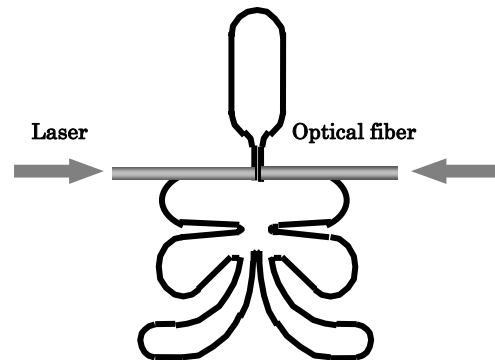


Fig.2 Structure of opto-fluidic conversion device

2.3 Opto-fluidic converter

Figure 3 shows the structure of the opto-fluidic converter. The 1st stage of this converter is the opto-fluidic conversion device. The output differential pressure generated by the conversion device is feeble. Therefore, it is amplified fluidically by the LPA of two stages which are 2nd and 3rd stage. The aspect ratio is 1.32 in both the 1st conversion stage and the 2nd stage, and that of 3rd stage is 0.66. The thickness of this converter is 0.5[mm]. We have analyzed the dynamic characteristics of the opto-fluidic conversion device which is 1st stage. In our experiments, we have not used this opto-fluidic converter itself but the expansion model.

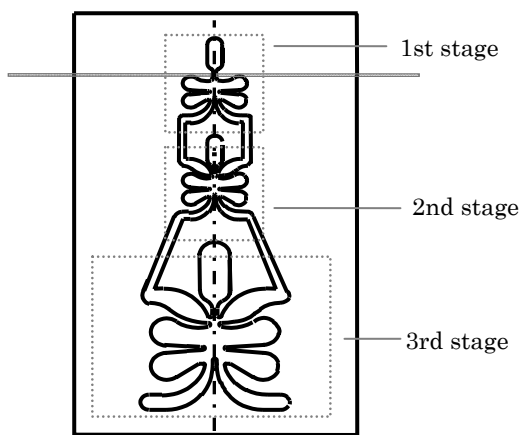


Fig.3 Structure of opto-fluidic converter

3. Experiment instrument

3.1 Expansion model

In analyzing the dynamic characteristics of opto-fluidic conversion device, considering the size of the measuring instrument, it was difficult to analyze the dynamic characteristics by using the conversion device of original size, because the conversion device is too small compared with the size of measuring instrument. Therefore, we make a model, which is expanded the conversion device of original size to double height and width size. Figure 4 shows the structure of this expansion model. It is made of stainless steel, and the thickness is 5.0[mm].

3.2 Bundled optical fiber

As the optical fiber for this model expanded to double height and width size, the bundle of optical fiber is used. The sectional area is 2.0[mm] × 5.0[mm], and the shape

of the bundled optical fiber is rectangular pillar. In addition, we make more two kinds of the bundled optical fiber, the sectional area of which is 1.0[mm] × 5.0[mm] and 3.0[mm] × 5.0[mm] respectively. The shape of those fibers is also rectangular pillar. Figure 5 shows the configuration of bundled optical fiber.

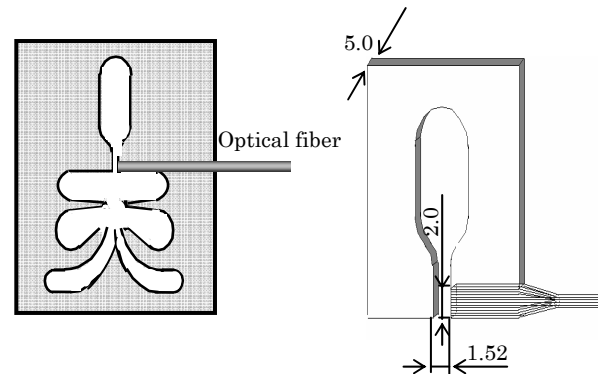


Fig.4 Structure of expansion model

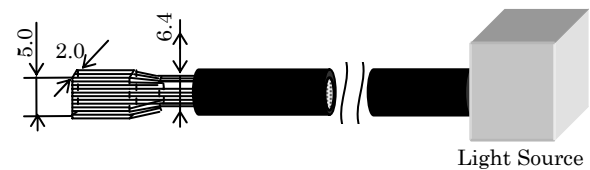


Fig.5 Configuration of bundled optical fiber

4. Experimental results

Three kinds of experiments on the dynamic characteristics are conducted by using the expansion model. The optimal sectional area of the three bundled optical fibers is examined from these experiments.

4.1 Temperature measurement of the optical absorber

The temperature change of the optical absorber influences the air flow in the opto-fluidic conversion device. Therefore, the time change of the temperature on the optical absorber is measured by using the expansion model and bundled optical fibers. The sectional area of bundled optical fibers are 1.0[mm] × 5.0[mm], 2.0[mm] × 5.0 [mm] and 3.0[mm] × 5.0[mm]. Figure 6 and Figure 7 show the measurement result concerning three bundled optical fibers. The result is shown by the approximation curve. Where, the supply pressure to the conversion device is 100[Pa], and the temperature of the fiber end is unified as 100[] in these bundled optical fibers. The

time when the light is begun to irradiate is set to 0[s] in Fig.6, and the time when the light disappears is set to 0 [s] in Fig.7.

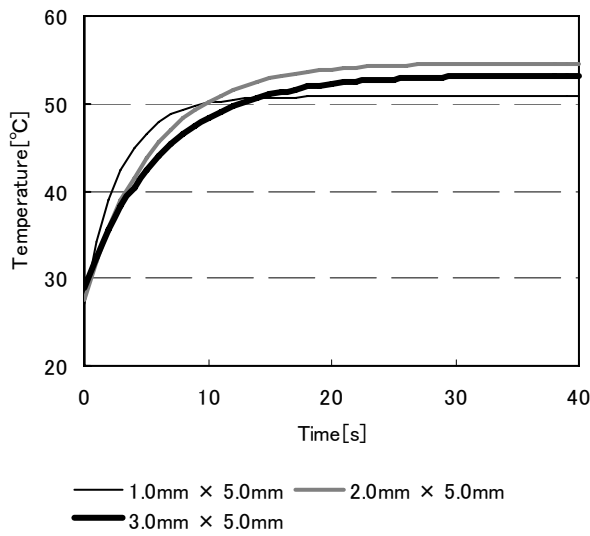


Fig.6 Temperature of the optical absorber, case of rise

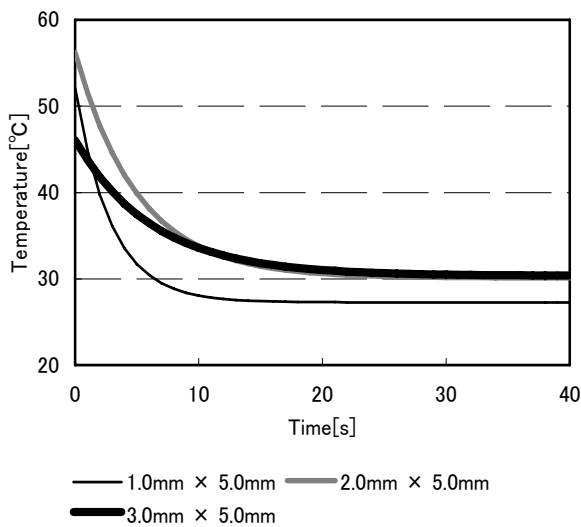


Fig.7 Temperature of the optical absorber, case of descent

From Fig.6 and Fig.7, it is shown that the time of transient response is proportional to the size of the sectional area of the bundled optical fiber. The difference of transient response time more than 10[s] appears between the result of bundled optical fiber of 1.0[mm] × 5.0[mm] and that of 3.0[mm] × 5.0[mm]. Therefore, we consider that an area of the optical absorber influences the time constant of a first order lag system.

4.2 Measurement of the output differential pressure

In this experiment, the output differential pressure from the opto-fluidic conversion device is measured. Figure 8 shows the measurement result of the output differential pressure concerning three bundled optical fibers. The sectional area of these fibers are 1.0[mm] × 5.0[mm], 2.0[mm] × 5.0[mm] and 3.0[mm] × 5.0[mm]. The result is shown by the approximation curve. Where, the supply pressure to the conversion device is 100[Pa], and the temperature of the fiber end is unified as 100[] in these bundled optical fibers. The time when light is irradiated is set to 0[s], too.

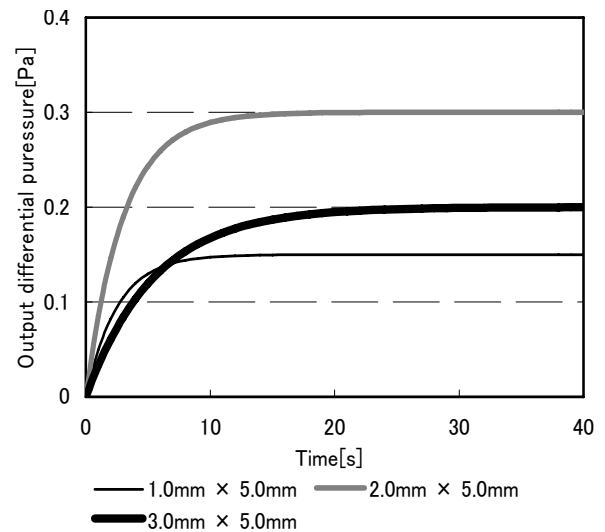


Fig.8 Output from the opto-fluidic conversion device

From Fig.8, it is shown that the sectional area of bundled optical fibers is not proportional to the output differential pressure from the conversion device. The bundled optical fiber of 1.0[mm] × 5.0[mm] doesn't generate the viscosity change effectively because the quantity of heat which gives to the supply jet is a little. By contrast, the bundled optical fiber of 3.0[mm] × 5.0 [mm] generates the viscosity change in the large range because there is much quantity of heat given to the supply jet. Therefore, it is considered that the output differential pressure is low when the bundled optical fiber of 1.0[mm] × 5.0[mm] or 3.0[mm] × 5.0[mm] is used. We consider that the bundled optical fiber of 2.0 [mm] × 5.0[mm] enables to obtain the highest output differential pressure.

4.3 Measurement of the pneumatic temperature change in the opto-fluidic conversion device

In this experiment, the time change of the pneumatic temperature in the opto-fluidic conversion device is

measured by using the expansion model. As shown in Fig.9, measurement positions are three places, where are 0.05[mm] (Region 1), 5.0[mm] (Region 2) and 12.0[mm] (Region 3) downward from a nozzle edge. The supply pressure to the conversion device is 100[Pa], and the temperature of the fiber end is unified as 100[] in three bundled optical fibers, the sectional area of which are 1.0[mm] × 5.0[mm], 2.0[mm] × 5.0[mm] and 3.0 [mm] × 5.0[mm]. Figure 10.1 and 10.2 show the temperature distribution of the Region 1 in the conversion device, and figure 11.1 and 11.2 show that of the Region 3 in the conversion device. The temperature distribution are two kinds of 3[s] and 30[s] later when the light is irradiated. Figure 10.1 shows the temperature distribution of 3[s] later, and figure 10.2 shows that of 30[s] later. Figure 11.1 shows the temperature distribution of 3[s] later, and figure 11.2 shows that of 30[s] later.

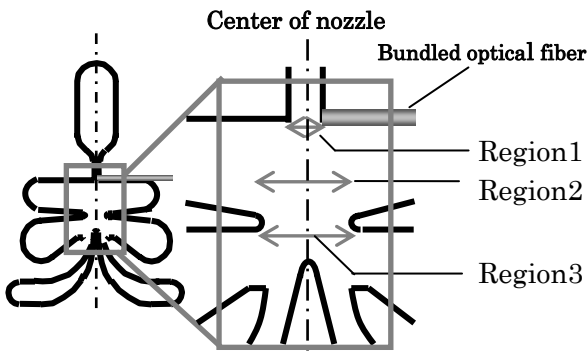


Fig.9 Measurement positions

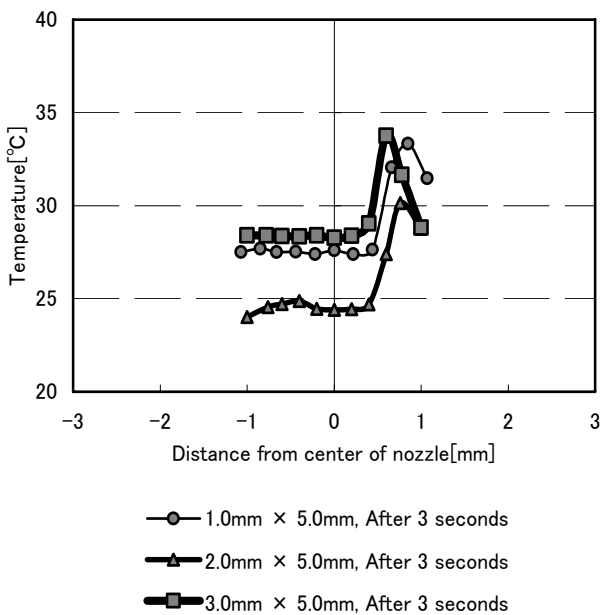


Fig.10.1 Temperature change in Region1(after 3 seconds)

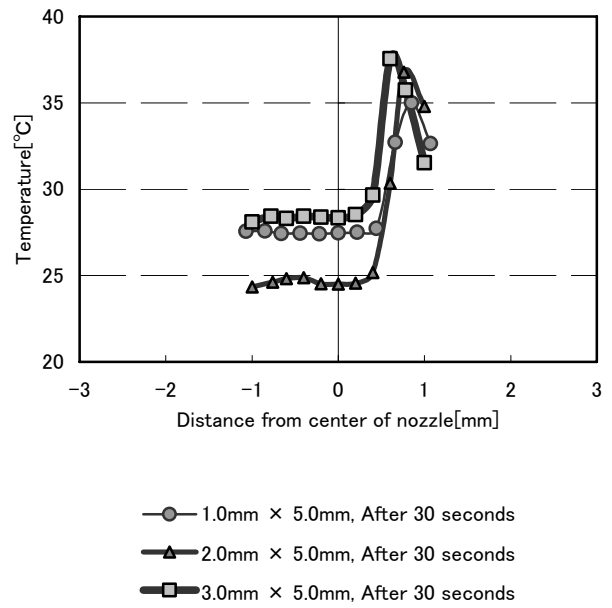


Fig.10.2 Temperature change in Region1(after 30 seconds)

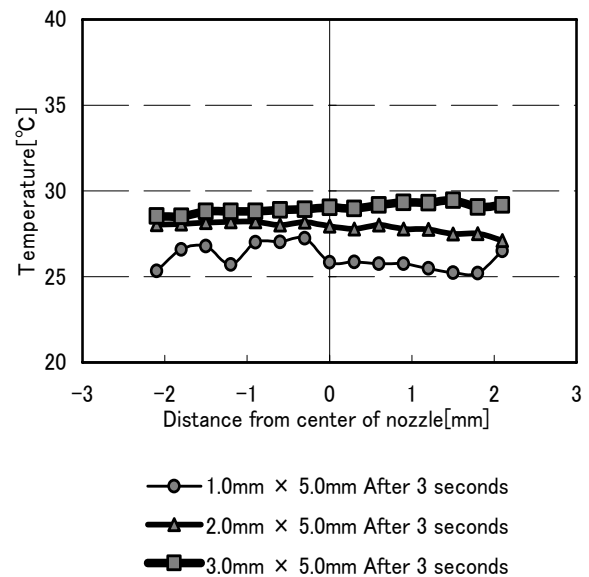


Fig.11.1 Temperature change in Region3(after 3 seconds)

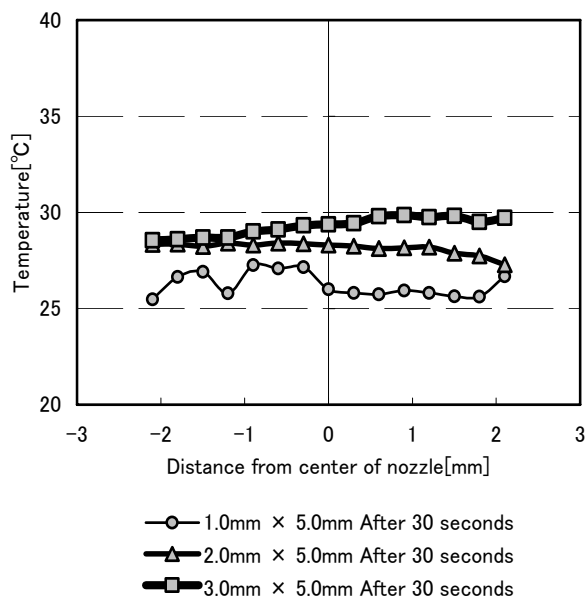


Fig.11.2 Temperature change in Region3(after 30 seconds)

From Fig.10.1, Fig.10.2, Fig.11.1 and Fig11.2, it is shown that the temperature change of the Region 1 is larger than that of the Region 3 in all bundled optical fibers. The temperature change becomes small as the measurement position moves to downward (i.e. from Region 1 to Region 3). It is considered that the temperature change of Region 1 is the largest compared with other measurement position because the Region 1 is the nearest measurement position from the bundled optical fiber. In Region 1 and Region 3, the temperature in the conversion device becomes the highest when the bundled optical fiber which is 3.0[mm] × 5.0[mm] is used.

5. Conclusion

In the present study, three kinds of bundled optical fibers have been made, which have the different sectional area. And three kinds of the dynamic characteristics on the opto-fluidic conversion device have been measured by using those fibers. Measurement results have indicated that the size of the sectional area of the bundled optical fiber has greatly influenced the output differential pressure from the conversion device and the pneumatic temperature in it. In addition, it has indicated that the quantity of heat generated on the optical absorber has been proportional to the size of the sectional area of the fiber. It is notable that the output differential pressure is low when the sectional area of the fiber is too large or is too small. We consider that the bundled optical fiber which has the sectional of 2.0[mm] × 5.0[mm] is optimal

in this test case. If the performance of the actual opto-fluidic conversion device is improved referring these data, the opto-fluidic control system advances for the practical use.

6. References

1. Keijiro Yamamoto, Characteristics of an Opto-Fluidic Converter Utilizing Photo acoustic Effect, Trans. SISE Japan, 1991, 27-12, pp1405-1411.
2. Tomoaki Kurihara, Osamu Oyama, Toshihiro Yoshimitsu and Keijiro Yamamoto, Dynamic Characteristics of Opto-Fluidic Conversion Device, SICE 5th Symposium on Fluid Control and Measurement.

DESIGN, SIMULATION AND EXPERIMENTAL TESTS OF HYDRAULIC HYDRO-SOUNDER

Tapio VIRVALO*, Arto LAINE**

*IHA, Tampere University of Technology, Finland

P.O.Box 589, 33101 Tampere

Tel. -358-3-31152262, Fax. -358-3-31152240

e-mail tapio.virvalo@tut.fi

** Patria Advanced Solutions Oy

Naulakatu 3, 33100 Tampere, Finland

ABSTRACT

Mines installed into sea are a serious threat to navigation during wars or other un-certain conditions. During years mines have become quite sophisticated. Every ship passing through the water emits sound, disturbs the Earth's magnetic field, and causes fluctuations in water pressure. Mine clearing is important and challenging task. Sea mines react to stimulus of ships. Noise caused by ships is one of remarkable stimulus. Mines reacting to noise are tried to clear with acoustic mine clearing equipment. In order to image noise generated by different ships quite large frequency range is required. High frequencies (> 100 Hz) can be achieved, for instance, with permanent magnet and magnetostrictive hydro-sounders. At low frequencies (≤ 60 Hz) hydraulic hydro-sounder might be a reasonable solution. In this paper the preliminary design, modeling and experimental tests of hydraulic cylinder driven hydro-sounder are presented.

KEYWORDS

Hydro-sounder, hydraulic servo

INTRODUCTION

Mines installed into sea are a serious threat to navigation during wars or other un-certain conditions. During years mines have become quite sophisticated. Yesterday's moored or drifting contact mine is still a threat, but today's modern naval arsenal also includes the bottom or moored influence mine. The influence mine lies on the bottom or

floats at the end of its tether and waits...sometimes for weeks or months. Every ship passing through the water emits sound, disturbs the Earth's magnetic field, and causes fluctuations in water pressure. Mines can be built and programmed to detect all of these changes. If an approaching ship emits enough noise, causes a sufficiently strong change in the surrounding magnetic field, or generates a significantly large fluctuation in

water pressure, it can cause the influence mine to detonate. Mine clearing is important and challenging task. Sea mines react to stimulus of ships. Noise caused by ships is one of remarkable stimulus. Mines reacting to noise are tried to clear with acoustic mine clearing equipment.

In order to image noise generated by different ships quite large frequency range is required. High frequencies (> 100 Hz) can be achieved, for instance, with permanent magnet and magnetostrictive hydro-sounders, Fig.1.



Figure 1. An example of magnetic hydro-sounder
At low frequencies ($\leq 60\text{Hz}$) hydraulic hydro-sounder might be a reasonable solution. The principle idea of the hydraulic test system is shown in Fig.2.

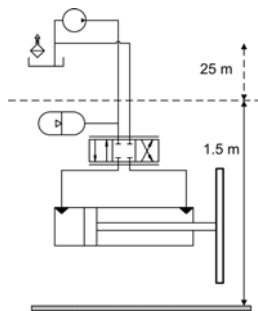


Figure 2, Basic idea of hydraulic hydro-sounder test system

The plate is moved by the hydraulic cylinder under water generating pressure waves. For practical reasons the initial feasibility tests are decided to realize in the laboratory where reasonable size water spool exists. The size of the spool is 6x5x10 (length, width and high). Based on experiences of preliminary tests with other types of hydro-sounders the diameter of the moving plate is

selected 400mm. Later also the plate of 600mm diameter is used.

GOALS OF FIESIBILITY STUDY

In the preliminary design stage the following specifications are set to 400mm plate

- * Maximum sin-wave frequency 50Hz with the position amplitude 2mm
- * Maximum position amplitude 90mm at low frequencies
- * Maximum velocity 1m/s
- * Maximum acceleration 200m/s^2

Because there is very little information available about the dynamic load of the plate in this kind of application experimental tests are necessary. Before experimental tests some simple modeling and simulations are considered also necessary.

With simulations responses to different amplitudes and frequencies of sin-wave reference signals are studied with some basic controllers. In this way the following issues are tried to find

- * Suitable reference signal
 - * Position
 - * Velocity
- * Required performance of servo valve
- * Size of hydraulic cylinder
- * Required supply pressure
- * Basic structure of controller
- * Specifications of position sensor

After simulations an experimental set-up is realized based on simulations and reasonably available components. The goals of experimental tests are:

- * To check performance
- * To find forces caused by water
 - * Inertia load
 - * Friction forces
- * To get information for more detail modeling

PRELIMINARY MODELLING

Quite large study of Internet and literature gave very poor results in the modeling of the moving of a round plate in water against its surface. The goal of the modeling is to find suitable abstract model for system and controller design purpose. As the first approximation of modeling interaction of the plate and water is considered as an inertia load and viscous friction. The inertia load is approximated as a mass of cylinder with the diameter of the plate and high of the double of the diameter. This leads to the inertia load of 50kg. Simple test with the paddle tells that water restricts the movement so far the paddle moves. On the other hand the inertia of water behaves totally different as mechanical inertia. In this stage the behavior of water inertia is modeled as follows:

```

if(vel>0.0 & acc>0.0) then !vel=velocity
wflag    =1.0 !wflag=flag
else if((vel>0.0 & acc<0.0) then !acc=acceleration
wflag    =0.0
else if((vel<0.0 & acc<0.0) then
wflag    =1.0
else if((vel<0.0 & acc>0.0) then
wflag    =0.0
end if

```

The effective water inertia is described as a second order system

$$m = \frac{\omega^2 \cdot wflip}{s^2 + 2 \cdot \delta \cdot \omega \cdot s + \omega^2} \cdot m_{WAT}$$

Where ω is estimated natural frequency of effective water mass (inertia), δ is natural damping factor of effective water mass (inertia), and m_{WAT} is estimated water mass.

Figure 4 shows as an example the responses of water inertia and the acceleration of the plate in an open loop control case. The viscous friction coefficient (force depending on the velocity of the plate) is estimated in this stage relatively high, 7000Ns/m.

Lot of simulations is done with this water model. According to simulations with this preliminary model the following conclusions can be made:

- * It is possible to achieve set performance goals

- * Open loop control is not good enough
 - * Position drift
 - * Low bandwidth
- * Closed loop velocity control with loose position control outer loop seems promising
 - * No position drift
 - * Lower phase shift than closed loop position control
 - * Feed forward loop improves performance.

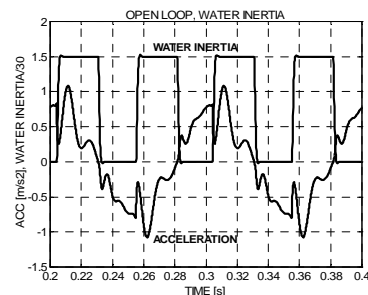


Figure 3. Responses of water inertia and acceleration of plate, simulated

EXPERIMENTAL TESTS

In order to get more exact information about the behavior and performance of hydraulic hydro-sounders an experimental test set-up realized in the laboratory circumstance.

Specifications of test set-up

Experimental set-up is realized with already available components, because the purpose of experimental tests is to confirm simulations and get more detail information for improving the water model

- * Cylinder 32/18-90 (piston dia., rod dia. stroke [mm])
- * Servo valve, nominal flow 40l/min with pressure drop 35bar/control notch
- * Supply pressure
- * Pipes between pump/tank and unit
 - * Inner diameter 16mm
 - * Length 25m
- * Accumulator 8litre
- * Analogue position sensor (potentiometer)

In order to achieve a symmetric structure two hydraulic units are assembled into the same water tight box as shown in Fig.4.



Figure 4. Test unit

Experimental tests

In order to find the inertia and friction load caused by water open loop measurements are done. Sin-waves with different amplitudes and frequencies are used as reference signals in the performance measurements of the closed loop control system in water. The cylinder chamber pressures, supply and return line pressures as well as the position of the plate are measured in all cases. The test unit is pinned by anchored it into the floor.

Open loop measurements in air

Firstly open loop measurements are done in air in order to find friction forces of the hydraulic cylinder. The procedure of open loop measurements is

- * Fixed start point is achieved with closed loop position control
- * Position control is switched off and after short delay the step-wise control signal of the valve is generated
- * When the plate reaches the fixed end point the control signal of the valve is switched step-wise off.

According to these measurements the velocity of the plate is a linear function of the valve control signal. The friction force as a function of the plate velocity is presented in Fig.5.

The hydraulic cylinder is normal low-price commercial cylinder and so the friction force is remarkably high, especially at higher velocities.

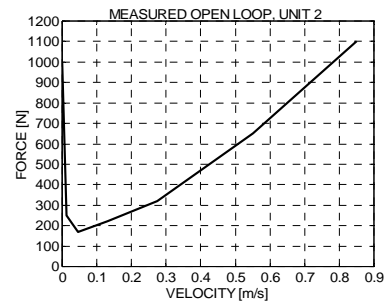


Figure 5. Measured friction force as a function of velocity, in air

Open loop measurements in water

The same kinds of open loop measurements are done in water. The plate velocity as a function of the valve control signal is shown in Fig.6.

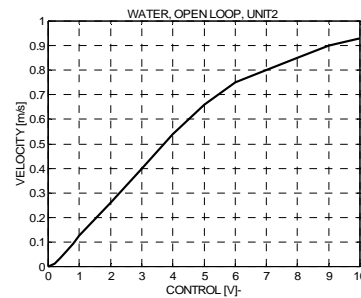


Figure 6. Measured plate velocity as a function of valve control signal (max 10V), in water

The friction force as a function of the plate velocity is presented in Fig.7. The velocity of the plate is not linear function of the control signal any more. Higher velocities than 0.6m/s water causes remarkably higher restrictive force than air. According to these measurements it seems that the velocity depending friction force is a non-linear function of velocity. Some tests done with the higher supply pressure confirm this. According to these preliminary tests it seems that a reasonable approximation is the third order dependence. This estimation is shown in Fig.8.

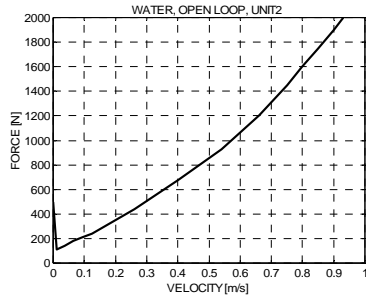


Figure 7. Measured friction force as a function of velocity, in water

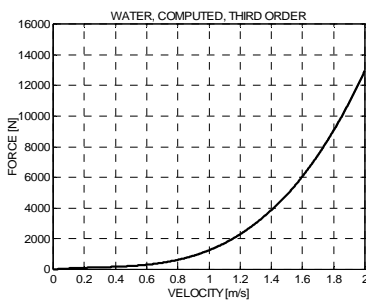


Figure 8. Estimation of friction force as a function of plate velocity in water

Estimation of water inertia is based on the measured cylinder chamber pressures and computed acceleration of the plate. The computed force acting on the plate is shown in Fig.9 and acceleration of the plate in Fig. 10. An interesting phenomenon can be observed in both figures. The force and acceleration/deceleration differ significantly each other.

Based on the same kinds of estimations in air the mechanical part of the inertia can be eliminated and this results water inertia 39kg. Figure 11 shows, as an example, the response of the return line pressure with maximum step-wise valve control signal. The long return line (25m) causes very high pressure peak in the acceleration stage limiting the reachable acceleration in step-wise control. In normal application cases

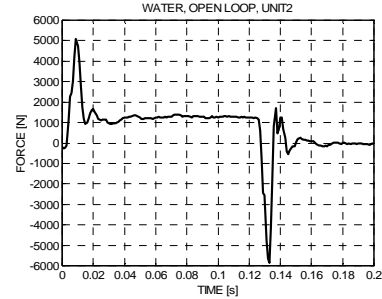


Figure 9. Measured force acting on plate, in water, control 50%

continuously oscillating reference signals are used. As an example, Figure 12 shows the return line pressure when the sin-wave reference signal with the amplitude 0.4m/s and frequency 40Hz is used.

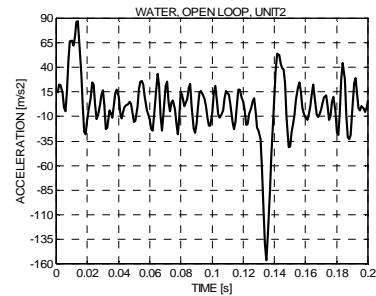


Figure 10. Measured acceleration of plate, in water, control 50%

Closed loop control in water

The purpose of closed loop control tests is to ensure sufficient performance of hydraulic hydro-sounder. The hydraulic, especially the cylinder and control valve, is not the best one, but a compromise between expected performance and available components.

A linear PI-controller and forward loop is used in these tests. The sampling time is 1ms and the tuning is made manually at the frequency of 20Hz. This tuning is a reasonable compromise, because the best tuning depends on the frequency, especially when forward loop is used.

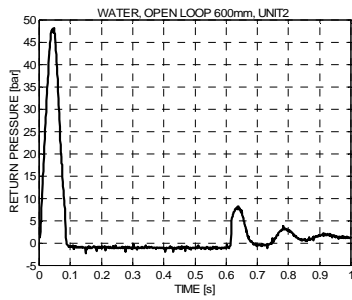


Figure 11. Measured response of return line pressure in step-wise control, control 100%, in water

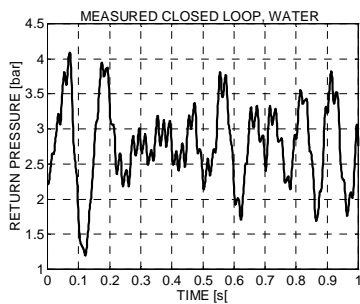


Figure 12. Measured response of return line pressure in sin-wave reference signal, in water

As examples the responses of velocity and position are presented in Fig.13 and 14. The reference signal is a sin-wave with the amplitude 0.4m/s and the frequency 50Hz. There is the remarkable phase shift $\approx -200^\circ$ and also amplitude damping -3db in the velocity response, Fig. 13. The performance depends mostly on the dynamic characteristics of the used servo valve. The steady state point of the plate is in the middle of the stroke. The amplitude of the position response is 1mm around the steady state point, Fig.14. The return line pressure oscillates with the amplitude about 5bar.

DISCUSSION AND CONCLUSIONS

Very rough approximation model of the behavior of water in this kind of application is valid so far that preliminary estimation of performance can be done. Water forms some kind of inertia load, but its behavior is strongly non-linear and does not resemble mechanical inertia load.

Water causes non-linear viscous friction which increases strongly as a function of the plate velocity. Most critical component is the control valve and high response valve is required in order to achieve good performance at frequencies of 50... 70Hz. Anyway, achieved results are so promising that R&D work can be continued.

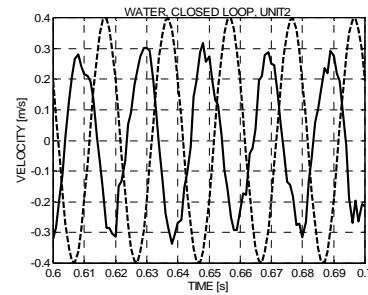


Figure 13. Velocity response (solid line), velocity reference (dash line) 50Hz, 0.4m/s in water

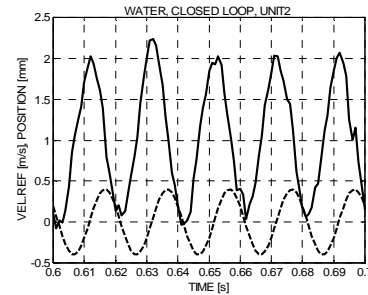


Figure 14. Position response (solid line), velocity reference (dash line) 50Hz, 0.4m/s in water

FURTHER WORKS

Based on open and closed loop measurements the model of inertia load and friction force of the plate and water combinations could be focused. With this more accurate model the required performance of the hydraulic cylinder and servo valve could be specified. Different control algorithms could also be studied effectively with the high quality model.

Experimental tests in real circumstances are also necessary after simulation and maybe further laboratory tests.

FLOW VS. PRESSURE CONTROL SERVOVALVES IN FORCE-BASED POSITION CONTROL APPLICATIONS

Antti MAKELA, Jouni MATTILA, Mikko SIUKO, Matti VILENIUS

Institute of Hydraulics and Automation,
Tampere University of Technology
P.O.Box 589
FIN-33101 Tampere, Finland
(E-mail: antti.h.makela@tut.fi)

ABSTRACT

In teleoperation applications torque controlled joints are often required. If hydraulic actuator is driven by flow control servovalve, a force-based position control requires tuning of inner loop force controller and force or pressure sensor. An alternative for flow control servovalves are pressure servovalves which are seldom used in industrial applications. Advantage of this technology should be that tuning of inner force-control loop should be avoided and also more importantly addition of pressure and/or force feedback sensors should not be required. Sensors are often the most likely component to fail while working in hazardous environments. Our aim is to compare three kinds of inner loop force controls. First, we use pressure servovalve in position control application without inner loop pressure or force sensors. In remaining two cases we use force control in the inner control loop with flow and pressure control servovalve. Three controller alternatives are compared and the results are discussed.

KEY WORDS

Pressure servovalve, flow servovalve, force control, position control

NOMENCLATURE

A: Cylinder pressure area
B: System's bulk modulus
V₀: System's dead volume
m: Load's mass
b: Load's viscosity friction
k: Load's stiffness

K_q : Flowservo's flowgain
 K_p : P-controller gain
 k_h : Cylinder's spring constant
 K_{PR} : Pressureservo's pressure gain
 t : Pressureservo's time constant

- X : Cylinder position
- X_R : Cylinder position reference
- \dot{X} : Cylinder velocity
- \dot{X}_R : Cylinder velocity reference
- \ddot{X}_R : Cylinder acceleration reference
- K_V : Velocity error gain
- e : Error
- ω_n : Natural frequency
- ζ : Damping
- QN : Flow

INTRODUCTION

The fundamental difference between electric and hydraulic actuators is that electric actuators are essentially torque sources whereas hydraulic actuators are velocity sources. In other words, with the electric DC-motors actuator output torque is proportional to motor input current. In case of hydraulics control input is proportional to actuator output velocity. This fundamental difference is not usually critical in traditional position control applications. However, in teleoperation applications torque controlled joints are often required. In hydraulics these applications are known as force-based position control applications, see Figure 1, where the principle of control structure is shown. In this case of usual servohydraulic hardware setup where hydraulic actuator (motor or cylinder) is driven by flow control servovalve, a force-based position control requires tuning of inner loop force controller. Inner loop force controller can be simple e.g. PI-type controller or more complex non-linear controller. Force feedback can either be based on pressure or force (load-cell) feedback.

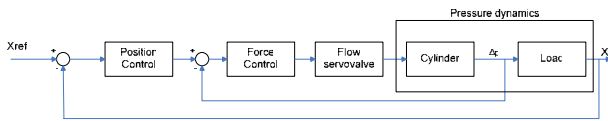


Figure 1 Force based position controller utilizing flow control servovalve and inner force control loop

An alternative for flow control servovalves are pressure control servovalves which are seldom used in industrial applications anymore most likely because of their high price. Pressure servovalves give pressure difference, which is proportional to input signal. Conventional pressure servovalves operate based on hydro-mechanical

pressure feedback principle and therefore do not require pressure feedback sensor. Therefore, the big advantage of this old almost forgotten technology should be that tuning of inner force-control loop should be avoided and also more importantly addition of pressure and/or force feedback sensors is not required. Sensors are often the most likely component to fail while working in hazardous environment. Still another advantage of pressure servovalves is the high bandwidth of valve response. For example, a commercial pressure servovalve blocked port pressure control bandwidth is close to 200 Hz [3]. This kind of pressure control bandwidth is very difficult to achieve with a controller combination of a servovalve and pressure feedback transducers. These design factors mentioned are of the major concern in application where high reliability, bandwidth and robustness are required. In the Figure 2 position controller utilizing pressure servovalve is shown. In this kind of control scheme no force/pressure feedback transducer is required and thus inner loop force controller is removed.

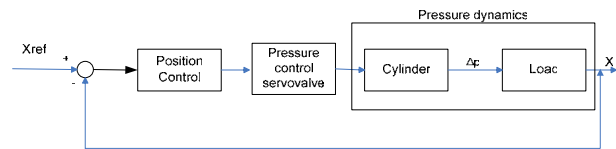


Figure 2 Force based position controller utilizing pressure control servovalve

In this study, we compare two alternatives, namely flow and pressure control servovalves in teleoperation application requiring inner loop force control. Our aim is to compare three kinds of force controls. First, we use pressure servovalve in position control application without inner loop pressure or force sensors. In remaining two cases we use force control in the inner control loop with flow and pressure control servovalve. The use of pressure control servovalve with pressure sensor has the advantage that in case of sensor failure force control still functions. Thus the operator should be able to complete the given task with somewhat decreased force feedback sensitivity. With this last option, if pressure control servovalve is operating under pressure sensor feedback, the force feedback accuracy should be as good as with flow control servovalve and pressure feedback combination. Therefore, pressure control servovalve should have the best robustness but also equally good force sensitivity as compared to flow control servovalve. Three controller alternatives are

compared and the results are discussed.

THEORETICAL BACKGROUND OF FORCE CONTROL

Flow servovalve's force control loop can be described by following block diagram [1]:

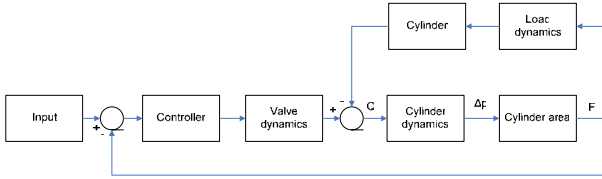


Figure 3 Flow servovalve's force control block diagram

The valve flow gain is K_q and controller gain is K_p

Cylinder pressure dynamics model can be described as an actuator transfer function from flow to pressure:

$$G_A(s) = \frac{2AB}{sV_0} \quad (1)$$

The feedback path of the system consists of the load transfer function from force to position and of the cylinder transfer function from position to flow:

$$G_L(s) = \frac{1}{ms^2 + bs + k} \quad (2)$$

$$G_p(s) = As \quad (3)$$

Collecting the transfer functions (1, 2, 3) together and describing the gains according to Figure 3 yields:

$$G(s) = 2K_q K_p \frac{AB(ms^2 + bs + k)}{s(V_0ms^2 + V_0bs + V_0k + 2A^2B)} \quad (4)$$

The hydraulic spring constant is defined as:

$$k_h = \frac{2BA^2}{V_0} \quad (5)$$

Applying equation (5) to (4) yields the open loop transfer function from voltage to force:

$$G(s) = k_h K_p \frac{K_q}{A} \frac{(ms^2 + bs + k)}{s(ms^2 + bs + k + k_h)} \quad (6)$$

From transfer function (6) can be seen that the poles of the load become the zeros of the open loop transfer function of the system. The actuator transfer function will not affect the zeros, which means that they can not be changed with PID-type controller as shown in [2]. As indicated in [2], these lightly damped open-loop zeros limit the bandwidth of the closed-loop force system.

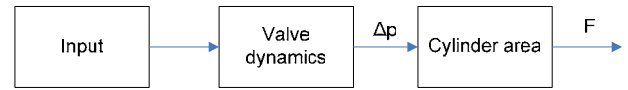


Figure 4 Pressure servovalve's force control block diagram

On the other hand, in the case of pressure control servovalve, the gain from input current to pressure difference is K_{PR} . Fast valve dynamics can assumed to obey first order model with a time constant τ . Cylinder area is A and the model from valve input current to output force is:

$$G(s) = \frac{K_{PR}}{ts + 1} A \quad (7)$$

As we can see, there are no zeros in open loop, so bandwidth is bigger and force control should be also faster. According this theory, flow servovalve should be controlled with some other controller than PID-type, if we want to get as fast response as pressure control servovalve has.

CONTROLLERS TUNING PRINCIPLES

As described above pressure control servovalve doesn't require inner loop force/pressure controller. One of the test control cases was pressure control servovalve with inner-loop control with pressure feedback. Feedforward control must be used in this case. Pressure servovalve needs some input current so that it would keep pressure difference. Anyway P-type controller gives signal only if there is some error.

For flow control servovalves typically a P- or PI-type of force/pressure controller is required for inner loop force control. In this study, we used P-type controller due to faster response. As described above pressure control servovalve doesn't necessarily require inner loop force/pressure controller. However, we also try in third test case pressure control servovalve with inner-loop pressure feedback. Inner loop pressure controller is a P-controller in parallel with pressure demand.

Upper-loop is also a simple PD-type position controller with desired acceleration as a new input to the system is described by following equation:

$$F = m(\ddot{X}_R + K_V(\dot{X}_R - \dot{X}) + K_P(X_R - X)) \quad (8)$$

The final closed-loop system becomes under this choose of feedback law:

$$\ddot{e} + K_V\dot{e} + K_P e = 0 \quad (9)$$

The error equation (9) can be transformed to the s-domain, which results the following:

$$s^2 + 2\omega_n\zeta s + \omega_n^2 = 0 \quad (10)$$

$$s^2 + K_V s + K_P = 0 \quad (11)$$

, where

$$K_V = 2\omega_n\zeta s \quad (12)$$

$$K_P = \omega_n^2 \quad (13)$$

Where second equation corresponds to well known second order characteristic equation with damping ζ and natural frequency ω_n . In the servocontrol the damping ratio of $\zeta = 1.0$ is highly desirable because it corresponds to situation of the fastest possible non-oscillatory response of the system to a step input. With the choose of $\zeta = 1.0$, simple relation holds for feedback gains in:

$$K_V = 2\sqrt{K_P} \quad (14)$$

MEASURED RESULTS

In order to compare the performance of three different inner loop force/pressure controller in force based position, experiments were carried out in 1 DOF linear testbed. The specifications for the experimental system are as follows

- Cylinder 40/28-710, load mass was 250 kg.
- Flow control servovalve: Bosch-Rexroth closed loop proportional valve NG6, QN = 40 l/min at $\Delta p = 35$ bar per notch. Natural frequency about 100 Hz, when input amplitude is +/- 5 %.
- Pressure control servovalve: Moog series 15-010. Rated flow capacity of 55 l/min at 105 bar per notch. Block port natural frequency is about 250 Hz.
- Pressure sensors: Kistler K-line 300bar
- Supply pressure is 70bar and maximum flow is enough so that valves doesn't saturate

Position, velocity and acceleration motion profiles for point to point motions are required to be smooth functions of time. Therefore, a quintic polynomial is used for desired position profile in measurements. Amplitude of the motion profile was 3.5 cm and a rise was time 0.5 seconds.

In Figures 5 and 6, the results with pressure control servovalve without inner feedback loop force controller are shown. In experimental system, stability limit for upper-loop position controller was found to be 6500 and a value used for it was 6000.

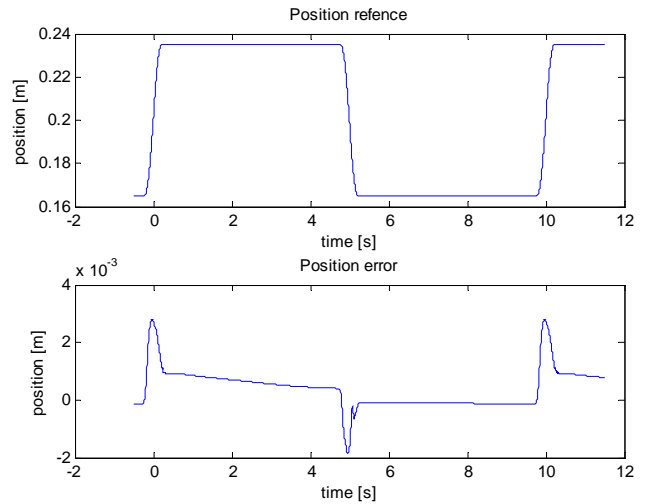


Figure 5 Position control response with pressure control servovalve

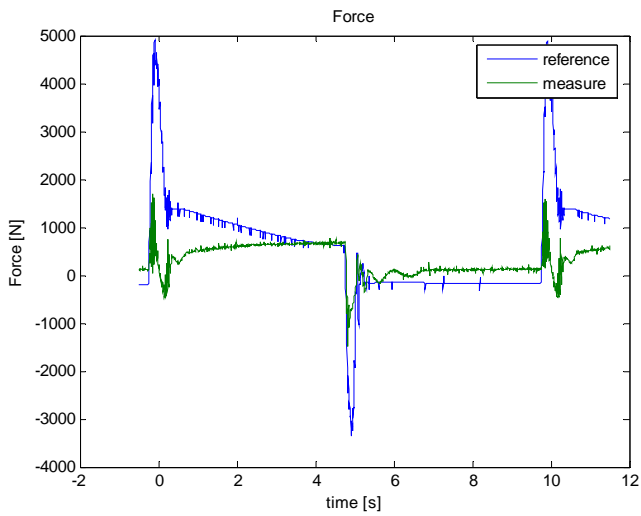


Figure 6 Force control responses with a pressure control servovalve

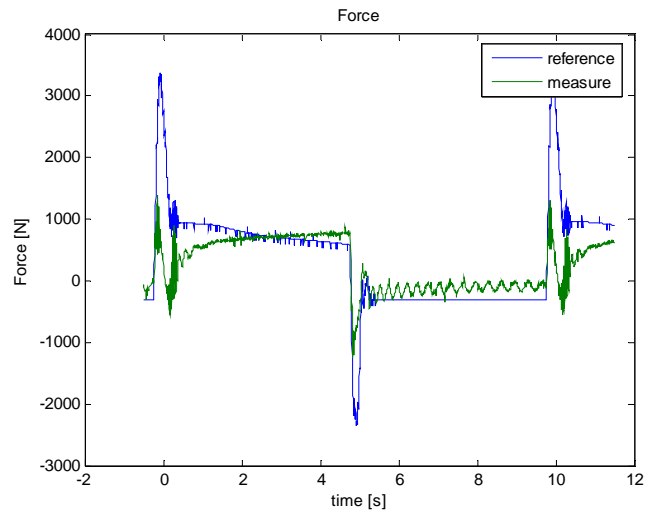


Figure 8 Force control response with a pressure control servovalve

Next Figures 7 and 8 show results with a pressure control servovalve with the inner-loop force controller. For this experiment position controller gain was reduced to 3000 and inner-loop force control gain was set to 0.22. Stability limit for inner loop control was found to be 0.26.

Finally, Figures 9 and 10 show, a flow control servovalve responses, with inner loop force control gain 0.00004 when its stability limit was 0.0001. In this case, outer loop's position controller gain was 28000, when its stability limit was 30000.

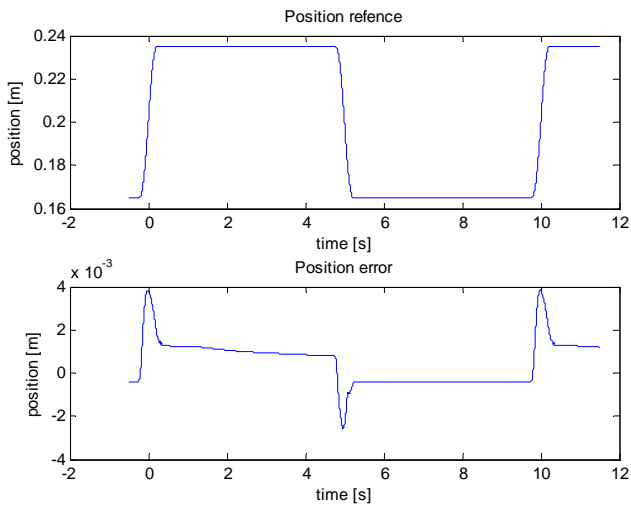


Figure 7 Position control response of a pressure control servovalve

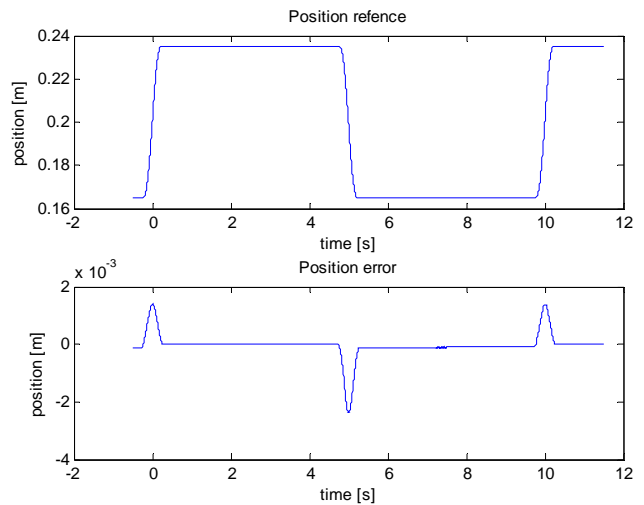


Figure 9 Position control response of a flow servovalve

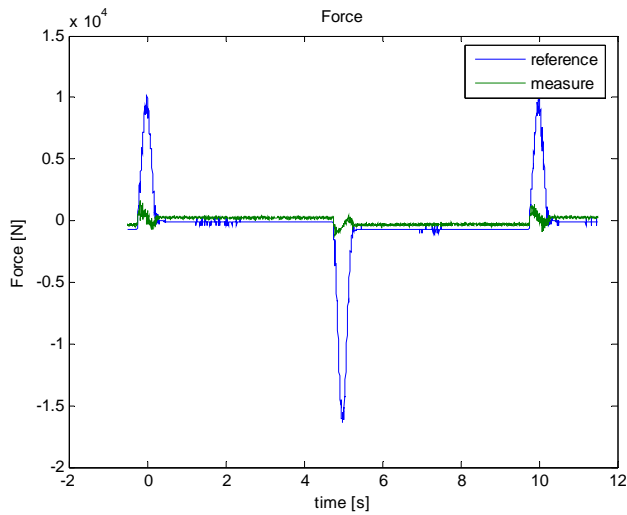


Figure 10 Force response of a flow servovalve

As we can see from measured results, flow servovalve's position tracking error is the lowest. Also static position accuracy of the flow servovalve is very good and it is equal to both motion directions. In both control cases with pressure control servovalve, the static accuracy depends on motion directions. Most likely, a symmetric cylinder is a cause of that. For the pressure control servovalve, as can be seen from the Figures 5 and 7, the motion settling time is very long and depends on motion direction. In typical manipulator application even with symmetric actuators (e.g. vane actuators), pressure valve offsets can be a problem due to a different load force direction. As expected, without a contact with the environment phase of the motion, inner-loop force controller doesn't improve the performance of the pressure control servovalve. Therefore, series of additional tests have to be carried out in the future with a realistic combination of both free space and contact phase motions.

Comparing force tracking capabilities, it can be noticed that flow servovalve is quite poor in dynamic force tracking but the static force accuracy is good. With pressure control servovalve, the settling time of force response is very slow while valve is correcting small position error as can be seen from Figure 6 and 8.

CONCLUSIONS

Pressure servovalve works quite well in force-based position control, and they can be considered for teleoperation applications in harsh environments. Pressure control servovalves are easy to tune by few tuning rules. Flow servovalves also provides good force-based position control results. However, with flow control servovalves, significant amount of effort has to put into careful selection of pressure transducers, sensor signal conditioning and to robust tuning of the inner-loop force controller's etc.

The best properties of the pressure control servovalves are that they are easy to tune and have very robust design. The concern about using pressure servovalves are their price and availability in the near future. A pressure control servovalve used in is this study is manufactured in accordance with MIL-speciation and therefore should be reliable and proven technology. However, some of the other valve manufacturers have already discontinued their pressure control servovalve program.

In near future, more tests are needed to be carried out in a rotary test joint subject to non-constant gravity force and contact with the compliant environment.

REFERENCES

1. Koivisto H., Mattila J., Makela A., Siuko M., and Vilenius M., On pressure/force control of a water hydraulic joint, The Ninth Scandinavian International Conference on Fluid Power, SICFP'05, June 1-3, Linköping, Sweden
2. Alleyne, A., 1999, On the Limitations of Force Tracking Control for Hydraulic Servosystems, ASME Journal of Dynamic Systems, Measurement and Control, Vol. 121, pp. 184-190
3. Moog series 15, pressure control servovalves

AN ADAPTIVE PRESSURE CONTROLLER DESIGN OF HYDRAULIC SERVO SYSTEM WITH DEAD ZONE

Kazuhisa ITO

Department of Mechanical Engineering, Faculty of Science and Technology

SOPHIA University

7-1, Kioicho, Chiyoda-ku, Tokyo 1028554, Japan

(E-mail: kazu-ito@me.sophia.ac.jp)

ABSTRACT

This paper develops a design of adaptive pressure controller for hydraulic servo valve with unknown dead zone. In general to reduce leakage flow, the servo valves adopt positive lap structures. This makes dead zone larger and is obstacle for precise positioning control. To compensate of such dead zone and unknown physical parameters of system, adaptive control strategy is examined for simple pressure control system. First it is assumed that only the flow gain of servo valve can be known by experiment and the adaptive controller is designed. This controller is examined on water hydraulic servo system which has larger leakage and positive lap for lower viscosity of tap water. The experimental results show that the better tracking performance is obtained comparing with PI or conventional adaptive controller without dead zone compensation. Then the controller is extended for unknown flow gain case.

KEYWORDS

Water Hydraulic Servo System, Dead Zone, Adaptive Control, Lyapunov Design, Robustness

INTRODUCTION

In electrohydraulic servo valves with high positioning performance, positive lap structures are adopted between land and sleeve to attenuate the leakage of fluid in general. In addition, a nozzle-flapper structure is also adopted to reduce friction. However, when the nonlinearities caused by these structural properties are neglected in designing control system, it often causes deterioration in the control performance. In the water hydraulic case, which is paid attention for its lower environmental load, the high availability and the high energy density owing to lower compressibility, this characteristic is more obvious. Especially the dead zone and/or the leakage flow around neutral position of spool displacement should be compensated to improve the control performance of hydraulic actuators.

In this research, we discuss the design of an adaptive controller to track a given desired pressure compensating the dead zone in servo valve as well as unknown physical parameters. In general, the dead zones depend on the direction of spool displacement of a servo valve, and some approach has been reported to overcome this nonlinearity in oil hydraulic systems. In [1] and [2], the dead zone was estimated by using neural network technique and PWM signal was generated to cancel the effect. On the other hand, the research results on applying the adaptive control technique to compensate the effect of dead zone directly are very few[3]. In this paper, an adaptive controller which compensate unknown dead zone is constructed and the performance is examined by experiments. In addition, the adaptive controller is extended to unknown flow gain case.

PROBLEM FORMULATION

The hydraulic circuit discussed in this paper is shown in Figure 1.

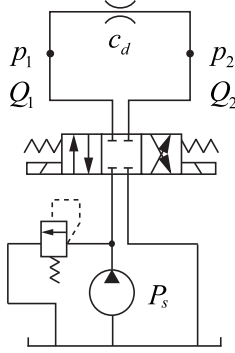


Figure 1: Hydraulic circuit

By linearizing the flow equation around neutral position of sool in servo valve and introducing load pressure $p = p_1 - p_2$, the pressure dynamics is given by

$$\dot{p} = -\text{sgn}(p)\theta_1\sqrt{|p|} - \theta_2p + f(u) \quad (1)$$

where $\theta_i > 0$ ($i = 1, 2$) and $\text{sgn}(\cdot)$ is the signature function. The input nonlinearity f can be described

$$f(u) = \begin{cases} u - \theta_3, & u \geq \theta_3 \\ 0, & -\bar{\theta}_3 \leq u \leq \theta_3 \\ u + \bar{\theta}_3, & u \leq -\bar{\theta}_3 \end{cases} \quad (2)$$

where u is input to be determined later. The parameters $\theta_3, \bar{\theta}_3 > 0$ are positive and negative dead zone, respectively, depending on the servo valve displacement direction (See Figure 2).

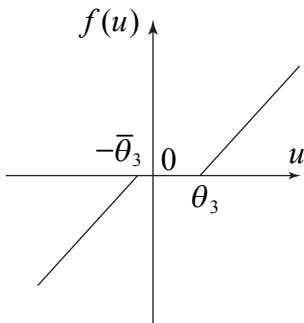


Figure 2: Dead zone of servo valve

The problem that should be solved in this paper is defined as follows.

Problem 1 Find an adaptive controller that makes the load pressure p track to the reference pressure p_r guaranteeing global boundedness of all signals in the system

$$\begin{aligned} u &= u(p, \hat{\theta}) \\ \dot{\hat{\theta}} &= \phi(p) \end{aligned} \quad (3)$$

where $\hat{\theta}$ is adaptive parameter. █

Here we assume that the gain of input u is known in Figure 2 and in fact this can be almost done by experiment. However, in general, this parameter depends on working point therefore in later, we discuss another adaptive controller design considering this unknown input positive gain.

CONTROLLER DESIGN

The desired pressure response is given by

$$\dot{p}_r = -\alpha p_r + \alpha r \quad (4)$$

where $\alpha (> 0)$ is a design parameter and r is a reference signal. Defining pressure error as $e = p - p_r$, we have error system

$$\begin{aligned} \dot{e} &= \dot{p} - \dot{p}_r \\ &= -\alpha e + \alpha(p - r) - \text{sgn}(p)\theta_1\sqrt{|p|} - \theta_2p \\ &\quad + \begin{cases} u - \theta_3, & u \geq \theta_3 \\ 0, & -\theta_3 \leq u \leq \theta_3 \\ u + \bar{\theta}_3, & u \leq -\bar{\theta}_3 \end{cases} \end{aligned} \quad (5)$$

In the following, we design the controller and discuss the stability, depending on the magnitude of input u .

Case (i) : $u \geq \theta_3$ or $u \leq -\bar{\theta}_3$

Introducing adaptive parameter $\hat{\theta}_i$ ($i = 1, 2, 3$), we give adaptive input as

$$u = -\alpha(p - p_r) + \hat{\theta}_1\text{sgn}(p)\sqrt{|p|} + \hat{\theta}_2p + \hat{\theta}_3 \quad (6)$$

Then Eq.(5) can be expressed

$$\dot{e} = -\alpha e + \tilde{\theta}_1\text{sgn}(p)\sqrt{|p|} + \tilde{\theta}_2p + \tilde{\theta}_3 \quad (7)$$

where $\tilde{\theta}_i = \hat{\theta}_i - \theta_i$ ($i = 1, 2, 3$). The Lyapunov-like function is constructed as

$$V_1 = \frac{1}{2} \left(e^2 + \sum_{i=1}^3 \frac{1}{\gamma_i} \tilde{\theta}_i^2 \right) \quad (8)$$

and the time derivative of V_1 along the solution of error system Eq.(7) is evaluated as

$$\begin{aligned} \dot{V}_1 &= -\alpha e^2 + \frac{\tilde{\theta}_1}{\gamma_1} \left(\dot{\hat{\theta}}_1 + \gamma_1\text{sgn}(p)\sqrt{|p|}e \right) \\ &\quad + \frac{\tilde{\theta}_2}{\gamma_2} \left(\dot{\hat{\theta}}_2 + \gamma_2pe \right) + \frac{\tilde{\theta}_3}{\gamma_3} \left(\dot{\hat{\theta}}_3 + \gamma_3e \right) \end{aligned}$$

where $\gamma_i > 0$ ($i = 1, 2, 3$). This leads to the parameter update law

$$\dot{\hat{\theta}}_1 = -\gamma_1\text{sgn}(p)\sqrt{|p|}e, \quad \dot{\hat{\theta}}_2 = -\gamma_2pe, \quad \dot{\hat{\theta}}_3 = -\gamma_3e \quad (9)$$

Using Eq.(9), we have $\dot{V}_1 = -\alpha e^2$ and Barbalat's Lemma [4] shows the pressure error goes to 0 and all signals are bounded. The similar discussion can be shown in the case for $u \leq -\bar{\theta}_3$ and the positive definite function V_2 and is omitted. Therefore, in these cases we have Eq.(6) as the adaptive control input for $V = \frac{1}{2}(V_1 + V_2)$ outside of the dead zone.

Case (ii) : $-\bar{\theta}_3 \leq u \leq \theta_3$

In this region the input u is invalid. However we consider the behaviour of the dead zone compensation parameter $\hat{\theta}_3$.

(a) $p > 0$ and $u < 0$

We have $e > 0$ and the right-hand side of the error dynamics

$$\dot{e} = \alpha(p_r - p) - \theta_1 \text{sgn}(p) \sqrt{|p|} - \theta_2 p \quad (10)$$

is negative. This makes e a monotonically decreasing and there exists a time t_0 such that $e(t_0) = 0$ crossing from positive value.

(b) $p > 0$ and $u > 0$

We have $e < 0$ and the right-hand side of Eq.(10) is negative. This keeps e be decreasing. At the same time the fact that the parameter update law guarantees $\theta_i > 0$ ($i = 1, 2, 3$) and monotonically increasing. This leads that the input u is positive and being monotonically increasing. This implies that there exists a time t_1 such that $u(t_1) > \theta_3$ and the situation moves to above Case(i).

(c) $p < 0$ and $u > 0$

We have $e < 0$ and in a similar to (a), there exists a time t_0 such that $e(t_0) > 0$.

(d) $p < 0$ and $u < 0$

We have $e > 0$ and in a similar to (b), there exists a time t_1 such that $u(t_1) < -\bar{\theta}_3$ and the situation moves to above Case(i).

Therefore the input signal surpass the dead zone after finite time even if the magnitude of input u becomes smaller than the dead zone.

Theorem 1 Consider the pressure control system with dead zone Eq.(1),(2) and desired pressure model Eq.(4). The adaptive input Eq.(6) and parameter update law Eq.(9) solve the Problem1. ■

EXPERIMENTAL RESULTS

To evaluate the effectiveness of the proposed controller, the pressure control experiment was done. The dead zone of the servo valve used this time was estimated almost as $\theta_3 = 0.3$ [V], $\bar{\theta}_3 = 0.4$ [V] by experiment. The external reference r is a rectangular wave signal that changed at each 10[s], and the design parameter is $\alpha = 3$. We examined the PI controller and the normal adaptive controller without dead zone compensation[5] as well as proposed

controller. The PI control parameters are determined by try and error.

The experimental result that the maximum reference pressure is set to 3[MPa] is shown in Figure 3. From this figure, the normal adaptive controller without dead zone compensation shows lower performance in reference signal change. The PI controller have better tracking performance, however, the small vibration can be seen around zero reference pressure for dead zone. The proposed adaptive controller shows best tracking performance for both reference signal change and zero state.

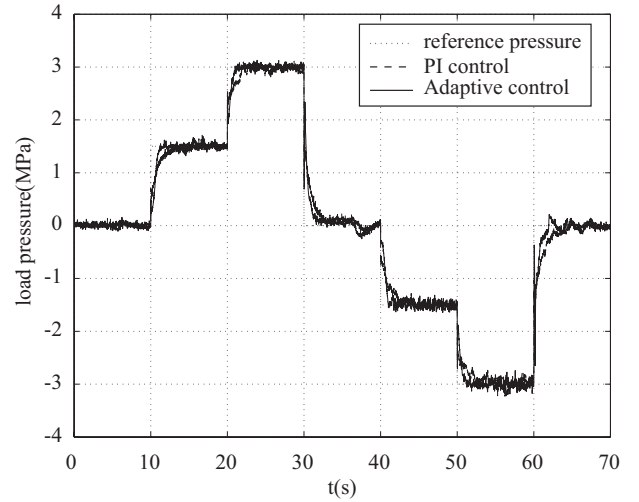


Figure 3: Experimental result: maximum reference pressure 3[MPa]

Another experimental result that maximum reference pressure is close to corresponding dead zone is shown in Figure 4. In this system, the dead zone corresponds to the pressure from +0.6[MPa] to -0.8[MPa] approximately. In

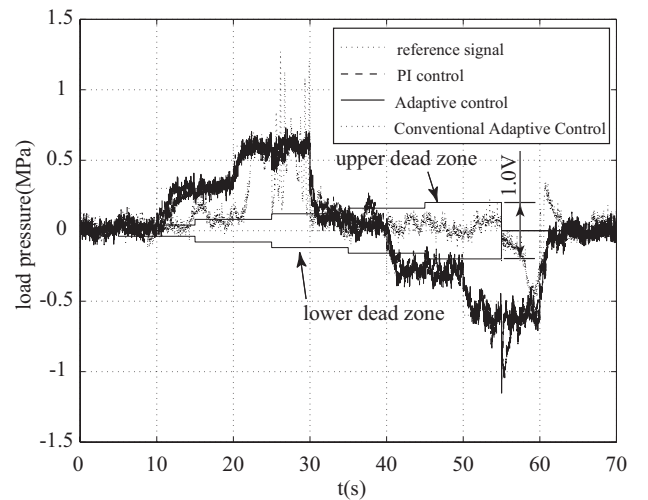


Figure 4: Experimental result: maximum reference pressure 0.6[MPa], with software dead zone

addition, the external stepwise software dead zone from 0 to 1.0[V] is also applied to examine the robustness of each controller. In this result, the sensor noise is relatively larger therefore the tracking performance becomes lower for all cases. The proposed controller can only almost keeps better tracking performance for smaller reference signal and software dead zone. And it also shows best performance on the 0 pressure regulation. It is observed that the normal adaptive controller fails reference tracking. This is on the fact that the adaptive controller is not possible have good approximation of nonlinear function with larger bias term by only the combination of linear and the square root functions. PI controller also shows lower performance than that shown in Figure 4 and the vibration becomes larger.

EXTENSION OF CONTROLLER

In previous section, it was assumed that the flow gain of the servo valve was known. However, this flow gain changes depending on the operation point generally, therefore we solve the design problem including the unknown flow gain estimation.

The flow gain is assumed to be θ_3 , $\bar{\theta}_3 (> 0)$ and nonlinear function $f(u)$ of the input of Eq.(1) is modified as follows (See Figure 5).

$$f(u) = \begin{cases} \theta_3(u - \theta_4) & , u \geq \theta_4 \\ 0 & , -\bar{\theta}_4 \leq u \leq \theta_4 \\ \bar{\theta}_3(u + \bar{\theta}_4) & , u \leq -\bar{\theta}_4 \end{cases} \quad (11)$$

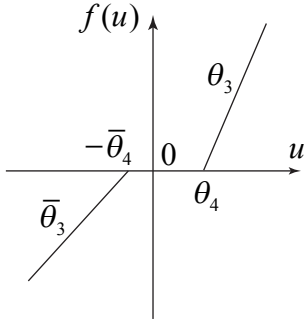


Figure 5: Dead zone of servo valve with unknown flow gain

Adaptive Controller Design

The modified error system is given by

$$\dot{e} = -\alpha e + \alpha(p-r) - \text{sgn}(p)\theta_1\sqrt{|p|} - \theta_2 p + \begin{cases} \theta_3(u - \theta_4) & , u \geq \theta_4 \\ 0 & , -\bar{\theta}_4 \leq u \leq \theta_4 \\ \bar{\theta}_3(u + \bar{\theta}_4) & , u \leq -\bar{\theta}_4 \end{cases} \quad (12)$$

Motivated by R.Marino's idea, the inverse parameters are introduced to estimate θ_3 , $\bar{\theta}_3$ [6].

Case (i) : $u \geq \theta_4$

Defining the adaptive parameter $\hat{\theta}_i$ ($i = 1, \dots, 4$), we construct the adaptive input as

$$u = \hat{\theta}_4 + \frac{v}{\hat{\theta}_3} \quad (13)$$

$$v = -\alpha(p-r) + \text{sgn}(p)\hat{\theta}_1\sqrt{|p|} + \hat{\theta}_2 p \quad (14)$$

Then error dynamics can be expressed as

$$\begin{aligned} \dot{e} &= -\alpha e + \alpha(p-r) - \text{sgn}(p)\theta_1\sqrt{|p|} - \theta_2 p \\ &\quad + \theta_3(\hat{\theta}_4 - \theta_4) + \frac{\theta_3}{\hat{\theta}_3} v \\ &= -\alpha e + \alpha(p-r) - \text{sgn}(p)\theta_1\sqrt{|p|} - \theta_2 p \\ &\quad - \theta_3\tilde{\theta}_4 + \frac{\tilde{\theta}_5}{\hat{\theta}_3} v \end{aligned}$$

where $\tilde{\theta}_i = \theta_i - \hat{\theta}_i$ ($i = 1, \dots, 5$) and

$$\theta_5 = \frac{1}{\theta_3}, \quad \hat{\theta}_5 = \frac{1}{\hat{\theta}_3} \quad (15)$$

Therefore

$$\begin{aligned} \dot{e} &= -\alpha e + \alpha(p-r) - \text{sgn}(p)\theta_1\sqrt{|p|} - \theta_2 p \\ &\quad - \theta_3\tilde{\theta}_4 + \left(1 - \frac{\tilde{\theta}_5}{\hat{\theta}_3}\right) v \\ &= -\alpha e - \text{sgn}(p)\tilde{\theta}_1\sqrt{|p|} - \tilde{\theta}_2 p - \theta_3\tilde{\theta}_4 - \frac{\tilde{\theta}_5}{\hat{\theta}_3} v \\ &= -\alpha e - \text{sgn}(p)\tilde{\theta}_1\sqrt{|p|} - \tilde{\theta}_2 p + \tilde{\theta}_3 \frac{v}{\hat{\theta}_3} - \tilde{\theta}_4\theta_3 \end{aligned} \quad (16)$$

We give a positive definite function

$$V_1 = \frac{1}{2} \left(e^2 + \sum_{i=1}^4 \frac{1}{c_i} \tilde{\theta}_i^2 \right), \quad c_i > 0 \quad (17)$$

and evaluate its time derivative along the solution of Eq.(16):

$$\begin{aligned} \dot{V}_1 &= -\alpha e^2 - \frac{\tilde{\theta}_1}{c_1} \left(\dot{\hat{\theta}}_1 + c_1 \text{sgn}(p)\sqrt{|p|}e \right) \\ &\quad - \frac{\tilde{\theta}_2}{c_2} \left(\dot{\hat{\theta}}_2 + c_2 p e \right) \\ &\quad - \frac{\tilde{\theta}_3}{c_3} \left(\dot{\hat{\theta}}_3 - c_3 \frac{v}{\hat{\theta}_3} e \right) - \frac{\tilde{\theta}_4}{c_4} \left(\dot{\hat{\theta}}_4 + c_4 \theta_3 e \right) \end{aligned}$$

Noticing that all unknown parameters are positive, we have parameter update law:

$$\begin{aligned} \dot{\hat{\theta}}_1 &= -c_1 \text{sgn}(p)\sqrt{|p|}e, \quad \dot{\hat{\theta}}_2 = -c_2 p e, \\ \dot{\hat{\theta}}_3 &= c_3 \frac{v}{\hat{\theta}_3} e, \quad \dot{\hat{\theta}}_4 = -c_4 e \end{aligned} \quad (18)$$

Eq.(18) guarantees e goes to 0 and the boundedness of all signal in pressure control system.

Case (ii) : $u \leq -\hat{\theta}_4$

Different from **Case (i)**, we give the input as

$$u = -\hat{\theta}_4 + \frac{v}{\hat{\theta}_3} \quad (19)$$

$$v = -\alpha(p-r) + \text{sgn}(p)\hat{\theta}_1\sqrt{|p|} + \hat{\theta}_2p \quad (20)$$

Similarly, defining $\tilde{\theta}_j = \bar{\theta}_j - \hat{\theta}_j$ ($j = 3, 4, 5$) and we introduce

$$\bar{\theta}_5 = \frac{1}{\bar{\theta}_3}, \quad \hat{\theta}_5 = \frac{1}{\hat{\theta}_3} \quad (21)$$

Then we have the error dynamics and Lyapunov-like function as

$$\dot{e} = -\alpha e - \text{sgn}(p)\tilde{\theta}_1\sqrt{|p|} + \hat{\theta}_2p + \tilde{\theta}_3\frac{v}{\hat{\theta}_4} + \tilde{\theta}_4\bar{\theta}_3 \quad (22)$$

$$V_2 = \frac{1}{2} \left(e^2 + \frac{1}{c_1}\tilde{\theta}_1^2 + \frac{1}{c_2}\tilde{\theta}_2^2 + \sum_{i=3}^4 \frac{1}{c_i}\tilde{\theta}_i^2 \right), \quad c_i > 0 \quad (23)$$

To make $\dot{V}_2 < 0$, we have the parameter update law

$$\begin{aligned} \dot{\hat{\theta}}_1 &= -c_1 \text{sgn}(p)\sqrt{|p|}e, \quad \dot{\hat{\theta}}_2 = -c_2pe, \\ \dot{\hat{\theta}}_3 &= c_3\frac{v}{\hat{\theta}_3}e, \quad \dot{\hat{\theta}}_4 = c_4e \end{aligned} \quad (24)$$

With Eq.(24), we arrive same result in Case (i).

Case (iii) : $-\hat{\theta}_4 \leq u \leq \hat{\theta}_4$

Similar to the previous section, we can show that the input signal surpass the dead zone after finite time even if the magnitude of input u becomes smaller than the dead zone.

In this control system, we have the Lyapunov-like function

$$V = \frac{1}{2}(V_1 + V_2) \quad (25)$$

for whole system. Note that if Case (ii) is turned off when Case (i) is valid and vice versa depending on in which side the spool is. Then the following theorem is obtained from the above discussion.

Theorem 2 Consider the pressure control system with dead zone Eq.(1),(11) and desired pressure model Eq.(4). The adaptive input Eq.(13),(14),(19),(20) and parameter update law Eq.(18),(24) solve the Problem 1. ■

Remark 1 In this design, some technical routine preventing from $\hat{\theta}_3, \hat{\theta}_3$ being divided by zero are needed in applications. ■

Numerical Examples

Figure 6 and Figure 7 show the numerical simulation of

pressure control and the input signal obtained by the proposed technique. The design parameter is set to $\alpha = 3$. The control performance is good even for small reference signal. The transient delay can be observed when the reference signature changes, however, this diminishes as adaptation develops. The adaptive control input also generate reasonable magnitude signal.

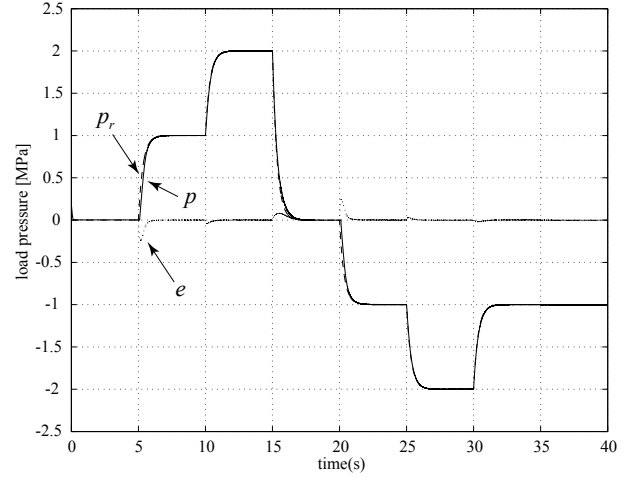


Figure 6: Simulation result: pressure error

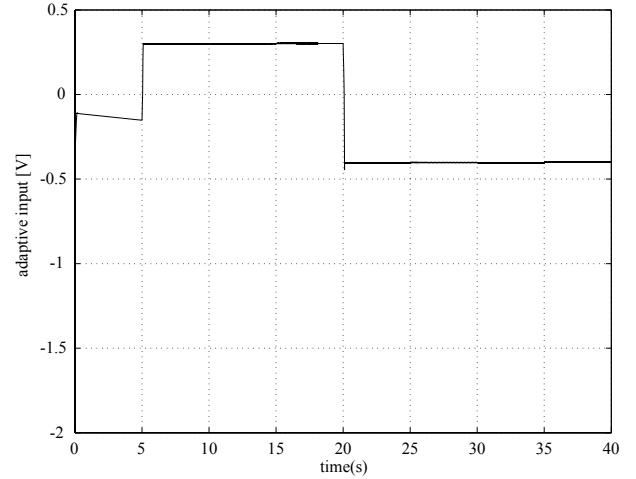


Figure 7: Simulation result: adaptive input

CONCLUSIONS

In this paper, two designs of adaptive controller for pressure tracking of servo valve with dead zone are discussed. Both methods compensate the dead zone directly. The effectiveness of former controller was evaluated in experiment and it is shown that the tracking performance is rather good for small reference pressure comparing with PI or conventional adaptive controller. Motivated by

R.Marino's idea, the latter method can accommodate unknown flow gain and simulation result show good performance. In future, we will obtain the experimental result on latter method and also for water hydraulic motor and water hydraulic cylinder control with these two control strategy.

References

- [1] Nishiumi, T., Katoh, H. and Konami, S, Quasi-Adaptive Position Control of an Electro-Hydraulic Servo Motor System Using Neural Network Approach, Proc. of 2nd Int. Workshop on Computer Software Design, 2001, Analysis and Control of Fluid Power Systems, pp.116-123.
- [2] Katoh, H., Nishiumi, T. and Konami, S., Precise Positioning Control For A Hydraulic Motor System With Dead Zone Using A State Feedback Neural Network, Proceedings of the 5th JFPS International Symposium on Fluid Power, 2002, Nov.13-15, pp.199-204, Nara.
- [3] Recker, D.A., Indirect Adaptive Nonlinear Control of Discrete Time System Containing a Deadzone, Int. J. of Adaptive Control and Signal Processing, 1997, Vol.11, No.1, pp.33-48.
- [4] Khalil, H.K. *Nonlinear Systems* 2nd Edit., Prentice Hall, 1996.
- [5] Landau, Y.D., *Adaptive Control –The Model Reference Approach–*, Marcel Dekker Inc., 1979
- [6] Marino, R., Shen, T. and Verreli, C.M., Robust transient stabilization of a synchronous generator with parameter uncertainty, Proceedings European Control Conference, 2003, Cambridge, pp.1-4.

FEEDBACK LINEARISATION APPLIED ON A HYDRAULIC SERVO SYSTEM

Torben O. Andersen¹, Michael R. Hansen², Henrik C. Pedersen³, Finn Conrad⁴

^{1,3} Institute of Energy Technology, Aalborg University
Pontoppidanstraede 101, DK-9220 Aalborg East, Denmark
(E-mail: toa@iet.aau.dk)

² Institute of Mechanical Engineering, Aalborg University
Pontoppidanstraede 105, DK-9220 Aalborg East, Denmark

⁴ Department of Mechanical Engineering, Technical University of Denmark
Nils Koppels Allé, DTU-bygning 404, DK-2800 Lyngby, Denmark

ABSTRACT

Generally most hydraulic systems are intrinsically non-linear, why applying linear control techniques typically results in conservatively dimensioned controllers to obtain stable performance. Non-linear control techniques have the potential of overcoming these problems, and in this paper the focus is on developing and applying several different feedback linearisation (FL) controllers to the individual servo actuators in a hydraulically driven servo robot to evaluate and compare their possibilities and limitations. This is done based on both simulation and experimental results.

KEYWORDS

Feedback linearisation, hydraulic servo system.

NOMENCLATURE

A_p	:	Cylinder piston area
B_t	:	Viscous friction coefficient
C_L	:	Leakage coefficient
F_L	:	External load force on the piston
K_v	:	Valve discharge coefficient
M_{eq}	:	Equivalent mass being accelerated
p_A, p_B	:	Cylinder chamber pressures
p_L	:	Load pressure, defined as $p_L = p_A - p_B$
p_S	:	Supply pressure
p_T	:	Tank pressure
u	:	Control signal to servo valve
x_P	:	Cylinder piston position
V_A, V_B	:	Volume in cylinder chambers
β_F	:	Effective oil bulk modulus

INTRODUCTION

In the last decades electrical drives have become increasingly popular, due to the advances in power electronics and frequency inverters, but hydraulic servo-systems still find a variety of applications in industrial motion control due to its high size-to-torque ratio [1]-[4]. The use of hydraulics is for instance still widespread in areas of machining plants, mining etc. [5]. Often however, these hydraulic drives are controlled using linear controllers, which degrade the obtainable performance of the drive, as most hydraulic systems are intrinsically non-linear and have time-varying parameters. The non-linearities, combined with large parameter ranges means that is difficult to achieve satisfactory performance, as the linear controllers have to be dimensioned conservatively to

ensure stability. In addition, the natural damping in these system are in general very low. Non-linear control techniques have the potential of overcoming these problems, and in this paper, the problem of tracking control of electro-hydraulic servo actuators using feedback linearisation applied to a hydraulically driven test robot is addressed. In its simplest form, feedback linearisation in this way amounts to cancelling the non-linearities in a non-linear system, so that the closed-loop dynamics become linear and may hence be controlled by linear controllers.

SYSTEM DESCRIPTION

The system considered in this paper is a two degrees-of-freedom rotary arm manipulator with a high-frequency servo valve controlled hydraulic cylinder driving each link. An illustration of the system is shown in Figure 1. This system is, as many hydraulic systems, characterised by the highly non-linear nature of the servo valve pressure/flow characteristic, friction effects, a very low damping ratio and dynamics that strongly depends on the operating point and the physical parameters describing the system.

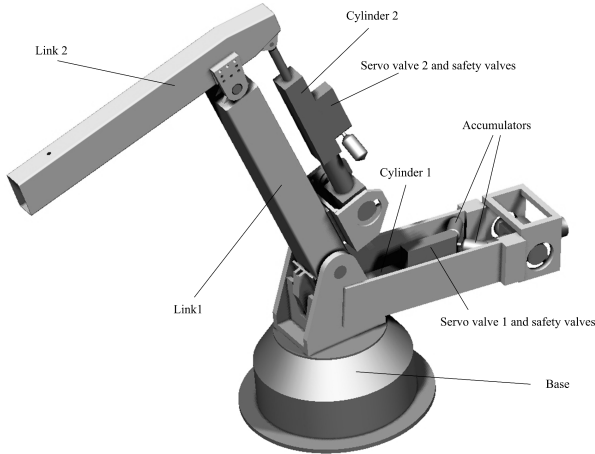


Figure 1 3D illustration of the hydraulic servo robot used as test case.

Considering each of the servo valve controlled cylinders separately, these may be model by the following equations. The force balance equation applied to the cylinder piston is given by:

$$M_{eq}\ddot{x}_P = p_L A_P - B_t \dot{x}_P - F_L \quad (1)$$

Neglecting the dynamics of the servo valve, the flow

through the servo valve may be described by:

$$Q_A = \begin{cases} K_v u \text{sign}(p_S - p_A) \sqrt{|p_S - p_A|} & , u \geq 0 \\ K_v u \text{sign}(p_S - p_B) \sqrt{|p_S - p_B|} & , u < 0 \end{cases} \quad (2)$$

$$Q_B = \begin{cases} K_v u \text{sign}(p_B - p_T) \sqrt{|p_B - p_T|} & , u \geq 0 \\ K_v u \text{sign}(p_A - p_T) \sqrt{|p_A - p_T|} & , u < 0 \end{cases}$$

The cylinder chamber pressures are found from the continuity equation:

$$\dot{p}_A = \frac{\beta_F}{V_{A,0} + A_P x_P} (Q_A - A_P \dot{x}_P - C_L p_L) \quad (3)$$

$$\dot{p}_B = \frac{\beta_F}{V_{B,0} - A_P x_P} (A_P \dot{x}_P - Q_B + C_L p_L) \quad (4)$$

INPUT-OUTPUT LINEARISATION OF THE HSS MODEL

The above model is the basis for the input-output linearisation. Representing this as a state model, with the state vector $\underline{x} = [x_P \ \dot{x}_P \ p_A \ p_B]^T$:

$$\dot{\underline{x}} = \begin{bmatrix} x_2 \\ \frac{1}{M_{eq}} (A_P (x_3 - x_4) - B_t x_2 - F_L) \\ \frac{\beta_F}{V_A} (-A_P x_2 - C_L (x_3 - x_4)) \\ \frac{\beta_F}{V_B} (A_P x_2 + C_L (x_3 - x_4)) \end{bmatrix} + \begin{bmatrix} 0 \\ 0 \\ \frac{\beta_F}{V_A} H(x_3, x_4) \\ -\frac{\beta_F}{V_B} I(x_3, x_4) \end{bmatrix} u \quad (5)$$

where $H(x_3, x_4) = Q_A$ and $I(x_3, x_4) = Q_B$ are the flow expressions given by Eq. (2).

Compensation of Pressure Dynamics

In the following the feedback linearisation approach will be used to compensate for non-linearities related to the pressure dynamics. This is done by considering only the part of the model, with the state vector $\underline{x}^T = [p_A \ p_B]$:

$$\dot{\underline{x}} = \begin{bmatrix} \frac{\beta_F}{V_A} (-A_P x_2 - C_L (x_3 - x_4)) \\ \frac{\beta_F}{V_B} (A_P x_2 + C_L (x_3 - x_4)) \end{bmatrix} + \begin{bmatrix} \frac{\beta_F}{V_A} H(x_3, x_4) \\ -\frac{\beta_F}{V_B} I(x_3, x_4) \end{bmatrix} u \quad (6)$$

Define the output as the force:

$$y = A_P (p_A - p_B) = A_P (x_3 - x_4) \quad (7)$$

Following the approach in [6], we set up the quantities:

$$\nabla h = [A_P \quad -A_P] \quad (8)$$

$$L_g h = \nabla h g \quad (9)$$

$$= \frac{\beta_F A_P}{V_A} H(x_3, x_4) + \frac{\beta_F A_P}{V_B} I(x_3, x_4)$$

$$L_f h = \nabla h f \quad (10)$$

$$= \left(\frac{\beta_F A_P}{V_A} - \frac{\beta_F A_P}{V_B} \right) (-A_P x_2 - C_L(x_3 - x_4))$$

where $L_f h$ is the Lie derivative of the scalar function h with regard to the vector function f . The Lie derivative and repeated Lie derivatives being defined as:

$$L_f h = \nabla h f = \frac{\partial h}{\partial \underline{x}} f(\underline{x}) \quad (11)$$

$$L_f^i h = L_f(L_f^{i-1} h) = \nabla(L_f^{i-1} h) f \quad i = 1, 2, \dots \quad (12)$$

with $\nabla = \left[\frac{\partial}{\partial x_1} \quad \frac{\partial}{\partial x_2} \quad \dots \quad \frac{\partial}{\partial x_n} \right]$ denoting the gradient operator.

Since $L_g h \neq 0$ the control law is selected as:

$$u = \frac{1}{L_g h(\underline{x})} (-L_f h(\underline{x}) + \nu) \quad (13)$$

which yields a force tracking system that converges exponentially to zero, if the desired force trajectory and its first derivative is known. If the control law is substituted into the system it results in the feedback linearised system:

$$\dot{y} = A_P(\dot{x}_3 - \dot{x}_4) = \nu \quad (14)$$

The plant describing the piston position is given by Eq. (5). Hereby the last two equations are feedback linearised by the control law in Eq. (13), and the first two equations, describing the motion of the piston, are linear. Differentiating the second equation of the system yields:

$$\begin{aligned} \ddot{x}_P = \ddot{x}_2 &= \frac{1}{M_{eq}} \left(A_P(\dot{x}_3 - \dot{x}_4) - B_t \dot{x}_2 - \dot{F}_{ext} \right) \\ &= \frac{1}{M_{eq}} \left(\nu - B_t \dot{x}_2 - \dot{F}_{ext} \right) \end{aligned} \quad (15)$$

or:

$$M_{eq} \ddot{x}_P + B_t \dot{x}_P + K = \nu \quad (16)$$

where K denotes the external forces and disturbances.

Controller Design

The above feedback linearisation yields a system model described by Eq. (16). The control law is selected as:

$$\begin{aligned} \nu &= \hat{M}_{eq}(\ddot{x}_d - k_a \ddot{e} - k_v \dot{e} - k_p e) + \hat{B}_t \dot{x}_P + \hat{K} \\ &= \underline{v}^T \hat{\underline{a}} \end{aligned} \quad (17)$$

where $\underline{v}^T = [\ddot{x}_d - k_a \ddot{e} - k_v \dot{e} - k_p e \quad \dot{x}_P \quad 1]$ and $\hat{\underline{a}}^T = [\hat{M}_{eq} \quad \hat{B}_t \quad \hat{K}]$. The constants \hat{M}_{eq} , \hat{B}_t and \hat{K} are estimates of the true values. If $\tilde{\underline{a}}$ is defined as $\hat{\underline{a}} - \underline{a}$, Eq. (17) can be rewritten as:

$$M_{eq}(\ddot{e} + k_a \ddot{e} + k_v \dot{e} + k_p e) = \underline{v}^T \tilde{\underline{a}} = \tilde{\underline{a}}^T \underline{v} \quad (18)$$

which, if Laplace transformed yields:

$$e = \frac{1}{s^3 + k_a s^2 + k_v s + k_p} [M_{eq}^{-1} \underline{v}^T \tilde{\underline{a}}] \quad (19)$$

If $\hat{\underline{a}} = \underline{a} \Rightarrow \tilde{\underline{a}} = 0$ resulting in exponential decay of the error.

The closed-loop error dynamics of Eq. (18) can be described by the following state-space equation:

$$\begin{aligned} \dot{\underline{x}} &= \underline{A} \underline{x} + \underline{B} \left[\frac{1}{M_{eq}} \tilde{\underline{a}}^T \underline{v} \right] \\ e &= \underline{C} \underline{x} \end{aligned} \quad (20)$$

where:

$$\begin{aligned} \underline{x} &= \begin{bmatrix} e \\ \dot{e} \\ \ddot{e} \end{bmatrix}, \underline{A} = \begin{bmatrix} 0 & 1 & 0 \\ 0 & 0 & 1 \\ -k_a & -k_v & -k_p \end{bmatrix} \\ \underline{B}^T &= [0 \quad 0 \quad 1], \underline{C} = [1 \quad 0 \quad 0] \end{aligned} \quad (21)$$

When designing the controller the constants k_a , k_v and k_p can be found by pole placement of the system in Eq. (20). Summarised the feedback linearised pressure controller (FLPC) is implemented as:

$$u = \frac{1}{L_g h(\underline{x})} (-L_f h(\underline{x}) + \nu) \quad (22)$$

$$\nu = \hat{M}_{eq}(\ddot{x}_d - k_a \ddot{e} - k_v \dot{e} - k_p e) + \hat{B}_t \dot{x}_P + \hat{K}$$

where

$$L_g h = \nabla h g = \frac{\beta_F A_P}{V_A} H(x_3, x_4) + \frac{\beta_F A_P}{V_B} I(x_3, x_4)$$

$$\begin{aligned} L_f h &= \nabla h f \\ &= - \left(\frac{\beta_F A_P}{V_A} + \frac{\beta_F A_P}{V_B} \right) (A_P x_2 + C_L(x_3 - x_4)) \end{aligned}$$

Using this controller as a pure state feedback, simulated position tracking errors may be seen in Figure 2. The errors are plotted when applying a sinusoidal reference input for both the two cylinders, making these move from one end position to the other and back in three seconds. To test robustness a mass step of 50 [kg] is applied to the tool center point of the test robot after 6 seconds.

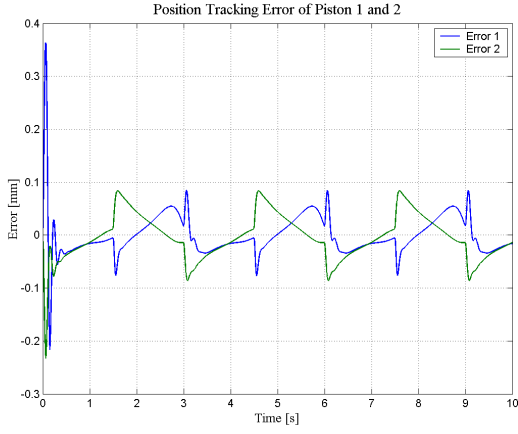


Figure 2 Simulated errors of HSS 1 and HSS 2 using the FLPC. A mass step of 50 [kg] is applied after 6 [s].

A SIMPLIFIED FL CONTROLLER (FLSC)

The strategy derived above requires measurement of the piston acceleration, and in this section a simplified model is derived. This is done by neglecting the pressure dynamics in the cylinder chambers, assuming the pressure build up to be instantaneous, whereby the flow from the servo-valve is set equal to the displacement flow of the cylinder piston. Neglecting the pressure dynamics yields:

$$A_P \dot{x}_P + C_{LP} p_L = \frac{K_v}{\sqrt{2}} u \sqrt{p_S - p_T - \text{sign}(u) p_L} \quad (23)$$

Why the control law u is chosen as:

$$u = \frac{\sqrt{2} A_P (\nu - \lambda p_{Lx})}{K_v \sqrt{p_S - p_T - \text{sign}(u) p_L}} \quad (24)$$

where p_{Lx} is the load pressure (applied by the feedback linearisation) and λ is a scaling factor. Equation (23) can now be written as:

$$A_P \dot{x}_P + C_{LP} p_L = A_P (\nu - \lambda p_{Lx}) \Leftrightarrow \quad (25)$$

$$p_{Lx} = -\frac{A_P \dot{x}_P + C_{LP} p_L - A_P \nu}{A_P \lambda} \quad (26)$$

Substituting the load pressure p_{Lx} into the motion Eq. (1) gives:

$$M \ddot{x}_P = A_P p_{Lx} - B_t \dot{x} - F_L \Rightarrow$$

$$\begin{aligned} \nu &= \frac{M \lambda}{A_P} \ddot{x}_P + \frac{B_t \lambda + A_P}{A_P} \dot{x}_P + \frac{F_L \lambda + C_{LP} p_L}{A_P} \\ &= a_1 \ddot{x}_P + a_2 \dot{x}_P + a_3 \end{aligned} \quad (27)$$

If the theory, used in the previous section, is applied to the this second-order system, the control law becomes:

$$\nu = \hat{a}_1 (\ddot{x}_d - k_v \dot{e} - k_p e) + \hat{a}_2 \dot{x}_P + \hat{a}_3 = \underline{v}^T \underline{\hat{a}} \quad (28)$$

where $\underline{v}^T = [\ddot{x}_d - k_v \dot{e} - k_p e \quad \dot{x}_P \quad 1]$, $\underline{\hat{a}}^T = [\hat{a}_1 \quad \hat{a}_2 \quad \hat{a}_3]$ and the constants \hat{a}_1 , \hat{a}_2 and \hat{a}_3 are estimates of the true values.

This results in a system, where the closed-loop error dynamics can be described by the following state-space equation:

$$\begin{aligned} \dot{\underline{x}} &= \underline{A} \underline{x} + \underline{B} \left[\frac{1}{a_1} \underline{\hat{a}}^T \underline{v} \right] \\ e &= \underline{C} \underline{x} \end{aligned} \quad (29)$$

with:

$$\begin{aligned} \underline{x} &= \begin{bmatrix} e \\ \dot{e} \end{bmatrix}, \underline{A} = \begin{bmatrix} 0 & 1 \\ -k_v & -k_p \end{bmatrix} \\ \underline{B}^T &= [0 \quad 1], \underline{C} = [1 \quad 0] \end{aligned} \quad (30)$$

Summarised the controller is implemented as:

$$u = \frac{\sqrt{2} A_P (\nu - \lambda p_{Lx})}{K_v \sqrt{p_S - p_T - \text{sign}(u) p_L}} \quad (31)$$

where

$$\nu = \hat{a}_1 (\ddot{x}_d - k_v \dot{e} - k_p e) + \hat{a}_2 \dot{x}_P + \hat{a}_3$$

Adjusting the controller parameters based on pole placement, with the desired pole locations being $\sigma = -100 \pm 40i$, simulated position tracking errors are shown in Figure 3.

Experimental Results of the FLSC

To verify the performance of the controller, this is implemented and tested on the laboratory setup. Implementation of the algorithm showed sensitivity to noise in both the position and pressure signals, why both of these had to be filtered using second-order digitally implemented filters. As a consequence hereof the controller parameters needed to be changed, so the poles were placed as $\sigma = -20 \pm 20i$, which degraded the performance of the controller. Experimental measurements using this controller are shown in Figure 4.

Comparing the simulated and the experimental results it is seen that the measured tracking errors are approximately an order of magnitude larger than the simulated due to the readjusted controller parameters.

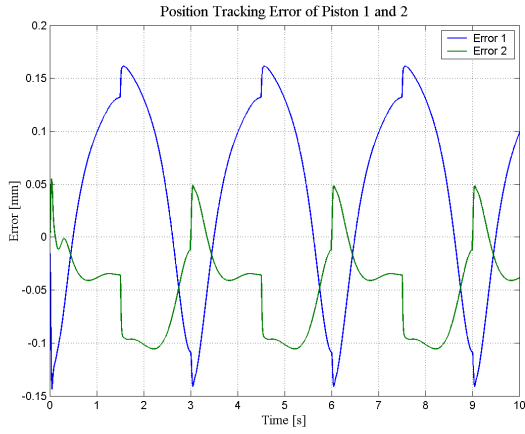


Figure 3 Simulated errors of HSS 1 and HSS 2 using the FLSC.

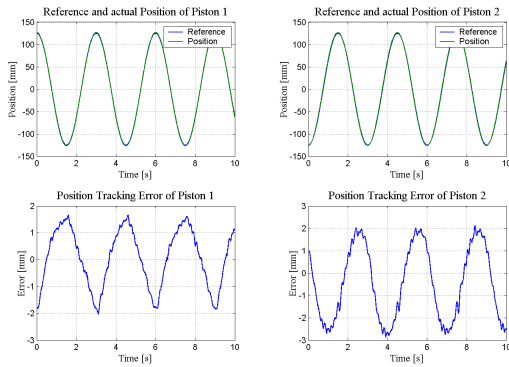


Figure 4 Errors of HSS 1 and HSS 2 using the FLSC on the laboratory setup.

ADAPTIVE FEEDBACK LINEARISED SECOND-ORDER CONTROLLER (AFLSC)

In the previous section the system parameters are estimated and consequently the controller the parameters are adjusted conservatively. In order to compensate for these parameter variations an adaptive controller has been implemented. For the error equation (29), a standard adaptive control law including both an “integral” and a “proportional” part is chosen to:

$$\hat{\underline{a}} = -\text{sign}(a_1^{-1})\gamma e \underline{v} - \text{sign}(a_1^{-1})\alpha \frac{d}{dt}(e \underline{v}), \quad \gamma, \alpha > 0 \quad (32)$$

The controller with adaptation capabilities to account for unmodelled dynamics is thus implemented as:

Control law (AFLSC):

$$u = \frac{\sqrt{2}A_P(\nu - \lambda p_{Lx})}{K_v \sqrt{p_S - p_T - \text{sign}(u)p_L}} \quad (33)$$

where

$$\nu = \hat{a}_1(\ddot{x}_d - k_v \dot{e} - k_p e) + \hat{a}_2 \dot{x}_P + \hat{a}_3$$

Adaptation law (AFLSC, expanded):

$$\begin{bmatrix} \dot{\hat{a}}_{1q} \\ \dot{\hat{a}}_2 \\ \dot{\hat{a}}_3 \end{bmatrix} = \begin{bmatrix} \dot{\hat{a}}_1 \\ \dot{\hat{a}}_2 \\ \dot{\hat{a}}_3 \end{bmatrix} = \begin{bmatrix} c_1 \\ -\gamma_2 e \dot{x}_P - \alpha_2 \frac{d}{dt}(e \dot{x}_P) \\ -\gamma_3 e - \alpha \frac{d}{dt}(e) \end{bmatrix}$$

with $c_1 = -\gamma_1 e(\ddot{x}_d - k_v \dot{e} - k_p e) - \alpha_1 \frac{d}{dt}(e(\ddot{x}_d - k_v \dot{e} - k_p e))$.

A schematic illustration of the implementation is shown in fig. 5. Simulation results for this controller are shown in fig. 6 and experimental results are given in fig. 7.

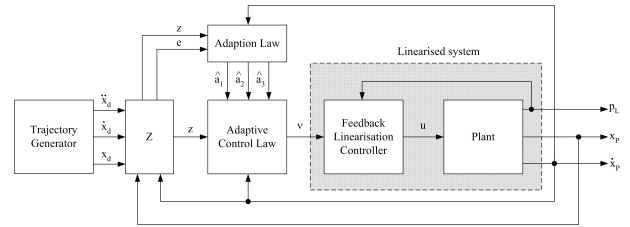


Figure 5 Block diagram of the system using the AFLSC.

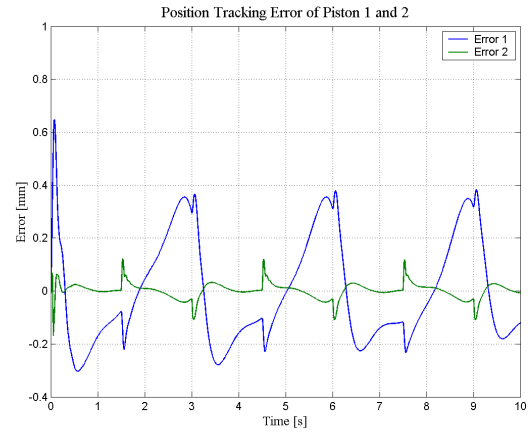


Figure 6 Simulated errors of HSS 1 and HSS 2 using the AFLSC.

As seen from the results the performance of the AFLSC is very good and the steady-state errors on both cylinder

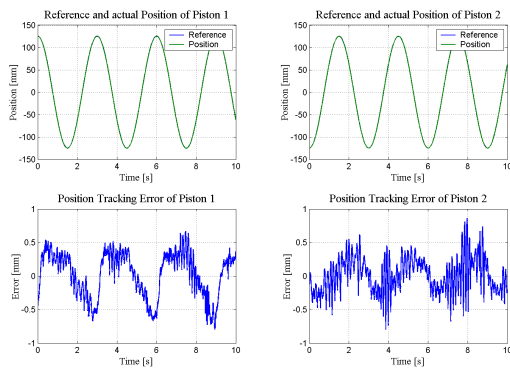


Figure 7 Errors of HSS 1 and HSS 2 using the AFLSC on the laboratory setup.

pistons are limited to ± 0.5 mm. From the position tracking errors, shown in fig. 7, it may be seen that it is very chattered, due to the velocity signal being obtained by differentiating the position signal and filtering.

CONCLUSIONS

The focus of this paper has been the development and comparison of several feedback linearisation controllers applied on a hydraulic servo robot. In the first controller (FLPC) a part of the model was linearised, namely the pressure dynamics. This linearisation results in a linear control system, but with varying inertia, which showed good performance both in the case of varying parameters and robustness to load changes. The disadvantages of the controller is the number of needed state measurements. The second controller (FLSC) was based on a model reduced to a second-order system, by neglecting the pressure dynamics. The controller showed very good performance in the simulation, but was sensitive to noise in the laboratory, why the controller parameters had to be retuned, decreasing the performance considerably.

To improve the performance of the FLSC, the AFLSC was developed by adding an adaptive control scheme, whereby the performance was improved significantly. Though the AFLSC is fairly complex, the controller parameters are easily adjusted. Common for the controllers considered are that they are very robust to mass variations, as a stepwise increase in the tool centre point mass by 50 [kg] has no significant influence on the resulting position tracking error response.

REFERENCES

- [1] Edge K.A., On the Control of Electrohydraulic Systems - Some Recent Research Contributions, The Eight Scandinavian International Conference on Fluid Power, SICFP'05, May 7-9, Tampere, Finland.
- [2] DeBoer C.C., Yao B., Velocity Control of Hydraulic Cylinders with only Pressure Feedback. School of Mechanical Engineering, Purdue University, IMECE01/DSC-2B-3, ASME International Mechanical Engineering Congress and Exposition New York, November 2001.
- [3] Hansen P.E., Autonomous and Adaptive Control of Hydraulic Actuator Systems. Department of Control and Engineering Design, Technical University of Denmark, PhD Dissertation, October 1997.
- [4] Andersen T.O., Hansen M.R., Pedersen H.C., Conrad F., On the Control of Hydraulic Servo Systems - Evaluation of Linear and Non-Linear Control Schemes, To be presented at The Ninth Scandinavian International Conference on Fluid Power, SICFP'05, June 1-3, 2005, Linköping, Sweden.
- [5] Jelali M., Kroll A. Hydraulic Servo-systems - Modelling, Identification and Control. ISBN: 1-85233-692-7, Springer Verlag London 2003.
- [6] Slotine E. J.-J., Li W. Applied Nonlinear Control. ISBN: 0-13-040890-5, Prentice-Hall, Inc. New Jersey 1991.

A SLIDING MODE FUZZY FORCE TRACKING CONTROLLER FOR PNEUMATIC CYLINDERS

Bin XU*, Yasuhiro HAYAKAWA** and Shunmugham R. PANDIAN*

* Department of Electrical Engineering and Computer Science
Tulane University
New Orleans, LA 70118, USA
(E-mail: bxu@tulane.edu)

** Department of Electrical and Control Engineering
Nara National College of Technology
Nara 639-1058, Japan

ABSTRACT

The problem of control of force exerted by pneumatic cylinders on the environment is of interest in industrial automation and systems such as legged robots. In this paper, a sliding mode fuzzy force control algorithm is proposed for pneumatic cylinders. The environment is assumed to be “soft” or compliant and modeled as a spring. The advantage of the new controller is that being based on fuzzy logic, knowledge of the cylinder dynamics or disturbances such as friction is not necessary. The control law implementation is based explicitly on contact force measurements. The proposed algorithm is simple, robust, and easy to implement. Results of experimental implementation are presented to illustrate the practical effectiveness of the new method.

KEY WORDS

Fuzzy force control, Sliding mode, Pneumatic cylinders, Soft environment

INTRODUCTION

Pneumatic actuators and systems are widely used in industrial automation because of their advantages of low-cost and high payload-to-weight/volume ratios. Further, they find applications in robotics, rehabilitation systems, as well as energy conversion.

However, further development and use of pneumatic actuators is limited by their difficulty of precise control. Pneumatic actuators have nonlinear, high-order dynamics and parametric uncertainties due to friction and air compressibility. The performance of conventional PID controller is limited under these conditions.

Accurate position and trajectory control of pneumatic actuators and air motors has been achieved by means of advanced control techniques such as sliding mode control and adaptive control, e.g. [1]-[3]. These techniques are developed based on full-order model-based compensation for the nonlinear dynamics which includes the chamber pressure dynamics. The performance achieved is comparable to that of conventional electric actuators [4].

Interaction with an environment is involved in many industrial assembly and automation operations, as well as systems such as legged robots and object handling.

Thus, the control of the contact force exerted on the environment is a major task. There are basically two types of environment: one is "hard" environment with infinite stiffness while the other is "soft" environment which undergoes deformation and can be modeled as spring, damper and mass system.

The problem of force control has been extensively studied for electrically actuated mechanisms and manipulators as well as hydraulic actuators, e.g. [5]-[6]. However, limited research has been conducted for the case of force control of pneumatic actuators and pneumatic robots, e.g. [7]-[10]. It has focused on linearized or nonlinear model-based force control and therefore is either limited in accuracy or complex to implement.

Intelligent control methods, using fuzzy, neural nets, or genetic algorithms, are well-suited for force control of pneumatic actuators, since they are not model-based and the environment is often unknown. However, research on intelligent control of pneumatic cylinders has mainly been limited to position control, e.g., [11]-[12].

The authors have recently applied the sliding mode control (SMC) approach to pneumatic cylinders in contact with a "hard" environment, i.e., the environment with infinite stiffness [13]. The SMC has advantages of simplicity, high performance, and robustness to matched uncertainties. However, in the absence of good model-based compensation – which requires knowledge of high-order system dynamics – the technique requires large switching gains which may lead to chattering and excitation of unmodeled dynamics. The adaptation of the switching gains further requires knowledge of system dynamics [2].

In this paper, we consider the force tracking control problem for pneumatic cylinders in contact with a "soft" environment, which is modeled as a spring of finite stiffness. In order to avoid modeling the high-order dynamics of cylinder and valves for controller design, we focus on the fuzzy logic approach for tuning gains. As is well known, fuzzy logic controllers are effective intelligent controllers for various applications, e.g., [14]. Because fuzzy controllers are often designed based on intuitive standpoint, they are often more understandable. However, due to the linguistic expression of fuzzy controller, it is difficult to guarantee the stability of control systems. Nevertheless, by designing sliding mode type fuzzy logic controller, the performance and stability can be ensured and meanwhile the number of fuzzy rules can be reduced [15].

The proposed sliding mode fuzzy controller (SMFC) has the advantages of not requiring knowledge of the cylinder and valve dynamics, and ensures precise and robust performance in the presence of disturbances through adaptation of switching gains and parameters. Experimental results are presented for an industrial-type cylinder to illustrate the effectiveness of the proposed SMFC.

DYNAMICS OF CYLINDRICAL ACTUATORS

Consider the schematic shown in Fig.1 of a pneumatic cylinder in contact with a soft environment modeled as a spring. Proportional servovalves are used at the two chambers to precisely control the air flow.

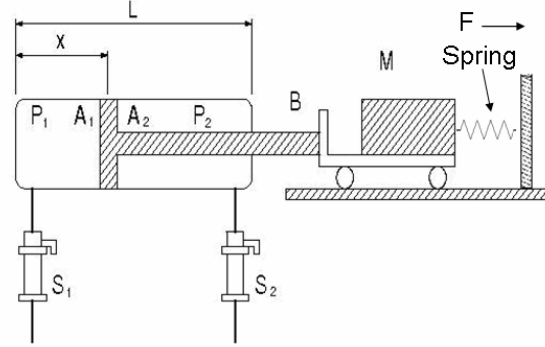


Figure 1. Model of cylindrical actuator

Here, P_1, P_2 are the chamber air pressures, A_1, A_2 are the ram areas, and S_1, S_2 are the valve cross-section areas. M is the mass of the external payload and the piston, and B is the coefficient of viscous friction and the damping. x is the position of the piston endpoint, and L is the stroke of the piston. F is the force exerted on the environment, represented here as a spring.

The dynamics of piston motion is given by

$$M\ddot{x} + B\dot{x} + d + F = A_1(P_1 - P_a) - A_2(P_2 - P_a) \quad (1)$$

where P_a is the atmospheric pressure, and d represents disturbance due to static and Coulomb friction. Assuming, without loss of generality, that $A_1 = A_2 = A$, the piston dynamics becomes

$$M\ddot{x} + B\dot{x} + d + F = A(P_1 - P_2) \quad (2)$$

Under the assumption of no friction, from Eq. (2) we have

$$P_1 - P_2 \equiv \Delta P = \frac{1}{A}(M\ddot{x} + B\dot{x} + F) \quad (3)$$

The dynamics of pressures P_1 and P_2 is expressed by nonlinear relations as [1]

$$\dot{P}_1 = \frac{f_1}{x} \frac{e_1}{h_1} u_1 - k \frac{\dot{x}}{x} P_1 \quad (4)$$

$$\dot{P}_2 = \frac{f_2}{(L-x)} \frac{e_2}{h_2} u_2 - k \frac{\dot{x}}{(L-x)} P_2 \quad (5)$$

where h_i and e_i are positive constants, f_1 and f_2 are nonlinear functions and u_i are voltage inputs to the valves ($i = 1, 2$).

Further, the valve dynamics is usually quite fast compared to the piston and pressure dynamics, and so can be neglected.

If the piston is in contact with the environment at x , the force on the environment can be modeled as a pure elastic restoring force as [5]

$$F = K(x - x_e) \quad (6)$$

where K is the coefficient of stiffness, and the equilibrium point of contact x_e is treated as constant for a stationary environment.

Equations (2)-(6) can be combined to express the system dynamics in terms of the contact force F and its derivatives. Model-based feedback (and feedforward) control for force tracking can then be designed using explicit force measurements. The details of this procedure are omitted here due to lack of space.

Note that the above dynamic equations are not used in the design of the SMFC. However, they can be used to obtain bounds on the switching gains and parameters of the controller as well as proof of stability.

DESIGN OF SLIDING MODE FUZZY FORCE CONTROLLER

Sliding Mode Controller

In the trajectory tracking problem, the force trajectory is required to track the reference force trajectory $F_r(t), t \in [0, T]$, where T is the terminal time. We assume that the desired force and its first two derivatives $\dot{F}_r(t), \ddot{F}_r(t)$ exist and are continuous over $t \in [0, T]$.

From the literature on force control of single and multiple manipulators, it is well known that integral force control provides both robustness and elimination of steady state error, e.g., [16]. So, we introduce an

additional state variable in the form of $\int_0^t F d\tau$.

Accordingly, the state vector of the resulting second-order system is defined as

$$\mathbf{X} = \left[\int F d\tau \quad F \right]^T \quad \text{and} \quad \mathbf{X}_r = \left[\int F_r d\tau \quad F_r \right]^T$$

Let the force tracking error be

$$\mathbf{E} = \left[\int \Delta F d\tau \quad \Delta F \right]^T = \mathbf{X}_r - \mathbf{X}$$

For the sliding mode controller, we choose a linear, time-invariant sliding surface as

$$s(t) = \mathbf{c}^T \mathbf{E} \quad (7)$$

where $\mathbf{c}^T = (c_1 \quad 1)$ and c_1 is a real constant. Note that on the sliding surface, $s(t) = 0$, which means that when the system state is on the sliding surface the system dynamics is of first order as

$$c_1 \int \Delta F d\tau + \Delta F = 0$$

Therefore, by choosing $c_1 > 0$, we can ensure that the reduced-order subsystem is stable on the sliding surface. Next, we choose the switching feedback gains to guarantee that the sliding surface is reached from anywhere in the state space. The sliding mode controller gains are obtained from the condition for reachability of the sliding surface:

$$s\dot{s} < 0 \quad (8)$$

We specify the control algorithm in the form [13]

$$u_i = \Phi_i^T \mathbf{E} + \Lambda_i \operatorname{sgn}(s), (i = 1, 2) \quad (9)$$

where $\Phi_i = (\varphi_{i1} \quad \varphi_{i2})^T$ and

$$\varphi_{i1} = \begin{cases} \alpha_{i1} & , \text{ if } s \int \Delta F d\tau > 0 \\ \beta_{i1} & , \text{ if } s \int \Delta F d\tau < 0 \end{cases}$$

$$\varphi_{i2} = \begin{cases} \alpha_{i2} & , \text{ if } s \Delta F > 0 \\ \beta_{i2} & , \text{ if } s \Delta F < 0 \end{cases}$$

and Λ_i is a scalar relay gain.

Fuzzy Gain-Tuning

Consider the sliding surface and the sliding mode controller as defined by Eqs. (7), (9). The control performance largely depends on the values of parameter c_1 and the feedback/relay gains. In order to avoid the problems of gain tuning with regular SMC, in this section we propose to use the Mamdani-type fuzzy logic controller (FLC) to adaptively tune these gains based on several sets of fuzzy rules. The structure of the proposed sliding mode force controller is shown in Fig. 2.

The general form for the j -th rule of a single-input, single-output Mamdani-type FLC is as follows:

Rule R_j :

IF z is A_j THEN y is $B_j \quad j = 1, 2, \dots, m$

where z is the input variable to the controller, y is the output variable, and A_j and B_j are the fuzzy sets for z and y respectively.

Next, we fuzzify the normalized z by means of predefined triangular membership function of the elements z as in Fig. 3.

Finally, we use the correlation-minimum inference method to geometrically sum the consequences of the active associations and apply centroid defuzzification to find the crisp values of normalized y . Then, we denormalize it to obtain the actual output value. The resulting equations are given by Eqs. (10) – (12).

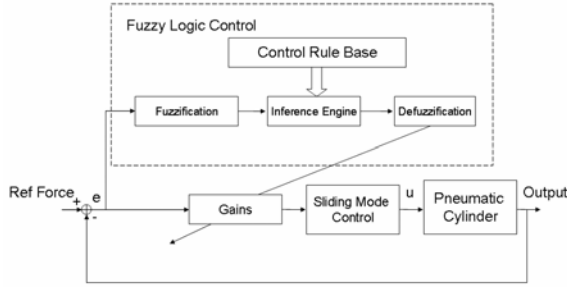


Figure 2. Sliding mode fuzzy force controller

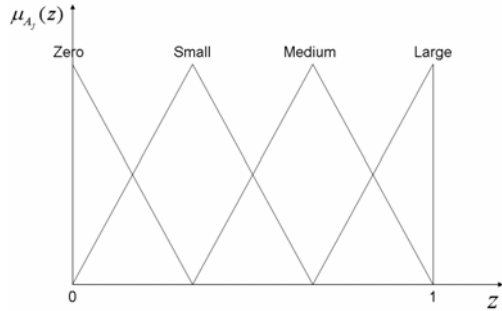


Figure 3. Fuzzification of z

$$\mu_{R_j} = \sup \min \{ \mu_{A_j}(z) \quad \mu_{B_j}(y) \} \quad (10)$$

$$\mu_{C_j} = \sup \min \{ \mu_{R_1}(y) \quad \mu_{R_2}(y) \quad \dots \quad \mu_{R_m}(y) \} \quad (11)$$

$$Y = \frac{\int \mu_{C_j}(y) y dy}{\int \mu_{C_j}(y) dy} \quad (12)$$

where μ_{R_j} is the output of the membership function value of the specific input value according to the

specific fuzzy rule. μ_{C_j} is the overall output of the membership function of the specific input by taking the minimum value among different output membership values. Y is the actually output obtained by defuzzification.

The parameter c_1 determines the slope of the sliding line and therefore, the larger it is the faster will the system response be. Therefore, based on this characteristic we set up the fuzzy rules as shown in Table 1.

The fuzzy logic tuning for the gains α_{i1} , α_{i2} and Λ_i is similar to that for c_1 based on different inputs and fuzzy rules, e.g. Table 2 shows the rule base for tuning α_{i1} . For simplicity of implementation, we may set $\beta_{ij} = -\alpha_{ij}$.

Table 1 Rule base for c_1

Fuzzy Rules	$\left \int \Delta F dt \right $			
	Zero	Small	Medium	Large
c_1	Zero	Small	Medium	Large

Table 2 Rule base for α_{i1}

Fuzzy Rules	$\left \int \Delta F dt \right $			
	Zero	Small	Medium	Large
α_{i1}	Zero	Small	Medium	Large

EXPERIMENTAL RESULTS

The effectiveness of the proposed sliding mode fuzzy force controller is illustrated in this section with results of experimental implementation on an industrial double-acting piston-driven pneumatic cylinder. The experimental setup used is shown in Fig. 4.

The external payload is moved by the piston against a soft environment. In the experiments, two 3-port 2-way proportional servovalves are connected to the left and right side input ports of the pneumatic cylinder respectively.

The force sensor reading is fed to the control program through a 12-bit A/D converter, and the output to the servovalves are from a D/A converter in the PCI data acquisition card inside a desktop PC, based on a 2 GHz Pentium processor. The program is written in Visual C++, and implemented with a sampling period of about 1 msec. The integral force error is obtained as difference

of the desired integral force signal and the numerically integrated values of the filtered force signal.

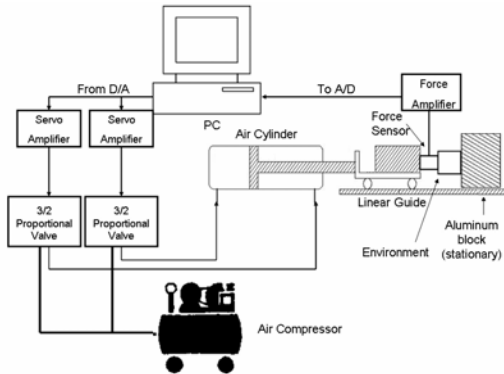


Figure 4. Schematic of experimental system

Figure 5 shows the case of tracking a cycloid trajectory. While the trajectory tracking is accurate, there is a significant initial error due to static friction [17]. Figures 6 and 7 show the results of tracking low and high frequency sine wave reference trajectories without payload, respectively. It can be seen that the tracking performance is accurate and robust with reference to speed of reference trajectory.

In order to investigate the robustness of the proposed sliding mode fuzzy controller, experiments with various payloads have been conducted. Figures 8 and 9 show the results of tracking low and high frequency sine wave with the payload of 3 kg. By comparing to Figure 6 and 7, the results show that the proposed controller provides a robust performance with different payload. However, there is significant error for each case due to the friction. The results presented here highlight the important role of cylinder and servovalve friction in limiting the accuracy of force tracking by pneumatic cylinders. This result is similar to earlier findings on effect of friction on cylinder position tracking [17]. Future research will focus on the friction learning and compensation to improve the controller's performance.

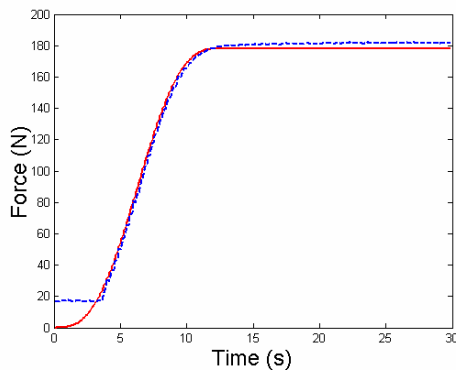


Figure 5. Tracking of cycloid force trajectory

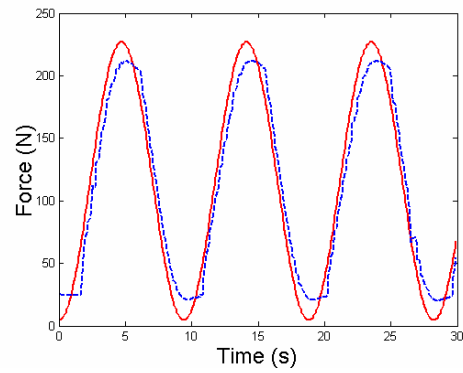


Figure 6. Tracking of low frequency sine wave without payload

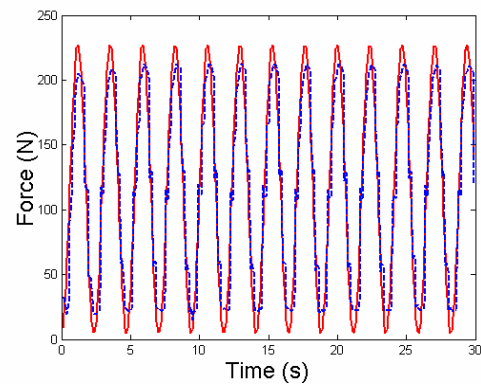


Figure 7. Tracking of high frequency sine wave without payload

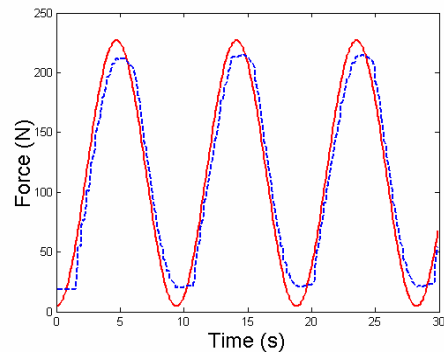


Figure 8. Tracking of low frequency sine wave with the payload of 3 kg

The major advantage of SMFC is that instead of manually tuning gains as in PI and conventional sliding mode control, the fuzzy gain tuning makes use of heuristic fuzzy logic rule base to adapt the gains. This adaptation of gains also can be expected to result in significant energy efficient performance.

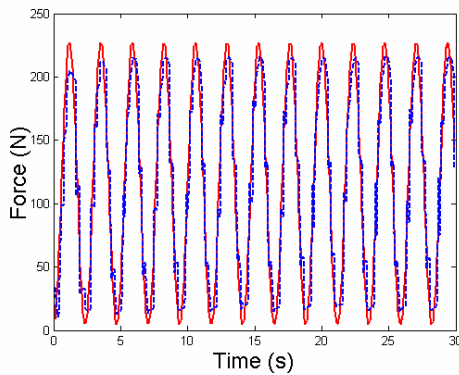


Figure 9. Tracking of high frequency sine wave with the payload of 3 kg

CONCLUSION

A sliding mode fuzzy force controller for control of interaction forces of a pneumatic cylinder actuator in contact with a “soft” environment has been proposed in this paper. The proposed controller has the advantages of simple and easy implementation and robust performance for trajectory tracking. The experimental results validate the effectiveness and robustness of the proposed controller.

ACKNOWLEDGEMENT

The authors would like to thank SMC Corporation for their support of the research.

REFERENCES

1. S.R. Pandian, Y. Hayakawa, Y. Kanazawa, Y. Kamoyama, and S. Kawamura, “Practical design of a sliding mode controller for pneumatic actuators”, *ASME J. Dynamic Systems, Measurement and Control*, 1997, **31**, pp. 666-674.
2. S.R. Pandian, F. Takemura, Y. Hayakawa, and S. Kawamura, “Practical design of adaptive model-based sliding mode control of pneumatic actuators”, *Fluid Power Systems: J. of Japanese Hydraulics and Pneumatics Society*, 2000, **31**, pp. 107-114.
3. F. Takemura, H. Mizutani, S.R. Pandian, Y. Hayakawa, and S. Kawamura, “Design and Control of a Vane-type Pneumatic Motor”, *Trans. of Japan Society of Mechanical Engineers*, 2000, **68-C**, pp. 117-124. (in Japanese).
4. S.R. Pandian, F. Takemura, Y. Hayakawa, and S. Kawamura, “Control performance of an air motor: Can air motors replace electric motors?”, *Proc. IEEE Int. Conf. Robotics and Automation*, Detroit, MI, 1999, pp. 518-524.
5. R. Carelli, R. Kelly, and R. Ortega, “Adaptive force control of robot manipulators”, *Int. J. Control*, 1990, **52**, pp. 37-54.
6. R. Liu and A. Alleyne, “Nonlinear force/pressure tracking of an electro-hydraulic actuator”, *ASME J. Dynamic Systems, Measurement, and Control*, 2000, **122**, pp. 232-237.
7. J.E. Bobrow and F. Jabbari, “Adaptive pneumatic force actuation and control”, *ASME J. Dynamic Systems, Measurement, and Control*, 1991, **113**, pp. 267-272.
8. J.E. Bobrow and B.W. McDonell, “Modeling, identification, and control of a pneumatically actuated force controllable robot”, *IEEE Trans. Robotics and Automation*, 1998, **14**, pp. 732-742.
9. M. Belgharbi, S. Sesmat, D. Thomasset, and S. Scavarda, “Force tracking control of an electro-pneumatic actuator using a linearized model around the reference trajectory”, *Proc. Bath Workshop on Power Transmission and Motion Control*, Bath, UK, 1998.
10. E. Richer and Y. Hurmuzlu, “A high-performance pneumatic force actuator system: Part I-Nonlinear mathematical model, Part II-Nonlinear controller design”, *ASME J. Dynamic Systems, Measurement, and Control*, 2000, **122**, pp. 416-434.
11. M.C. Shih and C.Q. Hwang, “Fuzzy PWM control of the positions of a pneumatic robot cylinder using high speed solenoid valve”, *JSME International Journal, Series C*, **40**, p 469-475, 1997.
12. S.H. Choi, C. Ahn and C.O. Lee, “Application of fuzzy logic adaptor to the position control of a pneumatic system using on-off valves”, *ASME, The Fluid Power and Systems Technology Division*, **2**, p 21-28, , 1995.
13. B. Xu, S.R. Pandian, S. Kawamura and Y. Hayakawa, “A sliding mode force controller for pneumatic cylinders”, *Proc. Int. Fluid Power Expo Tech. Conf.*, 2005, Las Vegas, NV, pp.451-458.
14. C.W. de Silva, “Intelligent control: fuzzy logic applications”, CRC Press, Boca Raton, FL, 1995.
15. R. Palm, “Sliding mode fuzzy control”, *Proc. Int. Conf. Fuzzy Systems*, San Diego, CA, pp.519-526, 1992.
16. L.S. Wilfinger, J.T. Wen, and S.H. Murphy, “Integral force control with robustness improvement”, *IEEE Control Systems Magazine*, pp. 31-40, 1994.
17. S.R. Pandian, F. Takemura, Y. Hayakawa, and S. Kawamura, “Pressure observer-controller design for pneumatic cylinder actuators”, *IEEE Trans. Mechatronics*, 2002, **7**, pp. 490-499.

A Study on Control and Measurement of a Power-Assisted Chair

Yuta FUJIMAKI, Kazunao SAKAINO, Masamichi FUKUTA, and Kazushi SANADA

Department of Mechanical Engineering, School of Engineering, Yokohama National University
79-5 Tokiwadai, Hodogaya-ku, Yokohama City, Kanagawa, 240-8501, Japan
(E-mail:sanada@ynu.ac.jp)

ABSTRACT

A power-assisted chair using pneumatic system has been studied by the authors. The chair aims to help the user to stand up with assistance force generated by a pneumatic cylinder. In this study, a pneumatic cylinder, control valves, a compressor, a microcomputer and electric power sources are integrated in the chair. Control and measurement techniques using the microcomputer are described in this paper.

KEY WORDS

Pneumatics, Power-assisted chair, Microcomputer control

1. INTRODUCTION

The shift to aging society is progressing rapidly in advanced countries including Japan. Lack of nurses becomes a social issue. Therefore, equipments for welfare attract interests of many researchers. For examples, assist systems for human walking were studied by Tsuchiya [1] and Raparelli [2]. A silicone outer fence mould actuator was studied by Hayakawa [3]. A flat tube actuator was studied by Tsukagoshi [4].

Human friendly robots were studied by Noritsugu [5]. In these studies, pneumatics was applied because of the advantage of compressibility and cleanliness of air. As a key word to cover this research field, a term "Soft Mechanisms" has been proposed by Prof. Noritsugu [5]. The authors also have studied a power-assisted chair that helps the user to stand up using a pneumatic cylinder [6]. The seat is tilted by a pneumatic cylinder and the seat angle is detected in order to control assist force. In this paper, control and measurement techniques of an

integrated power-assisted chair using a microcomputer are described. A pneumatic cylinder, control valves, a compressor, and a controller are installed inside the chair. In a section 2, the integrated power-assist chair is introduced. In a section 3 and 4, the system configuration and control and measurement techniques are described in details. Experimental results are discussed in a section 5. Finally, the results are summarized in a section 6.

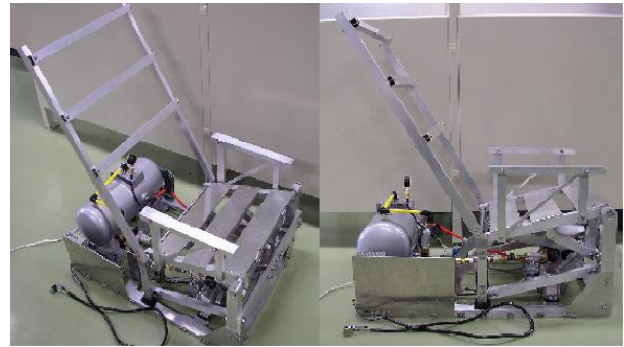


Fig. 1 Integrated power-assisted chair

Nomenclature

F	assistance force	(N)
M	weight	(kg)
P	pressure	(Pa)
θ	seat angle	(degree)

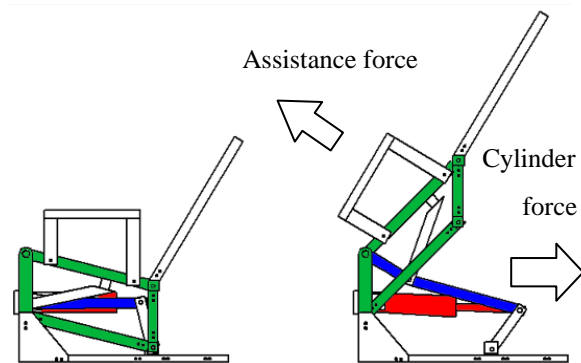


Fig. 2 Slider crank mechanism

2. Integrated Power-assisted Chair

The integrated power-assisted chair is shown in Fig. 1. A pneumatic cylinder, a proportional pressure control valve, a compressor and a tank were mounted on a base frame of the chair. The pneumatic cylinder was connected to the seat by a link mechanism. The link mechanism is shown in Fig. 2. Cylinder force was generated almost in a horizontal direction, and it is transferred to the seat by the slider crank mechanism. Force of the seat assists user's motion of standing-up and sitting-down. A ratio of the assist force to the cylinder force is named as a force transfer ratio in this study.

3. System Configuration

System configuration is shown in Fig. 3. A microcomputer board (H8 microcomputer shown in Fig. 4) was used in order to control the pneumatic cylinder and the compressor. The microcomputer has not a display and a keyboard. Therefore, a remote control panel was made as the interface device. Using the control panel, main power supply can be switched. In addition, a rotary potentiometer was used in order to input the weight of the user.

A commercial compressor for tires and balls was used. It is enough small to be installed inside the chair. Compressed air is supplied to a proportional pressure control valve through a filter, a drier, and a check valve. Cylinder pressure is controlled by the proportional pressure control valve.

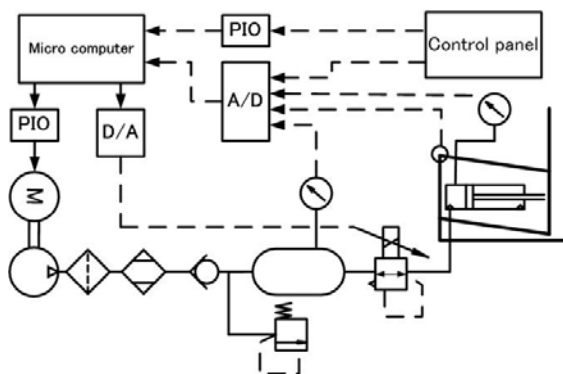


Fig. 3 System configuration

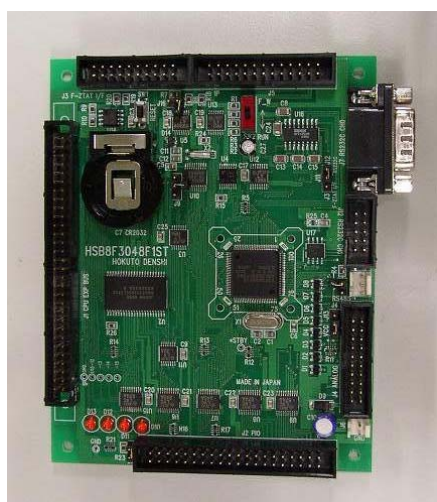


Fig. 4 H8 Microcomputer board

Seat angle is detected by a rotary potentiometer attached at the rotary joint of the seat. Seat angle, cylinder pressure, and tank pressure are input to the microcomputer through AD or PIO interfaces. The main role of the microcomputer is to control cylinder pressure. The pressure control technique is based on calculation using the seat angle, the weight specified by the control panel, and the pressure of the cylinder. The details will be described in the next section. Another role is on/off control of the compressor. If the tank pressure is larger than the high value, the compressor is turned off. If it is smaller than the low value, the compressor is turned on. The control signal is sent to the compressor through a solid-state relay switch.

4. Control System

First of all, static characteristics of the proportional pressure control valve were measured. The results are shown in Fig. 5 as a function of input voltage. Hysteresis was observed corresponding to standing-up and sitting-down motion. Therefore, the characteristics were approximated using two straight lines representing stand-up and sit-down motion, respectively.

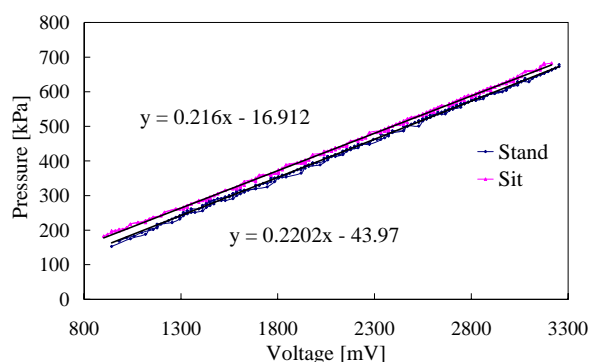


Fig. 5 Static characteristics of a proportional pressure control valve

A control technique of assistance force is explained. Assistance force was determined based on a concept of knee torque compensation. Human body was approximated by a link model as shown in Fig.6. The link parameters, such as mass, inertia and center of gravity, can be found in a reference [7]. According to our experiments, in the case of standing-up motion, the angle of the upper body with respect to a vertical line does not change so much. Therefore, the angle of upper body is assumed to be constant ($\theta_3 = 30^\circ$). A static balance of moments around a knee joint is written as:

$$T_2 = m_2 g d_2 \sin \theta_2 - l_2 F + m_3 g (l_2 \sin \theta_2 + d_3 \sin \theta_3)$$

$$\therefore T_2 + l_2 F = m_2 g d_2 \sin \theta_2 + m_3 g (l_2 \sin \theta_2 + d_3 \sin \theta_3) \quad (1)$$

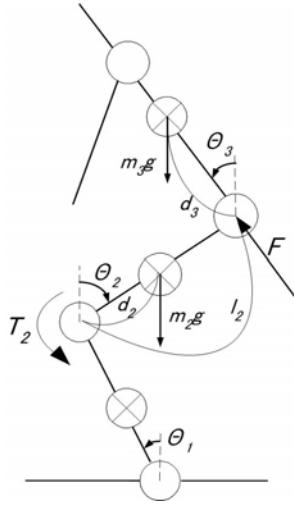


Fig. 6 Three link model of a human body

The assistance torque in the knee joint $l_2 F$ is controlled to be a half of knee torque without the assistance force. Therefore,

$$T_2 = l_2 F \quad (2)$$

Substituting Eq.(2) into Eq.(1), the assistance force F is obtained as:

$$F = \frac{m_2 g d_2 \sin \theta_2 + m_3 g (l_2 \sin \theta_2 + d_3 \sin \theta_3)}{2 l_2} \quad (3)$$

According to the design of the chair, a geometrical relationship between θ and θ_2 is written as:

$$\theta_2 = \frac{\pi}{180} (105 - \theta) \quad (4)$$

Substituting parameter values into Eq(3) and approximating the curve of the assistance force F as a function of the angle θ by a second order polynomial of θ , the approximated equation is obtained as:

$$F = (-0.0004\theta^2 - 0.022\theta + 4.9908) \times M, \quad (5)$$

where M is mass of the human body that will be input by the user.

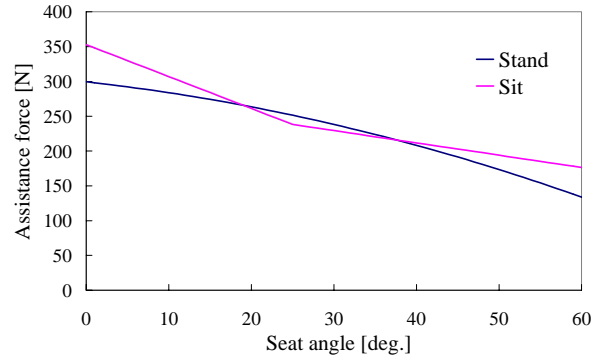


Fig. 7 Assistance force ($M = 60\text{kg}$)

Therefore, the assistance force for standing-up motion can be plotted as a function of the seat angle as shown in Fig. 7 for the weight $M=60$ kg. Assistance force for sitting-down motion can not be obtained at present. Therefore a virtual spring concept [6] was applied.

The block diagram of the control system is shown in Fig. 8. Valve characteristic $V(P)$ and assistance force $F(\theta)$ are obtained according to above mentioned techniques. $D(\theta)$ is a force transfer ratio.

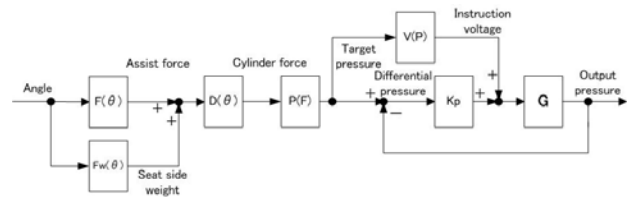


Fig. 8 Block diagram of a control system

The seat angle is detected and desired assistance force is calculated. To determine cylinder pressure, a force component of the seat weight that is parallel to the assistance force or perpendicular to the seat should be added to the desired assistance force.

Multiplied by the force transfer ratio, desired cylinder force and desired cylinder pressure are determined. The cylinder pressure is controlled by feedback and feed-forward control.

There are two main control modes corresponding to standing-up motion and sitting-down motion. In experiments where only these two modes were considered for the valve control, chattering phenomena occurred and the valve became unstable. The chattering may be caused by noise. In order to suppress the chattering, a state transition chart having six modes shown in Fig.9 was applied. In the figure, $\Delta\theta$ is the increment of the seat angle during one control period. The initial state is “Start”, and it transits to “Sit”, “Stand” or “Stop” mode depending on the value of $\Delta\theta$. For an example, the “Sit” mode is a buffer mode for going to the next mode “Down”. In the “Sit” mode, the valve is not controlled. When $\Delta\theta$ is negative, the state transits from the “Sit” mode to the “Down” mode. Otherwise, the state stays there for $\Delta\theta = 0$ or it goes to the “Stand” mode for $\Delta\theta > 0$. In the “Down” and “Up” mode, the valve is controlled. During the “Down” mode, when $\Delta\theta$ becomes positive, the state transits from “Down” to “Start” mode. Using the state transition chart, chattering was suppressed in experiments.

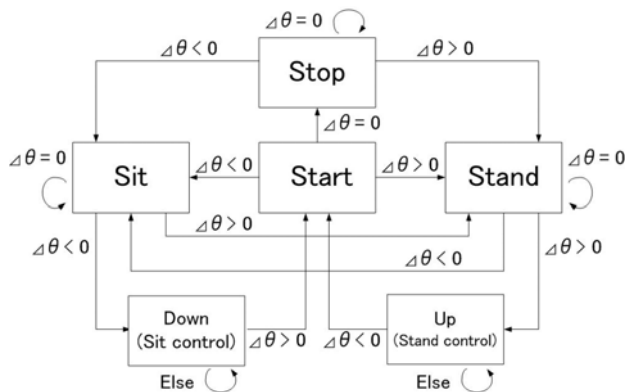


Fig. 9 State transition chart

5. Experimental Results

Controlling the chair by the proposed method, experiments were carried out. Cylinder pressure was measured for standing-up and sitting-down motions. Measured results of cylinder pressure are shown in Fig. 10. The cylinder pressure well followed the target values. The system stability was very much sensitive to the proportional gain of the feedback control of cylinder pressure.

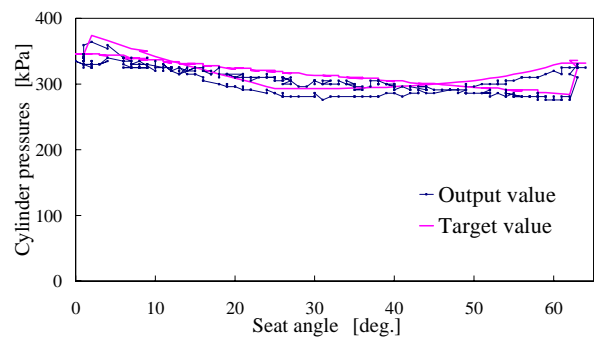


Fig. 10 Experimental results of cylinder pressures

6. Conclusion

In this research, control and measurement techniques of the integrated power-assisted chair were proposed. A concept of knee torque compensation was applied. A microcomputer (H8 microcomputer) had an enough performance. State transition chart was useful to avoid chattering. Because the commercial compressor produced noise and vibration, a silent and small size compressor must be designed in the future.

Acknowledgement

This research was carried out as an Interdisciplinary Project of Yokohama National University.

References

- [1] G. Tsuchiya, O. Oyama, and T. Toshimitsu, Development of Pneumatic Assist System for Human Walk, Proceedings of the Fifth JFPS International Symposium on Fluid Power, Nara 2002, 2002, p.333/338.
- [2] T. Raparelli, P. Beomonte Zobel, and F. Durante, Development of Pneumatic Knee Orthosis, Proceedings of the Fifth JFPS International Symposium on Fluid Power, Nara 2002, 2002, p.305/308.
- [3] Y. Hayakawa, H. Mori, R. Tsuda, M. Aichi, et. al., Development of a Silicon Outer Fence Mold Actuator with Human Compatibility, Proceedings of the Fifth JFPS International Symposium on Fluid Power, Nara 2002, 2002, p.321/326.
- [4] H. Tsukagoshi, A.Kitagawa, and Y. Kamata, Wearable Fluid Power by Means of Various Flat Tube Actuator, Proceedings of the Fifth JFPS International Symposium on Fluid Power, Nara 2002, 2002, p.31/36.
- [5] T. Noritsugu, D. Sasaki, and M. Takaiwa, Application of Pneumatic Soft Mechanism to a Human Friendly Robot, Proceedings of the Fifth JFPS International Symposium on Fluid Power, Nara 2002, 2002, p.61/66.
- [6] K. Sanada, A Study on Control Techniques for Power-assisted Chair, Proceedings of the Fourth JHPS International Symposium on Fluid Power Tokyo '99, 1999, p.175-180.
- [7] D.A.Winter, Biomechanics and Motor Control of Human Movement, Second Edition., John Wiley & Sons, Inc., Toronto, 1990.

APPLICATION OF INTELLIGENT SWITCHING CONTROL OF PNEUMATIC ARTIFICIAL MUSCLE MANIPULATORS WITH MAGNETO-RHEOLOGICAL BRAKE

Diep Cong Thanh TU * and Kyoung Kwan AHN**

* Graduate School of Mechanical and Automotive Engineering,
University of Ulsan, Korea

(E-mail: tdcthanh@yahoo.com, tdcthanh@hotmail.com)

** School of Mechanical and Automotive Engineering,
University of Ulsan, Korea

San 29, Muger 2dong, Nam-gu, Ulsan, 680-764, Korea
(E-mail: kkahn@ulsan.ac.kr)

ABSTRACT

A pneumatic artificial muscle actuator (PAM actuator), has been regarded during the recent decades as an interesting alternative to hydraulic and electric actuators because of these advantages such as high power to weight ratio, low cost, readily available and cheap power source, inherent safety and mobility assistance to humans performing tasks. However, problems with the air compressibility and the lack of damping ability have made it difficult to realize motion with high accuracy, high speed and with respect to various external inertia loads in order to realize a human-friendly therapy robot (HFTR).

An intelligent phase plane switching controller, which harmonizes a phase plane switching control (PPSC) algorithm, conventional PID controller and the adaptabilities of neural network, is newly proposed in this study. In order to realize satisfactory control performance, Magneto-Rheological Brake (MRB) is equipped to the joint of the manipulator. The experiments were carried out in practical PAM manipulator and the effectiveness of the newly proposed control algorithm was demonstrated through experiments, which proved that the stability of the manipulator could be improved greatly in a high gain control without regard to the change of external inertia loads.

KEY WORDS

Pneumatic Artificial Muscle, Magneto-Rheological Brake, Phase Plane Switching Control, Neural Network

1. INTRODUCTION

The PAM is undoubtedly the most promising artificial muscle for the actuation of new types of rehabilitation therapy robots. However, the air compressibility and the lack of damping ability of the PAM actuator bring the dynamic delay of the pressure response and cause the oscillatory motion. Therefore, it is not easy to realize the performance of transient response with high speed and with respect to various external inertia loads in order to realize a HFTR. The limitations of PAM manipulator have promoted research into a number of control strategies, such as an adaptive controller [2], sliding mode control [2], fuzzy PD+I learning control [3], robust control [4], feedback linearization control [5], and so on. Though these systems were successful in

addressing smooth actuator motion in response to step inputs, the manipulator must be controlled slowly in order to get stable, accurate position control and the external inertia loads were also assumed to be constant or slowly varying. Therefore, intelligent control techniques have emerged to overcome some deficiencies in conventional control methods in dealing with complex real-world systems. An intelligent using a neuro-fuzzy controller [6], a hybrid using fuzzy and neural network [7] and a learning vector quantization neural network [8] were proposed. However these control algorithms were not yet to reconcile both damping and response speed in high gain control.

To overcome these problems, Electro Rheological Fluid (ERF) Damper has been applied to the PAM manipulator [9]. The results show that the ERF damper

is one of effective methods to develop a practically available HFTR by using the PAM manipulator. However, some limitations still exist, such as the damping torque was not tuned adaptively and ERF require extremely high control voltage (kV), works in narrow range of temperature and high nonlinearity. Thus, the goal of this paper is to implement a MRB, to develop a fast, accurate position control system by intelligent PPSC using neural network which will tune the damping torque adaptively and without regard for the changes of external inertia loads. The experiments were carried out in practical PAM manipulator and the effectiveness of the newly proposed control algorithm with an intelligent PPSC using MRB was demonstrated through experiments.

2. EXPERIMENTAL SETUP

2.1 Experimental apparatus

The schematic diagram of the PAM manipulator is shown in Fig. 1. The hardware includes an IBM compatible PC (Pentium 1 GHz), which calculates the control input, controls the proportional valve (FESTO, MPYE-5-1/8HF-710 B) and MRB (LORD, MRB-2107-3 Rotary Brake), through D/A board (Advantech, PCI 1720), and two PAM (FESTO, MAS-10-N-220-AA-MCFK). The braking torque of MRB is controlled by D/A board through voltage to current converter, Wonder Box Device Controller Kit (LORD, RD-3002-03). The joint angle is detected by rotary encoder (METRONIX, H40-8-3600ZO) and the air pressure into each chamber is also measured by the pressure sensors (FESTO, SDE-10-10) and fed back to the computer through 24-bit digital counter board (Advantech, PCL 833) and A/D board (Advantech, PCI 1711), respectively. The external inertia load could be changed from 20[kg·cm²] to 200[kg·cm²], which is a 1,000[%] change with respect to the minimum inertia load condition. The experiments are conducted under the pressure of 0.4[MPa] and all control software is coded in C program language. A photograph of the experimental apparatus is shown in Fig 2.

2.2 Characteristics of MRB

Construction of MRB was shown in Fig. 3. The rotor in Fig. 3 is fixed to the shaft, which can rotate in relation to housing. Between rotor and housing there is a gap filled with MRF. Braking torque of MRB can be controlled by the electric current in its coil. An apparent viscosity of MRF is changed at few milliseconds after the application of a magnetic field, and goes back to the normal viscosity with no magnetic field.

The following experiments are performed to investigate the characteristics of MRB, which measurement data is shown in Fig. 4. MRB is connected with a torque transducer and a servomotor in series. In this experiment, the rotational speed is changed from

100[rpm] to 1000[rpm] and the current applied for MRB is changed from 0[A] to 1[A]. Figure 4 shows the damping torque with respect to the change of the input current (a) and rotational speed (b) of MRB. From Fig. 4, it is clear that the damping torque of MRB is independent of rotational speed and almost proportional to input current. Thus an equation (1) holds between the inputs current I and damping torque T_b

$$T_b = f(I) = a + bI \quad (1)$$

Here, a and b are constant.

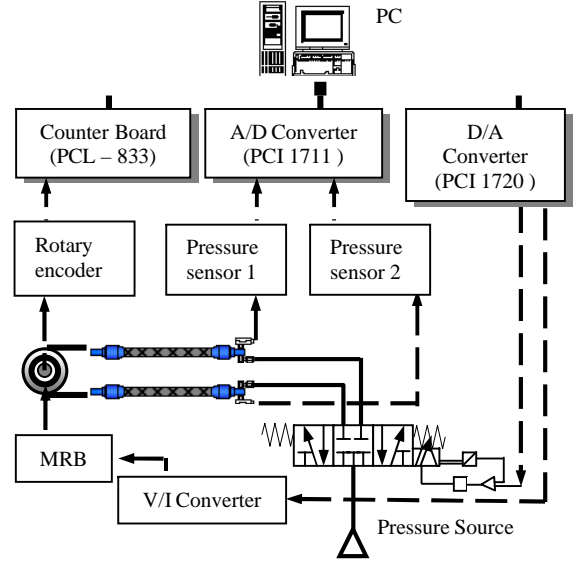


Figure 1 Schematic diagram of PAM manipulator

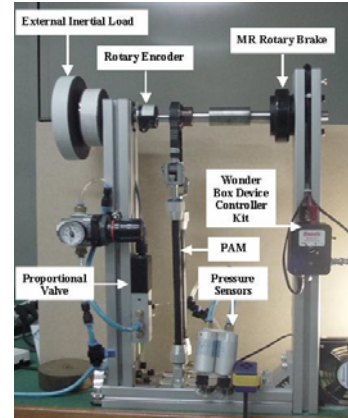


Figure 2 Photograph of the experimental apparatus

3. CONTROL SYSTEM

3.1 Positioning control system

To control this PAM manipulator, a conventional PID control algorithm was applied. The controller output at sampling sequence k can be expressed as:

$$u(k) = K_p e(k) + u(k-1) + \frac{K_p T}{T_i} e(k) + K_p T_d \frac{e(k) - e(k-1)}{T} \quad (2)$$

where $u(k)$, $e(k)$ are the control input to the control valve and the error between the desired set point and the output of joint, respectively.

MRB is one of effective methods because of working in only the regions where the acceleration or deceleration is too high. The structure of the PPSC algorithm is shown in Fig. 5.

Here, s is Laplace operator, T_a is torque produced by manipulator, T_c is constant torque and K_{ED} determines a gain for the torque proportional to the angular speed $\dot{\theta}$, V_c is a control voltage of source calculated from Eq. (1) to produce T_c . A direction of a damping torque is every time opposite to the rotary direction of the arm. Eq. (3) below indicates that the damper produces a torque T_b .

$$T_b = (-K_{ED}\dot{\theta} + T_c)\text{sign}(\dot{\theta}) \quad (3)$$

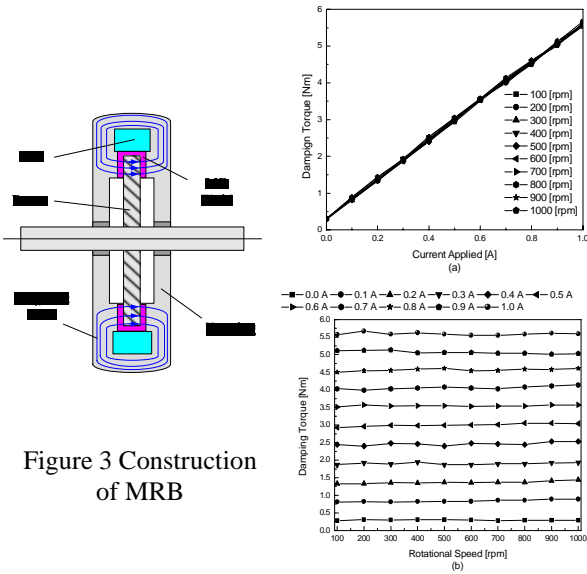


Figure 3 Construction of MRB

Fig. 4 Characteristics of MRB

3.2 PPSC algorithm

The damping torque T_b improves the damping performance of the manipulator. In the region that the joint angle of the arm approaches to the desired angle, $a \sim b$, $c \sim d$ in Fig. 6(a), the current is not applied not to interfere the movement of the arm, since the high response speed is required. In the region the arm passes the desired angle, i.e. the diagonally shaded areas of $b \sim c$, $d \sim e$ in Fig. 6(a), a current is applied to improve the damping performance to converge to the desired angle quickly. To determine whether the magnetic field should be applied or not, the phase plane shown in Fig. 6(b) is used. The horizontal axis in the phase plane corresponds to joint angle deviation e between the desired angle θ_r and the joint angle θ , and the vertical axis corresponds to the derivation of the deviation $\dot{e} = -\dot{\theta}$. Each point $a \sim e$ on the phase plane corresponds to each point $a \sim e$ in Fig. 6(a). Here, the regions with the application of current are controlled by h , the gradient of the line, which is shown in Fig. 6(b).

The region under the application of the damping torque expands as $|h|$ decrease.

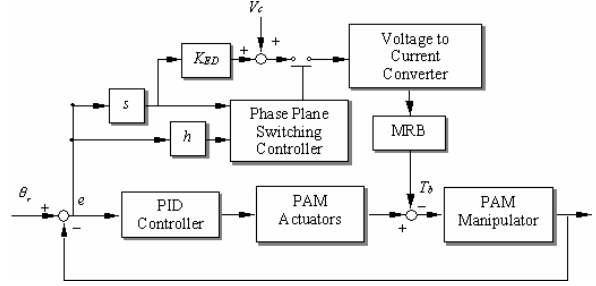


Figure 5 Block diagram of PPSC

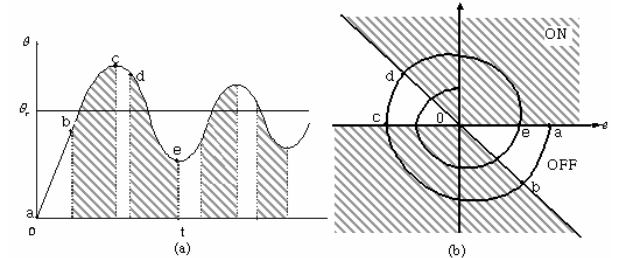


Figure 6 Concept of PPSC

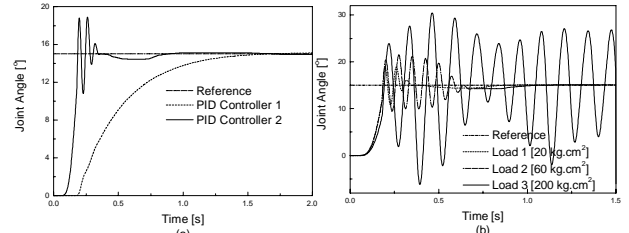


Figure 7 Experimental results of PID controller

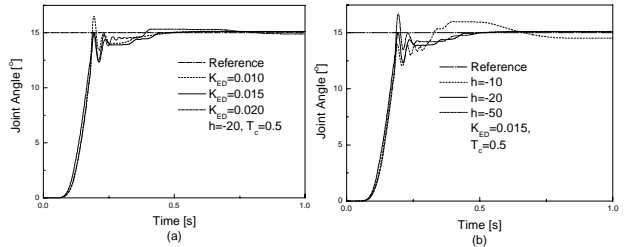


Figure 8 Experimental results of PPSC

3.3 Experimental results of PID and PPSC algorithm

Experiments were carried out with 3 cases of external inertia loads (20, 60, 200[kg·cm²]). Figure 7(a) showed the experimental results of the PID controller where the minimum external inertia load 20[kg·cm²] was used with the following 2 control parameters $K_p = 200 \times 10^{-6}$, $K_i = 1 \times 10^{-6}$, $K_d = 70 \times 10^{-6}$ (PID controller 1) and $K_p = 1000 \times 10^{-6}$, $K_i = 10 \times 10^{-6}$, $K_d = 130 \times 10^{-6}$ (PID controller 2). It is obvious that it is difficult to satisfy both the damping and response speed. The manipulator must be controlled slowly in order to have a good stability. On the contrast, the

overshoot and oscillation are always included if one wants fast response. In addition, experimental result with PID controller 2 was shown in Fig. 7(b) where the external inertia loads change from 20[kg·cm²] to 200 [kg·cm²]. From these results, it was understood that the system response became more oscillatory according to the increase of the external inertia load and became unstable with ten times bigger external inertia load with respect to the minimum inertia load condition.

Next, the experiments were carried out in practical PAM manipulator and the control parameters of the PPSC algorithm, were set to be $T_c = 0.4$, $h = -20$ with various K_{ED} ($K_{ED}=0.10, 0.015, 0.020$) in experiment with load 20[kg·cm²] and $K_{ED} = 0.015, T_c = 0.4$ with various h ($h=-10, -20, -50$) in the experiment with load 60[kg·cm²] in Fig. 8(a) and 8(b), respectively. These parameters were obtained by trial-and-error through experiments. From these experimental results, it is understood that the settling time becomes very big in some value of design parameters of switching controller. To guarantee the control performance, the control parameters must be tuned adaptively and we newly proposed PPSC using neural network (PPSCNN), which is explained in detail in next section.

4. PROPOSED PPSCNN

4.1 Structure of PPSCNN

It is obvious that the PPSC algorithm is limited because the K_{ED} parameter is constant. This means that the damping torque is not adaptable and optimal in any case. Here, we propose a PPSCNN, which has the adaptability of control parameter to minimize the error. With the capacity of learning and adaptability of neural network, the proposed controller can solve these problems. The damping torque will be tuned adaptively and optimally in order to minimize the position error without respect to the variation of external inertia loads. Figure 9 shows the structure of newly proposed PPSCNN. In Fig. 9, the proportional gain K_{ED} was modified by neural network. The block diagram of neural network is shown in Fig. 10. Here $K_E(k)$, $K_{ED}(k)$, $e(k)$, $e_D(k)$, $x(k)$ and $f(x)$ are the proportional gain, the derivative gain, the system error between desired angle output and output of joint of the PAM manipulator, the difference of the system error, control input of MRB and sigmoid function of neural network, respectively. The sigmoid function, $f(x)$, which has a nonlinear relation is presented in the following equation:

$$f(x) = \frac{2(1 - e^{-xY_g})}{Y_g(1 + e^{-xY_g})} \quad (4)$$

where x is the input of sigmoid function and Y_g is the parameter determining its shape. Figure 11 shows the shapes of sigmoid function with various Y_g .

We have two-layered nonlinear neurons. Neural networks are trained by the conventional back propagation algorithm to minimize the system error between the output of joint of the PAM manipulator and desired angle. In Fig. 10, the input signal of the sigmoid function in the output layer, $x(k)$, becomes:

$$x(k) = K_E(k)e(k) + K_{ED}(k)e_D(k) \quad (5)$$

$$e(k) = \theta_r(k) - \theta(k), \quad e_D(k) = \frac{e(k)(1 - z^{-1})}{\Delta T} \quad (6)$$

ΔT : sampling time, z : operator of Z-transform, k : discrete sequence

$\theta_r(k)$ and $\theta(k)$ are desired angle and output of joint of the PAM manipulator, respectively.

The damping torque of newly proposed PPSCNN can be obtained as the following equation:

$$T_b(k) = (abs(f(x(k)))) + T_c)sign(\dot{\theta}) \quad (7)$$

where function $sign(\dot{\theta})$ is the sign of angular speed, and function $abs(f(x(k)))$ is the absolute value of the output of neural network.

4.2 Learning algorithm of neural network

In order to get the optimal value of damping torque, the control parameters K_E and K_{ED} must be adjusted automatically in order to minimize the position error. To tune K_E and K_{ED} , the steepest descent method using the following equation was applied.

$$K_E(k+1) = K_E(k) - \eta_E \frac{\partial E(k)}{\partial K_E} \quad (8)$$

$$K_{ED}(k+1) = K_{ED}(k) - \eta_{ED} \frac{\partial E(k)}{\partial K_{ED}}$$

where η_E and η_{ED} are learning rates determining convergence speed, and $E(k)$ is the error defined by the following equation:

$$E(k) = \frac{1}{2}(\theta_r(k) - \theta(k))^2 \quad (9)$$

Using the chain rule, we get the following equations:

$$\frac{\partial E(k)}{\partial K_E} = -\frac{\partial \theta(k)}{\partial u} f'(x(k))e^2(k) \quad (10)$$

$$\frac{\partial E(k)}{\partial K_{ED}} = -\frac{\partial \theta(k)}{\partial u} f'(x(k))e(k)e_D(k)$$

$$f'(x) = 4 \frac{e^{-xY_g}}{(1 + e^{-xY_g})^2} \quad (11)$$

As done by Yamada and Yabuta [13], for convenience, $\frac{\partial \theta(k)}{\partial u} = 1$ is assumed. Eq. (8) is expressed as follows:

$$K_E(k+1) = K_E(k) + \eta_E e(k) e(k) \frac{4e^{-xY_g}}{(1+e^{-xY_g})^2} \quad (12)$$

$$K_{ED}(k+1) = K_{ED}(k) + \eta_{ED} e(k) e_D(k) \frac{4e^{-xY_g}}{(1+e^{-xY_g})^2}$$

From Eq. (12), it is obvious that the damping torque will be auto-tuned adaptively and optimally. However, from the experimental results, it is understood that Y_g is difficult to determine in some cases. Thus, in case of PPSCNN, the experimental results were shown in both cases (with and without tune Y_g). The shape function Y_g was auto-tuned by the following equation.

$$Y_g(k+1) = Y_g(k) - \eta_{Y_g} \frac{\partial E(k)}{\partial Y_g} \quad (13)$$

$$= Y_g(k) + \eta_{Y_g} e(k) \left(\frac{4x(k)Y_g(k)e^{-xY_g} + 2e^{-2xY_g} - 2}{(1+e^{-xY_g})^2} \right)$$

Here, η_{Y_g} is learning rates determining convergence speed of shape function.

The effectiveness of the newly proposed PPSCNN will be demonstrated through experimental results with various external inertia loads.

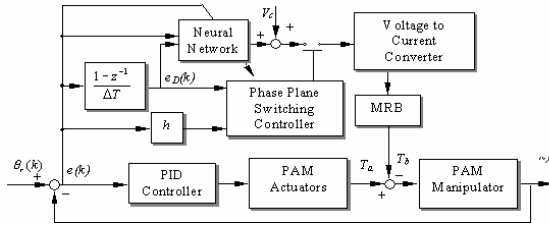


Figure 9 The structure of PPSCNN

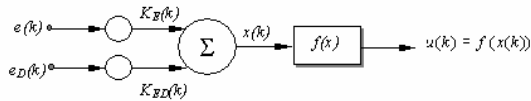


Figure 10 The block diagram of neural network

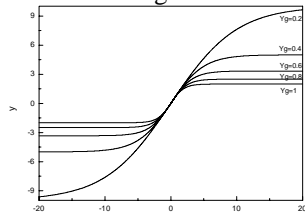


Figure 11 The sigmoid function shapes

4.3 Experimental results

The initial control parameters of PPSCNN were set to be $T_c = 0.25$, $h = -10$, $K_E = 0.010$, $K_{ED} = 0.010$, $Y_g = 1$, $\eta_E = 350 \times 10^{-8}$, $\eta_{ED} = 1 \times 10^{-8}$ and $\eta_{Y_g} = 8 \times 10^{-3}$. These control parameters were obtained by trial-and-error through experiments.

Figure 12 shows the comparison between the conventional PID controller 2, the PPSC algorithm and the proposed PPSCNN with respect to various external loads. In the experiments, the joint angle of PAM manipulator was in good agreement with that of

reference by using PPSC. With up to ten times bigger external inertia load with respect to the minimum external inertia load, a good control performance was also obtained in this case. However, it has too large settling time due to the fixed control parameter of PPSC. It was found that a good control performance and strong robustness were obtained without respect to the variation of external inertia load, the overshoot was almost reduced and the steady state error was reduced within $\pm 0.025^\circ$ by using PPSCNN. It is clear that the newly proposed controller using neural network with auto-tuning shape function was very effective in any case of external inertia loads.

The effectiveness of the newly proposed PPSCNN was shown in detail in Fig. 13 with respect to various external inertia loads. From these figures, it is understood that the damping torque was not applied for fast response when the manipulator started to move and the damping torque was generated by MRB to the rotational axis of PAM manipulator in order to reduce the overshoot and oscillation when the manipulator reaches the desired angle. In addition, during the experiments of the PAM manipulator, the control parameters K_E , K_{ED} and the shape function of neural network, Y_g , were tuned adaptively by neural network to minimize the position error. Indeed in the experiment, it is difficult to get an optimal value of Y_g . But with newly proposed intelligent control algorithm, the shape function of neural network will be tuned adaptively and optimally in any case of load condition. And the damping torque was applied and released frequently according to the approach to the desired angle.

5. CONCLUSION

A novel intelligent PPSC using MRB is newly proposed and applied to the PAM manipulator in this study. In order to reconcile both damping and response speed in high gain control, a MRB had joint to the manipulator, which damping torque will be tuned adaptively and optimally by the capacity of learning and adaptability of neural network with auto-tuning shape function.

From the experimental results, it was verified that the newly proposed control algorithm presented in this study was very effective in high gain control, good control performance, fast response and strong robust stability with respect to the 1,000% change of external inertia loads and the steady state error with respect to various loads was reduced within $\pm 0.025^\circ$.

ACKNOWLEDGEMENT

This work was supported by Ministry of Commerce, Industry and Energy (MOCIE) of Republic of Korea, through the Research Center for Machine Parts and Materials Processing at the University of Ulsan.

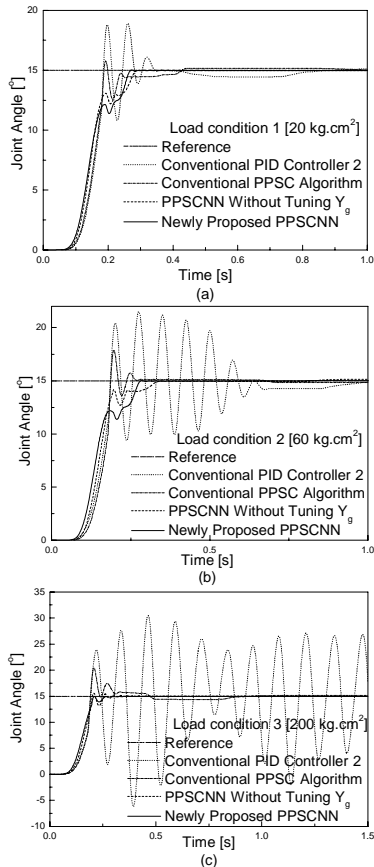


Figure 12 Comparison between PID controller 2, PPSC and PPSCNN with various external inertia loads

REFERENCES

1. Caldwell, D.G., Medrano-Cerda, G.A. and Goodwin, M.J., Control of pneumatic muscle actuators, IEEE Contr., Syst., Mag., 1995, 15-1, pp.40-48.
2. Tondu, B. and Lopex, P., Modeling and control of Mckbben artificial muscle robot actuators, IEEE Contr., Syst., Mag., 2000, 20-1, pp.15-38.
3. Chan, S.W., Lilly, J.H., Repperger, D.W. and Berlin, J.E., Fuzzy PD+I learning control for a PM, IEEE Int., Conf., Fuzzy Systems, 2003, 1, pp.278-283.
4. Guihard, M. and Gorce, P., Dynamic control of an artificial muscle arm, Proc., IEEE Int., Conf., Systems, Man and Cybernetics, 1999, 4, pp.813-818.
5. Kimura, T., Hara, S., Fujita, T. and Kagawa, T., Control for pneumatic actuator systems using feedback linearization with disturbance rejection, Proc., Conf., American Control, 1995, 1, pp.825-829.
6. Iskarous, M. and Kawamura, K., Intelligent control using a neuro-fuzzy network, Proc., IEEE Int., Conf., Intelligent Robots and Systems, 1995, 3, pp.350-355.
7. Folgheraiter, M., Gini, G., Perkowski, M. and Pivtoraiko, M., Adaptive Reflex Control for an Artificial Hand, Proc., Sym. on Robot Control, 2003.
8. Ahn, K.K. and Thanh, T.D.C., Improvement of the control performance of pneumatic artificial muscle manipulator using an intelligent switching control method, KSME, Int., Jour., 2004,8-8, pp.1388-1400.

9. Noritsugu, T., Tsuji, Y. and Ito, K., Improvement of control performance of PAM manipulator by using ER fluid damper, Proc., IEEE Int., Conf., Systems, Man and Cybernetics, 1999, 4, pp.788-793.

10. Yamada, T. and Yabuta, T., Neural network controller using autotuning method for nonlinear functions, IEEE Trans., Neural Networks, 1992, 3, pp.595-601.

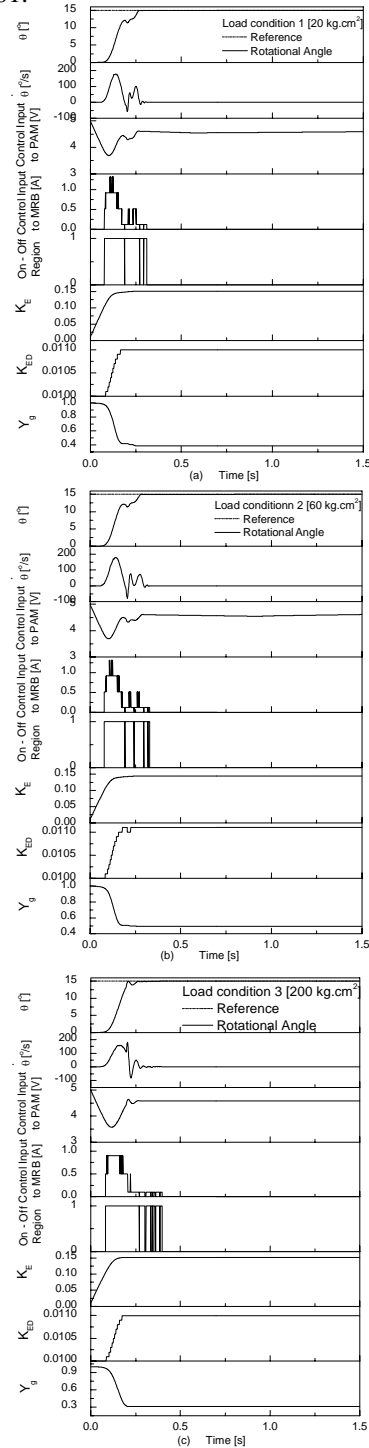


Figure 13 Experimental results of the newly proposed PPSCNN with various loads

Soft Mechanism by using a Sponge-Core-Soft-Rubber Actuator for Welfare Machines

Yasuhiro Hayakawa*, Naoyoshi Ueda*, Shogo Hirota* and Shunmugham Raj Pandian**

* Department of Electrical and Control Engineering
Nara National College of Technology
22 Yata-cho, Yamato-Koriyama, Nara, 639-1080 Japan
(E-mail: hayakawa@ctrl.nara-k.ac.jp)

** Department of Electrical Engineering and Computer Science Department
Tulane University
6823 St. Charles Avenue New Orleans, LA, USA
(E-mail: pandian@eecs.tulane.edu)

ABSTRACT

In care activity or rescue activity, hands that can grasp creatures are sometimes needed. Therefore, it is considered that the soft mechanism that uses pneumatic elements is useful to realize such hands. In this paper, we propose a new type of soft actuator (Sponge-Core-Soft Rubber Actuator) in which a sponge rubber is covered with silicon rubber. The structure of the sponge rubber is divided into two types. One is single-layer type and the other is two-layer type (a flat type and a clipping type). In order to clarify the differences in characteristics of each actuator, we examine the basic characteristics of the actuators. Further, the control performances of both position and force are studied to realize a hybrid element. From some experimental results, the control performance of the two layers type actuator is illustrated.

KEY WORDS

Key words, Sponge Rubber, Soft mechanism, Force Estimation, Force Control

NOMENCLATURE

F: Output force,
Fr: Desired force
F_r: Desired Force
K_p, K_i, K: Gain
P: Inner Pressure in the Actuator
P₀: Initial Pressure in the Actuator
Pr: Desired Pressure
V: Input Voltage to Valve
V₀: Neutral Voltage

INTRODUCTION

Recently, many types of robots have been used in factory automation. Since these robots usually grasp hard material objects in these tasks, the robot hand has a mechanical structure. However, when the robot grasps a soft material object such as foods and creatures, the hand needs a force sensor to control the grasping force. In this case, it takes much time and effort to control the grasping force.

Therefore, when the hand grasps the soft material object, it is considered that a pneumatic element that is used at the grasping parts is useful to realize a flexible hand by

making use of pneumatic compressibility. Further, by pressure measurement in the element, it is possible to estimate the external force. As a result, there is no need to use a force sensor to measure the external force. Moreover, by controlling the inner pressure of the pneumatic element, the shape of the grasping part can be changed.

That is to say, by making use of pneumatic components, it is possible to realize a hybrid element that has both a position control function and a force control function.

Therefore, an actuator that has both active elements (position control and force control) and passive elements (compressibility) can be used to develop a soft mechanical interface between a robot hand and an object. Thus, since pneumatic actuators have flexibility because of compressibility of air[1], it is considered that pneumatic systems are very useful to realize the above soft mechanical system. In order to realize the system, some kinds of pneumatic actuator such as Flexible Micro Actuator[2] and Rubber Actuator have been proposed in literature. However, when these actuators are burst by some accidents, the rapid deformation of the actuator is caused by air release. As a result, user has some trouble in operating them. Therefore, in order to eliminate these problems, we propose a new type of pneumatic soft actuator in which a sponge rubber is covered with silicon rubber.

In this paper, the structure of the actuator is explained in Section 2. Further, in Section 3, basic characteristics of the proposed element are clarified from some experimental results. Moreover, position and force control performances are examined in section 4. Finally, in Section 5, force sensing performance is illustrated.

SOFT MECHANISM

In factory, many kinds of robots are used to operate many objects. At this time, when the robot hand operates a hard object as shown in Fig.1, the grasping force F is dependent on a weight of the grasping object. On the other hand, when the robot operates a soft material that is shown in Fig.1, the hand has to be realize a force control to operate the object. Further, since the shape of the object is changed by the grasping force, the tip of the hands part have to be moved to grasp the object. However, when the hand grasps a creature,

Moreover, Furthermore, in recent years, human support machines are needed. In this case, we have to investigate the structure of hand part that contacts with human body. So, in order to realize the hand mechanism with human compatibility, we propose a new type of pneumatic rubber actuator. As you know, by making use of both rubber elasticity and pneumatic compressibility, the actuator can realize a passive motion. Moreover, the pneumatic actuator is easy to control generation force by adjusting the inner pressure of the actuator. Thus, the

actuator can be used as an active element that is constructed with position and force control. So, in this study, we propose a new type of hybrid element by using pneumatic power.

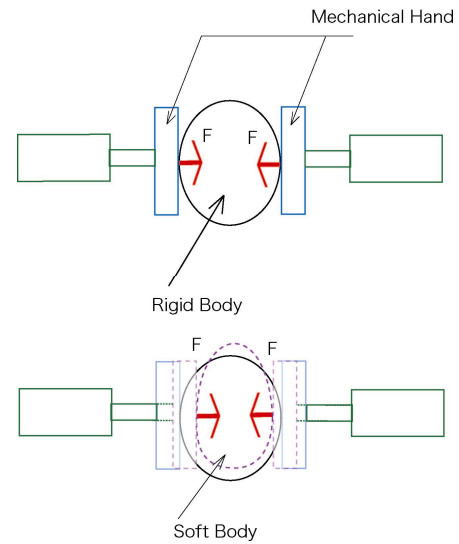


Fig.1 Mechanical Hand

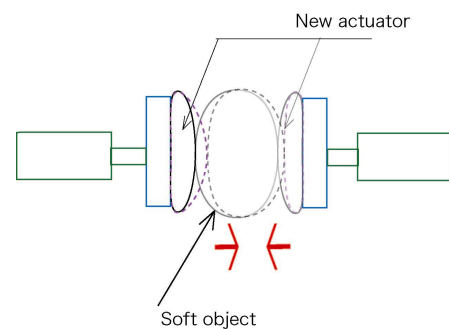


Fig.2 Soft Mechanical Hand

SPONGE-CORE-SOFT RUBBER ACTUATOR[3]~[8]

Structure of Actuator

In order to develop a soft mechanism actuator whose inherent stiffness is controllable, we apply pneumatic system to the actuator. The structure of the actuator is shown in Fig.3. The actuator is constructed with two materials. One is a silicon rubber and the other is sponge rubber. Furthermore, since the sponge is coated with silicon rubber, air can be charged into the sponge chamber. In this study, the number of sponge layer is two. As this time, the actuator expands when air is charged into the sponge chamber.

The actuator has sponge layer inside the silicon rubber. Therefore, when the actuator is made to burst by some accidents, the sponge material can support the object by its inherent stiffness. As the results, the actuator can ensure safe operation.

Furthermore, in order to improve the two layers type actuator, a clipping type actuator is proposed. The structure of the sponge is shown in Fig.4. In Fig.4, the two layers type actuator is divided into four structures(Type1 (Standard Type), Type2(Clipping Type), Type3(Outer Coat One Layer Type) and Type4(Outer Coat One Layer and Clipping Type)).

Experimental Setup

We investigate dynamics of the actuator when air is charged into the sponge chamber. In the experiment, two types of sponge are used. One is ECZ type whose density is $16 \pm 1.5 \text{ kg/m}^3$ and the other is EMM type whose density is $52 \pm 3 \text{ kg/m}^3$. The size of the actuator is $80 \times 80 \times 20 \text{ mm}$. The experimental set up is shown in Fig.5. The pressure in the sponge chamber is measured by a pressure transducer. Further, we use a laser sensor to measure the displacement of the actuator.

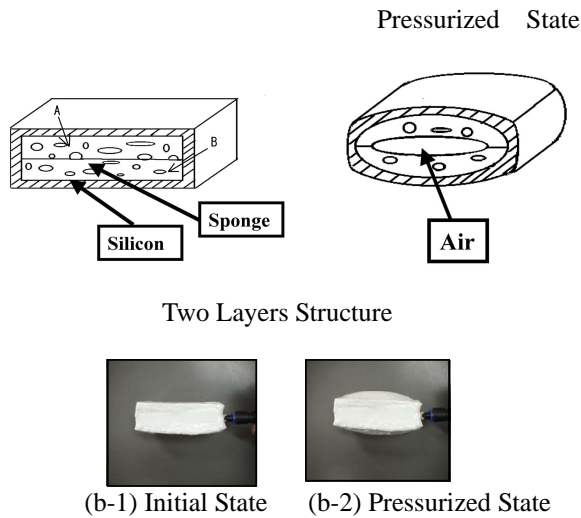


Fig.3 Schematic View of Pneumatic Sponge-Core-Soft Rubber Actuator

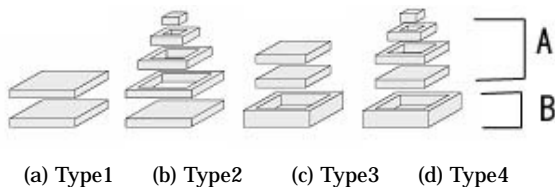


Fig.4 Structure of Sponge Plate

FORCE CONTROL PERFORMANCE

Step Response

In this section, we consider force control performance of the actuator with respect to each sponge type as shown in Fig.4. At first, we investigate the step response of force control. In the experiment, each type sponge structure (Type1-Type4) is investigated with respect to each sponge material (ECZ and EMM).

In the experiment, hierarchical feedback control scheme[9] is applied to the force control of the actuator. The control equations are as follows. Thus, at the first step, the desired pressure is derived from Eq(1). And input volt to the valve is calculated from Eq(2).

$$Pr = K_p (Fr - F) + K_i \int (Fr - F) dt \quad (1)$$

$$V = V_0 + K(Pr - P) \quad (2)$$

The experimental results are shown in Fig.6. From the results, it is considered that the response time is slow because of both low pressure level and rubber elastic force. Further, settling time and steady state error of each sponge type are shown in Table 1 and Table 2. In this experiment, the desired force is 5[N].

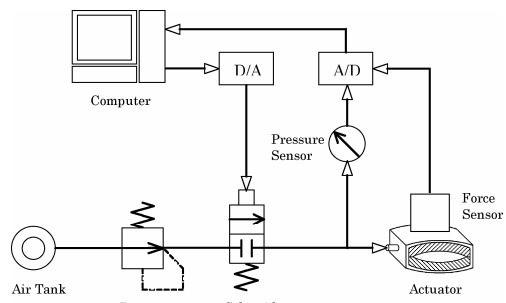


Fig.5 Experimental Setup

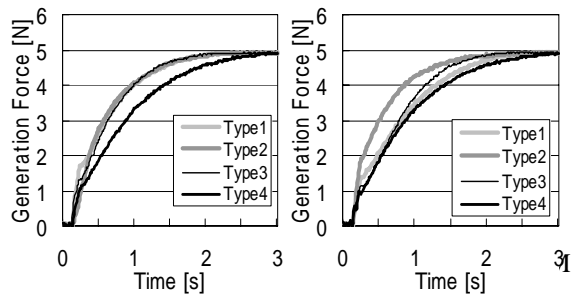


Fig.6 Experimental Results of Force Control

Table1 Settling Time

Table2 Steady State Error

(unit:[s])

(unit: $10^{-3} \times [N]$)

	ECZ	EMM
Type1	2.16	2.61
Type2	2.23	2.25
Type3	2.14	2.11
Type4	2.90	2.92

	ECZ	EMM
Type1	1.96	5.35
Type2	3.64	1.47
Type3	0.51	2.89
Type4	4.05	3.43

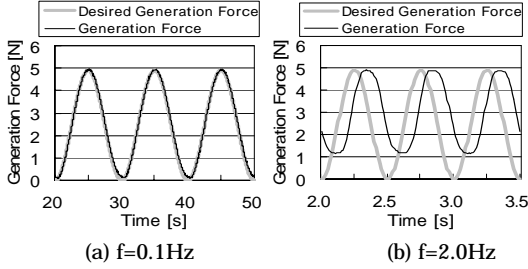


Fig.7 Experimental Results of Frequency Response with Force Control (ECZ-Type3)

From experimental results, it is seen that the result of Type3 (Sponge material is ECZ) is much better than the other types. Further, in the case of Type3, it is considered that the deformation of the element is easier than the case of Type1 because of their structure.

Frequency Response

In order to ascertain the frequency characteristics of the actuator, we measure the output force as a function of the sinusoid pressure fluctuation. The sample response of the experimental result with respect to Type3(ECZ) is shown in Fig.7.

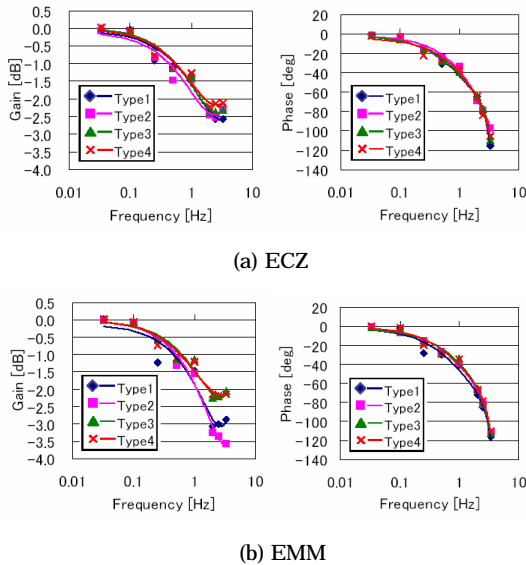


Fig.8 Bode Diagram

Furthermore, the Bode diagram with $[F/F_r]$ is shown in Fig.8.

From these experimental results, it is cleared that with respect to the ECZ, there is almost no difference between each sponge structure (Type1 – Type4). On the other hand, in the case of EMM the gains of Type3 and Type4 are much larger than that of Type1 and Type2. Furthermore, when we use Type3 and Type4, it is better to use these sponge types in the high frequency region (over 1Hz). As a result, it is cleared that Type3 is useful to realize a good performance of force control from the result of both step pressure and frequency response.

FORCE SENSING PERFORMANCE

Force Estimation

To understand the performance of external force estimation we use the Type3 sponge structure as shown in Fig.4. Here, the sponge material is ECZ and the size of the actuator is $80 \times 80 \times 20$ mm. The experimental setup is shown in Fig.9. In the experiment, an initial pressure P_0 is charged into the actuator. Next, a force sensor is attached to the plate on the element(Actuator) under the condition that the actuator is sealed up. At this time, we measure both inner pressure and compression force of the force sensor. The relation between the pressure in the actuator and force with respect to each initial pressure is shown in Fig.10. In the experiment, the initial pressure is increased from 0 to 9kPa. From the experimental result, an external force estimation equation is derived as follows.

$$F = \frac{P - P_0}{a_1 P_0^3 + a_2 P_0^2 + a_3 P_0 + a_4} \quad \begin{cases} a_1 = -0.00008 \\ a_2 = 0.0006 \\ a_3 = 0.001 \\ a_4 = 0.3004 \end{cases} \quad (3)$$

Here, F is an external force.

In order to indicate the usefulness of the Eq.(3), we measure the pressure in the actuator under the condition that a mass is placed on the plate of the element. At this time, the external force is calculated from Eq.(3). The result of external force estimation is shown in Fig.11. Here, the initial pressure is 6kPa. From this result, it is clear that the average error is 0.44N and maximum error is 1.03N. Thus, the estimation equation is useful to estimate external forces.

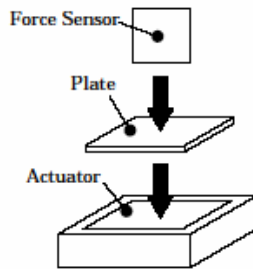


Fig.9 Experimental Setup

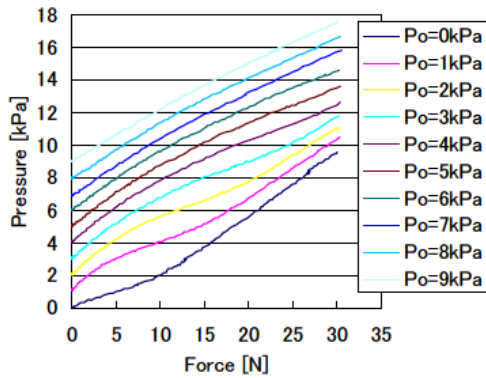


Fig.10 Experimental Result of Force Measurement

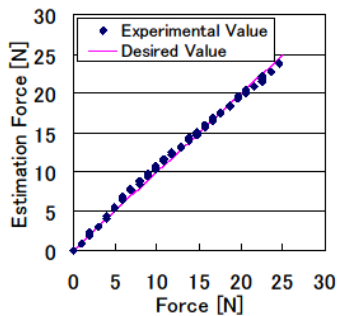


Fig.11 Experimental Result of External Estimation Force

CONCLUSIONS

In this paper, we have proposed a new type of hybrid element by using sponge-core-soft rubber actuator in which a sponge rubber is covered with silicon rubber in order to realize a soft mechanism of a hand. Through several experimental results, the force control characteristics of the proposed element were clarified. Furthermore, we verified the external force estimation capability of the element.

ACKNOWLEDGMENTS

This research was partially financed by Grant-in-Aid for Scientific Research(c) (2) (Project Number: 16560234). Moreover, support for this research was provided in part by SMC Co., Ltd.

REFERENCES

- (1)Y.Hayakawa, T.Yamamoto,N.Iseki and Y.Amano, "Development of an Autonomous Transfer Machine with Human Compatibility by using Pneumatic Actuators", Proceedings of the European Medical & Biological Engineering Conference (1998)
- (2)K.Suzumori, S.Iikura and H.Tanaka,"Applying A Flexible Micro-actuator to Robotic Mechanisms", IEEE Control Systems, 12-1, 21-27 (1992)
- (3)Y.Hayakawa, H.Mori and R.Tsuda, etc , "Basic Study to Develop an Active Supporter with Human Compatibility", Proceedings of the Symposium of Welfare Technology (2001)
- (4)Y. Hayakawa, H. Mori, R. Tsuda, M. Aichi, S. Hamasaki, S. Higashiura, T. Kodaka and S. Kawamura , "Development of a Silicon Outer Fence Mold Actuator with Human Compatibility", Proceedings of the Fifth JFPS International Symposium on Fluid Power (2002)
- (5)Y. Hayakawa, H. Mori, M. Aichi, T.Kodaka (Nitta) and S.Higashiura(Nitta), "Study on an Active Supporter Using Pneumatic Foaming Rubber Actuator Coated with Silicon Rubber", Proceedings of the 2nd European Medical and Biological Engineering Conference (2002)
- (6)Y. Hayakawa, K. Morishita and M.Aichi,"Control Performance of a Pneumatic Silicon Outer Fence Mold Actuator", SICE Annual Conference in Fukui (2003)
- (7)Y. Hayakawa, K. Morishita and M. Aichi,"Study on a New Mechanism of a Silicon Outer Fence Mold Actuator", 7th International Symposium on Fluid Control, Measurement and Visualization (2003)
- (8)Yasuhiro Hayakawa, Mina Aichi and Kensuke Morishita,"Basic Characteristics of a Silicon Outer Fence Mold Actuator with Human Compatibility", 1st International Conference on Computational Method in Fluid Power Technology (2003)
- (9)S.Kawamura, K.Miyata, H.Hanafusa and K.Ishida,"A Hierarchical Feedback Control Scheme for Pneumatic Drive System", SICE, Vol.26, No.2, pp 204-210 (1999)

DEVELOPMENT OF RODLESS TYPE FLEXIBLE PNEUMATIC CYLINDER AND ITS APPLICATION FOR LONG STROKE MCKIBBEN TYPE ACTUATOR

Tetsuya AKAGI* and Shujiro DOHTA**

* Department of Intelligent Mechanical Engineering, Faculty of Engineering,
Okayama University of Science
1-1, Ridai-cho, Okayama, 700-0005, Japan
(E-mail: akagi@are.ous.ac.jp)

** Department of Intelligent Mechanical Engineering, Faculty of Engineering,
Okayama University of Science
1-1, Ridai-cho, Okayama, 700-0005, Japan

ABSTRACT

Recently, virtual reality systems that feed back to human senses have only been realized as visual and acoustic feedback. However, they are not enough to realize the force feedback system for hands, arms, legs and so on. The actuators required for such a system need to be flexible so as not to injure the body. The purpose of our study is to develop a flexible and lightweight actuator which can be safe enough to be attached to the human body. We propose new types of flexible pneumatic actuator that can be used even if the actuator is deformed by external force. In this study, we tested rodless type flexible pneumatic cylinders that have a self holding function for positioning under the condition of no supply pressure. We also developed a new type of McKibben artificial muscle that has a long stroke of more than 80 % of its original length. As a result of our experiment, we can confirm that the tested cylinder is useful to be applied in a positioning system because it consumes less air under the condition of holding. By using the tested McKibben actuator, we can realize a long stroke lifting motion of a dumbbell whose mass is 6 kg.

KEY WORDS

Rodless Type Flexible Pneumatic Cylinder, Self Holding Function, Long Stroke McKibben Type Actuator, Soft Actuator

INTRODUCTION

Virtual reality has been flourishing as an interactive information technology. Recently, virtual reality systems that feed back to human senses have only been realized as visual and acoustic feedback. However, they are not enough to realize the force feedback system for hands, arms, legs and so on. Furthermore, due to the ageing in Japanese society and the decreasing birthrate, an important problem of providing nursing care for the elderly has occurred. As a result, it is

necessary to develop systems to aid in nursing care[1]. The actuators required in such a feedback control system, as for power assisted nursing care of the elderly, need to be flexible so as not to injure the body. The purpose of our study is to develop a flexible and lightweight actuator which can be safe enough to be attached to the human body. We had proposed and tested new types of flexible pneumatic actuators that can be used even if the actuator is deformed by external force[2][3].

In this study, we investigate the friction in a rodless type

flexible pneumatic cylinder proposed in our previous studies[4][5]. We also aim to develop a new type of McKibben artificial muscle that has a long stroke of more than 80 % of its original length.

RODLESS TYPE FLEXIBLE PNEUMATIC CYLINDER

Construction and operating principle

Figure 1 (a) and (b) show the construction of two types of rodless flexible pneumatic cylinders. We call the former, as shown in Fig.1(a), a “Double type” and call the latter a “Single type”. The double type cylinder consists of a flexible tube as a cylinder and gasket, two steel balls as a cylinder head and a slide stage that can slide along the outside of the tube. The slide stage has two rollers set on the inner bore of the stage in order to press and deform the tube toward the center of the tube. The construction of the single type cylinder as shown in Fig.1(b) is similar to that of the double type. The single type cylinder uses one steel ball as a cylinder head. The steel ball is held by two pairs of brass rollers from both side of the ball. Compared with the double type, we aim to decrease the friction of the cylinder by decreasing the contact area between the inner ball and inner wall of the tube.

The operating principles of both cylinders are as follows. When the supply pressure is applied to one side of the cylinder, the cylinder head (inner steel balls) are pushed. At the same time, the balls push rollers and move the slide stage while they deform the tubes. In the double type, the two balls of the cylinder head are not connected to each other, that is, each ball can move independently. Therefore, the balls can move along the curved tube in the same manner as a straight tube.

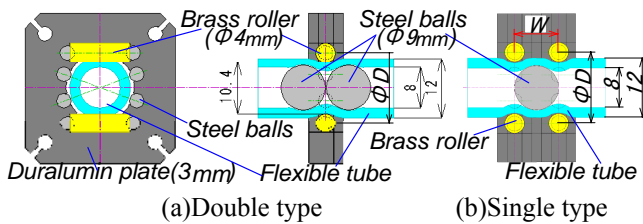
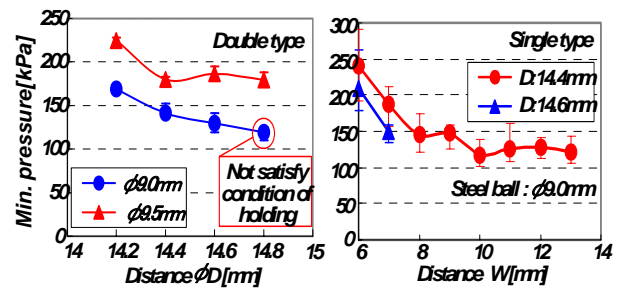


Fig.1 Construction of rodless type flexible pneumatic cylinder

Minimum driving pressure for actuation

Figure 2 (a) and (b) show results of minimum pressure for actuation of double and single type cylinder using various center distances D and W (as shown in Fig.1) between the two pairs of rollers as a design parameter. In case of the double type cylinder, as shown in Fig. 2(a), we investigated the relation between the center distance D and minimum pressure of the cylinder. In

case of the single type cylinder, as shown in Fig.2(b), we investigated the relation between the center distance W and minimum pressure using optimal value of distance D of 14.4 or 14.6 mm that can be obtained from Fig.2(a). Vertical lines show the scatter in measured values. From Fig. 2(a), we can see that the cylinder using a distance D of 14.6 mm and an inner steel ball with a diameter of 9.0 mm shows the lowest driving pressure of 130 kPa. From Fig. 2(b), it can be seen that the minimum driving pressure of the single type cylinder is gradually approaching the constant value of 120 kPa in the case using the center diameter W of more than 10 mm. It can be seen that the lowest driving pressure of the cylinder is 120 kPa. We can reduce about 7.8 % of the friction compared with the double type of cylinder.



(a) Double type

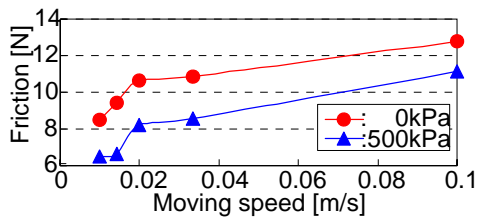
(b) Single type

Fig.2 Minimum driving pressure of rodless type flexible pneumatic cylinder

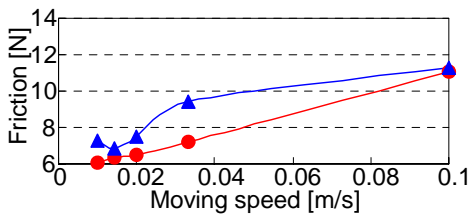
Frictional characteristics

In order to investigate frictional characteristics for actuation of the tested cylinders, we measured the pulling force when we gave a motion to the slide stage of the cylinder at constant speed. Figure 3(a) and (b) show the relation between moving speed of the slide stage and frictional force of the double type and single type cylinder, respectively. In Fig.3, each symbol ▲ and ● shows the experimental results under the condition when supplied pressure of 500 kPa is applied or not to the both side of cylinder chambers. In the case using double type cylinder as shown in Fig.3(a), we can see that the frictional force under the condition of no supply pressure is about 1.4 times as large as the case when supply pressure of 500 kPa is applied to the cylinder. On the other hand, in the case using the single type cylinder, it can be seen that the frictional force when supply pressure is applied to the cylinder becomes larger than the results with no supply pressure. We think that it is caused by following reason: In the case of double type cylinder, the frictional force depends on the contact area between inner steel balls

and inner wall of cylinder tube. When supply pressure is applied to the cylinder, the cylinder tube expands and the contact area between the inner balls and the tube decreases. Then it makes the friction decrease. On the other hand, in the case of single type cylinder, the contact area between an inner steel ball and the tube depends on an arrangement of two pairs of brass rollers and the inner steel ball. When the cylinder tube expands with supply pressure of 500 kPa, the contact area between brass rollers and outer bore of the tube increases. So, it makes the friction increase. As a result mentioned above, we can conclude as follows. The double type cylinder has an advantage that it is possible to hold more easily the slide stage at a certain position than in the case using an ordinary pneumatic cylinder on the market, because the tested cylinder has a feature that the frictional force of the cylinder without input pressure is higher than the case when supply pressure is applied. This means that the tested cylinder has a “self holding function” for positioning under the condition of no supply pressure. This is one of important merits of this cylinder.



(a) Double type



(b) Single type

Fig.3 Frictional characteristics of rodless type flexible pneumatic cylinder

MCKIBBEN ACTUATOR WITH ADJUSTABLE STROKE

Construction and operating principle

The tested flexible pneumatic cylinder has some merits such as long stroke pushing and pulling motion, high speed motion of more than 1 m/s and self holding function for positioning. However, the generated force of the cylinder, that is about 15 N with supplied pressure of 500 kPa, is not so enough to apply a force

feedback system for human. Therefore, we should consider to increase the generated force of the flexible actuator. A McKibben artificial muscle has been flourishing as a flexible and wearable actuator because of its simple configuration, flexible property and lightweight. Usually, McKibben artificial muscles can generate larger force compared with their weight. However, the actuator can not act a long stroke motion such as more than 25 % of their original length. Then, we aim to develop a new type of flexible actuator by combining the rodless type flexible pneumatic cylinder and McKibben artificial muscles. Figure 4 shows the construction of the tested actuator. It consists of an ordinal McKibben artificial muscle that is made of a silicone rubber tube coated with nylon mesh and a slide stage that can slide along the outside of the tube. The slide stage has two rollers with outer diameter of 8 mm set on the inner bore of the stage in order to press the tube toward the center of the tube. A chamber of McKibben artificial muscle is divided into two chambers by using the slide stage. The rollers in the stage and rubber tube keep the seal even if supply pressure is applied to both chambers. Figure 5 shows the operating process of the tested actuator. The operating principle of the actuator is as follows. The slide stage is fixed. When a free end of the actuator (we call it “A side” for short) as shown in Fig.5② is pressurized, the actuator generates smaller pulling force than the case using a usual McKibben actuator. Then, the tube length of the opposite side (we call it “B side” for short) of the actuator becomes shorter by pulling force. In this condition, we add to pressurize “B side” of the actuator as shown in Fig.5③. “B side” of the actuator works as same as a usual McKibben actuator. Therefore, it can generate larger force than the case when we pressurize only to “A side” of the actuator. After exhausting the air in the B side of chamber, this causes the loosening between the slide stage and the B side of tube end.

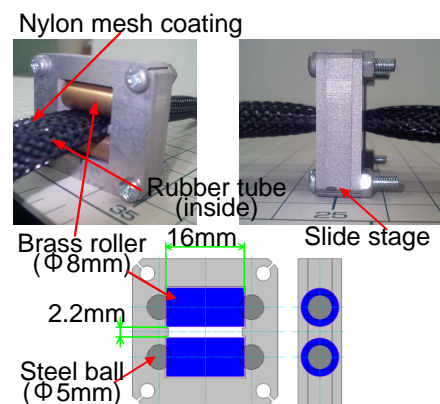


Fig.4 Construction of the McKibben actuator with adjustable stroke

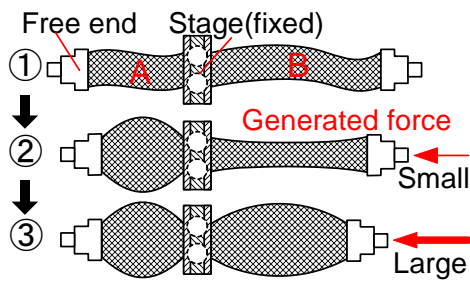


Fig.5 Operating principle of tested McKibben actuator

By repeating these operations (①→②→③→②→③…), we can adjust the stroke of the tested actuator statically. It means that the tested McKibben actuator can work a long stroke pulling motion under the condition when there is sliding friction between an object connected with the actuator and the table.

Generated force of tested actuator

Figure 6 shows the relation between supplied pressure in “A” or “B” side of chamber and generated force of the tested actuator. In the experiment, we use the tested actuator with a whole length of 500 mm without connectors and changed the ratio of lengths between “A” and “B” side of tubes every 100 mm. The results as shown in Fig.6 include two types of experimental results. One is the generated force when we only pressurized “A side” of the actuator. The other is the case when we added to apply supply pressure to “B side” of the actuator under condition when “A side” is pressurized at 400 kPa. In Fig.6, each symbol shows the results using various combinations of lengths of “A” and “B” side of the actuator. Each input pressure into “B side” of chamber for each experimental condition is given until a leakage occurs between “A” and “B” side chamber. From the left side in Fig.6, we can see that each relation between input pressure and generated force when we apply the pressure to “A side” is almost same even if the length of “A side” of the actuator is changed. Maximum generated force in this case is about 21 N. From the right side in Fig.6, it can be seen that the generated force becomes larger than the case when “A side” of chamber is pressurized only. The maximum generated force in this case is about 5 times as large as the previous case; that is about 110 N. This value is almost the same as the case using a usual McKibben actuator. We can see that the generated force increases according to length of “B side” of the actuator even if we give a same input pressure. It means that the tested actuator has same characteristics of a usual McKibben actuator that can generate larger force according to the tube length of the actuator. In the experiment, we found a leakage between two

chambers of the actuator when supply pressure becomes larger. The leakage is generated as follows. When supply pressure in two chambers becomes larger, the rubber tube expands. Then the thickness of the tube becomes smaller. It generates the leakage between two chambers at the point of slide stage. Therefore, the maximum generated force depends on the sealing characteristics of the actuator. We think that it is possible to increase the generated force of the actuator by improving the construction of the slide stage and rubber tube so as to keep the seal for higher input pressure.

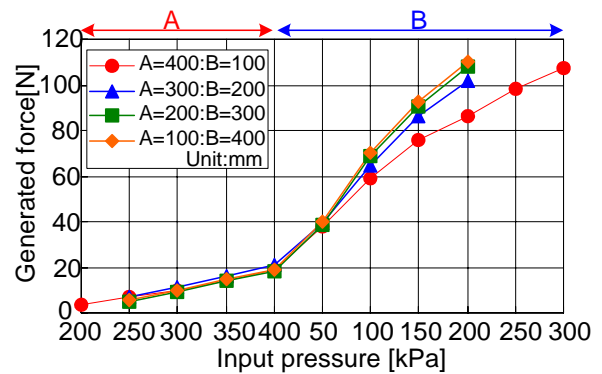


Fig.6 Experimental results of tested McKibben actuator

LONG STROKE MCKIBBEN TYPE ACTUATOR

Construction and operating principle

The tested McKibben actuator mentioned above can act a long stroke motion by changing the length of the tube connected with the load statically. However, the tested actuator could not realize a long stroke motion under the condition of constant load. Therefore, we proposed and tested a new type of McKibben actuator that can work continuously in a long stroke motion. Figure 7 shows a construction of a long stroke McKibben type actuator and experimental equipment for measuring the generated force of the actuator. The actuator consists

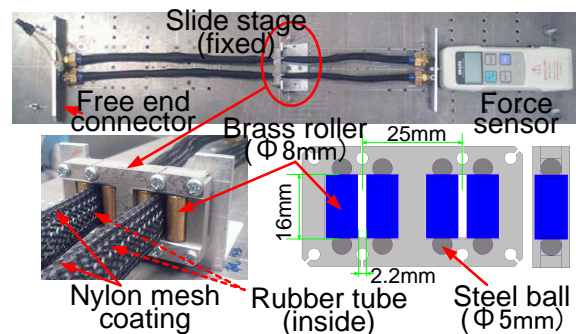


Fig.7 Construction of long stroke McKibben type actuator and its experimental equipment

of two McKibben actuators with adjustable stroke that both actuators are arranged parallel with distance of 25 mm. Each end of two actuators is connected with an aluminum plate. One end of the actuator can move freely; that is a free end. The other is connected with a load or a digital force sensor (IMADA Co.Ltd. DSP-100). The slide stage and the force sensor are fixed on the table.

The operating process of the long stroke motion using tested actuator is shown in Fig.8. We call the upper side chambers of stage “A side”. Each a left and right chamber located under the stage is called “B side” and “C side”, respectively. The operating principle of the actuator is as follows. One end of the actuator (“B side” and “C side”) connected with a load that was set toward the ground. The other (“A side”) located on upper side of the fixed stage. First, we apply constant supply pressure to “A side” of chambers. At the point of the fixed stage, the “A side” of tubes generate a small pulling force toward the upper side as shown in Fig.8②. By expanding of “A side” of tubes, the tubes are hard to pull down toward “B and C” side even if a larger downward pulling force is applied to the tubes. It is caused that “A side” of tubes function as a stopper at the point of narrow clearance between two rollers. In the condition, when we pressurize “C side” of chamber, “C side” of tube works as a McKibben artificial muscle and generates larger upward force. Then the distance between the stage and the lower side end connector becomes a little shorter, an axial deflection in “B side” of tube is produced as shown in Fig.8③. At the same time, “B side” of tube is pulled into the slide stage by pulling force generated in “A side” of tubes and stretched tightly between the stage and connector. In the same manner as the previous one, when the pressurized chamber is changed from “C side” to “B

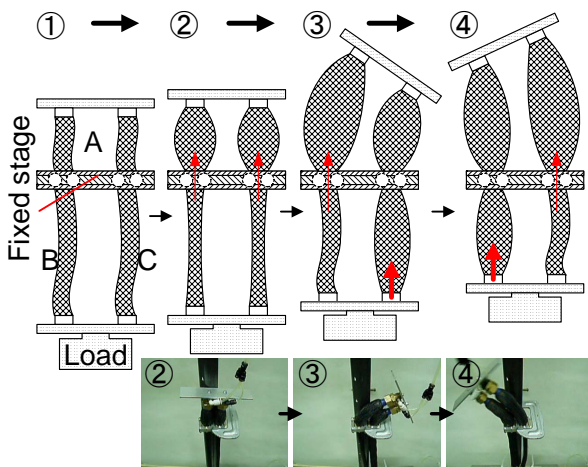


Fig.8 Operating principle of long stroke McKibben type actuator

side”, the distance between the stage and the end connector becomes shorter while the actuator holds a lifting force of the load as shown in Fig.8④. By repeating these operations (②→③→④→③→④…), the actuator can realize a continuous lifting motion with a long stroke of more than 80 % of its original length even if it is under the condition of the constant load such as a gravity. And we can control the position of the load by adjusting the number of repetitions of these operations (③→④→③→④…).

Experimental results of long stroke lifting motion

Figure 9 shows the view of a long stroke lifting motion using the tested actuator. In Fig.9, each figure shows the state of the actuator with time. The number of left end in each figure shows the time from the beginning of the moving. In the experiment, the actuator is set in the vertical position and the slide stage is fixed on a pole. The lower end of the actuator is connected with a stainless dumbbell whose mass is 6 kg. The length of the actuator without inlets and connectors is about 500 mm. The operation of the actuator is done as follows. First, “A side” of chamber is pressurized with supply pressure of 400 kPa as shown in Fig.9①. Then, we give supply pressure of 400 kPa to “B and C side” of tube alternately every 1 second through two on/off control valves (Koganei Co.Ltd. G010HE). It can be seen that the tested actuator can realize the long stroke lifting motion of about 400 mm for 9.4 seconds while the free end connector moves as an oscillating motion. From Fig.9③ and ⑤, we can confirm that it is hard to pull down the tubes under condition of pressurized in upper chambers even if the axial deflection in a lower side of tube is produced. By exchanging the pressurized chambers and the procedure of operation in the actuator, the actuator can move toward opposite direction, because the moving direction of the actuator depends on its operation, it does not depend on the direction of the load.

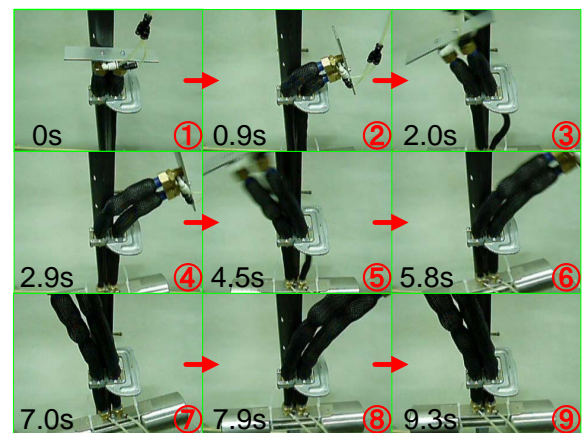


Fig.9 View of a long stroke lifting motion using tested actuator

Generated force of tested actuator

In the same manner of the McKibben actuator with adjustable stroke, we investigate the relation between the input pressure and the generated force of the long stroke McKibben type actuator. Figure 10 shows the relation between supply pressure in “A side” or “B” and “C” side of chamber and generated force of the tested actuator. The experimental conditions for measuring the generated force are almost the same as the case using the McKibben actuator with adjustable stroke. As a point of difference from the previous experiments, we gave the same supply pressure to both “B” and “C” side of chambers in measurement. In Fig.10, each symbol shows the results using various combinations of lengths of “A”, “B” and “C” side parts of the actuator. From Fig.10, we can see that the relation between the input pressure and generated force of the actuator is similar to previous results as shown in Fig.6 such as an increasing tendency of generated force when we apply the pressure to both side (A, B and C side) of chambers. It can be seen that the maximum generated force using the tested actuator is about 2 times as large as previous one, that is about 220 N, because two adjustable actuators were used in the actuator. As a result, we can confirm that the maximum generated force of the actuator depends on the sealing characteristics, because the generated force of a McKibben actuator becomes larger according to supply pressure. Therefore, it is possible to develop the actuator that can generate higher force by changing the configuration of the slide stage and material of the rubber tube and coating.

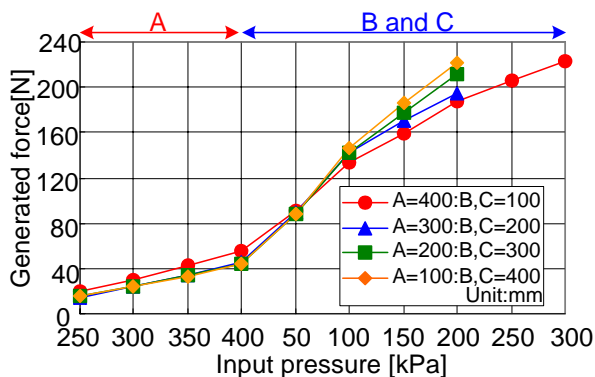


Fig.10 Experimental results of long stroke McKibben type actuator

CONCLUSIONS

This study aiming at the development a new type of McKibben artificial muscle and investigation about the friction characteristics of the single and double type

rodless flexible pneumatic cylinder can be summarized as follows:

- 1) As a result using the single type cylinder, we found that the frictional force increases according to input pressure. We conclude that it is caused that the contact area between rollers and the tube increases according to expansion of tube for supply pressure.
- 2) In case of double type cylinder, we found that the frictional force with no input is about 1.4 times as large as the case when supply pressure of 500 kPa is applied because of decreasing the contact area between the inner steel balls and tube according to input pressure. As a result, we can confirm that the tested cylinder has a self holding function for positioning under the condition of no supply pressure.
- 3) We proposed and tested the McKibben actuator with adjustable stroke that is combined the rodless type flexible pneumatic cylinder and a usual McKibben artificial muscle. As a result of experiment, we found that the maximum generated force is about 110 N, and this limit depends on the sealing characteristics of the actuator.
- 4) We proposed and tested the long stroke McKibben type actuator that has a parallel arrangement of two McKibben actuators with adjustable stroke. As a result, the tested actuator can realize a long stroke lifting motion, such as more than 80 % of its original length, of a dumbbell whose mass is 6 kg.

Finally, we express our thanks that a part of this research was supported by Okayama Prefecture Industrial Promotion Foundation in Japan.

REFERENCES

1. K.Yamamoto et al, Development of Wearable Power Assisting Suit, *Proc. of FLUCOME2003*, Sorrento, 2003,113.pdf, pp.1-6.
2. T.Akagi, S.Dohta and et al, Development of a Flexible Pneumatic Actuator with a Flexible Tube, *Proc INTERMAC2001 Joint Tech. Conf.*, Tokyo, 2001,F-1093.pdf, pp.1-10.
3. T.Akagi and S.Dohta, Development of a Flexible Pneumatic Cylinder with a Flexible Tube, *Proc. of FLUCOME2003*, Sorrento, 2003,076.pdf, pp.1-6.
4. T.Akagi and S.Dohta, Development of Rodless Type Flexible Pneumatic Cylinder and Its Application, *Proc. of Actuator2004*, Bremen, 2004, pp.751-754.
5. T.Akagia and S.Dohta, “Development of Flexible Pneumatic Rotary Actuator Using Flexible Cylinder”, *Proc. of FA2004*, Denver, 2004, JS012.pdf, pp.1-4.

Development of Pneumatic Wearable Power Assist Device for Human Arm "ASSIST"

Daisuke Sasaki, Toshiro Noritsugu, Masahiro Takaiwa and Yusuke Kataoka

Graduate School of Natural Science and Technology

Okayama University

3-1-1 Tsushimanaka , Okayama , 700-8530 Japan

(E-mail:[daisuke, toshiro,takaiwa]@sys.okayama-u.ac.jp)

ABSTRACT

In order to realize an assist of independent life for people in need of care and relieve a physical burden for care worker, an active support splint driven by pneumatic soft actuator (ASSIST) to support a human arm has been developed. ASSIST is constructed with the appliance and the rotary-type soft actuator. Since a weight and hardness of device involve a danger of causing a serious accident for users or neighbors, this device is constructed with components which are a lightweight and have a mechanical softness. In this paper, the structure of developed device is described, and then the control method based on the center of pressure is proposed. Finally, the assist effectiveness using the proposed control method is experimentally discussed.

KEY WORDS

Soft mechanism , Soft actuator , Pneumatic rubber muscle , Wearable robot

INTRODUCTION

Owing to a growth of advanced age society, it is predicted that a ratio of an elderly in a population will increase from current 20[%] to 36[%] in 2060[1]. In addition, an increase in a people in need of care is also predicted. Actually, a ratio of people in need of care in an elder population which was 10[%] in 2000 had increased to 15[%] in 2003[1]. Thus a decrease in a young people who engages in a care worker and an increase in an elderly in need of care have become serious problem in Japan.

However, 30% elderlies in all ones in need of care have slight symptoms, then they can live independently if disabled physical functions are assisted. From above reasons, many kinds of power assist device have been developed [2,3]. 3DOF robotic exoskeleton [2] of a floor type device can effectively assist a human upper limb according to an enough

generated force. A wearable robotic orthosis[3] can support a working motion for a muscular weak human even if it is constructed with simple elements such as a spring-dumper system. However, a compatibility of a weight, size and a function, a hardness of components are technical issues to improve an operability and a human friendliness for preventing a serious accident for the users or neighbors. On the other hand, ASSIST[4] shown in **Fig.1** has a high human friendliness according to constructing with a pneumatic soft actuator which has a flexibility of a material, a power source and a high power weight ratio. It is the main advantage for the medical or the welfare application that the developed device has a flexibility due to not only the power source but also the body of actuator. However, the developed ASSIST has to solve a technical issue about controlling a device based on a human intention to improve a maneuverability. In this pa-

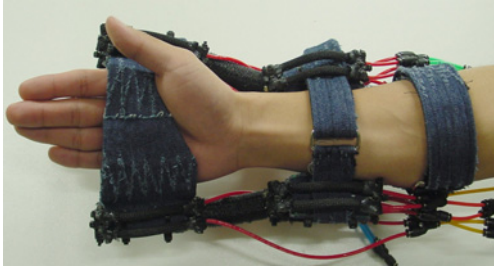


Fig.1: ASSIST to support a wrist

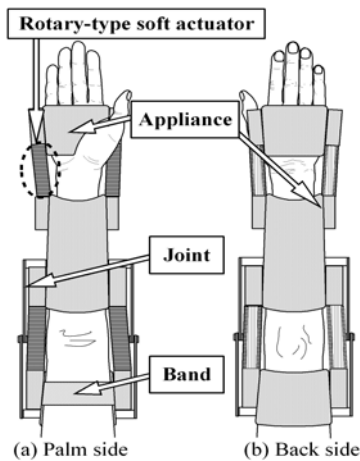
per, ASSIST extended an assisting part to a human elbow is described. In addition, a control method based on a human intention is proposed. Finally, a effectiveness of ASSIST operated on the proposed method is experimentally evaluated.

STRUCTURE OF ASSIST

Fig.2 shows the outlook and the structure of ASSIST.



(a) Outlook



(b) Structure

Fig.2: ASSIST to support an arm

ASSIST is constructed with an appliance made by forming a plastic used as an interface between an actuators and a human body. The joint are put for restricting the movable angle of ASSIST under an average maximum bending angle of a Japanese male. In this section, the structure and the characteristics of components are discussed.

The rotary-type soft actuator for an elbow consists of a rubber tube and a polyester bellows as shown in **Fig.3(a)**. The outer and inner diameters and length of rubber tube are 20, 14, 290[mm], respectively as shown in Fig.3(b). Both ends of rubber tube are plugged by polyurethanes with diameter 14[mm] and length 100[mm]. The outer diameter of polyester bellows are 40[mm] as shown in Fig.3(c). The bellows is reinforced with a fiber along the axial direction as shown in the figure. Depending on the reinforcement, when the compressed air is supplied into the actuator, the actuator expands to the circumferential direction as shown in **Fig.4**.

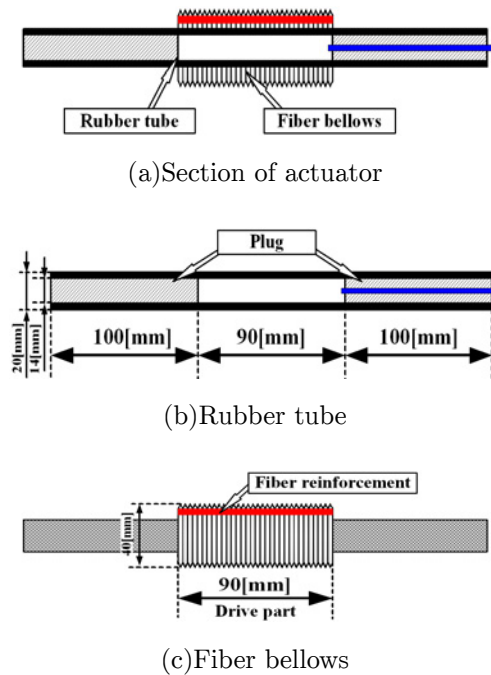


Fig.3: Rotary-type soft actuator

Fig.5 shows the fundamental characteristics of actuator. Fig.5(a) shows the relation between inner pressure and bending angle under unloaded condition. Fig.5(b) shows the relation between bending angle and generated torque. The torque is calculated from the generated force of actuator fixed at each angle as shown in **Fig.6** when the maximum pressure is determined 500[kPa] in considering with-standing pressure of the actuator.

Fig.7 shows the torque characteristic of ASSIST



(a) Initial state



(b) Pressurized state

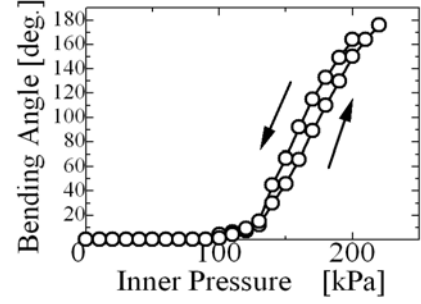
Fig.4: Outlook of rotary-type soft actuator

when two actuators are put in the forearm appliance. A mass of a forearm and a palm of male is about 2.5[kg][5]. A center of gravity of them is assumed to locate on a center of a forearm[6], about 2.8[Nm] per one actuator is required to keep a posture of a forearm horizontally. From the results, the torque of ASSIST to keep a posture and to lift a load about 4[kg] can be obtained in the movable angle.

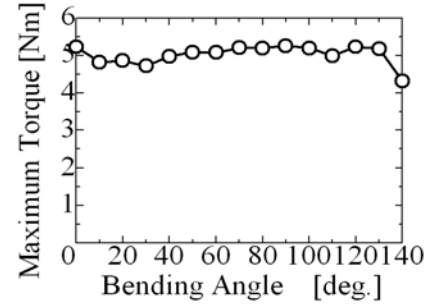
OPERATION BASED ON HUMAN INTENTION

Two tactile soft sensor is put in the appliance as shown in **Fig.8** to detect the contact force between the appliance and the forearm. **Fig.9** shows the structure of developed sensor. Developed sensor is made by two vinyl chloride sheets and sponge as shown in Fig.9(a). An extent of an oblique line in Fig.9(b) represents a welded part. When the external force is applied to the sensor, the inner pressure is increased according to the decrease in the inner volume. By detecting the inner pressure, the external force can be detected. **Fig.10** shows the fundamental characteristic of the developed sensor.

When the forearm bends as shown in **Fig.11**, the angle between the appliance and the forearm increases or decreases by $\delta\theta_i$. According to $\delta\theta_i$, the center of pressure between the appliance and the forearm is changed on y axes shown in **Fig.12**. The



(a) $P-\delta\theta$



(b) $\delta\theta-\tau_{max}$

Fig.5: Fundamental characteristics of actuator

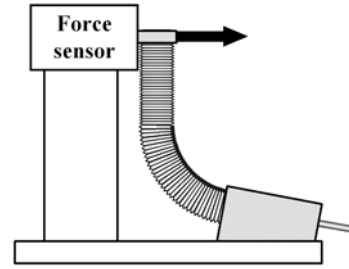


Fig.6: Experimental condition

origin is the middle point between the centers of the sensor. A center of pressure y_a is calculated as:

$$y_a = \frac{l(F_1 - F_2)}{2(F_1 + F_2)} \quad (1)$$

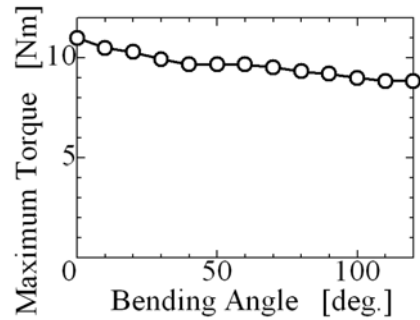


Fig.7: Torque characteristic of ASSIST

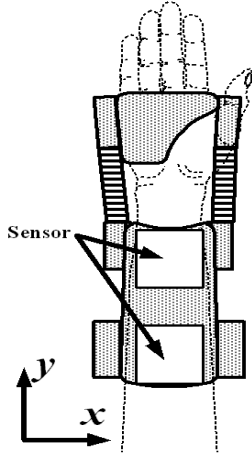


Fig.8: Arrangement of tactile soft sensor

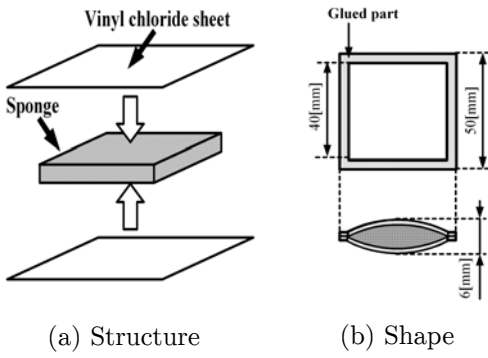


Fig.9: Structure of tactile soft sensor

F_1, F_2 represent the detected forces by tactile soft sensors, l is the distance between the center of the sensors. In this device, l is 150[mm].

Fig.13 shows a block diagram of a control system based on the center of pressure. In the figure, y_{ini} is the initial center of pressure, P, P_r are the measured and reference inner pressure. P_{min} is the pressure to abolish the dead zone of the actuator. $\theta, \theta_r, \delta\theta_i$ are the bending angle of ASSIST, the bending angle

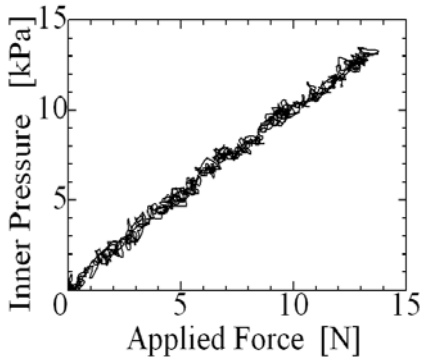


Fig.10: Characteristic of tactile soft sensor

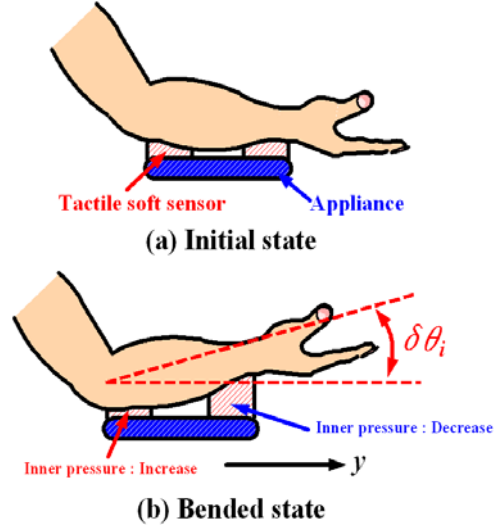


Fig.11: Principle of operation

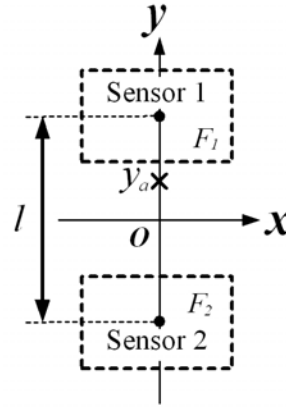


Fig.12: Detection of center of pressure

of the elbow, the angle between the appliance and the forearm.

In case the bending angle of ASSIST θ does not follow θ_r intended by a human, the angle between the appliance and the forearm increases or decreases by $\delta\theta_i$ as compared with the initial state. Then, let the center of pressure is y_a when $\delta\theta_i$ is produced, the difference δy between y_{ini} and y_a can be regarded as the parameter of the bending angle error. According to controlling the inner pressure P of the actuator by the reference one P_r obtained from P_{min} and the output of PI controller δP for the input δy , ASSIST can follow the movement of the forearm without measuring θ and θ_r . The inner pressure is controlled by the flow control type servo valve (FESTO MPYE-5-1/8 LF-010B) and the pressure sensor (COPAL PA-500-502G).

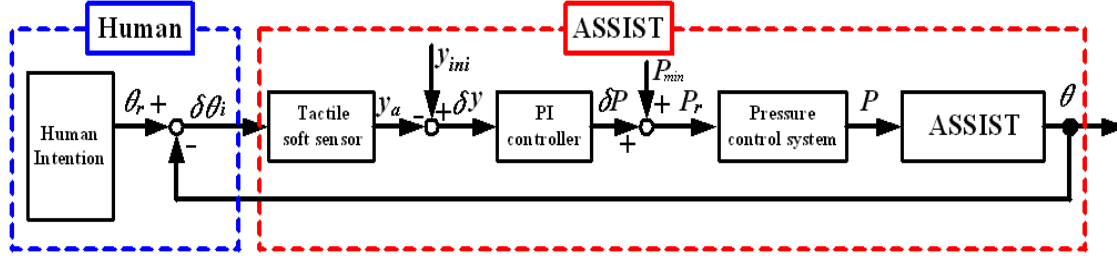


Fig.13: Control system

EXPERIMENT

• DETECTION PRECISION

The center of pressure is measured to verify a detection precision. In the experiment, an acrylic plate (Width 50[mm], Length 200[mm], Thickness 3[mm]) is put on the tactile soft sensors attached to the appliance as shown in Fig.14. A force is applied to the acrylic plate at distance of 20[mm], and the applied force is 10[N].

Fig.15 shows the experimental result. From the figure, since the center of pressure can be detected exactly, it is expected that ASSIST can be controlled using the center of the pressure.

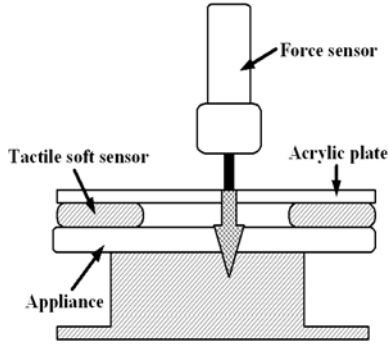


Fig.14: Experimental equipment

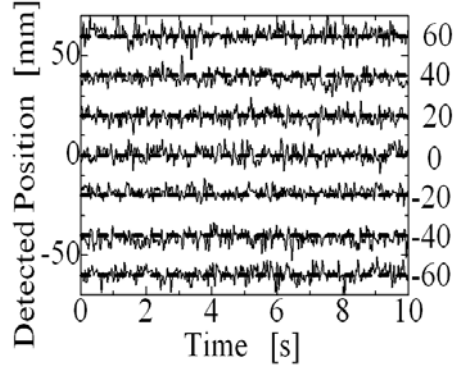


Fig.15: Detection precision of center of pressure

These results mean that the actuator can change the bending angle depending on the change of θ_r .

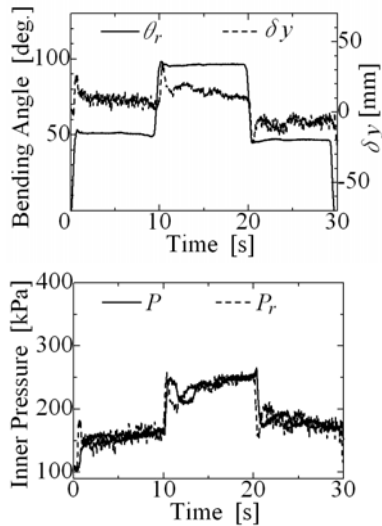
From the above, ASSIST can be operated by using the proposed control method. The effectiveness of ASSIST operated by the proposed method is discussed in the following. In this experiment, a subject bends an elbow under the load 3[kg] put on the forearm as shown in Fig.17(a). ASSIST is put the load on the forearm appliance as shown in Fig.17(b). Fig.18 shows the results. EMG signal is measured at a biceps muscle of the upper arm. Since the magnitude of EMG is decreased, a human who equips with ASSIST can bend the forearm by the less muscular force as compared with a human without ASSIST.

• FUNDAMENTAL EXPERIMENT

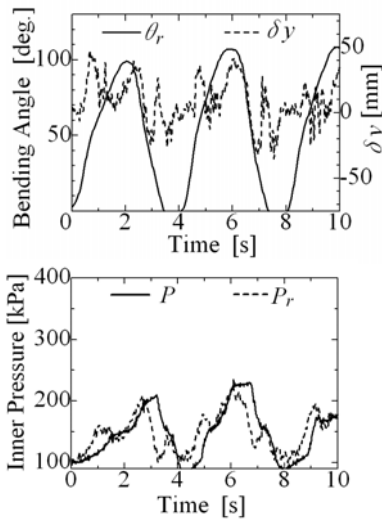
Fig.16 shows the experimental result when the subjects bends the forearm stepwise and sinusoidally to verify the proposed control method. In the step motion, in order to confirm that ASSIST can be stopped at an intended angle, the subject who equips with ASSIST increases or decreases the bending angle of the forearm at intervals of 10[s]. The forearm is bended with 4[s] period in the sinusoidal motion. The bending angle of the elbow θ_r is changed stepwise and sinusoidally, even though it is desirable that $\delta\theta$ is 0, the reference pressure P_r can be obtained according to change of $\delta\theta$ as shown in figures.

CONCLUSION

The movement of the forearm can be detected by introducing the center of pressure calculated from the tactile soft sensor. Therefore, ASSIST can be operated by the movement of the forearm as the human intention input signal. In addition, when the human forearm lifts a load, ASSIST operated by the proposed method is effective to realize the power assist based on a human intention.



(a) Step motion



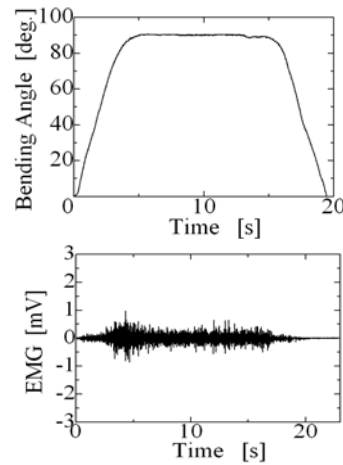
(b) Sinusoidal motion

Fig.16: Experimental results

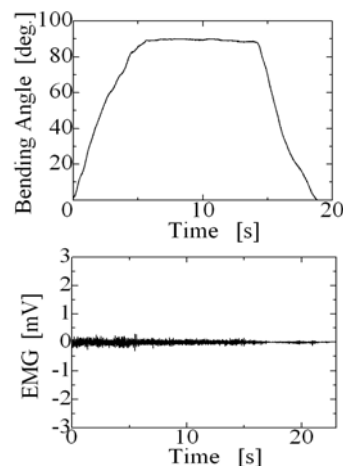
(a) Without ASSIST (b) With ASSIST

Fig.17: Experimental condition

[6] M.Sato, et al.:“Human engineering numerical standard handbook”,Gihodo Shuppan Co.,Ltd., (1999) (in Japanese)



(a) Without ASSIST



(b) With ASSIST

Fig.18: Verification of effectiveness

References:

- [1] Ministry of Internal Affairs and Communications: “Statics of Japan 2004”, (2004)(in Japanese)
- [2] K.Kiguchi, M.H.Rahman and T.Yamaguchi: “Adaptation Strategy for the 3DOF Exoskeleton for Upper-Limb Motion Assist”,Proc. of the 2005 IEEE International Conference on Robotics & Automation, pp.2307-2312 (2005)
- [3] J.C.Moreno,F.J.Brunetti,J.L.Pons,J.M.Baydal,R. Barber:“Rationale for Multiple Compensation of Muscle Weakness Walking with a Wearable Robotic Orthosis”,Proc. of the 2005 IEEE International Conference on Robotics and Automation, pp.1926-1931 (2005)
- [4] D.Sasaki,T.Noritsugu,M.Takaiwa:“Development of Active Support Sprint Driven by Pneumatic Soft Actuator(ASSIST)”,Journal of Robotics and Mechatronics, Vol.16,No.5,pp.497-503 (2004)
- [5] J.Kohara, et al.:“Measurement of human body”,Japan Publication Service, (1986) (in Japanese)

A STUDY ON TELEOPERATION OF FLUID POWER SYSTEM OVER INTERNET

Shuyi JING*, Ato KITAGAWA*, Pingdong WU**

* Department of Mechanical and Control Engineering, Tokyo Institute of Technology
Tokyo, 152-8550 JAPAN
(E-mail: jsy@cm.ctrl.titech.ac.jp)

**Mechatronics Center, Beijing Institute of Technology
Beijing, 100081 CHINA

ABSTRACT

The main objective of this research is to demonstrate experimentally the feasibility of teleoperating a hydraulic system over Internet in real time. The teleoperation is based on the client/server architecture. Time delay caused by Internet is the main problem of the teleoperation system. After discussing the characteristic of uncertain time delay and the format of communication protocol, this paper introduces a control algorithm with prediction. Combining with the characteristic of time delay and TCP/IP protocol, this method can compensate the time delay existing in forward and feedback path. Moreover, the operator can operate transparently the master just as operating the remote object. A hydraulic master slave system is developed as a test rig and experimental results verify the feasibility of the compensator.

KEY WORDS

Teleoperation, Impedance, Time delay, Master slave, Fluid power

NOMENCLATURE

B : viscous coefficient (Ns/m)
 F_m : operating force of the operator on the master (N)
 F_s : contact force of the slave (N)
 K : stiffness (N/m)
 M : inertia (kg)
 t : time (s)
 U : actuator-driving force (N)
 V : (reference) velocity (m/s)
 Z : impedance (Ns/m)

Subscripts

e : object
 m : master
 o : target
 s : slave

1 INTRODUCTION

The main purpose of teleoperation system is to extend the distance between an operator and an object. If an operator can operate a remote object smoothly, it will become reality that an experiential doctor conducts a telesurgery, or an engineer telecontrols a robot to work in some dangerous place, etc. For these significant aspects, many researchers have focused their attentions on the related works [1], and presented several examples of successful control over Internet in both theory and application. Anderson and Spong proposed a control law for Master-slave system with any non-varying time-delay based on passivity and scattering theory for the first time [2]. Adriana Vilchis presented a slave robot in new architecture for tele-echographic examination [3]. Tachi reported the

master slave system by teleexistence with advanced presence [4].

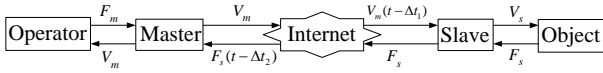


Figure 1 A master slave teleoperation system over Internet

A simplified sketch of this research is given in figure 1. The master slave teleoperation system takes on the precise job to operate a remote object over Internet. The slave consists of a hydraulic robot. Because the utilization of hydraulic actuators is attractive in several situations, due to their standard, safety and high load capacity, as well as their reliable performance. Hydraulic systems are, however, complex and nonlinear which may pose problems when applying control laws. For example, the fact that oil is compressible under high pressure, along with high load inertia may reduce the natural frequency. Furthermore, the performance of hydraulic valves is highly sensitive to payload. Finally, external and internal leakage, Coulomb friction, fluid flow dead band all result in parameters change of the system. These practical considerations make the successful implementation of control strategies rather difficult. Moreover, the hydraulic system is teleoperated. In this research, we will integrate an internal closed-loop position control on cylinder of hydraulic system with a much higher frequency than the external open-loop control. The teleoperation system aims at making the operator teleoperate the hydraulic system with high transparency.

2 A MASTER SLAVE TELEOPERATION SYSTEM

2.1 The Bilateral Impedance Control Method

A teleoperation system consists of a master, a slave, an operator and an object. In order to make equations derivation more intuitive [5], one degree of freedom (DOF) teleoperation system is considered. Before the Internet is introduced, there is no time delay in the communication. Assuming that the slave may not depart from the object, the dynamics of the master and the slave are modeled as follows in the form of impedance:

$$F_m - U_m = Z_m(s)V_m \quad (1)$$

$$U_s - F_s = Z_s(s)V_s \quad (2)$$

where

$$Z_m(s) = M_m s + B_m + \frac{K_m}{s} \quad (3)$$

$$Z_s(s) = M_s s + B_s + \frac{K_s}{s} \quad (4)$$

If the internal control input of master $U_m = F_s$ and $V_s = V_m = V_o$ is assumed, the system block diagram of impedance control becomes figure 2. The input and output relation between the master and the slave is expressed with the Eq. (5) and (6).

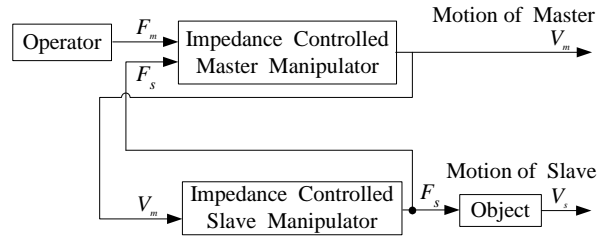


Figure 2 Schematic diagram of impedance control method

$$F_m - F_s = Z_o(s)V_o \quad (5)$$

$$U_s - F_s = Z_o(s)V_o \quad (6)$$

Here, the slave follows the master at the same speed. If target impedance $Z_o(s)$ is set small enough, then $F_m = F_s$ can be obtained. This indicates that the operator can operate the object transparently.

2.2 The Control Technique over Internet

This research aims at realization of teleoperation of the master and the slave over Internet. The control block diagram is shown in figure 3, and the following Eq. (7) and Eq. (8) can be obtained from figure 3.

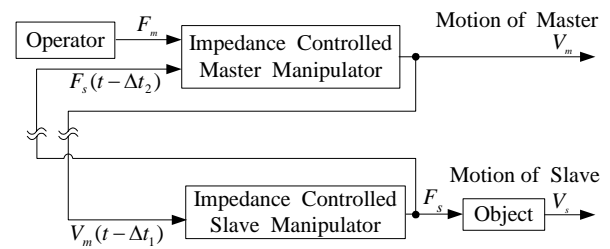


Figure 3 Schematic diagram of impedance control method over Internet

$$F_m - F_s(t - \Delta t_2) = Z_o(s)V_m \quad (7)$$

$$U_s - F_s = Z_o(s)V_m(t - \Delta t_1) \quad (8)$$

The forward time delay of a communication course is shown as Δt_1 , and the backward time delay of a course is shown as Δt_2 . Therefore, it is different from the ideal Eq. (5) and (6) in the case of real time.

3 EXPERIMENT SETUP

In this paper, experiment setup of the teleoperation system over Internet is depicted in figure 4.

The teleoperation system allows the operator to operate the master handle in one degree of freedom (DOF) in a line of 10cm with a maximum force of 200N. The master controller gathers force from the operator and then transmits it to the slave controller continuously every 10ms. The slave robot is consisted of a hydraulic system. Measured force from the object is also transmitted every 10 ms to the master controller.

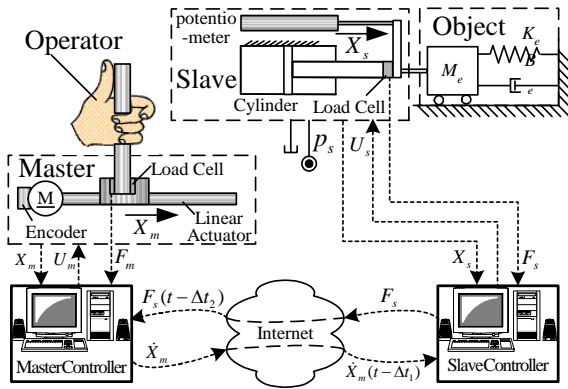


Figure 4 Schematic diagram of experiment setup

An external open-loop position-force control integrated with an internal closed-loop position control on cylinder of hydraulic system was implemented.

4 INTERNET

4.1 Characteristic of Time Delay

Considering the reliability and credibility of network [6, 7], TCP/IP protocol is adopted in this paper.

Figure 5 (a) is one example of the results of Internet-induced time delay between Kitagawa lab in Tokyo of Japan and Beijing of China. From figure 5 (a) (b), the Internet-induced time delay and its uncertainty is clear. In almost all of receiving time, packets are dropped off completely.

4.2 Format of Datagram

The teleoperation is based on the client/server architecture. Figure 6 shows the format of communication datagram. The unit of datagram is byte. In the forward path, master controller writes control signal and timestamp into datagram. On the other hand, in the feedback path, slave controller writes feedback signal, timestamp that remote computer received, and timestamp that remote computer send into datagram.

4.3 Simulation about Internet

To make results more convictive, we use the same time delay pattern with every result in this paper. However, time delay is uncertainly changing in the real communication process because of Internet routing or congestion etc. Therefore, we simulate Internet as figure 1 by making the time delay between the master and slave the same as typical data of time delay over Internet. The front part with 10s in a set of typical data with 30s is shown in figure 5.

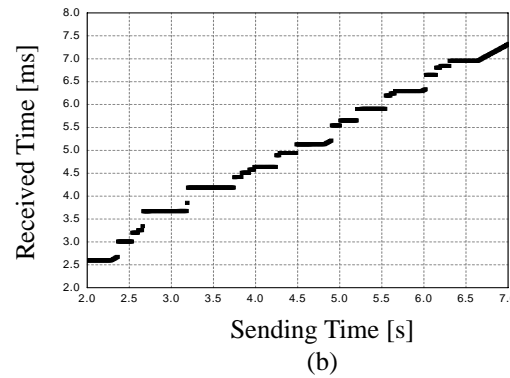
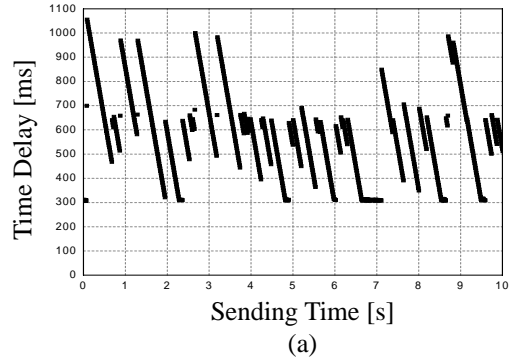


Figure 5 Internet-induced time delay between Tokyo and Beijing

Sequence number	Control signal	Feedback signal	Timestamp sent by local computer
Timestamp received by remote computer	Timestamp sent by remote computer		

Figure 6 Format of communication datagram

5 EXPERIMENT RESULTS WITHOUT PREDICTITION

In this paper, the parameters are set as followings.

$$M_o = 0.05[\text{kg}], B_o = 0.4[\text{Ns/m}], K_o = 0$$

$$M_e = 0, B_e = 0, K_e = 1500[\text{N/m}]$$

Here, we just take a spring as the object.

5.1 Experiment Result without Internet

In the case of direct communication between the master and the slave, the signal is transmitted as figure 7. The experimental result by the setup in figure 4 without Internet is shown in figure 8. Figure 8 (a) describes displacements of the master and the slave. In the figures of displacement in this paper, "master" expresses the displacement X_m of the master and "slave" expresses the displacement X_s of the slave, or the displacement of the object. The figure shows that the slave robot follows the master well.

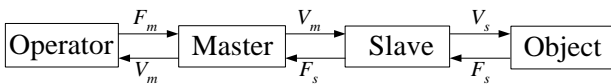
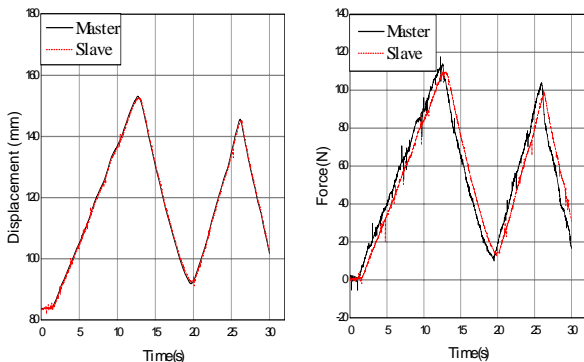


Figure 7 A master slave system without Internet

Figure 8 (b) shows force of the master and the slave. In the figure of force in this paper, "master" expresses the force F_m applied by the operator, and "slave" expresses the reaction force F_s from the object. The figure shows that the force from the operator and the reaction force from an object are almost the same. Therefore, it shows that the master slave system works well in figure 8.



Displacement of master and slave (a)

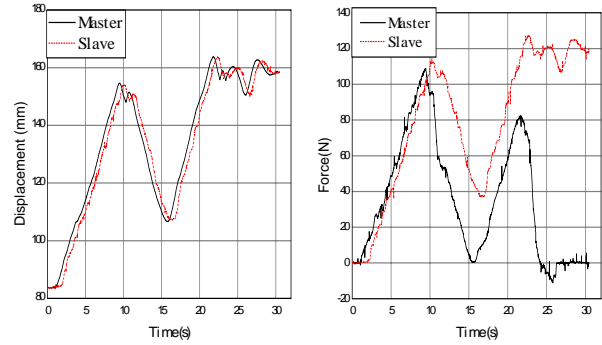
Force of master and slave (b)

Figure 8 The result without Internet

5.2 Experiment Result over Internet

If the signal is transmitted over Internet as figure 1 and figure 3, the experiment result is shown as figure 9. Figure 9 (a) indicates that system becomes unstable, but the slave still follows the master well. Figure 9 (b) shows that the system becomes unstable and operator cannot continue operation any more. Because of the existence of Δt_1 and Δt_2 in Eq. (7) and (8), the difference of force between master and slave becomes larger and larger. This is the reason why the

system becomes unstable and it is impossible for the operator to operate the object over Internet. Due to time delay from Internet, the teleoperation system even cannot retain stability. Therefore, some special compensator is necessary.



Displacement of master and slave (a)

Force of Master and slave (b)

Figure 9 The result over Internet

6 DYNAMIC PREDICTOR

6.1 Teleoperation with Predictor

The analysis above indicates that Internet-induced time delay is changing uncertainly. Thus, compensator should compensate the changes of Internet-induced time delay, to ensure the dynamic characteristic and stability of system. In this paper, we utilize the prediction control theory, which corrects an object model in the master side with history information, and schematic block diagram of the system is shown as figure 10. Where, \bar{F}_s is the reaction force from the object model.

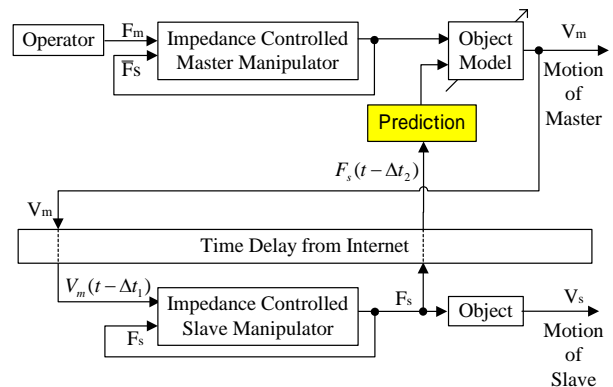


Figure 10 The schematic diagram of prediction control

6.2 Dynamic Principle of Prediction

The operator teleoperates an object by a master slave

system over Internet. For system stability, this research compensates suitably by designing a dynamic predictor. The strategy exploits a particular kind of linear plant model called the ‘controlled autoregressive integrated moving average’ (CARIMA) model

$$A(q^{-1})y(t) = B(q^{-1})u(t-1) + \frac{\xi(t)}{1-q^{-1}} \quad (9)$$

Where $A(q^{-1})$ and $B(q^{-1})$ are polynomials of degrees n_a and n_b in the backward shift operator q^{-1} and $\xi(t)$ is an uncorrelated random noise, $u(t)$ and $y(t)$ represent the input and the output, respectively. Since the noise filter, represented by the last term in Eq. (9), has a pole at $z=1$, a nonzero mean disturbance is produced in the CARIMA model.

As the primary of this research, we assume that the object persist one parameter of its rigidity, or its viscosity, e.g. viscosity. Here introduces $b(t)$ as the spring constant, and the j -step ahead prediction of $b(t)$ and $F_s(t)$, i.e. $\hat{b}(t)$, $\hat{F}_s(t)$, are obtained from Eq. 10 and Eq. 11.

$$\hat{b}(t) = \frac{1}{n_2 - n_1 + 1} \sum_{j=n_1}^{n_2} F_s(t-j) \quad (10)$$

$$\hat{F}_s(t) = \frac{1}{n_2 - n_1 + 1} \sum_{j=n_1}^{n_2} F_s(t-j) + [\hat{b}(t) * (\sum_{j=0}^{(n_1+n_2)} X_j)] \quad (11)$$

Where n_1 is the minimum output horizon and n_2 is the maximum output horizon. The objective of predictive control law is to determine future control signals, based on future predicted plant outputs and a given sequence of future set points. Because 30 steps is a little further, to reduce the calculation, we define n_1 and n_2 as below. From the time delay, we define n_1 as the last one of $F_s(t)$ that we have gotten. Because of the sliding-window protocol of TCP, and the characteristic of figure 5, so we define n_2 as (n_1+50) .

Moreover, we use the following cost function:

$$J(n_1, n_2) = E\left\{ \sum_{j=n_1}^{n_2} [\hat{F}_s(t) - F_s(t)]^2 \right\} \quad (12)$$

If $J(n_1, n_2)$ is bigger than the threshold value, it indicates that predicted $\hat{F}_s(t)$ is too different from $F_s(t)$.

In this situation, the slave cannot follow the master, so the system will be obliged to stop to avoid danger.

6.3 The result with Prediction

The result with prediction is given in figure 11. Compared with the figure 8 (a), figure 11 (a) shows although there is time delay in displacements between the master and the slave, the system has become stable.

This figure shows that the slave robot follows the master well. Compared with figure 8 (b), figure 11 (b) shows although there is time delay in force between the master and the slave, the force from the operator and the force to the object are almost the same. It just means that operator can operate remote hydraulic system transparently.

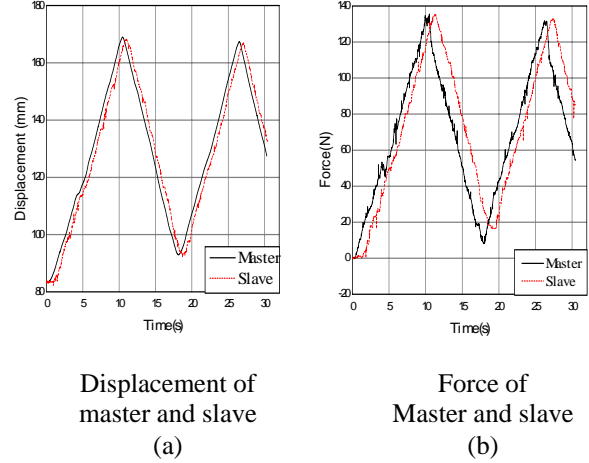


Figure 11 The result over Internet with dynamic compensator

As the result of the experiment, figure 12-figure 14 shows the force of the operator. Without Internet, figure 12 shows that the master system is in so good situation that the force of the operator is nearly the same as the object reaction force in the operation process. The difference of two curves depends on the master dynamic characteristic, and nonlinear hydraulic systems, which is not objective of this research. However, under communicating over Internet without compensator, figure 13 shows that operator cannot feel the object as a spring any more. With prediction, figure 14 shows that operator move the master over Internet, just like moving object directly.

7 CONCLUSIONS

This paper presented a research on teleoperation of a hydraulic robot with time delay over Internet. After describing the control mechanism of master slave system, the characteristic of uncertain time delay caused by Internet, and the format of communication protocol are discussed. Another emphasis is the designation of the compensator to solve the instability caused by time-delay. The control algorithm on line with prediction brought out in this paper can guarantee the stability of the system effectively. Moreover, this paper demonstrated experimentally the feasibility of operating the remote object by the hydraulic setup over Internet in real time.

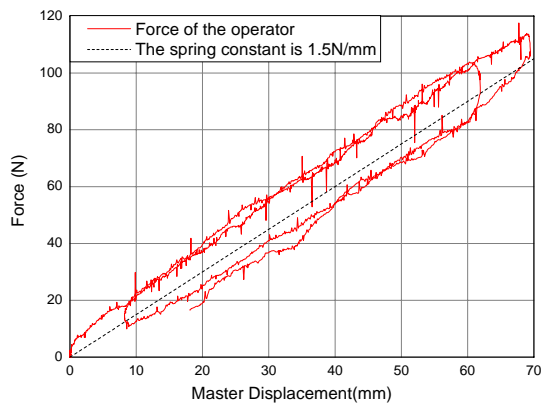


Figure 12 Force of the operator without Internet

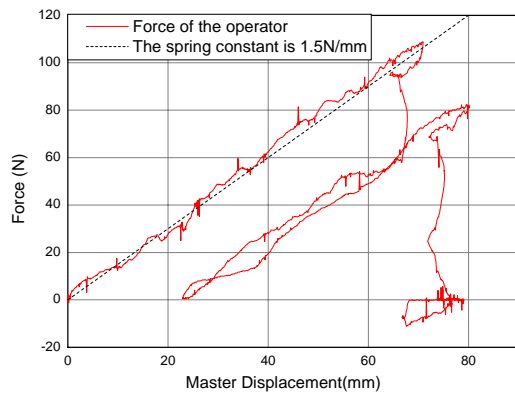


Figure 13 Force of the operator over Internet without predictor

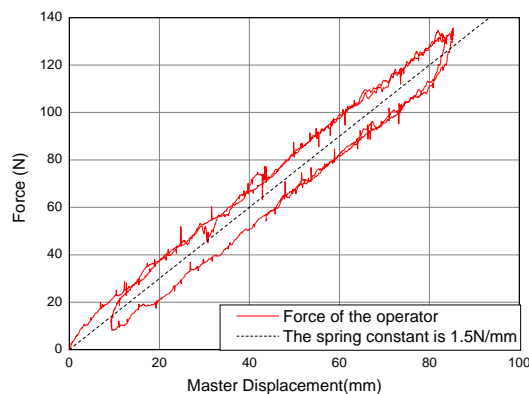


Figure 14 Force of the operator over Internet with predictor

REFERENCES

1. Bicchi, A., Scilingo, E.P., and De Rossi, D., "Haptic Discrimination of Softness in Teleoperation: The

Role of the Contact Area Spread Rate," IEEE Transactions on Robotics and Automation, vol. 16, no. 5, pp. 496–504, Oct. 2000.

2. Anderson, R.J., Spong, M.W., "Bilateral Control of Teleoperators with Time Delay," IEEE Transactions On Automatic Control, vol. 34, no. 5, pp. 494-501, May 1989.
3. Vilchis, A., Troccaz, J., Cinquin, P., Masuda, K., and Pellissier, F., "A New Robot Architecture for Tele-Echography," IEEE Transactions on Robotics and Automation, vol. 19, no. 5, pp. 922–926, Oct. 2003.
4. Susumu TACHI, "Robotics Research toward Next-Generation Human-Robot Networked Systems," Proceedings of the 35th International Symposium on Robotics, Paris France, March 2004.
5. Canghai LIU and Ato KITAGAWA, Impedance Control of Hydraulic Master-Slave Robot. 2nd FPN International Scientific Forum on Developments in Fluid Power Control of Machinery and Manipulators, pp.113-116, 2000.
6. Douglas E. Comer, Internetworking with TCP/IP Volume 1, 2: Principles, protocols, and architecture (third edition) Englewood Cliffs, NJ: Prentice-Hall International, Inc.1995.
7. X.F. Wang, and P.D. Wu, "Basic study of hydraulic teleoperation system based on Internet," The Proceedings on Spring Conference of Fluid Power System Society of Japan, pp. 4-6, June 2002.

Study on designing a biped robot With bi-articular muscle type bilateral servo systems

*Takeshi Matsuoka, **Yukio Saito, ***Hiroshi Negoto

*Department of intelligent mechanical engineering, Tokyo Denki University
Oaza-Ishizaka, Hatoyama, Saitama, 350-0394 Japan
(E-mail:04smn31@ed.ccs.dendai.ac.jp)

** Department of intelligent mechanical engineering, Tokyo Denki University
***Frontier reseach and development center, Tokyo Denki University

ABSTRACT

At present, biped robots are designed having motors on each joint. But human have actuators that span two joints, and the antagonistic pair actuator drives two joints at the same time. In these days, the effects of this study that is source of fast motor such as jump or running are investigated on Body moment study and Biology. This study shows the basic principle and the driving mechanism of the new actuator, called bilateral servo system developed in our laboratory, having the bi-articular operation to adjust a biped robot, and characteristics of the actuator that driving joint. As for those characteristics, this paper expresses the bilateral servo system and the robot that use the actuators.

Keyword

bilateral servo, rotary actuator, bi-articular muscle, biped robot

NOMENCLATURE

F_m	: Force of master
F_s	: Force of slave
A_{ma}	: Section area of master (Master cylinder, Bottom side)
A_{mb}	: Section area of master (Master cylinder, Rod side)
A_{sa}	: Section area of slave (Slave cylinder, Bottom side)
A_{sb}	: Section area of slave (Slave cylinder, Rod side)
P_1	: Pressure of bottom side
P_2	: Pressure of rod side

INTRODUCTION

Biped robots have a long history. In Japan, it has began since 1970s. In 1983, Prof. Kato in Waseda University developed a robot that can walk by itself. WL-10 has achieved reliable walking with reliability.

At present, many robots have achieved movement walking with ZMP (Zero Moment Point) control systems. In 1993, they attached upper body on the robot developed without it, and learning control which stability standard is ZMP has learned, at a simultaneous period, the study that makes amends for tree axis moment by the upper body.

And then, from 1996 a biped robot has known as a realistic thing like P2 introduced by HONDA. The posture control of those intelligent biped robots has one motor on each joint, and past system consists of

cooperative control of each joint. We have created a bi-articular actuator that is a bilateral servo system, and systematized posture and force. And as we reproduced antagonistic operating, the robot gets rapid movement and peculiar operation to animals with tedium.

About the peculiar operation of animals, Van Ingen Schenau's group reported that bi-articular muscles are power source and operation that takes energy generate from sgementure of limbs. By same group, at winter Olympic in1998, it is known that many athletes who bi-articular muscles flourished.

N.Hogan reported that bi-articular muscles took part much in setting and tracks of stiffness in work coordinate system. And Kumamoto verified this concept with analysis and robot-arm. In a word, bi-articular actuators are not only human mechanism but also effective means of control problems of robots that have operation with tedium.

When muscles of living things are divided roughly, it becomes mono-articular muscles and bi-articular muscles as shown Figure .1. Especially, bi-articular muscles could drive two joint by itself. As for the actuators, animals could operate rapidly and stably.

By the way, as shown Figure .1, hamstring and rectus femoris in large thigh are bi-articular muscles that span between hip joint and knee joint. And then, gastrocnemial in under thigh is bi-articular muscle that span between knee joint and foot joint.

The characteristics of humans and animal's motion control are summarized as follows.

- 1) Basically, it is fussy, but can operate smooth, quick and rapid with open loop.
- 2) Motions such as running or walking are cotrolled in spinal cord level, and it is the sending part of cooperation motion.

THE MECHANISM OF POWERED LOWER LIMBS OPERATION SIMULATION WITH VISUAL NASTRAN

The bi-articular actuator drawn with CATIA was linked with a Visual Nastran for operation simulation (Figure 2). Here, as a source of driving, movement type actuator soon is installed between two piston heads. The relation between force and velocity is made linear for simplification and we operated simulation. Figure 3.1 shows the specification of the actuator. The result is shown in Figure 3.2, 3.3.

THE CONTROL SYSTEM OF BI-ARTICULAR MUSCLE TYPE ACTUATOR

The control system is shown in Figure 4. The device needs to read signals from a pressure sensor and a potentiometer for each feedback. The control unit with analog to digital conversion machine can read amplified signals.

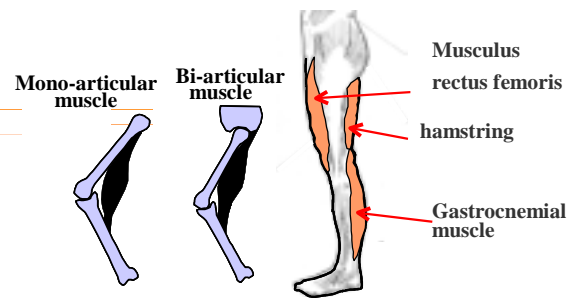


Figure .1 Mechanism of bi-articular muscle

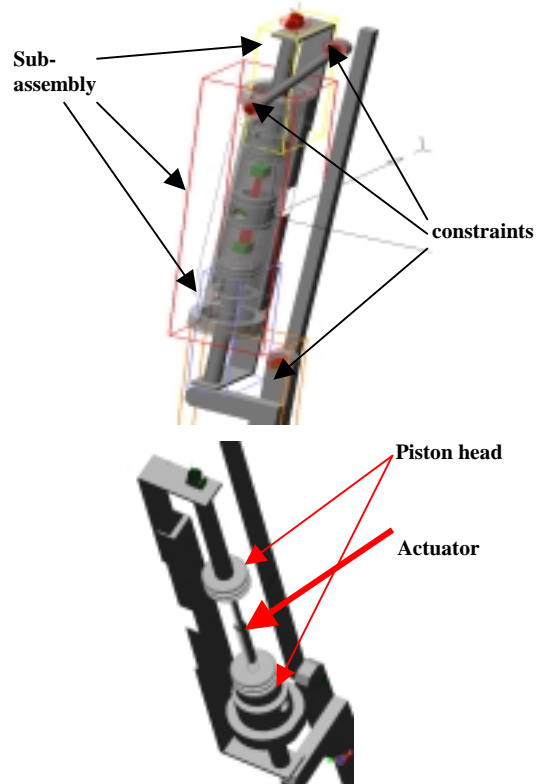


Figure .2 Link of CATIA assembly model and Visual Nastran

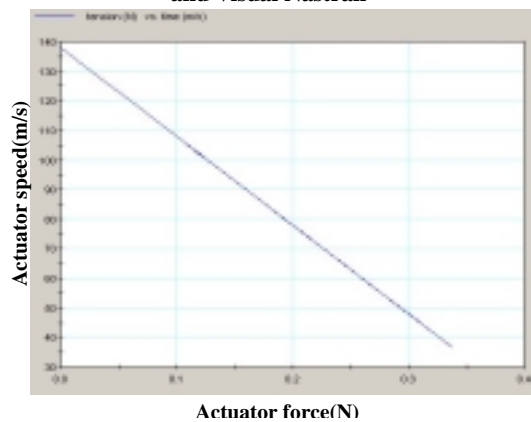


Figure 3.1 Specification of actuator

The PWM control system can drive motors and open-shut solenoid valves, and the device can drive both one and two joints.

BI-ARTICULAR ACTUATOR COMPOSED ON BILATERAL SERVO SYSTEM

Figure 5 shows the bilateral servo system that can reproduce operation of a bi-articular muscle. This mechanism consists of master cylinder with a single rod and a slave cylinder with double rods united by tube in parallel. The master cylinder consists of a rotation - straight-line conversion mechanism and a motor. This master cylinder has three pressure sensors and three potential meters. And then, the slave has an operation of bi-articular muscle, and it can drive two joints with switch of electromagnetic valve.

The thrust of master cylinder's rod, and we define the slave cylinder's thrust as F_m , F_s ,

$$\begin{cases} F_m = A_{ma} \cdot P_1 - A_{mb} \cdot P_2 & (1) \\ F_s = A_{sa} \cdot P_1 - A_{sb} \cdot P_2 & (2) \end{cases}$$

$$F_s = \frac{A_{sa}}{A_{ma}} \cdot F_m \quad (3)$$

Basically, the slave cylinder is driven by motor that set on the master cylinder. The thrust is generated by ratio of sections because of incompressible fluid in cylinders. So the torque and speed of the slave cylinder is described by difference of section. Table1 shows that relationship.

Table1 The relationship of ratio of sections and values

Ratio of section	Transmission force	Stroke
$A_{m1} < A_{m2}$	$F_1 < F_2$	$X > Y$
$A_{m1} = A_{m2}$	$F_1 = F_2$	$X = Y$
$A_{m1} > A_{m2}$	$F_1 > F_2$	$X < Y$

OPERATION CHARACTERISTICS WITH OPEN LOOP CONTROL

Figure .7 shows the device developed in our lab. And Figure 8 is the operation chart. The slave cylinder is set on hamstrings for re production of operation of bi-articular muscle. Therefore, this device can drive two joints at same time.

Diameters of master and slave are 50, 30 respectively. Measurements of potentiometers and change values

of pressure at two joints driving simultaneously are shown in Figure 8. A is a center part change value of pressure of the slave, B is the position of master, C is the bottom change value of pressure of the bottom of

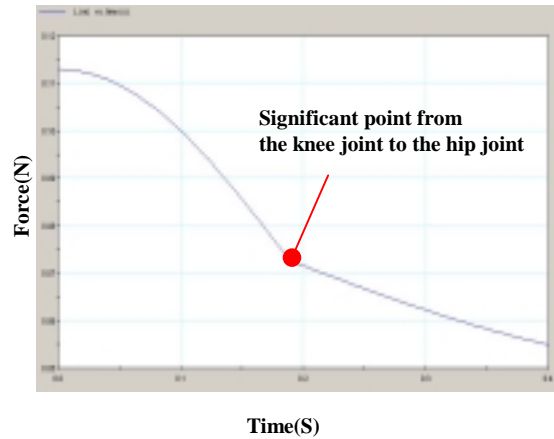


Figure 3.2 Length curve of actuator

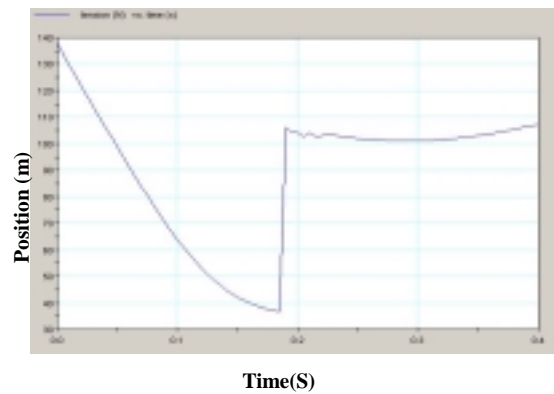


Figure 3.3 Actuator torque curve

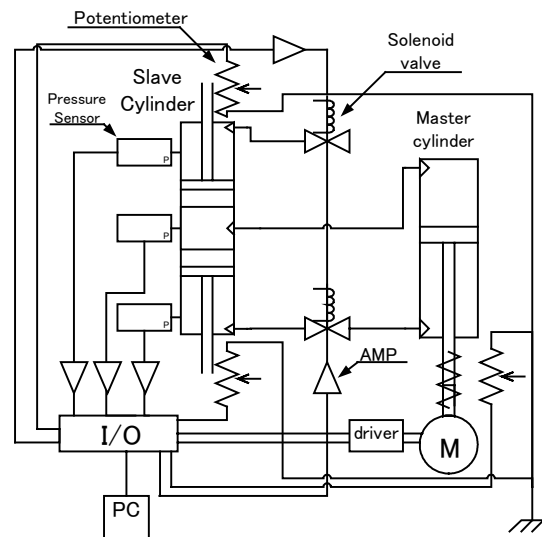


Figure .4 Bi-articular muscle actuator control method(1CH)

the slave, D is the position of bottom of slave, E is the position of the upper position of the slave, F is the change value of the pressure of the upper position of slave.

The effects shows that we get linear and stability operation with open loop control. And then, it is possible to control presser and potential with that characteristic.

If there is no feedback signal, we can drive motor on master and get stability operation.

Figure .6 shows driving of the actuator.

OPERATION EXPERIMENT BY POSITIONAL FEEDBACK CONTROL

We need to verify if the actuator can operate repeatedly with feedback signal or not for adjusting to biped robot. The operation way is to be converted displacement of slave cylinder, and then, when the value reach purpose values that set in PC, the valve switch. Figure 9 shows the effect. Figure .6 says that it is possible to be adjusted the actuator to robot's walking.

CONTROL SYSTEM OF ROTARY TYPE ACTUATOR

In general, motors are used on industrial-use robot's joints in rotary operation. In this study, we have designed a rotary type bilateral servo system. Figure .10 shows the rotary type bilateral servo system developed in our laboratory.

The rotary type actuator exchanges the slave cylinder of bi-articular muscle type actuator for the rotary actuator. Rotary actuator of old model couldn't keep arbitrarily control position. With this mechanism, it is possible to control position as for the antagonistic operation. And then, this actuator doesn't need power amplifier as for the difference of pressure on inside, so it is easier mechanism and lighter weight

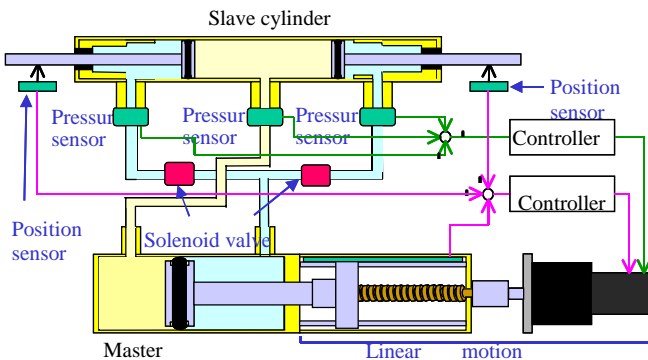


Figure 5 Bi-articular actuator composed on bilateral servo system

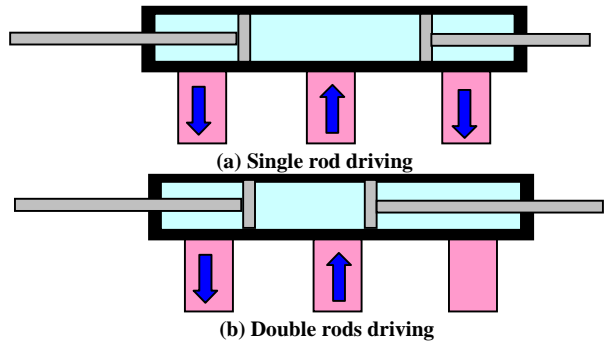


Figure .6 Driving way of the actuator

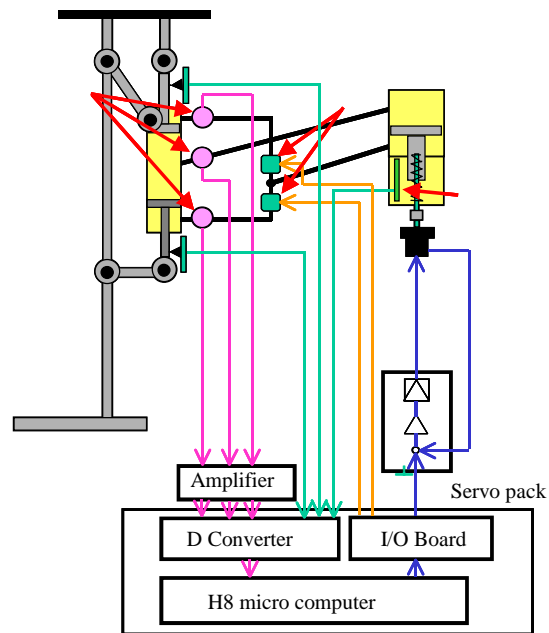


Figure .7 Device of experimentation

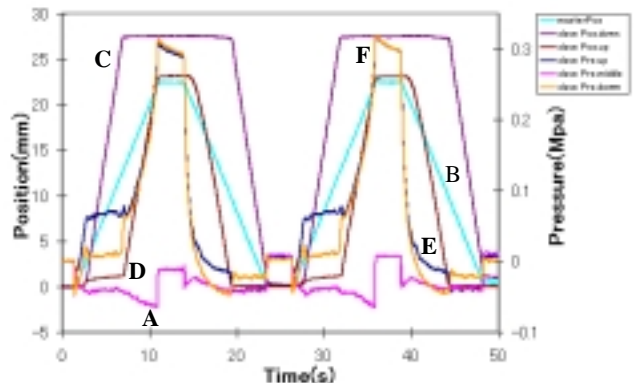


Figure 8 Measurement of potentiometers and change values of pressure

EXPERIMENT OF THE ROTARY TYPE BILATERAL SERVO SYSTEM

Position-feedback experiment

We have had a load test of bilateral servo system. The device of the experiments is shown in Figure 11.

The experiment results are shown in Figure 12, 13(horizontal, vertical).

The result shows that the line with 12kgf has a little overshoot and height of retentively.

Pressure-feedback experiment

The device of the experiments is shown in Figure 11.

The experiment results are shown in Figure 14, 15(horizontal, vertical).

The result shows that change of the line is extremely few with minute pressure changes.

And then, table2 compares weight with torque of this rotary actuator and General motor's

Biped robot and the Element technologies

On this study, we drew a draft of a robot that had an operation of bi-articular muscle at fast. Because of using this actuator, the robot can move not only one joint but also two joints at the same time. And the robot has freedom of degree enough, two DOF on hip joint, one DOF on knee joint, two DOF on ankle joint to walk straight. And the foot is designed that has two toes with load cells and heel to reproduce a foot bottom bow cap and to stand on those three points. This mechanism is to adjust to ruggedness geographical features for controlling posture. And then, toes can operate originally to produce floor reaction force.

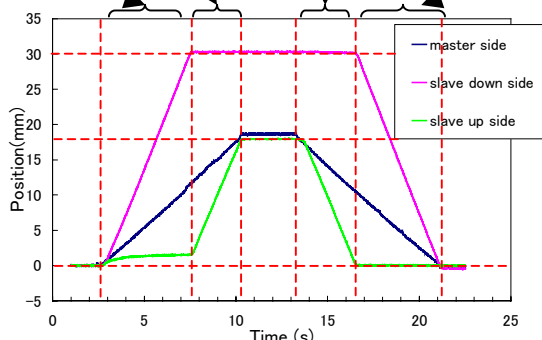


Figure 9 Measurements of potentiometer and change values pressure

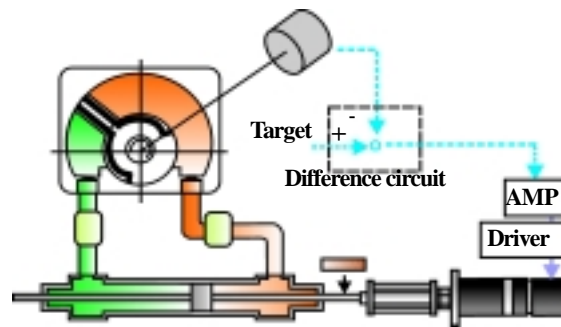


Figure 10 Rotary type bilateral servo system

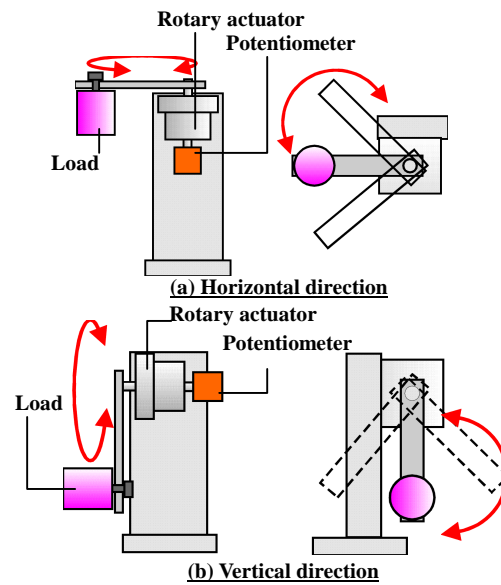


Figure .11 The device of experiments

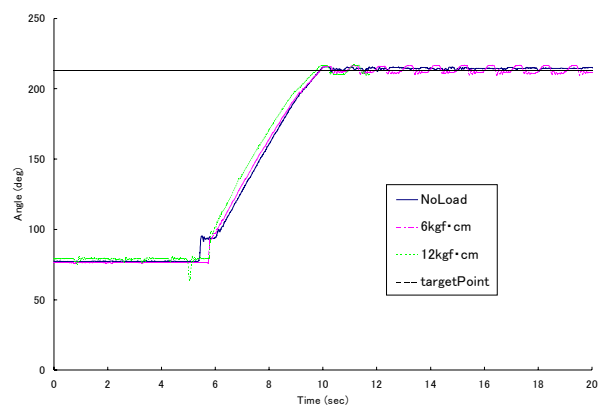


Figure 12. Experiment result of position feedback (Horizontal)

CONCLUSION

Generally, a biped robot has one actuator at each joint. We suggested the robot which one actuator moves joints of the both ends of a femur like human muscles. And the robot has rotary bilateral servo actuators at the hip joint and the ankle. The rotary actuator of the hip joint is used for the lateral elevation.

In this paper, the basic motions of those actuators were confirmed by simulation and experiment. Those results are as follows.

The smooth motion and the kick motion needed for walking of the robot were conducted by simulation and experiment of actuators imitating human bi-articular muscles, called as bi-articular muscle actuator.

(1) We confirmed that the rotary actuator for oscillating movement has slight pressure fluctuation by simulation and experiment of its basic motion.

(2) And we compared our rotary actuator to commercial rotary actuators and d higher positioning accuracy than commercial actuators.

(3) All actuators are bilateral servo system, and the power-assisting function by the control of position and force became possible.

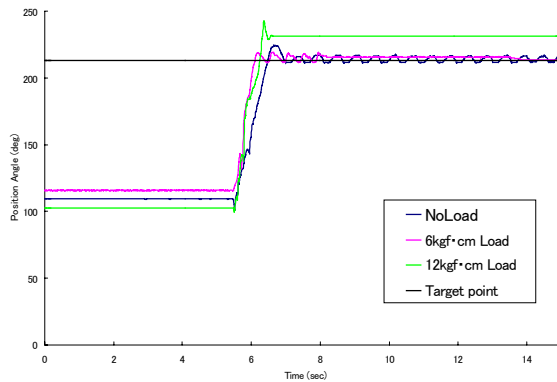


Figure .13 Experiment result of position feedback (Vertical)

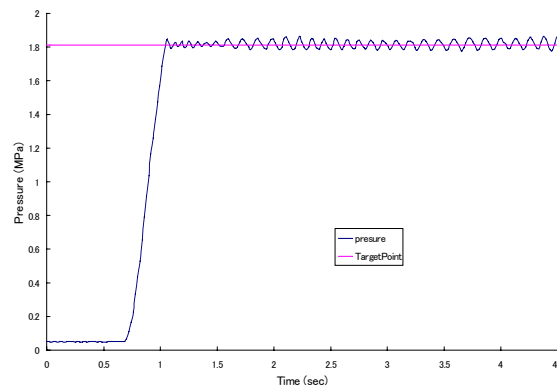


Figure .14 Experiment result of pressure feedback (horizontal)

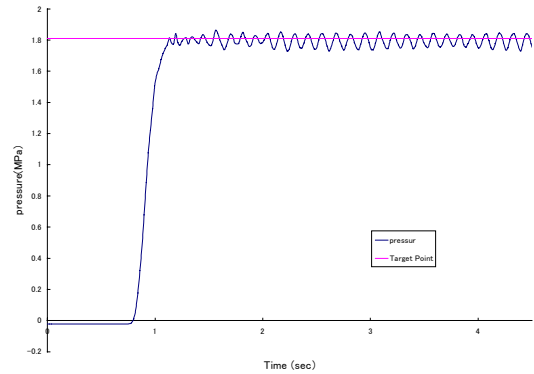


Figure .15 Experiment result of pressure feedback (vertical)

Table2 characteristics table of swing type bilateral servo

Mechanical part	Single Behn type rotary actuator	AC Motor (200W)
The maximum of movable area	270°	-
Official torque	66.35 N·cm (6.77kgf·cm)	59.0 N·cm (6.01 kgf·cm)
Weight	72g	3200g

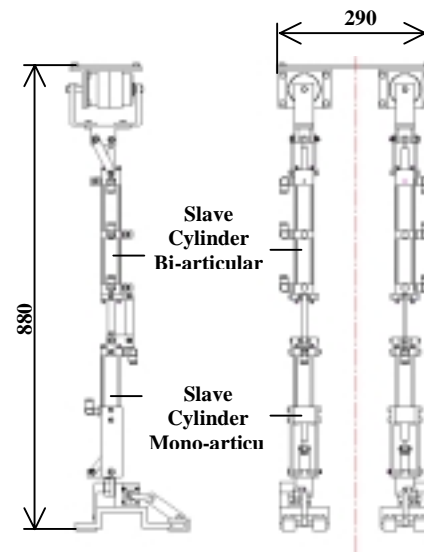


Figure 16 Appearance of the robot

References

- [1]T.Osima, T.Fujikawa, M.Kumamoto: Functional Evaluation of Effective Leg Muscular Strength Based on a Muscle Coordinate System Composed of Bi-articular and Mono-articular Muscle-Estimation of Functional Effective Muscular Strength from Output Force Distribution-, The Japan Society for Precision Engineering,.Vol.67, No.11, pp1824-1828, 2001

DEVELOPMENT OF PALPATION SIMULATOR USING PNEUMATIC PARALLEL MANIPULATOR

Masahiro TAKAIWA* , Toshiro NORITSUGU*

* The Graduate School of Natural Science and Technology,
Okayama University
3-1-1 Tsushimanaka, Okayama, 700-8530, JAPAN
E-mail: takaiwa@sys.okayama-u.ac.jp
toshiro@sys.okayama-u.ac.jp

Abstract

Nowadays, the breast cancer, over ahead of stomach one, holds the highest cancer incidence rate among Japanese women. Detection of breast cancer is done by palpation diagnosis, which require doctor to have highly experienced technique. In this study, we develop a palpation simulator which forms a woman's actual breast model holding active controlled variable stiffness property. A pneumatic parallel manipulator is employed as mechanical part of our simulator. In order to display a concrete stiffness feeling to human (doctor), control strategy is proposed where the contact point is detected using an idea of graphical intersection test. A reference stiffness is realized by constructing a compliance control system. By regulating the reference stiffness value according to the contact point, a palpation motion is executed. The validity of the proposed palpation system are confirmed through some experiments and analysis.

KEYWORDS

Palpation simulator, Pneumatic servo system, Parallel Manipulator

INTRODUCTION

Among the Japanese women, The disease rate of breast cancer became the most highest one, over ahead of that of stomach cancer[1]. However, if the cancer is identified as it is still just a part of breast, the existence rate is reported to be 92 %, which shows the importance of early detection simultaneously.

Detection of breast cancer is implemented by both palpation diagnosis and Mammography (X-ray photograph of breast). Palpation motion requires for doctor to have a highly skilled technique. From a view of medical education, there is strong need for palpation simulator and some equipment using robot technology or VR one are being developed[2][3].

In this study, we aim at developing a palpation simulator which has a actual breast model to be touched

by human in natural manner. In the mean while, importance of self diagnosis is also pointed out. Our simulator can be also used as a reference model of women's self diagnosis.

In order to realize such an palpation simulator, 3-D breast model holding a spatially different stiffness on its surface is required. Actually, some palpation simulators has already come onto the market, but they don't have function to adjust position or magnitude of stiffness as we will.

In this study, a pneumatic parallel manipulator is introduced to sustain a 3-D breast model. Parallel manipulator has a feature of multiple d.o.f. for its compactness and it enables minute force regulation property owing to the air compressibility. A contact point is detected using an idea of graphical intersec-

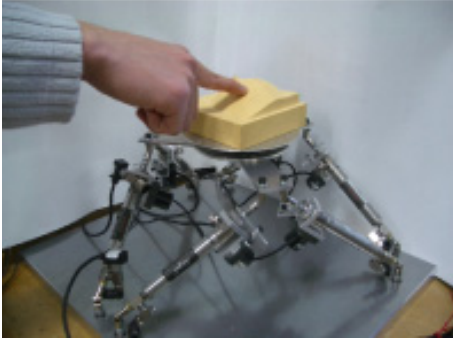


Figure 1: Developed Palpation Simulator



(a) Pneumatic parallel manipulator

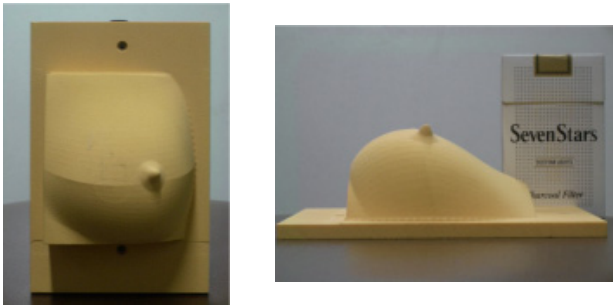
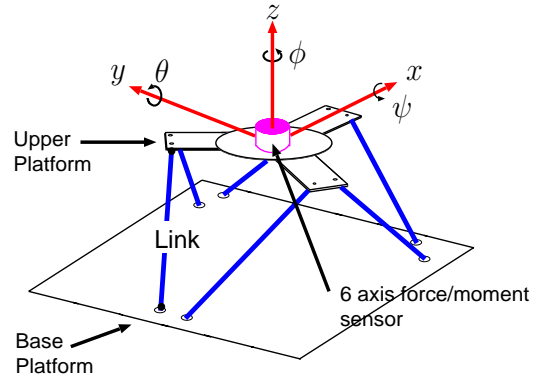


Figure 2: Breast shape model



(b) Schematic diagram

tion test and the reference compliance is realized by constructing a compliance control system on the parallel manipulator.

The validity of the proposed palpation equipment are confirmed through some experiments.

Developed Palpation Simulator

Outline of Simulator

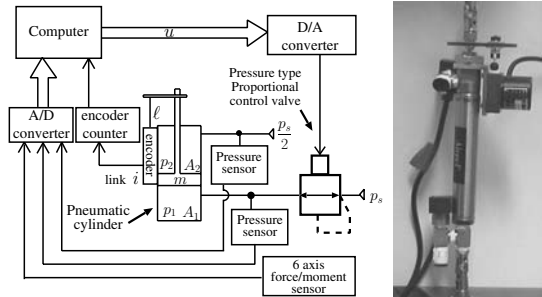
Fig.1 shows the developed palpation simulator. A 3-D breast model is attached with a upper platform of a pneumatic parallel manipulator via 6 axis force/moment sensor. Human(doctor or woman) pushes or trace any point of the model as shown in the figure and feels spatially different stiffness, which is realized by a parallel manipulator.

Fig.2 shows the manufactured breast shape model designed using 3-D modeling software and manufactured by 3-D modeling machine with the material of chemical wood.

Pneumatic Parallel Manipulator

Fig.3 (a) shows the developed pneumatic parallel manipulator works as compliance displaying mechanism.

The position/orientation of the upper platform is expressed by a hand vector $\mathbf{h} = [x, y, z, \phi, \theta, \psi]^T$ using roll-pitch-yaw angle notation. The origin of hand



(c) Pneumatic driving circuit and unit of link

Figure 3: Pneumatic parallel manipulator

coordinate frame \mathbf{h} is set at a center point of upper platform(namely at center point of force/moment sensor) when manipulator stands in a standard posture. Force/moment vector works at an origin of \mathbf{h} is defined as $\mathbf{f}_m = [f_x, f_y, f_z, \tau_\phi, \tau_\theta, \tau_\psi]^T = [\mathbf{f}_t^T, \boldsymbol{\tau}^T]^T$.

In the mean while, Fig.3(c) shows the pneumatic driving circuit of one cylinder. A friction in a cylinder makes compliance control performance worth. The employed pneumatic cylinder(Airpel Co. Ltd., 9.3 mm in internal diameter, 50mm in rod stroke) is a special made type ant its friction is negligible. Pressure in each cylinder's chamber, p_1 , p_2 are detected by pressure sensors and the displacement of piston rod ℓ is measured by wire type linear encoder. The

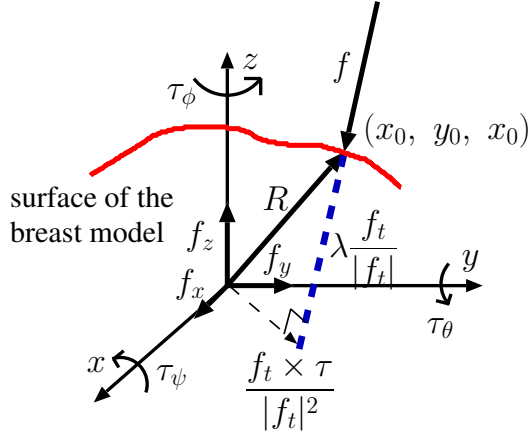


Figure 4: Geometrical model

A/D converter is of 12 bit resolution.

A control signal u calculated every sampling period (5 ms) in a computer corresponds to an input voltage of a pressure control valve through D/A converter (resolution of 12 bit), which regulates the pressure of head side chamber. The piston rod side chamber is pressurized at constant pressure. Supply pressure p_s is set to be 400 kPa. Control algorithm is implemented based on RT-Linux.

Detection of Contact point

Fig.4 shows the geometrical model of breast surface, where contact force \mathbf{f} is applied at a contact point represented by position vector $\mathbf{R} = [x_0, y_0, z_0]^T$.

As you see that, force vector \mathbf{f} is simply derived from the balance of translational force around the origin of \mathbf{h} as

$$\mathbf{f} = \mathbf{f}_t \quad (1)$$

As shown in Fig.4, position vector \mathbf{R} can be described using an arbitrary parameter λ as the following equation[4].

$$\mathbf{R} = \frac{\mathbf{f}_t \times \boldsymbol{\tau}}{|\mathbf{f}_t|^2} + \lambda \frac{\mathbf{f}_t}{|\mathbf{f}_t|} \quad (2)$$

Up to the former work, we assumed that the surface of breast model could be expressed by numerical formula and we obtained \mathbf{R} by substituting Eq.2 into that formula, therefore the shape of the breast model is limited to be a simple geometric one like a spherical shell[5].

In this study, a novel scheme to detect contact point is proposed to eliminate the geometric limitation in the former work based on an idea of graphical intersection test.

When we design a geometric breast model using 3-D CAD at a computer, an output file of "DXF

```

0
SECTION
2
ENTITIES
0
3DFACE
8
3
10 //...the 1st point x coordinate value
103.669060
20 // y coordinate value
0.211670
30 // z coordinate value
0.000008
11 //...the 2nd point x coordinate value
103.632797
21 // y coordinate value
0.000122
31 // z coordinate value
0.000008
12 //...the 3rd point x coordinate value
104.156570
.
.
.

```

Figure 5: Sample of DXF file

file" is obtained, which is widely used as a standard CAD data file. In this study, this DXF file is utilized not only to manufacture the actual breast model at a modeling machine but also to detect contact point.

DXF file is a text type one as shown in Fig.5 and it contains position data of all polygon which form the surface of a breast model. Begin with a phrase of "3DFACE", the x, y, z position of each vertex of a polygon is described in the sequence and these "3DFACE" notation blocks are described for all polygons.

Therefore by repeating a trial of intersection test between one polygon and a line vector shown as blue dot line in Fig.4 for all polygons, contact point can be detected[6].

COMPLIANCE DISPLAYING SCHEME

Control system

Fig.6 shows the proposed position based compliance control system[5]. The measured force/moment \mathbf{F}_m is fed back through a compliance matrix $\mathbf{K}^{-1} =$

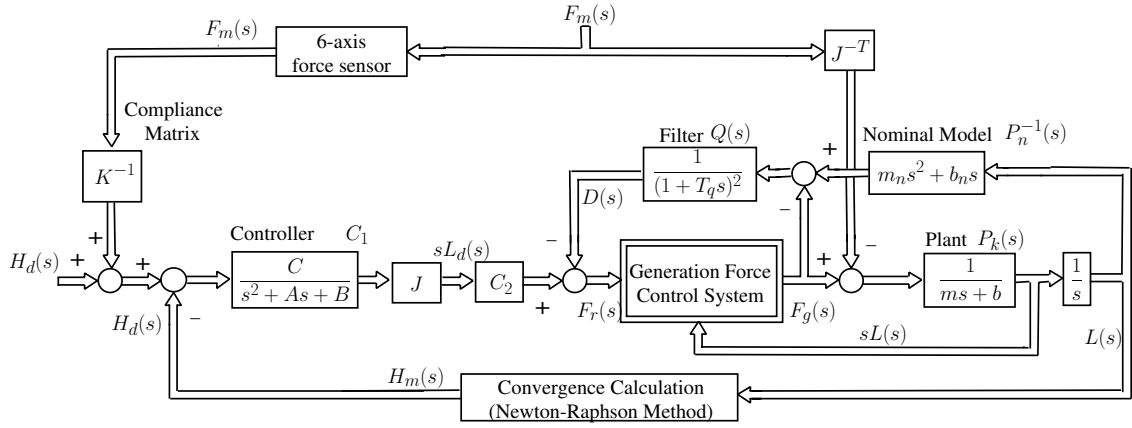


Figure 6: Compliance control system

$diag[K_x^{-1}, K_y^{-1}, K_z^{-1}, 0, 0, 0]$. The inner position control system is designed in order that the closed loop transfer function may follow the 3rd order system shown in Eq.(3).

$$\frac{H}{H_d} = G_r = diag\left\{\frac{C}{s^3 + As^2 + Bs + C}\right\} \quad (3)$$

The inner block with a doublet represents a force control system of generating force F_g based on disturbance observer, which works to lower the influence of piston rod velocity that acts as disturbance on force response as well as to make F_g to follow to the reference value with time constant T_{pn} [5].

EXPERIMENTAL RESULTS

Detection property of contact point

Fig.7 shows the result of contact point detection. As shown in figure (a), small hollows are arrayed on the surface of a breast model in a lattice with 10 mm intervals and force is applied at these hollows in normal direction for the surface. Figure (b), (c), (d) show the detected contact point for $(x,y)=(40\text{mm},60\text{mm})$ (most closer to sensor), $(20\text{mm},60\text{mm})$ and $(60\text{mm},20\text{mm})$ (most apart from sensor), respectively. A force/moment sensor is mounted at a position of $(40\text{mm},50\text{mm})$. A large detection error(maximum 2 mm in the case (d)) can be confirmed as the contact point apart from the point of a force/moment sensor. Improvement of detection accuracy is under the current consideration.

The contact detection property for continuous following contact motion as shown in Fig.8 is also verified. Fig.9 shows the static pictures cut out with 0.1 s interval on OpenGL graphic screen, where a white

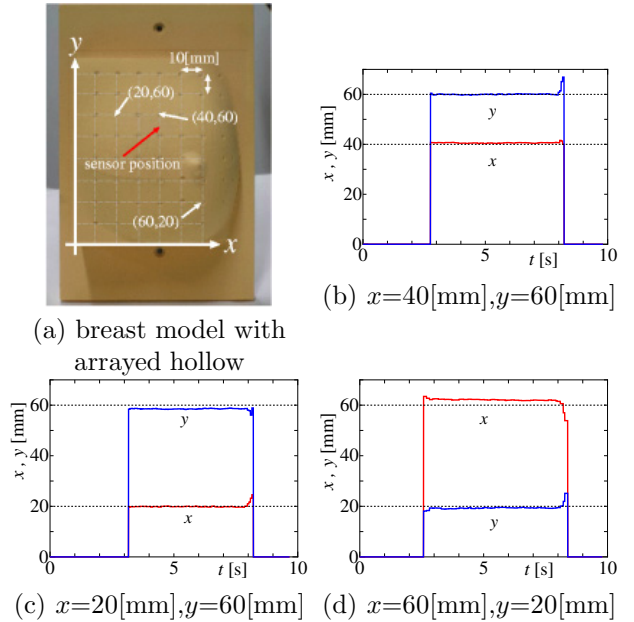


Figure 7: static contact point detection

line shows the contact force vector. The state of continuous contact motion is well confirmed.

Compliance control property

First the basic compliance control property is verified. Through actual measurement of breast stiffness of a subject(woman,36 years old), the stiffness is obtained to be about 0.03 N/mm on an average. It is said that the stiffness of lump is as about 5 times stiff as that of peripheral region of lump. Therefore we set the reference stiffness of lump as 0.15 N/mm and that of peripheral region as 0.03 N/mm.

Fig.10 shows the basic compliance control property, where all of the stiffness K_x, K_y, K_z are set as equal

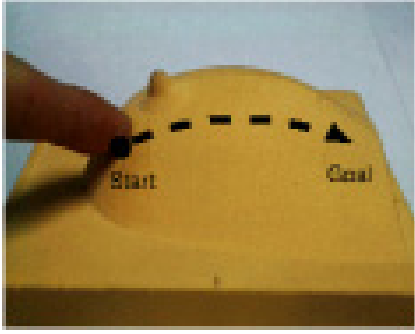


Figure 8: Continuous contact motion

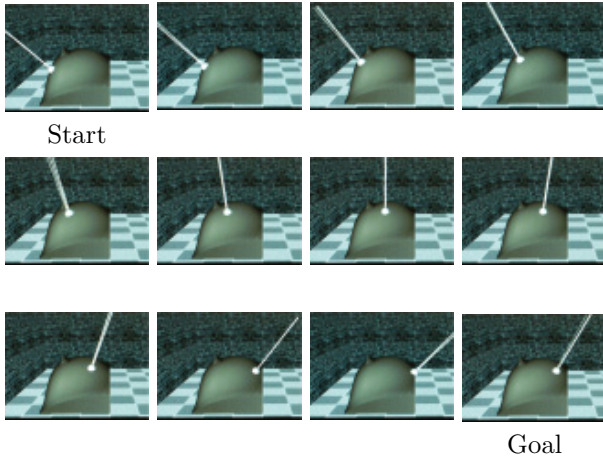


Figure 9: Contact point detection for continuous motion

and a force is applied for the direction in order that the displacement for all x, y, z axis may become almost equal. The minimum realizable stiffness was 0.01 N/mm as shown in Figure (a) and it is confirmed that the stiffness can be regulated every 0.01 N/mm from Figure (a), (b) and (c). By the way, a most popular force displaying device on the market, PHANTOM Desktop, has a minimum realizable stiffness of 1.5 N/mm , which show that our palpation simulator can display 1/150 times soft feature as that of this market device. The reference stiffness of lump (0.15 N/mm) and that of peripheral one (0.03 N/mm) is confirmed to be realized in the steady state. Happening of large stiffness at transient time is mainly caused by a positioning response lag.

Fig.11 shows the compliance control property, where reference stiffness is changed from 0.03 to 0.15 N/mm for several angular frequency. Until the stiffness change with 0.5 Hz , almost the reference stiffness can be realized, which corresponds to the case, for example, that human can feel lump with 20 mm diameter of 0.15 N/mm stiffness by moving over by their finger with velocity of 10 mm/s as shown in figure (d).

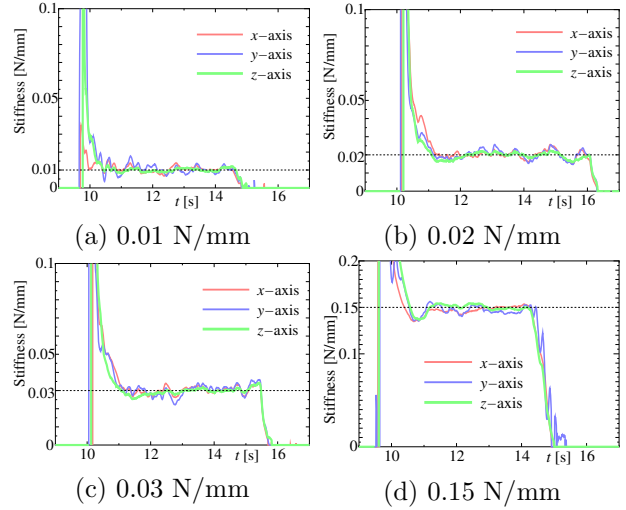


Figure 10: compliance control property (for static state)

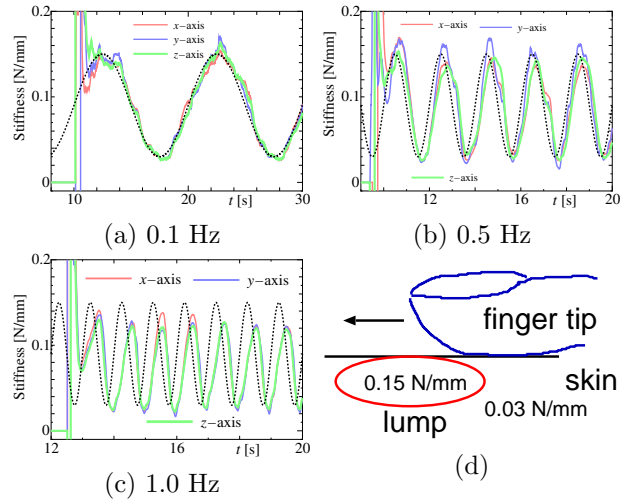


Figure 11: compliance control property (for sinusoidal variation)

Fig.12 shows the recognition property of virtual lump. A sphere with diameter of 20 mm as a lump model is considered within the breast model and human traces over the lump by reciprocating motion in parallel with x axis. The spatial position of finger is obtained by the contact point of breast model and position/orientation of parallel manipulator. The figure (a) and (b) correspond to the case of moving velocity of 10 mm/s and 20 mm/s , respectively. In both figures, (i) shows the realized stiffness (red line) and (ii) expresses the trajectory of finger tip. As mentioned in the former experiment of Fig.11, almost satisfactory recognition property can be confirmed for the case of motion of 10 mm/s . However for the case of smaller lump such as 10 mm diameter, which equiva-

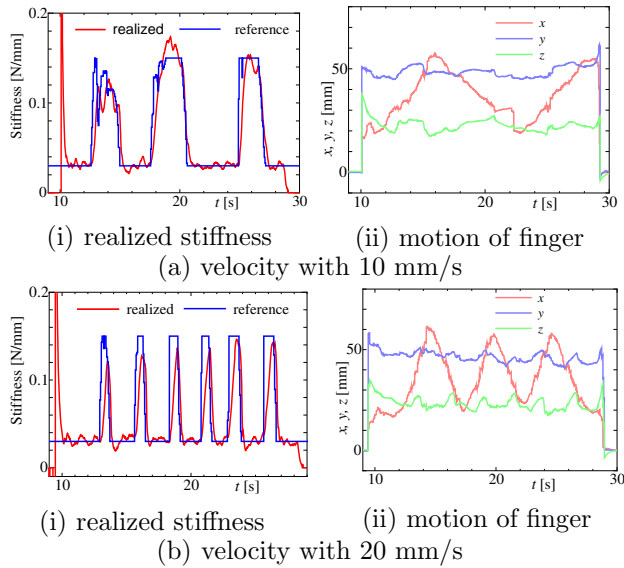


Figure 12: recognition of lump

lent to the case of (b) (20 mm diameter with 20 mm/s motion), the recognition property is lowered. This is mainly caused by a dynamics of inner position control system and that control system is caused by pressure response lag. Further improvement in the dynamic recognition is under consideration.

CONCLUSION

In this study, we developed a mechanical equipment to be applied as a palpation simulator using a pneumatic parallel manipulator.

We proposed a contact point detection scheme using an idea of graphical intersection test, which brought an advantage that any form of 3-D model could be applied as the object surface. Consequently the palpation simulator for, such as, stomach or abdomen can be developed.

Compliance control system is constructed on a parallel manipulator to display desired compliance corresponds to that of lump.

Through some experiments, control performances both in detecting the contact point and in displaying the reference stiffness are confirmed. The minimum realizable stiffness is attained to be 0.01 [N/mm] and the stiffness can be regulated with a resolution of 0.01 N/mm.

The further improvement of compliance displaying performance for the recognition in dynamic motion to feel a realistic lump is under the current investigation.

Acknowledgment

This research was supported by the Ministry of Education, Science, Sports and Culture, Grant-in-Aid for

Scientific Research, 16760202, 2004.

References

- [1] *T.Kitagawa, H.Tsukuma et al*, Prediction of cancer incident in Japan, *Cancer statistics 1999*, *Shinohara Shuppan, Tokyo*
- [2] *V.Daniulaitis, M.O.Alhalabi, H.Kawasaki, Y.Tanaka, T.Hori*, Medical Palpation of Deformable Tissue using Physics-Based Model for Haptic Interface RObot(HIRO), *Proc. of 2004 IEEE/RSJ Int. Conf. on Intelligent Robots and Systems*, pp.3907-3911
- [3] *K.Inoue, R.Uesugi, T.Arai, Y.Mae*, Development of Haptic Device Using Flexible Sheet, *Journal of Robotics and Mechatronics, Vol.15, No.2, pp.121-127, 2003*
- [4] *J.K.Salisbury, Jr.*, Interpretation of Contact Geometries from Force Measurements, *Proc. of*
- [5] *M. Takaiwa and T. Noritsugu*, Development of Force Displaying Device Using Pneumatic Parallel Manipulator and Application to Palpation Motion, *Proc. of ICRA 2003, CD-ROM pp.4098/4103*
- [6] *Samuel R. Buss*, 3-D Computer Graphics, *CAMBRIDGE UNIVERSITY PRESS, pp.99-107, 260-263, 2003*
- [7] *T. Murakami and K. Ohnishi*, Advanced Control Technique in Motion Control, *The Nikkan Kogyo Shinbun Ltd., Japan, 1990*

Study of Robot with the Ability to Detect Land Mines Using Pneumatic Bilateral Servo System

Kiyomi Takei*, Yukio Saito*, Shingo Koizumi*, Hiroshi Negoto**

* Dept. of Intelligent Mechanical Engineering, Tokyo Denki University
Ishizaka, Hatoyama, Hiki, Saitama 350-0394, Japan
(kiyomi@saitolab.n.dendai.ac.jp)

**Frontier Research and Development Center, Tokyo Denki University

ABSTRACT

In this research, we selected Pneumatic Bilateral Servo System (PBSS) consisting of master and slave cylinders as an actuator system for the land mine apparatus. Usually the master side operates the slave side in PBSS. But we realized in our system that position and power controls are made by comparing and feeding back physical information between the master and the slave. It also makes possible that the slave operates the master on the basis of this information. For the above reasons, PBSS is suited to be the actuator for the land mines apparatus. In this research, we work on the following tasks based on PBSS as the basic system.(1) Construction of pneumatically-controlled bilateral servo system(2) This system becomes harmless on the environment and human. (3) Making this system can sense and be controlled by minute pressure change by the 100-gram weight.

Keywords

bilateral servo system, land mine, demining, direct probe measuring

NOMENCLATURE

F_{in} : Total load force on slave cylinder
 f : Total viscosity coefficient
 M_{sp} : Total mass of rod and piston
 L : Load force
 x : Displacement of piston
 AS_r : Sectional area of slave cylinder in rod side
 AS_b : Sectional area of slave cylinder in bottom side
 P_r : Pressure of rod side
 P_b : Pressure of bottom side
 F_r : Force of pressured P_r slave piston
 F_b : Force of pressured P_b slave piston
 p : Initial pressure in a cylinder
 n : Ratio of specific heat

INTRODUCTION

Background

Now, land mines, 70 million from 60 million, are laid underground in 88 countries. Those were laid underground or dissemination. Every year, about 100,000 land mines are removed, and about 60 people die with land mines. It will take 600 years to 700 years to remove all land mines at present speed.

Land mines are removed by deminers using metal detectors, mine prodders, mine dogs, etc. When using a prodder, a deminer repeats stabbing it to the ground at a slant carefully.

There are many land mines at any area. Treading or touching land mines, people become limb amputation, or blindness, loss of hearing, or death. Actually, about 26,000 people are sacrificed and injured by land mines each year. It means that one person per 20 minutes dies. Most of land mines are plastic antipersonnel land mines it is very difficult to detect those. Therefore, exact land mine detection by deminers is needed.

In this paper, we describe our land mine detection system with pneumatic bilateral servo actuators. The goal of this research is to establish the method of mine detection and cleaning by our robot with high safety, assuredness and expedition.

Present Situation of Land mine Detection and Positioning of This Research

Recently, many research organizations are studying about prevention from damage by land mines.

Sato et al.⁽¹⁾⁽²⁾⁽³⁾ are researching the underground search radar that distributes short pulse microwaves from the transmitting antenna toward the ground and detects microwaves reflected by objects. Many parts of landmines are made from plastic and wood. This radar can detect metal and nonmetal objects.

Shimoi et al.⁽³⁾⁽⁷⁾ are researching the infrared camera system to measure temperature distribution of the ground. The ideal photography condition is that the temperature difference becomes largest at the sunrise and the twilight. The device detects the position of land mines, measuring the temperature difference between landmines underground and the surface. This device has characteristics to be able to measure widely from a remote place and to visualize easily the temperature distribution but is too expensive.

Hirose et al.⁽⁴⁾⁽⁵⁾⁽⁷⁾ are researching the contact-type probe system. This system recognizes materials of a land mine, for example plastic and steel, analyzing sound of collision between the sensor probes and a land mine when setting the probe in the ground. The probe consists of the direct operated impact driving function and the shock and vibration sensors. The former sends shockwave towards the probe, controlling the compressed air by solenoid valve. The latter detects the shockwave. It is possible to recognize shape of a land mine, detecting shockwave by these probes arranged in parallel.

Nonami et al.⁽⁶⁾⁽⁷⁾ are researching the high sensitive magnetic mine detector to detect metals, recognizing slight magnetic field. The characteristics are the compact size and the high sensitivity, and less subject to the disturbance from

earth magnetism and commercial alternator. Now, the land mine detection robot COMET walking by 6 legs with detector.

In this research, applying the pneumatic bilateral servo actuator, we aspire for the realization of high reliable land mine detection technology.

In our case, it searches by setting probe in the ground and detects land mines directly. The system analyzes materials by heating an object by the heater in the probe head, and understands shape of an object by the detection sensor arranged in a matrix. The structure is simpler than other detection system and the cost for the realization and the maintenance fee are cheap.

We will mount this system on the Gorilla type 4 leg walking robot with PBSS actuators, and can realize the land mine detection and demining anywhere.

THE BASIC EXPERIMENTAL EQUIPMENT OF MINE-DETECTING

Most of land mines are buried from 20 mm to 100 mm under the ground and are detonated with from 0.4kg from 1kg of the load. The experimental equipment is shown in figure 1. This equipment has 3 pneumatic bilateral servo actuators and the slave cylinder is moved along each axis.

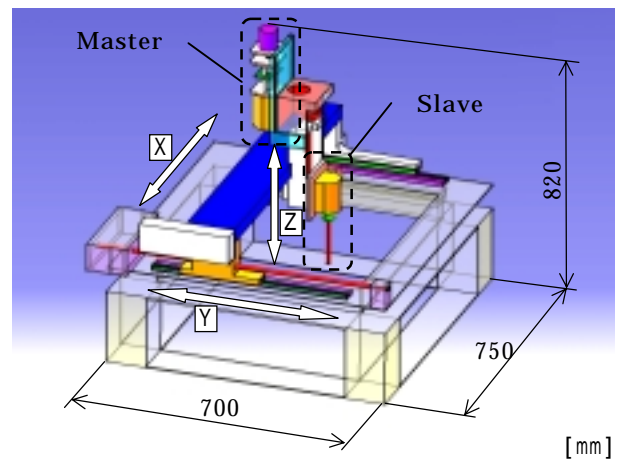


Figure 1 PBSA experimental equipment

In the experiment, the probe is repeatedly inserted into the ground for detecting imitations of land mines, moving in a reticular pattern. When the probe touches an object, it judges from the difference of pressure in PBSA that it is a landmine or not.

BILATERAL SERVO ACTUATOR SYSTEM

In size of most antipersonnel landmines the external diameter is over 80mm, the thickness is over 30 mm and the weight is more than 100 g less than 250g. Shape of antipersonnel land mines is a plastic ellipse or a wood cuboid.

In this research, the pneumatic bilateral servo actuator (PBSA) in figure 2 is used.

The PBSA consists of a master cylinder and a slave cylinder that are linked to each other by tubes and filled with compressed air. When the torque transmitted by the ball screw of the motor moves the piston of the master cylinder, the piston of the slave cylinder is moved by antagonistic effect. When the rod of the slave cylinder is moved by external force, the force is transmitted to the piston of the master cylinder by antagonistic effect.

The probe is connected to the rod of the slave cylinder and set in the demining machine. When the probe head touches to a landmine, pneumatic pressure in cylinders changes, and the force is detected as variation of pressure by the pressure sensor. At the time, displacements of the pistons are detected by potentiometers.

The advantage of PBSA is written as follows.

- (1) It is possible to reduce in size and weight of a device because a PBSA driven by a small motor generates high torque.
- (2) Pressure loaded to the probe is directly detected by sensors.
- (3) Impact strength between the probe and a target is buffered by compressed air in cylinders and the air is low-pollution.

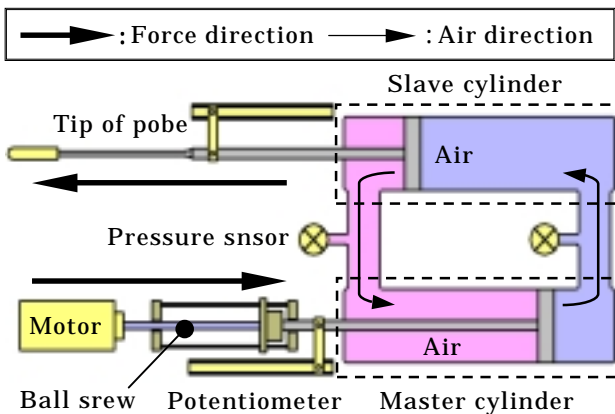


Figure 2 Schematic of the pneumatic bilateral servo actuator (PBSA)

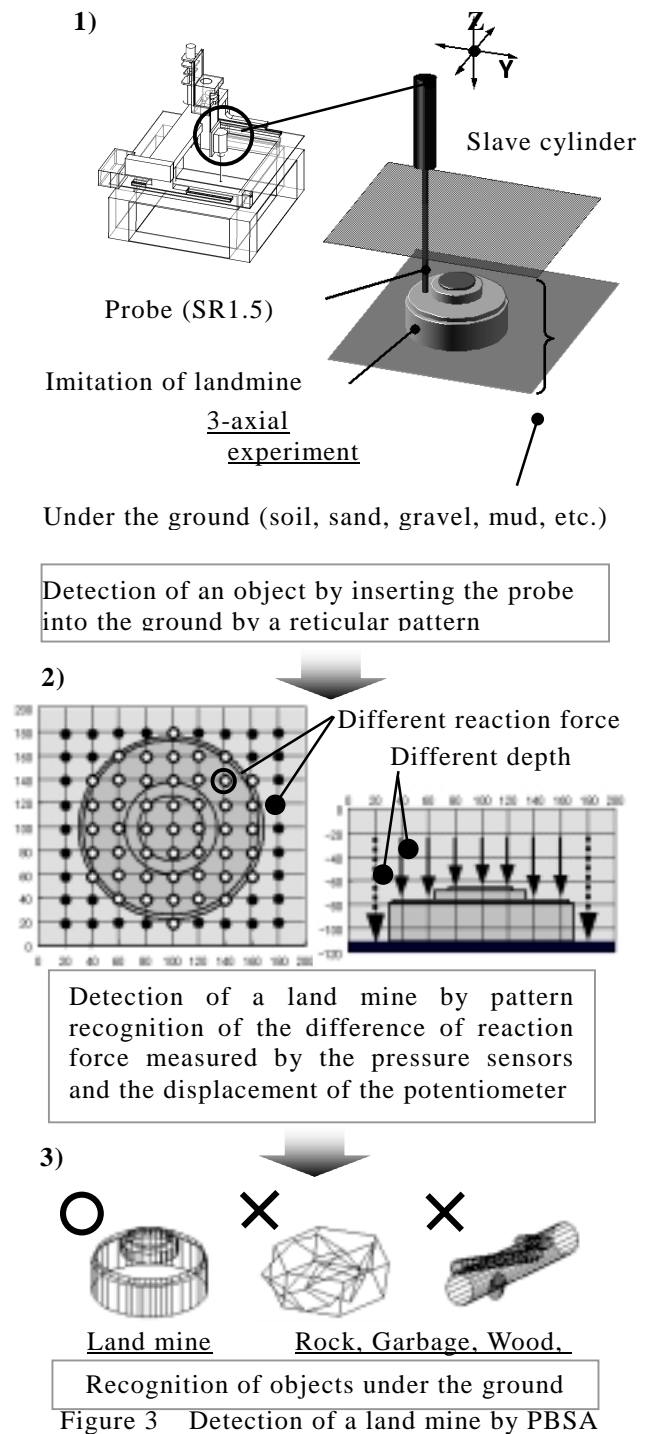


Figure 3 Detection of a land mine by PBSA

BASIC PRINCIPLE OF PBSA

A symmetric bilateral servo mechanism gives emphasis to positioning accuracy. But the demining by positioning control of the mechanism is impossible. To detect a land mine, it is important to detect the reactive force when a plodder, hits to a land mine. Therefore, force-reflecting bilateral

servo actuators are needed. It is especially needed to detect reaction force by a plodder. The motion equations of force-reflecting PBSA in figure 4 are as follows.

$$m\ddot{x} + f\dot{x} = F_{in} \quad (1)$$

we obtain

$$\ddot{x} = \frac{F_{in}}{m} - \frac{f}{m} \dot{x} \quad (2)$$

where

$$m = M_{sp} + L \quad (3)$$

$$F_{in} = F_b - F_r = P_b \cdot AS_b - P_r \cdot AS_r \quad (4)$$

The equation of adiabatic change of master and slave cylinder are expressed as follows.

$$P_r = p \left(\frac{V_r}{V_r + dV_r} \right)^n \quad P_b = p \left(\frac{V_b}{V_b + dV_b} \right)^n \quad (5)$$

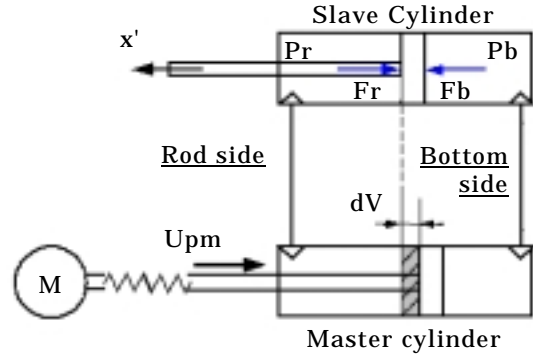


Figure 4 PBSA system

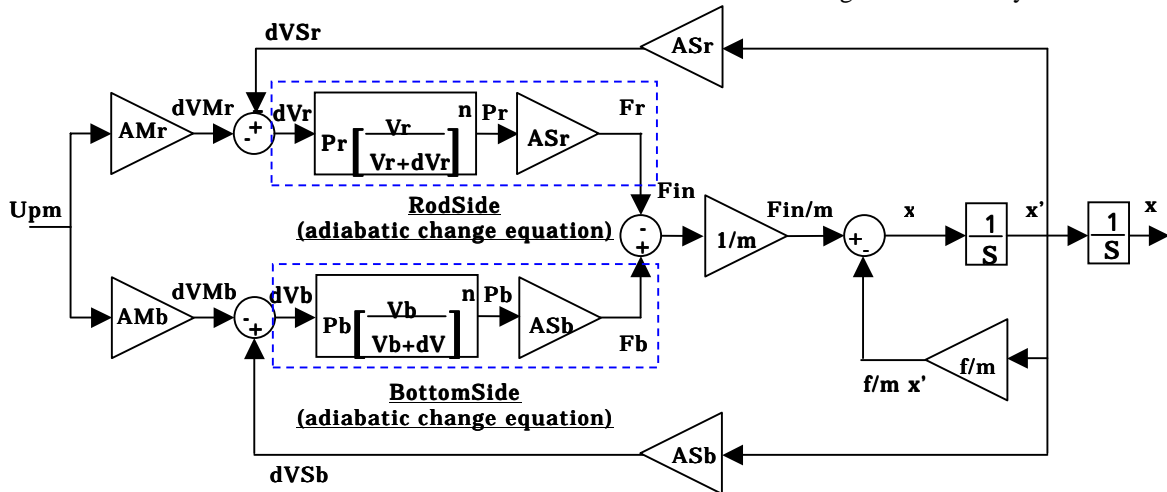
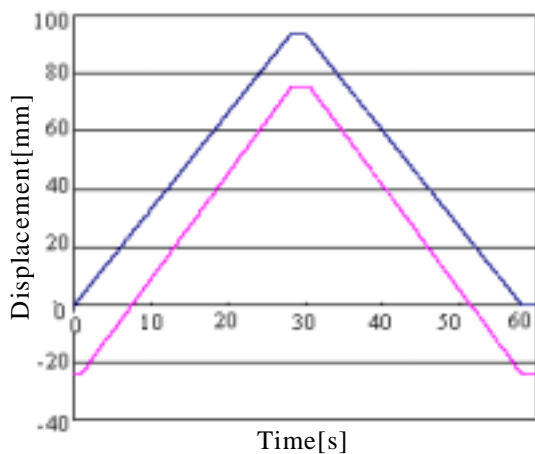
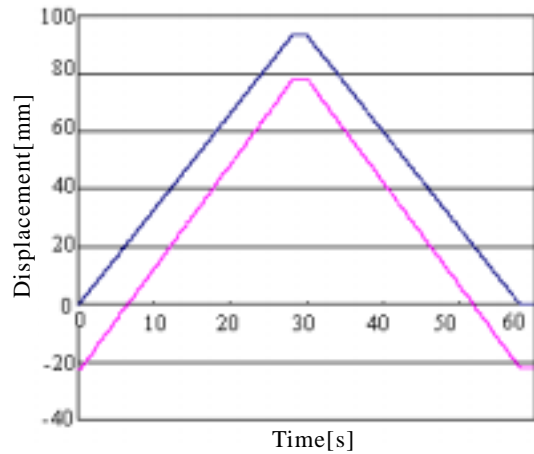


Figure 5 Block diagram of PBSA

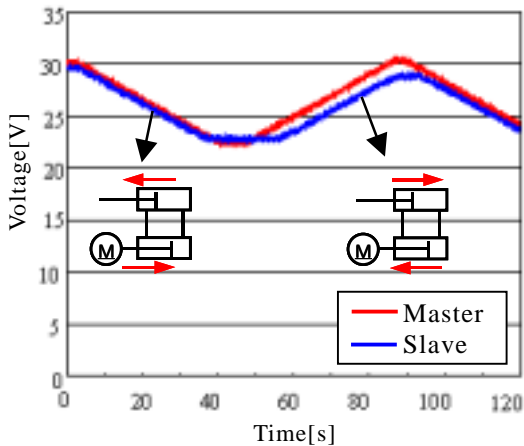


(a) Air pressure : 0.15 [MPa]

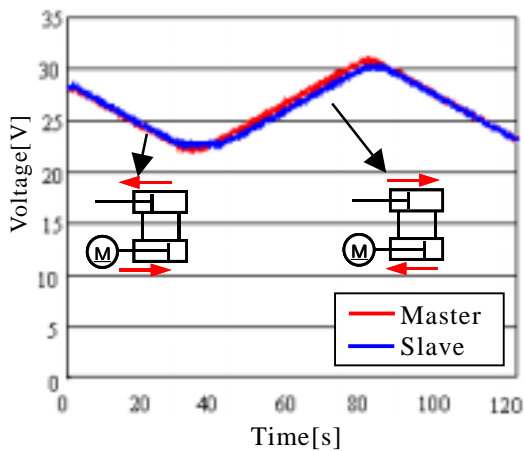


(b) Air pressure : 0.35 [MPa]

Figure 6 Response experiment (Simulation)



(a) Air pressure : 0.15[MPa]



(b) Air pressure : 0.35[MPa]

Figure 7 Response experiment (Experiment equipment)

Figure 5 shows the block diagram of the simulation.

Figure 6 (a) and (b) of simulation result when pressured by 0.15[MPa], 0.35[MPa] shows each response from input of master movement to output of slave piston. We can see response (a) is late a little.

Figure 7 shows the result of the experiment the response from master to slave motions. From figure 7 (a), we can confirm to be late response wave than (b). The time lag of right wave in (a) can be thought due to the difference cross-section area of piston and bottom side.

We developed the experimental equipment of PBSA

We confirmed that the higher the air pressure is, the higher the response is.

PBSA CHARACTERISTIC EXPERIMENT

Loading characterization

A land mine explodes with force from 0.4kg to 1kg. Therefore, it is needed to detect slight change of load when the probe touches a land mine. We are experimenting the response to loads of our PBSA. Table 1 shows the condition. Figure 8 shows the change of positions of reaction force from slave piston. When each load in table 1 are applied to the rod of the slave cylinder. The position of piston and the pressure in cylinders changed over 50 g proportionally. We confirmed to be able to measure a slight load to the probe from the change of pressure in cylinders. And then we will experiment to know smallest measure limit of PBSA by changing load force smaller.

Table 1 The condition of the response experiment

Air pressure[Mpa]	0.2	
Load[gf]	0, 30, 50, 70, 100, 120, 150, 170, 200	
Measuring time[sec]	30	
Sampling rat[Hz]	100	
Measurement part	CH1	Position of the piston (Master cylinder)
	CH2	Position of the piston (Slave cylinder)
	CH3	Pressure (Bottom side)
	CH4	Pressure (Rod side)

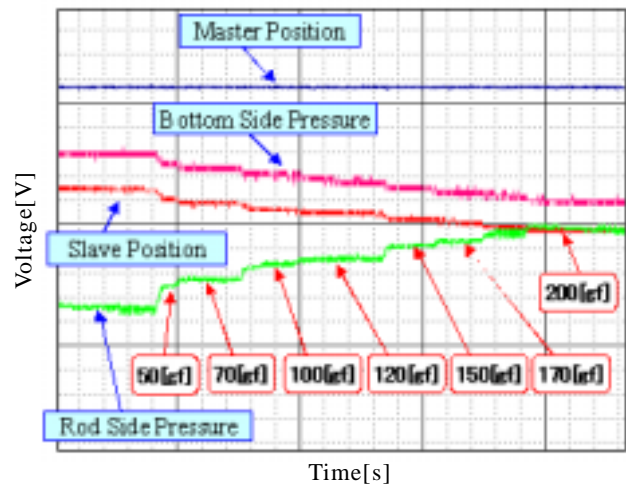


Figure 8 Loading characteristic experiment

Pressure sustainment

There are many land mines in an area. Therefore, our PBSA has to keep the air pressure in cylinders for a long time. Figure 9 shows the result of the measurement of the air pressure in cylinders. The initial pressure was 0.3 MPa. The pressure reduced after 15 minutes. After that, the pressure was kept

about 2 hours. From this result, we confirmed that it is possible to use our PBSA for a demining for a long time.

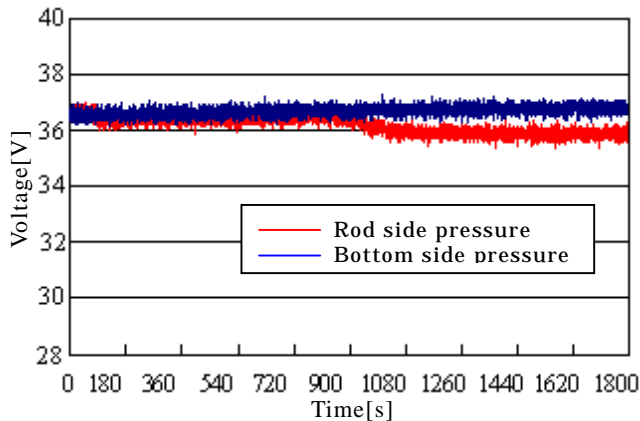


Figure9 Pressure sustainment experiment

CONCLUSION

We described the method to detect land mines, about 10 cm under the ground, by a prodder. The points are as follows.

- (1) The vertical insertion of the probe for the mine detection into the ground at a constant speed and even interval. (In case of the mine detection by deminer, a deminer slides the prodder on an object under the ground and makes a distinction between a mine and other objects from the reaction force.)
- (2) The pattern recognition of land mines from reaction force when inserting the probe in a reticular pattern.
- (3) The experiment of load measurement by the force feedback control and by the positioning control.
- (4) The detection of reaction force over 50 gf. And the quick start and stop by antagonistic effect by compressed air in the bottom and rod side cylinders.
- (5) A slight pressure reduction in more than 2 hours. (It was possible to keep running the system without recruitment of compressed air.)

In this paper, we described the basic experiment for the demining robot. We will develop the demining robot by application of our quadrupedal walking robot "Gorilla". The removal of plants at areas where land mines are buried in the ground is an issue.

REFERENCES

1. Motoyuki Sato, The state of the art of the

abandoned land mines by GPR, Proceedings of workshop on humanitarian detection and disposal of antipersonnel land mine, 2004, pp.49-54

2. <http://cobalt.cneas.tohoku.ac.jp/users/sato/index-j.html>
3. Nobuhiro Shimoi, Qingjiu Huang, Hiroaki Uchida, Daisuke Komizo, Kenzo Nonami, The smart sensing method for mine detection using time difference IR images, Collected papers of lectures on robotics and mechatronics 2000, The Japan society of mechanical engineering, 2000, pp.2A1-71-097(1)-2A1-71-097 (2)
4. Takeshi Kama, Keisuke Kato, Shigeo Hirose, Study of Probe-type Mine Detecting Sensor(Design and Experiments for the Impulsive Probing), Collected papers of lectures on robotics and mechatronics 2000, The Japan society of mechanical engineering, 2000, pp.1P1-69-108(1)-1P1-69 -108(2)
5. <http://www.mece.ualberta.ca/staff/fyfe/landmine.html>
6. Kenzo Nonami, Nobuhiro Shimoi, Hiroaki Uchida, Qing Jiu Huang, Daisuke Komizo, Jinok Shin and Aoki Toguri, Development of Six-Legged Walking Robot and Radio-Controlled Helicopter Robot, Dynamics and Design Conference 2000 CD-ROM, The Japan society of mechanical engineering, 2000
7. Nobuhiko Shimoi, Technology for Antimine, Morishitashuppan, 2002, pp.66-127

EXPERIMENTAL INVESTIGATION OF HYBRID VEHICLE

Ken ICHIRYU

Department of Mechatronics , Faculty of Engineering,

Tokyo University of Technology 1404-1 Katakura, Hachioji Tokyo 192-0982

Japan

(ichiryu@cc.teu.ac.jp)

Abstract

For energy saving, many attempts were tried in off-highway, highway vehicle and tram .First, we studied SATV vehicle of breakthrough and rescue purpose which is composed of hybrid power line CPS for low speed and MMT for high speed running.

Second, we studied CPS vehicle composed of variable P/M and energy recovery of flywheel.

In the last, we introduced flywheel driven FST tram prototype performance recently developed . This system is controlled by switching valve using fixed P/M.

KEY WORDS

HST HMT CPS Switching System

NOMENCLATURE

HST Hydrostatic Transmission

HMT Hydro-mechanical Transmission

CPS Constant Pressure System

FST Fluid Switching Transmission

INTRODUCTION

At present, to prevent global earth warming problem, automobile exhaust gas reduction and saving energy are becoming very important problem .

Roughly speaking, there are two methods to solve this problem.

1) First is of course, improvement of prime mover engine itself and many attempts are

tried such as digital engine technology and operation of engine always at good fuel consumption point .

2) Second way is improvement of power transmission line efficiency. This is especially important in hydraulic operated off-highway vehicle. In this field, HST is a fundamental element where large starting torque generation , wide speed ratio and transmission efficiency are three important parameters to consider .

To obtain wide required speed ratio of vehicle, one considers simple combination of variable P/M at first . But, partial efficiency

of P/M is not sufficient and limitation of usable capacity is 1/3-1/5 of rated capacity .

To avoid this problem , gear change or driving motor switching applying 2 motor driving system .

Importance of transmission efficiency is dependent on vehicle running duty cycle . For example, in wheel loader , running duty is not so frequent and above mentioned HST is applied .

But in tractor, running performance is important. Therefore, hydro mechanical transmission (HMT) is applied which combines hydraulic machine and planetary gear . To achieve required speed range , many kind of complicated system was developed combining speed and torque summation mechanism as fundamental element .

Third way is to construct hybrid system to absorb vehicle kinetic energy at braking by combining auxiliary power source.1),2)

Energy accumulation system is classified as follows

1) Engine +Electric Generator

Energy accumulation device is, such as battery, capacitor and flywheel

2) Engine+Hydraulic Pump/Motor

Energy accumulation device is accumulator and flywheel.

Here, according to the selection of hydraulic machine,pump/motor type ,different hydraulic system is created .

If we choose conventional variable P/M, constant pressure system (CPS) or secondary regulating system is possible to apply.

If we wish to choose combination of constant volume P/M, switching valve system will be one candidate .

1 CPS and HMT COMBINED SUPER ALL VEHICLE DEVELOPMENT

Crawler vehicle is recently gaining attention by its good snow driving performance . At the same time , it has the potential application as rescue vehicle . In this kind of purpose , necessary function is to reach disaster area as fast as possible from city center . Therefore high speed running performance inside city and break through performance of deserted area are demanded .3)

For this purpose , we studied SATV (SUPER ALL TERRAIN VEHICLE) using CPS and HMT combined power line as shown in Fig.1.

In SATV, low speed drive is by 4 hydraulic motor in front and rear and high speed drive is by rear HMT .Power flow of CPS and HMT is shown in Fig.2 .

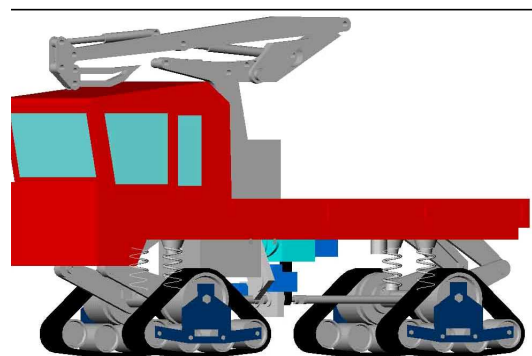


Fig.1 SATV Concept

1.1 CPS DRIVE

Power line from engine is composed of two lines CPS and HMT . At CPS drive, engine is connected to CPS gear box and HMT line is disconnected . Drive unit motor is connected to front and rear axle through clutch. By selecting clutch operation, it is possible to realize independent front or rear drive .

In CPS drive, flywheel is adopted . Detailed discussion of this system is omitted here , because another CPS was introduced in next chapter .

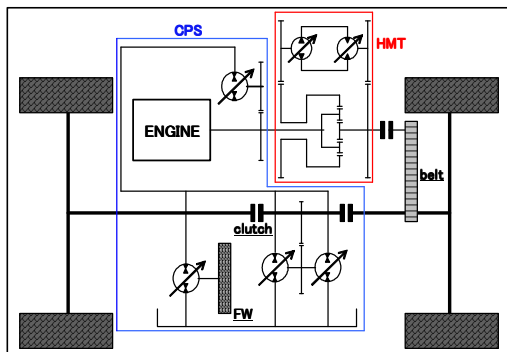


Fig.2 Power line of SATV

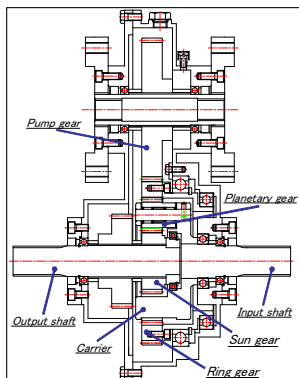


Fig.3 Developed input split HMT

1.2 HMT DRIVE

Power from HMT is transferred to drive shaft and crawler through output pulley. HMT is a combination of HST and planetary gear with CVT performance by HST and high efficiency by planetary gear.

There are two type of single HMT of input and output split type .

Hydraulic power ratio is compared with input split and output split. When hydraulic power ratio is zero, power transmission is made by planetary gear train only, without hydraulic power loss .

Therefore, at this speed ratio, transmission efficiency becomes best .In this time, we selected input split from control purpose. Manufactured HMT is shown in Fig.3. We confirmed fundamental performance of it by bench and experimental SATV vehicle.

2 CPS DRIVEN NEW CAR DEVELOPMENT

2.1

FUNDAMENTAL CONFIGURATION OF CPS WITH FOUR VARIABLE HYDRAULIC P/M

As shown in above, conventional drive method frequently applied for heavy vehicle is HST . This method has good transmission performance. But, braking energy storage is not possible and combination with hydraulic actuator or consumer is also difficult. In a word, HST application is limited only traction without energy recovery.

On the contrary, CPS is more flexible hydraulic system which is capable to coexist

with drive line and actuating system.4),5)

In the following, new CPS system is explained ,shown in Fig.4.

There are four variable hydraulic machines, that is, 1) engine coupled variable pump/motor, 2) flywheel coupled variable pump/motor 3) two driving variable pump/motors.

For energy storage , it is common to use hydraulic Acc (accumulator) . But, this system is assumed not fitted for light vehicle because Acc weight is heavy.

The system of FFC P/M (fluid force couple type pump/motor) connected to flywheel is shown in Fig.5. Let explain principle of energy storage by flywheel unit.

A) Deceleration

By pressing brake, capacity(eccentricity ratio) of drive unit FFC-P/M is set to the pump side in proportional to brake pedal displacement .

By this action, FFC discharges high pressure oil to the CPS high pressure line and vehicle is decelerated by braking torque . In this state , discharged oil makes rise the pressure of high pressure line and flywheel side FFC is regulated to act as hydraulic

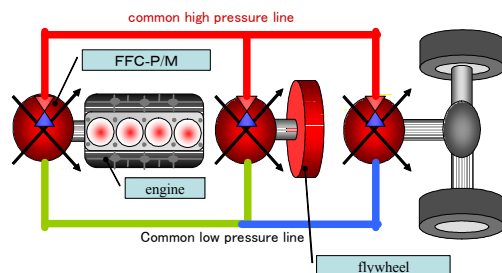


Fig.4 Car drive system by CPS

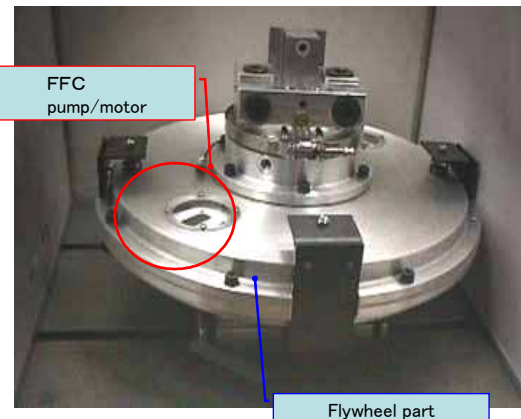


Fig.5 Flywheel driven by FFC motor to absorb discharged oil . Then, flywheel begins to rotate . That is, braking energy is converted to flywheel rotation .

B) Acceleration

When operator pushes acceleration pedal , capacity of drive unit FFC is set to the value of pedal displacement . As the result, pressure of high pressure line decreases and flywheel FFC acts as pump to discharge oil to compensate for pressure decrease. Revolution speed of flywheel decreases due to energy discharge. That is, flywheel rotational energy is converted to the vehicle acceleration.

In the case where flywheel accumulating energy is sufficient in the process of flywheel discharge and absorbing energy, engine is possible to stop to enhance fuel economy.

In the case of engine restart, engine drive FFC is set to the motoring action with simultaneous firing of injector .

In this state, as engine FFC absorbs high pressure oil, pressure of CPS line decreases . Therefore, flywheel rotation is required to be higher than certain limit.

2.2 STATIONARY TEST OF FLYWHEEL ENERGY STORAGE AND DISCHARGE

Measurement of flywheel energy storage efficiency was attempted by the process “ engine start –flywheel acceleration(energy storage)-engine stop-flywheel deceleration (energy reuse)-engine-restart-flywheel acceleration-flywheel deceleration ” without vehicle running .

By this test, efficiency of the hydraulic system is possible to evaluate . Control parameters are selected for each test condition .From this, system pressure is confirmed regulated nearly constant , by engine and flywheel action .

2.3 FLYWHEEL ENERGY STORAGE TEST OF RUNNING CONDITION

After stationary test, we conducted running test by using vehicle as shown in Fig.6 . After engine stops and flywheel reaches maximum speed , FFC coupled to flywheel starts to discharge oil to the high pressure line and vehicle accelerates by the energy of flywheel .

When the flywheel speed reduces to the lower limit ,then braking command is given to the driving FFC .

By this action, flywheel speed is once more increased to absorb braking energy .

Let calculate regenerative braking energy efficiency .

Ratio of energy stored in flywheel and energy restored in flywheel in the process of

vehicle start and stop is energy accumulation efficiency .

Efficiency of acceleration of vehicle by flywheel η_A and regenerative or braking energy η_B are defined as follows ;

$$\eta_A = J_V N_V^2 / J_{FW} (N_{F1}^2 - N_{F2}^2) \quad (1)$$

$$\eta_B = J_{FW} (N_{F3}^2 - N_{F2}^2) / J_V N_V^2 \quad (2)$$

Where, N_{F1} ; flywheel maximum revolution

N_{F2} ; flywheel minimum revolution

N_{F3} ; flywheel revolution at regeneration

N_V ; driving unit maximum revolution

J_V ; vehicle equivalent moment of inertia of driving unit shaft

J_{FW} ; flywheel moment of inertia

Total efficiency η is product of η_A and η_B ,

thus ,

$$\eta = (N_{F3}^2 - N_{F2}^2) / (N_{F1}^2 - N_{F2}^2) \quad (3)$$

These calculation includes CPS hydraulic system and vehicle driving efficiency .

So that , efficiency is total vehicle driving and energy storage efficiency .

By experiment , driving efficiency

$\eta_A = 70\%$,braking energy recovery efficiency

$\eta_B = 40\%$ and total efficiency $\eta = 30\%$ are obtained .

The reason why η_A , η_B different is not clear ,just now .

At acceleration of vehicle , flywheel rotational energy is converted to vehicle velocity through two FFC units .Also at braking, vehicle braking energy is transferred to flywheel through two FFC .

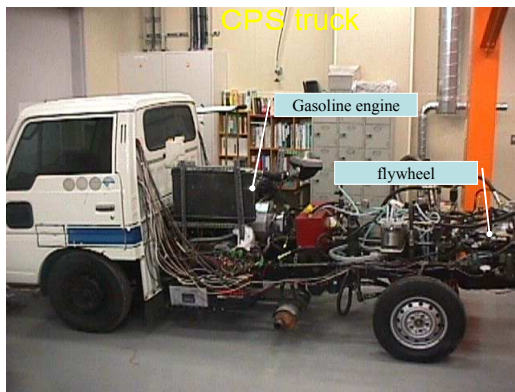


Fig.6 Test truck driven by CPS

3 FLUID SWITCHING TRANSMISSION

Contrary to using variable P/M, new approach to use constant P/M with switching valve named FST was developed recently .(6)

Developed 3 axis 6 wheel automatic steering bogie machine is prototype for tram application ,equipped with small engine and large flywheel for energy storage as shown in Fig. 7 .



Fig.7 Tram model driven by FST

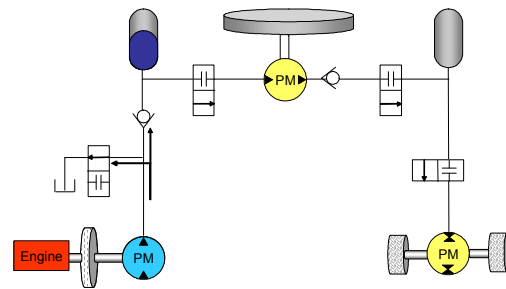


Fig.8 FST hydraulic diagram

Flywheel is specially designed to minimize rotational loss and capacity is 13.0 Kgm² ,about 6 times larger than CPS car .

. Basic hydraulic diagram is shown in Fig.8. Switching circuit is constructed in engine –flywheel and flywheel-driving motor .

Driving command is inputted by mono lever and on-off valve is controlled by FST algorithm. Flywheel is accelerated to the top speed by engine. Then, by this flywheel energy, tram is accelerated to the desired speed . Braking energy is also recuperated to the flywheel .

FST hydraulic circuit is simple because only using switching valve and gear P/M instead of complicated variable P/M. Tram acceleration and deceleration are confirmed fundamentally same as of above mentioned CPS.

System total efficiency at running is estimated high due to using fixed P/M and switching valve. In this system, surge phenomena takes place due to rapid switching of fluid line. If we have effective measures to this problem , FST is also applicable to hybrid vehicle.

CONCLUSION

Experimental investigation of hybrid vehicle was conducted including SATV composed of CPS and HMT and flywheel car driven by CPS.

Further, FST was reviewed which was driven by switching principle .

- 1) CPS and HMT combined power transmission system was proposed for SATV.
- 2) By actual running test, braking energy was possible to recuperate in CPS car.
- 3) By switching valve system FST , simple and effective driving system for tram is possible to realize.

In closing this paper, we sincerely thank Mr.Narahara for SATV project , Mr.Kita for CPS and Mr.Itoh of Yukigaya Co. for FST system to their support . Finally, we thank member of Ichiryu laboratory for their cooperation .

REFERENCES

1. P.L.Matheson,J.S.Stecki;Development of Hybrid Diesel Hydraulic System for large commercial vehicle; P1251, SICFP03,May,2003
2. E.Karlson;TheVolvocity bus ImechE, C157/81 143/151(1981)
3. K.Ichiryu ; Present and future of hybrid car , Autumn Seminar 2002 JFPS ,2002
4. R.Kordak; Hydrostatic Drives with control of the secondary unit , The Hydraulic Trainer,6,Mannesman
5. K.Kawamura;Study on hybrid vehicle using CPS with Flywheel , SICFP 2005
6. Seki and Itoh; An examination of LTV and its Transmission equipped on board,p91-93, Itoh amd Seki; The JFPS Spring meeting 2004,p34-39,May 2004,Tokyo

Application and study on the Hydraulic Switching Power Control

Sumiko SEKI* and Takahiko ITOH*

* Department of Electronic and Mechanic Development
Yukigaya Seigyo Laboratory
2-12-12-203 Shin-Yokohama, Kohoku-ku, Yokohama, 222-0033 Japan
(E-mail: seki_yukigaya@nifty.com, itoh_yukigaya@mbe.nifty.com;)

ABSTRACT

Recently, a technology on the machines under computer control is become established. However huge working power of the hydraulic mechanics is difficult to control with taking efficient power transmission and its precision. Then hydraulic switching power control system is contrived based on analogy between electric circuit and fluid circuit. Hydraulic and electric switching devices are called valves as both circuits on nomenclature. The hydraulic switching control on huge working power have been disclose only a few years ago, at first in the world on JFPS Spring Meeting on Fluid Power”, May 2002 in Japan. This paper is described process of some experiment to have evidence to practical use of the Hydraulic Switching Control. We have obtained patents about the hydraulic switching control as a new theory on the Fluid Power Systems, and registered it as the trade mark “FST” means Fluid Switching Transmission. Outline of the performance of the FST is also described in this paper.

KEY WORDS

Key words, Hydraulic switching, Electronic switching, Fluid switching Transmission, FST

NOMENCLATURE

Q_m : output torque of motor
 Q_p : input torque of hydraulic pump
 I : inertia of flywheel
(sum of inertia on motor shaft)
: angular velocity of flywheel
 a : on/off condition of un-loader valve
 i : current of electric power sauce
 EsI : output voltage of electric power sauce
 EcI : output current of electric power sauce
 LI : inductance of reactor cil
 b : on/off condition of switching device

INTRODUCTION

The concept of hydraulic switching for power control and regulate the fluid conditions on the hydraulic power system was have not existed in the world, it is as same as a seen on electronics a half century ago. It was believed that the power switching on high frequency on heavy load, it was believed that makes severe vibration as parasite oscillations.

We have succeeded to suppress the violence of transient in the power electronics, based on the way of the electron beam deflection and fly back circuit on CRT control, especially for color CRT display.

Usually, human lives in the world that is dominated by the ILLUSION. However on the physical object like as the mechanical constructions, the vibration makes serious obstructions, it is much different from the human sense and sensitivity of human.

The technology of FST (Fluid Switching Transmission : is only our registered trademark) is facing the difficulties on vibrations not only physical but also illusion of human sensitivities.

The switching technology on the hydraulic power system will be judged from the quite otherwise. We have succeeded on a trial of the production of hydraulic power switching servo controllers reciprocate, it has brought the great successful result of the trial for us.

We continued the development of the hydraulic power control by switching since 1973, accompany with the research on the electronic switching power control, to increase their transferring efficiency on the power transmission and suppression of unparadonable obstructions will be eliminated.

We have disclosed the hydraulic switching technologies on May 2002, applied for a patent simultaneously, and we have obtained the patent of the theory on hydraulic switching technology recently, what is said⁽¹⁾⁽²⁾⁽³⁾⁽⁴⁾⁽⁵⁾⁽⁶⁾.

We will discuss about the technology of power switching on the hydraulic and electric field of technology, and investigate the analogy of the hydraulic switching technology with the electronic switching power control. The prototype of rail vehicles will be introduced in this paper which are produced by us, in order to prove the performance of the hydraulic switching technology as a transmission, both to hydraulic and electric switching power control systems.

The three units of original servo systems are shown in Figure 1, they are a part of prototype produced at first, controlled by hydraulic power switching. These servo actuators are produced 1973 in order to cut down the energy consumption of a hydraulic servo systems working in a factory as productive facilities, and the FST servo control system succeeded to save the energy more than 99% of conventional servo control systems in that was running in the factory.

These original models have mechanical output of reciprocate.

The servo control system has an excellent ability as power transmission if designed appropriately.

We have produced plot type of LRV (Light Rail Vehicle) to prove the performance of power switching control systems as the transmission of vehicles on board.

Figure 2 shows the plot type of trolley less electric vehicle powered by the EDLC (Electric Double Layer Capacitor) on board, the vehicle is driven by electrostatic energy at first in the world, tt is shown in Figure 2 has electronic power switching controllers as transmission, for powering and regenerative brake.

Figure 3 is the vehicle powered by the thermal engine and flywheel hybrid, and the power is controlled by the bilateral FST⁽⁷⁾⁽⁸⁾⁽⁹⁾⁽¹⁰⁾.

The vehicle shown in Figure 3 is powered by the kinetic energy stored in the flywheel on board, and on braking, kinetic energy that was kept in vehicle returns to the flywheel as regenerative brake system.

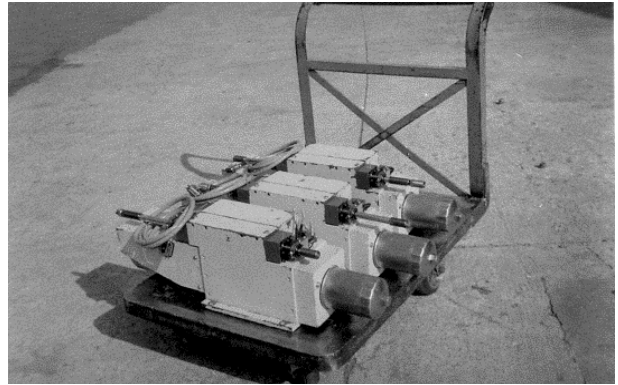


Figure 1 Switching servo control produced 1973



Figure 2 Trolley less electric vehicle EDLC on board



Figure 3 Hybrid flywheel vehicle FST on board

The FST is a high performance transmission, and the FST vehicle has the powering system equivalent to that of the electric systems.

FST have been proved that its operating efficiency is 100% on theoretically, same to that of the electronic switching power control designed proper.

The analogy between hydraulic system and that of electricity is often appears on the books telling technical theory, however almost of them are mistake of slip.

The excellent power transmission will perform energy regeneration on the powering system, and regeneration

demands a support of accumulators of high performance that will be introduced below

THE POWER SWITCHING

Generally importance of the power switching on the power systems have been well known on the field of technology, the electronic switching technology have only grow to a standard system of power controllers.

However we have completed hydraulic power switching control system more than 30 years ago as servo controllers, however, we did not disclosed them.

The most basic hydraulic switching circuit diagram of the "FST" is shown Figure 4.

Figure 5 shows the electronic circuit diagram equivalent with the FST circuit what is shown in Figure 4.

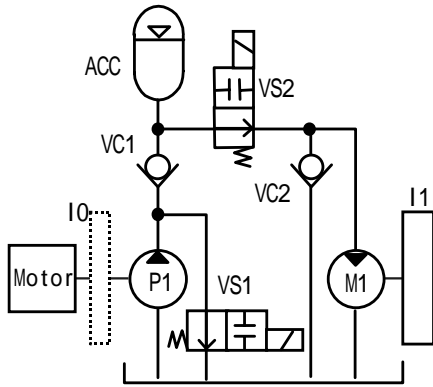


Figure 4 Circuit diagram of the FST

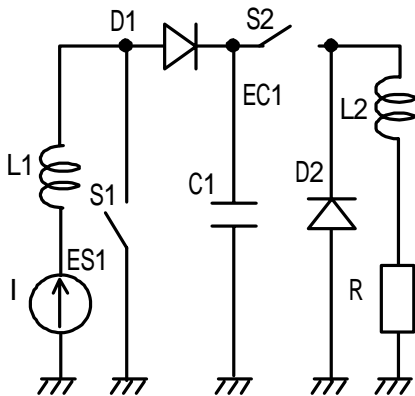


Figure 5 Circuit diagram of a switching converter

Figure 6 to Figure 9 are supplementary explain about the principles of FST.

Function of VS1 in Figure 4 behaves like as the un-loader valve, but its usual operating frequency is much higher than generally used un-loader valves.

It is operated synchronize to clock frequency or self oscillating frequency that is decided by the way of

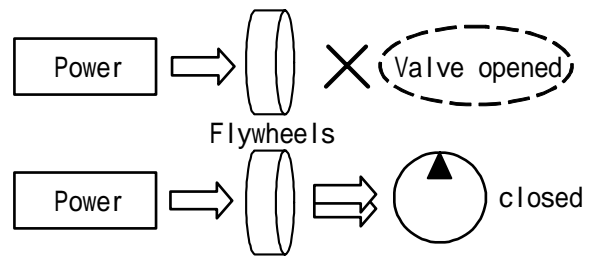


Figure 6 Inertia makes two phases

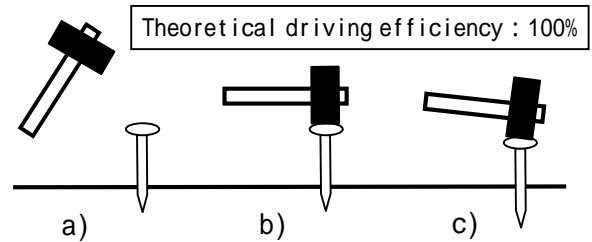


Figure 7 Drive a nail

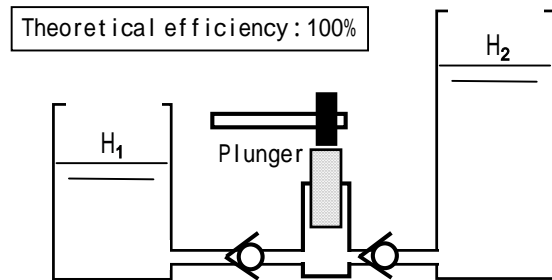


Figure 8 Drive a plunger pump by hammer

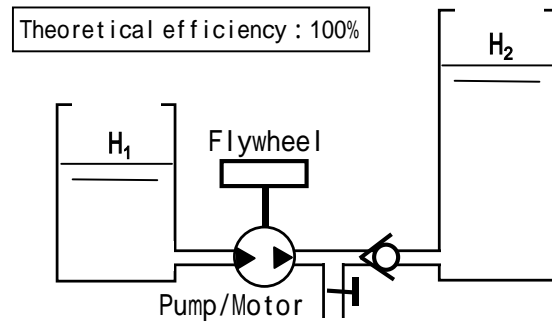


Figure 9 Inertia makes boost the hydraulic pressure

feedback loop from the hydraulic pressure in the accumulator ACC 4 in Figure 4.

Figure 6 shows the behavior of torque transfer, when the un-loader valve is switched, on the rotating motor shaft installed hydraulic pump and flywheel or incidental inertia instead of flywheel.

When the un-loader valve is opened, the angular velocity of flywheel increased by the motor torque.

The un-loader valve is closed the hydraulic pump will be driven by larger torque than motor torque, sum of the torque of motor and flywheel.

Some of similar examples of switching action were described before, on the analytical explanation.

Figure 7 shows a process of driving a nail into a wooden block. The kinetic energy of hammer is converted into a thrust to drive a nail, and the efficiency on driving nail is 100%, if the coefficient of elasticity, "E"=1, between the head of hammer and the nail, theoretically.

An example similar to the nail drive is shown in Figure 8. A plunger works as a ram, that is driven by a hammer, then, they make a piston pump, and boost up the hydraulic pressure H1 to H2.

Theoretical efficiency of this plunger pump also presents 100% on the pressure boost.

An improved pressure booster is shown in Figure 9, equivalent to the boosters in Figure 7 and 8.

This booster system works as rotary machine, generally, the rotary machines are superior to reciprocate for practical use, especially its continuative transfer ability is excellent, and the power density of rotary machines are better than that of reciprocate.

An example of switching control hydraulic power system will be analyzed on the equations.

Q_m : torque, motor generates, Q_p : loaded torque of hydraulic pump, I : sum of inertia on the pump driving shaft, ω : angular velocity of the driving shaft.

The motion is shown by Eq. (1).

$$Q_m - aQ_p - Id \frac{d\omega}{dt} = 0 \quad (1)$$

$a=1$: VS1 is closed

$a=0$: VS1 is open

On the electric circuit that equivalent with hydraulic switching circuit, the voltage boost is practiced as the followings; i : source current, $ES1$: voltage of source, $L1$: inductance of $L1$, $EC1$: output voltage on the terminal of C1.

The relation between current and voltage is shown by Eq. (2), it is equivalent with Eq. (1).

$$ES1 - bEC1 - L1 \frac{di}{dt} = 0 \quad (2)$$

$b=1$: S1 is open (OFF)

$b=0$: S1 is closed (ON)

There are various way to present the power switching both to mechanical and electric engineering field.

Then, we will present a typical response on switching both to hydraulic and electronic switching.

Figure 10 shows the angular velocity of flywheel connected with hydraulic pump and motor coaxially, and the magnetic flux density in the core of inductor on

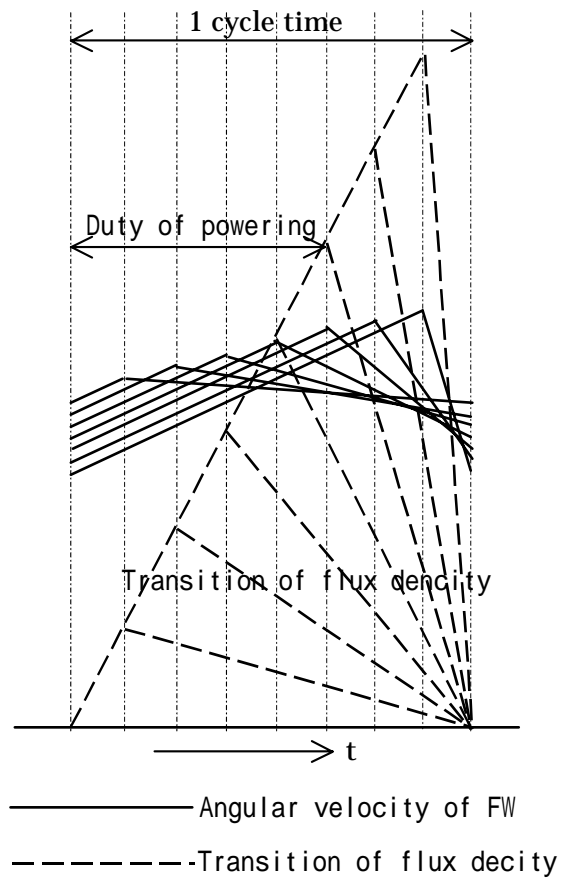


Figure 10 Transition of angular velocity and flux

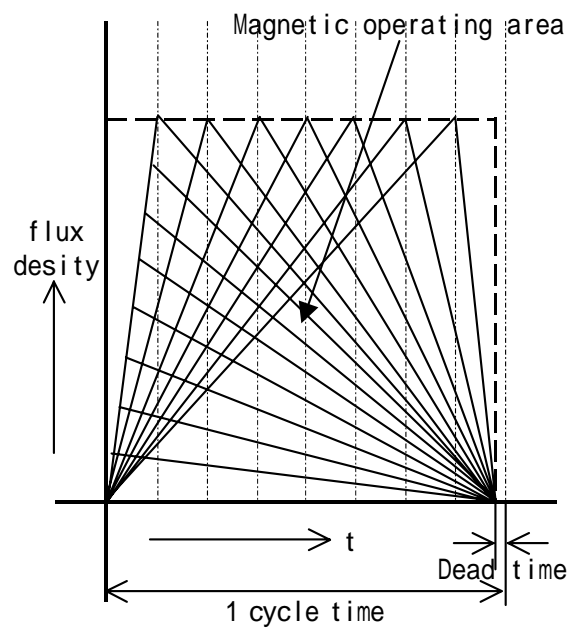


Figure 11 Magnetic flux density on 2nd quadrant

a pressure and a voltage booster.

The transition of magnetic flux density in the inductor core on chopper converter is shown in Figure 11, generally magnetic cores of inductor are operated on the 1st quadrant and 3rd quadrant of the B-H plain, and operating area is limited by characteristics of magnetic core.

The hydraulic switching system is equivalent with electronic switching system, but it is not equal on all, there are various inconsistency between on both system. Generally the switching power controls are applied pulse width modulation (PWM).

There are various method to apply PWM for switching, but they are belongs to the system of synchronous to clock, or hysteresis control that has no clock pulse.

You can chose whichever you like above two ways of PWM control, but if anything asynchronous hystersis control is better than others, limited on hydraulic system.

Anyway the switching power control is constructed of reciprocal transitions of the energy accompany with oscillation

APPLICATIONS

We have produced many instruments to prove the performance of switching power control not only hydraulic power systems but also on the electric power control systems.

Figure 12 shows the Flywheel Hybrid Rail Vehicle controlled by the hydraulic switching transmission on left hand, and on right the Electric Rail Vehicle powered by the electrostatic energy stored in the Electric Double Layer Capacitor (EDLC) on board. ⁽⁸⁾⁽⁹⁾⁽¹⁰⁾

Close up of the flywheel rail vehicle is shown in figure 13, the instrument panel and bench seat for operator is seamed on the head of the vehicle.

Middle of the vehicle, under the seat, flywheel is mounted, reserve tank and the circuit hydraulic switching transmission are on near the tail of vehicle, accumulators are also mounted top of the hydraulic control circuit.



Figure 12 Rail vehicles have switching on board

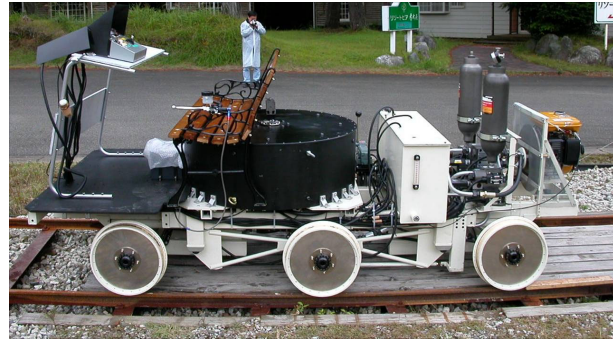


Figure 13 Flywheel hybrid vehicle controlled FST

The thermal engine is mounted on tail end of the vehicle it is shown in Figure 13.

The vehicle runs powered by the flywheel on board which is increased its angular velocity by the engine power and regenerative braking power.

The vehicle on the right hand in Figure 12 is the prototype of rail vehicle powered by EDLC on board.

The variable range of FST-transmission is boundless and the efficiency as transmission have been measured over 99% on wide range of convert ratio.

POWER ACCUVULATORS

It is important for us that reduce energy consumption of vehicles and other instruments, so we continued to develop of high efficient motor, transmission and power accumulator.

The high efficient vehicles must be equipped regenerating brake and high efficient bilateral transmission onboard.

We have established switching power transmissions on electronic and hydraulic power control, and we found the necessity of power accumulators not only on hydraulic bat electric power switching systems.

We made a trial to develop the power accumulators since 1975.

One of successful power accumulator is the EDLC and other is the Flywheel covered with floating shrouds.

Newly developed flywheel as power accumulators has floating shrouds rotating coaxially with flywheel, the flywheel able to rotate up to super sonic velocity on its tangential velocity in the atmospheric air pressure.

The flywheel is shown in Figure 15, this is mounted on board FST vehicle, it wears three layer of shrouds, in Figure 13, upper half of shrouds are removed for exhibition.

Figure 16 shows a cross section of the flywheel.

The aerodynamic theory of reducing drag force of the flywheel in atmospheric air pressure environment is our patent.

Figure 17 shows EDLC which has huge electro static capacity of 2,000 and 1,200 Farad, we have continued development of powering by the EDLC, and our first EDLC vehicle was succeeded 1988.

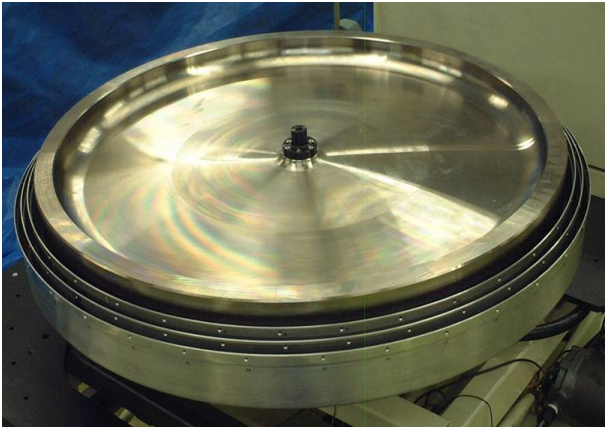


Figure 15 Flywheel with bottom shroud

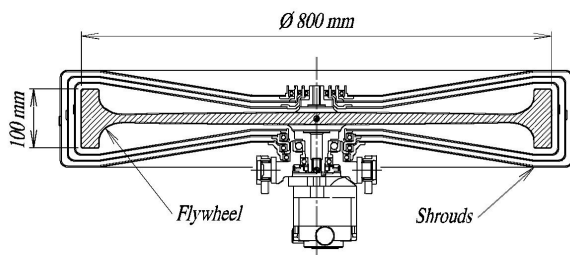


Figure 16 Cross section of flywheel and shroud



Figure 17 Electric Double Layer Capacitor

Now, we are converting a conventional marine Diesel engine into the FST control engine, in order to present the effect of FST on Diesel engines.

The FST involves the concept of dynamics, on the rotary inertia it makes transmission, on the reciprocate, FST makes most efficient hydraulic system.

The FST engine will complete in September 2005, and it will begin the test run.

The full detail of the experiment is will be disclosed near future.

We have chose 4-stroke cycle Diesel engine in this project in order to prove the performance of FST.

The difficulties applying to 4-stroke will be solved by the FST engine control systems.

CONCLUSION

We proved that the FST is one of best way to keep the efficiency of transmissions, thermal engine and other powering systems. The best way to reduce consumption of energy is the increase of efficiency on systems, we believe.

The power switching is completed on the electric power control technology, but it was not exist on the hydraulic power system.

We succeeded to make practicable hydraulic power switching at first in the world, so we cannot find any publish about hydraulic power switching yet.

REFERECE

- (1) The 8 th National Symposium on Power and Energy Systems (SPES 2002)
Itoh, Seki, Aoyama and Shimada, Flywheel for energy storage, p365-368, June 18 2002, Tokyo.
- (2) Itoh, Seki, Aoyama, Shimada and Suzuki, The new theory and technology on hydraulic transmission, JFPS Spring meeting 2002, p34-39, May 23 2002, Tokyo.
- (3) Seki and Itoh, An Examination of a LRV and its Transmission equipped onboard, p91-93,
Itoh and Seki, The equivalent Hydraulic Transmission on Electric Transmission, p94-96,
Itoh and Seki, The JFPS Spring meeting 2004, p34-39, May 26 2004, Tokyo.
- (4) Itoh, Trolley less vehicle and energy accumulator, Rolling Stock & Technology, No89, September 2002, Rail & Tech. Publishing Co.Ltd.,
- (5) Itoh, The proposal on hydraulic control technology, Hydraulic & Pneumatics, Vol.42 No.5, p49-55, 2003
- (6) Itoh, Switching control on the hydraulic power system, Hydraulic & Pneumatics, Vol.42 No.7, p55-60, 2003
- (7) Itoh, An application of shrouded flywheel, Hydraulic & Pneumatics, Vol.43 No.12, p4-10, Oct. 2004, Nippon kogyoshuppan.
- (8) Itoh and Ski, We produce a LRV and constructed a railroad for experiment, S4-2-6 p265-268, J-RAIL-01, December 12 2002, tokyou
- (9) Seki and Itoh, Application of Electric Double Layer Capacitor for LRV and EV, S4-1-2, p329-332, J-RAIL2002, November 27 2002, Kobe
- (10) Itoh and Seki, Light-Rail-Vehicle running only by the storage energy of on board EDLC ,and steering by the Automatic Control Links, 3302, P247-250, TRANSLOG2002, December 11 2002, Kawasaki

Valve actuator and fuel injection pump driver on Diesel Engine

Takahiko ITOH* and Sumiko SEKI*

* Department of Electronic and Mechanical design
Yukigaya Seigyo Laboratory
2-12-12-203 Shin-Yokohama, Kohoku-ku, Yokohama, 222-0033 Japan
(E-mail: itoh_yukigaya@mbe.nifty.com; seki_yukigaya@nifty.com)

ABSTRACT

Marine Diesel engines are converting their fundamental futures, they are compelled to suppress the emissions of CO₂, NO_x, and others maintaining the conference around the thin layer of the earth surface, then these engines are beginning to convert their design concept now. However, it seemed for us that is processing by poor technology and concept, such as the applying computers and electric controls only. The principal reforms of the engines are remove their camshaft, tappets, mechanical push rods, rocker arms and mechanical injection pumps and the tasks are depend to computer and electric control. The engines applied the new concept has some small advantage to traditional engines, easy start and reverse, etc, but facing serious difficulties of its reducing thermal efficiency. This paper describes that the compatibility of suppress the emissions keeping high thermal efficiency of the engine. We are remaking an engine will be changed from conventional engine to the innovative one applying our patent HYDRAULIC SWITCHING TECHNOLOGY.

KEY WORDS

Key words, hydraulic switching, CVT, equivalent to electric switching, fuel injection, valve actuator

NOMENCLATURE

$D1$: smaller diameter of stepped booster piston
 $D2$: larger diameter of stepped booster piston
 $D3$: diameter of pluger
 Ph : pressure of hydraulic fluid
 Pf : pressure of fuel oil
 Qm : torque of mortar
 Qp : torque of hydraulic pump
 I : inertia of rotary part of pump
 Es : sauce Voltage
 LI : reactor inductance

INTRODUCTION

We have established hydraulic switching servo control system in 1973, but we have not disclosed it over 30

years. The hydraulic power switching technology has been disclosed in the JFPS spring meeting held in Tokyo on 2002, at first in the world, simultaneously we applied patents and obtained it ⁽¹⁾⁽²⁾⁽³⁾.

Recently, marine Diesel engines are beginning to undergo a transfiguration by the requirement for suppression of their emissions and smoke.

On uni-flow two-stroke marine Diesel engines exhaust valves are changed to hydraulic push rod already instead of mechanical push rods and rocker arms ⁽⁴⁾⁽⁵⁾.

The hydraulic control systems of the engines reduce its thermal efficiency.

We have made a plan to increase the thermal efficiency of these engines drastically applying the FST, which is a hydraulic transmission applying hydraulic power switching technology equivalent to the electric power switching control, suited for the reciprocate.

CONVENTIONAL FUEL INJECTION

Figure 1 shows a cross section of the conventional fuel injection pump. An electrically controlled booster pump

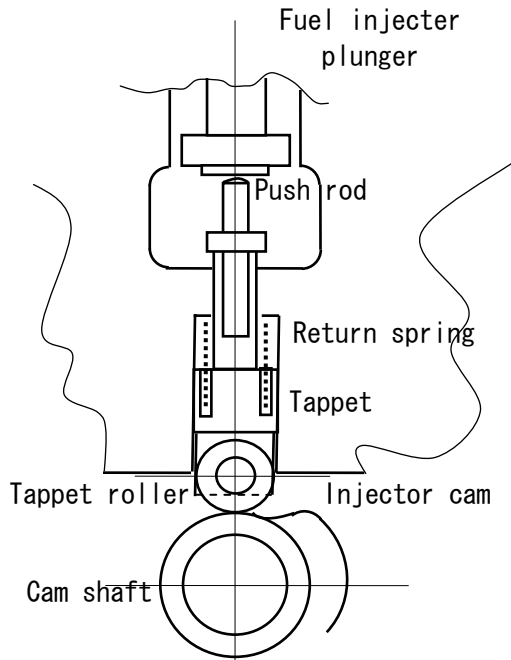


Figure 1 Conventional fuel injection pump

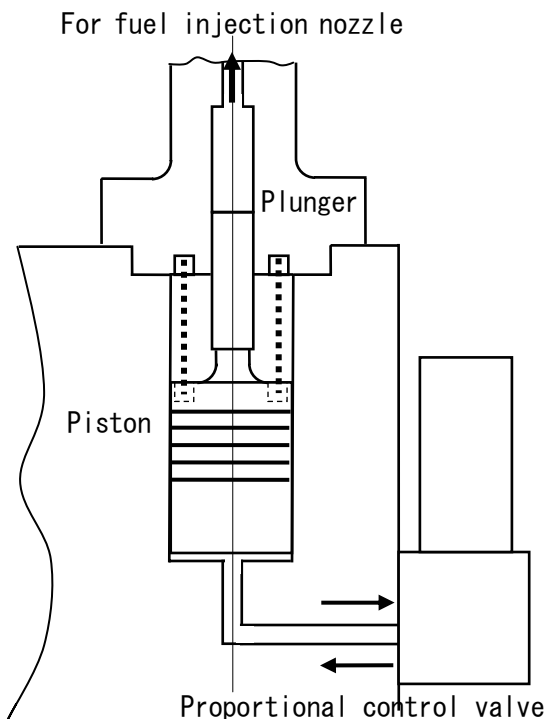


Figure 2 Electrically controlled fuel pressure booster

as fuel oil booster is shown in figure 2.

Figure 3 is an example of fuel oil pressure transition in the boosted fuel oil pipe of the conventional engine.

Figure 4 is an example of double injection electrically controlled pressure transition of boosted fuel oil.

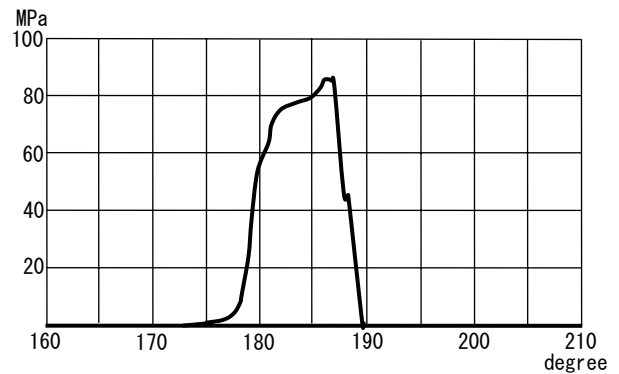


Figure 3 Fuel pressure transition conventional engine

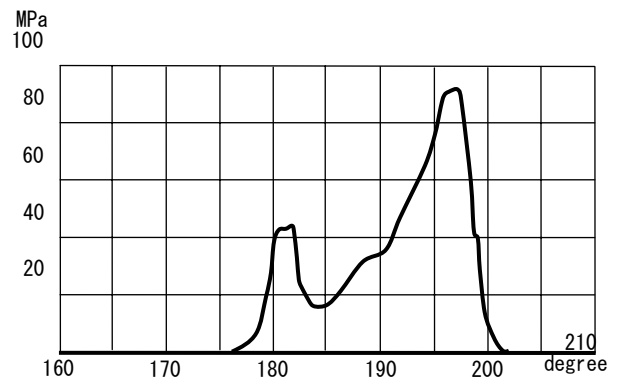


Figure 4 Fuel oil pressure transition hydraulic booster

The boosted fuel oil pressure transition pattern of electrically controlled injection is variable, to have best compromise to improve the relation between thermal efficiency and emission of NOx.

It is well known that high rate fuel injection on TDC, combustion gas generates high density of NOx. The air in cylinder is compressed to a maximum pressure and minimum entropy on the TDC, then high rate fuel injection generates high density of NOx by the combustion of high temperature and high pressure.

Progressive injection or double injection reduces NOx emission, however the injection pattern of this way spoils thermal efficiency of the engine⁽⁴⁾⁽⁵⁾.

We continue the experimental simulation of progress the thermal efficiency of a Diesel engine, by means of applying the FST technologies, for fuel oil pressure booster and valve actuators of the engine.

The compatibility between emission and high thermal efficiency of the engines will be completed.

THE REVILUTION ON FUEL INJECTIN

The increase in dissipation of energy on the electrically controlled fuel injection system makes increase in fuel consumption of the engine, and reduces its net thermal efficiency.

The FST(Fluid Switching Transmission / Technology) will make the revolution on technology of suppression of NOx and smoke emission⁽⁷⁾⁽⁸⁾⁽⁹⁾.

FST is the registered trademark of a hydraulic control system that is developed and applied the patent to us, and it means “Fluid Switching Transmission” and “Fluid Switching Technology”.⁽¹⁾⁽²⁾

Figure 5 shows cross section of injection system driven by the FST, the fuel injection pump has similar structure to the conventional or electrically controlled one.

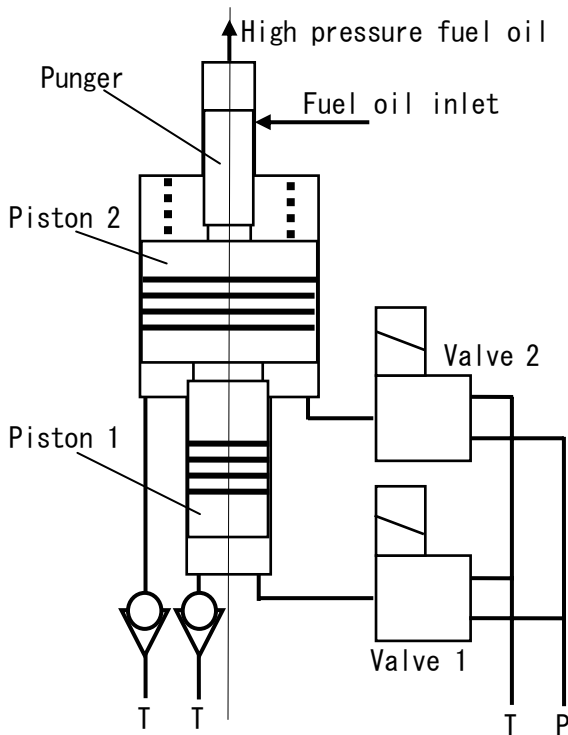


Figure 5 FST fuel pressure booster

The FST fuel injection pump is a mechanism of the hydraulic pressure boosters, and the plunger actuator piston has multiple steps of its diameter coaxially. Piston 1 generates lower pressure in the fuel oil, and piston 2 makes middle pressure by the differential area on the step of diameter.

The valve 1 is opened, and the valve 2 is closed, plunger makes lowest fuel oil pressure by the hydraulic pressure delivered on the area of small diameter piston.

When the valve 2 is open, and the valve 1 is closed, fuel oil pressure is made by differential area of the piston, middle level of pressure is given to the fuel oil.

The both valves are opened fuel oil pressure rises to the maximum injection pressure.

A simulated transition of fuel oil pressure transition is shown in figure 6.

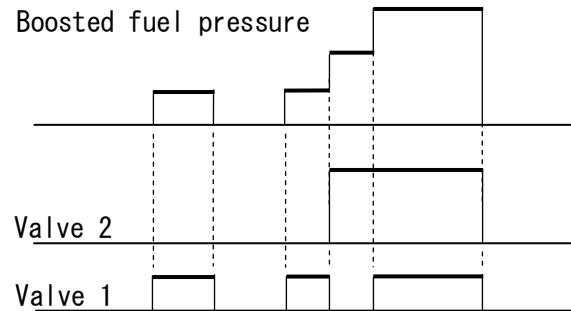


Figure 6 Bit control and boosted pressure

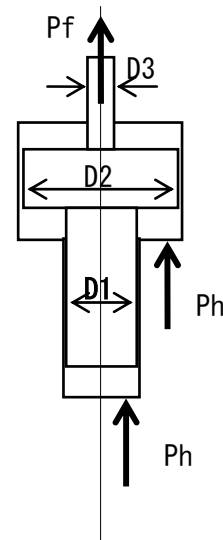


Figure 7 Pressure balance on multiple piston

Figure 7 shows an illustration of fuel oil pressure booster equipped multi diameter pistons D1 and D2. When Ph is loaded piston diameter D1, boosted pressure Pf is equation (1)

$$Pf1=(D1/D3)^2 Ph \quad (1)$$

Next, for middle pressure,

$$Pf2=(D2-D1)^2/D3^2 Ph \quad (2)$$

And the most pressure is given by area of diameter D1, it is made by the way of feeding pressure Ph both to the area of D1 and D2 of the piston which has a fuel injection plunger and multi diameter piston.

The highest pressure of fuel oil for injection is given as

following equation.

$$P_f3=(D2/D1)^2Ph \quad (3)$$

The energy need to fuel injection is the sum of each step of injection pressure transition.

The injection power is increase with boosted fuel oil pressure proportionally, Figure 7 shows a simulated chart of the energy consumption on fuel injection of trendy one and the FST fuel oil booster.

Figure 8 shows injected quantity of the fuel by pressure.

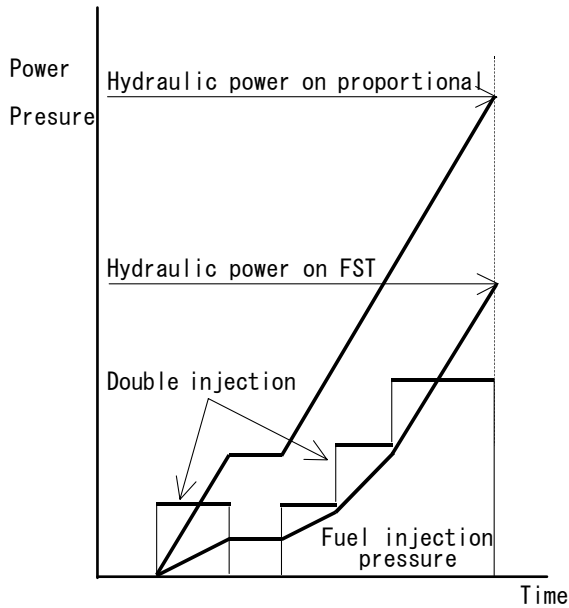


Figure 7 Power consumption on fuel injection

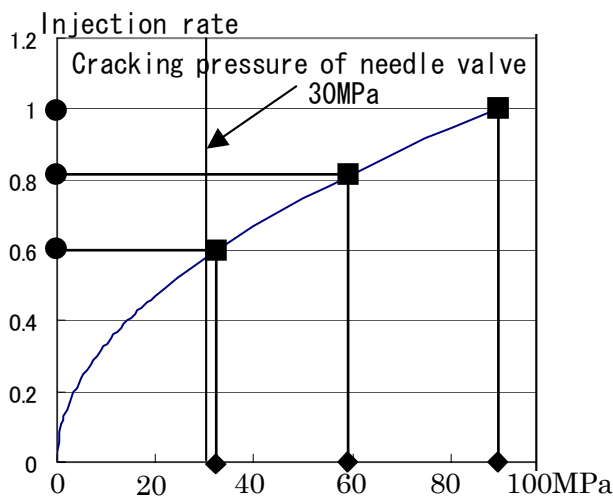


Figure 8 Fuel injection pressure and quantity

REGENERATING VALVE ACTUATORS

We continue the improvement on large scale of Diesel engines applying FST technology for not only their fuel oil pressure booster but also valve actuators.

The hydraulic circuit of the FST is shown in figure 9. Figure 10 is an electric circuit equivalent to the FST.

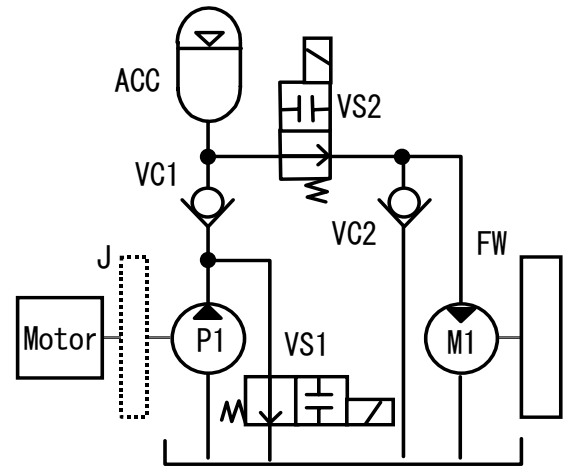


Figure 9. Schematics of the FST

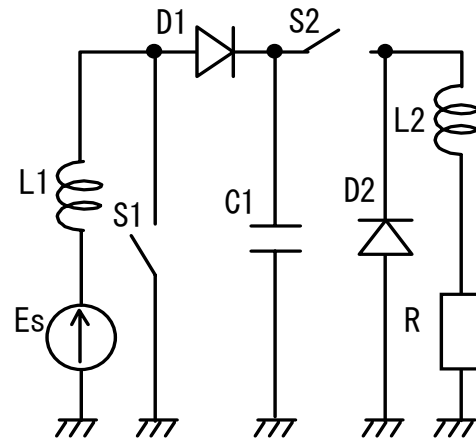


Figure 10 An equivalent circuit to the FST

The FST(Fluid Switching Transmission) is a newly proposed technology on hydraulic transmission.

The principle of FST is the hydraulic power switching technology equivalent to electric power switching control technology.

The principal movement is shown differential equation (4), and (5) is the equation of Figure 10, as a reference.

$$Qm-Qp-Id \omega/dt=0 \quad (4)$$

$$Es-EC1-L1di/dt=0 \quad (5)$$

On the electric switching power control, electric energy is stored in inductors converted to magnetic energy and on the next timing, return to electric energy alternately, synchronized with the electric current chopping.

On the hydraulic switching control, we have newly proposed, hydraulic energy is converted to kinetic energy in inertia like as by flywheels, and return to hydraulic energy on next timing as like as the process of electric power switching on electronic controllers.

So the FST makes converter of hydraulic pressure, and its efficiency for transmission is 100% on theoretically as same to the electric switching converters, and its capability of converting ratio to transfer is more than range of 30, in the area of high efficient operating.

Figure 11,12,13 show cross section hydraulic valve actuators.

Fig 11 shows conventional valve actuator that replaced mechanical push rod to the hydraulic push rod, Figure 12 shows electrically controlled exhaust valve actuator developed by marine engine sellers in Europe recently, and Figure 13 shows a model of valve actuators consist of newly developed FST power control technology.

The FST marine Diesel engines will save much deal of fuel consumption up to 4% of fuel consumption of trendy marine Diesel engines.

Figure 14 shows comparison of energy consumption on hydraulic valve actuator of traditional, trendy and FST.

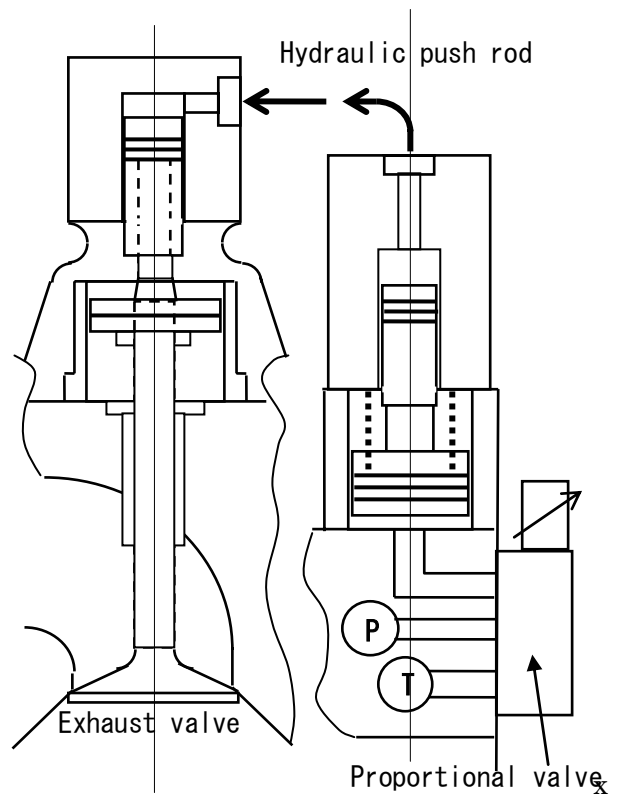


Figure 12 Controllable hydraulic valve system

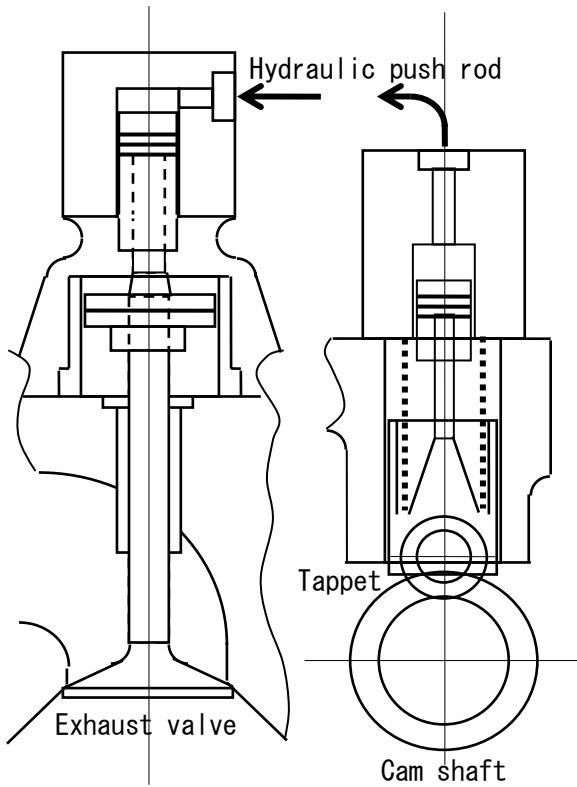


Figure 11 Conventional hydraulic valve system

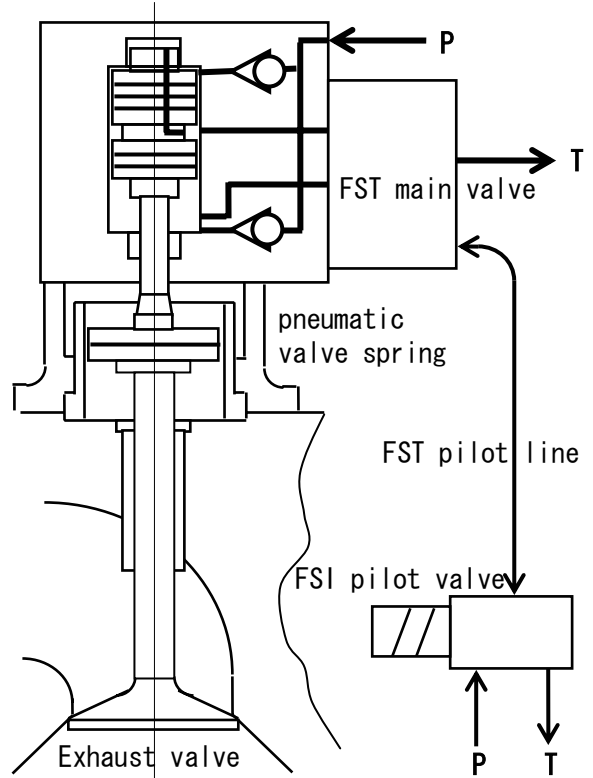


Figure 13 FST valve system

The FST valve actuator and trendy one which has a cam shaft and tappets, regenerates energy that is consumed on the way of opening valves. However the trendy engines regenerates no energy.

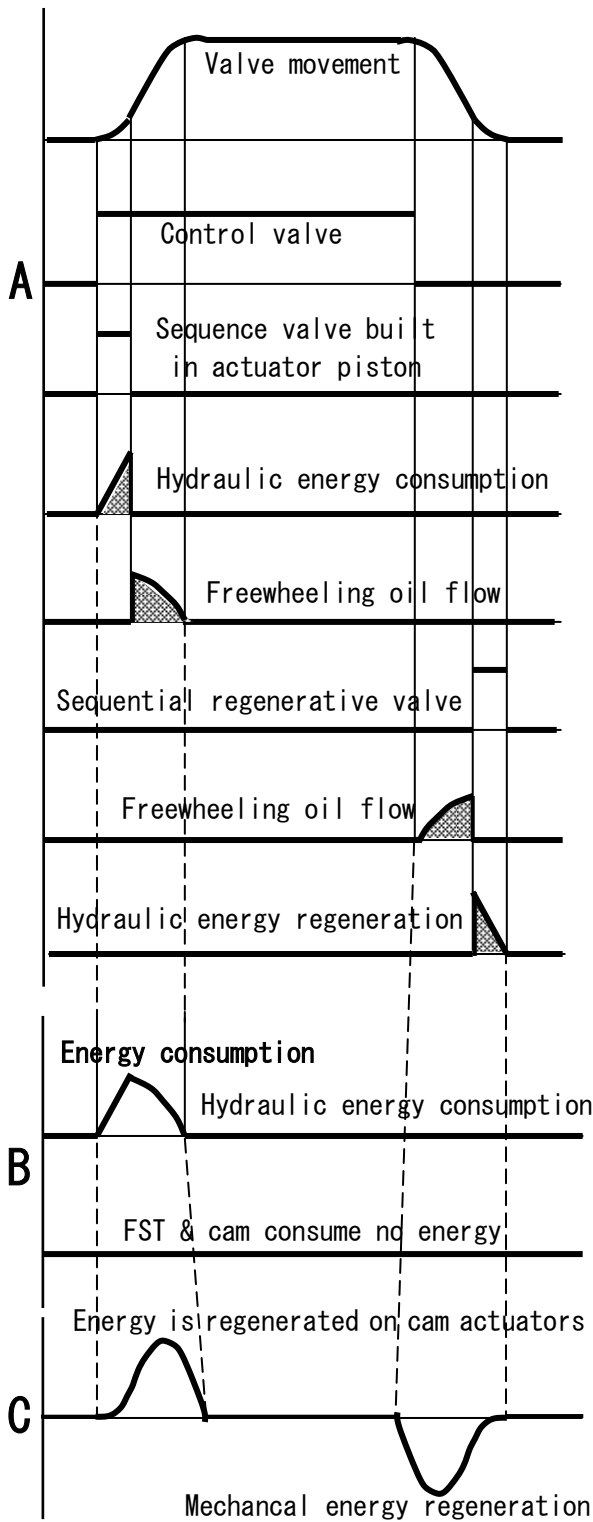


Figure 14 Valve movement and hydraulic flow

EXPERIMENT OF THE ENGINE APPLIED FST

Now, we are converting a conventional marine Diesel engine into the FST controlled one, in order to present the effect of FST on Diesel engines.

FST involves the concept of dynamics, on the rotary inertia in transmission, on the reciprocate machines FST makes most efficient hydraulic system.

The FST engine will complete in September 2005, and it will begin the test run. The full detail of the experiment is will be disclosed in near future.

We have chose 4-stroke cycle Diesel engine in this project in order to prove the performance of FST.

The difficulties applying to 4-stroke will be solved by the FST engine control system.

CONCLUSION

We proved that the FST is one of best way to keep the compatibility with emission and thermal efficiency of Diesel engine and other thermal engines.

The FST will make some compatibility with thermal efficiency and emissions for thermal engines on Reciprocate.

REFERECE

- (1)Itoh, Seki, Aoyama, Shimada and Suzuki, The new theory and technology on hydraulic transmission, JFPS Spring meeting 2002, p34-39, May 23 2002, Tokyo.
- (2) Seki and Itoh, An Examination of a LRV and its Transmission equipped onboard, p91-93The JFPS Spring meeting 2004, May 26, Tokyo.
- (3)Itoh,Seki, The equivalent Hydraulic Transmission with Electric Transmission, p94-96, The JFPS Spring meeting 2004, May 26, Tokyo.
- (4)Egeberg, Knudsen, Sorensen, The Electrically Controlled ME/ME-C series will lead the Two-stroke Diesel Engine Concept into the Future, paper No.: 82 CIMAC Congress 2004, Kyoto
- (5)Sakaguchi, Sugihara, Development of Electronically Controlled Engine "Mitsubishi UEC Eco-Engine" paper No.: 221, CIMAC Congress 2004, Kyoto.
- (6) Itoh, Trolley less vehicle and energy accumulator, Rolling Stock & Technology, No89, September 2002, Rail & Tech. Publishing Co.Ltd.,
- (7) Itoh, The proposal on hydraulic control technology, Hydraulic & Pneumatics, Vol.42 No.5, p49-55, 2003
- (8) Itoh, Switching control on the hydraulic power system, Hydraulic & Pneumatics, Vol.42 No.7, p55-60, 2003
- (9) Itoh, An application of shrouded flywheel, Hydraulic & Pneumatics, Vol.43 No.12, p4-10, Oct. 2004, Nippon kogyoshuppan.

Innovative solution for climbing and cleaning on smooth surfaces

Guido BELFORTE, Giuliana MATTIAZZO, and Roberto GRASSI

Department of Mechanics
Technical University “Politecnico di Torino”
Corso Duca degli Abruzzi 24-10129-Torino-Italy
E-mail: roberto.grassi@polito.it

ABSTRACT

A new generation of cleaning robots for domestic applications based on all-pneumatic technology is on study; the project deals with three main fields: motion, cleaning and drying. Referring to motion, an innovative design using pneumatic cylinders as structural elements is being tested; the implementation of a control made with digital valves permits to reduce costs, decrease setup times and leads to a unit which can be easily reconfigured for various applications. A recently developed series of vacuum cups allows the unit to stick itself on surfaces even if dirty or wet; innovative design and materials were studied to guarantee a firm grip in extreme conditions such as metal or glass covered by lubricating fluids. The structure used for motion system and the solutions for control the unit are shown. The cleaning system is based on pneumatic motor driving of rotating brushes with water injection between them. The drying system is based on fluidic concepts and driven by compressed air; studies about Coanda effect were carried on trying to extract water directly from wet surface without contact. Computational Fluid Dynamic simulations and experimental tests were carried on to validate the models; comparative analysis about performances and fluid consumption are here presented.

KEY WORDS

Cleaning, Climbing robot, Pneumatics, Vacuum cups , Window

INTRODUCTION

The study and production of robots for domestic application is a relatively recent research field. This kind of robot is actually in continuous development. Huge surface cleaning, and even glass windows or building walls is on study in industrial fields with very different characteristics and innovations. The robot presented in this paper, developed at Politecnico di Torino, deals with a field of application not yet studied:

small sized windows cleaning in domestic environment. Such a prototype must present some particular aspect that deal with indoor applications; first of all low cost and limited complexity. For that reason the robot was built with the only degrees of freedom really essential and with pneumatic technology. Moreover a cleaning unit must have the smallest interference with the workspace; then recovering of washing fluid is essential. The most important study of this prototype is about an innovative drying unit capable to collect detergent and

avoid spoilt. The unit uses compressed air. By means of Coanda effect it generates an air stream on a curved surface close to the window; washing fluid is then extracted directly from the glass and conveyed for further recycling.

STATE OF THE ART IN VERTICAL SURFACE CLEANING

A huge amount of robot is used to transport tools and operate in remote areas [8] [9]. The state of the art in windows cleaning consists mainly in applications over huge surfaces [4] [5] [10].

An innovative robot, developed for cleaning vertical walls and smooth surfaces in general, comes from Institute for Problem in Mechanics of Russian Science Academy [1] ; it consists in a transportation system on which can be mounted several technological modules. The transporter is a round shaped carter with a wheeled platform inside; by mean of electric motors the wheels allow it to move in all directions. The main body is similar to a turtle and an electric fan provide vacuum inside of it; along the perimeter, a gasket permits to hold inner pressure preventing air (vacuum) losses and to slip on the surface reducing friction. Washing fluid is injected near the cleaning unit from a nozzle connected to a pump.

The Institute for Material Sciences, university of Hannover and Schmalz, a German company, had developed a small robot called Hydra [2] that can climb on vertical surfaces; so it may be useful for cleaning applications. Four suction cups allows the unit to stick on the surface; the motion is demanded to pneumatic actuators with polymer made pneumatic cylinders. Hydra can overcome obstacles less than 40 mm height; cleaning modules can be connected to the main body.

Another interesting solution is Oktoput, developed to clean huge glass surfaces onboard cruise ships; it is made of two structures, relatively translating, and can travel in all directions. Its mass is approx 140 kg and its length is about 1 m; the main power source is electric, carried by a 220 V cable. It can move at an average speed of 1 m/min carrying an efficient cleaning unit based on rotating brushes; the grip is assured by eight suction cups of approx 30 cm diameter each.

The robot developed at the Technical University of Turin is based, as the others, on vacuum cups, but its main characteristics are an extremely simple motion system and an innovative cleaning unit; it can recycle the cleaning fluid with a vacuum recovery unit based on Coanda Effect.

STRUCTURE OF THE ROBOT

The robot workspace will be a window, so in order to define an example of structure it was simplified as a

vertical, rectangular shaped, surface approx 1 by 1.5 meters wide; the unit will have to describe the whole space during operation following a defined path. The active degrees of freedom are limited to two, moreover a self aligning system keeps the robot in vertical position; so the motion system allows the robot to climb vertically and translate side by side. Then the self alignment equipment provides a further passive degree of freedom. The cleaning operation does not require particular displacement precision, so a step motion can give enough mobility combined with a simple structure and control; for these reason a Cartesian structure with pneumatic linear actuators was designed. In figure 1 the kinematics is shown: by extending and retracting legs the robot is able to move in both directions step by step.

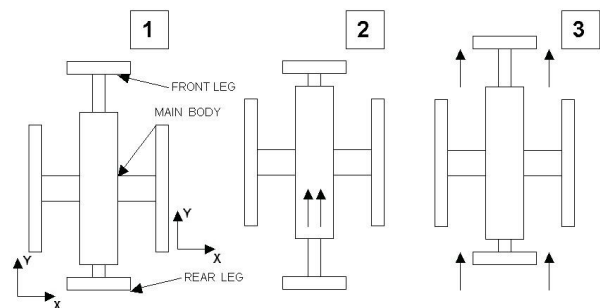


Figure 1: Motion sequence for Y direction , alternative translation of body and legs allows climbing

The march direction need to be held parallel to the external structure of the window so the easier solution is to suspend the robot like a pendulum: by rotating the body around the upper cylinder it is able to gain a vertical displacement even if it is hanged to the surface in a wrong way. The first group of vacuum cups is mounted on an I shaped frame with an hollow arc of circle, shown in figure 2, that acts as a circular guide; it permits relative rotation between frame and robot body of approx 10 degrees.

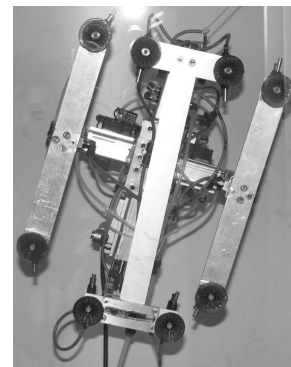


Figure 2: The robot on a Plexiglas window, rear view that shows the self alignment in action.

The main body consists in four pneumatic cylinders, mounted at a 90 degrees angle, that allows horizontal X and vertical Y motion; the four cylinders are integrated on a central rectangular shaped structure in aluminum. In that way, by using cylinders as structural elements, this compact very light structure can be used to mount cleaning elements or water nozzles; pneumatic actuation allow to fully integrate motors (cylinders) in the whole system in a perfect synergy between actuation and structural elements. Moreover pneumatics guarantee a good reliability with relatively less maintenance and is very cheap; for these reason it was chosen as the best technology for the application. The motion unit can be completed with different implements, so the available fields of operation are extended to all the situations in which transportation of tools might be required; for this goal the structure presents free spaces in the whole body and a maxim payload of approx 50% of total mass.

In figure 3 the whole robot is shown during a test on a plastic surface. The side legs are visible during extension; on every suction cup there is a pneumatic ejector that generates vacuum.

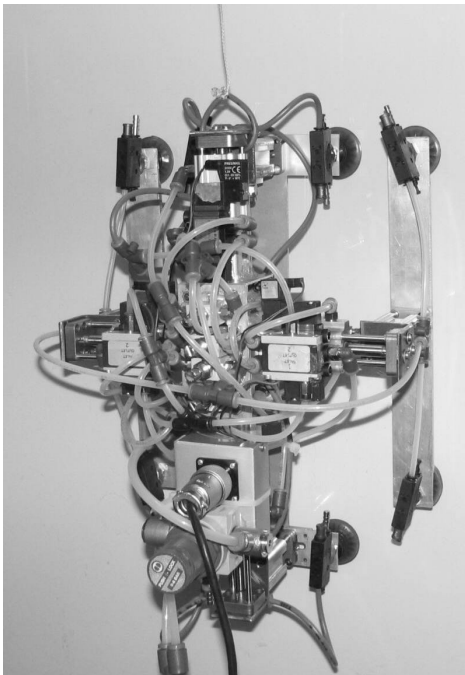


Figure 3: The motion system during a test on a vertical plastic surface.

In order to move the robot along a vertical glass surface, the grip must be firmly and safely assured. Variable forces tend to disengage the unit: as robot mass, that is approx 3 kg; payload due to tools and supply cables; external reaction forces due to particular working. The grip unit consists in eight suction cups.

To assure a correct engage, a wide range of suction cups

was analyzed in order to find the best solution. The working environment is the main factor that influences suction cup material: the cup will be working in an extremely wet condition, water and detergent fluid will affect grip performances and weariness resistance. An eventual slip may cause vacuum losses and the whole grip system might become ineffective. The most suitable cup for our application is made in polyurethane with oversized gasket and a diameter of 35 mm. These particular cups do not leave impressions even on extremely smooth surfaces, so during operation the robot will not leave any sign.

COANDA EFFECT DRYER

The robot was designed to wash and clean glass surfaces, so it must be able to leave the surface clean and dry; moreover the indoor application requires less interactions with the environment. Using brushes and water may cause spoilt of fluid and such event does not happen; for this goal a system able to collect all used water and eventually recycle it was studied. The application of Coanda effect leads to a unit based on a surface, like an aircraft wing, on which an high speed air stream can stick and therefore be driven in a given direction; [7] the air stream, running close to the glass surface, extract water directly and launches it in a direction expected to be perpendicular. Due to the robot structure it can move on the surface in two direction, so the dryer must be able to operate according to the motion; in order to keep the surface clean the drying system will be designed as a rectangular line around the main body. Every side of this rectangle is made of a single drying element; in that way the correct drying in every direction is granted.

In order to design the unit a numerical analysis was carried on. Given its workspace, the dryer is assumed to be a wing shaped element; so a circular hollow body was designed, with a line shaped outlet that permits to drive air from inside to the external surface.

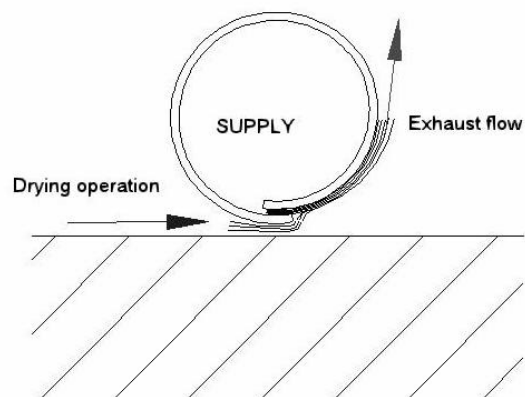


Figure 4: Section of the first prototype.

After having defined a profile section, the volume to be studied is obtained from. Given the solid geometry the mesh is constructed with particular care; therefore the simulation has been carried out in three dimensions, since some 2D tests, limited to the profile section have given poor results. The volume object of simulation spreads around the unit. The program simulates fluid behavior in a cylinder 25 mm diameter around the tube; beyond this distance the effects due to the wall are negligible. In figure 5 the section geometry with linear dimensions is shown.

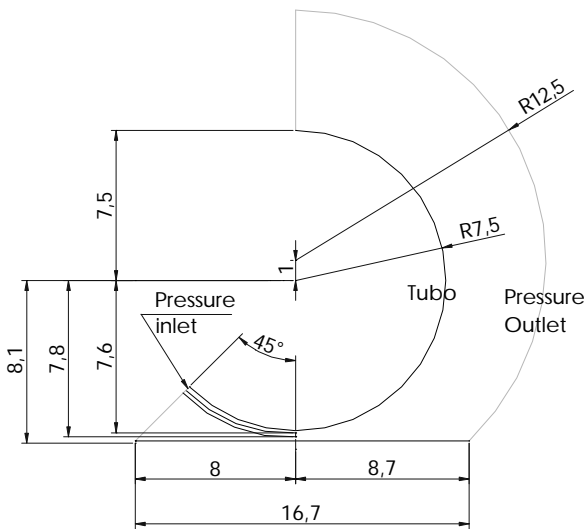


Figure 5: Geometry of the model.

The section, named Pressure Inlet is the system input. The program sets up the pressure in these points as a contour condition; that will be called supply pressure. The mass flow in that particular section will be called supply air flow and is the effective fluid consumption of the object. The section has subsequently been extruded to obtain a profile of 35 mm length. In order to better evaluate sensitive areas, such as the external curved surface, the mesh has a variable size and is more accurate near the surface. Proceeding that way may be useful in every area in which velocity gradient is supposed to be higher; so the calculation is more accurate only where required and in less important areas the separation is wider. The picture of figure 6 shows a trace of the mesh; in the lowest part there is a line that in solid model represents a wall. To be noticed a more accurate grid between wall and dryer, in that way the interaction between dryer and glass surface will be analyzed with particular care to the distance.

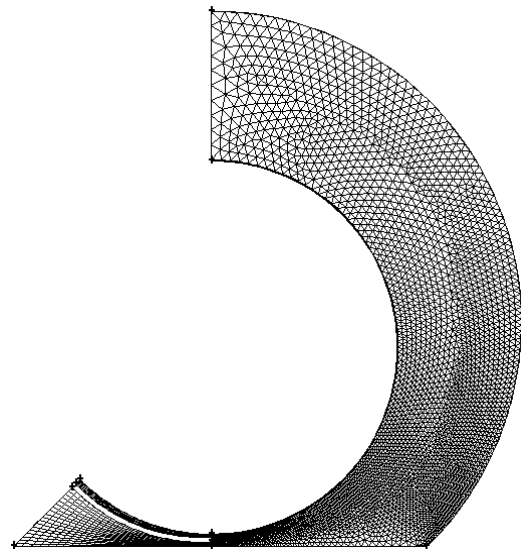


Figure 6: Variable sized mesh.

This model was simulated with pressure supply levels between 0.1 and 0.8 bar; increasing the pressure a first evaluation of air speed is obtained. From these results it is clear that with supply pressure above 0.4 bar the flow has a great Reynolds number and becomes turbulent. In that case the viscous model K-epsilon is used. The results can be represented by graphics. For example air velocity may be represented in a 2D graphic along a section, as shown in figure 7: in that case the pressure supply is set to 0.4 bar and the mass flow rate is about 220 g/min.

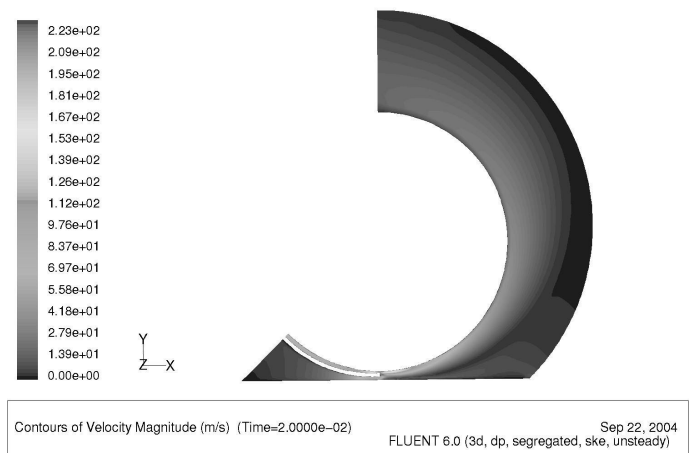


Fig.7 : 2D velocity magnitude plot at supply pressure of 0.4 bar.

From the figure it can be noticed that in the area next to the wall the velocity presents a maximum; so in these area the airflow is effectively stuck on the surface according to Coanda's theory. Moreover downside of the supply area, between glass surface and the lowest part of the dryer, the flow is particularly intense with an airspeed of 90 m/s. This is the most interesting aspect because in this area the water extraction effect is generated. After having analyzed the obtained results it was possible to define a useful profile. A good combination between tube diameter and inlet thickness was defined in order to guarantee an high airspeed.

The theoretical profile was subsequently realized and a first prototype was obtained for experimental tests. In order to validate the model the supply air consumption was evaluated, this is an important characteristic that deals with energy requirements of the system. For this proposal a series of simulations was conducted with variable levels of supply pressure and theoretical data about air consumption were obtained. The air consumption of the prototype is evaluated by giving it a defined supply pressure, then measuring the mass flow rate with a ROTA flow meter at different level of pressure. In figure 8 experimental data of air consumption, in g/min, are compared with simulation.

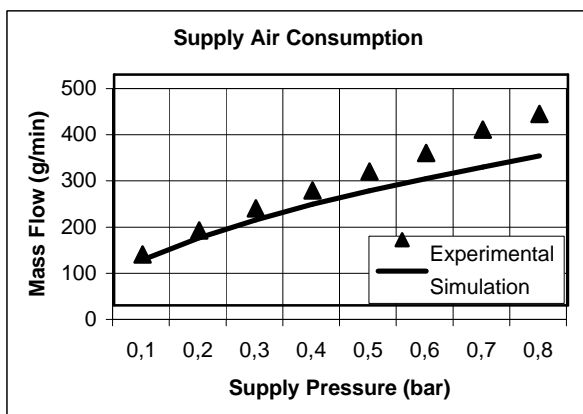


Fig.8 : Air consumption vs supply pressure, experimental data compared with simulation

As noticeable from the figure, experimental data are slightly higher than simulated. The difference between these data increases with supply pressure. This effect is probably caused by the enlargement of inlet section; it is due to the strain of the tube subjected to pressure.

The prototype was subsequently integrated onboard and preliminary evaluation tests were conducted.

The first results are encouraging; the robot climbs on an extremely wet surface and the drying unit extract water leaving glass properly clean and dry.

CONCLUSIONS

A prototype of a working robot was designed and tested. A Coanda dryer was produced with satisfactory results. Further activities will be carried on to improve the drying capability. In particular a deeper analysis of this application of Coanda effect is required, regarding the geometry, with the goal of reducing supply air consumption maintaining the drying skills.

REFERENCES

1. V. Gradetsky, M. Rachkov, S. Kalinichenko, E. Semenov : Service robot for cleaning vertical surfaces. IARP Workshop, Genova, October, 1997, pp. 120-126.
2. Un Robot "Scalatore" Rivista di Meccanica N° 1074 Maggio 1995, p.80de
3. Nishi A. : Development of Wall-climbing Robots, Computers Elect. Enginering Volume 22, pp. 123-149, 1996
4. Elkmann N., Felsch T., Sack M., Horting J.: Innovative service Robot for façade cleaning of Difficult-to-Access areas, Proc. 2002 IEEE/RSJ International Conference on Intelligent Robots and Systems
5. Schraft R.D., Simons F.: Facade and window climbing robots for cleaning and inspection, CLAWAR Newsletter, Issue 11 November 2003 pp. 12-16
6. Carpenter P. W., Green P.N.: The aero acoustic and aerodynamics of High-speed Coanda devices, part 1: conventional arrangement of exit nozzle and surface, Journal of Sound And Vibration (1997), pp. 777-801
7. www.jetfan.com
8. S.Yokota, H. Kobayashi, K. Kabawata: Development of a mobile system using leg-type crawlers for rough terrains, CLAWAR Newsletter 2002 p. 899.
9. M.Armada, P.Gonzales de Santo, M.Prieto : Climbing and walking robot for the petrolchemical industry and for underwater applications, CLAWAR Newsletter 2002 p. 939.
10. O.Derriche, K.Kouiss : A cleaning robot for spherical buildings, CLAWAR Newsletter 2002 p. 993

DEVELOPMENT OF A SENSOR-LESS ELECTRO-HYDRAULIC VALVE ACTUATOR FOR A CAM-LESS ENGINE

Hirohisa TANAKA*, **Nozomi TOYODA***

Department of Mechanical Engineering, Faculty of Engineering
Yokohama National University
Tokiwadai, Hodogaya, Yokohama, 240-8501, Japan

ABSTRACT

A fully electronically controllable valve-actuator has potentials of improving volumetric efficiency at gas exchange, and of presenting variable compression-ratio. This paper describes a new type of hydro-mechanical position-servo electro-hydraulic valve actuator for a cam-less engine. The piston is positioned hydro mechanical feedback mechanism, which balances the flow rate of the feedback slot to the pilot valve. The feedback-slot opens its area in proportion to the piston displacement. This mechanism succeeds to decelerate the landing-velocity of 0.2m/s at a working speed of 1.0m/s for valve lift of 12mm, and to actuate the valve at a volumetric efficiency of 95% within lag times of opening 18ms and closing 8ms, that is possible to work at an equivalent engine rotational speed of 2100rpm. The actuator is energized by the hydraulic power source of flow-rate of 6.7L/min and pressure of 14MPa.

KEYWORDS

Engine-valve actuator, Hydro-mechanical servo piston, Landing-velocity control, Switching valve

INTRODUCTION

A fully electronically controllable valve-actuator has a potential not to improve volumetric efficiency of intake or exhaust gas exchange, but to present variable compression ratio. An electro-hydraulic actuator⁽¹⁾ has a feature of high force density but motion speed is usually not so quick at a limited power compared to an electro-magnetic actuator⁽²⁾. This paper describes a new trial of a hydro-mechanical position servo actuator that improves speed and efficiency for a 2800rpm cam less engine. The actuator positions the valve without any electronic position sensor by using a new type of hydraulic piston with feedback slot, and this makes it possible to reduce the landing velocity. This type of actuator falls into unstable at a design of too small under lap of the feedback slot and high-pressure operation. The stability is

examined by linear theory first, and more detail design parameters are fixed by using bond graphs analysis. It clarifies power waste and landing speed simultaneously by simple expression. The prototype is designed to actuate a valve of 430g mass, 12mm in displacement within delay of 18ms, and to close the valve within the landing velocity of 0.2m/s at a control pressure of 14MPa.

HYDRO-MECHANICAL POSITION CONTROL ACTUATOR

A schematic view of the pilot operated hydraulic piston with feedback slot is shown in Fig.1. The sectional area of the upper chamber is smaller than the pilot one, and it closes the valve stationary by high-pressure fluid through the slot. The piston opens when the pressure in the pilot chamber is reduced by opening the pilot valve. The flow rate from the

pilot valve and the feedback slot should be balanced, and then the piston is stopped at a settled pilot valve opening because the slot is designed to have a opening area in proportion to the piston displacement.

LANDING VELOCITY CONTROL

Linear analysis is important for over viewing the dynamics of the actuator. The piston motion is expressed by

$$m \frac{d^2x}{dt^2} + b \frac{dx}{dt} + k_s x = A_s P_s - A_c P_c - F_d \quad (1)$$

where m , b and k_s are equivalent mass, damping coefficient and spring constant, A_s and A_c are cross sectional areas of piston, and P_s and P_c are constant supply pressure and control pressure in the pilot chamber.

The continuity of fluid flow in the pilot chamber including fluid compressibility is expressed by

$$Q_c - Q_p + A_c \frac{dx}{dt} = \frac{V_c}{K} \frac{dP_c}{dt} \quad (2)$$

where the pilot flow rate Q_p is expressed by

$$Q_p = C_{dp} A_p \sqrt{\frac{2}{\rho} P_c} \quad (3)$$

Flow rate from the feedback slot Q_c by

$$Q_c = C_{dc} S_x \sqrt{\frac{2}{\rho} (P_s - P_c)} \quad (4)$$

where the opening area of the feedback slot S_x is given by

$$S_x = a_x W_c (x + x_l) \cos \theta. \quad (4)$$

W_c is the width of the feedback-slot and a_x is the area gain expressed by depth against stroke, θ is slope angle of slot, and x_l is under lap of opening slot at valve closure.

Linearized flow characteristics of pilot valve in Eq.(3) and slot (4) are expressed by

$$Q_p = k_{qp} x_p + k_{cp} P_c \quad (5)$$

$$Q_c = k_{qc} x - k_{cc} P_c \quad (6)$$

where k_{qp}, k_{qc} are flow gains, and k_{cp}, k_{cc} are pressure–flow coefficients. The linearized flow continuity is

$$k_{qc} x - k_{cc} P_c - k_{qp} x_p - k_{cp} P_c + A_c \frac{dx}{dt} = \frac{V_c}{K} \frac{dP_c}{dt} \quad (7)$$

Laplace transformed formula of valve motion and flow

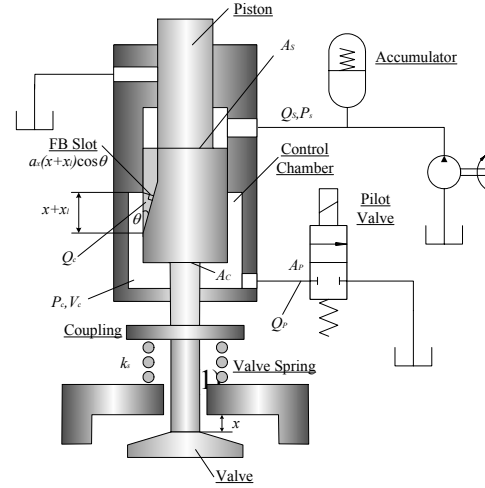


Fig.1 Schematic view of the sensor-less valve actuator with a hydro-mechanical feedback slot

continuity are expressed by

$$\left(k_{cc} + k_{cp} + \frac{V_c}{K} s \right) P_c = (k_{qc} + A_c s) x - k_{qp} x_p \quad (8)$$

$$(m s^2 + b s + k_s) x = -A_c P_c - F_d. \quad (9)$$

The block diagram of the valve actuator is described in **Fig.2**, where parameters are expressed as follows.

$$k_{ce} = k_{cc} + k_{cp}, \quad \omega_s = \sqrt{\frac{k_s}{m}}, \quad \zeta_s = \frac{b}{2\sqrt{mk_s}} \quad (10)$$

The stability limit of this mechanism is expressed by using Hurwitz criteria.

$$4\zeta_s^2 + \frac{2\zeta_s \{ \alpha + \omega_s^2 T_v (T_c + \alpha T_v) \}}{\alpha \omega_s T_v} + \frac{1}{\alpha} \left(\frac{T_c}{T_v} - 1 \right) > 0 \quad (12)$$

where $\alpha = k_s k_{ce} / (k_{qc} A_c)$, $T_v = V_c / (K k_{ce})$ and $T_c = A_c / k_{qc}$

Evaluating the stability of Eq.12, we can get $T_v = 1.31 \times 10^{-9}$ (s), $T_c = 5.56 \times 10^{-3}$ (s) and $T_c / T_v > 1$, so that the Eq.12 is always realized.

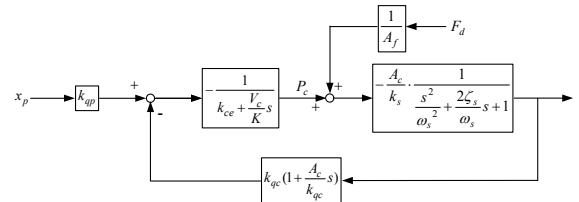


Fig.2 Block diagram of the electro-hydraulic valve actuator

BOND GRAPHS ANALYSIS AND EXPERIMENT

Valve landing-velocity and power waste are examined by using bond graph analysis in this section.

Bond graphs of the actuator A single bond expresses two physical meanings of flow and effort that denote a combination of velocity and force in mechanical elements, or flow-rate and pressure in hydraulic elements. **Figure 3** expresses the bond graph of the actuator. The discharge flow SF (Q_s) from a pump is regulated by a relief valve R (resistance) through the hydraulic accumulator C (capacitance), and pressurized fluid is flown into the pilot valve R through the feedback slot R . The opening area of the feedback-slot R is expressed by a linear function of the actuator displacement in the mechanical spring C (k_s).

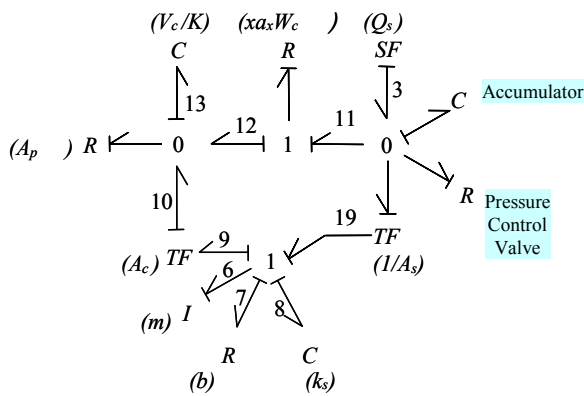


Fig.3 Bond graphs of the electro-hydraulic valve actuator operated by a switching pilot valve

Effect of mass on the response and landing speed **Figure 4** simulates the effect of mass on the response and landing velocities at a limited design of flow rate 6.7L/min and pressure 14MPa. We can see that the opening delay is a shortly improved by using lighter mass of 200g from 430g. **Figure 5** shows also a simulated result of the velocity and flow-rate for positioning the 430g-actuator. The actuator is decelerated within 0.2m/s at landing.

Comparison of bond graphs analysis and measurement

Figure 6 shows a comparison of bond graphs analysis and measurement of the step response x of the 430g-actuator. The high speed switching pilot valve is operated within lag time of 0.8ms by using an electric quick driver⁽³⁾. The actual landing of the actuator is decelerated strongly at $x = -0.5\text{mm}$

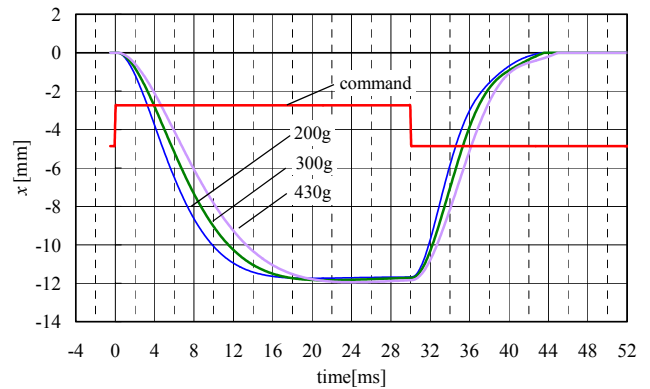
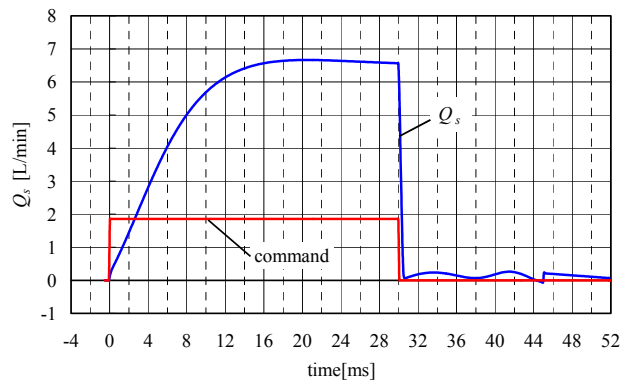
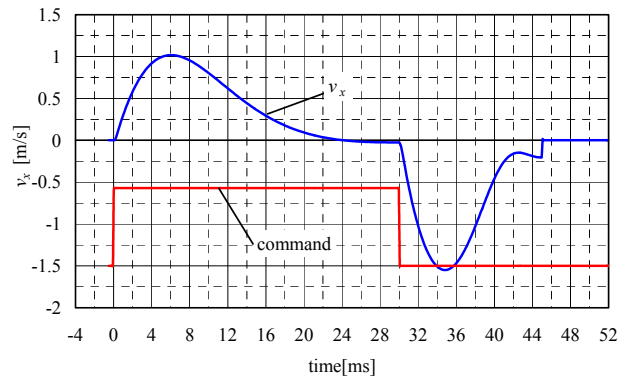


Fig.4 Effect of mass on the step response of the valve actuator by Bond Graphs Analysis at $P_s = 14\text{MPa}$



(a) Flow rate from the inlet port



(b) Valve landing velocity

Fig.5 Flow rate (a) and valve landing velocity (b) by Bond Graphs Analysis at $P_s = 14\text{MPa}$

that will be caused by the reduction of the discharge coefficient of the feedback slot at a high pressure control. **Figure 7** is a calculated example of using the reduced discharge coefficient from 0.7 to 0.2 at $x = -0.5\text{mm}$.

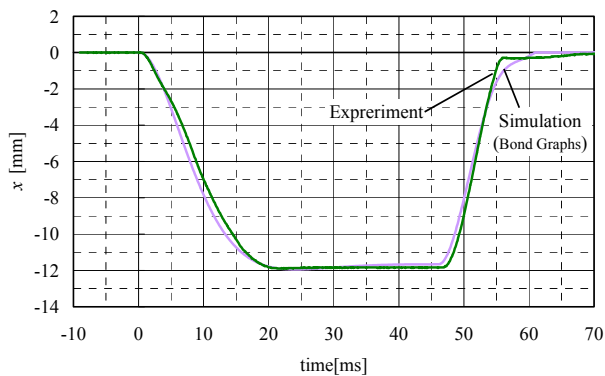


Fig.6 Comparison of the measurement and Bond Graphs Analysis of the valve motion at $P_s=14\text{MPa}$.

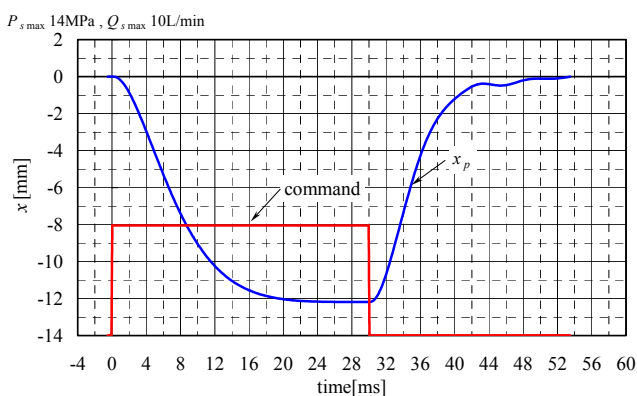


Fig.7 The strong deceleration of the landing velocity at $x=-0.5\text{mm}$ is explained by the reduction of the flow coefficient of the feedback slot from 0.7 to 0.2 in the bond graphs analysis.

Displacement control by pressure The valve lift is influenced by the supply pressure due to the valve spring. The spring is used to close the valve at normal condition. **Figure 8** shows experimental results of the effect of the supply pressure on the lift. The lift changes from 6.8mm at 10MPa to 12mm at 14MPa linearly. This means that the lift is also controllable by the pressure besides the pilot valve opening..

Response speed measurement **Figure 9** shows measurement of frequency response of the actuator at the fixed valve opening crank angle of 120 degrees. The frequencies of 6, 12 and 18 Hz are equivalent to engine rotational speeds of 700, 1400 and 2100 rpm. The valve actuator opens 12mm in stroke and closes at a regulated landing speed. The actuator is difficult to work over the engine rotational-speed of 2800 rpm at a limited hydraulic

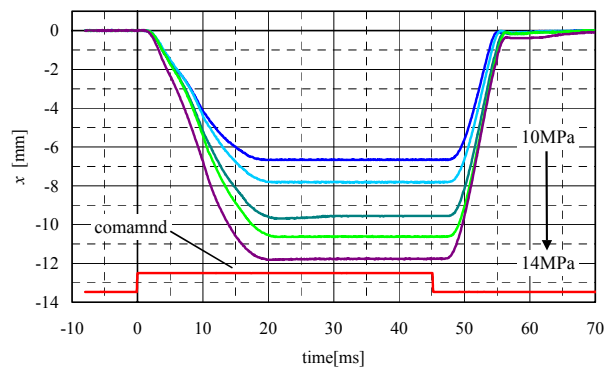


Fig.8 Measurements of the effect of the supply pressure on the valve lift

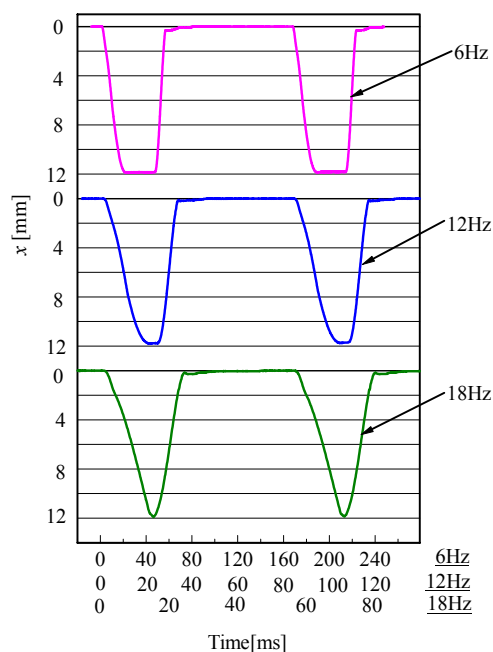


Fig 9 Measurement of step responses at three cyclic frequencies (We can see that all of the landing velocities are decelerated. Frequencies correspond to the engine rotational speeds of 700, 1400 and 2100rpm.)

power, however using high power-source in addition to larger pilot valve will solve this limit.

Landing velocity control by two pulse command The landing velocity is also controlled by using two-pulse command for strong deceleration. The pilot valve is opened again in a short time before landing as shown in **Fig.10**. We can see that the landing velocity becomes under 0.1mm/s.

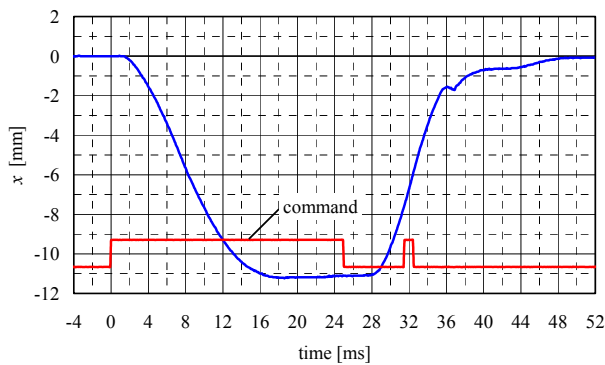


Fig.10 Measurement of the landing velocity deceleration by the two-pulse control

Figure 11 shows a quick response test result by using 2 switching valves per piston, which makes it possible to work the engine at a maximum rotational speed of 2400rpm

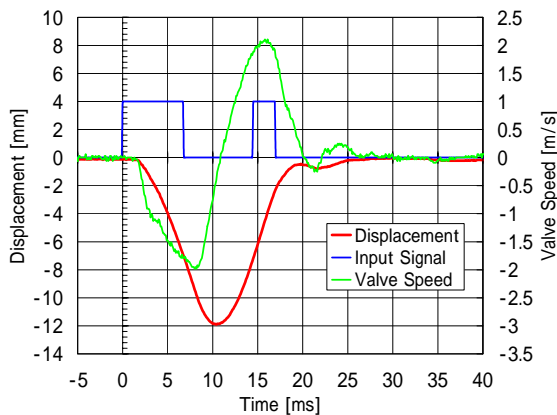


Fig.11 Quick response test by using 2 switching valves per piston for working the engine at a maximum rotational speed of 2400rpm

MESUREMENT OF VOLUMETRIC EFFICIENCY OF THE ACTUATOR

This actuator is controlled by a half-bridge hydraulic-circuit for saving the hydraulic power-waste. The loss is caused only by the piston leakage, which is measured as shown in **Fig.12**. The volumetric efficiency is given by the volume of leakage against that of one stroke of the piston

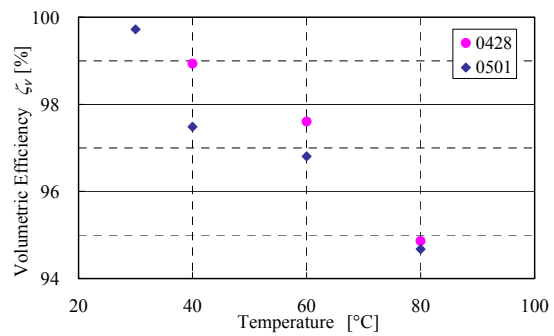


Fig.12 Measurement of volumetric efficiency of hydraulic valve actuator

CONCLUSION

A newly designed hydro-mechanical position-servo electro-hydraulic valve actuator for a cam-less engine is proposed. The piston is positioned by balancing the flow rate of the feedback slot and the pilot valve. The feedback slot is designed to be open the area in proportion to the piston displacement. This mechanism succeeds to decelerate the landing velocity of 0.2m/s at a working speed of 1.0m/s for valve lift of 12mm by the single pulse control, and to actuate the valve at a volumetric efficiency of 95% at lag times of opening 18ms and closing 8ms, that is possible to work at an equivalent engine rotational speed of 2100rpm. The actuator is energized by the hydraulic power source of flow-rate of 6.7L/min and pressure of 14MPa. A pair of intake- and exhaust-valve actuators is shown in Photo.1, and their outlook of mounting on a 6-cylinder 12L displacement engine. head in Photo 2..

ACKNOWLEDGEMENT

The authors would like to thank Dr. T.Urai for making the valve actuator.

REFERENCE

- (1) R. Uhlenbrock, J. Melbert and G. Lugert, "Smart Actuator for Sensor less Electromagnetic Variable Valve Actuation", SAE, ATTCE2001, Vol.5, Barcelona, No.2001-01-3278, p.85-90, 2001.
- (2) J. Aaltonen and M. Vilenius, "Electro hydraulic System for High Speed Gas Exchange Valve Actuation", 5th JFPS International Symposium at Nara, p.775-780, 2002.

(3) Y.Sato and H.Tanaka, "Effect of Eddy Current on the Switching Speed of a High Speed Switching Valve", Trans. of JHPS, Vol.24, 4, p.104-110, 1992 (in Japanese).



Photo.1 Electro-hydraulic valve actuator for gas exchange valve operated by high speed switching valves



Photo 2 Valve actuators mounted on a 12L engine head

The Inertia Simulation System Based on Hydrostatic Secondary Control

Jiao Zongxia, Shen Dongkai, Wang Xiaodong and Wang Shaoping

No.303 School of Automation Science and Technology
Beijing University of Aeronautics and Astronautics, Beijing 100083. P. R. China
E-mail: zxjiao@vip.sina.com

ABSTRACT

In the study on the braking system, the inertia simulator is necessary, which is generally realized by inertia plate. Its advantage is simple and accurate, whereas the disadvantage is the larger volume and difficult to be adjusted. This paper presents a novel scheme, which is realized by hydrostatic secondary control circuit. The inertia can be increased and decreased by electro-hydraulic servo control through momentum feedback, in which a dual variable servo pump is adopted, with the velocity and torque feedback loops applied. In the beginning, it is set as speed control mode until it reaches the braking speed. Meanwhile, it turns to the state of inertia simulator, which is the torque control mode, so as to keep the inertia as set value.

The function of inertia simulation system based on hydrostatic secondary control is to simulate the momentum, which is realized by momentum feedback control, and it can be calculated through accelerator and desired inertia. The variable pump is driven by constant pressure network, and the variable swashplate is controlled through servo valve. The torque feedback and speed feedback guarantee the control performance requirements. Since there are some problems of nonlinearity, instability, strength friction, etc. a hybrid fuzzy control method are adopted to get higher dynamic control precise and steady characteristics. It is concluded that the scheme and control method is available and validity.

KEYWORDS

Inertia Simulator; Hydrostatic Secondary Control

NOMENCLATURE

- J^* : simulated inertia;
- θ_L : angle of load;
- K_D : radian displacement coefficient;
- K_P : system pressure;
- J_m : secondary unit inertia;
- J_L : inertia of load;
- K_F : torque sensor coefficient;
- B_m : secondary unit damping constant;
- G_m : torque sensor elastic ratio;
- $\dot{\phi}$: Swash speed;
- T : torque;
- θ_m : angle of secondary unit

INTRODUCTION

By now, Antiskid Brake System (ABS) has been widely used in aeronautics, automobile and other fields. During the research and development, it is necessary to implement the braking tests in order to get optimal performance and designation parameters [5].

The inertia simulation device is needed in the test, which is used to simulate the real mass of the aircraft or automobile so as to obtain the inertia of tested system [4]. Conventionally, equivalent inertia plate is adopted, which is simple and accurate while the volume is large. So it is difficult to adjust the inertia smoothly in any direction according to the actual requirement.

Using hydrostatic secondary control circuit, the inertia can be increased and decreased smoothly by

electro-hydraulic servo control through momentum feedback, in which a dual variable servo pump is adopted, with the velocity and torque feedback loops applied. In the beginning, it is set as speed control mode until it reaches the braking speed. Meanwhile, it turns to the state of inertia simulator, which is the torque control mode, so as to keep the inertia as set value.

Secondary control is defined as the regulation of secondary component in constant pressure network. In the application, the system pressure is not always absolutely constant, considering the dynamic characteristics of oil source, pressure storage device and the disturbance of other factors to oil source. Hydrostatic secondary control system can work in four quadrants, that is, it can work in pump condition as well as motor condition. The energy losing is little and it can be recycled, besides, it is not sensitive to load variation.

Domestically or aboard, closed loop speed regulation is usually carried out by secondary control, and this is the speed control mode of inertia simulation. Now, some torque servo system based on this theory appears, such as load simulator[1, 2], and its maximal advantage is no extraneous torque, which means that it is not sensitive to load variation. Therefore, during braking test, there is little disturbance to output torque for braking pressure change.

SYSTEM ANALYSIS

The function of inertia simulation system based on hydrostatic secondary control is to simulate the momentum, which is realized by momentum feedback control, and it can be calculated through accelerator and desired inertia. The inertia simulation system is shown in Fig.1. Secondary control inertia simulation a kind of electro-hydraulic torque servo control system, in which the output torque is adjusted by the regulation of the swashplate angle in constant pressure network. In Fig.1, the inertia plate is used to simulate the road surface, and driven by secondary component output shaft. The two systems interfere with each other.

In order to work on the state of torque and velocity

feedback, the torque sensor and velocity sensor are mounted on the pump output shaft with a connected small inertia plate against braking disc, which is of mid value of the inertial simulated. Output torque and swashplate angle are fed to control computer by A/D, and the control computer controls the servo valve and actuator by given control law, so as to control the torque. In the testing system, the computer still to gather the

velocities of inertia plate and tyre wheel simultaneously in order to simulate the ABS under real condition. Pressure sensor is mounted for the sake of the variation observation of system pressure. Oil system's constant pressure must be regarded to guarantee the dynamic performance of system, so the fixed quantity pump and overflow valve system of wide frequency is adopted.

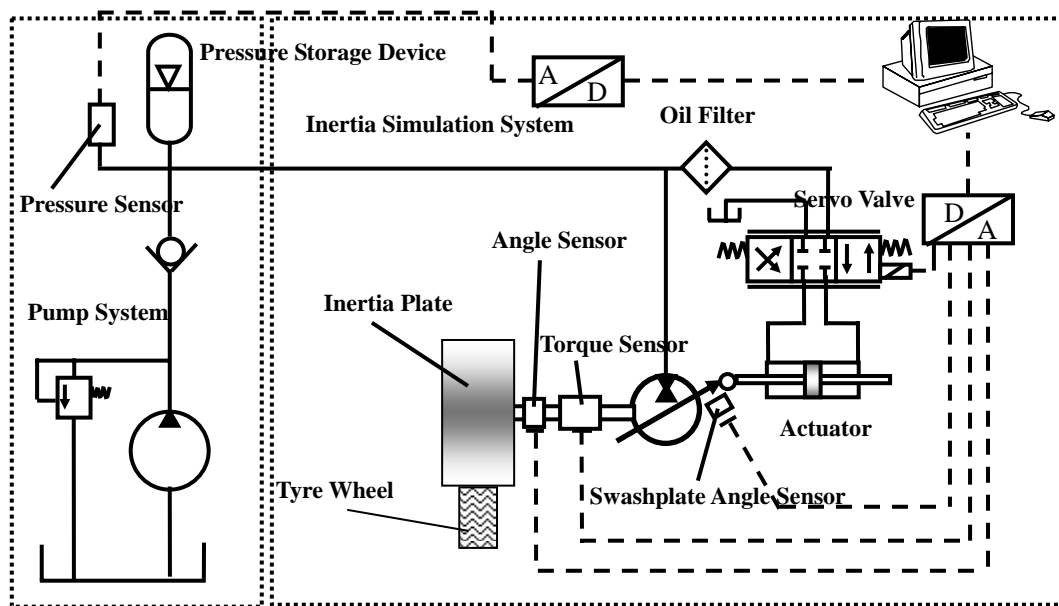


Fig.1. Diagram of Inertia Simulation System Based on Secondary Control

CONTROLLER DESIGNATION

The inertia simulator based on secondary control is not a complicated multi-variables coupling system, but there are certain nonlinearity and time varying characteristics in it. For instance, inertia simulation based acceleration signal of system presence delay, causing fluctuation of inertia torque, influencing system dynamic performance; the servo valve flux is the nonlinear function of oil pressure, load pressure and the valve core displacement, and it has a great effect on forward magnification coefficient of servo system; Furthermore, with the increasing simulation time, the oil temperature variation

induces the transformations of viscosity and elasticity, and this represents the time varying characteristic of system. Under this circumstance, the precise mathematical model is difficult to be obtained.

Fuzzy controller can't study by itself and eliminate the steady state error, but its implementation is very convenient for its simpleness, also it can improve the system robust effectively.

The integral control can be introduced in the controller in order to improve the steady state performance, which can eliminate the steady state error, but the dynamic response is slow, so integration [3] of PID controller and Fuzzy controller constitutes Fuzzy-PID compound controller to improve the steady state performance of Fuzzy controller,

which is shown in Fig.2.

In the big error range, it adopts fuzzy control, and in small error range uses PID control. The conversion between two controls is automatically carried out by

command programmed in advance. The conversion method includes direct switch, straight line switch and exponential switch, etc.

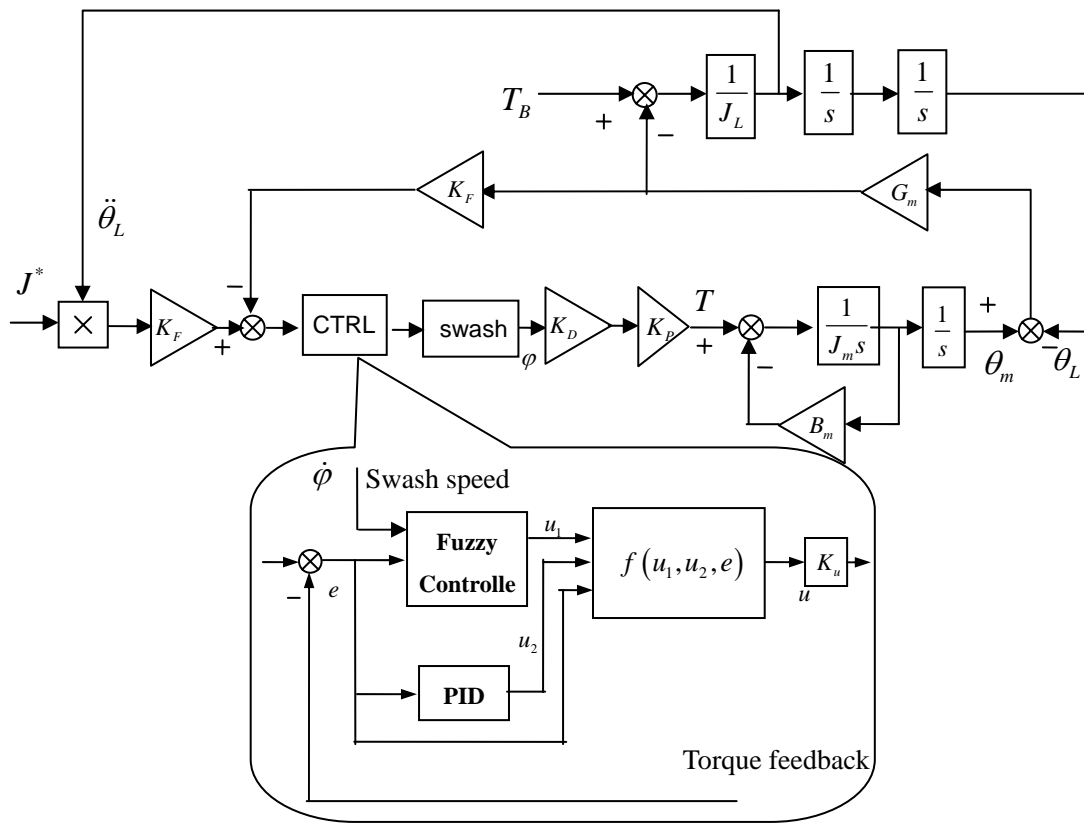


Fig.2. Diagram of Fuzzy PID Controller

In Fig.2 $f(u_1, u_2, e)$ is transition function of Fuzzy control and PID control. According to current error, to determine the controlled output u , u is a certain integration of u_1 and u_2 . According to the three conversion methods mentioned above, f can be calculated as follows.

$$u = \begin{cases} u_1 & |e| > \alpha \\ u_2 & |e| \leq \alpha \end{cases} \quad (1)$$

Namely, if absolute value of error is less than a certain

set value, the system uses the PID controller output, otherwise, uses the Fuzzy controller output. In the formula, $\alpha > 0$ is the threshold.

$$u = \begin{cases} u_1 & |e| > \frac{e_{\max}}{k_e} \\ u_1 \frac{k_e |e|}{e_{\max}} + u_2 \left(1 - \frac{k_e |e|}{e_{\max}}\right) & |e| < \frac{e_{\max}}{k_e} \end{cases} \quad (2)$$

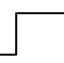
Namely, if absolute value of error is larger than a certain set value, the system uses the Fuzzy controller output, otherwise, uses the linear integration of the two

controllers as the ultimate output. In the output, the proportions of each controller is determined by coefficient k_e , where, $e_{\max} > 0$ is conversion threshold.

$$u = u_1(1 - \exp(-\alpha|e|)) + u_2 \exp(-\alpha|e|) \quad (3)$$

This method doesn't need to set threshold. It uses exponential relation to integrate from zero to infinite. The change speed along the exponential curve is determined by α . α is the larger, change is the steeper.

SIMULATION ANALYSIS

Brake sharply 

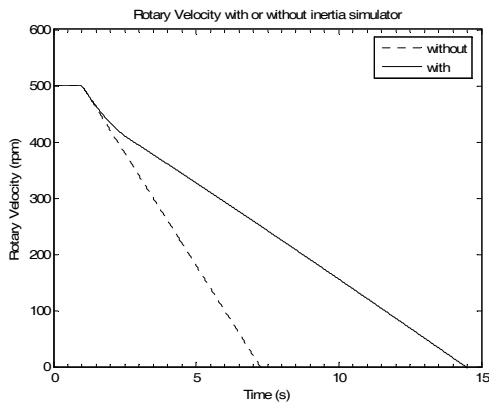


Fig 3. Velocity with or without inertia simulator

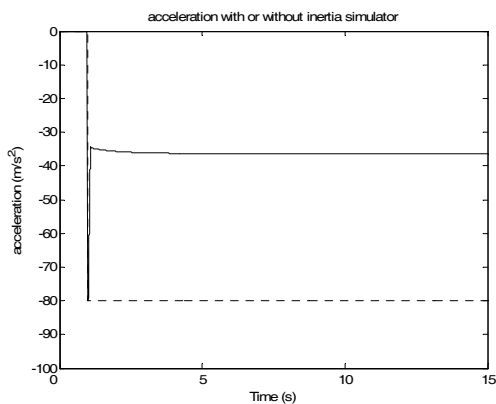


Fig 4. Acceleration with or without inertia simulator

Using the method mentioned above, some simulations are done. Firstly, the inertia plate is initialized to a velocity of 500rpm. After 1 second, change the braking torque to 100Nm directly like a step. While the inertia simulator is used, the total inertia is greater than the one which inertia simulator is not used. So the simulator suppresses the deceleration by reduce acceleration to a small constant of about 37Nm quickly. See figure 3 and figure 4.

In this case, the actual inertia changes sharply to the expected value with a little over shoot, so does the torque control performance, which the actual torque reaches the expected one. See figure 5 and figure 6.

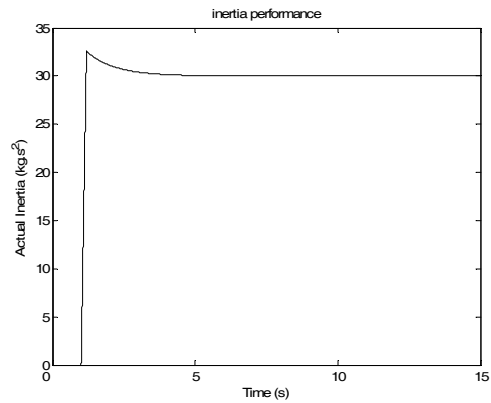


Fig 5. The actual inertia

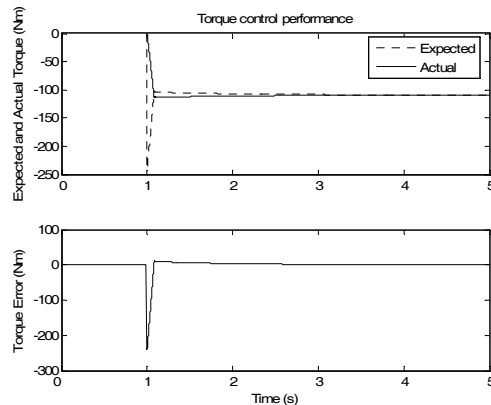
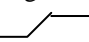


Fig 6. Torque tracing

Brake gradually 

Here, the inertia plate is initialized to a velocity of 500rpm. After 1 second, change the braking torque by adding 10Nm per second. While the inertia simulator is used, the total inertia is greater than the one which inertia simulator is not used. So the simulator suppresses the deceleration by reduce acceleration compared to the one without inertia simulator. See figure 7 and figure 8.

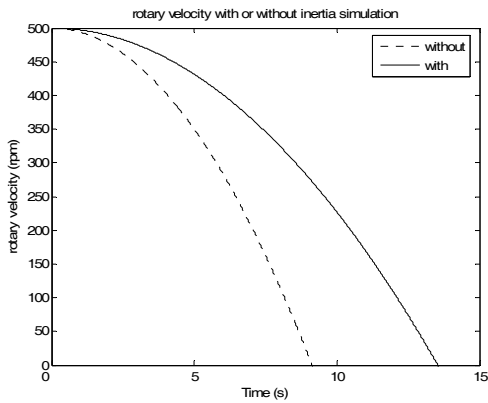


Fig 7 velocity with or without inertia simulator

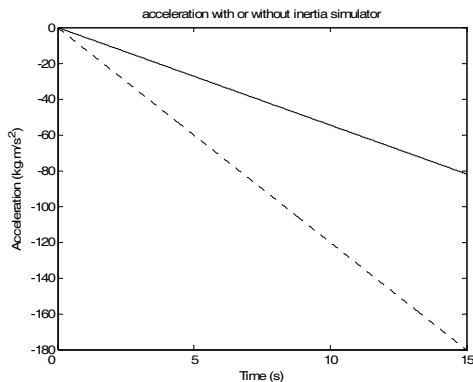


Fig 8. acceleration with or without inertia simulator
 In this case, the actual inertia changes sharply to the expected value with no over shoot. And the actual torque traces the expected one well. See figure 9 and figure 10.

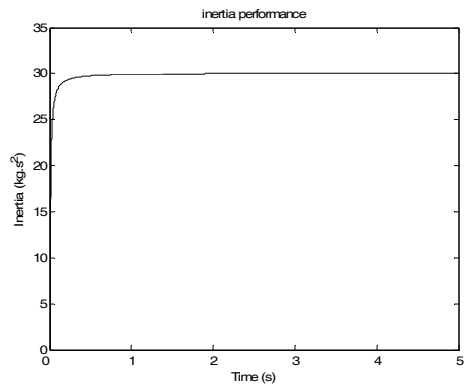


Fig 9 actual inertia

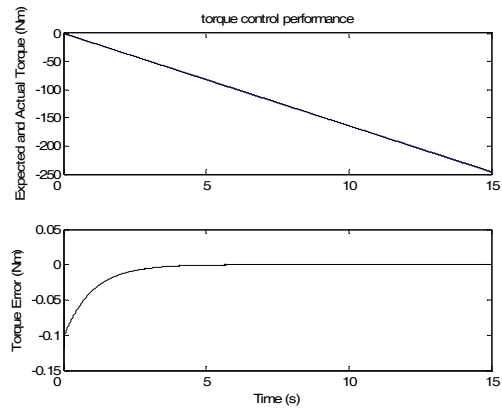


Fig 10. torque control performance

CONCLUSION

For the complex structure, nonlinear and mathematical model complexity of inertia simulation system based on secondary control, this paper presents a fuzzy control scheme, its structure is simple and performance is fine. The scheme characteristics are as follows.

The torque error and its change are two inputs of fuzzy control. The swashplate speed is the third input, and its membership function is specially designed to eliminate the influence of static friction torque and to minimize the time of zero speed;

Using pressure signal to carry out feed-forward compensation, according to the pressure change to adjust the system output gain so as to compensate the torque

fluctuation;

Integrating Fuzzy Controller and PID Controller organically, and using exponential conversion method to regulate the ultimate output proportion of two controllers.

The experiment results show that the control effect of fuzzy controller is fine, the system exceedance is small, and the response is rapid. It is also indicated that is necessary to introduce Fuzzy-PID control to eliminate steady error and minish dead area, and also necessary to introduce pressure variable gain to restrain the influence of pressure fluctuation.

ACKNOWLEDGEMENTS

The author appreciates, the valuable support provided by the Teaching and Research Award Program for Outstanding Young Teachers in Higher Education Institutions of MOE, P.R.C. and China Aeronautics Science Foundation (No.04E51013) for funding this project.

REFERENCES

- 1、 H.Berg and M Ivantysynova; Design and testing of a robust liner controller for secondary controlled hydraulic drive, Fluid power and control group, Department of Measurement and control, faculty of mechanical engineer, the MS April 1999 page375-386.
- 2、 Y M Jen, MSc and C B Lee; influence of an accumulator on the performance of a hydrostatic drive with control of the secondary unit, The MS, April 1993 page173-184.
- 3、 M. Martin, R. Tburton, and G.J. Schoenau, Analysis, Design and Compensation of Computer Controlled Hydraulic Load Simulator. Proceedings of ASME Winter Meeting, November 1992.
- 4、 W. A. Ragsdale, A GENERIC LANDING GEAR DYNAMICS MODEL FOR LASRS++, Unisys Corporation, NASA Langley Research Center,

Hampton, VA 23681-2199.

- 5、 Jeong-Woo Jeon; Ki-Chang Lee; Don-Ha Hwang; Yong-Joo Kim; Development of a dynamic simulator for braking performance test of aircraft with anti-skid brake system, Industrial Electronics, 2002. ISIE 2002. Proceedings of the 2002 IEEE International Symposium on Volume 2, 8-11 July 2002 Page(s):518 - 523 vol.2.
- 6、 Xu, Z., Taylor, D., Using motion platform as a haptic display for virtual inertia simulation. Information Visualization, 2003. IV 2003. Proceedings. Seventh International Conference on 16-18 July 2003 Page(s):498 – 504.
- 7、 Zongxia Jiao, Monika Ivantysynova, Xiaodong Wang, Load Simulator Based on Hydrostatic Secondary Control Technology, Sept. 2002, 23rd ICAS, TORONTO, Canada, pp.346.1~346.9

Electrohydraulic Proportional Metering Valve for Common Rail System

Sonam YUN*, Jae Seop RYU*, Byoung Kyu AHN*, Go Do KIM** and Jung Hyun JO**

* Intelligence and Precision Machinery Research Division,
Korea Institute of Machinery and Materials(KIMM)
171 Jang-dong, Yuseong-gu, Daejeon, 305-343 Korea
(E-mail: ysn688@kimm.re.kr)

** Technology Institute, SG Servo Inc.
57-6 Palyong-dong, Chanwon, Kyungnam, 641-846 Korea

ABSTRACT

In the common rail system with direct injection equipment in diesel engine, a proportional metering valve to control the fuel flow into the high pressure pump is used. The proportional solenoid actuator is suitable for metering valve because it has a constant attraction force in the control region independently on the stroke position and a fast motion response of the plunger. The force characteristics with respect to the stroke of the proportional solenoid actuator is strongly depending on the shape of the control cone, but it is difficult to design the control cone. In this paper, a proportional solenoid actuator of electrohydraulic proportional metering valve for common rail system was analyzed using finite element method and the shape of the control cone of the proportional solenoid actuator was optimized to get the constant force in the control region. The analysis results of the optimized proportional solenoid actuator were compared with the experimental results of the manufactured one.

KEY WORDS

Common rail system, Proportional solenoid, Proportional metering valve, PWM control, Fuel injection

NOMENCLATURE

L : Control cone length
 t_c : Control cone thickness
 W : Width between plunger and bobbin
 G_{ap} : Gap between plunger and control cone

INTRODUCTION

This study deals with a low pressure proportional metering valve with a proportional solenoid actuator for a common rail system of the diesel engine vehicle. This

actuator is installed at the inlet part of the high pressure fuel pump and has the function of controlling the flow rate from the low pressure fuel pump. This fuel flow is controlled in proportion to the engine RPM. So this control operation enables the engine to inject the optimal of fuel. Generally, diesel vehicles emit the toxic gases including nitrogen and produce noise during operation. These problems deteriorate the comfort of passengers, environmental pollution and energy saving, for which a improvement has been required. As the solution for the above-mentioned problems, the method, which involves the injection of high pressure and atomization of fuel, was developed to improve the

combustion process of diesel engines used in vehicles. It is also very important to optimally control the supply of the initial amount of fuel for atomization. However, there is further need for the optimal design of a low pressure proportional solenoid actuator[1][2]. This is a basic study on an optimal method of fuel injection and a low pressure proportional metering valve with a solenoid actuator[3][4][5]. Figure 1 shows a common rail system with a low pressure proportional metering valve with a solenoid actuator inside, which is the object of this study.

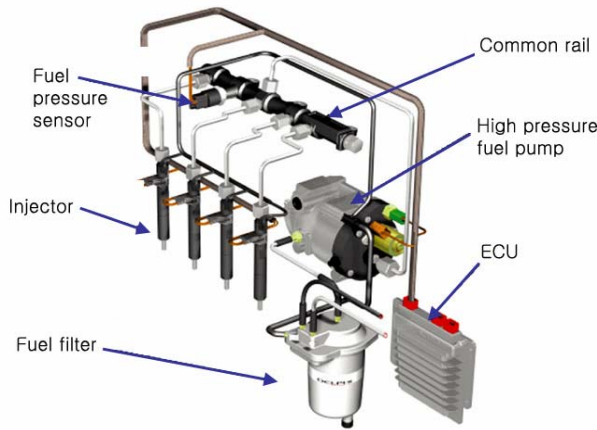


Figure 1 Common rail system of diesel engine

DESIGN OF PROPORTIONAL SOLENOID ACTUATOR

Figure 2 shows a low pressure proportional metering valve for a common rail, consisting of a coil, stationary core, plunger and poppet type flow control valve.

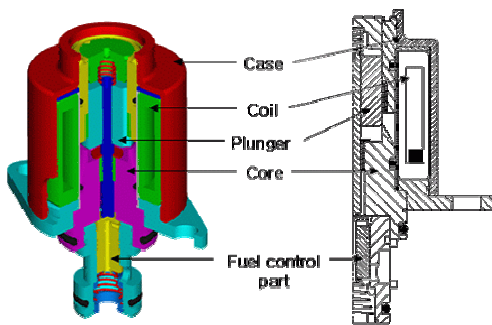


Figure 2 proportional metering valve for common rail

2.1 1st design

Figure 3 shows the proposed solenoid actuator in the first step of concept design. The control cone of the proportional solenoid plays a vital role of controlling

attraction force in proportion and its properties have to be understood through analysis. During the step of concept design, we conducted the analysis by inputting the design factors in Table 1 into the drawing of Figure 3. The specifications were input voltage 12[V], input current 1.1[A], and attraction force 10[N].

The a) in Figure 4 shows the experimental results when there is almost no gap between the control cone and the plunger and the thickness of the control cone, t_c , was fixed at 1.5mm. It was observed that the closer the plunger came to the stationary core, the lower the attraction force was. The b) of Figure 4 shows the experimental results when the thickness of the control cone was fixed at 0.5mm but there was no visible effect. We believe that it is resulted from the too-large magnetic flux leakage generated because there was no gap between the plunger and the control cone and because the width of the control cone, W , was very large[6][7][8].

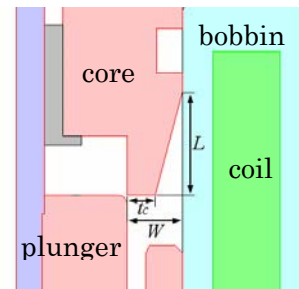
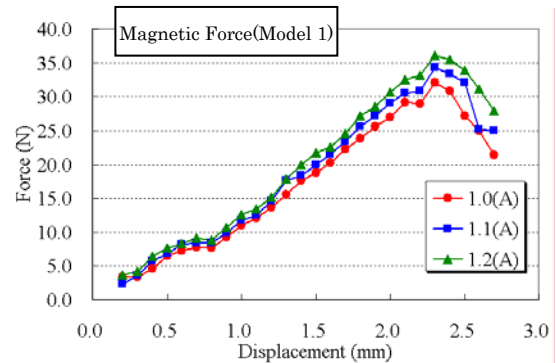


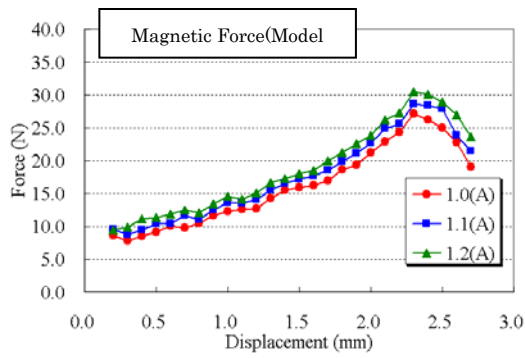
Figure 3 Analysis model_1

Table 1 Design parameters for model_1

Item	Model_1	Model_1(new)
W	3.0mm	3.0mm
L	5.6mm	5.6mm
t_c	1.5mm	0.5mm



a) Model_1



b) Model_1(new)

Figure 4 Analysis result of model_1

2.2 2nd design

Figure 5 shows new proposed models for compensating the attraction force shown in Model_1. Both a) and b) in Figure 5, are the experiment results, when conducted with the reduced values of control length, L , and width, W , compared to those of Model_1. And the b) in Figure 5 is the result when conducted with the width, W , of less than 1mm compared to a) in order to reduce magnetic flux leakage. It was confirmed that b) in Figure 6 has more excellent properties than a) However, the shape of the sealing part was not good in effectively preventing leakage and an optimal design technique is needed.

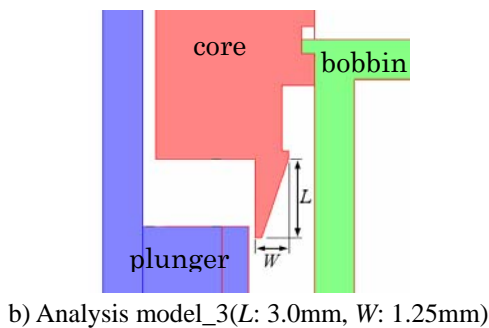
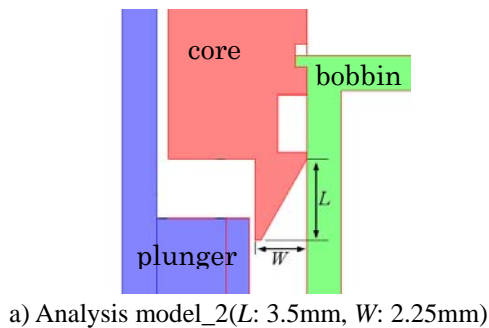
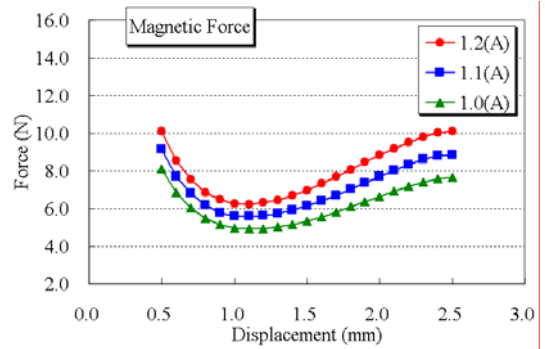
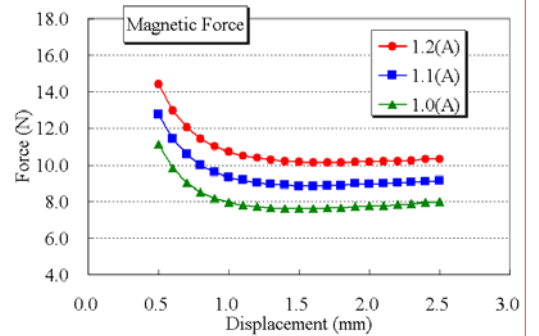


Figure 5 Proposed model_2 and model_3



a) Model_2



b) Model_3

Figure 6 Analysis results of model_2 and model_3

2.3 3rd design

Figure 7 is designed to provide an optimal solenoid actuator from the shape in Figure 5, which manufacturing condition and seal property were taken into consideration.

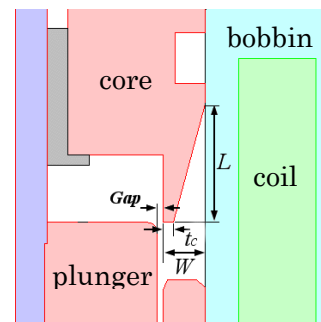
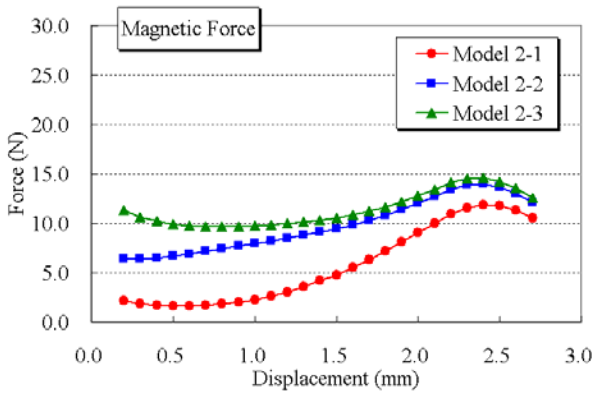


Figure 7 Final model for proportional solenoid actuator

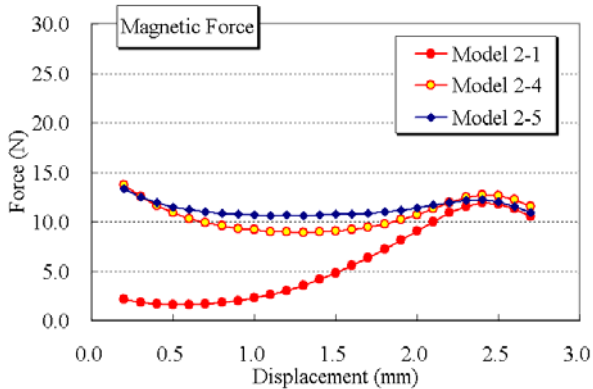
Table 2 Design parameters for final model

Item	Model 2-1, 2-2, 2-3	Model 2-4	Model 2-5
W	2.0mm	1.0mm	2.0mm
L	5.6mm	3.2mm	5.6mm
t_c	0.5mm	0.5mm	0.25mm
G_{ap}	0.25mm	0.25mm	0.25mm

Figure 8 shows the finite element results analyzed by inputting each design factors shown in Table 2. It was confirmed that in the case of $W= 2.0\text{mm}$, $L= 5.6\text{mm}$, $t_c= 0.25\text{mm}$, $G_{ap}= 0.25\text{mm}$, high attraction force was gotten and was constantly controlled regardless of changes of plunger stroke.



a) Model 2-1, 2-2, 2-3



b) Model 2-1, 2-4, 2-5

Figure 8 Analysis results of final models

EXPERIMENTAL RESULTS

3.1 Experimental apparatus

We made a prototype proportional metering valve with a solenoid actuator based on the analysis results in Table 2 and Figure 8, and in order to verify the actuator's performance, we composed the experimental apparatus shown in Figure 9. And then observed the flow and pressure property of the solenoid actuator from the experimental apparatus. To input the signals into the solenoid, we used the PWM controller presently embedded in leisure vehicles. Figure 10 is the photo view of the experimental apparatus.

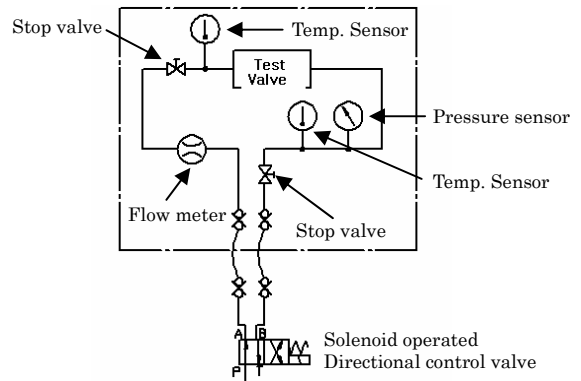


Figure 9 Hydraulic circuit of experimental apparatus

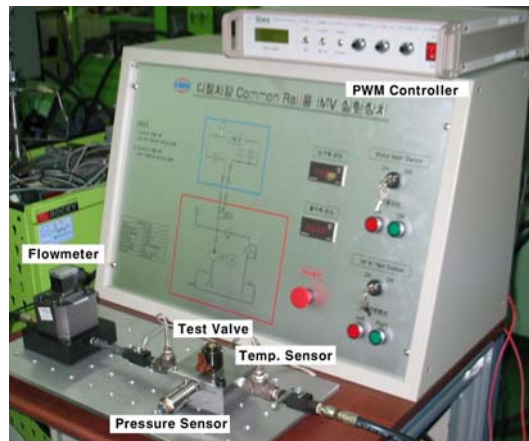
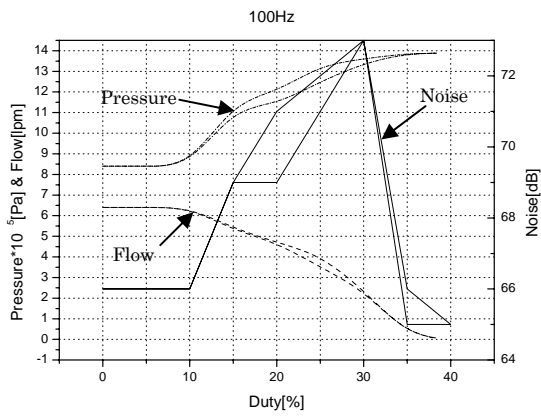


Figure 10 Photo view of experimental apparatus

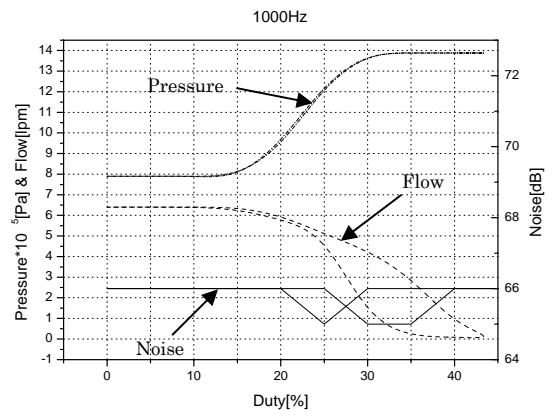
3.2 Experimental results

Figure 11 shows the experimental results of the prototype. after setting any number of frequency inputted into the proportional solenoid actuator, these are the results of the pressure of the valve and the flow in accordance with the manipulation of duty ratio. First, the noise was the least at the 1000Hz PWM signal input, but flow and pressure hysteresis were most excellent at the 400Hz PWM signal input. Because the reduction of the causes of noise to improve comfort is an important factor in designing a vehicle, there is a need to design a valve that has a good performance at high frequencies. We believe that a valve precision manufacturing can easily solve the problem.

Figure 12 shows the experimental results of the 2nd prototype. The 2nd prototype was precisely manufactured with better machinability, which was a trouble of the 1st prototype. Therefore, hysteresis at the high frequencies was improved, which was a problem of the 1st prototype.

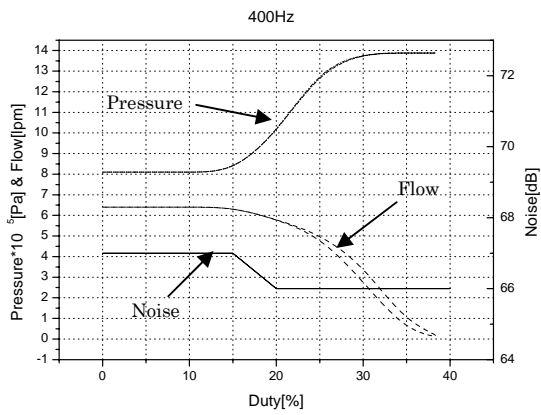


a) 100Hz PWM signal input

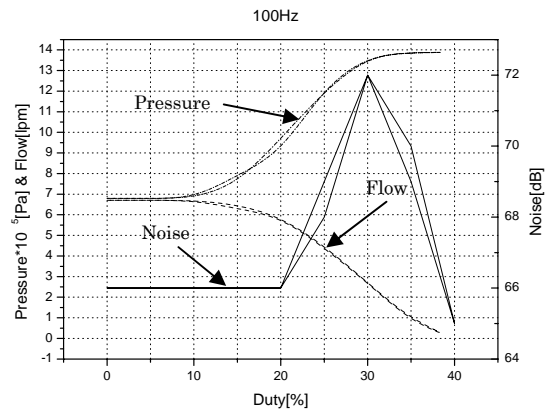


d) 1000Hz PWM signal input

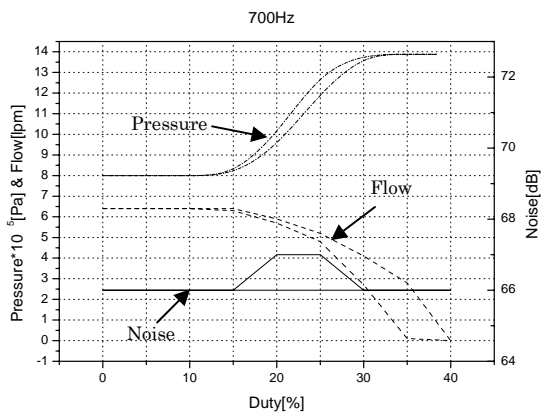
Figure 11 Experimental results of 1st prototype



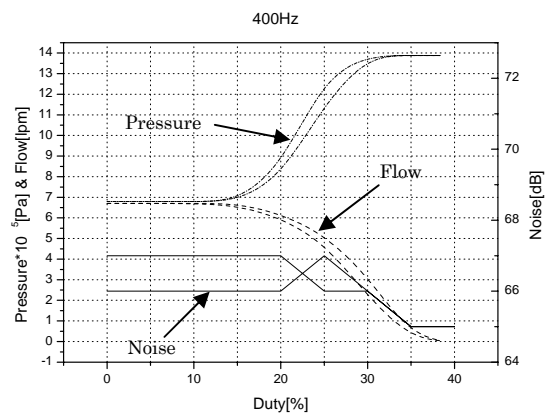
b) 400Hz PWM signal input



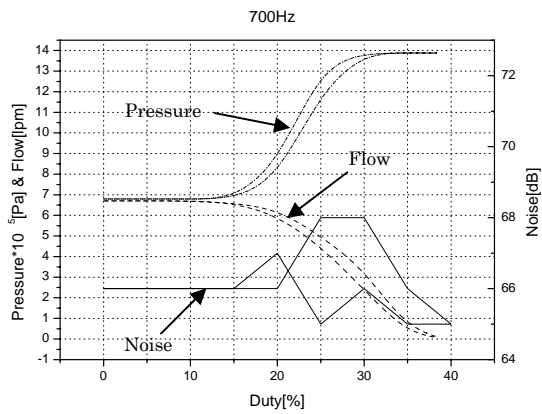
a) 100Hz PWM signal input



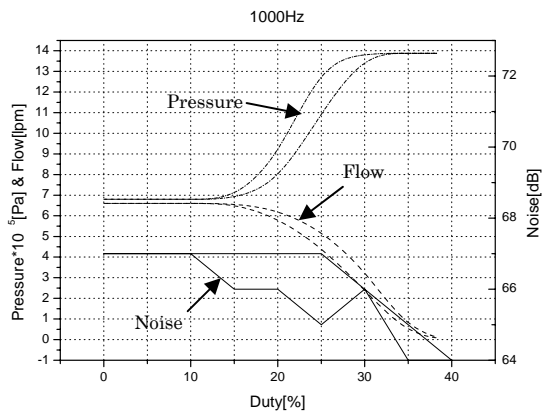
c) 700Hz PWM signal input



b) 400Hz PWM signal input



c) 700Hz PWM signal input



c) 1000Hz PWM signal input

Figure 12 Experimental results of 2nd prototype

CONCLUSION

In this study, we conducted an analysis of the electromagnetic and design of a low pressure proportional metering valve with a solenoid actuator from a leisure diesel vehicle applied to a common rail system, and we verified its performance by manufacturing it. The comparative factors such as noise, flow and pressure hysteresis depend on the given conditions of the PWM signal. It was verified that these problems could be easily solved through a precision process. In addition, the results of this study can be utilized in developing and improving the proportional metering valve with a solenoid actuator for the common rail system.

REFERENCES

1. Bruno P. Lequesne, Finite Element Analysis of a Constant-Force solenoid for Fluid Flow Control,

- IEEE, Tran. Industrial Application, 1988, 24-4, pp.574-581.
2. Grit Geiler, Modellbildung von Proportionalmagneten mittels konzentrierter Parameter, +P, 2001, 45-1, pp.49-52.
3. C.S. Koh, J.O. Kim, S.Y. Hahn and Osama. A. Mohammed, Optimum design of Voice Coil Motor with constant torque coefficients using evolution strategy, Journal of Applied Physics, 1994, 75-10, pp.6045-6047.
4. Sonam Yun, Kyungwoo Lee and Honghee Kim, Development of the Pneumatic Valve with Bimorph Type Piezoelectric Actuator, 1st International Workshop on Piezoelectric Materials & Applications in Actuator, 2004, p.118.
5. Jae Seop Ryu, Mi Ran Seo, Chang Seop Koh, Sonam Yun and Dong Soo Kim, Optimal Design of Constant-Force Solenoid for Pressure Control Using Axisymmetric Non-linear Parameterized Sensitivity Analysis, The 11th Biennial IEEE Conference on Electromagnetic Field Computation, 2004, p.390.
6. Sonam Yun, Electro-Magnetic Proportional Solenoid, JFPS, 2004, 35-5, pp.342-347.
7. Sonam Yun, Young-Bog Ham, Characteristics analysis of the solenoid valve for exhaust brake, Transactions of KSAE, 2005, 12-1, pp.190-195.
8. Sonam Yun, Jae-seop Ryu, Byung-Kyu Ahn, Mi-ran Seo and Chang-seop Koh, Optimal design of electro-magnetic proportional solenoid using genetic algorithm, Proceeding of the 50th national conference on fluid power, 2005, pp.243-247.

AN ENERGETIC COMPARISON BETWEEN VALVELESS AND VALVE CONTROLLED ACTIVE VIBRATION DAMPING FOR OFF-ROAD VEHICLES

Bastian EGGERS, Dr. Robert RAHMFELD, Prof. Monika IVANTYSYNOVA

Purdue University, Agricultural and Biological Engineering,
MAHA Fluid Power Lab
3601 Sagamore Pkwy North, Lafayette, 47904 IN, USA
Email: mivantys@purdue.edu

ABSTRACT

This paper presents a comparison of the energetic consumption of a valveless and a valve controlled active oscillation damping system for off-road machinery. Today only passive oscillation damping systems are subject to off-road machine series production. These systems offer the advantage of no additional primary energy use for damping. However, the disadvantages are the high costs and no adaptation possibility to the operating parameters. The recent developments where valve controlled linear actuators have been used for active damping had to face several problems with too low dynamics of today's implemented control valves and the high additional energy need. These disadvantages can be avoided by using valveless linear actuators for working functions and for active damping. In fact, throttling losses are omitted and, energy recovery is possible. It will be shown based on measurement and simulation results that a suitable damping quality can be achieved with valveless linear actuators. Therefore, some aspects of the controller design will be given. Hereby, a simple acceleration sensor and standard control hardware are used. The main part will describe the energetic modelling, whereby especially precise pump loss models have been developed. The energy consumption of both systems performing active damping is compared in detail.

KEYWORDS

Displacement control, Valveless, Valve control, Active Oscillation Damping, Energy Saving, Linear Actuators

NOMENCLATURE

A_K	cylinder area [m ²]
C_H	hydraulic capacity [m ⁵ /N]
c_{uc}	spring constant, undercarriage [N/m]
d_{uc}	damping constant, undercarriage [Ns/m]
m_B	boom mass [kg]
m_L	load mass [kg]
m_{Ch}	chassis mass [kg]
M_S	pump torque losses [Nm]
n	pump speed [rpm]
Q	volume flow [m ³ /s]

V_i	displacement volume [cm ³ /s]
y	cabin vertical position [m]
ϕ	boom angular position [°]

1 - INTRODUCTION

In today's off-road machines – especially mobile machines capable of driving at fairly high speeds of up to 40 km/h like wheel loaders – oscillating accelerations at the cabin and at the boom structure represent an important factor limiting the machines productivity and the operator comfort. The accelerations have their source in forces introduced into the machine structure from the ground

through the low damped wheels and undercarriage (Fig. 1). The accelerations lead to two major problems: a comfort problem for the driver in the cabin and a safety problem for the load transported by the machine (Fig. 2). Both problems lead to a reduction of the drive speed of the machine in case the acceleration grows beyond certain limits.

Currently, three hydraulic system concepts focussed on the reduction of the oscillating acceleration in mobile working machines exist. The most basic and widely implemented concept is a passive solution where the high pressure side of the hydraulic working actuators is connected by simple switch valves with high pressure hydro-pneumatic accumulators and shut off from the rest of the hydraulic circuit (e.g. Drake and Jaecks, 1991; Hosseini, 1992; Ufheil and Rector, 1996; etc.). This concept has the advantage of no additional primary energy necessary for the additional damping in the system. The disadvantages are the very limited frequency range in which the concept produces additional damping and the cost both for implementation and maintenance of the high pressure accumulators.

Using the main electrohydraulic valve block of the standard hydraulic system, or additional faster valves if more bandwidth is necessary (which is often the case), active oscillation damping can be implemented in mobile machinery (Latour and Biener, 2002; Patel et al, 1999; etc.). In this application the controller uses additional sensors for acceleration, pressure, force or a combination to produce an additional command input for the control valve. The oscillation reduction using valve control comes at the price of high additional primary energy. Valve controlled actuators – usually in combination with load sensing controlled pumps – are even for standard position control not an energy-efficient concept. For active oscillation damping the valve is commanded from negative to positive position in short time intervals. As soon as the valve is opened energy is lost at the valve itself. Using valve control, no energy can be recovered, e.g. while lowering a load, this becomes of higher importance for active damping as all additional energy for this task is lost and cannot even partly be reused. All energy lost is transformed into heat energy. This energy has to be transferred out of the system by additional cooling effort.

Using a hydraulic system concept with a displacement controlled (also pump controlled or valveless) actuator in closed hydraulic circuit, energy recovery is possible. The concept uses the hydraulic pump itself as final control element and has proven itself in earlier studies useful for the high bandwidth demanding task of active oscillation damping (Rahmfeld, Ivantysynova and Eggers, 2004). This concept has been analysed concerning its energetic behaviour and compared to a standard hydraulic system with valve controlled actuator and load sensing controlled pump. The results of the analysis and

the comparison will be presented in the main part of this document.

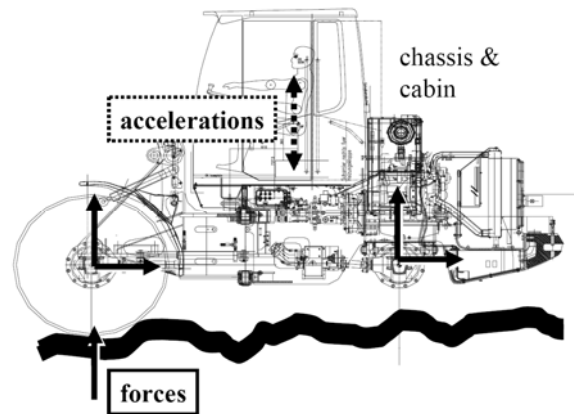


Fig. 1: Sources for accelerations at the cabin of an off-road working machine

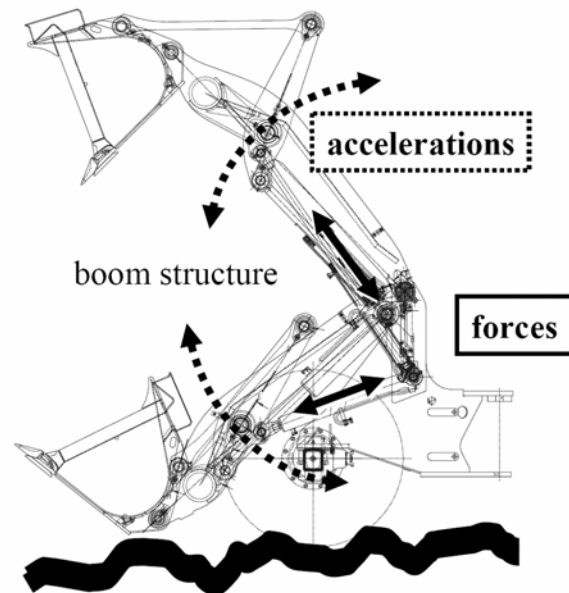


Fig. 2: Accelerations at the boom structure of a mobile working machine

2 - VALVELESS ACTIVE OSCILLATION DAMPING FOR OFFROAD VEHICLES

Rahmfeld (2002) developed a hydraulic circuit solution using single rod cylinders in closed circuit with an additional low pressure level to compensate for the different volume flows in and out of the two cylinder chambers (see also Rahmfeld, Ivantysynova and Weber, 2004). Using the variable displacement pump as final control element, this system has three major advantages over today's standard valve controlled systems:

1. higher energy efficiency by omission of throttling losses and the possibility of energy recovery,
2. simplification of the system itself by use of less components,
3. higher dynamic with easier control possible.

Fig. 3 displays the linear valveless actuator concept. The single rod cylinders (2) are controlled by the electrohydraulic variable displacement pump (1). The pilot operated check valves (3_1 , 3_2) allow volume flow from the low pressure line (LP) into the main hydraulic lines and back to compensate for the different volume flow in and out of the actuator chambers.

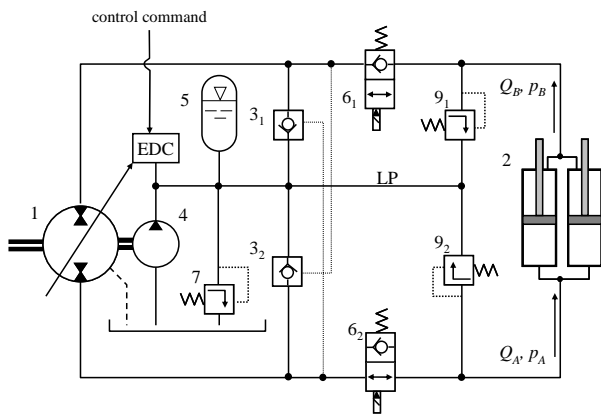


Fig. 3: Hydraulic circuit solution: Displacement controlled linear actuator

The low pressure level is equipped with a charge pump with fixed displacement volume (4) and a hydro-pneumatic low-pressure accumulator (5). Maximum low pressure is adjusted by a relief valve (7). The main hydraulic lines can be locked by two shut-off valves (6_1 and 6_2) and are connected to the low pressure line by two pressure relief valves (9_1 and 9_2). All required components could be integrated in the pump housing.

In a machine with more than one displacement controlled actuator like for the wheel loader, the low pressure lines can be coupled (Fig. 4) and the number of hydraulic system components can be reduced once more. Additionally, energy recovered by one displacement pump running in motoring mode can be reused by the other actuator or the hydrostatic transmission drive (19). In this case the energy is transferred through the distributing gear (17).

The application of valveless active oscillation damping has been implemented in a technology demonstrator wheel loader (pre-series) machine by Rahmfeld, Ivantynova and Eggers (2004). In this work a wheel loader with displacement controlled linear actuators has been equipped with two capacitive acceleration sensors at the boom structure and at the cabin. This type of sensor

proved to be cost efficient and as well as comparable to pressure sensors. The boom sensor signal could be used as input for additional acceleration controller implemented in the electric CAN-bus controller of the machine to act directly on the displacement control unit of the variable displacement axial piston pump of the lifting actuators. The potential of this concept could be demonstrated in experimental drive tests.

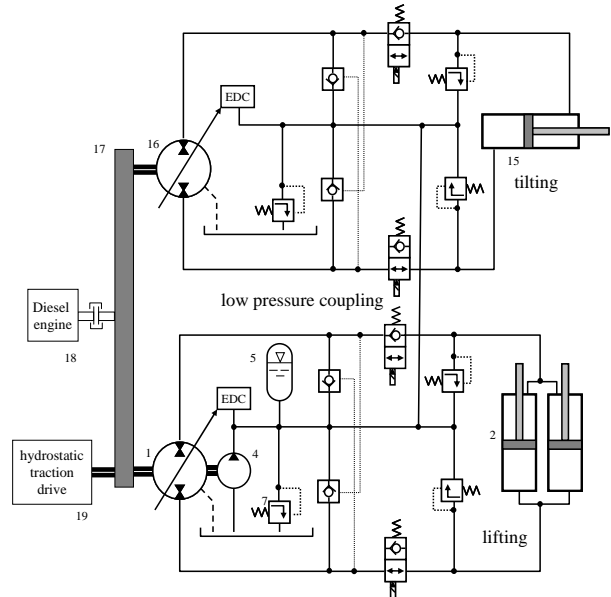


Fig. 4: Wheel loader with valveless working functions and coupled low pressure level

Within these earlier investigations measurement results of the electrohydraulic pump were analysed to reveal a strong amplitude dependency of the pump dynamics, as it is typical for nonlinear systems. Using these measurements a linear pump model could be created as a PT2 transfer element with a damping of $D_{\text{pump}} = 0.456$ and the eigenfrequencies for different commanded displacement volume amplitudes as

amplitude 30%:	$\omega_{\text{pump}} = 5.4 \text{ Hz} = 34 \text{ rad/s}$
amplitude 12.5 %:	$\omega_{\text{pump}} = 7.8 \text{ Hz} = 49 \text{ rad/s}$
amplitude 5 %:	$\omega_{\text{pump}} = 9.4 \text{ Hz} = 59 \text{ rad/s}$

Clearly the amplitude dependency of the pump dynamics becomes visible. Although this information may be sufficient to create a linear model of the hydraulic system and to proceed with a systematic controller design, these findings show the demand for a nonlinear model of the pump and its control system with similar behaviour for simulation purposes.

3 - CONTROL CONCEPT

Fig. 5 displays the linear block diagram of the control plant consisting of the electrohydraulic pump and the single rod cylinders. In case of manual control by the driver this system is controlled in open loop (OL) providing good control quality for the driver. As soon as no input is produced through the joystick, the system switches to closed loop (CL) maintaining the angular position of the boom ϕ with the help of the position controller. This controller is enhanced with two nonlinear compensations for pump speed and kinematic to provide nearly maximum controller gain at all operating points. To facilitate acceleration control for the boom and the cabin of the machine, two additional control loops are implemented. The input for the control loops is provided by the acceleration sensors at the boom and the cabin.

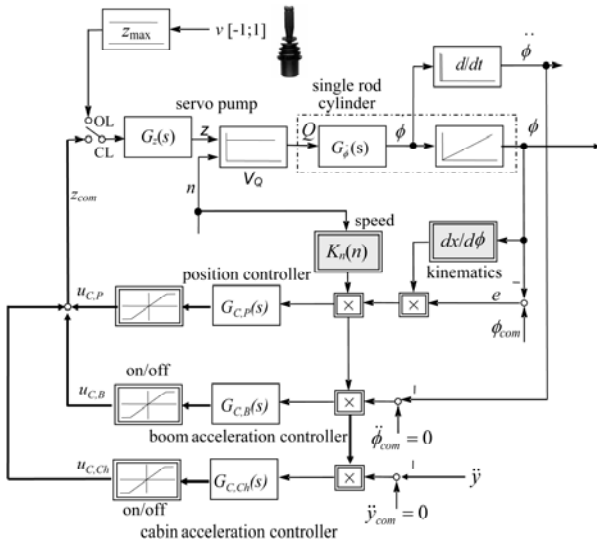


Fig. 5: Position and acceleration control loops

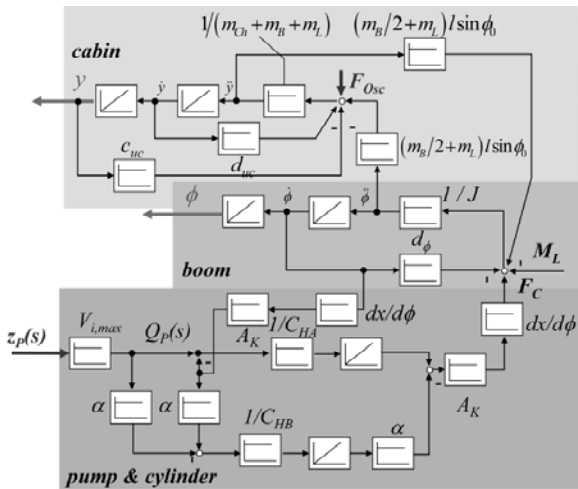


Fig. 6: Linearized block diagram of pump, cylinder, boom and cabin

To be able to design the acceleration controller systematically, linear models of the control plant and the mechanical model of the boom and the cabin have been created (Fig. 6). The model with two degrees of freedom – angular boom position ϕ and vertical chassis position y – is based on two differential equations: the equation of rotational motion around the connecting point between chassis and boom:

$$J \ddot{\phi} = -d_{\phi} \dot{\phi} + (m_L + m_B/2) l \sin \phi (g - \ddot{y}) + (A_K (p_A - \alpha p_B) - F_R(\dot{x}) - m \ddot{x}) \frac{dx}{d\phi} \quad (1)$$

and the equation of linear motion of the chassis

$$(m_{Ch} + m_B + m_L) \ddot{y} + d_{uc} \dot{y} + c_{us} y = (m_B/2 + m_L) l \ddot{\phi} + F_{Osc} \quad (2)$$

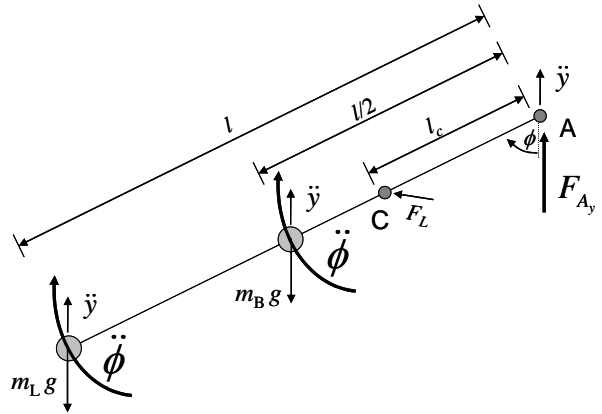


Fig. 7: Boom dynamic model

These equations can be derived by cutting the boom structure (Fig. 7) and the chassis model (Fig. 8) free. The cylinder force is calculated in this approach as:

$$F_L = A_K (p_A - \alpha p_B) - F_R(\dot{x}) - m \ddot{x} \quad (3)$$

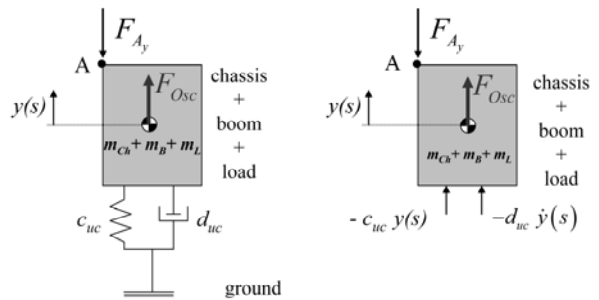


Fig. 8: Chassis dynamic model

Using this linearized model, controller up to the 1st order have been designed both for cabin and acceleration control. In nonlinear simulations good damping quality could be achieved using PDT1 controller, significant cabin acceleration reduction could not be produced due to the simplified cabin model. Selecting the pole of the boom acceleration controller near the cabin poles at approximately 1 rad/s and the zero at the frequency of the dominating pole pair of the differential cylinders at 53 rad/s made amplitude reductions of the acceleration of 35% possible using a model of the standard pump control system. The *Bode* diagram of the closed acceleration control loop can be seen in Fig. 9.

The energetic evaluation and comparison in this document focuses on equivalent acceleration amplitude reduction at the boom using the two different system solutions: valveless and load-sensing.

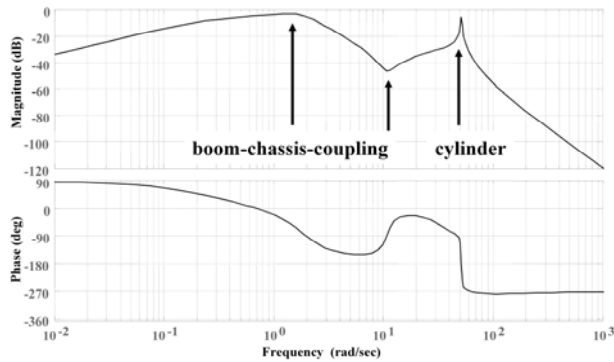


Fig. 9: Closed loop bode diagram, 1st order boom acceleration control

4 - ENERGETIC MODEL

To be able to calculate the necessary primary energy for a displacement controlled active oscillation (acceleration) damping approach the precise modelling of the energy losses of the hydraulic pump (and of the other hydraulic components) is crucial. Using displacement control, the pump can change between pumping and motoring mode. Loss models for the single quadrants of such a pump show significantly different behaviour especially around small displacement volumes. For the task of acceleration control the hydraulic pump is commanded from positive to negative displacement and vice versa in short time intervals. To ensure a smoothly running simulation model for these changes in displacement it is important to use a loss model with continuous behaviour at the operating points with little displacement volume and/or pressure difference.

Figure 10 displays the four single quadrant models of the torque losses of an axial piston swash plate type pump with a maximum displacement volume of 75 cm³/rev generated with the program *POLYMOD* based

on measurements (markers). *POLYMOD* represents a mathematical interpolation of the measurements by a polynomial as a function of pump speed, pressure difference and displacement for one oil temperature. The torque losses (Eq. 4) and the volumetric losses (Eq. 5) of the pump are defined through the coefficients of the polynomials K_M and K_Q . These coefficients are derived by selecting a surface fitting best to the measurement data using the method of least squares. The discontinuity becomes obvious in this figure. When the measurement data of all four quadrants is used for interpolation using *POLYMOD* a continuous model can be created (Fig. 11).

The *Sankey* (energy flow) diagram in Fig. 12 describes the main loss components of the displacement controlled actuator. For this application the electrohydraulic pump is the main loss source.

Furthermore the *Sankey* diagram demonstrates that the energy recovered in the displacement controlled system and reused in other actuators reduces the total amount of consumed primary energy by the machine and makes it more efficient. For this effect, it is assumed that the recovered energy at the pump shaft (the pump losses are also recovered) is used by other drives in the machine system like transmission, steering, braking, etc.

$$M_S(V_i, n, \Delta p)_{T=\text{konstant}} = \sum_{i_1=0}^{I_1} \sum_{i_2=0}^{I_2} \sum_{i_3=0}^{I_3} K_M(i_1, i_2, i_3) \cdot V_i^{i_1} \cdot n^{i_2} \cdot \Delta p^{i_3} \quad (4)$$

$$Q_S(V_i, n, \Delta p)_{T=\text{konstant}} = \sum_{i_1=0}^{I_1} \sum_{i_2=0}^{I_2} \sum_{i_3=0}^{I_3} K_Q(i_1, i_2, i_3) \cdot V_i^{i_1} \cdot n^{i_2} \cdot \Delta p^{i_3} \quad (5)$$

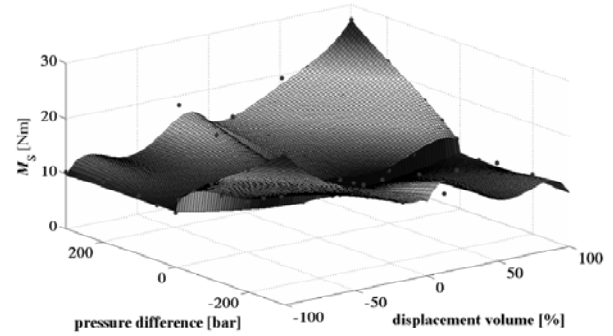


Fig. 10: Four combined single quadrant torque loss models

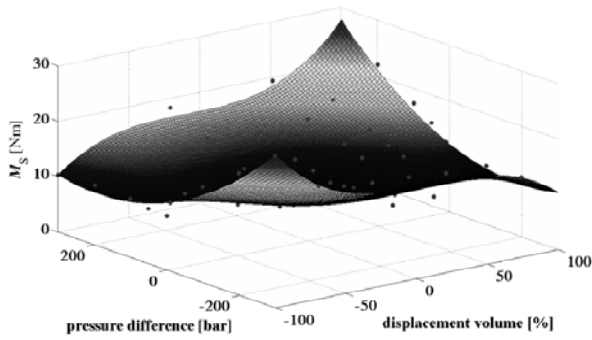


Fig. 11: Four quadrant torque loss model

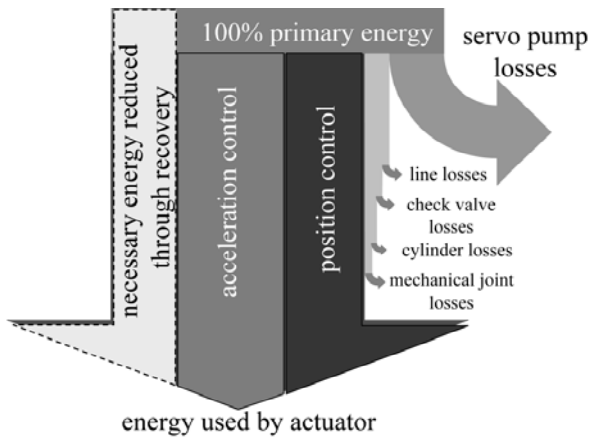


Fig. 12: Sankey diagram, displacement control

The loss behaviour of the hydraulic valves has been calculated based on the volume flow - pressure drop - diagrams issued by the manufacturers.

5 - VALVE CONTROLLED ACTIVE DAMPING

A standard open circuit hydraulic concept for active damping using valve control as primary and a load sensing controlled pump as secondary control element has been used in earlier applications for active oscillation damping (Latour and Biener, 2002; Berger and Patel, 1999; etc.). Fig. 13 compares the basic concept of valve and displacement control using simplified circuit diagrams.

To compare the primary energy necessary to provide equivalent damping quality using displacement control as well as valve control, additional to the nonlinear model of the displacement controlled machine, the model of a virtual valve controlled hydraulic system with a load sensing controlled pump as secondary control element has been developed. The dynamics of the load sensing valve have been tuned to produce equivalent damping quality as achieved with the displacement controlled system. To provide a useful primary position control, the

load sensing valve itself has been designed with zero overlap in contrast to a standard load sensing valve with positive overlap. I.e., the load sensing valve is during position control always actuated. The pure position control alone could be done more efficiently by a standard load sensing system, however, for active damping the valve is always in actuation.

The Sankey diagram of the valve controlled actuator in Fig. 14 demonstrates two important facts compared to a displacement controlled system: the system has two major loss sources – the pump and the main valve – and the consumed primary energy cannot be reduced with the help of energy recovery.

6 - SIMULATION MODEL BASED ON MEASUREMENTS

In earlier measurements (Rahmfeld, Ivantysynova and Eggers, 2004) only the quality of displacement controlled active damping was looked upon. Drive test were conducted with the focus on the amplitude reduction of oscillations at the boom structure of a wheel loader. The measurements left two questions unanswered: how much energy is necessary to provide the achieved damping quality and how much energy would be necessary by using a valve controlled load sensing system? To answer these questions a non-linear model of the hydraulic circuits and its components and a multi-body model of the boom structure and the cabin were used in combination with measurement based loss models for the hydraulic pump and other used components.

The pump and the remaining components of the hydraulic circuit for this simulation system as well as the position and acceleration controller have been generated as non-linear models in Matlab/Simulink 7.0. The multi-body models of the boom structure and the cabin have been created in Matlab/SimMechanics 2.0 providing the tools for a non-linear simulation within one program, avoiding a complex co-simulation, see Fig. 15.

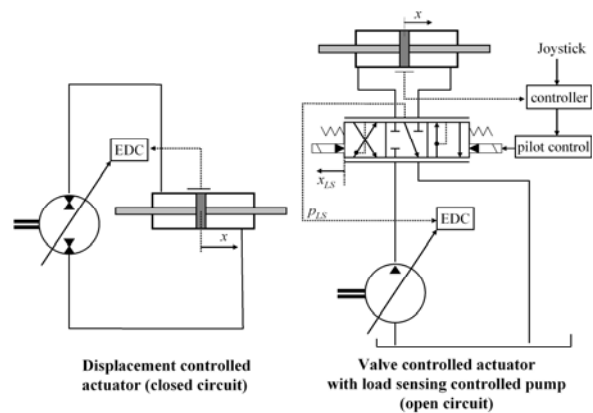


Fig. 13: Comparison: Displacement control – Load sensing valve control

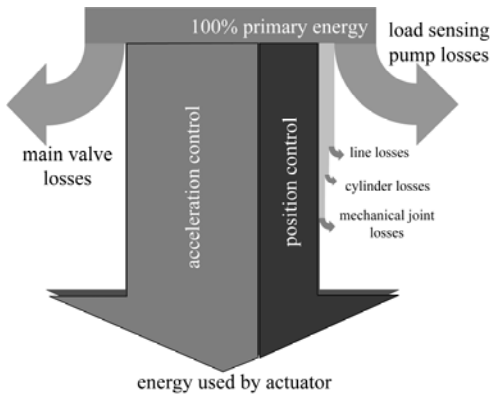


Fig. 14: Sankey diagram, valve control

The hydraulic circuit has been modelled with closed circuit displacement controlled on the one hand and for comparison as open circuit load sensing valve controlled. In both cases the same pump loss model has been used. In case of the valve controlled actuator the pump has been equipped with an electro-hydraulic pressure control system and a zero-overlap valve with enough bandwidth to produce a damping quality similar to the displacement controlled system. As multi-body model a model of the boom structure with one rotational degree of freedom was extended with a basic model of the chassis as a mass-spring-damper combination with one translation degree of freedom in vertical direction. This model offers the possibility to reproduce the accelerations at the cabin directly from the measured drive test results by introducing a force F_{Osc} (Fig. 6, 15) in vertical direction of the chassis. The force is generated using the inverted transfer function (Eq. 6) of the chassis dynamics and the acceleration measured at the chassis in the drive tests.

$$G_{osc}(s) = \frac{F_{osc}(s)}{\ddot{y}_{meas}(s)} = \frac{(m_L + m_B + m_{Ch})s^2 + d_{uc}s + c_{uc}}{s^2} \quad (6)$$

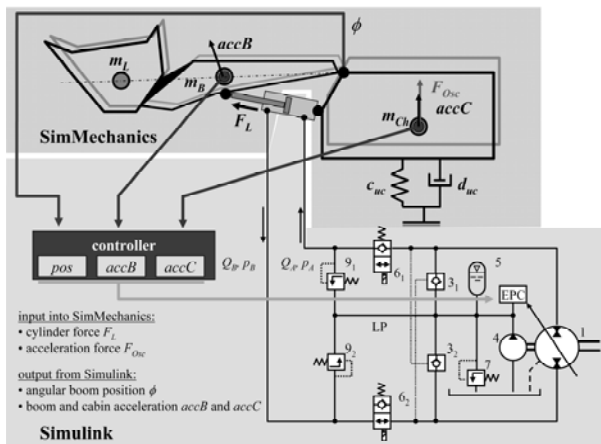


Fig. 15: Hydro-mechanical simulation using Matlab Simulink and SimMechanics

7 - COMPARISON FOR WHEEL LOADER DRIVING MANOUVRE

As basis for the comparison of the two hydraulic concepts concerning their energetic behaviour when used for active oscillation damping, the measurements of a drive test with deactivated control was selected. With these results the natural accelerations at the boom and at the cabin could be recreated to be counteracted by the designed acceleration controllers. Within the selected drive test the machine was driven over three groups of high obstacles (Fig. 16). The drive speed was approximately 10 km/h. Out of the drive test measurements a 12 s long phase was selected to be used as input for the non-linear simulation models. The utilized wheel loader has a maximum engine power of 82 kW.

Using the acceleration input and a selected first order acceleration controller the effective pump torque has been calculated for both system concepts. The calculations have been carried out for three different load scenarios: unloaded, loaded with 1 ton in the bucket and loaded with 2.5 ton. Figure 17 shows the effective pump torque of the pump for the LS valve controlled and the valveless system for the two most extreme load cases. It can be easily observed that the pump torque in the displacement controlled system drops below the minimum pump moment – indicated by the black horizontal line – as described in chapter 4. This means the pump is running in motoring mode, compensating for its own losses.

For an actuator moving not only the boom mass but an additional 2.5 ton of load, the pump is not only running in motoring mode in a high number of time frames but the pressure difference is high enough that the pump when running in motoring mode can drive other units running on the same shaft, i.e. the recovered energy is transferred mechanically to other units as steering pump, hydrostatic drive or others. Since the active oscillation damping will be used mainly while the machine is moving, it is very probable that the energy can be fully recovered. In fact the energy can be transferred to e.g. the transmission drive which will thereby take less torque from the combustion engine so that the engine can reduce the fuel injection. The engine itself will therefore have to produce less primary energy for the system and consume less fuel.

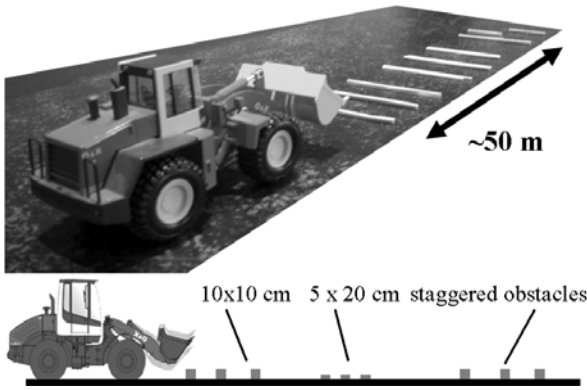


Fig. 16: Obstacle proving ground for drive tests

The effective pump shaft energy can be calculated using equation 7. The effective pump shaft torque defined

by the theoretical torque M_{th} and the torque losses M_S as presented in chapter 4 and stated in equation 8.

$$P_{mech} = 2\pi M_e n_{pump} \quad (7)$$

$$M_e = M_{th} + M_S \quad (8)$$

The mechanical work of the pump, running at constant speed n_{pump} , is calculated by integrating the pump shaft energy over the simulation time (Eq. 9).

$$W_{mech} = \int_0^T P_{mech}(t) dt = 2\pi n_{pump} \int_0^T M_e(t) dt \quad (9)$$

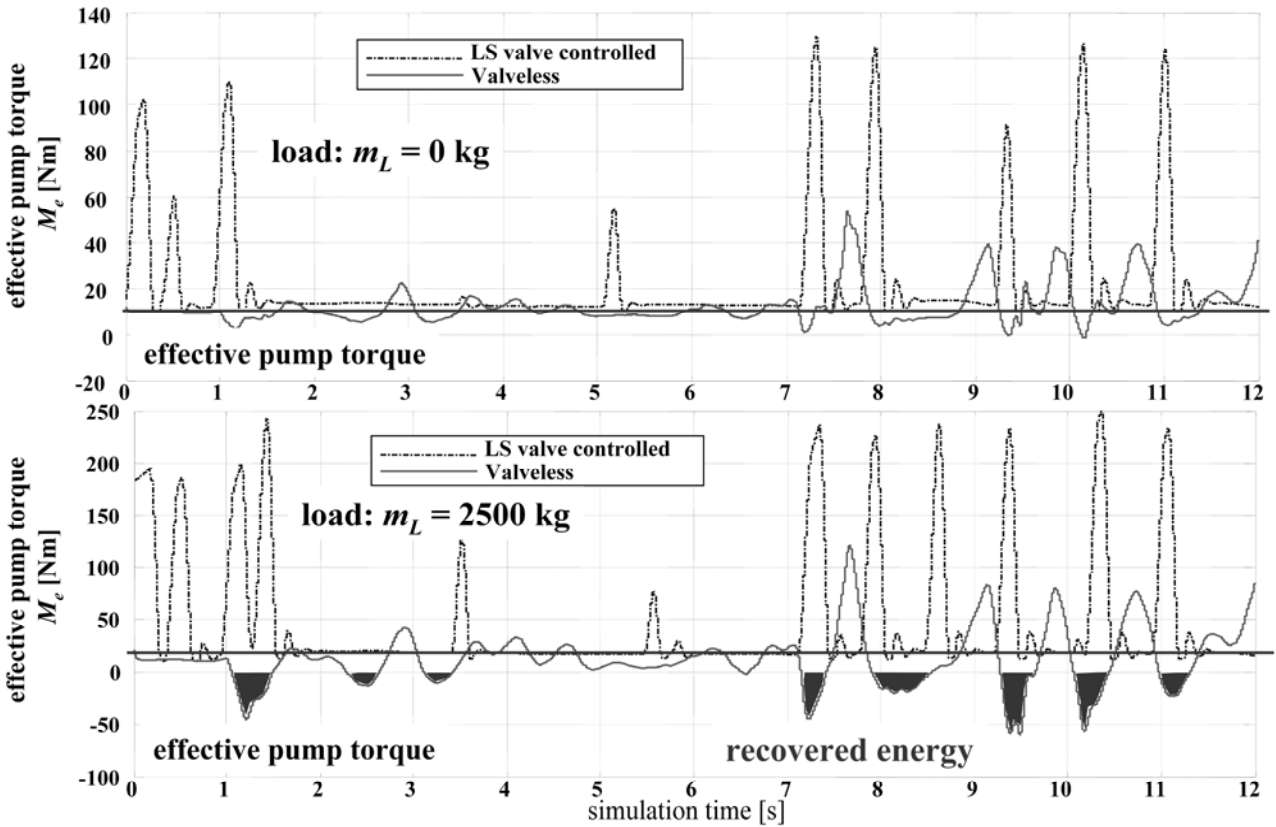


Fig. 47: Effective pump torque, two load cases (0 ton and 2.5 ton)

Figure 18 demonstrates the amount of primary energy consumed by the two compared system solutions for similar oscillation damping quality both for the position control of the boom structure (black) and parallel acting acceleration control (grey). The additional energy used for active damping is displayed in this graphic as percent of the energy amount used for position control. The amount of

energy saved through recovery in the displacement controlled system is marked in white. In this comparison the energetic advantage of the displacement controlled system – especially for high load – becomes obvious: a lower additional percentage of primary energy is necessary for the damping and a high amount of energy can be reused.

The simulation results for the three load cases reveal the energy amount for the simulation cycle as:

Load Sensing valve controlled

unloaded:	position control:	37.5 kJ
	acceleration control:	12.3 kJ (+ 33%)
2.5 ton load:	position control:	65.8 kJ
	acceleration control:	35.9 kJ (+ 55%)

Displacement controlled (valveless)

unloaded:	position control:	22.0 kJ
	acceleration control:	6.8 kJ (+ 31%)
	recovered energy:	0.0 kJ (0%)
2.5 ton load:	position control:	26.7 kJ
	acceleration control:	13.5 kJ (+51%)
	recovered energy:	-12.4 kJ (92%)

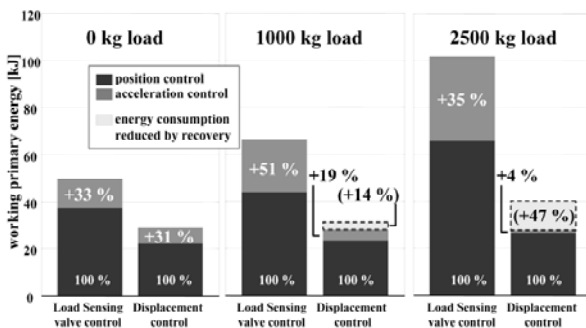


Fig. 18: Consumption of primary energy for position and acceleration control, valve control vs. displacement control

8 - SUMMARY AND CONCLUSION

To analyze the energetic behaviour of the two different drive concepts – load sensing valve control and displacement control – the loss behaviour of the hydraulic components of each system has been modelled and a four quadrant loss model for the hydraulic pump has been created. The models have been used in combination with extensive non-linear models of the dynamic behaviour of the hydraulic and the mechanic system to simulate two different system concept providing comparable damping quality. The simulations based on measurement results were used for an analysis of the energetic behaviour. A comparison could be carried out revealing strong advantages of the displacement controlled actuator especially for high load masses. The ability of a displacement controlled system to recover energy allows the system to reuse a large amount of the energy used to actively damp the boom structure by running the pump in motoring mode. For the first time this has been simulated to this extend.

In a valve controlled system providing similar damping quality not only is more energy consumed during the damping, all energy lost at the valve is converted into heat energy. This energy has to be transferred out of the system

with additional cooling and thereby additional energy consumption. This investigation proves why valve controlled active damping has not been implemented in series production off-road machines.

REFERENCES

- Berger, A. D. and Patel, K. B.** 1999. Active Ride Control System for Off-road Vehicles. *US Patent No. 5.897.287.*
- Drake, F. J. and Jaecks, B. K.** 1991. Hydraulic System for a Wheel Loader. *US Patent No. 5.195.864.*
- Frediani, S., Gianoglio, R. and Weber, J.** 2003. Electro Hydraulic Active Ride Control. *4. IFK (4th Int. Fluid Power Conference)*, pp. 129-138, Dresden, Germany.
- Hosseini, J.** 1992. Automatic Ride Control. *US Patent No. 5.147172.*
- Latour, Ch. and Biener, R.** 2002. Comparison of active and passive oscillation suppression systems for wheel loaders. *3. IFK (3rd Int. Fluid Power Conference)*, T4 Vol. 2, pp. 101-112, Aachen.
- Patel, K. B., Lin, H. C., Berger, A. D., Farag, W. and Khan, A. A.** 1999. EDC Draft Force Based Ride Controller. *US Patent No. 6.196.327.*
- Rahmfeld, R.** 2002. *Development and Control of Energy Saving Hydraulic Servo Drives for Mobile Systems.* Doctoral thesis TU Hamburg-Harburg (Germany), Vol. 12, No. 527, VDI-Verlag, Düsseldorf, Germany.
- Rahmfeld, R. and Ivantysynova, M.** 2003. New Displacement Controlled Linear Actuator Technology – a Suitable Control Element for Active Oscillation Damping. *The 8th Scandinavian Inter-national Conference on Fluid Power (SICFP'03)*, pp. 1139-1154, Tampere, Finland.
- Rahmfeld, R., Ivantysynova, M. and Eggers, B.** 2004. Active Vibration Damping for Off-Road Vehicles using Valveless Linear Actuators. *SAE Commercial Vehicle Engineering Congress and Exhibition, Chicago, USA.*
- Rahmfeld, R., Ivantysynova, M. and Weber, J.** 2004. Displacement Controlled Wheel Loader – a simple and clever Solution. *4th IFK (Int. Fluid Power Conference)*, pp. 183-196, Dresden, Germany.
- Ufheil, S. and Rector, S. W.** 1996. Programmable Ride Control. *US Patent No. 5.520.499.*

EXPERIMENTAL STUDY ON THE PERFORMANCE ESTIMATION EFFICIENCY MODEL OF A HYDRAULIC AXIAL PISTON MOTORS

Dong-Soo JUNG*, Hyoung-Eui KIM*, Heon-Sul JEONG**, Bo-Sik KANG*
Yong-Bum LEE*, Jong-Ki KIM* and E-Sok KANG***

* Mechanical System Reliability Research Group,
Korea Institute of Machinery and Materials
Yusung P.O Box 101, 171 Jang Dong, Yu Sung Gu, Taejun, Korea, 305-600
(E-mail: jds667@kimm.re.kr, khe660@kimm.re.kr, kbs668@kimm.re.kr, lyb662@kimm.re.kr,
bellflag@kimm.re.kr)

** School of Mechanical Engineering,
Kunsan National University
Miryong-dong #68, Kunsan, Chonbuk, Korea 573-701
(E-mail: hsjeong@kunsan.ac.kr)

***Department of Mechanical Design Engineering,
Chungnam University
220 Kung-dong, Yuseong-gu, Daejeon, Korea 305-764
(E-mail: eskang@cnu.ac.kr)

ABSTRACT

Performance of a hydraulic piston motor is very difficult to estimate in advance before experiment. But it is highly required because, if an efficiency model for performance estimation is already in hands, the model enables one to design a hydraulic motor with good efficiency at a designated operating point. Recently such a performance estimation model is developed by H.S. Jeong. In this paper, validity and accuracy of the performance model is studied by comparison with experimental efficiency test data.

KEY WORDS

Hydraulic Axial Piston Machine, Performance Estimation Model, Volumetric Efficiency, Mechanical Efficiency, Leak Flow Rate

NOMENCLATURE

C_{DVN} : discharge coefficient of valve notches
 C_{DPP} : discharge coefficient of piston ports
 C_{wSP} : discharge coefficient of shoe and pistons

f_p : equivalent friction coefficient of a piston
 f_{pBr} f_{vBr} : friction coefficient of bearings
 h_p : gap height between piston and cylinder
 h_s : gap height of slipper and swash plate

h_v : gap height of valve plate and cylinder block
 Q_L : leak flow rates of each parts
 M_L : loss moments of each parts
 n : rotational speed of a motor in rev/min
 V_g : geometrical displacement of a hyd. motor
 μ : viscosity of hydraulic oil
 η_v, η_{hm} : volumetric, hydro-mechanical efficiency

INTRODUCTION

The hydraulic system is used variously for construction heavy equipment, vehicle, ship, aircraft and so on. Because it has a great amount of power per load by unit and is easy to transfer the large amount of power and it is good to realize linear and rotational motion easily. The system consists of hydraulic pump generating hydraulic power and hydraulic motor converting hydraulic energy into mechanical power. These 2 components are the core element determining the efficiency of whole system.

These hydraulic components are usually operated under the unique condition, rotating speed and torque or pressure. Therefore, it is very important to select or build hydraulic pump and motor which have a high efficiency for organizing hydraulic system in the view point of energy consumption.

However, unique efficiency character and maximum efficiency point are determined for the model presented from manufacturers. Normally, it needs high cost and long time to develop new hydraulic pump and motor which have the maximum efficiency in the working point required for the object system.

But the requirement of hydraulic power representing the high efficiency is still unchanged in the each using area. For solving this problem, the research of estimation of efficiency characteristics for hydraulic system has been progressed in the design stage of hydraulic pump and motor by Europe and Korea.

This paper tries to analyze propriety, accuracy and effectiveness of efficiency estimation model from the result data of 36cc/rev hydraulic motor for the new efficiency estimation model of hydraulic piston motor.

The preceding studies for the subject are as follows.

- 1) 'Preliminary design of a hydraulic piston motor for achieving an user-defined optimal efficiency point (by Heon-Sul Jeong)
- 2) 'On the Instantaneous and Average Piston Friction of Swash Plate Type Hydraulic Axial Piston Machines (by Heon Sul Jeong and Hyoung Eui Kim).

1. MEASURE OF LOSS AND EFFICIENCY OF HYDRAULIC MOTOR

1.1 VOLUMETRIC LOSS AND MECHANICAL

LOSS

Various kinds of losses occur on each element of hydraulic piston motor during rotating and going-returning movement and interaction with flow. These losses could be divided into loss of working oil and the loss of hydro-mechanic. At first, loss of volumetric flow is described as below.

There are three contacting point between piston and cylinder, slipper and slope and cylinder block and valve plate in hydraulic piston motor.

Poiseulli flow leakage which is proportional to the pressure and to the cube of interval is generated through the interval between the movement contacting point

If there is a notch to relieve the pressure variation which is occurred when the piston moves between two ports of valve plate, then internal leakage is generated and this is one of losses. Meanwhile, there is 1% loss of volume in the working oil when the 150 bar of pressure is increased. This compression of fluid has same effect as the reduction of output flow. If the pump is operated with high speed, cavitations could be generated and then it is corresponded to the loss of volumetric flow

On the other hand, the examples of hydro-mechanical losses are as follows. Fluid lubrication film is formed at the contacting point and it has relative movement so that Newtonian flow is generated which is in proportional to speed and inverse proportional to the interval. The loss between piston and cylinder has Coulumb friction characteristics in proportional to the pressure variation. The slight loss of pressure is one of hydro-mechanical losses occurred when the piston moves to piston chamber through the two ports on the valve plate. Also churning loss generated because cylinder block and slipper in the housing filled with working oil rotates at high-speed and losses came out from the bearing installed at front and rear on input and output axis. They are also hydro-mechanical losses.

1.2 MEASUREMENT OF EFFICIENCY

For the measurement of efficiency of hydraulic motor, after realizing working area with wide range, rotating speed n and pressure variation Δp , in accordance with the definition of volumetric efficiency and mechanical efficiency, we shall measure 6 physical quantities like M, n, Q_1, Q_2, p_1, p_2 in each working condition.

But, there are some considerations and problems for measuring and analyzing the subject motor by using this method. First, we need to calculate displacement V_i from the measured data. We can get displacement V_i as inclination of output flow when the speed is increased under the $\Delta p = 0$ condition. But we can also

derive it from the efficiency measurement data. If the displacement V_i is miscalculated, the efficiency could be over 100%. Secondly, external leakage flow Q_{Le} is correlatively small so that flow meter with small capacity is needed. Simply, we can suppose $Q_{Le} = Q_1 - Q_2$ but it is difficult to use $Q_1 - Q_2$ as a leakage flow due to the limitation of resolution of flow sensor. Third, in the case of calculating the volumetric efficiency, it is one of trifle things to decide if Q_1 or $Q_2 + Q_{Le}$ or $n \cdot V_i + Q_{Le}$ as input flow. This is a problem related to the accuracy of flow meter used in

2.1 EXISTED EFFICIENCY MODEL

Mathematical model of hydraulic pump and motor is recognized as one of important fields in hydraulic engineering. Because, it is important to simulate the dynamic characteristics of hydraulic system and it is essential to perform the most suitable design of system function.

The model describing the efficiency in the working area $n - \Delta p$ is divided into polynomial model and performance coefficient model. Polynomial model is often used for representing the efficiency test data of the existed pump and motor mathematically. It expresses

Table 1 Models of leakage flow and torque loss of hydraulic pump

Wilson	$Q_p = \varepsilon_p V_p n_p - C_s \frac{V_p \Delta p}{2\pi\mu} - Q_R$ $M_p = \varepsilon_p \frac{V_p \Delta p}{2\pi} + C_f \frac{V_p \Delta p}{2\pi} + C_d \mu V_p n_p + M_c$
Schlosser	$Q_p = \varepsilon_p V_p n_p - C_s \frac{V_p \Delta p}{2\pi\mu} - C_{St} V_p^{2/3} \sqrt{\frac{2\Delta p_p}{\rho}}$ $M_p = \varepsilon_p \frac{V_p \Delta p}{2\pi} + C_f \frac{V_p \Delta p}{2\pi} + C_d \mu V_p n_p + C_h \frac{\rho V_p^{5/3} n_p^2}{4\pi}$
Thoma	$Q_p = \varepsilon_p V_p n_p - C_s \frac{V_p \Delta p}{2\pi\mu}$ $M_p = \varepsilon_p \frac{V_p \Delta p}{2\pi} + C_f \frac{V_p \Delta p}{2\pi} + C_d \mu V_p n_p + Ch \frac{\rho V_p^{5/3} n_p^2}{4\pi} + \frac{V_p p_c}{2\pi}$
Zarotti & Nevegna	$Q_p = \varepsilon_p V_p n_p - C_1 p_p - C_2 p_p^2 - C_3 p_p^2 n_p^{1.5} - C_4 p_p n_p (C_5 + \varepsilon V_p)$ $M_p = \varepsilon_p p_p V_p + n_p (C_1 + c_2 \varepsilon_p n_p) + C_3 p_p (1 + \frac{C_4 \varepsilon_p^2}{\sqrt{p_p}} + \frac{C_5 (\varepsilon_p + C_6)}{n_p + C_7}) + \frac{C_8}{(n_p + C_9)}$
Dorey	$Q_p = \varepsilon_p V_p n_p - C_s \frac{V_p \Delta p}{2\pi\mu} - \frac{p_p n_p V_p}{\beta} (V_r + \frac{1 + \varepsilon_p}{2})$ $M_p = \varepsilon_p p_p V_p + C_v^* \mu n_p V_p + C_f^* p_p V_p$
Ryberg	$Q_p = \varepsilon_p V_p n_p - C_s \frac{V_p \Delta p}{2\pi\mu} - a_0 \varepsilon_p V_p n_p - (a_1 + a_2 \varepsilon_p) \frac{V_p n_p \Delta p_p}{\beta} - a_4 V_p \Delta_p^2$ $M_p = \varepsilon_p \frac{V_p \Delta p}{2\pi} + (b_0 + b_1 \varepsilon_p) \frac{V_p \Delta p}{2\pi} + (b_2 + b_3 \varepsilon_p) \frac{V_p p_L}{2\pi} + b_4 \frac{ p_h + \delta p_L }{1 + (n_0 / n_{p0})^\gamma} \frac{V_p}{2\pi}$

Meanwhile, it is easy to realize $n - \Delta p$ condition as lattice type of regular space for understanding the efficiency characteristics according to the working area. However, this way needs much efforts to realize the working area which has exactly equal space. Therefore, it is good alternative plan to treat the measurement data by 3-dimension curve fitting method.

2. EFFICIENCY MODEL OF HYDRAULIC MOTOR

the efficiency by polynomial equations with speed.

n and pressure difference Δp as an independent variable. In case of variable volume type, volumetric ratio $\varepsilon = V / V_{\max}$ is selected as an additional factor.

Polynomial model is determined by the test data but performance coefficient model is the model that characteristics coefficient is achieved from the test data in mathematical formula based on the physical law. A number of efforts has been progressed to make the exact efficiency model from the wide-range working area

since Wilson established the model for leakage flow and moment loss in 1948. Huhtala has read that unfortunately he couldn't find any sufficient efficiency coefficient model after comparison of accuracy and merits and demerits of each model in the range of speed 500~3000 rpm and pressure 20~210 bar in the existed efficiency coefficient model shown as table 1.⁵⁾

2.2 NECESSITY OF EFFICIENCY MODEL FOR PERFORMANCE ESTIMATION

The efficiency model for performance estimation is the model that can estimate the working condition of given pump and motor, that is, efficiency in the speed and pressure. It should satisfy two conditions to be a useful efficiency estimation model. At first, the accuracy of efficiency estimation must be guaranteed in the working area. And moreover, the efficiency coefficient should be expressed as measurable dimensions of pump and motor.

The secure of guaranteed efficiency estimation model means that the efficiency characteristics can be estimated from the origin of pump and motor, so that it also means that we can estimate the efficiency of pump and motor in the designing stage without test. Finally, it has an important point that we can design the pump and motor which have a good efficiency at the point of working condition of object system.

2.3 NEW DEVELOPED EFFICIENCY MODEL FOR PERFORMANCE ESTIMATION

Under this condition, it can be summarized as follows.⁶⁾ After analyzing the physical law and the construction of piston motor, derived leakage flow and friction loss torque are as follows.

$$\begin{aligned} Q_L &= Q_{L\mu} + Q_{L\rho VN} + Q_{L\rho PP} + Q_{Lc} + Q_{L0} \\ &= C_{\mu}\Delta p / \mu + C_{\rho VN}\sqrt{\Delta p / \rho} + C_{\rho PP}\rho n^3 / \Delta p \\ &\quad + zC_c n\Delta p / \beta + Q_{L0} \end{aligned} \quad (1)$$

$$\begin{aligned} M_L &= M_{L\mu} + M_{L\rho VN} + M_{L\rho PSP} + M_{Lp} + M_{L0} \\ &= K_{\mu}\mu n + \frac{C_{\rho VN}}{2\pi}\Delta p\sqrt{\frac{\Delta p}{\rho}} / n + K_{\rho PSP}\rho n^2 \\ &\quad + K_p\Delta p + K_{p2}\Delta p^2 + M_{L0} \end{aligned} \quad (2)$$

Meanwhile, the definition of volumetric efficiency and mechanical efficiency of general hydraulic motor is like this,

$$\begin{aligned} \eta_v &= \frac{Q_{th}}{Q_{th} + Q_L} \\ &= \frac{V_g n}{V_g n + (Q_{L\mu} + Q_{L\rho VN} + Q_{L\rho PP} + Q_{Lc} + Q_{L0})} \end{aligned} \quad (3)$$

$$\eta_{km} = \frac{V_g \Delta p / 2\pi - (M_{L\mu} + M_{L\rho VN} + M_{L\rho PSP} + M_{Lp} + M_{L0})}{V_g \Delta p / 2\pi}$$

Therefore, the revised efficiency estimation model can be summarized as following two equations

$$\eta_v = \frac{V_g n}{V_g n + C_l \Delta p + C_{iN}\sqrt{\Delta p} + C_{ip}n^3 / \Delta p + C_c n \Delta p + Q_{L0}} \quad (4)$$

$$\eta_{km} = \frac{V_g \Delta p / 2\pi - K_{ip}n^2 - K_{iN}\Delta p\sqrt{\Delta p} / n - K_v n - K_p \Delta p - k_{p2}\Delta p^2 - M_{L0}}{V_g \Delta p / 2\pi} \quad (5)$$

According to the efficiency estimation model as mentioned above, characteristics coefficient of leakage flow like $C_{\mu}, C_{\rho VN}, C_{\rho PP}, zV_c, Q_{L0}$ and characteristics coefficient of loss torque like $K_{\mu}, K_{\rho VN}, K_{\rho PSP}, K_p, K_{p2}, M_{L0}$ are expressed by 11 efficiency characteristics coefficients.

2.4 FACTORS DETERMINING EFFICIENCY

11 characteristic coefficients of the equation (5) ~ (6) in the efficiency model are not be indicated because of the paper's limitation. However, with the standard dimensions, the efficiency characteristics are dominated by the following 14 efficiency determination factors.

Table 2 Factors determining efficiency

Factors Category	Factors Symbol
Interval of movement contacting point	h_p, h_s, h_v
Friction coefficient	$f_{Pi}, f_{P0}, f_{pBr}, f_{vBr}$
Flow coefficient	$C_{DVN}, C_{DPP}, C_{wSP}$
Etc.	$V_{Pmax}, K_{p2}, Q_{L0}, M_{L0}$

Meanwhile, viscosity and density of hydraulic oil and volumetric elasticity coefficient can be changed into equations expressed by 7 characteristic coefficients as follows.

$$\mu = \mu_0 e^{\gamma_{PP}} e^{-\gamma_T(T-T_0)} \quad (6)$$

$$\rho = \rho_0 \{1 + \kappa_P p - \kappa_T (T - 4_0)\} \quad (7)$$

$$\frac{\beta}{\beta_0} = \frac{1 + (p_0/p)^{1/\kappa} (V_a/V_F)(\beta/\kappa p)}{1 + (V_a/V_F)} \quad (8)$$

At last, the efficiency of hydraulic motor, that is the volumetric efficiency and the mechanical efficiency are determined by total 14 factors and 7 sub-factors which indicate the characteristics of hydraulic oil.

3. TEST ANALYSIS OF PERFORMANCE ESTIMATION EFFICIENCY MODEL

We compared and analyzed that the estimation data by efficiency test data and performance estimation efficiency model for Jeil Hydraulic JMF 36 piston motor which has 36cc/rev volume.

Comparatively, the density of hydraulic oil and bulk modulus are less effective and the viscosity has a great effect to the efficiency of hydraulic motor. This paper supposes that the efficiency determining sub-factors as characteristic hydraulic oil are foreknown from the proper references related to hydraulic oil.

3.1 RESULT OF EFFICIENCY ESTIMATION

From comparison between the efficiency test data and the efficiency model of equation (5) and (6), supposed 14 efficiency determining factors and the efficiency characteristic coefficients calculated from the factors can be arranged like the following table.

Table 3 Estimated efficiency determining factors and efficiency characteristic coefficient

Efficiency determining factors	h_p [μm]	h_s [μm]	h_v [μm]	f_p 10^{-5}	f_{PBr}	f_{vBr}
	8.3	4.0	10.2	9.20	5.5	0.5
C_{DVN}	C_{DPP}	C_{wSP}	V_{pmax} [cc]	$Kp2$ 10^{-16}	Q_{L0} [LPM]	M_{L0} [Nm]
2.2592	0.5265	0.2647	0.1091	0.0139	-0.258	4.3359
Volumetric efficiency characteristic coefficient	C_μ 10^{-14}	$C_{\rho VN}$ 10^{-8}	$C_{\rho PP}$ 10^{-7}	zV_c 10^{-6}	Q_{L0} [LPM]	
	0.9718	1.7735	3.4461	0.9821	-4.300	
Mechanical Efficiency Characteristic coefficient	K_μ	$K\rho VN$ 10^{-9}	$K\rho PSP$ 10^{-6}	$K\rho$ 10^{-7}	$Kp2$ 10^{-16}	M_{L0} [Nm]
	3.9140	2.8226	1.8906	1.5721	0.0139	4.3359

The error distribution graph which shows the relationship between the measured efficiency and efficiency estimation factors in the table 3 is shown in the Figure 1 and the average and the maximum error also shows very satisfying results like table 4.

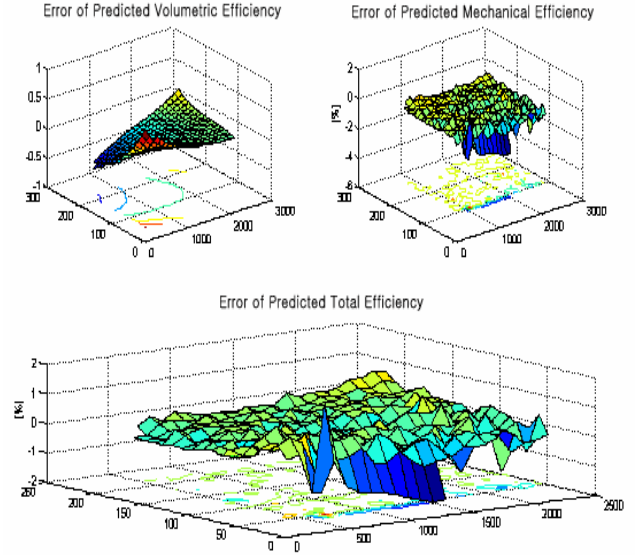


Figure 1 Error percentages of the model on efficiencies

Table 4 Statistics on performance estimation efficiency error

Total efficiency Estimation	Volumetric Estimation	Mechanical Estimation
Average error	Average error	Average error
0.248%	0.291%	0.417%
Total efficiency Estimation	Volumetric Estimation	Mechanical Estimation
Max. error	Max. error	Max. error
2.371%	1.776%	2.880%

3.2 COMPARISON BETWEEN TESTED AND ESTIMATED EFFICIENCY

The comparison between measured efficiency and estimated volumetric efficiency, mechanical efficiency and total efficiency of hydraulic motor from performance estimation efficiency model is shown as Figure 2 ~ 5. We performed the efficiency test by changing pressure and speed. Colored lines indicate pressure values in 'Total efficiency vs. speed' (fig. 2 and 3) and speed values in 'Total efficiency vs. pressure' (fig. 4 and 5). The height of the lines varies according to their values. The lines display 250~50 kgf/cm² of

pressure in fig. 2 and 3 and likewise, the lines display 2,500 ~ 300 rpm of speed in fig. 4 and 5.

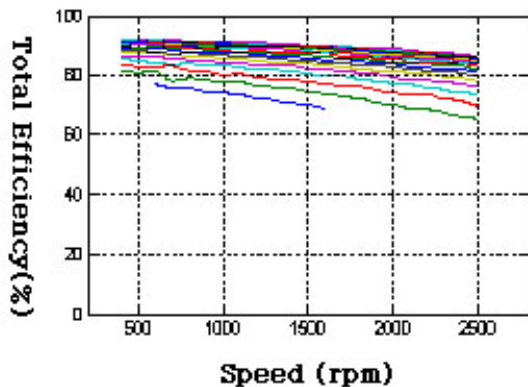


Figure 2 Total efficiency vs. speed(Experiment)

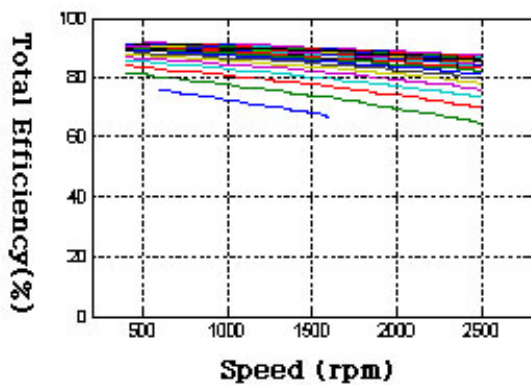


Figure 3 Total efficiency vs. speed(Calculation)

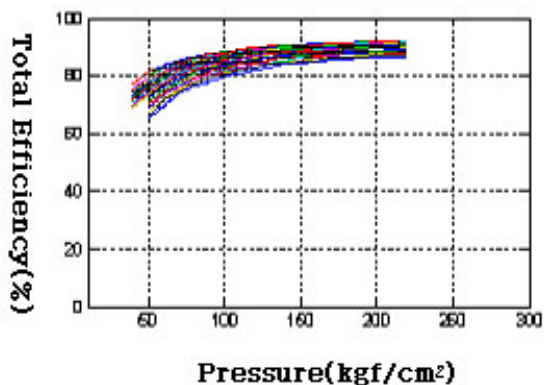


Figure 4 Total efficiency vs. pressure(Experiment)

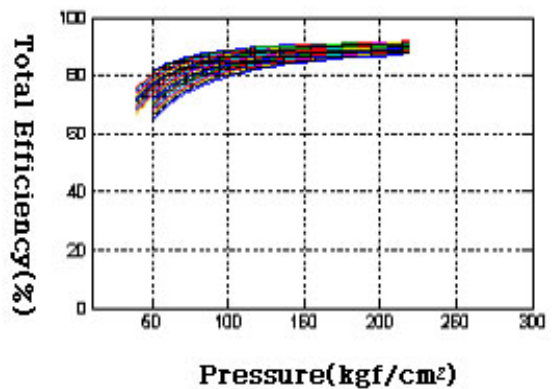


Figure 5 Total efficiency with pressure(Calculation)

As we can see the above diagrams, even though we compared in wide range like 300~2600 rpm speed and 20~270 bar pressure, the efficiency value of each point can be estimated very precisely and at the total point as well.

Meanwhile, we can get the following diagram, if we compare the leakage flow and the friction loss torque used in the working area.

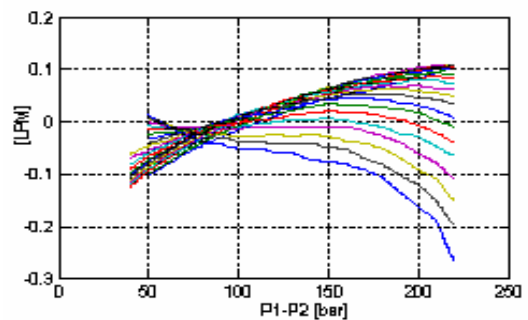


Figure 6 Predicted error of leakage flow with pressure

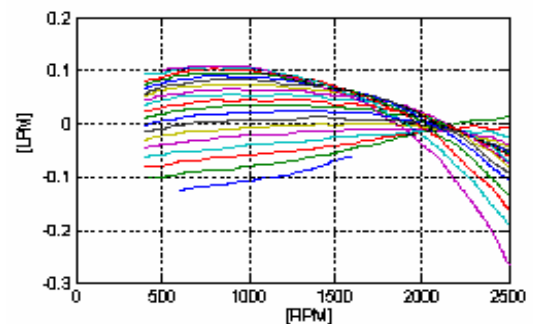


Figure 7 Predicted error of leakage flow with speed

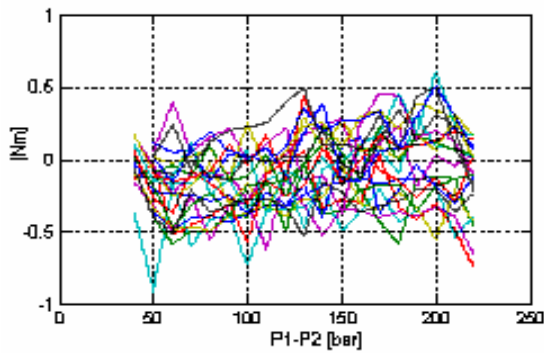


Figure 8 Predicted error of torque loss with pressure

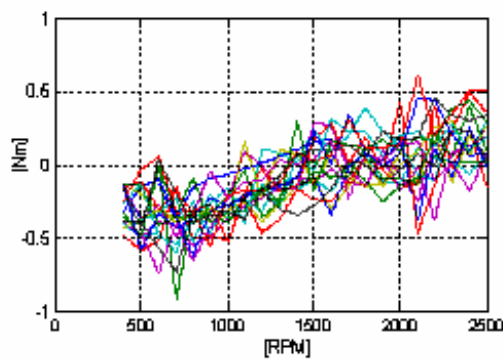


Figure 9 Predicted error of torque loss with speed

As we see in the diagram 5, the average of leakage flow and the maximum error are respectively 0.128 LPM and 0.368 LPM. And the average of losing torque and the maximum error are respectively 0.428 Nm and 2.461 Nm. They show a good result.

Seeing this, we can say that propriety and utility of performance estimation efficiency model in equation (5) and (6) are confirmed by experiments.

CONCLUSION

It is thought that hydraulic pump and motor must pass the efficiency test because, there was no efficiency model for hydraulic pump and motor which has accuracy in the wide working range.

But for designing of hydraulic system which has a good efficiency, the necessity of the performance estimation model from the design stage has been proposed for a long time.

Under this situation, this paper analyzed the propriety and utility of performance estimation efficiency model from test data of 45 cc/rev hydraulic motor for various types of losing elements and new developed performance estimation efficiency model.

The efficiency characteristics of this new model are determined by total 14 efficiency determining factors with the basic dimensions of pump and motors. And after comparing the test data and the performance estimation model from the new developed model at the rotating speed 300~2600 rpm and pressure 20~270 bar, we got the good result of average estimation as 0.248% and the maximum error as 2.37%.

These results are just assumption of efficiency determining factors to get the nearest result to the test data for estimated efficiency so that we can anticipate that it is possible to secure the performance estimation efficiency model.

Henceforth, if we have more elaborative model and make a database of efficiency determining factors from test data, we suppose that we can estimate the efficiency of pump and motor in the near future. Furthermore, we assume that it is possible to design and manufacture the most effective piston pump and motor in the various working condition.

REFERENCES

1. Heon-Sul Jeong, Preliminary design of a hydraulic piston motor for achieving an user-defined optimal efficiency point, 1st Int. Conf. on Computational Methods in Fluid Power Technology, Melbourne Australia, 26-28 November 2003
2. H.-S. Jeong, H.-E. Kim, On the Instantaneous and Average Piston Friction of Swash Plate Type Hydraulic Axial Piston Machines, KSME Int. J., Vol. 18, No.10, 2004. 10.
3. J. Ivantysyn, M. Ivantysynova, Hydrostatic Pumps and Motors, Akademia Books Int., ISBN 81-85522-16-2, 2001
4. W. E. Wilson, Performance criteria for positive displacement pumps and fluid motors, ASME Semi-annual Meeting 1948, paper No. 48-SA-14
5. Kalevi Huhtala, Matti Vilenius, Comparison of steady state models of hydraulic pump, 5th Scandinavian International Conference on Fluid Power, Linkoping, Sweden, 1997
6. Heon-Sul Jeong, Research on simulation and optimization program of hydraulic HST, NRL project 2nd year report of entrusted research project, Korea Institute of Machinery and Materials, 15 June 2004

Downsizing of Oil Reservoir by Bubble Eliminator

Ryushi SUZUKI *, Yutaka TANAKA **

* Opus System Inc.

3-18-7 Asagayaminami, Suginamiku, Tokyo 166-0004, JAPAN

(E-mail: rsuzuki@opussystem.com)

** Department of Art and Technology, Faculty of Engineering

Hosei University

3-7-2, Kajinocho, Koganeishi, Tokyo 184-8584, JAPAN

(E-mail: y_tanaka@k.hosei.ac.jp)

ABSTRACT

In mobile hydraulic systems such as commercial vehicles, hydraulic fluids are splashed and agitated in the reservoirs. To overcome air entrainment in oils, the overall dimensions should enclose a sufficient volume of oil to permit air bubbles to escape passively during the resident time of the fluid in the reservoir. However, in view point of environmental compatibility, energy saving, cost saving and safety, one trend in fluid power systems is to be designed in a more compact fashion and requiring less fluid in the reservoir. One of the authors has developed a newly device using swirl flow for bubble elimination capable of eliminating bubbles and of decreasing dissolved gases. This device is called the bubble eliminator. In this paper we focus on the technical issue of oil degradation for the air bubbles and oil temperature rise in the reservoir of a test hydraulic circuit. In our experiments, surrounding air is intentionally introduced from the oil surface by vibration of the reservoir in the hydraulic circuit. The bubble eliminator solves many problems concerning the air entrainment in hydraulic systems.

KEY WORDS

Aeration, Bubble eliminator, Mobile hydraulic system, Oil degradation, Swirl flow

INTRODUCTION

In recent years we are facing technical issues pertaining to environmental protection and energy conservation in fluid power systems. Because the earth is warming up and the cost of energy rising, we have to make a paradigm shift in design concept in fluid power technology. Engineers often times overlook problems caused by bubbles in fluids. Bubbles in operating fluids greatly affect the performance of fluid power systems and sometimes cause major problems [1]. For instance, temperatures of fluid with bubbles increase

significantly when the fluid is compressed and passes through pumps [2]. Therefore, it is important to eliminate bubbles from fluids in order to maintain the integrity of high quality products and system.

One of the authors has developed a newly device using swirl flow for bubble elimination capable of eliminating bubbles and of decreasing dissolved gases [3][4]. This device is called the bubble eliminator. In our previous study, we have reported that the developed bubble eliminator is useful for preventing oil temperature rising as a result of bubbles being under low, moderate and high system pressure conditions in the stationary

hydraulic systems [2][5]. It has also been confirmed through experiments and numerical simulation that the bubble eliminator is useful for removing dispersed bubbles from the fluid in stationary fluid power systems.

In mobile hydraulic systems such as commercial vehicles, hydraulic fluids are splashed and agitated in the reservoirs and air is entrained in the hydraulic fluids. To overcome air entrainment in oils, the overall dimensions should enclose a sufficient volume of oil to permit air bubbles to escape passively during the resident time of the fluid in the reservoir. However, in view point of environmental compatibility, energy saving, cost saving and safety, one trend in fluid power systems is to be designed in a more compact fashion and requiring less fluid in the reservoir.

In this paper the performance of the developed bubble eliminator concerning the effect of preventing the oil degradation and reducing the oil temperature rise is experimentally investigated. It is experimentally verified that the bubble eliminator can solve many problems concerning the air entrainment in mobile hydraulic systems.

TROUBLES CAUSED BY BUBBLES

Bubbles in fluid power systems are generated when dissolved air is released, external air is introduced mechanically, improper bleeding is made, there is fluid contamination, a reservoir is designed improperly, and/or air vents are improperly installed.

If bubbles are present in hydraulic fluid in a reservoir, they may be sucked into a pump whereby the bubbles will increase in volume due to pressure decrease at the suction line and then be compressed when higher pressure is introduced. When bubbles in the fluid are compressed adiabatically at high pressure the temperature of the bubbles rises significantly and the surrounding fluid temperature also rises. In addition to these well known phenomena, cavitation may lead to formation of reactive chemical intermediates that will affect secondary oxidation. Cavitation occurs when hydraulic fluid pressure is less than the vapor pressure in the fluid.

Bubbles in fluids greatly influence the performance of fluid power systems and may cause various problems such as: broad and high frequency vibration, higher noise emission, cavitation erosion, material damage, thermal degradation of oil [6], acceleration of oil degradation by oxidation [7], oil temperature rise, lubricity reduction by air emulsion [8], reduction of thermal conductivity, increase in compressibility, decrease in dynamic characteristics, decrease in pump output efficiency and bulk modulus change.

Thus, it is important to eliminate bubbles from the fluid

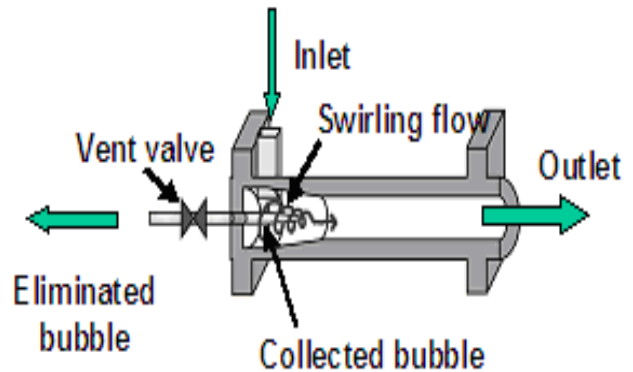


Figure 1 Principle of Bubble Eliminator

in order to preserve quality of fluid, attain sound system performance and avoid damage to components.

BUBBLE ELIMINATOR

Figure 1 illustrates the principle of the bubble eliminator. The device consists of a tapered-tube that is designed such that a chamber of circular cross-section becomes smaller and is connected with a cylindrical shaped chamber. Fluid containing bubbles flows tangentially into the tapered tube from an inlet port and generates a swirling flow that circulates the fluid through the flow passage. The swirling flow accelerates, and the fluid pressure along the central axis decreases as the fluid moves downstream. From the end of the tapered-tube, the swirl flow decelerates downstream and the pressure recovers as the fluid moves to the outlet.

There are certain position-dependent centrifugal forces created in all parts of the swirl flow, and the bubbles tend to move toward the central axis of the bubble eliminator due to the difference in centrifugal force between the fluid and the bubbles. Small bubbles are trapped in the vicinity of central axis of the swirling flow and collected near the area where the pressure is the lowest. When backpressure is applied at the downstream side of the bubble eliminator, the collected bubbles are ejected through a vent port.

The dissolved air in the fluid is also eliminated through bubbles extracted at the pump's suction side under negative pressure [9]. The bubble eliminator has the advantage of a simple structure, a low level of the pressure drop (a few hundred Pa) and of being a passive element without any power supply.

The bubble eliminator has been used in many industrial machines using fluids such as hydraulic systems, food machines and coater machines in paper products [10].

EXPERIMENTAL INVESTIGATION FOR OIL DEGRADATION

We firstly focus on technical issue to eliminate the air bubbles entrained in the oil to preserve oil quality . The oil degradation is accelerated with effective oxygen supply of air, the most influential factor in shortening the life of the oils.

In order to investigate the effectiveness of the developed bubble eliminator experimentally, changes of oil degradation are observed under three different conditions of bubbles for normal pump operating conditions during 96 hours of continuous running.

An experimental circuit of the hydraulic system is illustrated in Figure 2. The oil in a capacity of 5-liter reservoir pressurized by a piston pump flows through a relief valve and returns to the reservoir. The pump delivery flow rate is adjusted at a constant value of 9 liter/min. A relief valve is set at a supply pressure of 7 MPa. The downstream line of the relief valve is divided into two lines. One goes through the stop valve-(3), the bubble eliminator, the stop valve-(5) and an oil cooler to the reservoir. Another goes through the bypass line, in which the stop valve-(2) is incorporated, and the relief valve to the reservoir. A needle valve-(1) at the suction side of the pump is used to introduce external air into the hydraulic circuit. A thermistor type thermometer is installed in the reservoir.

For test, the axial piston pump (Yuken type AR16) is installed. During the test, the oil temperatures are kept at 60 ± 1 centigrade. The test is performed for base stock having viscosity of $32 \text{ mm}^2/\text{s}$. The test conditions are tabulated in Table 1. Different parameters such as the bubble eliminator “With” or “Without” and the air supply “On” or “Off” are set for the given pump delivery conditions. In cases of air supply “on”,

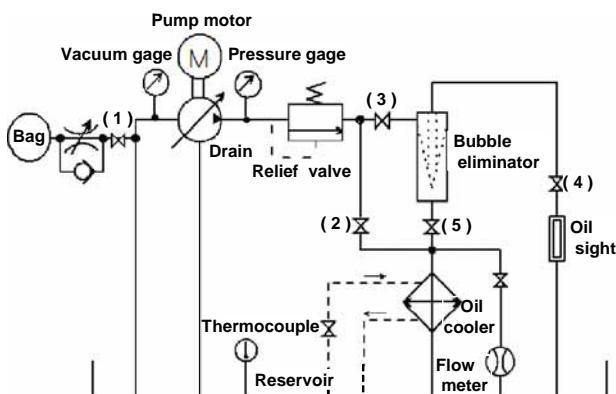


Figure 2 Experimental hydraulic circuit for oil degradation

Table 1 Test conditions

Case	Air supply	Time (Hours)	Bubble Eliminator
A	On	96	Without
B	Off	96	Without
C	On	96	With

660ml/min air is supplied from the pump suction side. To investigate processes of the oil degradation, the following analytical items and their procedure are selected:

- Color (ASTM D1500)
- TAN (ASTM D664)
- Viscosity (ASTM D445 - 3)
- Deposit (Millipore filter).

The changes of the oil property are investigated as a function of the operating time of 96 hours for all the data. Oil specimen is sampled once for every 24 hours. Table 2 to 4 show analytical results of the oil specimens under the test condition cases A, B and C. Figure 3 to Figure 6 show the change of the each analytical data plotted as a function of time.

It should be mentioned that much metal debris is observed in the deposit of the oil in the cases A and B.

Table 2 Performance in Case A

Test case \ Time(hour)	0	24	48	72	96
Color	1.0	0.5	5.0	6.5	7.0
Viscosity(40) [mm ² /s]	31.34	31.36	31.37	31.39	31.42
TAN[mgKOH/g]	0.01	0.01	0.01	0.02	0.03
Deposit[mg/100ml]	1.3	1.1	8.5	7.2	7.1

Table 3 Performance in Case B

Test case \ Time(hour)	0	24	48	72	96
Color	0.5	0.5	1.0	1.0	1.0
Viscosity(40) [mm ² /s]	31.35	31.36	31.37	31.43	31.45
TAN[mgKOH/g]	0.01	0.01	0.02	0.02	0.03
Deposit[mg/100ml]	1.2	2.9	2.7	1.4	1.6

Table 4 Performance in Case C

Test case \ Time(hour)	0	24	48	72	96
Color	1.5	0.5	1.0	2.5	6.5
Viscosity(40) [mm ² /s]	31.36	31.37	31.39	31.41	31.45
TAN[mgKOH/g]	0.01	0.01	0.01	0.01	0.02
Deposit[mg/100ml]	2.7	0.0	1.7	2.3	4.1

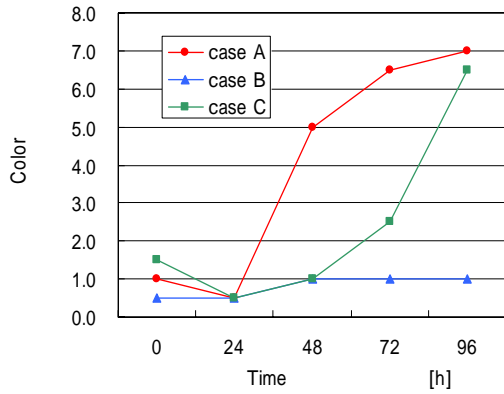


Figure 3 Color change in pump test

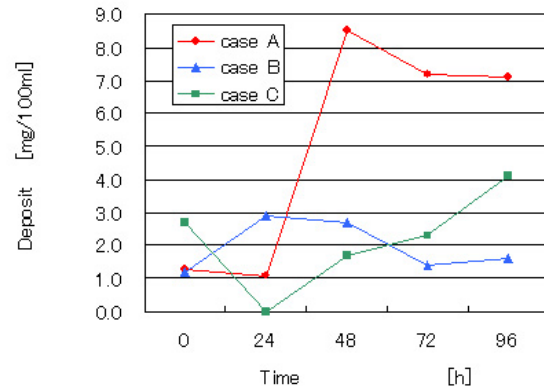


Figure 6 Deposit change in pump test

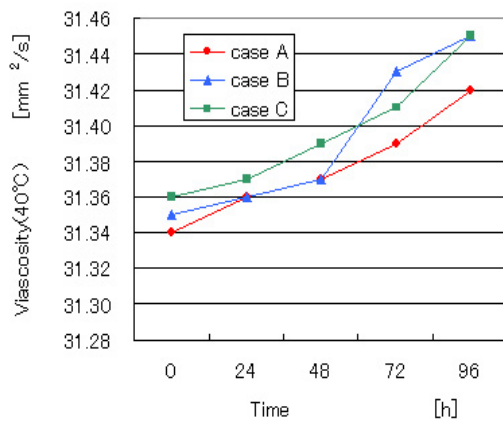


Figure 4 Viscosity change in pump test

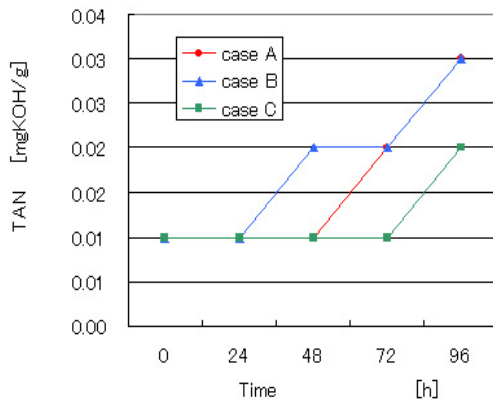


Figure 5 TAN increase in pump test

When bubbles in oil are compressed adiabatically at high pressure, the temperature of the bubbles rises sharply, resulting in generation of carbonaceous particles. Under poor lubricity caused by supplied air, wear debris is created on the boundary surface of the pump parts during pressure build-up.

In the cases A and C, much debris is produced regardless to the application of the bubble eliminator. In

these cases, the bubble eliminator located at the downstream side of the pump is unable to prevent generation of particle and wear debris on the boundary surface of the pump. The test results show clearly that the supplied air accelerate oil degradation and shorten the life of an oil.

The test oil is compressed to 7 MPa by the piston pump and then decompressed with the relief valve to a pressure close to atmospheric pressure then dissolved air is separated to cavitation air. If not removed, eventually cavitation air is compressed adiabatically and can reach high temperature in system.

In the case A, degradation of oil is caused by both supplied air and cavitation air. In the case B, cavitation air accumulated in the oil results in acceleration of oxidation. In the case C, the supplied bubbles together with cavitation air are eliminated and the TAN rise can be prevented as shown in Figure 5. The comparison of the above results leads to the conclusion that the bubble eliminator is useful in making oil life longer.

No significant difference can be observed in the results of the viscosity change as shown in Figure 4. The viscosity change should not be regard as an obvious indication for an advance degradation of oil.

EXPERIMENTAL INVESTIGATION FOR MOBILE CONDITIONS

In this section we focus on technical issue for the relationship between air bubbles in the oil and oil temperature rise in the reservoir. In our experiments, surrounding air is intentionally introduced in the oil from the oil surface by vibration of the reservoir in the hydraulic circuit. An overall experimental setup and the hydraulic circuit for vibration of the reservoir are shown in Figure 7 and Figure 8, respectively. A pump-motor, a reservoir, and the bubble eliminator are located on an active linear table. A hydraulic servo cylinder forcedly vibrates the active linear table in order to infuse air to the oil of the reservoir from surrounding air.

The bubble eliminator in a main line is located in

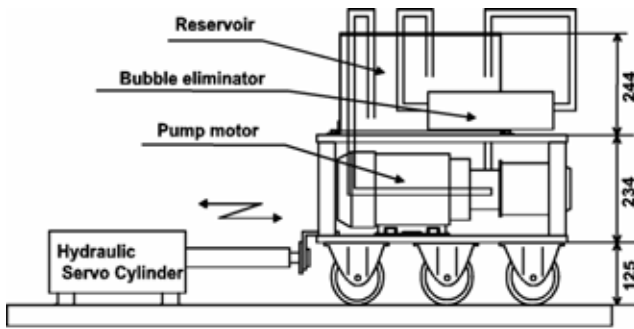


Figure 7 Overall experimental setup

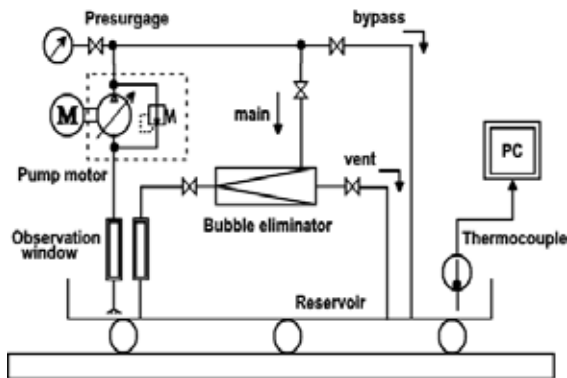


Figure 8 Experimental hydraulic circuit for mobile condition

Table 5 Test conditions for experiments

Case	Vibration Time	Bubble eliminator
A	0 min	Without
B	0 min	With
C	150 min	Without
D	150 min	With

parallel with a normal pipe of a bypass line. The reservoir and observation windows at the suction and return lines are made from transparent acrylic vessel and pipes, respectively. The air bubbles in the oil can be visually observed at the reservoir and the observation windows.

In our experimental hydraulic circuit the average flow rates delivered by the pump are kept at 12 L/min and the reservoir has a capacity of 3 Litter. It is assumed to be 1/20 model of the mobile construction machinery with the pump delivery flow rate of 240 L/min and reservoir capacity of 60 Litter.

The experimental equipment is forcedly vibrated with

the frequency of 1.2Hz and the amplitude of ± 20 mm in order to reproduce working environment of construction vehicles. Test conditions are tabulated in Table 5. There are four conditions A to D. In the case A and B, the experimental setup is not vibrated. In the case C and D, the experimental setup is vibrated during 150 minutes. Under the each condition, the oil temperature in the reservoir is measured by a thermocouple every 5 minutes during 150 minutes.

Typical experimental results of temperature rise in the reservoir are plotted in Figure 9. The temperature data are plotted as the values relative to the initial temperature. In the case A and case C, the oil flows through the bypath line. In the case B and case D, the oil flows through the bubble eliminator in the main line. Since it is considered that the bubbles are eliminated by the bubble eliminator, the oil temperature rise in the case B becomes lower than that in the case A. In the case D, the equilibrium temperature more dramatically decreases than one in the case A. This can be considered that the lower temperature rise is based on the cooling effect by the infused surrounding air and the bubble removal effect by bubble elimination. From these experimental results for measurement of oil temperature rise in the reservoir of the test hydraulic circuit, the bubble eliminator is effective in reducing the oil temperature rise under the mobile condition. The advantage obtained from the use of the bubble eliminator is a reservoir with light weight, smaller space, simpler configuration and lower cost.

CONCLUSIONS

In fluid power systems, air bubbles are the most influential factor to accelerate oil degradation. In this paper, it is experimentally verified that the bubble eliminator can effectively separate bubbles to prevent oil oxidation reactions, for extension of lifetime of oil. The authors have also examined the influence of the air

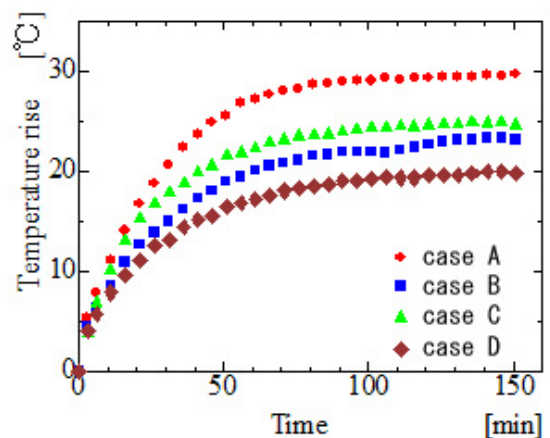


Figure 9 Typical experimental results of temperature rise (Case A, B, C, D)

bubble and the effect of the bubble eliminator to prevent temperature rise through the experimental investigations by using the oil hydraulic system. It is experimentally verified that the bubble eliminator can effectively reduce the oil temperature rise.

It must be borne in mind that the reduction of the entrained bubbles should be considered as one of the important design factors for the fluid power system. Concrete benefits obtained from the use of the bubble eliminator for the systems are:

- A reservoir with lighter weight, smaller space, simpler configuration, lower cost
- Slow fluid degradation, which extends lifetime of fluid
- Prevent pump and valve cavitations and noise
- Decrease in compressibility of oil
- Shorter heating time in cold environment
- Easier contamination control.

ACKNOWLEDGMENTS

The authors wish to thank Idemitsu Kousan Co.Ltd., for the offer of test oil and their valuable assistance with the experiment including measurements for the analytical items of the oil specimens. The contribution to this work provided by a student, Mr. Keiji Baba at the Hosei University is gratefully appreciated and acknowledged.

REFERENCES

1. Totten, G.E., Sun, Bishop, "Hydraulic Fluids: Foaming, Air Entrainment, and Air Release –A Review", SAE Technical Paper No.972789, 1997.
2. Suzuki, R., Tanaka,Y., Yokota, S. "Reduction of Oil Temperature Rise by Use of a Bubble Elimination Device in Hydraulic Systems, J. Society of Tribologists and Lubrication Engineers, 54-3, 1998, 23/27.
3. US Patent No. 5,240,477
4. Suzuki, R., Yokota, S., "Bubble Elimination by Use of Swirl Flow", IFAC Int. Workshop on Trends in Hydraulic and Pneumatic Components and Systems, Poster Paper 2, 1994.
5. Suzuki, R., Tanaka,Y., Yokota,S., "Bubble Elimination Device in Hydraulic Systems", Fluid Power Systems and Technology: Collected Papers ASME 1997, FPST-Vol.4/DSC-Vol.63, 1997-11, 131/135.
6. Matusyama Y., Takesue M., "Introduction of non-sludge type hydraulic fluids", Proc. JHPS International Symp. Fluid Power, 1996, 613/616.
7. Backe, Lipphardt, "Influence of the Dispersed Air on The Pressure", CI Mech. Eng., C97/76, 1976, 77/84.
8. Yano, H. and Yabumoto, J., "Expected Developments of the Bubble Elimination Device for Fluids," Mitsubishi Oil Co. Technical Review, No.76, 1991, 117/126.
9. Yutaka Tanaka, R. Suzuki, "Solution of Air Entrainment for Fluid Power Systems", Proceedings of the 49th National Conference on Fluid Power, IFPE2002, March 19-21, 2002, pp.57-62.
10. Suzuki,R., Tanaka,Y., Arai,K., Bubble Elimination for Coating Material, Proc. TAPPI 2001 Advanced Coating Fundamentals Symposium in San Diego, CL. 2001, 239/247.

Development of Energy Saving Power Steering

Fumihide KOZUMA*, Tsunefumi ARITA** and Hisashi TSUDA***

* Basic Technology Research and Development Center
KAYABA Industry Co., Ltd.

1-12-1 Asamizodai, Sagamihara, Kanagawa, 228-0828 Japan
(E-mail: kouzuma-fum@kyb.co.jp)

** Steering Engineering Department, Gifu North Plant
KAYABA Industry Co., Ltd.

2548 Dota, Kani, Gifu, 509-0298 Japan

*** Steering Engineering Department, Europe Branch
KAYABA Industry Co., Ltd.

Kimpler strasse. 336, 47807 Krefeld, Germany

ABSTRACT

This paper shows the energy saving power steering system, which was named as KEEPS (Kayaba Electronic Controlled Energy Saving Power Steering). In a conventional hydraulic power steering system, the hydraulic pump always supplies enough quantity of oil to the hydraulic circuit. This extra oil flow increases driving torque of the pump, thus the hydraulic power steering system wastes energy. On the other hand, KEEPS can control oil flow electrically in accordance with the condition of a vehicle. In the measurement test for energy consumption of the power steering system with the actual vehicle on test courses, KEEPS got 48% less at city mode, 41% less at highway mode and 39% less at country mode compared with the conventional hydraulic steering system.

KEY WORDS

KEEPS, Hydraulic Power Steering, Energy Saving, Electronic Control

INTRODUCTION

Recently under international environmental problems, saving fuel consumption of an automobile has been required, and the various regulations of fuel consumption have been implemented. These activities of reducing fuel consumption influence on not only engines but also automotive equipments, and high efficiency equipments are required. This situation applies to a hydraulic power steering system too.

In a conventional hydraulic power steering system, the hydraulic pump always supplies enough quantity of oil to the hydraulic circuit. The circuit has hydraulic resistances such as the steering gear and the hose, thus extra oil flow increases pressure loss in the circuit and driving torque of

the pump. As a result, unnecessary energy is consumed. And to improve the energy problem of power steering systems, various systems have been proposed. Those are variable displacement pump, EHPS (Electronic Hydraulic Power Steering), EPS (Electric Power Steering) and so on. The purpose of this paper is to confirm effect of energy saving by the newly developed power steering system.

CONCEPT OF ENERGY SAVING

Figure 1 is one experimental result concerning to the steering occurrence rate at various driving modes. In the city and the highway mode, about 80% of the steering occurrence angle is less than 5 degree. In the country mode, under 5 degree steering angle occupies about 50%

of all.

Figure 2 shows the relationship among driving torque and flow rate of a hydraulic power steering pump at constant pump speed. When flow rate goes to lower, pressure loss in the circuit and driving torque of the pump are decreased.

Therefore it is possible to reduce energy consumption of a hydraulic power steering system, if pressure loss and driving torque can be reduced by minimizing oil flow rate supplied from the pump into the hydraulic circuit in

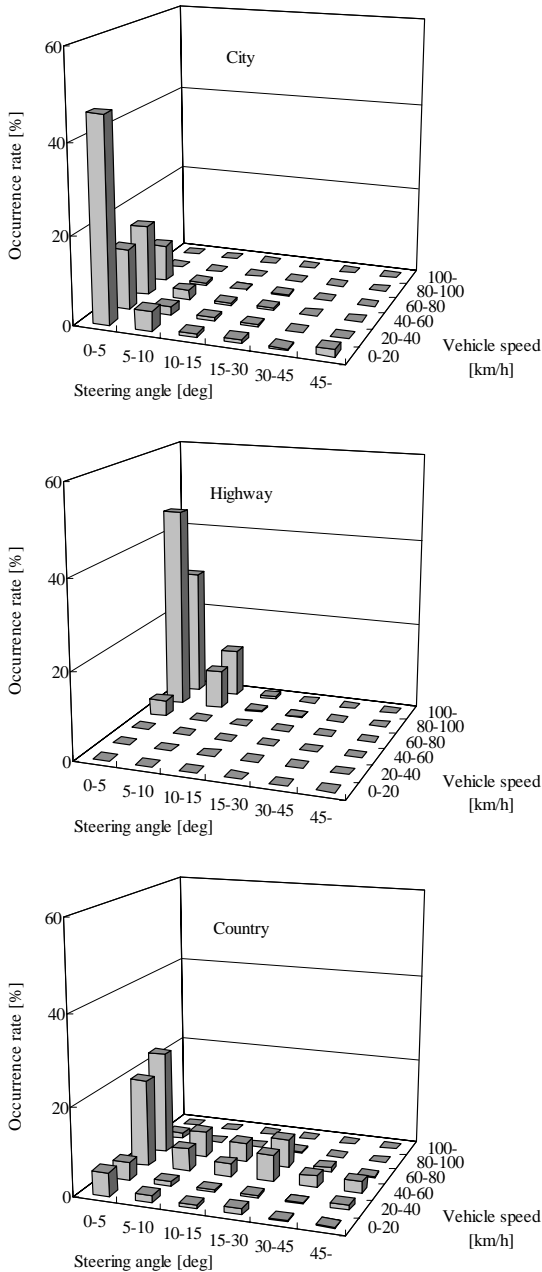


Figure 1 Steering occurrence rate

non-steering or no power assist mode.

SYSTEM CONFIGURATION

As shown in Figure 3, the system of KEEPS mainly consists of a pump assembly, a power steering gear and an electronic control unit (ECU). The pump and the steering gear are used as same as a conventional hydraulic power steering one. A proportional solenoid valve is adopted instead of a flow control valve in the pump assembly. ECU and sensors are newly adopted. Electric current that is defined by ECU controls oil flow rate.

In non-steering or no power assist mode, ECU orders the solenoid valve to close its flow area. Then by-pass flow rate is increased, and main flow rate is decreased approximately to 15% of normal one. Hereby load pressure of the pump is kept lower level and driving torque of the pump is also reduced. Figure 4 shows the comparison of pump driving torque at non-steering mode between a conventional power steering and KEEPS. On the other hand when a driver steers, ECU orders the

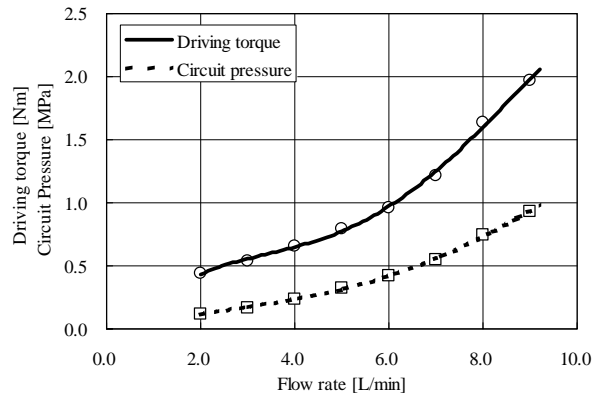


Figure 2 Pump driving torque

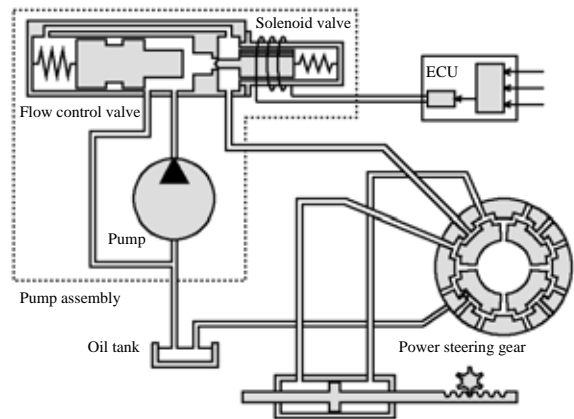


Figure 3 System configuration

solenoid valve to open its flow area and main flow rate is returned quickly to necessary quantity. Thus ECU controls main flow rate according to vehicle condition, KEEPS can realize energy saving and suitable steering feeling at the same time [1].

EXPERIMENTAL TESTS

We have practiced various tests to check the effects of energy saving by KEEPS. Below results were obtained using by the conventional hydraulic power steering system and KEEPS that were designed for the 2000cc-class passenger car.

Power consumption test on bench tester

This test is measurement of power consumption on a power steering bench tester using similar hydraulic circuit of an actual vehicle, and was executed in a European university. The bench tester can reproduce various driving conditions, to give pump speed and load force to steering gear. At the same time the bench tester can provide other information, for example vehicle speed and steering angle, which are necessary to KEEPS ECU. Power consumption

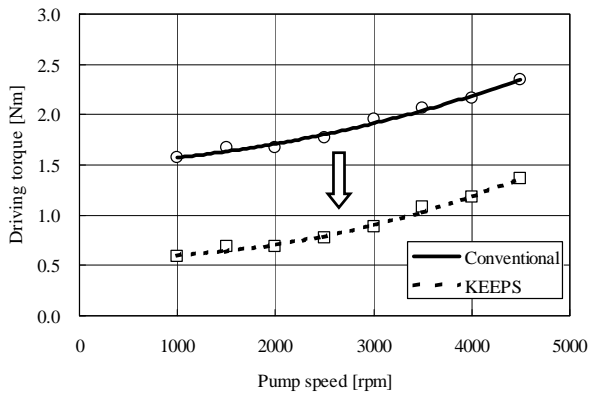


Figure 4 Comparison of driving torque

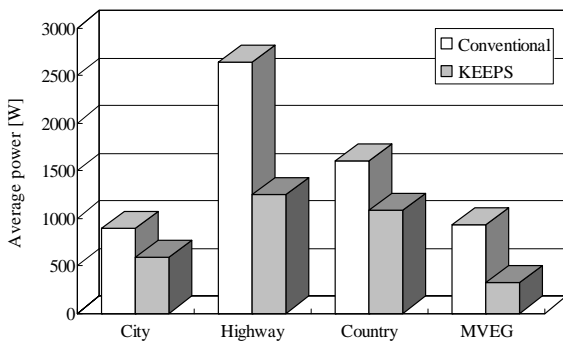


Figure 5 Result of power consumption test

of the power steering system is calculated from pump speed and driving torque measured directly. In this test, KEEPS reduced power consumption by 34% at city mode, 53% at highway mode, 32% at country mode and 66% at MVEG mode test as shown in Figure 5. In these test modes, only MVEG is under non-steering condition.

Fuel consumption test using actual car

This test is investigation of fuel consumption efficiency using an actual car on a chassis dynamometer, and was executed in a Japanese institute. The test on the chassis dynamometer is carried out under non-steering mode. The chassis dynamometer provides the vehicle running resistance according to vehicle speed. During under testing, environment of the vehicle such as temperature

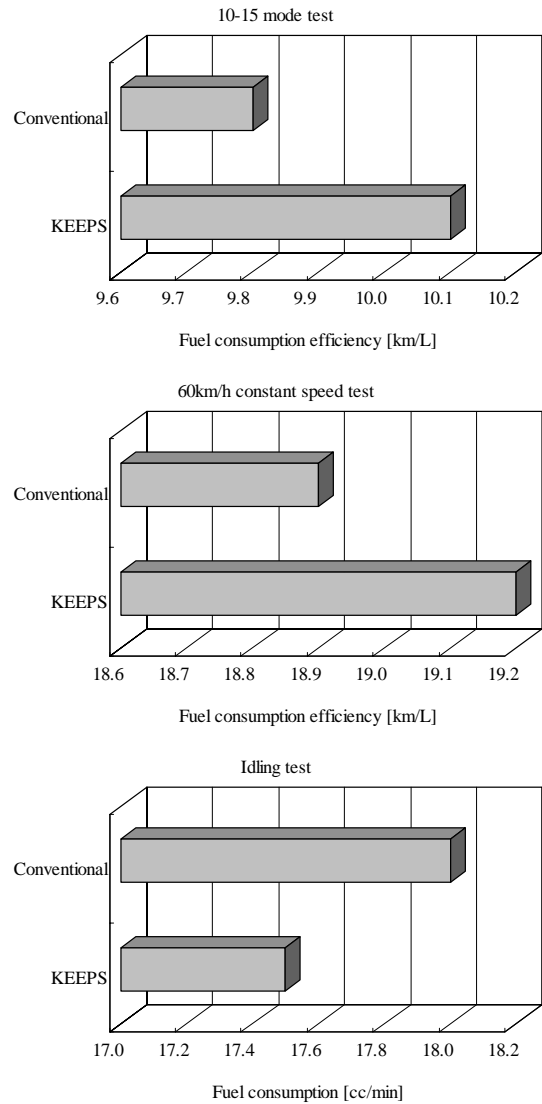


Figure 6 Result of fuel consumption test

and humidity is controlled steadily. Fuel consumption is measured from emission gas by carbon balance method. In this test as shown in Figure 6, KEEPS car got 3.1% improvement of fuel consumption at 10-15 mode test, 1.6% improvement at 60km/h constant speed test and 3.1% improvement at idling test.

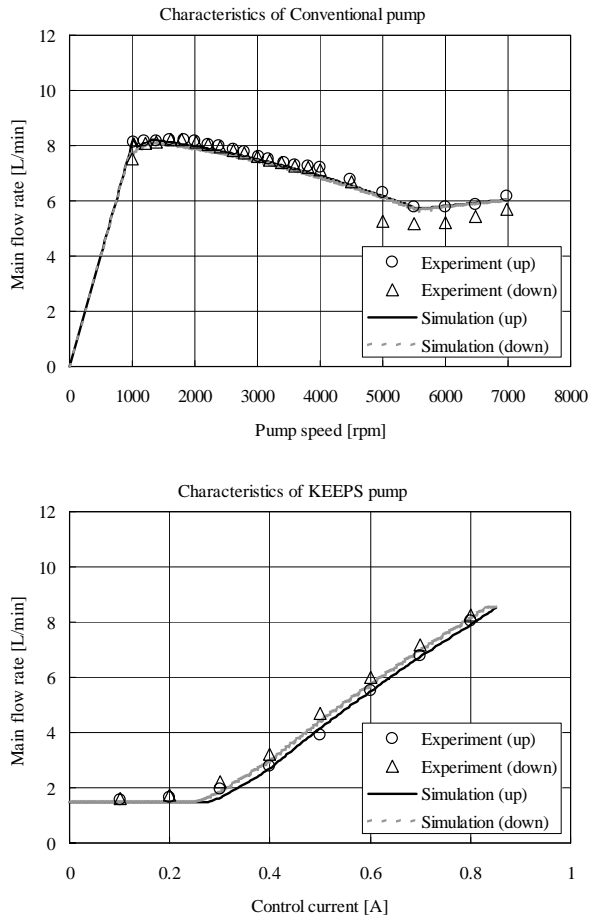


Figure 7 Flow rate characteristics of the pumps

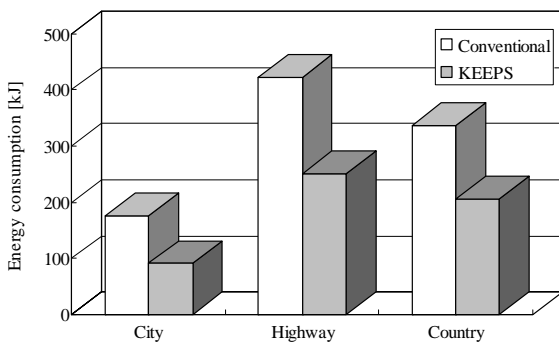


Figure 8 Comparison of energy consumption test results

Energy consumption test on test course

This test is estimation of energy consumption of power steering system, and was executed on test courses with an actual vehicle. Generally it is difficult to measure driving torque of a hydraulic power steering pump on a vehicle. Therefore we measured the mechanical efficiency of the pump before testing, and calculated driving torque, power and energy consumption from vehicle condition such as pump speed and circuit pressure.

On the other hand it is impossible to test or compare for various samples under the strictly same condition of a vehicle. To solve an above problem, we made the simulation program of the hydraulic power steering system. This program consists of mathematical models of a pump assembly, a power steering gear, hoses and ECU (KEEPS). Above elements are considered to dynamics and nonlinear characteristics, and the program can simulate behavior of the hydraulic power steering system to give condition around the system [2].

Figure 7 is the comparisons of the pump characteristics between experimental result and simulative one using the program.

In this test, KEEPS decreased energy consumption by 48% at city mode, 41% at highway mode and 39% at country mode as shown in Figure 8.

CONCLUSION

As above-mentioned, we confirmed effect of reduction of energy or fuel consumption by KEEPS. For example, in the measurement test for energy consumption of the power steering system with the actual vehicle on test courses, KEEPS got 48% less at city mode, 41% less at highway mode and 39% less at country mode compared with the conventional hydraulic steering system.

According to these result and rate of general driving mode [3], it is expected that KEEPS can decrease energy consumption of a hydraulic power steering by about 40-50%.

We will continue to improve KEEPS more as energy saving technology of the hydraulic power steering system.

REFERENCES

1. Takai, M. and Tsuda, H., Electronic Controlled Energy Saving Hydraulic Power Steering 'KEEPS', Kayaba Technical Review, 2002, No.25, pp.34-37
2. Kozuma, F., Simulation of Electronic Controlled Energy Saving Hydraulic Power Steering, Kayaba Technical Review, 2005, No.30, pp.77-81
3. Kabuto, K., Murayoshi, K., and Hashizume, H., Energy Efficient Power Steering Technology, Journal of the Japan Hydraulics and Pneumatics Society, 1993, 24-6, pp.650-657

DEVELOPMENT OF FIELD ROBOT (Steering mechanism and crawler tilting mechanism)

Hamad KARKI, Toshikazu YAMASHITA and Ken ICHIRYU

Department of Mechatronics, Faculty of Engineering
Tokyo University of technology
1404-1 Katakura, Hachioji, Tokyo, 192-0982 Japan
(E-mail: karki@ichry.mech.teu.ac.jp)

ABSTRACT

In many fields, all terrain vehicles are highly demanded with high performance and efficient energy consumption. Some vehicles run on four or six tires, and some vehicles run rubber tracks, called crawlers. In this paper, we will focus on crawlers and their applications. First, we will describe the vehicle's features, and its characteristics. A unique four-wheel-steering Z link mechanism is applied. Crawlers with a tilting mechanism are applied that enables the vehicle to run over steps and obstacles.

KEY WORDS

Four wheel steering, steering mechanism, crawler tilting mechanism

INTRODUCTION

We developed a multi purpose robot that could be applied in many fields, such as construction areas, agricultural areas, and hazardous areas for example landmine fields. Eventually, for every task there is a specific robot or machine, limited with particular features. This field robot has a wide field.

Background

In hazardous areas, man could be injured severely or could lose his life on the field. Therefore, wireless or remote controlling system is necessary to prevent such accidents. Some of these areas are difficult to reach and to proceed with the task. Therefore a new multi purpose field robot has been proposed.

Objective

The main purpose of this research is to develop an efficient and smart steering mechanism. That mechanism gives the robot a flexible structure to run through narrow areas. And undergo any kind of tasks at places with limited amount of space. The development

of the tilting mechanism is one of the objectives of this project. Tilting mechanism is a mechanism that enables the crawlers to incline or decline depending on the ground features. Obstacles such as stones, tree logs or even steps would not stop, or delay the robot from proceeding. Finally, develop a wireless network to control the whole field robot including the steering and tilting mechanism.

FIELD ROBOT FEATURES

Field Robot characteristics outline

The robot is powered by a diesel engine. The engine runs a two axial piston pumps. One of these piston pumps is a hydro static transmission called (HST). The HST drives four hydraulic motors installed to each crawler. On the other hand, the other piston pump drives the steering cylinders and the tilting mechanism. The crawlers could steer 90 degree to the right and 30 degree to the left. Front crawlers are attached to the body by a shaft that it enables the 2 crawlers swing. The whole system (PLCs, servo valves and HST) is controlled by a PC and a controller.



Figure 1 Field robot image

Table 1 Field robot specification

Dimensional Size	2.6/1.5/1.8 m
Wheel Base	1.980 m
tread	1.341 m
Weight	1600 kg
(Power Source)Engine	Ishikawajima Shibaura N843L-SH5(Diesel, 1.7 cc)
Drive	4 Wheel Drive
Transmission	HydroStatic Transmission
Steering	Front/rear independent steering
Steering angle	Right 90, left 30 degree
Undercarriage	Rubber tracks (crawlers)
Suspension	None (Swinging mechanism)
MAX SPEED	3.3 km/h

STEERING MECHANISM

In this robot a Z link steering mechanism is installed. That mechanism enables the four crawlers to rotate 90 degrees to the right and 30 degrees to the left. Thus steering range is 120 degrees. To rotate the crawlers with a hydraulic cylinder a Z link mechanism comes in handy as shown in the following figure.

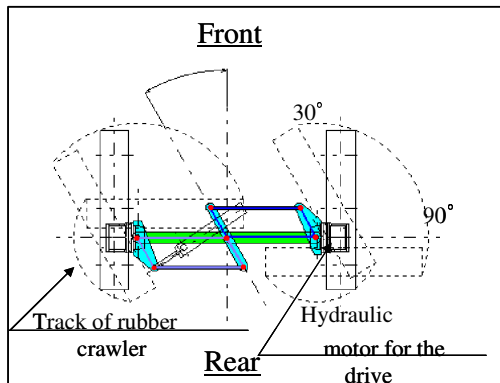


Figure 2 Steering mechanism

Four wheel steering enables the robot to steer its wheels to any direction as shown in the lower figure.

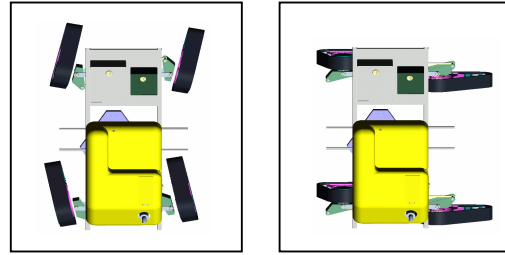


Figure 3 wheel steering applied

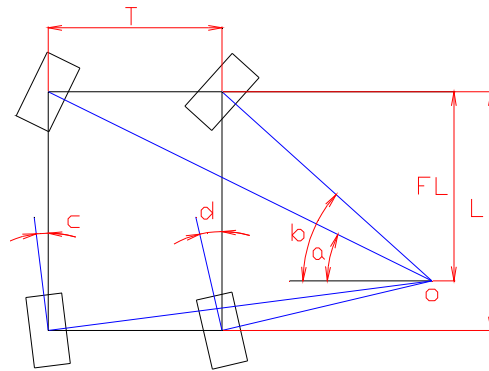


Figure 4 Minimum turning radius model

Ackermann steering geometry is a geometric arrangement of linkages in the steering of a car or other robots, designed to solve the problem of wheels on the inside and outside of a turn needing to trace out circles of different radii [1]. According to Ackermann steering geometry the following equations were derived.

This equation shows the minimum radius:

$$R = \frac{FL}{\sin a} + \sqrt{FL^2 + \left(\frac{FL}{\tan b} + Tf\right)^2} \quad (1)$$

However, pulling force:

$$FL = \frac{L}{\tan \frac{(a+b)}{2} + \tan \frac{(c+d)}{2}} \times \tan \frac{(a+b)}{2} \quad (2)$$

L : Distance between front and rear axis [m]

FL : Calculated axis distance[m]

T : Crawlers axis center[m]

a : Front outer wheel angle [rad]

b : Front inner wheel angle [rad]

c : Rear outer wheel angle [rad]

d : Rear inner wheel angle [rad]

That shows that a robot with 4 wheel steering mechanism could turn in smaller radius, compare to conventional vehicles steering mechanism

Servo control

Steering cylinders were actuated by proportional valve. As a result, bad response was observed, and skilled operator is necessary to perform the steering. Therefore, the proportional valves were replaced with servo valves to gain high positioning efficiency and sharp response. Each crawler weigh about 500 kgf defined as F_w and F_m is defined as the momentum torque acting on the kingpin, which is located between the steering cylinder and the crawler.

$$F_m L_1 = F_w L_2 \quad (3)$$

$$P_l = \frac{F_m}{A} \quad (4)$$

$$V_1 = Q_{70} \sqrt{\frac{A_1 P_s - F_m - A_2 P_T}{35(A_1^3 + A_2^3)}} [cm/s] \quad (5)$$

L_1 : Space between cylinder & kingpin [mm]

L_2 : Space between kingpin & crawler [mm]

P_s : Rated Pressure [kgf/cm²]

P_T : Hose pressure loss [kgf/cm²]

A_1 : Cylinder head cross-sectional area [cm²]

A_2 : Cylinder rod cross-sectional area [cm²]

V_1 : Cylinder extending speed [cm/s]

V_2 : Cylinder contracting speed [cm/s]

The equations above allow the selection of valves and potentiometers.

Steering control result

After replacing the proportional valves with servo valves, steering performance was improved in many stages. According to the command, response is faster and more accurate. Wireless control is more reliable, since the steering is controlled with servo controllers.

TILTING MECHANISM

Four rubber tracks known as crawlers are installed instead of the tires. Crawlers have bigger area contacting the ground, give it a strong grip and prevent it from slipping.

Rubber track

During work, normal vehicles use hydraulic assistant legs to increase the stability of the vehicle. While crawlers gives offers bigger stability to the vehicle, because of the tracks has big area that increases the ground resistance and prevent the vehicle from slipping.

However, when the robot runs back ward with obstacles behind, the crawlers rise up and the robot loses its balance. Such action starts to turn into problems. Therefore a new crawler tilting mechanism was introduces to the field robot. This titling mechanism prevents the crawlers to rise up while running backwards. And it assists the crawlers to rise when there are steps or obstacles ahead. A hydraulic cylinder was installed on the crawlers, to lift it up 30 degrees and lower it 30 degrees. As shown in the figure, the mechanism enables the crawler to run up 300 mm high step.



Figure 5 Crawler image

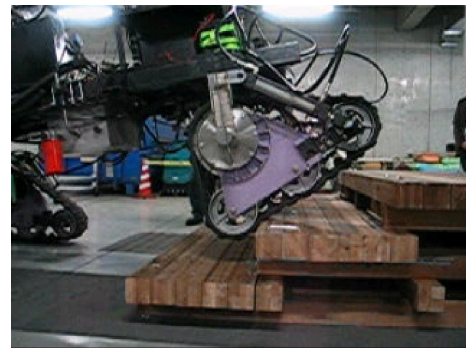


Figure 6 Crawler running over steps

Crawler tilting results

The experiment was to drive the robot up the stairs and back down. The stairs consist of 3 steps. Before running through the stairs the front crawlers are lift up. Then the robot is driven until the crawler starts running over the first time. At the same time the rear crawler tilting cylinder pushes the crawler downward to have a stronger grip of the ground. Technically front crawlers help to climb and the rear crawlers help to push the crawler forward. The experiment was held successfully. However for the crawlers were controlled manually, for safety reasons.

Wireless Control

In the field, sometimes man cannot accompany the robot for operations. Thus, a total wireless control system was proposed. AD5430 controller is installed in the robot. The controller is controlled by a personal computer through a wireless LAN. Engine ignition, HST, crawler tilting and steering cylinders are controlled through the controller.

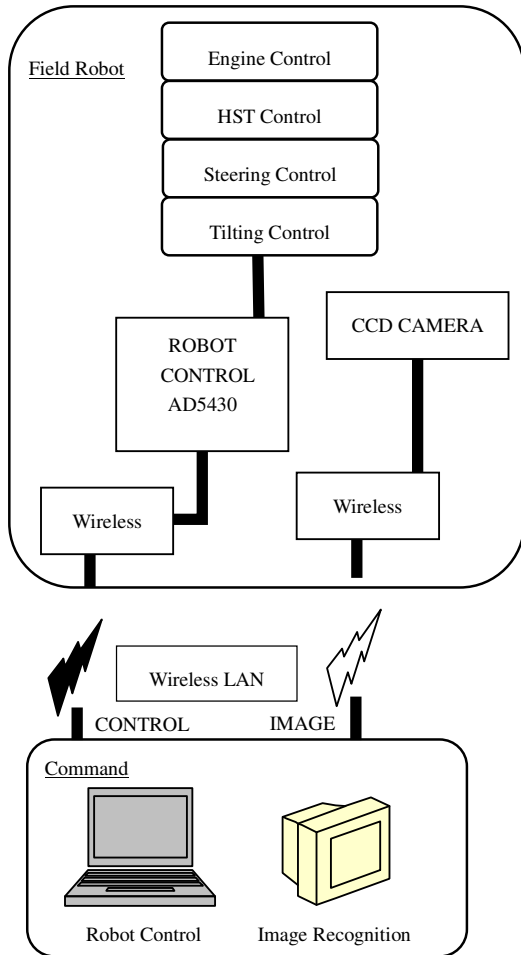


Figure 7 Wireless Control System

The Above figure shows that the controller AD 5430 gives commands PLC that turns on/off the engine, and to the stepping motor attached to the pump and feed back by rotary encoders installed to the crawlers. The steering cylinder is controlled and monitored since steering force differs in each running status. In addition to the crawling mechanism which eventually will be an automated system.

Running Experiments and results

The controller which controls the whole robot system is basically programs and system blocks created by MATLAB SIMULINK. And Virtual console is used to create a simple interface between the operator and the

field robot, in which the operator can control all the actuators and monitor the speed and other data from sensors.

The running test of the robot took place on a 300 meters long track. The at the distance of the 300 meters away from the operator the data transmission was weakened and slower and at 350 meters it lost its connection completely. In case the robot runs out of range accidentally the robot will automatically shut down and wait for another confirmed command signal. The displacement error is about 1.3% that is caused by the rubber crawlers which expand and extract according to the road features.

Conclusion

In this research, we developed a robot with many features that support it during its running off-road. In case of narrow areas, or small spaces the robot can steer through it with the new steering mechanism. In the other hand, when the robot faces obstacle the crawler tilt device will be activated to support the robot. Further experiments are expected on the crawler tilting mechanism.

Applications



Figure 8 Robot applied in landmine field

Applying this robot in landmine fields, demands several equipments, such heavy shield to prevent any serious damage in case of explosive accidents. Other equipments are required too, for example landmine sensors and defecting robotic arms.

REFERENCES

1. http://en.wikipedia.org/wiki/Ackermann_steering_geometry/
2. Yoram Koren, Robotics for Engineering, McGraw Hill International edition.
3. "Jissen Mechatronics, Hydraulics and pneumatics "Written by Ryouji Senda 1984
4. The Japan Society of Mechanical Engineers Basic chapter A5 of mechanical engineering handbook application fluidics. Japan Society of Mechanical Engineers.

WIRELESS TECHNOLOGY AND ITS APPLICATION IN PNEUMATIC SYSTEM

Xu Hongqing, Hao Pengfei, He Feng, Li Xinming

SMC-Tsinghua University Pneumatic Technology Center
Tsinghua University, Beijing 100084

ABSTRACT

It is well known that wireless technology has been widely used in communication. In recent years it has been ubiquitous in nearly every aspect of industry, medicine, environment and meteorology. The wireless technology will revolutionize these fields. This paper presents a wireless pneumatic system which consists of a controlled wireless pneumatic proportional valve based on SMC VEF-312 and a wireless transducer of flowmeter for monitoring the flowrate. The results about the application of wireless technology in pneumatic system were discussed.

KEY WORDS

wireless technology, pneumatic system

INTRODUCTION

As all known wireless technology has quickly development in past decades. Wireless communications is capable of reaching every location on the face of the earth. In recent years wireless technology has been ubiquitous in every aspect of industry, such as medical equipment, environment and meteorology, manufacturing and process control system. Although traditional hard-wired technologies continue to rein these fields, applications of wireless technologies will revolutionize these fields. For instance, nowadays manufacture factory usually has many sensors and actuators, which require cable and wire installation throughout a plant floor in order to connect between the sensors and the control house for both power supply and communications. Cables are easy to damage and need to be

removed and re-run. Therefore, the cost related to maintenance is usually prohibitive. The advent of wireless technology provides the solution to these problems. Using wireless technology, it can greatly reduce sensor installation cost, amount of cable, labor hours, faster installation and setup time and etc.

In this paper a controlled wireless pneumatic system is presented. The system consists of a controlled wireless pneumatic proportional valve based on SMC VEF-312 and a wireless transducer of flowmeter MFDN-15 for monitoring the flowrate.

1、Hardware system configuration

The hardware system configuration is shown in Figure 1. It consists of server PC, base station, flowmeter, electromagnetic valve, client station 1 and 2. Server PC uses Windows XP as operating system.

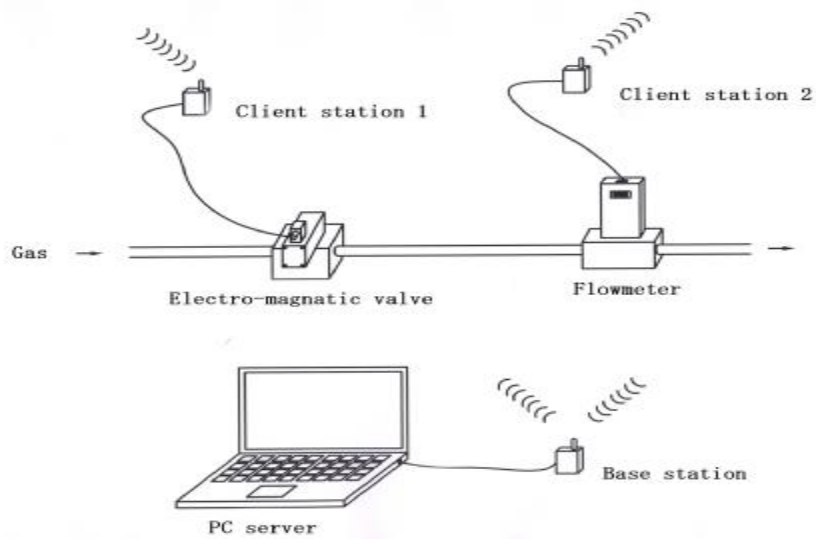


Figure 1: The hardware system configuration

1.1 Mass flowrate measurement

A mass flowmeter was built using the thermistor sensor, once the setpoint is reached the heat balance state that when the supplied energy is equal to the heat dissipation, the temperature of sensor is to keep constant. The supplied energy, which is a function of the fluid speed or flowrate, is detected using a special electronic circuit. The flowmeter is a MFDN-15 gas mass flowmeter designed by SMC-Tsinghua University Pneumatic Technology Center. It contains an amplification circuit, an analogy-to-digital converter and a microprocessor. The power supply voltage is in 12V. The range of measurement is 0-100L/min; the voltage output is 1-5 volts. The flowmeter was calibrated using a commercial flowmeter with high accuracy. The calibration shows that the flowmeter response is linear and repeatable shown in Fig.2.

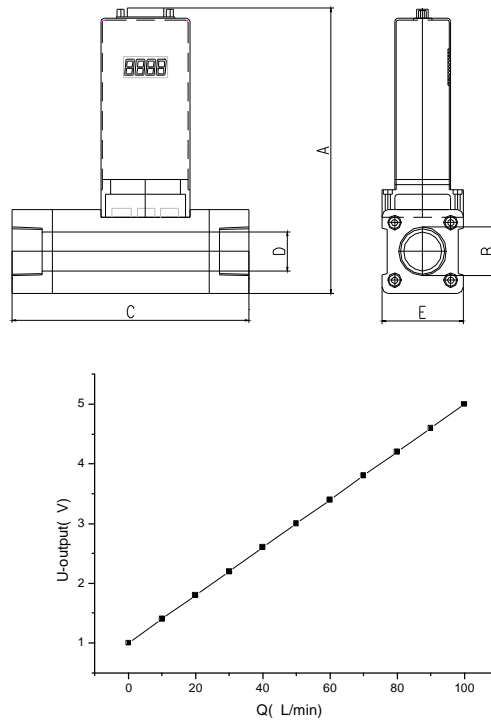


Figure 2 MFDN-15 gas mass flowmeter and its characteristic of output

1.2 Electro-magnetic proportional valve

Electro-magnetic proportional valve is VEF-312 made by SMC Corporation. It can adjust the gas flow of pneumatic air source system. The external power supply DC voltage is 24 volts. The range of control voltage is 0-5 volts. The opening of the valve is in variation with the operation voltage. The characteristics of proportional valve at the pressure of entrance 0.2 MPa is shown in Fig. 3.

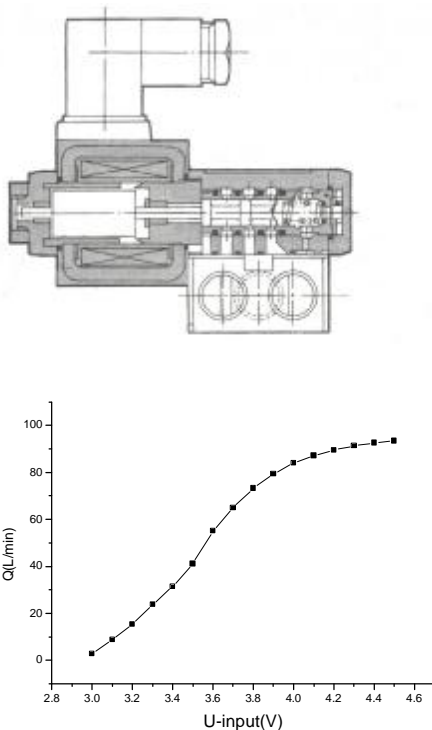


Figure 3 Flowrate output vs input voltage of VEF-312 valve

1.3 Transmitter and Receiver board

1.3.1 The base station module

Figure 4 is a block diagram of the base station module. The main component of the base station is a CC1000 wireless module, which has an RF transmitter, receiver and a base band modem. A microcontroller 43 is used to serve as central control unit, which sends the control and handshaking information to CC1000. RS-232 serial interface is used to communicate with the server PC.

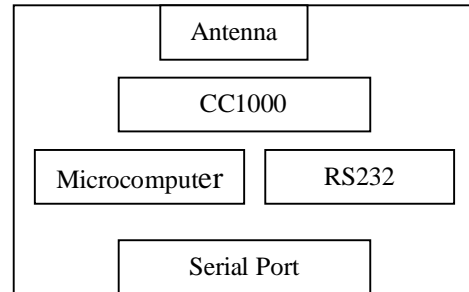


Figure 4 Base station

1.3.2 Client station 1

Figure 5 illustrates the block diagram of the client station, which consists of microprocessor (as an MCU), analog to digital converter module, CC1000 module, and a power supply unit. MCU is responsible for the following tasks: 1) control ADC for sampling 2) configure CC1000 by setting MAC (Measurement And Control) address and initializing the communication routines. 3) Encode the ADC output data using forward error correction (FEC) code and send the frames to CC1000 4) Process the acknowledgement information and the data request from CC1000. MAX187 from MAXIM is used for data sampling and analog to digital conversion.

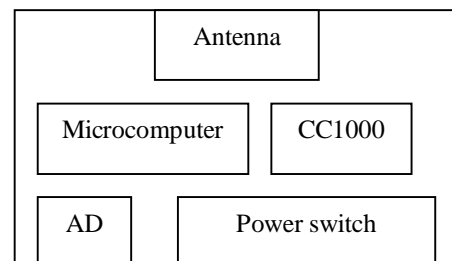


Figure 5 Client station 1

1.3.3 Client station 2

The block diagram of client station 2 is shown in Figure 6. The only difference between client station 2 and client station 1 is that the analog interface is changed to digital to analog converter (DAC). MAX5302 from MAXIM is used for this purpose.

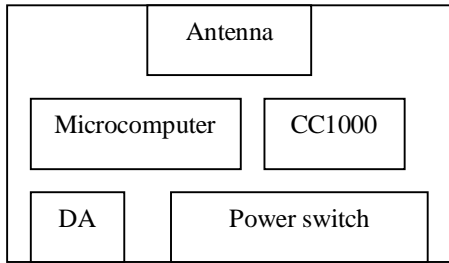


Figure.6 Client station 2

Frequency range	433.1-434.6 MHz
Number of Channels	11
Modulation scheme	FSK
Duplex mode	half duplex
Maximum transmit power	+10dBm
Receiver sensitivity	-105dBm
ADC resolution	12bits
Coverage	100m (Line of Sight)
Physical layer data rate	9.6kbps
Temperature range	-25-70C
Power supply voltage	12V

Table 1 System specifications

1.4 System specifications

The wireless system described in this paper transmits over unlicensed ISM band. The antenna can be placed externally or internally. The detailed specifications are listed in Table 1.

2 System software

Figure 7 shows the user interface of software and control program of base station module.

It was written using C ++ Builder 6.0. The following features are offered by the program: the initialization of CC1000 module, the program for monitoring serial port, the processing receiving data, display the dynamic results and sending control voltage value. Figure 8 shows a flow chart of initializing control program. The program of client station was written using the C51 programming language for a microprocessor.

It contains a control program for sampling data of A/D and D/A converters, setting and control for serial port of AT89C51 which is connected with CC1000 module. Sending data of frame channel coding and analyzing command words received.

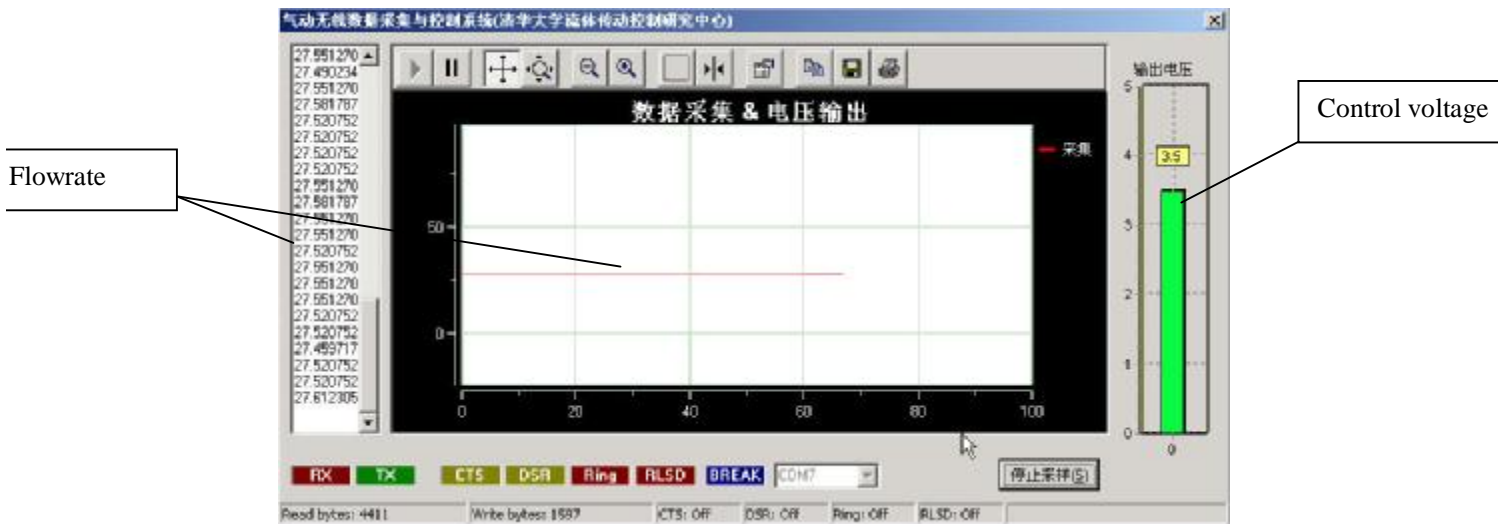


Figure 7. The user interface of software

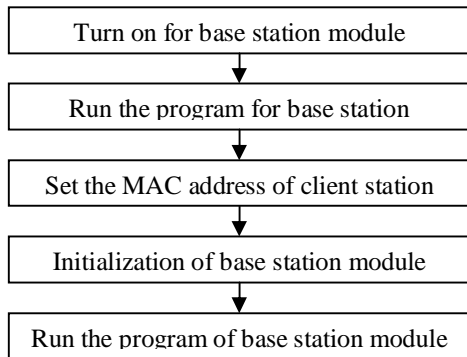


Figure 8. The flow chart of initializing control program for base station module

3 Wireless transceiver design and error protection mechanism

Fading and interference are two major factors affecting the performance and reliability of wireless communication. Our system adopts classical protection mechanism used in modern wireless access system, such as cellular and Wi-Fi, to make the communication more reliable. These mechanisms include channel coding, CRC check and ARQ.

3.1 Channel coding

Channel coding has been widely used in wireless communication systems to combat channel fading and interference. The theory is that by adding redundant information to the original source bits, the receiver can recover the source bits even if some of the received bits are wrong. This method can lower the bit error rate for the whole system.

After careful calculation and selection of the codes, we finally chose (8, 5) code. This particular code increases the Hamming distance to facilitate the error correction at the receiver side.

3.2 CRC check

CRC check is a method to check the integrity of the received packets. The transmitter adds a small segment of the checksum based on the source packets. This CRC segment along with the original source bits are transmitted to the receiver. The receiver uses the same equation to calculate the checksum. By comparing the local checksum with the received checksum, the receiver can know whether the received packet is correct or not.

CRC stands for cyclical redundancy check, which offers outstanding error detection performance. By combining the channel coding and CRC check, the error packets can be detected and recovered effectively, which reduces the error rate at the server. The flowchart of this process can be seen in figure 8.

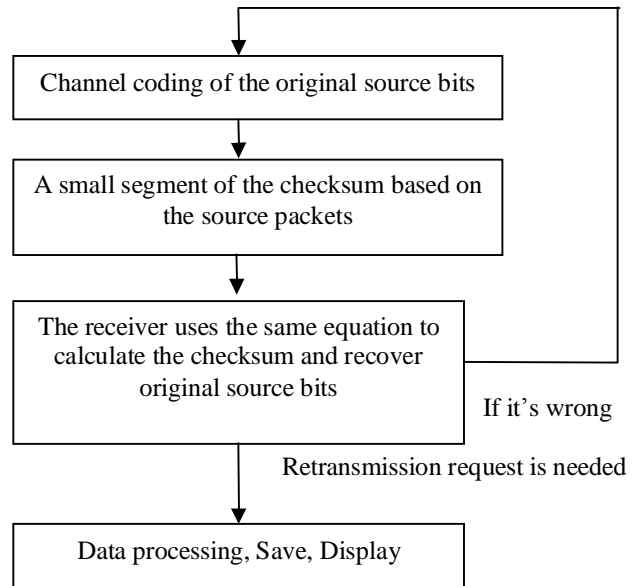


Figure 9. Flow chart of CRC check

3.3 ARQ (Automatic Retransmission request)

When the interference is severe, the error rate will go up significantly and the channel coding can not correct all the error bits. CRC check will fail in this case, which indicates the packet is not received correctly. A retransmission request for the current packet is generated and the received error packet is discarded. This retransmission mechanism can prevent the error packets from propagating to the server, which guarantees the reliability of the wireless communication.

4 Conclusions

We have successfully completed the design and development of a wireless measurement and control pneumatic system. It is easy to monitor and control a manufacturing process.

Right now this system is provided for showing experiment of laboratory. CC1000 module has 11 channels for client station. Therefore the system can be developed into a wireless network in duplex mode to realize multipoint measurements and control function.

REFERENCES

1. Jorgen Bach Andersen. Propagation Measurements and Models for Wireless Communication Channels. IEEE Com. Mag. Jan. 1995.
2. Arturo Herrera. Wireless I/O Devices in Process Control Systems, Sensors for Industry Conference USA Jan. 2004

DEVELOPMENT OF A PORTABLE PNEUMATIC POWER SOURCE USING PHASE TRANSITION AT THE TRIPLE POINT

Haifan WU*, Ato KITAGAWA* and Hideyuki TSUKAGOSHI*

* Department of Mechanical and Control Engineering,
Tokyo Institute of Technology
2-12-1, O-okayama, Meguro-ku, Tokyo, 152-8550 Japan
(E-mail: wuhaifan@cm.ctrl.titech.ac.jp)

ABSTRACT

This study is concerned with the development of a novel portable pneumatic power source applicable to self-powered mobile applications such as wearable actuator and rescue robot etc. Dry ice is chosen as a source of power for the pneumatic power source because it is nonpoisonous, easy to obtain and it expands 750 times in volume after being vaporized into gas. When dry ice is stored in the confined pressure container, it begins to liquefy after the pressure reaches the triple point (0.52[MPa(abs)], -56.6 °C). In this process the pressure remains constant until all the dry ice melt into the liquid. When the state remains at triple point, the pressure does not decrease even though the gas is released from pressure container. By using this physical property of carbon dioxide, and by controlling the heat transfer from the surroundings into the pressure container, a noiseless, large capacity and portable pneumatic power source is developed.

KEY WORDS

Pneumatic Power Source, Phase Transition, Dry Ice, Triple Point, Self-Powered

NOMENCLATURE

M : mass of dry-ice in pressure container
 Q : volumetric flow rate
 G : mass flow rate
 q : heat transfer rate
 T : output period (duration of an output flow)
 T_{ALL} : total output period ($= \sum T_i$)
 y : displacement of cylinder
 ΔH_v : heat of vaporization at the triple point of carbon dioxide=348[kJ/kg](-56.6 °C)
 ΔH_f : heat of fusion at the triple point of carbon dioxide=195.8[kJ/kg](-56.6 °C)

ΔH_s : heat of sublimation at the triple point of carbon dioxide=543.8[kJ/kg](-56.6 °C)

Subscripts

i : i th output

1. INTRODUCTION

The lack of suitable pneumatic power source is one of the dominant bottlenecks preventing the more widespread appearance of self-powered mobile applications such as wearable actuator and rescue robot etc. The pneumatic power source in these fields should achieve the following capabilities: 1) lightweight; 2) portable-size; 3) large capacity; 4) long life; 5) noiseless; 6) nonpoisonous; 7) low-price and 8) safety. This is a challenging list, and no current pneumatic

power source possesses all of these desirable characteristics. To solve the pneumatic power supply problem, many researches have been done in recently years^{1) ~3)}. However, new advances in portable pneumatic power source are still required.

This paper presents a novel portable pneumatic power source which is called Dry Ice Power Cell. Dry ice, which is the solid phase of the carbon dioxide, is chosen as the source of the power because it is nonpoisonous, easy to obtain, low in price and it expands 750 times in volume after being vaporized into gas. By using physical phase transition property of carbon dioxide at the triple point, and by controlling the heat transfer from the surroundings, a noiseless, large capacity, light and portable pneumatic source is developed. In this paper, the structure and the flow characteristic of the pneumatic power source is described in detail.

2. BASIC PRINCIPLE

The phase diagram for CO₂ is shown in Fig.1. Point O is the triple point of CO₂ (0.52[MPa(abs)], -56.6 °C) where solid, liquid and gas phases all coexist in equilibrium. Notice that the pressure at the point O is higher than atmosphere pressure. This means that the solid phase (dry ice) sublimates, that is it passes directly from the solid to the gas when left open to the atmosphere (point D), and liquid CO₂ cannot exist in this situation.

As illustrated in Fig.1 and Fig.2 (a) ~ (e), when dry ice is stored in the confined pressure container, the pressure increases steadily along the DO line (solid-gas boundary) because heat is added from the environment (a). When the pressure reaches triple point O, it stops increasing and solid begins to melt (b). In this situations, the heat addition results in change in internal energy, but no change in temperature and pressure. The heat addition from surroundings is saved in the liquid phase as the latent heat. Once all the solid has melted, no phase change occurs and the pressure rises farther along the OFA line (liquid-gas boundary) (c). At room temperature (25 °C), the pressure reaches 6.4[MPa (abs)] which is the pressure in cylinder of liquid carbon dioxide for daily use (point A).

When gas in the pressure container is released (for example, from point F), the pressure drops back down to point O along the FO line (d). Then the pressure holds constant at point O for a while. In this situation, the liquid begins to boil quite rapidly and also solid begins to reform (e). When all the liquid is gone and only reformed solid left, the pressure eventually drops back down to D along the OD line to normal atmospheric pressure (point D).

Notice that when the state remains at triple point, the pressure does not decrease even though the gas is released from pressure container. This is a useful property for pneumatic power source where a steady

pressure is always required.

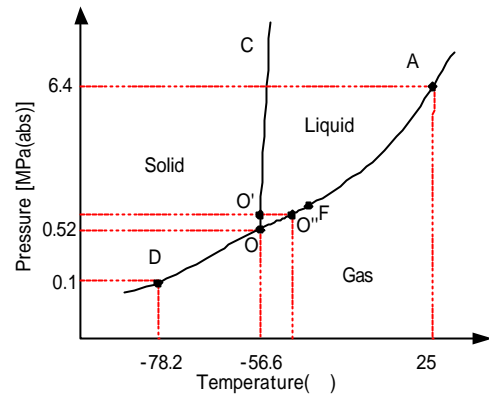


Fig.1 Sketch of the phase diagram for carbon dioxide (not to scale)

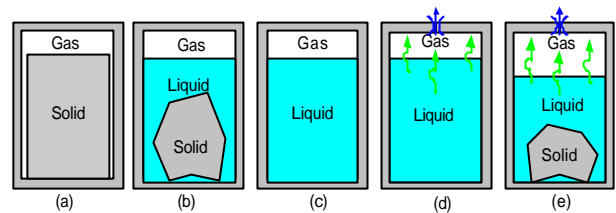


Fig.2 Phase transition process of the dry-ice in closed container

From the viewpoint of energy transfer, when gas is released at triple point pressure, part of the liquid changes to solid and emits the saved latent heat while other part absorbs this latent heat to improve its vaporization thus can hold the pressure. On the other hand, when liquid is gone, the pressure drops because of the required heat of vaporization for steady output flow rate can not be offered at that time. In other words, the liquid at the triple point acts just like an energy buffer, that is it saves energy transferred from the environment when solid melts and emits the saved heat when the output flow rate is released. The more the liquid, the longer the release duration can be achieved.

Making use of the physical property of carbon dioxide at the triple point, a novel pneumatic power source can be developed. By controlling the heat transfer from the surroundings, he developed pneumatic power source can hold the carbon dioxide in a pressure container at the state of triple point for a long time, thus achieves a fixed pressure (0.42[MPa]) pneumatic power source which can offer various output flow rate. The following describes the structure and the flow characteristic of the developed pneumatic power source in detail.

3. DESCRIPTION OF THE STRUCTURE

Developed Dry Ice Power Cell is illustrated in Fig.3. The dry ice (F) is stored in pressure container (E) which is surrounded by a can with composite wall consisting of an inner insulate layer (G) and an outer aluminum

can (H) with fin (I). The control mechanics consist of a double-acting cylinder (J), a pressure switch (D), a solenoid valve (A) and its drive circuit.

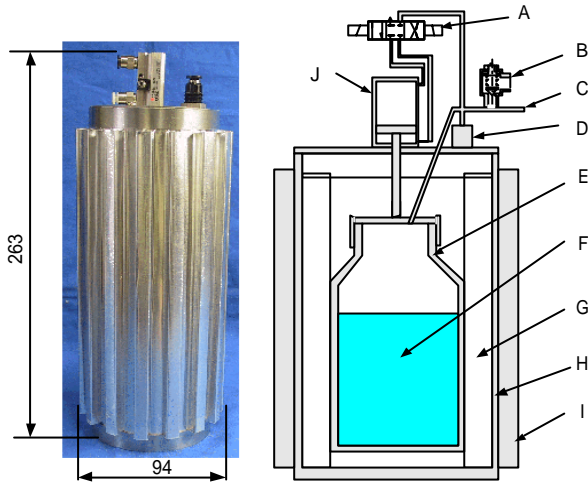


Fig.3 Photo and Model of Dry-ice Power Cell

When the pressure in the pressure container (E) falls below 0.42[MPa], solenoid valve (A) is switched on by pressure switch (D) and cylinder (J) extends to push the pressure container (E) down to contact closely with the bottom of the aluminum can (I). This position is called contact position later. On the other hand, when the pressure is higher than 0.45[MPa], solenoid valve (A) is switched off by pressure switch (D), and cylinder (J) retracts to lift the pressure container (E) up to separate it from the bottom of the aluminum can (I). This position is called separate position later. Because thermal resistance is small in the contact position and large in the separate position where an air space is inserted, the heat transfer rate from the environment to the pressure container can be controlled by this two position control. From the viewpoint of energy transfer, when the pressure reaches 0.45[MPa] a little higher than triple point pressure, all the dry ice in the pressure container has melted into liquid CO₂ which shows sufficient latent heat has been saved and no more heat transfer from the environment is needed. At this pressure, the separate position where heat transfer is not a lot is selected. Moreover, because the pressure rises slowly even in the separate position, the relief valve (B) is needed (setting pressure 0.5[MPa]) to prevent the pressure from rising farther.

The developed Dry Ice Power Cell weighs 600g, and can store 430g dry ice, thus the total weight is about 1kg. In order to explain the action of the Dry Ice Power Cell, the phase change and pressure change inside the pressure container is shown in Fig.4.

Firstly, pressure rises as the solid sublimates, then it stops rising and the solid begins to melt. The pressure rises again as all the solid melts to liquid. When the

pressure reaches 0.45[MPa], the pressure container is switched to the separate position and the heat transfer from the environment is slowed down. When the pressure reaches 0.5[MPa], the gas is released from relief valve to prevent the pressure from rising farther. After that, the outlet valve may be open to give the output. When the gas flows out, the pressure drops down to the pressure of the triple point and holds there the period of T_1 . During this process, the pressure container is switched back to the contact position and the liquid boils quite rapidly and the solid reforms.

When all the liquid is gone and only reformed solid survives, the pressure drops again and the output flow has to be shut off. Then the survival melts again, thus the second output period T_2 is given during a process just like ~. Accordingly, the third period T_3 , the fourth period T_4 ... output periods can be obtained if the solid reformed from previous output exists.

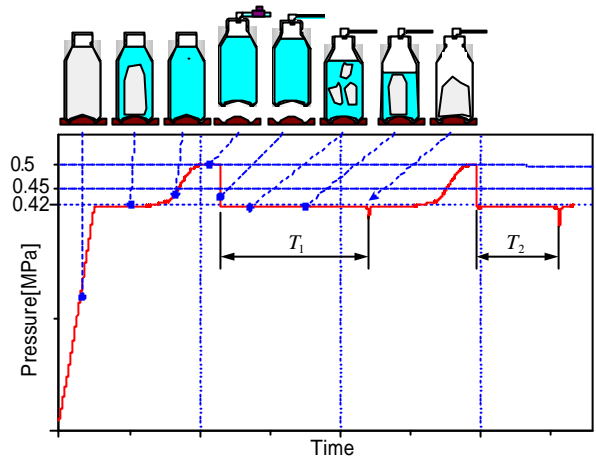


Fig.4 Principle of the Dry-ice Power Cell

4. EXPERIMENT

The experimental setup for flow characteristic of the Dry Ice Power Cell is illustrated in Fig.5.

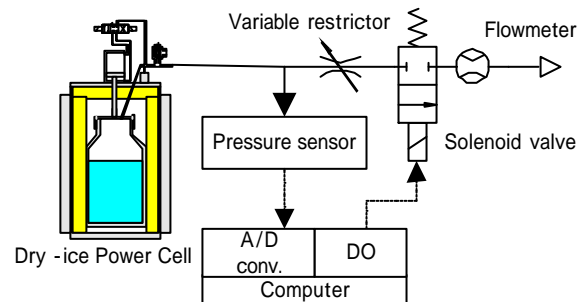


Fig.5 Schematic diagram of experimental setup 430g dry ice is stored in its pressure container. The output flow rate is controlled by a variable restrictor and

a solenoid valve to give an on/off output control. The output flow rate and the pressure in the pressure container are measured by a flowmeter and a pressure sensor. When the gas is released at flow rate Q at the pressure of triple point 0.42[MPa] , the output period $T_1, T_2 \dots$ are measured.

As shown in Fig.6, when output flow rate is 5, 7 and 20[L/min (nor)], experimental results show that as the output flow rate is increased, the first output period T_1 becomes shorter. This is because both vaporization and freezing occur more rapidly in larger output flow rate.

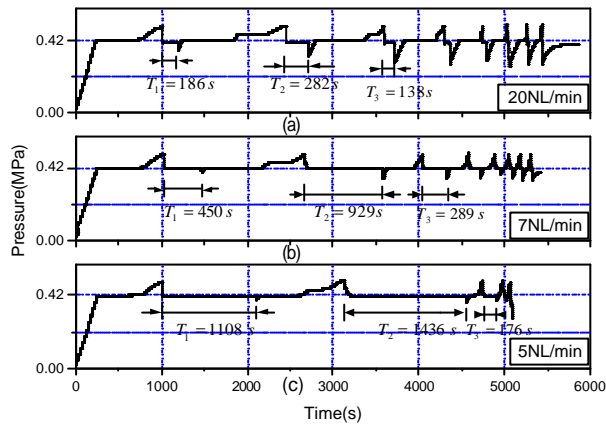


Fig.6 Experimental results of pressure with time

As shown in Fig.7, when output flow rate is 2, 3 and 4[L/min (nor)], all the gas is released at only one period T_1 . This means the immediate heat transfer alone is enough for offering these small flow rates and no solid reforms throughout the output period. Notice that only the contact position is selected throughout the output at 4[L/min (nor)] (Fig.6 (a)). However, when the output flow rate is less than 4[L/min (nor)], the separate position is needed because the heat transfer at the contact position is too large for that flow rate. The smaller the out flow rate, the more the separate positions.

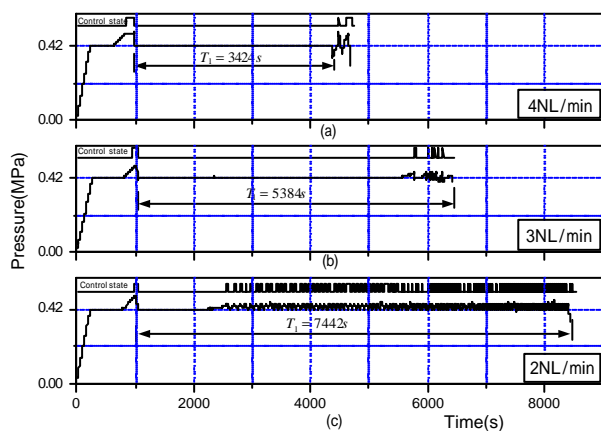


Fig.7 Experimental results of pressure with time

As shown in Fig.8, when Dry Ice Power Cell does not give any output flow, the liquid CO_2 can be preserved at the separate position for about 7.5 hours. The flow rate released from the relief valve during this process is about 0.4[L/min (nor)] .

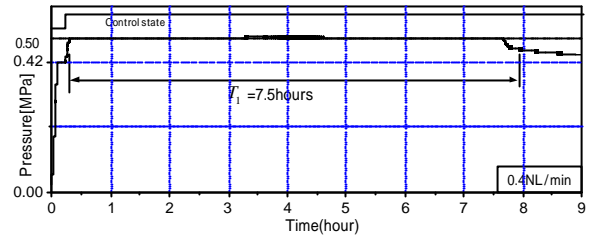


Fig.8 Experimental results of pressure with time

5. DISCUSSION

5.1 ENERGETICS

A simplified calculation can be given for roughly estimating the output capability of Dry Ice Power Cell. From neglecting the heat transfer during the output process, the heat emitted from the freezing process (195.8kJ/kg) simply equals the heat for vaporization (348kJ/kg), so that the mass of the output gas should be 36% (about 1/3) of the total initial liquid mass, and the rest 64% (about 2/3) should reform to solid. However, as illustrated in Fig.6, the experimental result shows that the first output period T_1 is less than not only 1/3 of the total output period T_{ALL} but also the second output period T_2 . The conflict between the calculation and the experiment is caused by uneven temperature distribution in the pressure container.

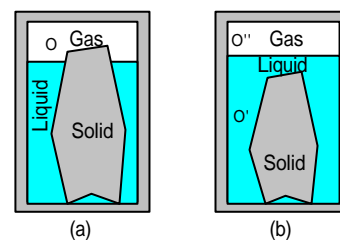


Fig.9 Temperature deviation near triple point

As illustrated in Fig.9, when the solid melts in the pressure container, the solid change it position from above liquid level (a) to sinking in liquid (b). This causes the boundary face which solid, liquid and gas phase all coexist to disappear. Although the pressure is even, the temperature distribution is not even and different temperatures can exist at the point O' and O'' as shown in Fig.1. The pressure rises even though the solid still exists in the pressure container.

In order to prove this explanation, the pressure container is shaken to make the temperature distribution even and enable to achieve a complete liquefaction. As shown in

Fig.10, (b) is from the experiment which pressure container is shaken to achieve complete liquefaction, while (a) is shown for comparison (the same as Fig.6 (a)) which the experiment is just done on a still table without any shake movement. When the pressure rises above the triple point pressure (Point A in Fig.10 (b)), the pressure container is hold to be shaken to make the temperature distribution even, thus the pressure drops down to triple point pressure. After that, the pressure rises again and again and needs to be shaken repeatedly. The existence of the solid can be confirmed in this process from the knocking sound inside the pressure container. At last, the pressure does not drop (point B) even though the pressure container is strongly shaken and no knocking sound occurs. This shows solid is not exist, and the complete liquefaction is achieved.

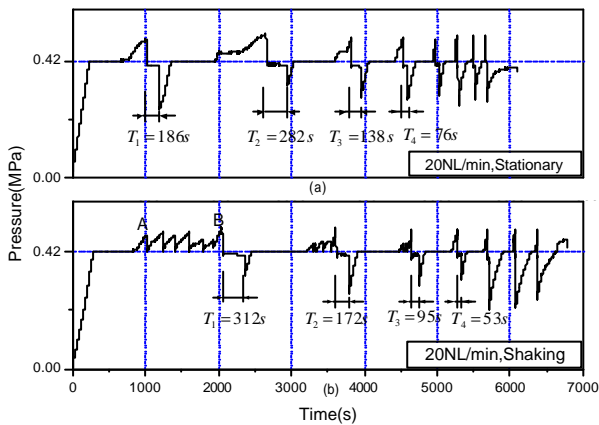


Fig.10 Experimental results of pressure with time

When the complete liquefaction is achieved, the output period at the flow rate of 20[L/min (nor)] is $T_1=312s$, $T_2=172s$, $T_3=95s$..., as shown in the Fig.10 (b), which is a geometric progression with the ratio of 0.55.

Since the temperature inside the pressure container is always constant at the triple point, the temperature of the environment does not change very much either, thus the heat transfer rate q should be almost constant. Therefore, the energy balance can be expressed in equation (1) which shows the heat emitted from freezing process plus the heat transferred from the environment equals the heat of vaporization. The conservation of mass can be expressed in the equation (2).

$$G\Delta H_s = q + \frac{M_i \Delta H_f}{T_i} \quad (1)$$

$$M_{i+1} = M_i - GT_i \quad (2)$$

So the ratio of output period geometric progression can be given by equation (3), which shows a constant ratio when the gas flows out at a constant mass flow rate G .

$$\frac{T_{i+1}}{T_i} = 1 - \frac{G\Delta H_f}{G\Delta H_s - q} \quad (3)$$

When flow rate is 20[L/min (nor)] and the ratio is 0.55, and heat transfer rate q equals 4.5[kJ/min]. However, the heat transfer rate q measured in this way shows that q is about in the range of 3.5~4.5 [kJ/min] as shown in Fig.11, which shows some increasing tendency as the output flow rate increases.

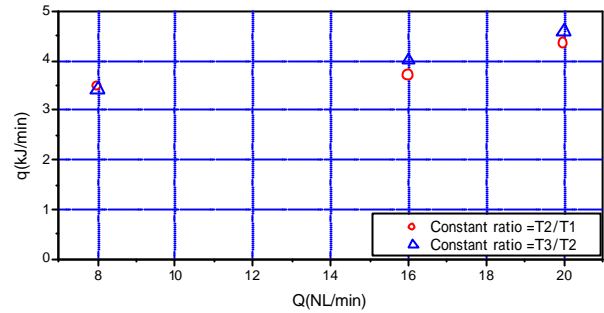


Fig.11 Experimental results of q vs. various flow rates Q

When the Dry Ice Power Cell is carried by a person, because there are often shake movement accompany by walking movement, the actual using condition of Dry Ice Power Cell is believed near the condition of complete liquefaction.

Developed pneumatic power source stores 430g dry ice, which can evaporate to 218L (nor) gas or 42L at pressure of 0.42[MPa]. The pressurized gas can do 18[kJ] (5Wh) work, and can give power as shown in Table 1. For example, when the output valve is full opened and 110L/min (nor) flow rate can be obtained for about 40 seconds, thus can output 150W power in 40 seconds.

Table 1 Output power of Dry-ice Power Cell

Q (L/min(nor))	T_1	T_{ALL}	Power(W)
0.4	7.5 hour	7.5 hour	0.6
4	57 min	57 min	5
20	5 min	11 min	27
110	40 second	2 min	150

5.2 APPLICATION TEST

The Dry Ice Power Cell is applied to the driving of a cylinder. The experimental setup is shown in Fig.12.

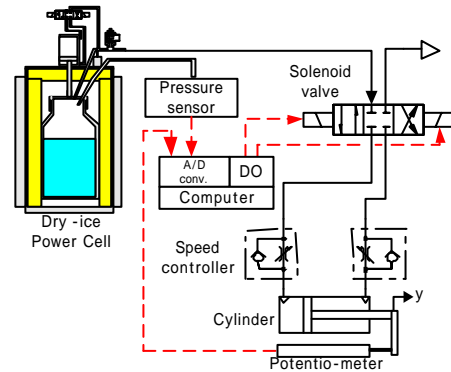


Fig.12 Setup of experiment

The cylinder is controlled by meter-out circuit, and the displacement of the cylinder y and the pressure in the pressure container are measured by potentiometer and pressure sensor. The working period of the cylinder is recorded.

Table 2 Parameters of experiments and T_i

No	Diameter (mm)	Stroke (mm)	Period (s)	T_i (min)	Mean flow rate (L/min(nor))
1	10	45	1	40, 6, 2	5
2	10	45	2	90	2.5
3	25	255	5	6,2,3,4,1,9,1,1	16

The experimental results of two cylinders in three conditions are listed in table 2. A cylinder of 10mm in diameter, 45mm in stroke is driven at a period of 1 second, and three periods of T_1, T_2, T_3 is achieved. The same cylinder is driven at a period of 2 second, only one period of 90 minutes output is achieved. A cylinder of 25mm in diameter, 255mm in stroke is driven at a period of 5 second, and output periods of $T_1 \sim T_4$ are achieved.

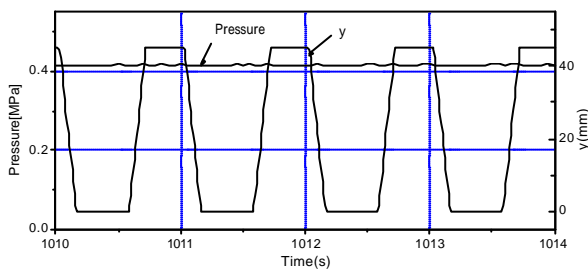


Fig.13 Experimental results (No.1)

The pressure in the pressure container and the displacement of the cylinder y of the experiment No.1 is shown in Fig.13. Notice that the pressure has only small fluctuation even though the output flow has an intermittent change. This shows the Dry Ice Power Cell can give intermittent output flow at a constant pressure and the air receiver is not necessary which is often necessary in the pneumatic system. This makes it very convenient for the pneumatic system to achieve small size and light weight.

5.3 SAFETY CONSIDERATIONS

Although the gas CO_2 is nonpoisonous, it causes some health problems when people breathe it in at high concentration. However, an adult in quiet breathe blows out CO_2 at the flow rate of nearly 0.45L/min, which is near 0.4 L/min (nor) the output of the Dry Ice Power Cell at separate position. A 2.4kW/h gas-heater generates 220L CO_2 within one hour, which is near the amount of the CO_2 generated by 430g dry ice. Therefore, Dry Ice Power Cell is safe even for using at home.

Because dry ice is obtained fom by-product stream from manufacturing processes, the Dry Ice Power Cell

makes no more CO_2 , and is considered to have little effect on increasing the amount of CO_2 in the atmosphere which can cause global warming.

6. CONCLUSIONS

A novel pneumatic power source is proposed in this paper. By using the physical property of carbon dioxide at the triple point, and by controlling the heat transfer from the environment into the pressure container, a noiseless, large capacity and portable power source which is named Dry Ice Power Cell is developed. Proposed pneumatic power source can be widely used in self-powered mobile applications such as wearable actuator and rescue robot etc.

REFERENCES

1. Toshiro, NORITSUGU., Jianhai HAN and Masahiro, TAKAIWA., Development of A Miniature Compressor Driven with a Linear Electromagnetic Actuator , Transactions of the Japan Fluid Power System Society, 2002, 33-4, pp.83-90.
2. Maolin, CAL, Toshinori FUJITA, Toshiharu, KAGAWA., Distribution of Air Available Energy in Pneumatic Cylinder Actuation, Transactions of the Japan Fluid Power System Society, 2002, 33-4, pp.91-98.
3. Goldfarb, M., Barth, E.J., Gogola, M.A. and Wehrmeyer, J.A.: Design and Energetic Characterization of a Liquid-Propellant-Powered Actuator for Self-Powered Robots, IEEE/ASME Transactions on Mechatronics, 2003, 8-2, 254/262

CHARACTERISTICS OF LEAK DETECTION BASED ON DIFERENTIAL PRESSURE MEASUREMENT

Harus L.G.*, Maolin CAI**, Kenji KAWASHIMA** and Toshiharu KAGAWA**

* Graduate student of Mechano-Micro Engineering Dept., Tokyo Institute of Technology

** Precision and Intelligence Laboratory, Tokyo Institute of technology

226-8503 Yokohama, Midori-Ku, Nagatsuta Chou 4259 Japan

(E-mail: harus@k-k.pi.titech.ac.jp)

ABSTRACT

This paper presents the first study on how the unbalance of temperature recovery after air charged has a significant effect on the accuracy and repeatability of air leak detection. From this viewpoint, temperature recovery time is derived and affecting parameters are investigated. In a leak detection based on differential pressure measurement, the leak is detected by measuring pressure difference between a reference component, which is leak tight, and a tested component using a differential pressure sensor. When the tested component is leaking, the pressure inside it decreases and the pressure difference with the reference is measured. However, when the required temperature recovery time is not satisfied, unbalance of temperature recovery due to a possibly small difference of heat transfer coefficient between the reference and tested component can produce pressure difference that is similar in size as a real leak and larger uncertainty. This phenomenon is described theoretically and the experimental data are in satisfactory agreement with the calculated results.

KEY WORDS

Air leak detection, Differential pressure, Temperature recovery

NOMENCLATURE

b	: Critical pressure ratio	$[\quad]$	P	: Differential pressure	$[\text{Pa}]$
C	: Sonic conductance	$[\text{m}^3/(\text{s} \cdot \text{Pa})]$	$(P = P_r - P_m)$		
C_p	: Specific heat at constant	$[\text{J}/(\text{kg} \cdot \text{K})]$	q	: Volume flow rate	$[\text{m}^3/\text{s}]$
	pressure		Q_L	: Leak rate	$[\text{cc}/\text{min}]$
C_v	: Specific heat at constant	$[\text{J}/(\text{kg} \cdot \text{K})]$	Q_{LG}	: Generated leak rate	$[\text{cc}/\text{min}]$
	volume		R	: Ideal gas constant	$[\text{m}^2/(\text{s}^2 \cdot \text{K})]$
G	: Mass flow rate	$[\text{kg}/\text{s}]$	S_h	: Heat effective area	$[\text{m}^2]$
h	: Heat transfer coefficient	$[\text{W}/(\text{m}^2 \cdot \text{K})]$	T_h	: Thermal-time constant	$[\text{s}]$
κ	: Ratio of specific heat	$[\quad]$	T_r	: Temperature recovery time	$[\text{s}]$
m	: Mass	$[\text{kg}]$	T_{rr}	: Required temperature	$[\text{s}]$
P	: Pressure	$[\text{kPa}]$		recovery time	
			V	: Volume	$[\text{cc}]$

	: Temperature	[K]
	: Differential temperature	[K]
e	: Measurement error	[cc/min]
σ	: Standard deviation	[cc/min]
ρ_o	: Air density	[kg/m ³]

Subscripts

m	: Master
t	: Tested

INTRODUCTION

The growing need for leak tight products has made researchers as well as leak tester manufacturer competing to develop a better leak tester. Various leak detection methods have been developed to satisfy the wide range of leak size down to 10⁻¹²cc/min depending on the application. In a leak detection based on differential pressure measurement, leakage is detected by measuring pressure difference between a reference and a tested component using a differential pressure sensor. As compared with only measurement of pressure inside the tested component chamber, measurement of differential pressure between the dual chambers, in which a leak-tight master is used as a reference, has several advantages. The waiting time for detection can be shortened, thermal instability can be reduced and influence of external environment change can be counterbalanced.

E.B. Arkilic described in his paper that temperature stability of the environment surroundings the low flow system and temperature stability within it influences the result. The more accurate the detection result and the smaller the leak size to be detected the higher the temperature stability requirement [1].

During the charging process in to a chamber, T. Kagawa demonstrated in his paper that pressure response within the chamber is affected by the heat transfer between the air in the chamber and the chamber wall [2]. Higher tested pressure takes longer temperature recovery time and bigger chamber volume also needs longer temperature recovery time. This must be considered when differential pressure measuring technique is going to be utilized for leak tester.

When two chambers are charged simultaneously, unbalance of temperature recovery due to a small difference of heat transfer coefficient occurs and produces differential pressure that is similar in size as a real leak and uncertainty to the air leak detection. In this paper, these phenomena are analyzed theoretically and verified experimentally.

MODEL AND ANALYSIS

When a chamber is charged as illustrated in Figure 1, temperature inside the chamber increases to a certain level and recovers to atmosphere temperature due to

heat transfer. And when the charging process is stopped during temperature recovery, the pressure inside the chamber decreases proportionally to the temperature change within the chamber [3]. To describe this phenomenon, first, the ideal-gas equation of state is derived as follow:

$$\frac{dP}{dt} = \frac{P}{\theta} \frac{d\theta}{dt} + \frac{R\theta}{V} G \tag{1}$$

From the conservation of energy, the following equation is obtained:

$$C_v m \frac{d\theta}{dt} = C_v G_u (\theta_a - \theta) + R G_u \theta_a + Q \tag{2}$$

As the atmosphere temperature is maintained constant at a certain level θ_a , the heat transfer rate passing through the chamber wall can be expressed as:

$$q = h S_h (\theta_a - \theta) \tag{3}$$

Based on Eq. (1), Eq. (2) and Eq. (3), the pressure and temperature change inside the chamber after charging process, can be expressed utilizing the following equations:

$$\frac{dP}{dt} = \frac{P}{\theta} \frac{d\theta}{dt} + \frac{R\theta}{V} G \tag{4}$$

$$\frac{d\theta}{dt} = \frac{R\theta}{C_v P V} [G(C_p \theta_a - C_v \theta) + h S_h (\theta_a - \theta)] \tag{5}$$

Where the mass flow rate to the chamber is expressed as [4]:

$$G = \begin{cases} C \rho_o P \sqrt{1 - \left(\frac{P/P_s - b}{1-b}\right)^2} \dots\dots \frac{P}{P_s} > b \\ C \rho_o P \dots\dots\dots \frac{P}{P_s} \leq b \end{cases} \tag{6}$$

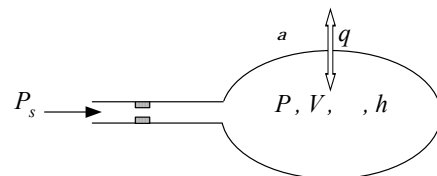


Figure 1 Air charged in to a chamber

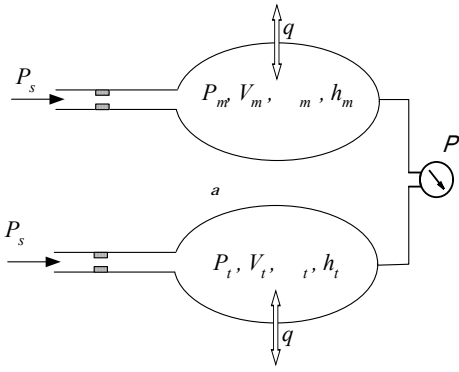


Figure 2 Air charged simultaneously to two chambers

The simulated results of pressure and temperature change within the chamber after stop charging at 6s, under pressure 500kPa and chamber volume 140cc are shown in Figure 3. As illustrated in the figure, the pressure within the chamber decreases as a result of temperature recovery.

In a differential pressure type air leak tester as displayed simply in Figure 2, two chambers are charged simultaneously to supply pressure before starting leak detection.

After charging process is stopped at $T_r = 6s$, to start leak detection, temperature difference due to inadequate temperature recovery produces differential pressure that is similar in size as a real leak even though tested chambers is leak-tight.

These phenomena are demonstrated theoretically in Figure 4. As illustrated in the figure, although the heat transfer coefficient is only 0.26% different between master and tested chamber, a 0.01K remaining unbalance of temperature recovery occur at this point due to inadequate temperature recovery time and this produces a pressure difference of 6Pa even though tested tank is leak-tight. When the charging is stopped at a longer time (i.e. 10s), the pressure difference becomes about 3.5Pa. It is clear that longer waiting time is necessary to create adequate temperature recovery and to eliminate the pressure difference not due to leak.

Leak size for dual chamber method is simply calculated based on the derivation of ideal gas equation:

$$\frac{V_t}{R\theta_t} \frac{dP_t}{dt} - \frac{V_m}{R\theta_m} \frac{dP_m}{dt} = \rho Q_L + \frac{P_t V_t}{R\theta_t^2} \frac{d\theta_t}{dt} - \frac{P_m V_m}{R\theta_m^2} \frac{d\theta_m}{dt} \quad (7)$$

If the two chambers are equal in temperature, volume and undergo identical thermal fluctuations, then the leak rate is given by:

$$Q_L = \frac{V}{R\theta} \frac{d\Delta P}{dt} - \frac{\Delta P V}{R\theta^2} \frac{d\theta}{dt} \quad (8)$$

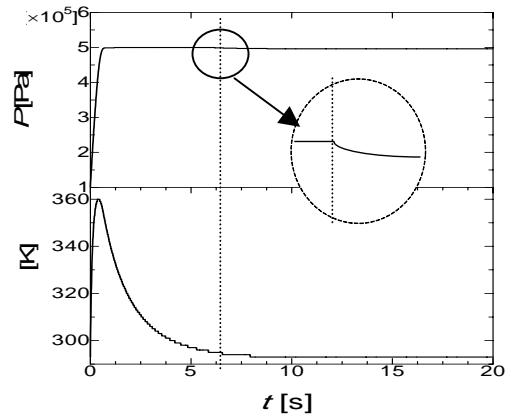


Figure 3 Pressure and temperature inside the chamber [Charging is stopped at 6s]

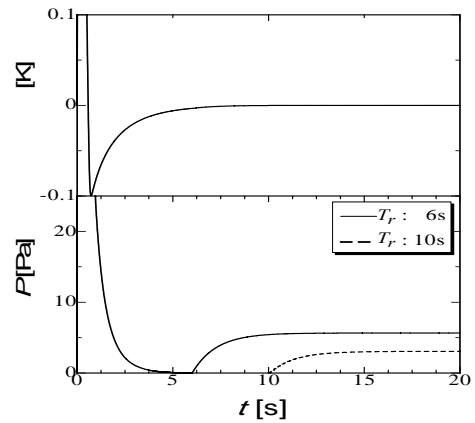


Figure 4 and P change between the two chambers [$h_m = 30W/(m^2K)$, $h_t = 30.08W/(m^2K)$]

Generally, the last part of Eq. (8) can be neglected since P and $\frac{d\theta}{dt}$ is very small as compared with $\frac{d\Delta P}{dt}$.

LEAK DETECTION

The developed leak tester

The developed leak tester as illustrated in Figure 5 consists of 5 main elements: PLC (Programmable Logic Controller), PC (Personal Computer), a reference and tested component, a differential pressure sensor and valves. The valves are controlled by the PLC based on the sequence as displayed in Figure 6. The room temperature is maintained constant at 20° C.

The applicability under high pressure and the leak-tightness of the leak tester before utilizing for leak detection are important to be guaranteed. By disassembling both master and tested chamber, the leak tester is charged up to 800kpa.

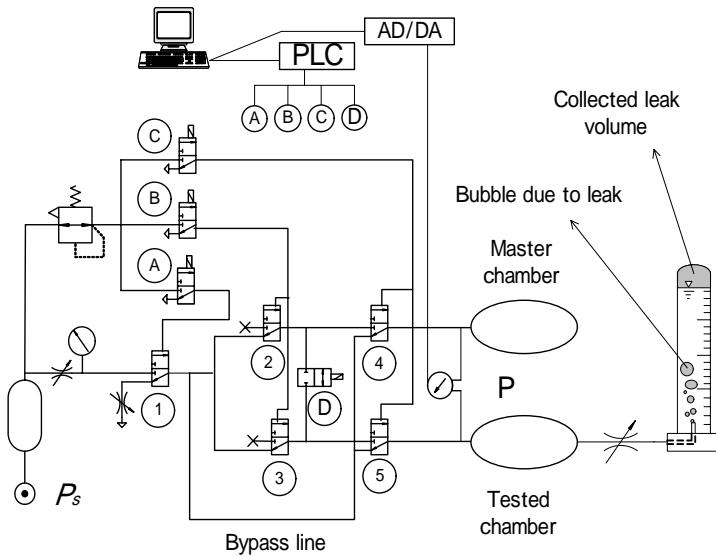


Figure 5 Developed leak tester

At the possible shortest temperature recovery time $6s$, the charging is stopped and the differential pressure response between reference and tested circuit is recorded, and repeated 5 times under the same experimental condition to guarantee the repeatability of the leak tester. As illustrated in Figure 7, the differential pressure responses after the charging process is stopped at $6s$ are stable, constant at zero level and high repeatability. The experimental result demonstrates the applicability of the developed leak tester under high pressure, pressure balance between reference and tested circuit, and the leak-tightness of the leak tester.

Characteristics of leak-tight chamber

As demonstrated in the simulated results that inadequate temperature recovery can produce pressure difference that is similar in size as the real leak although tested chamber is leak-tight. The experimental results, as displayed in Figure 8(a) and 8(b), are carried out under leak-tight tested chamber, 5 times repetitions and in two different T_r (i.e. $6s$ and $10s$). The results are in satisfactory agreement with the simulated results.

Since the charging process passing through a sudden enlargement from the pipe to the chamber, the experimental results also show the effect of inadequate temperature recovery to the range of uncertainty as demonstrated in Figure 8. Within 5 sample data, the range of uncertainty of the differential pressure response due to inadequate temperature recovery is larger when shorter T_r is applied.

Leak generation and detection results

As displayed in Figure 5, leakage is generated by a variable restrictor attached to the tested chamber. The generated air leak is measured by a mess cylinder filled with water connected at the end of the pipe.

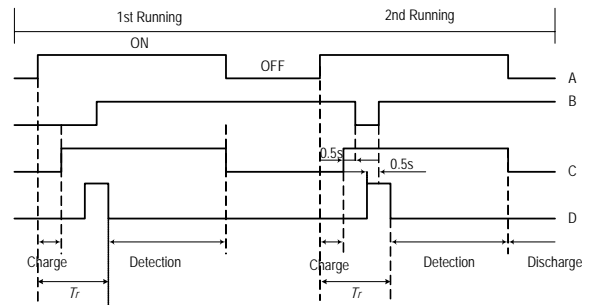


Figure 6 Valve control sequence

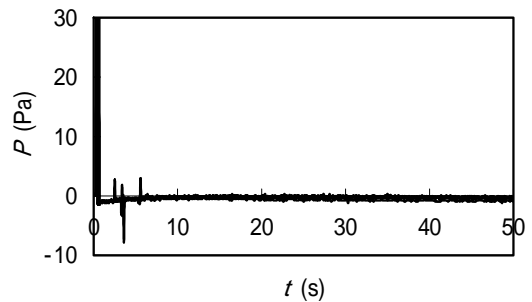


Figure 7 P response of leak tester

Based on the JPAS002-1984 standard for air leak measurement, the generated leak rate is the ratio of the collected air volume due to leakage in the top of the mess cylinder to time consumption t during leak detection.

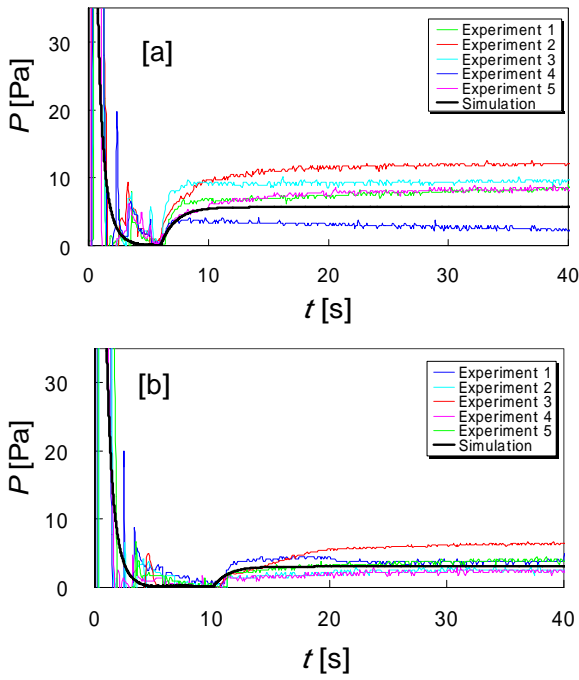


Figure 8 Simulated and experimental results of the P responses for leak-tight tested chamber, Experiment is carried out 5 times, $P=500\text{kPa}$ and $V=140\text{cc}$: [a] $T_r=6\text{s}$ and [b] $T_r=10\text{s}$

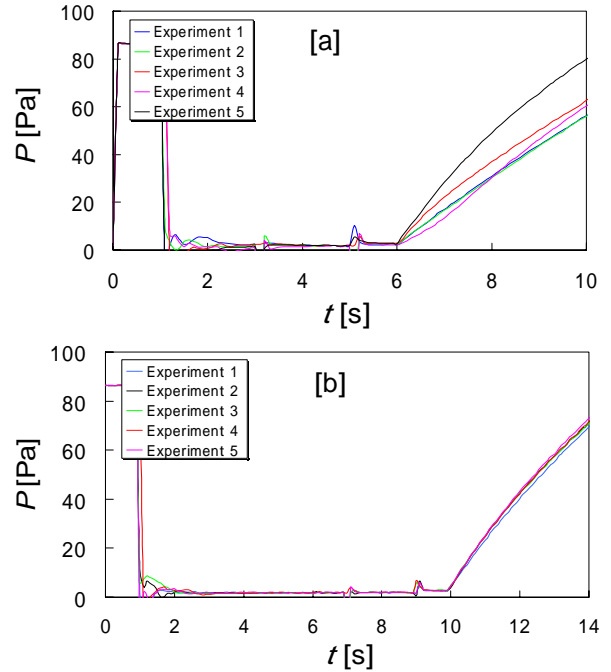


Figure 9 Differential pressure change under 5 times repetitions for $0.3\text{cc}/\text{min}$ generated leak from tested chamber for $P=500\text{kPa}$ and $V=140\text{cc}$: [a] $T_r=6\text{s}$ and [b] $T_r=10\text{s}$

The experiment on leak tested chamber was carried out by generating $0.3\text{cc}/\text{min}$ leakage from the tested chamber and five sample data were recorded at each temperature recovery time to investigate the repeatability of the detection results. The experimental results are summarized in Figure 9(a) and 9(b) for $T_r=6\text{s}$, and 10s respectively.

Figure 9(a) demonstrates that inadequate temperature recovery produces larger uncertainty or low repeatability which is shown by about 24Pa range of uncertainty of the differential pressure P change within 5 sample data due to $0.3\text{cc}/\text{min}$ generated leak. However, when the temperature recovery time T_r is set to be longer ($T_r=10\text{s}$), the differential pressure P response varies narrowly about 4Pa as demonstrated in Figure 9(b).

Table 1 displays the summary of the precision and accuracy of the detection results in various T_r and leak sizes which are indicated by the measurement error e and the standard deviation σ respectively.

REQUIRED TEMPERATURE RECOVERY

The uncertainty of the differential pressure responses for leak-tight tested chamber in various pressures and volumes are summarized in Figure 10.

Table 1 Measurement error and deviation
(a) $P=500\text{kPa}$ and $Q_{LG}=0.3\text{cc}/\text{min}$

T_r	e	σ
6	0.04	0.01
10	0.02	0.002
14	0.01	0.001

(b) $P=500\text{kPa}$ and $Q_{LG}=0.05\text{cc}/\text{min}$

T_r	e	σ
14	0.004	0.01
18	0.001	0.006
22	0.001	0.002

The experiments were carried out by taking the maximum range of uncertainty within five sample data for various pressures (i.e. 200kPa , 500kPa and 800kPa), various volumes (i.e. 140cc and 400cc) and 4s time increment (i.e. 6s , 10s , 14s and 18s).

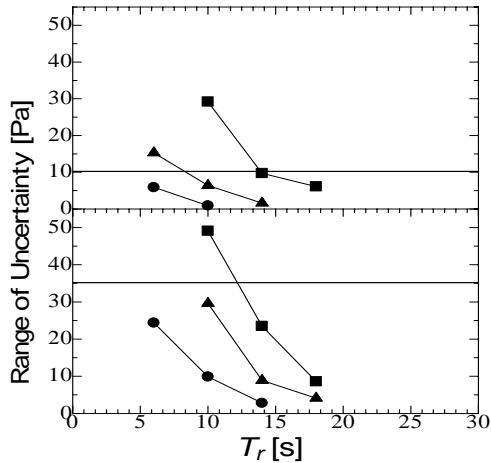


Figure 10 Range of uncertainty in various pressures

Higher accuracy requires lower uncertainty and a 0.001cc/min of accuracy requires less than 10Pa and 35Pa tolerable range of uncertainty of the differential pressure response for chamber volume 140cc and 400cc respectively. The required temperature recovery time T_{rr} is defined as the minimum temperature recovery time that can produce range of uncertainty less than 10Pa and 35Pa for chamber volume 140cc and 400cc respectively which is shown by the solid line in Figure10. And the experimental results of the T_{rr} are summarized in Figure 11 upper side.

It is clear that T_{rr} depends on the charged pressure and chamber volume. However, it is difficult to determine it by drawing the curve of uncertainty as shown in Figure 10, since it takes long time to conduct experiments under different T_r .

Here, we discuss the relation between T_{rr} and the thermal time constant. The thermal time constant is defined in the following equation [5].

$$T_h = \frac{C_v W}{S_h h} = \frac{C_v P V}{S_h h R \theta} \quad (9)$$

Because T_{rr} is also a parameter proportional to the charged pressure and related to chamber volume as shown in Figure 11 upper side, we calculate their ratio and show the result in Figure 11 lower side. It can be seen that the ratio is less than 6. Therefore, as a practical determination method, the required temperature recovery time can be approached by setting 6 times of the calculated thermal time constant for various pressures and volumes.

CONCLUSIONS

A differential pressure type air leak tester is studied.

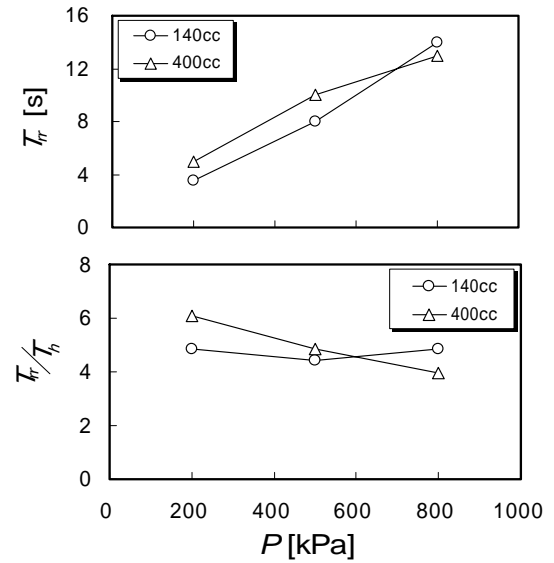


Figure 11 Required temperature recovery and thermal-time constant

Temperature recovery and its unbalance due to a small difference of heat transfer are discussed. This unbalance and inadequate temperature recovery produces differential pressure between master and tested chamber though the tested chamber is leak tight. Furthermore, this differential pressure is uncertain due to uncertainty of heat transfer. Due to the difficulty of determining the required temperature recovery time experimentally, its relation with thermal time constant has been investigated and proposed in this research to be utilized to estimate the required temperature recovery time that is very meaningful in leak detection field.

REFERENCES

1. Arkilic, E.B., Schmidt, M.A. and Breuer, K.S., Sub-nanomol per second measurement near atmospheric pressure, Journal of Experiments in Fluid, 1997, Vol. 2, pp.37-41.
2. Kagawa, T., Shimizu, M. and Morita, Y., Heat conduction effects of the chamber wall on the air pressure dynamics, Proceeding of Measurement and Automatic Control Association, 1987, Vol.23, No.8., pp.870-871.
3. Incropera, F.P. and Dewitt, D.P., Fundamental of Heat and Mass Transfer, 4th edition, John Wiley & Sons.
4. ISO6358: Pneumatic Fluid Power-Components Using Compressible Fluids-Determination of Flow rate Characteristics
5. Kagawa, T. and Shimizu, M., Non dimensional Pressure Responses of Pneumatic RC Circuit Considering Heat Transfer, Proceeding of Hydraulic and Pneumatic, Vol.19, No.4, pp.306-311.

Model of a nozzle-flapper type pneumatic servo valve and differential pressure control system design

Tao WANG*, Maolin CAI**, Kenji KAWASHIMA** and Toshiharu KAGAWA**

* Department of Mechano-Micro Engineering
Interdisciplinary Graduate school of Science and Engineering
Tokyo institute of Technology
4259 Nagatsuta-cho, Midori-ku, Yokohama, 226-8503 Japan
(E-mail: wangtao@k-k.pi.titech.ac.jp)

** Precision and Intelligence Laboratory
Tokyo institute of Technology
4259 Nagatsuta-cho, Midori-ku, Yokohama, 226-8503 Japan

ABSTRACT

In pneumatic position and force control systems, nozzle-flapper type servo valves are usually used for the pressure control. This paper proposes a linear model for a 4-port nozzle-flapper type pneumatic servo valve, which also includes the influence of the flow force, by deriving it from a full nonlinear model. The proposed linear model had a better agreement with experimental dynamics response than the former one which neglects the flow force. Furthermore, the proposed model was applied to achieve the differential pressure control between two symmetrical control chambers. A two degree-of-freedom (TDF) controller was designed based on the proposed model. The experiment results showed that differential pressure controllability could be improved for the reference input tracking and disturbance restraining by using the proposed model.

KEY WORDS

Differential pressure control, Nozzle-flapper type servo valve, Linear model, Flow force, TDF controller

NOMENCLATURE

B_f	damping coefficient of the armature-flapper	[N·m·s]
$b_{o1, o2}$	critical pressure ratio of the left and right fixed orifice	[-]
$b_{n1, n2}$	critical pressure ratio of the left and right nozzle-flapper	[-]
$C_{o1, o2}$	sonic conductance of the left and right fixed orifice	[s·m ⁴ /kg]
$C_{n10, n20}$	sonic conductance of the left and right nozzle-flapper at zero input current	[s·m ⁴ /kg]
$G_{c1, c2}$	mass flow rate of the left and right control side	[kg/s]
$G_{o1, o2}$	mass flow rate through the left and right fixed orifice	[kg/s]
$G_{n1, n2}$	mass flow rate through the left and right nozzle-flapper	[kg/s]
i	input current	[mA]
J	moment of the armature-flapper	[kg·m ²]
K_a	rotational stiffness of the flexure tube	[N·m/rad]
$K_{f1, f2}$	flow force coefficient of the flapper left and right side	[N/Pa]
K_m	magnetic rotational stiffness	[N·m/rad]
K_t	torque-motor gain	[N·m/mA]
l_f	distance from the nozzle to the pivot point of the armature-flapper	[m]

$m_{o1, o1}$	subsonic index of the left and right fixed orifice	[-]
$m_{n1, n2}$	subsonic index of the left and right nozzle-flapper	[-]
P_a	atmosphere pressure	[Pa]
$P_{c1, c2}$	left and right side control pressure	[Pa]
P_s	supply pressure	[Pa]
R	gas constant	[m ² /s ² ·K]
$V_{1, 2}$	volume of the left and right control chamber	[m ³]
T_e	time constant due to eddy currents	[s]
T_t	torque caused by electromagnetic forces	[N·m]
x	flapper tip displacement	[m]
x_f	distance from flapper tip to each nozzle at zero input current	[m]
ΔP	differential pressure between both control sides $\Delta P = P_{c2} - P_{c1}$	[Pa]
α	armature-flapper deflection	[rad]
θ	control chamber air temperature	[K]
ρ	air density for standard conditions	[kg/m ³]

INTRODUCTION

In many pneumatic position and force control systems, nozzle-flapper type servo valves are normally used for controlling small flow rates. For example, the air-spring type horizontal vibration isolation is mainly achieved by differential pressure control using a 4-port nozzle-flapper type pneumatic servo valve due to its simple construction, high sensitivity and wide frequency band [1]. Therefore, modeling the servo valve is important for designing a good performance control system. However, there was no general mathematic model describing a nozzle-flapper type pneumatic servo valve considering the flow force on the flapper. The nozzle-flapper type servo valve is usually treated as a proportional element with the torque motor dynamic and the flow force being neglected. The pneumatic control system with a nozzle-flapper element is generally approximated to a first order lag system assuming an isothermal state change for the air in the load chamber [2]. The conventional control approach for differential pressure control uses a PID controller regarding the system model as a first-order model, in which parameters are recognized by experiment directly.

In this research, a full nonlinear model of the nozzle-flapper type servo valve was derived including the torque motor dynamics and the flow force. The linear model is derived through linearizing the nonlinear model around its equilibrium state. Through the simulation and experiment for the dynamics response, the influence of the flow force is confirmed. Using the proposed linear model a two-degree-of-freedom control system is designed for the differential pressure between the two load chambers.

Dynamics of servo valve and control chamber

The differential pressure control system shown in Figure 1 consists of a 4-port nozzle-flapper type electronic-pneumatic servo valve with dual fixed orifices and dual nozzles and two load chambers called as Isothermal Chambers. The armature-flapper is moved by a torque motor consisting of a coil and vertically arranged magnets. Movement of the flapper changes the distance between it and both nozzles. This creates different pressures, P_{c1} and P_{c2} , in the control sides. In the steady state, the differential pressure, $\Delta P = P_{c2} - P_{c1}$, is proportional to the input current. The two Isothermal Chambers, in which the copper wires with the diameter of 50 μm are stuffed uniformly, are connected to the two control ports of the servo valve as load chambers respectively.

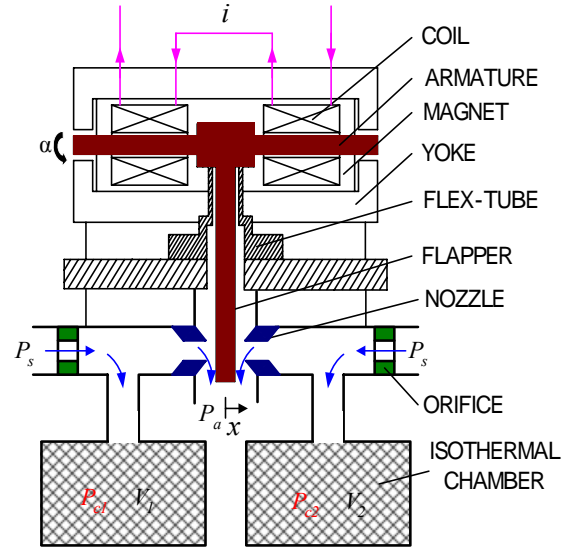


Figure 1 differential pressure control system

The torque T_t , driving the armature-flapper generated by the coil current considering the influence of the eddy current, is given as the following [3]:

$$T_e \dot{T}_t + T_t = K_m \alpha + K_i i \quad (1)$$

The moment around the pivot of the armature-flapper around is obtained by

$$J \ddot{x} / l_f = T_t - K_a \alpha + (K_{f1} P_{c1} - K_{f2} P_{c2}) l_f - B_f \dot{x} / l_f \quad (2)$$

The first term is torque of the torque motor as Eq. (1). The second term is the torque on the armature-flapper around the pivot, caused by the flex-tube which acts as an elastic support. The third term is the torque on the flapper around the pivot, caused by flow forces which are generated by air jet from the two nozzles.

In Eq. (2), the left and right side flow force coefficients are determined by the experimental approach using the following approximant equations [5].

$$K_{f1} = \frac{K_i}{l_j} \left[a_{11} - (a_{11} - a_{12}) e^{-\left(a_{13} \frac{x_f + x}{x_f} \right)^{a_{14}}} \right] \quad (3)$$

$$K_{f2} = \frac{K_i}{l_j} \left[a_{21} - (a_{21} - a_{22}) e^{-\left(a_{23} \frac{x_f - x}{x_f} \right)^{a_{24}}} \right] \quad (4)$$

With respect to the compressibility of air, the flow state through the fixed orifice and the nozzle-flapper can be sonic or subsonic depending upon the upstream/downstream pressure ratio. Firstly, the flow rate through the fixed orifice is given by

$$G_o = C_o \rho P_s \varphi_o(P_c) \quad (5)$$

where

$$\varphi_o(P_c) = \begin{cases} 1 & P_c/P_s \leq b_o \\ \left[1 - \left(\frac{P_c/P_s - b_o}{1 - b_o} \right)^2 \right]^{m_o} & P_c/P_s > b_o \end{cases}$$

G_o , C_o , P_c , b_o , m_o and φ_o , for the left and right side of the flapper are identified by attaching the subscripts 1 and 2 respectively.

The flow rates through the two nozzle-flappers are given by

$$G_{n1} = C_{n10} \rho \frac{x_f + x}{x_f} P_{c1} \varphi_{n1}(P_{c1}) \quad (6)$$

$$G_{n2} = C_{n20} \rho \frac{x_f - x}{x_f} P_{c2} \varphi_{n2}(P_{c2}) \quad (7)$$

where

$$\varphi_n(P_c) = \begin{cases} 1 & P_a/P_c \leq b_n \\ \left[1 - \left(\frac{P_a/P_c - b_n}{1 - b_n} \right)^2 \right]^{m_n} & P_a/P_c > b_n \end{cases}$$

In the above equation, φ_n , P_c , b_n , and m_n , for the left and right side of the flapper are identified by attaching the subscripts 1 and 2 respectively. The nozzle-flapper critical pressure ratio and subsonic index are considering constant with the flapper displacement change.

Air temperature inside the chamber is considered constant and isothermal state during pressure and flow rate change. It is because that the high heat capability of copper wire than air and large heat area between the copper wires and air inside the chambers. So air dynamics in two load chambers are obtained from air state equation [4].

$$G_c = \frac{V}{R\theta} \dot{P}_c \quad (8)$$

Applying the continuity equation to the 4-port nozzle-flapper servo valve, the following equation can be obtained:

$$G_c = G_o - G_n \quad (9)$$

G_c , K_c , V , P_c , G_o and G_n for the left and right side of flapper are expressed by attaching the subscripts 1 and 2 respectively.

Linear model for differential pressure model

The linear model is derived from the above nonlinear model at an equilibrium state. The equilibrium states are obtained for zero input, i.e., $i=0$ as follows:

$$\alpha_0=0, x_0=0,$$

P_{c10} and P_{c20} can be calculated from Eqs. (5)-(7) and (11) when the flow rate through the fixed orifice equals that through the nozzle-flapper; the flow state at the fixed orifice is subsonic and that at the nozzle-flapper is sonic.

$$C_{o1} P_s \left\{ 1 - \left(\frac{P_{c10}/P_s - b_{o1}}{1 - b_{o1}} \right)^2 \right\}^{m_{o1}} = C_{n10} P_{c10} \quad (10)$$

$$C_{o2} P_s \left\{ 1 - \left(\frac{P_{c20}/P_s - b_{o2}}{1 - b_{o2}} \right)^2 \right\}^{m_{o2}} = C_{n20} P_{c20} \quad (11)$$

Because the two control pressures at equilibrium are not zero, the pressure variations and flow rate variations dynamics to the input current variation derived in Appendix A, have the forms shown in Figure 2. This block diagram shows that a differential pressure control system for two fixed chambers with a nozzle-flapper type servo valve can be validly represented by a fourth order model. Furthermore, the flow force can be considered as the disturbances to flapper movement.

The specific servo valve used in the experiment system is part AS121005 as manufactured by the PSC Company. The control pressure change range is 300~400 kPa for the rated current of ± 100 mA and air supply pressure of 400 kPa. The rated differential pressure is 8.6 kPa for an input current of 10 mA. The two chambers with the

effective volume of 95 cm², in which the copper wires with the diameter of 50 μm and weight of 0.4 kg are stuffed uniformly, are connected to the two control ports

of the servo valve closely neglecting connecting section. The experiments were performed at a constant ambient temperature of 20 °C and a supply pressure of 400 kPa.

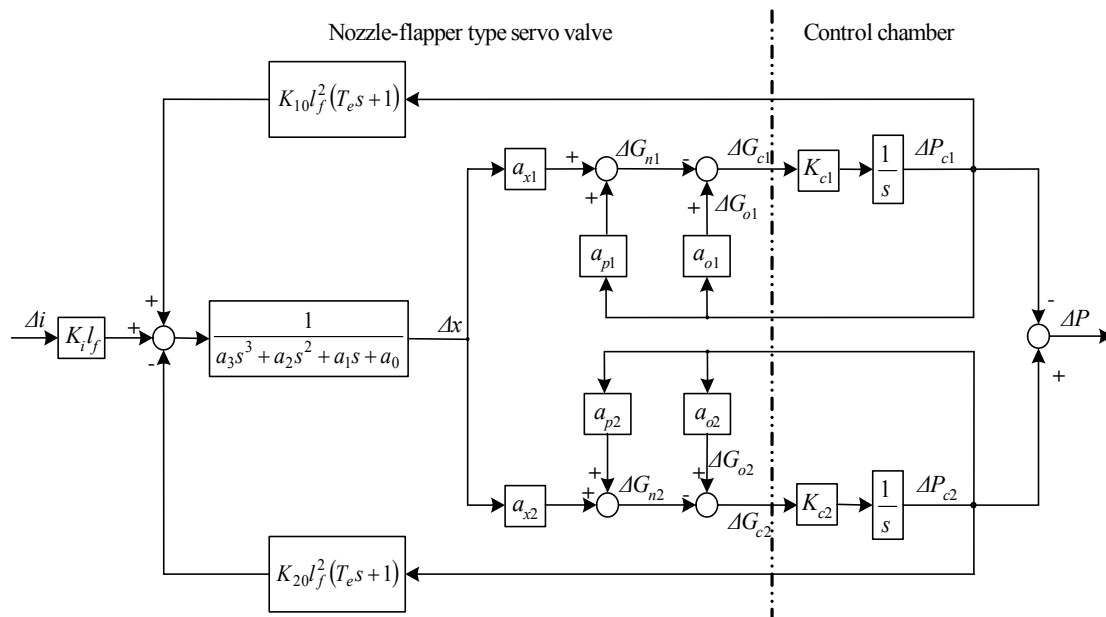


Figure 2 Schematic of a linear model for a combination of servo valve and control chambers

To validate the derived linear model, the step responses and frequency responses for the proposed model and experiment were achieved. Various step input currents were applied to the model and experimental setup. The input current was varied using step-up signals with magnitudes of ±10%, ±20% and ±30% of the rated current. There is good agreement between the results of the simulation and experiment, as shown in Figure 3. Furthermore, comparison between the results of the experiment and the simulation which neglects the flow force yields a steady state error of about 30%. This shows that flow force has the effect of reducing the pressure gain of the servo valve.

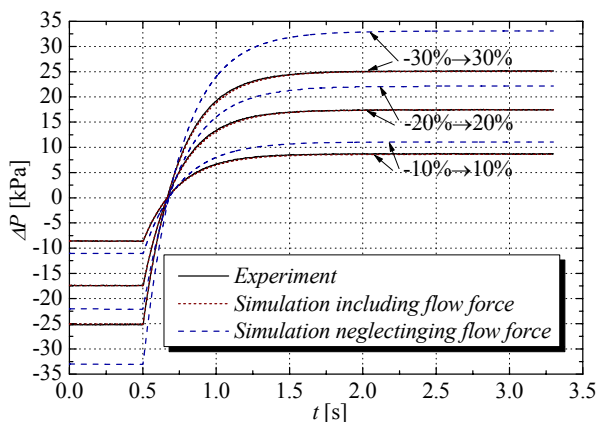


Figure 3 Step response of the differential pressure

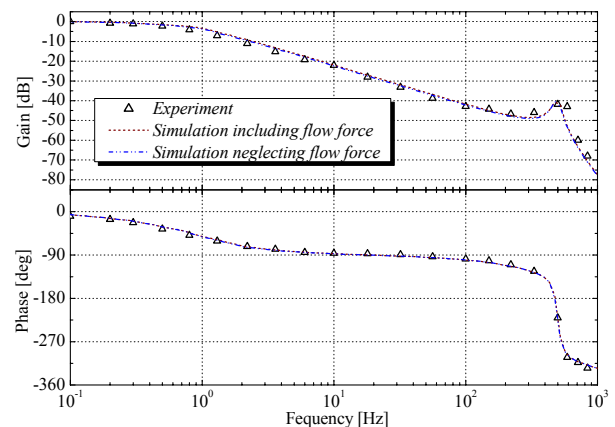


Figure 4 Frequency response of the differential pressure

The frequency response was obtained by superimposing a 5 mA swept sinusoidal current on a biased zero input current and is summarized in the bode diagram shown in Figure 4. From this bode diagram we may see that the gains for both the experiment and model descended to 3 dB at about 0.65 Hz. At about 400 Hz a peak appears in the bode diagram and corresponds to the resonant frequency of the armature-flapper. The influence of the flow force on frequency response is almost negligible. The dynamics of the system is mainly dominated by the air dynamics in the control chamber in the low frequency field. Many electro-pneumatic servo applications demand closed loop bandwidth far below

the servo valve bandwidth, therefore the dynamics of the combination of servo valve and control chambers can approximately be considered as a first order loop for the servo control design.

Control system control design

To obtain high performance control results for reference tracking and disturbance restraining simultaneously, a two degree-of-freedom (TDF) controller is designed for the differential pressure control. It comprises two components, a prefilter and a feedback compensator. The control system is shown as Figure 5.

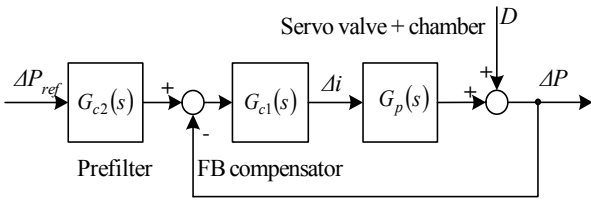


Figure 5 Differential pressure control system with a TDF controller

$G_p(s)$ is the transfer function of the combination of servo valve and control chambers shown in Figure 2. The FB compensator is designed as a PI controller consisting of a proportional coefficient K_p and an integral coefficient T_i :

$$G_{c1}(s) = K_p \left(1 + \frac{1}{T_i s} \right) \quad (12)$$

The prefilter is designed as follows:

$$G_{c2}(s) = \frac{1 + c_1 c_2 T_i s}{1 + c_2 T_i s} \quad (13)$$

Different outputs results for models, with and without flow force, with respect to input current show the flow force is mainly influencing the gain of the transfer function for servo valve show in Figure 3. Therefore the different controllers need to be designed for different models with respect to the same reference input.

In order to confirm control effect, using the models including and neglecting the flow force we designed the different controllers. The controller design is performed as the following. Firstly because the model has been established clearly shown as Figure 2, the parameters of the FB compensator can be tuned using simulating the model, no depending upon the experiment investigation, by the Critical Gain Method of Ziegler-Nichols shown as Table 1. Next the parameters of the prefilter are usually recommended as $c_1=0.4$ and $c_2=1.35$ referring to [6].

We introduced the parameters of the above two TDF controllers to the digital experimental control system respectively and compare the control results to the step input and step disturbances respectively.

Table 1 FB compensator parameters

No		K_p	T_i [s]
1	Model including the flow force	4.5	0.238
2	Model neglecting the flow force	3.375	0.270

Figure 5 shows the experiment step response using each TDF controller for a reference amplitude of 20 kPa. Better differential pressure response is achieved with the more accurate control model including the influence of the flow force and the rising time to 64% of the reference is 53 ms. Compared with it the rising time of the combination model and the control model neglecting the flow force of the servo valve are 257 ms and 73 ms respectively.

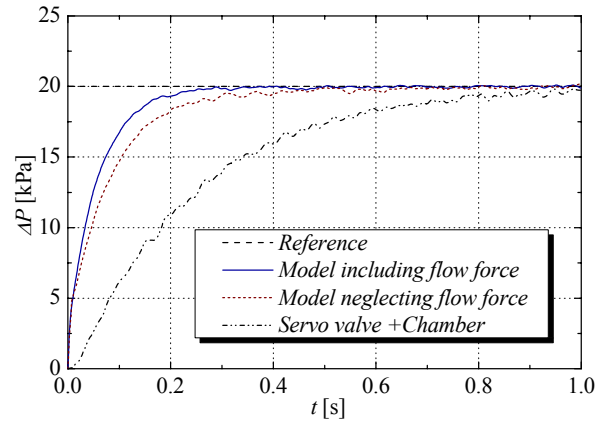


Figure 6 Step reference tracking responses

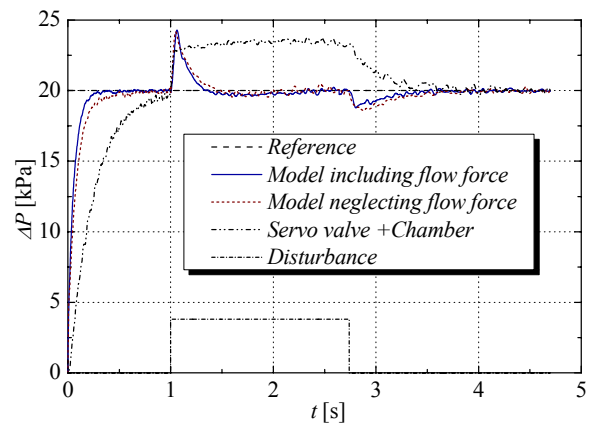


Figure 7 Disturbance restraining response

As a disturbance, an additional pressure with the amplitude of 3.7kPa and time interval of 1.74 s is added to right control chamber after the control system has settled to the steady state. Figure 7 shows that disturbance restraining response of the control model including the influence of the flow force and neglecting it at the steady state of 20 kPa. Quicker disturbance restraining effect with the control model including the influence of the flow force shows the differential pressure controllability could be improved.

Conclusion

A linear model for the differential pressure has been derived from the nonlinear model for a 4-port nozzle-flapper type pneumatic servo valve and two control chambers including the flow force of the servo valve. Simulation and experiment show that the flow force influences the steady state error of the servo valve dynamics. The differential pressure control system design using a TDF controller has been performed based on the two models including and neglecting the flow force. As expected and verified by the experiment, better control effect for reference input tracking and disturbance restraining is achieved for the proposed model including the flow force than the model neglecting it. It is signified that the differential pressure controllability can be improved by using the proposed model.

Appendix A: Derivation of the linear model

From the armature-flapper model in Eq. (1) and (2), a transfer function, relating the displacement due to input current and the control pressure can be derived as follows:

$$\frac{\Delta x(s)}{K_i l_f \Delta i(s) + (T_e s + 1) l_f^2 (K_{10} \Delta P_{c1}(s) - K_{20} \Delta P_{c2}(s))} = \frac{1}{a_3 s^3 + a_2 s^2 + a_1 s + a_0} \quad (A1)$$

where

$$a_0 = K_a - K_m, \quad a_1 = B_f + K_a T_e$$

$$a_2 = J + B_f T_e, \quad a_3 = J T_e$$

K_{10} is K_{f1} at the equilibrium position.

K_{20} is K_{f2} at the equilibrium position.

By linearizing Eq. (7) at the equilibrium position, the flow rate variation at the fixed orifice can be obtained from the control pressure variation as follows:

$$\Delta G_{o1} = a_{o1} \Delta P_{c1} \quad (A2)$$

$$\Delta G_{o2} = a_{o2} \Delta P_{c2} \quad (A3)$$

where:

$$a_{o1} = \left. \frac{dG_{o1}}{dP_{c1}} \right|_{P_{c1}=P_{c10}}, \quad a_{o2} = \left. \frac{dG_{o2}}{dP_{c2}} \right|_{P_{c2}=P_{c20}}$$

By linearizing Eqs. (8) and (9) at the equilibrium position ($x=x_0=0$, $P_{c1}=P_{c10}$, $P_{c2}=P_{c20}$), the flow rate variation at the nozzle-flapper can be obtained from the displacement variation and the control pressure variation as follows:

$$\Delta G_{n1} = a_{x1} \Delta x + a_{p1} \Delta P_{c1} \quad (A4)$$

$$\Delta G_{n2} = a_{x2} \Delta x + a_{p2} \Delta P_{c2} \quad (A5)$$

where:

$$a_{x1} = \left. \frac{\partial G_{n1}}{\partial x} \right|_{\substack{x=x_0 \\ P_{c1}=P_{c10}}}, \quad a_{p1} = \left. \frac{\partial G_{n1}}{\partial P_{c1}} \right|_{\substack{x=x_0 \\ P_{c1}=P_{c10}}}$$

$$a_{x2} = \left. \frac{\partial G_{n2}}{\partial x} \right|_{\substack{x=x_0 \\ P_{c2}=P_{c20}}}, \quad a_{p2} = \left. \frac{\partial G_{n2}}{\partial P_{c2}} \right|_{\substack{x=x_0 \\ P_{c2}=P_{c20}}}$$

The transform function of the dynamics in the control chamber shown as in Eq (10) can be written as follows:

$$\Delta G_{c1}(s) = K_{c1} \Delta P_{c1}(s) \quad (A6)$$

$$\Delta G_{c2}(s) = K_{c2} \Delta P_{c2}(s) \quad (A7)$$

where:

$$K_{c1} = \frac{R\theta}{V_1}, \quad K_{c2} = \frac{R\theta}{V_2}$$

REFERENCES

1. Shearer, J. E., Study of Pneumatic Process in the Continuous Control of Motion with Compressed Air-I, II, Transactions of ASME. 1956, Feb. pp.233-249.
2. Zalmanson, L. A., Components for Pneumatic Control Instruments, 1965, Pergamon Press.
3. Urata, E., Influence of eddy current on torque-motor dynamics, 4th IFK Workshop, 2004. Mar 24. pp. 71-82.
4. Kawashima, K. Fujita, T. and Kagawa, T., Flow Rate Measurement of Compressible Fluid using Pressure Change in the Chamber, Trans. of the Society of Instrument and Control Engineering, 2001, Vo1.1, No.1, 32, p.252-258.
5. Wang, T. Cai, M. Kawashima K and Kagawa, T., Modelling of Pneumatic Nozzle-flapper servo valves, Spring Symposium of JFPS, 2004, May 26, pp. 70-72
6. Hiroi, K., US5105138, Two degree of freedom controller, Kabushiki Kaisha Toshiba, Kawasaki, Japan, 1992, April 14.

EXPLICIT FINITE ELEMENT ANALYSIS OF TRACKING CAPABILITY OF ROTARY FACE SEAL FOR INDUSTRIAL FLUID POWER APPLICATIONS

Olof CALONIUS and Matti PIETOLA

Department of Mechanical Engineering
Helsinki University of Technology
P.O. Box 4400, FI-02015 TKK, Finland
(E-mail: Olof.Calonus@tkk.fi)

ABSTRACT

Seals are generally inexpensive machine elements, but in industrial fluid power systems the costs of sealing failure can be much higher than the cost of replacing the damaged seal due to, e.g., costs related to process downtime. Consequently, careful design evaluation is needed. In this study, the capability of a large diameter rotary face seal of spring-loaded type to respond to unwanted axial motion between the sealing surfaces caused by sudden changes in loading of components of the process machinery was evaluated.

Explicit finite element analysis, well suited for highly non-linear problems involving frictional contact, was used to compute the response of the seal to forced relative axial motion of the sealing surfaces. For condition monitoring, temporal variation of the total contact force exerted on the counterface, i.e., the sealing force during excitations was recorded, representing simple virtual sensor output describing the relation between axial motion and contact situation.

KEY WORDS

Explicit, Finite, Element, Face, Seal

NOMENCLATURE

B	: Seal cross-section width [mm]
b	: Spring cross-section width [mm]
E	: Young's modulus [N/m ²]
H	: Seal cross-section height [mm]
h	: Spring cross-section height [mm]
$PTFE$: Polytetrafluoroethylene
R	: Seal contact radius [mm]
r	: Radial coordinate [mm]
t	: Spring thickness [mm]
W	: Seal contact width [mm]
α	: Coefficient of thermal expansion [1/°C]
μ	: Friction coefficient [-]
ν	: Poisson's ratio [-]

ω	: Angular velocity [1/s]
ρ	: Density [kg/m ³]
σ_Y	: Yield stress [N/m ²]

INTRODUCTION

This study was motivated by a need to evaluate prospective seal designs of critical components in process machinery. In a previous study [1], an initial seal profile shape of two different sizes was investigated in which the seal lip had approximately the same radial location as the actuation zone of the spring. For this study, the seal profile was modified by changing the radial location of the lip in relation to the actuation zone of the spring in order to increase the contact pressure on

the oil side of the lip. The capability of the modified rotary face seal design to react to excessive axial motion between the sealing surfaces was investigated. In addition, for condition monitoring purposes, the contact situation between the seal and the counterface was monitored by recording the sealing force values during axial motion excitations.

METHODS

Seal model

The cross-section of the seal is shown in Figure 1. The dimensions were $R = 249$ mm, $W = 0.2$ mm, $B = 13$ mm, $H = 7$ mm, $b = 6$ mm, $h = 4$ mm and $t = 0.26$ mm. A corresponding axisymmetric finite element model of the seal was built, Figure 2. Abaqus/Explicit was used for solving the response to the axial excitations. The model comprised 450 CAX4R elements in the seal jacket and 168 CAX4R elements in the spring. The rotor, clamp and counterface were modeled as rigid parts.

Frictional contact was specified between the different parts. In the static joints between seal and clamp and seal and rotor the coefficient of friction was 0.1. The same value was chosen for the dynamic joint between seal and counterface because relatively high contact stresses were expected at the seal lip and sliding speed in the radial direction was expected to be low [2]. For the seal-spring contact pair three different friction coefficient values were tested: $\mu = 0.06, 0.18, 0.36$. The base value of 0.06 was chosen to represent friction between seal and spring at low sliding speeds [3]. The other values were chosen to model the effect that dirt and deposits could have on the dynamic behavior of the seal-spring contact.

Temperature dependent properties for the glass fiber filled *PTFE* material of the seal jacket [4] and the Hastelloy C-22 [5] spring were chosen according to Table 1. A Drucker-Prager material model was chosen for the *PTFE* material in Abaqus to be able to model the fact that the material had higher yield stress in compression than in tension. The same model was previously used in [1], in which the dependence between stress and plastic strain also was listed.

Analysis steps and loads

The actual analyses consisted of determining the response of the seal to relative motion between the rotor and the counterface. To be able to study the response, computations to obtain the operating conditions were conducted. The seal was first clamped against the rotor and subsequently compressed 0.9 mm against the counterface. Then the operating temperature distribution, the rotational body force and the pressure load were applied. The analyses were therefore carried out as four consecutive computational steps: 1) clamp, 2) compress, 3) apply operating conditions and 4) apply excitation.

The analysis time was 0.05 s in the three first steps and 2.05 s in the excitation step, 2.20 s in total. To speed up

the analyses in Abaqus/Explicit, mass scaling was used [6]; scaling factor 100 in steps 1)–3) and 400 in step 4). The temperature distribution in the seal profile was computed in a separate heat transfer analysis in Abaqus/standard. This was a simplified analysis in that only temperature boundary conditions corresponding to typical design requirements were applied. The temperatures in the response analyses varied from 100 °C at the contact zone of the seal lip to 60 °C in regions in contact with the oil and 40 °C in boundary regions elsewhere. The centrifugal effects were taken into account by applying a rotational body force ($\rho r \omega^2$, $\omega = 81.7$ 1/s) in the radial direction to the spring and the seal jacket. The parts of the seal jacket in contact with the oil were loaded with a pressure of 0.05 MPa.

Excitations

Forced displacement excitations were applied to the seal-clamp-rotor combination to produce relative motion between the seal and the counterface. During the excitations the rotor and the clamp were allowed to move only in the axial direction and the seal and the spring interacted with the other parts only through frictional contact.

Two different excitations were applied. Excitation 1 was produced from measurements of the relative motion between rotor and counterface in an industrial setting during a change in the loading of the machinery, Figure 3 (a). The displacement signals were obtained by twice integrating the output signals of accelerometers measuring motion in the axial direction. The relative motion signal was produced by filtering (band-pass 0.5-6 Hz) the displacement signals and computing their difference. This filtered relative motion signal is shown in Figure 3 (b) together with Excitation 2, a sinusoidal signal with an amplitude of 0.6 mm representing a situation of unwanted excessive relative motion.

RESULTS

Sealing force

The sealing force, i.e., the temporal variation of the total contact force exerted by the seal on the counterface, recorded the response to different excitations. Abnormal contact situations, loss of contact or excessive contact outside the seal lip, were easily detected, as shown in Figure 4 (a). During Excitation 1 the maximum, minimum and average values of the sealing force were 3.3 kN, 0.86 kN and 1.95 kN, respectively. These values were computed for $\mu = 0.06$ between seal and spring. The influence of seal-spring friction on the seal dynamics was found to be small as shown in Figure 4 (b). For all three values of μ tested, nearly the same force response was obtained.

Stresses and contact pressure

The contour plot in Figure 5 shows the axial stresses in the seal cross-section during normal operation (seal in base position after compression).

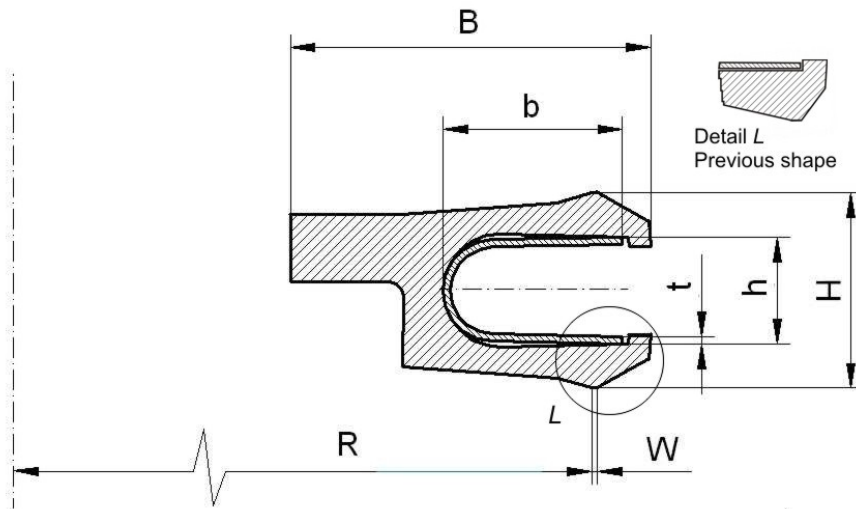


Figure 1 Cross-section of seal. Oil space on the right and air space on the left, towards the rotation axis. Dynamic sealing zone (W) will be in contact with the counterface. Upper parts of seal will be clamped against rotor. Detail L shows earlier seal lip design.

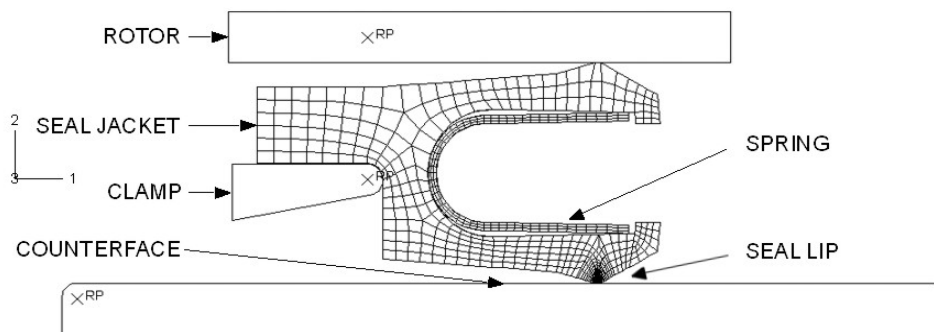


Figure 2 Finite element model of spring-loaded face seal. Configuration before clamping and precompression shown. Axial direction is vertical and radial direction is to the right.

Table 1 Material properties

Property	PTFE	Hastelloy
σ_Y	6 MPa @ 23 °C 1.8 MPa @ 120 °C	408 MPa @ 24 °C 373 MPa @ 93 °C
E	600 MPa @ 23 °C 205 MPa @ 120 °C	206 GPa @ 24 °C 203 GPa @ 93 °C
ν	0.46	0.3
ρ	2160 kg/m ³	8690 kg/m ³
α	1.9×10^{-4} 1/°C ⁽¹⁾	1.1×10^{-5} 1/°C

⁽¹⁾ For temperatures above 31 °C (3.3×10^{-4} 1/°C in range 19-31 °C)

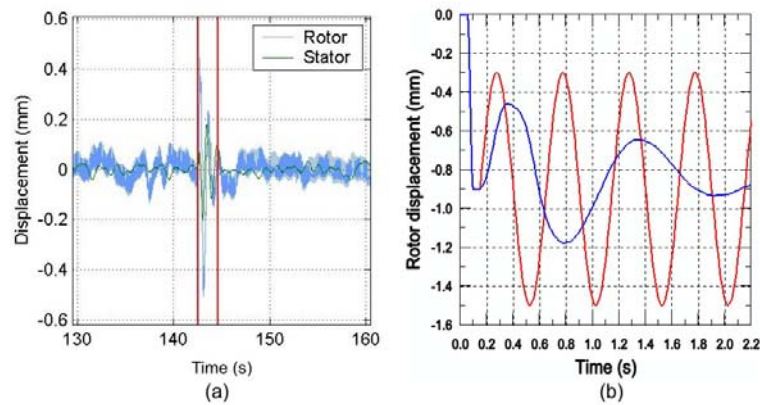


Figure 3 (a) Measured motion of rotor and counterface (stator) in process machinery. Change of loading at approximately 142 s. Excitation 1 has been produced from signals between vertical lines. (b) Excitations applied to the seal-clamp-rotor combination. Curve in middle is Excitation 1, produced from the filtered signals in (a). Sinusoidal curve is Excitation 2, an artificial motion signal used for studying the effects of excessive motion and diagnostic capability of the virtual total contact force sensor.

As a result of clamping, there were high compressive stresses, reaching -10 MPa, in the seal flange. At the end of Excitation 1 there were high tensile/compressive bending stresses in the spring ($+284 / -315$ MPa) and in the vertical part of the seal profile ($+4.6 / -4.7$ MPa). In the beginning of the excitation the highest stresses in the spring exceeded the yield stress. Yielding was restricted to few elements close to the symmetry line of the spring in the outer element layers.

Figure 5 also shows the stress field resulting from excessive contact between the vertical part of the seal and the counterface. A collision of this kind leads to permanent deformation of the profile with large plastic strains developing in the middle of the vertical part of the seal profile where there already were high compressive stresses during normal operation. In this region the axial compressive stresses reached -14 MPa and the equivalent plastic strains reached 7%. High axial compressive stresses were present in the seal lip at the contact zone. At the end of Excitation 1 the maximum compressive stress reached approximately -10 MPa. At the same time there were substantial radial compressive stresses in the seal lip reaching -5.6 MPa. High bending stresses also developed in the lower part of the seal between the vertical part and the lip. During Excitation 1 the highest values were ± 9 MPa.

Figure 6 shows close-ups of the seal lip of both an earlier design and the current design. The axial stress concentration due to contact was on the air side of the contact zone. The contact pressure distribution under the seal lip was roughly parabolic in shape, Figure 7. When the seal profile was in base position (corresponding to 0.9 mm compression) the contact pressure dropped to zero at the nodes closest to the oil side.

DISCUSSION

Current seal lip design

The current seal lip design was conceived under the hypothesis that by moving the seal contact zone somewhat towards the air side, the spring would exert more pressure on the oil side of the contact zone compared to the earlier design, c.f. Figure 6. A design in which the peak of the contact pressure distribution is located on the oil side is often considered a prerequisite for good sealing capability in lip seals [7–9]. It appears, see Figures 6 and 7, that the design change was not radical enough. The peak of the contact pressure distribution did not relocate to the oil side of the sealing zone. The lower part of the seal jacket still pivots about the air side edge of the seal lip during axial motion. Apart from the high stresses in the seal flange caused by clamping, there were three high stress regions. High bending stresses were found in the vertical part of the seal, next to the clamp, and in the horizontal part between the vertical part and the seal lip. During Excitation 1 plastic strains developed in the latter region. In the seal lip, near the contact zone, the compressive stresses clearly exceeded the yield stress.

Tracking capability

The tracking capability of the current seal was found to be adequate for coping with the measured axial motion (Excitation 1) produced by changes in loading of the machinery. However, as shown by the response of the seal to Excitation 2 (Figures 4 and 5), small changes in the motion amplitude can cause leakage or even damage the seal, if it is not protected against excessive compression by proper seal housing design.

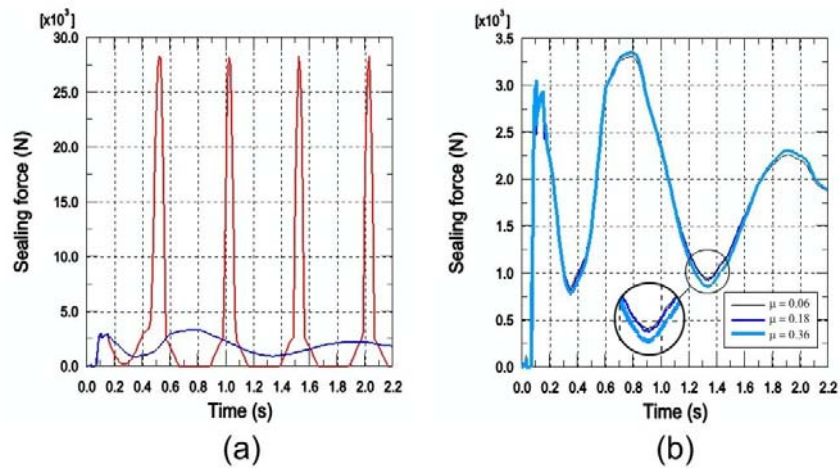


Figure 4 (a) Sealing force values corresponding to Excitation 1 (smoother curve) and to Excitation 2 (curve with spikes). Zero sealing force indicates loss of contact, while spikes indicate contact outside intended contact zone.
 (b) Effect of friction between seal and spring ($\mu = 0.06, 0.18$ and 0.36) on sealing force for Excitation 1. In the figure, the line width increases with the value of μ .

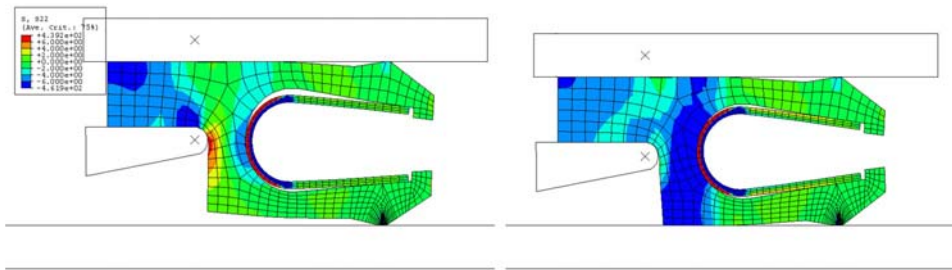


Figure 5 Vertical, i.e., axial stresses in seal profile. Seal in base position after compression shown left and vertical part of seal colliding with counterface due to excessive axial motion (Excitation 2) shown right. High compressive stresses are produced in the attachment flange and typical bending stresses are seen in vertical regions of seal and spring. The collision results in high compressive stresses in the vertical part of the seal and deformation of the profile.

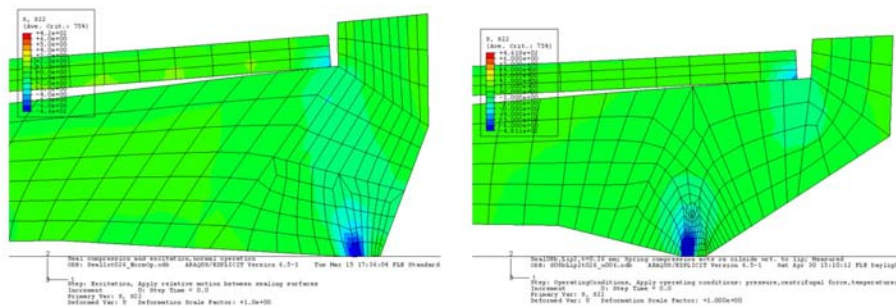


Figure 6 Vertical stresses in seal lip. Earlier lip shape shown left and current lip shape shown right. In both cases the highest compressive stresses are located towards the air side of the contact zone.

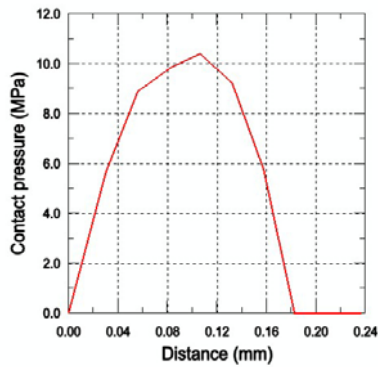


Figure 7 Contact pressure distribution under seal lip for current seal design. Seal profile in base position after Excitation 1.

Note that the seal maintains contact (non-zero sealing force) with the counterface during the first cycle of Excitation 2, Figure 4 (a). It is only after the collision that loss of contact occurs during the recession part of the motion cycle. As long as the seal is undamaged, a natural upper limit on the rebound travel is the precompression, 0.9 mm in this case [1].

For the axisymmetric model the sealing force appeared to be a simple but appropriate indicator describing the overall contact situation between seal and counterface. A similar indicator was the temporal variation of the internal energy (strain energy plus plastic dissipation). For example, the internal energy curve had spikes coinciding with situations of excessive contact, but the sealing force curve depicts this situation more clearly. Loss of contact can also be more easily discerned from the sealing force curve. Loss of contact directly leads to leakage and collision can lead to leakage because the shape of the seal jacket is likely to change permanently.

Finite element modeling

Mass scaling was needed to keep the analysis time reasonable. During the assembly steps 1) to 3), the scaling factor was not increased above 100 to avoid artificial inertial effects. During excitation a scaling factor of 400 was considered acceptable because as long as the seal lip stayed in contact with the counterface artificial inertial effects were not perceived. With these settings and a total analysis time of 2.2 s, the analysis was typically left to run overnight on a PC workstation. The mesh density was chosen so as to adequately describe the overall dynamic behavior of the seal profile. For contact related phenomena, e.g. wear, mesh refinement in the seal lip region is needed to produce a more accurate contact pressure distribution. Submodeling of the contact region could therefore be considered. For condition monitoring purposes a model of reduced computational complexity would, however, be needed to provide fast enough feedback. Further work should involve assessment of changes in the contact situation over time due to, e.g., wear and creep.

CONCLUSIONS

The studied seal design could handle the measured axial displacements between the sealing surfaces without loss of contact. However, there is not much allowance for larger displacements. The seal housing needs to be designed to protect the seal against excessive compression causing irreversible deformation.

It appears that the current seal lip design does not represent a significant improvement over the earlier design as a contact pressure distribution similar to the previous one was produced. The current design can be further improved by increasing the dimensions of the cross-section to account for larger displacements.

Increased friction between spring and seal did not influence the axial dynamic behavior of the seal for the range of tested friction coefficient values (0.06–0.36).

The total seal-counterface contact force output from the finite element model could be used as a virtual force sensor to monitor and record the contact variations during operation.

REFERENCES

1. Calonius, O. and Pietola, M., Explicit Finite Element Analysis of Spring-Energized Rotary Face Seal for Industrial Process Machinery, 18th Abaqus Users' Conference, Stockholm, Sweden, 18-20 May 2005.
2. Hoffman, C., Untersuchungen an PTFE-Wellendichtungen, Dissertation, Universität Stuttgart, Institut für Maschinenelemente, Bericht Nr. 61, 1995.
3. Sui, H., Pohl H., Schomburg U., Upper U., and Heine S., Wear and Friction of PTFE Seals, *Wear*, 1999, **224**, pp. 175-182.
4. Pohl, H., Computerunterstützte und experimentelle Untersuchungen von Manschettendichtungen aus glasfaserverstärktem PTFE-Compound, Dissertation, Universität der Bundeswehr, Hamburg 1999.
5. MatWeb Online Materials Database: www.matweb.com, accessed 31.10.2003.
6. Abaqus Analysis User's Manual, Abaqus Inc., Providence, 2004, Ch. 7.16 Mass Scaling.
7. Kawahara, Y., Abe, M. and Hirabayashi, H., An Analysis of Sealing Characteristics of Oil Seals, *ASLE Transactions*, 1980, **23**, pp. 93-102.
8. Müller H.K., Concepts of Sealing Mechanism of Rubber Lip Type Rotary Shaft Seals, *Proceedings of the 11th International Conference on Fluid Sealing*, 1987, pp. 698-709.
9. Salant R.F., Theory of Lubrication of Elastomeric Rotary Shaft Seals, *Journal of Engineering Tribology*, 1999, **213**, pp. 189-201.

THE CFD SIMULATION RESEARCH ON HYDRAULIC TRANSFORMER

Ma Jien, Xu Bing, Ouyang Xiaoping, Yang Huayong

The Key State Lab of Fluid Power Transmission and Control
Zhejiang University, Hang Zhou 310027, PR China
(E-mail: jienma@hotmail.com)
(Tell: +86 571 87952500 224)

ABSTRACT

A new hydraulic transformer (named NHT) prototype has been designed and tested by Zhejiang University in China. The results show that the HT can realize the function of transforming pressure, but its parameters such as efficiency and noise should be improved further. To help optimizing it, CFD-simulation using commercial software FLUENT is introduced. And the fluid field inside this hydraulic component can be theoretically analyzed. The velocity field and pressure distributing at different places such as the oil gap between the cylinder block and the valve plate, and between the valve plate and the end cap, or inside the cylinder chamber are founded. And the flow fields were analyzed in different rotate speeds and control angles. Besides the flow field was discussed under different grid cell numbers. The conclusions contribute to the understanding of the flow conditions inside the NHT and thereby supply dependences for optimization on the NHT.

KEY WORDS

CFD, Hydraulic transformer (HT), Simulation

INTRODUCTION

During the development of the secondary control, the idea of a hydraulic transformer enabling the extraction of controlled oil flow from the pressure net without incurring large valve losses was pursued [1]. Therefore, the new hydraulic transformer (named NHT) with three rather than two control kidneys was studied widely by

company INNAS, Linköping University, Caterpillar Inc, Rexroth, Zhejiang University and so on. Today, an improved NHT prototype has been designed and tested by Zhejiang University in China. And this prototype broadened the control angle of the NHT. The characters such as flow, pressure, efficiency and noise were tested on a Common Pressure Rail (CPR) system, which could provide a steady pressure at the supplying rail.

Currently CFD (computational fluid dynamic) have become popular in application of hydraulic components analysis [2]. This technique has made very good progress in recent years. That together with the increasing speed of computers makes CFD very interesting to use in this line of work [3]. Therefore, this paper introduced an application of CFD commercial software on study of the flow configuration and pressure distribution inside the NHT. The overall aim of this investigation is to contribute to the understanding of the flow conditions inside the NHT and thereby supply the dependences for further optimization on the NHT.

THEORETIC ANALYSIS

The structure of the new hydraulic transformer is similar to a conventional seven-cylinder, bent-axis axial piston pump, except that the NHT has three control kidneys rather than two. Therefore, the problems of bent-axis axial piston pump such as cavitations, volumetric loss, and noise are all faced while investigating the NHT. The NHT's control angle can be altered by turning around the valve plate, and the flow conditions inside the NHT are changed at different control angles.

Cavitations are the main reason to place a premium on noise of hydraulic components; therefore it goes by the name of cancer in liquid flow. Cavitation or the formation of gas filled bubbles occurs when the static pressure somewhere inside the NHT drops below a certain critical level [4]. These bubbles are transported to high pressure region of the NHT where they are compressed violently. These not only lead to increased volumetric loss and vibration levels but also could bring damage of the NHT if a gas bubble is located near a wall when it is compressed [2]. Hence, it is important to understand the phenomena involved inside the NHT in order to minimize the pressure drop and thereby utilize the available inside pressure in the most optimum way. A scope of our investigations is therefore to find where it might cavitate inside the NHT by resorting to CFD simulation tool.

EXPERIMENTS

A prototype of new hydraulic transformer is shown in Figure 1, which was designed by Zhejiang University. A diagram of the test setup is shown in Figure 2 and this is a CPR system, which means that all of the appliances in these are connected to the same rail and are offered the same "common" pressure. This system mainly consisted of a NHT, two fluid power pumps, two accumulators, three pressure transducers and three flow meters mounted at the inlet and outlet of the NHT, a cooling system, safe precaution units and a 200 l tank. Besides, a noise Fourier analyzer was added to register the noise level and the rotation speed was measured with an optical sensor.

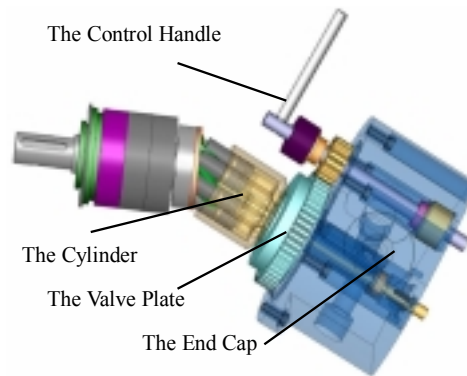


Figure 1 A prototype of new hydraulic transformer

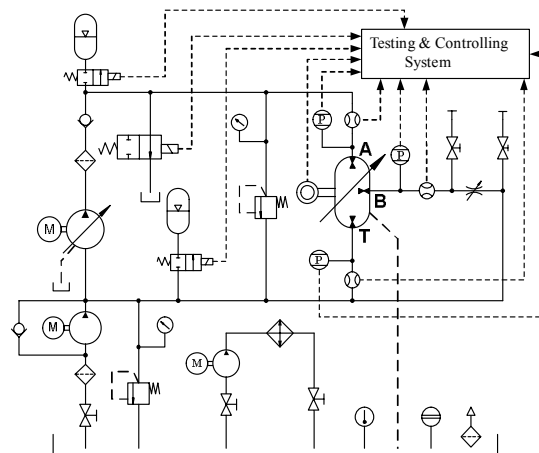


Figure 2 The test setup of a NHT

During a test procedure, the control angle was changed by the control handle of the NHT, which lead to the variety of delivery pressure. And the supply pressure for port A in Figure 2 would also be alternated to different levels by the variable pump. The noise level and the volumetric loss both increased while the rotation speed was largening. Such an increase could be studied in Figure 3 in the next page which shows the noise level and the volumetric loss as a function of the NHT rotation speed from test runs with an ordinary hydraulic oil of viscosity class ISO VG 46.

In order to investigate this further, some other approach was chosen. A way of using CFD and numerically determine the flow field inside the NHT was chosen in this investigation.

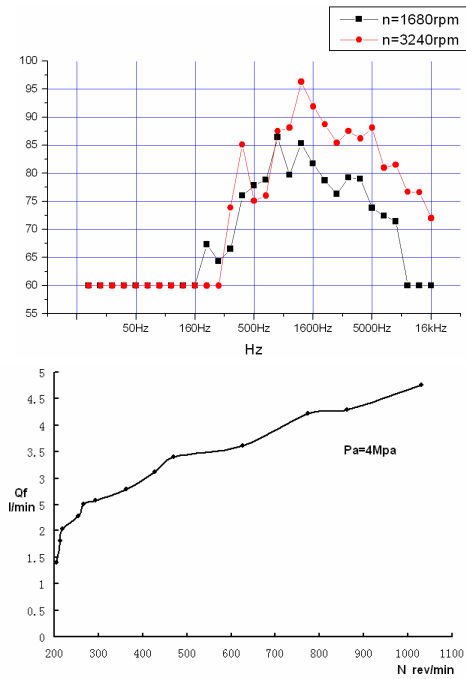


Figure 3 The noise level and volumetric loss characters with the rotation speed

CFD-SIMULATIONS

A commercial CFD software package called Fluent was used for all of the simulations in this research. This package consists of a pre-processor, Gambit for geometry and mesh generation; a combined solver; and a post-processor for analyzing and presentation of simulation results. The solver is based on the finite volume method (FVM) to discretize the governing equations for mass, momentum and energy transfer [5].

The internal flow geometry of the NHT comprises of three inlet/outlet manifolds, the cylinders, the valve plate, two thin gaps, one between the valve plate and the cylinder and another between the valve plate and the end cap. This geometry would introduce difficulties for analysis as the computational domain, and there is a need for simplification, otherwise the CFD-model will become very large and time-consuming to solve even on very powerful computers.

The final solution was to separate this geometry into two parts, the upper one and the lower one, which are represented in Figure 4 below with a control angle of 60°. Each part includes three geometries at different control angles with different rotation speeds. Specially, a two-dimensional CFD computations focus on the cylinders was analyzed to see the detailed flow situations at this part, because the flow field is very complex here

and cavitation is most likely to occur.

The properties of the fluid were chosen according to the same hydraulic oil with a fluid density of 910 kg/m^3 and a viscosity of 0.0048 kg/m-s that was used in the experiments and such a fluid makes it possible to use incompressible flow in the simulations.

Under normal operating conditions, the flow inside the NHT is probably laminar with some local disturbance of turbulent flow. Since the aim was to keep the simulation as simple as possible, laminar flow was used in the three-dimensional simulations. While as for the two-dimensional simulation turbulence model was chosen to reach the accurate results for the increase in computing effort is acceptable even at this flow situation. Three different viewing sections of the NHT are used to present the results in this paper:

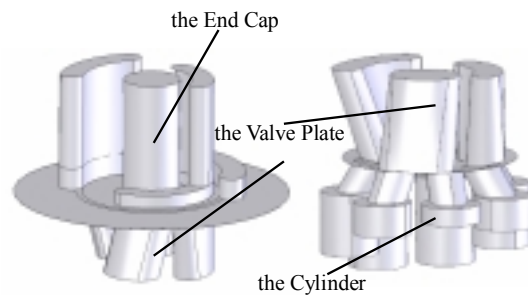
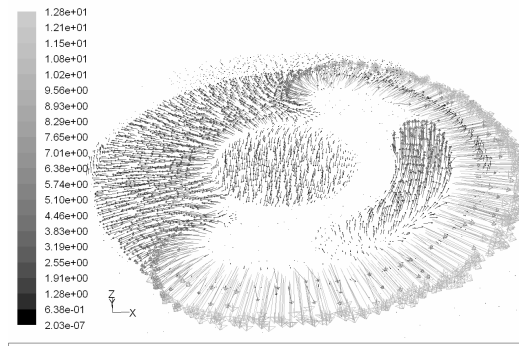


Figure 4 The 3D simulation geometries

Results of the upper part 3D simulation

The geometry of the upper part includes three inlet/outlet manifolds, part of the valve plate, and the thin gap between the valve plate and the end cap, which are shown on the left of Figure 4. The pictures in Figure 5 and Figure 6 show the surface of a cut-out at the middle section of the thin gap, including velocity vectors on the upper part and static pressure contours on the lower. The pictures in Figure 5 and Figure 6 are the results of the simulation at the same situations except for the different grid cell numbers.



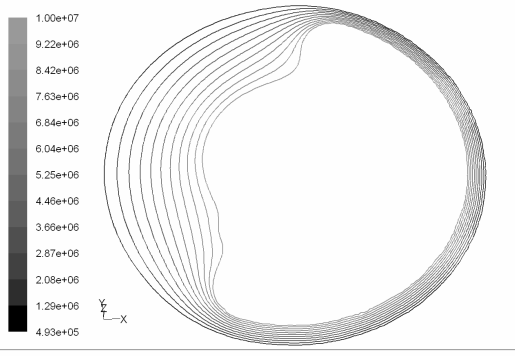


Figure 5 Velocity vectors and pressure contours of the upper part with a mixed grid cells number of 466 000

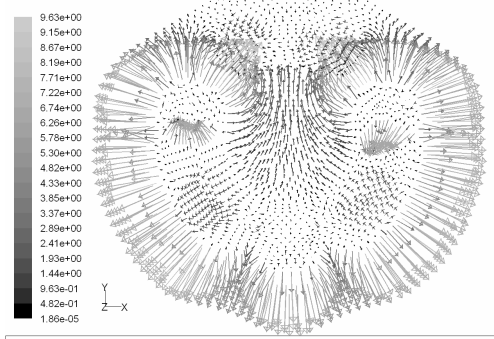


Figure 7 Velocity vectors and pressure contours of the lower part with a mixed grid cells number of 258 000

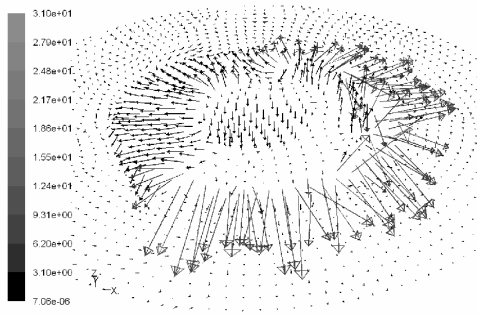


Figure 6 Velocity vectors and pressure contours of the upper part with a mixed grid cells number of 42 000

Results of the lower part 3D simulation

The geometry of the lower part includes the cylinders, part of the valve plate, and the thin gap between the valve plate and the cylinder, which are shown on the right of Figure 4. The pictures in Figure 7 and Figure 8 show the surface of a cut-out at the middle section of the thin gap, velocity vectors on the upper part and pressure contours on the lower. The pictures in Figure 7 and Figure 8 are the results of the simulation at the same situations except for the different grid cell numbers.

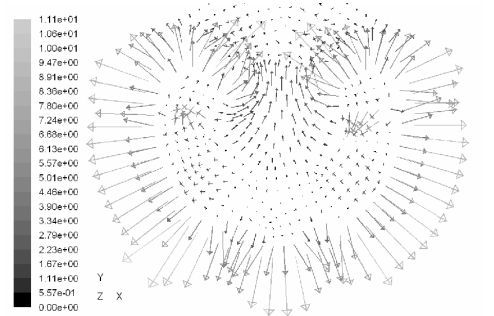


Figure 8 Velocity vectors and pressure contours of the lower part with a mixed grid cells number of 26 000

Results of the cylinders 2D simulation

The liquid flow in the cylinders is probably the most strong turbulent and likely to lead cavitation while a cylinder is just reaching or leaving a control kidney, which we named the opening area and the closing area. Because the valve plate of the NHT has three control kidneys and three typical control angles are investigated here, there were eighteen ($3 \times 3 \times 2$) groups of results totally. The pictures in Figure 9 show a group of results of cylinders' two-dimensional simulations at the control angle of 60° at the opening area of the high pressure kidney port A, velocity vectors on the upper and the corresponding pressure contours at the near following. The left part of these pictures represents the curvature of the valve plate port and the right represents a cylinder at different positions. The pressure levels of the pressure contours in these figures are the static pressure relative to the inlet pressure.

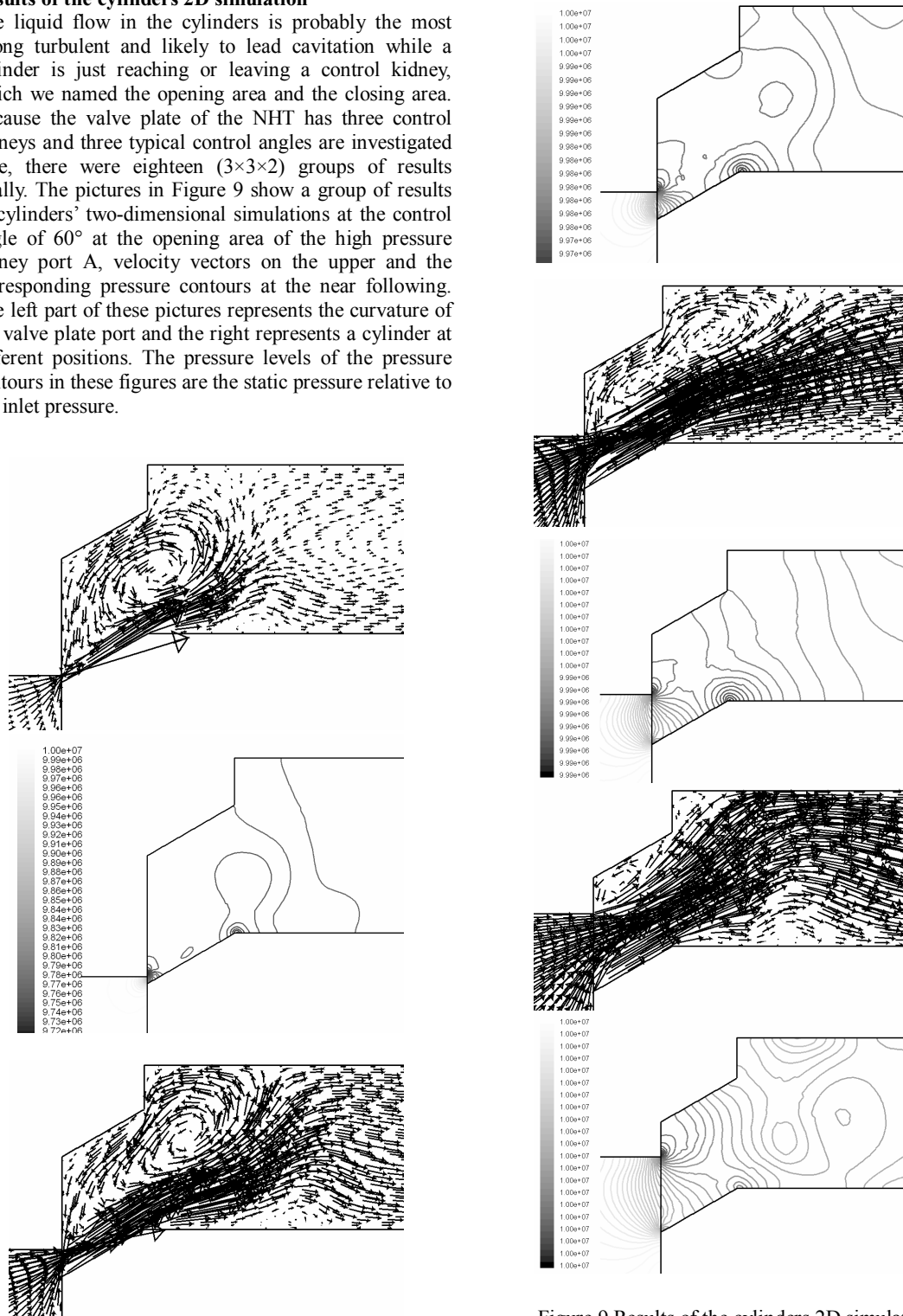


Figure 9 Results of the cylinders 2D simulation

DISCUSSION

According to Figure 5 to Figure 8, there are radial flow fields in the thin gaps because of the pressure difference. The volumetric loss can be calculated using this CFD software. Simulation results show that the volumetric loss is 7.8×10^{-5} l/min at the thin gap between the valve plate and the end cap and is 0.59 l/min between the valve plate and the cylinder with a rotation speed of 1000 rpm. While the experiment result from the right picture in Figure 3 revealed the volumetric loss of about 4.5 l/min at the rotation speed 1000 rpm. This can be concluded that the volumetric loss through the thin gaps is part of the total result under experiment and this is not the whole reason of volumetric loss. Another probable reason is the oil leaking at the cylinder. It can be studied from the figures that the volumetric loss is much lower at the thin gap between valve plate and end gap than that between the valve plate and cylinder. On the other hand, the liquid fields indicate that the total liquid loss includes not only the difference between measured inlet and outlet flow rate but also the liquid leaking inside the NHT from higher pressure kidney port to lower ones through the thin gaps. This phenomenon is difficult to observe and calculate through experiment.

The question is if the accuracy of the CFD-simulation is good enough to be used for the conclusions. Considering the complexity of the geometry, the cells number is probably a big source of error in the simulation. Therefore, results at different cells numbers were shown. And there is just a difference of smooth. Maybe to some extent the cell density only affects the accuracy of the value in each discrete point and not so much the flow field in general. So the results are relatively reliable.

The results in Figure 9 indicate the areas in the flow field with low pressure that could be important for cavitations. It is the area just behind the moving direction of cylinders, in which a vortex with low pressure generated according to these simulations. A smoother edge on the front of the cylinder will probably give a more favorable flow into the cylinder since it will reduce the size of the vortex. The results also show that the low pressure area at the high pressure kidney port A is much lower compare with the other two kidneys. The pressure of the low pressure areas is decrease with the rotating speed increasing, i.e. control angle increasing. Based on the theoretic analysis, this conclusion offers a possible explanation to the phenomenon that the noise level was heightened while the control angle increasing.

CONCLUSION

The simulation results correlate well with the experiments in this investigation. A possible explanation of the noise and the volumetric loss behavior is offered by the CFD-simulations. Furthermore, the use of CFD simulation tool can provide additional information on the

direct acting the NHT flow configuration and pressure distribution; thereby supply the dependences for further optimization on the NHT. In general this investigation reveals the usefulness of the CFD-simulations in the NHT design.

Acknowledgement

The authors would like to express their gratitude towards the National Natural Science Foundation of China for providing necessary funding of this project (the grants No.50305032).

REFERENCES

1. Prof. Dr-Ing. Dr. h. c. mult. Wolfgang Backe, What are the Prospects Facing New Ideas in Fluid Power, Fluid Proceedings of the Sixth International Conference on Power Transmission and Control ICFP'2005, pp. 6-15.
2. Roger Yang, CFD Simulation inside Hydraulic Valves, SAE off-Highway Engineering, June 2002.
3. P-E Wiklund, G C Svedberg, Three-dimensional CFD-a Possibility to Analyse Piston Pump Flow Dynamics, Advances of CFD in Fluid Machinery Design, 2003, PP. 159-170.
4. Pär-Eric Wiklund, Suction Dynamic of Axial piston Pumps, [D], Royal Institute of Technology, KTH, Sweden, 1998.
5. FLUENT Inc., User's Guide 6.0[M], USA: Fluent Inc., 2001.

Dynamic Characteristics of a Spool Valve Coupled with Electromagnetic and Mechanical Effects

Atsushi YUGE^{*}, Koki TOMIOKA^{**}, Kazuhiro TANAKA^{**}, Katsuya NAGAYAMA^{**},
Kimishiro TOKUDA^{**}

^{*} Nagasaki Research & Development Center
Mitsubishi Heavy Industries, LTD.
5-717-1 Fukahori-machi, Nagasaki, 851-0392, Japan

^{**} Department of Mechanical Information Science and Technology
Kyushu Institute of Technology
680-4 Kawazu, Iizuka-city, Fukuoka, 820-8502, Japan

ABSTRACT

A spool valve as a flow direction control valve has usually been used in a hydraulic system. In recent years, some hydraulic actuator systems need high accuracy control of the spool valve in order to control the delivery precisely. For the reason, it is very important practically to know dynamic motion of the spool.

To analyze the dynamic characteristics of the spool valve, it is necessary to consider the dynamic motion of the spool. Springs, solenoids and working fluid, which is pressurized by the pump in the circuit, support the spool. The motion of the spool is governed complicatedly by pressure force, flow force, electromagnetic force and mechanical spring force acting on itself. As a result, it is difficult to analyze the dynamic motion of the spool, and therefore, any commercial code to calculate the dynamic characteristics of the spool valve dose not exist at present.

Final target of this study is to develop numerical code to predict precisely the dynamic motion of the spool valve. As the first step, dynamic characteristics of a spool valve coupled with electromagnetic and mechanical effects have been conducted in the present paper.

KEY WORDS

System Dynamics, Coupled Analysis, Spool Valve, Electromagnetic Analysis

Nomenclature

A :	Vector Potential	[Wb/m]	m :	Mass of the Conductor	[kg]
B :	Magnetic Flux Density	[T]	n :	Normal Vector	[m]
c :	Damper Coefficient	[kg/s]	S :	Surface of the Conductor	[m ²]
F :	Vector of Force	[N]	T :	Maxwell stress tensor	[T ²]
f :	Force	[N]	V :	Vector of Velocity	[m/s]
J :	Current Density	[A/m ²]	V :	Velocity of the Conductor	[m/s]
k :	Spring Coefficient	[kg/s ²]	x :	Displacement of the Conductor	[m]
			v :	Reluctivity	[m/H]
			σ :	Electric Conductivity	[S/m]

INTRODUCTION

A spool valve as a flow direction control valve has usually been used in a hydraulic system. A spool in its valve is controlled by electromagnetic force. Therefore, it is necessary to predict behavior of the spool by analyzing dynamic characteristics of the spool valve.

As dynamic characteristics of the spool are affected by fluid force, electromagnetic force and mechanical force, the behavior of the spool is very complex. Hence, it is necessary to consider three forces as represented above to analyze completely the dynamic characteristics of the spool valve. However, any commercial codes to calculate the dynamic characteristics of the spool valve considering the above three forces dose not exist at present. So, it is important to establish a prediction way of dynamic behaviors of the spool valve coupled with the above three forces.

As the first step of the complete coupled analysis, the analysis coupled with electromagnetic system and mechanical system was carried out in this study. An electromagnetic field was three-dimensionally modeled by using a partial differential equation by the A-method. On the other hand, dynamic characteristics in a mechanical system were one-dimensionally modeled by using ordinary differential equations based on the Bondgraph method. In this paper, the following two steps were conducted to verify the coupled analysis;

- (1) To develop an analysis code for an electromagnetic field and to verify this program by comparing with the experimental results on a simple model.
- (2) To establish a way coupling with the A-method and the Bondgarph method.
- (3) A movable conductor which replaces the spool is connected to spring and damper. The behavior prediction of this conductor is simulated to verify the coupled analysis.

ANALYSIS METHOD

Analysis Method for Electromagnetic System

The electromagnetic analysis was carried out using the A-method. A vector potential is expressed as the following equation with a magnetic flux density.

$$\mathbf{B} = \nabla \times \mathbf{A} \quad (1)$$

After Maxwell equations are transformed using Eq. (1), the governing equation for the electromagnetic field is shown by the following equation.

$$\nabla \times (\nu \nabla \times \mathbf{A}) = \mathbf{J} - \sigma \frac{\partial \mathbf{A}}{\partial t} + \sigma \{ \mathbf{V} \times (\nabla \times \mathbf{A}) \} \quad (2)$$

In the above equation, the second term of the right-hand side indicates an influence of eddy current. This term means that the eddy current is caused by a temporal change of the vector potential. And the third term of the right-hand side indicates an influence of speed electromotive force.

The left-hand side of Eq. (2) has a high degree of freedom. Solutions of the vector potential should be specified under the coulomb gauge condition, which it is usually necessary to constrain the vector potential. However, to consider the coulomb gauge condition is not necessary in this analysis because the magnetic flux density, which is obtained by the vector potential using Eq. (1), has the uniqueness.

In this analysis, a movable conductor which replaced a spool moves temporally. In order to realize this situation, it was necessary to change the shape of grids temporally. Therefore, Eq. (2) was transformed according to a curvilinear coordinates system. After that, discretization of the equation was carried out using the finite differential method. In addition, a way of backward difference was used for digitization of time.

Electromagnetic Force

In the present study, the electromagnetic force is obtained by Maxwell stress tensor. The tensor is expressed as follows;

$$T = \begin{bmatrix} B_x^2 - \frac{1}{2} \mathbf{B}^2 & B_x B_y & B_x B_z \\ B_y B_x & B_y^2 - \frac{1}{2} \mathbf{B}^2 & B_y B_z \\ B_z B_x & B_z B_y & B_z^2 - \frac{1}{2} \mathbf{B}^2 \end{bmatrix} \quad (3)$$

where, subscripts x , y and z indicate each direction in the coordinate system. Using this tenor, the force which is acting on the conductor is expressed as following equation.

$$\mathbf{F} = \nu_0 \int T \cdot \mathbf{n} dS \quad (4)$$

The integration path of dS in the Eq. (4) is surface of the conductor. However, the magnetic flux density on this surface is apt to change steeply because the magnetic permeability has a big difference about hundreds times between the conductor and the air. Consequently, because accuracy of the force calculation which is derived from Eq. (4) depends on the integration path, the path needs to keep away from the conductor surface.

ELECTROMAGNETIC ANALYSIS FOR THE STATIC MODEL

Analysis Model

A calculation code developed for the electromagnetic field is verified using three-dimensional verification model which is proposed by Institute of Electrical Engineers of Japan (hereafter, Test-model). Figs. 1 (a) and (b) show the top view and the side view of the Test-Model, respectively. The unit in Fig. 1 is millimeter. Hatched areas indicate the conductor, the outline area indicates the coil area and the otherwise is the air area.

Analysis Condition

Analysis conditions are shown in Table 1. Here, the relative magnetic permeability of the conductor is constant. In order to achieve accurate force calculation, nonlinear electromagnetic analysis in which the reluctivity changes against B is required. However, the linear analysis was conducted in the present study because this study stands on the first stage. The difference between linear and nonlinear analyses will be clarified near future.

As the boundary condition, the vector potential should be equal to Zero at the infinite distance from the conductor. In this study, the calculation area sets up as a square one side of which is five times more than that of the conductor. And the boundary condition of the calculation area is $\partial A/\partial n = 0$. Consequently, the effect of the boundary condition was diminished and does not influence to the calculation result. The number of calculation grids is $51 \times 51 \times 71$ and shape of grids is unequally spaced grid.

Table 1 Parameters for Static Analysis

Parameters	Amount of Parameters
Current of Coil	3000 [AT]
Relative Magnetic Permeability of the Conductor	1000 [-]
Boundary Condition	$\partial A/\partial n = 0$
Number of Grid	$51 \times 51 \times 71$

Result

Figs. 2 and 3 show results of the magnetic flux density at $x = 31.25$ [mm], $y = 31.25$ [mm], $z = 100 - 200$ [mm] and $x = 46.875$ [mm], $y = 60$ [mm], $z = 0 - 200$ [mm], respectively. In these figures, the abscissa axis shows the distance in the z direction [m] and the ordinate axis shows the magnetic flux density [T]. The solid line means the calculation result and the rhombic symbols means experimental results⁽¹⁾.

In Fig. 2, the calculation result on the magnetic flux density is a little higher than the experimental result. As the measurement point recedes from the conductor

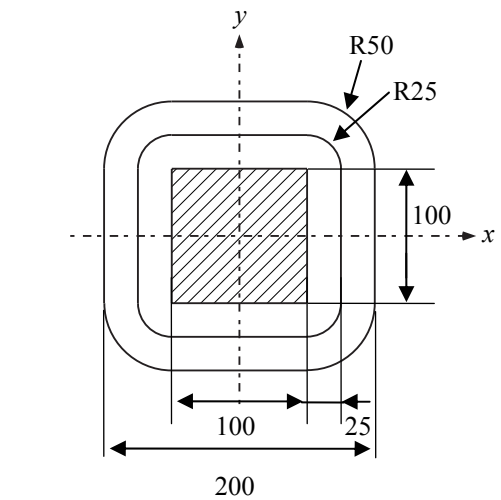
(as the value of z becomes bigger), the value of the magnetic flux density decreases. The calculation result and experimental result have the same tendency.

In Fig. 3, the calculation result is compared with the experimental result. These results have a little difference only at the $z=100$ [mm], however, these results agree well on the whole.

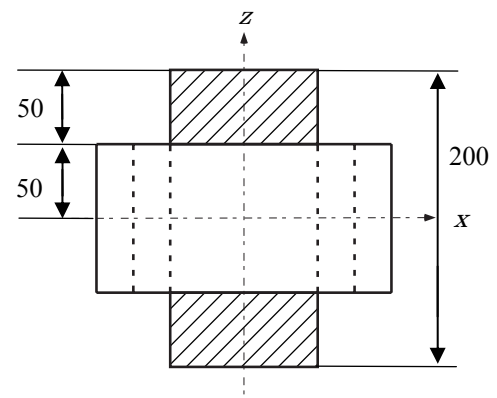
As the above discussion, the magnetic flux density of the calculation result and experimental result agree well, and the own-developed code is useful for the calculating the electromagnetic field.

ANALYSIS METHOD FOR MECHANICAL SYSTEM

The mechanical system was modeled by the Bondgraph method. This method is very convenient for modeling and simulation on various systems such



(a) Top View



(b) Side View

Fig. 1 Test Model for Static Analysis

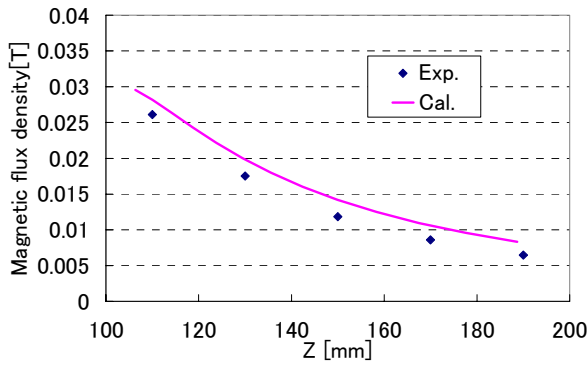


Fig. 2 Results at $x=31.25[\text{mm}]$ $y=31.25[\text{mm}]$

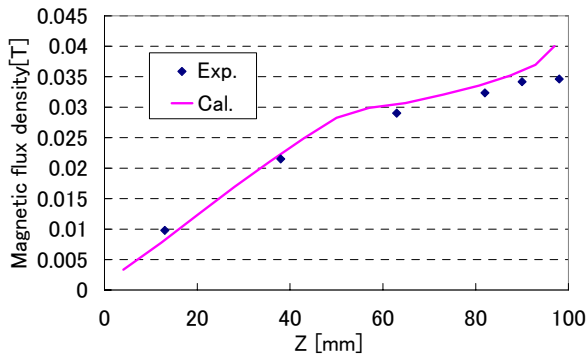


Fig. 3 Results at $x=46.875[\text{mm}]$ $y=60[\text{mm}]$

as mechanical systems because the method is based on the power transmission. Fig. 4 shows the system Bondgraph model of Spring-Mass-Damper system which is a representative model of the mechanical system. In the figure, SF element corresponds to the wall velocity as the boundary condition, SE element to the external force similarly, I element to the inertia effect by the mass, R element to the energy loss at the damper, C element to the energy storage at the spring, respectively. Characteristic equations in the elements are shown in Table 2.

Table 2 Characteristic Equations

Elements	Characteristic Equations
SE	$f = \text{electromagnetic force}$
SF	$V = 0$
C	$f = k \int V dt$
I	$V = \frac{1}{m} \int f dt$
R	$f = cv$

In the Bondgraph method, state space equations of a system are derived by combining the relationships in Table 2. In this study the state space equations were calculated by Runge-Kutta method.

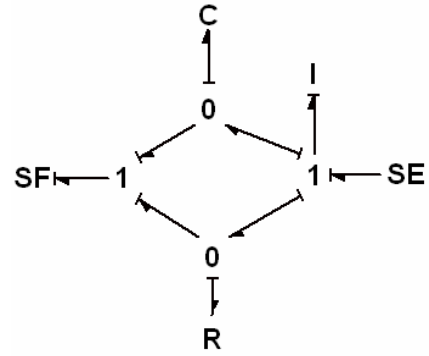


Fig. 4 Spring-Mass-Damper Model with Bondgraph

The final equations to be solved, which are derived from the Bondgraph method, are equal to the ordinary differential equation which is expressed by the following equation.

$$m\ddot{x} + c\dot{x} + kx = f \quad (5)$$

Dynamic characteristics of the mechanical system can be calculated successfully by Eq. (5) with Runge-Kutta method. In the future study, however, coupled analysis program will expand relations of the dynamic characteristics of the system such as the oil-hydraulic systems after the coupled analysis with the fluid system will be completed. Therefore, mechanical system was modeled by the Bondgraph method which is easily applicable to many systems such as fluid and mechanical systems.

COUPLED ANALYSIS

Coupling Way

Fig. 5 shows a flow chart of the coupled analysis method with an electromagnetic system and a mechanical system. This flow chart is explained as follows;

First, the vector potential is calculated using Eq. (2). Next, the electromagnetic force working on the conductor which is derived from Eq. (4) is calculated. The calculated force is substituted into the mechanical system as an external force, which is equal to an effort variable of SE element in Fig. 4 and the dynamic characteristics of the mechanical system is calculated. After that, the displacement of the conductor, which corresponds to the displacement of I element in Fig. 4, is calculated from the numerical results in the Bondgraph method. The calculation grids for the electromagnetic field are restructured because the conductor moves in the distance equal to this displacement. Finally, the vector potential is calculated using Eq. (2). Iterating these steps, the analysis coupled with the electromagnetic system and the mechanical system could be carried out in the

calculation of the dynamic characteristics of the spool valve.

Analysis Model

Fig. 6 shows the side view of the analysis model. The top view of the analysis model is the same as Fig. 1 (a). The unit of Fig. 6 is millimeter. The hatched areas indicate the conductor and the movable conductor. The outline area indicates the coil area and the otherwise is the air area. The size of the stationary conductor which is surrounded by the coil is 100*100*200. The size of the movable conductor which locates above the stationary conductor is 100*100*20. This movable conductor is constrained by the spring and the damper.

Analysis Condition

The movable conductor locates initially at the position which is shown in Fig. 6. The gap between the movable conductor and the stationary conductor is 20 [mm]. The movable conductor is fixed at this location until this analysis becomes steady. After this steady state is assumed to be the initial condition, the movable conductor can freely move.

The purpose of this analysis is to investigate the behavior of this movable conductor. The analyses were carried out under three kinds of conditions with different spring and damper coefficients. These conditions are shown in Table 3.

Table 3 Analysis Conditions

Parameters	Amount of Parameters
Time Step	1.0E-4 [s]
Current of Coil	3000 [AT]
Relative Magnetic Permeability of the Conductor	1000 [-]
Conductivity of the Conductor	1.03E+07 [S/m]
Number of Grid	51*51*81
Mass of the Conductor	1.56[kg]
Spring Coefficient	Case 1: 200[N/m]
	Case 2: 400[N/m]
	Case 3: 200[N/m]
Damper Coefficient	Case 1: 1.0[Ns/m]
	Case 2: 1.0[Ns/m]
	Case 3: 5.0[Ns/m]

Result and Discussion

Fig. 7 shows the displacement change of the movable conductor. The abscissa axis shows the time [s] and the ordinate axis shows the displacement [cm] of its conductor from the initial location. The solid line represents the result of Case 1, alternate long and short dash line the result of Case 2 and the dashed line the result of Case 3, respectively.

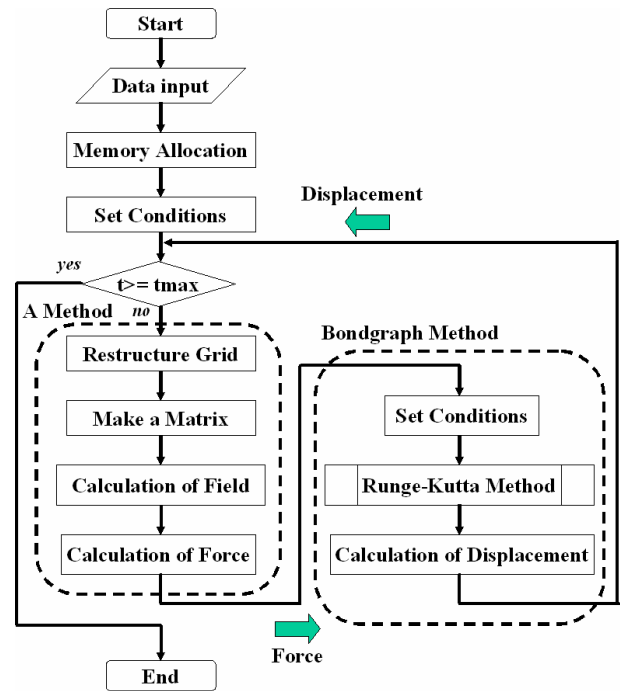


Fig. 5 Flow Chart of Coupled Analysis

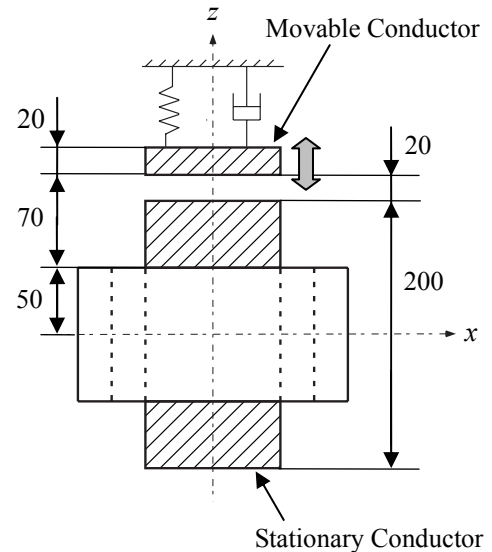


Fig. 6 Test Model for Coupled Analysis

Comparing results in Cases 1 and 2, the displacement in Case 2 is larger than that in Case 1. Because the spring coefficient in Case 2 is twice bigger than that in Case 1, the force in Case 2 which acts in the opposite direction by the spring force is stronger than that in Case 1. Additionally, comparing result of Cases 1 and 3, the both frequency is the same because the spring coefficient is the same. And the behavior of the movable conductor in Case 3 is more stable than that

in Case 1 because the damper coefficient in Case 3 is larger than that in Case 1. So, it is considered that this result is reasonable.

Frequency of the movable conductor is around 4.0 or 4.5 [Hz] approximately in all cases. However, theoretical frequency of the conductor in Case 1 and Case 3, which is derived from the natural frequency of the mechanical system, is 1.8 [Hz] and that in Case 2 is 2.5 [Hz] without the influence of eddy current. The eddy current which is generated and changes time-dependently at the conductor causes this frequency increase.

Generally it can be considered that the eddy current causes frequency decrease of the movable conductor, although there is a referenced paper⁽²⁾ that the natural frequency with eddy current becomes higher than that without eddy current. This feature would change according to the calculating conditions. It will become possible to explain the reason qualitatively after many parameter studies.

Fig. 8 shows the force working in z direction on the movable conductor. The abscissa axis shows the time [s] and the ordinate axis shows the electromagnetic force [N] working on the movable conductor. The negative and positive values indicate the repulsive force and the attractive force, respectively. The solid line represents the result in Case 1, the alternate long and short dash line the result in Case 2 and the dashed line the result in Case 3, respectively.

In this figure, the frequency of the force is around 4.0 or 4.5 [Hz] approximately in all cases. The frequency of the force in Fig. 8 corresponds to the frequency of the displacement in Fig. 7. In the analysis without the eddy current the frequency of the mechanical system changes according to the spring coefficient. However, in the coupled analysis, the frequency between in two cases with different spring coefficient was approximately same. This means that the effect of the eddy current was larger than that of the mechanical spring in this study.

When the movable conductor approaches the stationary one, the attractive force is decreased in all cases. Especially in Cases 1 and 3, the repulsive force was generated at the first vibration. On the other hand, when this movable conductor moves away from the stationary one, the attractive force was increased.

On the displacement of the movable conductor, its maximum displacement at the first vibration from the initial condition was 1.9 [cm] without influence of the eddy current and 0.7 [cm] with influence of the eddy current. The displacement was decreased by effect of the eddy current.

CONCLUSIONS

In order to establish the calculation method weakly coupled with mechanical and electromagnetic systems,

the program has been own-developed and the dynamic characteristics has been performed on the test model.

The calculation result and experimental result agree well under the static condition without considering the eddy current. In the dynamic calculations, the reasonable fact was obtained that the displacement of the movable conductor was diminished by the eddy current.

REFERENCES

1. A. Kameari and K. Koganezawa, IEEE Transaction on Magnetics Vol. 33, No. 2, pp. 1223-1226(1997).
2. Y. Tanaka and T. Horie, "Characteristics of the forced vibration with magnetic danmping", Int. Journal of Applied Electromagnetics and Mechanics 13, pp.45-51(2001/2002).

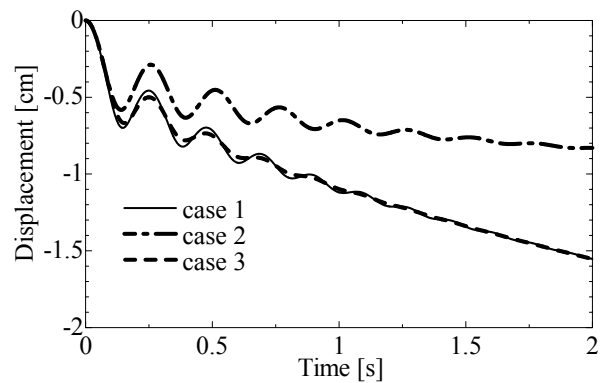


Fig. 7 Displacement of a Movable Conductor

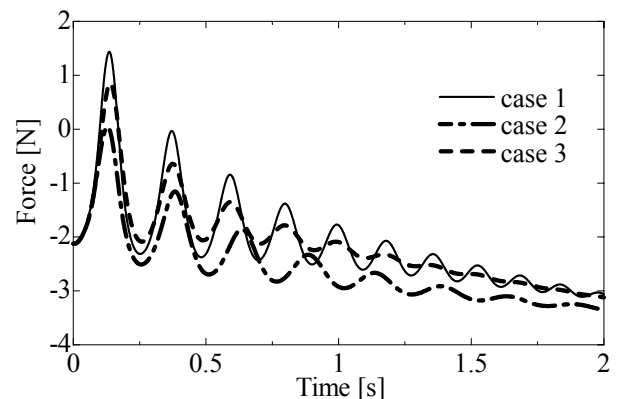


Fig. 8 Force Working on a Movable Conductor

Simulation of the Dynamic Characteristics of a Pneumatic Circuit by OHC-Sim

Yasuo SAKURAI*, Kazuhiro TANAKA**, Takeshi NAKADA*** and Takehisa KOHDA****

* Ashikaga Institute of Technology
268-1 Oomaecho, Ashikaga, Tochigi, 326-8558 Japan
(E-mail: ysakurai@ashitech.ac.jp)

** Kyushu Institute of Technology
680-4 Kawazu, Iizuka, Fukuoka 820-0067, Japan

*** Tokyo Denki University
2-1200 Muzai gakuendai, Innzai City, Chiba, 270-1382 Japan

**** Kyoto University
Yoshida-honmachi, Sakyo-ku, Kyoto 606-8501 Japan

ABSTRACT

OHC-Sim is a simulation package for design of an oil-hydraulic circuit and analysis of its dynamic characteristics. To make the design and the improvement processes of an oil-hydraulic circuit more effective and systematic, OHC-Sim had been developed with the support of JFPS and has been enhanced in the research committee in JFPS. OHC-Sim is executable on personal computers in Windows® environment, and provides easy design and improvement of an oil-hydraulic circuit based on the simulated results. However, in order to enhance the use of OHC-Sim, it is desirable that the simulation of the dynamic characteristics of a pneumatic circuit becomes executable on OHC-Sim. In this study, to enhance OHC-Sim to the simulation of a pneumatic circuit, the bond-graph models for pneumatic components are discussed. And, by using the user-customized function, these bond-graph models are registered to OHC-Sim, and the simulation of dynamic characteristics of a pneumatic circuit is carried out.

KEY WORDS

OHC-Sim, Pneumatic circuit, Simulation, Dynamic characteristics, Bond-graph method

NOMENCLATURE

A : area of piston [m^2]
 A_e : effective area [m^2]
 C_p : specific heat at constant pressure [$\text{J}/(\text{kg} \cdot \text{K})$]
 C_v : specific heat at constant volume [$\text{J}/(\text{kg} \cdot \text{K})$]
 M : mass of air in a chamber [kg]
 \dot{m} : mass flow rate [kg/s]
 P : absolute pressure [Pa]
 R : gas constant [$\text{J}/(\text{kg} \cdot \text{K})$]
 T : absolute temperature [K]
 t : time [s]

V : volume of a chamber [m^3]
 v : piston velocity [m/s]
 x : piston displacement [m]
 κ : specific heat ratio

Subscripts

A : atmosphere
 S : supply

INTRODUCTION

To make the design and the improvement processes of an oil-hydraulic circuit more effective and systematic, it

is effective to predict the dynamic characteristics of the circuit beforehand by computer simulation. And then, it is necessary to derive the mathematical model for the circuit and to construct the program for computer simulation. Therefore, some exclusive simulation packages had been developed, which provide the environment where an oil-hydraulic circuit can be designed and improved easily based on the simulated dynamic characteristics without deriving mathematical models and constructing simulation program.

OHC-Sim (Oil-Hydraulic Circuit Simulation package) is one of such simulation packages, and had been developed in Japan with the support of JFPS (the Japan Fluid Power System Society, formally The Japan Hydraulics and Pneumatics Society) [1]. And it has been improved and enhanced in the research committee of JFPS [2]. OHC-Sim has a user-friendly graphical user interface in Windows® environment, and provides easy design and improvement of an oil-hydraulic circuit referring to the simulated results by personal computer. Furthermore, the first version of the user-customized function [3,4], which is based on bond-graph method [5,6], had been developed to make it possible to register the models for new oil-hydraulic components to the database of OHC-Sim. By the development of this user-customized function, it becomes possible to carry out the simulation of the dynamic characteristics of a complicated oil-hydraulic circuit or a water-hydraulic one [7] in OHC-Sim.

However, in order to enhance the use of OHC-Sim much more, it is desirable that the simulation of the dynamic characteristics of a pneumatic circuit becomes possible on OHC-Sim. To realize this, it is necessary to derive the bond-graph models for basic pneumatic components in the shape that these models can be handled with OHC-Sim. Moreover, it is required that the maintenance of the models registered in the database is easy.

Pneumatic circuits have compressible fluid-flow and thermal fields. In constructing the bond-graph model for such a circuit, true or pseudo bond-graph has so far been employed. In addition, two kinds of bonds, which represent both fluid power and thermal power, have been used, and multi-port C and multi-port R elements have been frequently used in the model as well [5,6,8]. Therefore, the resulting bond-graph models are complicated, and the maintenance of the models becomes troublesome when the models are in the database. In addition to it, when multi-port C and multi-port R elements are used in the model, it is necessary to modify the main body of OHC-Sim and simulation program BGSP for OHC-Sim so as to use them.

In this study, the bond-graph models for pneumatic components are derived by using 1-port C and 1-port R elements. In deriving the bond-graph model for compressible flow field, pseudo bond-graph, in which

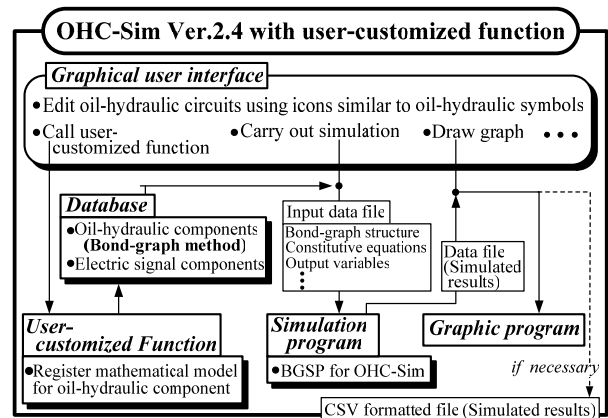
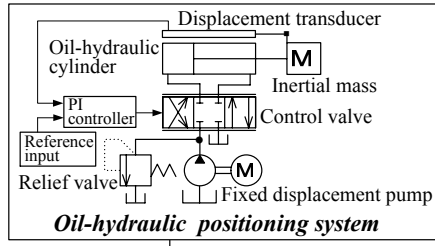


Figure 1 Basic structure of OHC-Sim

effort is absolute pressure and flow is mass flow rate, is employed so as to represent the continuity equation in the field easily. Furthermore, to confirm the usefulness of the proposed bond-graph models, the bond-graph models are registered to OHC-Sim by the use of the user-customized function and the simulation of dynamic characteristics of a pneumatic circuit is carried out.

OUTLINE OF OHC-Sim

The basic structure of OHC-Sim is shown in Figure 1. OHC-Sim is an exclusive simulation package for design of an oil-hydraulic circuit and analysis of its dynamic characteristics, and it is executable on personal computers in all Windows® environments. In OHC-Sim, an oil-hydraulic circuit can be constructed on the display with ease by using graphical user interface and connecting oil-hydraulic component icons similar to oil-hydraulic symbols as shown in Figure 2. In this figure, SU1~SU4 are the components called sensor. This component is used to pick up the physical quantity such as pressure, discharge or displacement. And, by copy and paste of the sensor, the physical quantity sensed by the sensor can be utilized to represent a feedback loop or a pilot line. The mathematical models for components are registered in the database of OHC-Sim, and these models are represented by bond-graph method. Based on these models, the mathematical model for the oil-hydraulic circuit on the display is automatically created, and the simulation of the dynamic characteristics of the circuit is carried out. As simulation program, BGSP for OHC-Sim is employed. BGSP [9] is a simulation program based on bond-graph method, had been developed in Japan, and has obtained a number of fruitful results [10]. The simulated results can be confirmed easily and quickly on the display. In addition, OHC-Sim has a user-customized function. By using this function, users can register the mathematical models for their own oil-hydraulic components to the database. By



Edit by OHC-Sim

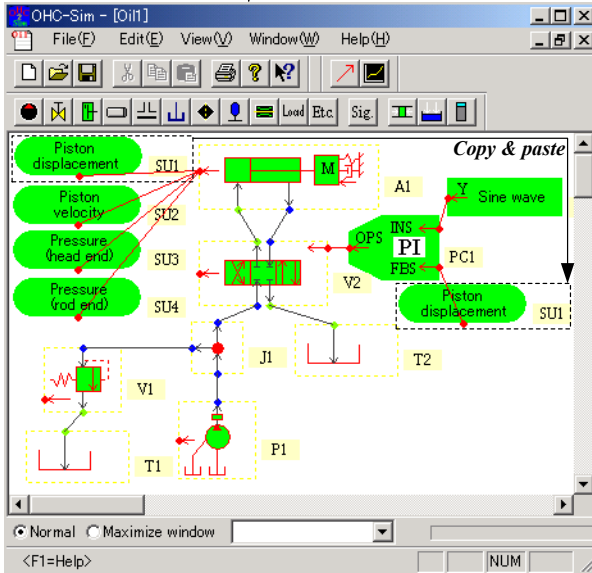


Figure 2 Edit of oil-hydraulic circuit by OHC-Sim

the development of this user-customized function, it becomes possible to carry out the simulation of the dynamic characteristics of a complicated oil-hydraulic circuit or a water-hydraulic one in OHC-Sim.

BOND-GRAPH MODEL FOR BASIC PNEUMATIC COMPONENT

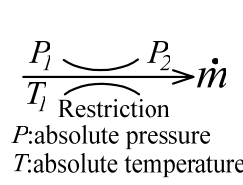
In this section, each bond-graph model for restriction and chamber of a pneumatic cylinder is derived. In constructing the bond-graph model for compressible flow field, pseudo bond-graph is employed, in which effort is absolute pressure and flow is mass flow rate. In mechanical field, true bond-graph is used, in which effort is force and flow is velocity.

Restriction

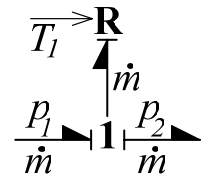
At a restriction shown in Fig. 3, the continuity equation yields

$$\dot{m}_1 = \dot{m}_2 = \dot{m} \quad (1)$$

where \dot{m}_i ($i=1,2$) is the mass flow rate through cross sections 1 and 2 in Fig. 3, respectively.



(a)Restriction



(b)Bond-graph model

Figure 3 Bond-graph model of restriction

The mass flow rate through the restriction can be expressed by Eq. (2) and (3).

$$0 \leq \frac{P_2}{P_1} < 0.528$$

$$\dot{m} = AeP_1 \sqrt{\frac{\kappa}{RT_1} \left\{ \left(\frac{2}{\kappa+1} \right)^{\frac{\kappa+1}{\kappa-1}} \right\}} \quad (2)$$

$$0.528 \leq \frac{P_2}{P_1} \leq 1$$

$$\dot{m} = AeP_1 \sqrt{\frac{2\kappa-1}{\kappa-1} \frac{1}{RT_1} \left\{ \left(\frac{P_2}{P_1} \right)^{\frac{2}{\kappa}} - \left(\frac{P_2}{P_1} \right)^{\frac{\kappa+1}{\kappa}} \right\}} \quad (3)$$

As can be seen from Eq.(1), flow \dot{m} is equal at the restriction. And, from Eqs. (2) and (3), flow \dot{m} is expressed as a function of effort P_1 and P_2 . Therefore, the restriction can be represented by 1-junction and an R-element as shown in Fig.3 (b). In order to calculate mass flow rate \dot{m} based on Eqs. (2) and (3), temperature T_1 is necessary. Therefore, temperature T_1 is inputted to R-element through the active bond which is denoted by full arrow and transmits a signal.

Chamber of pneumatic cylinder

In a head-end chamber of a pneumatic cylinder shown in Fig. 4, the heat transfer through a wall is assumed to be adiabatic to make the bond-graph structure simple. Then, the first law of thermodynamics yields

$$\frac{dU}{dt} = \dot{H} - P \frac{dV}{dt} \quad (4)$$

where U is the internal energy of air in the chamber of the pneumatic cylinder and \dot{H} is the enthalpy flux through the control surface.

Internal energy U and enthalpy flux \dot{H} are expressed as

$$U = C_V \rho VT \quad (5)$$

$$\dot{H} = C_P \dot{m} T^* \quad (6)$$

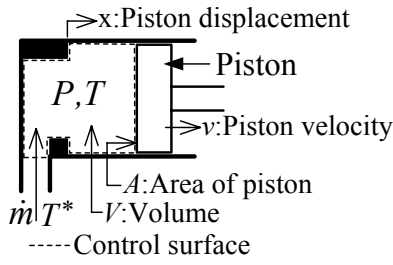


Figure 4 Head-end chamber of pneumatic cylinder

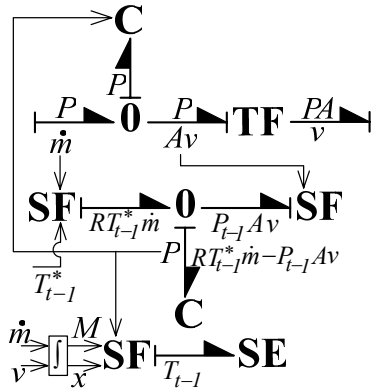


Figure 5 Bond-graph model for head-end chamber of pneumatic cylinder

where ρ is the density of air in the chamber and T^* is the temperature of air through the control surface. Substituting Eqs. (5)-(9) into Eq. (4), we obtain Eq.(10).

$$C_P - C_V = R \quad (7)$$

$$C_V = \frac{R}{\kappa - 1} \quad (8)$$

$$\frac{dV}{dt} = Av \quad (9)$$

$$\frac{dP}{dt} = \frac{\kappa}{V} (R\dot{m}T^* - PAv) \quad (10)$$

Assuming that T^* and P in the right-hand side of Eq. (10) can be replaced with the values at one time step before the time, we get Eq. (11).

$$P = \frac{\kappa}{V_{H0} + Ax} \int (RT^*_{t-1} \dot{m} - P_{t-1} Av) dt + P_{H0} \quad (11)$$

where V_{H0} is the head-end chamber dead volume and P_{H0} is the initial pressure at the chamber.

As can be seen from Eq.(11), effort P can be determined by integrating flow \dot{m} and v . And effort P is equal in the head-end chamber of the pneumatic cylinder. Hence,

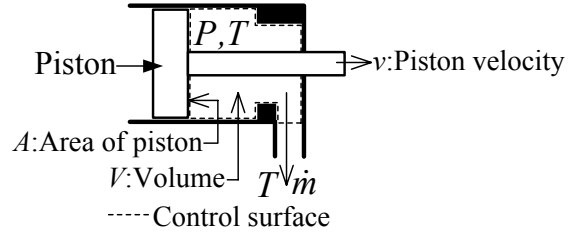


Figure 6 Rod-end chamber of pneumatic cylinder

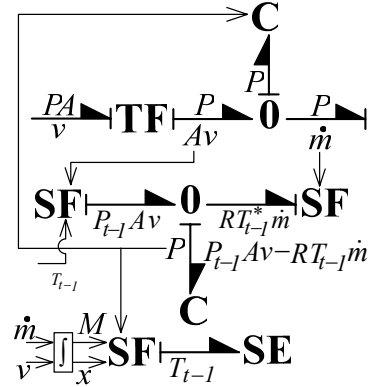


Figure 7 Bond-graph model for rod-end chamber of pneumatic cylinder

the head-end chamber of pneumatic cylinder shown in Fig.4 can be modeled by a C-element and 0-junction as shown in Fig. 5. However, in order to calculate effort P from Eq. (11), two SF-elements and a C-element is employed. And then, this C-element is used as a mere integrator. Furthermore, to calculate the temperature of air in the head-end chamber of pneumatic cylinder from Eq. (12), an SF-element and an SE-element are employed as a mere calculator. And then, the flow of the bond between these elements represents the temperature of air in the head-end chamber of pneumatic cylinder at one time step before the time.

$$T = \frac{PV}{MR} , T_{t-1} = T \quad (12)$$

Similarly, the pressure at the rod-end chamber of a pneumatic cylinder shown in Fig. 6 can be determined by Eq. (13).

$$P = \frac{\kappa}{V_{R0} - Ax} \int (-RT_{t-1} \dot{m} + P_{t-1} Av) dt + P_{R0} \quad (13)$$

where V_{R0} is the volume of the rod-end chamber when piston displacement x is equal to 0.

As seen from Eq.(13), effort P can be calculated by

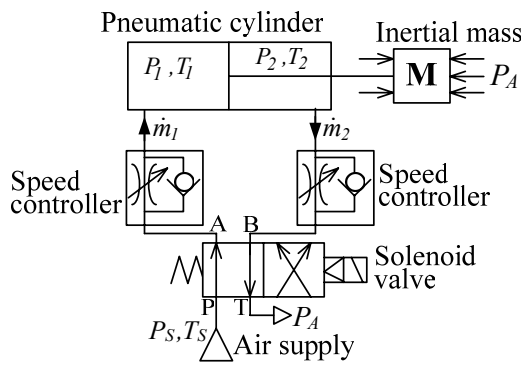


Figure 8 Pneumatic circuit

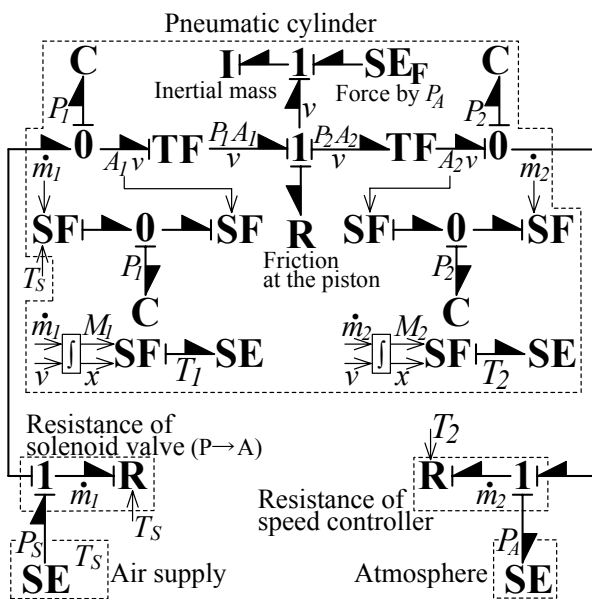


Figure 9 Bond-graph model for pneumatic circuit

integrating flow \dot{m} and v . And effort P is equal in the rod-end chamber of the pneumatic cylinder. Therefore, the rod-end chamber of pneumatic cylinder can be represented as shown in Fig. 7. Then, it should be noted that the temperature of air in the rod-end chamber is used in calculating the pressure of air in the chamber by Eq. (13).

SIMULATION OF DYNAMIC CHARACTERISTICS OF PNEUMATIC CIRCUIT BY OHC-Sim

In order to show the usefulness of the above-mentioned bond-graph models, the simulation of the dynamic characteristics of the pneumatic circuit shown in Fig. 8 was carried out. The bond-graph model for the circuit is shown in Fig. 9. Since the pressure and the temperature

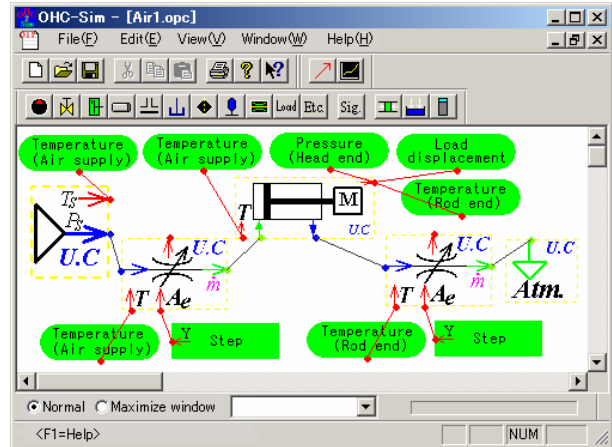


Figure 10 Edit of pneumatic circuit in OHC-Sim

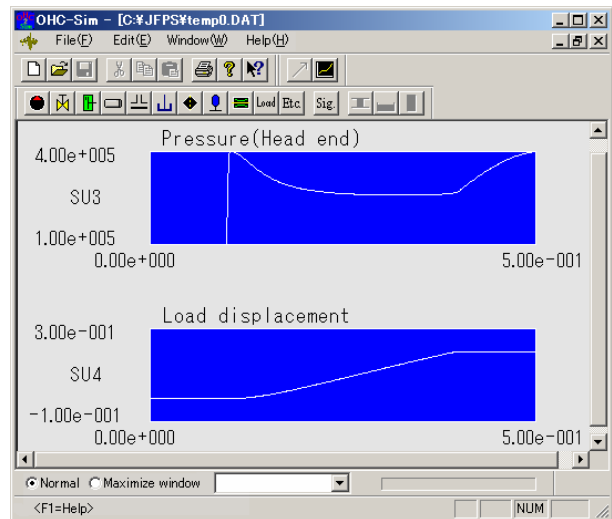


Figure 11 Simulated results

of air at the air supply are considered to be constant, the air supply can be modeled by an SE-element. When the flow through the solenoid valve or the speed controller located at the rod end of the pneumatic cylinder is assumed to be similar to that through the restriction shown in Fig.3, each valve can be regarded as an R-element. Then, the resistance of the speed controller includes the resistance between B-port and T-port of the solenoid valve. The pressure and the temperature of the atmosphere are constant. Therefore, the atmosphere can be represented by an SE-element.

The bond-graph model shown in Fig. 9 for each pneumatic component was registered to OHC-Sim by using the user-customized function. Figure 10 shows the pneumatic circuit constructed in OHC-Sim. To calculate the mass flow rate through the solenoid valve or the speed controller and the pressure at the head-end

chamber of the pneumatic cylinder, the temperature at the upstream component is necessary. Therefore, the temperature is inputted to these components by copy and paste of the sensor sensing the temperature at the air supply or the rod-end chamber of the pneumatic cylinder.

Figure 11 shows the simulated results of the dynamic characteristics of the pneumatic circuit in the case where the P-port is connected to the A-port of the solenoid valve at time 0.1s. As a result, it is shown that the simulation of the dynamic characteristics of a pneumatic circuit becomes possible on OHC-Sim by using the proposed bond-graph models.

CONCLUSIONS

The bond-graph models for pneumatic components were derived, which were composed of 1-port C element and 1-port R-element. Furthermore, in order to investigate the usefulness of the proposed bond-graph models, these models were registered to OHC-Sim by using the user-customized function, and the simulation of dynamic characteristics of a pneumatic circuit was carried out. Consequently, it was shown that the simulation of the dynamic characteristics of a pneumatic circuit became possible on OHC-Sim by adopting the proposed bond-graph models without modifying OHC-Sim. It is a great merit that the modification of OHC-Sim is not necessary when the proposed bond-graph models are employed in the modeling of pneumatic components. Next step will be to confirm the validity of the simulated results on OHC-Sim by comparing the simulated results with the experimental ones in various pneumatic circuits.

REFERENCES

1. Nakada, T., Tanaka, K., Kohda, T., Sakurai, Y. and Suzuki, K., Introduction of Innovative Program OHC-Sim for Oil-Hydraulic Circuit Simulation, Fluid Power (Proceedings of the 3rd JHPS International Symposium on Fluid Power), Yokohama JAPAN, 1996, pp.679-682.
2. e.g. Sakurai, Y., Kohda, T., Tanaka, K., Nakada, T., Enhancement of OHC-Sim (Oil-Hydraulic Circuit Simulation Package), Proceedings of 4th JHPS International Symposium on Fluid Power, Tokyo JAPAN, 1999, pp.225-230.
3. Sakurai, Y., Tanaka, K., Kohda, T., Nakada, T., Simulation Package OHC-Sim with User Customized Function, Proceedings of 7th Scandinavian International Conference on Fluid Power, Linköping SWEDEN, 2001, pp.127-141.
4. Sakurai, Y., Tanaka, K., Nakada, T., Kohda, T., Simulation Package OHC-Sim Ver.2.4 with User Customized Function, Proceedings of 1st International Conference on Computational Method in Fluid Power Technology, Melbourne AUSTRALIA, 2003, pp.111-121.
5. Rosenberg, R.C. and Karnopp, D.C., Introduction to Physical System Dynamics, McGraw-Hill, 1983.
6. Thoma, J.U., Simulation by Bondgraphs, Springer-Verlag, 1990.
7. Yata, Y., Nakada, T., Sakurai, Y., Tanaka, K., Dynamic Characteristics of Low-pressure Water Hydraulic System, Fluid Power (Proceedings of the 5th JFPS International Symposium on Fluid Power), Nara JAPAN, 2002, pp.161-166.
8. Thoma, J.U. and B. Ould Bouamama, Modelling and Simulation in Thermal and Chemical Engineering, Springer, 2000.
9. e.g. Kohda, T. and Nakada, T., Introduction of Bond Graph Simulation Program (BGSP), Fluid Power (Proceedings of the 2nd JHPS International Symposium on Fluid Power), Tokyo JAPAN, 1993, pp.173-182.
10. e.g. Sakurai, Y., Calculation of Dynamic Overall Efficiency of a Load Sensing Hydraulic System by Bondgraphs, Proceeding of IEEE International Conference on Industrial Electronics, Control and Instrumentation, Nagoya JAPAN, 2000, pp.1568-1573.

IDENTIFICATION OF THE PNEUMATIC SERVO SYSTEM USING THE SELF-EXCITED OSCILLATIONS

Petr NOSKIEVIČ*

* Department of Automatic Control and Instrumentation, Faculty of Mechanical Engineering
VŠB-Technical University of Ostrava
17. listopadu 15 , 708 33 Ostrava – Poruba, Czech Republic
(E-mail: petr.noskievic@vsb.cz)

ABSTRACT

The paper describes the identification of the variable critical gain and natural frequency of the pneumatic cylinder using the self-excited oscillations method. The pneumatic drives are characterized by the low stiffness of the pneumatic cylinder which depends on the piston position and determines the natural frequency of the cylinder. The variety of the stiffness in dependence on the piston position can be obtained using the curve describing the course of the critical gain and natural frequency in dependence on the piston position. This feature is a disadvantage by the closed loop control of the piston position. The low stiffness should be taken into the account by the design of the pneumatic servo system operated in the closed loop, because the natural frequency of the cylinder depends on the stiffness and limits the closed loop gain and quality of the step response of the controlled system. The identified curve can be used for the design of the adaptive controller with variable on the piston position dependent gain. The described approach is presented by the measurements and results realized on the test rig.

KEY WORDS

Pneumatic drive, Identification, Natural frequency

NOMENCLATURE

h stroke of the pneumatic cylinder
 K_M gain of the pneumatic cylinder
 K_{SV} gain of the servo valve
 K_{sn} gain of the transducer
 M output of the relay
 m mass
 n polytropic exponent of air
 p system pressure
 r_{ocrit} critical gain
 S piston thrust section
 T_{OM} time constant of the pneumatic cylinder
 T_{OSV} time constant of the servo valve
 T_{crit} period of the oscillations

V_{01} volume – inlet 1 of the cylinder
 V_{02} volume – inlet 2 of the cylinder
 ξ_M damping ratio of the pneumatic cylinder
 ξ_{SV} damping ratio of the servo valve
 ω_M angular frequency of the pneumatic cylinder
 ω_{SV} angular frequency of the servo valve
 ω_{0M} natural frequency of the pneumatic cylinder
 ω_{0SV} natural frequency of the servo valve

INTRODUCTION

The pneumatic servo actuators are very important drives with a wide range of applications in mechatronics. The design of the high dynamic pneumatic drives operated in the closed loop as a position servo drives is not

simple task. The dynamic properties of the pneumatic servo drive – the pneumatic servo valve, pneumatic cylinder and tubes must be taken into the account by the controller design [2, 3]. We can use the mathematical modeling to obtain the dynamic model and use the simulation program to analyze the dynamic behavior of the system in different working points. This approach needs the parameterization of the mathematical model and their verification. Some parameters are given from the drive specification, some must be estimated or identified by the experiment [3]. The pneumatic drive is characterized as a low damped system with lower stiffness and natural frequency as the hydraulic drive. The reason is the higher compressibility of the air as oil. The natural frequency of the pneumatic cylinder varies with the piston position and influences the controller tuning. Their course in dependence on the piston position can be useful for the design of the controller of the position closed loop controlled system.

The paper describes the identification of the natural frequency of the pneumatic cylinder using the self-excited oscillations by the arranging a non linear element in the feedback [1], Figure 1. It is recommended to set the amplitude of the relay characteristic normally to 10%, max 20% of the command value. The oscillations occur in the output and should be similar to the sinus signal. It is also possible to use the saturation element with the same amplitude and with the proportional gain little bit higher as the critical gain. This approach allows to identify the natural frequency and the damping ratio too after evaluation of the results using the simplified linear model of the pneumatic drive given by the transfer function of the second order system and using the stability analysis of the closed loop system.

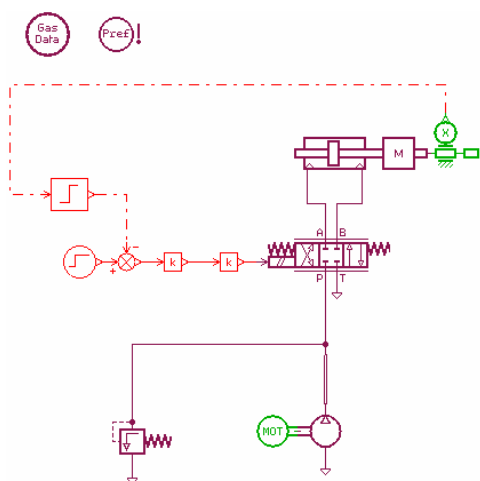


Figure 1 Pneumatic drive with non linear element in the feedback

ANALYSIS OF THE PNEUMATIC DRIVE

The typical structure of the pneumatic servo drive consists of the pneumatic cylinder controlled by the servo valve that allows continuously to control the mass flow through the variable resistances into the chambers of the pneumatic cylinder. The Figure 2 shows the block diagram of the closed loop position control of the pneumatic cylinder. The dynamic behavior of the main elements of the pneumatic drive can be described by the linear model after neglecting the nonlinearities. The transfer function

$$G_1(s) = \frac{K_M}{T_{0M}^2 s^2 + 2\xi_M T_{0M} s + 1} \quad (1)$$

describes the dynamics of the pneumatic cylinder, the transfer function

$$G_2(s) = \frac{K_{SV}}{T_{0SV}^2 s^2 + 2\xi_{SV} T_{0SV} s + 1} \quad (2)$$

describes the dynamic properties of the servo valve. The transfer function G_C in Figure 2 describes the controller.

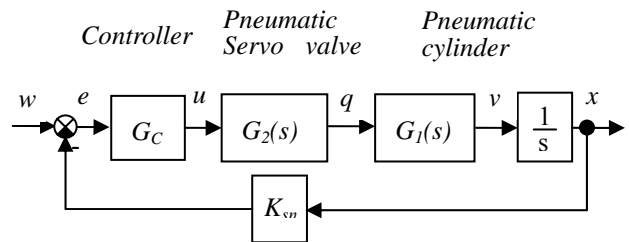


Figure 2 Block diagram of the closed loop position control

Because the bandwidth of the servo valve is higher than the natural frequency of the pneumatic cylinder, the dynamics of the servo valve can be neglected and in the following analysis the servo valve can be described only by the gain K_{SV} . After this simplification and for the proportional controller described by the gain K_R the transfer function of the closed loop system has the form

$$G(s) = \frac{K_0}{T_{0M}^2 s^3 + 2\xi_M T_{0M} s^2 + s + K_0}, \quad (3)$$

where K_0 is the gain of the open loop system

$$K_0 = K_R K_{SV} K_{sn} K_M. \quad (4)$$

The stability analysis of this linear system allows to

express the critical gain K_{0crit} in marginal stability

$$K_{0crit} = \frac{2\xi_M}{T_{0M}} = 2\xi_M \omega_{0M} . \quad (5)$$

In this formula ω_{0M} is the natural frequency of the pneumatic cylinder and ξ_M is the damping ratio of the pneumatic cylinder. These parameters limited the critical gain of the closed loop system, the controller gain and in this way the step response and quality of the control of the positioning system.

Using the results of the mathematical modeling of the pneumatic drive and under assumption that the thermodynamic processes can be good enough described as the polytropic or adiabatic (for $n=\kappa$) processes the natural frequency of the pneumatic cylinder can be calculated from the formula

$$\omega_{0M} = \sqrt{\frac{S^2 np}{m} \left(\frac{1}{Sx + V_{01}} + \frac{1}{S(h-x) + V_{02}} \right)} . \quad (6)$$

The natural frequency of the pneumatic drive which limits the controller tuning is variable in dependence on the piston position. The Figure 3 shows the typical course of the natural frequency.

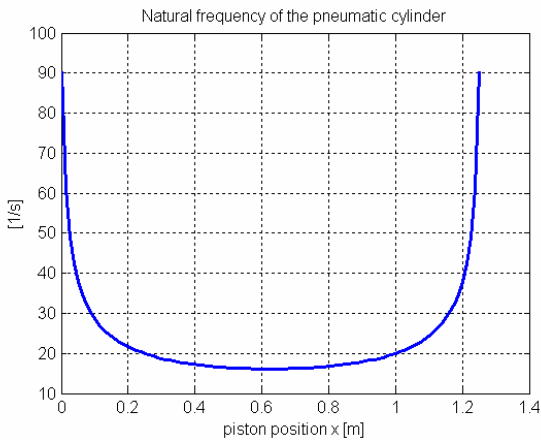


Figure 3 Natural frequency of the pneumatic cylinder

This natural frequency is the angular frequency of the non damped oscillations. Relations between the natural frequency ω_{0M} and the angular frequency ω_M of the observed oscillations of the margin stability is depending on the damping ratio ξ_M of the pneumatic cylinder and is given by

$$\omega_M = \omega_{0M} \sqrt{1 - \xi_M^2} . \quad (7)$$

The pneumatic cylinder is characterized by the very low damping. The damping ratio is typically less than 0.2.

For $\xi_M = 0.2$ becomes the expression (7) the form

$$\omega_M \doteq 0.98 \omega_{0M} . \quad (8)$$

For ξ_M less than 0.2 the difference between ω_M and ω_{0M} is less than 2%. The difference is smaller than the standard occurring final error by the experimental identification. For this reason it is possible in some cases to identify the angular frequency ω_M as a natural frequency ω_{0M} .

IDENTIFICATION USING THE SELF-EXCITED OSCILLATIONS

The identification method based on the self-excited oscillations is very simple and allows in very simple way to identify the angular frequency of the oscillations on the marginal stability.

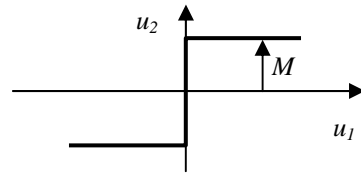


Figure 4 Relay characteristic of the non linear element

The oscillations occur after arranging the nonlinear element in the feedback. It is possible to receive the same result after placing the non linear element in the forward side of the closed loop system. It is suitable as a non linear element to use element with the relay characteristic, see Figure 4.

The closed loop pneumatic positioning system with the non linear element in the feedback is shown in Figure 1. After the oscillations occur the typical form of the output signal is shown in Figure 5.

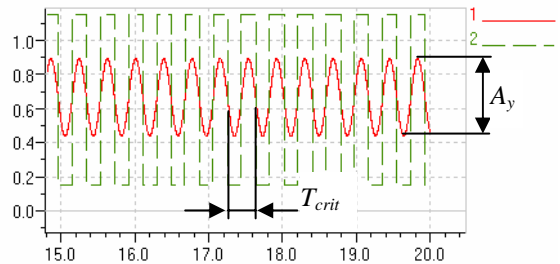


Figure 5 Self-excited oscillations of the piston of the pneumatic cylinder
Solid line – piston position
Dashed line - output from the non linear element

Using the theory of this identification method described for example in [1] the critical gain of the closed loop system is given by

$$r_{0crit} = \frac{4M}{\pi A_y} . \quad (9)$$

The values of the variables A_y and M can be obtain from the course of the self-excited oscillations and from the output of the relay characteristic, see Figure 5 and 4. The angular frequency of the critical oscillations can be expressed as

$$\omega_{crit} = \frac{2\pi}{T_{crit}} . \quad (10)$$

In accordance with the expression (5) for the critical gain of the pneumatic positioning system the values of the formulas (9) and (5) should be the same that means

$$K_{0crit} = r_{0crit} , \quad (11)$$

resp.

$$2\xi_M \omega_{0M} = r_{0crit} \quad (12)$$

and the critical frequency or period determines the angular frequency of the piston oscillations ω_M , which can be calculated from

$$\omega_M = \frac{2\pi}{T_{crit}} . \quad (13)$$

Using the expression (7) the natural frequency of the pneumatic cylinder is given by

$$\omega_{0M} = \frac{2\pi}{T_{crit} \sqrt{1 - \xi_M^2}} . \quad (14)$$

From the expression (12) can be calculated the damping ratio of the pneumatic cylinder

$$\xi_M = \frac{r_{0crit}}{2\omega_{0M}} . \quad (15)$$

After substitution of the expression (14) in the expression (15) we obtain the expression for the damping ratio which respects the difference between the natural frequency ω_{0M} and angular frequency ω_M of the pneumatic cylinder

$$\xi_M = \frac{r_{0crit} T_{crit}}{\sqrt{16\pi^2 + T_{crit}^2 r_{0crit}^2}} . \quad (16)$$

Provided that the described difference (8) between the ω_{0M} and ω_M for lower damping is accepted the simplified expressions can be used for the direct calculation of the natural frequency and damping ratio of the pneumatic cylinder from the measured values

$$\omega_{0M} \cong \omega_M = \frac{2\pi}{T_{crit}} \quad (17)$$

and

$$\xi_M = \frac{r_{0crit} T_{crit}}{4\pi} . \quad (18)$$

APPLICATION OF THE METHOD AND EXPERIMENTAL RESULTS

The described method was applied for the experimental identification of the natural frequency of the pneumatic cylinder of the test rig installed in the laboratory.

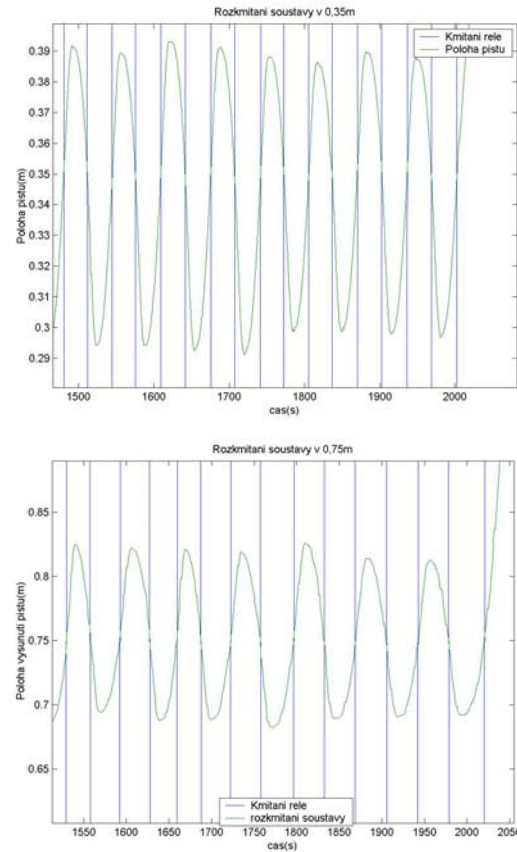


Figure 6 Measured self-excited oscillations of the piston of the pneumatic cylinder at the position $x = 0.35\text{m}$ (up), at the position $x = 0.75\text{m}$ (down)

The same drive and identification experiment was simulated in MATLAB – Simulink using the created mathematical model and in the simulation program AMESim, Figure 1, 5. The following drawings in Figure 6 show the measured signals at two different positions of the piston [4]. The evaluated values and approximated course of the natural frequency of the pneumatic cylinder compared with the analytical values

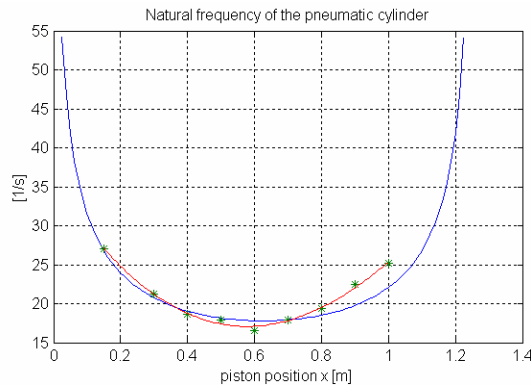


Figure 7 Natural frequency of the pneumatic cylinder – calculated analytically (6) and evaluated from the measurement “*”

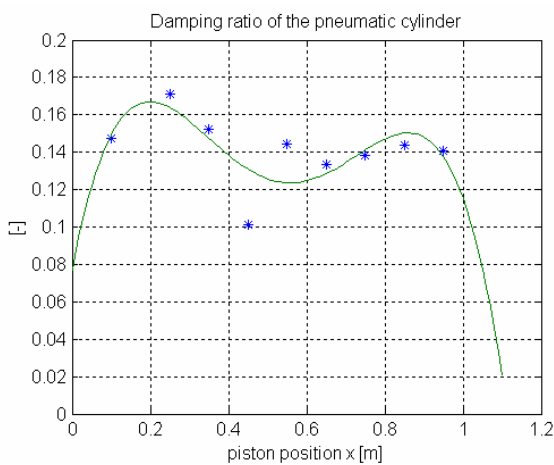


Figure 8 Damping ratio of the pneumatic cylinder – evaluated from the measurement “*” and polynomial approximation

calculated from the expression (6) are depicted in Figure 7. The values of the damping ratio calculated from the expression (16) and approximated by the polynomial function in dependence on the piston position are shown in Figure 8.

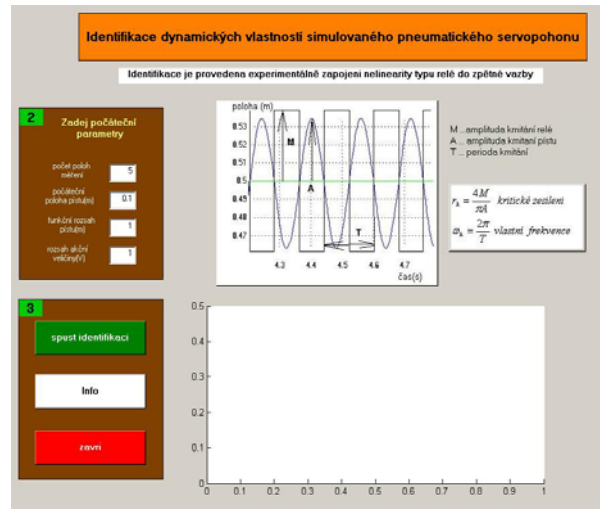


Figure 9 Control panel of the identification using the self-excited oscillations

The created program in MATLAB-Simulink with the Real Time Toolbox controls the identification process and realizes the calculation of the identified parameters of the pneumatic drive. The program controls the motion of the piston, the achieving of the desired positions and in each position starts the identification procedure. After measuring the excited oscillations the calculation of the critical gain and natural frequency runs automatically. The control panel of this program is shown in Figure 9.

CONCLUSIONS

The simple method for identification of the dynamic properties of the pneumatic drive based on the self-excited oscillations was presented in this paper. This method allows to calculate the natural frequency of the pneumatic cylinder, the critical gain and damping ratio at different positions of the piston. These values can be used for the controller tuning, for the design of the adaptive controller with variable gain. Simple realization is the advantage of this approach. The application of this method was presented by the identification of the pneumatic cylinder installed on the test rig.

ACKNOWLEDGMENTS

The author wishes to thank for supporting this research work by the project of the Grand Agency of the Czech Republic No: 101/03/0648, “Digital Control of Linear Actuators of Mechatronic Systems”.

REFERENCES

1. Macháček, J.: Identifikace soustav pomocí nelinearity ve zpětné vazbě (Identification using the non linearity in the feedback. In Czech.), Automatizace, Volume 41, No.9, pp. 559-564. ISSN 0005-125X.
2. Noskievič, P., Simulation of a pneumatic servo drive, Proceedings of the 5th Bergen International Workshop on Advances in Technology, Chapter 6, 14pp., Bergen University College, 2004, ISBN 82-7709-073-0.
3. Noskievič, P., Modelování a identifikace systémů System Modeling and Identification, In Czech). I.vydání, Ostrava, Montanex a.s., 1999, ISBN 80-7227-030-2.
4. Steiger, R., Řízení mechatronických systémů (Control of Mechatronic Systems, In Czech). Diploma thesis, Faculty of Mechanical Engineering, VŠB-Technical University of Ostrava, 2005.

DEVELOPMENT OF MODEL SELECTION PROGRAM FOR COMPLEX PNEUMATIC CIRCUITS

Shihong ZHANG*, Huping ZHANG*, Mitsuru SENOO*, and Naotake ONEYAMA*

* Technology Research Division, SMC Corporation Tsukuba Technical Center
4-2-2, Kinunodai, Yawara-mura, Tsukuba-gun, Ibaraki, 300-2493 Japan

ABSTRACT

Pneumatic system is applied in a wide range of industries. There are many kinds of pneumatic circuits that are used in different applied cases, such as transportation, clamp, press, etc. Among those pneumatic circuits, pneumatic circuit with only one cylinder controlled by one valve is primary for application, while branch circuit, which is consisted of multiple cylinders controlled by one valve, and manifold circuit, which is consisted of multiple cylinders controlled by multiple valves, is commonly applied in practices. In this paper, a simulation program for complex pneumatic circuits, especially for branch circuits and manifold circuits, is developed for model selection and characteristic calculation. Firstly, outline and specifications of the simulation program is introduced; secondly, modeling and simulation method of branch circuit and manifold circuit are explained; finally, an example of application is presented to verify the accuracy of the simulation program.

KEY WORDS

Pneumatic System, Branch Circuit, Manifold, Model Selection, Simulation

INTRODUCTION

Pneumatic system is applied to various fields for transportation, clamp, press, and so on. As applications are different, the pneumatic circuits are various. The basic circuit with one cylinder controlled by one valve is the most primary, while the branch circuit, which is consisted of multiple cylinders controlled by one valve, and the manifold circuit, which is consisted of multiple cylinders controlled by multiple valves, are more popular^{1), 2)}. The software named Pneumatic Model Selection Program was developed to support the model selection and characteristic simulation of basic circuit in version 2. And it is enhanced to simulate complex

pneumatic systems such as branch circuits and manifold circuits in the last version.

In the following sections, firstly, outline and guidance of the software version 3 is introduced; then, modeling and simulation method of branch circuit and manifold circuit are introduced; finally, an example of application is presented.

OUTLINE OF PROGRAM

The Pneumatic Model Selection Program Ver.3 can be executed in WindowsNT4.0 and Windows 98/2000/XP. Its CD-ROM version and Web version have been developed at the same time.

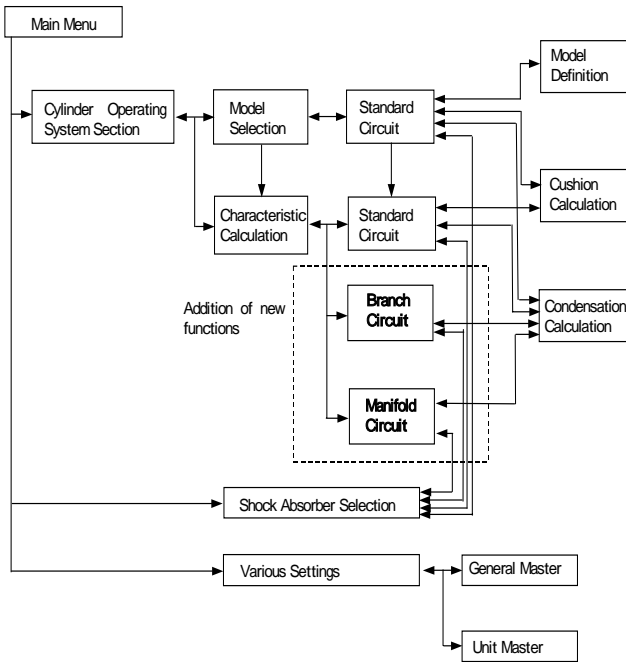


Figure 1 Configuration of Model Selection Program

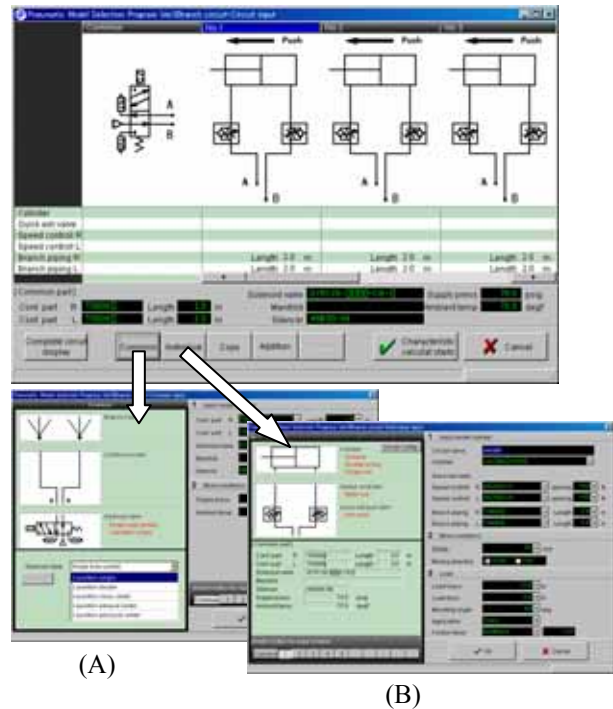


Figure 2 Input screens for branch circuit

Figure 1 shows configuration of the Pneumatic Model Selection Program. The software includes three main parts, the model selection for cylinder operating system, the characteristic calculation for cylinder operating system, and the model selection for shock absorber. With the help of the model selection for cylinder operating system, product models with proper size are automatically selected for basic circuits. With the help of the characteristic calculation for cylinder operating system, all dynamic characteristics are simulated for basic circuits, branch circuits and manifold circuits. Furthermore, cushion capacity and condensation probability for circuits can be calculated with the software, too.

CALCULATION SCREENS

Branch Circuit

Input screens of branch circuit are displayed in the figure 2. Total number of multiple cylinders controlled by a valve should not be allowed more than 10 in one branch circuit in the software.

When the “Common” button is clicked, an input screen will be popped up. Supply pressure, ambient temperature, and the model specifications for pipes, valve and silencer can be set in the common circuit input screen, as it is showed in the figure 2 (A).

Clicking the “Individual” button will open another input screen. The model and specifications for cylinder, flow controller and pipe can be set in the individual circuit

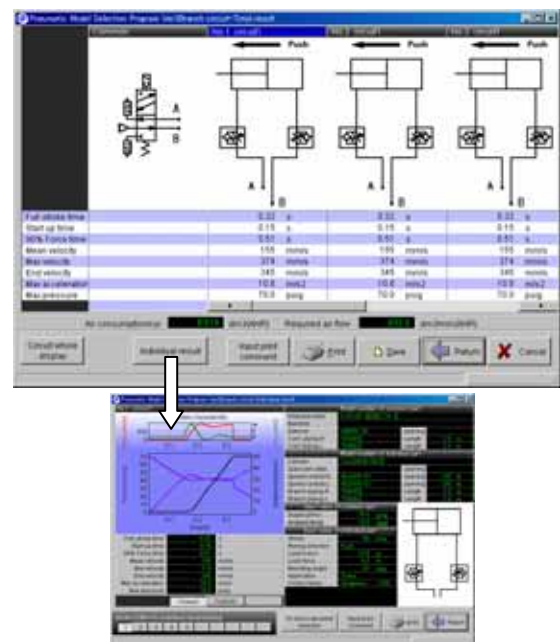


Figure 3 Output screens for branch circuit

input screen, as it is showed in figure2 (B). Cylinders of single action type and double action type are allowed at the same time in branch circuit.

For convenience of circuit design, functions of copy, add, and delete are also included for individual circuits in branch circuit input screen.

After all conditions are input, and the “Calculation” button is clicked, dynamic characteristics of branch circuit will be automatically calculated by simulation. Figure 3 shows output screens for calculation results of branch circuit. Stroke time, start time, final velocity, etc. are displayed for all cylinders in the branch circuit output screen.

Detail results of every cylinder will be showed if the “Individual Result” button is clicked. Cushion capacity can be calculated by clicking the “Cushion” button. And if necessary, proper model of shock absorber can be selected by clicking the “To shock absorber section” button.

Manifold Circuit

Figure 4 shows input screens of the manifold circuit. The maximum number of valves is 20 in one manifold circuit in the software.

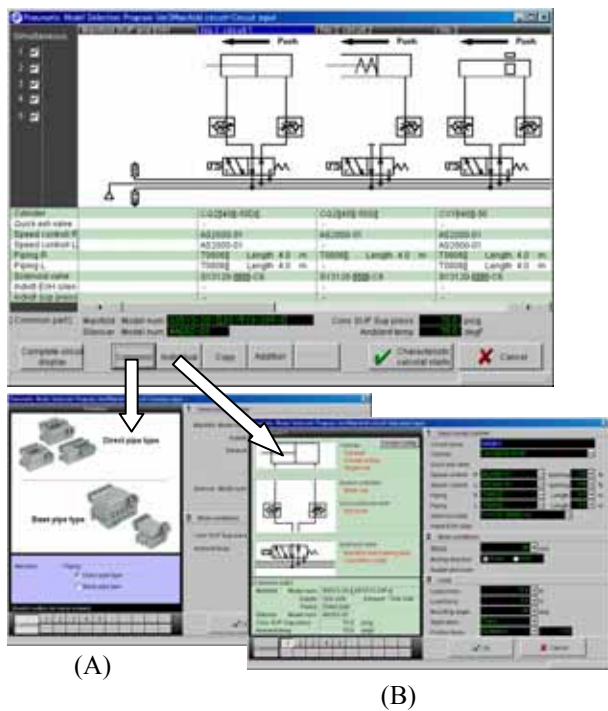


Figure 4 Input screens for manifold circuit

After the “Common” button is clicked, the common circuit input screen will be appearing as it is showed in Figure 4 (A). Supply pressure, ambient temperature, and model specifications for pipes, silencer can be set in this screen. Supply port and exhaust port can be set as one side type or both side type according to the specification of manifold.

After the “Individual” button is clicked, the individual input screen will be opened as it is showed in the figure 4 (B). Model and the specifications for cylinder, valve, flow controller and pipe can be set in this screen. Exhaust ports and supply ports of valves can be set as

common type or individual type according to specifications of valve-manifold unit, after the “Circuit Configuration” button is clicked.

For convenience of circuit design, copy, add, and delete functions are also provided for individual circuits in the input screen of manifold circuit.

In the manifold circuit input screen, individual circuits that are driven simultaneously can be chosen and set before simulation starts.

After all conditions are input, and the “Calculation” button is clicked, dynamic characteristics of manifold circuits will be automatically calculated by simulation.

Figure 5 shows output screens of calculation results of manifold circuit. Stroke time, start time, finally velocity, etc. are displayed for every cylinder in the manifold circuit output screen.

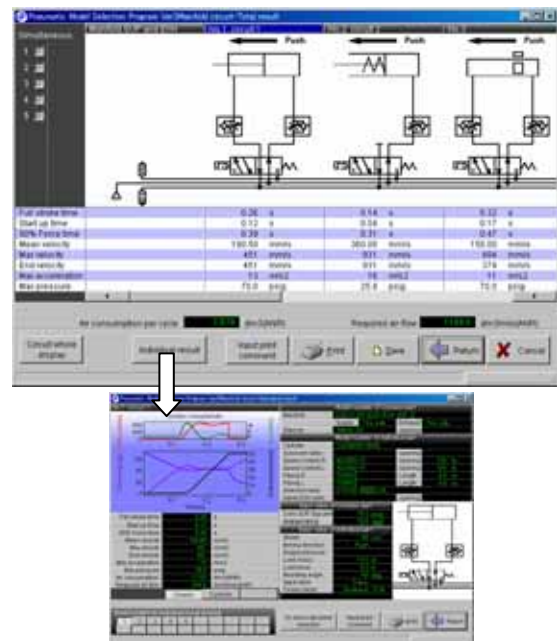


Figure 5 Output screens for manifold circuit

As same as branch circuit, detail results of every cylinder in manifold circuit are showed after the “Individual Result” button is clicked. Cushion capacity can be calculated by clicking the “Cushion” button. And if necessary, proper model of shock absorber can be selected by clicking the “To shock absorber section” button.

MODELS AND EXAMPLES

Modeling

Pipes, cylinders and valves in all kinds of circuits are separately simulated with the distribution pipe model, the cylinder basic equations, and the ISO flow rate

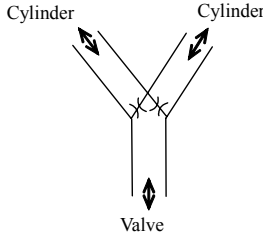


Figure 6 Model of branch circuit

characteristic equations.²⁾ Branch circuit and manifold circuit are simulated with the models described as follows.

Figure 6 shows the model of branch circuit. Considering pressure loss in branch circuit, instead of traditional method of loss rate, a fixed flow conductance is applied to model the resistance effect of branch circuit. Air flow from valve through every branch to all cylinders is considered, but air flow from one branch to the others is neglected in the model.

Choked air flow through branch circuit is calculated with equation (1).

$$G = Cp\rho_0 \sqrt{\frac{T_0}{T}} \quad (1)$$

Where G [g/s] is mass flow rate; C [dm³/(s·bar)] is conductance of branch circuit; p [bar] is absolute pressure of upstream air; $\rho_0=1.185$ [g/dm³] is air density of the standard reference conditions; $T_0=293.15$ [K] is air temperature of the standard reference conditions; and T [K] is upstream air temperature.

Subsonic air flow through branch circuit is calculated with equation (2).

$$G = Cp\rho_0 \sqrt{\frac{T_0}{T}} \sqrt{1 - \left(\frac{p_a - b}{1 - b} \right)^2} \quad (2)$$

Where p_a [bar] is absolute pressure of downstream air; b [-] is critical pressure ratio of branch circuit.

Figure 7 shows the model of manifold circuit. Lumped modeling is applied to inner volume of manifold. Supply volume is treated as a charge chamber, and exhaust volume is treated as a discharge chamber. State change of air is assumed to be isothermal both in charge process and in discharge process.

When equation of air state is applied to discharge chamber, change of air pressure is expressed with equation (3).

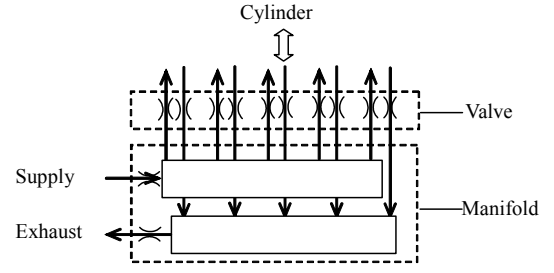


Figure 7 Model of manifold circuit

$$\frac{dp_d}{dt} = \frac{RT_d G_d}{V_d} \quad (3)$$

Where p_d [Pa] is absolute pressure of discharge chamber; t [s] is time passed; $R=287$ [J/(kg·K)] is gas constant; T_d [K] is air temperature of discharge chamber; G_d [kg/s] is mass flow rate of discharging; and V_d [m³] is volume of discharge chamber.

When equation of state is applied to charge chamber, change of air pressure is expressed with equation (4).

$$\frac{dp_u}{dt} = \frac{RT_u G_u}{V_u} \quad (4)$$

Where p_u [Pa] is absolute pressure of charge chamber; T_u [K] is air temperature of charge chamber; G_u [kg/s] is mass flow rate of charging; and V_u [m³] is volume of charge chamber.

Calculation Example

As an example, simulation and experiment results of a branch circuit is presented. It is a pneumatic system with five different cylinders controlled by one valve. The load of every cylinder is 1kg on the top of piston as showed in the figure 8.

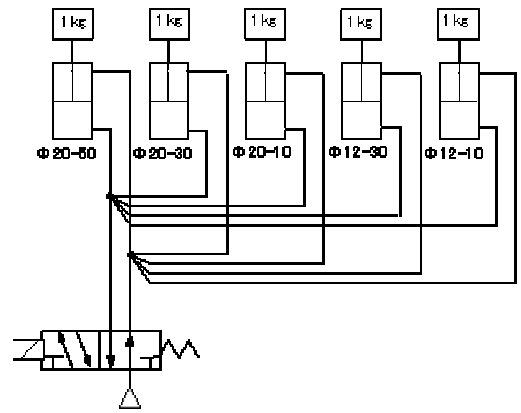


Figure 8 Example of calculation

REFERENCE

1. Huping ZHANG: Model Selection Program for Pneumatic System, Journal of Fluid Power System, Vol33, No.4, pp.216/261, (2002)
2. Huping ZHANG, Mitsuru SENOO, Kotaro KURIHARA, Hidetsugu FUJITANI, Naotake ONEYAMA: Development of Model Selection Software of Pneumatic Components, Proceeding of the 3rd International Symposium on Fluid Power Transmission and Control, Harbin, China, 566/571, (1999)

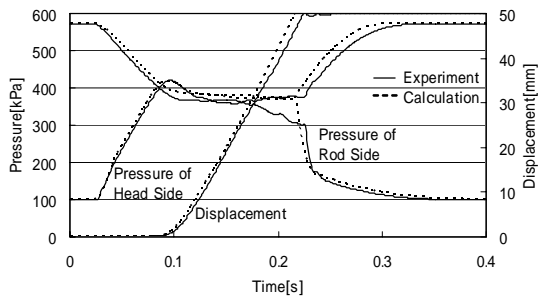


Figure 9 Results of push-out process

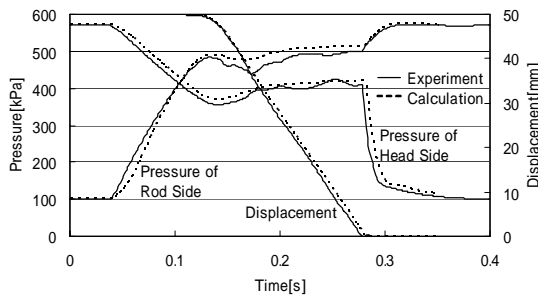


Figure 10 Results of pull-in process

Pressure in rod side chamber and head side chamber of the cylinders, and displacement of the pistons are tested in practical experiments. And the circuit is simulated with the Pneumatic Model Selection Program too, to get all dynamic characteristics.

One of the cylinders in the branch circuit is with 20mm diameter and 50mm stroke. Figure 9 shows the results of push-out process of the cylinder. The simulation results are in close agreement with the experiment results. Figure 10 shows the results of pull-in process of the cylinder. The simulation results are also in close agreement with the experiment results.

CONCLUSION

Firstly, outline and guidance of the Pneumatic Model Selection Program is introduced in this paper. Secondly, modeling and calculation method of branch circuit and manifold circuit is explained. Thirdly, a practical example of branch circuit is presented. Obviously, with the help of the Pneumatic Model Selection Program, design of complex pneumatic system, such as branch circuits and manifold circuits becomes easy and efficient.

ACKNOWLEDGEMENT

Finally, thanks for association from Professor Kagawa's Laboratory of Tokyo Institute of Technology.

Dynamic Characteristic and Power Consumption on an Electro-Pneumatic Hybrid Positioning System

Hiroshi HIGO*, Yasuo SAKURAI**, Takeshi NAKADA***,
Kazuhiro TANAKA*, and Katsuya NAGAYAMA*

* Department of Mechanical Information Science and Technology,
Kyushu Institute of Technology

680-4 Kawatsu, Iizuka, Fukuoka, 820-8502 Japan

** Department of Mechanical Engineering,
Ashikaga Institute of Technology

286-1 Oomae, Ashikaga, Tochigi, 326-8558 Japan

*** Department of Environment Integration and design,
Tokyo Denki University

2-1200 Muzaigakuendai, Inzai, Chiba, 270-1382 Japan

ABSTRACT

This paper deals with the dynamic characteristics of an electro-pneumatic hybrid positioning system. This system is composed of a pneumatic, an electric and a mechanical driving sub-system. The pneumatic driving system controls the pressure supporting the inertial mass, which means that the pressure is correspondent to the gravitational force acting on it. And the electric driving system with small capacity moves the inertial mass vertically through a ball screw as a mechanical driving sub-system. In the present study, in order to developing the electro-pneumatic hybrid positioning system, the mathematical model of this system has been refined by comparing calculation data with the experimental results, especially by measuring precisely frictional force of the ball screw. And the power consumption as well as the dynamic characteristics has been investigated numerically when the inertial mass is moved vertically upwards and downwards during one cycle by the electric driving system through the ball screw. The data on the power consumption during one cycle will be useful to select a suitable driving motor at the design stage.

KEY WORDS

Electro-pneumatic hybrid positioning system, Dynamic characteristics, Pressure control, Bondgraphs, Modeling

NOMENCLATURE

A_e : Effective area of the cylinder	[m ²]
A_r : Area of rod side cylinder	[m ²]
A_h : Area of head side cylinder	[m ²]
C : Frictional loss coefficient	[Ns/m]
F : Force	[N]
k : Specific heat ratio	[-]
K : Rigidity of coupling	[Nm/rad]
I_z : Momentum of shaft	[kgm ²]
l : Lead of ball screw	[m]
\dot{m} : Mass flow rate	[kg/s]
M : Inertial mass	[kg]
P : Pressure	[Pa]
Q : Flow rate	[m ³ /s]
R : Gas constant	[J/(kgK)]
T : Temperature	[K]

v : Velocity	[m/s]
ω : Rotational speed	[rad/s]
τ : Torque	[Nm]

INTRODUCTION

A pneumatic system has some advantages such as safety, ease to maintenance, environment, and so on. Then the pneumatic system is used various automation machines. However, the pneumatic system is difficult to control velocity and positioning of an inertial mass precisely [1-2]. To improve these disadvantages, an electro-pneumatic hybrid system is proposed [3]. In this system, supplied air pressure supports an inertial mass and the positioning of the inertial mass is controlled by a servomotor. This mechanism can easily control the positioning of the inertial mass more precise than a

pneumatic system.

However, when this actuator moves with suddenly large inertial mass, the servomotor faces unpredictably large torque and stops automatically. To avoid this stopping, it is important to predict the load of the servomotor precisely by analyzing the dynamic characteristics of the system.

Bondgraph method is very convenient to predict the system dynamic characteristics and calculate power consumption. The method is available in various systems composed mechanical, electrical and hydraulic components because it is based on the viewpoint of power conservation. This method has been used for prediction of dynamic characteristics and designing real systems [4-6]. In order to establish a design method of an electro-pneumatic hybrid system, the Bondgraph method is surely useful.

The objectives of this study are followings.

1. To investigate frictional loss of the electro-pneumatic actuator by experiment.
2. To construct a mathematical system model of the electro-pneumatic actuator.
3. To compare experimental results with calculated results when this actuator is operated and to verify the mathematical model of the system.

ELECTRO—PNEUMATIC ACTUATOR

Figure 1 shows the electro-pneumatic hybrid actuator. The Electro-pneumatic actuator consists of a servomotor, a cylinder, a ball screw, a rod and a air supply system. The servomotor is combined with the ball screw. The rod is combined with the nut. The bottom part of ball screw is inside the rod, when the servomotor is driven, the ball screw rotates, the nut moves and the inertial mass also moves.

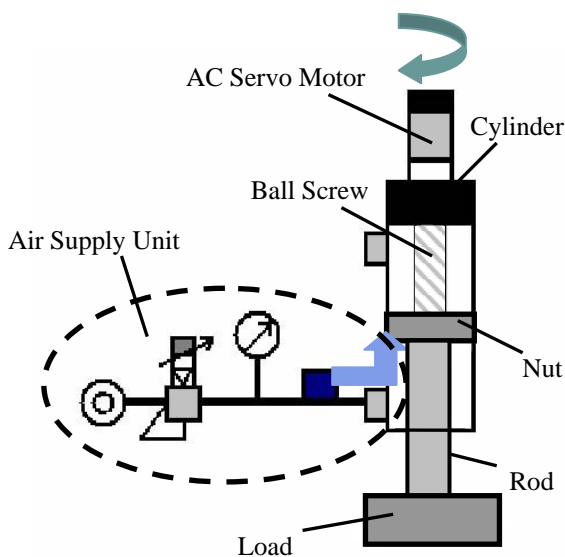


Fig. 1 Schematic of Electro-pneumatic actuator

The pressure of air supply system is correspondent to gravitational force acting on an inertial mass. Therefore, even a servo motor with low-capacity can control a large inertial mass.

EXPERIMENTAL EQUIPMENT

Experimental equipment is shown in Fig. 2. The pressure of the air supply unit is controlled by an electric-pneumatic regulator and is provided into the rod side of the cylinder. The pressure of another side chamber is atmospheric pressure. PC controls the electro-pneumatic regulator and angular velocity of the servomotor for precise positioning. In the experiment torque and rotational degree of the servomotor are measured.

SIMULATION MODEL

Generally, a physical system consists of electrical, mechanical, fluid, thermal system and so on. Because power flows between elements in physical systems, the systems can be expressed using power train. Bondgraph method is one of the system expression method based on power train.

When power flows from a system to a sub-system, these two elements can be connected by a line, called bond, which indicates power flow, as shown in Fig.3. Power is the product of effort and flow variables in each system, shown in Table 1. Consequently, the power bond has two power variables, effort and flow. In Bondgraph method, an element indicates a physical quantity in each field, shown as Table 2.

Table1 Variables

	Rectilinear system	Rotational system	Fluid system
Effort	Force	Torque	Pressure
Flow	Velocity	Angular Velocity	Volume flow rate

Table2 Elements

Element	Mechanical system	Rotational system	Fluid system
SE	Force	Torque	Pressure
SF	Velocity	Angular Velocity	Volume flow rate
R	Friction	Friction	Fluid Friction
I	Mass inertia	Momentum inertia	Mass inertia
C	Spring	Spring	Capacity

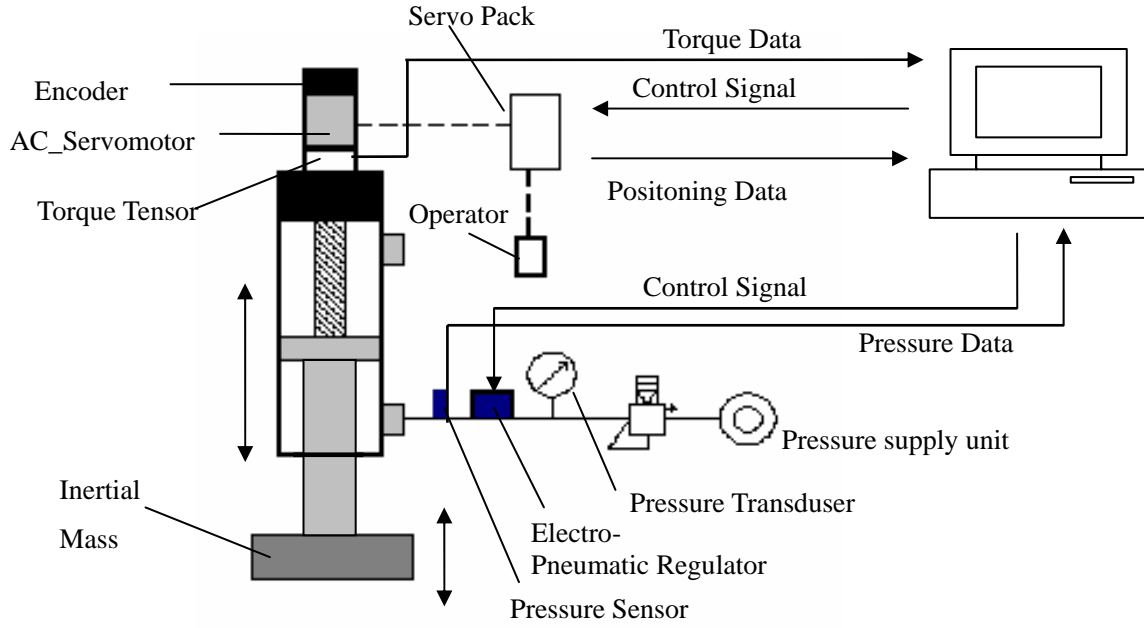


Fig. 2 Experimental apparatus

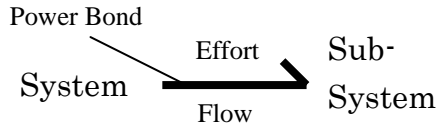


Fig. 3 Bond

$$\dot{m}_2 = A_e P_1 \sqrt{\frac{\kappa}{RT_1} \left\{ \left(\frac{2}{\kappa+1} \right)^{\frac{\kappa+1}{\kappa-1}} \right\}} \quad (2)$$

$$\left(0.528 \leq \frac{P_3}{P_1} \leq 1 \right)$$

A system bondgraph model of the electro-pneumatic actuator is shown in Fig. 4.

Output pressure of an air supply unit is assumed to be constant. Then an air supply unit is modeled by 'Se: Air supply unit' element. The following equation can be used for this element.

$$P_1 = const \quad (1)$$

Subscript indicates the number of bond.

An electric-pneumatic regulator is modeled by 'R: Valve' element and its constitutive equation is expressed as follows.

$$\left(0 \leq \frac{P_3}{P_1} < 0.528 \right)$$

$$\dot{m}_2 = A_e P_1 \sqrt{\frac{2\kappa}{\kappa-1} \frac{1}{RT_1} \left\{ \left(\frac{P_3}{P_1} \right)^{\frac{2}{\kappa}} - \left(\frac{P_3}{P_1} \right)^{\frac{\kappa+1}{\kappa}} \right\}} \quad (3)$$

Where A_e is effective area of the electric-pneumatic regulator, P_1 is pressure of air supply unit, T_1 is temperature of air.

'C: Compressibility' element means compressibility of the air in the rod end chamber of the pneumatic cylinder. Its constitutive equation is expressed as follows.

$$P_4 = \frac{\kappa}{V_0 + Ax} \int (RT_{t-1} \dot{m} - P_{t-1} Av) dt + P_0 \quad (4)$$

Where P_0 is initial pressure of rod-end chamber, V_0 is initial volume of rod-end chamber, T_{t-1} is calculation

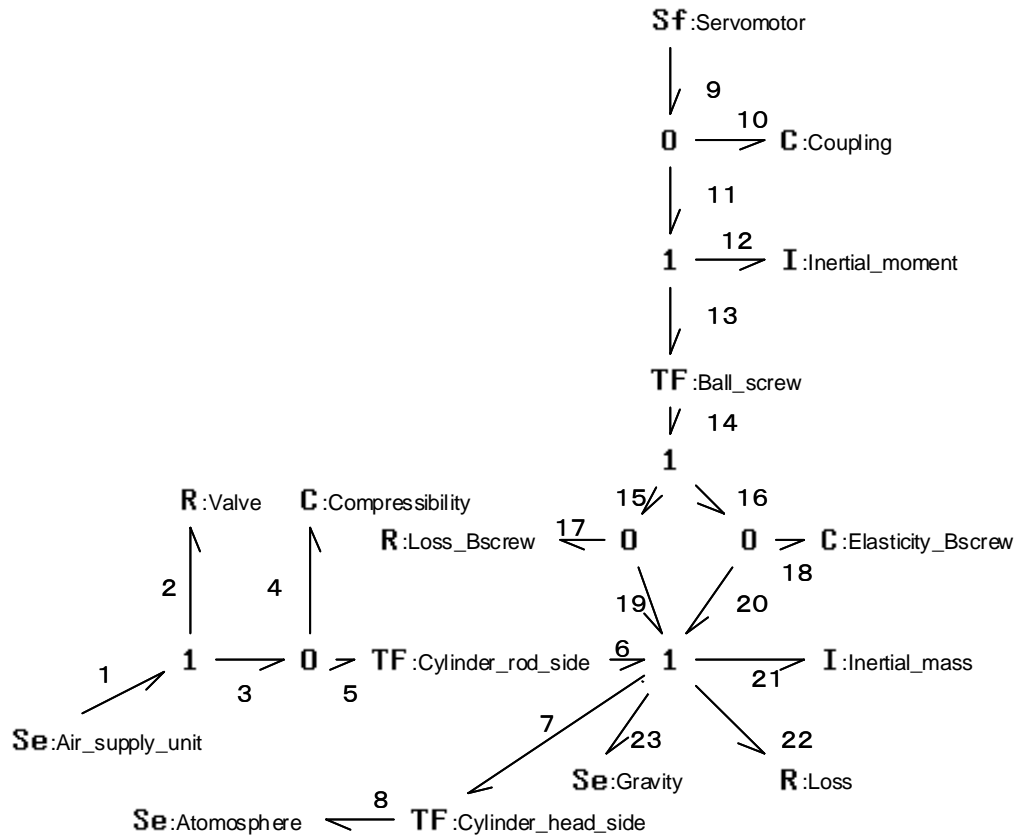


Fig. 4 System bondgraph model

result of temperature, P_{t-1} is calculation result of pressure. Each variable are calculational results before 1time step.

'TF1:Cylinder_head_side', 'TF1: Cylinder_rod_side' mean pressure area of piston, and its constitutive equation is expressed as follows

$$F_6 = A_r P_5 \quad (5)$$

$$Q_5 = A_r v_6 \quad (6)$$

$$F_7 = A_h P_8 \quad (7)$$

$$Q_8 = A_h v_7 \quad (8)$$

Where A_r is area of rod side chamber, A_h is area of head side chamber. By these elements, pressure is changed mechanical force.

'Sf: Servomotor' element represents angular velocity of a servomotor. The objective of present study is to establish a mathematical model of an electro-pneumatic hybrid positioning system. Therefore, the accurate mathematical model of the servomotor was not derived.

Angular velocity ω_9 is measured in experiment and used as an input to the system in simulation.

'C: Coupling' element means the torsion rigidity of the coupling, this equation is represented as follows.

$$\tau_{10} = K \int \omega_{10} dt \quad (9)$$

where K is rigidity of coupling.

'I: Inertial_moment' element means moment of ball screw. This equation is represented as follows

$$\omega_{12} = \frac{1}{I_z} \int \tau_{12} dt \quad (10)$$

where I_z is the inertial momentum of shaft

A ball screw is represented by 'TF: Ball screw' element for change from rotation motion to liner motion, and its constitutive equation is expressed as follows

$$v_{14} = \frac{l}{2\pi} \omega_{13} \quad (11)$$

$$\tau_{13} = \frac{l}{2\pi} F_{14} \quad (12)$$

where l is lead of ball screw.

'R: Loss_Bscrew' and 'C: Elasticity_Bscrew' element mean the characteristic of a nut.

'I: Inertial mass' means an inertial mass. This constitutive equation is expressed as follows

$$v_{21} = \frac{1}{M} \int F_{21} dt \quad (13)$$

'R: Loss' means frictional loss of cylinder. It is difficult to decide a frictional loss of a cylinder from using only parameters of equipment. Accordingly, this parameter is measured by experiment. Therefore this constitutive equation is expressed as

$$F_{22} = C \cdot v_{22} \quad (v_{22} < -0.01 \quad \text{or} \quad 0.01 < v_{22}) \quad (14)$$

$$F_{22} = \text{const.} \quad (-0.01 < v_{22} < 0.01) \quad (15)$$

'Se: Gravity' indicates gravity force of an inertial mass. It is constant value.

$$F_{23} = Mg \quad (16)$$

RESULTS AND DISCUSSION

1. Frictional loss

Frictional force is measured by experiments. The pressure which is controlled by an electric-pneumatic regulator is set at the constant value correspondent to the gravitational force of an inertial mass. By rotating the servomotor, an inertial mass moves upwards or downwards. The relationship between force of the cylinder and moving velocity of the inertial mass is followings.

F , force of the nut is calculated by pressure P , torque τ and inertial mass M (Eq.(17)). Pressure and torque were measured. The coefficient of frictional force is calculated by Eq.(18).

$$F = \frac{2\pi}{l} \tau + PA_e - Mg \quad (17)$$

$$C = \frac{F}{v} \quad (18)$$

Fig. 5 shows the measured results of the frictional force. It can be seen from this figure that the frictional loss is affected by the velocity of inertial mass.

Relationship between the velocity and frictional coefficient is expressed as

$$C = 213.7v^{-0.79} \quad (\text{Upward}) \quad (19)$$

$$C = 179.0v^{-0.86} \quad (\text{Downward}) \quad (20)$$

The frictional coefficient used here was taken from the experiment and was placed R element for the simulation.

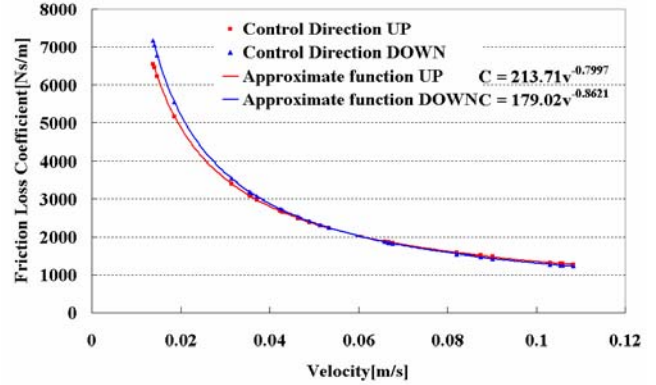


Fig. 5 Frictional Loss

Table3 Experimental Parameters

Parameter	Value
Valve effective area [m ²]	6.0 × 10 ⁻⁵
Estimated valve effective area [m ²]	1.2 × 10 ⁻⁵
Ratio of the specific heat of the air [-]	1.4
Initial temperature [K]	293
Gas constant [J/kg K]	287.3
Cross sectional area of the cylinder [m ²]	2.63e-3
Initial volume of the cylinder [m ³]	2.63e-4
Initial pressure [MPa] (absolute)	0.224
Inner diameter of the cylinder tube [m]	6.3 × 10 ⁻²
Diameter of the cylinder rod [m]	2.5 × 10 ⁻²
Weight [kg]	31.7
Constant dynamic friction [Ns/m]	160
Friction loss coefficient (UP) [Ns/m]	706.59v ^{-0.73}
Friction loss coefficient (DOWN) [Ns/m]	435.61v ^{-0.66}
Elasticity of the nut (Gap ≥ 0.1 [mm])	1.1 × 10 ⁸
Gap(Damper coefficient) [Ns/m]	1.0 × 10 ⁵
Lead of the ball screw [m/r]	5.0 × 10 ⁻³
Inertial moment [kgm ²]	4.06 × 10 ⁻⁵
Rotational elasticity of the coupling [Nm/rad]	120.9

2. Dynamic characteristics and power consumption

The experiment of dynamic characteristic of the

electro-pneumatic actuator is performed. Prior to the experiment, the position of the inertial mass was set at the lowest point and the control of the pressure acting on the inertial mass was started.

The input signal to determine angular velocity of servomotor was added to the servomotor controller. And then, inertial mass moved upwards by 100 mm, then stopped, and moved downwards by 100 mm. These experiments were carried out at same angular velocities of the servomotor. Experimental results are inputted as the angular velocity in the simulation. Table 3 shows experimental parameters. Only parameters of friction loss coefficient and input angular velocity are the experimental data and the others are catalogue value.

Simulation and experimental results are shown in Fig. 6. It can be seen from this figure that the experimental result and calculation result are agree well when inertial mass is moved. However, when inertial mass is stopping, calculation result is different from experimental ones. It might be thought that static friction at a moment when the servomotor stops is different in each case of experiments. When the mass moves downwards, the calculation data is stable compared with experimental data. This is because the capacity of the electro-pneumatic regulator is not suitably determined. If new regulator with more capacity is used, the both data will agree well. Any well, the data comes to a close match with an only minor discrepancy.

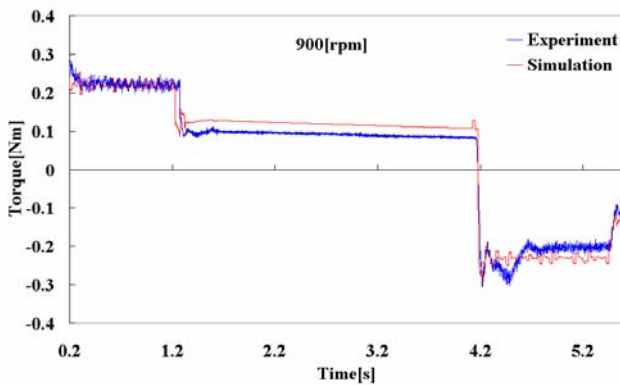


Fig. 6 Torque

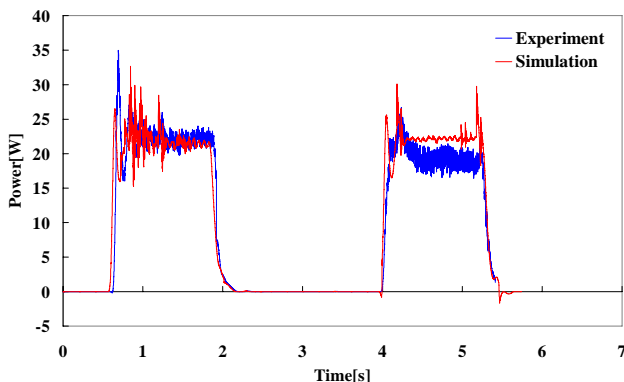


Fig. 7 Power of servomotor

Fig. 7 is comparison of calculation results with experimental ones on servomotor power. From this figure, calculation result and experimental one are agree well. Therefore, it is seemed that this model can predict the power of servomotor of electro-pneumatic hybrid actuator.

CONCLUSION

The mathematical model of the electro-pneumatic hybrid actuator was proposed to predict the system dynamic characteristics and power consumption. The frictional loss of the actuator, which is the most difficult parameter to be determined in the system, was measured precisely at moving upwards and downwards during the cycle. As a result, calculation result agrees well with experimental results. This proved that this mathematical model can predict dynamic behaviors of the system and the power of servomotor.

ACKNOWLEDGEMENT

The authors would like to thank SMC Co, Ltd. for providing the experimental apparatus and helpful suggestions.

REFERENCES

1. SHIH, Ming chang and LUOR, Niarn-liang. Self-tuning Neural Fuzzy Control the Position of a Pneumatic Cylinder Under Vertical Load. Proc of 6th FLUCOME, Sherbrooke CANADA, Cd-ROM, 2000.
2. Baihai ZHANG, Bondgraph Modeling and Simulation of Dynamic Characteristics of a Pneumatic System with an Air Cushion Cylinder, 5th JFPS International Symposium, 339-342, (2002).
3. Y.SAKURAI, K.TANAKA, T.NAKADA, Dynamic Characteristic On An Electro-Pneumatic Hybrid Positioning System, 7th Int. Symp. on Fluid Control, Measurement and Visualization, 2004
4. E. Benjamin Wylie, Victor L. Streeter, Fluid Transient in Systems, p. 2-9, PRENTICE HALL 1993.
5. Rosenberg R.C. and Karnopp D.C. *Introduction to Physical System Dynamics*, McGraw-Hill, 1983.
6. Thoma J. *Simulation by Bondgraphs*, Springer-Verlag, 1990.

Study on the Over-shoot of Cylinder Halfway Stop System

Wei FAN*, Guangzheng PENG*, Yu ZHOU*, Huping ZHANG**

* Department of Automatic Control
Beijing Institute of Technology
Beijing, 100081, China
(E-mail: fanwei@bit.edu.cn)

** Technology Research Division
SMC Corporation
Tsukuba, 300-2493, Japan

ABSTRACT

This paper makes modeling and simulation for some simple cylinder halfway stop systems with valves of different center configuration. Simulation gives the displacement curves of the piston in the working stroke and over-shoot values are also obtained according to each kind of halfway stop system. Furthermore, experimental systems are built and displacement curves are also achieved in these experimental systems, which has validated the simulation research. Comparison analysis and characteristic summary are dealt with different systems.

KEY WORDS

Cylinder halfway stop system, Over-Shoot, Modeling, Simulation and experimental investigation

NOMENCLATURE

A : Area of the piston (m^2)
 Qm : Mass flow (Kg/s)
 R : Gas constant ($287JKg^{-1}K^{-1}$)
 L : Full stroke of the cylinder (m)
 T : Temperature (K)
 x : Displacement of the piston (m)
 t : Time (s) ;
 k : Specific heat ratio, $k=1.4$ for the air
 X_0 : Initial remaining length of the cylinder
 C_q : Flow coefficient (0.7)
 A_q : Synthesis flow area of the valve, the speed controller, and the cube (m^2)
 M : Mass of the air (Kg)
 a : Coulomb friction (N)

b : Slip friction coefficient
 F_1 : Friction between the piston and the cylinder (N)
 F_2 : Friction between the load and the linear rail (N)
 M_w : Mass of the load and the piston rod (Kg)
 F : Total friction (N)

Subscripts

'1' and '2': Parameters of left and right sides respectively.

'a' and 's': Parameters of atmosphere and air supply respectively.

INTRODUCTION

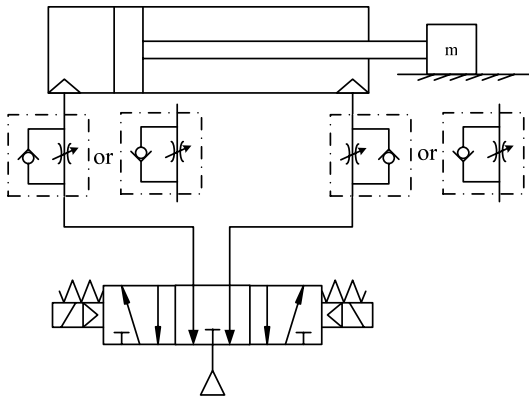
Cylinder halfway stop system, made up of 3 positions and 5 ports valve, exhausted-center or closed-center, and speed controllers of meter-in or meter-out, is widely

used in safe doors of machines as its simplicity and low-cost. However, over-shoot often occurs because of some difficultly unavoidable factors such as gas compressibility, switching delay of the solenoid valve, and so on when the cylinder is controlled to halfway stop. Therefore, it is significant for life safety to know this over-shoot in designing phase. In this paper, modeling, simulation and experimental investigation for the cylinder halfway stop system are completed, which can provide theoretical foundation and practical validity.

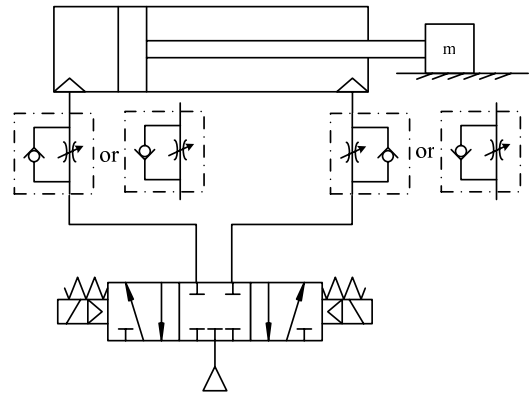
MODELING

Simple cylinder halfway stop system is controlled by the exhausted-center or closed-center valve of 3 positions and 5 ports, with speed controllers of meter-in or meter-out. Therefore, four familiar loops, as shown in Fig.1, will be studied in this research. The different kinds of speed controller only shows different flow characteristics in and out of the cylinder. So, generally speaking, the four loops can be classified to two types, exhausted-center and closed-center systems by the valve configuration. To simplify the modeling and calculation, conventional hypotheses are quoted as following.

- 1) The working medium, air is the ideal gas.
- 2) The air supply is stable with no fluctuation.
- 3) Internal Leakage of the cylinder and the valve is neglected.
- 4) The working course is adiabatic, and it is approximately a thermodynamic static course.



(a) Exhausted-center system



(b) Closed-center system

Fig.1 Simple cylinder halfway stop system

Exhausted-center system

The piston of the cylinder is initialized to the left position. The initial pressure of left side is atmospheric pressure and that of the right side is pressure of the air supply. Then, the valve is controlled, the left side of the cylinder is charged and the right side discharged, the piston is moving to right. When the piston arrives halfway, the valve is switched to center. Because the valve is exhausted-center, the left side is discharged and right side continues to be discharged. For any solenoid valve, there is switching delay when it is controlled. This delay time must be considered when simulation.

The pressure equations:

Left side is charging course,

$$\frac{dp_1}{dt} = -\frac{kp_1}{X_{01} + x} \cdot \frac{dx}{dt} + \frac{kRTQ_{m1}}{A_1(X_{01} + x)} \quad (1)$$

Right side is discharging course,

$$\frac{dp_2}{dt} = \frac{kp_2}{X_{02} + L - x} \cdot \frac{dx}{dt} - \frac{kRTQ_{m2}}{A_2(X_{02} + L - x)} \left(\frac{p_2}{p_s}\right)^{\frac{k-1}{k}} \quad (2)$$

The flow equations:

Left side is charging course,

$$Q_{m1} = C_q A_q p_s \sqrt{\frac{2}{RT}} \varphi\left(\frac{p_1}{p_s}\right)$$

$$\varphi\left(\frac{p_1}{p_s}\right) = \begin{cases} \sqrt{\frac{k}{k-1} \left[\left(\frac{p_1}{p_s}\right)^{\frac{2}{k}} - \left(\frac{p_1}{p_s}\right)^{\frac{k+1}{k}} \right]} & 0.528 \leq \frac{p_1}{p_s} \leq 1 \\ \left(\frac{2}{k+1}\right)^{\frac{1}{k-1}} \sqrt{\frac{k}{k+1}} & 0 \leq \frac{p_1}{p_s} \leq 0.528 \end{cases} \quad (3)$$

Right side is discharging course,

$$Q_{m2} = C_q A_q p_2 \sqrt{\frac{2}{RT}} \varphi\left(\frac{p_a}{p_2}\right)$$

$$\varphi\left(\frac{p_a}{p_2}\right) = \begin{cases} \sqrt{\frac{k}{k-1} \left[\left(\frac{p_a}{p_2}\right)^{\frac{2}{k}} - \left(\frac{p_a}{p_2}\right)^{\frac{k+1}{k}} \right]} & 0.528 \leq \frac{p_a}{p_2} \leq 1 \\ \left(\frac{2}{k+1}\right)^{\frac{1}{k-1}} \sqrt{\frac{k}{k+1}} & 0 \leq \frac{p_a}{p_2} \leq 0.528 \end{cases} \quad (4)$$

The force equations:

$$M_w \cdot \frac{d^2 x}{dt^2} = p_1 A_1 - p_2 A_2 - F \quad (5)$$

In Eq. (5), F is the total friction in the system, which is composed of two parts. One is the friction F_1 between the piston and the cylinder. When the pressure difference between both sides of the piston is not greater than the maximum friction of the piston, the piston is static and the friction is the force owing to the pressure difference. When the pressure difference between both sides of the piston is greater than the maximum Coulomb friction of the piston, the piston is moving and the friction is proportional to the velocity of the piston [3]. The other is the Coulomb friction F_2 between the load and the linear rail.

$$F = F_1 + F_2$$

$$F_1 = a \cdot \text{sign}\left(\frac{dx}{dt}\right) + b \frac{dx}{dt} \quad (6)$$

$$F_2 = \mu \cdot mg \cdot \text{sign}\left(\frac{dx}{dt}\right)$$

Closed-center system

It is little different from the exhausted-center system. When the valve is switched to center, both the left and right sides are closed because the valve is closed-center. Air in both sides is regarded as the ideal gas. So, it can be modeled with the ideal gas state equation. Similarly, there is switching delay when the valve is controlled. This delay time should be considered when simulation. Except for the pressure equations, flow equations and fore equations, the ideal state equations are also used in the modeling.

Left side,

$$M_1 = \frac{X_{01} p_a A_1}{RT} + \int Q_{m1}$$

$$p_1 A_1 (X_{01} + x) = M_1 RT \quad (7)$$

Right side,

$$M_2 = \frac{(L + X_{02}) p_s A_2}{RT} - \int Q_{m2} \quad (8)$$

$$p_2 A_2 (L + X_{02} - x) = M_2 RT$$

SIMULATION

Based on above modeling, simulation is done with the tool of Simulink of Matlab for the system made up of the cylinder of MB32-400, the valves of SY5420 (exhausted-center) or SY5320 (closed-center), the speed controllers of AS2311F (meter-in) or AS2301F (meter-out), which are all from SMC. In order to acquire actual parameters, some test experiments are carefully done. The first experiment is to test the switching delay time of the valves. Experimental system is built up as shown in Fig.2. By acquiring the output pressure of the valve, we can get the pressure response of port A, shown in Fig.3 (for SY5320, $p_s=0.5\text{MPa}$), when the left solenoid is electrified, which indicates obvious switching delay, about 30ms. This experiment adopts the interrupt at 100K sample rate with the FIFO of the DAQ card as the A/D DAQ method.

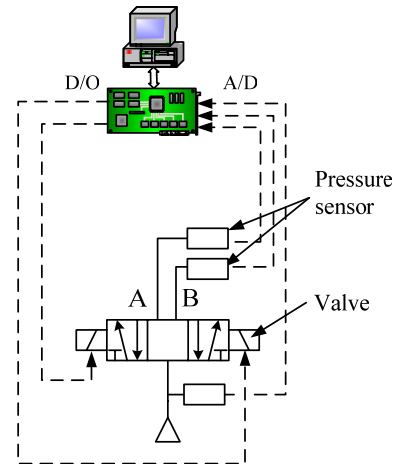


Fig.2 Experimental system to test the switching delay time of the valve

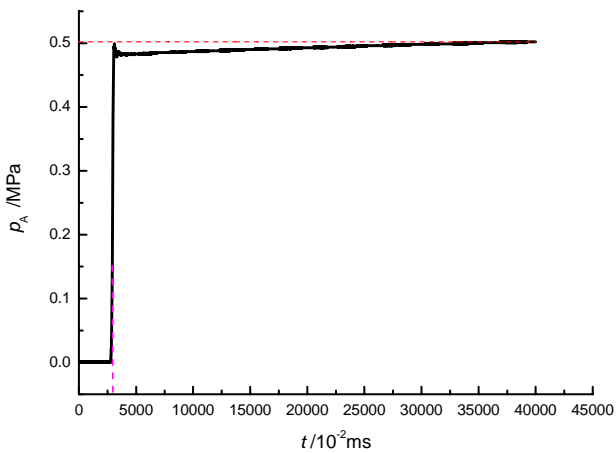


Fig.3 Experimental results of testing the switching delay time of the valve

The second experiment is to test the flow area of the speed controllers, the valve and the cube with the traditional methods of discharging in the velocity. The third experiment is to test the maximum Coulomb friction between the piston and the cylinder. It can be calculated by acquiring the pressure of the left and the right sides when the piston starts to move by adjusting the speed controllers.

Fig.4 (for the system of the cylinder MB32-400, load=30Kg and $p_s=0.5\text{MPa}$) gives the displacement curves of the piston in the working stroke and over-shoot values according to each kind of halfway system.

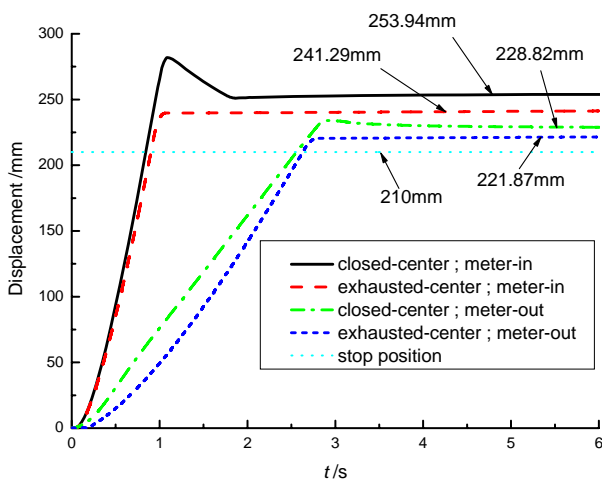


Fig.4 Simulation of the over-shoot of simple cylinder halfway stop system

Through simulation, we can analyze the factors

influence on the over-shoot. Over-shoot of the closed-center system is greater than that of the exhausted-center system. Over-shoot of the meter-in system is greater than that of the meter-out system. Besides, simulation shows that the more mass of the load the more over-shoot, and the switching delay time of the valve also has much influence on the over-shoot.

EXPERIMENTAL INVESTIGATION

Experimental systems are built as the Fig.5 shows. The DAQ hardware is from ADVANTECH of Chinese Taiwan. The displacement of the piston rod is measured by a raster code sensor and acquired by the PCL-833, and the Digital I/O is realized by PCI-1710, PCLD-782 and PCLD-785. The DAQ software is developed with NI/LabVIEW.

The experiment course is expressed as following. Firstly, the solenoid B is electrified, the piston goes to the left position. Then, the solenoid A is electrified and B un-electrified, the piston moves to right. When it arrives the halfway, e.g. the magnetism switch in the middle of the full stroke is on, A and B are simultaneously un-electrified, the valve is switching to the center, and the cylinder implements halfway stop. The displacement curves can be also achieved during the experiment course.

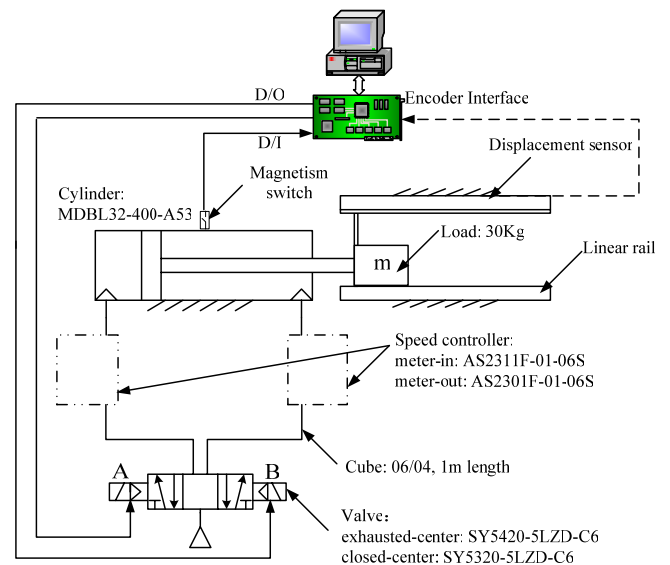
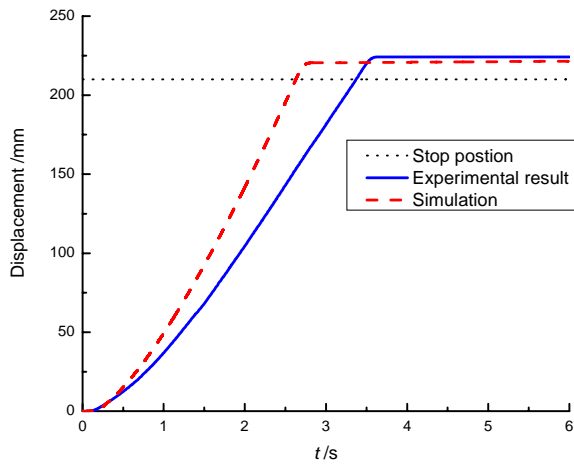
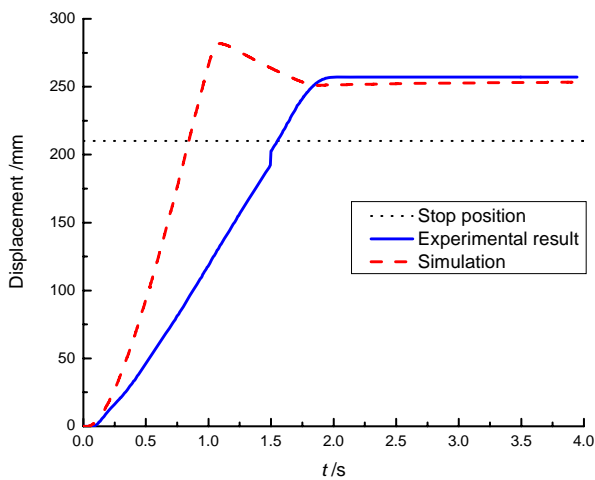


Fig.5 Experimental system of simple cylinder halfway stop system

Fig.6-a (for the system of MB32-400, exhausted-center, meter-out, load=30kg and $p_s=0.5\text{MPa}$) and Fig.6-b (for the system of MB32-400, closed-center, meter-in, load=30kg and $p_s=0.5\text{MPa}$) show the comparison between the simulation and experiment results.



(a) System of MB32-400, exhausted-center, meter-out, load=30kg and $p_s=0.5\text{MPa}$



(b) System of MB32-400, closed-center, meter-out, load=30kg and $p_s=0.5\text{MPa}$

Fig.6 Comparison between simulation and the experimental result

Some possible reasons result in the difference between the simulation and the experiment.

- 1) The air supply of experiments is not stable. Due to the dynamic response of the regulator, the flow of air supply can not satisfy the ideal supply as the modeling. So, the response of experimental result is slower than that of the simulation.

- 2) The friction model of cylinder in the simulation may not be accurate.
- 3) The valve response has obvious influence on the over-shoot.
- 4) The hypotheses in the simulation ignore the internal leakage of the cylinder and the valve and neglect the thermodynamic exchange.

These factors will be deeply studied in the future research work to make the simulation more accurate. Our final destination is to provide actual over-shoot of every halfway stop system by our simulation software when engineers design this kind of system.

CONCLUSION

Modeling and simulation of simple cylinder halfway stop system are completed. Over-shoot of the piston is achieved by simulation. And factors taking effect on the over-shoot are also analyzed. Besides, experimental systems are set up to validate the simulation. The research lays foundation for the future software to provide the over-shoot in the designing phase for engineers.

REFERENCES

1. Jun WU. Pneumatic Project Handbook. Publishing Company of National Defense Industries.
2. Hanchao C., Yongcai S. Air Pressure Transmission and Control. Publishing Company of Beijing Industry Institute.1987, 6.
3. Raparelli T, Manuello B A, Mazza L. Experimental and numerical study of friction in an elastomeric seal for pneumatic cylinders. Tribology International Volume. 1997, 30(7), pp. 547-522.
4. KOSAKIT, Manabu S. An Analytical and Experimental Study of Chaotic Oscillation in a Pneumatic Cylinder. Proc.of 1st. FPNI-PhD Symp. Hamburg 2000, pp. 303-310.
5. Haotao L., Ying D. MATLAB Procedure Design Tutorial Publishing Company of High Education.2002, 8.
6. SMC Pneumatic Components Manual (The Third Edition), SMC Corporation, 1999.
7. Baihai Z. Application of Dummy Instrument in Pneumatic Component and System Test. Machine Tool and Hydraulic, 2002,3, pp.169-172.

Calculation of Flow Field of Diffused Pneumatic Silencer

Zhang Xi-wen Zhang Yan Li Heng He Feng

SMC-Tsinghua University Pneumatic Technology Center
School of Aerospace, Tsinghua University, 100084, Beijing, China
(E-mail: zhangxiw@tsinghua.edu.cn)

ABSTRACT

Diffused pneumatic silencer has been widely used in pneumatic fields because of its small dimensions and high performance on noise reduction. Numerical simulation of its interior and exterior flow field is important to studying the gas flow in the silencer and the flow structure outside the silencer, understanding the mechanism of its noise reduction. Porous media model and Darcy-Forchheimer principle are used as the basic theoretical frame in this paper. The unified governing equations are used to describe the compressible flow in and out of the silencer. Robust numerical scheme is used to discretize the equations and the TDBC(Time-dependent boundary conditions) is used to treat the non-reflect boundaries. The detailed structures of the inner and outer flow field of the diffused pneumatic silencer are gotten. The results of the simulation display the characteristics of the flow in the silencer. And the structure of the flow outside the silencer that can be compared with the experimental data is gotten.

KEY WORDS

Diffused pneumatic silencer, Numerical simulation, Flow field

INTRODUCTION

Pneumatic technology is widely applied in many fields of industrial production, but its application brings exhaust noise, which contaminates circumstance, disservices health, and reduces efficiency of production. Diffused pneumatic silencer is widely used in pneumatic fields because of its small dimensions and high performance on noise reduction. Numerical simulation of its interior and exterior flow field is significant for the study of the gas flow in the silencer and the flow structure outside the silencer, understanding the mechanism of its noise reduction, optimum design of the structure of the silencer.

Porous anechoic material is the main component in a diffused pneumatic silencer, and the gas flow through the porous media is compressible gas flow in which pressure, density and velocity change conspicuously. As a result, the flow field in diffused pneumatic silencer is so difficult that few numerical investigations have been made so far.

There are two kinds of conventional numerical methods which simulate the flow in the district where porous materials and pure fluid couple: one uses Darcy or Forchheimer equations and slip boundary conditions, and the other uses Brinkman or Brinkman-Forchheimer equations^[1]. However, the governing equations in these

methods aim at special flow problems, so the scope to use them is limited. In addition, there is no uniform method to choose governing equations, that is, governing equations are chosen empirically.

The numerical simulation method basing on porous media model was initially used to simulate the flow and heat exchange in nuclear reactors and exchangers. There are many pipes and flakes in a exchanger, so a great number of meshes are needed to simulate the flow in detail. Patankar and Spalding^[2] (1974) gave out a method which adopts distributive resistance, it was called porous media model method. In this method, the influence of solid structure (pipes in a exchanger) on mass is reflected with porosity and surface permeability, the influence on momentum is reflected with distributive resistance; the influence on energy is reflected with distributive heat source, then the flow can be simulated with sparser meshes. Using this method, Sha^[3] simulated the flow in a

vapor generator and core of a nuclear reactor, Karayannis and Markatos^[4] simulated the flow in a exchanger, Prithiviraj and Andrews^{[5][6]} simulated the flow in a three-dimensional exchanger.

In this paper, porous media model is adopted, compressible gas flow in and outside a diffused pneumatic silencer is described with uniform and modified N-S equations, and the source terms in equations are determined with Darcy-Forcheimer law. Equations are discretized by using NND format which has good stability and high accuracy, no-reflect boundary conditions are dealt with by using time-dependent boundary conditions. Numerical simulation on the flow field in and outside a diffused pneumatic silencer is made, inner and external flow fields of a diffused pneumatic silencer are got, and the results of numerical simulation on external flow field can be compared with experiment.

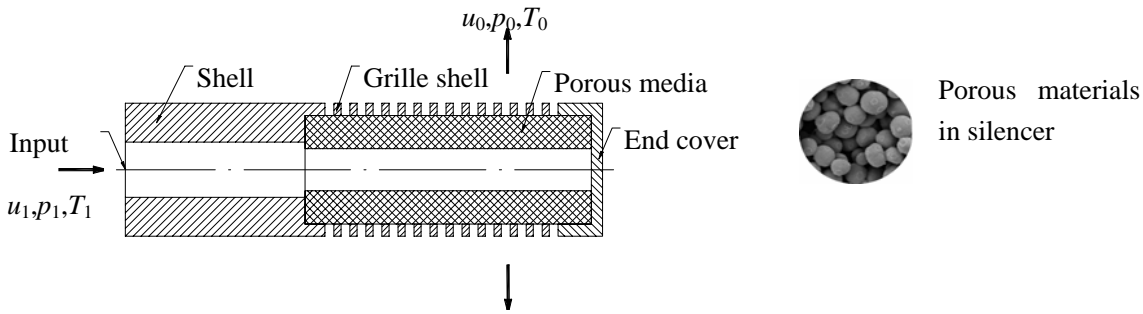


Figure 1. Structure of a diffused pneumatic silencer

DIFFUSED PNEUMATIC SILENCER

A diffused pneumatic silencer is composed of three parts: a silencer shell, porous materials and a end-cover. Its structure can be seen in figure 1.

PHYSICAL MODEL

In figure 1, high pressure gas which has the temperature of T_1 , density of ρ_1 , pressure of p_1 goes through a silencer at the axial velocity of u_1 , because of the resistance of the end cover, the gas will effuse in the radial direction, and the velocity turns to u_0 , pressure turns to p_0 , density turns to ρ_0 , temperature turns to T_0 . This is the compressible axis-symmetrical flow which goes through a zone coupling porous media and pure fluid.

EXPERIMENT PARAMETERS

Experiment about the gas flowing in a silencer was performed, the purpose was to provide necessary parameters for numerical simulation and validate the result of numerical simulation. The velocity of the gas flowing into a silencer is 65.1m/s, and the pressure is 1.6602×10^5 Pa, the gas pressure turns to 1.013×10^5 Pa after effusing the silencer, the temperature is 298K, porosity of porous materials is 0.86, permeability K is $1.21 \times 10^{-11} \text{m}^2$, and the inertia coefficient C_F is $0.91 \times 10^5 \text{m}^{-1}$.

GOVERNING EQUATIONS

N-S equation for integral unsteady axis-symmetrical compressible fluid is shown below^[7]

$$\frac{\partial}{\partial t} \iiint_V \rho dV + \iint_S \bar{n} \cdot \bar{A} dS + \iiint_V \frac{S}{r} dV = 0 \quad (1)$$

where \underline{Q} is a variable to be resolved, $\underline{\bar{A}} = (\underline{E} - \underline{E}_v)\underline{\bar{e}}_x + (\underline{F} - \underline{F}_v)\underline{\bar{e}}_r$, \underline{E} and \underline{F} are non-viscous fluxes in the directions of x and r respectively, \underline{E}_v and \underline{F}_v are viscous fluxes in the directions of x and r respectively, \underline{S} is the source term in the axis-symmetrical N-S equation.

According to the porous media model [2], modified N-S equation for unsteady axis-symmetrical compressible flow in porous media can be gotten from (1)

$$\frac{\partial}{\partial t} \iiint_V a_v \underline{Q} dV + \iint_S a_n \bar{n} \cdot \bar{A} dS + \iiint_V a_v \frac{\underline{S}}{r} dV + \iiint_V a_v \frac{\underline{S}_{por}}{r} dV = 0 \quad (2)$$

where a_v is volume porosity, a_n is surface permeability in the direction of \bar{n} . \bar{A} , \underline{Q} and \underline{S} have the same definitions as in (1). \underline{S}_{por} is the source term of distributive resistance in the porous media and heat source. When $a_v = a_n = 1$, $\underline{S}_{por} = 0$, (2) will be (1), which is normal N-S equation. Source term \underline{S}_{por} is shown below, distributive resistances R_x and R_r , heat source \underline{Q}_{rb} is relative to investigated flow.

$$\underline{S}_{por} = \begin{pmatrix} 0 \\ R_x \\ R_r \\ \underline{Q}_{rb} \end{pmatrix} \quad (3)$$

Perform the coordinate transformation below on equation (2)

$$\begin{cases} \xi = \xi(x, r) \\ \eta = \eta(x, r) \end{cases} \quad (4)$$

then the physical plane can be transformed to computational plane, resolve the equation on computational plane, detailed formulations for coordinate transformation, fluxes and the source term can be found in reference [7].

IDENTIFICATION OF SOURCE TERM

To simulate the flow in porous media correctly, the source term \underline{S}_{por} must be identified appropriately. The flow in porous media is very complex, the flow characteristics are different along with the variety of flow status, so the source term should be relative to the flow status of the simulated flow. To identify the expression of source term, the flow status should be known first. Hitherto most researchers regard the Reynolds Number based on aperture (Re_p) [8] and the Reynolds Number based on permeability (Re_K) [9] as the criterion of flow status. Usually, when $Re_K < 1$, the

flow is normal Darcy flow, that is, there is linear relation between pressure gradient and velocity. When $1 < Re_K < 10$, the flow is not Darcy flow, the linear relation between pressure gradient and velocity is not tenable, Forcheimer modification to flow equation is needed, but the flow is still laminar flow [9], this kind of flow is the so-called Darcy-Forcheimer flow. Along with the increase of velocity, the flow in porous media will turn to turbulent flow. How to differentiate the turbulent flow in porous media has been a problem in the research domain, there is not a definite criterion so far. Seguin's recent experiment [10][11] indicated that the laminar flow in porous media can maintain until $Re_p < 150 - 200$, when Re_p is larger than a given value, flow will turn to turbulent flow, the given value is relative to the structure of porous media, usually it is above 300. Equation (2) can simulate all kind of flows in porous media, when simulating laminar flow, only the expression of source term need to be identified; when simulating turbulent flow, it is necessary to introduce appropriate turbulence model and corresponding governing equations. There is only study on numerical simulation for laminar flow in this paper.

Steady Darcy-Forcheimer flow in porous media complies with Darcy-Forcheimer law [12] below:

$$\nabla p = -\frac{\mu}{K} \bar{V} - C_F \rho_f |\bar{V}| \bar{V} \quad (5)$$

where K is permeability, C_F is Forcheimer inertia resistance coefficient, ρ_f is the density of fluid, \bar{V} is Darcy velocity, μ is the dynamic viscous coefficient, $|\bar{V}|$ is the modulus of velocity, $|\bar{V}| = \sqrt{u_x^2 + u_r^2}$.

The relation between Darcy velocity \bar{V} and fluid velocity \bar{u} is:

$$\bar{V} = a_v \bar{u} \quad (6)$$

then the expression (5) can be written as

$$\nabla p = -\frac{\mu}{K} a_v \bar{u} - C_F \rho_f a_v^2 |\bar{u}| \bar{u} \quad (7)$$

In porous media model, distributive resistances [2] are identified with the expression below

$$\nabla p + \begin{pmatrix} R_x \\ R_r \end{pmatrix} = 0 \quad (8)$$

Comparing (7) with (8), expressions of distributive resistances can be given out below.

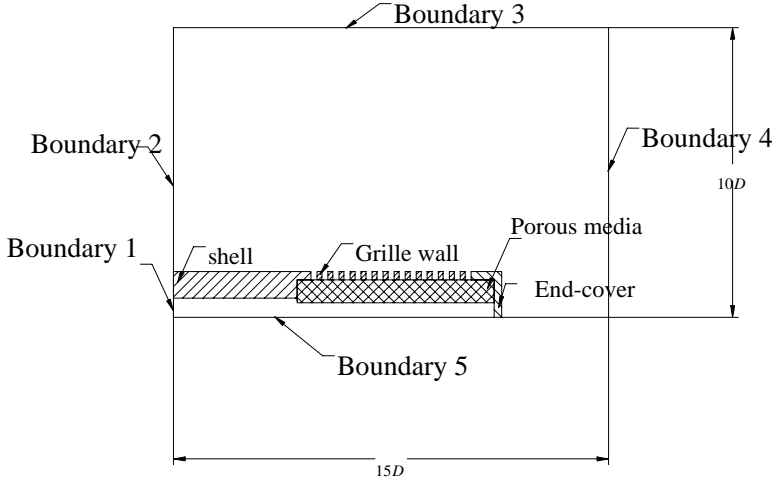


Figure 2. Computational zone

$$R_x = \frac{\mu}{K} a_v u_x + C_F \rho_f a_v^2 |\bar{u}| u_x$$

$$R_r = \frac{\mu}{K} a_v u_r + C_F \rho_f a_v^2 |\bar{u}| u_r \quad (9)$$

For the flow in porous media without heat source, $Q_{rb}=0$.

For Darcy flow in porous media, set C_F in the expressions of distribute resistances in (9) to 0, porosity and inertia coefficient in (9) are determined in experiment.

NUMERICAL METHOD

Finite volume method was adopted to resolve equation (2). After the coordinate transformation, the equation was discretized on structural meshes. The viscous flux terms of the governing equations are computed by second-order central difference scheme and the non-viscous flux terms are discretized by the second order NND scheme^[13]. The NND scheme belongs to TVD up-wind scheme, it has good stability and artificial viscosity is not needed in calculations. After spatial discretization, equations are integrated by the TVD type 3-stage Runge-Kutta scheme^[14], which has third-order accuracy and its effectiveness is well proven in the calculation of time dependent problems.

COMPUTATIONAL ZONE AND GRID

As shown in figure 2, computational zone comprises inner zone, porous materials zone and external zone, although two solid zones, silencer shell and end cover are in computational zone, they are not calculated during computation. The computational zone has an axial length of 15D and a radial width of 10D, D is the inner radius of

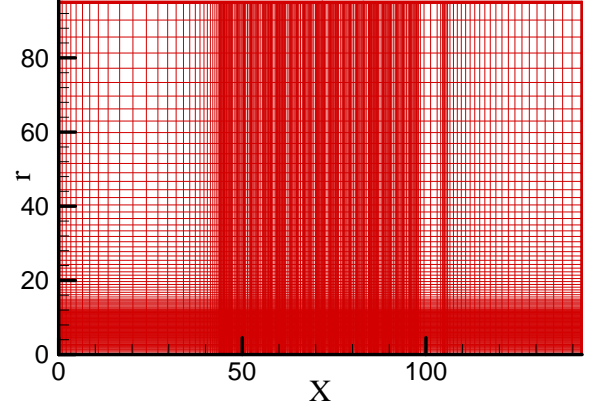


Figure 3. Computational grid

anechoic materials. Grid networks of 302(x)×121(y) were chosen to use, as shown in figure 3.

BOUNDARY CONDITIONS

There are five kinds of boundaries in computational zone: subsonic inflow boundary, subsonic outflow boundary, axisymmetric boundary, far-field non-reflecting boundary and adiabatic non-slip wall boundary condition. Time dependent boundary conditions (TDBC) which was given by Thompson and Lele were used to deal with far-field non-reflecting boundary, details can be found in references[15] [16] [17]. Five kinds of boundaries are shown in figure 2.

Boundary 1 is subsonic inflow boundary, subsonic inflow conditions are given, including temperature, axial velocity, and radial velocity.

Boundary 2 and 4 are far-field non-reflecting boundaries, far-field non-reflecting boundary conditions are given.

Boundary 3 is subsonic outflow boundary, subsonic outflow condition is given, which is outflow pressure.

Boundary 5 is axisymmetric boundary, axis-symmetrical conditions are given, that is, set radial velocity to be 0; for other parameters, their one-step differential coefficient in the direction of r are set to be 0 as well.

Surfaces on the solid structures in computational zone are given adiabatic wall boundary conditions, that is,

$$\text{set axial and radial velocities to be 0, and } \frac{\partial T}{\partial n} = 0.$$

TURBULENCE MODEL

The flows studied in this paper comprise three flow domains: flow in the silencer, flow in anechoic materials, and flow outside the silencer. Flow in the silencer has

high velocity and large Re , so it belongs to turbulent flow. Flow in anechoic materials has low velocity ($<10\text{m/s}$), and $Re_p < 30$, $Re_k > 2$, according to the criterion^{[8][9][10][11]}, the flow belongs to no-Darcy laminar flow in porous materials. Flow outside the silencer is considered to be turbulent flow, too. In this paper, RNG $k-\varepsilon$ turbulence model^{[18][19]} given by Yokhot and Orszag is used to deal with turbulent flow.

NUMERICAL RESULTS AND DISCUSSION

Pressure and velocity distributions on the axis in silencer are shown in figure 4 and figure 5, respectively. As shown in these figures, pressure and velocity are constant in the entrance section (domain enclosed by shell), after entering domain enclosed by porous materials, because the flow section reduces, velocity increases and pressure decreases. Gas in silencer is blocked by the end cover, so it effuses through anechoic materials in the radial direction, as a result, axial velocity decreases gradually and pressure increase meantime. In the domain outside the silencer, axial velocity was reduced to be 0, pressure turns to be atmospheric pressure. It can be seen that the pressure and velocity in the silencer are non-uniform.

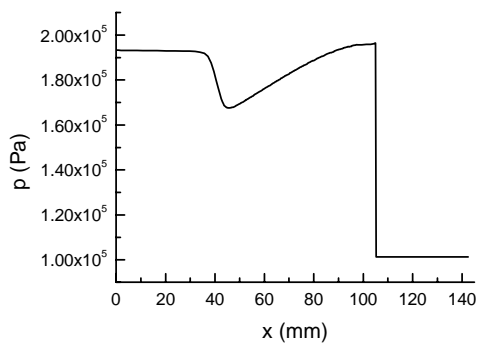


Figure 4. Pressure distribution on the axis

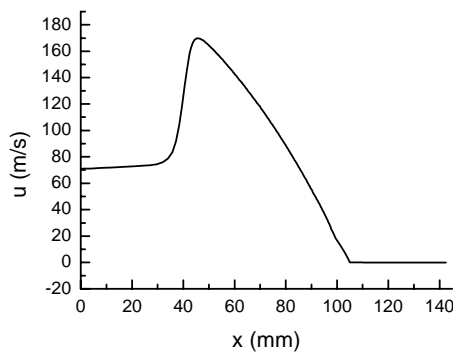


Figure 5. Axial velocity distribution on the axis

Flow fields distribution outside the silencer are shown in figure 6, 7, 8, which denote the distributions of radial velocity at three positions, which has a distance of 1mm, 3mm and 5mm from the out surface of anechoic materials. In these figures, velocity outside the silencer is very non-uniform, compare the experimental result with the result of numerical simulation, it can be seen that numerical simulation describes the flow field well.

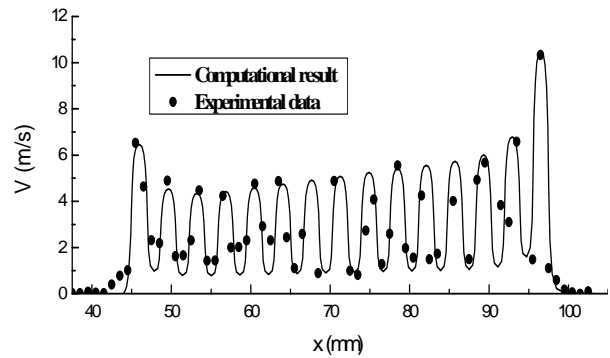


Figure 6. Radial velocity distribution (1mm from the surface of anechoic materials)

In addition, the characteristics of the flow field outside the silencer are: velocities of gas beside the silencer's two ends are higher than those in the middle of the silencer, and the velocities in the middle increase from left to right (figure 6). The flow field has the special structure due to the pressure distribution of the flow in the silencer. Radial velocity distribution on inner surface of anechoic materials is nearly uniform, it is shown in figure 10. There are a pressure drop and a minus radial velocity of large magnitude in figure 9 due to the contractibility of inflow area section. If presume that porosity and permeability of the porous materials are constant, there should be high outflow velocity at the position where pressure in anechoic materials is high, shown in figure 10.

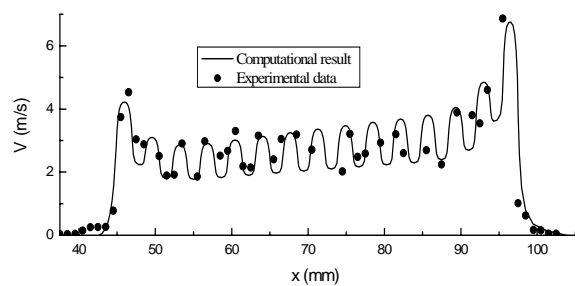


Figure 7. Radial velocity distribution (3mm from the surface of porous media)

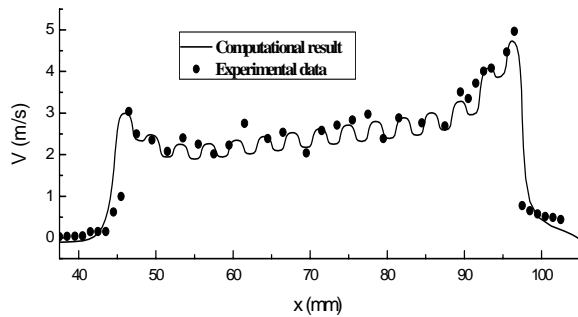


Figure 8. Radial velocity distribution
(5mm from the surface of porous media)

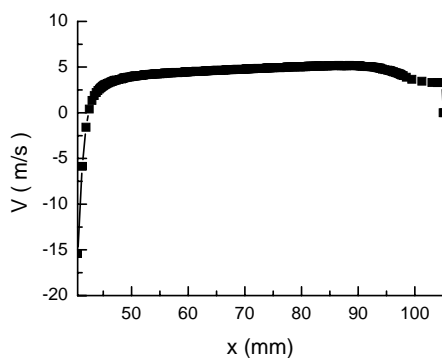


Figure 9. Radial velocity distribution (inner surface)

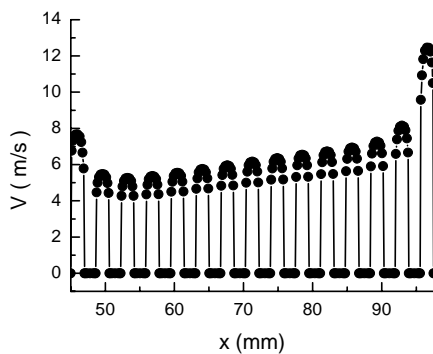


Figure 10. Radial velocity distribution
(external surface)

CONCLUSIONS

(1) With the use of porous media model, modified N-S equations, time-dependent boundary conditions(TDBC) for non-reflecting boundary, and NND schemes are adopted to numerically simulate the inner and external flow fields of a diffused pneumatic silencer, results of numerical simulation agrees well with experimental results.

(2) Results of simulation disclosed the characteristics of inner flow field and the distribution of external velocity of the silencer.

(3) Outflow velocity distribution is special non-uniform, it is determined by pressure distribution in the silencer. Inner pressure distribution and outflow velocity distribution can be improved by improving the structure of the silencer, such as modifying inner area section, reducing the area of shell and end-cover which cover anechoic porous materials. Velocity distribution's change can observably affect the noise elimination of a silencer.

REFERENCES

1. Li Heng, Zhang Xiwen, Journal of the University of Petroleum. 2000, 24(5):111-116 (in Chinese)
2. Patankar S.V., Spalding D.B., Heat exchangers: Design and Theory Source Book, McGraw-Hill, New-York, 1974,155-176.
3. Sha W.T., Yang C.I., Kao T.T. J.Heat Transfer,1982,104:417-425
4. Karayannis N. and.Markatos N.C.G, Proceedings of the 10 th International Heat Transfer Conference, Brighton, UK,The Industrial Sessions Papers,1984:13-18
5. Prithiviraj M., Numerical Heat Transfer Part A-Applications, 1998,33(8):799-816
6. Prithiviraj M., Andrews M.J., Numerical Heat Transfer Part A-Applications, 1998,33(8):817-828
7. Guo Yanhu, Ph. D Dissertation in Tsinghua University ,1996(in Chinese)
8. Marcos H.J.Pedras, Marcelo J.S. de Lemos, Int.Comm.Heat Mass Transfer, 2000,27(2):211-220
9. Nield D. A., Bejan A., Convection in Porous Media, New York, Springer-Velag Inc.,1999
10. Seguin D., Montillet A., Comiti J., Chemical Engineering Science, 1998,53(21):3751-3761
11. Seguin D., Montillet A., Comiti J., Chemical Engineering Science, 1998,53(22):3897-3909
12. Forchheimer P., Hydraulik(3rd ed.), Leipzig, Berlin: Teubner,1930
13. Zhang HX, Zhuang FG. Advances in Applied Mechanics, 1992, 29:143-165
14. Chi-Wang Shu., SIAM Journal on Scientific & Statistical Computing, 1988, 9:1073-1084
- 15.Thompson K.W. J Comput Phys, 1990, 89: 439-461.
16. Poinot T.J., J Comput Phys, 1992, 101: 104-129.
18. Yakhot V., Orszag S.A.. J Sci Comput, 1986, 1: 39-51.
19. Yakhot V., Orszag et al. Phys Fluids, Ser. A, 1992, 4 (7): 1510-1522.
20. Patankar S.V., Sparrow E.M., Ivanovic M. Int. J. Heat Mass Transfer, 1978, 24: 269-274.

USING INVERSE MODELS FOR DETERMINING ORIFICES MASS FLOW RATE CHARACTERISTICS

Rosario DE GIORGI*, Sylvie SESMAT* and Eric BIDEAUX*

*Laboratoire d'Automatique Industrielle, INSA de Lyon
25, avenue Jean Capelle, 69621 Villeurbanne, France
eric.bideaux@insa-lyon.fr

ABSTRACT

Information concerning the flow rate of pneumatic components is essential for both selecting the right component at the design stage and validating different performances of a circuit. Recently, new procedures based on the measurement of the transient response for the charge or the discharge of a tank have been proposed. These procedures are corresponding to an inverse approach that enables the mass flow rate in a component to be identified. The presented work investigates these new approaches and discusses the problem related to the use of inverse models. The heat transfer problem, which appears to be the main difficulty, is illustrated in order to analyze the relevancy of the thermal hypothesis.

KEYWORDS

Pneumatic, Inverse model, Heat exchange, Mass flow characteristic

NOMENCLATURE

Physical parameters

b	: critical pressure ratio	
C	: sonic conductance	[m ³ /s/Pa]
h	: specific enthalpy	[J/kg]
h_{conv}	: convection coefficient	[kg]
k	: polytropic index	
m	: mass	[kg]
P	: static pressure	[barA]
Q	: heat	[J]
$q_{h,out}$: outlet enthalpy flow rate	[W]
$q_{m,out}$: outlet mass flow rate	[kg/s]
S	: surface of thermal exchange	[m ²]
t	: time	[s]
T	: static temperature	[K]
U	: internal energy	[J/kg]
V	: volume of the tank	[m ³]
ρ	: density	[kg/m ³]

Physical constants

c_v	: specific heat at constant volume
r	: gas constant = 287J/(kgK)
γ	: ratio of specific heat = 1.4

Index and indices

0	: starting time of discharge
i	: generic time of discharge
r	: reference value
u	: upstream
d	: downstream
V	: tank
W	: wall of the tank
∞	: infinite time

Although the mass flow rate characteristic of a pneumatic component has to be as accurate as possible for modeling purposes, only a reference associated to a specific procedure has to be defined in order to compare several components and to make a selection for design purposes. The difficulty in the case of the pneumatic technology relies on the lack of theoretical models allowing a simple and accurate characterization of the flow rate to be used both for modeling purposes and classification of components.

The ISO6358 standard [1] is based on a mathematical approximation of the mass flow rate characteristic and describes the experimental conditions and the bench assembly in the case of a constant section orifice. This mathematical approximation of the mass flow rate is a function of the pressure ratio and of the upstream pressure and temperature (1). Although the use of this standard is restricted to the characterization of single orifices, it proposes an approach that is usable both for modeling purposes and classification of components. However, the time and the need of an expensive equipment required to achieve the measurement using the 6358 standard are the main drawbacks for its extension in an industrial context.

$$\begin{cases} q_m = C\rho_0\sqrt{\frac{T_r}{T_u}}P_u \cdot \sqrt{1 - \frac{P_d - b}{P_u - b}} & \text{if } \frac{P_d}{P_u} \geq b \\ q_m = C\rho_0\sqrt{\frac{T_r}{T_u}}P_u & \text{if } \frac{P_d}{P_u} < b \end{cases} \quad (1)$$

Recently, some other procedures based on the measurement of the transient response for the charge or the discharge of a tank have been proposed. Kagawa et al. [2, 3], Benchabane et al. [4] and Kuroshita et al. [5] have proposed such methods [6, 7] to identify the sonic conductance C and the critical pressure ratio b , the mass flow rate being obtained from the pressure response using an approximation of the solution of the tank state equation. These last procedures are corresponding to an inverse approach for identifying the mass flow rate in a component. Although it allows the experimental procedure to be shortened, the accuracy of the results are strongly related to the parameters of the experimental rig.

The presented work investigates one type of these new approaches, the discharge of a tank, and discusses the problem related to the use of inverse models in the case of identification problems.

The heat transfer problem, which appears to be the main difficulty when an inverse approach is used, is here illustrated in order to analyze the relevance of the thermal hypothesis (heat exchange, polytropic model). Although the isothermal chamber technique introduced by Kagawa [2] is an interesting but costly solution for solving the heat transfer problem, it is shown in this paper that any type of tank may be used if the heat

transfer phenomena has correctly been identified. The results show the requirement of a precise model in order to reach the adequate accuracy needed for the extension of this approach to an usable orifice characterization procedure.

2 THERMODYNAMICAL MODEL OF A PNEUMATIC CHAMBER

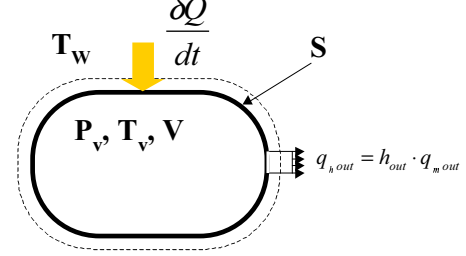


Figure 1: Pneumatic chamber

Considering the discharge of a tank (Figure 1), if the chamber volume is large enough, the kinetic energy of the fluid in the chamber can be neglected. The mass conservation law and the internal energy conservation law (2) enable the complete description of the dynamic behavior of the gas in the chamber. Considering the heat exchanged with the environment, without any mechanical work, the first law of the thermodynamics can be applied to this opened system.

$$\begin{cases} \frac{dm}{dt} = -q_{m,out} \\ \frac{dU}{dt} = -q_{h,out} + \frac{\delta Q}{dt} \end{cases} \quad (2)$$

With the hypothesis of a perfect gas, and assuming that, at any time, the pressure P_V , the temperature T_V and the density ρ_V of the gas are uniform in the chamber and equal to their mean value according to space, the state model of the system can be described by the following system of differential equations (4) using pressure and temperature in the volume as new state variables (3).

$$\begin{cases} P = \frac{r}{c_v V} \cdot U \\ T = \frac{1}{mc_v} \cdot U \end{cases} \quad (3)$$

$$\begin{cases} \frac{dP_V}{dt} = -\frac{r\gamma T_V}{V} \cdot q_{m,out} + \frac{\gamma - 1}{V} \cdot \frac{\delta Q}{dt} \\ \frac{dT_V}{dt} = \frac{(\gamma - 1)T_V}{P_V V} \left(-rT_V q_{m,out} + \frac{\delta Q}{dt} \right) \end{cases} \quad (4)$$

3 INVERSE MODEL

If we consider the complete discharge of a tank through an orifice (Figure 2), according to the ISO6358

standard [1], the determination of the mass flow rate characteristics of the orifice (critical pressure ratio b and sonic conductance C) requires the measurement of the mass flow rate through the orifice, the upstream and downstream pressures, and the upstream temperature. Assuming that the transient flow is negligible compared to the main flow, the mass flow rate passing through the orifice is equal, at any time, to the mass flow out from the tank.

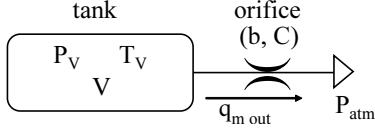


Figure 2: Scheme of a tank discharge through an orifice

Considering the previous system equation (4), and assuming that the pressure and temperature are known at any time, the determination of the output mass flow rate corresponds to an inverse problem. There are 2 equations and 2 unknown variables : the mass flow rate and the heat exchanged. The inverse model (5) shows that the pressure P_V and the temperature T_V have to be once differentiated. As P_V and T_V are obtained from measurements, a noise reduction procedure can be required.

$$\begin{cases} \frac{\delta Q}{dt} = \frac{\gamma V P_V}{(\gamma - 1) T_V} \cdot \frac{dT_V}{dt} - V \cdot \frac{dP_V}{dt} \\ q_{m,out} = -\frac{V}{r T_V} \cdot \frac{dP_V}{dt} + \frac{V P_V}{r T_V^2} \cdot \frac{dT_V}{dt} \end{cases} \quad (5)$$

4 EXPERIMENTAL RESULTS

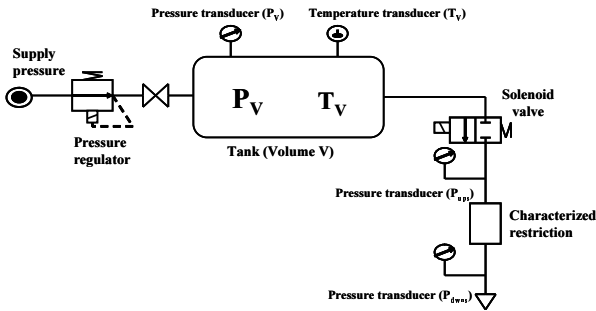


Figure 3: Experimental rig for the discharge method

In order to show a validation of this inverse methodology, the discharge of a standard steel tank (45 liters) through a 135° bend fitting (5 mm internal diameter) was realized (Figure 3). The initial pressure in the tank is imposed by the pressure regulator. When the initial pressure and temperature are stabilized in the tank, the solenoid valve is opened to start the complete discharge. Both pressure and temperature are measured in the tank, and additional pressure transducers enable the fitting upstream and downstream pressures to be recorded.

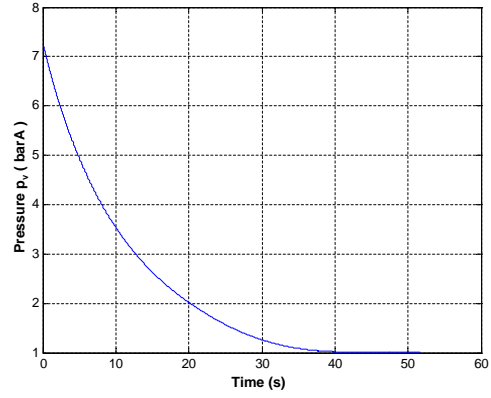


Figure 4: Measured pressure during the discharging process

The temperature was also indirectly measured using the 'stop method' described by Kawashima [3]. The procedure consists in several partial discharges always starting from the same initial conditions (P_V^0 and T_V^0), which have to be the initial conditions of the complete discharge test. When the pressure in the tank reaches the value P_V^i , the discharge is interrupted by closing the solenoid valve, and the pressure P_V^∞ and the temperature T_V^∞ are measured. The mass of the gas in the tank being constant, it is possible to accurately calculate the temperature at which the discharge is stopped using the Charles law (6). Kawashima [3] has estimated that the error of this method is less than 0,3K.

$$T_V^i = T_V^\infty \cdot P_V^i / P_V^\infty \quad (6)$$

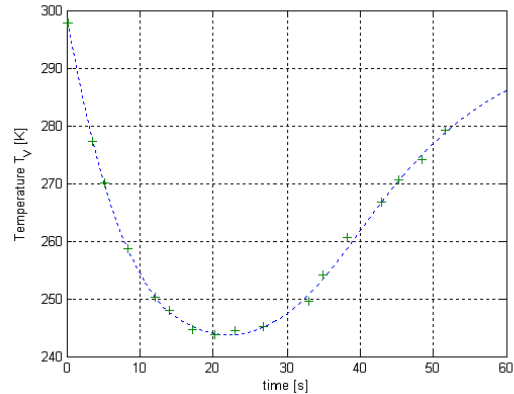


Figure 5: Measured temperature of the tank using the 'stop method' and its approximation

Figure 4 shows the measured pressure during the discharge test from 7 bars to the atmospheric pressure. Figure 5 gives the measured temperature using the stop method and the polynomial approximation, which has been introduced to solve the inverse problem. Using the inverse model (5), the instantaneous mass flow rate and

heat exchanged (Figure 7) can be computed from these data and their derivative. In this ideal case (Figure 2), computing the output mass flow rate and measuring the instantaneous pressure and temperature in the tank, enable the mass flow rate characteristic of the orifice through which the tank discharges to be determined (Figure 6), and the sonic conductance and the critical pressure ratio to be identified [1].

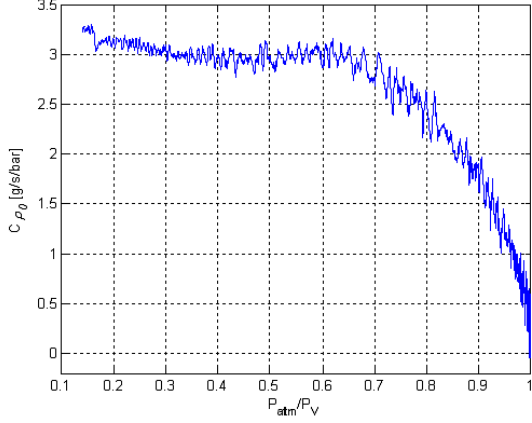


Figure 6: Mass flow rate characteristic $\frac{q_{m,out}}{P_V} \cdot \sqrt{\frac{T_V}{T_0}}$ as a function of the pressure ratio $\frac{P_{atm}}{P_V}$

5 HEAT EXCHANGE ANALYSIS

The thermal power exchanged during the discharge is now studied in order to verify if a polytropic law could describe pressure and temperature in the tank during this process, before developing a discussion on the use of a convection law.

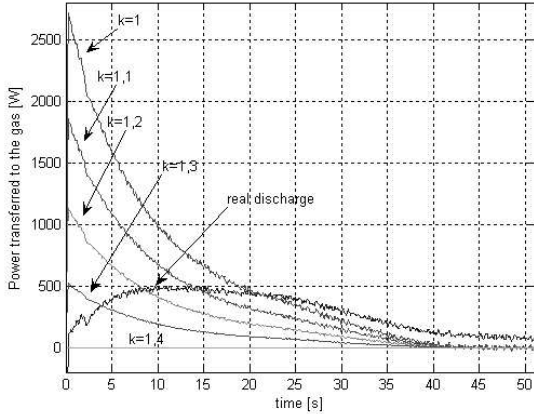


Figure 7: Evolution of thermal exchanged power

The heat exchanged computed from the inverse model (5) can be compared to the heat exchanged in the case of a polytropic evolution of the gas (7) considering different polytropic coefficient k but the same evolution of pressure in the tank. Using (4) in (7), the thermal power exchanged, considering a polytropic model to

describe the discharge, is given by (8).

$$(1 - k) \cdot \frac{dp}{P} + k \cdot \frac{dT}{T} = 0 \quad (7)$$

$$\frac{\delta Q}{dt} = -\frac{(\gamma - k)}{k(\gamma - 1)} \cdot V \frac{dP_V}{dt} \quad (8)$$

According to equation (2) the exchanged power is considered positive when it is transferred from the environment to the gas. Figure 7 shows that the heat transfer reaches a maximum at the discharge half time, and though, that a polytropic law can not properly describe the heat transfer during the discharging process of the tank. However, figure 7 shows clearly the importance of the heat transfer during the discharge, and the need of a proper thermal exchange model in order to implement the discharge method using a standard tank.

Yingzi [8] and Benchabane [4] have also determined the polytropic index according to time in the case of a tank discharge. Considering a global polytropic transformation between the initial time t_0 and the time t and using equation (9), figure 8 confirms obviously the results of the previous works showing a large variation of the polytropic index during the discharge going from nearly an adiabatic process to an isothermal one.

$$k_{t_0}(t) = \frac{1}{1 - \frac{\ln(\frac{T_V}{T_V^0})}{\ln(\frac{P_V}{P_V^0})}} \quad (9)$$

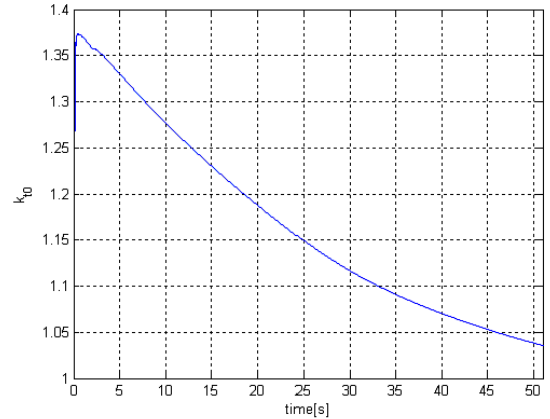


Figure 8: Polytropic index according to time calculated from initial conditions P_V^0, T_V^0

It is thus necessary to study more precisely the heat exchanges taking place between the gas in the tank and the environment. Classical hypotheses used in pneumatic chambers rely on the assumption that the thermal conductivity and the heat capacity of the wall material are sufficiently large compared to those of air, the wall temperature is therefore considered as a constant and the heat exchanged can be described

by a convection heat transfer model expressed by the Newton's Law using a convection coefficient h_{conv} .

$$\frac{\delta Q}{dt} = h_{conv} \cdot S \cdot (T_W - T_V) \quad (10)$$

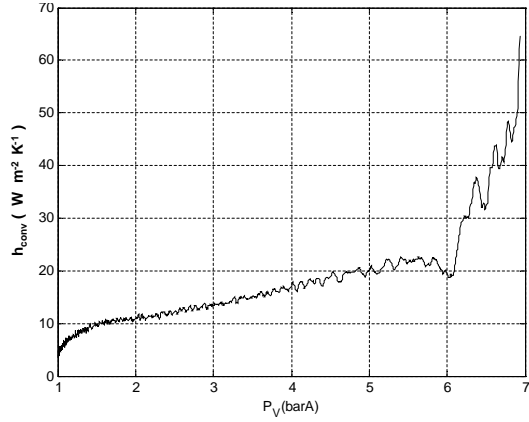


Figure 9: Convection coefficient vs tank pressure during the discharge process

Figure 9 confirms that the convection coefficient h_{conv} is not a constant, but is a function depending on the flow characteristics. Several models are used in the litterature. For example, Yingzi [8] has proposed a convection coefficient that varies from a reference value as a function of both relative pressure and mass flow rate. Det [9] has used a simplified Eichelberg's model [10] to calculate h_{conv} (11), where h_{conv}^r is the convection coefficient corresponding to the reference pressure P_V^r and temperature T_V^r . Considering P_V^0 and T_V^0 as the reference pressure P_V^r and temperature T_V^r , Figure 10 shows that this model is still unable to give a correct evaluation of h_{conv} for the whole time range.

$$h_{conv} = h_{conv}^r \sqrt{\frac{P_V \cdot T_V^r}{P_V^r \cdot T_V}} \quad (11)$$

The previous results show clearly that the heat exchange phenomena is complex. Further works have to be carried on to overcome this problem both for simulation accuracy and proper orifice characterization; the isothermal discharge seems nowadays the best way to avoid this problem.

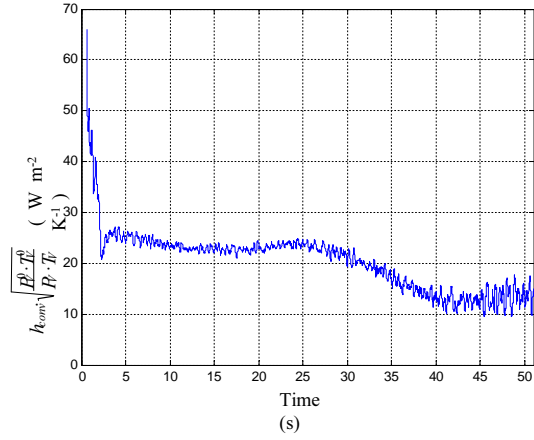


Figure 10: Variation of h from Eichelberg's simplified model

6 LIMITATION OF THE INVERSE APPROACH

The main limitation of the inverse methodology is the difficulty of the measure of the instantaneous temperature due to thermocouples time response. Different solutions have been proposed such as the 'stop method', but this method is time costly since each measured point of temperature requires the stabilisation of the pressure and of the temperature in the tank. This method is nevertheless interesting for the identification of the thermal hypothesis for a type of tank [2].

The NF E49-300 standard [7] is based on slow discharges (2 to 5 minutes) for which the time response of the thermocouple can be neglected. But it requires very large tanks. Moreover the thermocouple location in the tank [5] can be critical on which temperature is really measured.

Kagawa [2], and subsequently the japeese standard [6] avoid this problem by using an isothermal tank. But the difficulty is the implementation of this isothermal tank, its costs and its lifetime (conservation of its isothermal property in the time with the materials pollution).

A last solution that avoids the measure of the temperature, relies on either the knowledge of the heat exchanged for a given tank or the use of an accurate thermal exchange model. Then, according to our hypotheses, the inversion problem consists to solve a single non linear differential equation (12) that gives T_V and to use the output equation (13) for determining the mass flow rate $q_{m out}$:

$$\frac{dT_V}{dt} = \frac{(\gamma - 1)T_V}{\gamma P_V V} \left[V \cdot \frac{dP_V}{dt} + h_{conv} S (T_W - T_V) \right] \quad (12)$$

$$q_{m out} = -\frac{V}{\gamma r T_V} \cdot \frac{dP_V}{dt} + \frac{(\gamma - 1)}{\gamma r T_V} \cdot h_{conv} S (T_W - T_V) \quad (13)$$

Then it is possible to obtain the temperature and the output mass flow rate only from the tank pressure

measurement. At this state of our research, this methodology has to be validated in regard with:

- the existence or the identification of a correct model of the heat exchange term associated to a given tank, which has necessarily to take into account the variation of the convection coefficient,
- the repeatability and the precision of the procedure, firstly using the same experimental rig but realizing discharges from different initial pressures, and secondly testing with different types of orifices.

7 CONCLUSION

The proposed approach shows that it is possible to compare different components to each other using the discharge procedure with a normal tank. The only condition is that the heat exchanged model must be well-known. This requires a first precise study of the tank to be used. It has been done in our case by an indirect measure of the temperature using the stop method enabling the heat exchanges to be known by the resolution of the inverse model.

This study of the heat exchanges in the tank has shown the necessity of a better knowledge of them and thus the elaboration of other macroscopic models than the classically used polytropic ones.

The inverse methodology has to be extended to cases where it is not possible to make all the restrictions negligible compared to the orifice to be characterised. This could also avoid on one hand the oversizing of the experimental rig used for the discharge method, and on the other hand the design of specific equipments (fittings, pressure tubes,...).

REFERENCES

- [1] International Standard ISO 6358. *Pneumatic Fluid Power Components using Compressible Fluids - Determination of Flow-rate Characteristics*, 1989. 15p.
- [2] T. Kagawa, K. Kawashima, and T. Fujita. Effective area measurement method using isothermal chamber. *Hydraulics and Pneumatics*, Vol. 26(1):pp. 76–78, 1995.
- [3] K. Kawashima, T. Kagawa, and T. Fujita. Instantaneous flow rate measurement of ideal gases. *Transaction of ASME Journal of Dynamic Systems, Measurement and Control*, vol. 122:174–178, march 2000.
- [4] S. Benchabane, M. Bonis, and J.P. Lecerf. Economic measurement of iso pneumatic coefficients. In *11th Aachen Fluidtechnisches Kolloquium*, volume 3, pages 131–141, 1994.
- [5] K. Kuroshita, Y. Sekiguchi, K. Oshiki, and N. Oneyama. Development of new test method for flow-rate characteristics of pneumatic components. In *Power Transmission and Motion Control, PTMC'04*, pages pp. 243–256, Sept. 2004.
- [6] JIS B 8390. *Pneumatic Fluid Power Components using Compressible Fluids - Determination of Flow-rate Characteristics*, 2000.
- [7] NF49-300. *Transmissions pneumatiques - Méthode de caractérisation des coefficients de débit pneumatique par vidange de réservoir*, 2000. 22p.
- [8] J. Yingzy, L. Jun, and W. Zuwen. Study on the process of charging and discharging in pneumatic system. In *4th International Conference on Fluid Power Transmission and Control*, New Achievements and Ideals in Fluid Power Engineering ('97 ICFP), Hanzhzhou (China), Sept. 9-11 1997.
- [9] F. Det, S. Scavarda, and E. Richard. Simulated and experimental study of charging and discharging of a cylinder using an electropneumatic servovalve. *First JHPS Int.Symp. on Fluid Power, Tokyo*, pages 199–206, March 1989.
- [10] C. Eichelberg. Some new investigations of old combustion engine problems. *Engineering*, 148(27):463–466, 1939.

The Simulation of the Sampling Pipes and Sampling Holes Network with an Aspirating Smoke Detector

Linn CHENG*, Hua ZHOU* and Huayong YANG*

*The State Key Lab of Fluid Power Transmission and Control,
Zhejiang University,
38 Zheda Road, Hangzhou, 310027 China
(Email: linn_cheng1001@yahoo.com.cn)

ABSTRACT

Aspirating smoke detector uses aspirating fan to draw air from the protected area via a network of the sampling pipes and holes, analyses the air and generates warning signals when the concentration of the smoke in the air is over the limit. After the analysis from the view of hydrodynamics, the physical and mathematical models are established. By programming and calculating, the sampling holes' flow rate and the transport time in which the air is drawn from the sampling holes to the detector are got. If each sampling hole's flow rate is not balanceable or the longest calculated transport time exceed 120 seconds (according to NFPA 72), the diameters of the sampling holes are optimized. The calculated results are compared with the experiments, the errors are less than 10%. It is proved that the physical and mathematical models can be used practically.

KEY WORDS

Simulation, Network, Mathematical Model

NOMENCLATURE

p	:	the pressure
Q	:	the flow rate
v	:	the velocity
A	:	the area
μ	:	flow coefficient
λ	:	frictional resistance coefficient
ζ	:	local resistance coefficient

INTRODUCTION

In order to reduce the danger of fire, fire autoalarm is required on many occasions. Aspirating smoke detector is one kind of fire autoalarm and is invented in the 1970's in Australia. Aspirating smoke detector does not sense smoke, temperature, flame passively, but aspirate and sample smoke actively. This kind of detector can quickly and dynamically identify various polymer molecule and smoke particle in the air and can give an alarm duly.

Aspirating smoke detector is a system that uses an aspirating fan to draw air from the protected area via a network of the sampling pipes and sampling holes. It is

shown in figure 1. The sampled air is then passed through a high sensitivity precision detector that analyzes the air and generates warning signals when the concentration of the smoke in the air is over the limit. The network of the sampling pipes and sampling holes is the passage of the sampled air. Not only the air near the detector but also the air in the whole room which is high-speed or quiescent can be analyzed by the network.^[1,2]

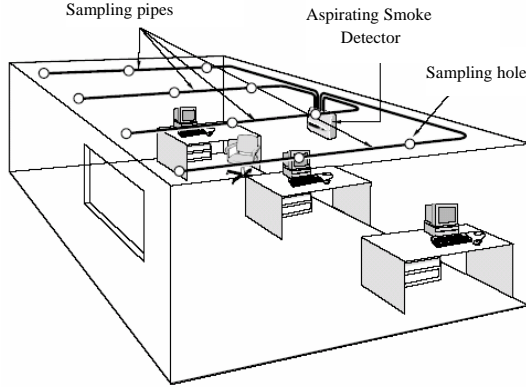


Figure 1 The sampling pipes and sampling holes network with an aspirating smoke detector

The network of the sampling pipes and sampling holes is regarded as the impedance of the aspirating smoke detector and we can analyze it from the point of view of hydrodynamics. The air flow rate percentage of every sampling hole can be got. Together with the characteristic curve of the aspirating smoke detector, the sampling holes' flow rate and the transport time in which the air is drawn from the sampling holes to the detector are got.^[3-5]

MATHEMATICAL MODELS

The sketch of the sampling pipe and sampling holes is shown in figure 2. Point '0' is a sampling hole in the end cap of the sampling pipe and it can make the sensitivity of every sampling hole nearly equivalent. Point '1', point '2' to point 'n-1' is sampling hole in the sampling pipe. Air is drawn to the detector through them. Point 'n' is the place where the sampling pipe connects to the detector. After the analysis of air's flow in the whole room and in the network of the sampling pipe and sampling holes, the physical and mathematical models are established based on the continuity equation and Bernoulli equation.



Figure 2 The sketch of the sampling pipe and sampling holes

For point '0', the equation is shown as:

$$0 = p_0 + \frac{\rho v_0^2}{2} + p_0' \quad (1)$$

p_0 is the pressure inside the sampling pipe at point '0', v_0 is the air velocity in the sampling pipe at point '0', ρ is air density, p_0' is the resistance at point '0'.

For the other sampling holes, the equation is shown as:

$$p_i + \frac{\rho v_i^2}{2} = p_{i+1} + \frac{\rho v_{i+1}^2}{2} + p_{li} \quad (2)$$

p_i is the pressure inside the sampling pipe at point 'i', and the differential pressure between the inside and outside of the sampling pipe is the reason why air can be drawn. p_{li} is:

$$p_{li} = \mu \cdot \frac{\rho}{2} \cdot \left(\frac{Q_i}{A_i}\right)^2 \quad (3)$$

where μ is flow coefficient, Q_i is the air flow rate in the sampling hole 'i', A_i is the area of the sampling hole 'i'. v_i is the air velocity in the sampling pipe at point 'i' and v_i is:

$$v_i = \frac{Q_{li}}{A_p} \quad (4)$$

where Q_{li} is the air flow rate inside the sampling pipe between the point 'i' and point 'i+1' and it is the sum of the air flow rate Q_0 , Q_1 , Q_2 to Q_i , A_p is the sectional area of the sampling pipe.

p_{li} is the resistance to air inside the sampling pipe between the point 'i' and point 'i+1' and consists of frictional resistance p_y and local resistance p_j .

$$p_y = \lambda \frac{l}{d_p} \frac{\rho v_i^2}{2} \quad (5)$$

$$p_j = \zeta \frac{\rho v_i^2}{2} \quad (6)$$

where λ is frictional resistance coefficient, l is the pipe length, d_p is the diameter of sampling pipe, ζ is local resistance coefficient.

From point 'n-1' to point 'n':

$$p_{n-1} = p_n + p_{in-1} \quad (7)$$

Provided that the flow rate of the sampling hole in the ending cap, Q_0 , is 1, the flow rates of the sampling holes in the sampling holes, Q_1 to Q_{n-1} , can be got by equation (1), equation (2) and equation (7). The flow rate percentage of each sampling hole can be got. Based on the theory of hydrodynamics, the characteristic equation of the whole network is:

$$\sum p = SQ^2 \quad (8)$$

where p is the whole resistance of the network, S is the impedance of the network and decided by the network, If the sampling holes and the sampling pipe in the network are the same S is the same. Q is the whole flow rate of the network.

When the detector is connected with the network and runs, the pressure which the detector provides will compensate the resistance of the network. And here the flow rate is the practical flow rate of the whole network and the detector. Combined the equation (8) with the actual characteristic curve of the detector, the flow rate is got. The actual characteristic curve of the detector is got by the experiment and is shown in figure 3.

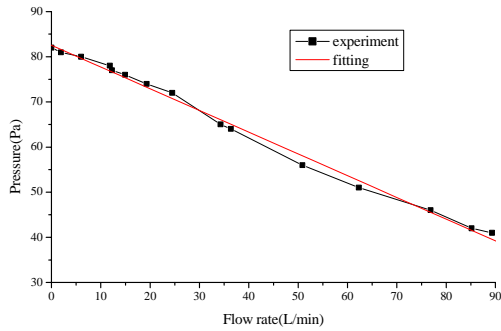


Figure 3 The actual characteristic curve of the detector

With the whole flow rate of the network, Q , and the flow rate percentage of each sampling hole, each sampling hole's flow rate, Q_i , can be got. And by equation (4), the air velocity in the sampling pipe can be got. The transport time in which the air is drawn from the sampling holes to the detector will be calculated.

If the flow rate in each sampling hole is very different, the sensitivity and stress of each sampling hole are not balanceable. Then the diameters of the sampling holes should be optimized to make the network balanceable. Suppose that each sampling hole's flow rate, Q_i , is alike and:

$$Q_i = Q_a = \frac{Q}{n} \quad (9)$$

Q_a is the average of each sampling hole's flow rate. The area of the sampling hole 'n-1', i.e. the area of the sampling hole near the detector can be calculated. Then the area of the sampling hole 'i' ($i=n-2, \dots, 1,0$) can be got. The diameter d_i of the sampling holes 'i' is:

$$d_i = \sqrt{\frac{4A_i}{\pi}} \quad (10)$$

In order to make the design and installation easy, d_i should be adjusted. The span of value is 2.5mm to 6mm and the interval of value is 0.5mm. d_i equals to the most approximate value. The sampling holes' flow rate and the transport time in which the air is drawn from the sampling holes to the detector based on the new diameter of the sampling holes d_i are got. The flow rate in each sampling hole of the network is the most balanceable in this way.

If the calculated transport time from the end cap of the network to the detector exceeds 120 seconds (according to the National Fire Protection Association, NFPA 72), the diameter should be adjusted. And at the same time, the balance of the sampling holes' flow rate should be taken into account. Provided that the diameter of the sampling hole in the end cap is the maximum, here the diameter is 6mm, and the other sampling holes' flow rate is the same as the flow rate of the sampling hole in the end cap, here the flow rate is 1, we can calculate the diameter of the sampling hole 'i' ($i=1,2, \dots, n-1$), d_i . Then adjust d_i . The span of value is 2.5mm to 6mm and the interval of value is 0.5mm. d_i is the most approximate value. The sampling holes' flow rate and the transport time in which the air is drawn from the sampling holes to the detector based on the new diameter of the sampling holes d_i are got. If the calculated transport time from the end cap of the network to the detector still exceeds 120 seconds, we must change the structure of the network, such as the length of the sampling pipe, the number of the sampling holes.

EXPERIMENTAL STUDY AND RESULTS

Four different suits of networks of the sampling pipes and sampling holes are built in a large room. And a set of aspirating smoke detector is used. When the smoke nears to the end cap the timing begins and when the detector generates warning signals the timing ends. The transport time is got and compared with the calculated one.

The sketches and the records of the networks in experiment are shown in Table 1. In order to be explicit, the experiments are numbered. The comparison of transport time is shown in Table 2. The errors of transport time between the experiments and the calculated are small.

Table 1 The sketches and the records of the networks in experiments

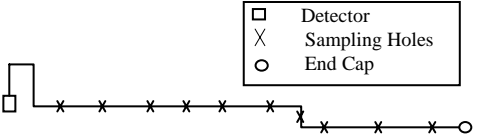
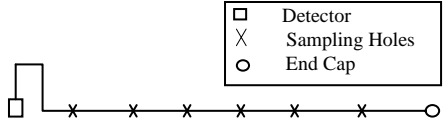
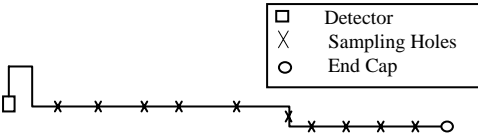
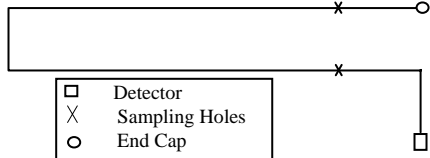
<p style="text-align: center;">No.1 Experiment</p>  <p>Experiment parameter and result: The number of the sampling holes: 11. The length of the sampling pipe: 48.5m. The bend (from the end cap): 11.2m, 15.8m, 40.7m, 43.7m, 45.7m. The space between the sampling holes (from the end cap): 2.2m, 3.4m, 4.3m, 3.6m, 5.7m, 4.0m, 3.6m, 4.2m, 4.0m, 3.6m, 9.9m. The diameter of the sampling hole (from the end cap): 4mm, 3mm, 3mm, 3mm, 3mm, 3mm, 3mm, 4mm, 4mm, 3mm, 3mm.</p>	<p style="text-align: center;">No.2 Experiment</p>  <p>Experiment parameter and result: The number of the sampling holes: 7. The length of the sampling pipe: 39.3m. The bend (from the end cap): 26.7m, 35.1m, 36.5m. The space between the sampling holes (from the end cap): 4.5m, 4m, 4m, 4m, 3.8m, 4.1m, 14.9m. The diameter of the sampling hole (from the end cap): 4mm, 3mm, 3mm, 3mm, 3mm, 3mm, 3mm.</p>
<p style="text-align: center;">No.3 Experiment</p>  <p>Experiment parameter and result: The number of the sampling holes: 11. The length of the sampling pipe: 46.05m. The bend (from the end cap): 17.2m, 19.2m, 38.95m, 41.85m, 43.25m. The space between the sampling holes (from the end cap): 2.7m, 3.6m, 3.9m, 4.3m, 3.9 m, 4.3m, 4.5m, 4.2m, 1.75m, 3.3m, 9.6m. The diameter of the sampling hole (from the end cap): 4mm, 3mm, 3mm, 3mm, 3mm, 3mm, 3mm, 3mm, 3mm, 3mm, 3mm.</p>	<p style="text-align: center;">No.4 Experiment</p>  <p>Experiment parameter and result: The number of the sampling holes: 3. The length of the sampling pipe: 41.13m. The bend (from the end cap): 20.19m, 20.9m. The space between the sampling holes (from the end cap): 4.19m, 32.71m, 4.23m. The diameter of the sampling hole (from the end cap): 3.5mm, 3.2mm, 3.2mm.</p>

Table 2 The comparison of the transport time

Experiment:	No. 1	No. 2	No. 3	No. 4
Transport time (experiment): [s]	77.72	57.97	64.03	77
Transport time (calculated): [s]	82.3	60.52	66.03	79.25
Error: [s]	4.58	2.55	2	2.25

CONCLUSION

The transport time based on the mathematical models accords with the experiment by and large. The choice of flow coefficient μ , frictional resistance coefficient λ and local resistance coefficient ζ is based on empirical formulas and they are simplified while calculating. It is the main reason caused the errors of the transport time between the calculated and the measured. The errors are less than 10% and the precision can be accepted in engineering calculation. The mathematical models are correct and available. They can be used to forecast the transport time of the network and direct the design and the installation of the network.

REFERENCES

1. VESDALaserPlus Air Sampling System, Beijing Huamaijinwei Electronic Fire Protection System Corporation.
2. GST Aspirating Air Intelligent Fire-Prewarning Detector Design Manual, Haiwan Security Technology Corporation.
3. Xiangduo Fu, the Network of Fluid Transport, China Architecture & Building Press, 2001, pp 41-67.
4. Jingchao SHENG, Hydraulic Hydrodynamics, China Mechanics Press, 1980, pp 118-171.
5. Yaoqing LU, Design Manual of Heat and Ventilation, China Architecture & Building Press, 1987, pp 773-901.

CONCURRENT CONTROL OF VELOCITY-FORCE CONTROL AND ENERGY-SAVING CONTROL IN HYDRAULIC VALVE-CONTROLLED CYLINDER SYSTEMS

Mao-Hsiung CHIANG*, Fei-Lung YANG**, Yih-Nan CHEN**, Lien-Wang LEE*,
Yih-Chen YEH*, and Shih-Tang SHENG*

*Institute of Automation and Control,
National Taiwan University of Science and Technology,
Taipei 106, Taiwan.
(E-mail: mhchiang@mail.ntust.edu.tw)

**Department of Engineering Science and Ocean Engineering,
National Taiwan University,
Taipei 106, Taiwan.

ABSTRACT

High servo control response and high energy-efficiency are requested in hydraulic servo systems of current hydraulic machines. This investigation concurrently implements energy-saving control and velocity-force control for simultaneously realizing high velocity-force control response and high energy-efficiency for hydraulic valve-controlled cylinder systems. The velocity-force control of the hydraulic cylinder, including 1st stage of velocity control and 2nd stage of force control, can be applied in hydraulic machines, i.e. injection moulding machines. The energy-saving control implemented here contains load-sensing control, constant supply pressure control and constant supply power control. The concurrent control of energy-saving control and velocity-force control of the hydraulic valve-controlled cylinder system becomes a two-input and two-output control problem. For that, an intelligent control strategies using fuzzy sliding mode control is developed. The experimental comparisons of the four different systems, including velocity-force control with load-sensing control, velocity-force control with constant supply pressure control, velocity-force control with constant supply power control and velocity-force control without energy-saving control, are implemented for the same velocity-force profile. The minimum consumed powers in each system are compared. The feasibility of the concurrent control of energy-saving control and velocity-force control is verified experimentally.

KEY WORDS

Key words, concurrent control, velocity-force control, energy-saving control, fuzzy sliding mode control, hydraulic injection moulding machine

INTRODUCTION

Improving the servo control performance and the energy-saving ability is a significant task for today's hydraulic injection moulding machines (HIMM) in face of the competition with electromechanical injection moulding machines (EIMM) [1]. The velocity control, pressure control and phase switching control of the

HIMM have been discussed and published in general terms [1-5]. In the conventional HIMM, the clamping force was controlled indirectly by means of the pressure control of the clamping cylinder via a servo valve. However, direct clamping force control can perform more accurate clamping force response. Specific research on the clamping FC of the HIMM is still rare. Besides, researches on the HIMM are usually

concentrated on the improvement of servo control performance, and rarely on the improvement of energy efficiency. However, the enhancement of energy efficiency in HIMM has become very important and a decisive factor in competition with the EIMM [1]. The study about the integrated control of the velocity control (VC) and energy-saving control (ESC) in the HIMM was published firstly in the research of Chiang, et al. [3]. Chiang et al. [6] discussed the parallel control of path control and ESC in hydraulic valve-controlled cylinder systems (HVCCS). As the clamping force control only requires high pressure but few volume flow such that only low power is in demand, and the energy efficiency is very low in the conventional HIMM. With the inherent lower efficiency, it is expected that the integrated control system can make a substantial improvement. In this paper, a novel solution is implemented for the integrated control of the velocity-force control and the energy-saving control for simultaneously realizing accurate velocity-force control response and high energy efficiency in the HIMM.

Today's HIMMs are mostly fitted with HVCCS, therefore the integrated control of velocity-force control and energy-saving control in the HVCCS could prove to be a significant improvement of the high velocity-force control performance and high energy efficiency for the HIMM. The conventional HVCCS with a relief valve and constant displacement pumps for setting the maximum supply pressure, perform good servo control response, but have low energy efficiency. For that reason, the energy-saving control, such as load-sensing control (LSC) and constant supply pressure control (CSPC), is introduced to improve the energy efficiency in the HVCCS. The LSC enables the supply pressure to be adjusted according to the load-sensing pressure of the hydraulic actuator thereby achieving the energy-saving effects by keeping a constant difference between the supply pressure and the load-sensing pressure [3,6,7]. Moreover, the integrated control of velocity-force control and energy-saving control in HVCSS is more complicated than the force control or velocity control alone, therefore it is indispensable to develop an appropriate controller to provide the excellent velocity-force control response as well as high energy efficiency for the HIMM.

TEST RIG LAYOUT

Figure 1 schematically depicts the test rig that can be divided into a HVCCS and an electro-hydraulic variable displacement pump system (EHVDPS). The HVCCS works for realizing velocity-force control of the injection cylinder of HIMM; the EHVDPS realizes the energy-saving control in the HIMM. Therefore, the concurrent control system, composed of the velocity-force system and the energy-saving control system, is a TITO control system. Besides, the

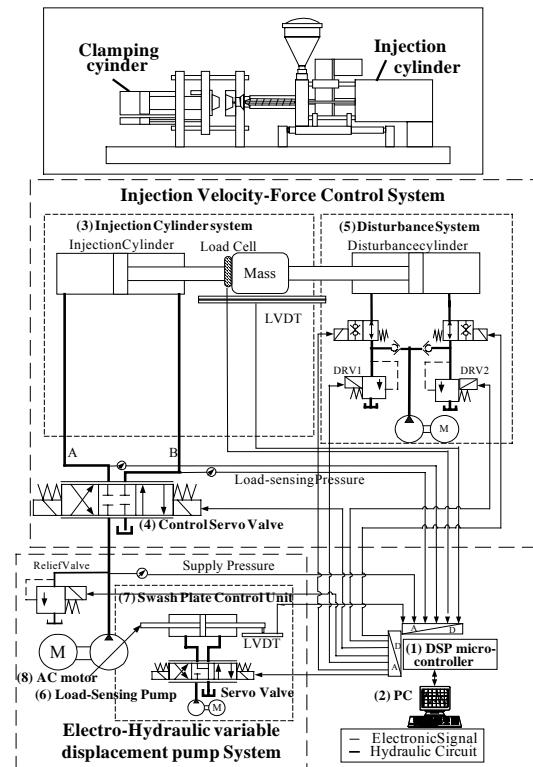


Figure 1 Test rig layout of the integrated control system for injection moulding machines

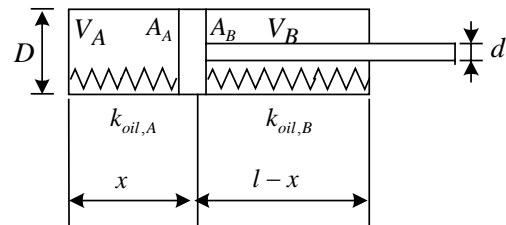


Figure 2 Equivalent springs of disturbance cylinder chambers

DSP-based control hardware can be realized for real industrial applications.

Injection velocity-force control system

This system is composed of: (3) an injection cylinder system, (4) a control servo valve and (5) a disturbance system. The injection cylinder system, including an injection cylinder, a load cell and two pressure transducers. The velocity and force signals are measured by the position sensor and load cell, and fed back to the velocity-force controller. The pressure from the load-sensing valve into the hydraulic cylinder, namely the load-sensing pressure p_{LS} , is measured and fed back for energy-saving control.

The disturbance cylinder acts as an equivalent spring for injection force control in this study by means of closing

the two solenoid valves. Due to the oil compressibility, the chamber oil of disturbance cylinder can act as hydraulic springs, as shown in Figure 2 [11].

Energy-saving control system

The energy-saving control is implemented by means of the EHVDPS that incorporates: (6) a swash plate piston pump with variable displacement (load-sensing pump), (7) a swash plate control unit, and (8) an AC induced motor. The displacement of the swash plate axial piston pump is adjusted by the angle of the swash plate, which is altered by the swash plate control unit via a small HVCCS with position control of the swash plate.

CONTROLLER DESIGN

In this study, fuzzy sliding mode control is used for decreasing the fuzzy rule numbers. The FSMC is an approach that incorporates the fuzzy control with the sliding-mode control. In many fuzzy control systems, the fuzzy rule base depends on both the control error e and the control error rate \dot{e} , which complicates the fuzzy inference rules and the membership functions. For that reason the FSMC introduces a sliding surface function σ to reduce the number of input variables and fuzzy inference rules.

$$\sigma = (\alpha e + \dot{e}) = ZERO \tag{1}$$

where α is a positive constant that depicts the slope of the fuzzy sliding surface $\sigma = ZERO$, which is a straight line in the phase plane, as shown in Fig. 3(a). Since the

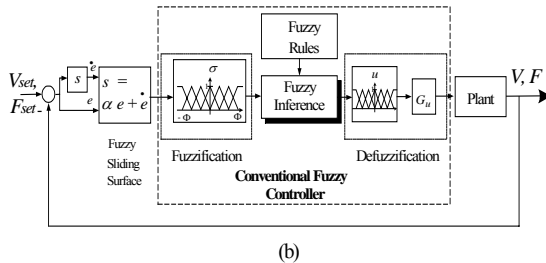
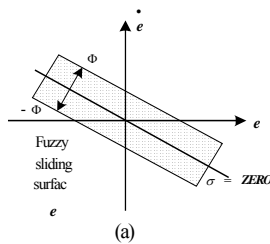
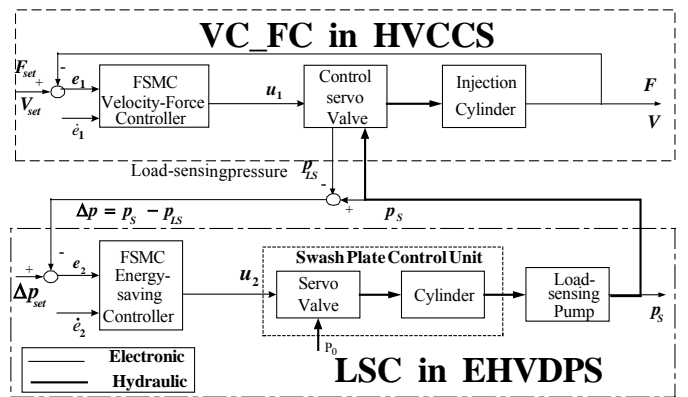
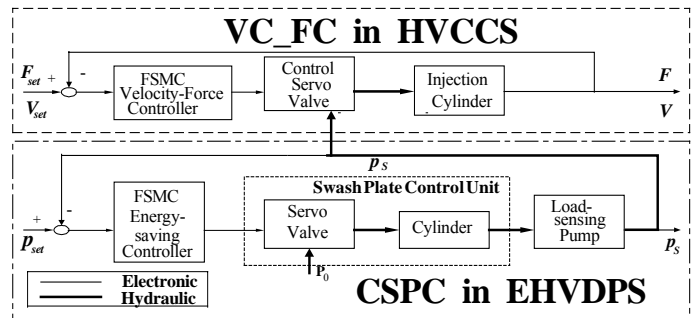


Figure 3 Fuzzy sliding-mode control
(a) fuzzy sliding surface σ
(b) Block diagram of FSMC

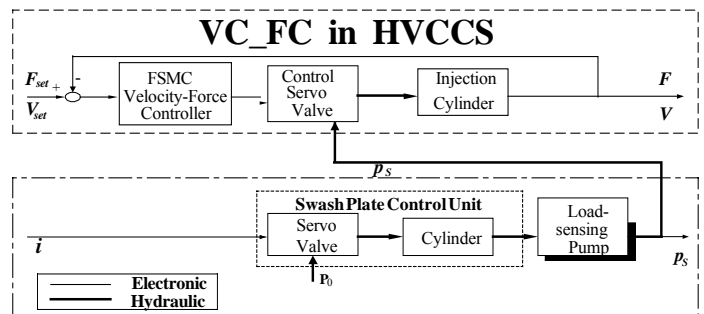
robustness is inherent in the sliding-mode control, the stability and robustness of the conventional fuzzy controller can be assured. In addition, it can at the same time improve the chattering phenomena which occurs in the sliding-mode control. In this study, the sliding surface σ and the control input u are both divided into 7 sections by the membership function set. Therefore, instead of 7×7 fuzzy rules with control error e and error rate \dot{e} in the conventional fuzzy control, the FSMC can reduce the fuzzy rules into 7 rules with the fuzzy sliding surface σ . The Mamdani method is used in the fuzzy inference, and the centroid method is used for defuzzification. The block diagram of the FSMC is illustrates in Fig. 3(b). The control block diagrams are shown in Fig. 4.



(a)



(b)



(c)

Figure 4 Block diagrams of the concurrent control systems
(a)(VC_FC + LSC) (b)(VC_FC + CSPC) (c)(VC_FC - ESC)

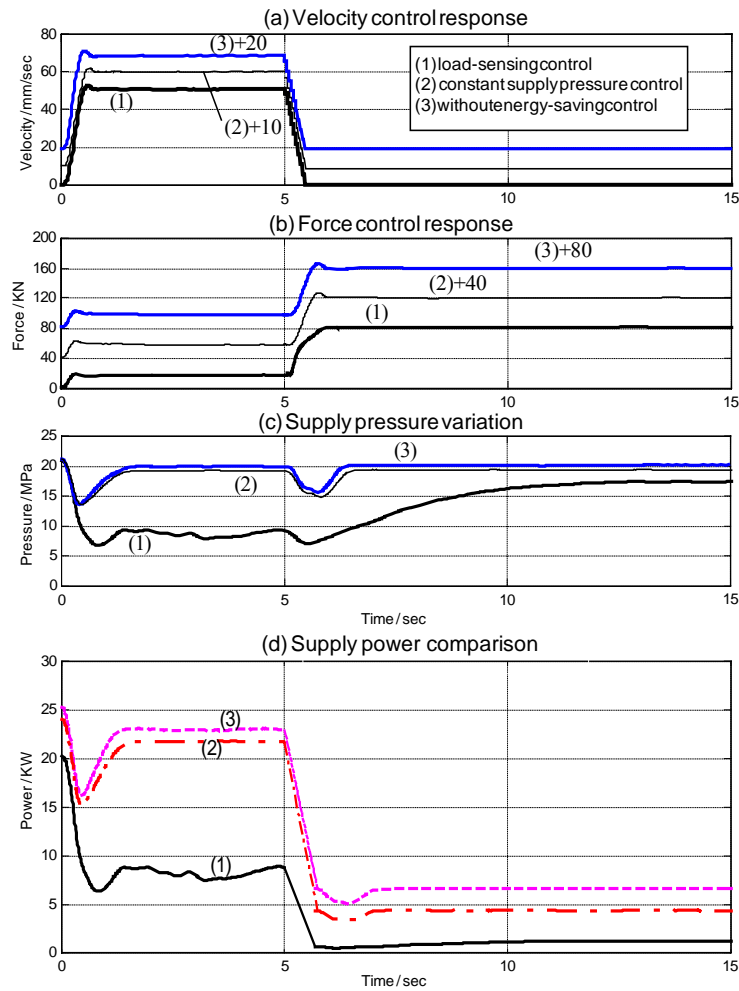


Figure 5 Experimental comparison of three different concurrent control systems: (1) velocity-force control with load-sensing control, $\Delta p_{set} = 2$ MPa (0~5sec), $\Delta p_{set} = 3$ MPa (5~15sec) (2) velocity-force control with constant supply pressure control, $p_{Sset} = 19$ MPa, (3) velocity-force control without energy-saving control, $p_{Smax} = 21$ MPa

EXPERIMENTAL RESULTS

The injection cylinder performs with constant velocity control firstly for constant feeding of plastic material. Subsequently, force control is performed for moulding injection. Thus, the velocity-force control is requested for the injection cylinder.

The new concurrent control of injection velocity-force control and energy-saving control with FSMC is implemented and verified experimentally. At first, the experiments of the injection velocity-force control are implemented without energy-saving control using FSMC, i.e. (VC_FC-ESC). After that, two different energy-saving control systems, such as load-sensing control (LSC) and constant supply pressure control (CSPC), are integrated with the velocity-force control,

i.e. (VC_FC+LSC) and (VC_FC+CSPC).

The nominal experiment conditions are chosen as: the sampling frequency $f_s = 200$ Hz, the oil temperature $T_{oil} = 30 \sim 40$ °C, and the maximum supply pressure $p_{Smax} = 21$ MPa.

At last, in order to evaluate the energy-saving effects, the pump energy consumption of the three concurrent control systems, i.e. (1)(VC_FC+LSC), (2)(VC_FC+CSPC) and (3)(VC_FC-ESC) are compared.

Figure 5 indicates the experimental comparison of the concurrent control for the velocity-force control with set velocity $V_{set} = 50$ mm/sec and set force of $F_{set} = 80$ kN under three different energy-saving control systems, namely (1) (VC_FC+LSC), $\Delta p_{set} = 2$ MPa (0~5sec), $\Delta p_{set} = 3$ MPa (5~15sec) (2) (VC_FC+CSPC), $p_{Sset} = 19$ MPa, (3) (VC_FC-ESC), $p_{Smax} = 21$ MPa. As shown in

Fig. 5(a), velocity control is performed during 0~5sec and can be achieved in all the three systems without obvious control performance difference. Figure 5(b) shows the force control comparison during 5~15sec. The force control performance is almost the same. Figure 5(c) shows the supply pressure variation of the three systems. The supply pressure of (VC_FC+LSC) varies with the load-sensing pressure. The supply pressure of (VC_FC+CSPC) can be controlled to keep constant supply pressure 19 MPa; The supply pressure of (VC_FC-ESC) almost reach the maximum supply pressure $p_{Smax} = 21$ MPa set by the relief valve. Figure 5(d) clarifies the pump supply power of the three concurrent control system, which can be computed by

$$P_{EM} = \frac{P_p}{\eta_{mech}} = \frac{P_s \cdot Q}{\eta_{mech} \cdot \eta_{vol}} = \frac{P_s \cdot Q}{\eta_{total}} = \frac{P_s \cdot n \cdot q_{max} \cdot x_p}{\eta_{total} \cdot x_{p,max}} \quad (2)$$

where

- P_{EM} : power of electrical motor
- η_{total} : total efficiency of pump
- η_{mech} : mechanical efficiency of pump
- η_{vol} : volumetric efficiency of pump
- P_s : supply pressure
- Q : volume flow of pump
- q_{max} : max. displacement of pump
- n : rotational speed
- $x_{p,max}$: max. swash plate angle of pump
- x_p : swash plate angle of pump

p_s and x_p are directly measurable by the pressure transducer and the position sensor. The constant rotational speed in the EHVDPS is at $n = 1760$ rpm. The total efficiency of the pump can be estimated from the pump performance curve supported by the pump supplier. The (VC_FC+LSC) system consumes the least power. The (VC_FC+CSPC) system performs also with energy-saving ability.

CONCLUSIONS

This paper develops the new strategy for the concurrent control of injection velocity-force control and energy-saving control in a hydraulic injection machine. The experimental results verify the feasibility of the integrated control systems in the H IMM, including (VC_FC+LSC) and (VC_FC+CSPC). for simultaneously achieving excellent velocity-force control performance and high energy efficiency.

REFERENCES

- [1] Duffner, E., Will the last bastions of stationary fluid technology really fall, or are electro-mechanical driven injection moulding machines a fashion trend?, Proc. of the 3. International Fluid Power Conference (3. IFK), Aachen, Germany, Vol. 1, 2002, 27-36.
- [2] Helbig Injection moulding machine with electric-hydrostatic drives, Proc. of the 3. International Fluid Power Conference (3. IFK), Aachen, Germany, Vol. 1, 2002, 67-82.
- [3] Chiang, M-H, Lee, L-W and Tsai, J-J, Concurrent implementation of high velocity control performance and high energy efficiency for hydraulic injection moulding machines, Int J Advan Manufac Techno, Vol.23, 2004, pp.256-262.
- [4] Alleyne, A. and Havlicsek, H., Nonlinear control of an electrohydraulic injection molding machine via iterative adaptive learning, IEEE/ASME Trans on Mechatronics, 4:3, 1999, pp.312-323.
- [5] Chiu, C.-P., Wie, J.-H. and Shih, M.-C., Adaptive model following control of the mold filling process in an injection molding machine, Polymer Eng and Sci Vol.31, 1991, 1123-1129.
- [6] Chiang, M.H., Yu, D.D., Lee, L.W., Parallelregelung der Bahnsteuerung mit Energiesparungsregelung für einen ventilgesteuerten hydraulischen Zylinderantrieb mit robustem H_∞ -optimalem Regler (in German), Ölhydraulik und Pneumatik O+P, 2/2005, 2005.
- [7] Chiang, M.H. and Chien Y.W., Parallel control of velocity control and energy-saving control on a hydraulic valve controlled system using self-organizing fuzzy sliding mode control, JSME International Journal, Series C, Vol.46, No.1, 2003, pp.224-231.
- [8] Alleyne, A. and Liu, R., On the limitations of force tracking control for hydraulic servosystems, ASME J of Dynamic Systems, Measurement, and Control, 121:2, 1999, pp.184-190.
- [9] Niksefat, N. and Sepehri, N., Design and experimental evaluation of a robust force controller for an electro-hydraulic actuator via quantitative feedback Theory, Control Eng Prac 8, 2000, 1335-1345.
- [10] Alleyne, A. and Liu, R., A simplified approach to force control for electro-hydraulic systems, Control Eng Prac 8, 2000, 1347-1356.
- [11] Murrenhoff, H., Servohydraulik (in German), Lecture Notes, RWTH Aachen, 1998, Germany.

ADAPTIVE FAULT DIAGNOSIS OF HYDRAULIC ACTUATION SYSTEM

Shaoping Wang*, Mingshan Cui, Jian Shi and Zongxia Jiao

* No.303 School of Automation Science and Technology,
Beihang University, Beijing, 100083, China
(E-mail: shaopingwang@vip.sina.com)

ABSTRACT

Hydraulic actuation system is typical displacement control system whose performance is subjected to random inputs from noise, random disturbance from pump vibration or parameter changes. Through importing the integral item of residual error in different rank, this paper establishes the Proportion-Integral Observer (PIO) that can eliminate the influence of random input, parameter excursion and inherent disturbance and realize the fault diagnosis robustly. In order to reach the high fault coverage and low false alarm, this paper provides twin-threshold and corresponding fault decision-making strategy that not only considers the inherent noise existed in the system but also can manifest the fault information effectively. Application and simulation of hydraulic actuator system indicates that the adaptive fault diagnosis can detect the failure in high precision at the stochastic condition.

KEY WORDS

Fault diagnosis, Proportion integral observer, Twin-threshold, Hydraulic actuation system

NOMENCLATURE

u : input command
 K_q : flow gain of servo valve
 T_v : time constant of servo valve
 E_y : bulk module of elasticity
 V_t : volume of cavity
 K_c : flow-pressure gain of servo valve
 K_s : rigidity of output pole
 A : available area of piston
 K_b : the gain of displacement sensor
 M : piston mass
 D : damping coefficient of piston
 X_r : piston displacement
 X_p : load output
 F : load force
 $G(s)$: load transfer function

INTRODUCTION

Hydraulic actuation system is a key component in flight control system, which performance and fault diagnosis is very important in application. With many nonlinear characteristics existed in hydraulic actuation system such as load flow of servo valve, friction of mechanical structure, fluid compressibility and coupling with hydraulic pump, it makes failure mechanism complex and failure diagnosis difficult [1]. Fault diagnosis method based on mathematic modeling is to design a diagnostic observer that can describe the system performance and detect the failure in certain direction with the residual error between actual system and observer [2]. However, it is difficult to decoupling and determine the failure location actually if some random factors exist, for example the modeling error

and disturbance. So it is necessary to study a robust way to separate the failure characteristics from estimated information effectively [3].

Directing to the disturbance existed in hydraulic actuation system, this paper presents the diagnostic observer based on PIO, which imports the integral item of residual error in observer to be suitable to the influence of random input [4]. Considering the inherent disturbance existed in hydraulic actuation system, its output varies with input signal and outside disturbance, so the fixed error threshold is difficult to cover the failure effectively. This paper presents an adaptive twin-threshold, which consists of fixation and variant items and can be adjusted with the input signal and disturbance. The simulation and application indicate that the adaptive observer based on PIO and twin-threshold can diagnose the failures of hydraulic actuation system effectively.

ADAPTIVE FAULT OBSERVER DESIGN

Although the normal fault observer is designed to pick up fault characteristic from residual error usually, it is easy to be get into trouble by some random factors, which always produces false alarm or fail to report. In order to extract the failure information from residual error effectively, PIO is designed to eliminate the influence of random input and unknown disturbance.

PIO Model in One-dimension

Given the linear time-invariant system:

$$\begin{cases} \dot{x} = Ax + Bu + Dd \\ y = Cx \end{cases} \quad (1)$$

Where $x \in R^n$ is state vector; $u \in R^p$ is system input; $d \in R^m$ is unknown disturbance; $y \in R^q$ is system output; D is allocation matrix of unknown input; A , B , C is coefficient matrix separately.

In order to realize the effective fault diagnosis under random input, not only the difference between actual output and estimation output but also its integral are inducted in observer, and construct the PIO as follows.

$$\begin{cases} \dot{\hat{x}} = A\hat{x} + Bu + K_p(y - \hat{y}) + Df \\ \dot{\hat{f}} = K_I(y - \hat{y}) \end{cases} \quad (2)$$

Where \hat{x} is the estimation of the state; f is failure vector; \hat{y} is observer output; K_p is proportion gain of observer; K_I is integral gain of observer. Define the state error vector as:

$$e = \hat{x} - x \quad (3)$$

Then from equation (2) and (3), the dynamic equation of e and f can be formulated to give

$$\begin{pmatrix} \dot{e} \\ \dot{f} \end{pmatrix} = \begin{pmatrix} A - K_p C & D \\ -K_I C & 0 \end{pmatrix} \begin{pmatrix} e \\ f \end{pmatrix} - \begin{pmatrix} D \\ 0 \end{pmatrix} d \quad (4)$$

With proper selecting of K_I and K_p , all the eigenvalues of matrix $\begin{bmatrix} A - K_p C & D \\ -K_I C & 0 \end{bmatrix}$ are at the left

hand side of the complex plane and the PIO converges to the state of plant. So the observer based on PIO can approach the hydraulic actuation system even if the disturbance exists.

If sensor fails, the dynamic model can be expressed as:

$$\begin{cases} \dot{x} = Ax + Bu + Dd \\ y_1 = C_1 x \\ y_2 = C_2 x + F_2 f_s \end{cases} \quad (5)$$

Where f_s is failure vector of sensor, F_2 is the corresponding fault distribution matrix. Defining $C = \begin{pmatrix} C_1 \\ C_2 \end{pmatrix}$, the output of PIO can be described as

$y_2 = C_2 \hat{x} + F_2 \hat{f}_s$, then the failure vector can be obtained as

$$\hat{f}_s = (F_2^T F_2)^{-1} F_2^T (y_2 - C_2 \hat{x}) \quad (6)$$

If actuator fails, the dynamic system become

$$\begin{cases} \dot{x}(t) = Ax(t) + Bu(t) + Dd(t) + Ef_a(t) \\ y = Cx \end{cases} \quad (7)$$

Where E is the fault distribution matrix and f_a is failure vector of actuator. Then the residual error can be solved from the error differential equation as

$$\begin{aligned} \varepsilon(t) = & e^{(A - K_p C)t} \varepsilon(0) + \int_0^t e^{(A - K_p C)(t-\tau)} D [f(\tau) - d(\tau)] d\tau \quad (8) \\ & + \int_0^t e^{(A - K_p C)(t-\tau)} E f_a(\tau) d\tau \end{aligned}$$

Where $\varepsilon(0)$ is original value of estimated error. Equation (8) provides the failure direction of actuator.

If the system is no fault i.e. $f_a = 0$, then $\varepsilon = 0$. As such the estimation f is the estimation of disturbance d under proper selection of K_p, K_I . Otherwise

$f_a \neq 0$ if actuator fails, its residual error can be described as:

$$\varepsilon(t) = \int_0^t e^{(A-K_p e)(t-\tau)} E f_a(\tau) d\tau \quad (9)$$

PIO Model in Multiple-dimension

When unknown disturbance is not constant, the performance of PIO based on one-dimension is not satisfied with the requirement of error modification. Hence the PIO in multiple-dimension is presented to estimate the disturbance signal in multiple dimension. For polynomial form of multiple dimension disturbance shown as follows:

$$d(t) = a_0 + a_1 t + a_2 t^2 + \dots + a_q t^q \quad (10)$$

Where a_i is coefficient of polynomial ($i=1,2,\dots,q$). Establish the state space equation under polynomial disturbance as follows.

$$\begin{pmatrix} \dot{d}_0 \\ \dot{d}_1 \\ \dot{d}_2 \\ \vdots \\ \dot{d}_q \end{pmatrix} = \begin{pmatrix} 0 & 1 & 0 & \dots & 0 \\ 0 & 0 & 1 & \dots & 0 \\ 0 & 0 & 0 & \dots & 0 \\ \vdots & \vdots & \vdots & \ddots & \vdots \\ 0 & 0 & 0 & \dots & 0 \end{pmatrix} \begin{pmatrix} d_0 \\ d_1 \\ d_2 \\ \vdots \\ d_q \end{pmatrix} \quad (11)$$

Where $d_i(t)$ is the i^{th} unknown disturbance vector whose rank is r_i ($i=1,2,\dots,q$), its state can be

described as $d_0 = d(t)$, $d_1 = \dot{d}_0$, $d_2 = \dot{d}_1$, ..., $d_q = 0$ separately.

On this condition, the all-rank integral items of residual error are acceded to observer, and construct the PIO in multiple dimension as follows.

$$\bar{A} = \begin{pmatrix} A & D_1 & D_2 & \dots & D_q \\ 0 & \Delta_1 & 0 & \dots & 0 \\ 0 & 0 & \Delta_2 & \dots & 0 \\ \vdots & \vdots & \vdots & \ddots & \vdots \\ 0 & 0 & 0 & \dots & \Delta_q \end{pmatrix} \quad (12)$$

$$\bar{C} = (C \ 0 \ 0 \ \dots \ 0)$$

Where $D_i = [P_i \ 0 \ \dots \ 0 \ 0]_{n \times (r_i+1)}$, $P_i \in R^{n \times 1}$ is the row vector which include uncertainties, noise and unknown input. Δ_i is the unit matrix shown as follow:

$$\Delta_i = \begin{pmatrix} 0 & 1 & \dots & 0 \\ 0 & 0 & \dots & 0 \\ \vdots & \vdots & \ddots & \vdots \\ 0 & 0 & \dots & 0 \end{pmatrix}_{(r_i+1) \times (r_i+1)} \quad (13)$$

With considering the influence of polynomial disturbance, all-rank integral items of residual are imported in PIO so as to realize the estimation. The existence condition of multiple PIO is that (\bar{A}, \bar{C}) can be observed. Its block diagram is expressed in Figure 1.

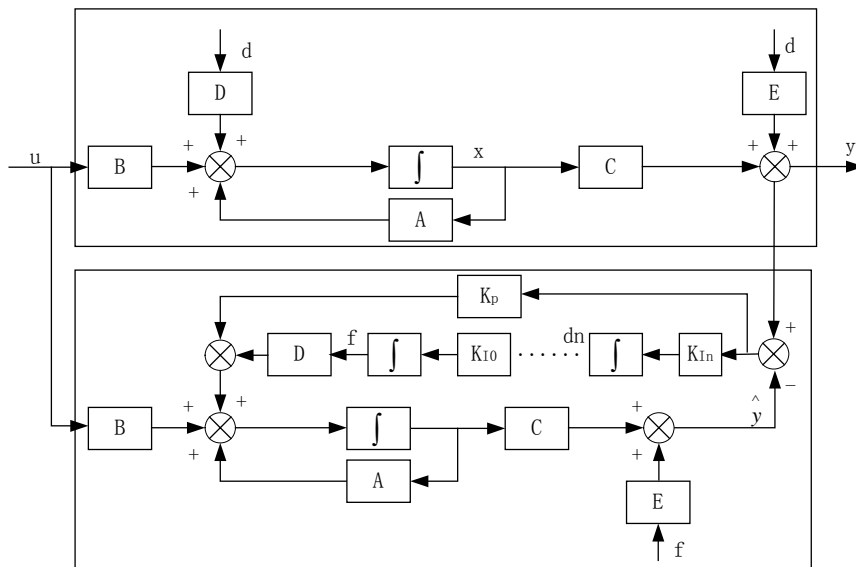


Figure 1 PIO in multiple dimension

It is proved that the dimension of PIO is $n + \sum_{i=1}^q (r_i + 1)$,

which increases with the rank of unknown disturbance. Due to the function of various integral items, PIO is suitable to stochastic system with some noise, unknown input and disturbance.

Twin Threshold

Fault detection and diagnosis are always executed with proper threshold that determine the failure coverage and false alarm. Considering the inherent noise and measurable error existed in control system, it is necessary to provide the preliminary threshold that can describe its inherent disturbance in normal condition. At the same time, the variance due to failures should also be represented in threshold. So the single threshold is not possible to realize the fault diagnosis effectively under random condition. The adaptive twin-threshold include two items as follows.

$$T(t) = T_0(t) + T_1(t) \quad (14)$$

Where $T(t)$ is adaptive twin-threshold, $T_0(t)$ is constant part considering inherent disturbance, $T_1(t)$ is time-variant part that describe the fault variety of system. The failure can be diagnosed according following decision-making strategy:

(1) If residual error is larger than $T_0(t) + T_1(t)$, it determines that the system fails to a certainty.

(2) If residual error is between $T_0(t)$ and $T_0(t) + T_1(t)$, it is doubtful that the failure occurs and begin to monitor. After three times, it determines that the system fails. Otherwise the system is normal.

(3) If residual error is less than $T_0(t)$ at all the time, the system is normal.

The twin-threshold is adaptive to the fault diagnosis of dynamic system, which has higher fault coverage and lower false alarm because the disturbance and fault variance are considered in threshold design. Suppose the allowable error of component in system is $E_i, i=1,2,\dots,n$, its gain is $R_i, i=1,2,\dots,n$ separately. The maximum error of system can be described as $T_1 = E_{\max} = \sum_{i=1}^n |E_i|$, which is the worst condition. $T_0(t)$ is determined by inherent disturbance.

Figure 2 shows the adaptive twin-threshold, in which curve 2 is the adaptive twin-threshold of certain detected signal $T(t) = T_0(t) + T_1(t)$ and curve 1 covers the variance of inherent disturbance $T_0(t)$.

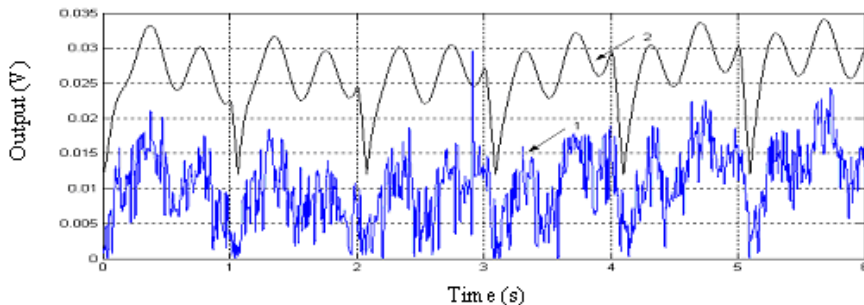


Figure 2 Adaptive twin threshold of a certain signal

It is obvious that the twin-threshold can solve the conflict between false alarm and fail to report of fault diagnosis in great degree so as to improve the robust. In practice, the adaptive twin-threshold is difficult to cover all the failure absolutely especially to the abnormal point shown in Figure 2. For example, the value at 2.8 second is greater than twin-threshold whereas the system is normal in general.

APPLICATION OF HYDRAULIC ACTUATION SYSTEM

PIO Design

Hydraulic actuation system is a key component that can be driven by command to realize the displacement control, which consists of displacement sensor, amplifier, servo valve and cylinder. Its block diagram is shown in Figure 3.

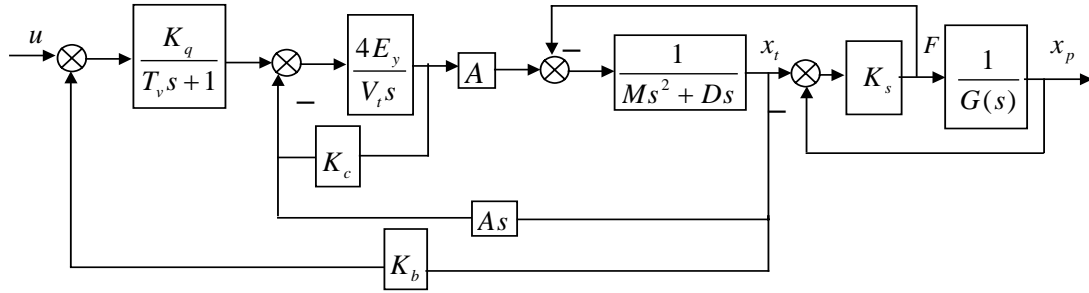


Figure 3 The block diagram of hydraulic actuation system

Establish the state space model of hydraulic actuation system as:

$$\dot{x} = \begin{pmatrix} -6.2834 \times 10^2 & 0 & -1.4138 \times 10^3 & 0 & 0 \\ 2.4459 \times 10^3 & -2.237 \times 10^3 & 1.5061 \times 10^8 & 0 & -1.5061 \times 10^8 \\ 0 & 0.5 & -3.5 \times 10^4 & 0 & 3.5 \times 10^4 \\ 0 & 0 & 3.5 \times 10^4 & -5 & -3.5 \times 10^4 \\ 0 & 0 & 0 & 0 & 1 \end{pmatrix} x + \begin{pmatrix} 1.4138 \times 10^4 \\ 0 \\ 0 \\ 0 \\ 0 \end{pmatrix} u + \begin{pmatrix} 0 \\ 2.1515 \times 10^3 \\ -0.5 \\ 0 \\ 0 \end{pmatrix} F \quad (15)$$

$$y = \begin{pmatrix} 0 & 0.56841 & 0 & 0 & 0 \\ 0 & 0 & 0 & 0 & 1 \end{pmatrix} x + \begin{pmatrix} 0 \\ 1 \end{pmatrix} f_s$$

Adopting the eigenvalue configuration, design the Luenberger observer and PIO whose integral gain is $K_i = 64.542$. If the system is normal with inherent noise of square signal with amplitude 10 and period 2s, the PIO output can be described as the real line and the output of Luenberger observer is shown as broken line in Figure 4.

It is obvious that the output residual error is less than the one of Luenberger observer, so PIO has the better

performance comparing with the Luenberger observer. Figure 5 shows the estimation effect of PIO in multiple dimension, in which curve 1 shows the disturbance existed in system and curve 2 is the corresponding estimation of PIO. It indicates that PIO can approach the model of stochastic system effectively.

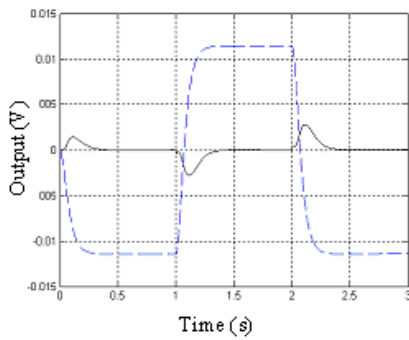


Figure 4 Comparison between PIO and Luenberger observer

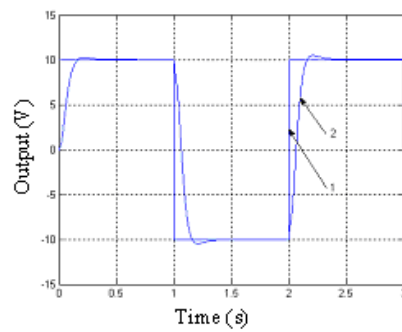


Figure 5 Comparison of disturbance and its estimation

If the sensor fails gradually according to the following rule:

$$f_s = \begin{cases} b_2 * \sin(2\pi / 10) & 1.2s \leq t \leq 3s \\ 0 & \text{others} \end{cases} \quad (16)$$

Then obtain the output residual of system shown in Figure 6, in which the real line is the residual of normal system and the broken line is the residual under sensor failures. It indicates that PIO can detect the fault sensor effectively.

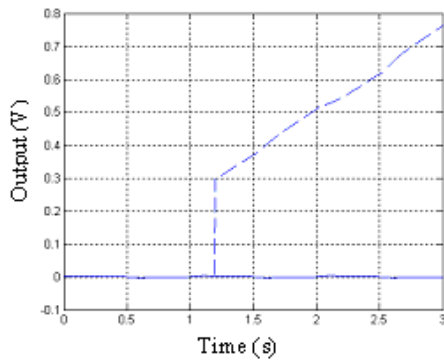


Figure 6 The residual under failures

Twin Threshold of Hydraulic Actuation System

Usually, parameter variable, flow pulse and Gauss noise can affect the threshold, so consider the inherent disturbance to determine T_0 and accumulate the tolerance of all components to determine T_1 shown in

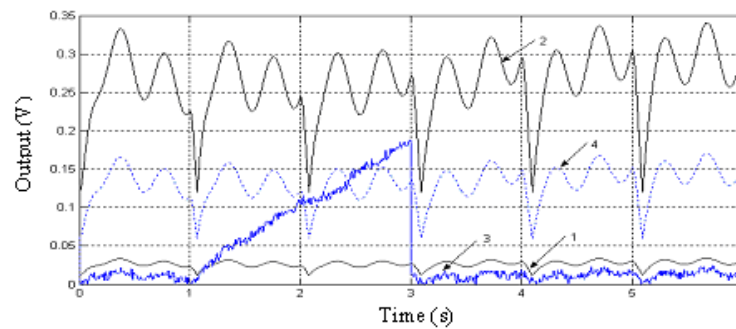


Figure 7 Fault diagnosis based on twin-threshold

In Figure 7, the failure occurs at 1.0 second. The residual error exceeds T_0 at 1.1 second, and went on until the residual error is greater than $1/2(T_0 + T_1)$ at 2.7s. After detecting for 30 clock period, PIO determines the gradual failure according to the fault diagnosis strategy, and remove the fault sensor in 3.0 second, so the system recovers to normal condition.

CONCLUSIONS

This paper provides the PIO and twin-threshold to hydraulic actuation system so as to improve the adaptability in fault diagnosis. Application indicates that the performance of PIO is better than the Luenberger observer, and twin-threshold not only can detect various failures rapidly but also can improve its robusticity.

REFERENCES

1. Li Faming, Study on Decoupling of Redundant

Figure 2. Select the control period is 10ms and let $T_1 = 10T_0$, then obtain the twin threshold in Figure 7, in which curve 1 expresses the threshold T_0 , curve 2 denotes the threshold $T_0 + T_1$, curve 3 is the residual under gradual failure and curve 4 means the median of $T_0 + T_1$.

The corresponding decision-making strategy is shown as follows:

- (1) If $\varepsilon > T_0 + T_1$, system fails.
- (2) If $T_0 < \varepsilon < 1/2(T_0 + T_1)$ and last for 30 times in 60 clock period, then the system fails, otherwise the system is normal.
- (3) If $1/2(T_0 + T_1) < \varepsilon < T_0 + T_1$ and last for 20 times in 40 clock period, then the system fails, otherwise the system is normal.
- (4) If $\varepsilon < T_0$, the system is normal.

1. Actuator, Master Dissertation of Beihang University, 2000.

2. Zhou Donghua, Fault Diagnosis and Fault Tolerant of Control System, Mechanical Industry Press, 1998.

3. Shafai B. and S. Nork, Simultaneous Disturbance Attenuation and Fault Detection Using Proportional Integral Observers, Proceedings of American Control Conference (ACC), Anchorage, AK., pp. 1643-1649, 2002.

4. Kang Ming, Fault Diagnosis of Fault Tolerant Control System, Master Dissertation of Beihang University, 2004.

ACKNOWLEDGEMENT

This work was supported by National Natural Science Foundation of China under grant number 60371043, Beijing Natural Science Foundation under grant number 4012009, and Chinese Excellent Talent Plan of New Century.

APPLICATION OF CONTROL THEORY TO THE IMPROVEMENT OF A VANE PUMP FOR FASTER DYNAMIC RESPONSE

Arie PERRY

Israel Aircraft Industries (IAI), MLM Division
P.O.Box 45 Beer Yaakov, 70350, ISRAEL
E-mail: arieperry@hotmail.com

ABSTRACT

Pump dynamic response, the speed in which a pump can build up pressure due to disturbance, system flow demand, is one of its most important characteristics. In high performance hydraulic control systems, normally we utilize a fast response, but expensive, variable displacement pressure compensated Piston Pump. Inexpensive Vane Pumps cannot be used because their very poor dynamic behavior, which is inherent from their construction and principle of operation. In this paper we apply Control Theory to analyze and investigate vane pumps and consequently suggest a possible re-design to improve their dynamic response. Performing stability, disturbance and speed of response analysis reveals that pump dynamic behavior is dominated by the parameter ratio B_{vf} / K_{sp} (B_{vf} – viscous coefficient, K_{sp} – spring constant). Upon completion of our study, we carried out a quantitative calculation of those parameters for a specific re-designed vane pump. In the re-designed vane pump speed of response was improved by factor of 35 and can now be used in high performance hydraulic servo systems, where high bandwidth is required.

KEY WORDS

Vane, Pump, Control, Dynamic, Response

NOMENCLATURE

M	: Regulating ring mass	(Kg)	δ	: Ring – Plate clearance	(m)
R	: Regulating ring radius	(m)	ξ	: Pump damping ratio	dimension-less
B_{vf}	: Viscous coefficient	(N / rad / sec)	ω_n	: Pump natural frequency	(rad / sec)
K_{sp}	: Spring constant	(N / m)	P_{op}	: Operating pressure	(bar)
K_{pv}	: Pressure coefficient	(N / bar)	P_{dp}	: Desired / Set pressure	(bar)
K_e	: Flow coefficient	(lpm / rpm / m)	Q_p	: System flow demand	(lit / min)
K_{lk}	: Leakage coefficient	(lpm / bar)	C_c	: Oil compliance	(lit / bar)
N	: Pump speed of rotation	(rpm)			

INTRODUCTION

The introduction of the variable displacement vane pump dynamic model is a significant contribution to the field of hydraulic pumps. It enabled the control of pump performance characteristics via theoretical trade offs during the design process. We studied and analyzed this model relating to the B_{vf} / K_{sp} ratio, found the lower and upper limits of the spring constant K_{sp} and defined best possible value for viscous friction B_{vf} , for a faster pump. The study included building of the necessary block diagrams, derivation of the relevant transfer functions in S domain and applying Routh Criteria, Steady State and Dynamic analyses.

The results of the study of pump parameters, related to a specific pump, are as follows:

- B_{vf} has been decreased significantly
 $B_{vf \text{ new}} = 1 / 20 B_{vf \text{ old}}$
- K_{sp} has been increased (stiffer spring)
 $K_{sp \text{ new}} = 1.75 K_{sp \text{ old}}$

The newly designed pump shall have the following parameters, which dominate dynamic response:

$$B_{vf} / K_{sp \text{ new}} = 1 / 35 B_{vf} / K_{sp \text{ old}}$$

The numerical values are a result of the re-design of the specific vane pump used in a previous research, which also contributed the pump nonlinear block diagram.

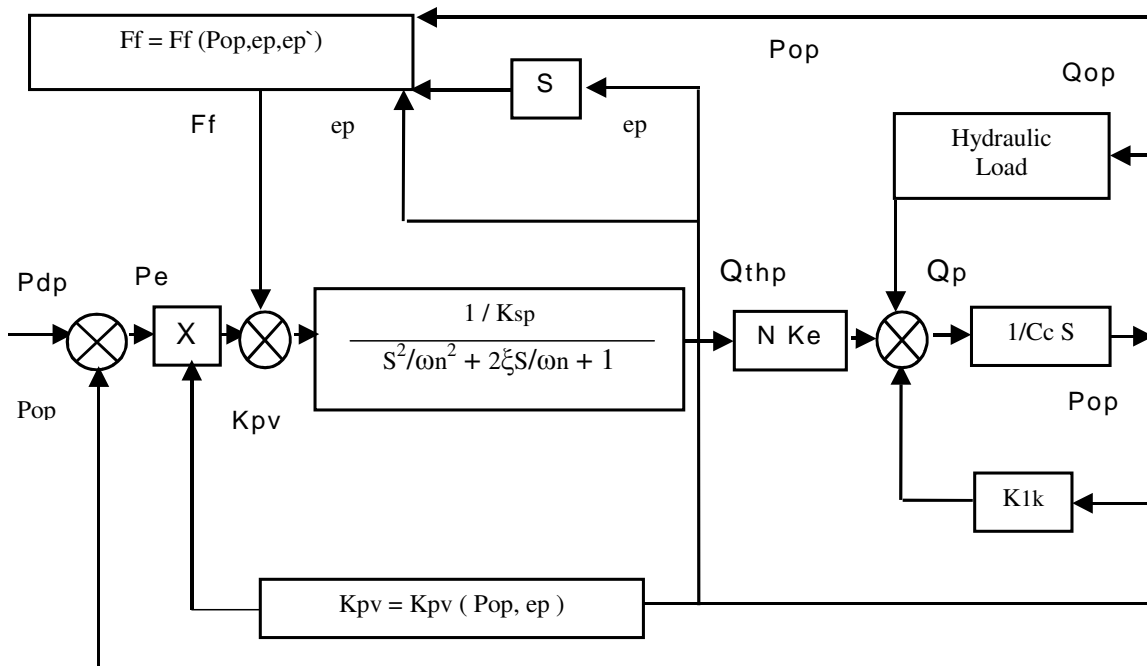


Figure 1: Pump nonlinear block diagram

STABILITY AND DISTURBANCE ANALYSIS

In order to study pump stability, we shall perform a linearized analysis of pump parameters neglecting the nonlinearities of the previous block diagram. The pump $Pop/Pdp(s)$ transfer function derived from the linearized block diagram has the form (see figure no. 2):

$$\frac{Pop}{Pdp} = \frac{K_{pv} N K_e}{(MS^2 + B_{vf}S + K_{sp})(CcS + K_{1k}) + K_{vp} N K_e} \quad (1)$$

which we shall put also in the standard form and apply Routh Stability Criterion for stability analysis.

Pump regulating operation is a feedback system, with the following linearized block diagram:

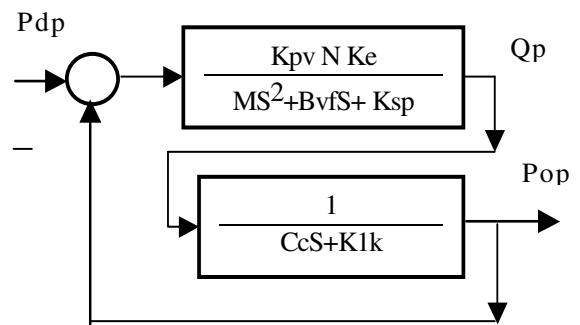


Figure 2: Pump linear block diagram with Pdp input

Pop / Pdp(s) in the standard form, equation no. (2):

$$\frac{Pop}{Pdp} = \frac{\frac{Kpv N Ke}{KpvNKe + KspK1k}}{\left[\frac{MCc}{KpvNKe + KspK1k} \right] S^3 + \left[\frac{BvfCc + MK1k}{KpvNKe + KspK1k} \right] S^2 + \left[\frac{BvfK1k + KspCc}{KpvNKe + KspK1k} \right] S + 1}$$

From the Routh Criterion we obtain the condition for stability, i.e. the constraint on spring constant Ksp:

$$(Bvf Cc + M K1k) (Bvf K1k + Ksp Cc) - M Cc (Kpv N Ke + Ksp K1k) > 0 \quad (3)$$

since $Bvf Cc^2 \neq 0$, we solve for Ksp in equation no.(3) to get the following condition, equation no. (4):

$$Ksp > \frac{M Cc Kpv N Ke - Bvf^2 Cc K1k - M Bvf K1k^2}{Bvf Cc^2}$$

This mathematical condition provides the relationship between the spring constant Ksp and the other pump parameters, for a stable pressure compensated pump. From the equation, maximum pump natural frequency can be obtained, dividing by $Bvf Cc^2$ and neglecting the elements with minus sign to get the Ksp / M ratio:

$$Ksp / M = \omega_n^2 > Kpv N Ke / Bvf Cc \quad \text{and from here:} \\ \omega_n \max = (Kpv N Ke / Bvf Cc)^{1/2} \quad (5)$$

Let us turn now to the pump Steady State analysis. The steady state gain, from equation no. 2:

$$Gss = Kpv N Ke / (Kpv N Ke + Ksp K1k) \quad (6)$$

$$\text{or} \\ Gss = 1 / [1 + (Ksp K1k / Kpv N Ke)] \quad (7)$$

Since K1k, Kpv, N, Ke are given for a specific pump, steady state gain is inversely proportional to Ksp (spring constant) i.e. $Gss \propto 1 / Ksp$. Softer spring means higher steady state gain and better pump pressure regulation. Dynamic point of view, however, indicates opposite requirement namely a stiffer spring, because too soft a spring (equation no. 4) will cause system instability. The conclusion is that the spring constant has to be large enough to ensure stability, and small enough to have a good pressure regulation, a tradeoff must be performed. Another useful transfer function is pump pressure / disturbance. When a pressure compensated pump is operating under normal conditions, the desired input

Pdp the (desired / set pressure) is usually kept constant. Pump dynamics is exercised by “disturbing” Qp flow demand of the system supplied by the pump.

The relevant linear block diagram with Qp as input:

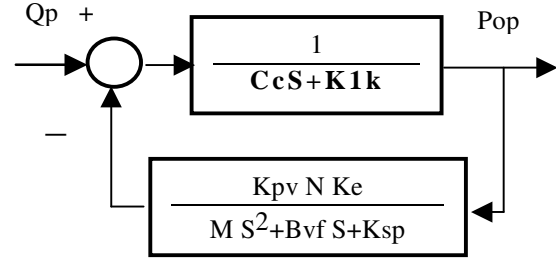


Figure 3: Pump linear block diagram with Qp input

The transfer function Pop / Qp (s) is obtained from the block diagram, equation no. (8):

$$\frac{Pop}{Qp}(S) = \frac{-(MS^2 + Bvf S + Ksp)}{(MS^2 + Bvf S + Ksp)(Cc S + K1k) + KpvNKe}$$

Or in its standard form, equation no. (9):

$$\frac{Pop}{Qp} = \frac{\left[\frac{-Ksp}{KpvNKe + KspK1k} \right] \left(\frac{S^2}{\omega_n^2} + \frac{2\xi S}{\omega_n} + 1 \right)}{\left[\frac{MCc}{KpvNKe + KspK1k} \right] S^3 + \left[\frac{BvfCc + MK1k}{KpvNKe + KspK1k} \right] S^2 + \left[\frac{BvfK1k + KspCc}{KpvNKe + KspK1k} \right] S + 1}$$

where $\omega_n^2 = Ksp / M$ is pump natural frequency, and $2\xi / \omega_n = Bvf / Ksp$ is viscous damping ration.

Routh Criterion, is identical to previous study of Pop / Pdp (s), so no additional information can be obtained.

The steady state gain $Gss = -1 / (KpvNKe / Ksp + K1k)$ is directly proportional to Ksp, or $Gss = \alpha Ksp$ since again K1k, Kpv, N, Ke are given for a specific pump. From disturbance considerations a softer spring gives smaller pressure changes, on the other hand will cause to instability, so we see again trade off is necessary.

DYNAMIC RESPONSE ANALYSIS

Having applied Routh Criteria and performed stability and disturbance analysis we found the constraints on the spring constant Ksp, and realized that there must be a tradeoff between soft spring for better pump regulation and smaller disturbances, and stiff spring for stability. We now turn to the analysis and investigation of the other parameter of importance Bvf, the viscous friction coefficient, in order to find ways for its improvement.

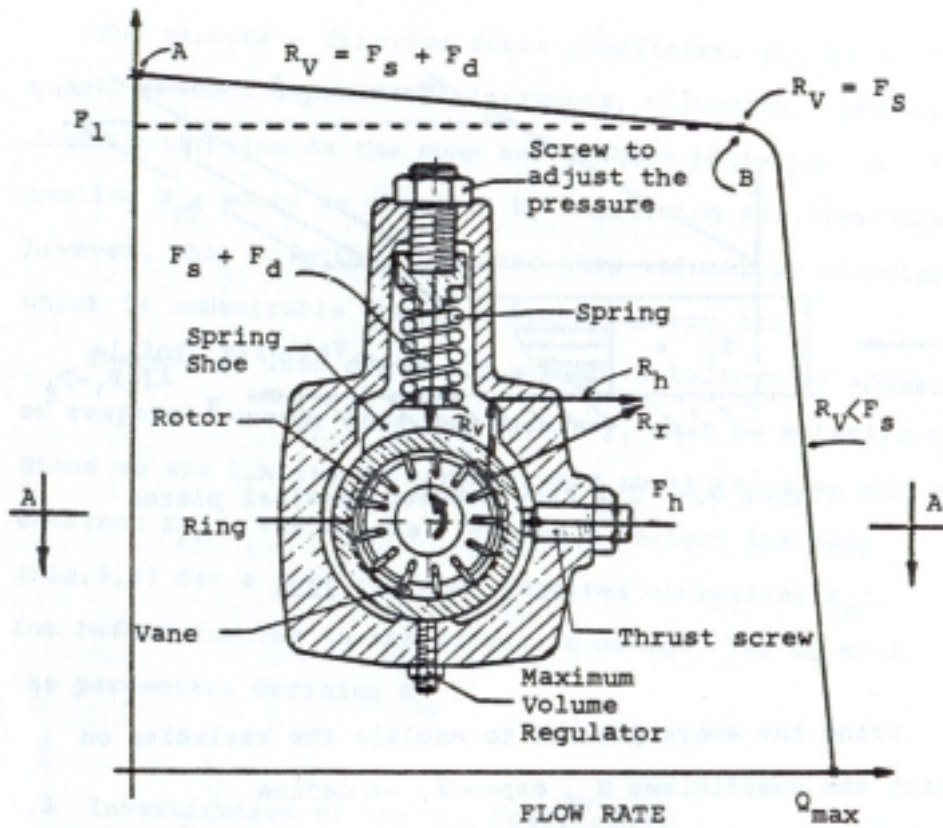


Figure 4: Typical variable displacement vane pump

Again, by quick pump response we mean “fast” pressure build up due to system flow demand Q_p (flow disturbance). For a given operating point pump dynamic behavior is defined by the values of M , B_{vf} and K_{sp} , dominated by the ratio B_{vf} / K_{sp} . For a typical pump B_{vf} / K_{sp} is in the range of 10^{-2} ($B_{vf} / K_{sp} = 0.05$), and the ratio $M / K_{sp} = 1 / \omega n^2$ in the range of 10^{-6} ($\omega n = 1068$ rad / sec), the other parameters being constant. Pump P_{op} / Q_p (s) transfer function can therefore be simplified to a second order system in the denominator, and a first order system with a time constant B_{vf} / K_{sp} in the nominator, equation no. (10).

$$\frac{P_{op}}{Q_p} = \frac{-\left[\frac{K_{sp}}{K_{pv}NKe + K_{sp}K_{lk}}\right] \left(\frac{B_{vf}}{K_{sp}}S + 1\right)}{\left[\frac{B_{vf}Cc + MK_{lk}}{K_{pv}NKe + K_{sp}K_{lk}}\right]S^2 + \left[\frac{B_{vf}K_{lk} + K_{sp}Cc}{K_{pv}NKe + K_{sp}K_{lk}}\right]S + 1}$$

This transfer function is usually used in the literature as the mathematical model for pump dynamic behavior. For a fast dynamic response the nominator time constant B_{vf} / K_{sp} has to be small, i.e. B_{vf} small and K_{sp} large.

INVESTIGATION OF THE B_{vf} PARAMETER

We assume that the K_{pv} , N , Ke , Cc , K_{lk} parameters are not controllable by the designer, and we can't choose a stiff spring constant K_{sp} , due to stability constraints. The B_{vf} parameter is a function of the oil viscosity, ring clearances and leakage patterns. Smaller B_{vf} can be obtained by increasing clearances, however this would decrease volumetric efficiency and increase energy losses. We shall concentrate now on minimizing B_{vf} .

$$B_{vf} = \mu l h / \delta \quad (11)$$

It is directly proportional to gap / friction surface, ($l \times h$) and inversely to gap clearance δ , therefore to get smaller B_{vf} we need bigger gap clearances and less ring friction. The flow between the plates, leakage in our case,

$$Q_{leak} = [(h \delta^3) / (12 \mu l)] \Delta p \quad (12)$$

Is directly proportional to the pump pressure drop Δp and sensitive to clearance δ^3 , meaning bigger gap higher leakage. On the other hand we need bigger gaps for smaller B_{vf} , definitely contradicting requirements.

Referring to pump construction to define the parameters in Q_{leak} and B_{vf} equations, let us look at pump cross section in figure 5. Ring is “pressed” between two plates

which seal the pumping chambers. Leakage Q_{leak} is proportional to pressure drop Δp between Delivery port (High pressure) to Suction port (Low pressure).

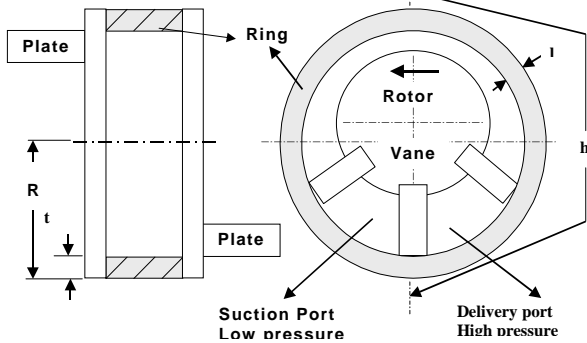


Figure 5: Pump ring – rotor configuration

Explanation of parameters l , h , δ : dimensions $h \sim \pi R$ and $l = t$, in B_{vf} parameter, friction surface $h \times l = 4 \pi R l$. The conclusion is that B_{vf} is large because the friction surface $4 \pi R l$ is large and gap is small (\sim zero), since as mentioned earlier ring is “pressed” between plates, an inherent construction in vane pumps.

THE NEW PUMP DESIGN

Having performed qualitative and quantitative analyses of parameters B_{vf} and K_{sp} , affecting pump speed of response, we came to the following conclusions:

1. – The spring constant K_{sp} is defined by regulating accuracy requirements and stability constraints, result of a trade-off process to reach its final numerical value.
2. – Parameter B_{vf} which depends on pump physical parameters $B_{vf} = \mu l h / \delta$, can be controlled by designer, and can be modified by re-designing the pump.

We suggest the following re-design procedure:

1. – Substantially increase the clearance δ , and decrease ring friction surface $h \times l$ ($4 \pi R l$), obtaining a much, much smaller B_{vf} parameter.
2. – Eliminating the pressure drop Δp across the ring, thus eliminating (minimizing) leakage Q_{leak} .
3. – Utilization of a piston to balance the pressure setting spring and doing so obtain higher flexibility in choosing the spring constant K_{sp} .

The following figure shows the new pump regulating ring, the balancing piston, and the two pressure equalizing chambers P_i and P_o .

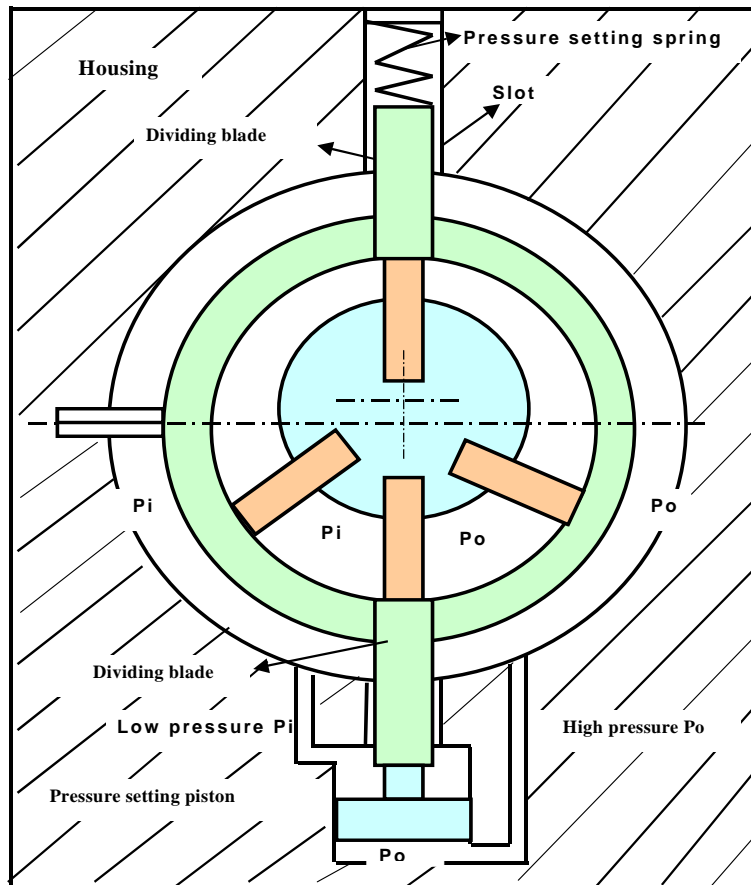


Figure 6: The “new pump” with the re-designed ring

The pressure equalizing chambers P_i and P_o eliminate Q_{leak} which is now limited across the two dividing blades, in the slots close to the spring and to the piston. Blades and ring are manufactured in one piece.

Rotor, vanes and dividing blades have the same width H and ring width is $h = H - 2\delta$. Clearance δ is now large, enables oil to enter both sides of the ring to be pressure balanced ($\Delta p = 0$ and $Q_{leak} = 0$). Side force is balanced by the thrust screw, so dividing blades can move freely in their slots. Since the ring is pressure balanced, the regulating force is zero, vertical regulation is provided by the newly designed piston actuated by the differential pressure $P_o - P_i$. Parameter K_{pv} is replaced now by the piston area A_p which can be designed at will.

Before we conclude the paper with a quantitative evaluation of an improved pump under the new conditions, let us summarize what are the achievements of our study and the concurrent re-design.

1 – Ring is pressure balanced $\Delta p = 0$, in both, high and low pressure chambers. The only forces on the ring are spring and piston, so it is designed with smaller thickness (5 mm not 9.5 mm) and smaller mass M .

2 – No case drain leakage $Q_{leak} \sim 0$ (or close to zero).

Almost no leakage means energy saving and overall higher pump efficiency. The leakage across the dividing blades is negligible, parameter K_{lk} is negligible.

3 – Regulating method is now based on piston force $A_p * (P_o - P_i)$ balancing the spring force $F_s + F_d$. We can control regulating force by varying the area A_p , which enables enormous flexibility in choosing spring K_{sp} .

4 – Finally, we decrease substantially the friction area between the ring and the plates ($h * l$) at least by an order of magnitude, and control the gap δ , so the friction coefficient $B_{vf} = \mu l h / \delta$ is decreased significantly.

SUMMARY OF RESULTS

We shall summarize now the concluding results of our study / investigation relating to a specific pump with the following parameters, see figure 7.

$$\S \delta_{new} = 2 \times \delta_{old}$$

or greater, depending on the oil viscosity

$$\S B_{vf\ new} = 1 / 20 B_{vf\ old}$$

after substituting the new parameters

$$\S M_{new} = 1 / 2.3 M_{old}$$

smaller ring mass due to new design

$$\S G_{ss} = - 1 / [K_{lk} + N K_e (K_{pv} / K_{sp})]$$

Steady state gain which was dominated by the ratio K_{pv} / K_{sp} is now controlled by A_p / K_{sp} .

$$\S K_{sp\ old} = 30 N / bar$$

obtained from accuracy / stability considerations

$$\S K_{sp\ new} = 1.75 K_{sp\ old}$$

$$\S D = 25mm \quad (A=490 \text{ mm}^2) \text{ Piston of diameter (Area)}$$

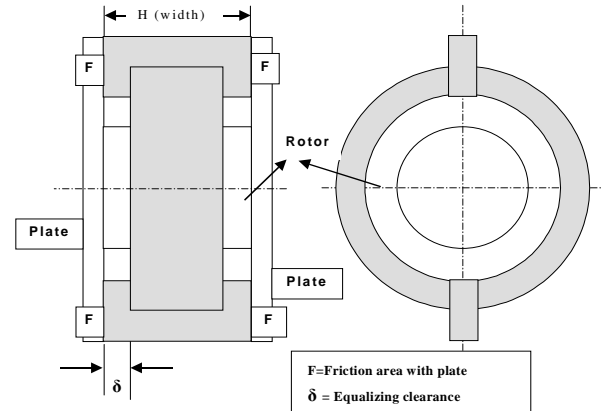


Figure 7: The new ring

The new design gives the designer an additional degree of freedom and grate flexibility to control pump speed of response without effecting accuracy and disturbance resistance. The final result of our study and re-design in B_{vf} / K_{sp} ratio is a tremendous improvement in pump dynamic response (band width) !

$$B_{vf} / K_{sp\ new} = 1/35 B_{vf} / K_{sp\ old}$$

CONCLUSIONS AND FURTHER STUDY

- The paper describes the application of control theory, analysis, evaluation and improvement of vane pump based on a Dynamic Model provided in the literature.
- The analysis concluded in the pump re-design, several of its important parameters, and in significant improved pump dynamic behavior (fast speed of response).
- In order to validate the results, a prototype has to be built and tested to study the actual pump behavior.
- The improved high bandwidth vane pump could now be utilized in high performance hydraulic servo systems.
- The new pump could be a part of the new generation hydraulics- Integrated Hydraulic System (pump, control servo-valve, actuator, sensors integrated in one unit).
- The governing mathematical model, the algorithms defining pump behavior, should be implemented in software and computer analyzed for optimization.

REFERENCES

1. Arie Perry
A theoretical and experimental study of hydraulic power supplies, Ph.D. Thesis, 1983, The Ohio State University Columbus, Ohio, USA
2. Herbert E. Merritt, Hydraulic Control Systems, 1967, John Wiley & Sons, USA
3. John F. Blackburn, Gerhard Reethof, J, Lowen Shearer, Fluid Power Control, 1969, MIT Press, USA

ROBUST CONTROL OF AN ELECTROHYDRAULIC SERVO SYSTEM UTILIZING ONLINE ESTIMATE OF ITS NATURAL FREQUENCY

Hideki YANADA* and Kazumasa FURUTA**

* Department of Mechanical Engineering, Faculty of Engineering
Toyohashi University of Technology
1-1, Hibarigaoka, Tempaku-cho, Toyohashi, 441-8580 Japan
(E-mail: yanada@mech.tut.ac.jp)

** Harmonic Drive Systems, Inc.
1856-1, Oaza-maki, Hotaka-machi, Minamiazumi-gun, 399-8305 Japan

ABSTRACT

This paper deals with online parameter estimation of an electrohydraulic servo (EHS) system and with robust control of the EHS system utilizing the parameter estimated online. In this study, the natural frequency of the EHS system is estimated using pressure sensors based on the equation of motion and equation of continuity, and the estimate of the natural frequency is utilized to enhance the robustness of the EHS system combined with a parallel feed-forward compensator (PFC). The optimal value of one of the PFC parameters is strongly influenced by the natural frequency of the EHS system and is adaptively varied using the estimate of the natural frequency. It is shown that the natural frequency of the EHS system can be estimated relatively accurately using the method proposed, and that the robustness of the EHS system to the plant parameter variations can be enhanced by adapting the PFC parameter.

KEY WORDS

Electrohydraulic servo system, Robust control, Parameter estimation, Parallel feedforward compensator

NOMENCLATURE

A_i :	piston area (i=1,2)	t :	time
B_e :	effective bulk modulus of fluid	u_p :	control input (servo current)
e_y :	error ($= y_p - y_m$)	V_i :	volume of fluid under compression (i=1,2)
F_L :	external force plus frictional force of cylinder	v :	piston velocity
J_e :	evaluation function	x_s :	spool displacement
K :	gain of EHS system	y_a :	output of augmented plant
k_e :	proportional gain	y_m :	output of reference model
m :	load mass	y_f :	output of PFC
p_i :	pressure (i=1,2)	y_p :	piston displacement
p_s :	supply pressure	α :	PFC parameter
q_i :	flow rate (i=1,2)	β :	PFC parameter
r :	reference input	ζ :	damping ratio of EHS system
s :	Laplace variable or differential operator	λ_h :	break frequency of highpass filter
		λ_l :	break frequency of lowpass filter
		ω_n :	natural angular frequency of EHS system

INTRODUCTION

An electrohydraulic servo (EHS) system usually suffers from parametric variations and disturbances. When the magnitudes of the parametric variations and/or the disturbances are large, the control performance of the EHS system degrades to some or a great degree even in the case where a robust control scheme such as sliding mode control or H infinity control is used. In such a case, an adaptive algorithm needs to be incorporated. This paper treats an online estimation of the natural frequency of the EHS system, which is the most important of the linearization parameters, as well as the update of the controller parameters using the estimate of the natural frequency.

Simple adaptive control (SAC) theory is considered to be one of the most promising control theories due to its simple structure and high robustness [1-3]. In order for the SAC scheme to be applied, a plant must be almost strictly positive real (ASPR). Most plants including EHS systems, however, do not satisfy the ASPR condition. In such a case, a feedforward compensator is added in parallel with the plant, and the compensator is called the parallel feedforward compensator (PFC). The PFC is added in order for the augmented plant, which is the parallel combination of the plant and the PFC, to satisfy the ASPR conditions [1].

Some methods to determine the structure of the PFC have so far been proposed [1], but no clear method to determine the parameters included in the PFC has been proposed to date. Because of this, the PFC parameters are usually determined by trial and error. The PFC parameters have a strong influence on both the ASPR conditions and the response characteristic of the plant output. In addition, the optimal values of the PFC parameters are strongly dependent on the plant parameters. Therefore, the control performance may degrade when the plant parameters are largely varied, even though the ASPR conditions are maintained.

This investigation aims at developing a robust controller by which a good performance is always attained even under large variations of the EHS system's parameters. In this paper, a method to tune the PFC parameters online, which is based on the value of the natural frequency of the EHS system estimated online, is proposed and the usefulness of the scheme is examined. The organization of the paper is as follows. First, the EHS system used is described, Second, the structure of the PFC used and the ASPR conditions of the augmented plant are given. Third, the selection criterion of the PFC parameters is proposed. Fourth, the online estimation algorithm of the natural frequency of the EHS system is presented. Fifth, the simulation and experimental results are given. Finally, the conclusion is described.

CONTRL SYSTEM HARDWEAR

In this paper, the position control of an EHS system is treated. Figure 1 shows a schematic of the EHS system for position control. The stroke, the internal diameter and the piston rod diameter of the hydraulic cylinder are 0.2m, 0.032m and 0.018m, respectively. The rated flow rate, pressure and current of the servo valve are $7.5 \times 10^{-4} \text{ m}^3/\text{s}$, 14MPa and 0.03A, respectively. The reference input, r , which is supplied by a function generator, and the outputs of a potentiometer and pressure sensors are read into a computer through a 12 bit analogue-to-digital (A/D) converter. The control input is calculated by the computer according to a control scheme and supplied to a servo-amplifier through a 12 bit digital-to-analogue (D/A) converter.

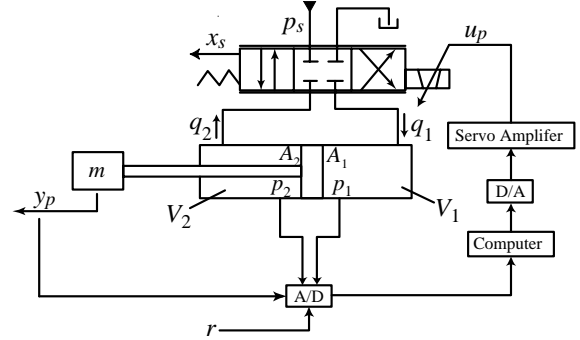


Figure 1 Schematic of position control EHS system

PFC AND ASPR CONDITION

By approximating the asymmetric cylinder as a symmetric one and by neglecting the dynamics of the servo valve, the transfer function of the EHS system can be given by

$$G_p(s) = \frac{Y_p(s)}{U_p(s)} = \frac{K\omega_n^2}{s(s^2 + 2\zeta\omega_n + \omega_n^2)} \quad (1)$$

where Y_p and U_p are the Laplace transforms of the plant output (position), y_p , and the control input (servo current), u_p , respectively.

A PFC is added to the plant as shown in Fig.2. The transfer function of the PFC can be given by the following equation [4]:

$$G_{pfc}(s) = \frac{\beta(s+11\alpha)}{(s+\alpha)^2} \quad (2)$$

The augmented plant is given by $G_a(s) = G_p(s) +$

$G_{pfc}(s)$. The ASPR conditions for an SISO system are given by the following [5]:

- C1) The relative degree is 0 or 1.
- C2) The coefficient of the highest-order term in the numerator polynomial is positive.
- C3) The system is minimum phase.

The above conditions C1 and C2 can be easily satisfied by selecting the PFC as given by Eq.(2) with $\beta > 0$. By applying the Hurwitz's stability criterion to the numerator polynomial of the augmented plant, $G_a(s)$, it can be seen that the condition C3 holds if the PFC parameters are selected to satisfy the following inequality:

$$\begin{aligned}
 & -121 \frac{\beta}{K} \left(\frac{\alpha}{\omega_n} \right)^3 + (2662 \frac{\beta}{K} + 440) \zeta \frac{\beta}{K} \left(\frac{\alpha}{\omega_n} \right)^2 \\
 & + \left[484 \zeta^2 \left(\frac{\beta}{K} \right)^2 + 84 \zeta^2 \frac{\beta}{K} + 99 \frac{\beta}{K} + 18 \right] \frac{\alpha}{\omega_n} \\
 & + 22 \zeta \left(\frac{\beta}{K} \right)^2 + 26 \zeta \frac{\beta}{K} + 4 \zeta > 0
 \end{aligned} \quad (3)$$

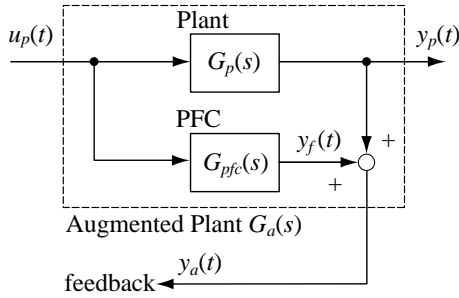


Figure 2 Augmented plant

Equation (3) shows that whether the augmented plant is ASPR or not is determined by three dimensionless parameters: α/ω_n , β/K and ζ . Substituting variable values into the three dimensionless parameters and calculating Eq.(3) yield the boundary surface between the ASPR and non-ASPR regions as shown in Fig.3. As can be seen from Fig.3, taking into account the fact that the value of ζ is seldom less than 0.1 for EHS systems, the augmented plant becomes ASPR when the value of α/ω_n is in the range $0 < \alpha/\omega_n \leq 2$. In addition, the ASPR region widens with increasing ζ , and the value of β/K does not have a great influence on the ASPR condition. Therefore, if the value of α/ω_n can be kept in the range $0 < \alpha/\omega_n \leq 2$ even under a large variation of ω_n , it is possible for the augmented plant to be ASPR.

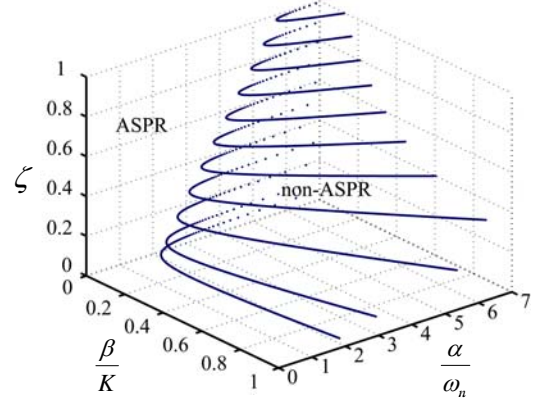


Figure 3 Boundary surface between ASPR and non-ASPR regions

SELECTION CRITERION OF PFC PARAMETERS

Even if the augmented plant is ASPR, the response of the plant may be oscillatory or slow. In order to find out the optimal values of α/ω_n and β/K , the tracking performance was examined in simulation using the feedback system shown in Fig.4 under the variable conditions of the plant and PFC parameters. The simulation was conducted using MATLAB/Simulink.

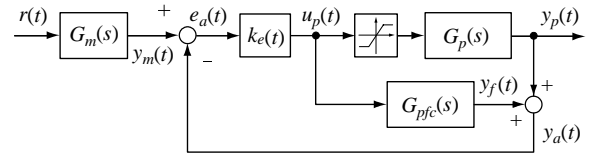


Figure 4 Evaluation system of tracking performance

A rectangular reference input whose value and frequency are 0.10 ± 0.05 m and 0.3 Hz was used. The tracking performance was evaluated by the following function:

$$J_e = \int_0^{t_f} |e_y(t)| dt \quad (4)$$

$$e_y(t) = \begin{cases} y_p(t) - y_m(t) & |y_p(t) - y_m(t)| > \varepsilon \\ 0 & |y_p(t) - y_m(t)| \leq \varepsilon \end{cases} \quad (5)$$

$(\varepsilon = 0.0002\text{m})$

where t_f stands for half of the period of the rectangular input.

Figures 5 and 6 show examples of the simulation results. Though not clearly seen from Figs.5 and 6, the simulations have shown the following:

- R1) The range of α/ω_n where the evaluation function becomes minimum is hardly changed by the values of the plant parameters and β , and is $1 \leq \alpha/\omega_n \leq 3$.
- R2) The range of β/K where the evaluation function becomes minimum is affected by the values of ζ and α and hardly affected by the other parameters.

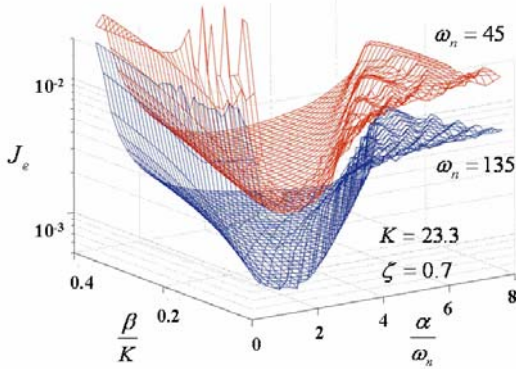


Figure 5 J_e vs. dimensionless PFC parameters (effect of ω_n)

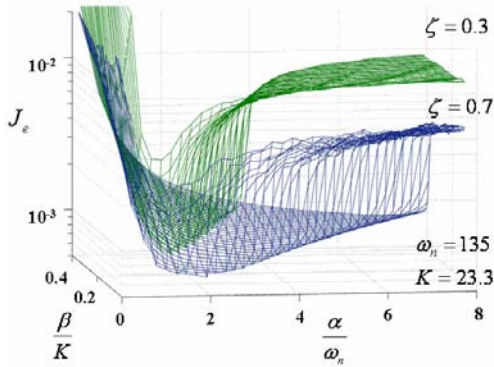


Figure 6 J_e vs. dimensionless PFC parameters (effect of ζ)

Taking these results and the results regarding the ASPR conditions given in the previous section, a method to determine the PFC parameters is proposed as follows:

- P1) For the parameter α , an arbitrary value in the range of $1 \leq \alpha/\omega_n \leq 2$ is selected, e.g., $\alpha = 1.5\omega_n$. In the control scheme proposed in this paper, the value of α is varied according to the variation of ω_n .
- P2) For the parameter β , a constant value is used. The value is determined by trial and error in order that a good response is obtained under the condition of the

maximum K and the minimum ζ .

ESTIMATION OF NATURAL FREQUENCY

A theoretical expression of the natural angular frequency of the EHS system shown in Fig.1 can be give by

$$\omega_n = \frac{A_1 + A_2}{2} \sqrt{\frac{B_e}{m} \left(\frac{1}{V_1} + \frac{1}{V_2} \right)} \quad (6)$$

The values of the piston areas are known and those of the volumes in the cylinder can be known by measuring the piston position. Therefore, if the values of the load mass and effective bulk modulus of fluid can be obtained, the value of the natural frequency can be calculated. In this paper, the values of the mass and effective bulk modulus are estimated online separately using the equation of motion and equation of continuity, respectively.

The equation of motion of the system shown in Fig.1 is written by

$$m \frac{dv}{dt} = p_1 A_1 - p_2 A_2 - F_L \quad (7)$$

Multiplying both sides of Eq.(7) by $1/(s + \lambda_l)$ (a first-order lowpass filter) and $s/(s + \lambda_h)$ (a first-order highpass filter, $\lambda_h \ll \lambda_l$) yields

$$m(v_h - \lambda_l v') = A_1 p'_1 - A_2 p'_2 \quad (8)$$

where

$$v_h = \frac{s}{s + \lambda_h} v, \quad v' = \frac{s}{(s + \lambda_h)(s + \lambda_l)} v$$

$$p'_1 = \frac{s}{(s + \lambda_h)(s + \lambda_l)} p_1, \quad p'_2 = \frac{s}{(s + \lambda_h)(s + \lambda_l)} p_2 \quad (9)$$

In the derivation of Eq.(8), an assumption $sF_L = \dot{F}_L \approx 0$ was introduced. The velocity, v , is estimated by a Kalman filter and the pressures, p_1 and p_2 , are measured by pressure sensors.

By letting the estimate of m be \hat{m} , the prediction error ε_m is defined as

$$\varepsilon_m = \hat{m} \varphi_m - (A_1 p'_1 - A_2 p'_2) \quad (10)$$

$$\varphi_m = v_h - \lambda_l v' \quad (11)$$

Using the weighted least-squares method, a parameter update law is derived, which is given in discrete form

by

$$\hat{m}(k) = \hat{m}(k-1) - \frac{\gamma_m(k-1)\varphi_m(k)}{\lambda + \varphi_m^T(k)\gamma_m(k-1)\varphi_m(k)} \varepsilon_m(k) \quad (12)$$

$$\gamma_m(k) = \frac{1}{\lambda} \left[\gamma_m(k-1) - \frac{\gamma_m^2(k-1)\varphi_m^2(k)}{\lambda + \varphi_m^2(k)\gamma_m(k-1)} \right] \quad (13)$$

where λ is the weight and

$$\hat{m}(0) = \hat{m}_0, \quad \gamma_m(0) = \gamma_{m0} > 0$$

The equations of continuity are described by

$$\frac{V_1}{B_e} \frac{dp_1}{dt} = q_1 - A_1 v \quad (14)$$

$$\frac{V_2}{B_e} \frac{dp_2}{dt} = A_2 v - q_2 \quad (15)$$

Likewise, multiplying both sides of Eqs.(14), (15) by $1/(s + \lambda_i)$ and substituting the estimate, \hat{B}_e , for B_e yield the following prediction error:

$$\varepsilon_{B_e} = \hat{B}_e^{-1} \varphi_{B_e} - [q_{1l} + q_{2l} - (A_1 + A_2)v_l] \quad (16)$$

$$\varphi_{B_e} = V_1(p_1 - \lambda_1 p_{1l}) - V_2(p_2 - \lambda_2 p_{2l}) \quad (17)$$

where the subscript l indicates the lowpass filtered variables. The values of the flow rates, q_1 and q_2 , are calculated using the nonlinear flow rate characteristic equations of the servo valve; the spool displacement is estimated by assuming the spool dynamics as the first-order system. A parameter update law for \hat{B}_e similar to Eqs.(12),(13) is obtained.

By substituting \hat{m} and \hat{B}_e for m and B_e in Eq.(6), the estimate, $\hat{\omega}_n$, of ω_n can be calculated.

RESULTS

In this investigation, in order to make clear the effect of the online tuning of the PFC parameter, a simple proportional control with a variable gain shown in Fig.7 was used. The block written as Estimator includes the algorithm to estimate the natural frequency. The PFC parameter α was adaptively varied according to the variation of the value of the natural frequency; the adaptive rule was $\alpha = 2\hat{\omega}_n$. Another parameter β was kept at a constant value determined offline in advance. The proportional gain was generated according to the following adaptive rule with a constant weight, γ :

$$k_e(t) = k_{e0} + \gamma |e_a(t)| \quad (18)$$

$$e_a = y_m - y_a \quad (19)$$

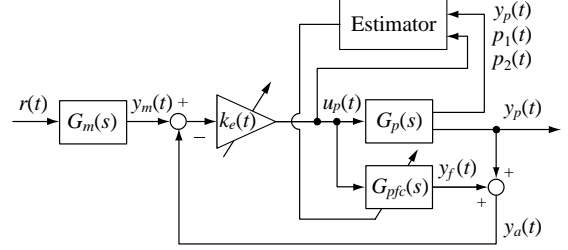


Figure 7 Block diagram of control system

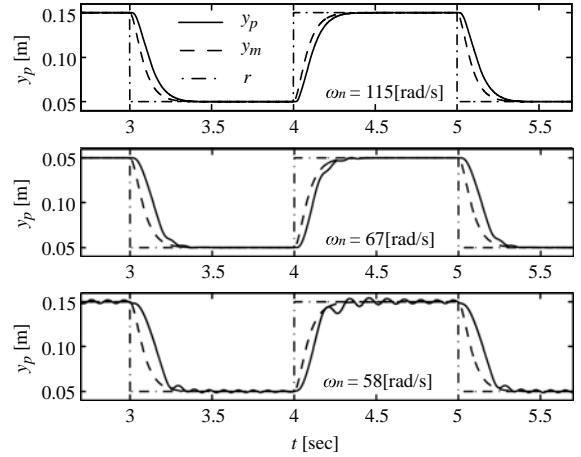


Figure 8 Simulation results under constant α (conditions: $\alpha = 2\hat{\omega}_n$, $\hat{\omega}_n = 115$ rad/s (fixed), $\beta = 0.52$)

Figure 8 shows simulation results obtained under the condition that the PFC parameter α was kept at a certain value. When the natural frequency of the EHS system is identical to the design value (115 rad/s, upper figure), the response is good. In case where the natural frequency is decreased to 67 rad/s (middle figure) due to the increase of the load mass and/or the decrease of the stiffness of the fluid, the response is deteriorated to some degree but not bad. In this case, the real value of α/ω_n is 3.4. However, a further decrease in the natural frequency to 58 rad/s, which leads to the increase in α/ω_n to 4.0, causes an oscillatory motion (lower figure). As can be seen from Fig.8, the control performance may be deteriorated under a constant α when the variation of the plant parameters is large.

Figure 9 shows a simulation result obtained when the estimation of the natural frequency and the adaptation of the parameter α were made. Before $t = 5$ sec, the

parameter α is fixed at a constant value (230rad/s) designed using the value of the natural frequency initially estimated (115rad/s). In the same manner as the lower figure in Fig.8, an oscillatory motion takes place. At the instant the estimation of the natural frequency and the adaptation of α accompanying it start at $t = 5$ sec, the response becomes smooth. This is because, as can be seen from the lower figure in Fig.9, the natural frequency can be quickly estimated in a relatively good accuracy. The usefulness of the control scheme proposed has been demonstrated by simulation.

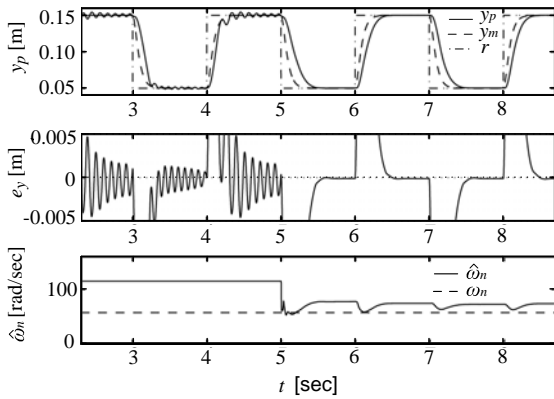


Figure 9 Simulation result under adaptive α (conditions: $\alpha = 2\hat{\omega}_n$. $\hat{\omega}_n$ is estimated online. $\beta = 0.52$. Initial value of ω_n used for PFC design is 115rad/s. Real value of $\omega_n = 58$ rad/s. Estimation of ω_n and adaptation of α start at $t = 5$ sec.)

An experimental result is shown in Fig.10. The experimental conditions are almost the same as those in the simulation shown in Fig.9, except for the initial value of the natural frequency of the EHS system. The dashed and dash-dot lines in the lower figure in Fig.10 show the values of the natural frequency estimated offline by two methods: the least-squares method using the ARX model and the self-excited vibration method [6]. The results obtained by the two estimation methods are roughly identical and the mean value (60rad/s) of the two can be regarded as the true natural frequency. The response is very steep in the vicinity of the reference input ($y_p = r = 0.15$ m) before the adaptation of α begins at $t = 5$ sec. However, after the beginning of the adaptation of α at $t = 5$ sec, the response becomes smooth near both at $y_p = r = 0.15$ m and at 0.05m. The estimation of the natural frequency is made relatively quickly and accurately, though not so fast compared to the simulation shown in Fig.9. The usefulness of the control scheme proposed has been demonstrated also by experiment.

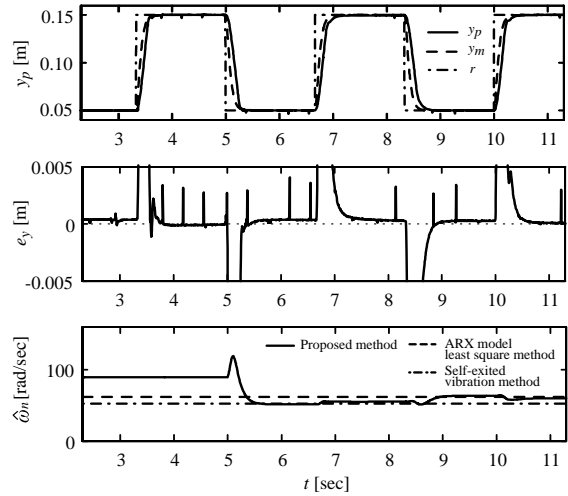


Figure 10 Experimental result under adaptive α (conditions: $\alpha = 2\hat{\omega}_n$. $\hat{\omega}_n$ is estimated online. $\beta = 4.2$. Initial value of ω_n used for PFC design is 90rad/s. Real value of $\omega_n \approx 60$ rad/s. Estimation of ω_n and adaptation of α start at $t = 5$ sec.)

CONCLUSION

In this paper, a criterion to determine the values of the PFC parameters, an online estimation method of the natural frequency of an EHS system and an adaptive, robust control scheme with the PFC have been proposed. It has been shown that the natural angular frequency can be estimated online in a relatively good accuracy by the method proposed, and that the control performance of the EHS system can be enhanced by adaptively changing a PFC parameter according to the variation of the natural frequency.

REFERENCES

1. Kaufman, H., Barkana, I. and Sobel, K., Direct Control Algorithms : Theory and Applications, Springer, 1997.
2. Iwai, Z., Egarashi, T., Hino, M., Takahashi, M. and Kyoizumi, K., Trans. Japan Soc. Mech. Engrs. (Ser. C), 1995, **61**-590, pp.3991-3998.
3. Tsukamoto, N. and Yokota, S., Trans. Japan Fluid Power System Soc., 2003, **34**-6, pp.126-133.
4. Iwai, Z. and Mizumoto, I., Int. J. Control, 1992, **55**-6, pp.1453-1470.
5. Zeheb, H., IEEE Trans., 1986, **AC-31**-11, pp.1055-1057.
6. Nishiumi, T., Ichiyangi, T., Katoh, H. and Konami, S., Trans. Japan Fluid Power System Soc., 2005, **36**-1, pp.1-7.

DESIGN OF ROBUST POSITION/PRESSURE CONTROLLER FOR CYLINDER USING HYDRAULIC TRANSFORMER

Tomohiro UENO*, Kazuhisa ITO**, Weidong MA*** and Shigeru IKEO**

* Division of Science and Technology, Graduate school of SOPHIA University

** Department of Mechanical Engineering, Faculty of Science and Technology
Sophia University

7-1 Kioicho, Chiyoda-ku, Tokyo 102-8554, Japan

(E-mail: {tomohi-u,s_ikeo}@sophia.ac.jp, kazu-ito@me.sophia.ac.jp)

*** Basic Technology R&D Center, Engineering & Production Div.

Kayaba Industry Co., Ltd.

1-12-1 Asamizodai, Sagamihara-shi, Kanagawa 228-0828, Japan

(E-mail:ma-wei@kyb.co.jp)

ABSTRACT

In this paper, the position/pressure control of a hydraulic cylinder using a hydraulic transformer is studied. A hydraulic transformer based on FFC pump/motor is used as a control component to drive the cylinder with a load horizontally. The two-degree-of-freedom (2DOF) design technique is applied to obtain the positioning controller with tracking performance and robustness for uncertainties while the structure of pressure controller is given by internal model principle to compensate stepwise disturbance. With these controllers the nonlinear friction torque, the leakage of the transformer and the load force acting on the cylinder can be compensated and the experimental results show that the sufficient accuracy of position and pressure are obtained.

KEY WORDS

CPS, Hydraulic transformer, Position control, Pressure control, 2-DOF

NOMENCLATURE

A	: area of cylinder piston [m ²]	D	: displacement [cc/rev]
B_c	: viscous damping coefficient of cylinder [kg/s]	J	: moment of inertia [kg·m ²]
	viscous damping coefficient of transformer	q_{le}	: leakage flow [m ³ /s]
B_{ht}	: [kg·m ² /s]	F_L	: load force [N]
		m	: mass of load and piston [kg]
		p	: pressure [MPa]

- p_s : pressure of constant pressure source [MPa]
 p_{1r} : desired pressure of load [MPa]
 q : flow [m³/s]
 T : torque [N·m]
 T_f : nonlinear friction torque [N·m]
 y : cylinder displacement [mm]
 y_r : Desired cylinder piston position[m]
 ω : rotational speed [rad/s]
 k : rate of spring [N/mm]
 l : Initial distance from rod to spring[mm]

Subscripts

- 1 : cylinder head chamber
 2 : cylinder rod chamber
 A : variable unit of transformer
 B : fixed unit of transformer
 y : velocity controller
 P : pressure controller

INTRODUCTION

The importance of energy saving in hydraulic power transmission system is increasing. Since the valve control strategy of hydraulic cylinder drive systems has relatively larger pressure loss, especially for large cylinders, a hydraulic cylinder drive with hydraulic transformer has been developed. The circuit consists of constant pressure power source, transformer and cylinder, as shown in Figure 1. The hydraulic transformer is constructed by combining a fixed displacement pump/motor and a variable displacement one which are connected by a driving shaft. The power is transmitted from the transformer to the cylinder without controlling the valve. The major advantage is that energy can be recovered and stored in accumulator in the common pressure line when the cylinder is being retracted under load [1]-[3]. The hydraulic transformer used in this paper consists of two FFC pump/motor. The Fluid Force Couple (FFC) pump/motor has high efficiency in wide operating range [4], [5].

In this research, we consider a design of robust positioning/pressure controller of hydraulic cylinder with transformer. Disturbances, *e.g.* nonlinear friction torque, leakage flow of transformer and load force, affect the performance of the positioning/pressure controller. These effects can not be compensated only by feedforward controller because it is difficult to describe them mathematically in detail a priori. Moreover, to

accommodate some uncertainties on physical parameters, the feedback loop design is also used. Therefore in this paper, the 2DOF controller design method is introduced for positioning control, not only to compensate disturbance and parameter uncertainty but also to ensure the tracking performance for given drive pattern. 2 DOF method is now widely used in mechanical system control [6]-[9] and with is able to specify the performance quantitatively by adjusting controller parameters. And in pressure control, we design the controller via internal model principle to decide the structure. The cylinder is set horizontally and the load spring simulates a work in pressing machine. The proposed controllers are examined in experiment and evaluate its performance.

EXPERIMENTAL DEVICE AND DRIVE PATTERN

Experimental device

The schematic diagram of the experimental system used in this research is shown in Figure 1. The transformer is connected to the head side of hydraulic cylinder. In this research the rod side of a cylinder is connected to the constant pressure system to realize heavy load. The cylinder displacement y and displacement of transformer D_A , the rotational speed of transformer ω and pressure in cylinder head chamber p_1 are taken into a controller. The displacement of variable pump/motor is $D_{Amax}=48.9$ [cc/rev] and the displacement of fixed pump/motor is $D_B=19.6$ [cc/rev]. The diameter of hydraulic cylinder is 50[mm]. The rate of spring is $k=362.6$ [N/mm]. The Initial distance from rod to spring $l=157$ [mm].

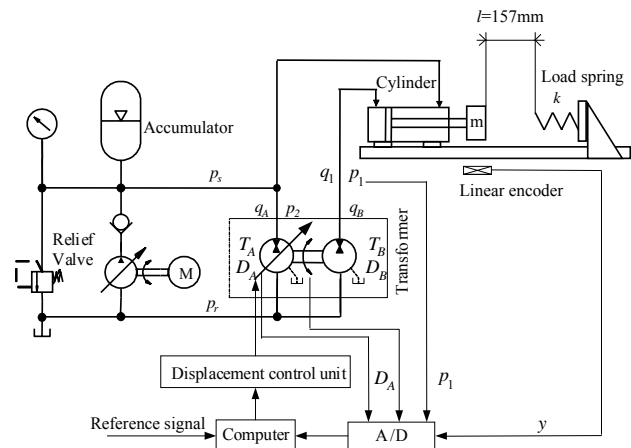


Figure 1 The experimental setup

Drive pattern

The drive pattern of the cylinder used in this research simulates the hydraulic pressing machines. Figure 2 shows a cylinder drive pattern used in this research. A load spring is supposed to be a work. In the cylinder position control, the reference step signal changes two

phases and this implies an actual approaching motion of pressing machines. The cylinder velocity is controlled in the higher velocities before reaching the load spring. After touching load spring, the controller keeps lower cylinder velocity until the pressure exceeds a predetermined threshold. Then we switch from the position control to the pressure control as a pressing process.

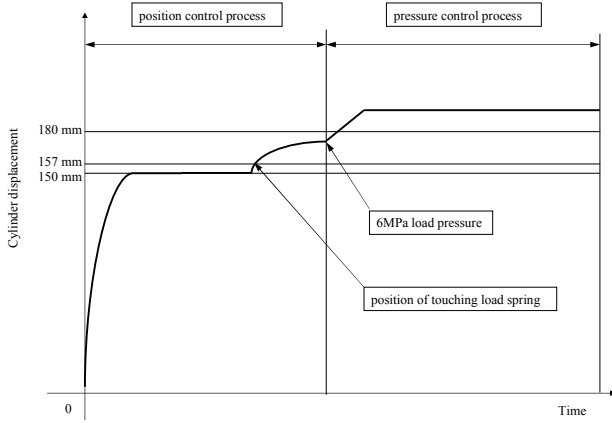


Figure 2 Cylinder drive pattern

MODELING

To derive the mathematical model of the system shown in Figure 1, we assume that the dynamics of piping are negligible and tank pressure $p_r=0$. The plant model can be reduced to lower dimension by ignoring the compressibility of the hydraulic oil. The leakage flow, the nonlinear friction torque and the load force are treated as disturbances. Then as the equation of motion of transformer, the flow rate and the cylinder motion, we obtain the following.

$$D_A p_s = J\dot{\omega} + B_{ht}\omega + D_B p_1 + T_f \quad (1)$$

$$q_1 = A_1 \dot{y} = \omega D_B - q_{le} \quad (2)$$

$$A_1 p_1 = m\ddot{y} + B_c \dot{y} + F_L = m\ddot{y} + B_c \dot{y} + A_2 p_2 + k(y-l) \quad (3)$$

$$F_L = \begin{cases} p_2 A_2, & \text{before contacting with spring} \\ p_2 A_2 + k(y-l), & \text{contacting with spring} \end{cases} \quad (4)$$

where l is the initial distance from cylinder to the load spring.

System model for positioning control

The cylinder displacement y is given as:

$$y(s) = G_y(s) (D_A(s) + d_y(s)) \quad (5)$$

where $G_y(s)$ is the transfer function of the nominal

system from D_A to y , and $d_y(s)$ is a disturbance which includes nonlinear friction torque T_f , leakage flow q_{le} and load force F_L , and $G_y(s)$ is given as:

$$G_y(s) = \frac{y(s)}{D_A(s)} = \frac{K_y}{J_y s^2 + B_y s} \quad (6)$$

$$K_y = \frac{D_B p_s}{A_1}, \quad J_y = J + \frac{D_B^2 m}{A_1^2}, \quad B_y = B_{ht} \quad (7)$$

$$d_y(s) = -\frac{D_B}{A_1 p_s} F_L(s) - \frac{1}{p_s} T_f(s) - \frac{J s + B_{ht}}{D_B p_s} q_{le}(s) \quad (8)$$

$$F_L(s) = p_2 A_2 + k(y-l) \quad (9)$$

System model for pressure control

On the other hand, the pressure in the cylinder head chamber p_1 is expressed as:

$$p_1(s) = G_{p1}(s) (D_A(s) + d_{p1}(s)) \quad (10)$$

where $G_{p1}(s)$ is a transfer function from D_A to p_1 and $d_{p1}(s)$ is a disturbance which includes nonlinear friction torque T_f , leakage flow q_{le} and load force F_L and $G_{p1}(s)$ is given as:

$$G_{p1}(s) = \frac{p_1(s)}{D_A(s)} = \frac{K_{p1}}{a_1 s^2 + a_2 s + a_3} \quad (11)$$

$$K_{p1} = D_B p_s (m s^2 + B_c s + k), \quad a_1 = A_1^2 J + D_B^2 m, \quad (12)$$

$$a_2 = A_1^2 B_{ht} + D_B^2 B_c$$

$$d_{p1}(s) = \frac{A_1 (J s + B_{ht}) s}{a_1 s^2 + a_2 s + a_3} F(s) - \frac{D_B (m s^2 + B_c s + k)}{a_1 s^2 + a_2 s + a_3} T_f(s) - \frac{(m s^2 + B_c s + k)(J s + B_{ht})}{a_1 s^2 + a_2 s + a_3} q_{le}(s) \quad (13)$$

$$F_L(s) = p_2 A_2 + k(y-l) \quad (14)$$

CONTROLLER DESIGN

In this paper, cylinder velocity control and force control is considered. Figure 3 and Figure 4 show block diagrams of the position and the pressure control systems, respectively. For notational convenience, subscripts y and p_1 stand for the cylinder position control system and the pressure control system, respectively. We design each controller via 2-DOF and internal model principle.

Position controller system

Figure 3 shows the block diagram of feedback type 2-DOF control system for position control. In this figure, r is desired position, u control input, y controlled variable, d disturbance, w disturbance from parameters variation, n sensor noise.

According to the parameterization of 2-DOF control system, controllers are given as

$$C_A(s) = \frac{1}{G_y(s)} \cdot \frac{Q(s)}{1-Q(s)} \quad (15)$$

$$C_B(s) = \frac{1}{G_y(s)} \cdot \frac{G_M(s)}{1-G_M(s)} \cdot \frac{1}{1-Q(s)} \quad (16)$$

where $G_M(s)$ is a reference model and $Q(s)$ is a stabilizing filter.

The transfer function from desired value r to controlled variable y is given as

$$W_{ry}(s) = \frac{y(s)}{r(s)} = \frac{C_B(s)G_y(s)}{1 + C_A(s)G_y(s) + C_B(s)G_y(s)} = G_M(s) \quad (17)$$

The sensitivity function $S(s)$ is given as

$$S(s) = \frac{y(s)}{w(s)} = \frac{1}{1 + C_A(s)G_y(s) + C_B(s)G_y(s)} = (1-Q(s))(1-G_M(s)) \quad (18)$$

The complementary sensitivity function $T(s)$ is given as

$$T(s) = \frac{y(s)}{n(s)} = \frac{C_A(s)G_y(s) + C_B(s)G_y(s)}{1 + C_A(s)G_y(s) + C_B(s)G_y(s)} = 1 - S(s) \quad (19)$$

The disturbance response is given as

$$W_{dy}(s) = \frac{y(s)}{d(s)} = \frac{G(s)}{1 + C_A(s)G_y(s) + C_B(s)G_y(s)} = S(s)G_y(s) \quad (20)$$

From Eq.(17), $W_{ry}(s)$ can be designed with $G_M(s)$, and from Eq.(18), (19) and (20) $S(s)$, $T(s)$ and $W_{dy}(s)$ can be designed with $G_M(s)$ and $Q(s)$. $S(s)$ is sensitivity index for disturbance rejection performance. And $T(s)$ is an index for robust stability and shows the sensor noise rejection performance. According to mixed-sensitivity design of H-Infinity control theory, it is desired that $S(s)$ is small in lower frequency domain while $T(s)$ is small in higher frequency domain in practical application.

In the case of positioning control, the $G_M(s)$ is considered as a second order model:

$$G_M(s) = \frac{1}{t_r^2 s^2 + 2\zeta_r t_r s + 1} \quad (21)$$

where $\omega_r (=1/t_r)$ and ζ_r are natural angular frequency and damping coefficient, respectively.

$Q(s)$ is given by the nominal model

$$Q(s) = \frac{3t_N s + 1}{t_N^3 s^3 + 3t_N^2 s^2 + 3t_N s + 1} \quad (22)$$

By substituting equations (21) and (22) into equation (15) and (16) and setting $B_n=0$, we have

$$C_A(s) = \frac{J_y}{K_y} \frac{3t_N s + 1}{t_N^3 s + 3t_N^2} \quad (23)$$

$$C_B(s) = \frac{J_y}{K_y} \frac{1}{s(t_r^2 s + 2\zeta_r t_r)} \frac{t_N^3 s^3 + 3t_N^2 s^2 + 3t_N s + 1}{t_N^3 s + 3t_N^2} \quad (24)$$

Before touching load spring, the controller parameters were selected as $t_r = 0.44$, $\zeta_r = 1.11$ and $t_N = 0.15$ to ensure the velocity response considering the saturation characteristic of displacement of variable displacement pump/motor. The primal stepwise reference position is 150[mm] and second one 180[mm]. After touching the load spring, the controller parameters were selected as $t_r = 1$, $\zeta_r = 1$ and $t_N = 0.15$ to push the load spring as slowly as possible.

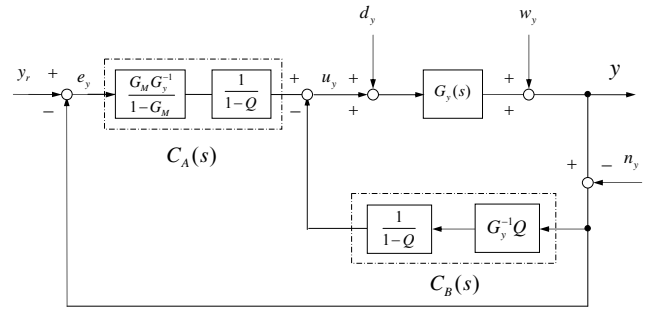


Figure 3 Cylinder position control system

Pressure control system

As the cylinder rod extends, the pressure p_1 increases. Therefore we switch the controller from position tracking to pressure tracking control imaging hydraulic pressing machines. Since the dynamics to be controlled is changed from Eqs. (6) to (11), the controller switching is made depending on the pressure threshold; when the threshold is exceeded, the controller is changed from position controller to pressure controller.

For given constant reference pressure, disturbance torque and leakage flow can be considered as constants. This implies that the controller should contain at least one integrator to track the reference pressure via internal model principle without steady state error. To consider a sufficient condition for the pressure controller, we define $G_{er}(s)$ and $G_{ed}(s)$ as transfer functions from reference $r(s)(=r_0/s)$ to error $e(s)$ and from input disturbance to error, respectively. Then, by applying the final value

theorem, the steady-state error e_∞ is given by

$$\begin{aligned}
 e_\infty &= \lim_{t \rightarrow \infty} e(t) \\
 &= \lim_{s \rightarrow 0} \{G_{er}(s)r(s) + G_{ed}(s)d(s)\} \cdot s \\
 &= \lim_{s \rightarrow 0} \left\{ \frac{1}{1 + G(s)C(s)} \frac{r_0}{s} - \frac{G(s)}{1 + G(s)C(s)} \frac{d_0}{s} \right\} \cdot s \quad (25) \\
 &= \lim_{s \rightarrow 0} \frac{r_0 - G(s)d_0}{1 + G(s)C(s)}
 \end{aligned}$$

where d_0 is constant disturbance gain.

This result shows that a controller should contain at least one integrator to make steady state error reduce to zero.

The controller of the following structure is then given as

$$C_{p1} = k_p + \frac{k_i}{s} \quad (26)$$

where k_p and k_i are PI control parameters to be determined.

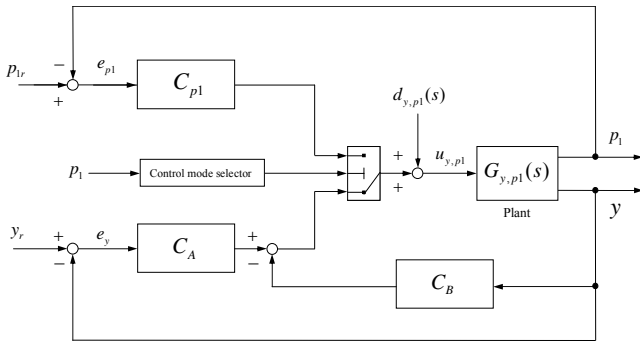


Figure 4 Positioning and pressure control system

EXPERIMENTAL RESULT AND CONSIDERATION

Figure 5 shows the experimental results on pressure in cylinder head chamber p_1 , cylinder displacement y and displacement of the variable unit D_A during position and pressure control. The constant system pressure is set to be 5[MPa] in all experimental results and the load mass $m=60$ [kg]. It is observed that the cylinder tracks to the reference model without the overshoot both in positioning and pressuring control phase. Moreover, we can see some delay in initial response, about 0.3[s]. This can be considered as the influence of dead zone in transformer. In the position control before reaching the load spring, good position tracking performance to reference model is achieved, and the settling time is about 4 seconds. In position control after touching load spring, the disturbances of nonlinear friction torque and load force of acting on cylinder can be compensated and

the settling time is about 0.5 seconds.

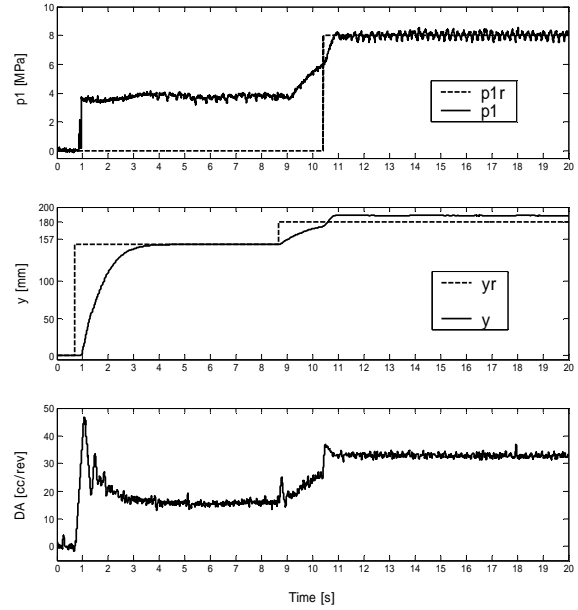


Figure 5 Experimental result

CONCLUSION

In this paper, the robust position/pressure control performance of cylinder using hydraulic transformer connected to constant pressure supply is examined. In positioning control, the feedback type 2-DOF controller is implemented and PI control system based on internal model principle is applied to pressure control. The experimental results show that the disturbances of nonlinear friction torque, the leakage of the transformer and load force of acting on cylinder can be compensated and the good positioning/pressuring accuracy is obtained. As a future work, we improve a speed of response by introducing nonlinear controller. Moreover the energy saving performance should be discussed.

REFERENCES

1. Feuser, A., Kordak, R. and Liebler, G., Hydrostatic Drives with Control of the Secondary Unit, The hydraulic Trainer, 1989, Vol.6, Mannesmann Rexroth GmbH., pp.62-66.
2. RICHTER, M., Moderne Antriebskonzepte im Pressenbau, Ölhdraulik und Pneumatik, 1996, Nr.40-10, pp.688-694.
3. Nakao, H, Transformer and its control, Hydraulics & Pneumatics, 1999, Vol.38, No.13, pp.13-18 (in Japanese).
4. Ma, W., Ikee S., Research on hydraulic cylinder

driving system using hydraulic transformer, Proc. of FLUCOME'03, 2003, CD-ROM

5. Kita, Y., Nomura, Y., Nakakohji, Y. and Sugawara, Y., New variable displacement pump/motor, FLUCOME '85, 1985, pp.467/472
6. Umeno, T. and Hori, Y., Design of Robust Servosystems Based on the Parametrization of Two Degree of Freedom Control Systems, Trans. IEE Japan, 1989, Vol.109-D, No.11 (in Japanese).
7. Dote, Y., Harashima, F.: Motion control, Corona publishing, 1993, pp.93-108 (in Japanese).
8. Yamamoto, T. and Yokota S., Application of H_∞ control theory for 2-DOF control system, Trans. JSME, 1998, Ser. C, Vol. 64, No. 617, pp. 177/184 (in Japanese).
9. Mochizuki, Y. and Matsui, T., A design of two-degree-of-freedom digital controller, Trans. JSME, 1992, Ser. C, Vol.58, No.538, 1992, pp.1086 /1091 (in Japanese).
10. Ma, W. and Ikeo, S., Position control of hydraulic cylinder using hydraulic transformer, Transactions of JFPS, 2003, Vol.34, No.5, pp.99/105 (in Japanese).
11. Ma, W., Ikeo, S. and Ito, K., Position Control of Hydraulic Cylinder Using Hydraulic Transformer, Trans. JSME, 2004, Ser. C, Vol.70, No. 694, pp. 1758/1763 (in Japanese).

TRENDS IN DESIGN OF WATER HYDRAULICS

- MOTION CONTROL AND OPEN-ENDED SOLUTIONS

Finn CONRAD

Department of Mechanical Engineering, Technical University of Denmark
DTU - Building 404, Kgs. Lyngby, Denmark
E-mail: finn.conrad@mek.dtu.dk

ABSTRACT

The paper presents and discusses a R&D-view on trends in development and best practise in design of both low-pressure and high-pressure tap water hydraulic components and systems for motion control as well as open-ended solutions various industrial applications. The focus is on the advantages using ordinary tap water and the range of application areas are illustrated with examples, in particular within the food processing industry, humidification operations, water mist systems for fire fighting, high water pressure cleaners, water moisturising systems for wood processing, lumber drying process and mobile machines and equipment that operate in environmentally sensitive surroundings. Today's progress in water hydraulics includes electro-water hydraulic proportional valves and servovalves for design of motion control solutions for machines and robots. The remarkable property is that the components operate with pure water from the tap without additives of any kind. Hence water hydraulics takes the benefit of pure water as fluid being environmentally friendly, easy to clean sanitary design, non-toxic, non-flammable, inexpensive, readily available and easily disposable. The low-pressure tap water hydraulic systems cover up to around 50 bar, and 2-4 kW having a strong potential to compete with pneumatic and electrical solutions in many applications. The high-pressure water hydraulic systems cover typically up to 160 bar pressure from pump and to motors and actuators 140 bar. Recently, dedicated pumps and accessories running with sea-water as fluid are available. A unique solution is to use reverse osmosis to generate drinking water from sea-water, and furthermore for several off-shore applications. Furthermore, tap water hydraulic components of the Nessie® family and examples of measured performance characteristics are presented and the trends in industrial applications and need for future are discussed.

KEY WORDS

Water hydraulics, Actuators, Motion Control, Robot Manipulator, Open-ended Systems, Water Mist.

INTRODUCTION

Globally, the benefits for industries and societies are based on the nature of water due to the following properties: environmentally friendly fluid, non-flammable, fire and explosion proof, easy to clean sanitary design, non-toxic, inexpensive, readily available and easily disposable. The remarkable property is that the components operate with pure water from the tap without additives of any kind, [1] and [22]. The business sales history confirms that the use of modern water hydraulics shows a growing turnover as for Danfoss High-Pressure Water Solutions in Figure 1.

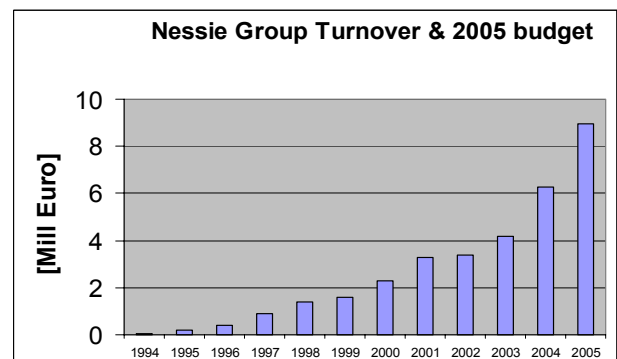


Figure 1 Trend in turnover of Danfoss Nessie Group

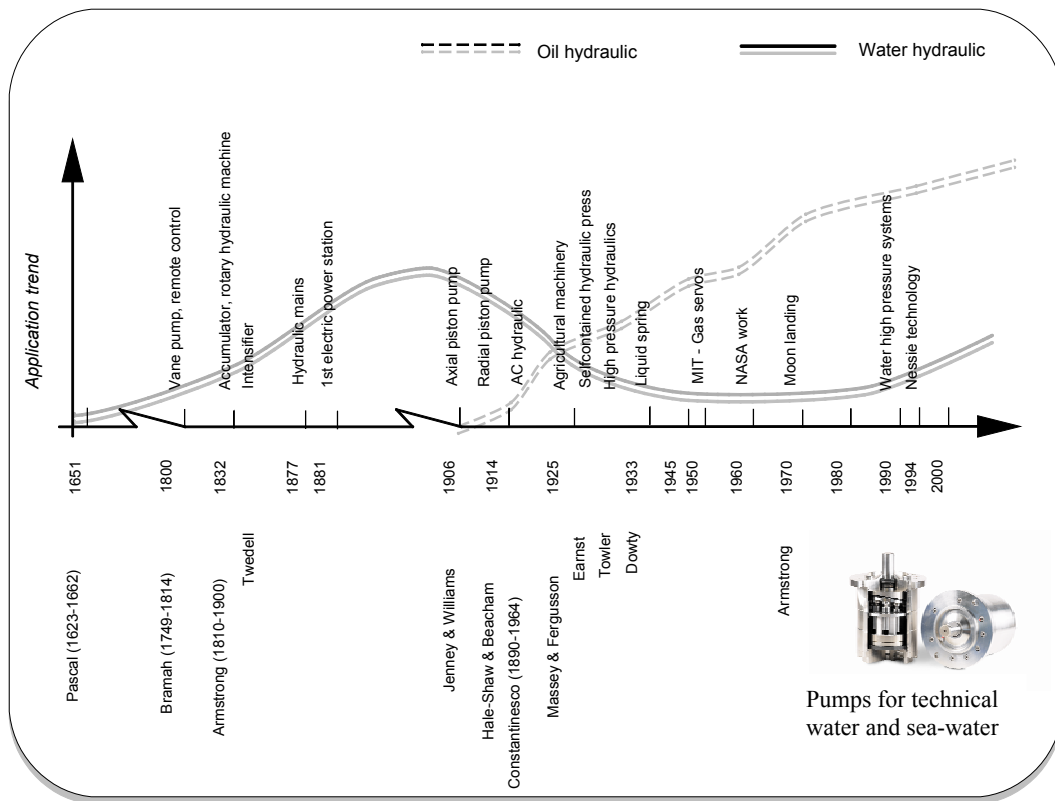


Figure 2 Hydraulics application trends and key milestones.[2]

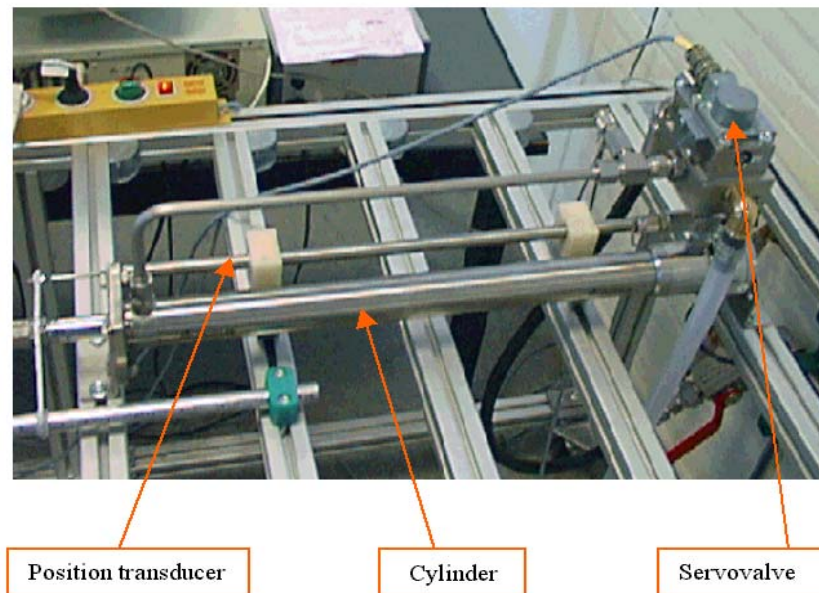


Figure 3 DTU Test water hydraulic servo actuator with a Nessie power supply

Figure 2 illustrates the development and applications of water hydraulics versus oil hydraulics, [2]. The Century BC Ctesibus invented a two-piston pump designed for

pumping water. Later in 1795 Joseph Bramah was the inventor of the unique *the hydraulic press*. In 1994 Danfoss introduced the first generation of modern tap

water components known as the Nessie® family of products for high-pressure tap water hydraulic systems that operate typically up to 140 bar. Since 1997 Danfoss has introduced such a second generation of low-pressure and low-power tap water hydraulic components that operate up to 50 bar. Figure 3 shows a running R&D test water hydraulic servo actuator for motion control since 1997 at Technical University of Denmark, DTU. The benefits of water relative to mineral oil, bio oil and water-oil emulsion are illustrated in Figure 4.

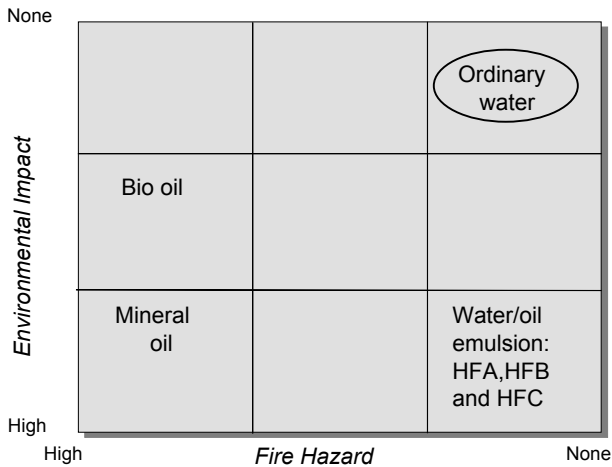


Figure 4 Water versus bio oil, mineral oil and emulsions

The significant advantages and benefits:

- No pollution of the environment (since most processes create leakage and fluid spills)
- Low operational and power media costs, i.e. purchase, storage, disposal
- Non-flammable explosion-proof fluid, safe and suitable for use in hazardous applications (lower insurance costs, etc.)
- High fluid power density, high power efficiency and high torque to inertia ratio compared to electric drives and pneumatic drives
- Workers do not breathe harmful oil vapours or risk exposure to skin and eyes.

The compressibility gives the liquid its ability to store and transfer energy with a remarkable power density, i.e. a very high torque to inertia ratio. However the bulk modulus of pure ordinary water is $2.4 \cdot 10^3$ MPa, approximately 50% larger than that for mineral oil ($1.6 \cdot 10^3$ MPa), and the velocity of sound in water (1,480 m/s at 20 °C) is around 10% faster than the velocity of sound in mineral oil (1,300 m/s at 20 °C). Thus a water hydraulic robot could be significantly faster than an oil hydraulically or an electrically driven robot.

A group of frontrunner companies as Danfoss High-Pressure Water Solution have their water hydraulic products and systems on the market, and the number and the areas of application are increasing since shown at the exhibition area 'The World of Water Hydraulics' at the Hanover Fair 1997 and 1999.

Today's R&D trends strengthen development and best practise in design of both low-pressure and high-pressure tap water hydraulic components and systems for motion control as well as open-ended solutions for customers within various industrial applications. The advantages using ordinary tap water and the range of application areas are illustrated in this paper with examples, in particular within process industries, the food processing industry, pharmaceutical industry, humidification operations, water mist systems for fire fighting, high water pressure cleaners, water moisturising systems for wood processing, lumber drying process, mining, steel and cobber industry, nuclear industry, and mobile machines and equipment that operate in environmentally sensitive surroundings. Today's progress in water hydraulics includes electro-water hydraulic proportional valves and servovalves for design of motion control solutions for machines and robots. Many industrial applications required particulars cautions that water hydraulics can provide [1]. On the other hand, water has low viscosity relative to mineral oil, and can in general only be recommended applied for supply pressure up to 160 bars.

Water is the most natural fluid in the world and nothing in nature is more closely associated with cleanliness, freshness, and purity than pure water. Therefore the use of pure water from the tap without any kind of additives for hydraulic systems suited for motion control and power transmission for machines and equipment, and water mist systems is a *natural approach*.

RESEARCH AND DEVELOPMENT

The research and development challenges were to find engineering solutions to the specific problems in design and manufacturing of water hydraulic components and industrial systems suitable for using pure tap water as the pressure fluid, [2]-[26]. Briefly, the main specific problems to overcome are

- avoid *corrosion*, using right combination of materials and surface finishes
- avoid *flow erosion* due to very low viscosity and turbulent flow
- control of *lubrication* with water; *tribology*, design internal parts and gaps
- surface treatment, tribology, achieving low friction surfaces with water lubrication

- control of *internal leakage* to secure satisfaction of high power efficiency
- control of *external leakage* to secure satisfaction of high power efficiency
- optimisation of the water nozzle performance for generation of water mist and moisturising units.

These challenges have been undertaken by Danfoss and other companies and by researchers. Today, companies have water hydraulic components, systems and solutions on the market, and the number of products and the areas of application are increasing as illustrated in turnover in Figure 1 and Figure 2.

TEMPERATURE AND PRESSURE RANGE

The permitted operational temperature range is $+3\text{ }^{\circ}\text{C}$ to $+50\text{ }^{\circ}\text{C}$ max. due to the nature of pure water, Figure 5. Today, as an example the pressure range of the Nessie® products is up to 160 bar. Furthermore, the range for components and water pressure up to 50 bar and for medium power range up to 4 kW are available.

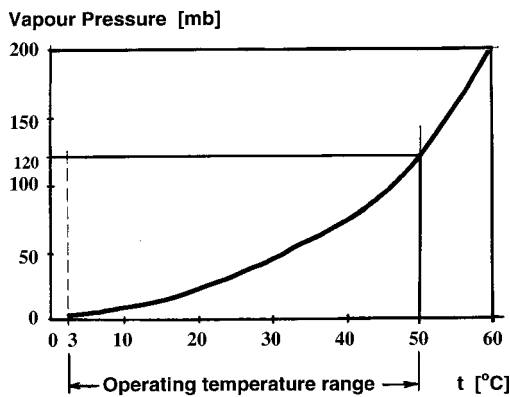


Figure 5 Vapour pressure characteristic of water

The maximum temperature of $+50\text{ }^{\circ}\text{C}$ is in many cases not a strong constraint because thermal conductivity of water is 4-5 times that of mineral oil! This means, that water hydraulic systems tend to require less cooling capacity. Heating is often a consequence of flow losses due to flow resistance.

VISCOSITY AND MATERIALS FOR DESIGN

In that respect need of cooling, water benefits from its much lower viscosity when compared to mineral oil, bio oil and oil/water emulsion, Figure 6. The dynamic viscosity of mineral oil (30 cSt at $55\text{ }^{\circ}\text{C}$ and atmospheric pressure) is around 30 times that of pure water (1 cSt at $20\text{ }^{\circ}\text{C}$ and atmospheric pressure).

Dynamic Viscosity η [m Pa s]

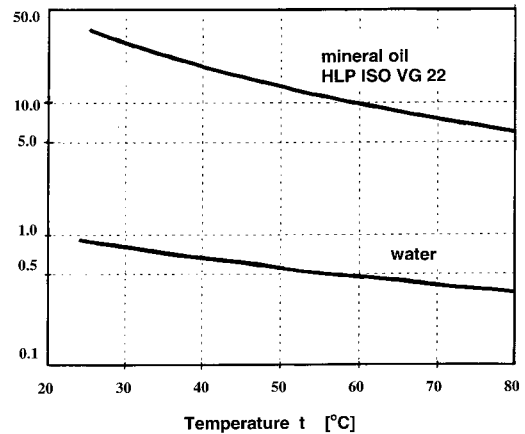


Figure 6 Viscosity of water and mineral hydraulic oil

That means using water the diameter of pipes, hoses and cooling systems is smaller size than that for oil hydraulics for the same power range. The specific heat of water is 2 times that of mineral oil, that means water has the double ability to absorb heat.

The viscosity of water is significant lower than the viscosity of hydraulic oils; with a factor of one to two orders depending of the actual oil. Assuming conditions for laminar volume flow according to Hagen-Poiseuille's law the leakage flow Q_L through the gap can be calculated from the following equation

$$Q_L = \frac{bh^3}{12L\eta} \Delta p \quad (1)$$

where b is the width, L is the length, h is the high of the gap, η is the dynamic viscosity and Δp is the pressure drop. For equal gaps in a water hydraulic machine (e.g. gap between piston and bore), the ratio of leakage water relative to leakage of a typical hydraulic oil is

$$\frac{Q_{L,W}}{Q_{L,O}} = \frac{\eta_{Oil}}{\eta_{Water}} \cong 30 \quad (2)$$

In order to reduce the leakage flow of water hydraulic components to the same level achieved for oil hydraulic components, the size of the gap has to be reduced according to the ratio

$$\frac{h_{water}}{h_{oil}} = \sqrt[3]{\frac{\eta_{Water}}{\eta_{oil}}} = 0.32 \quad (3)$$

In most cases, the radial gap, for example in piston pumps, cannot be reduced in practice, because there is a risk for locking the pistons due to thermal expansion caused by friction between mechanical parts. In design of water piston pumps, the gap clearance between piston and bore can be reduced to less than 10 μm without difficulties. Further, according to the inverse Reynold's equation, the spot underneath an elastic seal relative to a rod where $\frac{dp}{dx} = 0$ then the height of the gap is h_0 is proportional to $\sqrt{\eta}$. Comparing this value for water hydraulic relative to oil hydraulic gives the ratio

$$\frac{h_{0,\text{water}}}{h_{0,\text{oil}}} = \sqrt{\frac{\eta_{\text{water}}}{\eta_{\text{oil}}}} = \frac{1}{\sqrt{30}} = 0.18 \quad (4)$$

The global gaps for oil hydraulics is in the region of around 1/10 μm . That means, for the same given conditions the gap for water hydraulics should be a factor 0.18 less against the seal.

Due to the lower viscosity of water the dynamic pressure that builds up is significant lower compared to the same conditions with oil in wedge gaps. Assuming equal length of the wedge gap, the mean gap width has to be reduced according to the ratio

$$\frac{h_{m,\text{water}}}{h_{m,\text{oil}}} = \sqrt{\frac{\eta_{\text{water}}}{\eta_{\text{oil}}}} = \frac{1}{\sqrt{30}} = 0.18 \quad (5)$$

The same assumption could approximately holds for the micro-hydrodynamics at the wedge gaps of the surface structure. This implies that gaps have to be much smaller to build up the same hydrodynamic bearing forces as with oil. In this case it is important to avoid the risk of contact between solid parts and risk of higher wear.

Use of *hydrostatic bearing* is an efficient solution for separating the bearing surfaces. Furthermore, use of materials with low friction and resistant to wear is important. Stainless steel W. No. 1.4057 and reinforced polymer PEEK from the polyetherketone family are used by Danfoss for the sliding and sealing gaps of pumps and motors.

An increasing numbers of engineers and managers are considering water hydraulics as an emerging technology that can offer significant advantages to solve motion and force control tasks as a single technology and/or combined with other technologies. The trend shows the increasing number of application areas for modern tap water hydraulic components, in particular the used for design of environmental friendly industrial machinery, robots, and systems.

SOLUTIONS FOR WATER HYDRAULICS

Due to the significant advantages of tap water hydraulics, water hydraulic system solutions can often compete with pneumatic and electrical solutions in many industrial areas and with oil hydraulics in situations where machines and equipment have to operate in environmentally sensitive surroundings. Typical important application areas for tap water hydraulic solutions are:

- open-ended systems
- closed loop hydraulic systems
- combined open-ended and closed loop systems
- food processing industry
- chemical and pharmaceutical industry
- mining industry
- steel industry
- nuclear industry
- wood processing
- lumber drying processes
- humidification (energy saving, HVAC)
- water mist fire protection and fighting systems
- high pressure water cleaners

During the last few years Danfoss High-Pressure Water Solution developed dedicated APP pumps and accessories for sea-water and technical water to be available on the market. A unique breakthrough is the process called

- *Reverse Osmosis* (drinking water from sea-water)

Super Duplex stainless steel to operate with sea-water.

It is not more difficult to design water hydraulic systems than oil hydraulic systems as long as the required guidelines and design rules recommend for water hydraulics are followed by the design engineers, the technicians and service personnel.

WATER HYDRAULIC MACHINES

Today, water hydraulics is applied in design of modern mobile machines that have to operate in environmentally sensitive surroundings. In the following paragraphs two examples are presented.

Environmental waste packer lorry

All hydraulic functions for lifting and filling on the designed Waste Packer Lorrys for the Gothenburg Municipal are shown one of them in Figure 7.



Figure 7 Water hydraulic waste packer lorry

The functions are controlled and operated by water hydraulics to protect the environment in the city. The benefits are no risk of oil spill drops or product contamination, and easy to clean. The vehicles have el-hybrid motors.

A water hydraulic axial pump drives the hydraulic system, PAH 80, providing a flow of 115 l/min @ 140 bar. A water hydraulic motor MAH 12.5 drives the winch. All the linear motions such as open/closing tail gate, ejector plate, skip shaker, bin lift, carriage plate and packer plat are controlled by the 36 water hydraulic valves that drive the 11 water hydraulic cylinders. The control system includes a PLC. In order to operate degrees below freezing points, harmless propylenglycol has been added (sugar based glycol that a.o. is use in the food industry ad sweetener). A significant benefit is no risk of hydraulic oil spill drops on roads, and do reduce the use of annual around 18,000 hydraulic oil for machines per year in Gothenburg. In Sweden around of 40,000 ton of oil hydraulics are coming from leaks, and 1 litre of hydraulic oil can spoil a farmer area for crops or 25,000 drinking water reservoir. In many cases water hydraulics are solutions for environmental areas.

TAP WATER HYDRAULIC MACHINERY DESIGNED FOR HYGIENE IN FOOD INDUSTRY

Some typical examples of design for hygiene are presented in the following to illustrates application areas where tap water hydraulics can offer a design for hygiene solution in the food processing industry, which can not been solved by use of a bio-oil based hydraulic system. Compared with pneumatic solutions, water hydraulic solutions have the significant advantages of easy to flush and clean according to the requirements and regulations in the food processing industry, lighter weight of cutting tools (saws etc.) due to higher power density, much higher efficiency and saving energy costs. A tap water hydraulic driven meat burger-machine is shown in Figure 8. A motor is driving the spindle for the meat cutting of beef meat, and two water cylinders for motion control are used to form the five

meat burgers in one row, and one cylinder for moving the forming tool horizontally. The machine is very environmentally friendly and very easy to clean daily.



Figure 8 Tap water hydraulic driven burger-machine



Figure 9 Ice fill machines for 400 ice per minutes with one motor, 3 linear servo cylinders and 3 end cylinders

An automatic controlled ice fill machine for Tetra Pak Hoyer in Denmark with a capacity of 400 ice per minutes driven by electro water hydraulics with one motor, 3 linear servo cylinders and 3 end cylinders is shown in Figure 9.

An automatic control tobacco cutter machine for Universelle Germany is shown in Figure 10 with two water hydraulic cylinders to avoid no risk of pollution, easy cleaning and save energy.



Figure 10 Automatic control tobacco cutter machine driven by water hydraulics with two cylinders

A water hydraulic drive unit for wing press equipment for the aero plane factory of Palamine in UK want to avoid no pollution on ground, no fire risk and no oil is shown in Figure 11.

INDUSTRIAL HIGH PRESSURE WATER CLEANING

A very important industrial application of tap water hydraulics is high-pressure water cleaners. A typical example is cleaners for malt reservoirs in beer breweries shown in diagram in Figure 12. A pump, PAH 32, generates a pressure up to 160 bar. The pump supplies the two high-pressure clean guns connected to a main water supply ring net via quick couplings. The installation supplies the user with a very flexible and effective high pressure cleaning system.

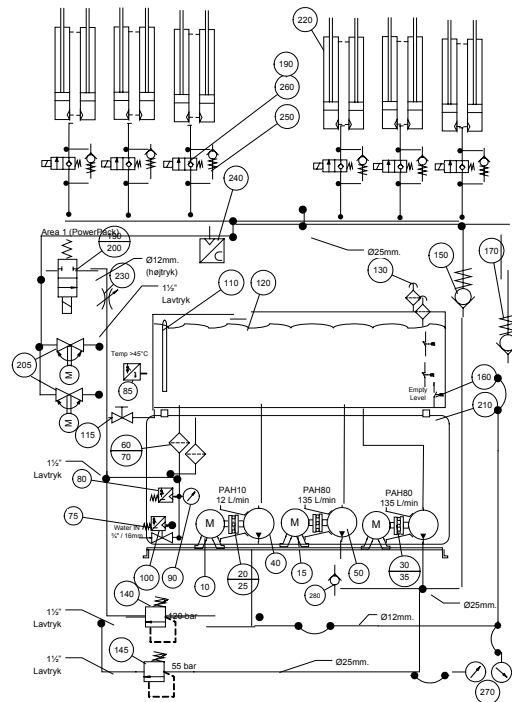


Figure 11 Water hydraulic drives for wing press equipment for an aero plane factory

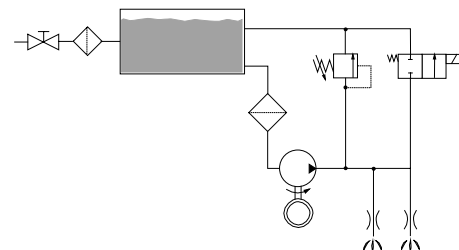


Figure 12 Diagram of a high pressure water cleaner

The high power density gives a very compact cleaner unit. Further advantages are no oil lubrication due to lubrication of the components by the tap water itself, and the system requires minimum maintenance.

HUMIDIFICATION

Today's several installations of humidification units with pumps, nozzles and accessories are in use for high-pressure water mist. It is needed indoor such as in super markets selling fruits and in textile industry. Indoor air quality is determined by a number of factors. Humidity is one of the most important measures directly affecting human beings as well as animals, plants and almost any material. Therefore, the ability to adjust humidity, both humidifying and dehumidifying, is of importance and found in numerous applications and industries.

Human beings, for example, feel most comfortable at humidity between 40 and 60% rH and a temperature of 22°C / 72°F. Correct humidity minimizes risk of infection with contagious disease, growth of bacteria or fungi, as well as impacts on performance of man and machine. There are hundreds of examples of how humidity affects productivity of manufacturing processes and the quality of products.

A high-pressure pump boosts water to a pressure typically between 70-100 bar. Specially designed water nozzles atomize the water in billions of extremely small droplets. The water mist jets are injected either directly into the open space or into the duct system of an air-handling unit as shown in Figure 13. A humidification controlled green house for crops is shown in Figure 14.

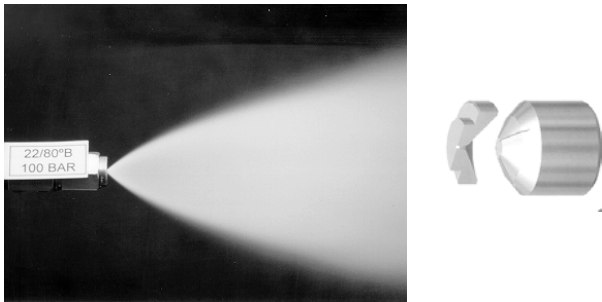


Figure 13 A nozzle and generation of water droplets

The principle works adiabatically, which means that the evaporation heat required for transferring water from liquid state into gas is obtained by the surrounding air, resulting in a temperature decrease called adiabatic cooling effect.

WOOD PROCESSING

Special designed water mist solutions are installed for wood processing, in particular for sawmills to avoid dust and to improve lubrication and cooling of saws as

shown in Figure 15 as well as for lumber drying shown in Figure 16.



Figure 14 Humidification control in green house



Figure 15 Wood processing for sawmills

A new water hydraulic based Lumber Drying Concept has been developed and tested, see Figure 16. This concept offers faster drying of lumber in a kiln with substantial benefits to capacity, wood quality and the overall economy.



Figure 16 Control of process for lumber drying in a kiln

Optimum profitability in the lumber business depends on the knowledge and experience of handling lumber as living wood material. Automation has become an indispensable tool for optimising the lumber drying process. A newly developed high-pressure water moisturising unit, making up the core of this concept (Nessie® Wood Concept) that improve the control of the lumber drying process. The new high-pressure water moisturising unit operates at pressures between 80-100 bar and special design nozzles generate extremely small water droplets evaporating immediately.

A vital part of the system is the nozzles that distribute the water droplets into the kiln. In Figure 13 is shown a nozzle and generation of water droplets. The system consists of a tank, a pump, a motor, valves, nozzles and a control system. The evaporated water quickly covers the total surface of the lumber in a kiln. The results are tangible

- Shorter payback time of the kiln plant: a markedly shortened drying period increases capacity.
- Increased wood quality thanks to a more lenient drying process.
- Reduction of waste.
- Higher product selling price.

The high-pressure unit provides these benefits by ensuring optimum controlled climatic conditions in all phases of the drying process: *heating, drying and conditioning*:

In the *heating phase* air humidity must be increased in order to obtain intense heating of the lumber – otherwise the danger of cracking and deteriorating is immediate. The humidity supplied by the Nessie high-pressure water moisturising unit condenses evenly on the surface of the entire pile, thus providing lenient heating of the lumber. Moreover, the heating phase can be reduced to 4-6 hours, compared to the 14-24 hours typically required by traditional moisturising of softwood. Applying the high-pressure water moisturising unit furthermore renders the widespread sprinkling of heat exchangers superfluous. The accurate process control ensures that the exact water amount for optimum climatic conditions in the kiln is obtained, leaving out any need for additional evaporation. This cuts down maintenance and replacement costs for otherwise rapidly corroding heat exchangers.

In the *drying phase* the climatic conditions in the kiln are likewise controlled by means of high-pressure water. The technology is superior to steam applications that may cause increased energy supply and thus undesirable increase of temperature. Experience from some 200 applications already running world-wide shows that accurate and quickly reacting temperature control can be obtained when utilising high-pressure water technology in the drying phase. Additionally, water

consumption is as low as 1 litre per cubic metre softwood per drying hour if you replace a traditional low-pressure water application with a high-pressure water moisturising unit.

In the *conditioning phase* lumber is moisturised with water in order to reduce tension and to equalise the humidity quotient throughout the lumber. Using high-pressure water, an even distribution of droplets on the lumber surface is achieved.

Steam applications make up an alternative to the Nessie high-pressure water moisturising unit. However, supplying steam may cause undesirable heating at the beginning of the conditioning phase. This adverse effect cannot occur using the high-pressure application, since it works on cold water exclusively.

A key advantage is that lumber drying with the new high pressure water moisturising unit only requires one system for the entire process: heating, drying and conditioning. The range of droplets before steam generation is 70 times shorter compared to traditional low-pressure systems (on identical temperature conditions). The drop size is 7 times smaller. The system is the most even and all-embracing evaporation on the market.

FIRE PROTECTION AND FIGHTING SYSTEMS

Very effective tap water hydraulic fire protection and fighting systems have been developed and taken in use. Figure 17 shows an typical fire fighting application.



Figure 17 Fire fighting by high pressure water hydraulics for generation of water mist

The water pressure is generated by a PAH 32 pump (max. 160 bar and max. flow 44 l/min) and a pressure relief valve secure protection against excessive pressure. The water mist system replaces Halogen systems (CFC) that have the disadvantage of damaging the ozone layer. The water mist is generated through special designed nozzles and small quantities of water can be used to extinguish fires, including those involving hydrocarbons and electrical controls

WATER HYDRAULIC MARITIME MACHINERY

Novel Boatscrubbers, a developed automatic boat washer to control and drive by high pressure water hydraulics for motion control and rotation of the brushes to clean the boats is shown in Figure 18.



Figure 18 Automatic water hydraulic boat washer

The benefits are significant due to the solution means that the boat-body can be paint with a silicone process to eliminate the pollutions from traditional boat painting that contains dangerous particles that seriously pollute the seabed of the harbours and sea-water.

REVERSE OSMOSIS - DRING WATER FROM SEA-WATER

Recently, a unique breakthrough with the success of development, design and implementation the process called

- *Reverse Osmosis* (drinking water from sea-water)

by novel dedicated pumps and valves using Super Duplex stain steel to operate with sea-water. A dream of generation drinking water from sea-water by reverse osmosis process is today reality by using dedicated APP pumps and VCM valves from Danfoss.



Figure 19 Drinking water from sea-water by reverse osmosis process by APP pumps and VCM valves

Figure 19 illustrates drinking water from sea-water from an installation from Lanzarote has resulted in an overall low as 2.65 kW/m³ fresh water production and saving running costs.

TRENDS IN R&D FOR WATER HYDRAULICS

The novel developed DTU robot manipulator with three joints, each controlled by a servovalve for a water hydraulic rotary vane actuator, has three links and is able to sustain a maximum load of 85 Kg with 1.9 m of extension, shown in Figures 20, 21, and 22. For a dexterous use, a load of 50 Kg has not to be exceeded. The slave arm weighs around 90 Kg and the actuators generate 2156 Nm, 1056 Nm and 448 Nm, respectively.

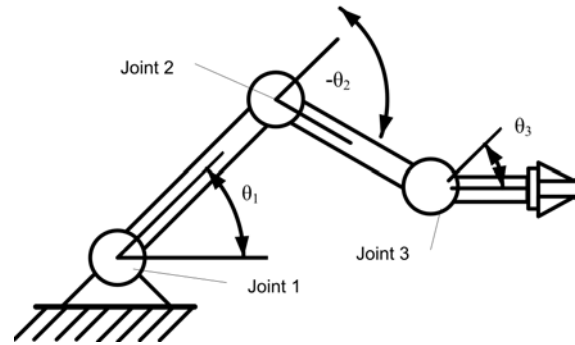


Figure 20 Schematic of the 3 DOF robot manipulator

The robot arms have servovalves to control flow rates. This solution allows the use of rigid connection between the servovalves and the actuator.

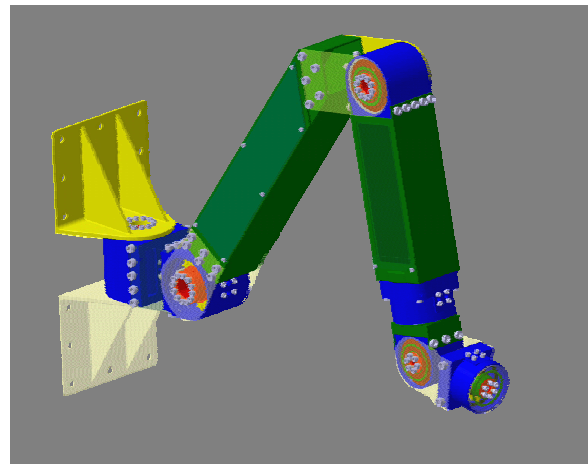


Figure 21 CATIA model of the arm 1 and arm 2 of the 6 DOF robot manipulator

The results [26] include engineering design and test of the proposed simulation models compared with IHA Tampere University's research measurements from a similar robot manipulator driven by tap water hydraulic components, Rameda, 2004, [24]. Simulation results behaviour of the tool point centre (TPC) of the slave manipulator arm with 3 DOF is shown in Figure 23.

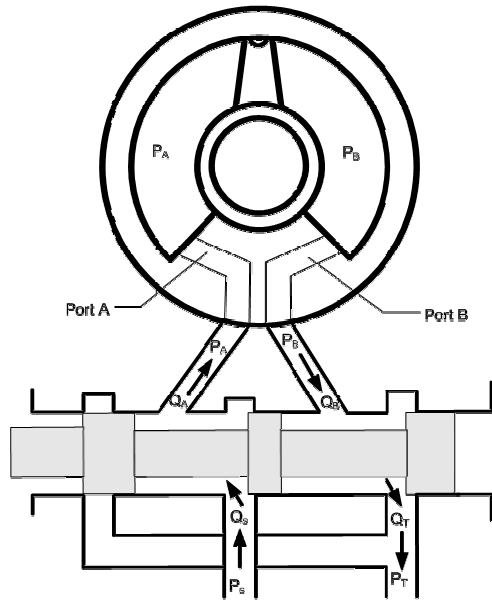


Figure 22 Schematic of water hydraulic vane actuator

A typical motion control application the slave arm was tested by defining the following complete test path trajectory build up by geometric elements as part of circles, strait lines, corner and ramp as reference input to the robot controller.

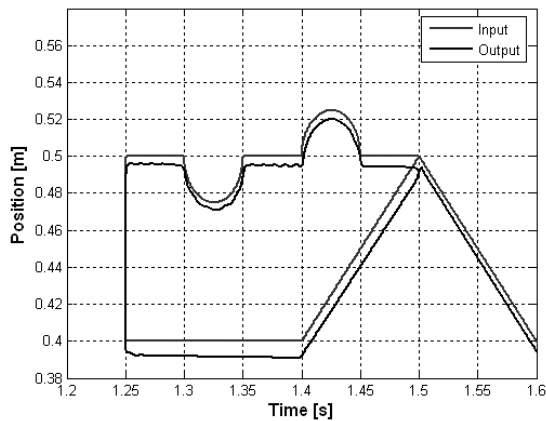


Figure 23 Tool point centre trajectory following a complete reference input path shape

The CUT's water hydraulic test rig facility with actuator operates arm, water hydraulic valves and cylinders shown in Figure 24 was built for R&D activity. It includes power supply, input signals generator, sensors for pressure, temperature, flow rate and position measurement system. As applied for the DTU water hydraulic test facility similar hydraulic components for the CUT test rig are mainly Danfoss Nessie products, including proportional valves, [23 and 25].



Figure 24 A CUT water hydraulics test manipulator

CONCLUSION AND OUTLOOK

Trends confirm that design of water hydraulic application is a *natural approach* to solve many of the major environmental pollution problem and problems in industries, which cannot accept contamination of products and problems of fire and explosion risk.

The contributions presents and discusses a R&D-view on trends in development and best practise in design of both low-pressure and high-pressure tap water hydraulic components and systems for motion control as well as open-ended solutions various industrial applications. The business sales history confirms that the use of modern water hydraulics shows a growing turnover per year. Important industrial applications and the benefits are presented with focus on process industries such as food industry, pharmaceutical processes, water mist fire fighting systems, high water pressure cleaners, water moisturising systems for a humidification, wood processing (sawmills and lumber drying processing), and industrial mobile machines and municipal machines working in environmentally sensitive surroundings.

Recently, a unique breakthrough with the success of development, design and implementation the process called *Reverse Osmosis* (drinking water from sea-water) by novel dedicated axial pumps and valves using Super Duplex stain steel to operate with sea-water.

Today's challenge is to include design of water hydraulic systems and industrial solutions in education of engineers, and research for PhD students. Several universities have undertaken the challenge, and more and more universities do include water hydraulics as an important technology complementary to oil hydraulics, pneumatics and electrical power engineering to best practice for design of solutions for the future.

ACKNOWLEDGMENTS

The author thanks Danfoss for contributions and the permission to use figures.

REFERENCES

- [1] *Modern Water Hydraulics - Your Choice for the Future*, National Fluid Power Association - NFPA, USA, 1995.
- [2] Conrad F. *Pure Tap Water Hydraulic Control Systems - Design and Applications*, Chapter 7 in *Advantages in Hydraulic Control Systems*, Editor Jacek S. Stecki, Studies in Subsea Engineering -96/1, Dept of Mechanical Engineering, Monash University, 18-19 April 1996.
- [3] Conrad F., A. Adelstorp *Pure Water Hydraulic Systems and Applications*, 9th Bath Int. Fluid Power Workshop, Bath 9-11 Sept. 1996. Editors C.R. Burrows and K.A. Edge, University of Bath, England. RSP, Research Studies Press LTD, John Wiley & Sons. Fluid Power Series, Volume 9. UK, 1997.
- [4] Trostmann E., P.M. Clausen *Fluid Power Control Based on Pure Tap Water*, Proc. 12th AFK, Aachen Conference on Fluid Power Technology, 12-13 March, Institut für fluidtechnische Antriebe, IFAS, RWTH, Aachen, Germany, 1996.
- [5] Yamashina, C., S. Miyakawa, E. Urata *Development of Hydraulic Cylinder Control System* Proc. 3rd JHPS Int. Symp. on Fluid Power, Yokohama'96, Japan, 1996.
- [6] Koskinen, K. T., E. Mäkinen, M. J. Vilenius, T. Virvalo *Position Control of Water Hydraulic Cylinder*, Proc. 3rd JHPS Int. Symp. on Fluid Power, Yokohama'96. Japan.
- [7] Matsui, T., H. Koseki *Motion Control of Water Hydraulic Servo Systems*, Proc. 3rd JHPS Int. Symp. on Fluid Power, Yokohama'96. Japan, 1996.
- [8] Clausen, P. M., E. Trostmann *Back to the Future with Nessie Water Hydraulics*. Proc. 5th Int. Conference on Fluid Power - SICFP'97, Vol. 1, pp. 261-276, Linköping Univ. Sweden, 28 - 30 May 1997.
- [9] Hyvönen, M., K.T. Koskinen, J. Lepistö, M.J. Vilenius *Experiences of Using Servo Valves with Pure Tap Water*. Proc. 5th Int. Conference on Fluid Power – SICFP'97, Vol. 2, pp. 21-32, Linköping, Univ. Sweden, 28 - 30 May 1997.
- [10] Conrad F., A. Adelstorp *Tap Water Hydraulic Control Systems for Medium Power Application Areas*, 10th Bath Int. Fluid Power Workshop, Bath 10-12 Sept. 1997. Editors C.R. Burrows and K.A. Edge, University of Bath, England. RSP, Research Studies Press LTD, John Wiley & Sons. Fluid Power Series, Vol.10, UK, 1997.
- [11] Adelstorp, A., *New Motor and valves for Tap Water*. Fluid Power Theme Days 97 in IHA 97 - Water Hydraulics, Tampere Univ. of Technology, 25-26 Sept. 1997.
- [12] Sørensen, P., *Latest Development in the Application of Water Hydraulics*. Fluid Power Theme Days 97 in IHA - Water Hydraulics, Tampere Univ. of Technology, 25-26 Sept 1997.
- [13] Bech, T., S. Olsen, P. Klit *Design of Pumps for Water Hydraulic Systems*. Proc. 6th Scandinavian Int. Conference on Fluid Power – SICFP'99, Vol. 1, pp. 231-241, Tampere Univ. of Technology, Finland, 26 - 28 May 1999.
- [14] Tammisto J., P. Kunttu, K.T. Koskinen, M. Vilenius *Development of Water Hydraulic Arc-Cylinder Pump and Motor*. Proc. 6th Scandinavian Int. Conference on Fluid Power – SICFP'99, Vol. 1, pp. 208-217, Tampere Univ. of Technology, Finland, 26 - 28 May 1999.
- [15] Shinoda, M., C. Yamashina, S. Miyakawa *Development of Low-Pressure Water Hydraulic Motor*. Proc. 6th Scandinavian Int. Conference on Fluid Power – SICFP'99, Vol. 1, pp. 208-217, Tampere Univ. of Technology, Finland, 26 - 28 May 1999.
- [16] Pohls, O., O. Rantanen, T. Kuikko *Sea Water Hydraulic Axial Piston Machine*, Proc. 6th Scandinavian Int. Conference on Fluid Power – SICFP'99, Vol. 1, pp. 2219-229, Tampere Univ. of Technology, Finland, 26 - 28 May 1999.
- [17] Voight, K. *Basis for a New Product Programme for Fluid Connections in Water Hydraulics*. Proc. 6th Scandinavian Int. Conference on Fluid Power – SICFP'99, Vol. 1, pp. 191-206, Tampere Univ. of Technology, Finland, 26 - 28 May 1999.
- [18] Hollingworth, B. *A Servo Valve for Operation in Less than Ideal Conditions*, Proc. 6th Scandinavian Int. Conference on Fluid Power – SICFP'99, Vol. 1, pp. 255-259, Tampere Univ. of Technology, Finland, 26 - 28 May 1999.
- [19] Koskinen, K.T. *Proposals for Improving the Characteristics of Water Hydraulic Proportional Valves Using Simulation and Measurement*, Thesis for degree of Doctor of Technology, 121 pages, Tampere Univ. of Technology, Finland, October 1996.
- [20] Conrad F. *Tap Water Hydraulic Machines and Tools*, Chapter 6 in *Developments in Hydraulic Power Control and Machinery and Manipulators*, Editor Andrzej Garbacik & Jacek S. Stecki, pp. 125-153, Fluid Power Net Publication, Cracow 2000, ISBN 83-86219-71-8.
- [21] Hilbrecht, B. *Water as Pressure Medium in Water Hydraulic Systems*, Int. Exposition for Power transmission and Technical Conference, NFPA, 4-6 April 2000.
- [22] Conrad, F., B. Hilbrecht, H. Jepsen *Design of Low-Pressure and High-Pressure Tap Water Hydraulic Systems for Various Industrial Applications*. SAE Transaction 2000, Society of Automotive Engineers, Inc, USA 2000.
- [23] Conrad, F., J. Pobedza, A. Sobczyk *Experimental-based simulation of water hydraulic mechatronics test facilities for motion control and operation in environmentally sensitive application areas*. Intl. Conference on Computational Methods in Fluid Power Technology. Methods for solving practical problems in Design and Control. Editor J. S. Stecki. Fluid Power Net Publication, 26-28 November, Melbourne, Australia 2003.
- [24] Raneda, A. *Impedance Control of a Water Hydraulic Manipulator for Teleoperation Applications*, Doctoral Thesis, IHA, Tampere University of Technology, Finland, 2004.
- [25] Conrad, F., J. Pobedza, A. Sobczyk *IT-Tool Concept for Simulation and Design of Water Hydraulic Mechatronic Test Facility for Motion Control in Environmentally Sensitive Application Areas*, ASME Proc. Intl. Congress on Mechanical Engineering and Expo, Anaheim, Cal., USA, November 2004.
- [26] Conrad, F., Francesco Roli *Development of a novel water hydraulic vane actuator applied for control of a two-links test manipulator*. Power Transmission and Motion Control – PTMC 2005, University of Bath, Professional Engineering Publishing Limited, London and Bury St Edmunds, UK 2005.

APPLICATION OF ADAPTIVE CONTROLLER TO WATER HYDRAULIC SERVO CYLINDER

Hidekazu TAKAHASHI*, Kazuhisa ITO** and Shigeru IKEO**

* Division of Science and Technology, Graduate school of SOPHIA University
7-1 Kioicho, Chiyoda-ku, Tokyo, Japan
(Tel: +81-3-3238-3873, E-mail: tak-hide@sophia.ac.jp)

** Dept. of Mech. Eng., Faculty of Science and Technology
SOPHIA University
7-1 Kioicho, Chiyoda-ku, Tokyo, Japan
(Tel: +81-3-3238-3606, E-mail: kazu-ito@me.sophia.ac.jp, s_ikeo@sophia.ac.jp)

ABSTRACT

Water hydraulic servo system is an attractive system source for its environmental safety. In this system, the problem for precise control is the uncertainties and/or the unmodeled dynamics which includes parameter variations depending on driving conditions and nonlinearity of system e.g. friction force, flow equation and so on. In this paper, we discuss the control performance of adaptive positioning controller for water hydraulic servo cylinder. This controller method aims to reduce the tracking error tend to zero for given reference signal asymptotically and ensures controller parameters keep being bounded. Based on the least square method, parameter update law is given and adaptive tracking controller is constructed. The robustness is examined experimentally for supply pressure changes and load fluctuations.

KEY WORDS

Water hydraulic system, Servo valve, Cylinder, Adaptive control, Position control

INTRODUCTION

In recent years manufacturers and users have been requested to take much care of mineral oil. Hence the water hydraulic technique using pure tap water as a pressure medium became a hot issue again with an increase of our concerns for global environment problems and also with the technological advances on materials, machining and lubricity. This was also motivated by its high safety for fire hazard in production plant, easy availability and low cost. Water hydraulic system now has been applied to food processing,

semi-conductor industry, forest industry, atomic power industry and so on [1], [2]. Among them, the PID control strategy is mainly used as a control system design for its simplicity and intuitive interpretation of control parameters. However, comparison with conventional oil hydraulics, the precision of positioning and rotational velocity control of water hydraulics are relatively lower. This is due to the uncertainties including physical parameter changing, unmodeled dynamics and disturbance. In water hydraulic case, fluctuation of load and supply pressure lead to parameter change while the friction, the leakage flow and the dead zone work as

disturbance. As a result, PID controller is hard to accommodate such uncertainties [3]. This motivates to apply adaptive control method to compensate such uncertainties and make the closed-loop system to keep the specified performance and be more robust.

In this paper, the nominal system is assumed to be linear, and we discuss the positioning controller design for water hydraulic cylinder drive system using adaptive control theory. More specified, based on the general least square method or the fixed trace method as a parameter update law, we construct adaptive tracking controller, and examine its robustness for parameter changes.

WATER HYDRAULIC SYSTEM

WATER HYDRAULIC SYSTEM

A schematic diagram of the water hydraulic servo system that forms the basis of this study is shown in Figure 1. The experimental water hydraulic servo system consists of a water hydraulic power unit, double rods type water hydraulic cylinder and water hydraulic servo valve. The cylinder connected to the load cart set up horizontally. The position of the cylinder detected by the linear encoder on the cart is taken into the PC through the digital counter. The control input u generated in PC is sent to a servo amplifier. Primary specification is shown in Table 1. The control system designed in the next section is implemented on the dSPACE, and the experiment is performed.

Table 1 Specification of the experimental set-up

cylinder (double rods type)	ƒ25×ƒ14×300st.
load	100 [kg], max.
water hydraulic power unit	14.0 [MPa], max.
servo valve	20 [L/min] (@ 7[MPa])
working fluid	30±1[deg C] (tap water)
linear encoder	320 [mm] : stroke 0.5 [μm] : resolution

CONTROLSTRUCTURE

A precise modeling of water hydraulic cylinder control system is a very difficult problem due to its inherent highly nonlinearities and uncertainties. Especially in initializing the experiment, it is necessary in this study to set the servo valve spool at a neutral position by hand and this routine makes the dead zone be differed value each time. Thus in this study, we introduced a closed loop control system as a pre-feedback from cylinder

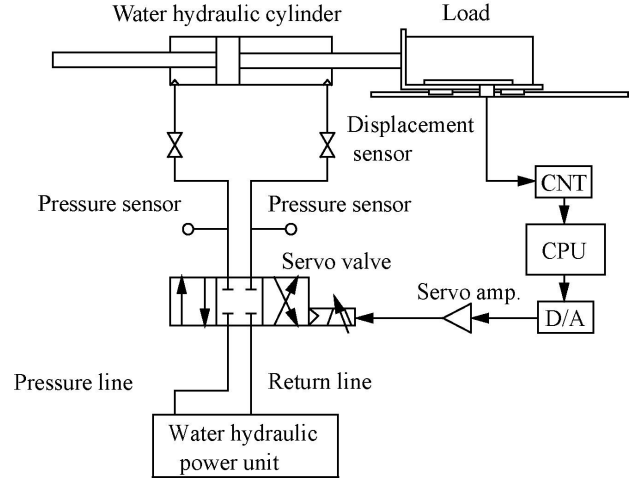


Figure 1 Water hydraulic servo system

reference position $x(t)$ to measured cylinder position $y(t)$ shown in Figure 2. Therefore we can ignore this nonlinearity including the spool position drift and we can treat it as a new plant. We choose the pre-feedback gain as $K_p=0.7$ [V/mm] from experiments.

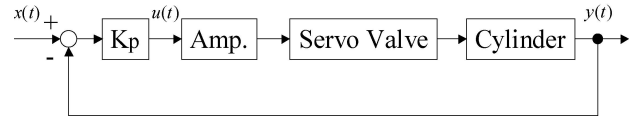


Figure 2 Block diagram of controlled system

DISCRETE TIME ADAPTIVE CONTROLLER

We consider following discrete linear time invariant SISO system.

$$y(k) = \frac{z^{-d} B(z^{-1})}{A(z^{-1})} u(k) \quad (1)$$

where $y(k)$ and $u(k)$ are the measurable input and output respectively, and $A(z^{-1})$ and $B(z^{-1})$ are polynomials in the unit delay operator of the form

$$A(z^{-1}) = 1 + a_1 z^{-1} + \dots + a_n z^{-n}$$

$$B(z^{-1}) = b_0 + b_1 z^{-1} + \dots + b_m z^{-m}, \quad b_0 \neq 0$$

The orders n and m as well as the time delay $d \geq 1$ are assumed to be known. In this study, $n=2$, $m=1$ and $d=1$. For the pole assignment of closed loop and the following Diophantine equation is employed [4], [5].

$$D(z^{-1}) = A(z^{-1})R(z^{-1}) + z^{-d}H(z^{-1}) \quad (2)$$

where

$$\begin{aligned} R(z^{-1}) &= 1 + r_1 z^{-1} + \dots + r_{d-1} z^{-(d-1)} \\ D(z^{-1}) &= 1 + d_1 z^{-1} + \dots + d_n z^{-n} \\ H(z^{-1}) &= h_0 + h_1 z^{-1} + \dots + h_{n-1} z^{-(n-1)} \end{aligned}$$

In Eq.(2) the polynomial $D(z^{-1})$ defines the closed loop poles and in this study an appropriate choice is $D(z^{-1}) = (1-0.1z^{-1})^2$. The design parameter $D(z^{-1})$ determines unique solution $R(z^{-1})$ and $H(z^{-1})$ through Eq.(2), and each degrees are

$$\deg H(z^{-1}) = n-1, \quad \deg R(z^{-1}) = d-1 \quad (3)$$

From Eq.(1) and (2), the following equation is derived as the nonminimal expression for a plant:

$$D(z^{-1})y(k) = \mathbf{q}^T \mathbf{f}(k-d) \quad (4)$$

where

$$\begin{aligned} \mathbf{q}^T &= [b_0, (b_0 r_1 + b_1), \dots, b_m r_{d-1}, h_0, h_1, \dots, h_{n-1}] \\ \mathbf{f}^T(k) &= [u(k), u(k-1), \dots, u(k-m-d+1), \\ &\quad y(k), y(k-1), y(k-n+1)] \end{aligned}$$

Given a reference input y_m , the output error equation is

$$D(z^{-1})[y(k+d) - y_m(k+d)] = 0 \quad (5)$$

From Eqs.(2) and (5), control input $u(k)$ is derived as follows.

$$u(k) = \frac{1}{b_0} [D(z^{-1})y_m(k+d) - \hat{\mathbf{q}}^T \bar{\mathbf{f}}(k)] \quad (6)$$

where

$$\begin{aligned} \mathbf{q}^T &= [b_0, \bar{\mathbf{q}}^T] \\ \mathbf{f}^T(k) &= [u(k), \bar{\mathbf{f}}^T(k)] \end{aligned}$$

When plant parameters are unknown in Eq.(6), we generate control input $u(k)$ as follows with adjustable parameters ($\hat{\cdot}$).

$$u(k) = \frac{1}{\hat{b}_0(k)} [D(z^{-1})y_m(k+d) - \hat{\mathbf{q}}^T(k) \bar{\mathbf{f}}(k)] \quad (7)$$

The overall block diagram of the discrete-time adaptive tracking control system is shown in Figure 3, where

$$\hat{B}_R(z^{-1}, k) = B(z^{-1})\hat{R}(z^{-1}) - \hat{b}_0 \quad (8)$$

The stability proof of this scheme is given in [5] and [6].

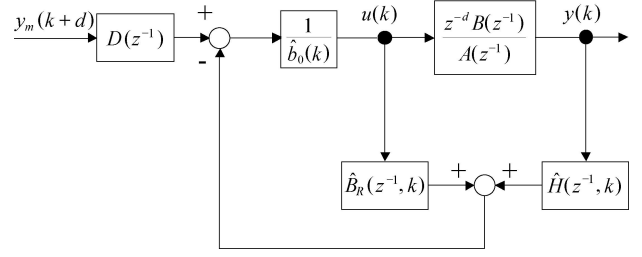


Figure 3 Discrete-time adaptive tracking control system

As a parameter update algorithm, we adopt the following recursive least square method with variable gain.

$$\begin{aligned} \hat{\mathbf{q}}(k) &= \hat{\mathbf{q}}(k-1) - P(k-1)\mathbf{f}(k-d)\mathbf{e}_1(k) \\ P(k) &= \frac{1}{\mathbf{I}_1(k)} \\ &\quad \cdot \left[P(k-1) - \frac{\mathbf{I}_2(k)P(k-1)\mathbf{f}(k-d)\mathbf{f}^T(k-d)P(k-1)}{\mathbf{I}_1(k) + \mathbf{I}_2(k)\mathbf{f}^T(k-d)P(k-1)\mathbf{f}(k-d)} \right] \end{aligned} \quad (9)$$

where

$$\begin{aligned} \mathbf{e}_1(k) &= \frac{-D(z^{-1})y(k) + \hat{\mathbf{q}}^T(k-1)\mathbf{f}(k-d)}{1 + \mathbf{f}^T(k-d)P(k-1)\mathbf{f}(k-d)} \\ 0 < \mathbf{I}_1(k) \leq 1, \quad 0 \leq \mathbf{I}_2(k) < \mathbf{I}, \quad P(0) = P^T(0) > 0 \end{aligned}$$

If we choose $\mathbf{I}_1(k)=1$, $\mathbf{I}_2(k)=1$, then Eq.(9) gives general least square method. On the other hand, if we choose $\mathbf{I}_1(k)$, $\mathbf{I}_2(k)$ so that $\text{tr}P(k)=\text{tr}P(0)=\text{constant}$, then Eq.(9) gives fixed trace method [5].

EXPERIMENTAL RESULTS

In this chapter we examine and discuss the robustness of adaptive control for supplied pressure changes and load fluctuations. More specified, we adopt general least square method or fixed trace method as a controller parameter update law, and discuss its control performance. The initial values of adjustable parameters and gain-update matrix of adaptive controller are $\mathbf{q}(0)=[1.5, 0, 0, 0]^T$, $P(0)=10^{-6}I$, respectively, independent of the system information a priori, and I is a fourth order identity matrix. Figure 4 and Figure 5 show experimental results of the position control and the position error in adaptive control with least square or fixed trace method. Experimental conditions are 5[MPa] of supplied pressure and 0[kg] of the mass of load. Figure 6 and Figure 7 are

for case of the supplied pressure 5[MPa] and the mass of load 100[kg]. Figure 8 and Figure 9 are in the case of the supplied pressure 7[MPa] and the same load mass.

From Figure 5, Figure 7 and Figure 9, it is seen that the changes of load or supplied pressure have few effects on the control performance in adaptive control with both least square and fixed trace method. However in the case of the least square update law, steady state error remains for 5-10[s] and for 15-20[s] while position error is about 20 μ m for 10-15[s].

In order to make clear the reason, friction characteristics of the cylinder and flow characteristics of the servo valve are investigated experimentally. As for friction characteristics of the cylinder, the difference between positive and negative direction of the cylinder position is small, thus we conclude that the effect of friction can be nearly ignored. On the other hand, flow characteristics of the servo valve used in this experiment differs depending on the direction of the spool displacement, and the direction of the spool displacement is negative both for 5-10[s] and for 15-20[s]. Figure 10 shows the experimental flow characteristics of the servo valve used in this experiment where the data between -0.5[l/min] and 0.5[l/min] is omitted for the sensor resolution. This implies that the flow characteristic differs for the direction of spool displacement.

As mentioned above, it is seemed that steady state errors in Figure 4 to Figure 9 are caused by flow characteristics of the servo valve. The other reason is that the norm of gain-update matrix P in the general least square method decreases rapidly as time goes by, and as a result the adaptive controller parameters are hardly updated. On the other hand, in the case of the fixed trace method, the norm of gain-update matrix P is constant, and controller parameters are always updated effectively. Therefore position error is about 1 μ m for 0-20[s], and the effect of nonlinearity of the servo valve used in this experiment could be compensated.

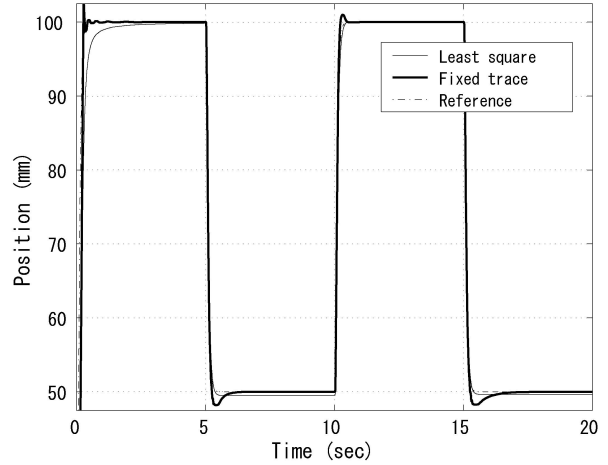


Figure 4 Experimental result: no load, supplied pressure 5[MPa]

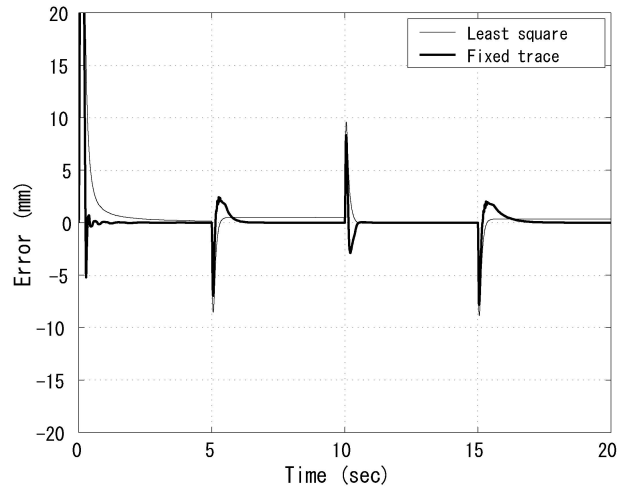


Figure 5 Experimental result (Error): no load, supplied pressure 5[MPa]

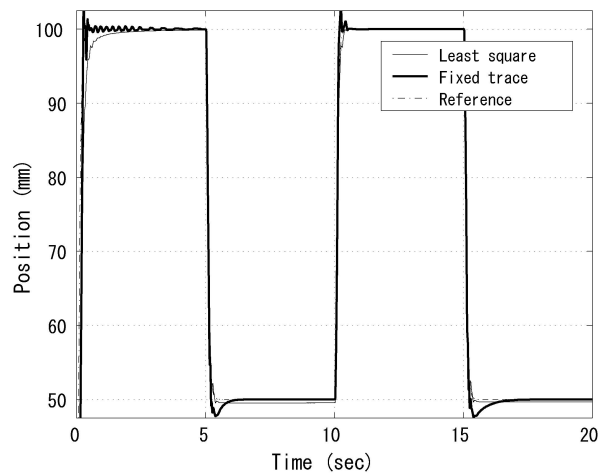


Figure 6 Experimental result: load 100[kg], supplied pressure 5[MPa]

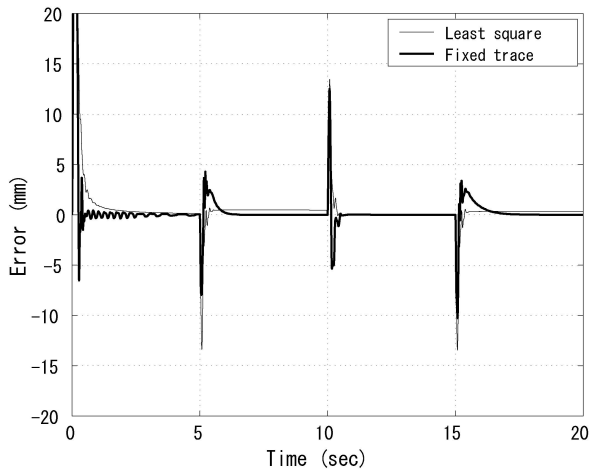


Figure 7 Experimental result (Error): load 100[kg], supplied pressure 5[MPa]

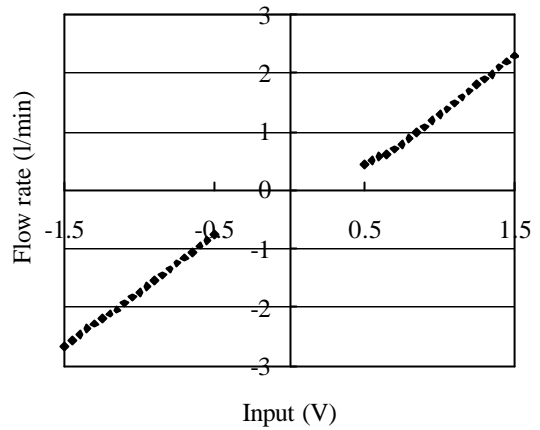


Figure 10 Experimental flow characteristics of the servo valve

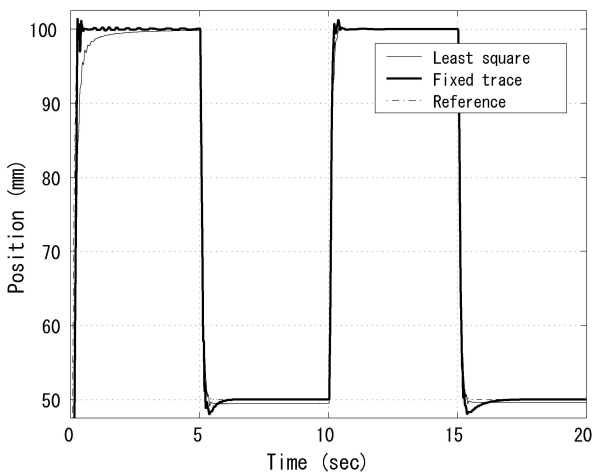


Figure 8 Experimental result: load 100[kg], supplied pressure 7[MPa]

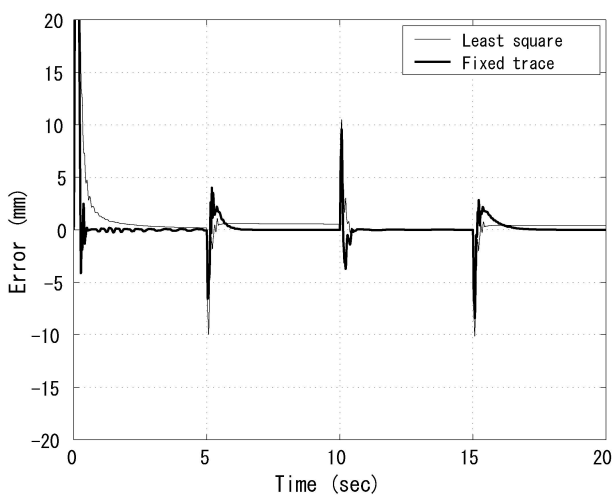


Figure 9 Experimental result (Error): load 100[kg], supplied pressure 7[MPa]

CONCLUSION

In this research, the control performance of adaptive control strategy for water hydraulic cylinder was examined. It is shown experimentally that the adaptive controller has the robustness for supplied pressure changes and/or the load fluctuations by using fixed trace method as a parameter gain update law. As for the cylinder used in this experiment, the effect of friction is very small, therefore the system dynamics can be treated as almost linear. The experimental results show that the application of adaptive controller to water hydraulic servo system is practical.

We consider more simple adaptive control strategy as a future work and the application for water hydraulic motor.

REFERENCES

1. Trostmann, E., Water Hydraulics Control Technology, 1996, Marcel Dekker, Inc.
2. Trostmann, E., Fround, B., Olesen, B.H., and Hilbrecht, B., Tap Water as a Hydraulic Pressure Medium, 2001, Marcel Dekker, Inc.
3. Terasaka, D., Ito, K. and Ikeo, S., PID-Control of Water Hydraulic Servomotor System, Fifth JFPS International symposium, 2002, Vol. 1, pp.443-448.
4. Landau, Y.D., Adaptive Control, 1980, Marcel Dekker, Inc.
5. Goodwin, G.C. and Sin, K.S., Adaptive filtering Prediction and Control, 1984, Prentice-Hall.
6. Goodwin, G.C., Ramadge, P.J. and Caines, P.E., Discrete-Time Multivariable Adaptive Control, IEEE Trans., 1980, AC-25-3, pp.449-453.

EXPERIMENTAL COMPARISON OF TELEOPERATION SCHEMES FOR HYDRAULIC MANIPULATORS

Ali MUHAMMAD, Jouni MATTILA, Mikko SIUKO and Matti VILENIUS

Department of Automation and Control/Institute of Hydraulics and Automation
Tampere University of Technology
Korkeakoulunkatu 6, Tampere, Finland
(E-mail: muhammad.ali@tut.fi)

ABSTRACT

Many studies have been conducted for quantitative/qualitative analysis and comparison of various teleoperation schemes. Position-position, force-position and 4-channels are to name a few. However most of this research has been focused on electrically actuated manipulators. This paper documents the comparative study of various teleoperation schemes explicitly for hydraulic manipulators. Identical water-hydraulic actuators have been used as master and slave. Three popular schemes of teleoperation: position-position, force-position and 4-channels have been implemented and tested. The results are compared on the basis of criteria established by other researchers for electrically actuated manipulators. The study has been done using manipulators with single degree of freedom to emphasize the comparison. The research has been carried out with a goal to extend the number of degrees of freedom in future to obtain a practical water-hydraulic teleoperation system useful in industrial applications such as International Thermonuclear Experimental Reactor (ITER).

KEYWORDS

Teleoperation, Hydraulics, Haptic, Robotics

NOMANCLATURE

F_e	: Environment force	X_{op}	: Operator position
F_m	: Master force	X_s	: Slave position
F_{op}	: Operator force	Z_{11}	: Max. transmittable impedance
F_s	: Slave force	Z_e	: Environment impedance
F_{12}	: Force tracking	Z_m	: Master impedance
h_{11}	: Free motion impedance	Z_{op}	: Operator impedance
h_{21}	: Position tracking	Z_s	: Slave impedance
K_p	: Proportional gain		
X_e	: Environment position		
X_m	: Master position		

INTRODUCTION

Hydraulics is always a choice of interest in industrial applications where high forces are required with compact size actuators. Simple construction and high reliability are added advantages of hydraulics. It has been proving its worth in applications like automobiles, excavators and airplanes with a high degree of reliability and low maintenance. With the developments in water hydraulics (water is used as a pressure medium rather than oil), scope of hydraulic applications has widened further. The characteristic advantages of hydraulics together with the characteristics of water as the pressure medium (fire and environmentally safe, chemically neutral, not activated not affected by radiation) are highlighted in critical applications such as remote handling operations in International Thermonuclear Experimental Reactor (ITER) [1].

Remote handling adds another dimension in control of hydraulic manipulators. It leads to the imagination of adding haptic interfaces with force feedback on hydraulic manipulators. It has been reported that haptic-augmented interactive systems seems to give about a two-fold performance improvement over purely graphical interactive systems [2].

Many studies have been conducted for quantitative/qualitative analysis and comparison of popular teleoperation schemes [3][4]. However, most of this research has been focused on electrically actuated manipulators. With new apparent needs and with advancement of water hydraulic components, heavy duty hydraulic manipulators will soon be employed in teleoperation applications.

Much research has already been done in past to teleoperate hydraulic manipulators in many industrial "situations". Working hydraulic teleoperation systems are under operation across the world to deal with tasks in hazardous conditions. However, most of these teleoperation schemes were developed for custom made manipulators with specific teleoperation capabilities. In summary no off the shelf techniques or general solutions are available.

With the development of ITER, once again, the need of such investigation has become evident. The manipulator has to have 6 degrees of freedom composed of water hydraulic actuators.

In authors knowledge no comprehensive and detailed studies have been performed to develop

and test methods for teleoperation of hydraulic manipulators. It is a first attempt to investigate the behavior of low pressure water hydraulic actuators under teleoperation. Both master and slave are identical water hydraulic cylinders (1 dof manipulators). The goal is to investigate and generalize the teleoperation techniques for water hydraulic manipulators, and widens the scope of application. The research will direct to extend the number of degrees of freedom to obtain a teleoperation system useful in industrial applications such as ITER.

In the following section we will discuss the implemented **teleoperation schemes**. A set of parameters will be mentioned under the section **evaluation criteria**. Hardware and software used for the experiment will be discussed under the heading of **experimental setup**. In the end **results** will be plotted and **conclusions** will be drawn.

TELEOPERATION SCHEMES

Lawrence [5] introduced a general and fundamental architecture for teleoperation. In this architecture both force and position information can be exchanged bilaterally between master and slave. However, the architecture can be modified to fit into any general scheme by setting the parameter values. The architecture also provides the description of optimized transparency in a teleoperation scheme. Transparency is the measure: how much the operator can have the feel of the task. An ideal teleoperation system should be transparent.

From the teleoperation point of view there is no reason not to use the position and force information bilaterally. However, from control point of view it is not possible many times. The reason could be the unavailability of sensors. Also introduced communication delays suggest the use of minimum transfer of information for system stability.

Lawrence architecture can be modified and can be implemented with the absence of certain communication channels. Ming [6] has mentioned and experimented with several schemes in his work. In the following paragraphs we will discuss the schemes of our interest.

Position-position scheme

As the name implies only the positions of master and slave are bilaterally exchanged through transmission channels. The architecture is also referred as position error scheme in text. Figure 1 illustrates the implemented control system.

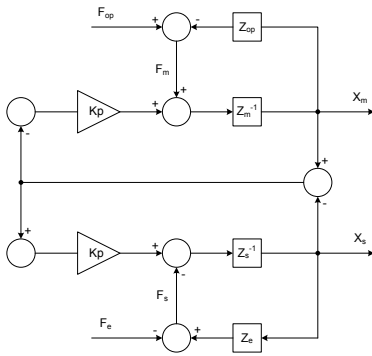


Figure 1 Position-position scheme

The forces acting on master and slave can be equated as in (1) and (2) below:

$$F_m = X_m - X_s \quad (1)$$

$$F_s = X_m - X_s \quad (2)$$

In some cases a scaling factor is required before the forces are reflected. However in this case it is set to one, so same forces are reflected at master and slave.

Force-position scheme

In this scheme position of master is transmitted to the slave, which tries to follow it as efficiently as possible. In the other direction force experienced by slave is transmitted to master, which is felt by the operator. The architecture is also referred as force reflection scheme by some authors.

The reflected force can be scaled up or down as per requirement. However, in this case the scaling factor is set to one, so the same force is experienced by master as by slave. Figure 2 depicts the control system of implemented scheme.

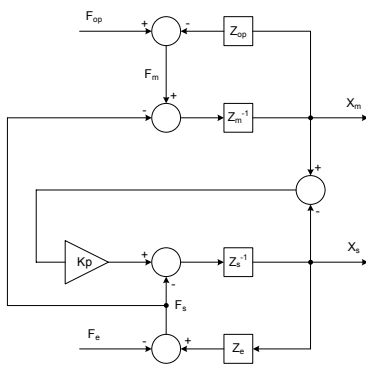


Figure 2 Force-position scheme

Forces acting on master and slave are described by equations (3) and (4) below:

$$F_m = F_s \quad (3)$$

$$F_s = X_m - X_s \quad (4)$$

4-channels scheme

As the name of the scheme suggests all the four channels of information mentioned in Lawrence [5] architecture are utilized to exchange information. Forces as well as positions of both master and slave are bilaterally exchanged. The presence of position and force sensors in both master and slave manipulators is thus compulsory.

The implemented scheme is shown in Figure 3. It can be observed that all the parameters are quite coupled together. It is hard to predict the behavior of the system if any one of them is modified.

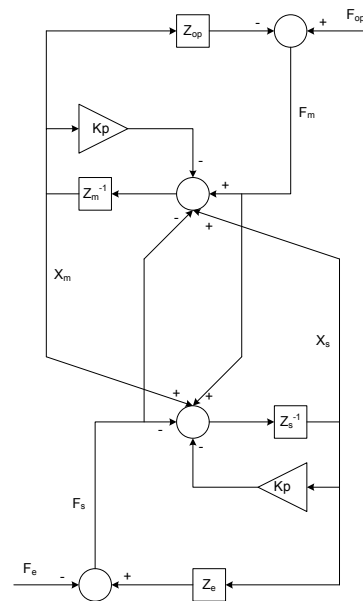


Figure 3 4-channels scheme

Figure 3 also indicates that no controllers have been implemented for communication channels. As both master and slave manipulators are connected to same control system, so the communication delays are neglected in this case. Also as master and slave are identical, so no scaling is required.

Equations (5) and (6) describe the forces acting on master and slave manipulators.

$$F_m = -F_{op} + F_s + X_m + X_s \quad (5)$$

$$F_s = F_e - X_s + F_m + X_m \quad (6)$$

$$F_s = 0 \quad (7)$$

EVALUATION CRITERIA

The sole criteria to evaluate the performance of master-slave systems is the operator, who can notice the difference in efficiency of various teleoperation schemes. However, from analytical point of view quantitative evaluation of such systems is important.

Aliaga [4] in his work has established criteria to evaluate and quantify the performance of a teleoperation system. According to him performance of a master-slave system can be experimentally evaluated by operating them under two basic conditions:

1. Unconstrained movement: Slave is moved freely in its environment. Mathematically this condition can be established in equation (7).

2. Hard Contact: Slave is made to contact and apply force against an infinitely hard surface. Mathematically this condition can be established in equation (8).

$$X_s = 0 \quad (8)$$

The four established parameters are obtained from the two-port representation matrices of a teleoperated system. He also has shown how a teleoperation system can be completely expressed in terms of these four parameters.

Aliaga [4] has tested the criteria with electrically actuated master-slave manipulators. However, in our case, the objective is to analyze the established parameters with hydraulic actuators. The parameters are summarized in Table 1 below.

Table 1 Evaluation parameters

Test Condition	Parameter	Relationship	Desired Value
Unconstrained Movement	Free motion impedance	$h_{11} = \frac{F_m}{X_m} \Big _{F_s=0}$	$\rightarrow 0$
	Position tracking	$h_{21} = \frac{X_s}{X_m} \Big _{F_s=0}$	$\rightarrow 1$
Hard Contact	Force tracking	$F_{12} = \frac{F_m}{F_s} \Big _{X_s=0}$	$\rightarrow 1$
	Maximum transmittable impedance	$Z_{11} = \frac{F_m}{X_m} \Big _{X_s=0}$	$\rightarrow \infty$

EXPERIMENTAL SETUP

Two identical water hydraulic cylinders presented in Figure 4 have been used to form a master-slave teleoperation system. Both cylinders are equipped with identical position encoders and force sensors.

Cylinders are connected to a real time system for control and data accusation, which operates at a frequency of 1 KHz. Position controllers have been implemented for master and slave. A stiffness value of 0.25 N/m has been chosen for both cylinders. A

hard contact surface has been provided for the slave. Teleoperation schemes mentioned before were implemented.

During the experiment the master cylinder is operated by the operator randomly; first in free motion region of slave and then slave against the hard contact surface. The position and force data from master and slave is acquired for a time period of 60 seconds. The obtained results are plotted in following section.

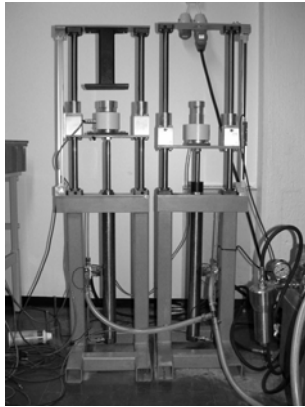


Figure 4 Master-slave hydraulic cylinders

RESULTS

Parameters h_{11} (free motion impedance), h_{21} (position tracking), F_{12} (force tracking) and Z_{11} (maximum transmittable impedance) have been obtained for each teleoperation scheme as per Table 1.

Figures 5, 6 and 7 show the plots of these parameters for each of the scheme.

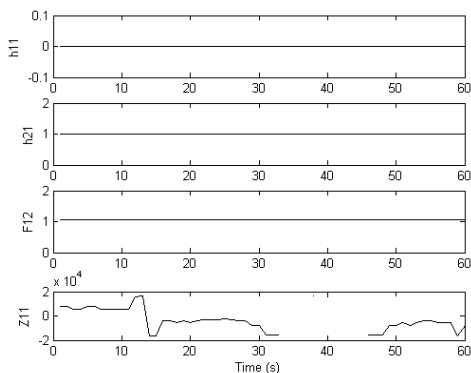


Figure 5 Position-position scheme

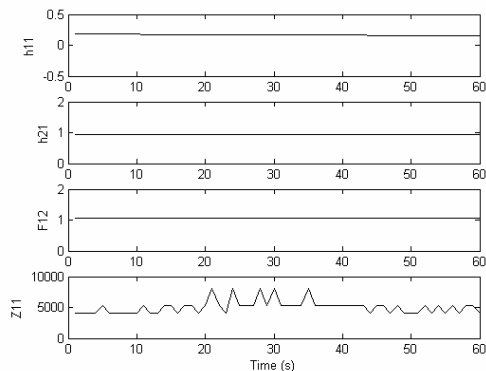


Figure 6 Force-position scheme

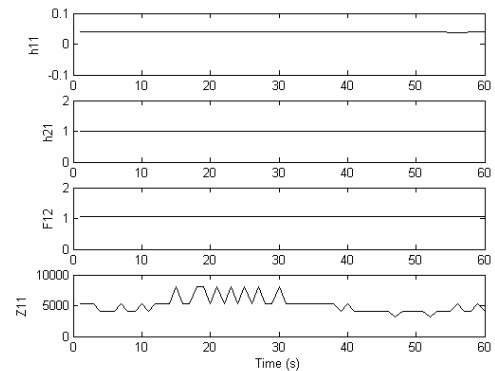


Figure 7 4-channels scheme

The plots establish the fact that same set of parameters (h_{11} , h_{21} , F_{12} and Z_{11}) can be utilized for the evaluation.

Position-position and 4-channels schemes provide the optimal performance. Results from force-position scheme are also satisfactory, apart from parameter h_{11} which is less closer to zero. Position-position scheme provides the best values of maximum transmittable impedance in this case.

CONCLUSION

Three schemes of teleoperation; position-position, force-position and 4-channels are implemented for the first time using identical low pressure water hydraulic cylinders as master and slave. Proposed criteria for the evaluation of teleoperation schemes have been used to analyze the master-slave system. The criteria had already been tested for electrically actuated manipulators. However the idea was to understand the utilization of same criteria for a hydraulic master-slave system.

It has been shown that mentioned parameters can be utilized for the evaluation of hydraulic teleoperation systems. Evaluation parameters have been obtained for each of the teleoperation schemes and used for the comparison purpose.

All master-slave schemes seem to give satisfactory performance. Highest values of maximum transmittable impedance were obtained with position-position scheme. Position-position and 4-channels schemes provide much lower values of unconstrained movement impedance than force-position scheme. All schemes provide good conformance of position and force tracking.

REFERENCES

1. Siuko, M., Pitkäaho, M., Raneda, A., J. Poutanen, J., Tammisto, J., Palmer, J. and Vilenius, M., "Water hydraulic actuators for ITER maintenance devices", *Fusion Engineering and Design* 69 (2003) pp. 141-145.
2. Frederick P. Brooks, Ming Ouh-Uoung, James J. Batter and P. Jerome Kilpatrick, Project GROPE, "Haptic Displays for Scientific Visualization", *ACM Computer Graphics*, 24(4):177-185, 1990.
3. Paloa Arcara, Claudio Melchiorri, "Control scheme for teleoperation with time delay: A comparative study", *Robotics and Autonomous Systems* 38 (2002) 49-64
4. Inake Aliaga, Angel Rubio, Emilio Sanchez, "Experimental Quantitative Comparison of Different Control Architecture for Master-Slave Teleoperation", *IEEE Transaction on Control Systems Technology*, Vol. 12, No. 1, January 2004
5. D. A. Lawrence, "Design Teleoperator Architecture for Transparency", *Proceedings of the IEEE International Conference on Robotics and Automation*, May 10-15, 1992
6. Ming Zhu, "Master-Slave Force-reflecting Resolved Motion Control of Hydraulic Mobile Machines", Master Thesis, The University of British Columbia, April 1994

ON PRESSURE/FORCE CONTROL OF A 3 DOF WATER HYDRAULIC MANIPULATOR

Jouni MATTILA, Mikko SIUKO, Matti VILENIUS

Institute of Hydraulics and Automation,
Tampere University of Technology
P.O.Box 589
FIN-33101 Tampere, Finland
(E-mail: jouni.mattila@tut.fi)

ABSTRACT

Force output of a hydraulic cylinder can be controlled by using either load cell or cylinder pressure feedback. Both forms of feedback have good features: load cells usually give more sensitive and accurate response to the external loads while pressure cells respond faster to changes in valve input and are much easier to install. Pressure feedback can easily be used also with rotary actuators but torque sensors are not widely available. In this study, force based motion controller design for 3-DOF water hydraulic manipulator is implemented. The target of this study is to compare the performance of load-cell feedback that is almost ideal feedback for force in terms of high sensitivity and accuracy to more practical and cost affective pressure feedback. Measured results with 3-DOF water hydraulic manipulator are presented in order to verify the findings.

KEY WORDS

Force based motion control, water hydraulics, force control, hydraulic manipulator

INTRODUCTION

Force control applications with hydraulic actuators are most commonly realized with pressure sensors and the force is measured indirectly from the chamber pressure signals. Main reason for this is the price of the pressure sensors compared to the price of the load cells, but load cells are also more difficult to assemble to the mechanical structure of the machine. One problem with both controllers is the disturbances caused by the change of volume flow and flow direction. The most vicious problem in the force control of hydraulic actuators is the seal friction inside the actuator. This leads to different characteristics between pressure signal and force signal based force controllers. Pressure signal based feedback reacts fast to changes on the valve input, but the static accuracy is not very good due to the seal friction. Seal friction is also the reason for the poor sensitivity for external forces. The seal friction can be compensated to some extent with complicated models, but due to the nature of the phenomenon it can never be fully compensated. Force signal based feedback is, on the other hand, faster to react to external forces and the static accuracy is better. Also sensitivity for external forces is higher.

In this study, force based motion control of a 3 DOF hydraulic manipulator is considered. In force based

motion control scheme shown in Figure 1, a force controller is an inner loop controller and an upper loop controller is PD-position controller with gravity compensation. With electric robots inner loop force/torque controller is not usually required because motor torque is proportional to input current. In hydraulics, servovalve input is proportional to actuator velocity. Therefore, for hydraulic applications demanding actuator force/torque control capability, inner loop force controller is required. In this paper, force based position control of water hydraulic manipulator is studied under pressure feedback and load cell force feedback. Measured results are presented.

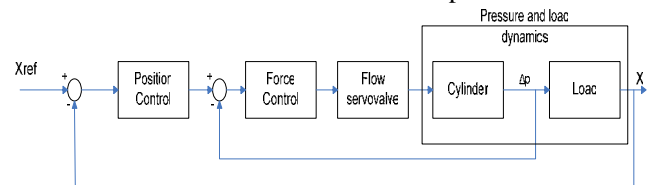


Figure 1. Force based position controller

PERFORMANCE COMPARISON

The performance of the force and pressure controllers were first compared in 1 DOF rotary joint driven by water hydraulic cylinder. Both controllers were simple proportional controllers with the same gain to allow comparison. Size of the cylinder is 32/25-300 mm, the

test joint maximum torque is above 1000Nm throughout the motion range, which is 120°. The cylinder is driven by a flow control servovalve.

The properties of both controllers were measured by its frequency response, step response and by a droop test. Frequency response measurement was used to define the bandwidth of two different control systems. The open-loop frequency response measurement of the test bench was first performed. The result from valve input to velocity without contact revealed bandwidth of 11.3Hz. The rest of the measurements were done with the boom in contact with stiff environment so that the reference force to the cylinder was 2500N. Input signal was band-limited white noise (BLWN) with peak amplitude of approximately 500N. Frequency responses were identified based on BLWN input and force output with ETFE (Empirical Transfer Function Estimate)-function of Matlab's Identification toolbox. Figure 2 shows the frequency response of pressure signal feedback with the bandwidth is about 20-21 Hz. Figure 3 indicates that the bandwidth of the pure force signal feedback is about 16-17 Hz.

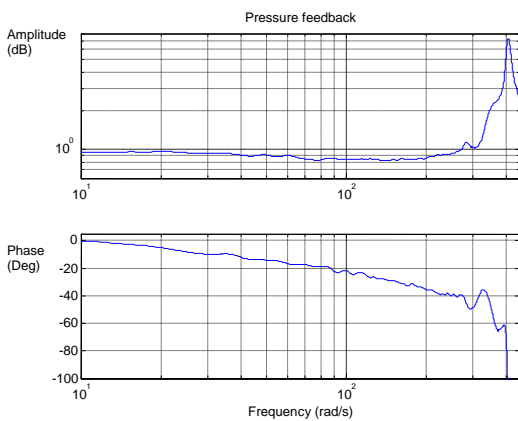


Figure 2. Frequency response of pressure signal feedback

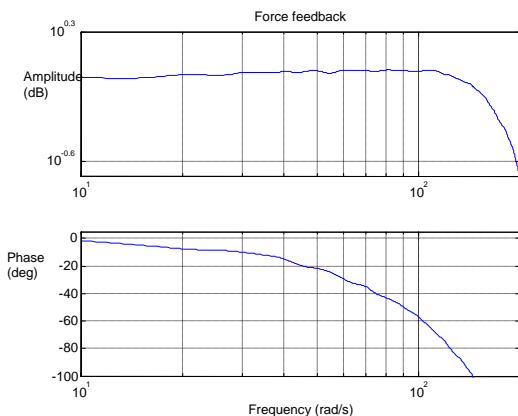


Figure 3. Frequency response of force signal feedback

Step responses were used to verify the results obtained from frequency response measurements. They were also measured when the boom was in contact with the stiff environment. Figure 4 shows the step responses of the force and pressure signal feedbacks. These graphs show that the pressure signal based feedback controller reacts faster to the change in valve input than force signal feedback controller.

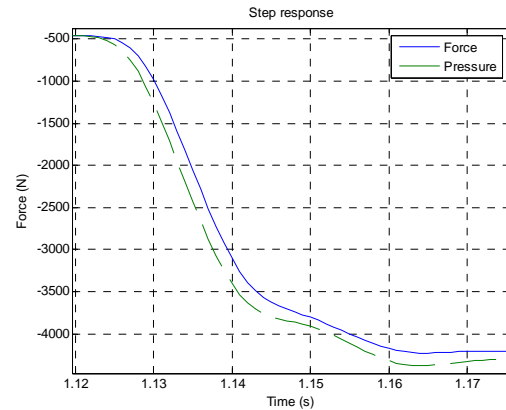


Figure 4. Step responses of force and pressure signal feedbacks

Droop measurements were made to compare sensitivities (backdrivability) between force and pressure signal feedbacks. The measurements were done by slowly moving the boom manually up and down. Ideally the increased cylinder velocity would not increase the motion resistance. From Figure 6 it can be seen that minimum force of about ± 500 Nm is required to move the rotary joint. On the other hand, Figure 5 indicate that with load-cell force feedback and force control, rotary joint responses to external load in fairly linear way without bias force.

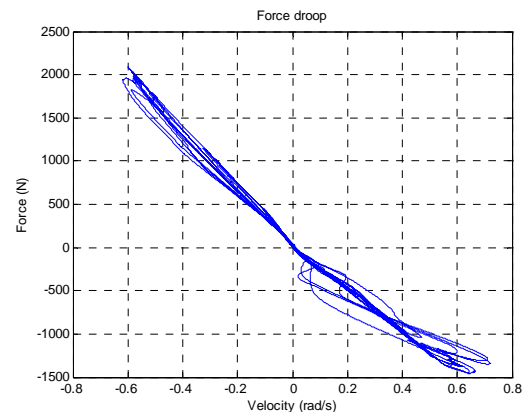


Figure 5. Force signal feedback droop

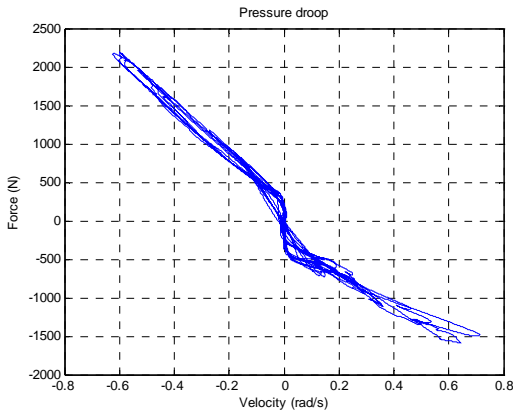


Figure 6. Pressure signal feedback droop

3 DOF MANIPLATOR MEASUREMENTS

Water hydraulic 3 DOF manipulator, shown in Figure 7, was tested with upper loop position and inner loop force or pressure feedback controller. 3 DOF manipulator operates in vertical plane with three actuators. Therefore, two joints are defining the vertical position in XY-plane and the third joint is defining the wrist orientation.

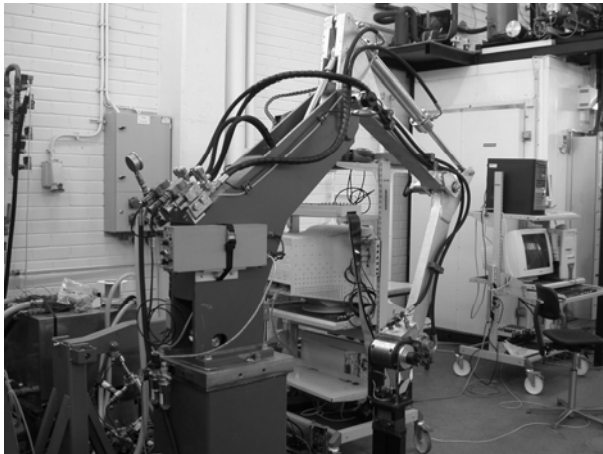


Figure 7. 3 DOF water hydraulic manipulator

Manipulator measurements were carried out under PD-position controller with gravity compensation. The X- and Y-coordinates describes the position of the third joint (wrist) axis. Wrist angle is defined as horizontal angle of the third joint. The schematic of the 3 DOF water hydraulic manipulator is shown in Figure 8.

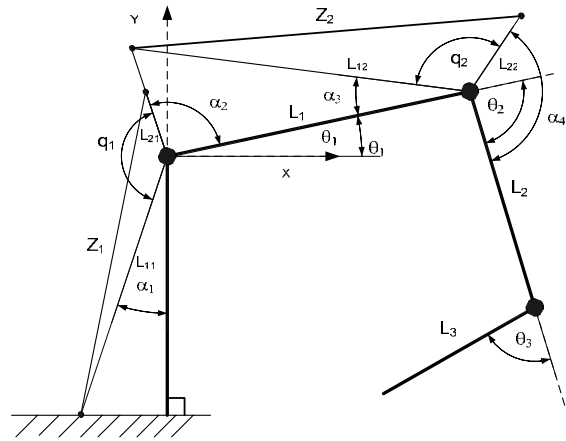


Figure 8. Schematic picture of 3 DOF water hydraulic manipulator

First and second joint are rotary joints driven by water hydraulic cylinders. Both cylinders are equipped with pressure transducers and load-cells installed on cylinder stroke axis. Third joint is vane actuator type and only equipped with pressure transducers. Therefore in both measurements presented, third joint has inner loop pressure feedback controller. Joint angles are measured by pulse encoders. Upper loop position controllers are simple PD-controllers with the same controller gains in both measurements

$$F_R = K_V(\dot{\theta}_R - \dot{\theta}) + K_P(\theta_R - \theta) \quad (1)$$

Trajectory generator is used to create joint motions between the Cartesian reference position. Inverse kinematics are used for converting Cartesian reference positions to joint angle references. Manipulator was programmed to execute a rectangular box in Cartesian space, shown in Figure 9, while keeping a constant horizontal wrist angle at -90 deg. Next measured results for force based motion controller with inner loop force feedback controller and inner loop pressure feedback controller are presented. Upper loop PD-controller has same gains in both measurements to allow inner loop performance comparison. Inner loop force/pressure controllers are simple proportional controller with about same gains. The gains of the pressure feedback controllers had to be decreased a little bit from values that worked good for force feedback inner loop controller. Although results therefore do not provide perfect comparison between two controllers, it is more important to show a benchmark result of force feedback based controller with quite modest time spend with whole motion controller tuning.

Measured results with inner loop force feedback controller

Inner loop controller in first measurement presented is using force feedback provided by load-cell installed on cylinder rod axis. Figure 9 shows the resulting Cartesian position reference and the calculated Cartesian position (forward kinematics) of the manipulator wrist (third) joint in vertical XY-plane.

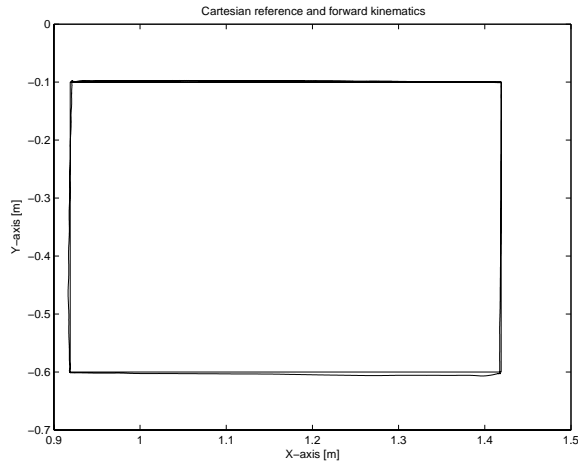


Figure 9. Cartesian reference and position

Cartesian space tracking error versus time is shown in Figure 10.

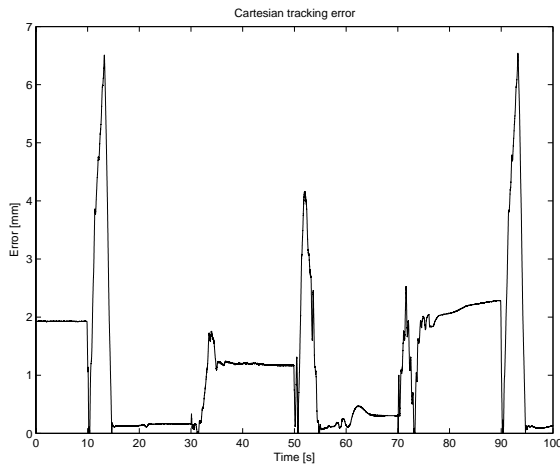


Figure 10. Cartesian tracking error

From Figure 10 it can be seen that static position accuracy is good but dynamic tracking accuracy should be somewhat improved. One reason for poor dynamic tracking accuracy is Cartesian space trajectory generator with trapezoidal velocity profile that results step-like acceleration/deceleration. Also, model-based control was not used in the upper loop controller for linearizing and decoupling of manipulator dynamics.

The measured joint positions and their references are presented in Figure 11.

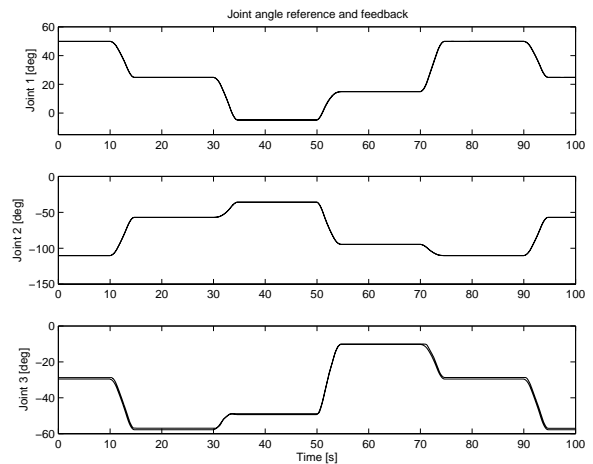


Figure 11. Joint angle references and measured angles

Finally, in Figure 12, resulting force reference and feedback signals are shown.

From Figure 12, it can be seen that force feedback tracks force reference quite well except that acceleration phase of the motion results large tracking error. This is in part due to step-like acceleration motion profile in Cartesian space.

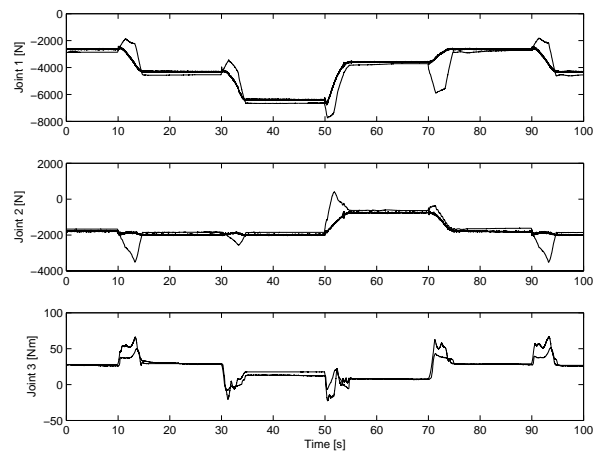


Figure 12. Joint force/torque and references

Measured results with inner loop pressure feedback controller

Second measurement was done by using pressure feedback controller as an inner loop of motion controller. Pressure signal feedback is more challenging control feedback signal than force feedback signal from load cell. This is in part due to direct effect of valve spool position to cylinder chamber pressure. This is because valve spool position is directly proportional to time derivate of pressure. On the other hand, load cell

feedback is less sensitive to fast servovalve spool movements. With pressure transducers sensor price has direct effect on sensor signal quality and bandwidth. In this study, medium priced pressure transducers were used and therefore more expensive sensors should have an effect to the results.

In next Figure 13, the result for pressure feedback controller is shown.

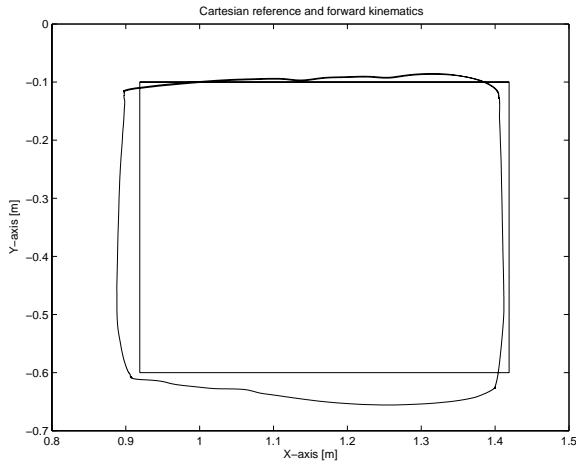


Figure 13. Cartesian reference and position with pure pressure feedback

Cartesian space tracking error versus time is shown in Figure 14.

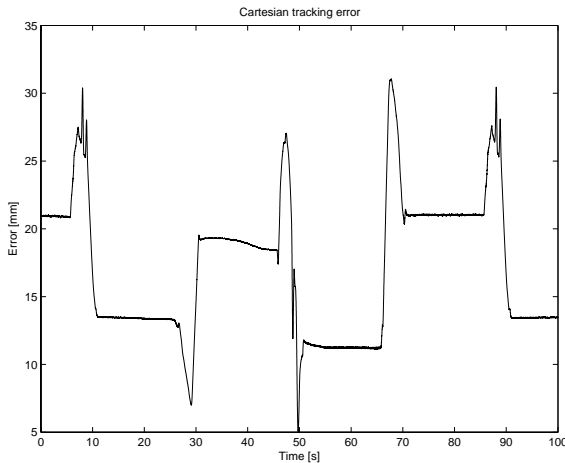


Figure 14. Cartesian tracking error with pure pressure feedback

By comparing Figure 10 and 14 it can be seen that Cartesian space tracking error is about decade bigger than with inner loop force controller. In next Figures 15 and 16 joint angle and force/torque tracking are presented.

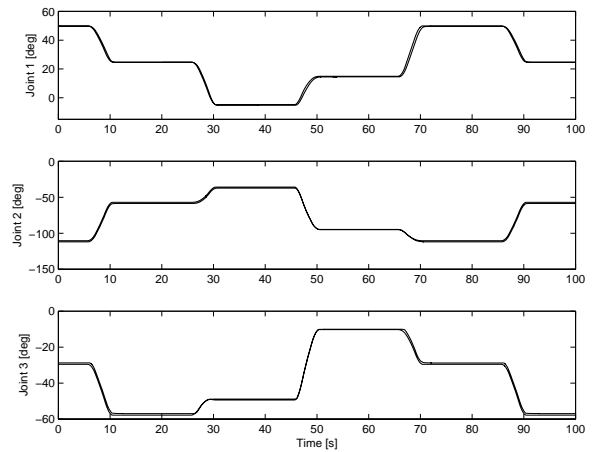


Figure 15. Joint angle references and measured angles with pressure feedback

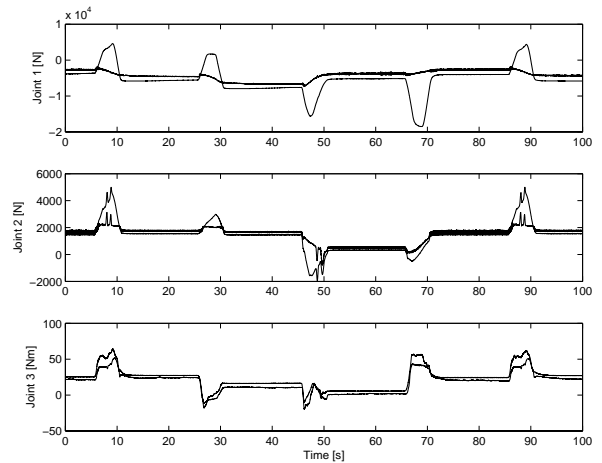


Figure 16. Joint force/torque references and measured with pure pressure feedback

By comparing the results obtained with two different inner loop controllers, it is evident that load cell force feedback controller is outperforming pressure feedback controller. The remarkable thing is that force feedback inner loop controller is quite easy to tune compared to pressure feedback controller. Alleyne [2] has shown the difficulty of tuning hydraulic force controllers mainly from theoretical point of view but theory presented holds for both pressure and force feedback. However, measured results especially with force feedback controller, show that force based motion control of hydraulic joints results quite satisfactory tracking accuracy both in position and force. Obtaining same kind of accuracies with pressure control based motion controller, on the other hand, requires much additional work and possibly model-based seal friction compensation control. The downside of these results is

that load cell feedback is feasible only at high-end robotic applications. For hydraulic rotary actuators like vane actuators pressure feedback is only feasible due to lack of torque feedback sensors of reasonable size and weight. As a continuing study, pressure feedback based inner loop controller will be improved and for that force feedback based results serve as a good benchmark.

CONCLUSIONS

In study pressure feedback based force control is compared to force feedback based controller. Measured results with 3 DOF water hydraulic manipulator are presented. Both inner loop controllers are simple proportional controllers with the about same tuning to allow comparison. Pressure sensor signal feedback quality did not allow as high proportional gain as force sensor signal did. Outer loop position controller is PD-controller also with the same tuning in both cases. Results showed that force feedback based motion controller is about decade better in Cartesian space position tracking accuracy as compared to pressure based motion controller. Difference in results can be explained to be mainly due to sensor signal quality and joint friction.

REFERENCES

1. Koivisto H., Mattila J., Makela A., Siuko M., and Vilenius M., On pressure/force control of a water hydraulic joint, The Ninth Scandinavian International Conference on Fluid Power, SICFP'05, June 1-3, Linköping, Sweden
2. Alleyne, A., 1999, On the Limitations of Force Tracking Control for Hydraulic Servosystems, ASME Journal of Dynamic Systems, Measurement and Control, Vol. 121, pp. 184-190

COMPARISON OF LINEAR CONTROLLERS FOR A HYDRAULIC SERVO SYSTEM

Torben O. Andersen¹, Michael R. Hansen², Henrik C. Pedersen³, Finn Conrad⁴

^{1,3} Institute of Energy Technology, Aalborg University
Pontoppidanstraede 101, DK-9220 Aalborg East, Denmark
(E-mail: toa@iet.aau.dk)

² Institute of Mechanical Engineering, Aalborg University
Pontoppidanstraede 105, DK-9220 Aalborg East, Denmark

⁴ Department of Mechanical Engineering, Technical University of Denmark
Nils Koppels Allé, DTU-bygning 404, DK-2800 Lyngby, Denmark

ABSTRACT

In many hydraulic control applications, classic linear controllers are still employed, although there exist a number of number of nonlinear control methods, which may be better suited for handling the intrinsic non-linearities often found in hydraulic systems. The focus of this paper is therefore on comparing different linear controllers, based on both simulation and experimental results, to determine what is obtainable when applying standard linear controllers to a hydraulic SISO servo system. The paper furthermore addresses how the performance may be improved by using internal pressure control and model based information to include feedforward information. The control strategies considered are all based on measurement of piston position and pressure only.

KEYWORDS

Pressure control, feedforward control, controller comparison

NOMENCLATURE

A_p	:	Cylinder piston area
B_t	:	Viscous friction coefficient
C_L	:	Leakage coefficient
K_q	:	Linearised flow coefficient
K_{qp}	:	Linearised flow/pressure coefficients
K_v	:	Servo valve coefficient
M_{eq}	:	Equivalent mass working on cylinder
p_L, p_S, p_T	:	Load, supply and tank pressure
u	:	Control signal
V_t	:	Total cylinder chambers volume
x_p, x_r	:	Cylinder and reference cylinder position
β_F	:	Effective oil bulk modulus

INTRODUCTION

Generally, hydraulic plants exhibit significant non-linearities and have time-varying parameters, which makes them difficult to control using linear controllers, as these typically have to be designed rather conservatively in order to ensure stability. Still, linear controllers are often applied to hydraulic systems [1], despite many non-linear control algorithms have been applied to hydraulic systems with success, see e.g. [1]-[4]. The main reasons for this are the simplicity of the linear control theory and the well developed set of rules and methods that exist, combined with the relative low knowledge of non-linear control theory within the hydraulic indus-

tri. Therefore, this paper focus on what performance, in terms of tracking errors and robustness, that is obtainable using standard linear controllers on a hydraulic servo system. It also considers what may be obtained if these are also combined with model based feedforward information. The paper furthermore addresses how the damping may be increased by adding an internal pressure feedback. Based on both simulation and experimental results the controllers are compared and their possibilities and limitations are outlined.

SYSTEM PRESENTATION

The hydraulic application considered here is a two-d.o.f. robotic manipulator, where each link is driven by a servo valve controlled symmetrical cylinder. Each of these servo valve and cylinder systems represents a hydraulic servo system (HSS) as considered in the following. A generalized model of such a system is characterized by the highly non-linear nature of the servo valve pressure/flow characteristic, friction effects, a very low damping ratio and dynamics that strongly depends on the operating point and the physical parameters describing the system. If the non-linear equations governing this system are linearised around an operating point, the transfer function, relating cylinder piston position to the servo valve input signal, may be written as [5]:

$$G(s) = \frac{X_P(s)}{U(s)} = \frac{K\omega_n^2}{s^2 + 2\zeta\omega_n s + \omega_n^2} \quad (1)$$

where the gain K , natural frequency ω_n and damping ratio ζ are given by:

$$K = \frac{k_q A_P}{B_t(C_L + k_{qp}) + A_P^2} \quad (2)$$

$$\omega_n = 2\sqrt{\frac{\beta_F}{M_{eq}V_t}(B_t(C_L + k_{qp}) + A_P^2)} \quad (3)$$

$$\zeta = \frac{4\beta_F M_{eq}(C_L + k_{qp}) + B_t V_t}{4\sqrt{M_{eq}V_t\beta_F(B_t(C_L + k_{qp}) + A_P^2)}} \quad (4)$$

Pressure Feedback

In order to increase the damping in the system an internal pressure feedback loop is implemented, as this has a stabilising effect on the HSS. The general idea is to measure the pressure difference in the servo-cylinder and feeding it back to the load flow reference of the servo-valve. However, instead of using a simple gain feedback, corresponding to a leakage term, the pressure is fed back through a high-pass filter which means, that only the high frequency pressure fluctuations will affect the load flow. A block diagram of the system with the pressure feedback loop inserted is shown in Figure 1.

The effect of the pressure feedback may be seen by closing the inner pressure loop, whereby the integrator part

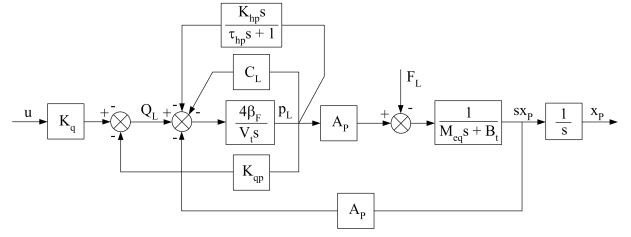


Figure 1 Block diagram of the system with and without pressure feedback through a high-pass filter.

$\frac{4\beta_F}{V_t s}$ in the original system is changed to:

$$\frac{4\beta_F}{(4\beta_F K_{hp} + V_t)s} \cdot \frac{\tau_{hp}s + 1}{\frac{V_t}{4\beta_F K_{hp} + V_t} \tau_{hp}s + 1} \quad (5)$$

The first term in Eq. (5) can be seen to reduce the gain of the system and the second term in Eq. (5) is a lead filter, which, if dimensioned correctly, may be used to increase the relative stability of the system. Implementing this filter, by choosing the time constant, τ_{hp} , below the natural frequency of the system and adjusting the gain, K_{hp} , to obtain sufficient phase margin and bandwidth, the systems frequency response may be changed as shown in the bode plot in Figure 2.

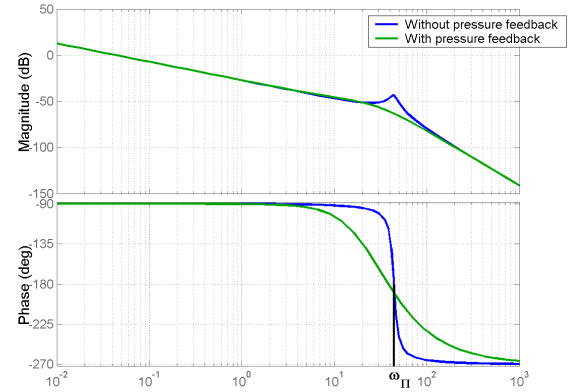


Figure 2 Bode plot of HSS to be controlled.

With the pressure control implemented, it shows that the resonance magnitude peak has been smoothed. This means, that the gain may be increased without encountering stability problems.

LINEAR CONTROLLERS

Linear controllers are typically designed based on worst case considerations, in order to ensure stability in the whole work space. The model given by Eq. (1) is based

on the cylinder being in the middle position and under the assumption that this is worst-case concerning stability, which is also the case for a constant inertia load. For the robotic manipulator the inertia load changes as a function of piston position, why the above is an approximation. The lowest eigenfrequency for each of the two cylinders are however so close to the middle position that this approximation is justified. This model is therefore used for determining the controllers and the controller parameters are adjusted, so the system fulfils the phase- and gain-margins requirements:

$$GM > 6[\text{dB}] \quad PM > 45^\circ \quad (6)$$

In the following the linear controllers considered are shortly described. These controllers are all found interesting due to the Bode plot characteristic of the system shown in Figure 2.

- **P-controller:** As the system both with and without the pressure control is a type one system, a proportional feedback results in tracking, why this is the simplest and most obvious controller to try.
- **PT/P-lead-controller:** From the system without pressure feedback the bode plot shows a fast decrease of the phase around the eigenfrequency, why adding a first order filter (PT) with a filterfrequency around ω_{II} may reduce the magnitude around the peak, but only change ω_{II} a little. The controller is:

$$G_{PT}(s) = K_P \frac{1}{\tau_i s + 1} \quad (7)$$

With the pressure control implemented it may be seen that adding phase to the system around the resonance frequency will increase the bandwidth of the system. Therefore a P-Lead controller is designed for this case:

$$G_{PD}(s) = K_P \left(\frac{\tau_d s + 1}{\beta \tau_d s + 1} \right) \quad (8)$$

- **PID-controller:** Since the system is of type one, the above controllers gives zero steady-state error, when the HSS is given a step input. If a PI or a PID controller is used, zero steady-state error will also be obtained for a ramp input. Practically the PID-controller is implemented as a PI-lead controller, in order to avoid problems with differentiation of high frequency noise:

$$G_{PID}(s) = K_P \left(1 + \frac{1}{\tau_i s} \right) \left(\frac{\tau_d s + 1}{\beta \tau_d s + 1} \right) \quad (9)$$

Simulation Results

The responses of the different controllers with and without pressure feedback are shown in Figure 3 and 4. The reference for both cylinders are sinusoidal, making each of the cylinders move from one end to the other and back in 3 seconds.

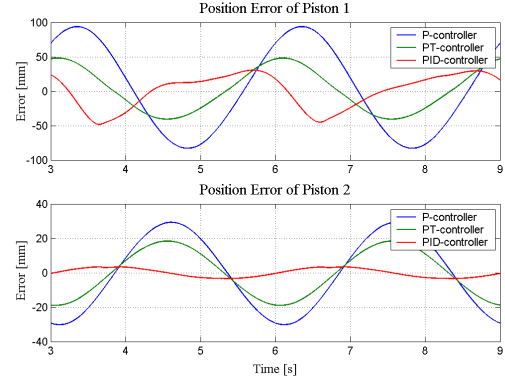


Figure 3 Simulated position tracking errors for the sinusoidal reference input, using the three controllers without pressure feedback.

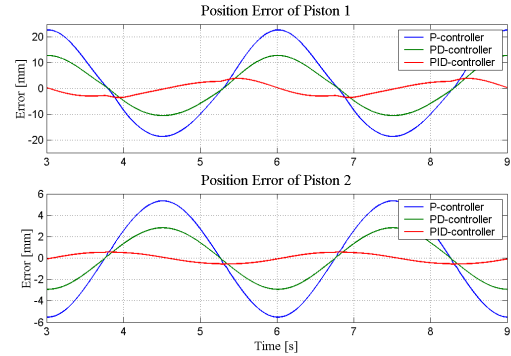


Figure 4 Simulated position tracking errors for the three controllers with pressure feedback.

Comparing the two figures it may be seen that the pressure feedback reduces the position error significantly. Still the errors are large, and typically not within limits for most of these types of servo systems. From the simulation results it may also be seen that the performance of the two servo systems are quite different, due to the different masses on the systems. Of the considered controllers it so also clear that the PID-controllers show the best results, and the PID-controller with pressure feedback is therefore the one tested on the laboratory setup.

Experimental Results

Originally the PID-controller was designed using a lead-filter for the D-part. When implemented in the laboratory the controller works, but the operation is noisy. In order to improve performance a critically damped second order filter in combination with the D-part reduces the noise significantly without reducing the performance, which implemented yields:

$$G_{PID}(s) = K_p + \frac{K_{pt}}{\tau_i s} + \frac{K_{pd}s}{\tau_d^2 s^2 + 2\tau_d s + 1} \quad (10)$$

Simulation results for the new PID controller with pressure feedback are shown in Figure 5, which also shows the robustness of the controller to a mass step of 50 [kg] applied after 6 [s]. Experimental results for this controller are shown in Figure 6. The results corresponds very well with the simulated ones.

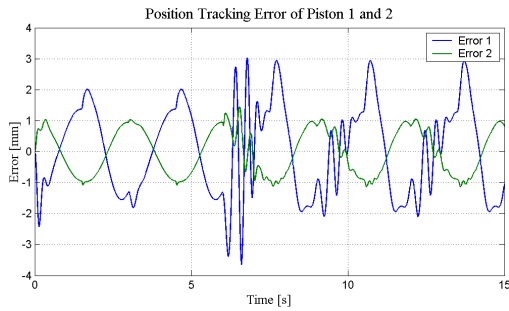


Figure 5 Simulated position tracking errors, using the PID controller with pressure feedback. A mass step of 50[kg] is applied after 6 [s].

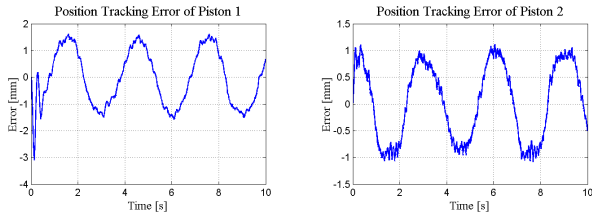


Figure 6 Measured tracking errors on the laboratory setup, using the PID controller with pressure feedback.

CONTROLLERS WITH FEEDFORWARD INFORMATION

The above controllers had a stabilising effect on the system. However when fast position tracking is required the controllers shows drawbacks such as phase lag, steady-state error and overshoot. Combining a standard controller with e.g. a velocity feedforward term may im-

prove performance in an often simple and intuitive matter, assuming the necessary system information is available. Hereby the linear controller only needs to compensate for the error between the estimated and the correct control signal, whereas the feedforward terms ensures the main part of tracking. Estimation of the feedforward control signal may in this case be done based on the reference trajectory. Alternative approaches may be to include feedforward terms to eliminate or reduce influence of measurable disturbances. In case of the robotic manipulator this could be measuring of the acceleration of link 2, as the inertia forces of this affects link 1. A brief discussion of different approaches for including feedforward terms in the controller structure may be found in [3].

Velocity Feedforward Controller (VFC)

To apply this method we need $x_r \in C^1$, which is also the case for the sinusoidal input. The general idea is then to continuously compute the servo-valve control input from knowledge of the system. Since, in steady state, the velocity of the piston is (assumed) proportional to the displacement flow, and hereby the flow from the servo-valve, the spool position corresponding to the wanted flow can be calculated from the orifice equation and fed forward, as shown in Figure 7.

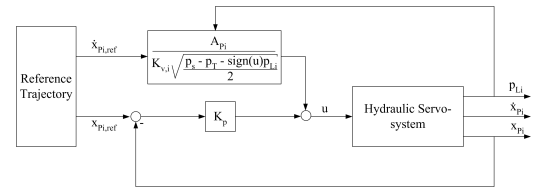


Figure 7 System with position feedback (proportional controller) and velocity feedforward control.

An expression for the load flow, corresponding to the average flow across the servo-valve orifices is given by:

$$Q_L = K_v u \sqrt{\frac{p_S - p_T - \text{sign}(u)p_L}{2}} \quad (11)$$

Similarly, the load flow may be related to the pressure dynamics as:

$$Q_L = A_P \dot{x}_P + \frac{V_t}{4\beta_F} \dot{p}_L + C_{LP} p_L \quad (12)$$

Which, if neglecting leakage reduces to:

$$Q_L = A_P \dot{x}_P + G \quad (13)$$

where G representing the pressure dynamics. Substitut-

ing Eq. (13) into Eq. (11) yields

$$\begin{aligned}
 u &= \Gamma \dot{x}_P + \nu \\
 \Gamma &= \frac{A_P}{K_v \sqrt{\frac{p_S - p_T - \text{sign}(u)p_L}{2}}} \\
 \nu &= \frac{g(p_L)}{K_v \sqrt{\frac{p_S - p_T - \text{sign}(u)p_L}{2}}}
 \end{aligned} \quad (14)$$

with Γ and ν in general being state dependent. With Eq. (14) representing the system dynamics, the control law takes the following form.

$$u = \hat{\Gamma}(\dot{x}_R + \text{Con}(x_R - x_P)) + \hat{\nu} \quad (15)$$

where $\hat{\Gamma}$ may be either estimated or calculated by measuring the load pressure p_L , based on Eq. (14). In the following ν is set to zero. Con denotes the (position) feedback controller implemented, x_R is the position reference, x_P is the actual position and \dot{x}_R is the velocity reference. If Γ is assumed constant, the feedforward term acts as a pre-filter and does therefore not affect system stability. If p_L instead is fed back and used for calculating Γ the system changes and becomes state dependent. The control law implemented is thus given by:

$$u = \underbrace{\frac{A_P}{K_v \sqrt{\frac{p_S - p_T - \text{sign}(u)p_L}{2}}}}_{u_{\text{feedforward}}} \dot{x}_R + \underbrace{\text{Con}(x_R - x_P)}_{u_{\text{feedback}}} \quad (16)$$

Three different types of the VFC have been tested on this basis, these are:

- VFCE with position measurement only (Estimated Γ)
- VFCA with position and load pressure measurement (Actual Γ)
- VFPC with pressure feedback (VFCA with pressure feedback though a high-pass filter)

All three types were tested with a PI controller in the (position) feedback loop.

Simulation Results

Simulation results for the three different controllers are shown in Figure 8-10.

In all the simulations a mass step of 50 [kg] is applied after 6 [s]. From the simulations it may be seen that the best result is obtained when Γ is calculated using measurement of p_L (VFCA), but without the pressure feedback, as this actually may increase the tracking error, when these are small, i.e. in the range of 0.5 – 1 [mm]. For the VFPC adjustment of the controller parameters resulted in the integral term being so small that the controller is implemented as a pure proportional controller instead.

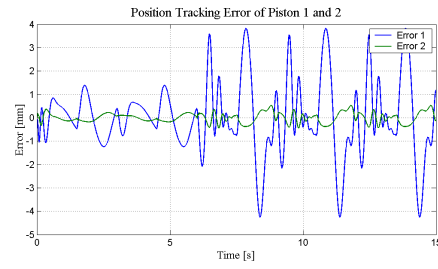


Figure 8 Simulated position tracking errors, using the VFCE and a PI-controller in the outer loop.

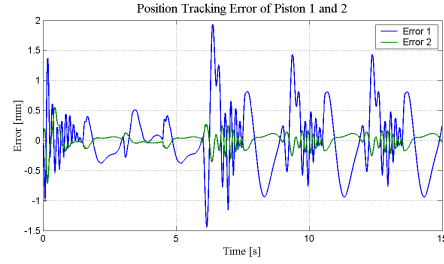


Figure 9 Simulated tracking errors, using the VFCA in combination with a PI-controller.

Experimental Results

All VFC strategies were tested in the laboratory to verify the simulation findings. The results of the measurements are shown in figs. 11-13.

Practical implementation showed that, due to noise, it was necessary to filter the measured p_L in the VFCA-scheme, in order to get stable and satisfactory performance. The filtering is done using a first order filter, however this did degrade performance, as the tracking error becomes much larger than in the simulation, as shown in Figure 12. For the VFPC-scheme the experiments showed that it was possible to implement the scheme without filtering the pressure signal, but the tracking error is still larger than what the simulation shows, cf. Figure 13 compared to Figure 9.

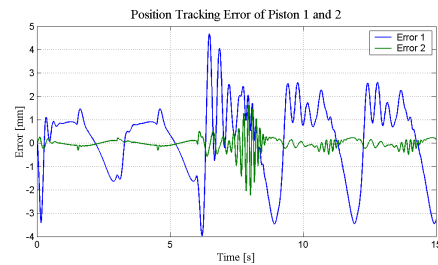


Figure 10 Simulated tracking errors, using the VFPC and a P-controller in the outer loop.

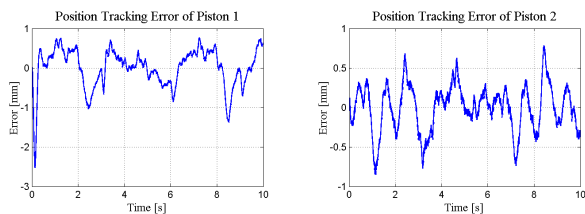


Figure 11 Measured tracking errors using the VFCE and a PI-controller in the outer position loop.

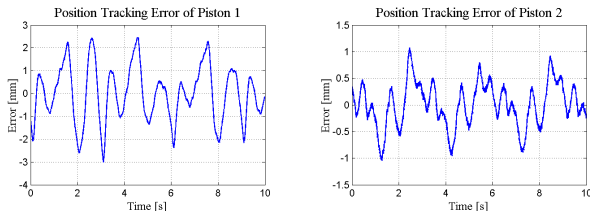


Figure 12 Measured tracking errors using the VFCA, with filtered p_L , and with a PI-controller in the position loop.

CONCLUSIONS

In this paper different linear controllers have been tested and compared, to determine what is obtainable when applying these to a highly non-linear hydraulic system. Based on both simulation and experimental results it was found that the linear controllers in their standard form are not generally sufficient to obtain acceptable performance. Including the pressure feedback dramatically improved performance. Of the standard controllers considered the PID-controller with pressure feedback shows the best response and also proved to be robust towards mass variation. In the practical implementation of the controller it was however necessary to include a filter on the derivative part to avoid noise problems. A disadvantage with this controller is as well that both a position and pressure transducer is required.

Considering the feedforward controllers, these all work well and have tracking errors better than for the PID-controller with pressure feedback. From both the experiments and simulation it was found that the best overall result is obtained with the simple VFCE strategy, using a PI-controller in the position feedback loop.

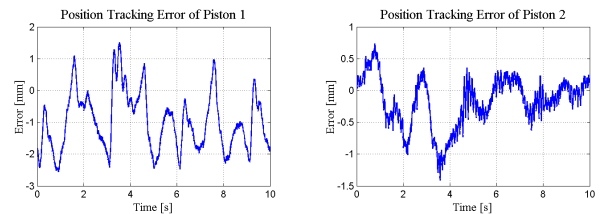


Figure 13 Measured tracking errors using the VFCE and a P-controller.

This although the VFCE in both simulation and experimentally shows very similar or better tracking errors. The advantages of the VFCE strategy is, besides being easy to implement, that it only requires a position measurement and it is not very sensitive to noise. The robustness towards mass variations on the other hand is not as good as for the PID-controller and the VCFA-scheme, which both requires pressure measurement, but still better than for the VFCE. Of the controllers considered the VFCA is the most robust to mass variations.

REFERENCES

- [1] Jelali M., Kroll A. Hydraulic Servo-systems - Modelling, Identification and Control. ISBN: 1-85233-692-7, Springer Verlag London 2003.
- [2] Edge K.A., On the Control of Electrohydraulic Systems - Some Recent Research Contributions, The Eight Scandinavian International Conference on Fluid Power, SICFP'05, May 7-9, Tampere, Finland.
- [3] DeBoer C.C., Yao B., Velocity Control of Hydraulic Cylinders with only Pressure Feedback. School of Mechanical Engineering, Purdue University, IMECE01/DSC-2B-3, ASME International Mechanical Engineering Congress and Exposition New York, November 2001.
- [4] Andersen T.O., Hansen M.R., Pedersen H.C., Conrad F., On the Control of Hydraulic Servo Systems - Evaluation of Linear and Non-Linear Control Schemes, To be presented at The Ninth Scandinavian International Conference on Fluid Power, SICFP'05, June 1-3, 2005, Linköping, Sweden.
- [5] H.E. Merritt, Hydraulic Control Systems, Wiley, New York, 1967.

COMPARING PNEUMATIC AND WATER HYDRAULIC POSITIONING SYSTEM FOR PROCESS VALVES

Tapio VIRVALO

IHA, Tampere University of Technology, Finland
P.O.Box 589, 33101 Tampere
Tel. -358-3-31152262, Fax. -358-3-31152240
e-mail tapio.virvalo@tut.fi

ABSTRACT

Pneumatic positioning actuators are very commonly used in the control of process control valves in petroleum, chemist and paper industries. During the last decade several ideas have been presented how to use water hydraulics in different applications. Low-pressure water is available in some process industrial applications a little bit the same way as pneumatic power. Lately very demanding performance specification requirements have been presented for positioners of process valves. In this paper requirements set to control components of pneumatic and low pressure water hydraulic drives in order to fulfil these high quality performance specifications are studied. Different experimental tests have been done with both systems and results show that the specification can be fulfilled, but quite high performance components are required.

KEYWORDS

Positioning, pneumatic position servo, water hydraulic position servo, process valves

INTRODUCTION

Pneumatic positioning actuators are very commonly used in the control of process control valves in petroleum, chemist and paper industries. Pneumatics has many advantages but also drawbacks in these applications. The main advantages are easy assembly and cost effectiveness and the most significant drawbacks are poor performance and large size.

During the last decade several ideas have been presented how to use water hydraulics in different applications. Applicability of water hydraulic servo systems in certain special applications has been also studied [1] [2] [3]. Low-pressure water is available in some process industrial applications a little bit the same way as pneumatic power. The performance requirements of pneumatic as well as low-pressure water hydraulic servo valves are studied in experimental tests.

Typically special low cost and quite poor performance valves are used in the control of process valves. However, some very demanding requirements have been presented to the performance of process valves. The steady state and dynamic specifications of the positioning of process valves are presented in [4] which is a de facto standard in process industry. En Tech has specified three different specification levels. The parameter values of dynamics for the most demanding cases are; $T_d=0.1s$, $T_{86}= 0.4s$ and $T_{ss}= 1s$, Figure 1. In addition the following specifications are valid: dead band 0.06%, step resolution 0.04%, total hysteresis 0.1%, and maximum overshoot 20% in the step size range $\pm 10\%$.

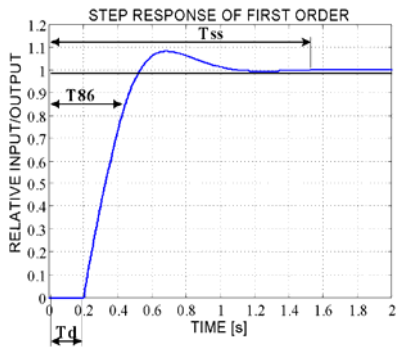


Figure 1. Performance criterion parameters

The studied application is shown in Figure 2 [5]. These kinds of positioning systems are used for instance in segment type process valves.

GOALS OF STUDY

The goals are to find if it is possible to achieve the specifications [4] with pneumatics and low pressure water hydraulics. The following goals are set:

- * To find out if the highest performance criterions of process valve positioning system can be fulfilled with both systems
- * To specify the specifications of the valid components of the system.
- * To specify the performance requirements of the controller.

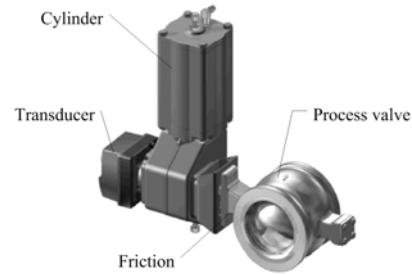


Figure 2. Process control valve (studied system)

SPECIFICATIONS OF SYSTEMS

A normal segment type process valve with standard pneumatic actuators is used in both cases, Figure 2. The rotation range of the segment is 90° . The control valve and position sensor are changed. In this study commercial pneumatic and water hydraulic servo valves are used.

The specifications of the pneumatic control system are as follows:

- * Cylinder 125/20-76 (piston/rod-stroke [mm])
- * Supply pressure 6bar
- * Servo valve, nominal volume flow 700l/min, supply pressure 6bar, pressure drop/notch 1bar, hysteresis $<0.5\%$, bandwidth 600rad/s
- * Position sensor, incremental encoder, resolution 0.01%

The specifications of the low pressure water hydraulic control system are as follows:

- * Cylinder 80/20-76 (piston/rod-stroke [mm])
- * Supply pressure 27bar
- * Servo valve, nominal volume flow 19l/min, pressure drop/notch 35bar, hysteresis $<3\%$, bandwidth 600rad/s
- * Position sensor, differential capacitive angle sensor
- * Analog-to-digital converter 14 bits.

The sampling time of the controller is 2ms in both cases. Considering the performance specifications and load characteristics this application is very demanding for both positioning system. Inertia loads are remarkably low in these kinds of applications. Friction forces are high mostly because of the seals of the process valve. High friction forces make the specifications of resolution and

hysteresis very challenging.

EXPERIMENTAL TESTS

Experimental tests are carried out both with pneumatic and pure water hydraulic systems. All components are commercial. The power supplies of both systems are taken from the main power units of the laboratory. The supply pressures are kept practically constant with an extra volume in the pneumatic supply line and an accumulator in the water hydraulic supply line.

Initial tests

In order to estimate friction forces and the velocity gain of the systems some open loop measurements are carried out. As an example open loop responses of both systems are shown in Fig.3 and 4. The maximum friction force is almost the same in both cases. The behaviour of the friction force in the pneumatic drive is more function of the piston position than in water hydraulic case. Remarkable difference is also in the relationship between the friction force and the maximum force and the dynamic behaviour of the friction forces.

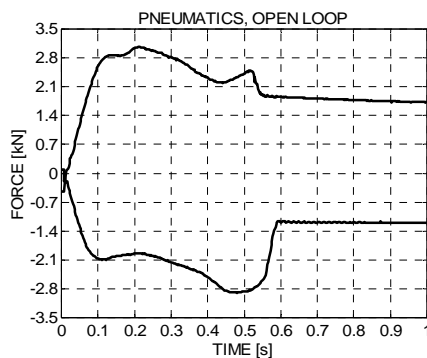


Figure 3. Measured friction force of pneumatic drive in both directions

The maximum friction force in pneumatic drive is about 45% and in water hydraulic drive about 22% of the maximum pressure forces. The pressure change rate is significantly lower in pneumatic drive than in water hydraulic drive in spite of that the maximum velocity of the pneumatic drive is significantly higher.

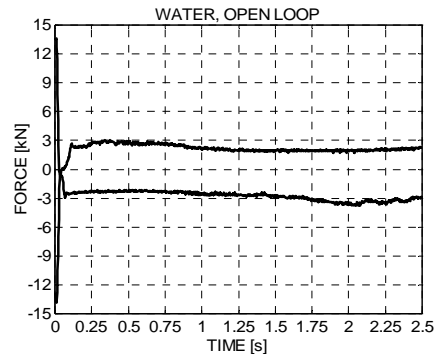


Figure 4. Measured friction force of water hydraulic drive in both directions

Performance tests

Because the specifications of the process valve positioner specify the performance of step responses, the following step responses are carried out. Figure 5 and 6 shows the position error responses of the pneumatic as well as water hydraulic drive, when the stroke length is about 10% corresponding about the 10mm stroke of the cylinders.

Both cases fulfil well the performance specifications. The responses of the water hydraulic drive behave nicely and quite symmetrically, but there are some un-certainties in the responses of the pneumatic drive. A simple non-linear P-controller is used in the water hydraulic case and a State Controller in the pneumatic case. Figure 7 and 8 shows responses of the position error of 1% strokes and Fig. 9 and 10 of 0.4% strokes, respectively.

All these responses fulfil the positioning accuracy and response time specifications. There are high frequency oscillations in responses of the water hydraulic drive, which are mostly due to the noise in the analogue position measuring system. The resolution of the position measuring system of the pneumatic drive can be clearly seen in the position error responses of Fig. 9. Because there is no overshoot in any one of the responses the tuning of the controllers might have been a little bit tighter. However the accuracy and response time requirements are fulfilled so there is no need to increase loop gains.

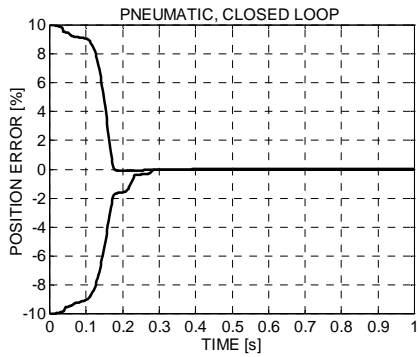


Figure 5. Measured position error responses, strokes 10%, pneumatics

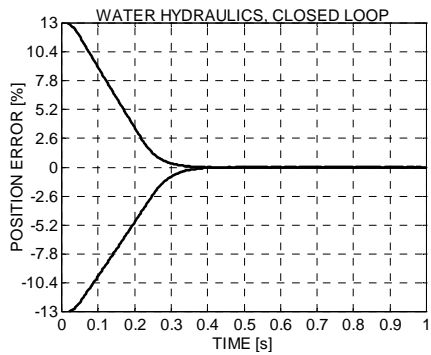


Figure 6. Measured position error responses, strokes 13%, water hydraulics

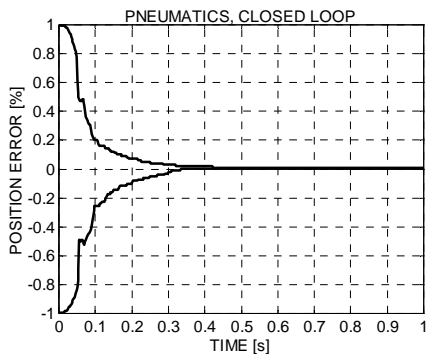


Figure 7. Measured position error responses, strokes 1%, pneumatics

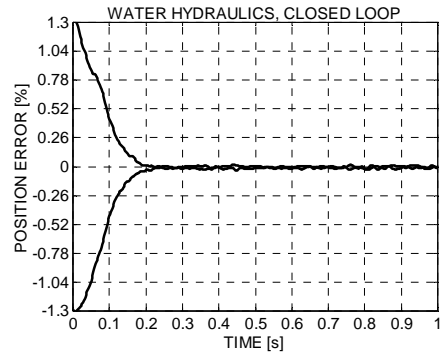


Figure 8. Measured position error responses, strokes 1.3%, water hydraulics

The specifications presented in Introduction chapter, dead band 0.06%, step resolution 0.04%, total hysteresis 0.1%, should be considered quite tough. In order to find those characteristics of both systems a continuous and discrete triangle shape wave reference signals have been used. As an example, the responses of the pneumatic drive to the continuous triangle wave are shown in Fig.11 and 12. The responses of the water hydraulic drive of discrete triangle wave are shown in Fig.13 and 14, respectively. As can be seen both system fulfil the performance specifications.

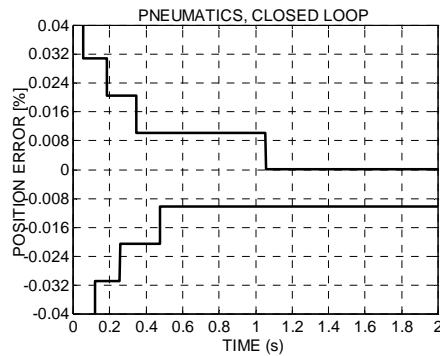


Figure 9. Measured position error responses, strokes 0.4%, pneumatics

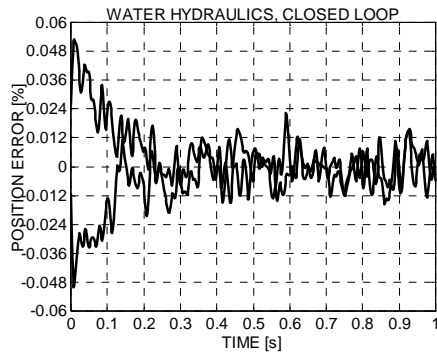


Figure 10. Measured position error responses, strokes 0.6%, water hydraulics

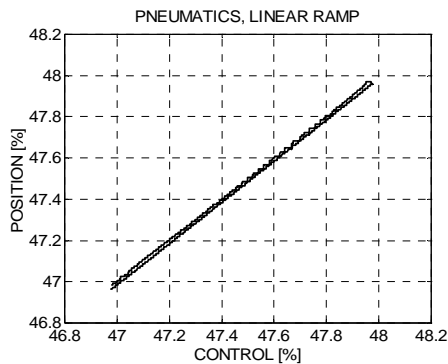


Figure 11. Measured position response of linear ramp (hysteresis), pneumatics

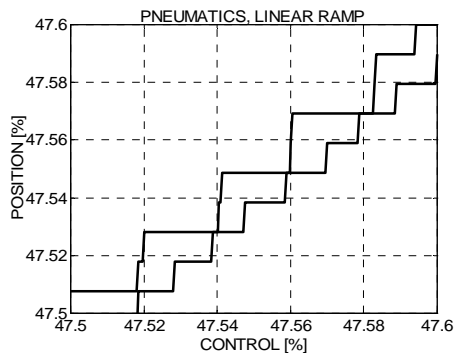


Figure 12. Zoomed measured position response of linear ramp (hysteresis), pneumatics

Differences in responses of two systems are mostly due to the used position sensors. There is significant noise in the position measurements of water hydraulic drive because

of analogue position sensor. The incremental encoder is used in the pneumatic drive and no noise has been noticed.

RESULTS COMPARED TO GOALS

Both studied systems fulfil all specifications set by [4], as can be seen in Figures above. All specified steady state positioning accuracy, dead band, resolution, hysteresis and response times are reached without big problems. When the zero point of valves is well tuned no drift or hunting takes place.

The most critical component in both cases is the servo valve. The servo valves used in this study are good quality commercial valves. Their size is quite suitable with the used supply pressures. The problem is their costs. These kinds of commercial servo valves, especially water hydraulic servo valve, are too expensive for these applications. The specified positioning accuracy, resolution, dead band and hysteresis require reasonable good position measurement system. The resolution should be at least around 0.01%, which means problems with analogue position sensors.

Because the maximum velocity of the cylinder is relatively low the high position loop gains can be used and so a non-linear P-controller is enough in the water hydraulic case. The pneumatic drive requires at least a State Controller. This not a big problem, because high resolution position feedback is needed anyway and so the required velocity and acceleration can be achieved by differentiate from position signal. The required sampling time is <10ms.

As a summary it can be said that with relatively high quality commercial components the highest specifications of steady state and dynamic behaviour set by [4] can be realized with pneumatics as well as with low pressure water hydraulics.

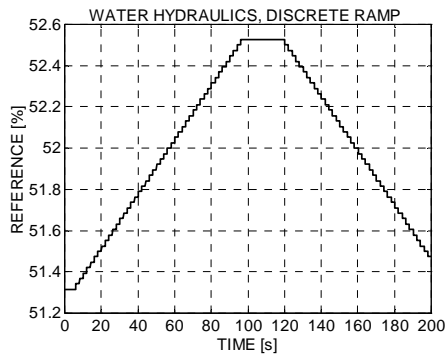


Figure 13. Measured discrete ramp, step 0.022%, water hydraulics

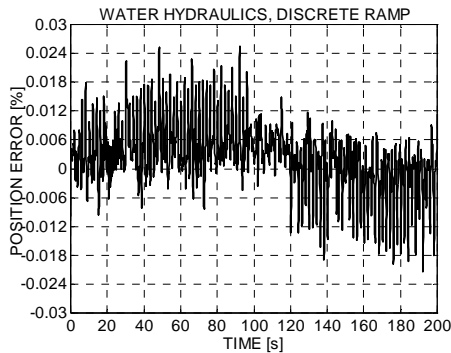


Figure 14. Measured position error, discrete ramp, water hydraulics

Discussion

In order to fulfil the performance specifications the steady state characteristics of servo valves should be around the specifications of the servo valve used in this study. Electric power of process valve control systems is very limited (around 5-10mW) which also might limit dynamic properties of servo valves. Some experimental tests are realized by using a second order low-pass filter in the control signal of the servo valves in order to reduce the dynamics of the servo valve. When the bandwidth of the filter is one tenth of the bandwidth of the servo valves and the damping lower ($\delta=0.5$) the overall behaviour of both systems do not differ remarkably from original behaviour. However, a State Controller is also needed in the water hydraulic drive and the controller the pneumatic drive has to be re-tuned.

CONCLUSIONS

According to this study the following conclusions can be made.

- * Highest steady state and dynamic performance specifications of positioners of process valves can be realized both with pneumatic and low pressure water hydraulic drives using commercial servo valves
- * High steady state performance of servo valves is required in both cases. Low hysteresis is the most important.
- * Dynamics of servo valves is not very critical. It could be one tenth of commercial servo valves.
- * Commercial servo valves are too expensive for these applications, especially water hydraulic servo valves.
- * Quite high resolution of position sensor is required. Resolution should be at least around 0.01% of the full stroke of positioners.

REFERENCES

1. Vuorisalo, M. & Virvalo, T. 2000. Comparing the control methods of fast water hydraulic on/off-valves in pressure control. The 7th Mechatronics Forum, 6th-8th September, 2000, Atlanta, Georgia, USA. 5 p.
2. Vuorisalo, M. & Virvalo, T. 2000. Smart material actuators for fluid power valves with different pressure mediums. 9th Annual Conference on MMV, 19th-21st, September, 2000, Harvey Bay, Queensland, Australia. p. 305-313.
3. Vuorisalo, M., Virvalo, T. & Anttonen, P. 2001. Different types of pilot stages for a water hydraulic control valve. ICFPi2001 April 3-5, 2001, Hangzhou, China. p. 435-439.
4. EnTech: Control Valve Dynamic Specifications, 1998.
5. Metso Automation, 3 R 20EN Issue 8/2001

DYNAMIC CHARACTERISTICS OF A DIRECT-PRESSURE SENSING WATER HYDRAULIC RELIEF VALVE

Kenji SUZUKI and Eizo URATA

Department of Mechanical Engineering, Faculty of Engineering
Kanagawa University
3-27-1 Rokkakubashi, Kanagawa-ku, Yokohama, 221-8686 Japan
(E-mail: suzuki@kanagawa-u.ac.jp)

ABSTRACT

This paper deals with dynamic characteristics of a direct-pressure sensing water hydraulic relief valve. Four hydrostatic bearings support the main valve to reduce hysteresis of static characteristics of the valve. Hence, Coulomb friction acting on the main valve is not available as damping force. A damping orifice is inserted between the main- and pilot valves to get a damping force for the main valve, while the orifice diameter affects on stability of the main valve. In addition, the motion of the pilot valve has large effects on the response of the relief valve itself. To show these influences, we compute the response to a step input of relief flowrate with the MATLAB/Simulink. The results show that the design parameters affecting the stability are followings: (1) the damping orifice diameter, (2) spring stiffness for the pilot valve, and (3) volume of a chamber between the damping orifice and the pilot valve.

KEY WORDS

Water hydraulic, Relief valve, Direct pressure sensing, Dynamic characteristic

NOMENCLATURE

A^* :	various areas (see Eq.(5)) [m ²]	K_i :	i -th order coefficient (see Eq.(12)) [-]
c_m, c_p :	viscous coefficient of main- and pilot valve, respectively [N·s/m]	K^* :	various proportional constants (see Eqs.(9),(16))
C_b, C_d :	discharge coefficient of a hydrostatic bearing orifice and a valve, respectively [-]	l_s :	axial length of clearance between pressure-detecting rod and sleeve [m]
d^* :	various diameters (see Figs.(2), (3)) [m]	m_m, m_p :	mass of main- and pilot valve, respectively (incl. 1/3 of corresponding spring mass) [kg]
d_i, D_i :	inner and outer diameter of the i -th throttle of main valve, respectively [m]	p^* :	pressure at various chambers [Pa]
h :	clearance of the first throttle when $x = 0$ [m]	P :	dimensionless pressure ($= p^* / p_s _{t=0}$) [-]
k_m, k_p :	spring constant for main- and pilot valve, respectively [N/m]	P_i :	dimensionless i -th pressure overshoot [-]
		P_0 :	dimensionless pressure increment [-]
		q^* :	flow rate (see Eqs.(10)-(15)) [m ³ /s]
		r_d :	damping ratio ($= B_2 / R$) [-]
		T_1 :	time to first overshoot [s]

T_d	: time from first overshoot to second one [s]
T_s	: settling time [s]
V^*	: volume of various chambers [m ³]
x	: displacement of main valve [m]
X	: dimensionless displacement of main valve [-]
x_0	: initial displacement of spring for main valve [m]
y	: displacement of poppet valve [m]
Y	: dimensionless displacement of poppet valve [-]
y_0	: initial displacement of spring for poppet valve [m]
α^*	: equivalent area (see Eq. (8)) [m ²]
β	: bulk modulus of fluid [Pa]
δ_s	: clearance between pressure-detecting rod and sleeve [m]
μ	: viscosity of fluid [Pa·s]
θ_p	: half cone angle of poppet valve [-]
ρ	: density of fluid [kg/m ³]

INTRODUCTION

Since viscosity of water is much lower than that of oil, internal leakage is liable to occur in water hydraulic valves than in oil hydraulic valves. Placing of a packing on sliding part prevents the internal leakage, whereas its Coulomb friction may causes stick-slip, hysteresis, and instability of the motion. To prevent these phenomena, flow through the clearance between a valve and a sleeve is utilised as pilot flow in a water hydraulic high-speed solenoid valve [1]. When the valve is eccentric to the sleeve, however, the flow through the clearance will increase and a hydraulic rock will be liable to occur.

In the water hydraulic relief valve dealt with this study, the main valve is supported by hydrostatic supports. Flow through the hydrostatic supports is utilised as pilot flow, by which internal leakage is reduced. A direct pressure-sensing technique [2] is adopted in the pilot valve to decrease pressure override. To suppress cavitation, pressure in relief flow is reduced by two serial restrictors in the main valve [3, 4].

Dynamic characteristics of a relief valve are studied by many authors. Some of the studies on a oil hydraulic relief valve are the followings: Shin [5] discussed static and dynamic characteristics of balanced-piston-type relief valve with various design parameters, whereas he has ignored the compressibility of oil; Yao [6] computed dynamic response of direct-pressure sensing relief valve only with one set of design parameters. For a balanced-piston-type water hydraulic relief valve, Hayashi et al. [7, 8] discussed the dynamic characteristics of the valve with some design parameters, including the connected pipeline. For the direct pressure sensing water hydraulic relief valve treated in this study, however, the analysis of dynamic characteristics has not been made.

In this study, effects of various parameters were investigated on the stability and dynamic response for

the direct pressure sensing water hydraulic relief valve. The design parameters that affects stability of the valve are shown.

STRUCTURE OF THE VALVE

Figure 1 shows the structure of the direct-pressure sensing water hydraulic relief valve treated in this study. The features are as follows:

- 1) The main valve is supported by a hydrostatic support to reduce Coulomb friction. The orifices for the hydrostatic bearings and clearance around the main valve are used as the restrictor from the supply pressure to the pilot pressure. Thus, the flow through the hydrostatic supports is utilised as the pilot flow.
- 2) To suppress cavitation, the main valve includes two annular throttles with nearly equal diameters. Both of the throttles employ a plane contact because a line contact is liable to change the static characteristics due to wear of the valve and the valve seat.
- 3) To reduce internal leakage from the pilot valve, a conventional poppet valve with a pressure-detecting rod is adopted. The displacement of the poppet valve is almost determined by the balance of forces due to the supply pressure and the pilot spring.
- 4) To stabilize the motion of the main valve, a damping orifice is placed between the main- and pilot valves.
- 5) The main valve is made up from three pieces to improve machining accuracy.

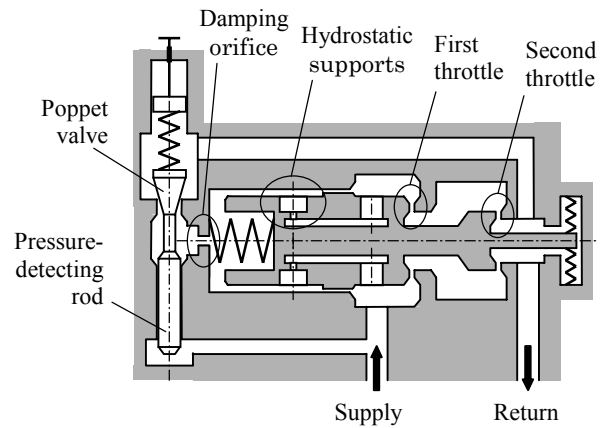


Figure 1 Schema of direct pressure sensing water hydraulic relief valve

SIMULATION MODEL

Figures 2 and 3 show the model drawing of the main valve and the pilot valve, respectively.

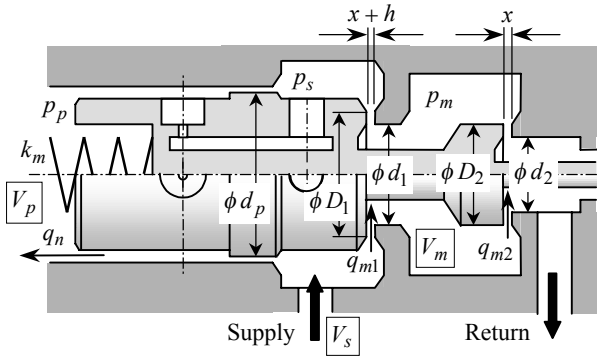


Figure 2 Model drawing of the main valve

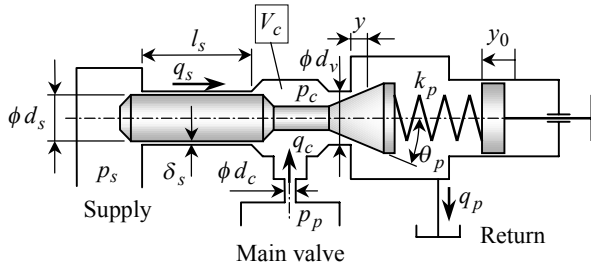


Figure 3 Model drawing of the pilot valve

For the analysis, following assumptions were made:

- Physical properties of the fluid are constant.
- Discharge coefficient is constant.
- Change of the chamber volume by displacement of the valve can be neglected.
- The valve undergoes no volumetric change under the pressure.
- The transient flow force can be neglected in the dynamic characteristics as it is small compared with the steady flow force.
- Coulomb friction acting on the valve can be neglected.
- The outlet fluid pressure is same as the tank pressure, that is negligibly small compared with the supply pressure.

Basic Equations

For each of the chambers, equations of continuity considering compressibility of fluid are established as:

$$\dot{p}_s = \frac{\beta}{V_s} (q_{in} - q_{m1} - q_n - q_s - A_{m1}\dot{x} - A_s\dot{y}), \quad (1)$$

$$\dot{p}_m = \frac{\beta}{V_m} (q_{m1} - q_{m2}), \quad (2)$$

$$\dot{p}_p = \frac{\beta}{V_p} (q_n - q_c + A_p\dot{x}), \quad (3)$$

$$\dot{p}_c = \frac{\beta}{V_c} (q_c + q_s - q_p), \quad (4)$$

where

$$A_{m1} = \frac{\pi}{4} (d_p^2 - d_i^2), \quad A_s = \frac{\pi}{4} d_s^2, \quad \text{and} \quad A_p = \frac{\pi}{4} d_p^2. \quad (5)$$

Equations of motion for main- and pilot valves are:

$$m_m\ddot{x} + c_m\dot{x} + k_m(x + x_0) = \alpha_s p_s + \alpha_m p_m - A_p p_p, \quad (6)$$

$$m_p\ddot{y} + c_p\dot{y} + k_p(y + y_0) = A_s p_s - K_f y p_c, \quad (7)$$

where

$$\alpha_s = \frac{\pi}{4} \left\{ d_p^2 - \frac{D_i^2 - d_i^2}{\ln(D_i / d_i)} \right\}, \quad (8)$$

$$\alpha_m = \frac{\pi}{8} \left\{ \frac{D_i^2 - d_i^2}{\ln(D_i / d_i)} - \frac{D_2^2 - d_2^2}{\ln(D_2 / d_2)} \right\},$$

and

$$K_f = \pi C_d d_v \sin 2\theta_p. \quad (9)$$

Equations of flow rate passing through each restrictors are written as:

$$q_{m1} = \text{sgn}(p_s - p_m) \pi C_d D_1 (x + h) \sqrt{2|p_s - p_m| / \rho} \quad (10)$$

$$q_{m2} = \pi C_d D_2 x \sqrt{2p_m / \rho} \quad (11)$$

$$q_n = \text{sgn}(p_s - p_p) K_b \sqrt{p_s} \sum_{i=1}^3 \left\{ K_i |1 - p_p / p_s|^i \right\} \quad (12)$$

$$q_c = \text{sgn}(p_p - p_c) K_c \sqrt{|p_p - p_c|} \quad (13)$$

$$q_s = \text{sgn}(p_s - p_c) K_s |p_s - p_c| \quad (14)$$

$$q_p = K_p y \sqrt{p_c} \quad (15)$$

where

$$K_b = \frac{\pi}{4} C_b d_b^2 \sqrt{2 / \rho}, \quad K_c = \frac{\pi}{4} C_d d_c^2 \sqrt{2 / \rho}, \quad (16)$$

$$K_s = \frac{\pi d_s \delta_s^3}{12 \mu l_s}, \quad K_p = \pi C_d d_v \sin \theta_p \sqrt{2 / \rho},$$

and K_i ($i = 1, 2, 3$) are calculated using the algorithm explained in [9], adding a few modification.

Method for Simulation and Estimation

MATLAB/Simulink was used for modeling of Eqs. (1)-(16). Runge-Kutta method of fourth-order was used as the solver. Although the time step for calculation was fixed step of 0.01 ms, the time step of data was 0.1 ms.

On a real situation of the relief valve usage, input flow rate to the valve varies from zero to the rated flow, namely, the valve closes initially. For the calculation of such situation, shorter time step and longer calculation time are required to prevent a memory-overflow. This

study is, however, mainly aiming at screening of change of response with various parameters, that the calculation was made with the main valve opened initially.

Before starting the calculation of the response, pressures and valve displacement at the initial relief flow rate were computed and read in as initial values. These values were approximation, so that vibration occurred just after starting calculation. However, the vibration disappeared after 0.2 s with all of the conditions. Step-change of the input flow rate to the valve was made when 0.25 s. The calculation of the response was made until 1.25 s. The pressures and the valve displacement were almost settled down after 1.25 s in most cases.

Since preset pressure varies slightly with each of the initial conditions, calculation results cannot compared with each other in their absolute values. Therefore, all pressure data were made dimensionless by the initial supply pressure.

Estimation method for the calculation results was as follows. Settling time was determined as the time until the main valve displacement was settled in the settled value $\pm 5\%$ of step width, where the step width is the difference between the initial- and settled values of the main valve displacement. As shown in Fig. 4, pressure increment P_o , pressure overshoot P_1 , peak rising time T_1 , damping ratio r_d and period of damped vibration T_d were found from waveform of supply pressure.

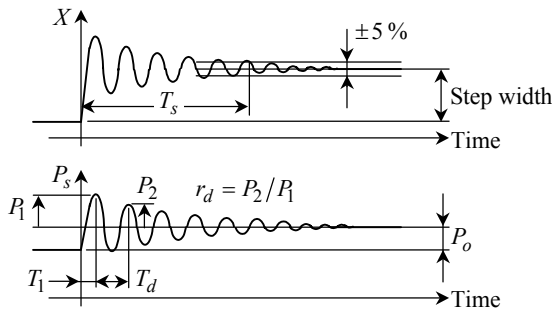


Figure 4 Measures of step response

Conditions for Calculation

Physical properties of fluid and reference parameters are listed in Table 1. The discharge coefficients C_d and C_b were assumed to be constant. The calculation was made varying the following parameters: mass of valves m_m and m_p , volume of chambers V_p and V_c , diameter of the damping orifice d_c , and spring constant for the pilot valve k_p . Variations of each of parameters were $-20, -10, 0, +10$ and $+20$ [%] of the corresponding reference value. The conditions for calculation were the followings:

- * Preset pressure: 7 MPa
- * Initial relief flow rate: 5 L/min
- * Step width of flow rate into the valve: 15 L/min

Table 1 Physical properties and reference parameters

$\mu = 0.5482$ [mPa·s]	$\rho = 988$ [kg/m ³]	$\beta = 2.2$ [GPa]
$C_d = 0.67$ [-]	$C_b = 0.67$ [-]	
$m_m = 65$ [g]	$m_p = 8$ [g]	
$d_c = 1.0$ [mm]	$k_p = 158$ [N/mm]	
$V_p = 1.46 \times 10^{-6}$ [m ³]	$V_c = 0.953 \times 10^{-6}$ [m ³]	
$V_m = 2.34 \times 10^{-6}$ [m ³]	$V_s = 0.01$ [m ³]	
$c_m = 0$ [N·s/m]	$c_p = 0$ [N·s/m]	

SIMULATION RESULTS AND DISCUSSION

Figure 5 shows dimensionless waveforms of the supply pressure and the valve displacement with conditions of Table 1. The estimated values are as follows:

- * Pressure increment P_o : 0.144 %
- * Pressure overshoot P_1 : 3.18 %
- * Peak rising time T_1 : 6.7 ms
- * Damping ratio r_d : 0.851
- * Period of damped vibration T_d : 25.1 ms
- * Settling time T_s : 540 ms

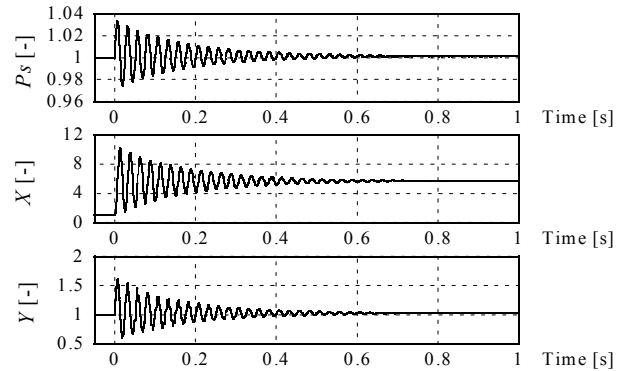


Figure 5 Step response

In the following, the variation of estimated values to the variation of each parameter will be shown. The pressure increment P_o is, however, shown lastly since it has been affected only by d_c and k_p .

Influence of m_m and m_p

Figure 6 shows the influence of mass of the main valve. T_1 and T_d did not change. However, all the other estimated values indicate that lighter main valve is preferable.

Figure 7 shows the influence of mass of the pilot valve. Any significant trend are not observed in this result. The waveforms of the pilot valve displacement (Fig. 8) show that lighter pilot valve is preferable on the damping for high frequency vibration.

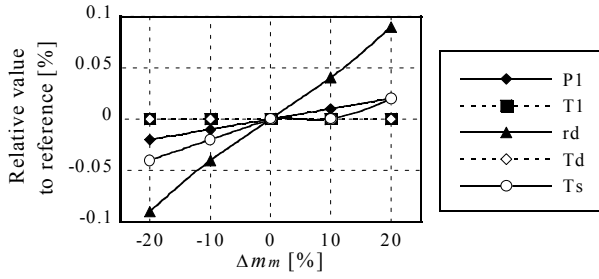


Figure 6 Influence of m_m

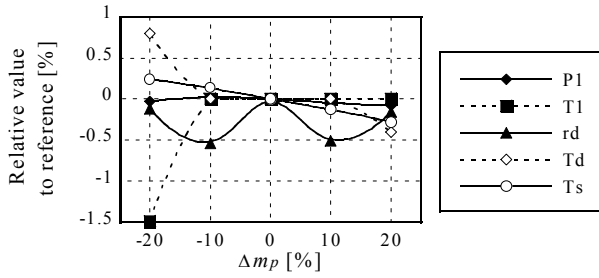


Figure 7 Influence of m_p

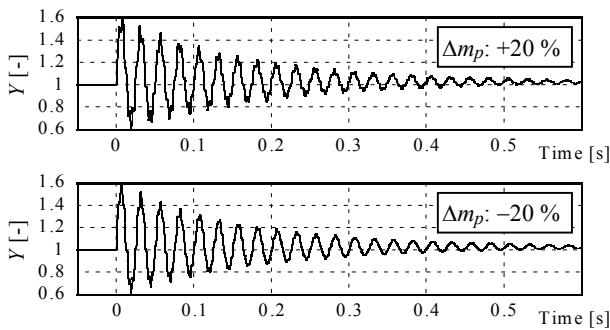


Figure 8 Waveforms of pilot valve displacement

Influence of V_p and V_c

Figure 9 and 10 shows the influence of V_p and V_c , respectively. Both graphs show clear tendency that large V_p and small V_c contributes the stability of the valve. Particularly, small V_c has much effect on decrease of the settling time.

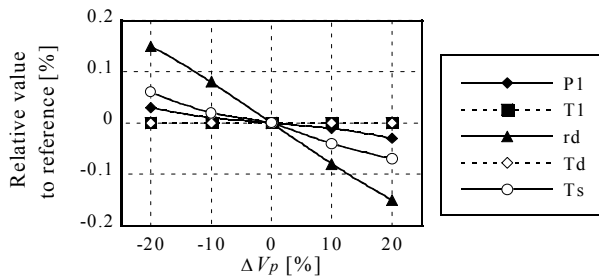


Figure 9 Influence of V_p

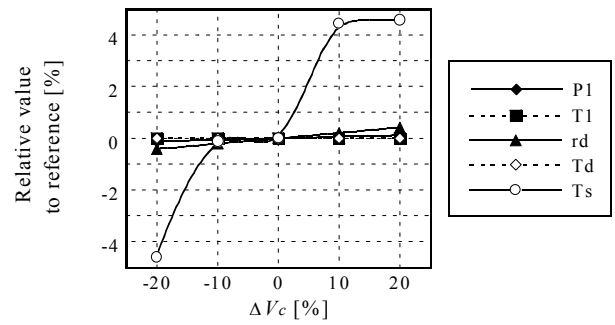


Figure 10 Influence of V_c

Influence of d_c

Figure 11 shows the influence of the damping orifice diameter, which indicates that the diameter has large influence on the stability. These phenomena resulted from the fact that the pressure difference between the orifice is inversely proportional to the orifice diameter to the power of four.

Small d_c made damped pressure vibration, whereas the overshoot, peak rising time and period of damped vibration became quite large. In contrast, if d_c was large, the overshoot, peak rising time and damping ratio became small, whereas the pilot valve vibrated with high frequency. In both cases, the settling time became longer. To summarize, there exists an optimal value for the damping orifice diameter. In addition, its small vibration has large influence on the stability of the valve. This implies that machining error has large influence on stability. To cope with the sensitivity of the orifice, a capillary would be preferable as the damping restrictor.

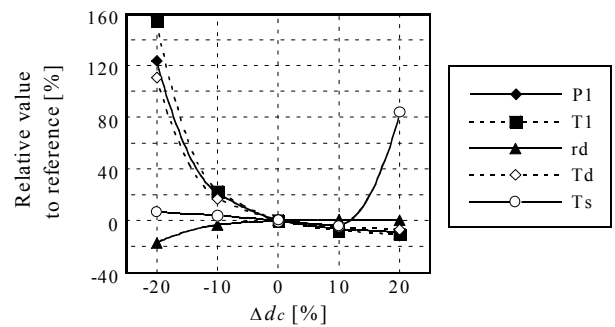


Figure 11 Influence of d_c

Influence of k_p

Figure 12 shows the influence of spring constant for the pilot valve. When a weak spring was used, the corresponding overshoot, peak rising time and period of damped vibration decreased, whereas the damping ratio increased. Behavior of the settling time does not show monotonic change with k_p , which suggest that a more precise analysis is necessary.

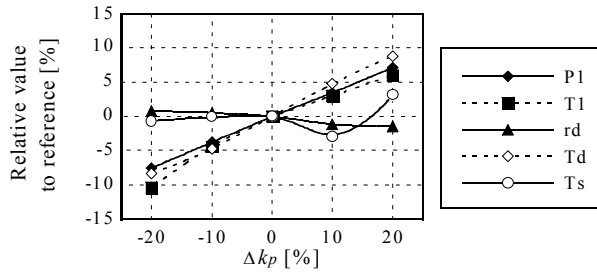


Figure 12 Influence of k_p

Influence of d_c and k_p on Pressure Increment

Figure 13 shows the influence of d_c and k_p on pressure increment. The pressure increment increases with increase of k_p and with decrease of d_c . Particularly, small d_c makes the pressure increment remarkably large, which implies that the pressure override becomes large.

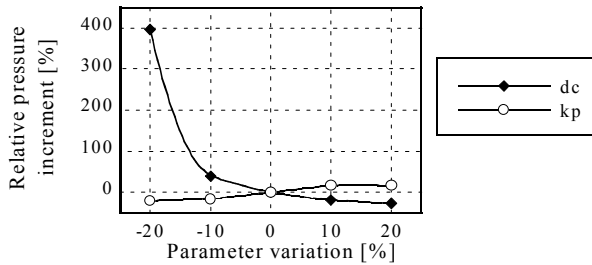


Figure 13 Affects of d_c and k_p on pressure increment

Overall Improvement

Based on the above investigation, the calculation was made again with variation of all six parameters as listed in Table 2. Although the damping ratio increases slightly, all the other estimated values decreased. The results are summarized in Table 3.

Table 2 Variation of six parameters

Δm_m : -20 %	Δm_p : -20 %	ΔV_p : +20 %
ΔV_c : -20 %	Δd_c : +10 %	Δk_p : -20 %

Table 3 Results with conditions of Tables 1 and 2

	Table 1	Table 2	Rel. value [%]
P_o [%]	0.144	0.106	-26.4
P_t [%]	3.18	2.75	-13.4
T_i [ms]	6.7	5.7	-14.9
r_d [-]	0.851	0.855	+0.47
T_d [ms]	25.1	22.2	-11.6
T_s [ms]	540	499	-7.65

CONCLUSION

Analysis of dynamic characteristics was made for a direct-pressure sensing water hydraulic relief valve, in which four hydrostatic bearings support the main valve to reduce hysteresis in the static characteristics of the valve. Investigation on the step response of the valve by simulation is presented for the various values of the design parameters. Stability of the valve was discussed with respect of pressure overshoot, peak rising time, damping ratio, period of damping vibration and settling time.

The factor affecting the stability most is the diameter of the damping orifice that is inserted between the main and pilot valves to give damping force to the main valve. In addition, the spring constant for the pilot valve and the volume of a chamber between the damping orifice and the poppet valve have much influence.

REFERENCES

- 1 Park, S-H, Kitagawa, A., Kawashima, M., Lee, J-K and Wu, P., A Development of Water Hydraulic High Speed Solenoid Valve, The Fifth JFPS Int. Sympo. on Fluid Power, **1**, 2002, pp.137-142.
- 2 Yao, D., Burton, R., Nikiforuk, P., Ukrainetz, P. and Zhou, Q., Research and Development of a Direct Pressure Sensing Relief Valve, Proc. The Fourth Int. Conf. on Fluid Power Transmission and Control, 1997, pp.150-155.
- 3 Berger, J., Kavitationserosion und Maßnahmen zu ihrer Vermeidung in Hydraulikanlagen für HFA-Flüssigkeiten, Dissertation der TH Aachen, 1983.
- 4 Suzuki, K., and Urata, E., Improvement of Cavitation Resistive Property of a Water Hydraulic Relief Valve, Proc. The Eighth SICFP, **1**, 2003, pp.265-276.
- 5 Shin, Y. C., Static and Dynamic Characteristics of a Two Stage Pilot Relief Valve, Trans. ASME J. Dyn. Syst. Meas. Control, 1991, **113**-2, pp.280-288.
- 6 Yao, D., Bitner, D., Burton, R. and Nikiforuk, P., Some Static and Dynamic Considerations in the Design of a Direct Sensing Pressure Relief Valve, Fluid Power Engineering: Challenges and Solutions, Tenth Bath Int. Fluid Power Workshop (Edited by K. A. Edge and C. R. Burrows), 1998, pp.214-229.
- 7 Nakanishi, T., Hayashi, S., Hayase, T., Shirai, A., Jotatsu, M. and Kawamoto, H., Numerical Simulation of Water Hydraulic Relief Valve, The Fourth JHPS Int. Sympo. on Fluid Power, 1999, pp.555-560.
- 8 Hayashi, S., Nakanishi, T., Hayase, T. and Shirai, A., Analysis of Dynamic Characteristics of Water Hydraulic Relief Valve, Trans. JFPS (in Japanese), 2002, **33**-7, pp.149-155.
- 9 Suzuki, K. and Urata, E., Analysis of Hydrostatic Bearing for Water Hydraulic Servovalve, The Sixth SICFP, **1**, 1999, pp.179-190.

DEVELOPMENT OF A LOW PRESSURE WATER HYDRAULIC ACTUATOR WITH SELF RECIPROCATING MOTION

Shigeru OSHIMA*, Tadashi KAGAWA**

* Department of Control and Computer Engineering
Numazu National College of Technology
3600 Ooka, Numazu, Shizuoka, 410-8501 Japan
(E-mail: oshima@numazu-ct.ac.jp)
** System Engineering, Advanced Engineering Course
Numazu National College of Technology
3600 Ooka, Numazu, Shizuoka, 410-8501 Japan

ABSTRACT

This paper concerns a newly designed water hydraulic actuator to make reciprocating linear motion without any directional control valves outside. It works with only supply of low pressure water, such as from tap water network. The object of this paper is to introduce the idea of construction and working principle of the actuator and to present some experimental results gained by prototypes. Two different prototypes, with a short stroke (approx. 20 mm) and a long stroke (approx. 200 mm), are produced. Fundamental performances were tested for the two types and good results were gained. Main piston's displacement, speed, force, and supply flow rate and pressure were measured under steady working conditions. The experimental results are presented and some considerations to improve the characteristics of them are also discussed.

KEY WORDS

Water Hydraulics, Actuator, Self Reciprocating Motion, Low Pressure

INTRODUCTION

Water hydraulic system which uses pure tap water as pressure medium has been paid attention for ten years more as a new environmental friendly drive system. It has advantages besides the environmental safety; cleanness, non-flammability, easiness of obtaining and disposing pressure medium, high power density, high stiffness and good controllability, etc.[1],[2].

The water hydraulic system has a great potential in the field of low-pressure level as well as the middle- and high-pressure levels. When the pressure level is low, the cost of the components becomes lower. A lot of research has been carried out in the field of low-pressure water

hydraulics. The aim of them is to realize the water hydraulic systems with low price of pneumatics and high power density and good controllability of oil hydraulics [3],[4].

Many applications of water hydraulics are found in industries, especially such as food processing industry where the machine and systems are required to have high tolerance to water cleaning and high hygienic standards [5]. The low-pressure water hydraulics has applications also in the field of nursing equipments to be used for caring handicapped or elder persons in institutions, and also it may be used for some domestic applications at homes when it can be driven by the low pressure water from household tap water network.

Concerning the water hydraulic components, there are less commercialized components in the low-pressure level rather than the middle- and high-pressure levels. Especially, actuator is needed to be developed further more in order to make the field of application of low pressure water hydraulics expand.

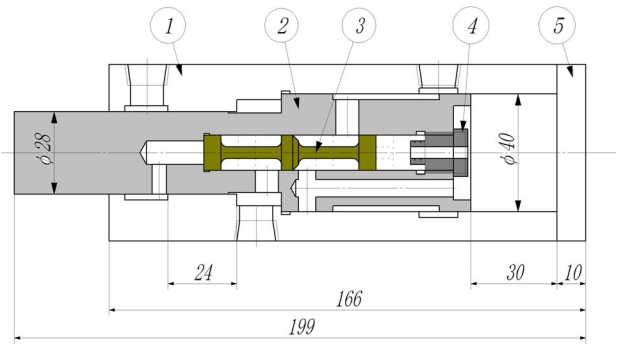
Commonly, the basic motions to drive machines are rotational and linear reciprocating motions. The rotation is generated by motors. A low-pressure water hydraulic motor with the maximum working pressure 2.0 MPa has been developed and in market [6]. Another motor driven by the pressure of tap water network is now under developing [7]. On the other hand, the linear reciprocating motion is generated by a water hydraulic cylinder, with usually using electro-magnetic directional control valves to switch the flow direction of water. But, the electro-magnetic valves tend to cause troubles when they are used at the places where will be wet and sometime under water. There are, however, practical applications in such situations to need just a simple reciprocating motion with a constant cycle time and a constant stroke, for example, the shaking equipments used in food processing and the feeder of a shower nozzles used in paper machines, etc.

This paper proposes a new type of a water hydraulic actuator which has possible applications in the situations mentioned above. It makes self reciprocating linear motion without any directional control valves outside. It works by only supply of low pressure water from a tap water network. It has advantages; easy usage, high stiffness and no danger of electric leakage. Two different prototypes, with a short stroke (approx. 20 mm) and a long stroke (approx. 200 mm), are produced. The construction of their important part, which switches the flow direction inside the main piston, is designed on the same concept. At first, the structure and working principle of the actuator is introduced and then the experimental results gained by the tests with each prototype are presented. Some considerations to improve the characteristics of them are also discussed.

STRUCTURE AND WORKING PRINCIPLE

Figure 1 shows the practical structure of the short stroke type. It consists of only five parts except for bolts. It has no sealing between the piston and the bore in the body to minimize friction. A small amount of leakage appeared to the outside through the clearance between the piston and the bore. At least, the sealing to prevent the leakage to the outside is absolutely necessary when it will be manufactured as a commercialized product. The material of the piston, spool and plug is stainless steel and the body and the end cover is brass.

The piston has two diameters, the bigger is 40 mm and



(1: Body, 2: Piston, 3: Spool, 4: Plug, 5: End cover)

Figure 1 Assembly drawing of the short stroke type

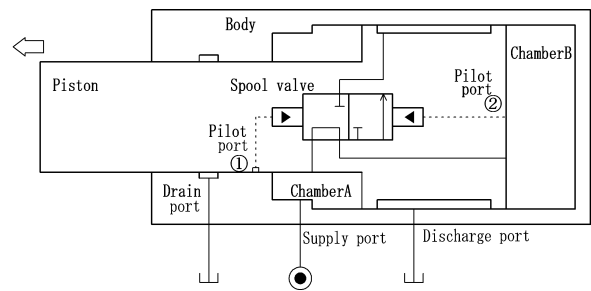
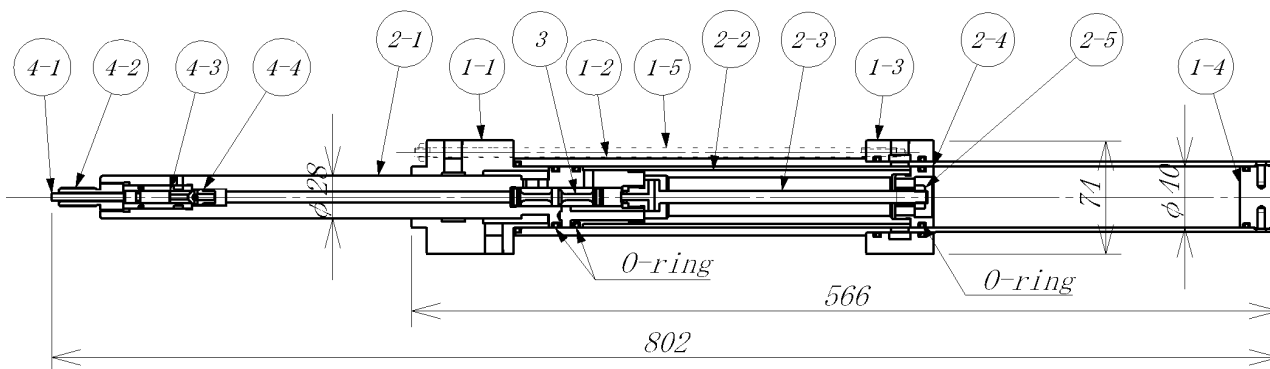


Figure 2 Schematic structure of the short stroke type

the smaller is 28 mm. It has, therefore, the two areas pressure acts on. One is $1,257 \text{ mm}^2$ on the right end of the piston and another is 641 mm^2 of the annular area at around the middle. Their ratio is almost 2:1.

A spool is installed in the piston and it makes a function of 3 way-2 position directional control valve as shown in Figure 2. It operates by difference of pressures act on its both the ends through the pilot ports 1 and 2. It switches the direction of the flow to and from the chamber B. When the position of the valve is as same as shown in Figure 2, the supply pressure comes to the chamber B as well as the chamber A and the piston moves to the left. On the other hand, when it is at another position, the chamber B connects to the discharge port and the piston moves to the right.

The position of the spool valve is determined by the position of the pilot port 1. When the pilot port 1 connects to the chamber A while the piston moves to the right, the position of the valve switches to the position as same as shown in Figure 2. Therefore, the piston changes the direction of its movement to the left. When the pilot port 1 connects to the drain port while the piston moves to the left, the spool valve switches to another position and the piston, therefore, changes the direction of its movement to the right. It is continuously repeated and the self reciprocating motion of the piston continues.



(1-1 to 1-5: Body, 2-1 to 2-5: Piston, 3: Spool, 4-1 to 4-4: Pilot valve)

Figure 3 Assembly drawing of the long stroke type

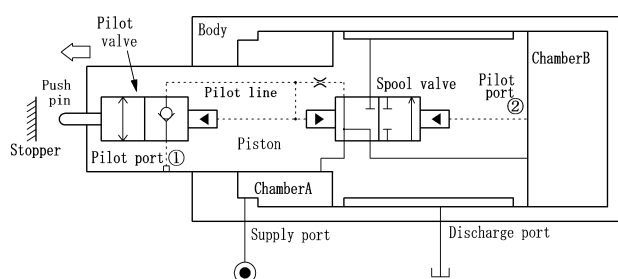


Figure 4 Schematic structure of the long stroke type

Figure 3 shows the structure of the long stroke type. The body consists of five parts; No.1-1 to 1-5. The No.1-2 is made of a stainless-steel pipe of which inner surface is finished by honing. The piston consists of five parts of No.2-1 to 2-5. The No.2 is also made of a stainless-steel pipe. The piston has two diameters, the larger is 40 mm and the smaller is 28 mm as same as the short stroke type. The piston has three O-rings on the larger diameter area. Grease is put on the O-rings to decrease the friction with the inner surface of the pipe of the body in which the piston slides. A spool is installed in the piston as same as the short stroke type. The major difference from the short stroke type is that the long stroke type has a pilot valve on a top of the piston, which consists of the four parts of No.4-1 to No.4-4. Due to the difficulty in producing, the same structure as the short stroke type was not available for the long stroke type. The material of the most parts is stainless-steel. The parts of No.1-1, 1-3 and 4-3 are made of brass.

The spool makes a function of 4 way- 2 position directional control valve as shown in Figure 4. It operates basically as same as in the short stroke type. The different point is that the pilot valve is installed on the pilot line connected to the pilot port 1. When the position of the valves are as shown in Figure 4, the supply pressure comes to the chamber B as well as the chamber A. The piston moves to the left. The left end of

the piston reaches the stopper and the push pin of the pilot valve is pushed in, the pilot valve switches the position and the pilot line is connected to the pilot port 1. The pressure in the pilot line decreases to the atmospheric pressure. The spool valve, therefore, switches its position to another position and the piston changes the direction of its movement to the right because the chamber B connects to the discharge port. When the pilot port 1 connects to the chamber A while the piston moves to the right, supply pressure comes through the pilot valve into the pilot line. It switches the positions of the spool valve and also the pilot valve. Then, it becomes the same situation as shown in Figure 4. The piston changes the direction of its movement to the left. As these steps are continuously repeated, the self reciprocating motion of the piston continues.

EXPERIMENTAL METHOD

Fundamental characteristics of the motion were tested for the both of the short stroke and the long stroke types. The piston's displacement, speed, force, and the supply flow rate and pressure were measured under steady working conditions.

The tests were carried out under the two kinds of load; inertia mass and constant force loads. As shown in Figure 5, the constant force load is given by using a magnetic brake (see (a)), and the inertia mass load was given by stacking iron plates on a plate with wheels (see (b)). The mass of each iron plate is 2 kg.

The water is supplied to the actuator through a common nylon tube of 5 m length from a tap water network. The maximum pressure at the tap is about 0.4 MPa. The flow rate is detected by a turbine flow meter, the supply pressure is by a strain gauge type pressure transducer, the displacement of the piston is by a magnetic displacement detector and the force is by a load cell to be available for the both of tension and compression. All the data is

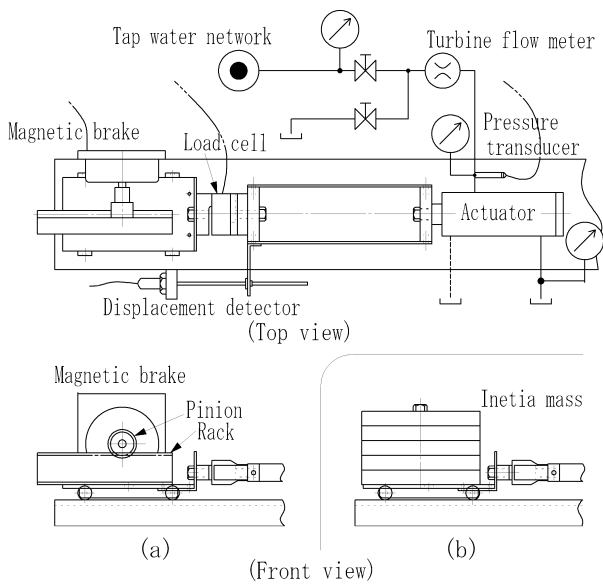


Figure 5 Test system

acquired by a computer with 1 ms and shorter sampling time.

EXPERIMENTAL RESULTS

Short Stroke Type

Figure 6 shows the displacement of the piston of the short stroke type when no inertia mass is loaded, and figure 7 shows that when the inertia mass is 10 kg. Supply water pressure is 0.28 MPa for the both cases. It is found that the good reciprocating motions are obtained in the both cases. The frequency of the reciprocating motion becomes larger as the inertia mass is smaller and the pressure is higher as shown in figure 8. The stroke of the piston changes with the change in pressure and inertia mass as shown in figure 9. The actuator does not work when the pressure is lower than 0.02 MPa.

Figure 10 shows the displacement of the piston of short stroke type when a force load is 50 N. Figure 11 shows the force detected by a load cell simultaneously with the data of displacement in figure 10. It is found that the actuator works well under such load condition. The critical force load is shown at each pressure in figure 12. The piston dose not reciprocate when the force load is larger than the critical value. The stroke of the piston changes with the change in force load and pressure as shown in figure 13. The stroke becomes smaller as the force load is larger. It dose not work when the pressure becomes lower so that the stroke becomes smaller than 0.0184 m.

Long Stroke Type

Figure 14 shows the displacement of the piston of the long stroke type when the inertia mass is 10 kg and the

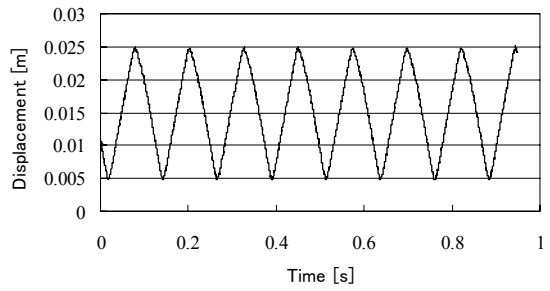


Figure 6 Displacement of piston in short stroke type (no inertia mass, at 0.28 MPa)

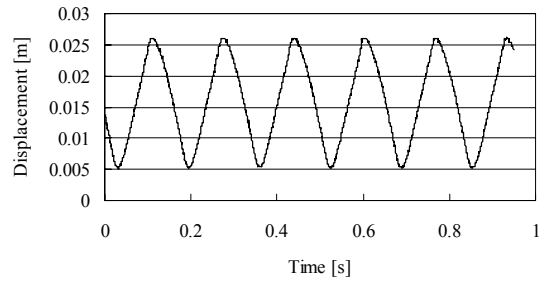


Figure 7 Displacement of piston in short stroke type (with 10 kg inertia mass, at 0.28 MPa)

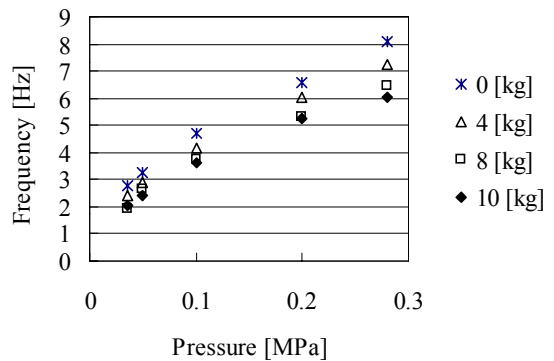


Figure 8 Frequency of the motion with change in pressure and inertia mass (short stroke type)

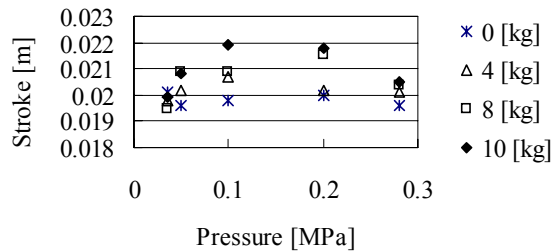


Figure 9 Stroke of the piston with change in pressure and inertia mass (short stroke type)

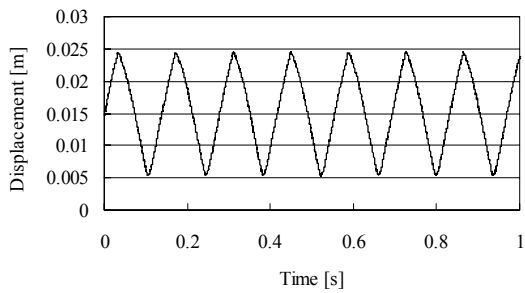


Figure 10 Displacement of the piston in short stroke type (with 50 N force load, at 0.28 MPa)

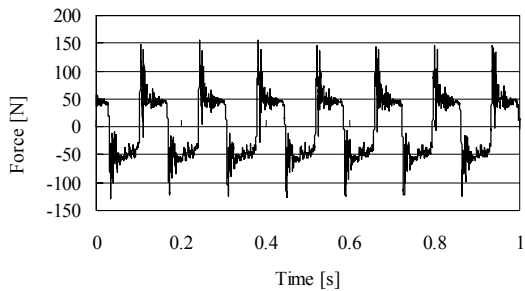


Figure 11 Detected force in the short stroke type (with 50 N force load, at 0.28 MPa)

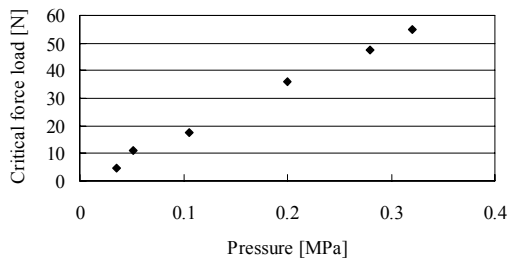


Figure 12 Critical force load in the short stroke type

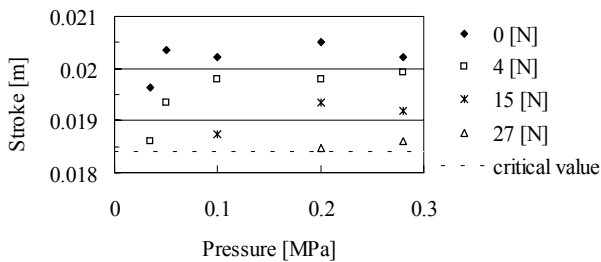


Figure 13 Stroke of the piston with change in pressure and load force (short stroke type)

pressure is 0.3 MPa. The stopper is located at the place to get the stroke 0.18 m. It is found that the reciprocating motion is continuously obtained, but the piston speed is slightly different between the forward and the backward movements. The stroke of the piston shows the two

different values as shown in figure 15; 0.18 m when the pressure is high and around 0.142 m when it's low. Due to the drain from the pilot port 1 while the piston moves backward, the piston changes the direction of movement from backward to forward before the pilot port 1 reaches the chamber A. When the pilot port 1 is covered with the bore of the body, the pressure in the pilot line rises and it makes the spool valve switch. It causes the shorter stroke. The frequency of the reciprocating motion becomes larger as the inertia mass is smaller and the pressure is higher as shown in figure 16.

Figure 17 shows the displacement of the piston of the long stroke type when a force load is 50 N. Figure 18 shows the force detected by a load cell simultaneously with the data of displacement in figure 17. It is clearly

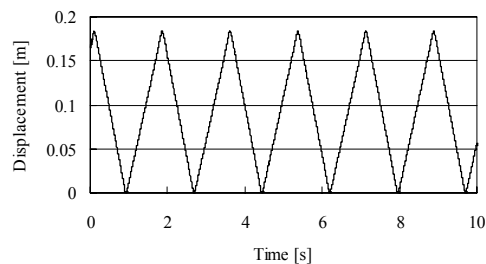


Figure 14 Displacement of piston in long stroke type (with 10 kg inertia mass, at 0.3 MPa)

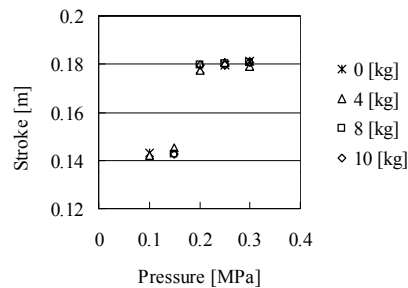


Figure 15 Stroke of the piston with change in pressure and inertia mass (long stroke type)

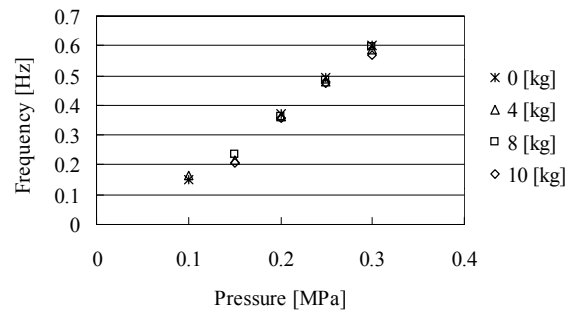


Figure 16 Frequency of the motion with change in pressure and inertia mass (long stroke type)

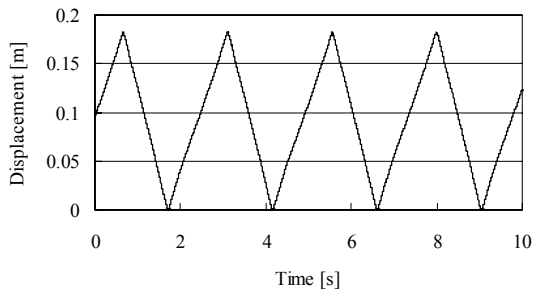


Figure 17 Displacement of the piston in long stroke type (with 50 N force load, at 0.3 MPa)

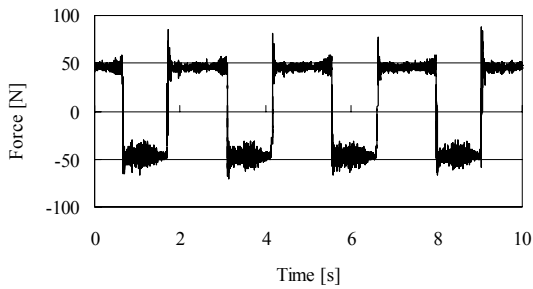


Figure 18 Detected force in the long stroke type (with 50 N force load, at 0.3 MPa)

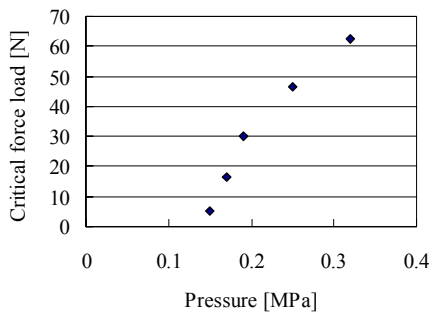


Figure 19 Critical force load in the long stroke type

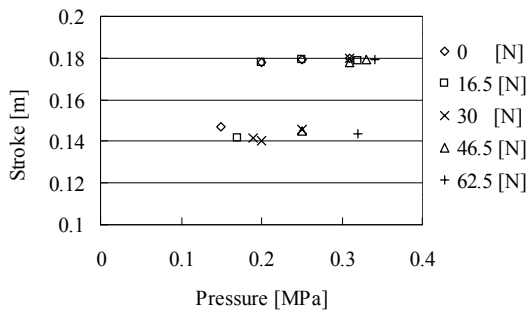


Figure 20 Stroke of the piston with change in pressure and load force (long stroke type)

found that the piston speed when moving forward is lower than backward. The critical force load is shown at in figure 19. Comparing with the result in figure 12, the critical value becomes extremely smaller as the pressure is lower. It is considered to be caused by the friction between the piston and the bore because the piston has O-rings. The stroke changes with the change in force load and pressure as shown in figure 20. The stroke gets the smaller value around 0.142 m when the pressure is lower and the force load is larger. As mentioned previously, the leakage through the pilot port 1 causes this.

It was found that the long stroke type still needs to be improved and it was important to decrease the friction between the piston and the bore and to make the leakage through the pilot port 1 close to zero when the piston is moving backward.

CONCLUSION

The low pressure water hydraulic actuator which makes self reciprocating linear motion with only supply of the low pressure water from tap water network is developed. Two different prototypes, a short stroke type and a long stroke type, were produced and tested. They showed good fundamental performances. But, especially, the long stroke type still needs to be improved.

REFERENCES

1. Modern Water Hydraulics – Your Choice for the Future, Leaflet of Introduction of Water Hydraulics by NFPA, (1995).
2. Urata E., Technological Aspects of the New Water Hydraulics, Proceedings of The Sixth Scandinavian International Conference on Fluid Power, 1999, pp.21-34.
3. Aaltonen, J. et al., Experiences On The Low Pressure Water Hydraulic Systems, Proceedings of the Fourth JFPS International Symposium, 1999, pp.357-363.
4. Kunttu, P. et al., Low Pressure Water Hydraulics - State of the Art, Proceedings of The Sixth Scandinavian International Conference on Fluid Power, 1999, pp.67-75.
5. Sørensen P., News and Trends by the Industrial Application of Water Hydraulics, The Sixth Scandinavian International Conference on Fluid Power-SICFP 1999, Tampere, Finland, 1999, pp.651-674.
6. Shinoda M. et al., Development of a Low-pressure Water Hydraulic Motor, Proceedings of The Fifth JFPS international Symposium, 2002, pp.187-192.
7. Tsukagoshi H., et al., Versatile Water Hydraulic Motor Driven by Tap Water, International Conference on Intelligent Robots and Systems IROS 2000, 2000, CD-ROM F-A2-2-1.

INNOVATIVE NEW ROV TECHNOLOGY UTILISING WATER HYDRAULICS

Gry Karin HAUGEN[♦] Finn CONRAD[♦] Mads GRAHL-MADSEN[♦]

[♦]Department of Mechanical and Marine Engineering, Bergen University College, Bergen, Norway
gry.haugen@hib.no mgm@hib.no

[♦]Department of Mechanical Engineering, Technical University of Denmark
Building 404, Kgs. Lyngby, Denmark
E-mail: finn.conrad@mek.dtu.dk

ABSTRACT

Today, Remotely Operated Vehicles, or ROV's, are the dominating type of vehicles for underwater operations and very much the working horse of the North Sea, and both the military and the scientific sectors are increasing their use of ROVs. An ROV is normally designed for underwater work using oil hydraulics or electricity for propulsion and tool control. ROV's using the surrounding water itself as the energy carrier for propulsion and tool control has never been successfully developed. The paper presents research results on a new ROV with water hydraulic propulsion system is being developed at Bergen University College. The design of the propulsion system is based on components available on the market. The ROV will have two thrusters for manoeuvring in the horizontal plane, and one thruster for vertical positioning. Static calculations and dynamic simulations have been performed to investigate the performance of the water hydraulic propulsion system. The simulations have been performed applying VisSim. The flow control valve has been tested to investigate the capability of flow regulation at low flow rates. Furthermore, this paper presents the selected experimental results and performance results.

KEY WORDS

Remotely Operated Vehicles ROV, Water Hydraulics

INTRODUCTION

The unmanned underwater vehicle industry, including both remotely operated vehicles (ROVs) and autonomous underwater vehicles (AUVs) is about 30 years old. A typical example of ROV for research in Norway is shown in Figures 1. During this period, these unmanned vehicles have evolved from unreliable prototypes developed for research and military use into essential everyday tools. Without ROVs many ocean industries such as deepwater oil and gas production would not exist. Applications range from simple 'remote eyeball' observation tasks to high precision seabed surveys and manipulative tasks such as pipeline connection and servicing of sub-sea oil and gas production installation. In March 1995 a designed and

tested Japanese ROV reached the deepest sea-water depth point of the Mariana Trench at 10,911 m (Hawley, Nuckols et al. 1996), [1].

Today, ROV's are the dominating type of vehicles for underwater operations and very much the working horse of the North Sea. The design of an ROV is normally based on oil hydraulics or electricity for propulsion and tool control. ROV's using the surrounding water itself as the energy carrier for propulsion and tool control has never been successfully developed.

Water hydraulics in its modern form has been available and in several industrial applications for more than 10 years, (Conrad, Hilbrecht and Jepsen, 2000), [2].

However, in relation to underwater technology not much work has been carried out. Even that oil hydraulics and water hydraulics are both fluid medium

water has other properties than hydraulic oils, Conrad, 2000, [2], (Backé,1999, [3]) and (Seabrook and Burrows, 1994), [4].

An ROV with water hydraulic propulsion system is being developed. The ROV is neutrally buoyant, has two thrusters for manoeuvring in the horizontal plane, and one thruster for positioning vertically, light and camera. Mathematical modelling and dynamic simulations using VisSim are undertaken for investigation of the performance of the water hydraulic propulsion system. The flow control valve was tested for the capability of flow control at low flow rates. Experimental results are presented and discussed.

REMOTELY OPERATED VEHICLES – ROV

The name a ROV (Remotely Operated Vehicle) is an underwater vehicle connected to the surface by an umbilical, which transfer electrical power, information and control signals to and from the surface work platform. Real-time communication between the surface and the vehicle allows for the operation and manoeuvring of the ROV as shown in Figure 1. The ROV system normally consists of the vehicle itself, an umbilical connected to the surface, a winch for handling of the vehicle and umbilical cable, a power distribution unit (PDU) and a control unit, see Figure 1.

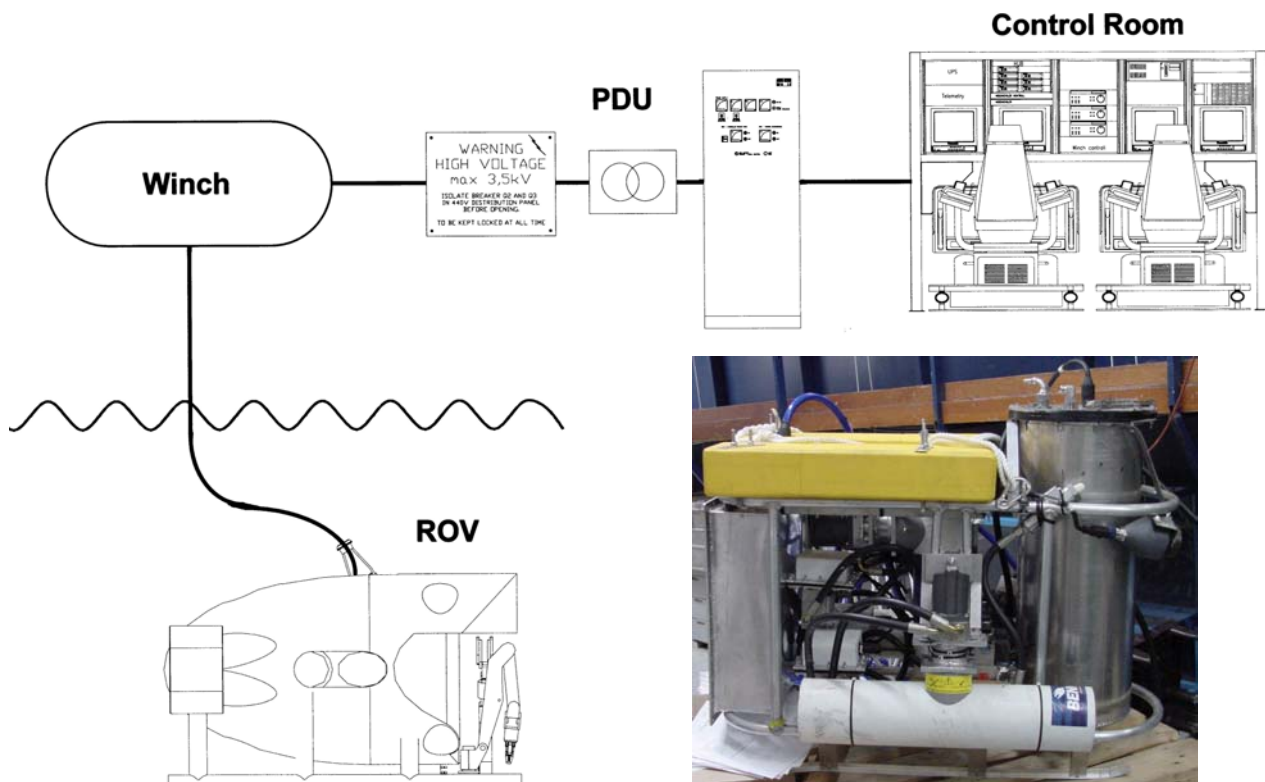


Figure 1. Underwater ROV System

<i>Observation</i>	<i>Survey</i>	<i>Inspection</i>	<i>Manipulative Tasks</i>
Visual observation with camera	Seabed observation, often together with acoustic mapping	Inspection of fixed structures, pipelines, cables and subsea systems	Requires manipulators and/or additional tools. Typical tasks are: installation and replacement of modules, valve operation, connecting subsea equipment during field development, pipeline tie-in etc.

Table 1

The ROV system normally consists of the vehicle itself, an umbilical connected to the surface, a winch for handling of the vehicle and umbilical cable, a power distribution unit (PDU) and a control unit, Figure 1. The main ROV tasks are described as in Table 1.

Cameras and light provide vision for the ROV pilot and other sensors like compass, pressure sensors and transponder provide additional information. A work class ROV is normally equipped with two hydraulically operated manipulator arms to perform various tasks.

The ROV can also be equipped with specialized tools to perform various tasks such as valve operation, sand blasting, wire cutting etc. The tasks for an ROV can be divided into active and passive. The passive tasks do not require manipulators or torque tools, such as observation, survey and inspection. Active tasks are defined as manipulative tasks.

NOVEL R&D ROV IN BERGEN

A novel ROV with a water hydraulic propulsion system as shown in Figure 2, and with light and camera is being developed at Bergen University College. Danfoss Nessie Water hydraulic components are used for the ROV propulsion system, and Sleipner Motor supplies the thrusters. Two thrusters operate the propulsion and turning of the ROV in the horizontal plane, and one

thruster to position the vehicle vertically. The ROV system consists of a control centre with joysticks for operation of the thrusters and to adjust focus of the camera. The ultimate goal, in respect of research is to develop a fully operational water hydraulic operated ROV and introduce new technology to the business. The project three main activities are

1. Water hydraulic propulsion and control systems
2. Hydrodynamic design and optimization
3. Instrumentation and navigation

Initial tests of the propulsion system have been carried out, revealing limitations with respect to speed control of the water hydraulic motors.

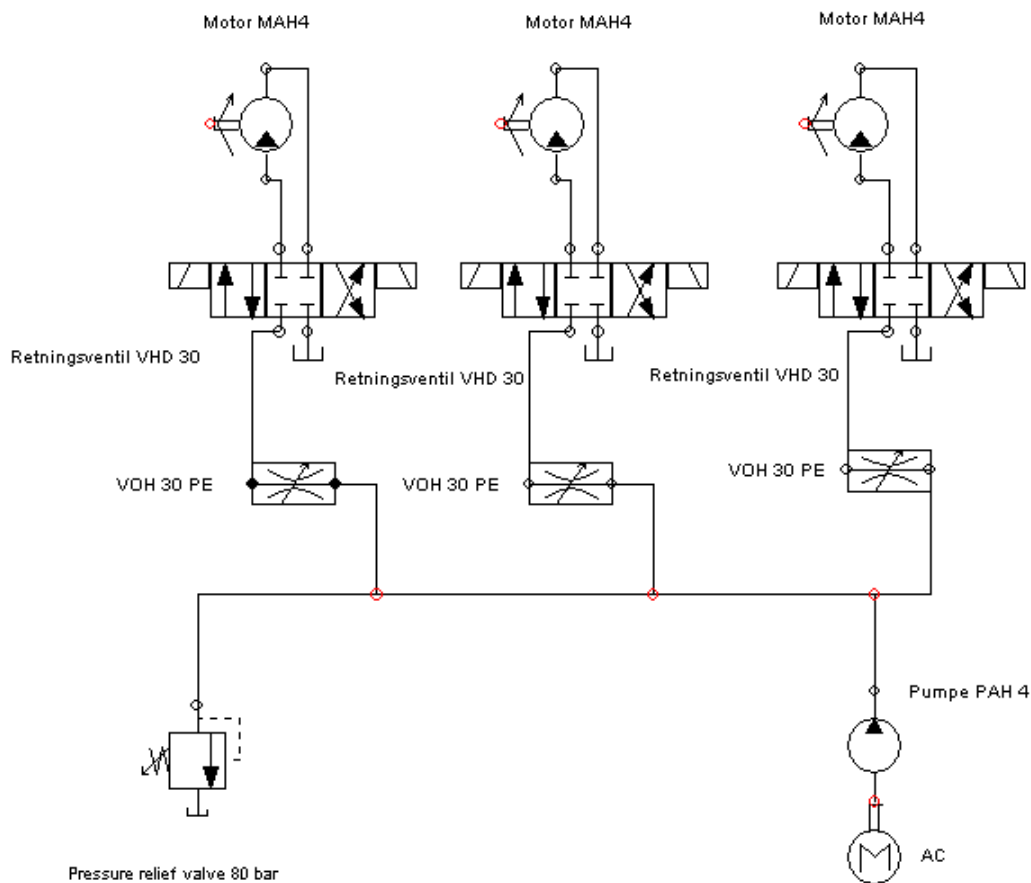


Figure 2. Hydraulic circuit of the novel ROV propulsion system

Only one motor could be running at a time, with little adjustment of the speed. An attempt to run two motors simultaneously failed, causing the first motor to stop as well. This could indicate a problem with the flow regulation, or a problem with the motors. Calculations to investigate the expected performance of the hydraulic system have therefore been performed.

One water hydraulic axial piston pump, Nessie PAH4 has $4 \text{ cm}^3/\text{rev}$ is driving the power supply system. The three water hydraulic axial piston motors, Nessie MAH4 have $4 \text{ cm}^3/\text{rev}$ do drive and control the three tunnel thrusters with a diameter of 125 mm via a gearbox. The applied 4/3 valve controls the rotational direction of the thrusters, and speed via the flow proportional control

valves, VOH 30. A 1.3 kW AC motor drives the water hydraulic pump, and a pressure relief valve at 80 bars prevents pressure build-up in the system.

MODELLING OF WATER HYDRAULIC PROPULATION SYSTEM

The volume of displaced water is expressed as by [5]

$$V = D_m \theta \quad (1)$$

where D_m is the displacement/radian and θ is total angular rotation for the motor. Hence, the flow rate is

$$Q = \frac{d}{dt}(D_m \theta) = D_m \omega \quad (2)$$

$$P = Q \cdot \Delta p \quad (3)$$

where Δp is the differential pressure over the motor.

The power is

$$P = T_m \omega \quad (4)$$

where T_m is the motor torque, and ω_m is the angular velocity. For an ideal motor with no friction, the mechanical power on the shaft is equal to the hydraulic power of the motor. Combining equation (3) and (4) an expression for the torque on the shaft is obtained

$$T_m = \frac{Q}{\omega} \cdot \Delta p = D_m \Delta p \quad (5)$$

The variation of density with pressure and temperature is

$$d\rho = \frac{\partial \rho}{\partial p} dp + \frac{\partial \rho}{\partial T} dT \quad (6)$$

Assuming isothermal conditions, the isothermal bulk modulus

$$\beta = \rho \frac{\partial p}{\partial \rho} \quad (7)$$

Equation (6) and (7) combines to

$$\dot{\rho} = \frac{\rho}{\beta} \dot{p} \quad (8)$$

The mass balance for a volume can be written

$$\frac{d}{dt}(\rho V) = w_{in} - w_{out} \quad (9)$$

where w_{in} and w_{out} is mass flow in and out of the volume V respectively. The product rule for derivation gives

$$\dot{\rho} = \frac{\rho}{\beta} \dot{p} \quad (8)$$

The mass balance for a volume can be written

$$\frac{d}{dt}(\rho V) = w_{in} - w_{out} \quad (9)$$

where w_{in} and w_{out} is mass flow in and out of the volume V respectively. The product rule for derivation gives

$$\dot{\rho} V + \rho \dot{V} = \rho(q_{in} - q_{out}) \quad (10)$$

where q_{in} and q_{out} are volume flow in and out of the volume. Equations (8) and (10) gives the mass balance

$$\frac{V}{\beta} \dot{p} + \dot{V} = q_{in} - q_{out} \quad (11)$$

Assuming an ideal motor, no internal or external leakage, and constant displacement volume gives

$$\frac{V}{\beta} \dot{p} = q_1 - q_2 \quad (12)$$

where q_1 is flow to the motor, and q_2 is flow from the motor. The flow from the motor gives

$$q_2 = \frac{D_m}{2\pi} \omega \quad (13)$$

Applying the Newton's Second law gives

$$T_m - T_L - T_f = J_m \dot{\omega} \quad (14)$$

where T_m is the motor torque, T_L is the external torque on the shaft from the thrusters, $T_f = B\omega$ is the viscous friction, and $J_m = I_m$ is the total mass moment of inertia of the motor

$$D_m \cdot (p_1 - p_2) - T_L - B\omega = I_m \dot{\omega} \quad (15)$$

Solved for the initial pressure p_{i1} , equation (15)

$$p_{i1} = \frac{D_m p_{i2} + T_L + T_s}{D_m} \quad (16)$$

Applying equations (16), (12) and (15) gives

$$\Delta p = \frac{1}{s} \frac{(q_1 - q_2) \beta}{V} \quad (17)$$

$$D_m \cdot (p_1 - p_2) - T_L - B\omega = J_m s^2 \theta_L \quad (18)$$

where angular velocity is $\omega = s\theta$.

EXPERIMENTAL RESULTS

The flow from the pump, and hence the angular velocity of each motor shaft and propeller is controlled with three electrically operated proportional flow control valves, Nessie VOH 30PE. The reaction time from closed to fully open is <150 ms, as shown in Figure 3.

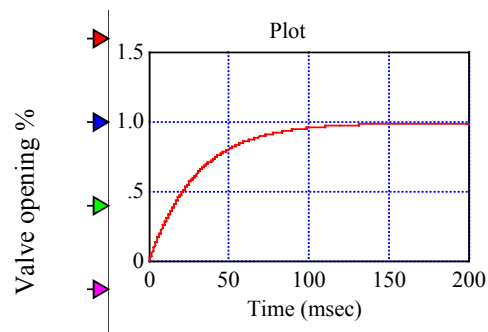


Figure 3 Opening time for proportional valve

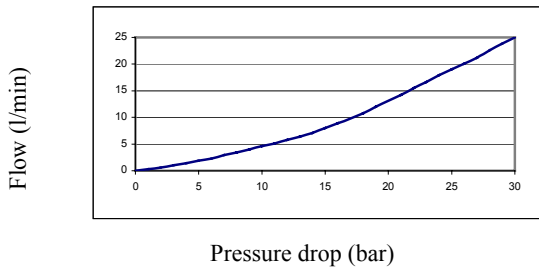


Figure 4 Flow characteristics for 4/3 directional valve

The rotational direction of each motor is controlled by three Nesses VDH 30 EC 4/3 directional valves. The measured flow characteristics of the directional valve are shown in Figure 4. The pressure drop for the 4/3 valve has been added to each curve at the corresponding flow for the proportional control valve. The flow versus rotational speed is shown in Figure 5 for motors.

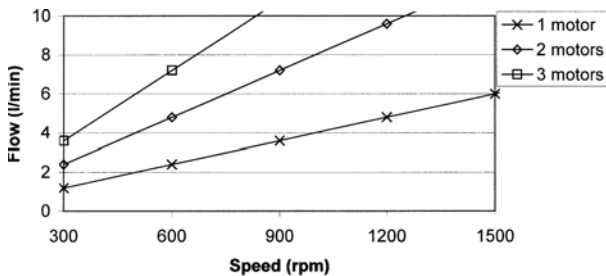


Figure 5 Flow and speed of the water hydraulic motor

The motors can be run from 300 to 4000 rpm. However, with the current used pump gives maximum available flow 5 l/min. The pressure drops versus torque are shown in Figure 6, up to the maximum torque at 8 kN.

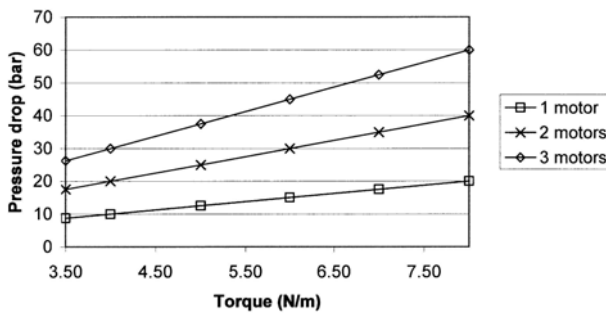


Figure 6 Pressure drop/torque of water hydraulic motor

The required flow versus rotational speed is shown in Figure 5 for motors running from 300 to 4000 rpm. However, with the current pump deliver 4 cm³/rev gives maximum available flow 5 l/min. The pressure drops versus torque for the motors are shown in Figure 6.

SIMULATION RESULTS

The hydraulic motor is modelled in VisSim based on equations describing the relationship between the supply

and return side pressures and flows, torques and angular velocity of the motor.

Two different scenarios have been simulated

1. One motor at minimum speed
2. One motor running with maximum available flow

One motor running at minimum speed

The motor is running around 300 rpm. The velocity, pressures and flows on the supply and return side are shown in Figures 7 to 11. The motor speed increases gradually to the steady state value at 310 rpm as shown in Figure 7. The pressure p1 at the supply side and the pressure p2 on the return side is shown in Figure 8. The flow q1 on supply and flow q2 return side of motor are shown in Figure 9. The limit of pressure p1 is approximately 23 Bar, while the pressure p2 reach at almost 2 Bar.

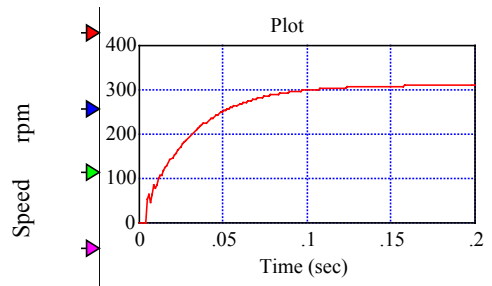


Figure 7 Rotational speed of motor

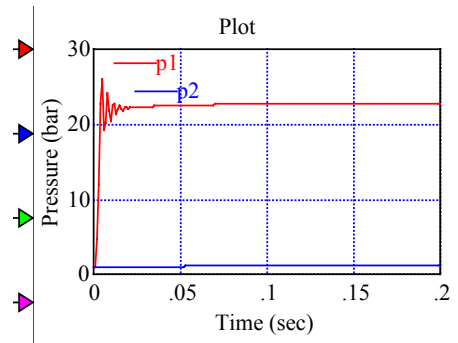


Figure 8 Pressure on supply and return side of motor

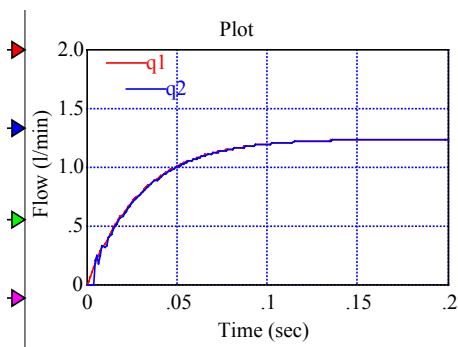


Figure 9 Flow on supply and return side of motor

The pressures will increase with increasing depth of the sea-water; these calculations are valid close to the surface. For a minimum speed of the motor, the flow through the motor stabilises at approximately 1.25 l/min. This shows that a regulation of the flow to around approximately 1.2 l/min after 0.1 second. Upwards is important to provide speed control of the motors to drive and control the thrusters.

One motor running speed with maximum flow

A simulation has been performed to establish the motor performance with a maximum flow from the pump of 5 l/min. As seen from Figure 10, one motor can be running at approximately 1250 rpm. This agrees well with the steady state values estimations shown in the previous paragraph on minimum flow rate.

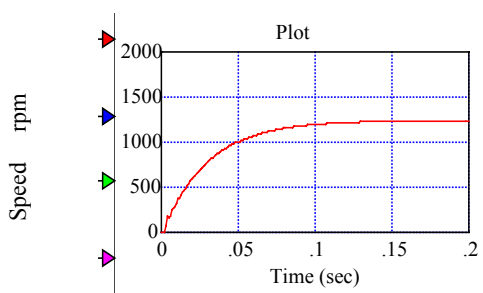


Figure 10 Rotational speed of motor

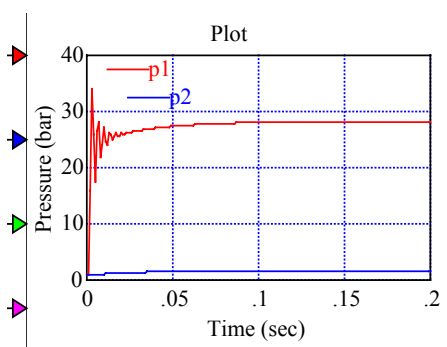


Figure 11 Pressure on supply and return side of motor

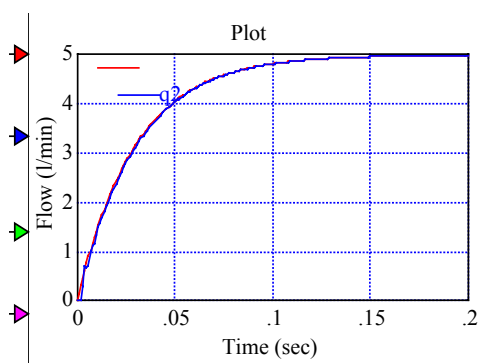


Figure 12 Flow on supply and return side of motor

Figures 11 and 12 show pressure p1 and pressure p2, flow q1 and flow q2. The limit of pressure p1 is

approximately 28 Bar, which is a little higher than the pressure at 300 rpm. This is due to the friction loss. The limit of the flow q1 through the motor is at around 5 l/min, which is the maximum flow from the pump.

CONCLUSION AND OUTLOOK

An novel ROV with water hydraulic propulsion system is being developed, designed and implemented at Bergen University College. The ROV has two thrusters for manoeuvring in the horizontal plane, and one thruster for positioning vertically, and equipped with light and camera. Initial tests of the propulsion system have been carried out, revealing limitations with respect to speed control of the water hydraulic motors. Only one motor could be running at a time, with adjustment of the speed. An attempt to run two motors simultaneously failed, causing the first motor to stop as well. This could indicate a problem with the flow regulation, or a problem with the motors. Modelling and dynamic simulations results to evaluate the performance of the water hydraulic propulsion system were presented. The results show that with a pump delivers flow at 4 cm³/rev, the system can be running in two different configurations

- One hydraulic motor with a velocity up to 1200 rpm and maximum torque (8 kN) on the motor shaft. This requires a power of about 0.9 kW as the minimum system pressure is 80 bar.
- Two hydraulic motors with a velocity up to 600 rpm and maximum torque (8 kN) on each motor shaft. This requires a power of about 0.9 kW.

Test results indicate that accurate flow regulation in the range of 0 – 5 l/min is as expected difficult to obtain. The used current flow control valve is oversized for the ROV system. There is a need for an available flow control valve for a smaller flow rate on the market to feet accurate regulation of the thrusters. Another flow control valve with better performance for the motor and thrusters speed control is needed for redesign, and to reduce the maximum flow through the valve. New system tests will be performed in the research project

References

- [1] Hawley, J. G., M. L. Nuckols, et al. *Design Aspects of Underwater Intervention Systems*, Kendall/Hunt Publishing Company, 1996.
- [2] Conrad, Finn, Bjarne Hilbrecht and Hardy Jepsen. *Design of Low-Pressure and High-Pressure Tap Water Hydraulic Systems for Various Industrial Applications*, Proceedings SAE Paper Number F7-A 2000-01-2614, Society of Automation Engineers Inc., USA 2000.
- [3] Backé, W. *Water- or oil-hydraulics in the future*, 1999.
- [4] Seabrook, C. and C. R. Burrows. *Water hydraulics - some design challenges*, ASME, USA, 1994.
- [5] Watton, John. *Fluid Power Systems*, Prentice Hall, USA, 1989.

EFFECT OF TANK DESIGN AND TWO-PHASED FILTRATION ON CLEANLINESS LEVEL OF WATER HYDRAULIC SYSTEM

Hannu RIIPINEN*, Sari SOINI**, Jaakko A. PUHAKKA**, Kari T. KOSKINEN* and Matti VILENIUS*

*Department of Mechanical Engineering, Institute of Hydraulics and Automation
Tampere University of Technology
P.O. Box 589, FIN-33101, Tampere, Finland
(E-mail: hannu.riipinen@tut.fi)

**Department of Environmental Engineering, Environmental Engineering and Biotechnology
Tampere University of Technology
P.O. Box 541, FIN – 33101, Tampere, Finland

ABSTRACT

Filtration in water hydraulic system may be problematic, due to chemical, physical and biological contamination. This contamination may cause quick increase in the pressure difference over the filter element. The aim of this research was to test different kinds of tank sizes and filter combinations and to determine their effects on water quality in a water hydraulic system. In this paper the results of these experiments are presented.

Experiments were made with pilot-scale water hydraulic systems. The systems induced no biological contamination and only a minimum amount of physical and chemical contamination. Filtered tap water was used as a pressure medium. The tested filter ratings ($\beta > 5000$) were from 10 to 90 μm depth type elements and the three different tank sizes 62, 105 and 148 litres. Experiments were made with water without amendments, and water with nutrient and particle contamination. The test periods were up to four weeks. Pressure difference over the filter, fluid flow and temperature are monitored. Microbiological analyses consisted of total number of cells, heterotrophic viable plate counts and the determination of biofilm formation. In addition, dissolved organic carbon concentration and particle counts were determined.

Solving the microbiological problems of water hydraulics requires new approach to tank design methods that support the long-term working of the water hydraulic system. It is possible to (1) reduce microbial growth in water and on surfaces with a proper tank design, (2) keep microbial growth under control and (3) considerably extend the filter lifetimes by using two-phased filtration in water hydraulic systems.

KEYWORDS

Water hydraulics, filtration, microbial growth, particle contamination

NOMENCLATURE

Bar: 10^5 Pascal
CFU: Colony forming unit [cfu/ml]

DOC: Dissolved organic carbon [mg/l]
EPS: Extra cellular polymer substance
ISO 4406 –glass: particle sizes $>5 \mu\text{m}$ / $>15 \mu\text{m}$
ISOMTD: ISO Medium Test Dust

R2A: Medium used to culture bacteria in low-nutrient environments

$\beta(x)$: (Number of particles $\geq (x)$ upstream) / (Number of particles $\geq (x)$ downstream)

INTRODUCTION

Microbial growth and particle contamination in water hydraulic systems have to be controlled. Filtration is a potential method to control the numbers of micro-organisms and particles in water hydraulic systems and to secure the proper functioning of the system. Micro-organisms retained on the filters grow in the filter element as biofilms and increase the pressure difference over the filter element. It has been shown that approximately 80 % of the micro-organisms of a water hydraulic system are on the filter element [1].

The aim of this research was to test different kinds of tank sizes and filter combinations and to determine their effects on water quality in a water hydraulic system. In this paper the results of these experiments are presented. In addition to tap water experiments, contamination simulation experiments were performed in order to illustrate the combined effect of organic contamination (R2A) and particle contamination on the filter elements in water hydraulic systems.

MATERIALS AND METHODS

The pilot-systems and the tested filters

Two pilot-scale water hydraulic systems were used to simulate the operation of a full-scale system (Figure 1 and 2). The flows produced by the pumps were 34 and 43 l/min. The temperatures of the systems were 35 ± 0.2 °C, which were set to maximize microbial growth in this kind of water hydraulic systems. The systems were made of acid proof stainless steel (AISI 316), only in suction line was used the rubber hose. The sampling ports were before, after or middle of the filter housings.

In the system 1 the fluid flow was monitored with ABB COPA-XE flow meter and in the system 2, with a Kytölä VLK-4FA rotameter. The temperature was measured with Pt100-sensor with Nokeval monitor. Pressure differences over the filters were measured with Huba Control pressure difference transmitter DTP 4-420 (0-4 bar, system 1) and Trafag pressure transmitter (0-40 bar, system 2). Measuring data was stored with GlobalLab-software. Particle counting was made using Pamas 3216 SBSS bottle sample analyser.

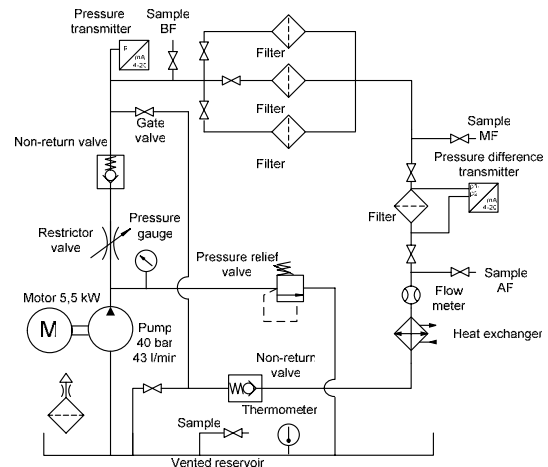


Figure 1 Pilot-system 1

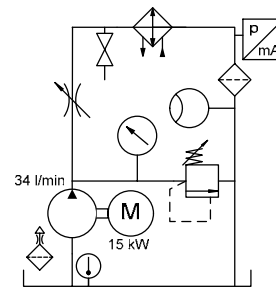


Figure 2 Pilot-system 2

The tested filters were 10 μm and 90 μm (absolute removal ratings $\beta(x) > 5000$) polypropylene cartridge filters produced by Pall Inc. The filter types were R1F100 and R1F900. The length of these filters was 254 mm and the diameters were 70 mm. These filters are disposable and can be used only once. [2]

Experimental set-up and processing of filters

Tap water was used as pressure medium in the experiments. Tap water was filtrated through 1.2 μm filter (Opticap 4" Capsule with Durapore Membrane and Milligard Media, Millipore) when filling the tank. P3 Clint CA was used as cleaning agent. The concentration of the cleaning agent in the system was 3 % during the 60 minutes cleaning period. After the cleaning the system was rinsed three times with filtered tap water. During the cleaning process, 10 μm polypropylene cartridge filter was used for the protection of the components from the harmful effects of potential particulate matter. The test filters were installed after the rinsing periods.

Water samples from the lines of the systems were aseptically taken into autoclaved bottles. Before the sampling the water was allowed to run for 2 to 3 minutes. Samples of polypropylene filter were prepared for scanning electron microscopy (SEM). The pieces were fixed in solution of 1 % glutaraldehyde in 0,1 cacodylate buffer at pH 7. After washing with distilled water, the pieces were dehydrated in ethanol series (70, 85, 95 and 99.5 %). The pieces were prepared in hexamethyldisilazine (HMDS) and air-dried at room temperature. They were stored in exicator. Before the actual investigation with SEM, the pieces were mounted on to SEM stubs and coated with gold. The coated pieces were investigated with a scanning electron microscope (Philips XL-30).

The heterotrophic viable plate counts were determined on R2A medium [3] and the total number of bacteria was determined by DAPI-staining. Also, pH and dissolved organic carbon (DOC) [4] were determined.

Contamination substances on the experiments

R2A was used as a biological contamination to induce microbial growth. ISOMTD was used to simulate particle contamination in the water hydraulic systems.

Depiction of the experiments

First three experiments were made to determine the effects of tank size in pure tap water system (experiment 1 105 litres, experiment 2 148 litres and experiment 3 62 litres), and these experiments were made with filtrated pure water.

Pre-filtration experiments 4 and 5 were made with filtrated pure water. The experiments 6 and 7 were made with filtrated tap water with additions of R2A on days 7 and 14. Experiments 8 and 9 were re-runs of experiments 6 and 7.

Experiment 10 was made to produce 90 µm filter elements which were loaded with different amount of biological contamination. Experiment procedure was as follows: experiment was started with four identical filters connected as shown in figure 1. After one week, when system was operated with pure water, the first of three pre-filters was taken out and it was put in particle test into pilot system 2 (Experiment 11). Experiment 10 continued with two pre-filters and R2A was also added into the system and after one week (two weeks of total running time) the second filter element was put in particle test (Experiment 12). The final phase of experiment 10 was the as previous. After this filter the last of the three pre-filters was put in particle test (Experiment 13).

RESULTS

Effect of the tank size

In experiments 1, 2 and 3, the pressure difference over the filter elements increased because of slight microbial growth and minimal particle contamination (Figure 3).

Experiments showed that when using pure tap water tank size was not important, taken that the tank is made of AISI316 and it has not dead flow areas. It can be seen from figure 3, that the system had more contamination in experiment 1, because cleaning was not efficient enough for new system.

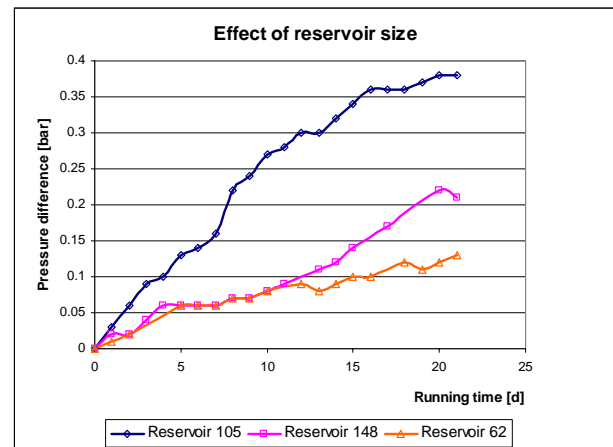


Figure 3 Development of pressure difference over R1F100 filter element (Experiments 1, 2 and 3)

It has been shown earlier that organic contamination can block the filter element quite fast causing system malfunction [5]. Thus, experiments with organic contamination alone were not necessary in this research.

Capability of pre-filtration system to reduce load of the main filter

Experiments 4, 5, 6 and 7 were done to study effects of pre-filtration (Figure 4). In the first two experiments the pressure difference over the filter element increased due to the slight biological and particle contamination. In the last two experiments the pressure difference over the filter element increased due to the slight particle and intense biological contamination.

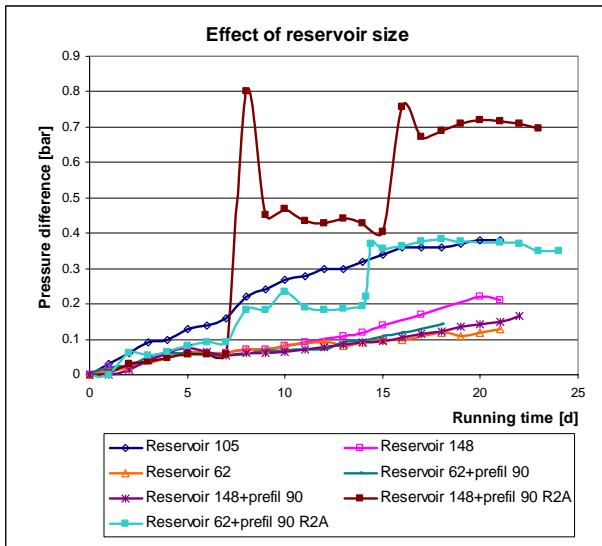


Figure 4 Development of pressure difference over R1F100 filter element (Experiments 1 to 7)

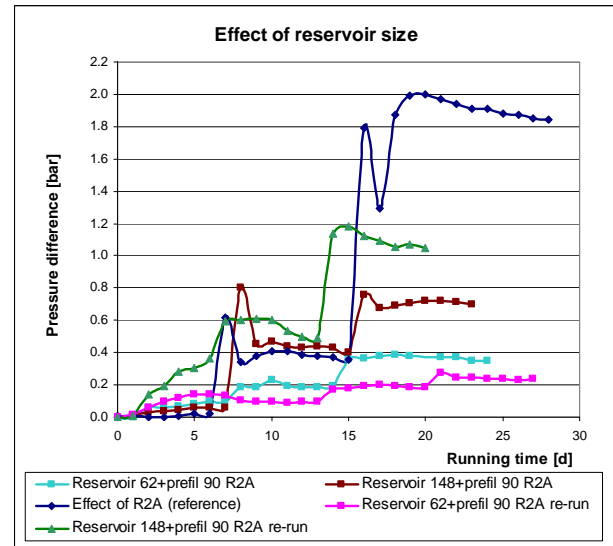


Figure 5 Development of pressure difference over R1F100 filter element (Experiments 6 to 9 and reference)

Pre-filtration was not necessary in case of pure water, but the advantage was clearly seen, when water was biologically contaminated. Absolute amount of biological contamination had a significant effect on the pressure difference over the 10 μ m filter element. The determination of this effect is really difficult, because microbial growth can not be precisely predicted in complex water hydraulic systems. In figure 5, the development of pressure difference in the experiments 6 and 7, the re-runs of them (experiments 8 and 9) and also a reference experiment [5] are shown.

The relative addition of R2A and temperature were the same in all experiments, in order to keep the environment as equal as possible. Only things which were changing were the quality of the tap water and the volume of the water in the system. In point of view microbiology the cell numbers were almost the same, when thinking the accuracy of the measuring and analysing methods and the nature of the microbial growth. Even in the laboratory conditions the effect of the microbial growth was not constant, which was seen when comparing experiments 6 and 8 and experiments 7 and 9.

When R2A was added the first time there no significant differences between the experiments, but the second additions change the situation and give a clear indication that pre-filtration reduces a load of the main filter when absolute amount of the biological contamination is considerable. This is mostly due the larger surface areas of the filters in the system.

Effect of organic contamination on 90 μ m filter element

Figure 6 shows how pressure difference over 90 μ m filter element changes during experiments with pure water or biologically contaminated water.

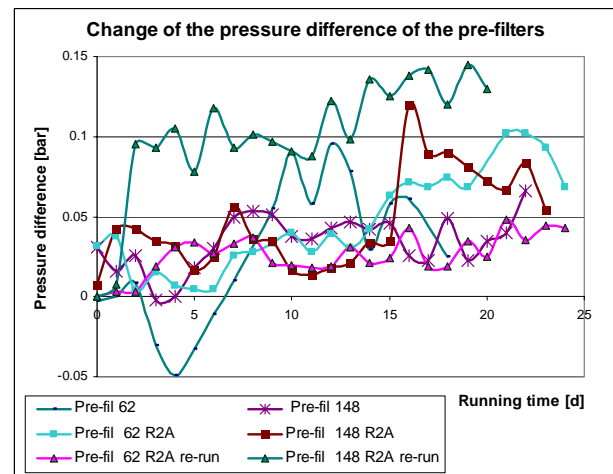


Figure 6 Development of pressure difference over R1F900 filter element (Experiments 4 to 9)

Biological contamination does not have significant effect on R1F900 filter. Average change of pressure difference was about 0.04 bar, which very low when compared with that of the 10 μm filters (Figure 5). Low flow volumes (43 l/min@3 parallel filters) through filters partly explained the difference. It has been observed that microbial attachment likely occurs in areas of low flow velocities [6]. In this case, the low flow velocity was not the problem.

Utilization of microbial growth to improve filtration ratio of 90 μm filter element

90 μm filter element is not capable of keeping particle contamination under control, because of its large bore size. On the other hand the 90 μm filter element has no pressure losses even then when it is loaded by organic contamination.

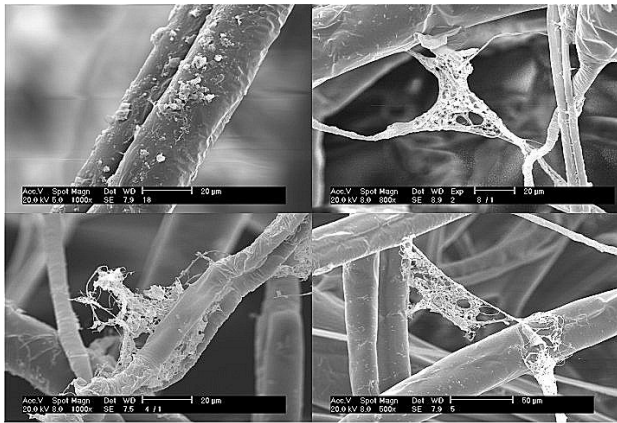


Figure 7 Biologically contaminated R1F900 filter element

In figure 8 is shown the changes in pressure differences over pre-filters and main filter (Experiment 10) are shown.

The most interesting outcome was that the main filter (90 μm) did not get clogged at all. The changes in pressure difference over pre-filters were mainly caused by flow restriction in the parallel line where the pre-filter number three was connected. During experiment 10 the flow tripled in that line.

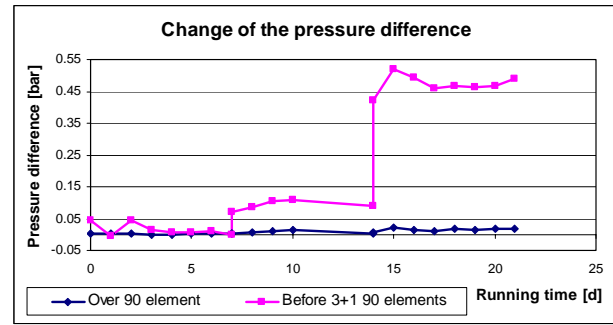


Figure 8 Development of pressure difference over R1F900 and R1F100 filter elements (Experiment 10)

In figure 9 experiment 11 was aborted because R1F900-element was not capable of filtering ISOMTD. Particle counts stayed in absolutely to high level and experiment was stopped to protect test equipment.

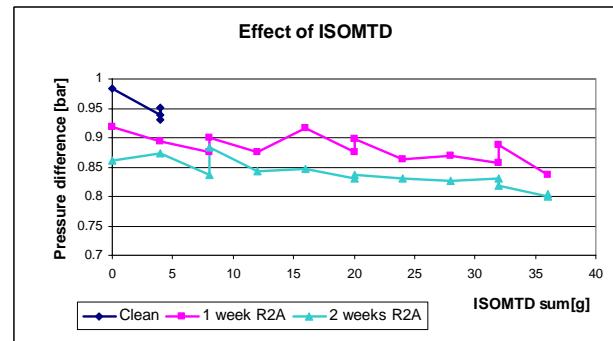


Figure 9 Development of pressure difference over R1F900 filter elements (Experiments 11, 12 and 13)

In experiments 12 and 13, there were not significant changes in pressure differences, but in experiment 12 ISO 4406 –glass was about 15/12 and in experiment 13 it was 11/8. This showed that 90 μm filter significantly improved its filtering grade, when biological contamination was introduced into the filter. At the same time the pressure difference was equal to clean filter element, when accuracy and resolution of measuring devices were taking into account.

The combined effect of biological and particle contamination in case of 10 μm filter has been reported very problematic [7]. Figures 10, 11 and 12 show how quick 10 μm filters have got clogged due to combined effect of biological and particle contamination. In these

experiments, R2A and ISOMTD were added in three different ways into the system.

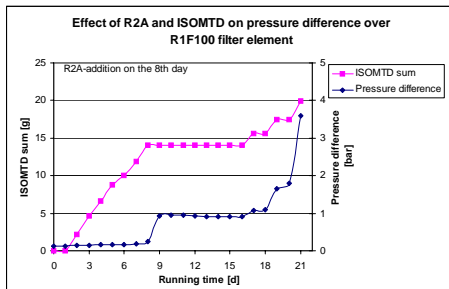


Figure 10 Development of pressure difference over R1F100 filter element (R2A addition on the 8th day) [7]

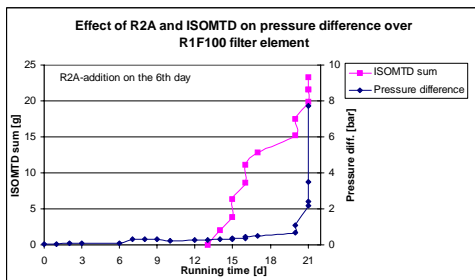


Figure 11 Development of pressure difference over R1F100 filter element (R2A addition on the 6th day) [7]

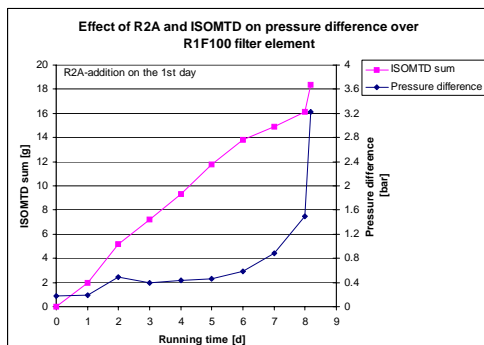


Figure 12 Development of pressure difference over R1F100 filter element (R2A addition on the 1st day) [7]

This kind of combined effect of particles and biofilm was not seen in experiments 11, 12 and 13 (Figure 9). This indicated that R1F900 –elements were working in

acceptable way (low pressure losses and low ISO-glasses), when organic contamination was present. In full-scale industrial applications the organic contamination is often present. This fact gives a possibility to consider using filter elements, which have larger bore sizes, because biological contamination improves the filtration ratio quite fast.

CONCLUSION

Experiments showed that when using pure water tank size is not important, but it is also known that microbial attachment likely occurs in areas where low flow velocities are, resulting in conclusion that unnecessary big tank construction may increase microbial problems. Pre-filtration is not necessary in case of pure water, but the advantage is clear, when water is biologically contaminated.

Combined effect of particles and biofilm can be reduced by using R1F900 –elements, which are working in acceptable way (low pressure losses and low ISO-glasses), when organic contamination is present.

REFERENCES

- [1] Varjus, S.H., Growth and Filtration of Microbes in Water Hydraulic Systems, Master of Science Thesis, Tampere University of Technology, 2001.
- [2] Pall Inc, Profile II polypropylene filters, USD1328b, 1997.
- [3] Reasoner, D.J. and Geldreich, E.E., Applied and Environmental Microbiology, 1985.
- [4] SFS-EN 1484, Water analysis. Guidelines for the determination of total organic carbon (TOC) and dissolved organic carbon (DOC), Suomen Standardoimislaitto SFS, Standard, 1997.
- [5] Riipinen, H., Varjus, S., Soini, S., Puhakka, J.A., Koskinen, K.T. & Vilenius, M. 2002. Effects of Microbial Growth on Filtration in Water Hydraulic System. Proceedings of the 49th National Conference on Fluid Power, March 19-21, 2002, Las Vegas, USA. USA. pp. 235-240.
- [6] Soini, S. M. Microbial ecology and control in water hydraulic systems. DrTech Dissertation. Department of Environmental Technology, Tampere University of Technology. Tampere University of Technology Publications 361. ISBN 952-15-0802-7. 161p. 2002
- [7] Riipinen, H., Varjus, S., Soini, S., Puhakka, J. A., Koskinen, K. T., Vilenius, M. (2002) Effects of Microbial Growth and Particles on Filtration in Water Hydraulic System, 5th JFPS International Symposium on Fluid Power, Nara, Japan, pp. 173-176.

FEASIBILITY STUDY OF CHAIN DRIVE IN WATER HYDRAULIC ROTARY JOINT

Antti MAKELA, Jouni MATTILA, Mikko SIUKO, Matti VILENIUS

Institute of Hydraulics and Automation,
Tampere University of Technology
P.O.Box 589
FIN-33101 Tampere, Finland
(E-mail: antti.h.makela@tut.fi)

ABSTRACT

In hydraulic manipulator applications effective joints movement range of above 180° is often needed. Vane actuator has maximum movement range about 270° . However, water hydraulic vane actuators are quite expensive to manufacture. Thus we investigate a possibility to use so called chain drive instead of vane actuator. Chain drive consists of two cylinders which are connected in series with a chain. Reduced model for chain-drive equals to symmetric cylinder and can be compared with a vane actuator of same size. Concerns with chain drive are the smoothness of sprocket turning around, stiffness of the chain and minimum required back-pressure level for keeping chain tension. In this paper a chain drive is designed, built and tested. We also compare chain drive's and vane actuator's properties mathematically from control point of view. We can conclude that chain drive's characteristics almost equal with vane actuator and it is much more cost effective.

KEY WORDS

Chain drive, vane actuator, dynamic properties

NOMENCLATURE

K_H	:hydraulic stiffness	ω_N	:natural frequency
B	:bulk modulus	d_N	:damping factor
A_2	:cylinder's piston rod side area	J	:load's inertia
V_0	:pressurized volume	D	:radian volume of vane actuator
R	:sprocket's radius		

INTRODUCTION

Hydraulic manipulator applications often require effective rotary joint movement range over 180 degrees. Most often, however, rotary manipulator joints are driven by cylinder which limits the maximum movement range to about 120 degrees. With the aid of four-bar transmission linear cylinder driven rotary joint can be extended from 120 degrees close to 180 degrees. Four-bar transmission is a widely used in elbow joints of heavy-duty hydraulic manipulators. However, as four-bar transmission consists of at least two additional rotary joints and links, the kinematic calibration and tolerance issues in robotic applications requiring high accuracy can easily become a problem.

An alternative for linear actuator driven joints is vane actuator which has maximum movement range is about 270 degrees. In heavy-duty oil hydraulic manipulators, however, vane actuators are seldom used. This is mainly because in these applications a low leakage and low price actuators are required. Low leakage requirement usually makes vane actuator seal friction level relatively high and thus limits the usability of the actuator. Still another drawback of vane actuators is that leakage across vane seal makes e.g. lock-valves ineffective in hydraulic load holding functions. Hydraulic cylinder actuator can be considered zero leakage actuators and thus load holding functions for them have proven to be effective.

However, in smaller scale purpose build hydraulic manipulator applications with a workspace less than 1-2 meters, vane actuators have proven to be effective solution due to robust design, compact size and large joint range. On the other hand, in water hydraulic applications vane actuator has some weaknesses. This is because water's viscosity is about ten times smaller than oil's which led to tight tolerances in manufacturing. This makes manufacturing of water hydraulic vane actuators quite expensive. Also as mentioned above leakage across vane seal makes e.g. lock-valves ineffective in hydraulic load holding functions. On the other hand, as well known, leakage cross actuator seal improves the dampening of the actuator, but it decreases position accuracy.

Because of above mentioned weaknesses vane actuators have, we investigate in this study a possibility to use cost-effective chain drive for rotary joint actuation. Chain drive consists of two hydraulic cylinders which are connected in series with a chain. Reduced model for

chain-drive equals to symmetric cylinder and thus can be easily compared with a vane actuator of same size.

HYDRAULIC ROTARY CHAIN DRIVE

The schematic of chain drive actuator is shown in Figure 1. Chain drive consists of two hydraulic cylinders which are connected in series with a chain and rotate a sprocket. Cylinder rodless sides are connected to tank and a servovalve is connected to rodsides of the cylinders. Reduced model of the chain actuator therefore equals to symmetric cylinder, making open-loop gain of the system equal to both directions. As well known, for example with zero load and critically lapped symmetric four way servovalve, the steady state pressures of symmetric cylinder chambers are equal to $P_s/2$ (supply pressure divided by two). Therefore, adequate chain tension can in some cases always be guaranteed if the application specifications are well known. This could be a case for example in some relatively low speed application. If the application specifications are not known exactly or the application requires for example high accelerations, minimum chain tension has to be provided for example with external pressure reducing valves, as shown in Figure 1. Downsides of the back pressure provided by pressure reducing valves is that they limit available torque output range of the actuator and make actuator design less compact. In addition to adequate back pressure function, chain design is of high importance. If the chosen chain stiffness is less or about the same magnitude as the stiffness of hydraulic cylinder, the result is complex 5 th order system that makes controller system design tedious task. Therefore, usual rule of thumb design requires that chain stiffness has to at least a decade higher than corresponding hydraulic stiffness.

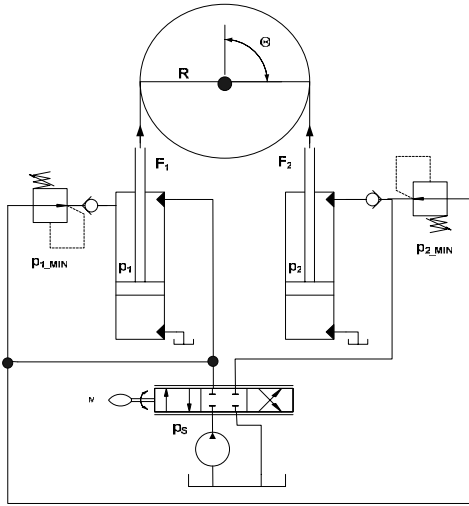


Figure 1 Schematic of chain drive

Prototype chain drive actuator design was based on following design parameters, which allow comparison with the vane actuator of approximately the same torque output.

- Maximum torque output of 525 Nm when maximum available supply pressure of 210 bar and back-pressure is 52 bar
- Maximum velocity of 180 deg/s with QN=6.8 l/min
- Maximum joint motion range of 275 deg.

Based on above specification, the following design was made.

- Two water hydraulic cylinder 32/25 - 550
- Triple chain wheel's with 42 teeth
- Distances between teeth are 15.875mm
- Sprocket radius of 106 mm.

With above design parameters following specification for chain drive actuator were achieved.

- Maximum torque 525Nm
- Maximum velocity of 195 deg/s
- Maximum joint motion range of 298 deg.

ACTUATORS PROPERTIES

The dynamic performance of the any hydraulic actuator is limited by its hydraulic natural frequency that is a

function of load mass and actuator hydraulic stiffness. Since the load of the both actuators is the same, the stiffness of the actuator will define the natural frequency of the actuators. Equation for hydraulic torsional stiffness of the vane actuator at its minimum value is [1]:

$$K_{H_VANE_1} = \frac{2BD^2}{V_0} \quad (1)$$

For cylinder driven chain actuator, the minimum hydraulic torsional stiffness is obtained:

$$K_{H_CHAIN_1} = \frac{2BA_2^2R^2}{V_0} \quad (2)$$

Vane actuator's and chain drive's natural frequency:

$$\omega_N = \sqrt{\frac{K_H}{J}} \quad (3)$$

A prototype vane actuator was build with following specification.

Following design was made:

- Ø 57mm axis
- Ø 83mm chamber
- 55 mm width

Following properties were achieved.

- Maximum torque is 525Nm
- $D = 2.503 \times 10^{-5} \frac{m^3}{rad}$.
- Maximum velocity $v = 43 \frac{deg}{s}$

For vane actuators it is convenient to integrate servovalve directly to vane actuator housing. Water flow paths are inside the chamber with diameter of 4mm and maximum length of 100mm. When vane actuator is at its middle position, its total pressurized volume is $V_0 = 8.0 \times 10^{-5} m^3$. For testbed load mass was 30kg at end of one meter long rod making its inertia about $J = 30kg \times m^2$. Water bulk modulus is about 1500MPa. These values result minimum natural frequency of $\omega_N = 4.5Hz$ for vane actuator.

Chain drive characteristics are given above. Servovalve is connected to cylinders with Ø4mm – 200mm pipe

making total pressurized volume equal to $V_0 = 8.113 \times 10^{-5} m^3$. These values result minimum natural frequency of $\omega_N = 4.9 Hz$ for chain drive.

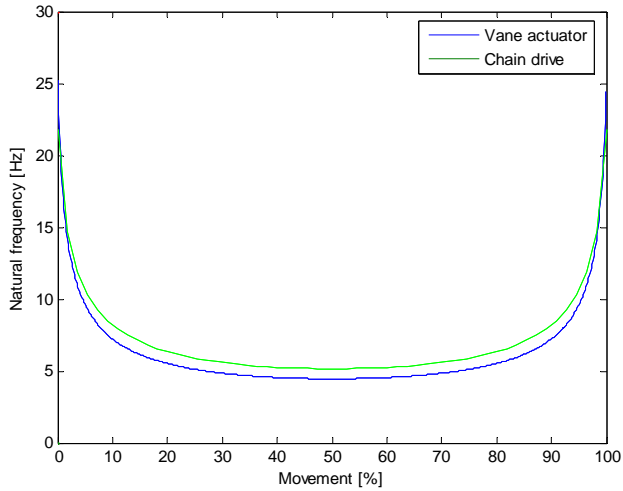


Figure 2 Natural frequencies of two actuators

Natural frequencies of two actuators as a function of actuator movement are plotted in Figure 2. From Figure 2 it can be seen that natural frequencies of the both actuators are about the same. The dampening of the hydraulic actuator is usually in the range of 0.05 - 0.2 and its value is hard to predict by theoretical analysis like given for example in [1]. However, the effective dampening ratio of the chain drive is expected to be lower than it is with vane actuator due to the relatively high cross seal leakage of the vane actuator [2]. Of course the dampening of the chain drive can be increased with leakage orifice across valve ports. However, leakage orifice will then destroy load holding functions that are required in robotic applications.

According to leakage measurements made with previous vane actuator prototype with nominal torque output of 1000Nm, the measured leakage factor across vane was $C_{LEAK} = 1.7 \times 10^{-7} \frac{m^3}{s} MPa$ in 35°C temperature and 210bar pressure difference. If we assume that leakage coefficient is directly proportional to achieved torque, then it will reduce 50% from above value. However, for chain drive there is hardly any leakage. Once available, measurements with lock valves will be performed to verify the load holding functionality of both actuators.

Open loop gain rules the static accuracy of the actuators. Maximum gain for hydraulic drive:

$$K_{max} = 2d_n \omega_n \quad (4)$$

According to Fig 2. natural frequency is little bit higher for chain drive. Damping factors are difficult to estimate, but they are about 0.2 for both actuators. Then maximum gain for vane actuator is $K_{max} = 11.3$ and chain drive $K_{max} = 12.3$. In theory both actuators static accuracies are almost same.

MEASURED RESULTS

Measurements were carried out with a chain drive testbed shown in figure 3. The testbed specifications were given above. Required nominal torque output of 525 Nm can be obtained with back pressure value of 5.2 MPa and therefore it was used in the experiments. It seems to be enough for this kind solution.

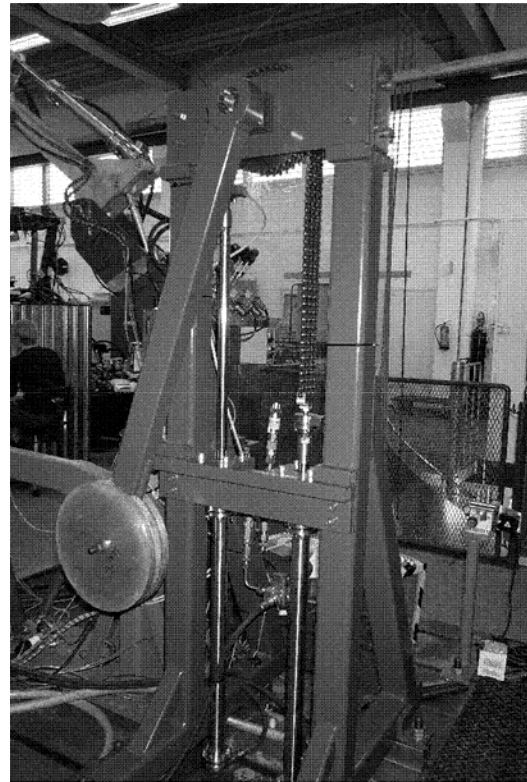


Figure 3 Chain drive testbed

Open loop natural frequency of vane actuator was measured by “hammer test” when load arm was in

horizontal position. From Figure 4, it can be seen that approximate natural frequency is about 5Hz making above natural frequency theory presented valid.

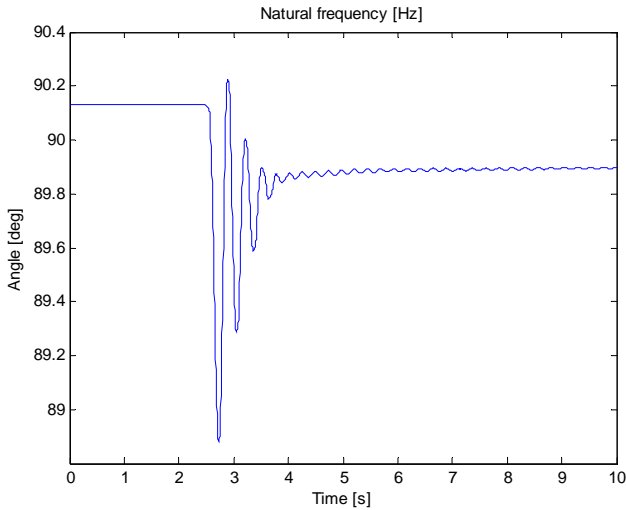


Figure 4 Natural frequency of chain drive actuator

Sprocket turning smoothness measurement test was done. Cylinder position was measured with linear encoder. Sprocket position was measured pulse encoder with 5000 pulse per round and it was interpolated to 25 – fold. As we can see there are some speed variations. Cylinder positions 24mm and 38.5mm and something over 50mm there are higher peaks. This is approximately same as teeth gap. Anyway greatest peak is about 0.6% above mean value.

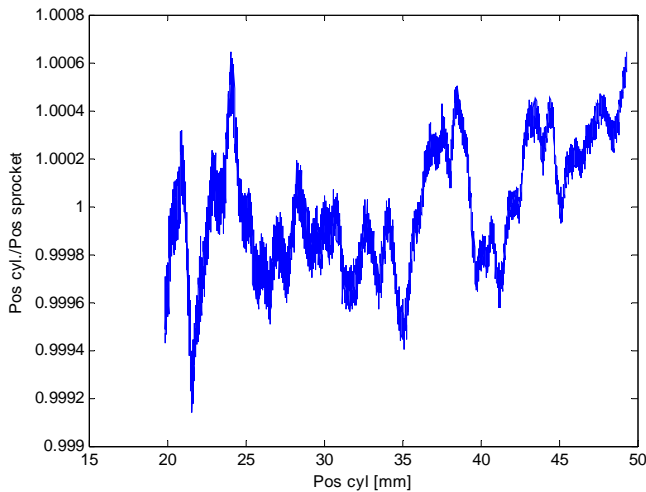


Figure 5 Sprocket turning smoothness

Simple proportional position controller was also tuned and measured in order to verify chain drive actuator dynamic performance under control. Step signal was used as reference. Controller gain was half of the maximum value given by stability criteria.

First measurements were done so that arm was driven to downwards. In next figures 6 and 7 position responses of the chain drive are shown. Static accuracy is 0.025 degrees in first response and -0.05 degrees in second response. So accuracies are relatively good to both directions

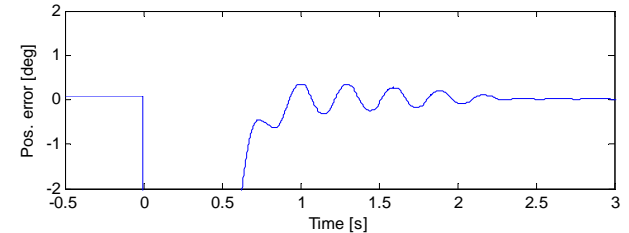
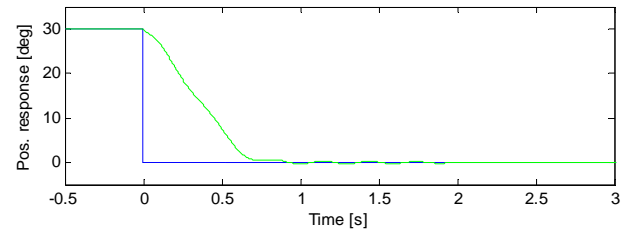


Figure 6 Step response and tracking error from 30 to 0 degrees

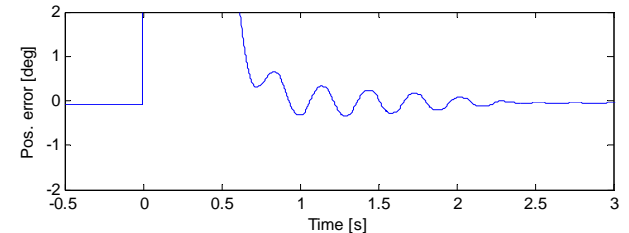
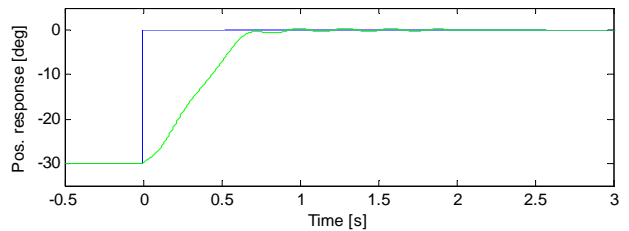


Figure 7 Step response and tracking error from -30 to 0 degrees

In figures 8 9 are shown next measurements. They were done so that arm was driven to horizontal position. Static accuracies are not as good as in previous measurement due to load force caused by gravity. In first response it is 0.25 degrees and second response it is 0.32 degrees. Valve inner leakage can affect worse accuracies. It can be noticed that gravity force causes some oscillation when arm is driven from 120 deg to 90 deg. When arm is driven to other direction oscillation is much less.

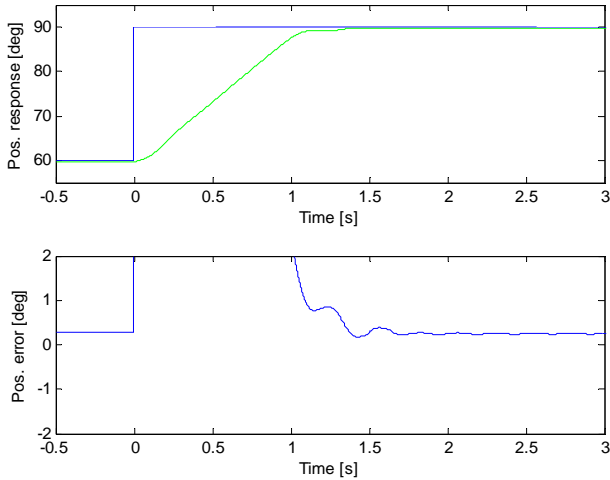


Figure 8 Step response and tracking error from 60 to 90 degrees

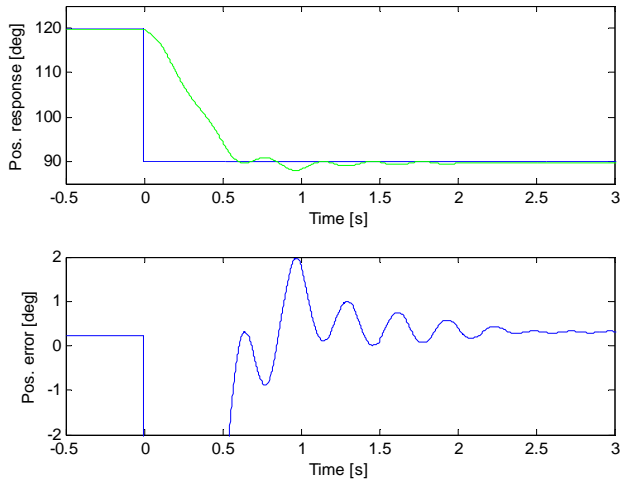


Figure 9 Step response and tracking error from 120 to 90 degrees

Based on measured results it can be assumed that designed chain stiffness seems to be adequate because it is invisible in position control measurements.

CONCLUSIONS

In this study new water hydraulic chain drive actuator was designed and tested. Chain actuator design was compared with vane actuator design of very similar design characteristics. Chain drive is a relatively inexpensive to build and zero-leakage actuator with satisfactory motion range of above 270 degrees. Zero-leakage characteristics are very important for load holding functionality point of view. The down side of the chain drive design is that its size is much bigger than vane actuator with similar maximum torque output and motion range. However, in many cases relatively big size of the actuator is not a problem. For example, sometimes chain drive actuator can be fitted e.g. into manipulator arm link. However, water hydraulic chain drive actuator is proved to very useful new actuator type when rotary motion range above 200 degrees is required at low cost and with zero-leakage characteristics.

This study was our first one concerning water hydraulic chain drive. Our future plan is to test different sprocket and cylinder radius combinations so that natural frequency is always same. Also some different hydraulic connections will be tested.

REFERENCES

1. Merrit, H. 1967. Hydraulic Control Systems, John Wileys & Sons inc.
2. Raneda, A., Siuko, M. and Virvalo, T., Torque control of a Water Hydraulic Vane Actuator Using Pressure Feedback, Proc. of ASME International Mechanical Engineering Congress and Exposition, 2002, New Orleans, USA

Development of Water Drive Spindle

Yohichi NAKAO* and Yuji SAGESAKA**

* Department of Mechanical Engineering, Faculty of Engineering
Kanagawa University
3-27-1 Rokkakubashi, Kanagawa-ku, Yokohama, 221-8686 Japan
(E-mail: nakao@kanagawa-u.ac.jp)
** Graduate School, Kanagawa University

ABSTRACT

A water drive spindle for diamond turning machines is proposed. The spindle uses water flow for driving the rotor by a water drive motor, for supporting the rotor by water hydrostatic bearings, as well as for coolant. As water is not only incompressible and clean but also low viscosity fluid, it is considered that a high-speed and precise rotational motion will achieve in the clean environments for ultra-precision machinings. The present paper reports a structure of the spindle as well as the operational principle of the spindle. In the present paper, theoretical equations used for designing the spindle is derived. The characteristics of the spindle are studied theoretically and experimentally.

KEY WORDS

Spindle, Water Hydraulics, Water Drive Built-In Motor, Water Hydrostatic Bearing, Ultra-Precision Machining

INTRODUCTION

A high-speed hydraulic motor has been presented in our studies^{[1]-[3]}. The performances of the motor have been studied theoretically and experimentally. In the experiments, the developed motor was driven by oil. However, the motor was designed so that it can be driven by not only oil flow but also air or water flow. Based on the studies concerning the high-speed hydraulic motor, a water drive spindle is developed in the present study. A final goal of the present study is to apply the water drive spindle for the ultra precision

machine tools, such as a diamond turning machine or a diamond grinding machine.

The spindle for the ultra-precision machine tools is required the following performances: (i) high rotational speeds, (ii) precise rotational motion with small run-out, (iii) large stiffness of the bearings and (iv) small thermal deformation of the spindle.

In order to attain the precise rotational motion, conventional spindles for the ultra-precision machine tools are commonly equipped with the air static pressure bearings and the electric built-in motor. In fact, precision machining can be performed by the

conventional spindle with a precision guide way and a single crystal diamond cutting tool.

Now, a further improvement of the machining accuracy is required. As a result, an advanced spindle is needed to achieve higher machining accuracy. From such viewpoint, the air static pressure bearings are not necessarily suitable to design the spindle with a large stiffness, because of the compressibility of air. Another problem of the conventional spindle is the heat generation at the built-in motor that induces the thermal deformation of the spindle.

In order to increase the stiffness of the static pressure bearings, the bearings are, in general, designed as follows: (i) the clearance of the bearings is small, (ii) the area of the bearing surfaces where the pressure acts is large. Accordingly, even small thermal deformation of the spindle, due to the heat generation at the built-in motor, will cause the mechanical contacts between the rotor and casing, which usually causes serious problems.

It is considered that a solution for designing advanced spindle is to use water for the lubricant fluid of the static pressure bearings, because water is the incompressible fluid with low viscosity. In addition, it will be also advantageous to use water for the coolant as well as the lubricant fluid, because the thermal conductivity of water is higher than that of air and oil.

In addition to the effective utilization of the water flow for the lubricant and coolant, the present paper proposes to use the water flow for driving the spindle. A basic design for driving the spindle, named as the water drive motor, has been studied in our previous studies^{[1]-[3]}. The water drive motor can be easily built in the rotor in place of the electric built-in motor.

The present paper first describes the operational principle of the spindle as well as theoretical equations of the spindle that are essential for the design of the

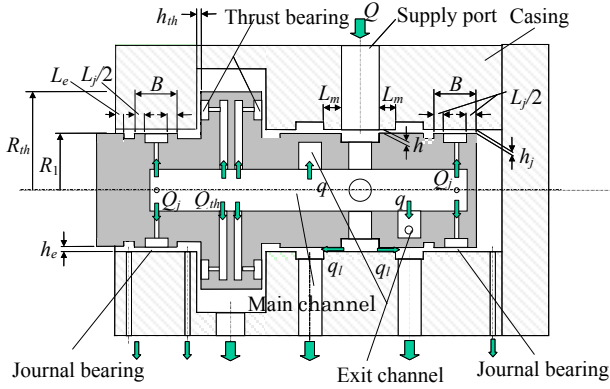
spindle. Spindles that have different rated powers and rotational speeds are studied theoretically and experimentally.

WATER DRIVE SPINDLE

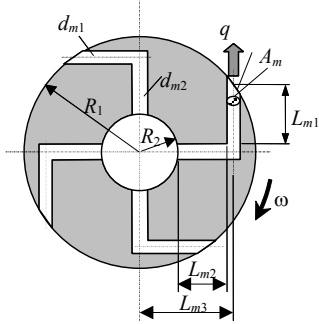
A structure of the water drive spindle is illustrated in Fig. 1. The spindle rotor is supported by the water hydrostatic bearings in the radial and axial directions and it has several flow channels inside the rotor. In order to lead water into the rotor, relatively large channels in the radial directions are present in the middle of the rotor. Water flows inside the rotor, because the main channel passes through the center of the rotor in the axial direction and several flow channels are fabricated for passing the water out from the main channel. The spindle is designed so as to use the water flow effectively to achieve the following three spindle functions.

(i) Water drive motor The spindle rotor has bend-shaped channels of small diameter, named as the exit channels, connecting between the main channel and the outer surfaces of the rotor. As illustrated in Fig. 1, the exit channels are located at two cross sections of the rotor. These exit channels enable the water flow to pass out from the inside of the rotor. The direction of the water flow changes significantly in the exit channels. Consequently, the torque used to spin the rotor is generated by the large change in the angular momentum of the water flow.

(ii) Water hydrostatic bearings Water hydrostatic journal and thrust bearings are designed as follows. Recesses are formed on the outer surfaces of the rotor. In addition, chokes of the bearings are located between the recesses and the main channel. Hence, the lubricant



(a) Spindle structure



(b) Exit channel

Fig. 1 Water drive spindle

water can pass out from the main channel through the chokes and the recesses in the radial and axial directions. This generates the static pressure distributions around the rotor to support the rotor.

(iii) Water cooling In addition to the working and lubricant fluid, water can be used as a coolant, to minimize the thermal deformation of the spindle. The thermal conductivity of water is higher than that of oil and air, which is an advantage for achieving better cooling performance.

THEORY

Primary configurations of the spindle are given in Figs. 1(a) and (b). The output torque T_l generated by the water flow rate q through one of the exit channels can be expressed by Eq. (1).

$$T_l = 2n\rho q \left(\frac{l_{m3}}{A_m} q - R_1^2 \omega + R_2^2 \omega \right) - 2\mu\pi R_1^3 \omega \left(\frac{2L_m}{h_m} + \frac{2L_j}{h_j} + \frac{L_e}{h_e} \right) - \frac{\mu\pi}{h_m} (R_{th}^4 - R_1^4) \omega \quad (1)$$

Here, ρ is the density of the water, μ is the viscosity of water and n is the number of the exit channels at a cross section of the rotor.

The pressure drop in the exit channels is dominant compared to that in the other channels. Hence, the relationship between the supply pressure p_s and the flow rate q can be represented as

$$q = \frac{A_m}{\sqrt{\kappa}} \sqrt{\frac{2p_s}{\rho}} \quad (2)$$

where,

$$\kappa = 1 + \lambda \frac{l_{m1} + l_{m2}}{d_m} + \zeta_1 + \zeta_2 \quad (3)$$

In Eq. (3), λ is the friction factor and ζ_1 and ζ_2 are the resistance coefficients of the exit channels. The leakage flow in the clearance between the casing and the rotor can be represented as

$$q_l = \frac{\pi h_m^3 R_1}{6\mu L_m} p_s \quad (4)$$

Thus, the flow rate of the water drive motor is given by $Q_m = 2(nq + q_l)$ (5)

The stiffness of the journal bearing can be given by

$$K_j = \frac{2BR_1}{h_j} \bar{P}_j p_{jr} \quad (6)$$

where, \bar{P}_j is a characteristic parameter determined by the pressure distribution on the journal bearing surface and p_{jr} is the recess pressure of the journal bearing. The flow rate of the journal bearing can be represented by

$$Q_j = \frac{\Theta_j h_j^3}{\mu} p_{jr} \quad (7)$$

where, Θ_j is a coefficient expressing the pressure flow relationship at the journal bearing surface.

Similarly, the stiffness and the flow rate of the thrust

bearing are given by

$$K_{th} = \frac{3\Pi_{th}A_{th}}{h_j} p_{thr} \quad (8)$$

$$Q_{th} = \frac{2\Theta_{th}h_{th}^3}{\mu} p_{thr} \quad (9)$$

where, p_{thr} is the recess pressure of the thrust bearing, and Π_{th} is a characteristic parameter determined by the pressure distribution on the thrust bearing surface, and Θ_{th} is also a coefficient expressing the pressure flow relationship at the thrust bearing surface. These coefficients \bar{P}_j , Θ_j , Π_{th} and Θ_{th} in Eqs.(6)-(9) can be obtained by solving the Reynolds' equation.

The total flow rate of the spindle is given by

$$Q_t = Q_m + 2Q_j + Q_{th} \quad (10)$$

Finally, the total efficiency of the spindle can be represented as

$$\eta = \frac{T_t \omega}{P_s Q_t} \quad (11)$$

DESIGNED SPINDLE

For designing the spindle, the rated performances, such as the output power, rotational speed and bearing stiffness, are specified. Accordingly, a designer has to determine the spindle dimensions so that the designed spindle attains, at least, the given rated performances. In addition, the designer is required to determine the optimum dimensions, which maximize the total efficiency of the spindle given by Eq. (11). In the present study, software for determining the optimum parameters has been developed based on the equations derived in the previous section.

In the present study, two spindles with different rated performances, named as Spindle 1 and Spindle 2, are designed using the software. The rated performances of the spindles, such as the output power P_r ; the rotational

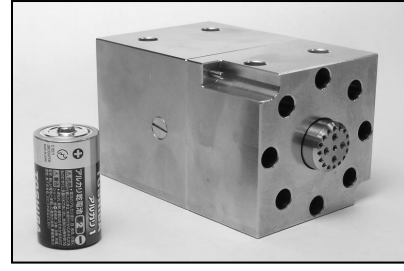


Fig. 2 Developed water drive spindle

speed N_r ; the stiffness of the journal bearing K_{jr} ; and the stiffness of the thrust bearing K_{thr} , are specified as follows:

(i) Spindle 1: $P_r = 50$ W, $N_r = 10,000$ rpm, $K_{jr} = 47$ N/ μ m and $K_{thr} = 12$ N/ μ m

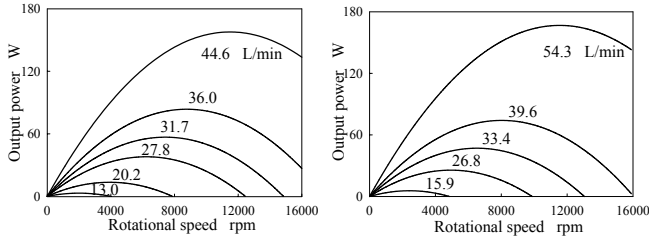
(ii) Spindle2: $P_r = 40$ W, $N_r = 4,000$ rpm, $K_{jr} = 85$ N/ μ m and $K_{thr} = 33$ N/ μ m

The developed spindle is shown in Fig. 2. Figures 3(a) and 4(a) show calculated output power. For example, Fig. 3(a) shows the output power of the Spindle 1. In this case, it is observed that the rated performance can be obtained when the total flow rate is 31.7 l/min. Similarly, the output power of the Spindle 2 becomes 40 W at 4,000 rpm by supplying the flow rate of 33.4 l/min, as shown in Fig. 4(a).

The total efficiency of the spindles are given in Figs. 3(b) and Figs. 4(b) as well. A disadvantage of the spindle is that the total efficiency is particularly low. It has been shown that a primary reason is the large pressure drop in the exit channels ^[3].

EXPERIMENTS

Experimental setup A schematic of the experimental setup is shown in Fig. 5. A water-piston pump was used to supply water to the spindle. A rotational speed of the spindle was measured by the pulse frequency from a photoelectric sensor that outputs one pulse per a rotation

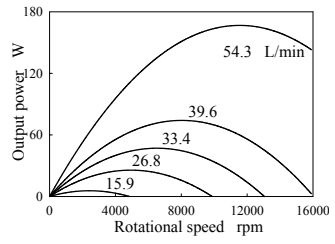


(a) Output power

(b) Efficiency

Fig. 3 Spindle characteristics

(Spindle 1)



(a) Output power

(b) Efficiency

Fig. 4 Spindle characteristics

(Spindle 2)

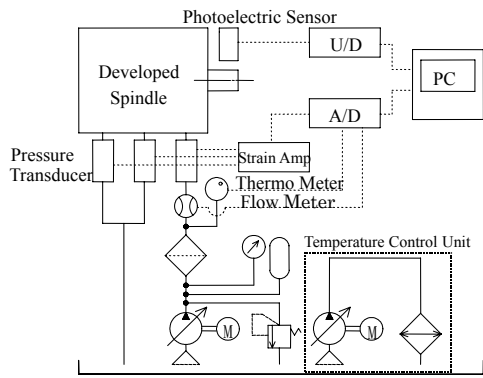


Fig. 5 Experimental setup

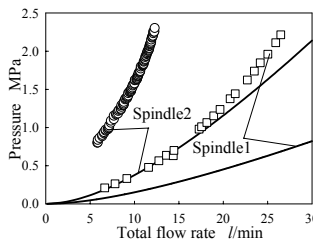


Fig. 6 Q_t vs. p_s

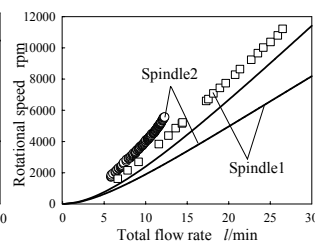


Fig. 7 Q_t vs. N

of the rotor. A water temperature control unit was equipped with a reservoir tank of water. Tap water was used for the experiments. During the experiments, the water temperature was controlled in the range from 19.8 to 20.8 degrees Celsius.

Experimental results As shown in Fig. 6, the highest supply pressure was approximately set to 2.3 MPa in both experiments. Figure 7 shows the relationships between the total flow rate and the rotational speed N . The results show the spindles can reach their rated spindle speeds.

The solid lines in Figs. 6 and 7 represent calculated rotational speed and supply pressure, i.e. pressure drop in the exit channels. It is observed that the supply pressure calculated with Eq. (2) differs significantly from the pressure measured in the experiments. It is considered that the friction factor and the resistance coefficients^[4] used for the calculations did not represent well the actual pressure flow relationships.

The calculated rotational speed also differs from the experimental results. As it is obvious from Eq. (1), once the primary dimensions of the spindle were determined, the flow rate q becomes the significant factor that determines the rotational speed. Furthermore, the flow rate q is determined by the recess pressures p_{rth} and p_{rj} , and Θ_j , Θ_{th} as well as the supply pressure p_s . The recess pressures p_{rth} and p_{rj} are determined by the pressure flow relationships of their chokes and Θ_j , Θ_{th} . Therefore, the results show that the characteristic values have to be measured in order to obtain better calculation results.

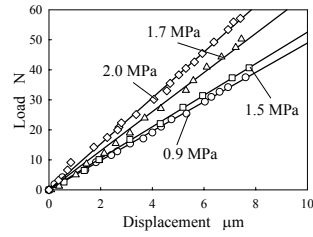
Stiffness of the water hydrostatic bearings was measured and then compared with the designed values. The relationships between the displacement and the load are shown in Fig. 8(a) and Fig. 9(a). The characteristics were measured for several supply pressures. The relationships between the supply pressures and the stiffness are shown in Fig. 8(b) and Fig. 9(b), respectively. We can observe that the stiffness increases in proportion to the increase in the supply pressures. At the rated operational condition, measured stiffness of the thrust bearing was 32 N/ μ m, which agrees well with

the theoretical value of 33 N/μm.

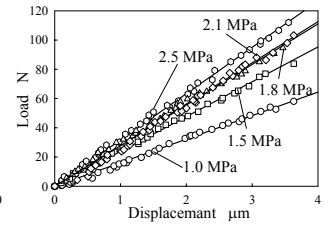
Stiffness of the journal bearings was measured as 7.7 N/μm. In the experiments, however, the loads were applied to an end of the rotor, which induces the moment effects on the bearings. Removing the moment effects from the original measured data, the stiffness in the radial direction becomes 49.0 N/μm per journal bearing. Since two journal bearings are present at both ends of the rotor, the total stiffness of the bearings in the radial direction becomes 98.0 N/μm. In contrast, the theoretical value of the stiffness was 87.9 N/μm. It is considered that the difference between the measured and theoretical values comes from the influence of the pressure flow relationships of the water hydrostatic bearings.

CONCLUSIONS

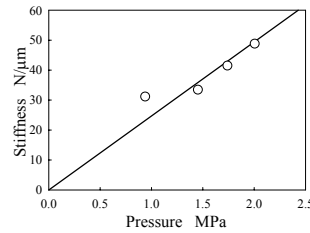
A water drive spindle for diamond turning machines was presented in this paper. The water drive spindle is designed so as to use water flow for driving, supporting and cooling the spindle. In the present paper, theoretical equations that are essential in designing the spindle were introduced. The characteristics of the spindle were studied through theoretical calculations and experiments. Two water drive spindles with different rated performances were designed and tested. The results showed that both of the spindles rotate at over the rated spindle speeds. It was shown that calculated performances of the spindles were not good agreed with the experimental results, due to lack of the experimental data on the pressure flow relationships of various flow channels of the spindle. Stiffness of the water hydrostatic bearings were also measured and the results were good agreed with the design values.



(a) Displacement vs. load



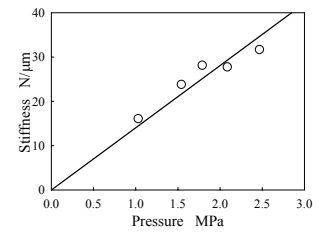
(a) Displacement vs. load



(b) p_s vs. stiffness

Fig. 8 Bearing stiffness

(journal bearing)



(b) p_s vs. stiffness

Fig. 9 Bearing stiffness

(thrust bearing)

This research work is financially supported by the Grant-in-Aid for Scientific Research (C) of Japan Society for the Promotion of Science.

REFERENCES

1. Y. Nakao and M. Mimura, Spindle motor driven by fluid energy for ultra-precision machine tool, Proc. of ASPE 2002 Annual Meeting, pp.215-218, (St. Louis, 2002-10).
2. Y. Nakao and M. Mimura, High-Speed Motor Driven by Fluid Power, Proc. of 5th JFPS, pp.543-548, (Nara, 2002-11).
3. Y. Nakao and M. Mimura, Study on Built-In Motor Driven by Fluid Energy for Ultra-Precision Machine Tool Spindle, Tras. Jpn. Soc. Mech. Eng. (Ser. C), (in Japanese) 71, 703, pp.1077-1084, (2005-3).
4. JSME Data Book: Hydraulic losses in pipes and ducts.

A STUDY ON THE APPLICATION OF BIRFIELD JOINT TO A WATER HYDRAULIC PISTON PUMP FOR LOW LEAKAGE AND LOW FRICTION PUMPING

Young-Bog Ham*, Yong-Bum Lee**, Kyung-Min Park***, Byung-Oh Choi*

* Intelligence and Precision Machinery Research Division, Korea Institute of Machinery and Materials, 171 Jang-dong, Yusung-gu, Daejeon 305-343, South Korea
(E-mail: hyb665@kimm.re.kr)

** System Engineering Research Division, Korea Institute of Machinery and Materials

*** Powertrain Development Center, P/T Project Planning Team, Ssangyong Motor Company

ABSTRACT

As water hydraulics is more and more highlighted in wide applications, many varieties of research on design, materials and manufacturing methods of water hydraulic components have been carried out. Especially, water hydraulic piston pump used to be the subject of study in relation to its relative sliding movement. In these relative sliding parts, the leakage and friction probably took place because of the characteristics of low viscosity and poor lubrication of water. In order to reduce the leakage and friction, the relative sliding parts are filled up nearly by using engineering plastic as an anti-wear material on sliding parts. Compared with an oil hydraulic system, a water hydraulic system has fundamental disadvantages of large friction, high leakage, high wear, corrosion, etc. A mechanism of rod type piston was considered to reduce friction of the piston's movement in a water hydraulic piston pump. Friction and leakage of the rod type piston was analyzed and compared with those properties of the conventional plunger type piston. An experimental device was set up to evaluate friction and leakage of those pistons. A PEEK piston was also tested as another alternative piston of a water hydraulic pump.

KEY WORDS

Water hydraulics, Piston, Pump, Birfield joint

NOMENCLATURE

A : contact area of viscous friction
 c : radial clearance
 d : diameter of piston
 e : eccentricity of piston
 F_c : coulomb friction force
 F_f : total friction force
 F_L : lateral force
 F_R : reaction force under piston shoe
 F_v : viscous friction force

h : thickness of oil film
 L : passage length
 L_1 : overlap length of piston
 L_2 : overhang length of piston
 P_d : discharge pressure
 r : tube radius
 v : velocity of relatively sliding
 α : inclination angle of tilting cam
 λ : coulomb friction coefficient
 μ : viscosity of oil
 ξ : inclination angle of piston rod

INTRODUCTION

In order to save oil energy and protect the environment, it is needed to reconsider the use of the existing oil hydraulic system, which uses a petroleum fuel. As a result, a water system is aroused our interest again in power transmission, and recently various studies have been conducted on water hydraulic systems that use a water as a hydraulic fluid, since water has cleaner and more economic advantages, as well as excellent safety against fire, ease of access, convenient management, and easy recycling, than oil. [1]

The most basic component in an oil or water hydraulic system is a pump, which make and supply the power on system. And, almost pump in water hydraulic system is adopted the piston pump for more high pressure on the system, when compares to other types. The water hydraulic piston pump is almost the similar structure of oil hydraulic piston one. However, the water hydraulic piston pump requires special design concepts for each sub components due to the difference in physicochemical properties between oil and water. [2]

Also, these researches on water hydraulic components and systems are made actively in Kitakawa Lab. of Tokyo Institute of Technology, Ikeo Lab. of Sophia University, and Sanada Lab. of Yokohama University, etc. In addition, the Nessie Water Hydraulics of Danfoss in Denmark and the Ebara Research Institute in Japan are producing and selling water hydraulic systems as well as pumps/motors, actuators, and valves.

PISTON AND BIRFIELD JOINT

In conventional piston type pumps, the plunger type piston is mostly used. But high friction is occurred between plunger type piston and cylinder bore through relative sliding movements, as shown in Figure 1.

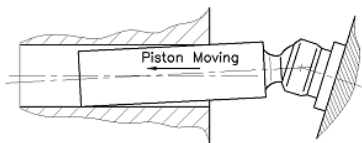


Figure 1 Tilted movement of the plunger type piston

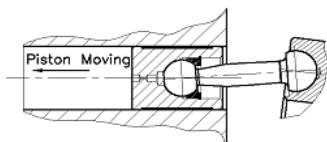


Figure 2 Parallel movement of the rod type piston

Because friction and wear results from the lateral force on the edge of both ends of a plunger type piston is

highly intensive, there is a need for another piston design that can reduce this lateral force.

In this paper, as a method to reduce the lateral force, rod type piston with a ball-socket joint of both spherical-surface ends, as shown in Figure 2, is applied. This will be make dispersion the concentrated load on the edges by offsetting the lateral force from the spherical joint, even though the piston is affected by the lateral force as it moves in the bore of the cylinder block.

However, the rod type piston requires an assisting mechanism for special operation. Generally, the plunger type piston is acted on the lateral force when the pump shaft rotates and the piston shoes slides on the swash plate, but the rod type piston is rotated and moved not by the lateral force but by the structural combination of the tilting cam and Birfield joint. Birfield joint is located between the pump shaft and the tilting cam, as shown in Figure 3, and supported to rotate with constant velocity.

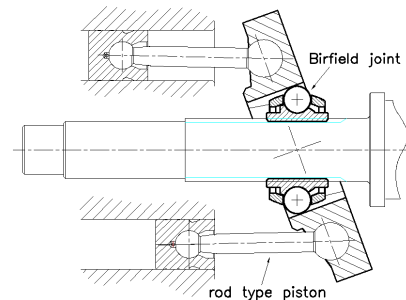


Figure 3 Birfield joint applied on a rod type piston and tilting cam

Besides, for smoother operation, the hydrostatic bearings are applied to the sliding components.

Figure 4 shows the rotary group of water hydraulic piston pump proposed in this study.

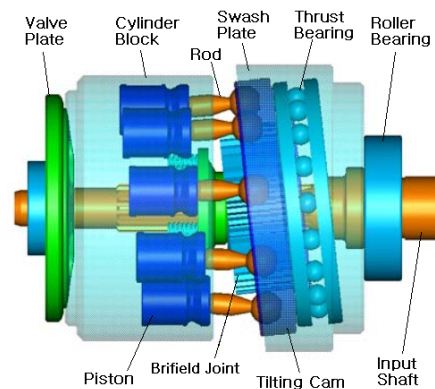


Figure 4 Water hydraulic piston pump consist of rod type piston and Birfield joint

FRICITION

Coulomb Friction of Plunger Pistons

In a plunger type piston pump, the power is transmitted through the side of the piston so that a strong lateral force is generated.

As shown in Figure 5, the lateral force takes or the strong concentrated force acts on each end of the piston, which is tilted to the side. The large concentrated force at the contact point makes coulomb friction and the viscous friction generated equally around the piston. The coulomb friction force is expressed the following Equation (1).

$$F_c = F_{c1} + F_{c2} = \lambda \cdot F_{L1} + \lambda \cdot F_{L2} \quad (1)$$

Here, λ represents the coulomb friction coefficient.

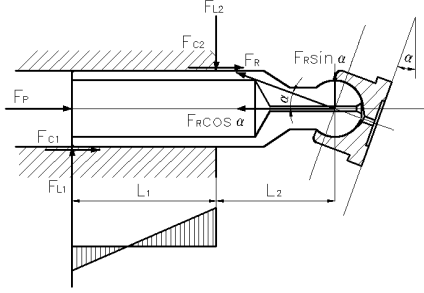


Figure 5 Inclined shape of the plunger piston in transferring the lateral force

In order to predict the effect of the coulomb friction, the equilibrium equation of the force can be used for the analysis.

From the equilibrium equation of the y-axis force and the moment for the zero point, it can be expressed as follows:

$$F_{L2} = F_{L1} + F_R \sin \alpha \quad (2)$$

$$F_R \sin \alpha \cdot L_2 - F_{c2} \frac{d}{2} - F_{L1} \cdot L_1 + F_{c1} \frac{d}{2} = 0 \quad (3)$$

The moment equilibrium equation in Equation (3) omitted the viscous friction because the viscous friction that works around the piston is proportionally distributed in the center point of the piston, zero.

If, F_R , which is the force applied to the piston shoe from the swash plate, is to be measured with the load cell, it is useful to express the coulomb friction F_{c1} , F_{c2} for F_R . If the coulomb friction is induced

using Equation (1), (2), and (3), it is as follows:

$$F_c = \lambda \left(1 + \frac{2L_2}{L_1} - \frac{d}{L_1} \lambda \right) F_R \sin \alpha \quad (4)$$

Equation (4) shows that the coulomb friction on the piston can be expressed with the proportion function of F_R , which is the force on the piston shoe from the tilting plate. In addition, the proportion coefficient is the value determined with the size and friction coefficients of the piston.

The coulomb friction force on the plunger piston is determined by the tilting angle of the swash plate, and the tilting angle usually ranges from 14 degrees to 18 degrees so it has a very large friction force.

In the motion equation for the piston movement direction (x-axis direction), if the inertia force and friction force of the piston are to be ignored, since they would be smaller than the force of the pressure, F_R , the force on the piston from the swash plate can be approximated as follow:

$$F_R \approx P_d \cdot \frac{\pi d^2}{4} \cdot \frac{1}{\cos \alpha} \quad (5)$$

When Equation (5) is substituted in Equation (4), it is as follows.

$$F_c \approx \lambda \left(1 + \frac{2L_2}{L_1} - \frac{d}{L_1} \lambda \right) P_d \frac{\pi d^2}{4} \tan \alpha \quad (6)$$

This shows that the coulomb friction force on the plunger type piston increases in proportion to the discharge pressure of the pump.

Coulomb Friction of a Birfield Joint and Rod type Piston

The configuration of a pump that applied a Birfield joint and rod type piston shown as Figure 4. Most of the torque is transmitted from the main shaft of the pump to the tilting cam through the Birfield Joint. As shown in Figure 6, out of the reacting force generated from the tilting cam; $F_R \sin(\alpha - \xi)$ which is generates torque, is transmitted through the Birfield Joint, so there is no lateral force at the sides of the piston.

The lateral force of the rod type piston, F_L , is affected by the tilting angle, ξ , of the piston rod. This can be expressed as Equation (7).

$$F_L = F_R \cos(\alpha - \xi) \sin \xi \quad (7)$$

Usually, the tilting angle, ξ , ranges from $\pm 1^\circ \sim \pm$

2° so the lateral force, F_L , is very small.

$$F_c = \lambda F_L = \lambda F_R \cos(\alpha - \xi) \sin \xi \quad (8)$$

When Equation (5) is substituted to Equation (8), it becomes Equation (9).

$$F_c \approx \lambda \cos(\alpha - \xi) \sin \xi \cdot P_d \cdot \frac{\pi d^2}{4 \cos \alpha} \quad (9)$$

The coulomb friction force of the rod type piston can be expressed with the proportion function of F_R , the force on the piston shoe from the tilting cam. The proportion function is very small due to the small effect of, and as a result, the coulomb friction is very small. Therefore, it can be determined that the rod type piston used in pump having the Birfield Joint has a smaller friction force than the force of the plunger piston, which is shown in Equation (6) and (9).[3],[4]

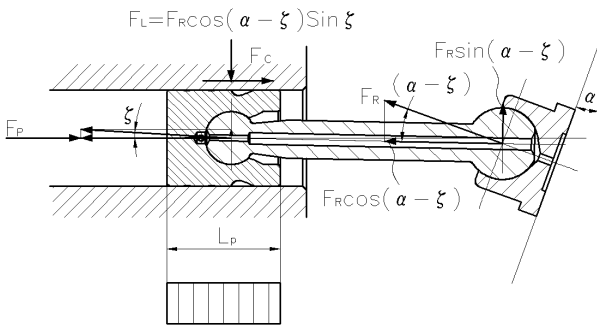


Figure 6 Force diagram of rod piston
Viscous Friction of Piston

Viscous Friction of piston

The friction force, F_f , in a normal hydraulic unit is combined from the coulomb friction force, F_c and viscous friction, F_v .

$$F_f = F_c + F_v \quad (10)$$

The viscous friction force generated from the united area between the cylinder bore and piston is as follows:

$$\tau = \mu \frac{\partial v}{\partial y} \quad (11)$$

Here, μ refers to the viscosity and $\frac{\partial v}{\partial y}$ represents the speed inclination. The viscous friction force, F_v , is expressed as follows.

$$F_v = \mu A \frac{v}{h} = \frac{\pi d L \mu}{h} \frac{dx}{dt} \quad (12)$$

Here, A refers to the contact area. The viscous friction force is irrelevant to the configuration of the piston. However, the rod type piston is very good for shortening the length of the contact point of the piston, $L = L_1$. When the length of the contact point of the piston is shortened, the contact area becomes smaller so that it receives a smaller viscous friction force than the plunger type piston.

LEAKAGE

As shown in Figure 7, the dynamic viscosity of water is 1/100 of that of petroleum oil (in a temperature of 20°C), so the leakage for the same clearance can be very different from that of oil.

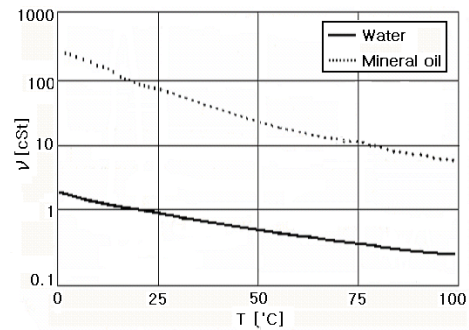


Figure 7 Kinematics viscosity of water and oil

The clearance between the piston and bore can be expressed as Figure 8. The leakage equation, which determines the leakage of this clearance, is expressed as follows: [5]

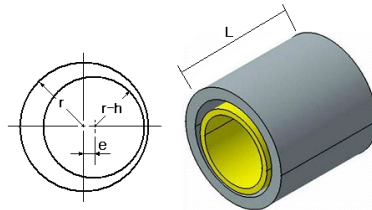


Figure 8 Clearance of piston and cylinder bore

$$Q = \frac{\pi r h^3}{6\mu L} \left[1 + \frac{3}{2} \left(\frac{e}{h} \right)^2 \right] (P_1 - P_2) \quad (13)$$

The biggest factors that determine the leakage flow rate, Q , are the contact length and the clearance. Therefore, when considering the viscosity of water, the clearance between the piston and the cylinder should have a very small value and the contact length should be increased in order to reduce the leakage.

However, an increase in contact length increases the viscous friction force, so it is difficult to have the right contact length. Therefore, a precise processing technique that minimizes the clearance of the contact point is required.

Equation (13) shows that the configuration of the piston is irrelevant to the leakage of the piston. However, the eccentricity (e) between the piston and the bore is affected by the configuration. As shown in Figure 5, the plunger piston has a maximum value for the eccentricity (e) when the inside of the bore is tilted. Therefore, the leakage flow rate will have a maximum value.

When the rod type piston and Birfield Joint are applied, the eccentric value (e) would be relatively small and so the leakage flow rate would also be small.

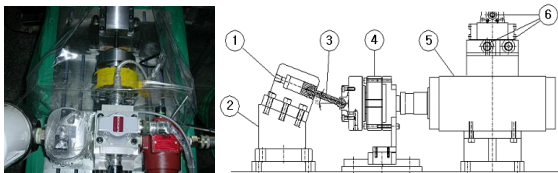
TEST

Test Equipment

As shown in Figure 9, 3 types of pistons were prepared for the test; plunger piston, rod piston, and PEEK plunger piston. In order to measure and compare the friction and leakage of these pistons, the test apparatus as Figure 10 was made.



Figure 9 Three types of pistons for test



- ① Connecting port of water hydraulic pump
- ② Cylinder block ③ Test piston ④ Load cell
- ⑤ Servo valve ⑥ Servo valve connector

Figure 10 Schematic diagram of test apparatus

Friction Test

The test was done with water pressure of 10 bar, 20bar, 30bar and 40 bar. In order to measure the friction, the sine wave signal was input to the servo valve to move the piston. As mentioned in previous, the shape of the piston (whether it is plunger type, rod type, and PEEK material) affects the Coulomb friction and is irrelevant to viscous friction. Therefore, the research mainly performed tests to measure the Coulomb friction and compared the results.

As shown in Equation (6) and (9), the Coulomb friction can be determined with the force from the tilting cam to the piston shoe, F_R . Therefore, F_R was measured using the load cell sensor.

The test was done on each piston in the same condition. The sizes of 3 types of pistons were all the same overhang length of piston. The cylinder bore and clearance sizes were all same.

Results of Friction Test

Figure 11 shows the signal graphs of load cell measured at the pressure of 30 bar. The signal of the plunger type piston changes greatly in proportion to the sine wave signal. The load cell signal is very high when the plunger piston enters the cylinder bore and it becomes low when the piston reverses from the cylinder bore. On the other hand, the rod type piston had lower load cell signal. There was hardly any difference in the signals of forward motion and reverse motion of the piston.

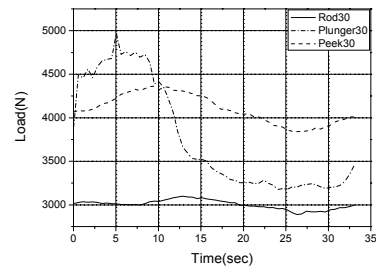


Figure 11 Load cell signals measured at the pressure of 30 bar

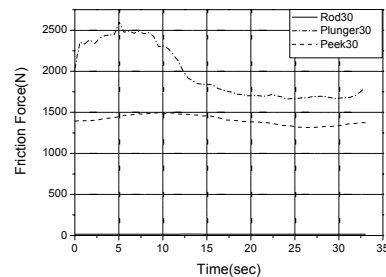


Figure 12 Coulomb friction for three types of piston at the pressure of 30 bar

CONCLUSION

Figure 12 shows the coulomb friction force for the three types of pistons. The friction of Figure 12 was calculated from the load cell signal of Figure 11.

Such test result matches the theoretical analysis. In other words, when the rod type piston is applied to the water hydraulic pump, the friction is very small and has excellent lubrication.

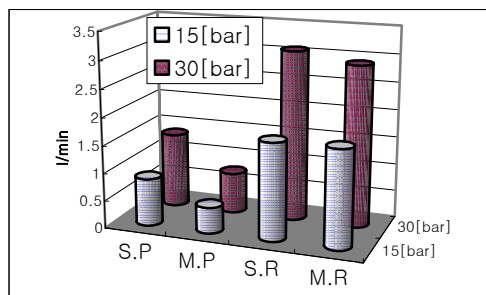
The friction for PEEK plunger type piston is smaller than friction for metal plunger piston, but it is much larger than the friction for rod type piston even though a new material, PEEK is applied as a material of plunger.

Leakage Test

The leakage test was done along with the friction test. The leakage test was done after 30-second initial operation and the system was settled to steady state. The leakage amount was measured using a stop-watch and electric weight scale. The test was done on each piston in the same condition. The sizes of 3 types of pistons were all the same overhang length of piston. The cylinder bore and clearance sizes were all same.

Results of Leakage Test

Leakage is not related to the material of pistons. The leakage test was done only on plunger type and rod type, and Figure 12 shows the leakage flow measured at the test.



S.P : Stopped Plunger, M.P : Moving Plunger
S.R : Stopped Rod, M.R : Moving Rod

Figure 12 Comparison of leakage flow

In 15 bar, the leakage flowrate of the rod piston doubled the leakage flowrate of the plunger piston when the piston is stopped. Even when the piston is operating, the leakage flowrate of the rod piston was four times greater than that of the plunger type. In 30 bar, the results were similar to the results in 15 bar condition.

The leakage of rod type piston was greater than the plunger type piston because the rod type piston was 1/2 the length of the plunger type piston and the resistance length for the leakage flow was shorter.

In other words, the length of the piston should be extended in order to reduce the friction and leakage flow with the rod type piston.

In the plunger type piston pump, the lateral forces on the edges of the plunger piston are the source of friction and wear, so a ball socket joint piston rod with spherical surface ends was proposed. When the rod type piston is applied, it is rotated and moved by the tilting cam, so a Birfield joint was applied to the space between the pump shaft and the tilting cam as a constant velocity joint.

The study examined friction in the piston and the cylinder for pumps with a plunger type piston and a rod type piston. As a result, the friction of the rod type piston was a lot smaller than the friction of the plunger type piston. The PEEK plunger piston has low friction compared to the metal plunger type piston but the friction is much larger than the friction of the rod type piston. The engineering plastic, PEEK, seems to be not so effective as the rod piston in reducing the friction of piston.

The leakage flowrate is irrelevant to the structure of the piston but it is determined by the contact or overlap length and clearance between cylinder bore and piston. In the test of the research, the rod type piston had twice larger leakage flowrate than the plunger and this is why the length of the rod type piston is 1/2 length of the plunger type. In order to reduce the leakage flowrate, the overlap length of the piston should be extended.

The study results show that the pump with the rod type piston and Birfield Joint is better than the conventional plunger type piston pump.

ACKNOWLEDGMENTS

The authors gratefully acknowledge financial support from the Korea Energy Management Corporation. (<http://racer.kemco.or.kr>)

REFERENCES

1. Karl-Erik Rydberg, "Energy Efficient Water Hydraulic Systems", ICFP, 2001.
2. Songlin Nie and Zhuangyun Li, "Design Techniques for Water Hydraulic Axial Piston Pumps(Motors)", NFPA, 2000, I00-16.5, pp 581-590.
3. R.A. Wehage, E.J. Haug, "Dynamic Analysis of Mechanical Systems with Coulomb Friction, Stiction, Impact and Constraint Addition-Deletion-I,II,III", Mechanisms and Machine Theory, 1986, Vol.21, No.5, pp.401-425.
4. Y. B. Ham, S. D. Kim, "A study on the application of tripod joints to transmit the driving torque of axial piston hydraulic motor", Proceedings of the 5th JFPS International Symposium on Fluid Power, NARA, November 14.2002, vol.2, pp 531-536.
5. Herbert E. Merritt, "Hydraulic control systems", John Wiley & Sons Inc, 1967, pp 9-13.

MECHATRONICS SYSTEM ENGINEERING FOR CAE/CAD, MOTION CONTROL AND DESIGN OF VANE ACTUATORS FOR WATER ROBOT APPLICATIONS

Finn CONRAD and Francesco ROLI

Department of Mechanical Engineering,
Technical University of Denmark
Building 404, Kgs. Lyngby, Denmark
E-mail: finn.conrad@mek.dtu.dk

ABSTRACT

The paper presents research results using IT-Tools for CAE/CAD and dynamic modelling, simulation, analysis, and design of a water hydraulic vane actuator for motion control of robot manipulator arm. Matlab/Simulink and CATIA are used as IT-Tools. The development and design a novel water hydraulic rotary vane actuator for robot manipulators is presented. The contribution proposes mathematical modelling, control and simulation of a novel water hydraulic rotary vane actuator applied to power and control a three-links manipulator. The results include engineering design and test of the proposed simulation models compared with IHA Tampere University's presentation of research measurements from a similar robot manipulator arm driven by tap water hydraulic components. Experimental and simulation results are compared for evaluation and verification of developed mathematical models of the motion control of the manipulator. Furthermore, presents performance results of to follow trajectories of path motion control.

KEY WORDS

Water hydraulics, Vane Actuator, Motion Control, Robot Manipulator

NOMENCLATURE

b_c	Coulomb friction coefficient	$[\text{m}^3/(\text{s Pa})]$	Q_A	Flow rate - chamber A	$[\text{m}^3/\text{s}]$
b_s	Static friction coefficient	$[\text{m}^3/(\text{s Pa})]$	Q_B	Flow rate - chamber B	$[\text{m}^3/\text{s}]$
b_v	Viscous friction coefficient	$[\text{Nm s/rad}]$	T_{ACT}	Torque – Vane actuator	$[\text{Nm}]$
K	Turbulent flow coefficient	$[\text{m}^3/(\text{s Pa}^{1/2})]$	θ_i	Angle position $i=1,2,3 \dots$	$[\text{rad}]$
ΔP	Pressure load	$[\text{Pa}]$	ω_i	Angle velocity	$[\text{rad/s}]$
P_A	Pressure in chamber A	$[\text{Pa}]$	ε	Parameter	$[\text{rad/s}]$
P_B	Pressure in chamber B	$[\text{Pa}]$	x_v	Servo valve spool position	$[\text{m}]$
P_s	Supply Pressure	$[\text{Pa}]$	T	Torque disturbance	$[\text{Nm}]$
P_{tr}	Transition pressure	$[\text{Pa}]$	D	Inertia - acceleration matrix	$[\text{N m s}^2/\text{rad}]$
Q	Valve orifice flow rate	$[\text{m}^3/\text{s}]$	h	Coriolis - centrifugal vector	$[\text{N m s/rad}]$
			c	Gravity vector	$[\text{N m /rad}]$
			b	Viscous friction vector	$[\text{N m s/rad}]$

INTRODUCTION

Three rotary vane actuators drive the robot manipulator studied in this paper. Water as pressure medium is chosen to drive the actuator. Water is a non-contaminant, fireproof, radiation proof and readily available. Many industrial applications as food processing, steel, mining, pharmaceutical and nuclear industry, require particular cautions that water hydraulics can provide [1]. On the other hand, water has low viscosity relative to mineral oil, and can in general only be recommended applied for supply pressure up to 160 bars. The limited motion range of hydraulic cylinders, confine their use in manipulators with few degrees of freedom. A water hydraulic rotary vane actuator may satisfy most of the requirements necessary to drive a dexterous manipulator and a specific water version could partially solve the problem of high leakage flow. The developed slave robot arm results in a multiply-purpose device suitable for an environmental friendly approach to the industrial processing.

DESCRIPTION OF THE MANIPULATOR

The novel developed robot manipulator with three joints, each driven by a water hydraulic rotary vane actuator, has three links and is able to sustain a maximum load of 85 Kg with 1.9 m of extension, shown in Figure 1, Figure 2, Figure 3 and Figure 4. For a dexterous use, a load of 50 Kg has not to be exceeded. The slave arm weighs around 90 Kg and the actuators generate 2156 Nm, 1056 Nm and 448 Nm, respectively. The robot arms have servovalves to flow rate control. This solution allows the use of rigid connection between the valves and the actuator.

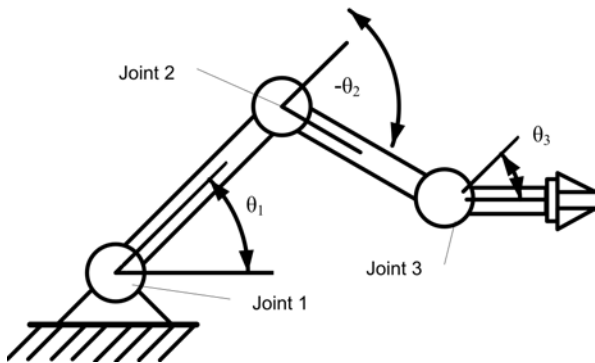


Figure 1 Schematic of the 3 DOF robot manipulator

Approach to the water hydraulic vane actuator

To simplify the model of the water hydraulic vane actuator the pump supply pressure is assumed to be constant at 140 bar to a four-way servovalve to control the flow rate to the vane actuator. A closed loop control system with position feedback is chosen to control the vane actuator movement. Since water hydraulics

components need small clearances, they are more expensive compared to the oil hydraulics mechanism. The servovalve is a Ultra Premier Range 4658 Series with the 9.6 l/min rated flow and a natural frequency of 22 Hz at 70 bar. The small natural frequency of the valve combined with position feedback control system to drive the arm's accuracy.

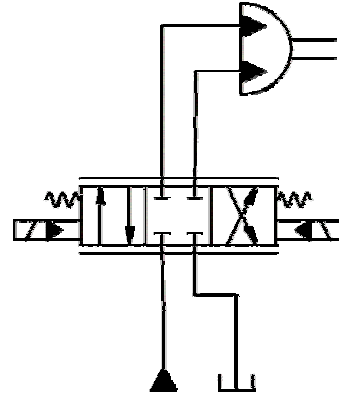


Figure 2 A water hydraulic vane actuator

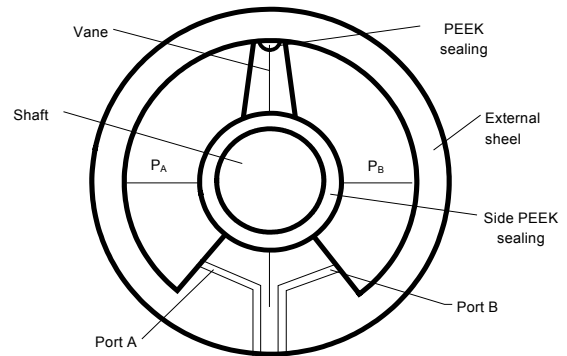


Figure 3 Schematic of the water hydraulic vane actuator

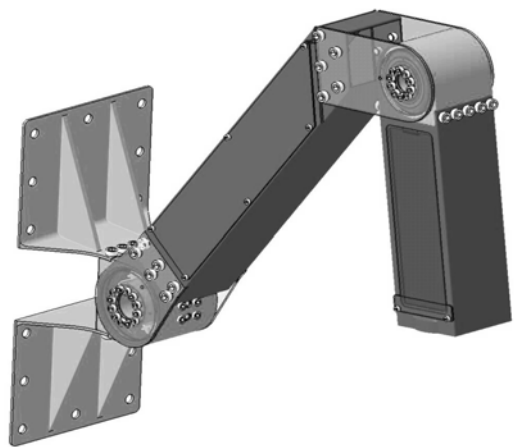


Figure 4 CATIA model of the arm 1 and arm 2 of the 3 DOF robot manipulator

SIMULATION MODEL

To simulate the performance of the slave robot arm a non-linear model was developed by modelling the different components of the water hydraulic rotary actuator system and robot manipulator arm.

The servovalve dynamics, from the input signal to the spool displacement is approximated with a second order transfer function figured out from the servovalve's flow gain and Bode plots from the datasheet.

The flow through the orifices is calculated switching from the laminar to the turbulent equation when the pressure difference became higher than the transition pressure P_{tr} . A second order interpolation, was developed by using the Lagrange method to keep the continuity of the first derivate in the transition point

$$Q = \frac{K(\Delta P - 3P_{tr})}{2P_{tr}^{3/2}} \quad (1)$$

The effects of friction could be modelled as a generalized force applied on the joint of the arm. Friction is a complex non-linear force that is difficult to model accurately, yet in many cases it can have a significant effect on the robot dynamics. A model that includes the viscous, the static and the Coulomb friction from components as proposed by [3]. Comparison between the complete and simplified viscous friction model is shown in Figure 5, and modelled by the following equation (2)

$$b = b_v \cdot \dot{\theta} + \text{sign}(\dot{\theta}) \cdot \left[b_c + (b_s - b_c) \cdot e^{-\frac{|\dot{\theta}|}{\varepsilon}} \right] \quad (2)$$

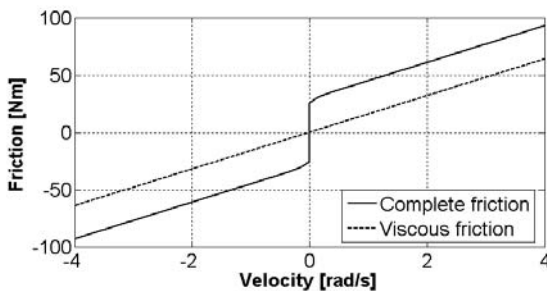


Figure 5 Comparison between the complete and simplified viscous friction model

In the following simulations, the friction model was reduced to only viscous term due to assuming a good engineering design to avoid Coulomb friction and sticktion. To test the water hydraulic rotary vane actuator a non-linear model developed was used to evaluate the performance. Test simulation results were

obtained by using the developed non-linear model shown as an overview diagram of the Simulink model in Figure 6.

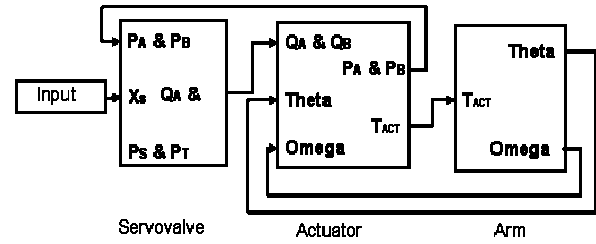


Figure 6 The non-linear model for test simulation

The general motion equations of the manipulator can conveniently be expressed through the direct application of the Lagrange-Euler formulation to non-conservative system. The approach for modelling of the considered test robot manipulator applying the robot model notation by Schilling, 1990, [3]

$$T = D(\theta)\ddot{\theta} + h(\theta, \dot{\theta}) + c(\theta) + b(\dot{\theta}) \quad (10)$$

Model Evaluation and Verification

To validate the developed models of the proposed water hydraulic vane actuator we did compare with experimental results by Rameda, IHA, Tampere University of Technology 2004, [4] of a similar vane actuator designed to work with oil and tested with tap water as fluid. The non-linear models are evaluated and verified against open-loop response of the valve-controlled rotary vane actuator.

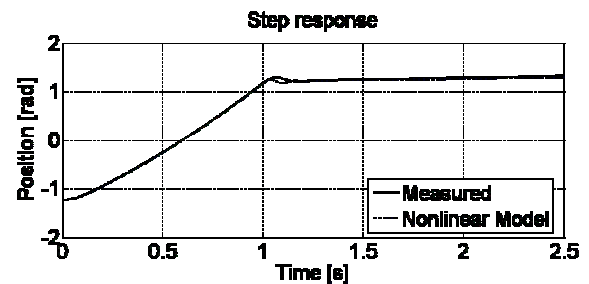


Figure 7 Open loop position response, simulated and experimental results.

The actuator is in vertical position (no gravity load in the zero position) with an inertial load of 31.2 Kg m^2 and weights attached at the end of the boom. The input signal to the servovalve was a step input (the valve was kept open for 1 second) to show the step response in Figure 7. The conclusion was that non-linear model could be used in this analysis because the simulation fit very well to the measured response. Furthermore, validation of the model and verification of the model was needed.

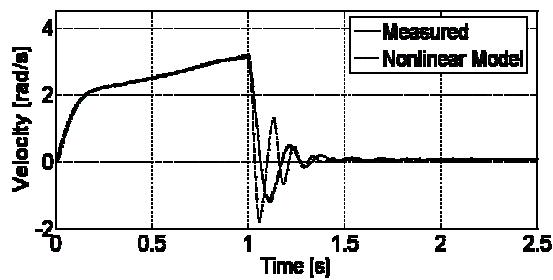


Figure 8 Open loop velocity response, simulated and experimental results

As shown in Figure 7 and Figure 8, during the valve opening, the non-linear model provides, with good accuracy, both the position and the velocity of the measured performance. However, there are errors of damping during the valve closing, probably due to the simplified friction model. In fact the friction force is the first cause of the damping and the operated model is mostly underrate at low velocity.

These errors are probably due to the simplified friction model, in fact, the friction force is the first cause of the damping and in our model is mostly underrate at low velocity. Since we did check the system stability by applying this model because it has a lower value of the damping rate compared to the measured velocity response (Figure 8) for the implemented robot manipulator arm by IHA, Tampere University of Technology [2].

THE NOVEL VANE ACTUATOR

A Mechatronic System Engineering approach was applied to develop and design the three links water hydraulic robot driven by rotary water hydraulic actuators.

The Figure 9 as illustrated the proposed IT-Tool controller design concept that integrates the development and design phases into a single design platform. It uses the Matlab Real-Time Workshop to generate C-code automatically from a Simulink block diagram, and then compile it, and download it to the real-time hardware. It can perform all steps of the control design process in one development environment. In a dSPACE system, input/output (I/O) can easily be specified and connected within the Simulink environment.

A view of the 3D CAD model of the proposed novel water hydraulic vane actuator is shown in Figure 10. The main materials used are stainless steel and PEEK. The fundamental components of the actuator are: the housing, the vane and the shaft. The rotor vane is fixed on the shaft and slides on the internal face of the

housing. To perform the sealing system the vane is composed of two pieces coupled together by bolts. This solution allows inserting different layer of sealing material for the two parts of the vane. The housing is made of three parts; a cylinder for the rotary vane, and two-side cover entrusted to close the pressure chambers and sustain the shaft. To secure the sealing between the vane and the side cover, two rings are applied with a rounded shape, to avoid corners in the contact surface.

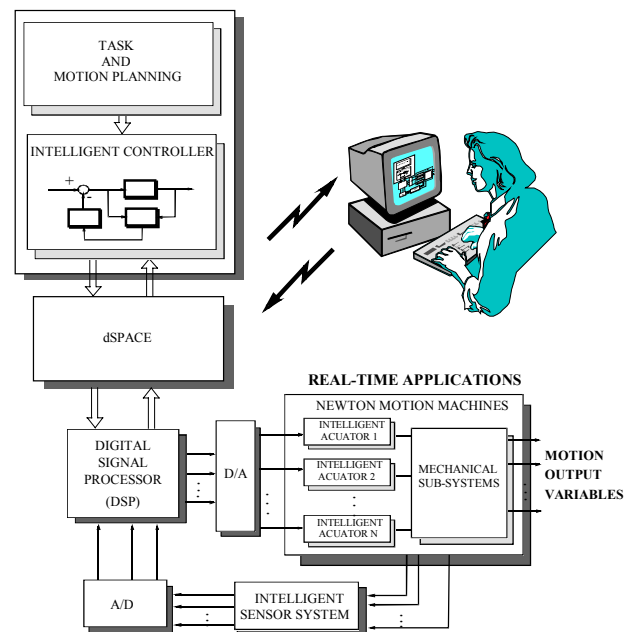


Figure 9 IT-Tools controller design concept

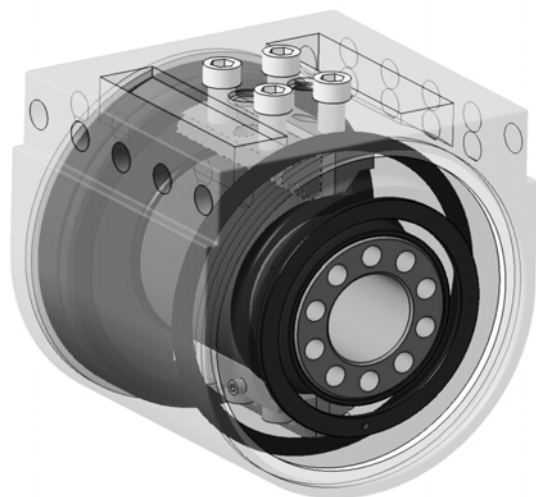


Figure 10 Shows a 3D CAD model of the novel water hydraulic vane actuator

The rings are fixed on the grooves machined in the shaft and in the housing. To sustain the shaft thrust bearings are used and fixed by pins and sleeve bearings forced on the lateral covers. Holes are machined in the housing, to perform the coupling of the arm and the stator vane. The side covers are ensured on the housing by spiral retaining ring, which thwart the pressure. Two flats coupled to the shaft close the actuator and the connection to the second robot arm.

The shaft is axial fixed by the contact between the flanges and the thrust bearing on the side covers. A second sealing system may be operating to isolate the external behaviour and assure that the entire leakage flows through the drain line.

TEST OF THE ROBOT MANIPULATOR ARM

To simulate the behaviour of the tool point centre (TPC) of the slave manipulator arm in a typical motion control application, the slave arm was tested by defining the following complete test path trajectory build up by geometric elements as part of circles, strait lines, corner and ramp as reference input to the robot controller.

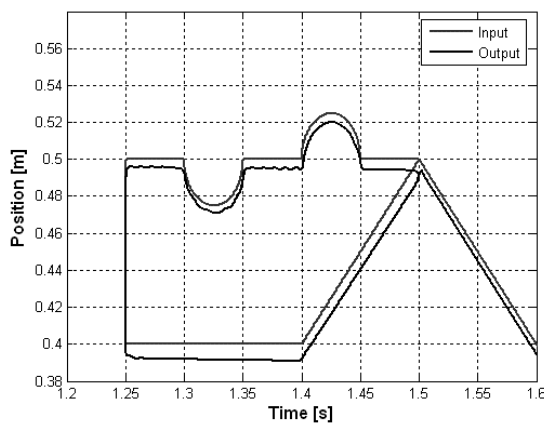


Figure 11 Tool point centre trajectory following a complete reference input path shape

Simulation result for motion control of the robot manipulator arm's TPC trajectory following a complete path trajectory is shown in Figure 12.

Position error following a complete shape is shown in Figure 12. The obtained results shows that even with a simple control system for the proposed novel water hydraulic vane rotary actuator with servovalve, the manipulator perform acceptable accuracy for many applications as long as the required maximum velocity fit to the load and robot manipulator arm design, and is limited.

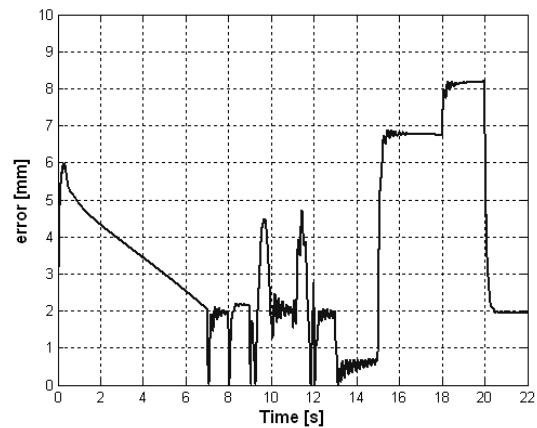


Figure 12 Position error following a complete shape

CONCLUSION AND OUTLOOK

The contributions presents research results using IT-Tools for CAD and dynamic modelling, simulation, analysis and design of water hydraulic actuators for motion control of machines, lifts, cranes and robots. Matlab/Simulink and CATIA were used as IT-Tools for the development and design a novel water hydraulic rotary vane actuator for robot manipulators. Furthermore, presents proposed mathematical modelling, control and simulation of water hydraulic rotary vane actuator applied to power and control a three links manipulator and evaluate the performance. The obtained results shows that even with a simple control system as a position feedback and an internal velocity feedback, the robot manipulator performance a good accuracy following trajectory at slow speed. In general, the simulated response with the linear model agrees well with the non linear model and with the presented measured response, and therefore the linear model can be used to simplify the controller design.

The applied mass located at the TPC of the robot arm decrease the hydraulic frequency benefits the system stability. On the other hand, the position error is approximately proportional to the external load. The control gains cannot be optimized for all the load range and therefore a compromise have to be made. All the control parameters have to be optimized.

The non-linear model can be used for prototype design instead the experimental design, at least for primary set up and provide good possibility to improve the control system. The water hydraulic rotary vane actuators have been developed to be driven by an robot controller, and has been designed to be improved for a 6 DOF water hydraulic robot manipulator arm research and application.

REFERENCES

1. F. Conrad, B. Hilbretch and H. Jepsen, Design of Low-Pressure and High-Pressure Tap Water Hydraulic Systems for Various Industrial Applications, SAE Transaction, USA, 2000.
2. H. Merrit, Hydraulic Control Systems, John Wiley & Sons Inc., New York, USA, 1967.
3. R. J. Shilling, Fundamentals of Robotics Analysis and Control, Prentice Hall, New Jersey, USA, 1990.
4. A. Raneda, Impedance Control of a Water Hydraulic Manipulator for Teleoperation Applications, Doctoral Thesis, IHA, Tampere University of Technology , Finland, 2004.
5. R. C. Dorf, R. H. Bishop, Modern Control Systems, Prentice Hall International, USA, 2005.

NUMERICAL SIMULATION OF A SLIPPER MODEL FOR WATER HYDRAULIC PUMPS/MOTORS IN MIXED LUBRICATION

Toshiharu KAZAMA

Department of Mechanical Systems Engineering
Muroran Institute of Technology
27-1, Mizumoto-cho, Muroran, 050-8585, Japan
(E-mail: kazama@mmm.muroran-it.ac.jp)

ABSTRACT

This paper presents a time-dependent mathematical model of a hybrid (hydrostatic/hydrodynamic) thrust pad bearing as a slipper of swash-plate type axial piston pumps and motors for the use of tap water under mixed and fluid film lubrication condition. Effects are examined of the load eccentricity, time-lag of changes in the supply pressure and load, surface roughness, recess volume, and the revolution radius. The bearing's motion is simulated three-dimensionally, including roughness interaction and asperity contact. Solutions are obtained regarding the friction, flow rate, power loss, and stiffness. Calculations indicate that the eccentric load causes local contacts. The preceding change in the load poses a larger motion of the bearing. The hydrodynamic effect becomes marked as the revolution radius increases. As the recess volume increases, the bearing stiffness decreases.

KEYWORDS

Water-hydraulics, Tribology, Hybrid/Hydrostatic bearings, Mixed lubrication, Piston pumps/motors

NOMENCLATURE

a	: Ratio of recess radius = R_1/R_2	\bar{r}_w	: Eccentric ratio of load = r_w/R_2
H	: Reference clearance	S_0	: Parameter = $\hat{S}_0 (R_2/H)^2 = 6\mu\omega(R_2/H)^2/p_{s0}$
h	: Clearance = h/H	\bar{T}	: Friction torque = $T/(p_{s0}R_2^3S_0)$
h_{0s}	: Pad center clearance = h_0/σ	\bar{V}_r	: Recess volume = $\hat{V}_r (R_2/H)^2 = 6\mu\omega V_r/(H^2KR_2)$
\bar{I}	: Moment of inertia = $\hat{I} (H/R_2)^3 = \omega H^3 I/(6\mu R_2^6)$	\bar{W}	: Load = $W/(p_{s0}R_2^2S_0)$
K	: Bulk modulus of lubricant	X, Y, Z	: Coordinates
\bar{L}	: Power loss = $L/(\omega p_{s0}R_2^3S_0)$	x, y, z	: Coordinates
\bar{M}	: Moment-load = $M/(p_{s0}R_1^3S_0)$	$\bar{\alpha}$: Inclination of pad = $\alpha R_2/H$
\bar{p}	: Pressure = $p/(p_{s0}S_0)$	β	: Parameter of restrictor = $\hat{\beta} (H/R_2)^3 = 4H^3 l_c/(3r_c^4)$
\bar{p}_r	: Recess pressure = $p_r/(p_{s0}S_0)$	$\Delta\tau$: Time lag of load = $\Omega\Delta t$
\bar{p}_s	: Supply pressure = $p_s/(p_{s0}S_0)$	ζ_0	: Parameter = $2W_0 \log a / [(1-a^2)p_{s0}R_2^2]$
\bar{Q}	: Flow rate = $Q/(\omega R_2^3)$	μ	: Viscosity
\bar{R}_0	: Radius of revolution = R_0/R_2	σ	: Surface roughness = $(\sigma_1^2 + \sigma_2^2)^{1/2}$
R_2	: Outer radius of bearing	τ	: Time = Ωt
\bar{r}, θ, \bar{z}	: Coordinates = $r/R_2, \theta, z/H$	$\bar{\Phi}_{x,y}$: Angle = $\Phi_{x,y}R/H$
		φ	: Azimuth of pad
		Ω	: Reference angular velocity

Ω' : Angular velocity of sliding plane
 ω : Angular velocity of pad

Subscripts:

a : Asperity
 f : Fluid
 m : Mean value
 x, y, z : x, y, z axes, respectively
 0 : Reference (High-pressure period)

INTRODUCTION

As a power transfer medium of hydraulic systems, nothing in nature is more human compatible and environmentally compatible than tap water: it is non-toxic, non-flammable, clean, easily disposable and readily available. In recent years, economic and environmental forces have helped water to regain its prominence as a hydraulic fluid [1][2].

Nevertheless, disadvantages and challenges of tap-water hydraulic systems remain: leakage resulting from water's low viscosity, erosion because of water's higher vapor pressure, and corrosion because of water's chemical reaction, in addition to bacterial growth and limited operating temperatures. In particular, lower viscosity and a lower viscosity-pressure index engender inferior lubrication.

As with oil-hydraulic pumps and motors, tap-water hydraulic pumps and motors are expected to function suitably in widely variant operating conditions. The efficiency and durability of the equipment are conspicuously influenced by tribological characteristics of the bearing and seal parts.

Swash-plate type axial piston pumps and motors take advantage of high power density based on high pressure and compactness, and high efficiency of variable displacement machinery. Main bearings and seal parts of the pumps and motors form a slipper, which functions as a hydrostatic bearing [3]. It is suitable for lubrication with low viscous fluids. Shute and Turnbull undertook a pioneering study [4]; later, Iboshi and Yamaguchi [3] as well as Hooke, et al. [5–6] contributed to study in this area by investigating characteristics of slippers and by discussing effects of operating conditions and geometry. Typical hydrostatic bearings are usually designed and used under the full film lubricating condition [7–8]. However, hydraulic pumps and motors strongly demand less leakage and compactness, which enforces smaller clearance of the same order as the roughness height. The bearings of real-life pumps and motors are thus required to operate in a mixed lubrication regime.

Yamaguchi and Matsuoka developed a mixed lubrication model that is applicable to bearing and seal parts of hydraulic equipment [9]. This model is based on a combination of the asperity-contacting model proposed by Greenwood and Williamson (GW model) [10] and the average flow model by Patir and Cheng (PC model) [11–12]. The former is a model for a contact mechanism of non-lubricated stationary rough surfaces. The latter is an approach using fluid film lubrication to the contact

phenomena of surface asperities. They fill the gap separating these two extreme models. Moreover, they include effects of adsorption of lubricants, elastohydrodynamic lubrication (EHL) and cavitation around asperities. Comparison of numerical results using the model and many experimental data for thrust washers and hydrostatic bearings [13–14] shows good agreement. Subsequently, Yamaguchi, et al. [15] expanded the model to include plastic-to-metal contact under water lubricated conditions, whereas the primary model specifically describes metal-to-metal contact under oil lubricated conditions.

In this study, the author applies the mixed lubrication model [9] to unsteady analysis [16] of a water-lubricated hybrid/hydrostatic thrust pad bearing, which is a model of a slipper of swash-plate type axial piston pumps and motors. Three-dimensional motion of the bearing is simulated and the tribological characteristics are discussed. Effects of interference in roughness asperities, contact between the surfaces and the time lag of the dynamic load are examined.

THEORY

Theoretical model

A hybrid thrust bearing that functions as hydrostatic and hydrodynamic bearings, lubricated with tap water, is shown in Fig. 1. Surface roughness, asperity contact, eccentric loads, and changes in the supply pressure and the load are considered. Heat generation resulting in a change in the physical properties of the lubricant and thermal distortion as well as elastic deformation of the bearing parts are neglected.

The load acting on the bearing and seal parts of hydraulic pumps and motors fundamentally changes cyclically and synchronously with the supply pressure. However, the load change can be slightly preceded or delayed because of factors such as friction and inertia of the parts in the equipment. Thus, the supply pressure p_s and the load W (<0) with a time lag $\Delta\tau$ between p_s and W are given as those in Fig. 2. Let $\Delta\tau$ be a negative value when the change in W is preceded by p_s . Revolution of the sliding plane with angular velocity Ω' as well as rotation with the angular velocity ω and reciprocation of the pad are included in the non-steady mixed lubrication modeling. The condition corresponds to a slipper of swash-plate type axial piston pumps and motors with slight inclination of the swash-plate, where the influences of pistons and ball joints are omitted.

Derivation of basic equations

The load-carrying capacity of asperities in contact is estimated by their capacities because of elastic and plastic contact. The asperity-contact pressure \bar{p}_a averaged over a small apparent area, is [9, 10, 13]:

$$\left. \begin{aligned} \bar{p}_{ae} &= (2/3)\bar{E}'(\eta\beta'\sigma^*)(\sigma^*/\beta')^{1/2} \\ &\quad \times [F_{3/2}(d_e^*) - F_{3/2}(d_e^* + w_p^*)] \\ \bar{p}_{ap} &= \pi\bar{H}_a(\eta\beta'\sigma^*)F_1(d_e^* + w_p^*) \end{aligned} \right\} \quad (1)$$

Therein, d_e^* is the separation, $\bar{E}' (=E'/(p_{s0}S_0))$ is the equivalent modulus of elasticity, $\bar{H}_a (=H_a/(p_{s0}S_0))$ is the hardness of the softer material, $w_p^*=(\beta'/\sigma^*)(2h_a/E')^2$, β' is the radius of asperity, η is the density of asperity and $\sigma^* (=0.7\sigma)$ is the standard deviation of the asperity-summit height. Subscripts e and p respectively represent the elastic and plastic deformation of asperities. In addition, the function F_m is expressed as the following.

$$F_m(h_s) = \int_{h_s}^{\infty} (s - h_s)^m \psi(s) ds \quad (2)$$

Therein, $\psi(s)$ is the standard probability density function, $=(2\pi)^{-1/2} \exp(-s^2/2)$. The standard plane of rough surfaces is either the summit mean plane or the surface mean plane. The former is used in the GW model and the latter in the PC model. The relation of $d_e^*=h_s$ ($h_s \geq 1.8$) and $d_e^*=1.5h_s-0.9$ ($h_s < 1.8$) holds for these mean planes [17]. Following the PC model [11–12], the average Reynolds equation is described as the following.

$$\begin{aligned} & \frac{1}{\bar{r}} \frac{\partial}{\partial \bar{r}} \left(\phi \bar{h}^3 \bar{r} \frac{\partial \bar{p}_f}{\partial \bar{r}} \right) + \frac{1}{\bar{r}^2} \frac{\partial}{\partial \theta} \left(\phi \bar{h}^3 \frac{\partial \bar{p}_f}{\partial \theta} \right) \\ &= \frac{\Omega'}{\omega} \bar{R}_0 \sin \theta \left(\frac{\partial \bar{h}_T}{\partial \bar{r}} + \frac{\sigma}{H} \frac{\partial \phi_s}{\partial \bar{r}} \right) + \left(\frac{\Omega'}{\omega} + 1 \right) \frac{\partial \bar{h}_T}{\partial \theta} \\ &+ \frac{\Omega'}{\omega} \frac{\bar{R}_0}{\bar{r}} \cos \theta \left(\frac{\partial \bar{h}_T}{\partial \theta} + \frac{\sigma}{H} \frac{\partial \phi_s}{\partial \theta} \right) + \left(\frac{\Omega'}{\omega} - 1 \right) \frac{\sigma}{H} \frac{\partial \phi_s}{\partial \theta} + 2 \frac{\Omega}{\omega} \frac{\partial \bar{h}_T}{\partial \tau} \end{aligned} \quad (3)$$

Therein, ϕ and ϕ_s are the factors of surface roughness [11–12]. The boundary conditions of the fluid pressure are determined by: $\bar{p}_f(a, \theta, \tau) = \bar{p}_r(\tau)$ and $\bar{p}_f(1, \theta, \tau) = \bar{p}_e$ (atmospheric pressure). Cavitation conditions are selected such that the negative values are replaced by zero during the calculation when $\bar{p}_f < 0$. Mean clearance \bar{h}_T^* is shown as the following [13].

$$\begin{aligned} \bar{h}_T^* &= \bar{h} + \frac{\sigma}{H} \int_{h_s}^{\infty} (s - h_s) \psi(s) ds \\ &= \bar{h}_0 + \bar{\alpha} \bar{r} \cos(\varphi - \theta) + (\sigma/H) F_1(h_s) \end{aligned} \quad (4)$$

The moment-load-carrying capacities \bar{M}_x and \bar{M}_y with regard to the x and y axes and the load-carrying capacity \bar{W} , because of contacting asperity and fluid, are computed respectively using the following integrals.

$$\bar{M}_{ax,fx} = \int_0^{2\pi} \int_a^1 \bar{p}_{a,f} \bar{r}^2 \sin \theta d\bar{r} d\theta \quad (5)$$

$$\bar{M}_{ay,fy} = - \int_0^{2\pi} \int_a^1 \bar{p}_{a,f} \bar{r}^2 \cos \theta d\bar{r} d\theta \quad (6)$$

$$\bar{W}_{a,f} = \int_0^{2\pi} \int_0^1 \bar{p}_{a,f} \bar{r} d\bar{r} d\theta \quad (7)$$

The integrals of the capacities are calculated numerically with the cavitation conditions ($\bar{p}_a=0$ and $\bar{p}_f = \bar{p}_r$ in the region of $\bar{r} < a$).

Considering the fluid compressibility and displacement

volume in the recess, the recess pressure \bar{p}_r satisfies the following relation.

$$\bar{V}_r \frac{\Omega}{\omega} \frac{d\bar{p}_r}{d\tau} = \bar{Q}_r - \bar{Q}(a) - \pi a^2 \frac{\Omega H}{\omega R_2} \frac{dh_0}{d\tau} \quad (8)$$

Therein, \bar{Q}_r and $\bar{Q}(\bar{r})$ ($a \leq \bar{r} \leq 1$) are the flow rates through the capillary restrictor and the bearing-land, given respectively as the following.

$$\bar{Q}_r = \pi(H/R_2)(\bar{p}_s - \bar{p}_r)/\beta \quad (9)$$

$$\bar{Q}(\bar{r}) = \frac{H}{R_2} \frac{\bar{r}}{2} \int_0^{2\pi} \left[\begin{aligned} & -\phi \bar{h}^3 \frac{\partial \bar{p}_f}{\partial \bar{r}} \\ & + \frac{\Omega'}{\omega} \frac{\bar{R}_0}{\bar{r}} \sin \theta \left(\bar{h}_T^* + \frac{\sigma}{H} \phi_s \right) \end{aligned} \right] d\theta \quad (10)$$

The equations describing the bearing-pad motion are thus written as the following.

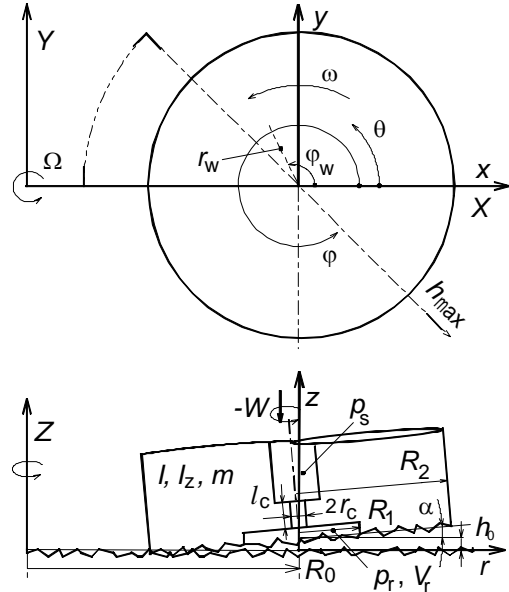


Fig. 1 Schematic diagrams and coordinates of the slipper model (hybrid thrust pad bearings)

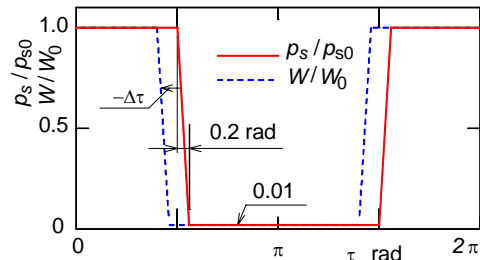


Fig. 2 Changes in supply pressure p_s and load W with a time lag $\Delta\tau$

$$\bar{m} \frac{d^2 \bar{h}_0}{d\tau^2} = \bar{W}_a + \bar{W}_f + \bar{W} - \bar{g} \bar{m} \quad (11)$$

$$\bar{I}_x \frac{d^2 \bar{\Phi}_x}{d\tau^2} - \bar{I}_z \frac{\omega}{\Omega} \frac{d\bar{\Phi}_y}{d\tau} = -\bar{M}_{ax} - \bar{M}_{fx} - \bar{M}_x \quad (12)$$

$$\bar{I}_y \frac{d^2 \bar{\Phi}_y}{d\tau^2} + \bar{I}_z \frac{\omega}{\Omega} \frac{d\bar{\Phi}_x}{d\tau} = \bar{M}_{ay} + \bar{M}_{fy} + \bar{M}_y \quad (13)$$

In those equations, $\bar{g} = g/(\Omega^2 H)$, \bar{I}_x , \bar{I}_y and \bar{I}_z represent the respective moment of inertia for the x , y and z axes, $\bar{\Phi}_x = -\bar{\alpha} \sin \varphi$ and $\bar{\Phi}_y = -\bar{\alpha} \cos \varphi$. Furthermore, the friction torque \bar{T}_a , because of the asperities in contact, and the torque \bar{T}_f , because of fluid acting on the sliding surface, are formulated as below.

$$\bar{T}_f = \frac{H}{6R_2} \int_0^{2\pi} \int_a^1 \left\{ \frac{\bar{r}^3}{h} \left[1 - \frac{\Omega'}{\omega} \left(\frac{\bar{R}_0}{\bar{r}} \cos \theta + 1 \right) \right] \left[\phi_f + \left(1 - 2 \frac{\sigma_1^2}{\sigma^2} \right) \phi_{fs} \right] - 3\phi_{fp} \bar{h} \bar{r} \frac{\partial \bar{p}_f}{\partial \theta} \right\} d\bar{r} d\theta \quad (14)$$

$$\bar{T}_a = \iint_{A_0} \bar{r} \left[\xi \bar{\tau}_p \left(\frac{\bar{\tau}_e}{\bar{\tau}_p} d\bar{A}_e + d\bar{A}_p \right) + (1 - \xi) \bar{\tau}_{ad} d\bar{A}_r \right] \quad (15)$$

Therein, $\bar{A}_0 (=A_0/R_2^2)$ is the land area, \bar{A}_r is the real contacting area, $d\bar{A} (=r d\bar{r} d\theta)$ is the apparent area, ξ is the parameter regarding an area-ratio of solid-contact asperities [9], $\bar{\tau} (= \tau/[6\mu\omega(R_2/H)^2])$ is the shearing strength, $\bar{\tau}_{ad}$ is shearing strength of the adsorbed film, and both ϕ_f and ϕ_{fs} are factors of roughness [11–12].

Defining the mean power loss \bar{L}_m during a single cyclic period by summing and averaging the power losses because of leakage flow rate \bar{L}_{Qm} and friction torque \bar{L}_{Tm} yields the following relationship.

$$\bar{L}_m = \frac{1}{2\pi} \int_0^{2\pi} [\bar{p}_s \bar{Q}_{out} + \bar{T}_a + \bar{T}_f] d\tau = \bar{L}_{Qm} + \bar{L}_{Tm} \quad (16)$$

The reference operating condition is representable as the ratio ζ_0 of the hydrostatic balance in the high-pressure period in a steady state defined by the following.

$$\zeta_0 = 2W_0 \log a / [\pi(1-a^2)p_{s0}R_2^2] \quad (17)$$

Therein, W_0 is the load (<0). The dynamic stiffness and moment-stiffness are defined as below.

$$\lambda = |\bar{W}_{\max} - \bar{W}_{\min}| / |\bar{h}_{0\max} - \bar{h}_{0\min}| \quad (18)$$

$$\lambda_M = |\bar{M}_{\max} - \bar{M}_{\min}| / |\bar{\alpha}_{\max} - \bar{\alpha}_{\min}| \quad (19)$$

Numerical technique

The Runge-Kutta method is used in solving the set of equations described in the previous section. The effects of cavitation and the inertia terms in the equations of motion are included in the following calculation [3].

The representative numerical parameters are specified as:

the ratio a of the recess radius is 0.683, the moment of inertia \hat{I} for the x and y axes is 9.3×10^5 , the moment of inertia \hat{I} for the z axis is 4.7×10^5 , bearing-mass \hat{m} is 9.3×10^5 , the revolution radius \bar{R}_0 is three, the outer bearing-radius R_2 is 10 mm, the load-eccentric ratio \bar{r}_w is 0.1, the operating parameter \hat{S}_0 is 2×10^{-7} , the recess volume \hat{V}_r is 1×10^{-10} , restrictor parameter $\hat{\beta}$ is 5.7×10^{10} , the parameter ζ_0 [13] is two-thirds, surface roughness σ/R_2 is 2×10^{-4} , roughness-ratio σ_2/σ_1 is unity, azimuth φ_w of the load is $\pi/2$, and the ratio of angular velocity Ω/ω is unity. The parameters regarding mixed lubrication are given by Ref. [15].

RESULTS AND DISCUSSION

Effects of load eccentricity

Figures 3 and 4 demonstrate the time evolution of the center clearance h_{0s} , pad inclination $\bar{\alpha}$ and the pad azimuth φ as well as the maximum contact pressure $\bar{p}_{a\max}$ and the leakage flow rate \bar{Q}_{out} [$=\bar{Q}_r(\bar{r}=1)$] in terms of eccentric ratio \bar{r}_w of the load, where the changes in \bar{p}_s and \bar{W} are synchronized ($\Delta\tau=0$).

As the ratio \bar{r}_w increases, the parameters h_{0s} , $\bar{\alpha}$ and φ become large in the low-pressure period and the pressure $\bar{p}_{a\max}$ increases in the high-pressure period. The leakage \bar{Q}_{out} peaks at the transition from the low-pressure to the high-pressure period, which is caused by the squeeze film effect.

Effect of time lag of loads

Figures 5–7 depict the variation of the center

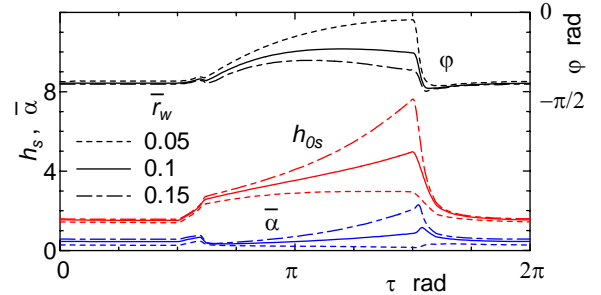


Fig. 3 Changes in center clearance h_{0s} , inclination $\bar{\alpha}$ and azimuth φ of pad in terms of eccentric ratio \bar{r}_w of load ($\Delta\tau=0$)

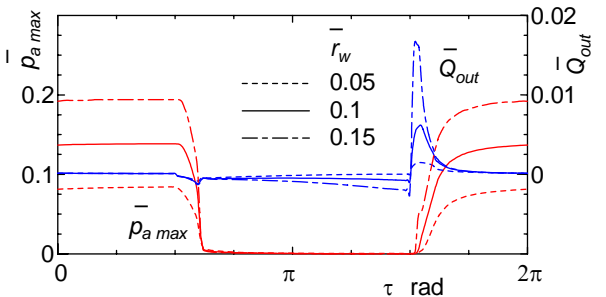


Fig. 4 Changes in maximum contact pressure $\bar{p}_{a\max}$ and leakage flow rate \bar{Q}_{out} in terms of eccentric ratio \bar{r}_w of load ($\Delta\tau=0$)

clearance h_{0s} and minimum clearance $h_{min s}$, leakage flow rate \bar{Q}_{out} , total friction torque \bar{T} ($\bar{T}_a + \bar{T}_r$) and the ratios of cavitation area \bar{A}_{cav}/\bar{A}_0 and contact area \bar{A}_{cnt}/\bar{A}_0 with time lag $\Delta\tau$ conditions. When the change in the load precedes that in the supply pressure ($\Delta\tau < 0$), the hydrostatic load-carrying capacity momentarily exceeds the load at $\tau \approx \pi/2$, which causes an imbalance and larger clearances in the low-pressure period. Jumping of the pad yields cavitation in the bearing-land; thereby creating the peaks of \bar{A}_{cav}/\bar{A}_0 . At another transition of the pressure and the load ($\tau \approx 3\pi/2$), the downward force becomes larger than that which is exerted upward, which consequently increases leakage \bar{Q}_{out} based on the squeeze film effect.

Conversely, when the change in the load delays ($\Delta\tau > 0$) at $\tau \approx \pi/2$, the downward force becomes larger and the pad is suppressed *vice versa*.

During the high-pressure period, the surfaces remain in contact ($\bar{A}_{cnt}/\bar{A}_0 = 1$) resulting in larger torque \bar{T} because of asperity-contact. On the other hand, during the low-pressure period, the area ratio \bar{A}_{cnt}/\bar{A}_0 is less than unity or equal to zero and \bar{Q}_{out} and \bar{T} are infinitesimal.

Effect of radius of revolution of pad

The radius \bar{R}_0 of the revolution of the pad corresponds to the respective pitch radius of the cylinder-bores of piston pumps and motors. Figures 8 and 9 show the effect of \bar{R}_0 on the bearing. As \bar{R}_0 increases, the maximum \bar{h}_{0max} of the center clearance increases, especially in the low-pressure periods, because of the hydrodynamic (wedge) effect; the minimum \bar{h}_{0min} changes less. The increase in hydrodynamic load-carrying capacity lessens the cavitation period $\tau_{cav}/2\pi$ and contacting period $\tau_{cnt}/2\pi$ in a cycle.

Effect of recess volume or liquid bulk modulus

The effect of the normalized recess volume \bar{V}_r on pad fluctuation is examined in Fig. 10. As \bar{V}_r increases, the bearing-stiffness $\bar{\lambda}$ decreases. By contrast, the moment stiffness $\bar{\lambda}_M$ remains almost constant. The mean power loss \bar{L}_m is determined by the power loss \bar{L}_{Tm} because of friction torque and the losses decrease slightly with increased \bar{V}_r .

It is noteworthy that parameter \hat{V}_r is equivalent to the inverse number of the bulk modulus K of the liquid. Therefore, if K is reduced, *e.g.* by containing bubbles in the liquid, the pad would fluctuate distinctly and the bearing-stiffness would decrease.

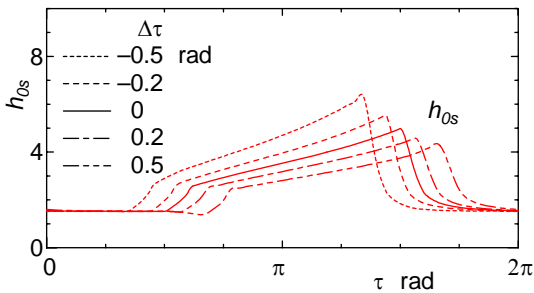


Fig. 5 Changes in center clearance h_{s0} in terms of time lag $\Delta\tau$ of the load

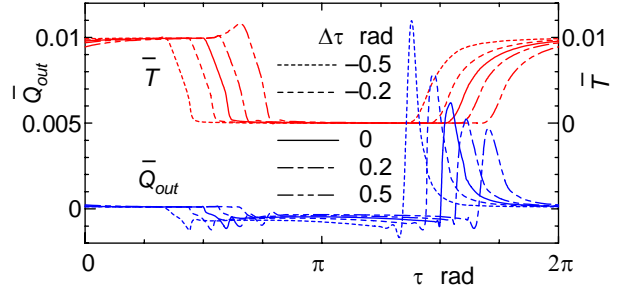


Fig. 6 Changes in leakage flow rate \bar{Q}_{out} and friction torque \bar{T} in terms of time lag $\Delta\tau$ of the load

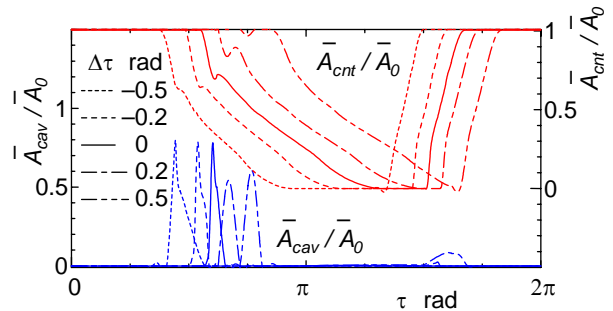


Fig. 7 Changes in cavitation area \bar{A}_{cav}/\bar{A}_0 and contact area \bar{A}_{cnt}/\bar{A}_0 in terms of time lag $\Delta\tau$ of the load

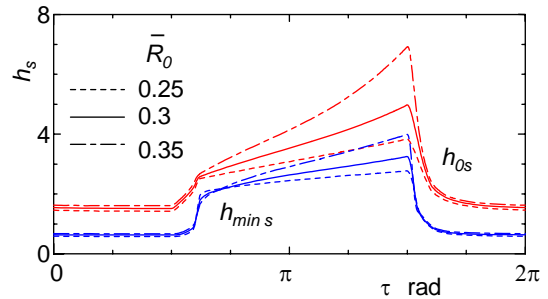


Fig. 8 Changes in center h_{s0} and minimum $h_{s min}$ clearances in terms of revolution radius \bar{R}_0

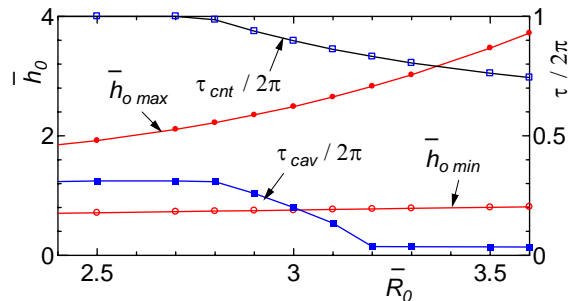


Fig. 9 Effect of revolution radius \bar{R}_0 on maximum clearance \bar{h}_{0max} , minimum clearance \bar{h}_{0min} , cavitation period $\tau_{cav}/2\pi$ and contacting period $\tau_{cnt}/2\pi$

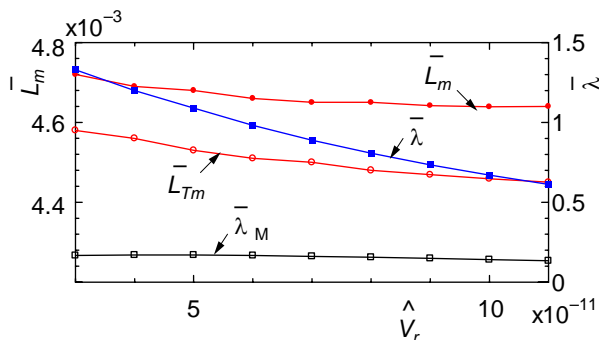


Fig. 10 Effect of normalized recess volume \hat{V}_r on mean power loss \bar{L}_m , mean friction power loss \bar{L}_{Tm} , dynamic stiffness $\bar{\lambda}$, and moment-stiffness $\bar{\lambda}_M$

CONCLUDING REMARKS

A hybrid thrust bearing as a slipper model of water hydraulic piston pumps and motors was developed in this study. It includes uneven contact because of alignment in mixed and fluid film lubrication, based on the GW model and the PC model. Numerical solutions of the time-dependence problem are obtained over a wide range of operation under water lubricated conditions.

The following conclusions were obtained: i) As the eccentric ratio of the load increases, the inclination of the pad increases, thereby causing local asperity-contact pressure. ii) The time lag between the supply pressure and the load influences the bearings' motion and tribological characteristics. In particular, the preceding change in loads engenders a larger motion of the pad. iii) The radius of revolution of the pad influences the bearing performance because of hydrodynamic wedge effect. iv) As the recess volume increases or the bulk modulus decreases, the bearing motion is enlarged, especially in the low-pressure period, decreasing the bearing stiffness.

ACKNOWLEDGEMENTS

The author would like to thank Professor Emeritus Atsushi Yamaguchi of Yokohama National University and Emeritus Professor Mitsuru Fujiwara of Muroran Institute of Technology for their thoughtful encouragement.

REFERENCES

1. Yamaguchi, A., Tap Water – Possibility as a Hydraulic Fluid, Journal of Japan Hydraulic and Pneumatic Society, 1978, 9-4, pp. 205–210. (in Japanese)
2. Modern Water Hydraulics – Our Choice for the Future, 1995, National Fluid Power Association.
3. Iboshi, N. and Yamaguchi, A., Characteristics of a Slipper Bearing for Swash Plate Type Axial Piston Pumps and Motors (1st Report), Bulletin of Japan Society of Mechanical Engineers, 1982, 25, pp.

- 1921–1930; (2nd Report), *ibid.*, 1983, 26, pp. 1583–1589; (4th Report), *ibid.*, 1986, 29, pp. 2539–2546.
4. Shute, N.A. and Turnbull, D.E., Minimum Power Loss of Hydrostatic Slipper Bearings for Axial Piston Machines, Proceedings of International Convention on Lubrication and Wear, Institution of Mechanical Engineers, 1963, pp. 3–14.
5. Hooke, C.J. and Kakoullis, Y.P., Effects of Non-Flatness on the Performance of Slippers in Axial Piston Pumps, Proceedings of Institution of Mechanical Engineers, Part C, 1983, 197, pp.239–247.
6. Hooke, C.J. and Li, K.Y., The Lubrication of Overclamped Slippers in Axial Piston Pumps--Centrally Loaded Behaviour, Proceedings of Institution of Mechanical Engineers, Part C, 1988, 202, pp. 287–293.
7. Williams, J.A., Engineering Tribology, 1996, Oxford Science Publications.
8. Hamrock, B.J., Fundamentals of Fluid Film Lubrication, 1994, McGraw-Hill.
9. Yamaguchi, A. and Matsuoka, H., A Mixed Lubrication Model Applicable to Bearing and Seal Parts of Hydraulic Equipment, Journal of Tribology, Transactions of ASME, 1992, 114, pp. 116–121.
10. Greenwood, J.A. and Williamson, J.B.P., Contact of Nominally Flat Surfaces, Proceedings of Royal Society, London, Series A, 1966, 295, pp. 300–319.
11. Patir, N. and Cheng, H.S., An Average Flow Model for Determining Effects of Three-Dimensional Roughness on Partial Hydrodynamic Lubrication, Journal of Lubrication Technology, Transactions of ASME, 1978, 100, pp. 12–17.
12. Patir, N. and Cheng, H.S., Application of Average Flow Model to Lubrication Between Rough Sliding Surfaces, Journal of Lubrication Technology, Transactions of ASME, 1979, 101, pp. 220–230.
13. Kazama, T. and Yamaguchi, A., Application of A Mixed Lubrication Model for Hydrostatic Thrust Bearings of Hydraulic Equipment, Journal of Tribology, Transactions of ASME, 1993, 115, pp. 686–691.
14. Kazama, T. and Yamaguchi, A., Experiment on Mixed Lubrication of Hydrostatic Thrust Bearings for Hydraulic Equipment, Journal of Tribology, Transactions of ASME, 1995, 117, pp. 399–402.
15. Yamaguchi, A., Okamoto, Y. and Wang, X., Friction Characteristics of PEEK for Bearing and seal Parts of Water Hydraulic Equipment, Transactions of Japan Fluid Power System Society, 2003, 34-2, pp. 40–45. (in Japanese)
16. Kazama, T., Yamaguchi, A. and Fujiwara, M., Motion of Eccentrically and Dynamically Loaded Hydrostatic Thrust Bearings in Mixed Lubrication, Proceedings of 5th JHPS International Symposium on Fluid Power, 2002, pp. 233–238.
17. Johnson, K.L., Greenwood, J.A. and Poon, S.Y., Simple Theory of Asperity Contact in Elastohydrodynamic Lubrication, Wear, 1972, 19, pp. 91–108.

Remote Control of Ordinary Backhoe Using Pneumatic Robot System

Takahiro SASAKI*, Kenji KAWASHIMA**, Takayuki NAGAI* and Toshiharu KAGAWA**

* Interdisciplinary Graduate School of Science and Engineering

** Precision and Intelligence Laboratory

Tokyo Institute of Technology

(E-mail: sasaki@k-k.pi.titech.ac.jp)

4259 Nagatsuda, Midori-ku, Yokohama-shi, Kanagawa, 226-8503, Japan

ABSTRACT

In disaster sites, the remote control of construction machinery is required to ensure the safety of the workers. However, the current remote control systems are limited in types of machines and numbers. A remote control system we have developed has advantages in portability and dexterity by using lightweight pneumatic robot arms. The effectiveness of the system has been confirmed with a small type backhoe. In this research, a system was developed to improve flexibility. First, the moving angle of the robot arm was enlarged. Then, the sliding system was developed to move the robot back and forth so that the robot arms can operate not only the levers to control the arm of the backhoe but also that of the acceleration. Moreover, CCD camera was attached to inform the vision from the backhoe. The system was applied to an ordinary backhoe whose bucket size is 0.28 m^3 . Some field tests were conducted and the effectiveness of the developed system was proven.

KEY WORDS

Key words; Pneumatic Robot, Pneumatic Artificial Muscle, Remote Control

INTRODUCTION

In disaster sites, the remote control of construction machinery is required to ensure the safety of the workers. However, the current remote control system is limited in types of machines and numbers. The remote control systems for construction machinery can be classified into two approaches. One is "Conversion Type" and the other is "Installation Type". The "Conversion Type" approach converts ordinary construction machinery into remote control systems^{[1][2]}. For example, a system has already been developed to realize remote control by replacing a valve in the construction machinery to a remotely controllable valve. Conversion type systems, though, require significant

time and effort because conventional remote-controlled construction machinery is larger than ordinary equipment and is available in only limited types and quantities.

On the other hand, the "Installation Type" approach is to install a remote-controlled robot system on ordinary construction machinery. Since the remote control can be successfully realized with any construction machinery near the disaster site, the quick restoration work is available. The system requirement for the "Installation type" is portability and easy installation to the construction machinery.

A remote control system we have developed from the "Installation Type" approach has advantages in portability and dexterity by using a lightweight

pneumatic robot arm. This system can easily be carried and installed on ordinary construction machinery. Using the developed pneumatic robot system, the effectiveness of the remote control system for construction machinery with a small type backhoe was confirmed^[3].

In this research, a system was developed to improve versatility and flexibility. A sliding system was developed so that the pneumatic robot arms can operate not only the levers to control the arm of the backhoe but also that of the acceleration. Moreover, we attached CCD camera to the robot system to inform the vision from the backhoe to the operator. We conducted some field tests to evaluate the effectiveness of the remote control system.

PNEUMATIC ROBOT SYSTEM

Pneumatic Robot Arm

Figure 1 shows pneumatic robot arms newly developed and the driving system of a joint. The pneumatic robot arm has six degree-of-freedom. Because the structural components are made of MC nylon, carbon rods, aluminum and the Pneumatic Artificial Rubber Muscles (PARMs)^[4] as actuators, the arm is very light in weight. The total weight of the arm is approximately 3 [kg]. Because the robot arm is lightweight, quake-resistant, portable and dexterous, it is effective in its role as part of a remote control system for construction machinery. Each angle is driven antagonistically with two PARMs connected to a link in parallel. A 5-port servo valve controls supply and exhaust air to PARMs^[3]. Then the difference of contraction of two PARMs creates joint torque as shown in Figure 1. A rotary encoder was set to each joint and the rotation angle was measured and controlled.

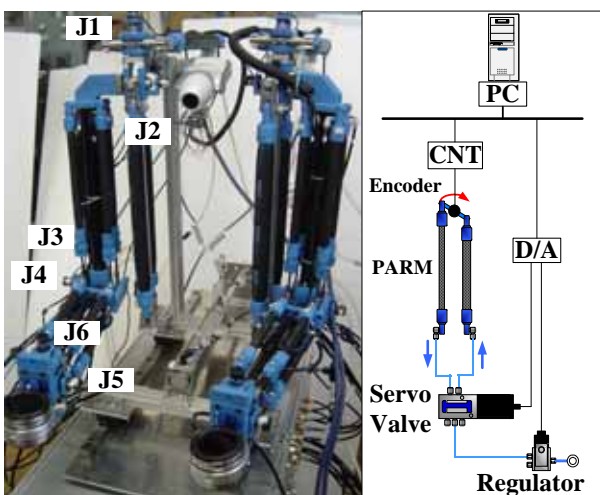


Figure 1 Pneumatic robot arms (left) and Muscular Driving System (right)

Table 1 Movable angle of robot arm (Shoulder joints)

	Available Angle [deg]	
	J1	J2
Previous Arm	± 28	± 28
New Arm	± 45	± 40

The robot arm contains of a wrist joint that enables the robot hand to move up, down, left, and right, the elbow joint which bends and twists the robot arm and the shoulder joint which turns the shoulder and rotates the entire arm. In previous research, available angle of each joint of the arm is about 30 [deg] and the robot arm can operate a small type backhoe because of short distance of the levers equipped with the backhoe. However, levers of the ordinary backhoe are separated. Therefore, we improved shoulder part of the robot arms to expand the available angle. The shoulder part, that is J1 and J2 in Figure 1, were newly developed. PARMs with 20 [mm] size in diameter and with 340 [mm] in length (MAS-20: manufactured by FESTO) were used the joints to improve the contracting length. As a result, larger available angle (over 40 [deg]) was realized as shown in table 1.

Sliding System

The acceleration lever of the backhoe is apart from the operation levers and the robot arm cannot reach it even the shoulder joints were improved because a human operator bend and rotate ones west to operate the levers. Therefore, a sliding system was developed to move the robot system back and forth as shown in figure 2. Linear sliders and a pneumatic cylinder were attached with the frames that fix the robot arms on the sliding guide. Therefore, robot arms can move about 200 [mm] backward and operate the acceleration lever.

Air Gripper is set to the tip part of the robot arm as shown in figure 1, therefore the robot arm can grasp not only the operation levers but also that of the acceleration of the construction machinery. The robot arm can rotates gripped lever using the wrist joint.



Figure 2 Sliding System

Control Box

Figure 3 shows control boxes for the pneumatic robot system. The boxes are divided into three units. One is a PC box which contains a PC board and sampling boards. Second one shown in figure 3-(a) contains pneumatic instruments such as servo valves and pressure regulators. The outer dimensions of the boxes are both 400 [mm] × 430 [mm] × 200 [mm]. The third box as shown in figure 3-(b) is power source unit supplying electric power to the PC unit and valve unit and an access point for wireless LAN network. The outer dimension of the box is 200 [mm] × 430 [mm] × 200 [mm]. The total weight of the robot system is about 40 [kg] and can be installed easily on construction machinery with minimal effort.

Remote Control System

Figure 4 shows a remote control system. An operator uses joysticks to input the target tip position for the robot arm from the master side. Then a laptop PC reads the joystick values and transmits the values to the control box at the slave side via wireless LAN (IEEE 802.11b). Then the robot arm, grasping the levers of construction machinery in advance, manipulates the levers according to the transmitted value. As a result, the joystick motion and the construction machinery levers are synchronized. We have confirmed that the response delay is less than 200 [ms] which is acceptable for remote control.

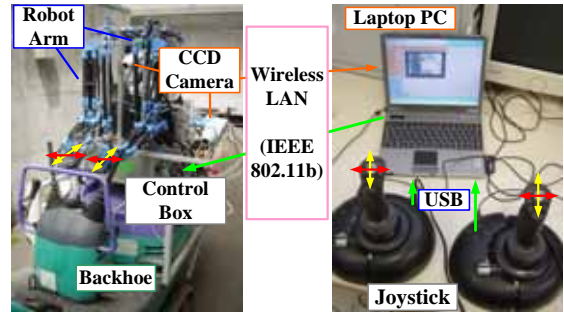
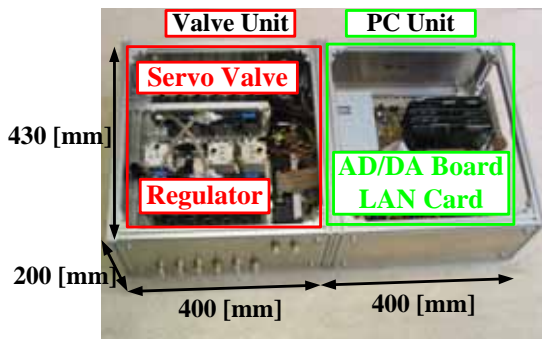


Figure 4 Remote control system

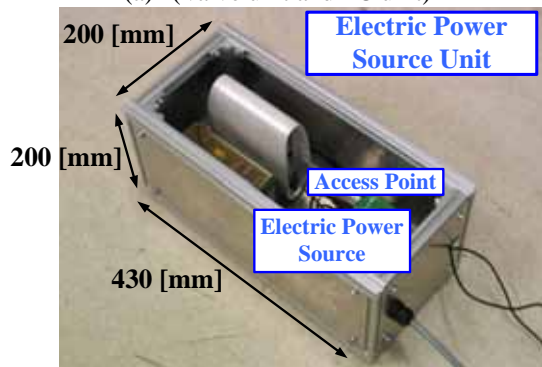
Generally, construction machinery such as a backhoe has two pairs of operation levers. One is to control a movement and the other is to control the arm of it. When an operator controls the construction machinery, one can choose and control any levers. According to the remote control, the operator is far from the machine, therefore it is difficult to move and control the robot arms precisely between two command levers. To make it easier to operate, we programmed the movement of changing the levers in advance by defining the trajectory of the movement. When an operator pushes a button on the joystick, the robot arms move to the lever from one side to another automatically. CCD cameras, which are helpful for remote control, are attached to the robot system. The vision from the CCD camera is provided to the operator through the wireless LAN.

EXPERIMENT

To confirm the availability of the system, we tried to apply the robot system to an ordinary backhoe. The backhoe used in the experiment was Grand Beetle 60SR (KOBELCO Construction Machinery Co., Ltd.) whose bucket size is 0.28 [m³]. Some experiments were conducted including the movement of the construction machinery. First, we removed the sheet from the backhoe and set the control boxes. Then, the robot arms were mounted on the boxes. About 30 minutes were needed with two persons to set up the system. Figure 5 is the photo of the remote control system installed in the operating room of the backhoe.



(a) (Valve unit and PC unit)



(b) Electric power source unit

Figure 3 Control box



Figure 5 Developed remote control system installed in the operating room of the backhoe

The contents of the experiment are as follows:

- (a) First, the backhoe moves forward.
- (b) Second, the robot arms change the levers.
- (c) Third, simulated excavating actions (move the boom forward and the arm down) and the backhoe rotate about 90 degrees to the left.
- (d) Simulated dumping actions (move the boom forward and open the bucket) are done and the backhoe rotates about 90 degrees to the right.
- (e) The robot arms change the levers.
- (f) Finally, the construction machinery moved backward.

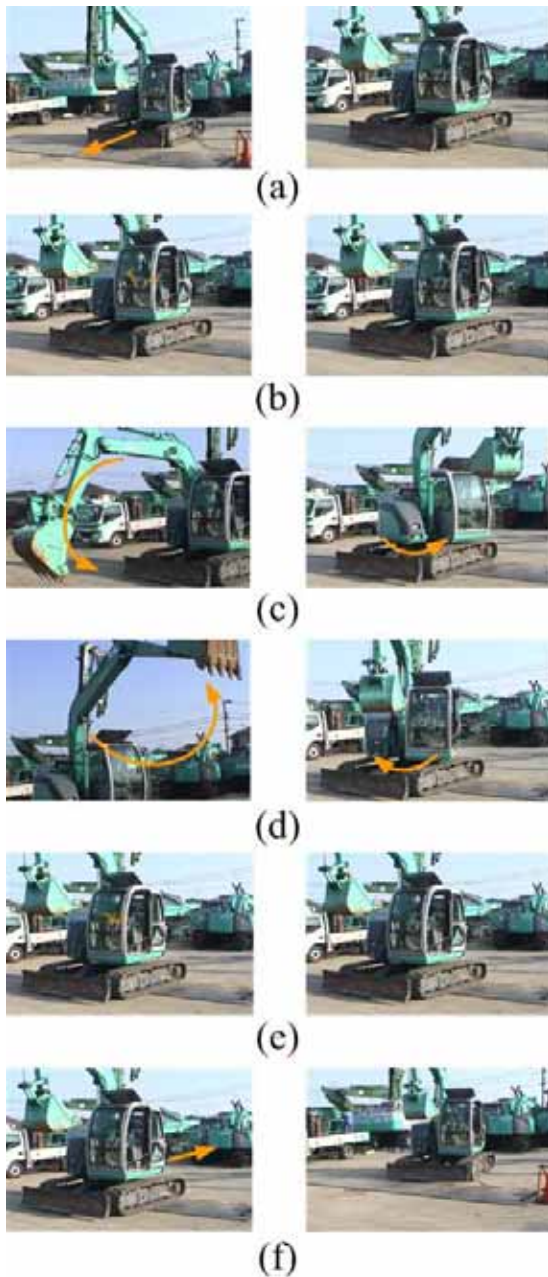


Figure 6 Remote control experiment

Table 2 Operation Time

Task in figure 6	(a)	(b)	(c)	(d)	(e)	(f)
Operation Time [s]	20	9	30	21	9	13

The remote control was conducted with the above-mentioned contents. Figure 6 shows the photos during the experiment and table 2 indicates the operation time of each task referred above. The operation was conducted smoothly and it took only 9 [s] for changing levers. The effectiveness was confirmed.

CONCLUSION

A lightweight remote control system of construction machinery was developed using pneumatic robot arms. We improved the system to realize the manipulation of an ordinary backhoe. Remote control experiments were conducted with an ordinary backhoe whose bucket size is 0.28 [m³]. The availability of the remote control system was confirmed from the field experiments.

ACKNOWLEDGEMENT

This research was supported in part by the “Development of Advanced Robots and Information Systems for Disaster Response” project of the Ministry of Education, Culture, Sports, Science and Technology in Japan, by FUJITA Corporation and by KOBELCO Construction Machinery Co., Ltd.

REFERENCES

1. Minamoto, M. and Matsunaga, K., Tele-presence information and remote-controlled task execution, Proceedings of the 1998 IEEE/RSJ Int. Conf. on Intelligent Robotics and Systems, Victoria, B.C., Canada, 1998, pp.1102-1106
2. Quang, H., Santos, M., Quang, N., Rye, D. and Durrant-Whyte, H., Robotic excavation in construction automation, IEEE Robotics and Automation Magazine, 2002, 9-1, pp.20-28
3. Kawashima, K., Sasaki, T., Miyata, T., Kagawa, T., Development of Remote Control System of Construction Machinery Using Pneumatic Robot Arm, Proc. of the 2004 IEEE/RSJ Int. Conf. on Intelligent Robotics and Systems, Japan, 2003, pp.3384-3389
4. Chou, C., Hannaford B., Measurement and Modeling of McKibben Pneumatic Artificial Muscles, IEEE Transactions on Robotics & Automation, 1996, 12-1, pp90-103

CONTROL OF A VIBRATION ISOLATION SYSTEM USING PRESSURE DIFFERENTIATORS AND SPOOL TYPE SERVO VALVES

Tomonori KATO*, Yosuke YAMAZAKI**, Koichi SAWAMOTO***, Kenji KAWASHIMA***
and Toshiharu KAGAWA***

* Department of Mechanical Engineering, Tokyo Metropolitan College of Technology
1-10-40 Higashi-oi, Shinagawa, Tokyo, 140-0011 Japan
(E-mail: kato@tokyo-tmct.ac.jp)

**Sumitomo Metals, 1-8 Fuso-cho, Amagasaki City, Osaka,

***Tokyo Institute of Technology
4259 Nagatsuta-cho, Midori-ku, Yokohama City, Kanagawa 226-8503 Japan

ABSTRACT

Active control type pneumatic isolation systems are widely used in semiconductor production processes. Most of them are actively controlled by nozzle flapper type servo valves, since they have fine characteristics as imperfect pressure integrators. But nozzle flapper type servo valves exhaust a lot of compressed air, for the sake of controllability. In this research, we firstly develop a pressure differentiator using an isothermal chamber, a cylindrical type laminar flow element and a differential pressure sensor. Then, by using the developed pressure differentiator and a spool type servo valve, an imperfect pressure integration system with much lower exhausted air flow rate compared to the system with nozzle flapper type servo valve, is constituted. Finally, the proposed pressure integration system is applied to the control of active vibration isolation system. The experimental results indicate superior performance of the developed system, especially in much lower energy consumption.

KEY WORDS

Pneumatics, Vibration Isolation System, Energy Saving, Pressure Differentiator

NOMENCLATURE

d : nominal length [m]	K : gain coefficient [Pa·s]
f : frequency [Hz]	L : length of slit [m]
f_c : cut-off frequency [Hz]	L_i : inlet length [m]
G : mass flow rate [kg/s]	P_a : atmospheric pressure [Pa]
	P_c : pressure in chamber [Pa]
	P_{do} : output signal of pressure differentiator [Pa]

- P_j : differential pressure[Pa]
 P_s : measured pressure [Pa]
 Q : volume flow rate [m^3/s]
 R : gas constant [J/(kg·K)]
 r_1 : Outer diameter [m]
 r_2 : Inner diameter [m]
 s : laplace operator [1/s]
 st : sampling time [s]
 t : time [s]
 T : time constant of the sensor [s]
 v : velocity in laminar flow element [m/s]
 V : volume of chamber [m^3]
 W : air mass in chamber[kg]
 x : displacement [m]
 θ : temperature in a chamber [K]
 θ_a : room temperature [K]
 μ : viscosity [$Pa \cdot s$]
 ρ_a : density of air at atmospheric pressure [kg/m^3]
 ρ_c : density of air when pressurized [kg/m^3]

INTRODUCTION

Since air is an ideal gas for design of vibration isolation systems, air spring systems are widely used in industry, as seen in machine tools or transportation systems[1]. Air spring systems are required such performances as steady-state stability, quick self-motion control, and good floor vibration isolation. In order to satisfy these demands, nozzle flapper type servo valves with linear and precise pressure controllability are widely used. But if pressure control with high gain is needed, nozzle flapper type servo-valve requires large amount of steady-state exhausted air flow rate, i.e. energy efficiency is sacrificed to controllability. Though there is a over lap type spool type servo valve which has much smaller amount of steady-state exhausted air flow rate and high flow rate gain, since it has strong non-linearity between its control signal to output flow rate, spool type servo valves have so far been difficult to use for precise pressure control like air spring systems.

In this paper, in order to reduce the affection by the nonlinearity and dead-point shift which spool type servo valves have, a pressure differentiator using an isothermal chamber[2][3], which we developed is applied to the pressure control in a pressure tank, as constituting a cascade pressure control system. Then, the cascade pressure control system is applied to the isolation table.

DEVELOPMENT OF PRESSURE DIFFERENTIATOR

Principle of the proposed pressure differentiator

As shown in Fig.1, the proposed pressure differentiator is composed of an isothermal chamber, cylindrical

laminar flow element, a diaphragm type differential pressure gauge and a pressure sensor. The cross sectional structure of a slit is shown in Fig.1. When the measured pressure P_s changes, air flows through the narrow slit between two plates, and pressure in chamber P_c changes slightly behind of P_s . By measuring the differential pressure $P_f = P_s - P_c$ with a diaphragm type differential pressure gauge, the differentiated value of P_s , dP_s/dt can be calculated.

Assuming the flow in the slit as a laminar flow, and taking equation of energy and Poiseuille law into consideration, the measurement principle of the sensor is explained as follows. The state equation for compressive fluids in a chamber can be written as Eq.(1).

$$P_c V = WR \theta \quad (1)$$

The following equation is derived by totally differentiating Eq.(1) and assuming that the chamber volume is constant:

$$\frac{dP_c}{dt} V = GR \theta + WR \frac{d\theta_a}{dt} \quad (2)$$

If the state of air in the chamber during charge or discharge remains isothermal, the following equation can be obtained from Eq.(2):

$$G = \frac{V}{R \theta_a} \frac{dP_c}{dt} \quad (3)$$

In Eq.(3), the average temperature in the chamber is equal to the room temperature. It is clear from Eq.(3) that if the volume of the chamber V and the room temperature θ_a are known, the mass flow rate G is proportional to the differentiated value of pressure in chamber P_s .

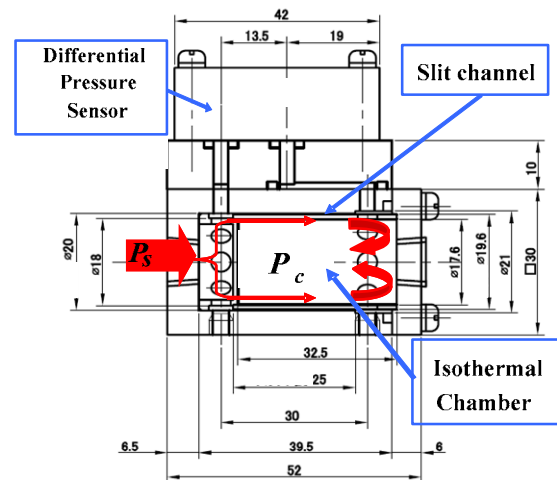


Fig.1 Structure of the proposed sensor

Suppose the width, outer and inner diameters and length of the slit are respectively r_1 , r_2 , h , L , and if flow in the slit is laminar, the relationship between the volume flow rate flowing through the slit Q and the differential pressure of both edges of slits can be expressed by Poiseuille law as

$$Q = \frac{\pi r_2 (r_1 - r_2)^3}{6 \mu L} (P_s - P_c) \quad (4)$$

Taking the density of air at atmospheric pressure ρ_a and the pressure in a chamber P_c into consideration, the mass flow rate can be expressed by the equation (5).

$$G = \rho_a \frac{P_c}{P_a} Q = \frac{\rho_a P_c \pi r_2 (r_1 - r_2)^3}{6 P_a \mu L} (P_s - P_c) \quad (5)$$

Defying the resistance coefficient of flow rate as $r_s = 6 P_a \mu L / \{\rho_a \pi r_2 (r_1 - r_2)^3\}$, equation (5) can be rewritten as

$$G = \frac{P_c}{r_s} (P_s - P_c) \quad (6)$$

The output signal of the differential pressure gauge can be written as

$$P_j = P_s - P_c \quad (7)$$

Therefore, from by Eq.(6) and Eq.(7), G can be written as follows.

$$G = \frac{P_c}{r_s} P_j \quad (8)$$

From Eq.(3) and (8), defining $K = \frac{r_s V}{R \theta}$ as the gain coefficient,,

$$\frac{dP_c}{dt} = \frac{P_c P_j}{r_s} \frac{R \theta}{V} = \frac{1}{K} P_c P_j \quad (9)$$

By laplace transform of Eq.(9), assuming a tiny pressure change from the equilibrium point of no differential pressure, $P_j(0)=0$, i.e., $P_s(0) \doteq P_c(0)$, Eq.(10) can be derived.

$$\begin{aligned} sP_c - P_c(0) \\ \cong sP_c - P_s(0) = \frac{1}{K} P_j P_c(0) \end{aligned} \quad (10)$$

Since $sP_s - P_s(0) = \int \left(\frac{dP_s}{dt} \right)$, and defining T as

$$T = \frac{K}{P_c} = \frac{6 P_a \mu L V}{P_c \rho_a \pi r_2 (r_1 - r_2)^3 R \theta} \quad (11)$$

the output of the differential pressure sensor P_j can be written as Eq.(12).

$$P_j = \frac{T}{1 + Ts} \int \left(\frac{dP_s}{dt} \right) \quad (12)$$

So, it is clear that the output value of the differential pressure sensor P_j is T times value of dP_s/dt , with 1st-order lag filter.

Now, suppose the divided value of P_j by T as the output of the proposed differentiator P_{do} , as Eq.(13).

$$P_{do} = \frac{1}{T} P_j = \frac{1}{1 + \left(\frac{K}{P_c} \right) s} \int \left(\frac{dP_s}{dt} \right) \quad (13)$$

When the desired frequency band of the differentiated value of P_s is much lower than the cut off frequency of the proposed sensor,

$$f_c = \frac{1}{2 \pi T} = \frac{P_c \rho_a r_2 (r_1 - r_2)^3 R \theta}{12 P_a \mu L V} \quad (14)$$

the proposed apparatus is effective as a pressure differentiator. The sensor in this research is fabricated with the specifications shown in Fig.1. The theoretical cut off frequency of the developed sensor at $P_c=180\text{kPa}$ abs is $f_c=317[\text{Hz}]$. For more information about the developed sensor, see the reference paper [2].

APPLICATION OF PRESSURE DIFFERENTIATOR TO ISOLATION TABLE

Cascade pressure control system

The pressure control system in vibration isolation system is required to satisfy the performance as an imperfect pressure integrator. For that reason, ordinarily, nozzle flapper type servo valves are widely used. But, in order to reduce the exhausted air flow rate from the servo valves, a cascade pressure control system using a spool type servo valve and the developed pressure differentiator is proposed. In Fig.1, suppose the affect by the volume change, $PA/V * dx/dt$, is negligibly small, measuring the differentiated value of pressure, dP/dt , is equivalent to measuring the flow rate. In order to realize an imperfect pressure integrator, a cascade pressure control system, with dP/dt as the minor loop, is constituted. The control cycle of the minor loop is designed as about 900 times of that of the pressure control loop. Therefore, the non-linearity and dead-point shift of the spool type servo valve are compensated, and the existence of the minor loop is almost negligible.

Procedure of experiment

Experiment was conducted with the apparatus shown in Fig.2. The volume of the isolator's chamber is $V=1.1 \times 10^{-3}[\text{m}^3]$, the mass of the table is $45.1[\text{kg}]$, and the surface area of the air spring is $72.4 \times 10^{-4}[\text{m}^2]$. The spool type servo valve used in the experiment is FESTO M5-SA. The gains are as follows : $K_x:500[\text{v/m}]$, $K_x I:250[\text{v/m}]$, $K_a:10[\text{V}/(\text{m/s}^2)]$, $K:2.53 \times 10^4$, $K_p:1.55$

$\times 10^{-4}$ [1/s], $K_{pd}:6.24 \times 10^{-4}$ [V/(Nl/min)], $K_{dp}:20$ [V/Pa].
 Fig.3 indicates the block diagram of the vibration isolation control system.

In the experiment, at 0s time, the control is started, and after settled at the set displacement, the steady state vibration of acceleration is compared to the value before the isolation table is controlled to float.

Experiment results

The experimental results are shown in Fig.4. The proposed control method can float the table without steady state error and unwanted vibration. achieves the vibration isolation performance within the amplitude of 2×10^{-3} [m/s²]. The result is no way inferior to that of nozzle flapper type servo valve.

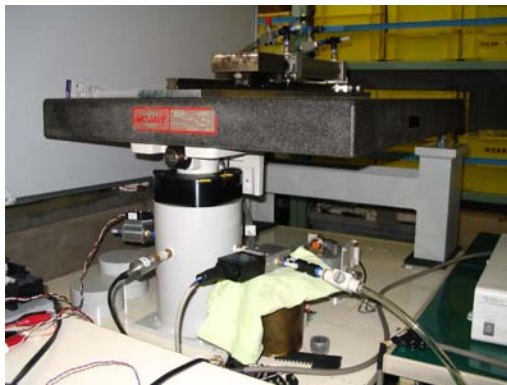


Fig.2 Picture of vibration isolation system

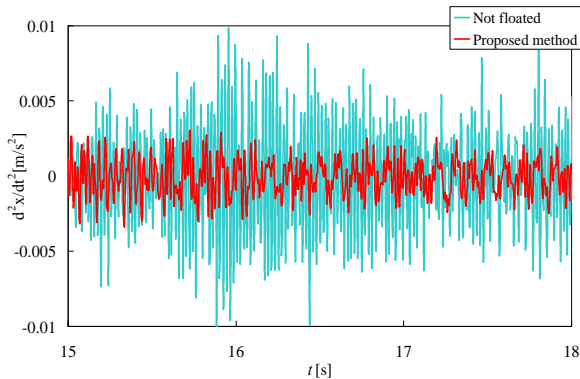


Fig.4 Experimental results of acceleration

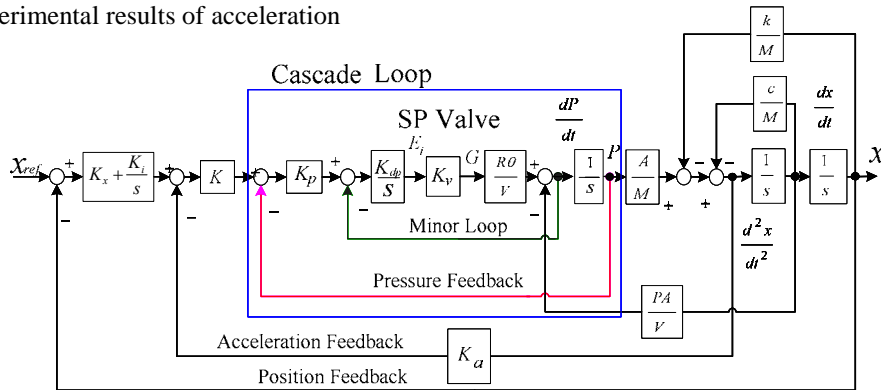


Fig.3 Block diagram of the proposed control method

Table 1 Comparison of exhausted air flow rate

Type of valve	Nozzle flapper	Spool
Exhausted flow rate[Nl/min]	15	0.4

Table 1 shows the comparison of the exhausted air flow rates on types of the servo valves. The proposed method can reduce the energy loss by exhausted air flow rate.

CONCLUSION

In this research, a pressure differentiator using an isothermal chamber and a cylindrical type laminar flow element is designed and fabricated.

Then, the developed pressure differentiator is applied to the pressure control of the tank of the isolation table, as constituting the cascade pressure control system. An imperfect pressure integrator is developed with a spool type servo valve and a developed sensor.

It is clarified that the proposed method can successfully control the vibration isolation table.

It is also clarified that there is a possibility of realizing the air spring system with much lower exhausted flow rate and higher maximum control flow rate.

REFERENCES

- [1]Wakui S : Incline Compensation Control Using an Air-Spring Type Isolated Apparatus, Precision Engineering, Vol.27, pp170-174 (2003)
- [2]KAWASHIMA K., KATO T., YAMAZAKI Y., YANAGISAWA M., KAGAWA K. : Development of slit type pressure differentiator using an isothermal chamber, Measurement Science and Technology, Vol.16, pp.1150-1156 (2005)
- [3]Kawashima K., Kagawa T. : Instantaneous Flow Rate Measurement of Ideal gases, Trans. ASME Journal of Dynamic Systems, Measurement and Control, Vol.122, pp.178-178 (2000)

Precise Position Control of Pneumatic Servo System Considered Dynamic Characteristics of Servo Valve

Takashi MIYAJIMA*, Hidekuni IIDA*, Toshinori FUJITA**, Kenji KAWASHIMA*** and
Toshiharu KAGAWA***

* Graduated School Student, Tokyo Institute of Technology
4259 Nagatsuda-cho, Midori-ku, Yokohama, 226-8503 Japan
(E-mail: miyajima@k-k.pi.titech.ac.jp)

** Department of Machinery System Engineering, Tokyo Denki University
2-2 Kandanishiki-cho, Chiyoda-ku, Tokyo, 101-8457 Japan

*** Precision and Intelligence Laboratory, Tokyo Institute of Technology
4259 Nagatsuda-cho, Midori-ku, Yokohama, 226-8503 Japan

ABSTRACT

Precise positioning system is required in the fields of semi-conductor manufacturing process. A pneumatic servo table system is one of a precise positioning system. The features of the table are little friction force and little heat generation. Generally, the controller of this system is designed by neglecting the characteristics of servo valves. However, in high frequency band, the response of this system becomes unstable because of the characteristics of the valves. In this paper, we demonstrate that by considering the characteristics of servo valves, the position control of a pneumatic servo table could be improved. First, the dynamic characteristics of servo valves were examined. It became clear that the characteristics could be described as a second-order system. Then, the servo table system was designed as a fifth-order system. It became clear that the position accuracy of this system were greatly improved.

KEY WORDS

Pneumatic System, Precise Positioning, Servo Valve, Pole Assignment

NOMENCLATURE

a	: acceleration	[m/s ²]	K_{vlv}	: valve gain	[m/(s ² V)]
f	: frequency	[Hz]	s	: Laplace operator	[1/s]
j	: jerk	[m/s ³]	Se	: effective area	[m ²]
K_a	: table acceleration gain	[V/(m/s ²)]	α	: parameter of α - β diagram method	[-]
K_n	: flow rate gain	[m/(s V)]	β	: parameter of α - β diagram method	[-]
K_p	: table proportional gain	[V/m]	ζ	: damping ratio	[-]
K_{ps}	: valve proportional gain	[V/m]	ω_0	: nominal angular frequency	[rad/s]
K_{sv}	: linearized servo valve gain	[m ² /V]	ω_n	: natural angular frequency	[rad/s]
K_v	: table velocity gain	[V/(m/s)]	(suffix)		
K_{vs}	: valve velocity gain	[V/(m/s)]	t	: value of servo table system	
			s	: value of servo valve	
			ref	: reference value	

INTRODUCTION

Precise positioning systems are very important in the fields of semi-conductor manufacturing process. In this region electro-motion systems are widely used, but the heat from the motor disturbs the position controllability and the machining accuracy.

To overcome the heat generation problem, we tried to construct pneumatic precise positioning system. The features of the pneumatic system are little heat and little magnetic field generation. However, the control of this system is very difficult because of the nonlinearity of pneumatic system such as stick-slip phenomena [1] [2].

We have developed a pneumatic servo table system with air bearing. The stick-slip phenomena were overcome by using air bearing. This system reached high positioning accuracy. However, in high gain region, the response of this system becomes unstable. The reason of this unstable response is the dynamic characteristics of the servo valve. Generally in a pneumatic servo system, the dynamic characteristics of the servo valve are neglected. Because the dynamic characteristics of the servo valve is sufficiently high compared to that of the pneumatic servo system.

In this paper, the dynamic characteristics of the servo valve were measured experimentally. It can be described as a second-order system. Therefore, the model of the servo table system considered the dynamic characteristics of the servo valve becomes a fifth-order system. After that, we proposed the design method of the controller of this system. To realize the proposal control method, the servo valve that can be set freely the dynamic characteristics is necessary. Then we developed a novel servo valve, which named as the precise position controllable servo valve.

By considering the dynamic characteristics of the valve, it is cleared that the rapidness and the position accuracy of this system are greatly improved.

PNEUMATIC SERVO TABLE

Pneumatic Servo Table

The pneumatic servo table system is one of a precise positioning system using air power. This system has an air bearing on the sliding surface to reduce friction force. By using an air bearing, this system can control the slider position accurately.

Figure 1 and 2 show the photo and the schematic diagram of this system. This system is constructed from a pneumatic actuator with air bearing, a pair of servo valves and a PC to control system.

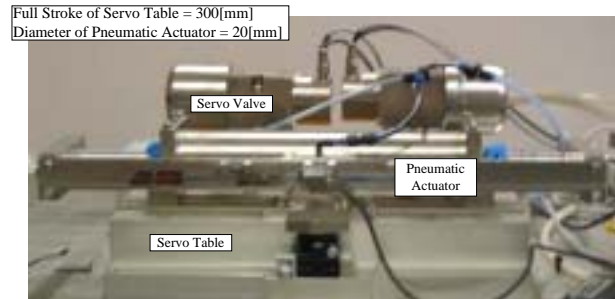


Figure 1 Photo of Pneumatic Servo Table System

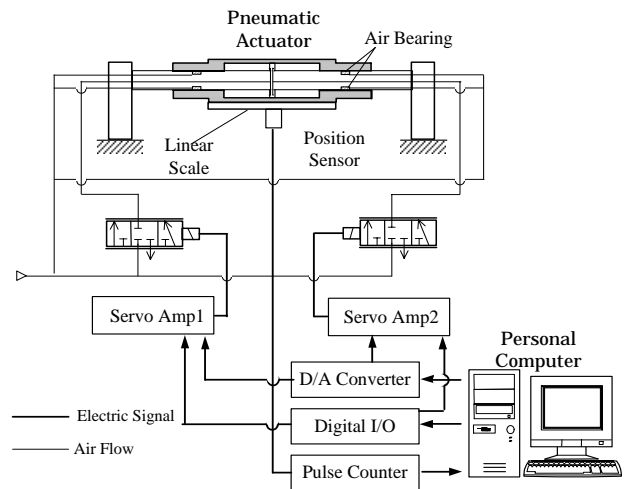


Figure 2 Schematic Diagram of Pneumatic Servo Table System

Third-order Model

From linearized equations of this system, the open-loop transfer function of the pneumatic actuator is given as a third order transfer function [3].

$$P_n(s) = \frac{K_n \omega_n^2}{s(s^2 + \omega_n^2)} \quad (1)$$

The natural angular frequency ω_n is under 60[rad/s]. On the other hand, that of the servo valve ω_{ns} is over 600[rad/s]. From this relation, the dynamic characteristics of the servo valves are negligible. By neglecting the dynamic characteristics of the servo valve, the open-loop transfer function of the servo valve is given by;

$$P_s(s) = K_{sv} \quad (2)$$

A PDD² control method was applied to this system. This control method feedbacks position, velocity and

acceleration. As a result, the closed-loop transfer function in the 3rd-order model is given by [3]

$$G_n(s) = \frac{K_{sv}K_nK_p\omega_{nt}^2}{D(s)} \quad (3)$$

$$D(s) = s^3 + K_{sv}K_nK_a\omega_{nt}^2s^2 + (1 + K_{sv}K_nK_v)\omega_{nt}^2s + K_{sv}K_nK_p\omega_{nt}^2$$

Figure 3 shows the block diagram of the 3rd-order model. We designed the feedback gains by α - β diagram method [4]. By using α - β diagram method, K_v and K_a are dominated by K_p , α and β .

$$K_a = \frac{\alpha K_p^{1/3}}{(K_{sv}K_n\omega_{nt}^2)^{2/3}} \quad (4)$$

$$K_v = \frac{\beta(K_{sv}K_nK_p/\omega_{nt})^{2/3} - 1}{K_{sv}K_n} \quad (5)$$

The parameter α and β are defined from a suitable gain margin and a phase margin. After that, K_v and K_a are dominated by K_p . In this third-order model, the rapidness and the position accuracy are dominated by the value of K_p . To improve these performances, the large value of K_p is required. However, this system becomes unstable in the experiments when K_p is increased.

This unstable phenomenon is considered to be because of the linearization of the system. Therefore, we studied the main factor of this instability. It became clear that the main factor was the dynamic characteristics of the servo valve. Therefore, the control model that considered the dynamic characteristics of the servo valve must be considered.

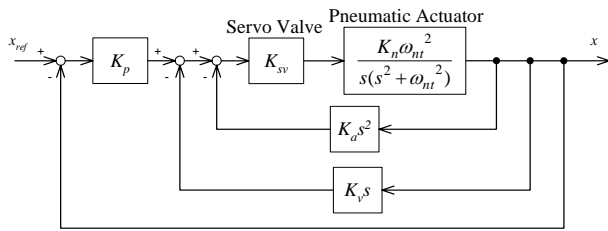


Figure 3 Block Diagram of 3rd-order Model

Fifth-order Model

We measured the dynamic characteristics of the servo valve experimentally. Figure 4 shows the experimental result of the dynamic characteristics of the servo valve made by FESTO MPYE-5-M5-010 B-SA.

It can be described as a second-order transfer function given in Eq. (6).

$$P_s(s) = \frac{\omega_{ns}^2}{s^2 + 2\zeta_s\omega_{ns}s + \omega_{ns}^2} \quad (6)$$

$$\omega_{ns} = 150[\text{Hz}], \quad \zeta_s = 0.35$$

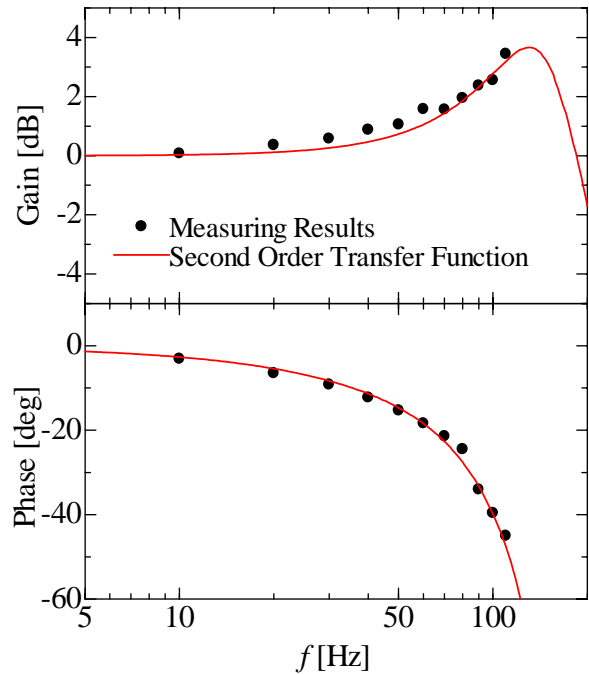


Figure 4 Bode Diagram of Commercially Available Servo Valve

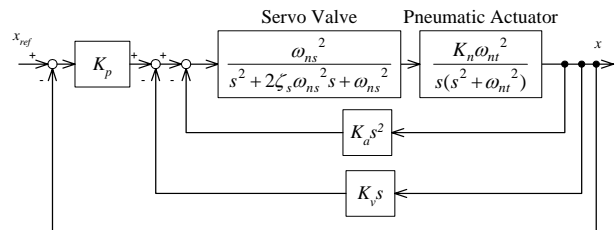


Figure 5 Block Diagram of 5th-order Model

From Eq. (1) and (6), the open-loop transfer function of this system with the dynamic characteristics of the servo valve is derived as a 5th-order function.

$$P_{all}(s) = \frac{\omega_{ns}^2}{s^2 + 2\zeta_s \omega_{ns} s + \omega_{ns}^2} \frac{K_n \omega_{nt}^2}{s(s^2 + \omega_{nt}^2)} \quad (7)$$

Then, the block diagram of whole system is shown as the Figure 5. The closed-loop transfer function is given by

$$G(s) = \frac{K_{sv} K_n \omega_{ns}^2 \omega_{nt}^2 K_p}{D(s)}$$

$$D(s) = s^5 + 2\zeta_s \omega_{ns} s^4 + (\omega_{ns}^2 + \omega_{nt}^2) s^3 + \omega_{ns} \omega_{nt}^2 (2\zeta_s + K_{sv} K_n \omega_{ns} K_a) s^2 + \omega_{ns}^2 \omega_{nt}^2 (1 + K_{sv} K_n K_v) s + K_{sv} K_n \omega_{ns}^2 \omega_{nt}^2 K_p \quad (8).$$

Root Locus on Fifth-order Model

We examined the varying of the pole of this system from the root locus. Figure 6 shows the root locus of this system. From Figure 6, it is cleared that the pole, which dominated by the servo valve characteristics, moves unstable plane when K_p is over 80.

To stabilize this system, a high performance servo valve that can set freely ω_{ns} and ζ_s is required. Then, we developed a novel servo valve which named the precise position controllable servo valve

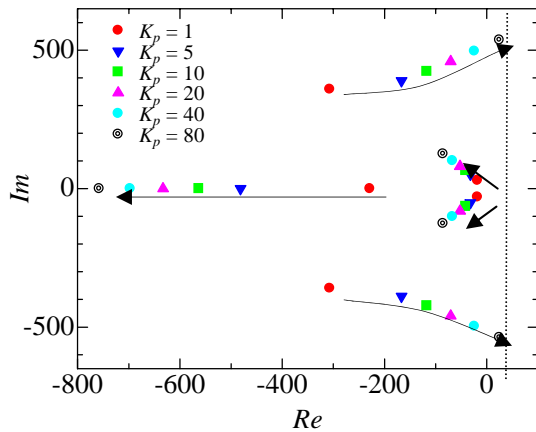


Figure 6 Root Locus of 5th-order Model

PRECISE POSITION CONTROLLABLE

SERVO VALVE

A pneumatic precise position controllable servo valve has been developed[5]. Figure 7 and 8 show the external view and schematic diagram of this servo valve.

To realize high dynamic characteristics, the performance of the displacement sensor to measure the spool position of the servo valve is very important. The resolution of this position sensor is submicron order. Because the friction force of the spool disturbs the controllability of the servo valve, we attached an air bearing to this servo valve.

The control method of this servo valve is the PD-control. Then, the block diagram of this valve is derived as Figure 9. The closed-loop transfer function of this servo valve is given by

$$P_{nv}(s) = \frac{K_{vlv} K_{ps}}{s^2 + K_{vlv} K_{vs} s + K_{vlv} K_{ps}} \quad (9).$$

From Eq. (6) and (9), the control gains are given by

$$K_{ps} = \omega_{ns}^2 / K_{vlv} \quad (10).$$

$$K_{vs} = 2\zeta_s \omega_{ns} / K_{vlv}$$

It is clear that we can design ω_{ns} and ζ_s at a certain value by gain tuning.

The response of this servo valve was examined. In this experiment, ω_{ns} and ζ_s was set 300[Hz] and 0.7. Figure 10 shows the step response of the spool position. The spool position is settled promptly. Figure 11 shows the frequency response of the spool position at the frequency of 50[Hz]. The spool position follows well with the reference trajectory.

Figure 12 shows the bode diagram of this valve. It is cleared that this valve can set ω_{ns} and ζ_s freely as we desired, and the dynamic characteristics are greatly improved compared with the commercially available one (Figure 4).



Figure 7 Photo of Precise Position Controllable Servo Valve

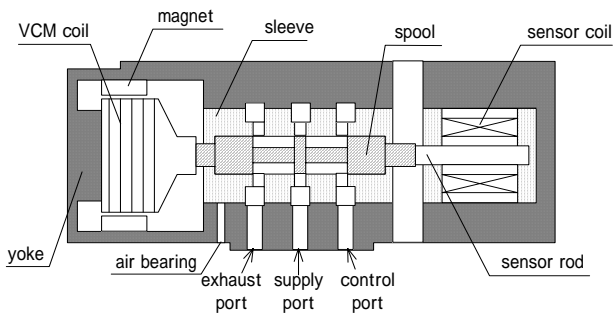


Figure 8 Schematic Diagram of Precise Position Controllable Servo Valve

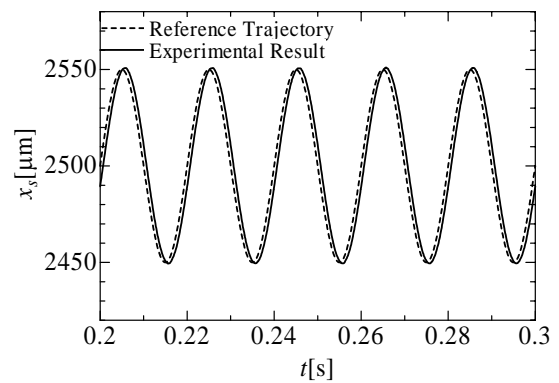


Figure 11 Frequency Response of Developed Servo Valve ($f=50[\text{Hz}]$)

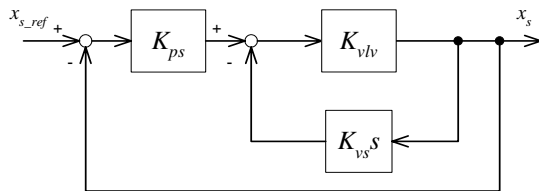


Figure 9 Block Diagram of Developed Servo Valve

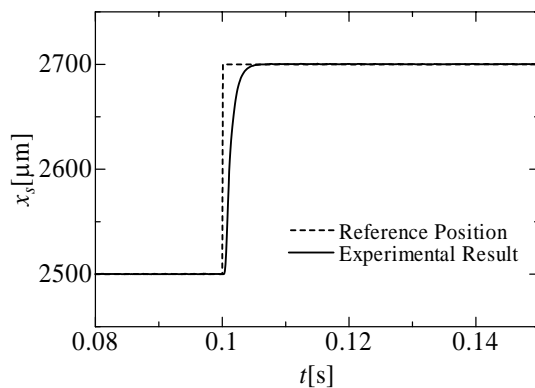


Figure 10 Step Response of Developed Servo Valve

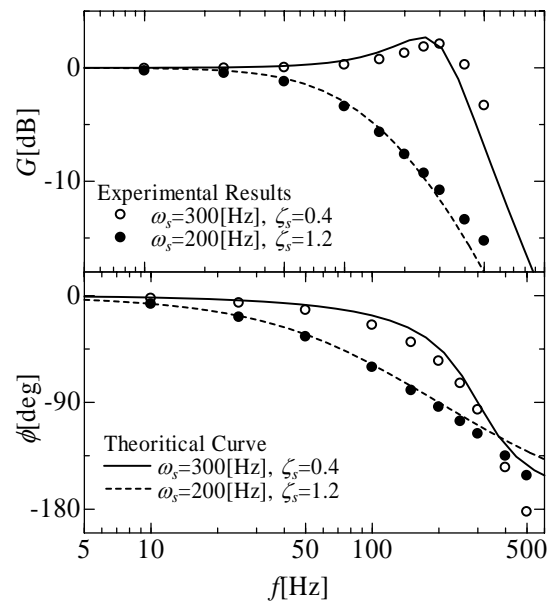


Figure 12 Bode Diagram of Servo Valve

CONTROL METHOD AND EXPERIMENTAL RESULTS

A control method for this fifth-order system was considered. We selected the pole assignment method as ITAE criterion. The ITAE criterion is given by

$$G(s) = \frac{\omega_0^5}{s^5 + 2.8\omega_0 s^4 + 5.0\omega_0^2 s^3 + 5.5\omega_0^3 s^2 + 3.4\omega_0^4 s + \omega_0^5} \quad (11).$$

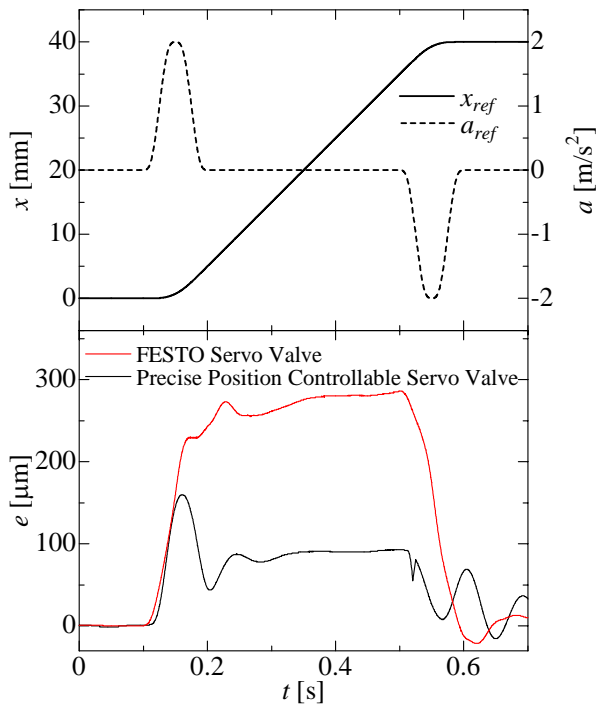


Figure 13 Reference Trajectory and Experimental Results

From Eq. (8) and (11), the dynamic characteristics of the servo valve and the feedback gains of the pneumatic servo table system were determined.

Figure 13 shows the experimental results of the proposal controller and that of the previous control method.

Upper figure shows the reference trajectories of the system. The position reference trajectory is designed as 5th-order curve to control this system accurately. Lower figure shows the position error of the servo table. It is clear that the position error is greatly improved compared with a commercial available servo valve by using ITAE criterion control method.

CONCLUSION

We constructed a pneumatic servo table system considered the dynamic characteristics of the servo valve. It became clear that the dynamic characteristics of the servo valve effects to the performance of the pneumatic servo table.

In this paper we introduced a precise position controllable servo valve. This valve can set freely the dynamic characteristics by gain tuning. We measured the dynamic characteristics of this servo valve. From the dynamic characteristics measurement, it is cleared that the dynamic characteristics of the servo valve is a twice of that of a commercially available one.

We constructed a pneumatic servo table system with the precise position control servo valve. The ITAE criterion pole assignment method was used for the gain tuning of this system.

The position following error of the servo table is reduced by the proposal control method. The maximum position error is reduced to half and the steady velocity error is reduced to one-third. It was shown that the controllability of the servo table is improved by using the precise position controllable servo valve.

We aim decrease of the following error of the servo table by studying better gain tuning method.

REFERENCES

1. Hamiti K., Voda-Besancon A., and Roux-Buisson H., Position Control of a Pneumatic Actuator Under the Influence of Stiction. *Control Engineering Practice*, 1996, 4-8, pp.1079-1088.
2. Uebing M., Vaughan N.D., and Surgenor B.W., Non Linear Dynamic Modeling of a Pneumatic Servo System. *The 5th Scandinavian International Symposium on Fluid Power 2*, 1997.
3. Kagawa T., Tokashiki L.R., and Fujita T., Accurate Positioning of a Pneumatic Servo System with Air Bearings. *Power Transmission and Motion Control*, 2000, pp. 257-268.
4. Nakata, Utility of Third-order Feedback Control (Japanese), 1978, 17-12
5. Takashi M., Kazutoshi S., Takashi S., Toshinori F., Kenji K., and Toshiharu K., Development of Pneumatic High Precision Position Controllable Servo Valve, *Proc. of IEEE/CCA*, 2004, pp.1159-1164.

RESEARCH ON PNEUMATIC POSITION CONTROL SYSTEM BASED ON A NEWLY-DEVELOPED ROTARY ACTUATOR WITH A BUILT-IN BRAKE

Yanhong BAI, Xiaoning LI and Baijun AN

SMC Nanjing Pneumatics Center, School of Mechanical Engineering,
Nanjing University of Science & Technology,
Nanjing 210094, China
(E-Mail: *xnli@public1.ptt.js.cn*)

ABSTRACT

In this paper, a newly developed pneumatic rotary actuator is introduced, which is specially designed for angular position control. The actuator incorporates a built-in air brake and an angular displacement sensor. The basic behavior of the brake is tested. On this basis, for angular position control some control systems are proposed. The first system is the on-off valve-based position control system, which has the advantages of simple control algorithm, easy implementation and lower cost. The second system is the proportional valve position control system with simple PID algorithm, which can reach a required positioning accuracy but with a lower stiffness against disturbance. The third system is the proportional valve position control system with a composite control strategy of PID combined with brake aided positioning, which can reach the same positioning accuracy and no overshoot with disturbance takes place, as compared with the simple PID.

KEY WORDS

Pneumatic rotary actuator; Position control; Brake; Proportional valve; PID algorithm

INTRODUCTION

Currently, there are mainly two approaches to implement the pneumatic position control. One is the pneumatic position servo system, in which the proportional /servo valve or on-off valve is used as a control device. This type of system has not been widely used due to its high cost and low stiffness with the effect of the compressibility of air. Another is the positioning system, in which the pneumatic actuator with brake is used. For this system, the positioning stiffness is higher, but the positioning accuracy is lower. Therefore, it is expected that a new control mode that combines the merits of the above-mentioned control systems would be researched and developed [1-3].

Because of the difficulty in the structure, there is not a market product of pneumatic rotary actuators with brake providing for use.

In this paper, the structure of a newly developed pneumatic rotary actuator with a brake (abbreviated as RAB) is introduced. For further control purpose, the basic property of the air brake is studied. On this basis, the angular position control of the new rotary actuator is demonstrated.

THE STRUCTURE AND OPERATION MECHANISM OF THE PNEUMATIC ROTARY ACTUATOR WITH A BRAKE

Structure of the Rotary Actuator with a Brake (RAB)

As shown in Fig. 1, the developed RAB consists of three components: pneumatic rotary actuator, brake unit and angular position detection unit. The photo of the RAB prototype is shown in Fig.2.

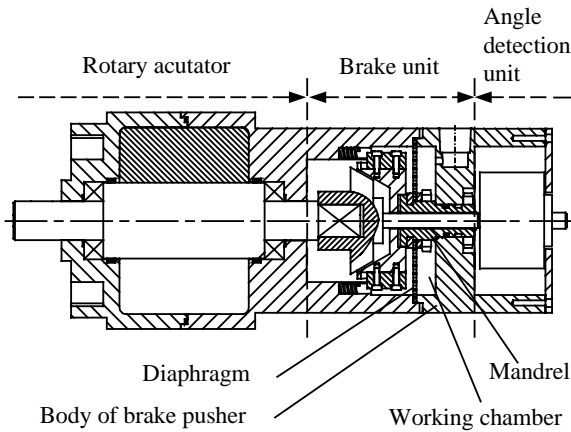


Fig. 1 Scheme of the RAB structure



Fig. 2 Photo of the RAB prototype

In the RAB, the component of the rotary actuator is similar to the structure of an ordinary pneumatic rotary actuator of vane-type. A rotary potentiometer is used as an angular displacement sensor, which is mounted in the component of angular position detection unit. The brake unit consists of a brake operator and a brake pusher. In following sections, the structure and operation mechanism of the brake unit will be introduced in detail.

Structure and Operation Mechanism of the Brake Pusher

As shown in Fig.1, the component of the pusher consists of the diaphragm, the hollow mandrel and the body of the brake pusher. The diaphragm is fixed on the mandrel and the mandrel is fixed on the body of the brake pusher. The diaphragm, the mandrel and the

body of the brake pusher form the working chamber. When pressurized air is charged into the working chamber, the deformation of the diaphragm is produced and a pushing force is exerted on the tapered disc B in the brake operator. If the air is discharged from the working chamber, the deformation of the diaphragm is removed and the pushing force is also removed. In order to measure the shaft speed, a rotary potentiometer should be connected to the shaft of the tapered disc A. So the mandrel is made hollow.

Structure and Operation Mechanism of the Brake Operator

As shown in Fig. 3, the brake operator mainly consists of the tapered disc A, the tapered disc B and the body of the brake operator. The tapered disc A is fixed on the rotary shaft and rotates together with the shaft. The tapered disc B is mounted in the body of the brake operator and its rotation is restricted only with the permission of linear motion along the direction of the shaft.

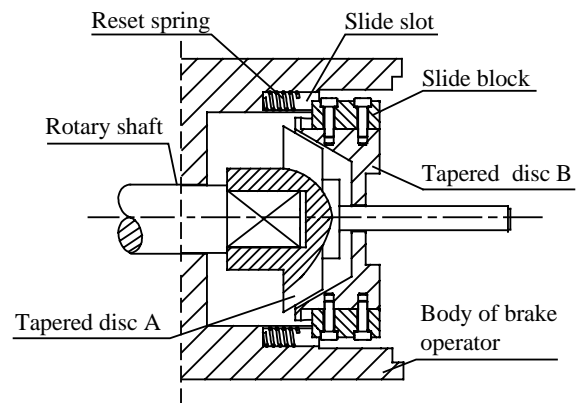


Fig. 3 Scheme of the brake operator

From Fig. 3, the operation mechanism can be illustrated. When tapered disc B is pushed by the diaphragm in the pusher component (see Fig. 1), it moves along the axial direction and exerts a force on the tapered disc A, so as to generate a friction torque on the shaft through the tapered disc A. The shaft rotation will be reduced or ceased with the torque. When the pushing force of the diaphragm is removed, the diaphragm will restore its initial state and the tapered disc B will return its initial position with the action of the reset springs.

HOLDING TORQUE OF THE BRAKE

Theoretical Analysis of the Holding Torque of the Brake

(1) Holding torque of the brake operator

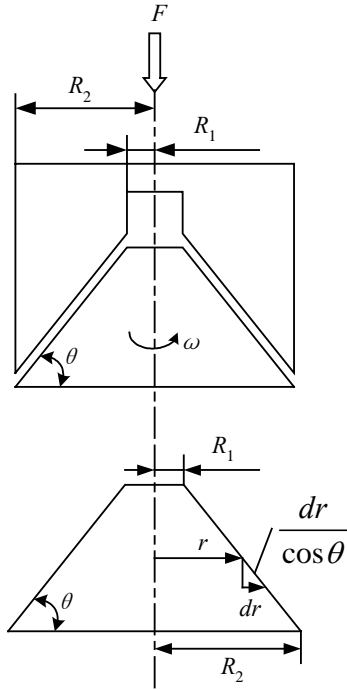


Fig. 4 Friction torque analysis of the tapered disc

The holding torque of the brake operator is the friction torque on the two conical surfaces of the tapered discs. According to Fig. 4, the pressure vertically exerted on the conical surface can be expressed as

$$p = \frac{F}{\pi(R_2^2 - R_1^2)} \quad (1)$$

Therefore, the friction torque on the conical surfaces exerted by the pushing force F is derived as

$$M = \int_{R_1}^{R_2} \frac{\mu p}{\cos \theta} 2\pi r^2 dr = \frac{2\mu F (R_1^2 + R_1 R_2 + R_2^2)}{3 \cos \theta (R_1 + R_2)} \quad (2)$$

Where θ is inclined angle of the conical surface, R_1 is top radius of the tapered disc A, R_2 is bottom radius of the tapered disc A, F is axial pushing force and μ is friction coefficient.

Eq. (2) indicates that the holding torque of the brake operator is proportional to the axial pushing force.

(2) Pushing Force of the Brake Pusher

The pushing force exerted by the brake pusher comes from the deformation of the ring diaphragm with the compressed air. The force analysis of the deformation of the diaphragm with small deflection is shown in Fig.5.

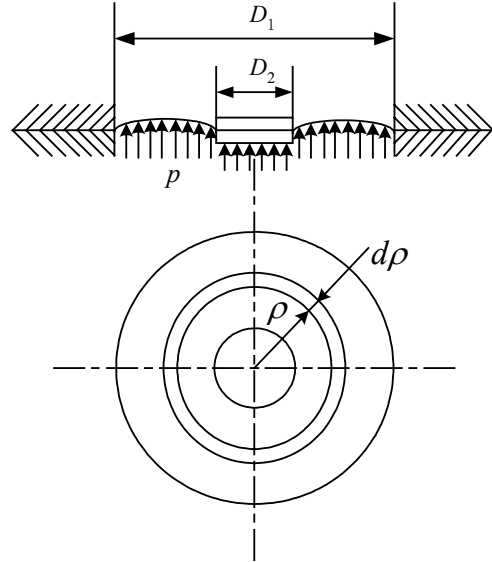


Fig. 5 Force analysis of the diaphragm

According to Fig.5, the pushing force produced by the diaphragm can be derived as

$$F = \int_{D_2/2}^{D_1/2} p \frac{D_1 - 2\rho}{D_2 - 2\rho} 2\pi\rho d\rho = p \frac{\pi}{12} (D_1^2 + D_1 D_2 - 2D_2^2) \quad (3)$$

Where D_1 is diameter of the working chamber, D_2 is diameter of the mandrel and p is air pressure in the working chamber.

Eq. (3) indicates that the pushing force produced by the diaphragm is proportional to the pressure in the working chamber. From Eq. (2) and (3), it can be seen that the holding torque of the brake is proportional to the pressure in the working chamber.

Experiments of the Holding Torque of the Brake

Experiments are carried out to measure the relation of the holding torque and the supply pressure. The measured curve is shown in Fig.6. From Fig. 6, it can be seen that the holding torque is approximately proportional to the supply pressure in the working chamber. This indicates that the experimental result is coincident with preceding theoretical analysis.

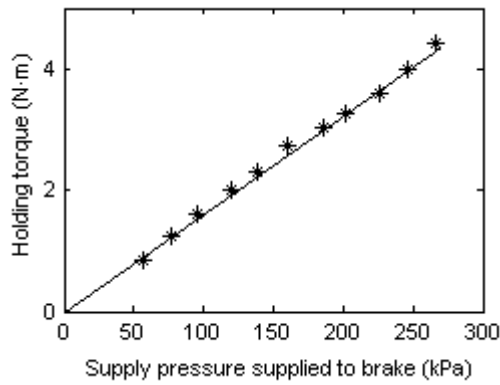


Fig. 6 Holding torque versus supply pressure in the brake working chamber

POSITION CONTROL OF THE RAB

RAB Position control system based on on-off valve

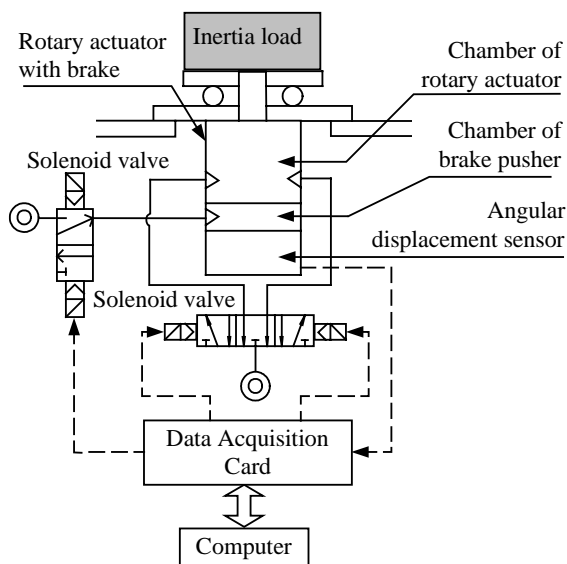


Fig. 7 Schematic constitution of the position control system based on on-off valve

As shown in Fig. 7, an on-off valve-based position control system is built up, in which ordinary solenoid valves are used for controlling the rotary actuator and the brake. Considering the response time of the solenoid valve and the braking distance of the brake, the actuator will continue to rotate for a certain time interval after the stop signal is sent. The rotating angular distance of the actuator within this time interval is defined as overrun-distance.

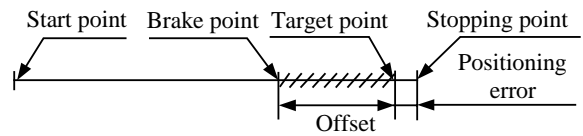


Fig. 8 Schematic of the positioning process with offset compensation method

Therefore to remove the practical influence on the accurate positioning, an offset compensation method is proposed. From Fig. 8, the principle of the offset compensation method can be illustrated. When the actuator rotates to certain position ahead of the target point, the stop signal is sent in advance. Thus the system will stop near the target point with less positioning error. Experiments are conducted with different loads and target positions. The measured positioning errors with 5 kg load are listed in Table 1.

Table 1 Positioning error measured with 5 kg load

Speed(°/s)	224			418			739		
Target position (°)	90	150	240	90	150	240	90	150	240
Positioning error (°)	0.26	0.25	0.48	0.78	0.91	0.02	1.18	0.13	0.33

Experimental results show that the positioning error is within the range of $\pm 2^\circ$ if the target rotary angle is beyond 90° . However if the target rotary angle is smaller than 90° , the speed of the actuator is unsteady in its running and the compensation value is difficult to be given. Experimental data involving this part has not listed yet. To improve the control performance with the smaller rotary angle, further research work is needed.

It can be seen that the position control system based on on-off valve has advantages of simple control algorithm, easy implementation and lower cost.

Position control system based on proportional pressure valve

In proportional valve-based position control system, two proportional pressure valves are used for controlling the pressure in the chambers of the rotary actuator. A solenoid valve is used for controlling the brake, as shown in Fig. 9.

To improve the performance, another control mode is explored. For this control mode, a composite control strategy of PID algorithm combined with brake aided positioning is adopted. As we know, the actuator would be decreased to a lower speed when it approaches the target points with PID control mode and could acquire a higher positioning accuracy. In this case if the actuator rotates at a low speed, the effect of the brake could be sufficiently obtained. This feature can

be utilized to form the basis of the composite control strategy, i.e., PID control algorithm combined the method of brake aided positioning.

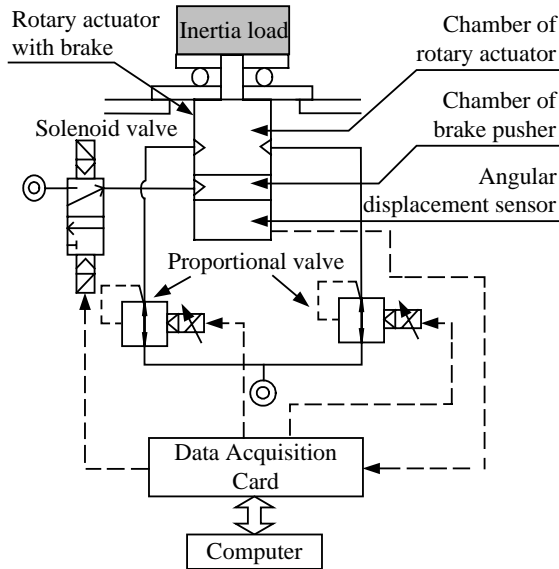


Fig. 9 Scheme of the position control system based on proportional pressure valve

We can describe the positioning strategy in detail. First, PID control algorithm is used for controlling the motion of the rotary actuator. Then, as the system enters into quasi steady state, the brake is operated to make the system into the steady state quickly, at the same time, PID algorithm is ceased and the proportional valves are switched off. The quasi steady state is defined as the state in which the error is kept within the desired precision range during a time interval.

The step response of the system with external force disturbance is shown in Fig. 10. From Fig. 10, it can be seen that with PID control the positioning precision is higher but there exists larger overshoot with disturbance. Adopting PID control strategy combined with brake aided positioning, the same positioning accuracy can be obtained and no overshoot with disturbance takes place, as compared with simple PID algorithm.

CONCLUSIONS

For meeting the practical requirement of a pneumatic rotary actuator with brake in industrial automation systems, a new pneumatic rotary actuator with brake (RAB) is developed and introduced. Based on this RAB, some control systems are presented and tested. The first one is the on-off valve-based position control system, which has the advantages of simple control algorithm, easy implementation and lower cost but with the default of low accuracy. To increase the

positioning accuracy, another proportional valve-based position control system with simple PID algorithm is presented, which can reach a required positioning accuracy but with a lower stiffness against disturbance. To improve the performance against disturbance, the third system is presented, which is the proportional valve position control system with a composite control strategy of PID combined with brake aided positioning. Experiments have shown that the system with the composite control strategy can reach the same positioning accuracy and no overshoot with disturbance takes place, as compared with simple PID algorithm.

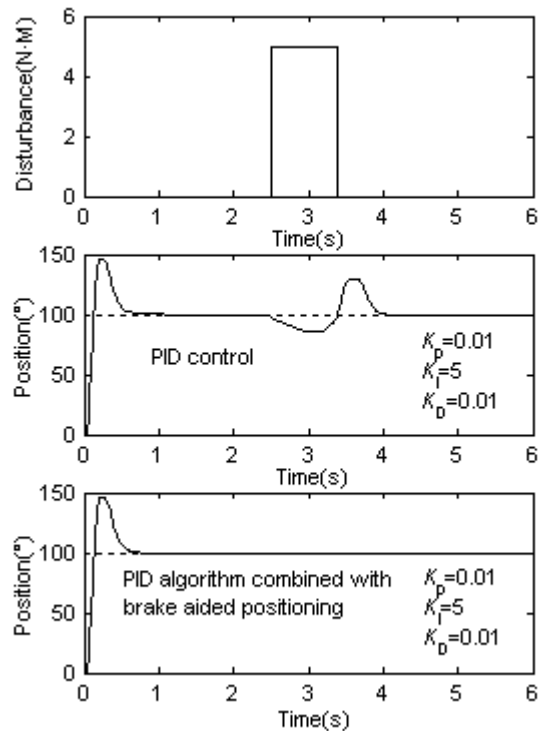


Fig. 10 Step response with external disturbance

REFERENCES

1. Wang, J., Pu, J. and Moore, P.R. Practical control strategy for servo-pneumatic actuator systems. *Control Engineering Practice*, 1999,7-12, pp. 1483-1488.
2. Van Varseveld, R. B. and Bone, Gary M. Accurate position control of a pneumatic actuator using on/off solenoid valves. *IEEE/ASME Transactions on Mechatronics*, 1997,2-3, pp.195-204.
3. Peng Guangzheng, Cheng Ping and Zhao Tong. A PWM Position Control System of Cylinder with a Built-in Brake. *Journal of Beijing Institute of Technology (in Chinese)*. 1999,19-3, pp.334-337.

Frictional energy analysis of a vane-type air pump for assisting paper handling via air flow in offset printing machines

Tadahiro UEKI * , Kazuo INABA ** and Junji SHIBATA ***

* Department of mechanical engineering ,Faculty of Engineering
Shibaura Institute of Technology
3-9-14, Shibaura, Minato-ku, Tokyo,108-8548 Japan
(E-mail: ueki@sic.shibaura-it.ac.jp)

** Napico CO.,LTD
1-16-10 Minamiooi Ota-ku, Tokyo,140-0013 Japan
***Management of Technology
Shibaura Institute of Technology
3-9-14, Shibaura, Minato-ku, Tokyo,108-8548 Japan

Today, the technical subject for the air pump used in the offset printing machine is to reduce sliding friction and wear of vanes. If we could improve the energy efficiency, we could successfully design a smaller air pump with a longer life. In this paper, first of all, total power consumption of the air pump was measured by axial torque and analyzed according to components of a frictional force. As a result, it was found that most of the power is consumed at the sliding face between vanes and housing cylinder in the air pump. The power increases significantly due to the sliding friction between the vanes and their guide slots of the rotor, especially when the vanes are forced to move inward. On the basis of these results, the importance of the sliding friction of the vanes was confirmed quantitatively and the arising mechanism of the sliding friction of a vane against the slot face of the rotor was investigated theoretically as well as experimentally, and finally, we proposed some counter measures to reduce the sliding friction of vanes.

1. Introduction

A Rotational moving-vane-type air pump for suction-blow (it is henceforth called an air pump for short) has a feature in operating two functions, suction and blow, by one set of pump. This air pump has a process of a suction and blow of air in a rotation of the rotor (one cycle), and this function has been utilized for handling papers in printing equipments as a source of air. For example, the air pump contributes to reducing the energy loss because the piping length can be shortened, also the air pump can adjust the pressure and amount of flow precisely. Therefore this air pump becomes the indispensable equipment to support the transfer and separation of papers in factories.

However the temperature of an air pump becomes 70 ~ 100 °C during the long running time and continuous operation and the lubricant oil becomes mist by the increase of the evaporation pressure and higher degree of vacuum. The mist of the lubricant oil becomes the source of the air pollution to damage the working environment and may produce the

inferior goods by sticking to the papers. Also it has lately drawn attentions that the worn-out lubricant oil becomes the industrial waste.

In the context of the facts shown above, a non-lubricant type dry air pump has drawn attentions and started to be developed and some have been already commercialized. However there are several technical problems such as excessive generation of heat and noise, and the increase of the power consumption. Furthermore the papers tend to be polluted by the carbon powder due to abrasion in exhaust air because the vane for dry air pump is made of carbon and also the structure of dry air pumps follows that of the conventional lubricious air pump. Eventually it is necessary to install the air filter in order to remove the carbon powder in air.

Although the importance of the characteristics of friction between the vane and the housing cylinder face for dry air pumps is commonly recognized, the pronounced rational solution has not been found because it is difficult to measure and observe the vane friction inside in a sealed housing.

There are some references ⁽¹⁾ which describe the

analysis of the dynamics about the motion of vanes in the oil pump whose structure is similar to the air pump, however it is not easy to presume the motion of the air pump from phenomena of oil pumps because there are clear differences between oil and air in terms of sliding conditions, pressure, etc... Therefore the systematic investigations on the motion of a vane and the characteristics of friction for the air pump are strongly required.

2. The objectives of the present research

Although the objectives of the present study are to obtain the basic data for the development of a dry air pump, the present paper describes the conventional lubricous air pump focusing on the mechanism of the behavior of the vane.

In fact, housing temperature of a dry air pump rises significantly due to the friction at the sliding area by the action of the vanes. However, authors consider

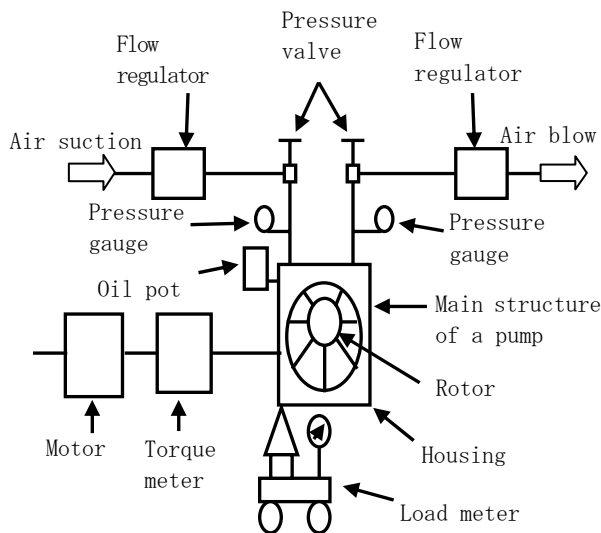


Fig.1 Constitution of the experimental system

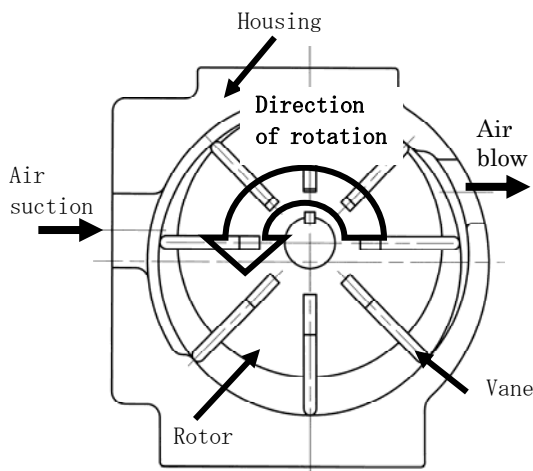


Fig. 2 Structure of a vane pump

that there is basically no difference in the mechanism of the behavior of vanes between the conventional lubricous air pump and the dry air pump. Therefore, the first step should be to clarify the mechanism of behavior of vanes with the conventional lubricous-type air pump which gives less temperature affection to the experiments. The quantitative analysis of the characteristics on the friction between the vane and housing at the sliding area in the lubricous type air pump may reveal the knowledge which contributes to obtain the fundamental view to improve the performance of the dry air pump.

3. Experimental arrangement

The friction force which is consumed between the vanes and housing was measured and analyzed based on the experimental data; i.e. the ratio of the friction component in the entire torque consumed, the effect on the friction of the vanes by the air pressure in the front room and the back room of the vane during the suction and exhaust, and the behavior of a vane which go in and out along the rotor slot.

Although the present study deals with the commercial air pump (Napico Ltd., suction pressure: 0.5kPa, exhaust pressure: 0.5kPa, air flow:300 l/min, total number of vanes: eight sheets), several parts have been modified in order to separate and measure the friction force at the sliding area. They are followings. First of all, the structure of a rotor and housing is rebuilt in rotating independently. A strain gauge which measures the operating torque between the motor and the main axis and also the strain gauge which measure the friction are mounted between the vane and housing at the sliding area. The sheath type

Table.1 Machine specifications and material

Specifications of air pump			
	Suction	Blow	
Pressure kPa	-60~0	0~60	
Flow rate l/min	100~260	260~240	
Rotation speed r. p. m	550 ~ 750		
Vane	Material	FC250	Hardness HB182
	Processing method		Milling machine Lathe
	Mass g	Plane	116.4 g
		Grooved	116.0 g
Housing	Material	FC250	Hardness HB280
	Processing method		Honing

thermocouple was mounted to the upper part of the housing for measuring the average temperature of the entire system. Fig 1 shows the experimental setup for the present study and Fig 2 show the description of the main structure of the air pump. The table 1 indicates the specifications and the materials of the pump used for the present study.

There are two kinds of the arrangement for the vanes. First of all, the number of the vanes is increased one by one following the order of the position of rotor slots. Second arrangement is that two vanes and four vanes are symmetrically mounted

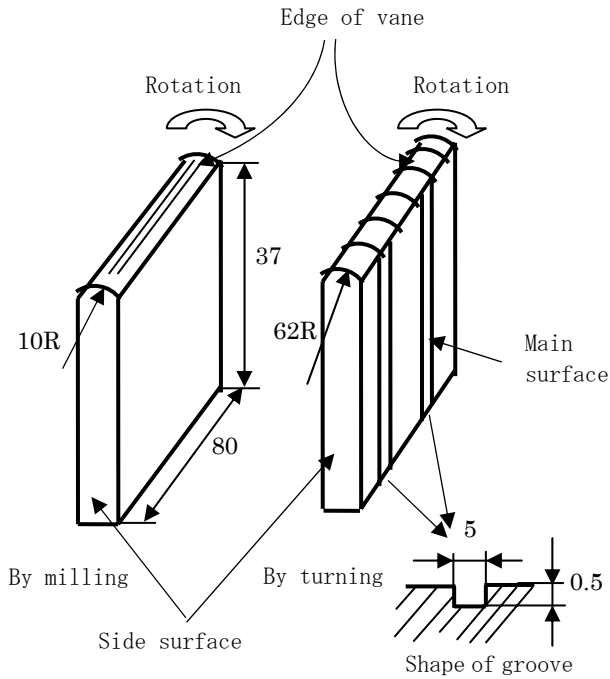


Fig. 3 Form and surface of a vane

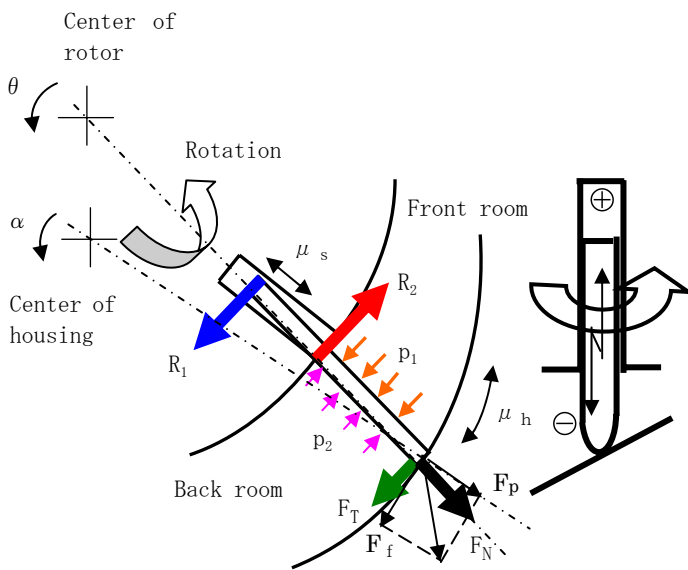


Fig. 4 Dynamic model for a vane movement

respectively about the axis. The number of rotation is increased by every 50rpm from 550rpm to 750 rpm and the experiments were carried out and followings were measured; ①the operation power of an air pump without the vanes.(the main power should be the friction consumed in the bearings which was about 0.7N for the present study), ②the friction between vanes and housing at the sliding area(it is measured as “the operating power of an air pump – power loss by bearings”), ③ the maximum temperature of the housing (measured by the thermocouple), ④the flow rate and pressure of the air blow and the air suction (measured by the ultra-sonic flux gauge and pressure gauge).

Fig 3 shows the shape of cast iron vanes. It is depicted that there are two different types of vanes; one of them has two grooves (depth 0.5mm×width 5mm) and the other has no grooves. This grooves is designed for penetrating the pressure of the bottom of the rotor slot to the vane room. The top of the vane which is the contact area was manufactured by a milling machine (curvature: 10R) and by a lathe (curvature: 62R) and the two kinds of curvatures were formed unwillingly due to the limitation of the manufacturing technique.

4. Statics analyses of a vane

The external force (Normal force F_N and Tangential force F_T to a vane main face, or Contact force F_c and Frictional force F_f to sliding surface) was expected to act to the rotating vane from the sliding surface as shown in Fig.4.

The frictional force F_f can be expressed as follows;

$$F_f = \mu \cdot m \cdot \left\{ \rho(\theta) - \frac{h}{2} \right\} \cdot \left(\frac{2\pi \cdot n}{60} \right)^2 \cdot \cos(\alpha - \theta) + \mu \cdot (\mu \cdot R_1(\theta) + \mu \cdot R_2(\theta)) \dots \dots \dots (1)$$

By solving the equations, the sliding friction F_f can be expected to be a function of the rotating angle θ of a rotor. For example Fig 6 shows the calculated value of the friction by neglecting the friction between the vane and a guide slot of a rotor, where we assumed that the sliding friction is generated only by the centrifugal force. The mass of a vane is about 0.0119 N and the centrifugal force at the number of rotation 650 r.p.m can be about 3.5N (maximum) ~ 2.3N (minimum) and up to 2.8N (the average). Here, by assuming the frictional coefficient between a vane and housing as $\mu=0.2$, the average sliding force (frictional force) P_{cal} becomes about 0.28N.

The fluctuation of the friction force in one rotation shows a sine curve. This is due to the eccentricity of the centre of the rotor and the accompanied change of the normal component of the force to the housing surface; in any case this fluctuation is small. On the

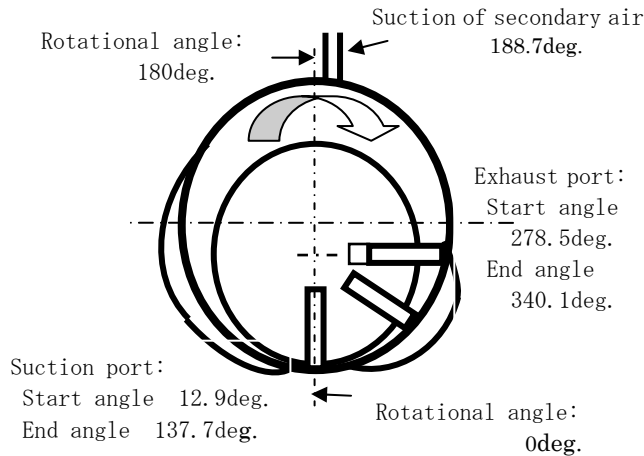
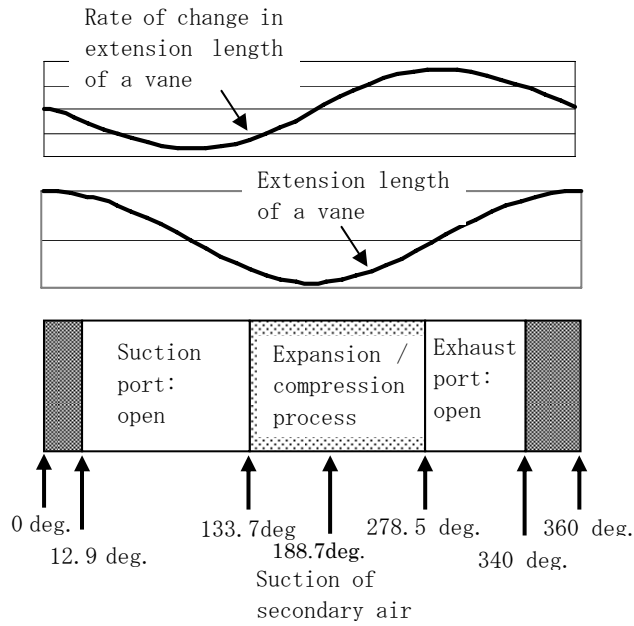


Fig. 5 Rotation angle of a rotor and pumping actions

other hand, it is confirmed that the absolute value and changing component are remarkably different from experiments as describe in the next section. It could be estimated that the friction at the clearance ($\mu R_1, \mu R_2$) between a vane and a rotor slot affects the sliding friction force of the vane F_t . For example, Fig 6 shows the sliding force on the housing cylinder by assuming the coefficient of the sliding friction along the guide slot of a rotor μ_s . The absolute value increases remarkably compared with the value for $\mu_s=0$ and the fluctuation curve becomes a sine wave with a rotating cycle. Also it becomes clear that the pattern of the fluctuation and phase is similar to the measured ones.

5. Result and Discussion

5.1 Performance of the air pump with one vane

Fig 5 shows the relation between the process of

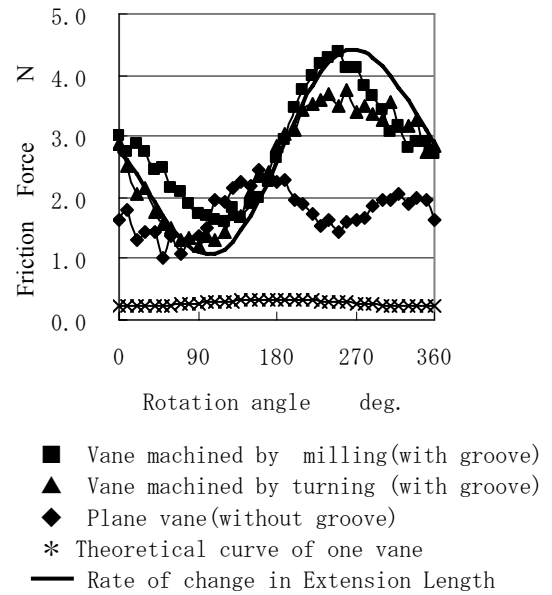


Fig. 6 Friction force for one vane which are machined by different processing methods

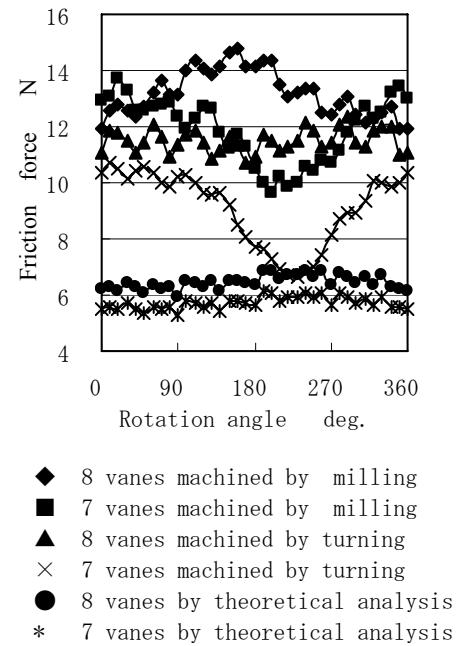


Fig.7 Comparasion of sliding power for 7 or 8 vane by different processing methods

suction and exhaust of an air pump corresponding to the rotating angle θ to the housing. While the vane goes in and out along the sliding surface of the housing cylinder in one rotation and operates the suction and exhaust by changing the volume of the vane room, the sliding force between the vane and the housing is fluctuated. At the moment, experiments by one vane provides the crucial

fundamental information for analyzing the resistance of the sliding vane because the pressure in the vane room does not change for one vane. The numerical shown in the same figure indicate the rotational angle (CCW) of the rotor whose basic point is the position of the minimum clearance between the rotor and housing.

Fig 6 shows the measured friction force at the sliding area between the top of vane and the housing cylinder, and calculated friction force by centrifugal force, together with protruding length of the vane.

There are clear similarity and difference for the vanes with and without grooves. The value becomes smaller for the vane without grooves and the value becomes larger near the exit of the exhaust, also there seems no repeatability and stability in the characteristics in case of the flat (without grooves) surface. This is because the sealed space enclosed by the rotor slots and the bottom of the vane causes the change in friction force which is affected by the vane pressure against the sliding area of housing, preventing the vane motion of going in and out due to the change of the pressure in the sealed space.

The motion of the vane without grooves is difficult to follow the centrifugal force by the rotation. This might be the reason why the sliding force is nearly constant. On the other hand, the vane with grooves shows a large periodical change in the sliding force which follows the change of the protruding amount of vanes. Similarly this change shows the similar tendency which does not depend on the roughness of the machined top surface of vanes. This change of the vane with grooves shows the tendency which is similar to the change ratio of protruding length of the vane as described in the previous section. The sliding force decreases at first and then increases with the rotating angle of the rotor from 0 to 180°. This is because the sliding force decreases at first because the vane is difficult to move with the rotating angle of rotor and then it begins to increase just after it started to move. The sliding force increases at first and then decreases in the rotating angle of 180 ~

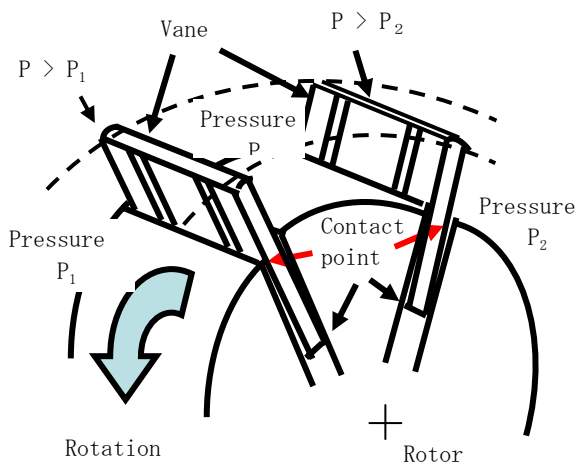


Fig. 8 Explanatory diagram of room pressure enclosed by a rotor and vanes

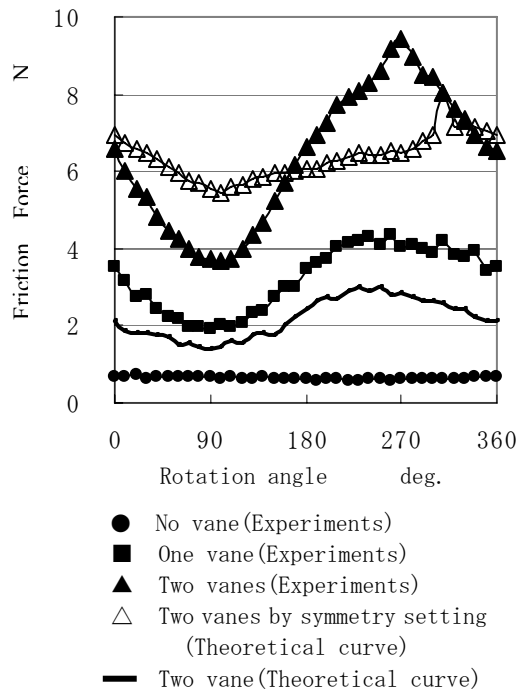


Fig.9 Relation between vane number and friction force of vanes

360°. The reason of the increase of sliding resistance is that larger protruding length of a vane hooks the corner of the rotor slot and prevents insertion and eventually the force is increased. Also the reason why the sliding force is decreased is that smaller protruding length of a vane becomes difficult to hook the corner of the rotor slot with the less effect of the pressure in the vane room. In any case it can be concluded that the effect due to the sealed space enclosed by the rotor slot and the bottom of the vane plays an important role.

5.2 The performance of the air pump with two and more vanes.

Fig 6, 7 and 9 show the relation between the number of vanes and the friction force. These figures show the fact that with rotating angle of the rotor, the minimum value of the sliding power against housing cylinder becomes larger with increase of the number of the vane. The reason why the sliding power decrease near the position of the exhaust port is that there is no resistance at the top of the specified vane because the vane is added one after another backward to the rotating direction of vane. Fig 7 shows the sliding power in terms of the rotational angle for the seven and eight vanes with grooves. As shown in the figure, there is no difference between vanes machined by the milling and lathe, and the sliding power of the housing is kept constant when the number of the vane is eight. On the other hand the sliding power start to decrease when the angle of the rotor is about 180 degree. This is because the

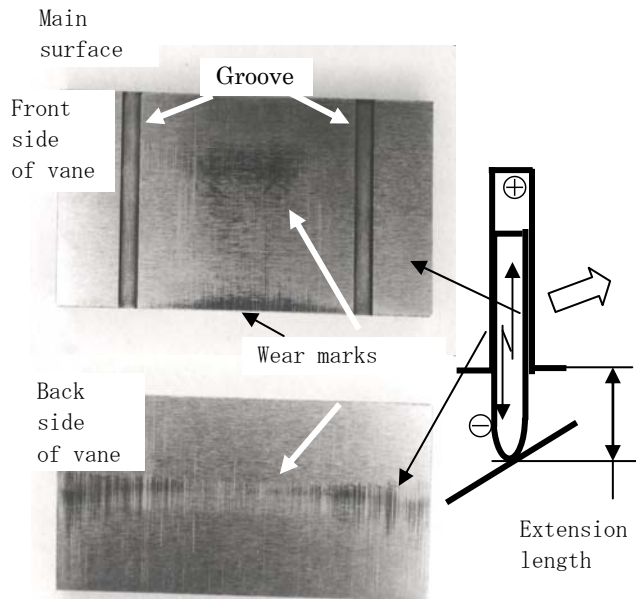


Fig. 10 Wear marks on both sides of a vane

volume of the advanced vane room is twice as large when the setting position of a vane is 0 degree. Also the sliding resistance decreases due to the decrease of the pushing power of the vane by the pressure in the vane room when the advanced vane passes the starting location of exhaust port (as shown in Fig 8).

Fig 9 shows the comparison of the sliding resistance of one and two vanes which are machined by lathe and have grooves. There are three patterns for the setting of two vanes, they are ①next to the slot of the rotor ②every other of the slot of the rotor ③axial symmetrically. In case of the sliding power, the two vanes which are set in one every other and that which are set continuously have same tendency as that for one vane. However in case of the symmetrical two vanes, it has completely different tendency whose fluctuation is smaller and shows the constant value. This is due to the averaging effect of the sliding power when the going in and out of the vane happened in the same phase for the axial symmetrical case.

The two vanes which are located next together and one every other show the clear difference in the sliding power against the housing cylinder. This is because the action of vacuum and compression are produced in the vane room enclosed by the two vanes. It can be assumed that the resistance of inward and outward-movement of the vane increases when the sliding face of the rotor slot and the corner of the rotor slot contact together with the vane which is pushed toward the direction of the next room when the pressure difference of adjacent vane rooms and sliding resistance between the surface of the housing and the corner of the rotor slot are added. In fact, under such a operating condition, wear marks are produced within a short time elapsed as shown in Fig

10, therefore the assumption would be reasonable.

The volume of the vane room is different twice as large for the two vanes next together, compared with the vanes one every other. Therefore it can be concluded that the effect of the pressure difference is caused by the ratio of the vane room capacity.

The bottom space of the vane depends on the vanes with and without-groove of the main face. This follows the same reason as for one vane.

Also it can be considered that the depth of the protruding and insertion of the vane affects the vane motion of going in and out. It is evident as shown in equation (8) that the protrude height of $e(\theta)$ is the factor to affect the reaction R_1 and R_2 . And it is also similar when the vane insert to the slot of rotor. Practically, however, it is strongly dependent on the sliding resistance rather than the height of the protruding as denoted before.

6. Conclusion

The authors discussed vane behaviors and frictional energy of a air pump experimentally as well as theoretically.

The results obtained in the paper are as follows:

(1) Most of the power of the air pump is consumed by the friction between vanes and a rotor as well as between the housing and vanes.

(2) The most important factor for the power consumption of the air pump is the friction between vanes and a rotor slit, which are influenced by reaction forces acting at the inlet corner of a rotor slit and an edge of a vane blade which contact the slit face of a rotor.

(3) Friction force between vanes and housing slide face is affected negligibly small by centrifugal force of vanes during the rotor rotation.

References

1. Ueno, Kataoka, Morimoto : Research (Friction Torque Characteristic by 2nd News Vane) on Characteristic of Amount Type Vane Pump of Good Changes, Oil Pressure and Air Pressure, 9-1, 38-45 (1978)
2. Friction Torque Characteristic of Inaguma and Hibi: Vane Pump, Oil Pressure and Air Pressure, 25-7, 81-87 (1994)
3. Ueki Tadahiro, Inaba kazoo, Shibata unji: Basic Research (the 2) about Vane of Vacuum and Press Pump, and Housing Wear, Collection of Japanese Tribology Meeting Drafts, 95-96 (2002-5)
4. Ueki Tadahiro, Inaba kazoo, Shibata unji: Basic Research (the 3) about Vane of Vacuum and Press Pump, and Housing Wear, Collection of Japanese Tribology Meeting Drafts, 63-64 (2002-10)
5. Ueki Tadahiro, Inaba kazoo, Shibata unji: Vane Friction Action of Movable Vanes Type Suction and Ventilation Air Pump Machine, Japanese Froude Power System Heisei 15 Spring Lecture Meeting, 105-107 (2003-5)

An Experiments and Characteristics Analysis of the Sealless Cylinder

Dong Soo Kim*, Sang Kyu Bae* and Young Cheol Kim **

* IT Machinery Research Center, Korea Institute of Machinery & Materials
171 Jang-Dong, Yuseong-Gu, Daejeon, Korea
(E-mail: kds671@kimm.re.kr)

** e-Engineering Research Center, Korea Institute of Machinery & Materials
171 Jang-Dong, Yuseong-Gu, Daejeon, Korea

ABSTRACT

This paper shows a performance analysis for conical type sealless cylinders and rod bearings. The pistons without seal have partly cylindrical and conical shapes. 2 dimensional Reynolds equation and FD(finite differential) numerical techniques are utilized for the performance analysis. The relationship among self-centering forces and leakage flows are investigated. Also, optimal design values for a sealless cylinder are presented. A prototype of sealless cylinder which had rod bearing with four pockets, five pockets, and six pockets was manufactured respectively. Leakage flow test is conducted to evaluate performance of piston and rod bearing in sealless cylinder.

KEY WORDS

Sealless Piston, Pneumatic Cylinder, Reynolds Equation, Self-Centering Force, Leakage Flow

NOMENCLATURE

Q_1, Q_2, Q_3 : Supply flow
 Q_A, Q_B, Q_C : Leakage flow
 h_1, h_2 : Membrane thickness
 c_1, c_2 : Clearance between piston and cylinder
 p_s : Internal pressure
 p_a : Atmosphere pressure
 L : Length of piston
 E : Eccentricity
 \dot{m} : Leakage flow

1. INTRODUCTION

Because the general cylinders use sliding seal, it causes the high friction force and adherence phenomenon when it operates in low speed, and the use of the cylinders is not proper in the clean room and high temperature and high pressure environment.

Accordingly, in this study, sealless cylinder attaching conical-type piston without seal is proposed to complement the handicap. This technology can be widely applied to servo actuator responding highly speedy and precise linear movement.

Fig. 1 shows the basic structure of the sealless cylinder. Piston A is composed of two parts of conical portion and cylindrical portion, and it has symmetry structure based on outlet groove in middle area. When the pressure is applied to inside of cylinder, self-centering

force happens, which becomes stronger when the piston moves to left and right sides reciprocally. Therefore, it has a function of composition bearing in which both static pressure effect and dynamic pressure effect act together. Part B is static gas pressure-supporting rod bearing, and Part C has the same function as plane seal. The following correlation can be drawn from flow conservation law.

$$Q_1 + Q_2 + Q_3 = Q_A + Q_B + Q_C \quad (1)$$

Sealless cylinder was originally proposed by Guido Belforte[1][2], he predicted the performance by deriving the approximate solution of 1D Reynolds equation for the non-moving cylinder. On the contrary, in this study, 2D Reynolds equation for reciprocal moving sealless cylinder was derived and the solutions were obtained by finite difference method, and then the optimized design conditions were proposed by performing the performance analysis of piston and rod bearing. Finally, feasibility of the design is verified by measuring the leakage flow after manufacturing of the test products.

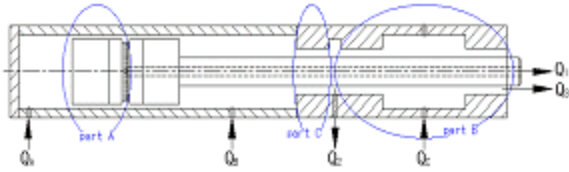
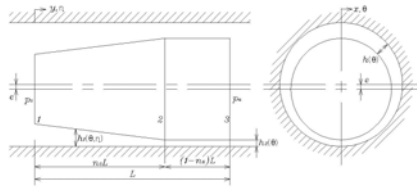
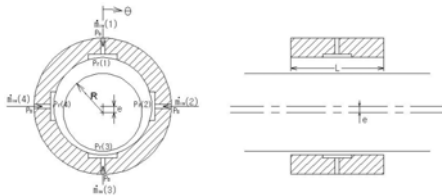


Figure 1 Sealless pneumatic cylinder



(a) Conical type piston



(b) Rod bearing

Figure 2 Geometry of the sealless cylinders

2. THEORY ON PERFORMANCE ANALYSIS

2.1 Performance analysis of piston

For performance analysis of sealless cylinder, conical type piston and rod bearing type are proposed as seen in Fig. 2(a),(b). Piston is composed of conical portion and cylindrical portion, high pressure, p_s , are acted on the side (face 1) and atmospheric pressure, p_a , are acted on the opposite side(face 3)

The thickness of air layer between piston and cylinder is as follows.

$$h_1 = c_1 + e \cos \theta \quad (0 \leq y < n_s L) \quad (2)$$

$$h_2 = c_2 + e \cos \theta \quad (n_s L \leq y \leq L) \quad (3)$$

Where, c_1 and c_2 represent the gaps at each position in radial direction. If $c_2 = c$ is assumed, the following equation can be drawn.

$$c_1 = c + s - \frac{s}{n_s L} y \quad (4)$$

The governing equation for the piston can be expressed as dimensionless Reynolds equation derived by assuming the constant temperature process in air layer.

$$\frac{\partial}{\partial \theta} (PH^3 \frac{\partial p}{\partial \theta}) + \Gamma \frac{\partial}{\partial \eta} (PH^3 \frac{\partial p}{\partial \eta}) = \Lambda \frac{\partial}{\partial \eta} (PH) \quad (5)$$

The dimensionless variables are as follows.

$$x = R\theta \quad (6)$$

$$y = L\eta \quad (7)$$

$$p = p_a P \quad (8)$$

$$\Gamma = \frac{R^2}{L^2} \quad (9)$$

$$\Lambda = \frac{6\mu R^2 U}{p_a c^2 L} \quad (10)$$

When eccentric ratio is defined as follow,

$$\varepsilon = \frac{e}{c} \quad (11)$$

The thickness of air layer can be expressed as dimensionless forms.

$$H_1 = \frac{c_1}{c_2} + \varepsilon \cos \theta \quad (12)$$

$$H_2 = 1 + \varepsilon \cos \theta \quad (13)$$

The boundary conditions are as follows.

$$P_{\eta=0} = P_s$$

$$P_{\eta=1} = 1 \quad (14)$$

$$P_{\theta=0} = P_{\theta=2\pi}$$

The leakage flow can be calculated as follow.

$$\dot{m} = \int_0^{2\pi R} \delta x \frac{p_a}{2p_a} p \left(Uh - \frac{h^3}{6\mu} \frac{\delta p}{\delta y} \right) \quad (15)$$

2.2 Performance analysis of rod bearing

Rod bearing is a kind of gas static pressure bearing. Piston rod reciprocally moves in axial direction, the rod is supported by using constant pressure. When high pressure, p_s , is supplied through orifice, constant pressure, p_r , is maintained, which supports the piston rod.

The thickness of air layer between rod bearing and rod is as follow.

$$h = c + e \cos \theta \quad (16)$$

The governing equation for rod bearing is the same as equation (4). The thickness of air layer can be expressed as dimensionless forms.

$$H = 1 + \varepsilon \cos \theta \quad (17)$$

The boundary conditions are as follows.

$$P_{\eta=0} = P_{\eta=1} = 1 \quad (18)$$

$$P_{\theta=0} = P_{\theta=2\pi}$$

The leakage flow can be calculated as follows.

$$\dot{m}_\theta = - \int_0^{2\pi R} \delta x \frac{p_a}{2p_a} p \frac{h^3}{6\mu} \frac{\delta p}{\delta y} \quad (19)$$

$$\dot{m}_\eta = \int_0^{2\pi R} \delta x \frac{p_a}{2p_a} p \left(Uh - \frac{h^3}{6\mu} \frac{\delta p}{\delta y} \right) \quad (20)$$

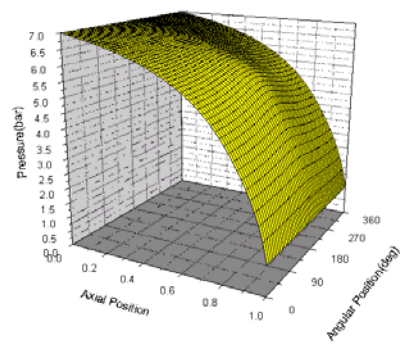
3. RESULT OF PERFORMANCE ANALYSIS

3.1 Calculation of pressure distribution

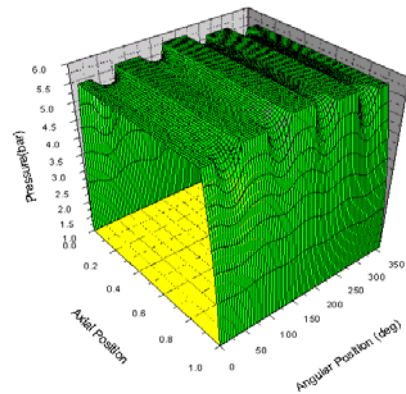
Fig. 3 is a calculating result of pressure distribution at , $\varepsilon = 0.5$, $n_s = 0.8$, $p_s = 7bar$. It can be predicted in the figure that self-centering force at the center region occurs due to pressure difference at $\theta = 0$ and $\theta = 180$.

3.2 Effect of eccentric ratio on performance

Fig. 4(a) and (b) show centering force and leakage flow against eccentricity variation of conical piston and rod bearing at $n_s = 0.8$. The centering force and leakage flow increase as eccentricity increases. It can be seen from Fig. 4(c) that the optimized values occur at $\varepsilon = 0.7$ for both conical piston and rod bearing by plotting the load/leakage value to maximize the centering force and to minimize the leakage flow.

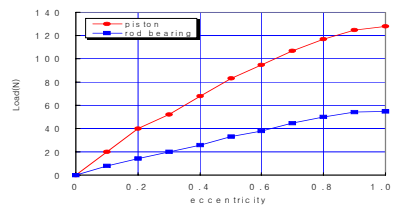


(a) conical piston ($\varepsilon = 0.5, \theta = 0.8$)

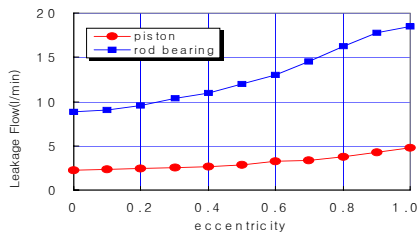


(b) rod bearing ($\varepsilon = 0.5$)

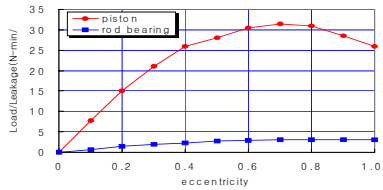
Figure3 Pressure distribution



(a) Load



(b) Leakage



(c) load/leakage

Figure4 Eccentricity vs. performance curve

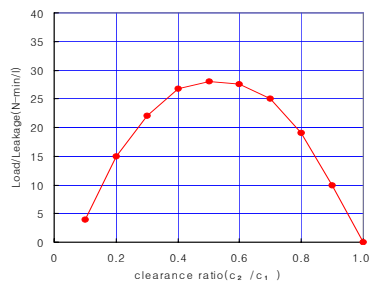


Figure5 Piston clearance ratio vs. performance curve

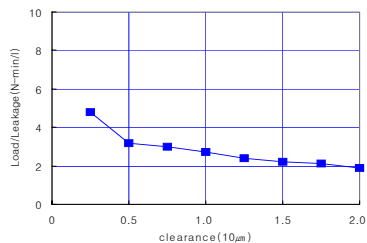


Figure6 Rod bearing clearance vs. performance curve

Table1. Dimensions of Sealless Cylinder

Contents	Length
Cylinder Diameter	50mm
Stroke	500mm
Total Piston Length	208mm
Cylindrical Piston Length	18mm
Conical Piston Length	82mm
Clearance	10 µ m
Tapered Length	20 µ m



Figure7 Drawing of Sealless Cylinder

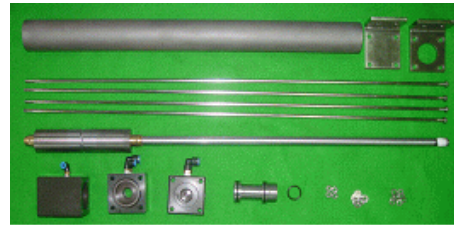


Figure8 Prototype of Sealless Cylinder

3.3 Clearance ratio and effect of clearance on the performance

Fig. 5 and Fig. 6 represent the variation of the load/leakage value against piston clearance ratio and rod bearing clearance to maximize the centering force and to minimize the leakage flow. In case of piston, the optimized value occurs when clearance ratio is 0.5, and in case of rod bearing, the clearance should be small. It is recommended in real design to determine the satisfactory clearance after fixing the maximum leakage flow.

4. OPTIMIZED DESIGN AND MANUFACTURING OF TEST PRODUCT

Sealless cylinder with optimized conditions based on analysis results was designed and manufactured. The design specification of the sealless cylinder is as Table 1⁽³⁾.

Fig. 7 is a drawing of the sealless cylinder, and Fig. 8 is a prototype of piston and rod bearing of manufactured sealless cylinder. Fig. 9 represents the type of rod bearing.

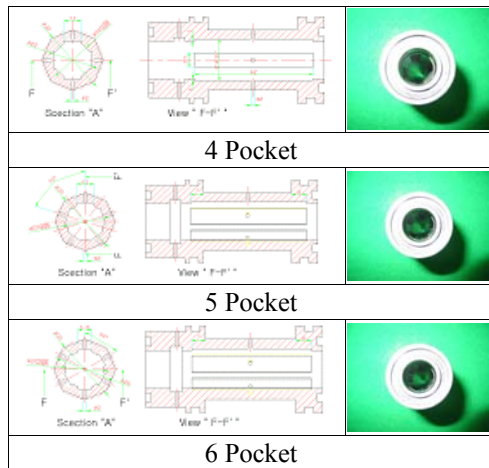


Figure9 Rod Bearing (4, 5, 6 Pockets)

5. LEAKAGE FLOW AND OVERALL PERFORMANCE EXPERIMENTS

5.1 A schematic of experimental apparatus and pictures

The experimental apparatus for overall performance evaluation was composed as Fig. 10. The compressed air is controlled by servo valve, load cell was attached to measure the friction force, position and velocity sensor, LVDT, was also attached, the sensors to measure pressure and flow rate was attached.

An air tank provides the cylinder through a FRL unit with Air. The equipped sensors can measure pressure and flux and the supplied Air can be controlled from servo valve. Also Load Cell and LVDT can measure friction, velocity and displacement at the edge of the cylinder. The acquired signals through sensors can be analyzed from PC.

Fig. 11 is a picture of controller part and mechanism part of the experimental apparatus for overall performance evaluation.

5.2 Experimental results

Fig. 12 is a result for reproducibility confirmation of servo actuator by input of triangle wave to servo valve. The Experiment was performed with a variation of controlling voltage from 5V to -5V under the condition of $P_a=1 \text{ MPa}$ and $Q=2500 \text{ /min}$. It is confirmed through two experiments that the time when maximum controlling voltage, 5V, occurs is identical.

Fig. 13 is a result for reproducibility confirmation of servo actuator by input of rectangular wave to servo valve like above experiment. As a result, the reproducibility of servo actuator was confirmed. Fig. 14 shows a result of dynamic characteristics of Gain/Phase/Hz by using sine wave.

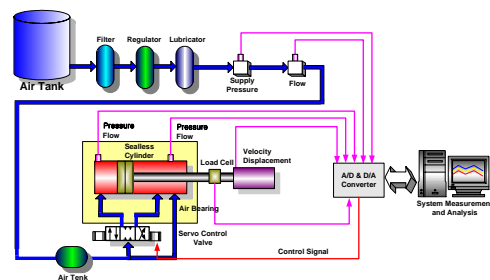


Figure10 Performance Experimental Apparatus



Figure11 Measurement Apparatus of Performance Tester Apparatus

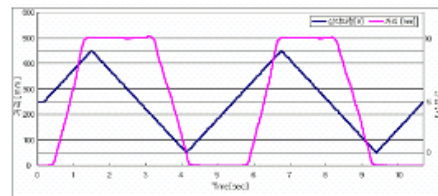


Figure12 Repeating test using triangle wave

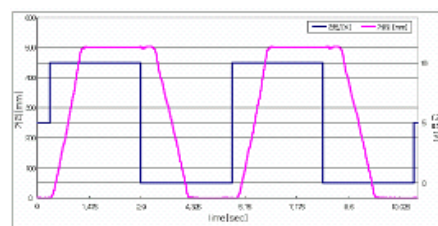


Figure13 Repeating test using rectangular wave

Fig 15 shows a measuring value of leakage flow of piston. Internal pressure was kept at 6 bars and it represents leakage flow at each position due to variation of stroke. At the initial stage, leakage flow is high, but it becomes lower as the piston operates. Finally, the difference of leakage flow is twice.

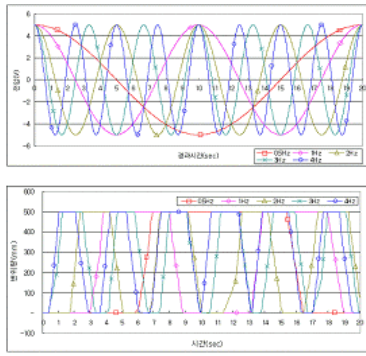


Figure14 Repeating test of Gain/phase/Hz using sign wave

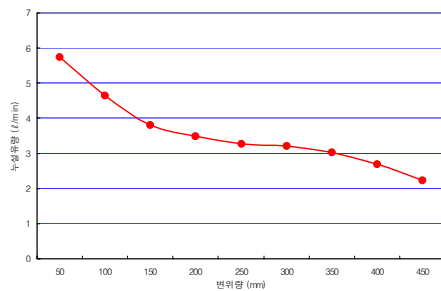


Fig. 15 Leakage flow of piston

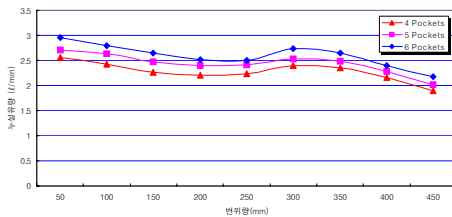


Fig. 16 Leakage flow of rod bearing

It was confirmed that precise manufacturing is excellent, judging from the fact of the leakage flow was evaluated to be approximately 2~6l /min which agrees with theoretical analysis result. Fig. 16 shows a measured leakage flow of rod bearing. The experiments using 4, 5, and 6 pocket bearing were performed. Internal pressure was kept at 6 bars and it represents leakage flow at each position due to variation of stroke. 4 pocket bearing has the smallest leakage flow, 2.5 l /min, which seems to be caused that the clearance was smelly fabricated compared with theoretical analytic value.

6. CONCLUSION

In this study, following conclusions were drawn from the results of the reproducibility of each wave shape, the dynamic characteristics experiments, and measured

leakage flow, varying the piston shape and rod bearing shape of sealless cylinder.

1. High performance sealless cylinder was manufactured by analyzing theoretically the bearing load and leakage flow.
2. Analysis on the conical type sealless cylinder was performed, 2D Reynolds equation on sealless cylinder moving reciprocally were derived, and then the solutions were obtained by finite difference method. It was confirmed that the results were applicable to the design.
3. From the experimental results through manufacturing of sealless cylinder, it was confirmed that 4 pocket bearing has the smallest leakage flow.
4. As the results of the leakage flow measuring, leakage flow of piston was evaluated to be approximately 2 ~ 6l/min, which agrees with theoretical analysis results. Rod bearing shows the leakage flow of 2.5 l/min, which seems to be caused that the clearance was smelly fabricated compared with theoretical analytic value.

ACKNOWLEDGEMENTS

This paper is a part of research project, "Development of High Performance Sealless Cylinder," which is industry basic project by Ministry of Commerce, Industry and Energy. The author gratefully acknowledges the financial support of the Ministry of Commerce, Industry and Energy.

REFERENCES

1. Belforte G., Raparelli T., Mazza L. and Trivella A., "Analysis and design of pistons for sealless pneumatic cylinders," Fluid Power, Forth JHPS International Symposium, pp459~464, 1999.
2. Belforte G., Raparelli T., Ferraresi C. and Trivella A., "New design of low friction cylinders," 12 Aachene fluidtechnishes kolloquium, Aachen, Germany, pp629-642, 1996.
3. Kim sung-jong, Kim dong-soo and Lee seung-hyun, "An Analysis and Test for Leakage Flow of Sealless Cylinder," KSME, 2004.
4. Kim young-cheol, Kim dong-soo, "Performance Analysis of pistons for Sealless Pneumatic Cylinder," KSTLE, 2004
5. Kim young-cheol, Kim dong-soo, "Lubrication and Leakage Performance Analysis for Sealless Pneumatic Cylinders," KSCFE, 2004

An Characteristics Analysis of the Fluidic Muscle Cylinder

DongSoo Kim*, SangKyu Bae*, Shin Huh** and SungIn Hong***

* IT Machinery Research Center, Korea Institute of Machinery & Materials
171 Jang-Dong, Yuseong-Gu, Daejeon, Korea

(E-mail: kds671@kimm.re.kr)

** Future Technology Department, Korea Institute of Machinery & Materials
171 Jang-Dong, Yuseong-Gu, Daejeon, Korea

*** Dept. of Mechanical Engineering, Chungnam National University
220 Gung-Dong, Yuseong-Gu, Daejeon, Korea

ABSTRACT

The fluidic muscle cylinder consists of an air bellows tube, flanges and lock nuts. Its features are softness of material and motion, simplicity of structure, low production cost and high power efficiency. Recently, unlikely the pneumatic cylinder, the fluidic muscle cylinder without air leakage, stick slip, friction, and seal was developed as a new concept actuator. In this study, we carried out the finite element modeling and analysis about the main design variables such as contraction ration and force, diameter increment of fluidic muscle cylinder. On the basis of finite element analysis, the prototype of fluidic muscle cylinder was manufactured and tested. Finally, we compared the results between the test and the finite element analysis.

KEY WORDS

Fluidic Muscle, Nylon Fiber, Contraction Ratio, Finite Element Modeling, Cord Angle

NOMENCLATURE

E: Elasticity coefficient
B: Thickness of air bellows
 D_0 : Diameter of air bellows
L: Length of cylinder
 p_1 : Internal pressure of cylinder
 ν : Poisson's ratio
 f : Contraction force
 θ : Cord angle

1. INTRODUCTION

Because the pneumatic cylinder generally uses sliding seal, it causes the high friction force and adherence phenomenon when it operates in low speed. Therefore, it has a disadvantage of difficult precise control during the driving of the cylinder. Many researches on the shape of piston and micro-cylinder have been performed to overcome that disadvantage ⁽¹⁾⁽²⁾. But these cylinders have disadvantages such as difficulty in manufacturing and high price.

Recently, unlikely the pneumatic cylinder, the fluidic muscle cylinder without air leakage, stick slip, friction, and seal was developed as a new concept actuator. It has the characteristics such as light weight, low price,

high response, durable design, long life, high power, high contraction, which is innovative product fulfilling RT(Robot Technology) which is one of the nation-leading next generation strategy technologies 6T as well as cleanness technology

In this study, finite element modeling is performed to analyze the characteristics of fluidic muscle cylinder, and then the optimized design variables are determined by analyzing the contraction force, contraction ratio, and the change of diameter and pressure. The characteristics are confirmed by manufacturing the fluidic muscle cylinder and performing the experiments.

2. THEORETICAL BACKGROUND

Exact mathematical modeling is needed to understand the characteristics of fluidic muscle cylinder. Fig. 1 shows a schematic analysis model of fluidic muscle cylinder .

A portion of the Internal pressure applied to the fluidic muscle cylinder, p , is used to expansion of rubber itself, the remaining is transferred to the fiber cord. When the outer pressure of the tube applied to the fiber cord is expressed as p_1 , equation (1) can be derived from the deformation correlation of axial stress and circumferential stress of the rubber tube.

$$p_1 = p - \frac{4EB(D^2 - DD_0)}{((2 - \nu)D^2 - \nu(D - D_0)^2)D_0} \quad (1)$$

Where E , B and D_0 represent the elastic coefficient of air bellows, thickness and internal diameter, respectively, and ν represents Poisson's ratio.

When the internal pressure applies to the fluidic muscle cylinder, the bellows expand in radial direction. The direction of expansion force is changed by fiber cord and then it becomes the contraction force(f_1),

$$f_1 = \frac{p_1 DL}{2 \tan \theta} \quad (2)$$

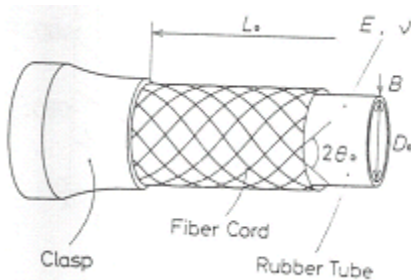


Figure1 Schematic diagram of fluidic muscle cylinder

Where, L represents the length of air bellows, and θ represents the cord angle. Simultaneously, the internal pressure causes the extension force of axial direction (f_2) to the end tip.

$$f_2 = \frac{\pi}{4}(D^2 + (D - D_0)^2)p_1 \quad (3)$$

The balance of the force regarding actuator can be expressed as equation (4) by equation (3)

$$f = f_1 - f_2 = \frac{p_1 DL}{2 \tan \theta} - \frac{\pi}{4}(D^2 + (D - D_0)^2)p_1 \quad (4)$$

Equation (4) shows that the contraction force (f) is proportional to the internal pressure, p_1 , the diameter, (D), and the length (L), but it inversely proportional to the cord angle.

The preceding theoretical equation can give a tendency regarding the characteristics of fluidic muscle cylinder, but it cannot evaluate the quantitative characteristics of the real products.

3. FINITE ELEMENT MODELING AND ANALYSIS

3.1 The structure of fluidic muscle

Fig. 2 shows the principal components of the fluidic muscle cylinder, which are composed of air bellows, flange, locking nuts. If the air pressure applies, the diameter of air bag increases and its length decreases. The cord papers aligned with nylon fiber are used to reinforce the rubber filled in high pressure for the tube, which is composed of 2 layers of cord papers.

The outer layer and inner layer are composed of rubber, in the medium each cord paper is aligned in the plus and minus angle on the basis of axis direction. Therefore, it plays a role to support most of load induced by air pressure.

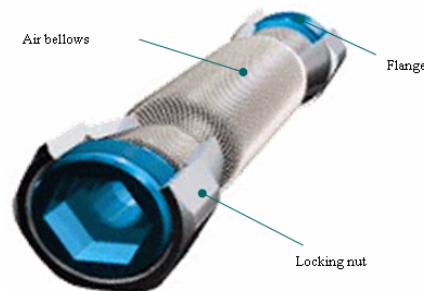


Figure2 Structure of fluidic muscle cylinder

The rubber thickness of air bellows is 0.4 mm, the rubber thickness of cord paper is 0.5 mm, the rubber thickness between cord papers is 0.4 mm, and the rubber thickness of outer region is 0.4 mm. The diameter of nylon cord is 0.5 mm, the gap between cords is 24ea/inch, and the cords are aligned in the angle of $\pm 30^\circ$ on the basis of axis direction.

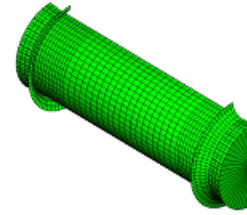


Figure3 FEA model of Fluidic muscle cylinder

3.2 Modeling and deformation analysis

The fluidic muscle cylinder is modeled by 3D 1/2 symmetry model, and is analyzed with ABAQUS, the tool of finite element analysis. The air bellows is modeled by using S4R finite-strain shell elements, 3D F3D3 and F3D4 hydrostatic fluid cavity elements are used to calculate the change of pressure and volume inside of air bag.

The air inside air bellows is modeled by regarding it as ideal gas, the standard density of the air is 1.204 kg/m^3 , the temperature of air is 23°C , the atmospheric pressure is 101.36 kPa .

The cord paper is composed of nylon fiber, which is modeled with skew rebar. Contact modeling between air bag and right & left locking nuts is expressed by defining contact pair between rigid element R3D4 and S4R shell elements. The boundary condition and restraint condition of the fluidic muscle restrain the degree of freedom in the center cutting point of both left and right locking nuts, and the center cutting point of right locking nut restrains corresponding degree of freedom according to analysis condition.

Fig. 3 shows finite element modeling of fluidic muscle cylinder. Mooney constant of rubber was used with the value of $C_{10} = 0.207 \text{ N/mm}^2$ and $C_{01} = 0.234 \text{ N/mm}^2$, elastic coefficient of nylon cord modeled with rebar is $E = 73,000 \text{ N/mm}^2$, and Poisson's ratio is $\nu = 0.3$.⁽³⁾

3.3 Analysis of performance change by cord angle change

Because the static characteristics of fluidic muscle cylinder generally depends on cord fixing angle, the effect of the change of cord fixing angle on the static characteristics of fluidic muscle cylinder was analytically predicted.

Fig. 4 shows the change of contraction ratio and diameter by cord angle change in the fluidic muscle cylinder with diameter of $\phi 10$, $\phi 20$, $\phi 40$ mm, and it is shown that as the cord angle decreases, contraction ratio and tube diameter increase.

Fig. 5 shows the contraction ratio and contraction force by the variation of cord angle. As the cord angle decreases, acted force and contraction ratio increase. The optimized value should be determined, considering that as the cord angle becomes smaller, the contraction force due to air pressure and slope increase, on the contrary tube diameter increases.

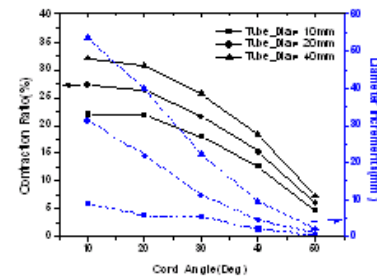
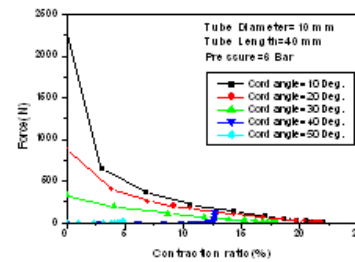
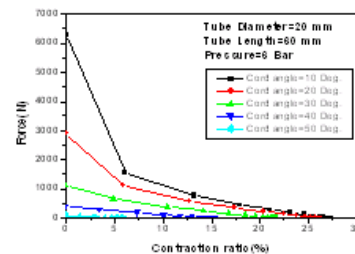


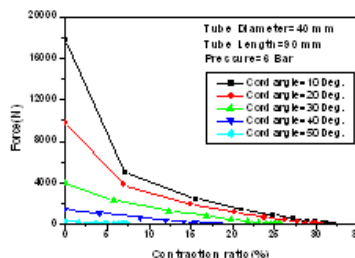
Figure4 Contraction ratio and diameter about the variation of cord angle



(a) $\phi 10$ mm



(b) $\phi 20$ mm



(c) $\phi 40$ mm

Figure5 Contraction ratio and force about the variation of cord angle

When the cord angle is 30°, proper maximum contraction ratio is maintained, so corresponding load is continuously acted. Accordingly, the cord angle of 30° shows the optimized performance.

3.4 Finite element analysis of manufacturing product

The characteristics according to the variation of cord angle which is main variable of fluidic muscle cylinder with the diameter of ϕ 10, ϕ 20, ϕ 40mm was analyzed, and then the optimized dimension and cord angle were determined and the analysis was performed. Fig. 6 shows FEA results of diameter increment ratio due to the variation of air pressure. From the figure it is confirmed that up to air pressure of 3 bar the slope of diameter increment ratio is steep, beyond that the slope becomes dull.

Fig. 7 shows FEA results of contraction ratio and contraction force due to the variation of air pressure from 1 to 6 bars. According to the results, the contraction ratio and contraction force have an increasing tendency as the air pressure increases.

When tube diameter is ϕ 10mm, the maximum contraction force was 327.7N, and maximum contraction ratio was 18.0% in case of 6bar air pressure.

When tube diameter is ϕ 20mm, the maximum contraction force was 1113.7N, and maximum contraction ratio was 21.7% in case of 6bar air pressure.

When tube diameter is ϕ 40mm, the maximum contraction force was 3930.0N, and maximum contraction ratio was 25.7% in case of 6bar air pressure.

From the analysis, the results on the deformation shape and the ratio of tube were obtained for the fluidic muscle cylinder with a diameter of ϕ 10, ϕ 20, ϕ 40 mm by finite element model for air pressure of 6 bar as shown in Fig. 8. And then the fluidic muscle cylinder was manufactured by reflecting the optimized conditions in the design. The Mises maximum stress of rubber occurs in the central region of tube, which are 1.05N/mm², 1.19N/mm², and 1.25N/mm²

4. MANUFACTURING OF THE PRODUCT AND EXPERIMENT

4.1 Design and manufacturing of the product

The fluidic muscle cylinder with optimized conditions was designed and manufactured on the basis of analysis results. Fig. 9 is the prototypes of assembled fluidic muscle cylinder with a diameter of ϕ 10, ϕ 20, ϕ 40 mm.

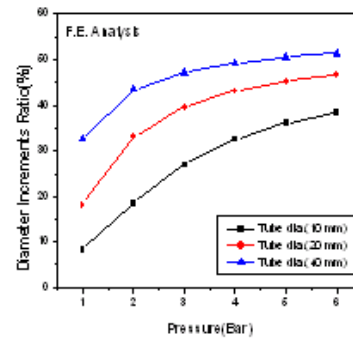
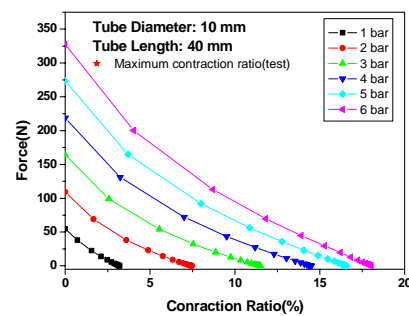
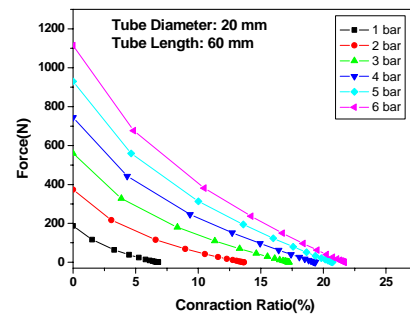


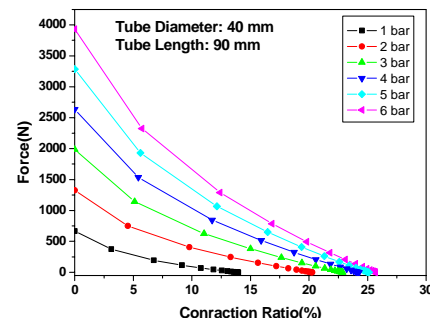
Figure6 FEA results of diameter increment ratio about the variation of air pressure



(a) ϕ 10 mm



(b) ϕ 20 mm



(c) ϕ 40 mm

Figure7 FEA results of contraction ratio and force about the variation of air pressure

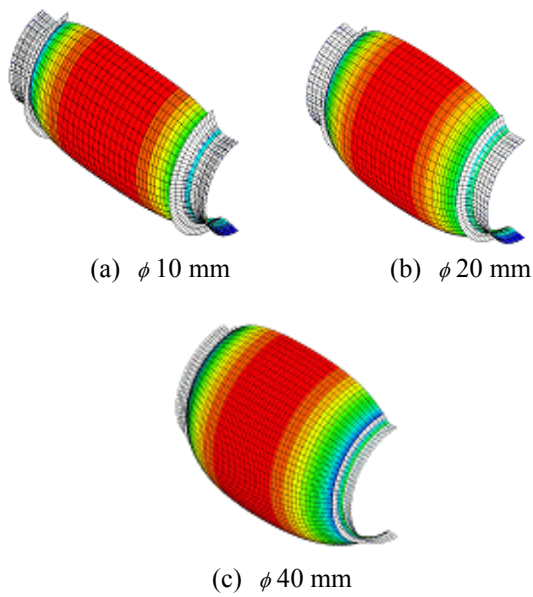


Figure8 Deformation shape of air bellows for air pressure of 6 bars (Cord angle= 30 deg.)



Figure9 Prototypes of fluidic muscle cylinder

4.2 Composition of experimental apparatus and experiment

The experimental apparatus for the performance evaluation was composed as Fig. 10. The compressed air is controlled by servo valve, load cell was attached to measure the force, position and velocity sensor, LVDT, was also attached, the sensors to measure pressure and flow rate was attached.⁽⁴⁾

Fig. 11 (a) and (b) show before and after pictures of pressure provision of manufacturing product. The contraction variation in the axial direction and expansion variation in the radial direction were measure and the contraction ratio was calculated by pressurizing the one side of cylinder and closing the other side.

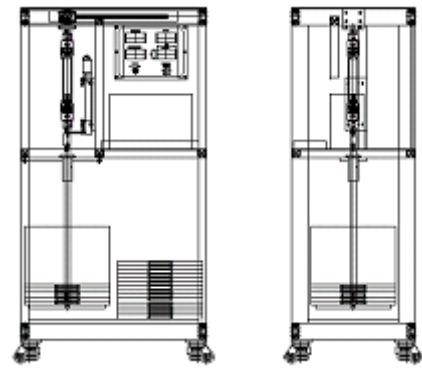


Figure10 Performance test apparatus



(a) Air pressure, $p = 0$ bar



(b) Air pressure, $p = 6$ bar

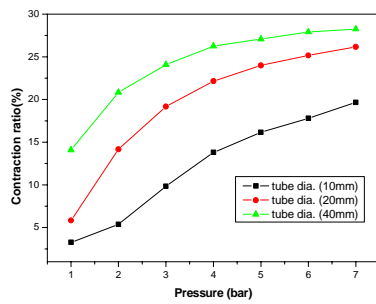
Figure11 Tests of fluidic muscle cylinder

4.3 Experimental results on contraction ratio and diameter incremental ration

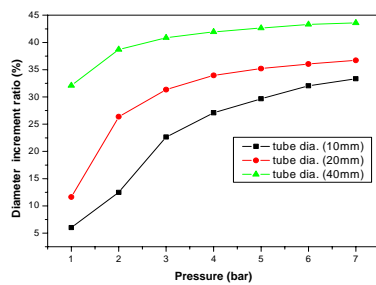
Fig. 12(a) and (b) shows contraction ratio of the cylinder in the axial direction and diameter increment ratio due to pressure variation. The contraction ratio increases as the diameter of bellows increases, especially when air pressure is more than 4 bars, the contraction ratio abruptly decreases. The diameter increment ratio increases as the diameter of air bellows increases, especially when air pressure is more than 3 bars, the increment ratio abruptly decreases.

Comparing the experimental results of contraction ratio with analysis results, the error was evaluated to be 0.2% in case of $\phi 10$ mm, 3.5% in case of $\phi 20$ mm and 2.2% in case of $\phi 40$ mm at the pressure of 6 bars. For the radial expansion ratio, the error was 4.7 % in case of $\phi 10$ mm, 4.3% in case of $\phi 20$ mm and 12.7% in case of $\phi 40$ mm.

Therefore, it is believed that the results of finite element analysis are reliable.



(a) Contraction ratio (%)



(b) Diameter increment ratio (%)

Fig. 12 Test results of contraction and diameter increment ratio

5. CONCLUSIONS

In this study, principal design variables were determined by performing the finite element analysis for the characteristics of fluidic muscle cylinder. As the results of manufacturing of the test product and the characteristics experiments, following conclusions were drawn.

1. Principal design variables were determined through the finite element analysis by predicting the contraction ratio, contraction force and diameter variation ratio as a function of cord angle.
2. On the basis of analysis results, the fluidic muscle cylinder with the diameter of $\phi 10$, $\phi 20$, $\phi 40$ mm was manufactured and then the experiments for contraction ratio and diameter variation ratio as a function of air pressure were performed.
3. On the basis of comparative results for the experimental values of the test product with the diameter of $\phi 10$, $\phi 20$, $\phi 40$ mm and analytical values, the errors of the contraction ratio and diameter variation ratio were less than 5 % and 12.7 %, respectively. But, it is believed that the results between experimental values and analytical values agreed well, considering non-linearity of rubber and anisotropic alignment of the cords.

4. It is confirmed that the deformation and characteristics of fluidic muscle cylinder can be predicted relatively well. On the basis of that it is believed that it can highly contribute to develop the new products.

ACKNOWLEDGEMENTS

This paper is a part of research project, "Development of Fluidic Muscle Cylinder," which is technology development project for components and materials by Ministry of Commerce, Industry and Energy. The author gratefully acknowledges the financial support of the Ministry of Commerce, Industry and Energy.

REFERENCES

1. G. Belforte, T. Raparelli, M. Velardocchia, "Study of the behavior of lip seals in pneumatic actuators", *Lubrication Engineering*, Vol. 49, No. 10, pp. 775-780, 1993.
2. G. Belforte, T. Raparelli, A. Trivella, "Study and development of innovative pneumatic microcylinders", *Conference of Hydraulics and Pneumatics*, Germany, pp. 235-248, 1995.
3. 横田, 小松建浩, "A Study on a Flexible Hydraulic Actuator for Space Manipulators," *日本機械學會論文集(C編)*, 57卷 542号 3222-3227, 1991.
4. C.W. Ju, "A Study on the Development for Fluidic Muscle Cylinder," 1st Final Report, 2004.

STIFFNESS REGULATION AND POSITION CONTROL TECHNOLOGY OF A PNEUMATIC MUSCLE ROBOT ARM

Yufen WEI, Xiaoning LI and Jianping LU

SMC Pneumatics Nanjing Center, School of Mechanical Engineering,
Nanjing University of Science and Technology,
Nanjing, 210094, China
(E-mail: xnli@public1.ptt.js.cn)

ABSTRACT

In the case that the high compliance and high safety are required, the use of pneumatic muscle for robot joints is a good choice. In this paper, a bio-mimic structure of pneumatic muscle robot arm is introduced and the differential pressure principle is applied to control the arm. In order to solve the practical problems that difficult regulation with pneumatic muscle and the lower accuracy of position control, a proportional stiffness regulation method with easy implementing feature is presented through theoretical analysis and experiments. On this basis, the position control of the joint with pneumatic muscle is implemented, for which the adaptive and self-learning neural-PSD controller is adopted. Tests indicate that the joint stiffness is easy to regulate by the method and joint operation shows a quick response and high accuracy.

KEY WORDS

Pneumatic muscle, Robot arm, Stiffness regulation, Adaptive neural-PSD controller

NOMENCLATURE

F	Contraction force	[N]
P	Input pressure	[MPa]
D	Muscle diameter	[m]
L	Muscle length	[m]
ε	Muscle contraction ratio	[%]
α	Muscle braided angle	[rad]
θ	Joint angle	[rad]
T	Joint torque	[Nm]
R	Radius of sprocket wheel	[m]
C	Joint stiffness	[Nm/rad]
u	Output of the controller	[MPa]

x	State variable	[rad]
e	Track error	[rad]

INTRODUCTION

Most robotic rotary joints are driven by electric servo-motors, step-by-step motors or sometimes by hydraulic motors. The joint structures driven by these actuators are usually complicated, heavy and lack of compliance. However, the human arm is light and flexible with the human musculature. So it is expected to find a kind of actuator with which the maximum similarity in function and shape of human arm would be acquired

based on the artificial pneumatic muscle.

There are two main problems for a robot arm driven by pneumatic muscle, that is, difficult regulation on joint stiffness and low accuracy in position control. Thus it is very important to investigate technique approaches for effective stiffness regulation and high precise position control with artificial pneumatic muscle.

In this paper, the research is focus on these problems. After describing the mechanical structure and working principle of the robot arm driven by pneumatic muscles, a proportional stiffness regulation method with easy implementing feature is presented through theoretical analysis and experiments. On this basis, the position control method for the joint is studied, which use the adaptive and self-learning neural-PSD control mode.

BIO-MIMETIC STRUCTURE AND WORKING PRINCIPLE OF THE ROBOT ARM

In most joints driven by electric motors or hydraulic motors, for regulating the speed difference between the driving motors and the actuating parts speed reducers must be used[1]. In this case the joints are lack of compliance due to their great stiffness. However, if pneumatic muscles are used to drive the joints the speed reducers can be removed owing to their suitable action speed.

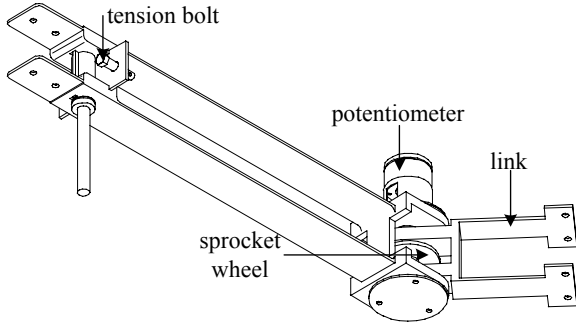


Figure 1 Mechanical structure of the robot arm

Figure 1 shows the mechanical structure of the robot arm developed by authors. From Figure 1 it can be seen that the pneumatic muscles are fixed on the arm skeleton, which transmits torque by a chain and a sprocket wheel when contracting with pressurized air. For regulating the initial length of the pneumatic muscles, a tension bolt is mounted on an end of the muscle skeleton. A potentiometer is used for measuring the rotary angle of the joint. The robot arm is about 300mm in length, 45mm in width, and 1.8kg in weight.

Figure 2 shows the working principle of the joint driven by two pieces of pneumatic muscles. At the initial state, both muscles are charged with air under initial pressure P_0 ,

and the rotary angle θ of the joint is zero. If the pressure are increased by ΔP in a pneumatic muscle and the pressure is decreased by ΔP in another pneumatic muscle, the joint would rotate around the direction with a contracting muscle owing to pressure increasing until the new force balance is reached.

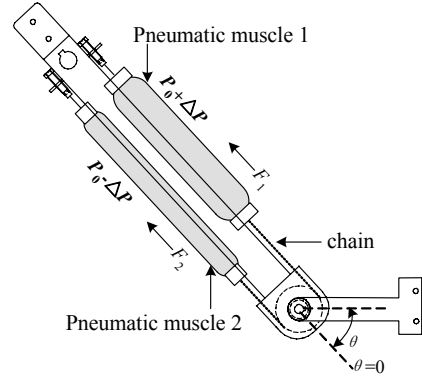


Figure 2 Working principle of the joint driven by pneumatic muscles

METHOD OF PROPORTIONAL STIFFNESS REGULATION

Requirement of Stiffness Regulation on Pneumatic Arms

The merit of use of a pneumatic muscle to drive a joint is with high compliance. However this leads to the decreasing of the stiffness. In some case for some tasks, the high stiffness is needed when overcoming greater loads, while the low compliance is permissible. Thus the stiffness regulation according to different tasks in robot working process is required. For this the force/length/pressure relation model of the pneumatic muscle should be built up.

The Force/Length/Pressure Relation Model

The pneumatic muscle used in our research is Mckibben muscle with 250mm in length, 20mm in width, 45g in weight, maximum pulling force with 0.5MPa is 250N. The force/length/pressure relation model is originally proposed in literature[2] as follows.

$$\begin{cases} F = \frac{\pi D_0^2}{4} P (a(1 - k\varepsilon)^2 - b) \\ \varepsilon = \frac{(L_0 - L)}{L_0} \\ a = \frac{3}{\tan^2(\alpha_0)}, b = \frac{1}{\sin^2(\alpha_0)} \end{cases} \quad (1)$$

For the muscle in our research, the initial parameters in Eq. (1) can be given as: $D_0=13.4\text{mm}$, $L_0=197\text{mm}$, $\alpha_0=21^\circ$, $k=1.14$. Figure 3 shows the comparison between experiment results and the theoretical results from Eq. (1). It can be seen that both results are well coincident[3].

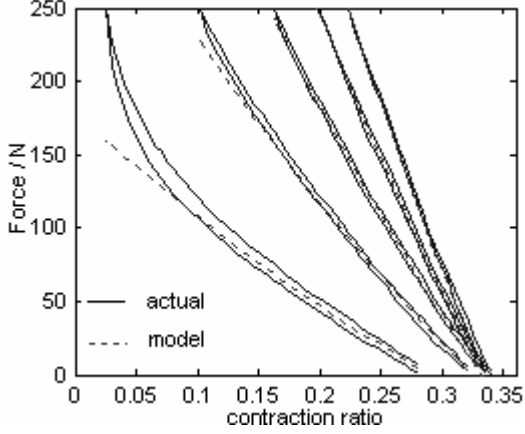


Figure 3 Comparison between experiment results and the theoretical results

Proportional Regulation of Joint Stiffness

Using the force/length/pressure relation model, the joint torque Eq.(2) can be derived according to its working process

$$T = K_1\Delta P - K_2P_0\theta \quad (2)$$

Where K_1 and K_2 are constants, dependent on pneumatic muscle's initial parameters(L_0, D_0, α_0, k)and structural parameters (ϵ_0, R) of the robot arm. In Eq. (2), when $T=0$ at balanced position the term of $K_2P_0\theta$ will equal the term $K_1\Delta P$. This derives following expression on θ and ΔP

$$\theta = \frac{K_1}{K_2P_0}\Delta P = G\Delta P \quad (3)$$

Where G is a static gain of θ with ΔP . The angular stiffness is the derivative of the torque function and can be expressed as

$$C = \frac{dT}{d\theta} = K_2P_0 \quad (4)$$

Because K_2 is a constant, the joint stiffness C is directly proportional to the initial pressure P_0 in the pneumatic

muscle. With the increasing of the initial pressure P_0 , the joint stiffness is increased. This feature can be used to actively regulate the joint stiffness when necessary.

Experiments for Regulation on Joint Stiffness

To validate the method to regulation on joint stiffness C , experiments are carried out, in which the output torque T and the joint angle θ must be measured to obtain the stiffness C from Eq. (4). Because of the limitation of the mechanical structure, it is very difficult to directly measure the output torque, so an indirect method is planned. As seen in Eq. (5), the static stiffness C is expressed as a function of K_1 and G and is also a function of θ and ΔP . If θ and ΔP can be measured, the static stiffness C can be calculated by Eq. (5).

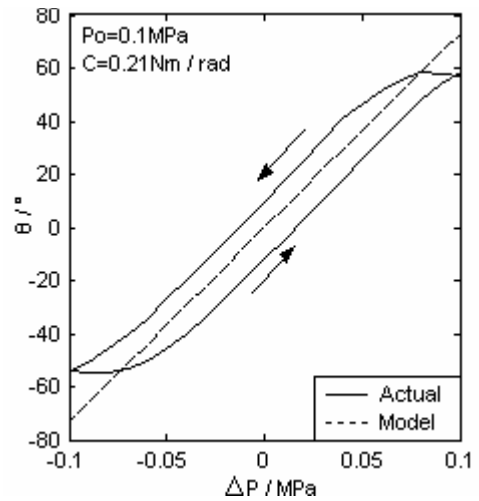
$$C = \frac{K_1\Delta P}{\theta} = \frac{K_1}{G} \quad (5)$$

We can define the joint compliance coefficient F as

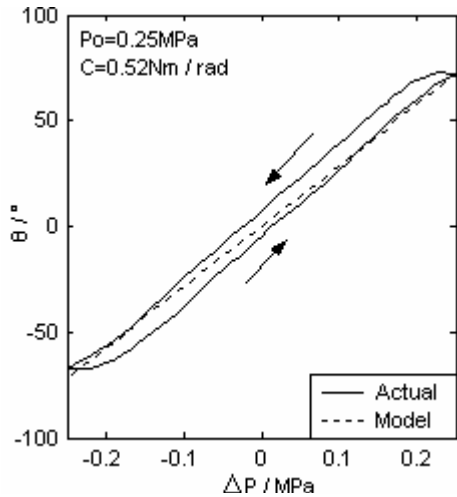
$$F = -\frac{d\theta}{dT} = -\frac{1}{K_2P_0} = -\frac{1}{C} \quad (6)$$

From Eq. (6), we can see that the F is inversely proportional to C . The increasing of F means decreasing C .

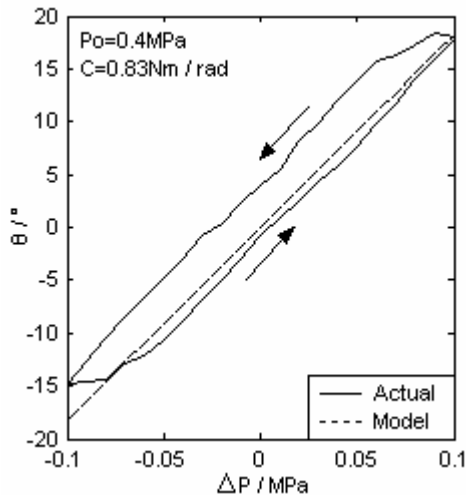
Figure 4(a) ~ (c) shows the variation of measured θ with ΔP with $P_0=0.1\text{MPa}$, 0.25MPa , 0.4MPa . From Figure 4, the G can be obtained by the slopes of the curves. Figure 5 shows the comparison between the model value and the measured value of the static gain G .



(a) $P_0=0.1\text{MPa}$



(b) $P_0=0.25\text{MPa}$



(c) $P_0=0.4\text{MPa}$

Figure 4 Variation of measured θ with ΔP

From Figure 5, it can be seen that the actual static gain G is very close to the theoretical value.

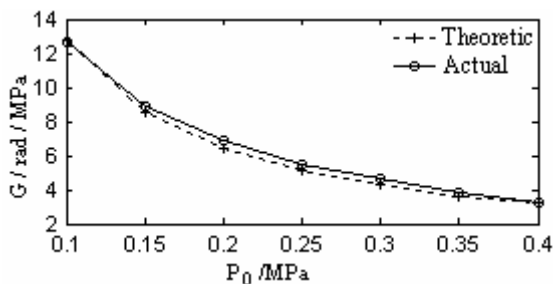


Figure 5 Comparison of the static gain G

Figure 6 shows the comparison between the model value and the measured value of the joint stiffness C . From Figure 6, it can be seen that the joint stiffness C is very close to the theoretical value. Therefore it can be deduced

that the theoretical C calculated by Eq. (5) can be used in real time controlling algorithm substituting the measured value.

For usual robot joint the stiffness or compliance is a fixed value when the structure is made, while for that driven by pneumatic muscles the stiffness or compliance can be regulated by regulating input pressure at any time. This provides the possibility of regulating the joint stiffness according to different loads or tasks in the joint controlling algorithm. On this basis, further controlling algorithm can be researched with different joint stiffness.

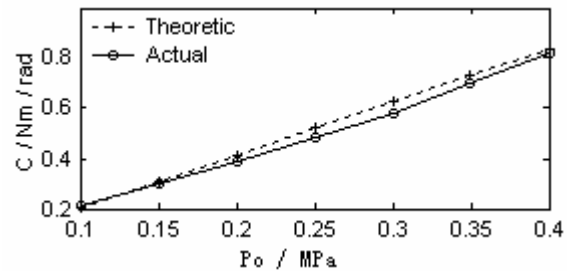


Figure 6 Comparison of the joint stiffness C

ADAPTIVE SINGLE NEURAL PSD POSITION CONTROL SYSTEM DESIGN WITH DIFFERENT JOINT STIFFNESS

Joint angle θ can be controlled in open-loop according to Eq. (3). However, because of its large hysteresis as shown in Figure 4, to obtain high accuracy θ could not be controlled merely by open-loop mode. So a suitable closed-loop control method should be studied and adopted.

Controller Design

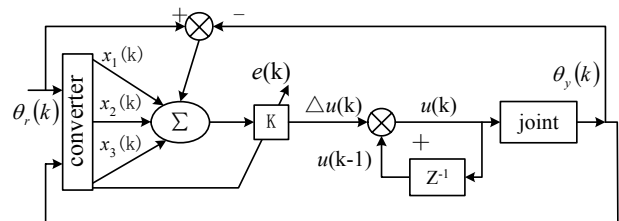


Figure 7 Diagram of adaptive single neural PSD control

Due to the air compressibility, the non-linearity and hysteresis in operation of pneumatic muscles, it is difficult to establish an accurate linear discrete model through experimental data. Therefore, to avoid the obstacle of the impossible accurate model, an adaptive and self-learning neural PSD controller without model is developed.

Diagram of this adaptive single neural PSD controller is shown in Figure 7[4][5].

The PSD controller is expressed as

$$u(k) = u(k-1) + K \sum_{i=1}^3 w'_i(k) x_i(k) \quad (7)$$

Where $u(k)$ is the output value of the controller, corresponding to the input pressure variation in pneumatic muscle; K is the proportional coefficient of neural ($K>0$); $x_i(k)$ ($i=1,2,3$) is state variable; $w'_i(k)$ ($i=1,2,3$) is weight corresponding to $x_i(k)$, $x_i(k)$ can be expressed as

$$\begin{cases} x_1(k) = e(k) = \theta_r(k) - \theta_y(k) \\ x_2(k) = \Delta e(k) = e(k) - e(k-1) \\ x_3(k) = \Delta^2 e(k) = e(k) - 2e(k-1) + e(k-2) \end{cases} \quad (8)$$

Where $\theta_r(k)$ and $\theta_y(k)$ are the set point and the actual value of joint angle. $w'_i(k)$ can be expressed as

$$w'_i(k) = w_i(k) / \sum_{i=1}^3 |w_i(k)| \quad (9)$$

Learning arithmetic of $w_i(k)$ is

$$\begin{cases} w_1(k+1) = w_1(k) + \eta_I z(k) u(k) [e(k) + \Delta e(k)] \\ w_2(k+1) = w_2(k) + \eta_P z(k) u(k) x_1(k) [e(k) + \Delta e(k)] \\ w_3(k+1) = w_3(k) + \eta_D z(k) u(k) x_1(k) [e(k) + \Delta e(k)] \end{cases} \quad (10)$$

Where η_I , η_P and η_D are learning rates of Integral, Proportional and Derivative terms of the controller.

The system performance is sensitive to Proportional coefficient K in controller. As K increases, the system response will become significantly faster, but the system could become unstable when K is sufficiently large. K can be regulated by the following learning arithmetic

$$\begin{cases} K(k) = K(k-1) + C \frac{K(k-1)}{T_v(k-1)} \\ \quad \text{for } \text{sign}(e(k)) = \text{sign}(e(k-1)) \\ K(k) = 0.75K(k-1) \\ \quad \text{for } \text{sign}(e(k)) \neq \text{sign}(e(k-1)) \end{cases} \quad (11)$$

$T_v(k)$ is given as follows

$$T_v(k) = T_v(k-1) + L^* \text{sign}(\Delta e(k) - T_v(k-1) \Delta^2 e(k)) \quad (12)$$

Where $0.025 \leq C \leq 0.05$, $0.05 \leq L \leq 0.1$. With the increasing of L , initial value of $T_v(k)$ and $K(k)$, regulation ratio of $K(k)$ is increased.

Experimental Results of PSD Control

To demonstrate the effectiveness of the controller, an experiment is carried out. The input pressures in pneumatic muscles are provided using pressure proportional valves with a time delay of 30ms being able to meet the requirement of the controller. By adjusting the input voltage of the pressure proportional valve, the force and contraction of pneumatic muscles can be controlled. The control algorithm and software are implemented using LabVIEW on a Pentium IV computer. The chosen sampling time interval is 30ms. Due to limitation of the range of normal working pressure the output value of the controller should be restricted as follow

$$0 < P_0 \pm \Delta P < 0.5 \text{MPa} \quad (13)$$

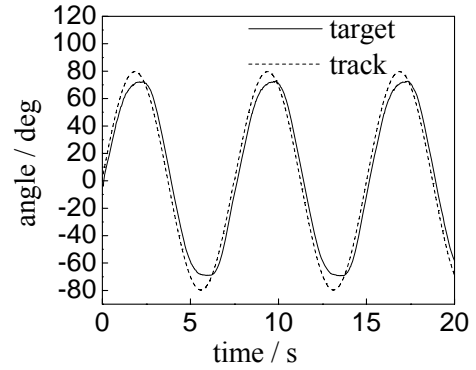


Figure 8 Response for a sine wave with open-loop (cycle=7.5s)

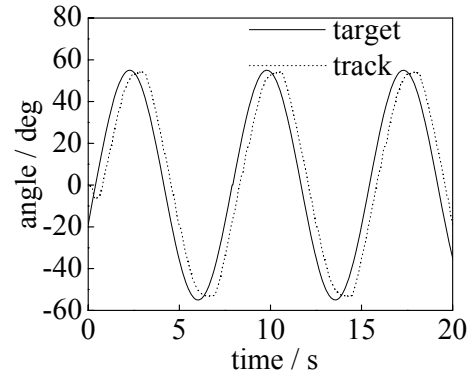
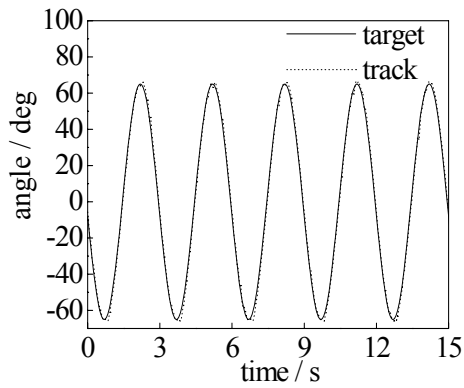
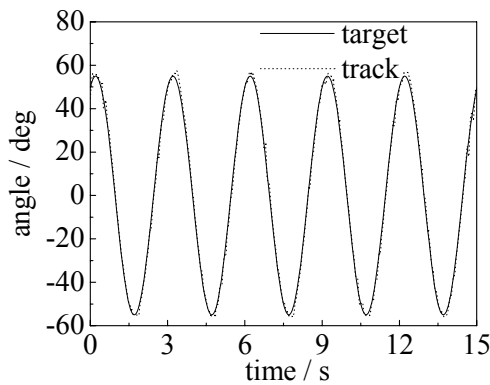


Figure 9 Response for a sine wave with PID (cycle=7.5s)



(a) $P_0=0.25\text{MPa}$



(b) $P_0=0.15\text{MPa}$

Figure 10 Response for a sine wave with adaptive single neural PSD (cycle=3s)

Figure 8 shows the steady state response for a sine wave with an open-loop control mode. From Figure 8, it can be seen that there are two defaults in output with open loop, one is the bigger track error between the target values and the track values and another is the longer response time.

Figure 9 shows the steady state response for a sine wave with a simple PID control mode. From Figure 9, it can be seen that the track error is decreased with the simple PID control mode.

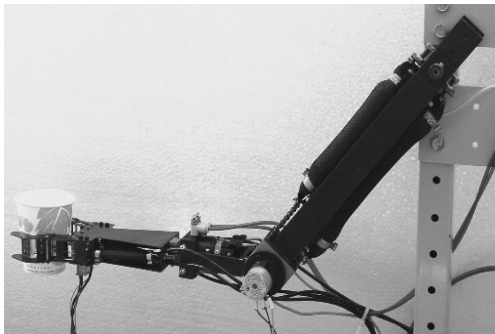


Figure 11 Practical operation of the arm

Figure 10(a) shows the steady state response for a sine

wave with adaptive single neural PSD ($P_0=0.25\text{MPa}$). Figure 10(a) shows the steady state response under the same conditions in Figure 10(b) but with different initial input pressure ($P_0=0.15\text{MPa}$). From Figure 10(a) and (b) it can be seen that the track error and response time are all decreased with adaptive single neural PSD control mode. Figure 11 shows a practical operation of the robot arm in grasping a paper cup. This is need necessary compliance and sufficient stiffness when the cup is full of water. With the help of the stiffness regulation method and the adaptive PSD control mode, the arm could complete the operation task without any problems.

CONCLUSION

In the case that the high compliance and high safety are required, the use of pneumatic muscle for robot joints is a good choice.

There are two main problems for a robot arm driven by pneumatic muscle, that is, difficult regulation on joint stiffness and low accuracy in position control. In this paper, the research has focused on these problems. First the mechanical structure and working principle of the robot arm driven by pneumatic muscles are introduced. Then a proportional stiffness regulation method with easy implementing feature is presented, which is derived from theoretical analysis and has been validated by experiments. On this basis, the position control method for the joint is studied, which use the adaptive and self-learning neural-PSD control mode. Experiments have shown that the adaptive PSD control mode is suitable for the joints driven by pneumatic muscles and has a good performance with smaller track error and shorter response time.

REFERENCES

1. Zong Guanghua, Liu Haibo and Chen Junshi, Translation. Manual of robot technology, Beijing: Science publisher, 1996.
2. Bertrand Tondou and Pierre Lopez, Modeling and control of McKibben pneumatic artificial robot actuators, IEEE Control System Magazine, 2000, 20(2): 15-38.
3. Wei Yufen, Study on driving characteristic of pneumatic muscle, Chinese Hydraulics & Pneumatics, 2004(7): 24-26.
4. Marsik J. A new conception of digital adaptive PSD control, Problems of Control and Information Theory 1983, 12 (4): 267-279.
5. Marsik J and Strejc V. Application of Identification free algorithms for adaptive control, Automatica, 1989, 25 (2): 273-277.

RESEARCH ON PNEUMATIC CYLINDER'S EXHAUSTED-AIR RECLAIMING CONTROL DEVICES

Yunxu SHI, Xiaoning LI and Yan TENG

SMC Pneumatics Nanjing Center, School of Mechanical Engineering,
Nanjing University of Science & Technology
Nanjing, 210094 China
(E-mail: xnli@public1.ptt.js.cn)

ABSTRACT

The air with certain pressure in a pneumatic cylinder is usually exhausted into the atmosphere after work process. It is of significant that the air energy can be saved and re-used. In this paper, the constitution of an exhausted-air reclaiming system for pneumatic cylinders is studied. To find the possible influence on the cylinder work process, the effect of the system on the cylinder velocity characteristics is also researched and different control switch points are tested. Experimental results show that attaching a reclaiming device would not cause bad influence on the velocity stability if the switch point could be properly controlled. Experiments also indicate that the switch control differential pressure ΔP_{sw} varies with P_c in the receiver and the supply pressure P_s would affect the velocity stability of cylinders. Therefore to reclaim more energy and make less influence on the cylinder velocity characteristics, the suitable differential pressure ΔP_{sw} and switching-point are also tested and suggested.

KEY WORDS

Air energy save, Air exhaust reclaim device, Velocity control characteristics, Control differential pressure

NOMENCLATURE

P_s	: Supply pressure	[MPa]
p	: Pressure	[MPa]
d	: Piston rod diameter	[m]
D	: Piston diameter	[m]
A	: Piston area	[m ²]
A_e	: Effective area of restriction	[m ²]
V	: Chamber volume	[m ³]
M	: Load Mass	[Kg]
F	: Force load	[N]
T	: Temperature	[K]
Q_m	: Mass flow rate	[Kg/s]
P_{c0}	: Initial pressure in receiver	[MPa]
ΔP	: Differential pressure	[MPa]
ΔP_{cr}	: Critical switch differential pressure	[MPa]
ΔP_{sw}	: Switch control differential pressure	[MPa]
v	: Piston velocity	[m/s]
x	: Piston displacement	[m]

ρ : Air density [kg/m³]

Subscripts

1	: Supply side
2	: Exhaust side
c	: Receiver

INTRODUCTION

In working cycles of pneumatic cylinders, the air with certain pressure in the discharging chamber is usually exhausted into the atmosphere directly. If a part of the exhausted-air could be reclaimed, great energy would be saved for an industrial pneumatic system. For this, a simple and direct method is to develop a system in which the discharging chamber of a cylinder should be connected with an air receiver and the exhaust air is reclaimed into the receiver for reuse. However, there might be some potential problems for this system. On the one side, when the pressure in the receiver is

increased near the pressure in the discharging chamber, the remaining air in the discharging chamber could not be reclaimed to the receiver and it should be discharged into the atmosphere. Moreover, the pressure in the receiver would vary with the increasing or decreasing of the air mass in it. Therefore it is necessary to control the connecting of the discharging chamber with the receiver and the air discharging from the cylinder (for short, expressed as exhaust switch). On the other side, the cylinder velocity characteristics might be changed when the cylinder circuit attached with an additional air-reclaiming device. Therefore, in order to reclaim more energy and make less influence on the cylinder velocity characteristics, the suitable control criterion and the switching-point for controlling the reclaiming process should be carefully studied and determined. Moreover, the reclaiming system should be simple in structure and low in cost.

In following contents, the constitution of the reclaiming system is introduced and the mathematical model of the system has been studied. Through theoretical analysis and experimental research, the varying law of the cylinder velocity characteristics when with reclaiming device is discussed and the criterion of control differential pressure at the switch points is determined. Then some suggestions for constitution and control of the exhausted-air reclaiming system are given.

THEORETICAL ANALYSIS

Mathematical Model of Exhausted-air Reclaiming System

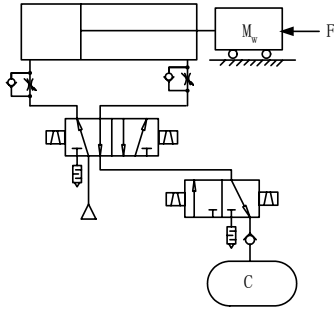


Figure 1 Constitution of the exhausted-air reclaiming system

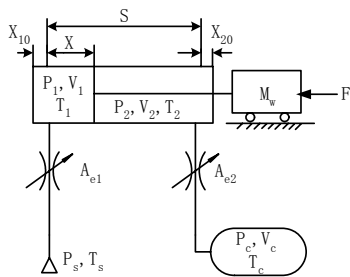


Figure 2 Working scheme of the exhausted-air reclaiming system

The exhausted-air reclaiming system is shown in Figure 1. To simplify calculation, some assumptions for the cylinder exhaust process should be made as follows [1]: (a) The thermodynamic process is adiabatic. (b) The supply pressure is constant and the temperature of supply air is equal to surrounding temperature. (c) The thermodynamic process of air in cylinder chambers is quasistatic process. (d) The internal and external leakage of the system is ignored.

The pneumatic working principle of the reclaiming system is shown in Figure 2. Applying the thermodynamics law to the charging and discharging chambers and the receiver, the mathematical model of the exhaust-air reclaiming system can be built up as follows [2][3]:

$$\frac{dp_1}{dt} = \frac{kRT_s Q_{m1}}{V_1} - \frac{kp_1}{V_1} \cdot \frac{dV_1}{dt} \quad (1)$$

$$\frac{dp_2}{dt} = -\frac{kRT_2 Q_{m2}}{V_2} - \frac{kp_2}{V_2} \cdot \frac{dV_2}{dt} \quad (2)$$

$$\frac{dp_c}{dt} = \frac{kRT_c Q_{m2}}{V_c} \quad (3)$$

$$\frac{d^2x}{dt^2} = \frac{1}{M_w} [p_1 A_1 - p_2 A_2 - F] \quad (4)$$

Where P_1 and P_2 are the absolute pressure in the charging and discharging chambers respectively, P_c is the absolute pressure in the receiver, A_1 and A_2 are the piston effective area respectively, R is the ideal gas constant, M_w is the mass load, F is the force load and Q_m is the simplified mass flow rate and is given in literature[4].

$$Q_m = \frac{A_e P_u}{\sqrt{RT_u}} \psi(\sigma) \quad (5)$$

$$\psi(\sigma) = \begin{cases} \frac{\sqrt{2}}{2}, & \sigma = p_d/p_u \leq 0.528 \\ \sqrt{2\sigma(1-\sigma)}, & 0.528 < \sigma \leq 1 \end{cases} \quad (6)$$

Where A_e is the effective flow area, P_u and P_d are the upstream and downstream pressure respectively, T_u is the upstream temperature and σ is the pressure ratio.

Theoretical Analysis of the Critical Switch Differential Pressure ΔP_{cr} in Exhausted-air Reclaiming

As shown in Figure 1, after several working cycles in piston's to-and-pro movements, the pressure in the receiver would be increased and the differential pressure ΔP between the discharging chamber and the receiver would be also reduced. Thus the piston velocity will be decreased gradually. Generally the working velocity range of a standard cylinder is 50 to 500mm/s. If the piston velocity is smaller than 50mm/s, the piston might

stop or cause a “stick-slip” phenomenon due to the influence of the friction force and the compressibility of air.

Therefore to avoid the stick-slip motion, the discharging chamber of a cylinder should be opened to the atmosphere at right time before stick-slip motion after a period of exhausted-air reclaiming process. The time point when the discharging chamber is switched from exhausted-air reclaiming process to directly discharging into the atmosphere is called exhaust switch point. The differential pressure between the discharging chamber and the receiver at the exhaust switch point is called critical switch differential pressure, expressed as ΔP_{cr} . If the differential pressure between P_2 in the discharging chamber and the P_c in receiver reaches the critical switch differential pressure ΔP_{cr} in reclaiming process, the directional valve should be switched to the process of the directly discharging into the atmosphere. At this moment, the pressure P_1 in the charging chamber is close to the supply pressure P_s (that is, $P_1 \approx P_s$) and the piston motion is probably at stable state. From Eq. (4), it can be seen that to sufficiently overcome the possible force load F the maximum permissible pressure in the discharging chamber should be

$$P_{2\max} = \frac{P_s A_1 - F}{A_2} \quad (7)$$

Assume that the thermodynamic process in chambers is isothermal process. The flow function $\psi(\sigma)$ adopts the subsonic phase in Eq. (6) when the differential pressure ΔP reaches the critical switch differential pressure ΔP_{cr} in the exhausted-air reclaiming process. Thus the mass flow through the effective flow area of the discharging pipes can be expressed as

$$Q_{m2} = \frac{\sqrt{2} A_{e2} P_2}{\sqrt{RT_s}} \sqrt{\sigma(1-\sigma)} \quad (8)$$

Assuming $\Delta p = p_2 - p_c$:

$$\sigma = \frac{p_c}{p_2} = \frac{(p_c - p_2) + p_2}{p_2} = 1 - \frac{\Delta p}{p_2} \quad (9)$$

Substituting Eq. (9) into Eq. (8), we get

$$Q_{m2} = \frac{\sqrt{2} A_{e2} P_2}{\sqrt{RT_s}} \sqrt{\frac{\Delta p}{p_2} - \frac{\Delta p^2}{p_2^2}} \quad (10)$$

Because the mass flow through the discharging chamber can also be expressed as

$$Q_{m2}' = \rho A_2 \frac{dx}{dt} = \rho A_2 v \quad (11)$$

Where, ρ is the air density in discharging chamber, x is the displacement of the piston and v is the piston velocity.

The ideal gas law can be written as

$$\rho = \frac{p}{RT} \quad (12)$$

Substituting Eq. (12) into Eq. (11), the mass flow equation can be expressed as

$$Q_{m2}' = \frac{P_2}{RT_s} A_2 v \quad (13)$$

From the continuity equation, we know that the mass flow out of the discharging chamber should be equal to the mass flow through the effective flow area of the exhausted-air side, which can be expressed as

$$Q_{m2} = Q_{m2}' \quad (14)$$

Substituting Eq. (10) and Eq. (13) into Eq. (14), we get

$$\frac{P_2}{RT_s} A_2 v = \frac{\sqrt{2} A_{e2} P_2}{\sqrt{RT_s}} \sqrt{\frac{\Delta p}{p_2} - \frac{\Delta p^2}{p_2^2}} \quad (15)$$

From Eq. (15), we obtain

$$\Delta p^2 - p_2 \cdot \Delta p + \frac{1}{2RT_s} \cdot \left(\frac{A_2 P_2 v}{A_{e2}} \right)^2 = 0 \quad (16)$$

Substituting the piston velocity $v = 50 \text{ mm/s}$ and the discharging chamber's pressure $P_2 \approx P_{2\max}$ into Eq. (16), the solution can be written as

$$\Delta P_{cr} = \frac{P_{2\max} - P_{2\max} \sqrt{1 - 0.0025 \cdot \frac{2}{RT_s} \cdot \left(\frac{A_2}{A_{e2}} \right)^2}}{2} \quad (17)$$

Assuming $\xi = \frac{2}{RT_s} \cdot \left(\frac{A_2}{A_{e2}} \right)^2$ and substituting it into Eq.

(17), the critical switch differential pressure ΔP_{cr} can be expressed as

$$\Delta P_{cr} = P_{2\max} \left(\frac{1 - \sqrt{1 - 0.0025 \cdot \xi}}{2} \right) \quad (18)$$

Where, $P_{2\max}$ is the maximum permissible pressure in discharging chamber being sufficient to overcome the force load, which is defined by Eq. (7).

The critical switch differential pressure ΔP_{cr} , as expressed in Eq. (18), is considered as the theoretical value of the minimum critical switch differential pressure. The practical switch differential pressure should be determined considering other real factors.

EXPERIMENTS ON EXHAUSTED AIR RECLAIMING SYSTEM

Experimental Equipment and Method

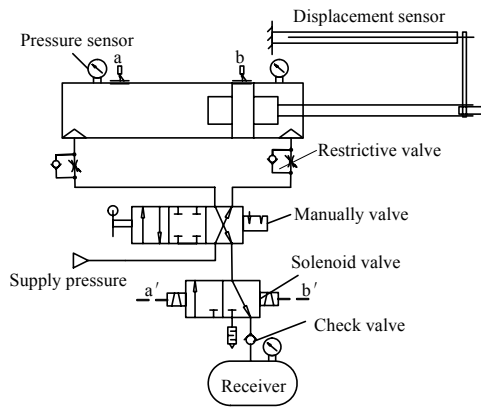


Figure 3 Experimental apparatus

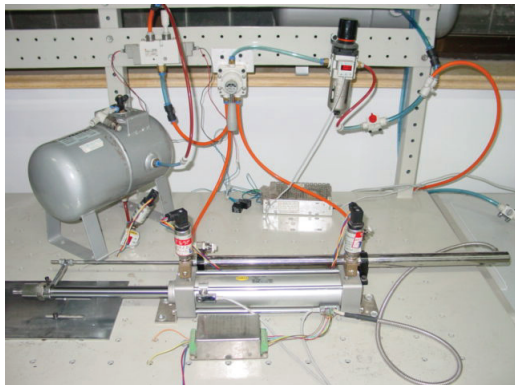


Figure 4 Photo of experimental device

The experimental apparatus is shown in Figure 3, which is used for validating the theoretical analysis and finding the real cylinder velocity characteristics when with the air reclaiming device. Figure 4 is a photo of the experimental device. Considering the similar process and working law with the extend stroke and the retract stroke of the cylinder, only the experiments for the retract stroke of the cylinder are reported and discussed. When the piston is at the position shown in Figure 3, the solenoid valve has been switched to the right side. Along

with the piston's return, the air in discharging chamber is being exhausted to the receiver. When the piston reaches the position of magnetic switch "a", the solenoid valve switches to the left side, the air in the piston rod chamber is exhausted into the atmosphere after the manually valve switches to the other side.

The diameter of the cylinder piston is 50mm and the stroke of the cylinder is 200mm, the volume of the receiver is 5 liter. In following sections to simplify the measuring in experiments, relative pressure is used if not demonstrative.

Influence on Cylinder's Dynamic Characteristics with Exhausted-air Reclaiming Device

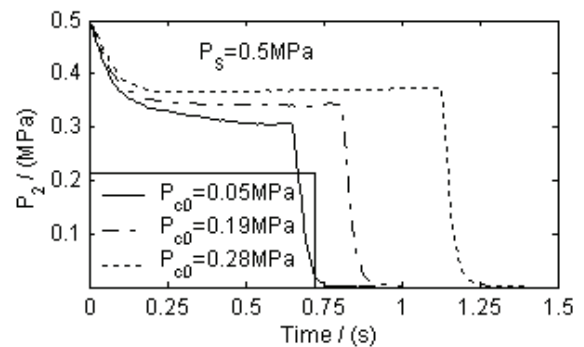


Figure 5 Variation of discharging chamber's pressure with different initial pressure in receiver

Figure 5 shows the variation of pressure in discharging chamber when the initial pressure P_{c0} in the receiver is 0.05MPa, 0.19MPa and 0.28MPa respectively in the process of exhausted-air reclaiming. From Figure 5, it can be seen that the initial pressure P_{c0} would affect the pressure curve of P_2 in discharging chamber.

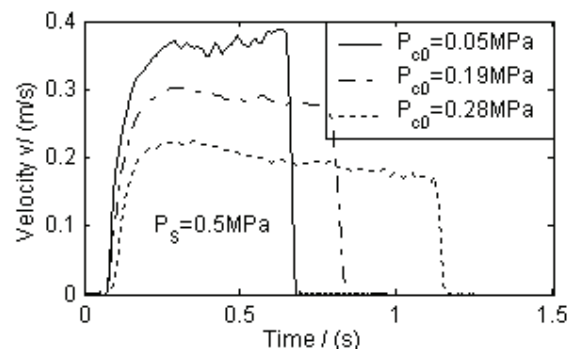


Figure 6 Variation of piston velocity with different initial pressure in receiver

Figure 6 shows the variation of piston velocity when the initial pressure in the receiver is 0.05MPa, 0.19MPa and 0.28MPa respectively in the process of exhausted-air reclaiming. From Figure 6, it can be seen that the higher

the initial pressure P_{c0} is, the lower the piston velocity and the longer the piston motion time interval. As shown in Figure 6, the higher the initial pressure P_{c0} , the smaller the velocity difference between the maximum and minimum piston velocity. Furthermore, it could be deduced that attaching a reclaiming device would not cause bad influence on the velocity stability but would increase the piston motion time under the same load condition if the switch point could be properly controlled.

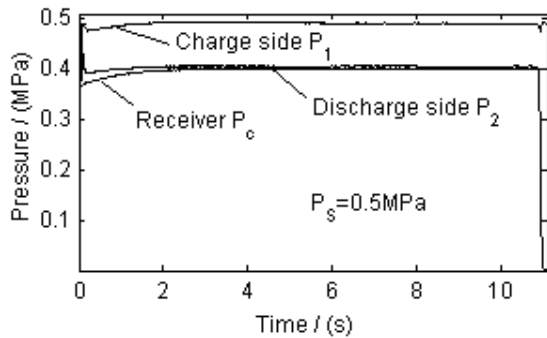


Figure 7 Variation of the pressure in cylinder chambers when P_c approaches P_2

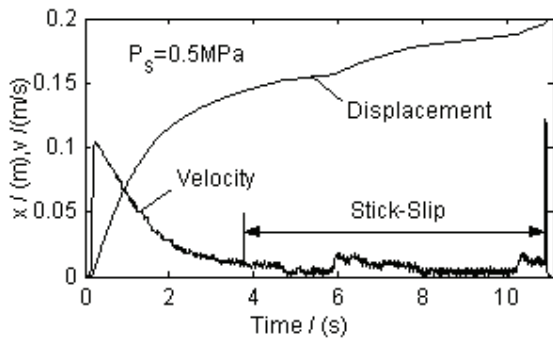


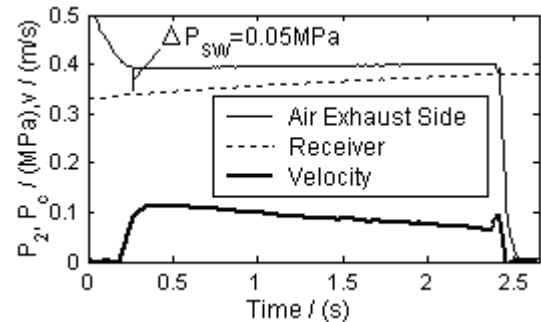
Figure 8 Variation of the piston velocity when P_c approaches P_2

The variation of the pressure in cylinder chambers and the piston velocity when the initial pressure P_{c0} in receiver approaches the stable pressure in discharging chamber are shown in Figure 7 and Figure 8 respectively. Figure 7 shows the pressure condition under which a variation in motion and velocity of the piston occurs. Further analyzing the velocity curve in Figure 8 can be seen that during reclaiming when P_c approaches P_2 the stick-slip motion might take place if the cylinder discharging chamber is keeping connection with the receiver. So the exhaust from discharging directly into the atmosphere and switch off the connection between the discharging chamber and the receiver should be started before P_c equals P_2 .

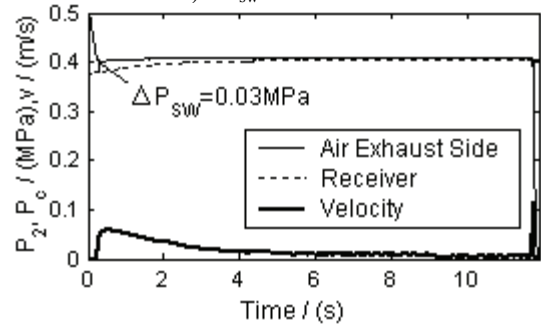
What is the more proper switch time point or the proper switch differential control pressure from reclaiming state

to the state of directly discharging into the atmosphere should be given by experiments.

Effect of Switch Control Differential Pressure ΔP_{sw} under Different Supply Pressure



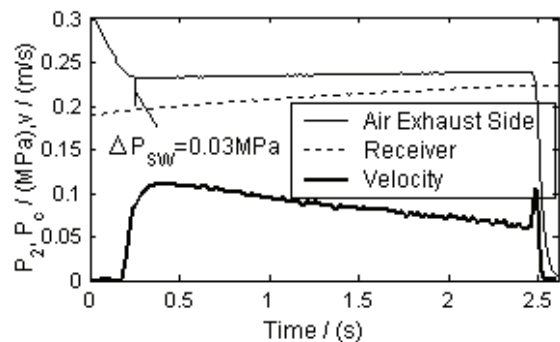
a) $\Delta P_{sw} = 0.05 \text{ MPa}$



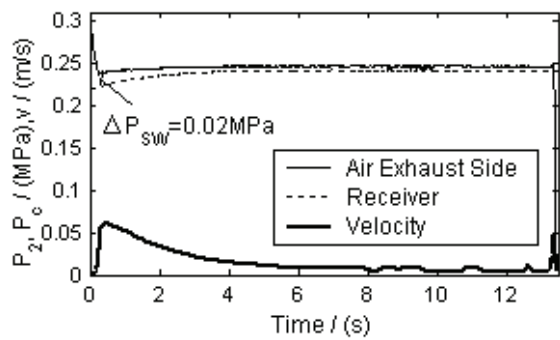
b) $\Delta P_{sw} = 0.03 \text{ MPa}$

Figure 9 Piston velocity with different switch control differential pressure ΔP_{sw} ($P_s = 0.5 \text{ MPa}$)

The piston velocity curves with different switch control differential pressure ΔP_{sw} are shown in Figure 9. When $\Delta P_{sw} = 0.05 \text{ MPa}$, the piston velocity is comparatively smooth and steady. However, when $\Delta P_{sw} = 0.03 \text{ MPa}$, the piston velocity fluctuates during the later stage and the stick-slip occurs. In this case the pressure P_2 has approached the permissible maximum pressure P_{2max} for overcoming a certain load and the motion time is obviously prolonged.



a) $\Delta P_{sw} = 0.03 \text{ MPa}$



b) $\Delta P_{sw} = 0.02 \text{ MPa}$

Figure 10 Piston velocity with different switch control differential pressure ΔP_{sw} ($P_s = 0.3 \text{ MPa}$)

The piston velocity curves with different switch control differential pressure ΔP_{sw} are shown in Figure 10. The piston velocity when $\Delta P_{sw} = 0.03 \text{ MPa}$ is more smooth and steady than when $\Delta P_{sw} = 0.02 \text{ MPa}$ and the motion time when $\Delta P_{sw} = 0.02 \text{ MPa}$ is longer than that when $\Delta P_{sw} = 0.03 \text{ MPa}$.

The above experiments reveal that the ΔP_{sw} varies with supply pressure P_s and the pressure P_c in receiver, and the smaller the ΔP_{sw} is, the greater the possibility of stick-slip motion of the piston and the motion time are. Although use of the smaller ΔP_{sw} to control the switch point would increase the reclaimed energy, the fluctuation might happen. So selection of the real switch control differential pressure ΔP_{sw} should be considered in all its aspects.

Variation of Switch Control Differential Pressure ΔP_{sw} with the Supply Pressure P_s

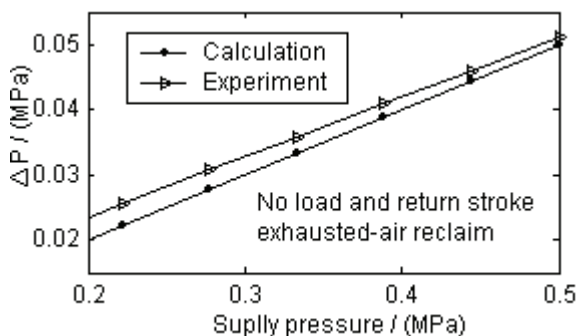


Figure 11 Variation of ΔP_{sw} and ΔP_{cr} with the supply pressure P_s

Variation of ΔP_{sw} and ΔP_{cr} with the supply pressure P_s is shown in Figure 11. From Figure 11, it can be seen that the trends of both curves of the theoretical calculation and the experiment are coincident and the ΔP_{sw} as while as the ΔP_{cr} are increasing with the increase of supply pressure P_s . Considering the results shown in Figure 7 to

Figure 9, we know that ΔP_{sw} also varies with P_c in receiver. The range of the ΔP_{sw} is normally within 0.02-0.05 MPa. This means that with different pressure P_c and P_s the switch control differential pressure ΔP_{sw} has to be changed. This will obviously increase the complication of the control system. So for simplicity and lower cost, we intend to select a determined value for the ΔP_{sw} . For reclaiming more energy, we expect to select a smaller set value of ΔP_{sw} . But it would not satisfy the velocity requirement with a higher supply pressure P_s or higher pressure P_c in receiver. If we select a higher set value of ΔP_{sw} , the velocity requirement could be well satisfied within a wide range from lower values to higher values of P_s and P_c . So for practicality we suggest that the value of ΔP_{sw} is determined as a set value and it can be set about 0.05 MPa under the given condition in our experimental reclaiming system.

CONCLUSIONS

In this paper, the constitution of an exhausted-air reclaiming system for pneumatic cylinders is studied. The effect of the system on the cylinder velocity characteristics and the control method are also researched through experiments. Experimental results show that attachment of a reclaiming device would not cause bad influence on the velocity stability but would increase the piston motion time under the same load condition if the switch point could be properly controlled, and experiments also indicate that the switch control differential pressure ΔP_{sw} varies with P_c in receiver and the supply pressure P_s of the cylinder. So the selection of ΔP_{sw} should consider some factors, such as the efficiency of reclaiming energy, simplicity and cost of reclaiming control method and the velocity stability of cylinder, etc. Therefore, we suggest that the value of ΔP_{sw} is determined as a set value and it can be set about 0.05 MPa under the given condition in our experimental reclaiming system.

REFERENCES

1. Wang Haitao, Bao Gang and et al. Study on cushion effect air supply pressure fluctuation. Proceedings of the fourth international symposium on fluid power transmission and control (ISFP'2003), 2003, 362~365.
2. Shi Yunxu and Li Xiaoning. The mathematic model and simulation of the exhaust reclaim velocity control system (In Chinese). Hydraulics and pneumatics, 2005(2): 25~28.
3. Li Jianfan. Dynamics of pneumatic systems (In Chinese). Guangzhou, SCUT press, 1991.
4. Y.Kawakami, J.Akao and et al. Some Considerations on the Dynamic Characteristics of Pneumatic Cylinders. The Journal of Fluid Control, 1988, (9): 22~36.

DRIVING CHARACTERISTICS OF A MICRO ARTIFICIAL MUSCLE ACTUATOR USING ELECTRO-CONJUGATE FLUID

Kenjiro TAKEMURA*, Shinichi YOKOTA* and Kazuya EDAMURA**

* Precision & Intelligence Laboratory,
Tokyo Institute of Technology
4259 Nagatsuta-cho, Midori-ku, Yokohama, 226-8503 Japan
(E-mail: takemura@pi.titech.ac.jp)

** New Technology Management, Co., Ltd.
2-9-1-306 Higashi-Shinkoiwa, Katsushika-ku, Tokyo, 124-0023 Japan

ABSTRACT

Soft robot inspired from natural systems is one of keywords in the robotic field in last decade. Accordingly, many types of artificial muscle actuators are developed. On the other hand, using an electro-conjugate fluid (ECF), which generates a powerful jet flow when subjected to a high voltage, we can construct a tiny pressure source. This paper proposes a novel micro artificial muscle actuator ($< 1 \text{ cm}^3$) utilizing the fluid. The essence of this study is to develop the micro artificial muscle integrated with micro pressure source, which enables us to construct an autonomous system and/or artificial muscle array. The contraction characteristics and normal force characteristics of the actuator were measured. The maximum contraction rate was around 16 % and the force generated was about 0.2 N with applied voltage of 6 kV. The experimental results confirmed the effectiveness of the proposed actuator.

KEY WORDS

Soft actuator, Micro actuator, Soft Robot, Functional fluid, Electro-conjugate fluid

INTRODUCTION

As robots are becoming widely used in many fields, a soft robot inspired from natural systems becomes one of the main research topics in the field of robotics and mechatronics, especially in the application requiring closer and safer interactions between humans and machines. The authors think the muscle of natural systems which potentially has flexibility is worthy of note, and that to create a new type of artificial muscle actuator might be a great research topic. As artificial muscle actuators, for example, several types of actuators have been developed. The artificial muscle actuator

which has the longest history is a pneumatic actuator such as McKibben type actuator. The constructions, numerical models, and applications of pneumatic actuators were widely studied [1][2]. It generates an extend-contract motion, however, there needs a bulky pressure source outside the actuator. Shape memory alloys are another example of artificial muscle [3][4]. They have great features as high power density, however, they suffer from slow response and heat problems. Polymer materials [5][6] might be a recent research trend on artificial muscle actuator, however, they are still not suitable for robotic application because they must be used in particular environments. A most

promising research of artificial muscle actuator in robotic field is electrically actuated dielectric elastomer films [7]. Although there reported several types of actuators as mentioned above, artificial muscle actuators are still being developed.

On the other hand, there is an interesting smart fluid or an electro-conjugate fluid (ECF) [8]. The fluid generates a powerful jet flow when subjected to a high voltage (~kV). This kind of phenomenon is known as an EHD (electrohydrodynamics) effect [9]. In our previous studies, the authors clarified the necessary condition for showing the effect, and the fluids meeting the condition are called ECFs. Although the mechanism of the effect has not been clarified yet, the ECFs are attractive for constructing new actuators. Hence, the authors applied the ECF effect on micro motors [10-12] and micro manipulators [13]. According to our previous studies on the ECF, the jet flow becomes more powerful with smaller electrode pair, which means, the ECF effect is suitable for micro actuation. Therefore, this paper proposes a new type of micro artificial muscle actuator using the ECF and clarifies its characteristics.

DRIVING PLINCPLE

Our previous studies proved the ECF effect is suitable for micro actuation [10-13], which means, it is easy to construct a micro pressure source using the ECF. Therefore, a new type of micro artificial muscle actuator can be realized as shown in Fig. 1. As the inner pressure of a fiber-reinforced flexible tube increases by a jet flow, which is generated at the pressure source using ECF, the tube contracts along the actuator axis because the fiber cannot extend.

One of the main accomplishments of this research is the incorporation of the pump (pressure source) in the actuator. This results in a very compact actuation system and therefore, we can place the actuator in an array just like natural muscles. This kind of design solution cannot be realized by pneumatic artificial muscle actuators previously developed because they need bulky pressure sources outside the actuator.

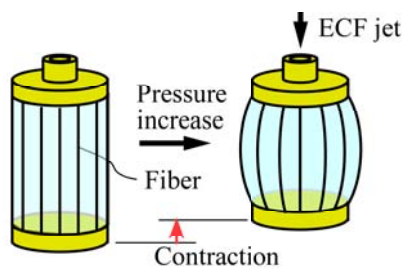


Figure 1 Concept of ECF micro artificial muscle

DESIGN AND MANUFACTURING

Here we briefly introduce a prototype of novel micro artificial muscle actuator. Fig. 2 shows a schematic illustration and actual view of the prototype. The prototype is composed of a fiber-reinforced silicone rubber tube, a micro pressure source using electro-conjugate fluid, a flexible ECF tank, and an external tank. This prototype is designed to confirm the driving principle of the micro artificial muscle actuator, so that each component is individually designed and produced. The fiber-reinforced silicone rubber tube is made of silicone rubber and aramid fibers with thickness of 35 μm and 12 fibers. The design parameters, tube thickness and number of fibers, are experimentally determined [14]. The outer dimension of the tube, $\phi 5 \times 10 \text{ mm}$, is determined so as the tube volume to be less than 1 cm^3 . The maximum contraction rate and force along tube axis measured at inner pressure of 10 kPa were 16 % and 0.18 N, respectively.

The micro pressure source using the electro-conjugate fluid includes a tiny electrode pair, consisting of a needle and ring electrodes as shown in Fig. 3 (the needle is connected to the GND, and the ring is to the positive). The diameter of the needle is 0.13 mm, and the inner diameter of the ring is 0.3 mm. An electrode spacer located between the electrodes keeps the

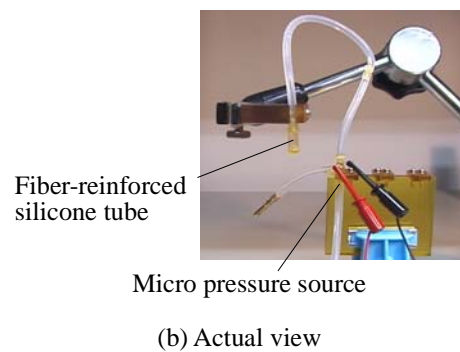
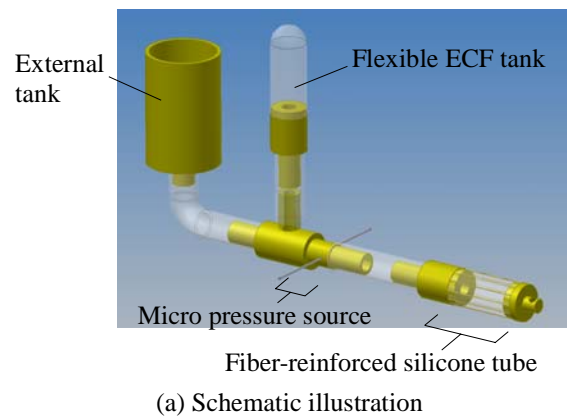


Figure 2 Prototype of micro artificial muscle actuator

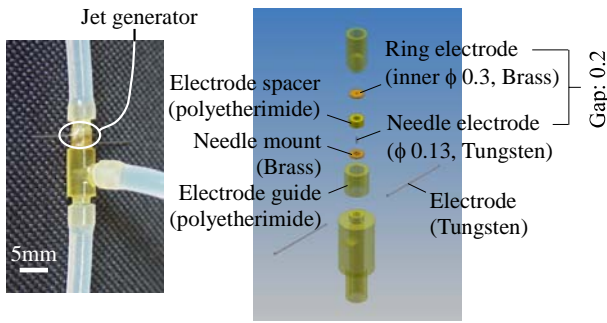


Figure 3 Micro pressure source (Jet generator)

electrode gap to be 0.2 mm. The micro pressure source generates up to around 10 kPa with applied voltage of 6 kV when dibutyl decanedioate, one of the electro-conjugate fluids, is used as a working fluid [14]. The flexible ECF tank and the external tank are filled with the ECF. A bulky external ECF tank was connected to the micro pressure source so that we could easily regulate the pre-pressure of the tube. In case of practical use, the external ECF tank should be removed (the actuator only needs the flexible ECF tank for drive).

EXPERIMENTS

Contraction Characteristics

The contraction characteristics of the prototype were measured. Fig. 4 shows the experimental result of static contraction with input voltages up to 6 kV. The contraction rate showed a quadratic curve against the input voltage. The maximum contraction rate was 0.16 at the input voltage of 6 kV. From the maximum contraction rate, the inner pressure of the actuator is expected to be around 8 kPa.

Fig. 5 shows the experimental results of dynamic contraction when the step input of 5 kV was applied. No overshoot was observed and the rise time was around 7.9 s. The dead region of 2 s shown in Fig. 9 is caused by the following phenomenon: The initial shape of fiber-reinforced silicone rubber tube had a hyperbolic cross-section, which means, narrow in the middle, because of the surface tension. Consequently, the pressure increase at the early phase was used to deform the initial shape to be a straight column.

Force Characteristics

The normal force generated by the prototype was measured. Fig. 6 shows the experimental result of static normal force. The static force measured here is that of so to say isometric contraction of natural muscle. The normal force showed a quadratic curve as the contraction rate did. This kind of characteristics is caused by the pressure characteristics, i.e., the pressure generated at the micro pressure source showed a quadratic relation against the applied voltage. The maximum normal force obtained was 0.18 N at the input

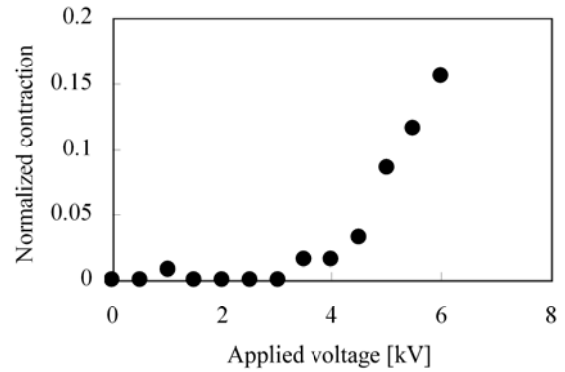


Figure 4 Static contraction

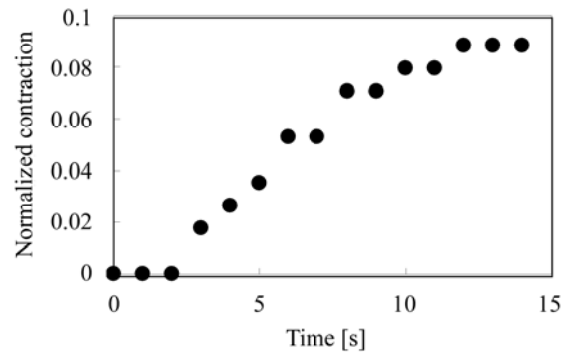


Figure 5 Step response of contraction

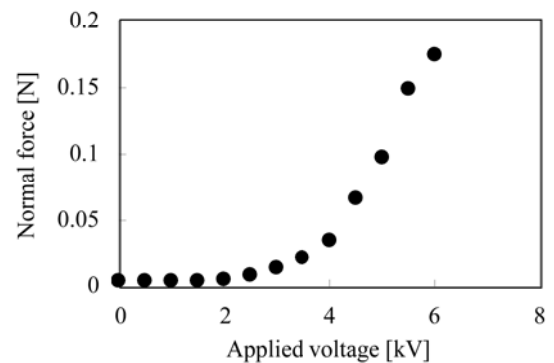


Figure 6 Static normal force

voltage of 6 kV. The inner pressure of 9 kPa might generate the normal force of 0.18 N, although it is expected to be 8 kPa from the contraction characteristic. The generative force of the actuator may seem to be small, however, note that the actuator with pressure source is extremely small. This means that higher actuation forces can easily be obtained by arranging several artificial muscle actuators in parallel.

Fig. 7 shows the experimental result of dynamic normal force with the step input of 5 kV. No overshoot was observed and the rise time was around 7.5 s. The response of the micro artificial muscle actuator was not so high, however, it can be improved by placing several electrode pairs in series-parallel in order to accelerate

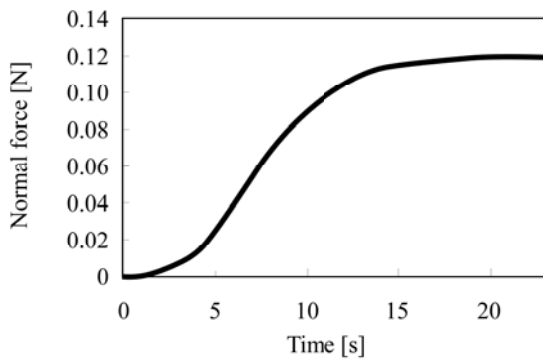


Figure 7 Step response of normal force

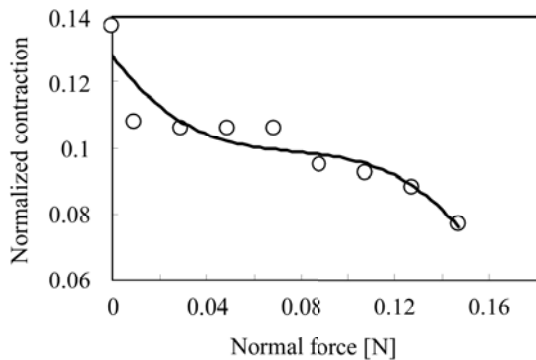


Figure 8 Isotonic normal force

the flow velocity of the ECF jet. Note that, the electrode pair required was extremely compact. Finally, the normal force of so to say isotonic contraction of natural muscle was measured when the input voltage was 5 kV. Fig. 8 shows the experimental result. The relation between normal force and contraction rate showed non-linear characteristic as that of natural muscles do.

PRACTICAL DESIGN SOLUTION

The prototype was for confirming the driving principle and for clarifying the basic driving characteristics of the micro artificial muscle actuator we proposed. It has the fiber-reinforced silicone rubber tube, the micro pressure source, the flexible ECF tank and the external tank, independently. For practical use, we have to integrate the components together.

Fig. 9 shows a practical design solution of the micro artificial muscle actuator. The flexible ECF tank is located around the fiber-reinforced silicone tube in order to maximize the space efficiency. To realize this purpose, the micro pressure source is combined with a tube/tank mount. With this design solution, the pressure source and tank are incorporated in the actuator. Hence, it is easy to be applied for actual systems and to be arranged in an array to obtain larger stroke and force.

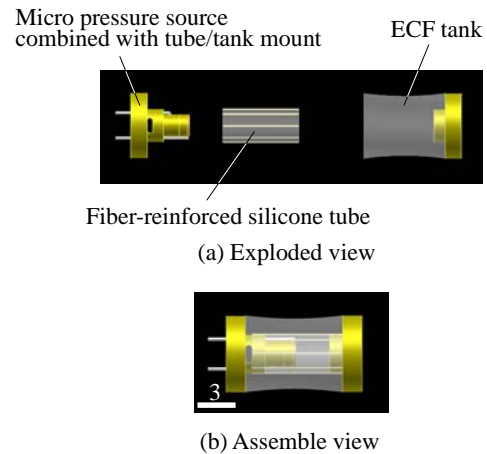


Figure 9 Practical design solution

CONCLUSIONS

A new type of micro artificial muscle actuator using electro-conjugate fluid was developed in this study. The main contribution of this research is the incorporation of the pressure source in the actuator, utilizing the ECF. This enables us to construct a compact artificial muscle actuator, and then, it is easy to apply the actuator to autonomous systems or to micro systems. Furthermore, we can arrange the artificial muscle actuators in an array just as natural systems do.

Our future study focuses on controlling the micro artificial muscle actuator. Also, we will be focusing on applications.

ACKNOWLEDGMENT

This study was supported in part by Grant-in-Aid for Exploratory Research #16656055, Grant-in-Aid for Scientific Research in Priority Areas #16078205, and Grant-in-Aid for Encouragement of Young Scientists (A) #17686013 of the Ministry of Education, Culture, Sports, Science and Technology of Japan.

REFERENCES

1. D. Sasaki, T. Noritsugu and M. Takaiwa, Development of Pneumatic Soft Robot Hand for Human Friendly Robot, *J. Robotics and Mechatronics*, Vol. 15, No. 3, pp. 164-171, 2003.
2. <http://www.shadow.org.uk/index.shtml>
3. H. Meier, L. Oelschlaeger, Numerical Thermomechanical Modelling of Shape Memory Alloy Wires, *Materials Science and Engineering A*, Vol. 378, pp. 484-489, 2004.
4. S. B. Choi, Y. M. Han, J. H. Kim, C. C. Cheong, Force Tracking Control of a Flexible Gripper Featuring Shape Memory Alloy Actuators, *Mechatronics*, Vol. 11, pp. 677-690, 2001.

5. <http://ndea.jpl.nasa.gov/nasa-nde/lommas/eap/WW-EAP-Newsletter.html>
6. Mihoko Otake, Yoshiharu Kagami, Yasuo Kuniyoshi, Masayuki Inaba, Hirochika Inoue, Inverse Kinematics of Gel Robots made of Electro-Active Polymer Gel, Proc. 2002 IEEE Int. Conf. Robotics and Automation, pp. 3224-3229, 2002.
7. Ron Pelrine, Roy Kornbluh, Qibing Pei, and Jose Joseph, High-Speed Electrically Actuated Elastomers with Strain Greater Than 100%, Science, Vol. 287, pp. 836-839, 2000.
8. Yasufumi Otsubo and Kazuya Edamura, Dielectric Fluid Motors, Applied Physics Letters, vol. 71, no. 3, pp. 318-320, 1997.
9. Seong-II Jeong, Jamal Seyed-Yagoobi, and Pierre Atten, Theoretical/Numerical Study of Electrohydrodynamic Pumping Through Conduction Phenomenon, IEEE Trans. Industry Applications, Vol. 39, No. 2, pp. 355-361, 2003.
10. Shinichi Yokota, Masakazu Hirata, Yutaka Kondoh, Koichi Suzumori, Atsushi Sadamoto, Yasufumi Otsubo, Kazuya Edamura, Micromotor Using Electroconjugate Fluid (Fabrication of Inner Diameter 2mm RE type ECF Motor), J. Robotics and Mechatronics, Vol. 13, No. 2, pp. 140-145, 2001.
11. Shinichi Yokota, Atsushi Sadamoto, Yutaka Kondoh, Yasufumi Otsubo, Kazuya Edamura, A Micro Motor Using Electro-conjugate Fluids (ECFs) (Proposition of Stator Electrode Type (SE-type) Micro ECF motors), Int. J. JSME, Ser. C, Vol. 44, No. 3, pp. 756-762, 2001.
12. Shinichi Yokota, A 2mm ECF micromotor, Proc. 7th Int. Conf. Mechatronics Technology (ICMT'03), pp. 361-366, 2003.
13. Ryutaroh Abe and Shinichi Yokota, A Micro Actuator using ECF-Jet with Needle-type Electrode, Proc. FLUCOME'03, CD-ROM, 2003.
14. Kenjiro Takemura, Shinichi Yokota and Kazuya Edamura, A Micro Artificial Muscle Actuator using Electro-conjugate Fluid, Proc. IEEE Int. Conf. Robotics and Automation, pp. 534-539, 2005.

DEVELOPMENT OF PISTON TYPE LINEAR ACTUATORS USING ELECTRO-CONJUGATE FLUID

Kentaro KASHU*, Takeshi NAKADA**, Yasuo SAKURAI*** and Toshinori FUJITA****

* Department of Precision Engineering, Faculty of Engineering
Tokyo Denki University

2-2 Kandanishikicho, Chiyodaku, Tokyo, 101-8457 Japan

** Department of Information Environment Integration and Design
Tokyo Denki University

2-1200 Muzaigakuendai, Inzai-city, Chiba, 270-1382 Japan

*** Department of Mechanical Engineering, Faculty of Engineering
Ashikaga Institute of Technology

268-1 Oomaecho, Ashikaga, Tochigi, 326-8558 Japan

**** Department of Machinery System Engineering, Faculty of Engineering
Tokyo Denki University

2-2 Kandanishikicho, Chiyodaku, Tokyo, 101-8457 Japan

ABSTRACT

An Electro-Conjugate Fluid (ECF) is considered as a functional fluid like electro-hydro dynamics fluid, and it has a remarkable property that a jet flow is generated between two electrodes when a high voltage is applied to the electrodes. In this study two types of linear actuators consisting of the pistons and cylinders using an ECF are proposed. The one has a structure of a coil type electrodes, and the other a structure of mesh type electrodes. The proposed actuators are fabricated, and their basic characteristics such as piston velocities vs. applied voltages to electrodes and the load characteristics are examined in the experiment. The experimental results show that the proposed linear actuators have the possibilities to be used as the functional linear actuators.

KEY WORDS

Linear Actuator, ECF, Jet Flow, Static Characteristics, Load-Velocity Characteristics

INTRODUCTION

An actuator is an essential component of robots and many other mechanical devices. There has been a growing demand for increasingly miniaturized and versatile actuators in recent years. This has spurred great interest in R & D for these components, both in solid-state actuators such as piezoelectric and electrostatic devices, and devices based on functional fluids, such as electro-rheological and magnetic fluids. Sumoto discovered that a dielectric fluid will rise against the pull of gravity along an electrode submerged in the fluid if a sufficiently high voltage is applied to the electrodes, a phenomenon subsequently called the Sumoto effect. More recently, Ohtubo et al. have

reported that application of a high voltage to electrodes submerged in certain types of dielectric fluids such as di-n-butyl dodecandioate causes an intense jet between the electrodes. The mechanism of this flow has yet to be explained, but since the jet effect is considerably more intense than those observed in other electrohydrodynamic (EHD) fluids, these dielectric media have been given their own designation, "electro-conjugate fluids" (ECF)[1]. ECF may enable construction of actuator systems with much simpler structures and driving circuits than conventional electric motors. There has been much research into different kinds of rotary motors based on ECF[2][3][4], pump modules employing EHD fluids[5], flow analysis of jets in opposed ring electrodes[6][7], and related topics.

This report describes the concept, fabrication and observed operating characteristics of a linear actuator based on ECF, a type of actuator which has received almost no attention from other researchers to the best of our knowledge. Piston-operated linear actuators of two configurations were fabricated using coil and mesh type electrodes. Operating characteristics were observed for both actuators, namely, the piston velocity with respect to applied voltage, static characteristics of current in the actuator at no load, and load-piston velocity. Future issues in the development of these actuators are also discussed.

CONCEPT AND FABRICATION OF LINEAR ACTUATOR

Since, in addition to rotary actuators, linear actuators have been widely used in industry, two types of ECF-based actuators were designed and constructed in this research. Both a coil and a mesh construction can be used for the electrodes in generating an ECF jet as the power source for a piston-operated linear actuator; accordingly, a coil-electrode linear actuator (coil-type actuator) and a mesh-electrode linear actuator (mesh-type actuator) were created.

Coil-Type Actuator

Figure 1 presents the coil-type actuator fabricated in this research. Let us consider the results of applying a voltage across the pair of helical coil-type electrodes shown in (a) with differing gap sizes of a and b . To simplify, let us assume here that $a < b$. In this model, an ECF jet is generated from the black coil toward the white coil in the gap a in Figure 1(a), from left to right, while an opposite jet is generated, from right to left, in the gap b . Since the gap a is smaller than the gap b , however, the strength of the jet in the gap a is greater than that in the gap b and therefore, the net effect is the excitation of an ECF jet from right to left. Applying an opposite voltage will cause a jet from left to right. Thus, controlling the polarity and intensity of the voltage applied to the helical coil pair controls the direction and intensity of the ECF jet. As shown in (b), directing the ECF jet into the cylinder inside the coil drives the piston in the cylinder. The number of turns in the fabricated coil was 4, the diameter was 18 mm, the length was 35 mm, and the material was tin-plated 1-mm wire. The electric power supplied to the coil was produced by a high voltage DC source through leads into caps placed at each end of the coils. The effective area of the piston was made of propylene and measured 12mm in diameter and 0.8 mm in thickness. The piston rod was made of 1-mm piano wire. The overall piston weight was 0.75g and the maximum stroke was 16 mm. Transparent polyvinyl chloride resin was used for the structure of the coil-type actuator. To examine the effect of the $a:b$ gap ratio on actuator performance, three coils were fabricated with gaps of $a = 1, 2$ or 3mm and $b = 4$ mm.

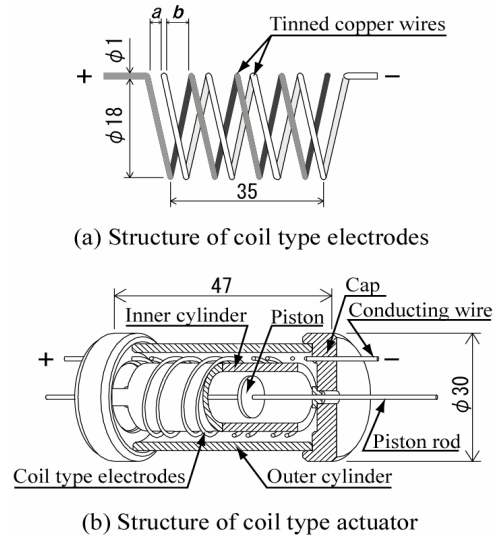


Figure 1 Configuration of coil type actuator

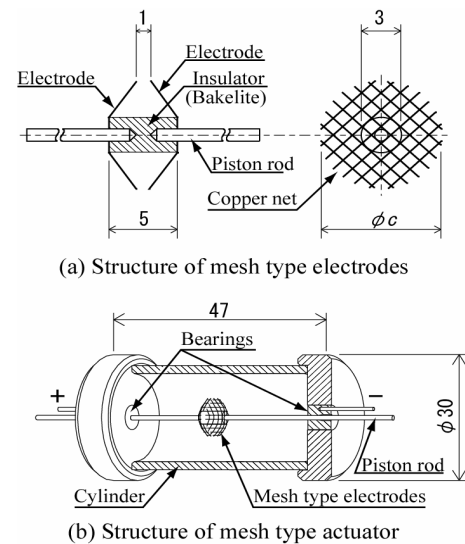


Figure 2 Configuration of mesh type actuator

Mesh-type Actuator

Figure 2 is a diagram of a mesh-type actuator. The electrodes shown in (a) were two opposed bowl-shaped meshes of 0.2-mm-diameter copper wire, woven at a spacing of 1 mm. A Bakelite rod 3 mm in diameter held the meshes in position while also insulating them from each other. Piston rod pieces were inserted along the axis at each end of the Bakelite rod and were electrically connected to each mesh. The piston rods were connected at their tips to a high-voltage source through a bearing (Figure 2(b)). The ECF jet was generated by charging the electrodes with the voltage through the piston rods. As shown in Figure 2(b), the mesh electrode structures also serve as pistons, driven directly by the jet.

In this research, meshes with three diameters (ϕ_c in Figure 2(a)) were used: 10, 13 or 15 mm. A preliminary experiment showed that a pair of flat meshes standing in parallel yielded almost no driving force to the pistons; the bowl-shaped electrodes were then fabricated and tested. This configuration has the advantage of a simpler construction than the coil-type actuator.

EXPERIMENTAL APPARATUS

Figure 3 shows the apparatus used for examining the basic operating characteristics of the linear actuators fabricated for this research. Each actuator was set in a vertical position in the cylinder. The base of the cylinder was placed in a container of ECF (not shown in the figure) in order to prevent leaks of the ECF from the bearing race of the piston. When the actuator was charged with a high voltage by the DC source, the piston, positioned at the floor of the cylinder by gravity, was raised by the action of the ECF jet under the influence of the electrodes. The speed of the piston was observed with a laser-based displacement/speed sensor. Also, the ground side of the electrode was connected in series with an exterior electric resistor (10 k Ω) in order to estimate the current by measuring the voltage drop across the resistor. Table 1 displays the principal physical characteristics of the ECF used in the experiment.

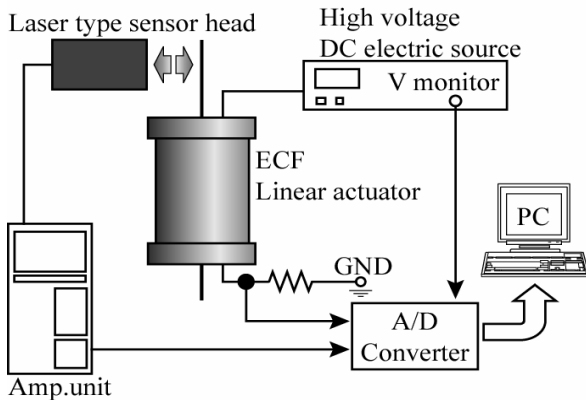


Figure 3 Experimental apparatus

Table 1 Properties of ECF

Boiling temperature	78 [°C]
Surface tension	0.014 [N/m]
Kinetic viscosity	0.4×10^{-6} [m ² /s]
Density	1430 [kg/m ³]
Firing point	None

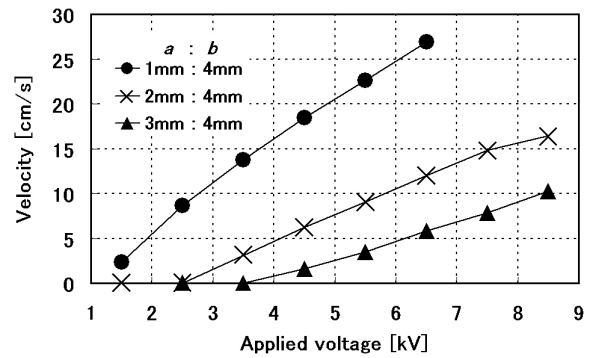


Figure 4 Static characteristics between piston velocity and applied voltage in coil type actuators with no load

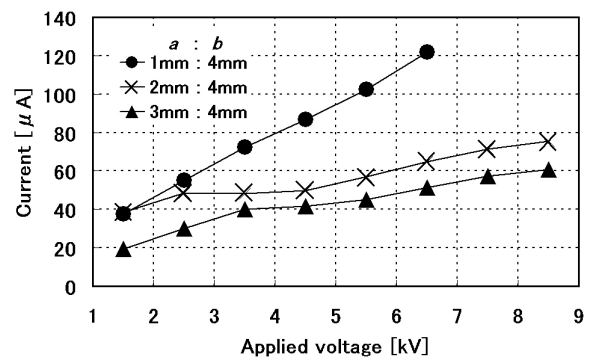


Figure 5 Static characteristics between current and applied voltage in coil type actuators with no load

STATIC CHARACTERISTICS OF THE ACTUATORS (NO LOAD)

Coil-Type Actuator

A coil-type actuator (see Figure 1(b)) was placed in the apparatus shown in Figure 3 and a DC voltage was applied to the helical coils. The speed of the piston forced upward by the operated ECF jet was recorded once it had reached a constant rate. The results are given in Figure 4. The symbols ●, ×, and ▲ represent the results for electrode spacing of 1, 2 and 3 mm, respectively. All cases showed a nearly proportionate increase in piston speed with applied voltage. Also, the smaller the dimension of the gap a , the greater the piston speed. This is consistent with the increase in ECF jet speed of the gap a shown in Figure 1(a). When the gap a was 1 mm and the voltage 6.5 kV, the piston speed was a considerable 27 cm/s. No results were recorded for higher voltages for the gap $a = 1$ mm because at high voltages, the piston speed did not become constant within the maximum stroke distance (about 16 mm) before the piston struck the top of the cylinder. It is reasonable to anticipate that higher piston

speeds would be attained at higher voltages.

It should also be noted that the minimum voltage necessary to initiate piston displacement diminished with gap size; at the gap $a = 1$ mm, this was 1.5kV. This voltage is expected to be greatly affected by the weight of the piston and the piston-cylinder friction.

The piston speed characteristics were found to be strongly affected by the gap ratio ($a:b$) and thus it will be necessary to identify the optimal electrode distance, given coil shape and dimensions. Figure 5 shows the observed current flow between the electrodes with applied voltage and electrode gap a . As seen in the piston speed characteristics in Figure 4, the current between the electrodes increased both with applied voltage and with diminishing electrode gap a .

Mesh-Type Actuator

The mesh-type actuator (see Figure 2(b)) was placed in the apparatus in Figure 3. The same experiments were performed as with the coil-type actuator, using the three mesh diameters (ϕ_c) 10, 13 and 15 mm. Figure 6 displays the observed relation between applied voltage and piston speed, and Figure 7, that between applied voltage and current flow between the electrodes. Figure 6 shows quite similar results to those for the coil-type actuator in Figure 4, i.e., all electrodes show a roughly linear increase in piston speed with voltage. However, in terms of the minimum voltage necessary to obtain starting, the mesh-type actuator required a higher voltage, and its results showed a greater scatter. As described later, this was attributed to the lower driving force generated by the present mesh-type actuator compared to the coil-type actuator; friction in the bearings and at other locations is expected to exert a relatively larger effect. The piston speed was highest when the $\phi_c = 13$ mm mesh was used; the speed was about equal to that observed with the 1-mm electrode spacing in the coil-type actuator. For mesh with $\phi_c = 10$ or 15 mm, no clear tendencies were observed in the relation between piston speed and electrode size. Figure 7 shows the current through the mesh structure between the electrodes; the current generally increases with electrode diameter. However, even though the current through the 13-mm-diameter electrodes was about midway between the levels at 10 and 15 mm, the piston speed at this diameter was highest, as shown in Figure 6. Further study is necessary into the relation of the electrode size to the current flow and piston speed. As the mesh electrode size increases, the electrode current and piston speed are also expected to increase, but piston mass and fluid resistance to the piston motion must also increase. The piston speed is determined by the equilibrium among all these factors. These interrelationships will have to be clarified before this actuator can be applied to real-world uses.

Time-Based Changes in Static Characteristics

We have discussed the characteristics of piston speed and current between the electrodes with respect to

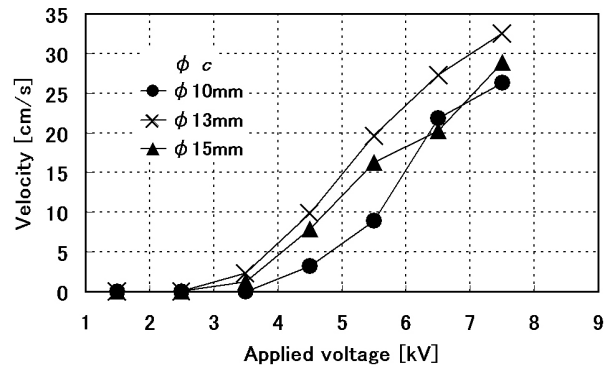


Figure 6 Static characteristics between piston velocity and applied voltage in mesh type actuators with no load

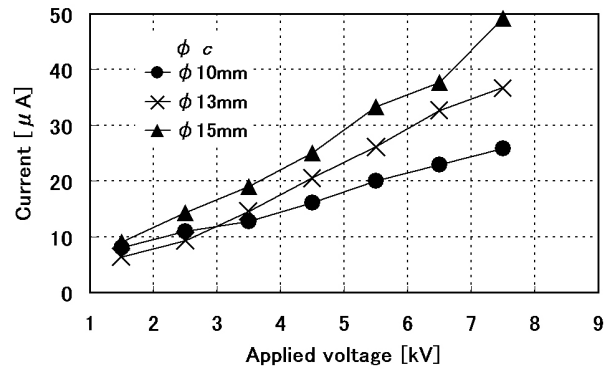


Figure 7 Static characteristics between current and applied voltage in mesh type actuators with no load

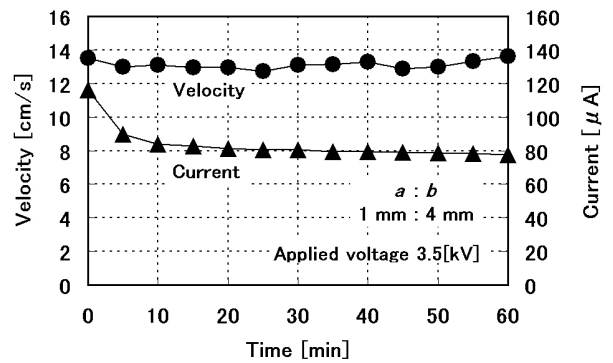


Figure 8 Static characteristics of piston velocity and current against elapse of time in coil type actuator with no load

applied voltage in coil-type actuators and mesh-type actuators. For practical application of these actuators, however, it is also important to examine how these characteristics change with time. Therefore, a coil-type

actuator with electrode spacing $a = 1$ mm and a mesh-type actuator with mesh diameter of 13 mm were subjected to voltage square waves of intensity 0 – 3.5 kV at a frequency of 0.1 Hz, causing reciprocating motion of the pistons, continuously for 60 min. Every 5 min, the piston speed and the current were observed, as shown for the coil-type actuator in Figure 8. The values of the piston speed hold constant. However, the current decreased somewhat during the 0-5 min period and subsequently became approximately constant. The mesh-type actuator exhibited the same pattern.

CHARACTERISTICS OF PISTON SPEED WITH ACTUATOR LOADING

The piston speed was again measured using the same method as described for the unloaded actuators in section 4, but this time, a range of weights were attached to the upper tip of the piston axle on the vertically displacing actuator (see Figure 3) The models tested were the coil-type actuator with a 1-mm electrode gap and the mesh-type actuator with 13-mm mesh, as these produced the highest piston speeds in the unloaded condition. The relations between piston speed and loading are shown in Figure 9 (coil-type actuator) and 10 (mesh-type actuator). The loads and piston speeds indicated by \blacktriangle , \times , and \bullet in Figure 9 represent voltages of 2.5 kV, 3.5 kV and 4.5 kV, respectively. Overall, these figures show the same drooping characteristic as seen in the torque-speed curve of a typical DC motor. It is easy to control the load by adjusting the voltage; this is a desirable trait for the purpose of control. In Figure 10, the \blacktriangle , \times , and \bullet symbols represent voltages of 4.5 kV, 5.5 kV and 6.5 kV, respectively. The mesh-type actuator showed the same trend for piston speed under load as the coil-type actuator did. The characteristics in Figures 9 and 10 were approximated by the broken lines, and then, the maximum power efficiency (mechanical power output/electrical power input, %) was calculated for each voltage. The coil-type actuator showed maximum power efficiencies at 2.5 kV, 3.5 kV, and 4.5 kV of 0.5%, 0.9% and 1.2%, respectively; the corresponding figures for the mesh-type actuator at 4.5 kV, 5.5 kV, and 6.5 kV were 1.3%, 1.5% and 1.7%, respectively. The maximum power efficiencies in both actuators improved with increased applied voltage. Also of interest, the electrical energy levels supplied to the coil-type actuator and mesh-type actuator at 4.5 kV were 400 mW and 90 mW, respectively. As mentioned above, the power efficiencies at this voltage were similar at 1.2% and 1.3%, respectively. ECF-based micromotors have attained experimental efficiencies as high as 17%. One of the issues for future models of these linear actuators will be to establish design guidelines for improving the power efficiency.

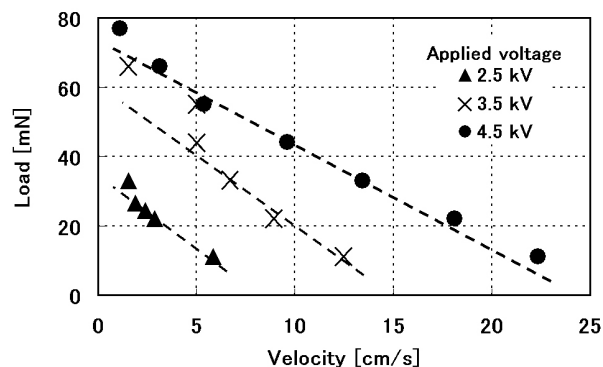


Figure 9 Static characteristics between load and applied velocity in coil type actuator ($a : b = 1[\text{mm}] : 4[\text{mm}]$)

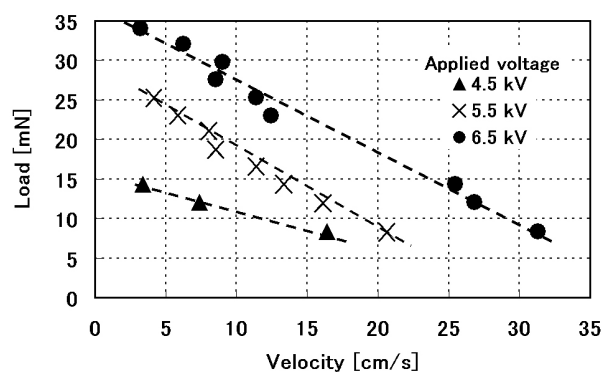


Figure 10 Static characteristics between load and velocity in mesh type actuator ($\phi 13$)

CONCLUSIONS

This report presents two linear actuators based on jet flows of electro-conjugate fluids (ECF), which have attracted interest as new functional fluids. Piston-type actuators were constructed using two different structures for the exciting ECF jets: a coil-based structure and a mesh-based structure. The basic static characteristics of these actuators were investigated. The main findings are as follows:

- (1) Both of the proposed linear actuators displayed fairly good static characteristics and potential for functional improvement.
- (2) In the coil-type actuator, the piston speed and the electric current flow between the electrodes grew approximately in proportion to the applied voltage. The mesh-type actuator showed similar characteristics. The coil-type actuator produced an unloaded piston speed of 27 cm/s when the electrode spacing was 1 mm and the applied voltage was 6.5 kV, at a current flow of 120 μA . This represents a moderately high piston speed.

(3) No large changes in function were noted in continuous cycling of either actuator for 60 min.

(4) Both actuators showed load-piston speed characteristics closely resembling the well-known torque-speed curve for a DC motor.

(5) The maximum power efficiencies were 1.2% at a supplied electrical power of 400 mW for the coil-type actuator and 1.7% at a supplied electrical power of 90 mW for the mesh-type actuator.

Future research on these linear actuators should aim to improve speed, and power efficiency. In particular, more detailed design data is required in order to optimize the coil and mesh electrode structures of the actuators and to investigate methods to prevent leakage of ECF.

REFERENCES

1. Shinichi, YOKOTA., Atsushi, SADAMOTO., Yutaka, KONDO., Yasufumi, OTSUBO. and Kazuya, EDAMURA., A Micro Motor Using Electro-Conjugate Fluids (ECFs) [Proposition of Stator Electrode (SE)-Type Micro ECF Motors] -(in Japanese), JSME Journal, 2000, 66-642, Series C, pp.627-633.
2. Shinichi, YOKOTA., Toshiyuki, NEMOTO., Yutaka, KONDO., Yasufumi, OTSIBO. and Kazuya, EDAMURA., A Micro Motor Using Electro-Conjugate Fluids (ECF) [Proposition of Rotor-Electrode (RE)-Type Micro ECF Motors]-(in Japanese), JSME Journal, 2000, 66-651, Series C, pp.275-280.
3. Shinichi, YOKOTA., Daisuke, SATO., Yutaka, KONDO., Yasufumi, OTSUBO. and Kazuya, EDAMURA., A Motor Using Electro-Conjugate Fluids (ECF) [Proposition of Disk Plate (DP)-Type ECF Motors] -(in Japanese), JSME Journal, 2001, 67-664, Series C, pp.356-361.
4. Shinichi, YOKOTA., So, KUWAJIMA.,and Kazuya, EDAMURA., Realization of a Higher Integrated Multi-layered DP-RE-type ECF Micro-Motor -(in Japanese), JSME Journal, 2004, 70-693, Series C, pp.239-245.
5. Tetsuya, AKAGI., Shujiro, DOUTA., and Hisashi, MTSUSHITA., Development of a Pumping Module Using EHD Fluid -(in Japanese). JSME Journal, 2002, 68-673, Series C, pp.98-103.
6. Seong-Il Jeong, Jamal Seyed-Yagoobi, Theoretical/ Numerical Study of Electrohydrodynamic Pumping Through conduction Phenomenon, IEEE Trans, on Industry Applications, 39-2(2003), pp.355-361.
7. S.I.Jeong and Seyed-Yagoobi, Innovative Electrode Designs for Electrohydrodynamic Conduction Pumping, 0-7803-7420-7/02, 2002, IEEE, 2204-2208.

MICRO-ELECTROHYDRODYNAMIC PUMP BY DIELECTRIC FLUID: IMPROVEMENT FOR PERFORMANCE OF PRESSURE USING CYLINDRICAL ELECTRODES

Ichiro KANO*, Kazuya MIZUOCHI* and Ichiro TAKAHASHI*

* Yamagata University, Mechanical Systems Engineering
4-3-16, Jonan, Yonezawa-shi, Yamagata Japan
(E-mail: kano@yz.yamagata-u.ac.jp)

ABSTRACT

This paper presents the improvements for the performance of a micro-electrohydrodynamic (EHD) pump and the fundamental model theory based on unipolar charge conduction. The EHD pump was fabricated with thin stainless wires which are the diameter of 0.3mm. An electrode pair consisted of one emitter electrode and two collector electrodes. The distance between the emitter and the collector electrode in an electrode pair had a 0.2mm. Static pressure tests have been performed with a dielectric fluid. In order to increase the pressure performance, the electrode pair was increased from one to five at the distance between the electrode pairs, 2.0mm. As a result, it is found that the increase of the electrode pairs improve the pressure performance. The EHD pump produces a static pressure about 700 Pa with five electrode pairs using Dibutyl Sebacate. Both experimental and theoretical pressure results show a liner relationship. This linear relationship confirmed the unipolar conduction concept theoretically.

KEY WORDS

Electrohydrodynamic (EHD), Pump, Dielectric Fluid, Static Pressure, Cylindrical Electrode,

NOMENCLATURE

L : length, m
 P : pressure, Pa
 V : voltage, V
 h : height, m
 r : radius, m
 ε : dielectric constant, F/m
 μ_e : Ion mobility, $m^2/V \cdot s$
 μ : Dynamic viscosity, $Pa \cdot s$
 ρ : Liquid density, kg/m^3
 σ : Electric conductivity, S/m

INTRODUCTION

With the advance of micro fabricated electro-mechanical devices, new applications such as micro pumps and micro actuators are expected. In these days, the electronic devices are demanded for reducing both volume and weight while increasing their complexity and power density. The micro pumps will be used in a micro fluidic pump in order to cool the electric devices. In micro-fabricated systems, the pumps without moving parts are of special interest. The electrohydrodynamic (EHD) pumps without vibration and dissipate power are electronically controllable and require no or little maintenance. These advantages make them attractive for

applications in micro-systems.

The EHD pumps use the Coulomb force by unipolar charge conduction to produce high pressure in a compact design pump without moving parts. The charges on a dielectric fluid are charged and directly discharged on the surface of electrodes. The fluid molecules are charged with electrodes and derived by the electric field between electrodes in the EHD pump [1].

The fact that dielectric liquids can be pumped by the injection of ions in applied electric field between the electrodes has been known for some time. Indeed, the theoretical and experimental investigations of the EHD pump were widely pursued in early 1960's. Stuetzer [2] and Pickard [3], [4] were the first researchers who proposed and studied the ion-drag EHD pump. Later, many researchers made further studies of the ion-drag EHD pump.

Crowley et al. [5] showed that high dielectric constant and low viscosity would lead to high flow velocity, while low electric conductivity and mobility would promote high efficiency.

With development of micro-fabricated technology, intense research efforts have been made toward micro-fluidic systems and micro-liquid handling devices [6], [7].

Otsubo et al. [8] used the jet flow produced by the injection of ions in Dibutyl Sebacate as the rotational power of motors. Yokota et al. [9] developed the micro-motors of a millimeter-scale outer diameter using Dibutyl Sebacate.

This paper presents the arrangements of the electrodes made by thin stainless wires to improve the pressure performance of the EHD pump (Figure 1). Also, this paper presents a fundamental model developed to design and characterization of the EHD pump.

EXPERIMENTAL SETUP

A photograph of the EHD pump is shown in Fig. 1. The overall dimensions of the micropump are $30 \times 30 \times 4.9$ mm and of the pumping channel are $24 \times 24 \times 0.9$ mm. The main body of the pump was made by the acrylic resin.

An arrangement of the electrodes is shown in Fig.2. The EHD pump was fabricated with the thin stainless wires which are the diameter of 0.3 mm. An electrode pair consists of one emitter electrode fixed on the center of the channel and two collector electrodes fixed on the channel walls. A distance between emitter and collector electrodes was 0.2 mm. The distance, L , between the electrode pairs was changed with 0.6, 2.0 and 3.4 mm. The number of the electrode pairs can be increased from one to five.

The static pumping tests of the EHD pump were performed with a Dibutyl Sebacate. This fluid has a relative dielectric constant, $\epsilon/\epsilon_0=4.8$ and a low electric

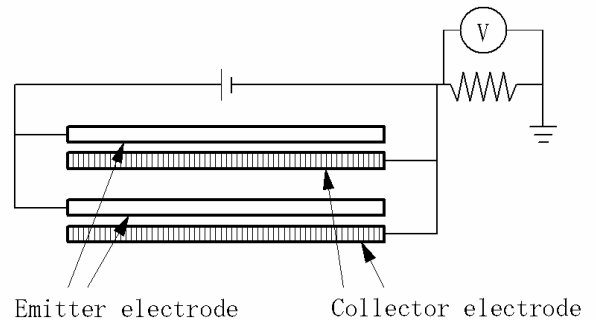
conductivity, $\sigma = 4.7 \times 10^{-10}$ (S/m). Other properties of this fluid are listed on Table 1.

A positive DC-voltage (KIKUSUI Model PHS10K_10) was applied to the emitter electrodes. A voltage drop on a resistance (100 k Ω) inserted in negative electrode is monitored by a multimeter (YOKOKAWA Model 7562) and the electric current of the pump circuit can be calculated from the measured voltage and the resistance.

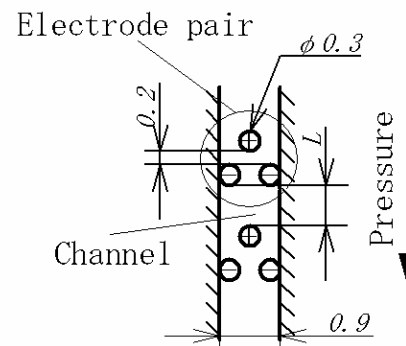
The outline drawing of static pressure measurement is shown in Fig. 3. The static pressure (zero flow rates) was measured using an inclined-tube manometer. The acrylic tubes for the inclined manometer have the inner diameter of 3 mm and the length of 1 m. All experiments were performed at a room temperature.



Figure 1 Top view of the EHD pump



(a) Top view



(b) Side view

Figure 2 Arrangement of the electrodes

Table 1 Properties of Dibutyl Sebacate

Properties	Dibutyl Sebacate (C ₁₈ H ₃₄ O ₄)
Relative dielectric constant ϵ/ϵ_0	4.8
Electric conductivity σ [S/m]	4.7×10^{-10}
Ion Mobility μ_e [m ² /V·s]	2.1×10^{-9}
Viscosity μ [Pa·s]	9.4×10^{-3}
Liquid density ρ [kg/m ³]	940

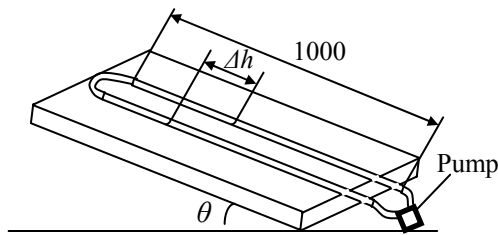


Figure 3 Outline drawing of static pressure measurement

EXPERIMENTAL RESULT

The static pressure of the EHD pump was determined using Dibutyl Sebacate as working fluid. The electrodes and the pumping channel were cleaned with ethanol to avoid the contamination of the fluid with impurities. The applying voltage was varied such as 0.2, 0.4, 0.6, 0.8 and 1.0 kV. When the voltage was applied to the electrodes, the liquid lifted height was recorded, while the voltage was raised by steps. The maximum point of the liquid height was recorded, since the liquid lifted height tends to decrease with time.

The measurement of static pressure for the various distances between two electrode pairs, L , is shown in Fig. 4. The distance, L , is changed such as 0.6, 2.0 and 3.4 mm. The electrodes layout of the one electrode pair is labeled P1. The distance between the emitter and the collector is 0.2mm (Fig. 1). The other layouts labeled such as P2L0.6, P2L2.0 and P2L3.4, have two electrode pairs with the distance, L , of 0.6, 2.0 and 3.4mm, respectively.

The static pressure of P2L2.0 shows the highest performance in these experiments. Therefore, it is evident that the case of $L=2.0$ indicates the best performance. The static pressure for P2L2.0 is up to 340 Pa at applying voltage of 1 kV.

The static pressure results by increasing the number of electrode pairs are shown in Fig. 5. All of the electrode distance between the electrode pairs, L , is the same as

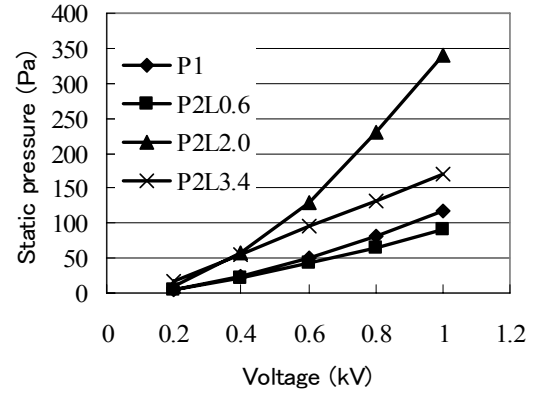


Figure 4 Static pressure as a function of applied voltage for the case of various electrode distances

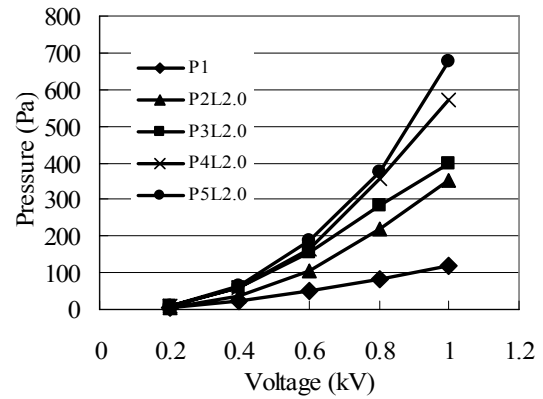


Figure 5 Static pressure as a function of applied voltage for the case of various number of electrode pairs

2.0 mm. The numbers of the electrode pairs are increased one to five in the EHD pump. We believe that the larger number of the pairs is the better pumping performance in this design. The static pressure for P5L2.0 was raised up to 700 Pa at applying voltage of 1 kV.

DISCUSSION

The simple formulas of the EHD pump for plane, cylindrical and spherical electrode were summarized by Stuetzer [2]. Stuetzer derived the static pressure of EHD pump with a cylindrical electrode as:

$$\Delta P \approx \epsilon \left(\frac{V - V_0}{r} \right)^2 \log \frac{r}{r_0} \quad (1)$$

where P is the pressure within the fluid, V is the applying voltage, ϵ is the permittivity and V_0 is the threshold voltage below which pressure is not obtainable. V_0 is

assumed to be zero in this paper. r is the radius of between the electrodes and r_0 is the radius of a electrode. The main dimensional parameters of this arrangement are indicated in Fig. 6.

According to Eq. (1), the pressure of the EHD pump is proportional to the square of the electric field when the electrodes are fixed.

The pressure drop is generated at an electrode pair and between the electrode pairs. The pressure drop between the electrode pairs is generated to the opposite direction of the pressure drop generated at an electrode pair. Although the electric field between the emitter and the collector are slightly affected by the other electrodes, we assumed that the electric field between the emitter and the collector is not interfered by the other electrodes. The total pressure drop is exerted by the electric filed between the emitter and the collector. Then, we have:

$$\Delta P \approx \sum_{n=1}^N \epsilon \left(\frac{V - V_0}{r} \right)^2 \log \frac{r}{r_0} - \sum_{n=1}^{N-1} \epsilon \left(\frac{V - V_0}{r'} \right)^2 \log \frac{r'}{r_0} \quad (2)$$

where r' is the radius between the electrode pairs and N is the number of the electrode pairs.

Figure 7 shows the comparison between the experimental and the theoretical values from Eq. (2). The relationships between experimental and theoretical pressure are not a liner except for P2L2.0, while we can expect that all relationships are linear from Eq. (2). The deviation from linear relationship would be caused by the impurities in the liquid.

Figure 8 shows the comparison between the experimental and theoretical pressure. The experimental pressures are the values in Figure 5 and the theoretical ones are from Eq. (2).

There are almost liner relationships between the experimental and the theoretical results. This linear relationship confirmed the concept of unipolar conduction theoretically. The results of pressure obtained with five pairs of the electrodes P5L2.0 show high performance. It is found that increasing the pair of the electrodes improve the pumping performance.

CONCLUSIONS

The improvement for the micro-EHD pump using the thin stainless wires was investigated and the static pressure generated by the pump was quantified. A fundamental theoretical model contributed to guide the design and characterization of EHD pump. The fundamental theory was based on a unipolar conduction model reported by Stuetzer [2]. The electrodes were consisted of several electrode pairs which have one emitter electrode and two collector electrodes. The number of electrode pair increased from one to five. The results of the static pressure demonstrated successfully the capabilities of the EHD pump. The EHD pump with

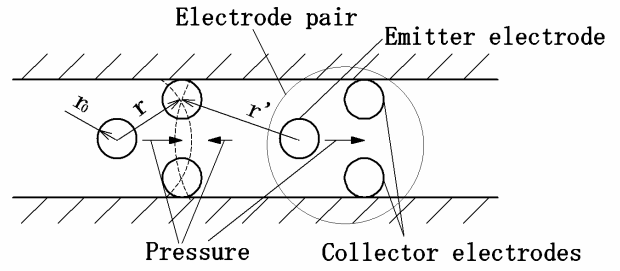


Figure 6 Arrangements and the parameters for cylindrical coordinates

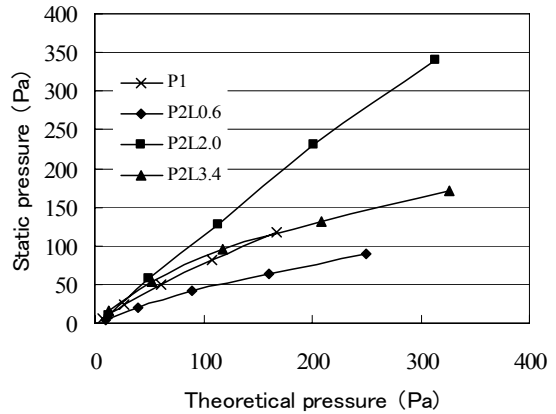


Figure 7 Relationship between experimental and theoretical pressure for the case of various electrode distances

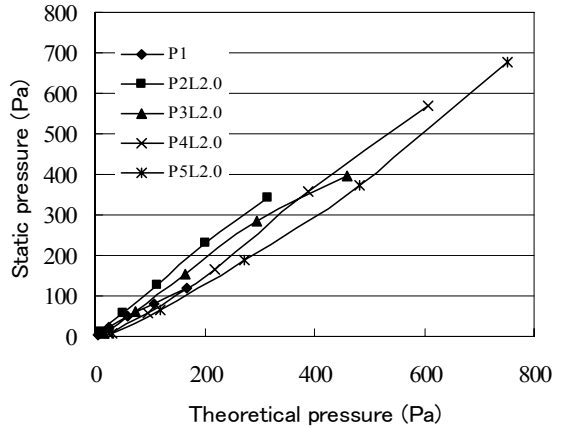


Figure 8 Relationship between experimental and theoretical pressure for the case of various numbers of electrode pairs

five electrode pairs produced a static pressure drop about 700 Pa using Dibutyl Sebacate.

The relationship between the experimental and the theoretical pressure showed a linear relationship. For the same boundary conditions of the electrode, the static pressures were proportional to the square of electric field strength. This linear relationship confirmed the concept

of unipolar conduction theoretically. As a result, it is cleared that the theoretical model is useful to design of the high performance EHD pumps.

REFERENCES

1. I. Kano and Y. Kano, Micro-electrohydrodynamic pump by dielectric fluid, The Sixth KSME-JSME Thermal and Fluids Engineering Conference, 2005, JH01, Jeju, Korea.
2. O. M. Stuetzer, Ion Drag Pressure Generation, *J. Appl. Phys.*, 1959, **30**-7, pp.984-994
3. W. F. Pickard, Ion-Drag Pumping I : theory, *J. Appl. Phys.*, 1963, **34**-2, pp.246-250.
4. W. F. Pickard, Ion-Drag Pumping II : Experiment, *J. Appl. Phys.*, 1963, **34**-2, pp.251-258.
5. J. M. Crowley, G. S. Wright and J. C. Chato, Selecting a Working Fluid to Increase the Efficiency and Flow Rate of an EHD Pump, *IEEE trans. Ind. App.*, 1990, **26**-1, pp.42-49
6. J.Darabi, M. Rada, M. Ohadi, and J. Lawler, Design, Fabrication and testing of an Electrohydrodynamic Ion-Drag Micropump, *J.Microelectromech. Syst.*, 2002, **11**-6, pp.684-690
7. J. Darabi and K..Ekula, Development of a chip-integrated micro cooling device, *Microelectronics J.*, 2003, **34**, pp.1067-1074
8. Y.Otsubo and K.Edamura, Dielectric Fluid Motors, *Appl. Phys. Letter*, 1997, **71**-3, pp.318-320
9. S. Yokota, Y. Kondoh, A. Sadamoto, Y. Otsubo and K.Edamura, A micro motor using electro-conjugate fluids (Proposition of stator electrode-type (SE-type) micro ECF motors), *JSME Int. J.* 2001 C, **44**-3, pp.756-762.

The new type actuator by applying the EHD phenomenon

— Development of the EGD Motor —

Sumitaka TERASAKA*, Shu KUDO*, Shinichi KURODA**, Hiroshi ABE***,
Junko NIITSUMA****, Tsuyoshi SAITOH***** and Kazuyuki MITSUI*

* Department of Machinery System Engineering
Tokyo Denki University

** Department of Chemistry (Materials Science)
Gunma University

***Department of Materials Science and Engineering
National Defense Academy

****Department of Motor Dysfunction

National Rehabilitation Center for the Disabled

*****Mechanical and System Safety Research Group
National Institute of Industrial Safety

ABSTRACT

The purpose of this study was to develop the new type actuator which has flexibility by using an EHD phenomenon for the application to the small machine or welfare system. The EHD phenomenon is a phenomenon that generates the flow in the insulating fluid by applying a high voltage electric field. Especially, rotation type actuator using an EGD phenomenon was developed by this study. And, EGD (Electro Gas Dynamics) phenomenon is a kind of the EHD phenomenon which occurs in the gas. Then, this actuator was called EGD motor. The EGD motor has one pair of electrode, one of these is a cylindrical electrode for a stator and another is L shaped electrode for a rotor. We changed the shape of electrode and measured the torque and rotation speed, to evaluate the rotational performance of the EGD motor

KEY WORDS

EHD phenomenon, EGD phenomenon, motor, actuator, compliance

INTRODUCTION

Various equipments are developed for the medical and welfare system. Especially, in the equipment for the welfare system, flexibility to the over-load is more necessary than a positioning accuracy. Then, compliance is necessary in the actuator to use for these equipments. However, because there are few things which have compliance in the existing electric actuator, advanced control technology is necessary in making these equipments have compliance. Moreover, a fluid power actuator which uses pneumatics has compliance, but a peripheral device such as a pump and a

compressor is necessary to use this actuator. Because of that, when this actuator is used, the whole of the system becomes large, and has the problem of the occurrence of the noise.

Therefore, if an actuator for the small system which has compliance can be developed, not only a welfare system but also application in many industry fields can be expected.

EHD PHENOMENON

The EHD phenomenon is a phenomenon that generates the flow in the insulating fluid by applying a high

voltage electric field. For example, the insulating liquid climbs toward the line electrode from the board electrode when the high voltage electric field was applied at that electrode arrangement in the liquid as shown in figure 1. And the gas which is evaporated insulating liquid, contrary to the EHD phenomenon in the liquid, flows from the line electrode to the board electrode when the line electrode is pulled up in the gas from the liquid. This flow of gas was called EGD (electro gas dynamics) phenomenon, and we developed prototype of actuator by applying this EGD phenomenon which flowed from the line electrode to the board electrode.

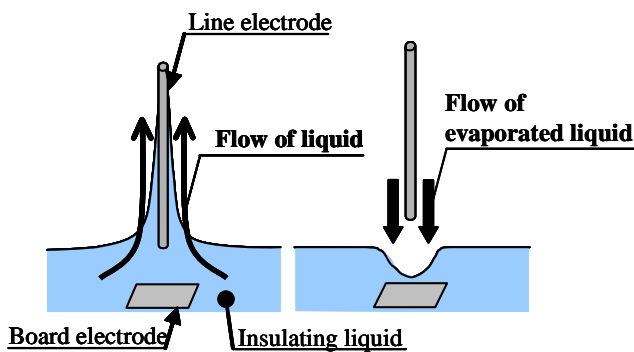


Figure 1 EHD phenomenon which liquid level rises, and EGD phenomenon which liquid level becomes dent

TYPE OF THE DEVELOPED ACTUATOR

In this study, we developed a rotation type of motor as a kind of actuator using the EGD phenomenon, because the motor is general actuator. Then we called that developed motor the EGD motor.

EGD MOTOR

Figure 2 shows the movement principle of the developed EGD motor. Parts which drive the EGD motor are composed of the cylindrical electrode and L shaped electrode. If the insulating gas is filled here, the voltage of the plus is applied to the cylindrical electrode, and L shaped electrode is connected with Gnd, the current of air by the EGD phenomenon is generated from the L shaped electrode toward the cylindrical electrode. L shaped electrode installed in the axis rotates by the reactive force of the EHD flow. It is thought that the number of parts is little and the miniaturization is easy because this EGD motor works only by a simple electrode structure and the gas. Moreover, it is thought that Moreover, it is thought that there are features with flexibility because driving source is a gas in the EGD motor.

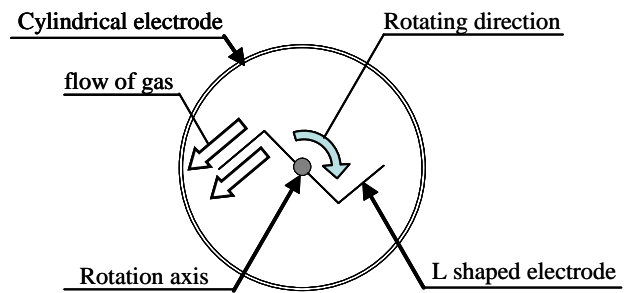


Figure 2 Movement principle of EGD Motor

PURPOSE

In this research, we aimed at the development of actuator which applied the EHD phenomenon. In evaluating the EGD motor from both sides of the miniaturization of the height of the cylindrical electrode and the miniaturization of the diameter of the cylindrical electrode, characteristic concerning the miniaturization of the EGD motor which used EGD phenomenon known as EHD phenomenon generated in the state of the gas was examined.

DEVELOPED EGD MOTOR

The appearance of the developed EGD motor is shown in figure 3 and the size of this motor is shown in figure 4. In this motor, the diameter is 96 mm, the height of bottom part is 20 mm and the height of lid is 10 mm. The size of the cylindrical electrode is 74 mm in the outside diameter, 60 mm in the inside diameter, and 13mm in height. Moreover, L shaped electrode is 20 mm in length, and 10 mm in width. The EGD motor was manufactured by the structure that the cylindrical electrode of various diameters and height was able to be exchanged easily.



Figure 3 Developed EGD motor

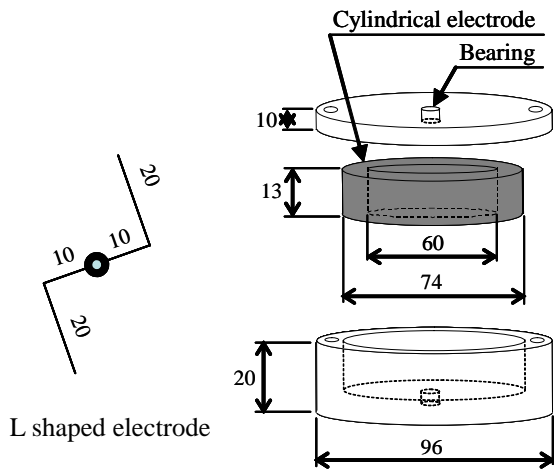


Figure 4 Size of EGD motor

EXAMINATION OF MAKING THIN TYPE

The EGD motor which changed only the height of the cylindrical electrode was manufactured, and the performance of the EGD motor was evaluated from the value of the starting torque and the no load rotational speed of the EGD motor which manufactured.

EXPERIMENT DEVICE

The rotating speed is measured with a reflecting plate and an optical speed indicator, and the torque is measured with the load cell which measures force by which the rotation axis winds up the string as shown figure 5.

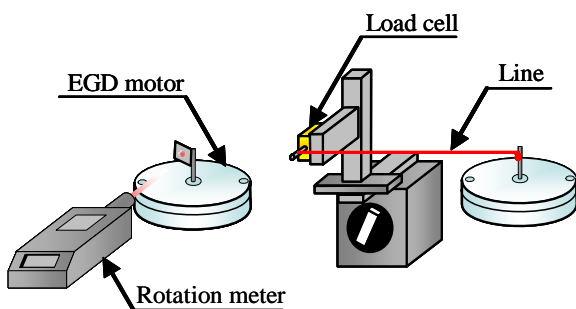


Figure 5 Experiment device

EXPERIMENT CONDITION

The experiment condition is shown below.
 Applied voltage: 18 kV (Voltage not discharged)
 Cylindrical electrode: Height 13 mm, 10 mm, and 8 mm
 The gas: The insulating fluid was put in the EGD motor, and the liquid was evaporated enough.
 Measurement frequency: Average five times

RESULT

Figure 6 shows the relation among the rotating speed, the torque, and height of the cylindrical electrode. The rotating speed showed the tendency to increase when the cylindrical electrode thinned. The maximum rotating speed of the EGD motor became 4741 rpm in 4 mm height. On the other hand, the torque became constant, and was about 20 μ Nm in each height.

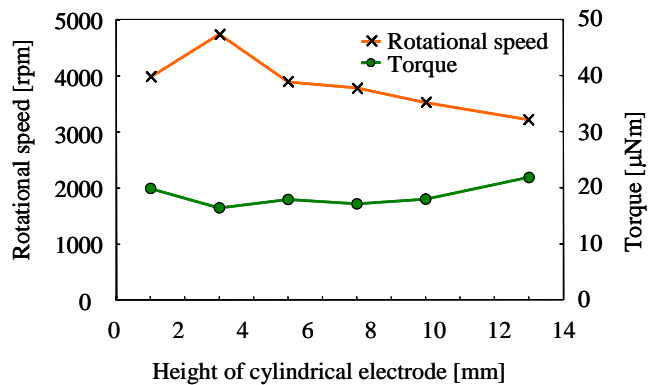


Figure 6 The relation among the rotating speed, the torque and the height of the cylindrical electrode

DISCUSSION

The rotating speed had increased by making the cylindrical electrode thin as shown by "Results". The force which is effective in the rotating direction weakens, because in a high cylindrical electrode, the gas which flows from the line electrode to the board electrode diffuses as shown figure 7(a). However, the flow of gas is bunched by low cylindrical electrode, and a bigger reactive force was able to be obtained as shown in Figure 7(b). Therefore, it can be said that EGD motor is suitable for making to the thin type because the rotating speed increase in changing height. The change in the value of torque did not appear so much. As shown in Figure 8, flow of the gas which generates the rotational force disturbs the rotational movement by hitting against other electrode on the other hand.

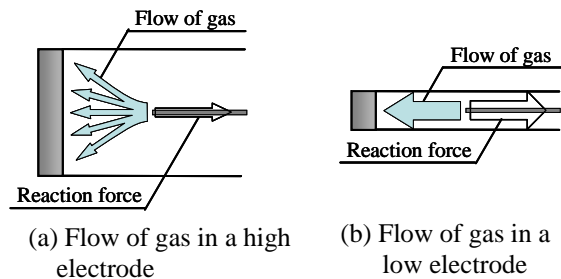


Figure 7 Influence by thickness of electrode

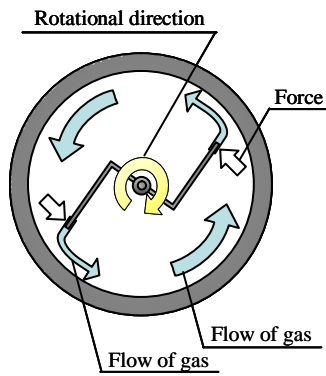


Figure 8 Influence which flow of gas in EGD motor exerts on performance

EXAMINATION OF MAKING SLIM TYPE

The inside diameter of the cylindrical electrode which be developed EGD motor was changed, to slim type was evaluated from idling speed and the starting torque.

EXPERIMENT CONDITION AND EXPERIMENT DEVICE

The experiment condition and the experiment device are shown below.

Applied voltage: 16 kV (Voltage not discharged).

Electrode: Inside diameter 45 mm, and 30 mm.

L shaped electrode was changed according to the ratio of inside diameters of the cylindrical electrode (Table 1).

Additionally, the experiment is a condition same as the examination of making thin type.

Table 1 Inside diameter of cylindrical electrode and relation of L type electrode [mm]

Inside diameter of cylinder electrode	L shaped electrode	
	I	-
90	10	20
60	7.5	15
45	5	10

RESULT

Figure 9 shows the relation among the rotating speed, the torque, and inside diameter of the cylindrical electrode in the slim type of motor. The rotating speed increases as the inside diameter of the cylindrical electrode becomes small, and the torque has decreased. Rotating speed became 2918 rpm at 30 mm in the inside diameter and torque became 8.5 Nm maximum at 60 mm in the inside diameter.

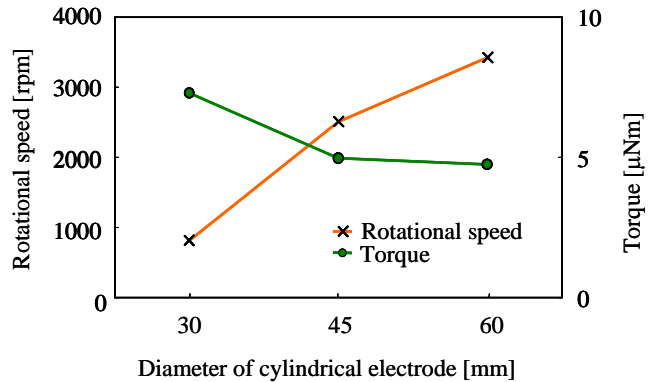


Figure 9 The relation among the rotating speed, the torque and the diameter of the cylindrical electrode

DISCUSSION

The rotating speed increases when the inside diameter of the cylindrical electrode becomes small and the torque has decreased. As these factors, the rotating radius of the line electrode becomes small by reducing the inside diameter of the cylindrical electrode, and moment of inertia decreases. And, it is thought that the rotating speed increases and the torque decreased as well as a general rotor. Therefore, it is thought that EGD motor can obtain the high revolution by making to a slim type as well as a usual electromagnetic motor.

SUMMARY

In this study, we developed the EGD motor using the EGD phenomenon which is a kind of the EHD phenomenon occurred in the gas. And, to investigate a change in the performance of the miniaturized EGD motor, we made a thin type of motor and slim type of motor. In the slim type of EGD motor, the rotating speed was increased compared with the original type of EGD motor, as well as a usual electric motor. In addition, in the thin type of EGD motor, the rotating speed was increased compared with the original type of EGD motor, as well as the slim type of EGD motor. As for the electric motor, increase of rotational speed in this thin type of motor was not seen.

A part of this study was financially supported by the Tokyo Denki University Science Promotion Fund.

REFERENCES

1. Sumitaka Terasaka, Akihiro Komiyama, Kazuyuki Mitsui, Shinichi Kuroda, Hiroshi Abe, Tsuyoshi Saitoh, Junko Niitsuma, Basic research on development of EHD motor, Japan Society for Precision Engineering, 2003

Basic performance of ER gel on one-sided structured electrodes

Yasuhiro KAKINUMA*, Tojiro AOYAMA* and Hidenobu ANZAI**

* Department of System Design Engineering, Faculty of Science and Technology
Keio University
3-14-1 Hiyoshi, Kouhoku-ku, Yokohama, 223-8522 Japan
(E-mail: kakinuma@sd.keio.ac.jp)

** Fujikura Kasei Co., Ltd.
5-13-1, Sakurada Washimiya-machi Kitakatsushika-gun, Saitama 340-0203, Japan

ABSTRACT

An electro-rheological Gel (ERG) is developed to overcome two shortcomings of Electro-rheological Fluid (ERF): sedimentation of ER particles and the seal structure required to allow the use of ERF in machine elements. The ERG shows a wide shear stress variation in response to an applied electric field. To apply an electric field to the ERG, it is necessary to sandwich the ERG between plane-parallel electrodes. However, it is impractical to wire both electrodes to a high voltage supply. In this study, one-sided electrodes are proposed to simplify the wiring structure. The basic characteristics of ERG on one-sided electrodes are evaluated experimentally. It is found that these electrodes exhibit nearly the same performance as the conventional plane-parallel type. The one-sided ERG mechanism is especially useful in applications involving rotating or sliding parts.

KEYWORDS

Electro-rheological Fluid, functional material, gel, one-sided electrodes

INTRODUCTION

Electro-rheological Fluids (ERF) [1, 2] are colloidal solutions whose viscoelastic properties vary with the applied electric field intensity. ERF are classified into two types, namely dispersed [3] and homogeneous [4], according to their flow behavior. Dispersed ERF and homogeneous ERF exhibit Bingham flow and Newtonian flow, respectively.

The research on homogeneous ERF has accelerated in recent years and its applications are put to practical use in the medical field, e.g., as assist devices for walking and rehabilitation [4]. On the other hand, the practical

shortcomings of dispersed ERF remain: the separation and sedimentation of ER particles over long-term use caused by the difference in density between the particles and the base oil. This reduces the ER effect [5, 6] and results in low-stability of ER devices. Another shortcoming is that a mechanical seal is required for machine element applications.

The present study reports the development of an Electro-rheological Gel [7, 8] that will overcome these shortcomings. This new ER material is produced by the hydrosilylation reaction, whereby the hydrogen-silicone and unsaturated compounds attach to the dispersed ERF via Si-H bonds. The ER particles are suspended in a gel component, and thus sedimentation of ER particles does

not occur. This suppresses the decrease in ER effect associated with precipitation. A seal structure is not needed in ERG applications because this is a solid-state system.

The mechanism of shear stress formation in ERG (Fig. 1) differs from that in ERF [8]. The initial state of the ERG sheet sandwiched between a pair of electrodes is shown in Fig. 1(a). The shear force between the upper electrode and ERG is very low in the absence of an electric field because the upper electrode is supported by slippery ER particles protruding from the gel surface. By contrast, the upper electrode makes contact with the sticky gel surface under a high electric field because the protruding particles retract into the gel so that dielectric polarized particles can attract each other as shown in Fig. 1(b). These changes in contact conditions at the interface between the electrode and ERG result in the shear force variation observed in response to the change in electric field intensity.

To obtain the ER effect in ERG, it is necessary to apply an electric field to ERG, which is sandwiched between the plane-parallel electrodes. However, it is impractical to wire both electrodes to a high voltage supply. Thus, the present study proposes one-sided electrodes in order to simplify the wiring structure. Using one-sided electrodes, the generation of the ER effect in ERF is confirmed by Furusho and Inoue [3]. In the present study, the basic characteristics of ERG on one-sided electrodes are evaluated experimentally and numerically.

STRUCTURE OF ONE-SIDED ELECTRODES

Figs. 2 and 3 show the structure and appearance of the one-sided electrodes fabricated. The aluminum electrodes are arranged alternately as cathode and anode on the insulating plate. Two types of one-sided electrodes having a different number of electrodes per unit length were designed: one with 10 electrodes where each electrode was 50×6.1×6 mm (L×W×H), the other with 15 electrodes where each electrode was 50×3.7×6 mm (L×W×H). The electrode gap in both types was 1 mm and the overall dimensions were 50×70 mm (L×W). An ERG sheet was formed on the electrodes with variable thickness. The ERG sheet was fixed on the one-sided electrodes because it was caught in slots between the electrodes.

The ER effect generated in the form of bridge-shaped electric field lines between the one-sided electrodes goes through the ERG sheet. To examine the ER effect on the one-sided electrodes, phenomena at the boundary between the ERG and the upper plate of the ITO glass were observed. As shown in Fig. 4, that the ERG surface changes into an adhesive surface under a 1.5-kV/mm electric field indicates that the ER effect of ERG is obtained using the one-sided electrodes.

STATIC PERFORMANCE OF ERG ON ONE-SIDED ELECTRODES

Shear test: experimental setup and procedure

Static performance of ERG on one-sided electrodes under an electric field was evaluated by the simple test

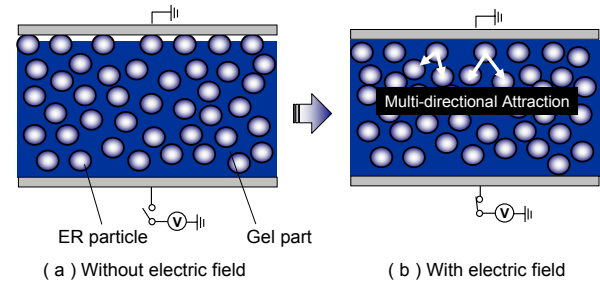


Figure 1 Mechanism of ER effect in ERG

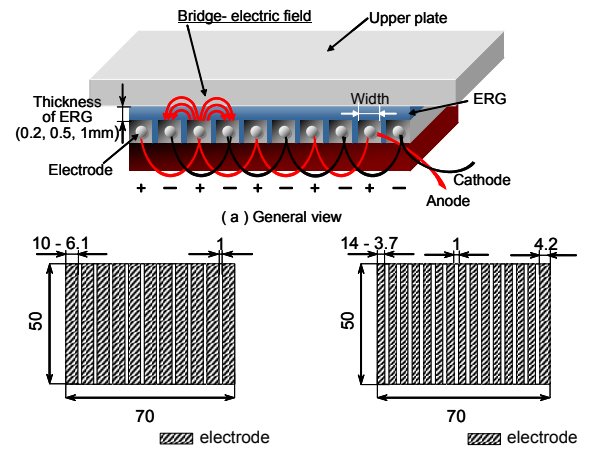


Figure 2 Structure of one-sided electrodes

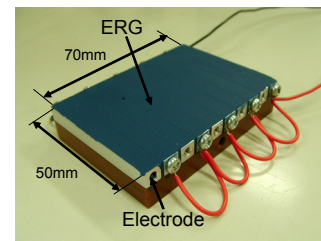


Figure 3 ERG sheet on one-sided electrodes

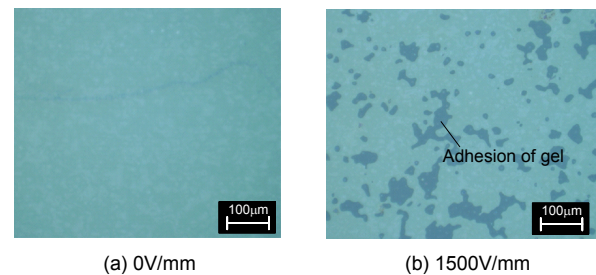


Figure 4 Observation at the boundary between ERG and the glass

stand schematized in Fig. 5. The upper plate made of Al was set on the ERG sheet formed on the one-sided electrodes. The variation in shear force between the upper plate and ERG sheet was measured while applying an electric field to the ERG. Shear motion was applied to the upper plate by a micrometer screw with motor-drive equipment. The shear force was measured by a strain gauge load cell attached to the slider plate. The displacement of the upper plate was measured by an eddy current displacement sensor. The behavior of shear force was monitored while varying the electric field intensity from 0 to 1.5 kV/mm. The shear length was set to 600 μm , and the shear speed was adjusted to 30 $\mu\text{m/s}$.

Relation between electric field intensity and shear stress

The behavior of shear stress under a variable electric field in both the 10- and 15-electrode-type electrodes are summarized in Figs. 6(a) and 6(b). An ERG sheet was formed on both one-sided electrodes with 0.2 mm thickness. When the displacement of the upper plate exceeds a certain value, the ERG sheet yields. Higher yield stresses are obtained under higher electric field intensities. Up to the yield point, the shear stress varies linearly with displacement because the upper plate and ERG are bonded by the ERG, which was rendered adhesive by the electric field. Above the yield point, the shear stress increases only gradually. This is due to the slip between the surface of the upper plate and the ERG sheet. Though the generated shear stress is lower than in double-sided electrodes, it is clearly possible to obtain the ER effect using an ERG on one-sided electrodes. Fig. 7 shows the relation between the applied electric field and generated yield stress. The generated yield stress increases exponentially with the applied electric field. By contrast, in the case of double-sided electrodes, the generated yield stress varies linearly with the applied electric field. This difference can be ascribed to the electric field lines going through the ERG, which increase exponentially in the case of one-sided electrodes, but linearly in the case of double-sided electrodes.

As shown in Fig. 7, the generated shear stress increases with the number of electrodes. To investigate the effects, if any, of the electrode structure on the generated shear stress, FEM analysis of the electric field is performed in one-sided electrodes at an electric field intensity of 1.5 kV/mm. Fig. 8 shows the FEM analysis results for the 15-electrode type. Clearly, the bridge-shaped electric field lines go through the ERG sheet. Perpendiculars dropped from the center of the cathode and anode to the boundary line between the ERG and the upper plate intersect the boundary at points A and B, respectively. In order to investigate the electric field distribution on line segment AB, 20 points are taken on the segment at equal intervals and the electric field intensity at each

point is determined. Fig. 9 shows the distribution of the electric field intensity on segment AB. The average of the electric field intensity between A and B is equal to the average electric field intensity at the boundary between the ERG and the upper plate. The average electric field intensity is given by

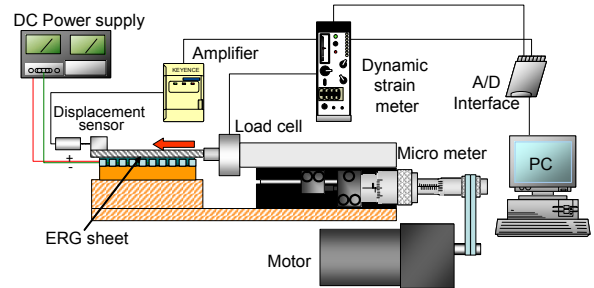
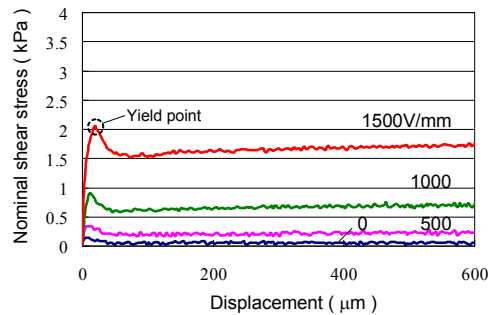
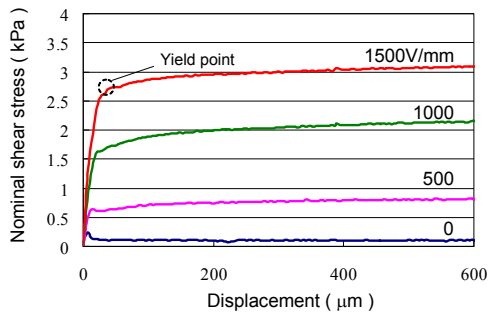


Figure 5 Experimental setup for shear test



(a) the total number of electrode: 10



(b) the total number of electrode: 15

Figure 6 Behavior of shear stress under variable electric field

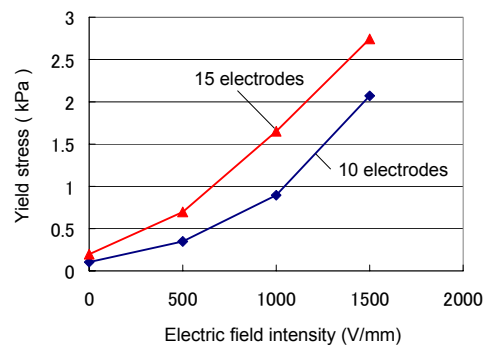


Figure 7 Relation between the generated yield stress and applied electric field

$$E_{ave} = \frac{\sum E_i}{20} \quad (1)$$

where E_{ave} is the average electric field intensity between the upper plate and the ERG sheet and E_i is the electric field intensity at each point on segment AB. The average electric field intensities using 10 and 15 electrodes are 336 and 465 kV/mm, respectively. The thinner the electrode width is, the higher the average electric field intensity, and hence, the higher the generated shear stress.

Based on the electric field analysis, a way to solve the yield stress from the average electric field intensity is proposed. In the case of the double-sided electrodes, the generated yield stress is roughly proportional to the applied electric field intensity. Fig. 10 shows the shear stress behavior in double-sided electrodes using the same ERG material. Under an applied electric field intensity of 1.5 kV/mm, the yield stress is about 9 kPa. Using this and the FEM analysis results, the relation between the estimated yield stress and average electric field intensity is formularized:

$$\tau_{est} = \frac{9}{1500} \times E_{ave} \quad (2)$$

where τ_{est} is the estimated yield stress. The estimated yield stress in the case of 10 and 15 electrodes is 2.0 and 2.79 kPa, respectively. These values determined by Eq. 2 match the results shown in Fig. 6 almost exactly. It appears that the generated yield stress depends on the average electric field at the boundary.

The average electric field intensity at the boundary seems to be determined by the ratio of the electrode gap to the electrode width. To generate the highest yield stress possible the ratio that gives the highest average electric field intensity at the boundary is determined. Then, at a constant electrode width, the influence of the electrode gap on the average electric field intensity is investigated by means of FEM analysis of the electric

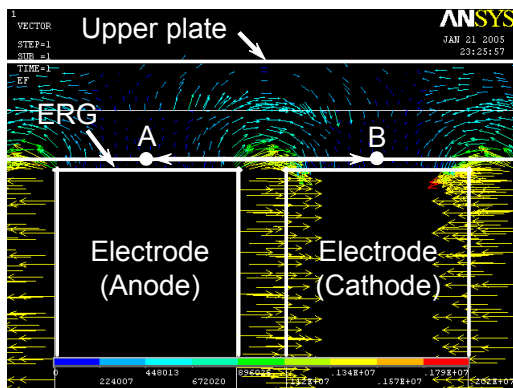


Figure 8 Distribution of electric lines

field. Fig. 11 illustrates the relation between the electrode gap and average electric field intensity, for an electrode width of 3.7 mm. The average electric field is calculated by Eq. 1. The maximum average electric field intensity occurs at an electrode gap of about 0.5 mm. That is, the most efficient design in terms of the generated yield stress would presumably be one-sided electrodes with an electrode gap of 0.5 mm and an electrode width of 3.7 mm.

From these results, it is possible to estimate the yield stress by FEM analysis, which helps in designing any device that incorporates the ERG.

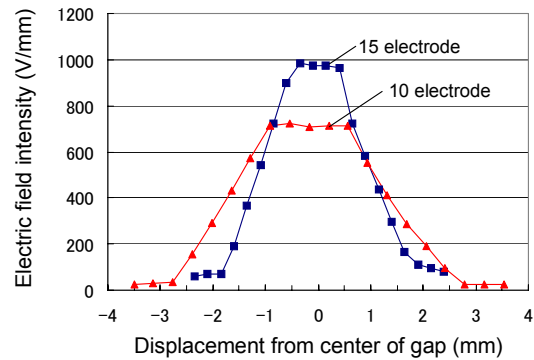


Figure 9 Distribution of electric field at the boundary between ERG and the upper plate

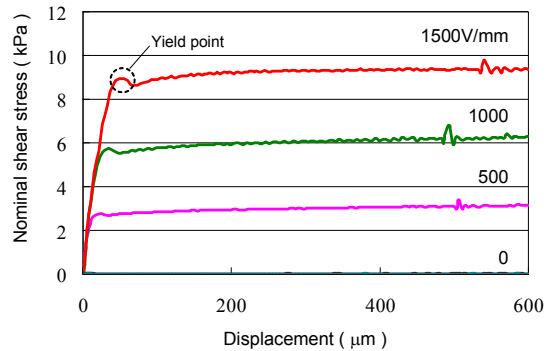


Figure 10 Result of shear test with both-sided electrodes

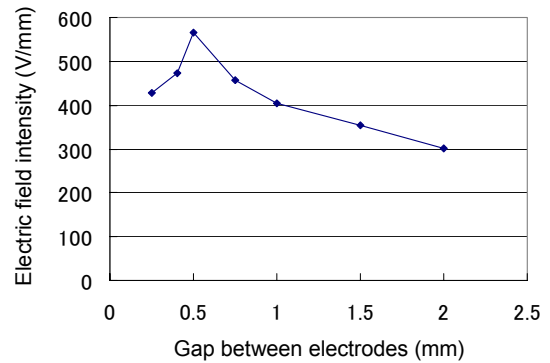


Figure 11 Relation between the electrode gap and average electric field intensity at the boundary

DYNAMIC PERFORMANCE OF ERG ON ONE-SIDED ELECTRODES

Procedure

The static performance assessment reveals that the ER effect can be obtained without wiring the upper plate. Then, to investigate the feasibility of using the ERG in a given device, e.g., as a clutch in a torque transfer device, its dynamic performance is analyzed experimentally. Fig. 12 shows the experimental setup for the vibration test. A 0.2-mm-thick ERG sheet and 15 one-sided electrodes are prepared. When vibrations are applied to the slider, the upper plate connected to it through a load cell is vibrated. In the absence of an electric field, the amplitude remained constant at 100 μm , while the frequency was varied from 5 to 100 Hz. The displacement amplitude and generated shear force were measured while applying an electric field to the ERG under vibration conditions. From the results of this test, the response of the ERG to the applied electric field is obtained.

Vibration test results

Fig. 13 shows the measurement results obtained at a frequency of 25 Hz. The electric field shown on the right vertical axis does not refer to the field at the boundary between the ERG and upper plate, but rather, to that between the electrodes. The vibration of the upper plate is quickly suppressed by the applied electric field as shown in Fig. 13(a): the amplitude of the electrode drops from 100 μm to less than 10 μm as a result of the applied electric field on the ERG. The shear stress is increased by the applied electric field as shown in Fig. 13(b); the shear stress amplitude increases from 1 kPa to more than 2.5 kPa.

Table 1 shows the dynamic responsiveness of the ERG on one-sided electrodes (the 15-electrode type), which differs little from the responsiveness of double-sided electrodes. ERG exhibits a very high ON responsiveness. However, the responsiveness of ERG in the CUT OFF operation is rather low. This is because the ERG is a passive material so that releasing the polarization charge in ER particles naturally requires time when the power supply is cut off.

Fig. 14 shows the relation between displacement of the electrode and shear stress over a period of cyclic vibration. When the applied electric field is relatively low, a hysteresis is observed between the displacement and the shear stress. This is presumably caused by the viscous damping of the ERG sheet, i.e., the damping effect due to the energy dissipation of viscous friction loss. By contrast, the vibration energy is converted into elastic energy as the electric field intensity exceeds 750 V/mm.

Fig. 15 shows the effect of the applied electric field intensity on the dynamic compliance of the upper plate.

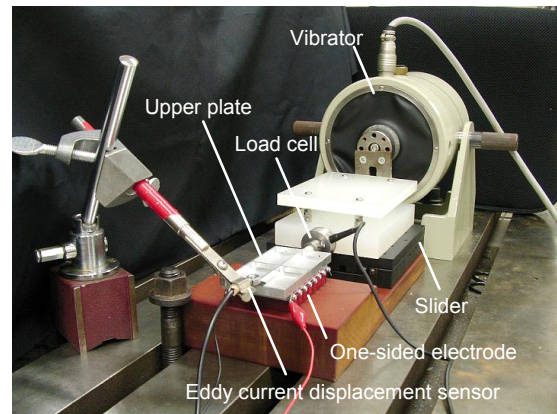


Figure 12 Experimental setup for vibration test

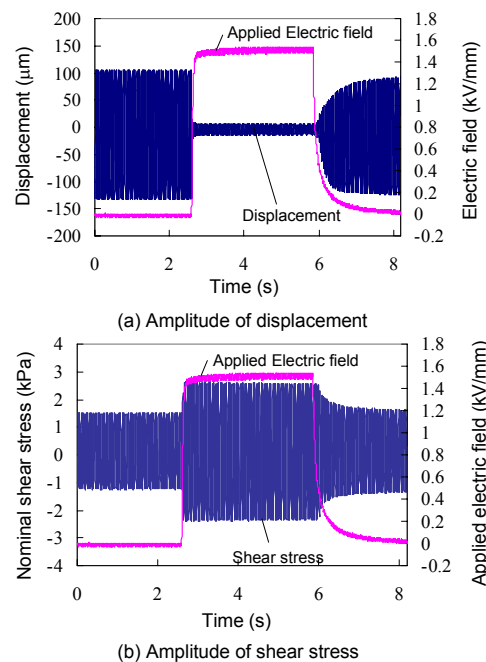


Figure 13 Result of vibration test at 25Hz

Table 1 Response time of ERG

	ON-response (ms)	OFF-response (ms)
ERG on one-sided electrodes	20~30	100~200

— 0V/mm — 150 — 300 — 450 — 600 — 750 — 900

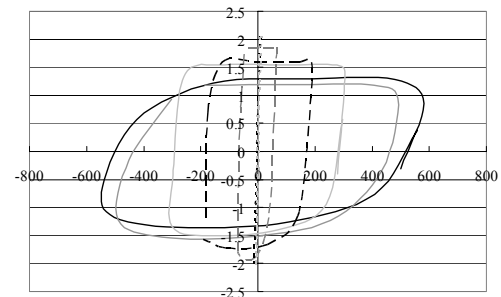


Figure 14 Influence of electric field intensity on hysteresis characteristics

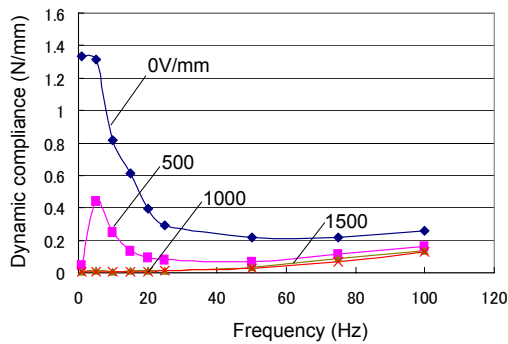


Figure 15 Relation between dynamic compliance and frequency of vibration

The peak value of the dynamic compliance curve decreased with increasing electric field intensity, indicating that the vibration of the upper plate can be effectively suppressed by the ERG on one-sided electrodes.

CONCLUSION

Using the developed ERG in a device with a rotating mechanism is problematic in that the ERG needs to be wired to the rotating part. To simplify the wiring mechanism, one-sided electrodes were proposed and applied to the ERG. The basic performance of the ERG on one-sided electrodes was analyzed experimentally and numerically. The relation between the generated shear stress and applied electric field was investigated via shear tests. Results indicated that the ERG on a large number of electrodes per unit length showed a large variation in shear force in response to changes in applied electric field intensity. Moreover, the yield stress clearly depends on the average electric field at the boundary between the ERG and the upper plate. Dynamic characteristics of the ERG on one-sided electrodes were determined through a simple vibration test. The results of this test showed the suitability of the ERG for use in vibration attenuators. It is expected that ERG on one-sided electrodes will find applications in, for example, clutch mechanisms, damping devices, and braking systems.

ACKNOWLEDGEMENT

This study was supported in part by Paradigm Shift from Intelligence to Life of 21st COE Program and JSPS Grant-in-Aid for Scientific Research (B).

REFERENCES

1. Nakano, M., and Nagata, T., ER Properties and Flow-induced Microstructures of an ER Fluid between Two Parallel Disk Electrodes in Squeeze Flow Mode, *International Journal of Modern*

2. Physics B, 2002, **16-17 & 18**, pp. 2555-2561
2. Jolly, M.R., and Nakano, M., Properties and Applications of Commercial Controllable Fluids, 6th International Conference on New Actuators, Bremen, Germany, 17-19 June, 1998, pp. 411-416.
3. Takesue, N., Furusho, J., and Inoue, A., Electro-rheological effects of liquid crystalline polymer on one-sided pattern electrodes, *Journal of Applied Physics*, 91-3,1, 2002, pp.1618-1623
4. Inoue, A., Ryu, U., and Nishimura, S., Caster-walker with intelligent brakes employing ER fluid composed of liquid crystalline polysiloxane, *Electrorheological Fluids and Magnetorheological Suspensions*, Nice, France, 9-13 July, 2001, pp. 23-29.
5. Tomas C. Halsey, *Electrorheological Fluids*, Science, **258**-5083, 1992, pp.761-766.
6. Klingenberg, D. J., Zukoshi, C. F., Studies on the Steady-Shear Behavior of Electrorheological Suspensions, *Langmuir*, 6, 1990, pp.15
7. Kakinuma, Y., Yakoh, T., Aoyama, T., Anzai, H., and Isobe, K., Development of Gel-structured Electro-rheological Fluids and their Application to Mechanical Damper Elements, the 8th IEEE International Workshop on Advanced Motion Control (AMC'04), Kawasaki, Japan, March 25 - 28, 2004, pp.541-545
8. Kakinuma, Y., Aoyama, T., Anzai, H., Sakurai, H., Isobe, K., Hino, T., and Tanaka, K., Development of Gel-Structured Electro-rheological Fluids and their Applications to the Control of Positioning, 8th International Research/Expert Conference (TMT 2004), Neum, Bosnia and Herzegovina, September 15 -19, 2004, pp.459-462

MAGNETORHEOLOGICAL (MR) FLUID AND ITS APPLICATIONS

Shigeru SHUTTO* and James R. TOSCANO**

* Lord Far East Inc. Japan Branch
8-11-1 Nishi-Shinjuku, Shinjuku-ku, Tokyo, 160-0023 Japan
(E-mail: s-shutto@lfe.cojp)

** Materials Business Unit, Lord Corporation
406 Gregson Drive, Cary, NC 27512-8012 USA
(E-mail: Jim_Toscano@lord.com)

ABSTRACT

Magnetorheological (MR) fluid is a functional, smart or controllable fluid, which responds to magnetic field, changing its rheological properties. The increased resistance to flow of an MR fluid is proportional to the strength of magnetic field. A typical MR fluid consists of iron particles, suspended in a carrier liquid such as synthetic oil or water. Proprietary additives, to discourage gravitational settling and promote particle suspension, are added to enhance lubricity, modify viscosity, and inhibit wear. In recent years devices and systems using MR fluid technology have been commercialized across wide industry applications, including automotive, industrial and civil engineering. In that development two key issues for the commercial success of MR fluid technology - durability and settling - have shown continual improvement as a result of formulation research. As a result, MR fluids today are strong, durable, adaptable and highly developed with fundamental material data and device design and models.

KEY WORDS

Key words, Magnetorheological, Smart Fluid, Functional Fluid, Automotive, Commercial

INTRODUCTION

Since the first patent was issued to inventor Jacob Rabinow in the 1940s, magnetorheological (MR) fluids have remained mostly a laboratory curiosity with little practical use. In the late 1980s and 1990s, however, researchers began to get serious about developing the commercial viability of MR fluids, especially when other technologies began to converge that made practical use a real possibility. Microprocessors, sensor technologies and increasing electronic content and processing speeds have created control possibilities that didn't exist in Rabinow's time. Battery technology, fueled by the advance of the burgeoning cell phone industry, as well as

new rare earth magnets now provide power in smaller packages than ever possible before.

Lord Corporation, after committing more than a decade of intense R&D, holds the world's most extensive patent portfolio on MR fluid formulations, devices and systems. The company has developed additives, lubricants and suspension aids to keep iron particles in place while preventing them from grinding away at seals, gaskets and metal components. The company also has compiled a body of scientific data through aggressive life cycle testing and installed commercial applications that clearly demonstrate the effectiveness, durability and performance of MR fluids, devices and systems.

DESCRIPTION OF MR FLUID TECHNOLOGY

MR fluids are materials that respond to a magnetic field with a dramatic change in rheological behavior. These fluids can reversibly change instantaneously from a free-flowing liquid to a semi-solid with controllable yield strength when exposed to a magnetic field. In the absence of an applied field, MR fluids are reasonably well approximated as Newtonian liquids when magnetic field is not given. For most engineering applications a simple Bingham plastic model is effective in describing the essential, field-dependent fluid characteristics, as shown in the model in Fig. 1.

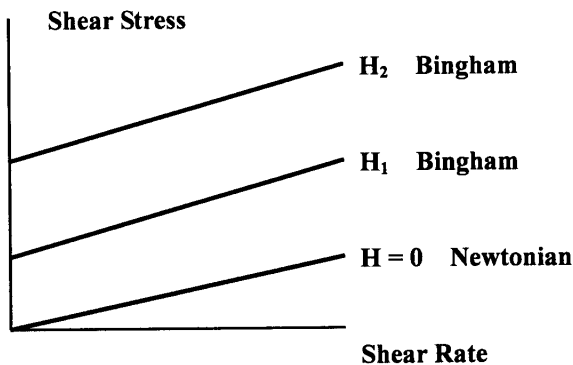


Figure 1 Stress-Strain model of Newtonian and Bingham fluids

A typical MR fluid consists of 20-40 percent by volume of relatively pure, 3-10 micron diameter iron particles, suspended in a carrier liquid such as mineral oil, synthetic oil, water or silicone oil. A variety of proprietary additives, similar to those found in commercial lubricants to discourage gravitational settling and promote particle suspension, are commonly added to Lord's state-of-the-art MR fluids to enhance lubricity, modify viscosity, and inhibit wear.

MR fluids made from iron particles exhibit maximum yield strengths of 50-100 kPa for applied magnetic fields of 150-250 kA/m. MR fluids are not highly sensitive to moisture or other contaminants that might be encountered during manufacture and usage. Further, because the magnetic polarization mechanism is unaffected by temperature, the performance of MR-based devices is relatively insensitive to temperature over a broad temperature range (including the range for automotive use).

MR fluids contrast with electrorheological (ER) fluids, which are often referred to as smart or functional fluids, in various performances and properties as in Table 1.

		MR	ER
⇒	Max. Yield Stress	50 - 100 kPa	2 - 5 kPa
	Max. Field	~ 250 kA/m (limited by saturation)	~ 4kV/mm (limited by breakdown)
	Viscosity	0.1-1.0 Pa-s	0.1-1.0 Pa-s
⇒	Operable Temp. Range	-40 to 150°C (limited by carrier fluid)	+10 to +90 °C (Ionic, DC) -25 to +125 °C (non-Ionic, AC)
⇒	Stability	Unaffected by most impurities	Cannot tolerate impurities
	Response Time	Milliseconds	Milliseconds
	Density	3 - 4 g/cm ³	1 - 2 g/cm ³
⇒	Power Supply (typical)	2 - 25 V @ 1 - 2 A (2 - 50 watts)	2 - 5 kV @ 1 - 10 mA (2-50 watts)

Table 1 Performance and properties of MR fluid and ER fluid

Most devices use MR fluids in a valve mode or direct-shear mode. Examples of valve mode devices include dampers and shock absorbers. Examples of direct-shear mode devices include clutches, brakes, and variable friction dampers.

DAMPING SYSTEM APPLICATIONS

Automotive Seat Suspension

MR fluid dampers had been used in seat suspensions for Class 8 trucks since 1998. The MotionMaster™ Ride Management System has proven capability to reduce topping and bottoming. Topping can lead to loss of control of the vehicle and bottoming can injure drivers. Seat vibration is monitored by the sensor, which sends signals to controller which controls electric currency to be given to the damper, which changes stiffness responding to vibration in 10 milliseconds.

Unlike standard air suspended seats the seating equipped with MotionMaster Ride Management system automatically adapts to both the driver's body weight and continually changing levels of shock and road vibration, improving driver responsiveness and control while reducing fatigue and risk of injury, Today 10,000+ buses, trucks and off-highway vehicles are equipped with the System. [1] - [4]

Cable-stay Bridges Stay Still

Stay cables are prone to vibration due to wind and rain effects. Smart dampers have the potential efficiency several times that of standard oil dampers. Lord's MR dampers were employed at the Dongting Lake Bridge, Hunan Province, China in 2003.

MR SYSTEM DEVELOPMENT AND OPTIMIZATION

Automotive Primary Suspensions

Year 2002 marked the first broad-based automotive application for MR fluid technology. Delphi Automotive Systems, the world's largest automotive industry supplier, has since developed and commercialized the MagneRide™ shock and strut system for a number of GM model cars and two future European vehicles slated for 2006. [5][6]

The Delphi mono-tube design employs an electro-magnetic coil wrapped around the passageway between two chambers filled with custom formulated MR fluid from Lord Corporation. When the piston moves within the damper body, MR fluid flows between these two chambers and through the coil. Varying current in the coil controls the magnetic field in the coil, adjusting the yield stress or resistance-to-flow of the fluid, proportionally to the field, up to 1,000 times a second. The design has no electromechanical valves or small moving parts. The iron particles in the MR fluid form a dense network of chains when a magnetic field is applied to them, increasing the damping in the shock. When the magnetic field is removed, particles revert to their free, unchained form, allowing freer movement of the damper and thus lower damping.

All four corners of the vehicle are independently controlled by the MagneRide system with the fluid (and thus damping force) in the four damper/struts changing in response to vehicle speed and sensed road and driving conditions such as pot holes and lateral forces in high-speed turns. The faster response time (less than 10 milliseconds) of MR dampers, compared to other semi-active shocks, enables the suspension system to adapt to changing road conditions and dampen sudden impacts when driving over rough terrain.

MagneRide shocks have fewer moving parts than conventional controllable shocks - 60 percent fewer parts than Delphi's conventional semi-active damper system. The MagneRide system also requires very little power. Peak power is 20 watts at each of the system's four dampers. MR dampers are also quieter in operation and simpler to assemble.

The MagneRide system was extensively tested for performance and durability under strenuous environmental conditions prior to launch in 2002 on the Cadillac Seville STS and Chevrolet Corvette. Today, the MagneRide system is additionally in production on the Cadillac SRX and XLR, will be on the Buick Lucerne 2006 model and will soon launch on two European vehicles.

The rheological properties of MR fluids depend on the concentration, size, distribution and shape of the iron particles, the carrier oil properties, additives, applied field, temperature and other variables. The interdependency of all of these factors is very complex and important to understand in optimizing the performance of these fluids within an MR device and control system for a particular application, as trade-offs must constantly be made in the design process.

Two areas of performance that received particular attention during Lord's decade-long MR development program in the 1990s were settling stability and durability (wear and seal life) as MR fluids, when first invented, were not stable to long-term settling and could be quite abrasive in use.

As with any micron scale particulate suspension in which a density mismatch exists between the particle and fluid, long-term settling must be controlled. The specific application dictates to what extent and how the settling will be controlled. For example, an MR damper used to control seismic forces in a building has very demanding settling requirements, requiring limited variation in iron concentration within the fluid for years with no agitation. To achieve this level of stability, the off-state of the fluid must be allowed to rise and the system effect is compensated in the design of the MR valve in the damper. Conversely, an automotive shock is unlikely to remain static for multiple years and low off-state damping is necessary to provide a large control range (from off to full on).

Settling behavior of suspensions is typically characterized in two ways: clear layer formation and ease of re-dispersion of the settled suspension. The paint industry has spent decades developing correlations for accelerating settling and predictability in settling behavior. One rarely buys a can of paint and finds that the solids in the bottom, which are more dense than the fluid, cannot be easily re-dispersed with a paint stirrer.

Similarly Lord has developed accelerated settling tests and developed correlations with real-time settling behavior. From these tests, we have been able to develop specifications for clear layer formation and re-dispersibility to satisfy the requirements of damper applications including automotive shocks. We know from our testing that as long as the clear layer in an MR fluid is less than 30010, the fluid in an MR automotive shock will re-disperse. In actual real-time and accelerated testing, Lord MR fluids do not exceed 20% clear layer in over 200 days of settling.

Delphi has tested MR shocks with the same accelerated settling tests that Lord uses for testing the base MR fluid. Shocks were stored horizontally or vertically and thermally cycled for multiple days to simulate settling for periods up to the equivalent of one year. At the end of the settling time, the shocks were carefully loaded into a test frame and the forces from the very first cycle of use were recorded. Figure 2 shows the results for a simulated test time of one year. While the first cycle shows an initial increase in force, by the second cycle, the damper produces forces identical with the original performance of the shock. Thus it takes only one stroke of the damper to completely re-disperse the MR fluid, even after 1 year of settling. Current MR fluid data from Lord indicates that our MR fluid formulation will continue to be re-dispersible, even after 10 years of storage .

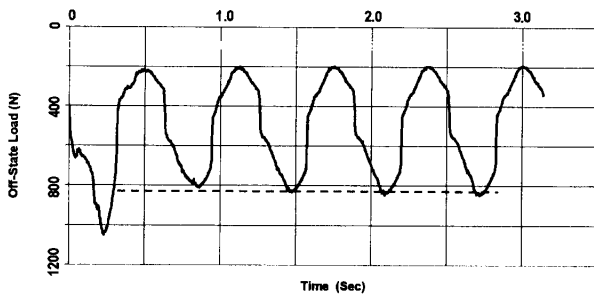


Figure 2 MR damper force during cycling immediately after one year of simulated settling

Shown in Figure 3 is the improvement in fluid durability over several years of formulation research.

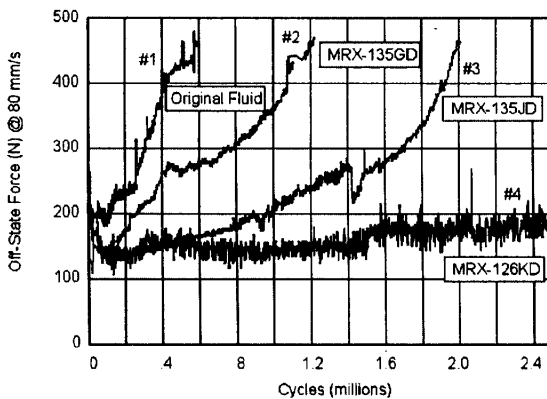


Figure 3 Historical durability test data in Lord Corporation MR fluids

The failure mechanism of an MR fluid is usually an increase in the off-state viscosity due to wear or breakdown of the iron particles, leading to lack of control range. Lord's patented additives prevent wear and breakdown while maintaining the magnetic performance of the fluid. Today MR fluids will last the

equivalent of hundreds of thousands of miles in an automotive shock application.

The ultimate test of any material is in actual use. In addition to accelerated and track testing, Delphi has recently tested shocks that have been in actual use for over two years. Shocks from vehicles from Texas and Michigan, with between 50,000 and 72,000 miles, were subjected to performance tests and further accelerated durability testing equivalent to the projected full life of the shocks (100,000 miles), to verify the long-term behavior of both the Lord MR fluid and MagneRide dampers.

All shocks tested, from both northern and southern climates, performed within original, as-made, specifications in laboratory testing. The on-state damping force changes were nominal, varying only 3-5%, even after an additional 50,000 miles of laboratory durability were added to the actual mileage on the shocks. See Figure 4.

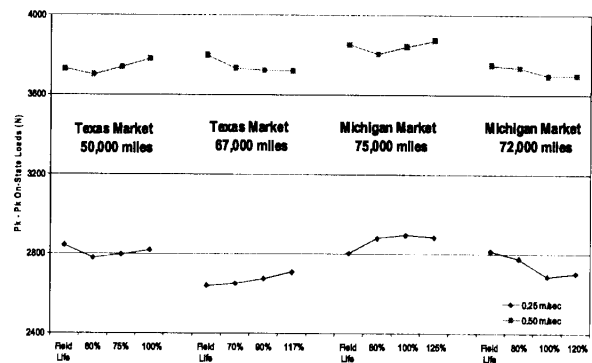


Figure 4 On-state shock performance from field life to 100,000+ miles (100% = projected life = 100,000 miles)

Similarly off-state forces and seal friction with and without side load showed only nominal change from the as-made specification to the field life plus additional 50,000 laboratory durability miles.

It is reasonable to conclude, after three years in the marketplace and many decades of accelerated testing by Lord and Delphi, the durability and stability of MR fluid and shocks are well proven. [7]

VEHICULAR STEER-BY-WIRE

Automotive design engineers are looking at a host of other potential applications for MR fluid technology, especially in the area of driver feedback, or "feel," that is often not optimized in electric, by-wire systems.

The trend in vehicle industries toward control-by-wire (steer-by-wire, shift-by-wire, throttle-by-wire, brake-by-

wire, etc.) has created a need for highly controllable, rugged, cost-effective devices to provide realistic force-feedback sensations to the operator, whether the manual device is a wheel, a joystick, a pedal, or a lever. Commercialized products for forklift vehicles use the Lord sMaRt Steering Brake™ to sense steering wheel position, control over-steer when the vehicle is moving quickly, and simulate the end-stop limit of driving wheel turn.

With MR fluid inside the Lord sMaRt Steering Brake, the rotor turns freely inside the housing in the absence of a magnetic field. But when the coil is energized, the magnetic field generated causes the iron particles in the MR material to form a chain, creating a resistive torque that is proportional to the current flow in the coil and reacts quickly to changes in the strength of the magnetic field.

The benefits in of MR technology in by-wire applications include:

- Continuously variable, speed-independent torque
- Quick response time (10 milliseconds)
- Smooth, realistic force feedback with high fidelity feel
- Real-time control
- High torque density - 10 times greater than DC motors
- Compact size
- No active forces generated
- Inherent system stability
- Low power consumption (typically 12V, 1 Amp max current)
- Compatible with vehicle electrical systems

United Kingdom-based lift truck manufacturer Linde has taken the technology of programmable feel the furthest in vehicular applications. Linde was the first (in 2000) to incorporate an advanced, fully integrated system developed by Lord, which provides high-fidelity tactile feel in Linde's all-electric active reach trucks with steer-by-wire control.

Linde incorporated the Lord sMaRt Steering Brake to improve operator control and safety, because the company realized during development that the vehicle was unsafe to operate without high-quality tactile feedback to the steering wheel. Linde considered using electric motors but rejected the idea due to high cost, size, weight, and energy usage. Linde eventually chose a Lord MR device because it produced a high-fidelity sense of "feel" to the operator with much lower cost, size, weight, and energy usage than electric motors. The Lord sMaRt Steering Brake is 60 percent smaller than comparable devices and produces the same amount of torque at fraction of the cost and power.

MR STATUS TODAY

Today, thousands of vehicles are in operation and more than 100,000 MR dampers, shock absorbers and brakes are in use. For automotive platform applications alone, anticipated annual growth in demand for MR devices is more than 1 million.

Production of fluid volume in 2004 reached several hundred tons. The cost of MR fluid ranges from about \$600 per liter for small quantities to about \$60 to \$180 per liter for large volume applications.

Lord Corporation's experience in the development of MR fluids, devices and systems has produced key insights, backed by solid data, into this remarkable technology. Over the past three years, Lord has offered MR Technology Workshops to train others in MR device and system design. Lord offers MR fluid and technology that is:

- Tailored for specific applications
- High strength
- Durable
- Robust
- Highly developed with fundamental material data and device design and models
- Extensive experience-based guidelines

REFERENCES

1. J.D. Carlson, J.L. Sproston, *Proceedings of Actuator 2000, 7th Int. Conf. on New Actuators*, 19-21 June, Bremen, Germany, 126-130 (2000).
2. J.D. Carlson, *Proceedings of the 3rd World Conference on Structural Control*, Vol. 1, 7-11 April, Como, Italy, F Casciati, Ed., Chichester: John Wiley 227-236 (2003).
3. Lord Corporation, *Rheonetic Magnetic Fluid Systems*, Publication No. PB8003, 1-10 (1996)
4. S.J. McManus, K.A. St. Clair, *SAE Technical Paper Series*, No. 2000-01-3408, Truck and Bus Meeting and Exposition (2000).
5. Delphi Energy & Chassis Systems, 2002, Pub. DE-00-E-019 02/02, <http://www.delphi.com/pdf/vpr/Magnaride.pdf> (2002).
6. General Motors Corp., (2002).
7. L.C. Yanyo, "Magnetorheological (MR) Fluid for Automotive Damping Systems Proceedings", *IIR Suspension and Damping Conference*, Germany (2004).

Flow of a Liquid Crystal Mixture in a Mini-Cylinder under Rotating Electric Fields

Tetsuhiro TSUKIJI*, Yuji MURATA** and Jun ITO**

* Dept. of Mech. Eng., Faculty of Science and Technology
SOPHIA University

7-1 Kioicho, Chiyoda-ku, Tokyo, Japan
(Tel: +81-3-3238-3818, E-mail: t-tukiji@sophia.ac.jp)

** Division of science and technology, Graduate school
SOPHIA University

7-1 Kioicho, Chiyoda-ku, Tokyo, Japan
(Tel: +81-3-3238-3873, E-mail: yuuji-m@sophia.ac.jp)

ABSTRACT

Flow visualization of a liquid crystal mixture in mini cylinders is conducted under application of the rotating electric fields. The mini cylinder with the electrodes on some parts of the inner surface of the cylinders is used. The cylinder is 1.0mm or 2.0mm in length and 1.1mm in diameter. The three-phase alternating currents and the rectangular wave voltages are used as the rotating electric fields. The frequency and the amplitude of the voltages are changed to investigate the effect of the unsteady electric fields on the flow phenomenon of the liquid crystal mixture. When the frequency and the voltage of the three-phase voltages are 60Hz and 260V the rotation speed of the liquid crystal is 14.3 r.p.m. On the other hand, when the frequency and the voltage of a rectangular wave voltage are 600Hz and 200V the rotation speed is 2.7 r.p.m.

KEY WORDS

Functional fluid, Liquid crystal, Rotating electric fields, Flow visualization

INTRODUCTION

Fluids whose rheological properties like an apparent viscosity can be controlled using electric or magnetic fields from outside are known as one of the functional fluids nowadays. Especially fluid whose properties can be controlled using the electric fields is said to be ER (Electro-rheological) fluids. Many research works about the welfare devices, the micro machine etc, as the

application of the ER fluids have been performed. Liquid crystal is one of the homogeneous ER fluids without precipitation and therefore has high reliability. The area for the application using the liquid crystal is expanding and many applications are expected in the future.

The authors examined the influence of the electric fields on the flow of the liquid crystal mixture in the circular tube with the electrodes on some parts of the inner surface of the tube [1]-[3]. As a result, the influence of

the electric fields on the characteristics between the pressure drop and the flow rate of the liquid crystal mixture became clear when it flowed in the circular tube electrode. Furthermore, we found that the liquid crystal mixture flows in the peripheral direction in a mini-cylinder with three sets of electrodes on the inner wall under application of three-phase alternating currents as the rotating electric fields [4]. The facing electrodes have an equal electrical current potential. Namely the liquid crystal mixture in itself causes the flow under application of the unsteady electric fields. Development of a micro-motor is expected using the mechanism mentioned above, but the mechanism of the liquid crystal mixture generating a flow is unclear in the present stage. In this study, the influence of the rotating electric fields on the flow of the liquid crystal mixture is examined in detail using two different cylinder electrodes. The inside diameter is smaller than the cylinder electrode made in a previous report [4]. The depths of the present mini-cylinder electrodes are 1 and 2mm. Especially the velocity distribution of the liquid crystal is investigated using PIV(Particle Image Velocimetry) processing. And we found that the liquid crystal mixture flows in the peripheral direction when the rectangular wave voltages are used as the rotating electric fields.

EXPERIMENTAL SETUP AND METHODS

In the present experiments, the liquid crystal mixture is used as one of the homogeneous ER fluid. This is the material that is mixed with some kinds of the nematic liquid crystals, and its viscosity is higher than the nematic liquid crystal. The liquid crystal mixture was supplied by MERCK Japan Co., Ltd. The isotropic nematic transition is 90.0 °C and smectic-nematic transition is - 44.0°C. The physical properties of the liquid crystal mixture used in the present study are shown in Table.1. Moreover those of the nematic liquid crystal are also shown in the same table.

Figure 1 shows a mini-cylinder of 1.1mm in inner diameter with the electrodes on the inner wall used in this experiment. Six electrodes are insulated every 0.2mm interval on the inner wall.

Figure 2 shows the experimental apparatus using three-phase alternating currents as the rotating electric fields to observe the flow of the liquid crystal mixture under the application of the electric fields. In this experiment, the electrodes facing each other have an equal electrical current potential. For example, the electrodes 1 and 4 have a same potential. The depth d is 1mm or 2mm. Three-phase alternating current shown in Figure 3 is applied on the electrodes in this cylinder electrode. The voltage curves ①, ② and ③ or ④, ⑤ and ⑥ come in that order. The voltage is applied in

the clockwise direction from top view. Flow of a liquid crystal mixture in the cylinder is visualized in the axial direction using a commercially available digital video camera. In addition, the effective value of the voltage to add on the electrodes of 1mm or 2mm in depth is changed between 0 and 260V and the frequency is also changed between 0 and 60Hz according to the change of the effective value in this experiment. Based on the present restriction of our device to generate the electric fields, the frequency and the effective value can not be changed independently. In this study, the frequency means the frequency of one-phase alternating current and the voltage means the effective value.

Table 1 Comparison of physical properties

Physical properties	Liquid crystal mixture (MLC6650)	Nematic liquid crystal (K15)
Operating temperature region	-44~90°C	23.1~35.5°C
Kinetic viscosity	76mm ² /s	20mm ² /s (20°C)
Anisotropy of dielectric constant	52.6	14.3
Double refraction index	0.1498	0.1952

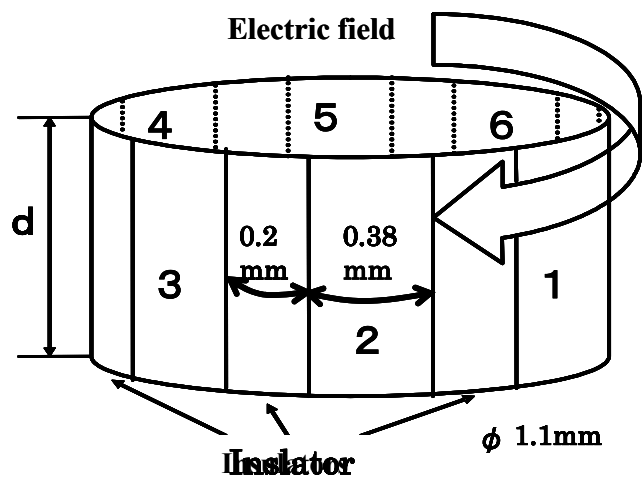


Figure 1 Mini-cylinder

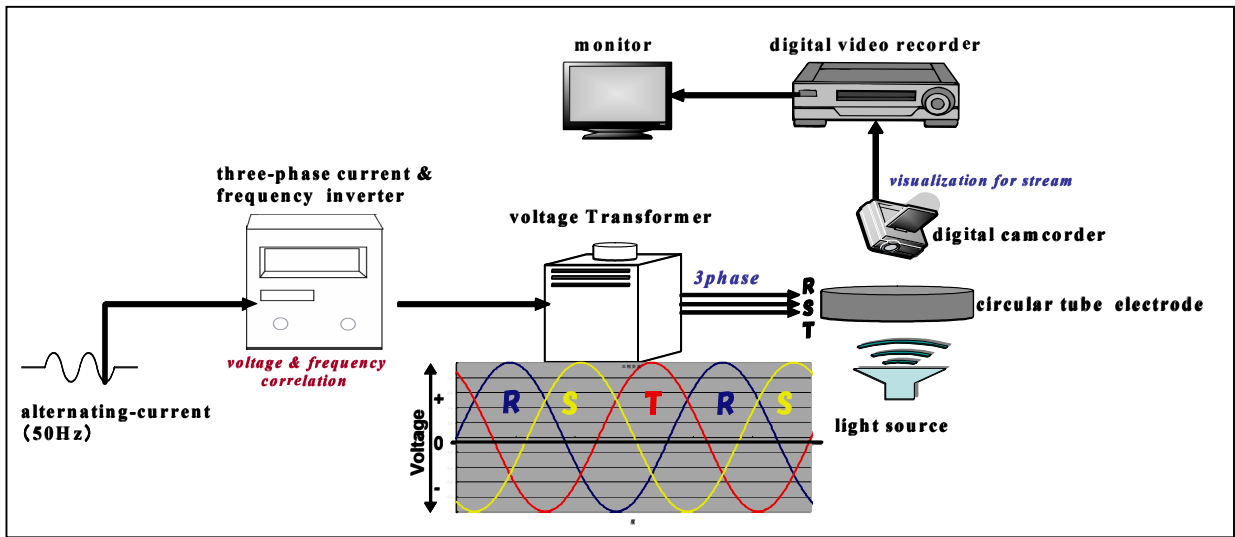


Figure 2 Experimental apparatus using three-phase alternating current

Figure 4 shows the experimental apparatus using the rectangular wave voltage as the rotating electric fields to observe the flow under the application of the electric fields. The electric field with 200V of maximum voltage rotates in the clockwise direction from a top view. For example, after the voltage is added between 1 and 2, it is added between 2 and 3, and so on. The frequency of 6Hz using a rectangular wave voltage means that the electric field rotates one round per a second. The frequency is changed between 0 and 1200Hz.

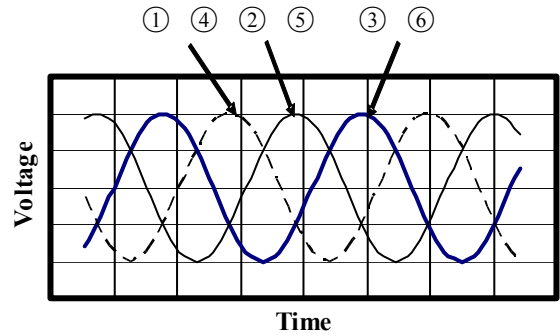


Figure 3 Three-phase alternating current

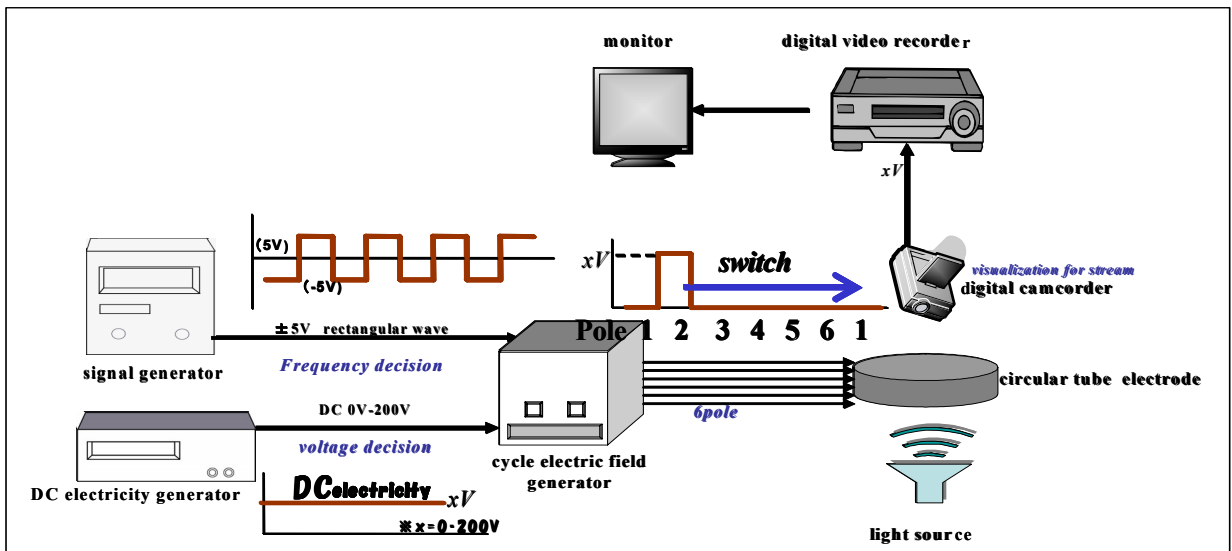


Figure 4 Experimental apparatus using rectangular wave voltage

EXPERIMENTAL RESULTS

Table 2 shows the flow states of the liquid crystal mixture when three-phase alternating currents are added on the electrodes in the cylinder with 1mm or 2mm in depth. The voltage is increased from 0 to 260V and the frequency is also increased from 0Hz to 60Hz according to the change of the voltage. In both the cylinder electrodes, the liquid crystal mixture does not flow without the electric field and it begins to flow when the electric field is applied on the electrodes. Furthermore, the frequencies of the voltage are about the same for two cases when the liquid crystal begins to rotate.

In addition, the flow visualizations under the application of the rectangular wave voltages in the circumference direction as a rotating electric field were conducted. Tables 3 and 4 show the results for $d=1\text{mm}$ and 2mm . The rotating flow occurred for the rectangular wave voltage, but the rotational speed of the liquid crystal mixture for $d=2\text{mm}$ is about 3 r.p.m. and is small compared with the case of three-phase alternating current.

We measured the rotational speed of the liquid crystal by observing a small air bubble moving in the circumference direction at 0.25mm of the radius from the visualized results using a commercially available digital video camera. The averages of the rotational speeds are shown in Figures 5 and 6. As a result, for both cases of $d=1\text{mm}$ and 2mm , the rotational speed under the application of the three-phase alternating currents increased greatly from 51Hz as shown in Figure 5. And for $d=2\text{mm}$, the rotational speed under the application of the rectangular wave voltage increased greatly from 200Hz to 600Hz as shown in Figure 6. On the other hand, it is almost constant from 600Hz. And for $d=1\text{mm}$, the rotational speed under the application of the rectangular wave voltage did not change in the range of the present experiments. In addition, the liquid crystal mixture did not rotate from 1Hz to 800Hz in the case of $d=1\text{mm}$. So there is no experimental data of the rotation between 200Hz and 800Hz for $d=1\text{mm}$ in Figure.6. The rotation speed for $d=2\text{mm}$ is about twice as fast as for $d=1\text{mm}$ between 800Hz and 1200Hz.

Furthermore, Figures 7 and 8 show the results analyzed using PIV(Particle Image Velocimetry) processing to obtain the velocity distributions. The liquid crystal mixture flows both in the circumference direction and the axial direction in the cylinder for $d=1\text{mm}$. On the other hand, it flows only in the circumference direction for $d=2\text{mm}$. In these figures, the smoothing processing is done several times to obtain only the velocity direction in the flow field.

Table 2 States under three-phase alternating currents ($d=1\text{mm}, 2\text{mm}$)

State	Frequency [Hz]	Voltage [V]	Remarks
Stationary	0	0	Stationary
Random	1-44	0-195	Liquid crystal mixture flows under electric field added.
Slow rotation	44-55	195-245	Liquid crystal mixture rotates slowly.
Fast rotation	55-60	245-260	Rotational speed is 7.9-14.3r.p.m.

Table 3 States under rectangular wave voltages ($d=1\text{mm}$)

State	Frequency [Hz]	Voltage [V]	Remarks
Stationary	0	200	Stationary
Random	1-800	200	Liquid crystal mixture flows under electric field added.
Slow rotation	800-1200	200	Rotational speed is 1.3r.p.m.

Table 4 States under rectangular wave voltages ($d=2\text{mm}$)

State	Frequency [Hz]	Voltage [V]	Remarks
Stationary	0	0	Stationary
Random	1-250	200	Liquid crystal mixture flows under electric field added.
Slow rotation	250-600	200	Liquid crystal mixture rotates slowly.
Fast rotation	600-1200	200	Rotational speed is 2.7r.p.m.

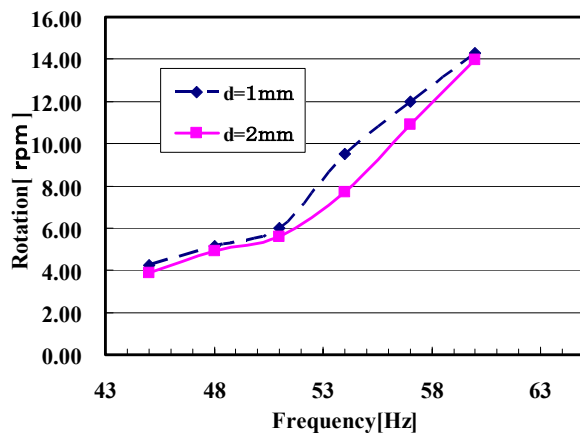


Figure 5 Rotational speeds per a minute (three-phase alternating currents)

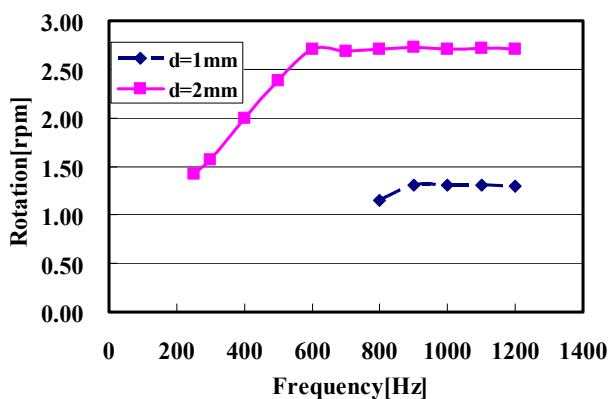


Figure 6 Rotational speeds per a minute (rectangular waves)

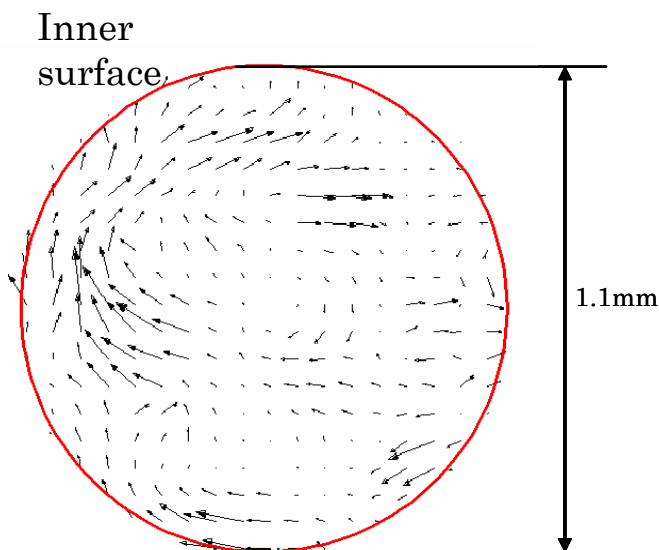


Figure 7 Results analyzed by PIV ($d = 1\text{mm}$, three-phase alternating current)

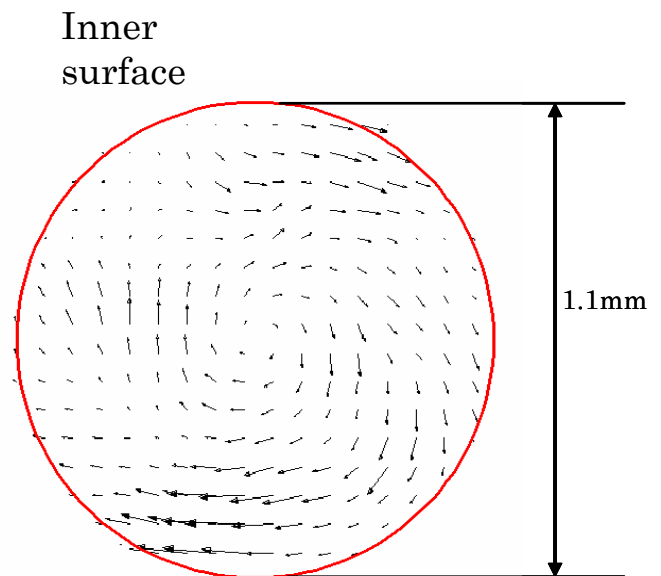


Figure 8 Results analyzed by PIV ($d = 2\text{mm}$, three-phase alternating current)

CONCLUSIONS

In this study, we added the three-phase alternating currents and the rectangular wave voltages as the rotating electric fields on the liquid crystal mixture in the mini-cylinder with the electrodes to generate the flow in the circumference direction. Some main conclusions are shown below.

1. In both the cylinder electrodes for $d=1\text{mm}$ and 2mm in depth under the application of the three-phase alternating currents, the liquid crystal mixture began to rotate when the frequency and the effective value of the voltage increased to 45Hz and 195V .
2. The liquid crystal mixture flows both in the circumference direction and the axial direction for $d=1\text{mm}$. On the other hand, it flows only in the circumference direction for $d=2\text{mm}$.
3. Using the PIV processing, we analyzed the velocity distributions of the flow in the cylinder electrodes and can grasp the state of the liquid crystal mixture rotating.
4. The rotational speed of the liquid crystal mixture increases when the frequency and the effective value of the voltages increase in the range of the present experiments. The maximum rotational speed was about 14.3 r.p.m.
5. When the rectangular waves of the voltage were added as rotating electric fields on the liquid crystal, it rotates. However the rotational speed was smaller than that in the case of the three-phase alternating currents.

ACKNOWLEDGMENTS

We thank Syouwarikagaku Co.,Ltd. for assistances to design our experimental rig, and MERCK Japan Co.,Ltd. for supplying us the liquid crystal mixture. Prof. Toshihiko Imato who belongs to Kyushu Univ. gave us many suggestions.

REFERENCES

1. Tsukiji, T., Nakayama, K., Koyabu, E. and Mitani, T., Influence of electric fields on the flow of a liquid crystal mixture in a circular pipe with electrode surface, Preprint of the Japan Fluid Power System Society, 2003, autumn, pp.174-179. (in Japanese)
2. Tsukiji, T., Koyabu, E., Nakayama, K and Mitani, T., Influence of electric fields on the flow of a liquid crystal mixture in a circular pipe with electrode surface, Transactions of the Japan Fluid Power System Society, 2004, 35-5,pp.84-88.(in Japanese)
3. Tsukiji, T., Koyabu, E., Tsuji, T. and Chono, S., Flow characteristics of a liquid crystal mixture in the circular pipe electrodes, DVD Proceedings of First International Conference on Flow Dynamics, 2004.
4. Tsukiji, T., Ito, J. and Koyabu, E., Study on the flow of a liquid crystal mixture in a circular pipe electrode, Preprint of the Japan Fluid Power System Society, 2004, autumn, pp.38-40. (in Japanese)

DYNAMIC CHARACTERISTICS OF LIQUID CRYSTAL FILM IN A SLIDE BEARING UNDER ELECTRIC FIELD

Yoshiki MATSUMURA*, Toshihiko SHIRAISHI** and Shin MORISHITA**

*Information Processing Center

Hitotsubashi University

2-1 Naka, Kunitachi 186-8603 Japan

*Graduate School of Environment and Information Sciences

Yokohama National University

79-7 Tokiwadai, Hodogaya-ku, Yokohama 240-8501 Japan

(E-mail: mshin@ynu.ac.jp)

ABSTRACT

This paper describes the viscosity variation of a liquid crystal under electric field, and its application to a controllable sliding bearing. Liquid crystal is known as a homogeneous organic liquid characterized by the long-range order of its molecular orientation. When an electric field is applied to a liquid crystal film as lubricant, the orientational order of molecules become parallel to the applied field, which causes apparent viscosity variation. In this paper, a controllable sliding bearing system was constructed and its dynamic characteristics were studied. When step load or sinusoidal load was applied to the bearing pad, the film thickness was successfully controlled by a conventional PID controller. The response frequency was also studied in the experiment.

KEYWORDS

Liquid crystal, Fluid lubrication, Electroviscous effect, Control, Step bearing

INTRODUCTION

Sliding bearings support the applied load by the pressure produced in lubricating oil or air which is subjected to shear deformation [1],[2]. In such sliding bearings, there is a gap between lubricated surface, and the friction force in lubricated sliding bearings is far smaller compared with the friction in ball bearings. Though sliding bearings are superior to ball bearings from the viewpoint of friction force, the lubricating condition in sliding bearings may be strongly governed by the design of bearing assembly and their operation conditions. The lubricating film thickness may be varied by the fluctuation of applied load, sliding velocity, temperature of lubricating oil, etc.

One of the primary factors which give influence on the lubricating condition is the viscosity of lubricant which has been thought to be invariable under constant tem-

perature and normal pressure level. We aim to control the viscosity of lubricant by the external signal introducing liquid crystal as lubricant in sliding bearings.

Liquid crystal is known to show Electrorheological (ER) effect under some electric field. The molecular shape of liquid crystal in nematic phase is considered to be elliptic cylinder and its primary direction of molecules can be controlled by the applied electric or magnetic field, and rheological properties varies in accordance with the field strength. It is also known that the main axis of molecules coincides the shear direction on lubricated surface, which induces decrement of the friction force without any electric nor magnetic field. In this sense, liquid crystal is superior to any other lubricating oil.

In the present paper, a small size model of sliding bearing system with liquid crystal was manufactured and dynamic characteristics of liquid crystal film was examined experi-

mentally. When some fluctuating load was applied to the sliding bearing, the film thickness was controlled by the applied electric voltage to the bearing surfaces. The applied voltage was controlled by a conventional PID controller, and the film thickness was tried to be kept constant even when the applied load to the bearing was varied. The friction force variation by the applied electric field strength was also studied.

LIQUIDCRYSTAL

Liquid crystal is an organic liquid characterized by the ‘long-range’ order of its molecular orientation [3],[4]. This molecular orientation changes in either of two ways, in a certain range of concentration and in a certain range of temperature, resulting in two types of liquid crystal referred to as lyotropic and thermotropic liquid crystal, respectively. Liquid crystal is also classified into high and low molecular weight types. A finer classification is made on the basis of the structure of molecular orientation. Two models of typical phase are shown in Fig. 1, nematic and smectic phases, and the rest two are known as cholesteric and discotic phase.

The most popular and mass-produced liquid crystal is low molecular-weight nematic or smectic phase one which has cylindrical and ellipsoidal shape. The isotropic shape and particular structure of liquid crystal molecules generate some directional properties in viscosity, optical properties, or dielectric constant. The major axis of each molecule has tendency to line up in the same direction statistically due to the interaction of each molecules. And it is known that the surface of partition walls give the influence on the direction of molecules within some distance from the walls and that the direction can be controlled by the applied electric or magnetic field.

In the application of liquid crystal as a lubricant, the orientation of molecules may reduce the friction force between the surfaces, and the magnitude of friction may vary according to the direction of molecules. With the aid of the

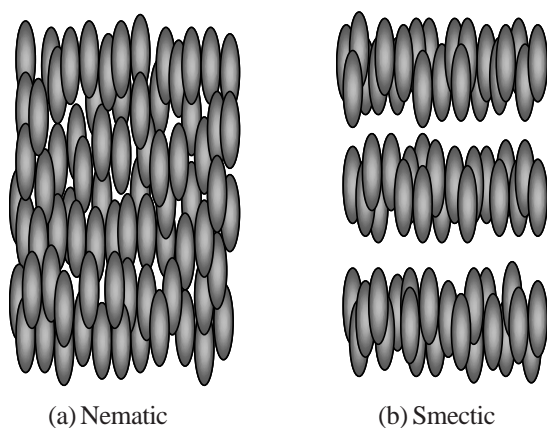


Figure 1 Molecular models of liquid crystal

magnitude of friction force and the shear rate, equivalent viscosity can be evaluated. The viscosity of nematic phase liquid crystal is known to be anisotropic, and three limiting viscosities, called Miesowicz viscosities, have been defined for the three typical orientations of liquid crystal molecules in relation to the shear flow, as shown in Fig. 2. Miesowicz viscosities generally increase in the order of $\eta_1 > \eta_3 > \eta_2$. When the director of the molecules is controlled by applied electric field, the viscosity may vary from η_1 to η_2 .

The liquid crystal used in the present study is a mixture of thermotropic liquid crystals of nematic phase, and originally developed for displays of computers or television sets. The main component is cyano-phenyl-cyclohexane, whose molecular structure is shown in Fig. 3. As shown in this figure, benzene nucleus and cyclohexane are banded together directly as a main part of the molecule, connected by cyano and alkyl on both sides. The bending stiffness of the main part of a molecule in mechanical sense is said to be large enough to represent rod-like structure, where we have no tool to evaluate the stiffness at this time. Electric anisotropy is caused by the difference of electric properties of molecules connected at each side, and because of this electric anisotropy, molecular orientation can be controlled by the applied electric field.

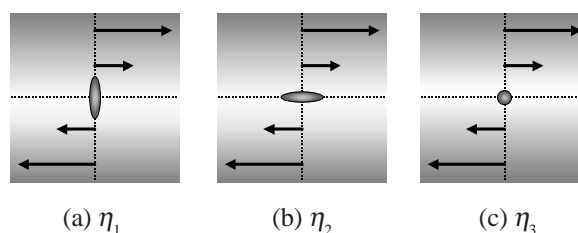


Figure 2 Miesowicz viscosity

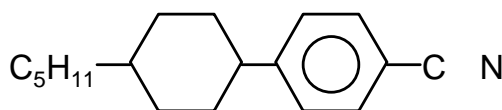


Figure 3 Molecular structure of a specimen

Table 1 Characteristics of a specimen

Clearing point	70 °C
Melting point	-6 °C
Viscosity (@20°C)	28 mPa·s
Dielectric anisotropy ($\Delta\epsilon$)	10.3
ϵ_{\parallel}	15.0
ϵ_{\perp}	4.7

Typical properties of the present liquid crystal are shown in Table 1. Clearing point means a transition temperature where turbid liquid becomes isotropic and consequently optically clear. The temperature where the solid of liquid crystal changes into a rather turbid liquid, is called melting point. Between the temperature range of clearing and melting point, the mesophase is thermodynamically stable. When external electric field is applied, the dielectric anisotropy of liquid crystal which is defined as the subtraction of the dielectric constant parallel to the major axis from that perpendicular to the axis, is one of the most important properties.

RHEOLOGICAL PROPERTIES OF LIQUID CRYSTAL

The typical electroviscosity of test sample measured by the rotational-type viscometer is shown in Fig. 4. The viscosity began to increase when the electric field strength reached a value of a few hundred V/mm, followed by a sudden rise in viscosity with a further increase in the electric field strength. Finally, the viscosity asymptotically reached a constant maximum value. Increasing the shear rate did not affect this pattern in the viscosity-electric field strength relationship; only a higher electric field strength was needed to reach a constant viscosity level. The observed pattern can be explained in relation to Miesowicz viscosity shown in Fig. 2.

EXPERIMENTAL SETUP

One of the simplest shapes of slide bearings may be a step bearing. It has a step around the middle of bearing pad in the sliding direction, and the pressure produced in the lubricant has triangular distribution. The position of peak pressure coincides the location of the step. The geometry of step bearing and the pressure distribution are shown in Fig. 5.

According to the basic theory of lubrication, the load

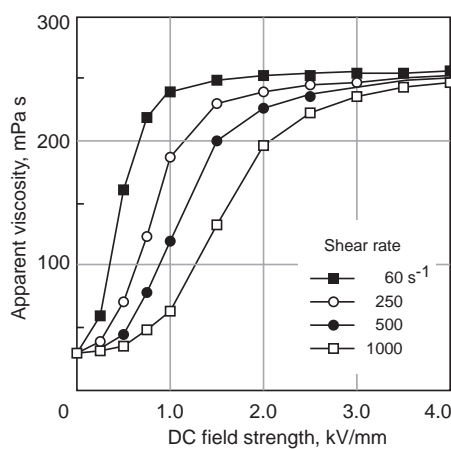


Figure 4 Apparent viscosity as a function of DC field strength under various shear rates

capacity per unit width of a step bearing is

$$P = \frac{3(a-1)k(1-k)}{a^3(1-k)+k} \cdot \frac{\eta UB^2}{h^2} = C_p \cdot \frac{\eta UB^2}{h^2} \quad (1)$$

where η is viscosity of lubricant, U is sliding velocity, B is length of bearing pad, and h is minimum film thickness. C_p is called 'load factor' and a and k are shape parameters defined as shown in Fig. 5. It is well known that the load factor reaches a maximum when the shape parameters are $a = 1.87$, and $k = 0.72$ for step bearings[2]. In the present experiment, k was set to 0.5 in order to eliminate the moment around the horizontal axis perpendicular to the sliding direction.

The step height was set to 0.1 mm, because the experiment will be conducted under the condition that the minimum film thickness should be set around 0.1 mm. Though the minimum film thickness varies due to the experimental condition, the shape parameter a will be around 2.0. The width of sliding pad is 20 mm, and the length is also 20 mm.

The sliding pad was made of insulator, while copper films as electrode were attached on the surface of the pad upward and downward of the step independently. Applying some electric voltage to one or both of the copper films, the liquid crystal as lubricant was subjected to electric field perpendicular to flow direction. The lubricant was supplied by dripping just upward of the bearing pad.

The experimental setup including the bearing pad is shown schematically in Fig. 6. The step bearing pad was set on a rotating disk driven by a variable-speed motor. The bearing pad was supported by two leaf springs deformable just in horizontal direction, and the bearing pad including the leaf springs could rotate in vertical direction around the center of the shaft set at the supporting point of weighting system. The static load was applied to the

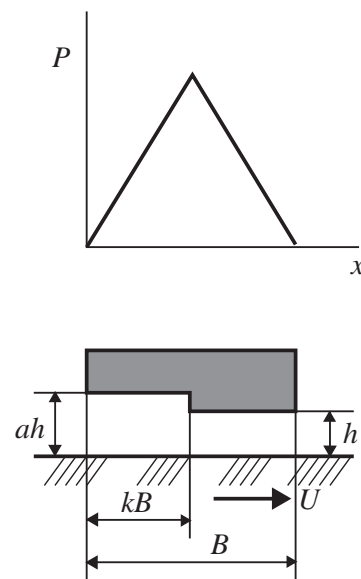


Figure 5 Step bearing and pressure distribution

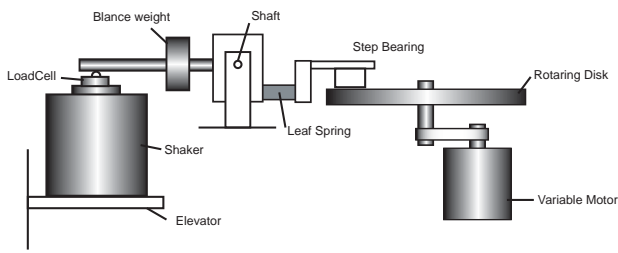


Figure 6 Experimental setup

bearing pad by setting a weight at the end of the torque arm, where a balancing weight was set at the other side of the arm. For applying fluctuating load to the sliding bearing, a magnetic exciter was installed at the end of the rod through a load cell. There were four kinds of weights, from 10 to 173 g. The diameter of rotating disk was 260 mm, and the bearing pad was set at 100 mm apart from the center of the disk. The lubricant was dripped 20 mm upward of the pad.

The film thickness of liquid crystal was measured by four eddy-current displacement sensors equipped at the corners of bearing pad. When the disk rotation was stopped and the bearing pad was slightly pressed against the disk, the film thickness (i.e. the distance between the surface of the disk and the bearing pad) was set to zero. The friction force acting between the disk and the bearing pad was measured from the strain on the leaf springs. All the data from the sensors were put into a personal computer through an A/D converter and proceeded by a conventional PID control algorithm.

RESULTS AND DISCUSSIONS

Typical properties under constant electric field

Before evaluating the properties of the bearing with liquid crystal as lubricant under some control system, the typical properties have been investigated under electric field. The film thickness and friction force were measured under constant electric field, and the applied voltage was changed stepwise from zero to 1,500 V, at the interval of 50 V. The rotating speed of disk was set to constant, and the temperature of lubricant was estimated to be constant at room temperature.

The film thickness variation under electric field is shown in Fig.7, under various applied constant load to the bearing pad. Under the applied voltage from zero to 0.4 kV, the film thickness decreased to some extent, followed by increase of the thickness with higher voltage. After the film thickness took the maximum under electric voltage of around 1.2 kV, it decreased as the applied voltage increased. This result was observed regardless of the magnitude of applied load.

The experimental results shown in Fig. 7 may be caused by mainly the force balance between Coulomb force and pressure variation due to viscosity increase. When the

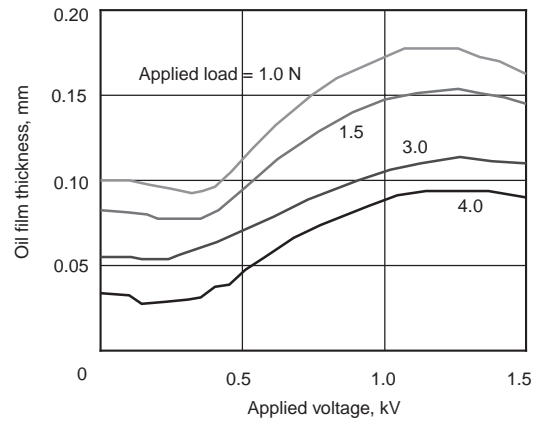


Figure 7 Oil film thickness as a function of applied voltage

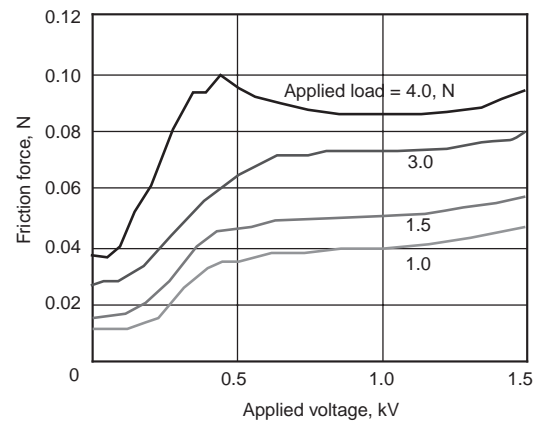


Figure 8 Friction force as a function of applied voltage

applied voltage is low, under 0.4 kV, the viscosity increment in electroviscosity effect is small as indicated in Fig. 4, compared with the increase of Coulomb force between the surfaces. Because Coulomb force acts as attraction force between the surfaces, the film thickness may be decreased. Further increase of applied voltage causes reversed relation between two forces, and the film thickness is increased due to viscosity increment. Beyond the applied voltage of 1.2 kV, the electroviscosity effect is decreased comparatively again, and the film thickness may be decreased. When the applied load to the bearing pad is increased, the film thickness curve shifted to downward almost in parallel. It is shown experimentally that the film thickness can be varied by the applied electric voltage to liquid crystal as lubricant.

The friction force variation under electric field is shown in Fig.8. The friction force was increased gradually as the electric voltage was increased. Further increase of electric voltage caused sudden rise of friction force, and approached to a maximal. The typical properties shown in Fig. 8 agree well with the results of viscosity variation as

shown in Fig. 4 qualitatively. When the applied electric voltage was high, the friction force decreased to some extent especially under large applied load, the cause of which is not revealed in this experiment.

Two identical electrodes are attached separately to the surface of step bearing, and the location effects of applied voltage to the film thickness were investigated. Three cases, voltage was applied to just inlet-side, just outlet-side, and both electrodes, were examined. When voltage was applied to both electrodes, the film thickness was increased largest of the three cases. In the case when just inlet-side electrode was effective, the film thickness was also increased, but the effect was less than that in the previous case. In the following experiment, the electric voltage was applied to just inlet-side electrode.

Film thickness control experiment

Control experiment was conducted to keep the film thickness to the appointed value regardless of the applied load variation. A controller should be constructed in addition to the experimental system shown in Fig. 6. A conventional PID controller was introduced because it is considered as one of the most reliable controller for linear systems. The required applied voltage was calculated by PID algorithm, based on all the signals from displacement sensors on the bearing pad and strain gauges on the leaf springs put into the personal computer through an A/D converter. The voltage signal was generated through a D/A converter set on the computer, and amplified for the signal for the step bearing.

When the applied load to the bearing pad was changed stepwise from 1.5 to 3.0 N, the time response of film thickness variation under constant disk rotating speed is shown in Fig. 9. The appointed film thickness was set to 0.1 mm. The result under constant voltage was also shown for comparison. As shown in Fig.9, the film thickness was controlled successfully, converged to the appointed value in 0.2 s after the sudden change of applied load.

A sinusoidal load was applied to the bearing pad by the magnetic exciter, and the results are shown in Fig.10. The frequency was set to 5.0 Hz. Before the controller started, the bearing pad was supported by the pressure produced in the lubricant and the film thickness fluctuated according to the applied load. The average film thickness was around 0.05 mm. After the controller started at 5.0 s, the film thickness was successfully controlled to 0.08 mm, which was set to the controller in advance. At the same time, the control voltage from the controller started to fluctuate synchronized to the frequency of the applied load. The upper limit of output from the amplifier was 1.0 kV, so the control voltage was also limited to the same value, as shown in Fig. 10.

The results by a sinusoidal load swept from 1.0 to 25.0 Hz are shown in Fig.11. While the film thickness fluctuated synchronized to the applied load around 0.04 mm without any control signal, the film thickness was well controlled around 0.08 mm with control signal. Under 5.0 Hz, the film thickness variation was limited up to 0.005 mm.

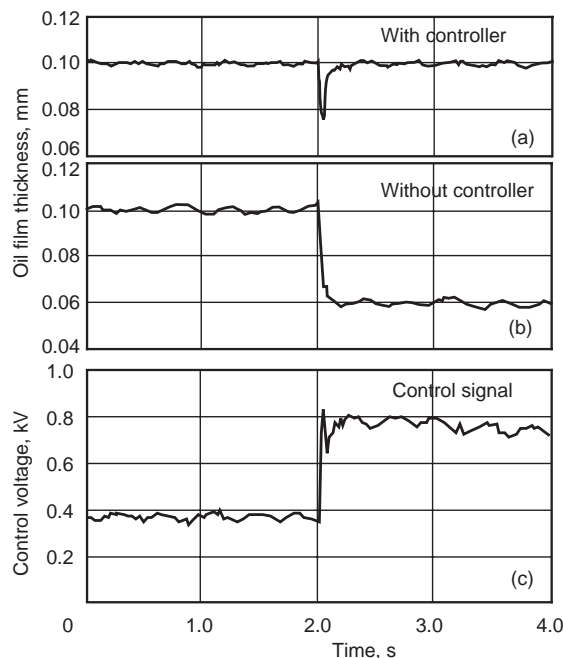


Figure 9 Oil film thickness with and without control under step load on the bearing

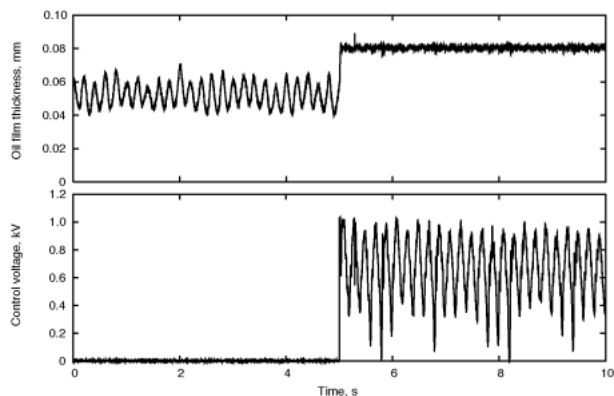


Figure 10 Oil film thickness with and without control under sinusoidal load on the bearing

The variation amplitude was well controlled up to 15 Hz by this control system compared with the results without the control signal. This may be caused by the output limit from the amplifier, and time history of the control signal had already reached to this limit around 10 Hz, as shown in Fig.11.

CONCLUSIONS

In the present paper, the control experiments of lubricating film thickness was conducted, in which liquid crystal was introduced as lubricant and electric field was applied to

liquid crystal in order to control the viscosity of lubricant. Liquid crystal has a great advantage in applying to lubricating fluid, because the friction force may be decreased by the molecular orientation expected especially near the surface of bearings without any field. In addition to that, the viscosity can be varied by the applied electric field strength.

In fact, liquid crystal is generally very expensive, and it cannot be used as lubricant for general purpose. But it is shown that the state of lubrication can be controlled by external signals experimentally in this system, which is expected as a turning-point in introducing such control system in fluid lubrication problems.

REFERENCES

- [1]Pinkus,O. and Sternlicht,B., Theory of Hydrodynamic Lubrication, McGraw-Hill, 213 (1961).
- [2]Cameron,A., Principles of Lubrication, Longmans, 132 (1966).
- [3]de Jeu,W.H., Physical Properties of Liquid Crystalline Materials, Gordon and Breach, 49 (1980).
- [4]Morishita,S.,Electroviscous effect of nematic liquid crystals, Tribology International, 26-6, 399-403 (1993).

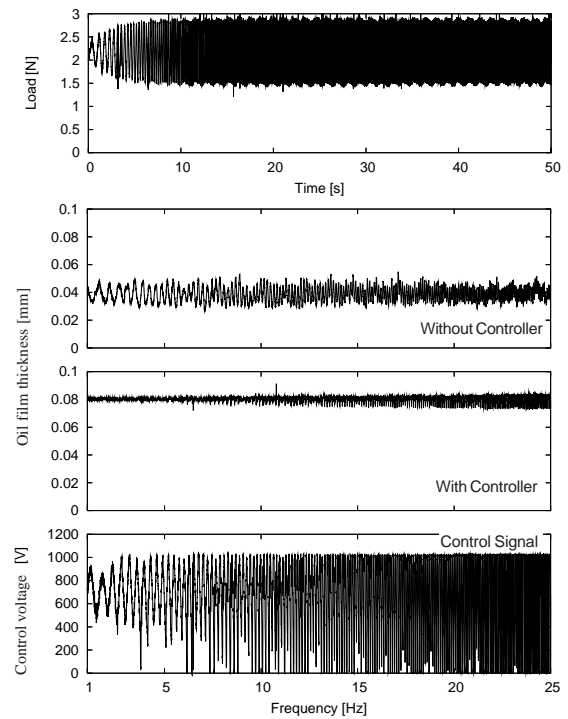


Figure 11 Results under sinusoidal applied load swept from 1 to 25 Hz

Development of ER Clutch for the Walking Support Machine

Katsushi SATOH*, Taro MABUCHI**, Yukio KAWAKAMI**, Hiroshi OKAMURA**

*Division of Functional Control Systems , Graduate School of Engineering
Shibaura Institute of Technology

**Department of Mechanical Control Systems, Faculty of System Engineering
Shibaura Institute of Technology

307, Fukasaku, Minuma-ku, Saitama-shi, Saitama-ken 337-8570 Japan

ABSTRACT

Walk training is good rehabilitation for old people and handicapped people. Then it is considered the effective measurement for decreasing bedridden people and wheelchair users. In walk training, they frequently use walkers, walking sticks, etc. It is a problem that these kinds of support tools are not flexible and mobile because their handicap conditions are different. New support tools are demanded to be intelligent and personalized.

We are developing a new walking support machine for old people and handicapped people, because they expect to move easily by themselves. The machine is equipped with two ER devices which compose an electrorheological fluid clutch (ER clutch) and a motor, and able to work with smooth power assistance or safety braking.

In this paper, we refer a developing concept in the new walking support system, and explain a mechanism and design of the ER devices. In addition, we also report some experimental results, because we have examined on characteristics of the ER devices.

KEY WORDS

ER Clutch, Walking Support Machine, Torque Transmission

INTRODUCTION

In aging society with declining birth rate, the population of the elderly people with some kind of functional disorders will be increased. The labor population of helper

will be decreased. Then, we have been studying about the development of the welfare equipment to assist the independence of the elderly people. Especially, muscular depression that becomes a problem with aging causes a moving decrease in the chance, and causes further muscular depression. Therefore, the maintenance and

recovery of the muscular power at the early stage are important preventive plans and handicapped persons will be decreased.

As for the equipment concerning the walking assistance, it is commercialized over many kinds, and the number of users is also increasing now. However, the use of these commodities in the place where there are walking obstacles of bump etc. is the large burden. The range of the action is inevitably limited. Therefore, they are used only as assistive device for people who can walk independently.



Fig.1: walking assistance equipment

We have been developing an intelligent walking support machine that can correspond to the walking situation of the road and user's trouble level as a movement support tool intended for handicapped persons and the preliminary group. To do the power assistance and the brake control for driving part of this walking support machine, the torque transmission device composed of the DC servo motor and the clutch with the ER fluid is used. In this paper, we mention about the construction of experimental prototype and the evaluational result of power transmission part, where ER device is used.

DESIGN CONCEPT OF WALKING SUPPORT MACHINE

Basic concept

We had examined walking pattern with existing walking support machine previous year. Our assumption of subject users and a basic concept of the power assistance system are given as follows.

Subject user

- a) Subject user is able to walk by themselves.
- b) The range of the action area is limited in a present walking assistance machine.
- c) The recovery is expected if undergoing rehabilitation though the trouble begins to appear a little in the leg strength.

Walking support concept

- i) User's leg strength is bring out to its maximum. User's will is perceived on that and the walking mode changes.
- ii) The turn able radius is assumed to be zero, in order to achieve effective small turn.
- iii) Gradual start, Safe braking.
- iv) The walking speed is maximum 4[km/h].
- v) The bump riding past is 50[mm] or less.
- vi) The gradability is about 10[deg].
- vii) Weight is about 15[kg].
- viii) Redundancy of safety device.

These settings will be introduced, however, the setting will be changed according to user's moving ability and life environments.

Assist method by walking support machine

When the set concept was achieved, the examination subjects was decided as follows as a content of the control.

- 1) In order to detect the object's posture and orientation of the movement, strain gauge is installed.
- 2) Confirmation of practicality and safety of ER clutch.
- 3) Detecting obstacles.
- 4) The mechanical brake besides the control brake is installed.

These items are choose, by the experiment aiming at commercialization in consideration of domination and the cost side.

Power transmission part(ER clutch)

The ER fluid has the characteristic that the viscosity is changed by the impressed voltage, and is excellent in conformity. Moreover, power more than the surrender stress is not transmitted. Therefore, the ER clutch that uses this characteristic can be expected a gradual start depending on the impressed voltage, compared with the the motor directly connected type. Even if there is abnormal control occurred, fear to reckless driving is alleviated while maximum transmission power is limited by the characteristic of ER of the clutch.

Then, main topic of this research is to develop the control method to realize smooth power support and a safe braking

at the practical use of the ER clutch. Moreover, we will evaluate about the ER device that can maximize the ER effect.

OUTLINE OF WALKING SUPPORT MACHINE

About the examination prototype

The prototype was developed in order to evaluate the performance and for further discussion(Fig.2). Both self-propelled and the joystick operation by driving program are developed.

The system configuration is as shown in Fig.3. The input signal of driving program or the joystick is sent to the control board by the personal computer. Distance of the movement is sent from the control board to the motor through the servo amplifier. The motor and the ER clutch are connected with the belt,



Fig.2: Prototype

and the speed is controlled by changing the impressed voltage of the ER clutch. Moreover, encoder information installed in the motor and the tire is sent back to the personal computer through the control board. By the way, sensors other than the encoder are not installed, but other sensors will be added if it's necessary while advancing the experiment in the future.

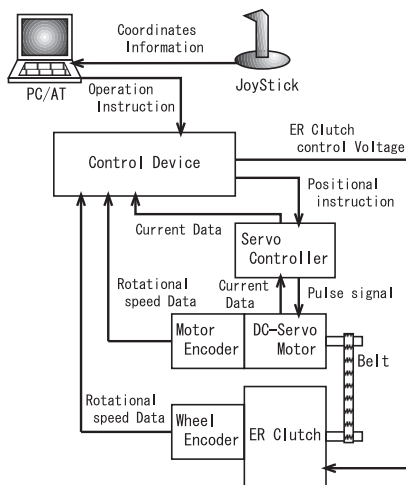


Fig.3: The system configuration

Control board

Open motion controller 'SPX-8000' (Fig.4) made by the techno company Ltd.. is used. This control board can possess the control of nine axis, and can send and receive the data respectively.



Fig.4: SPX-8000

Two axis for the motor control and the ER clutch control for both right and left are used (Total 4 axis). And the current and rotation of the motor and the rotational speed of the tire are monitored.

Motor

DC brushless motor (EC-40), the servo amp and the encoder, which are made by the maxon company are used. A basic characteristic concerning the motor is shown in Table.1. The diameter of the tire is 200[mm]. It follows that the output torque at the condition 4 [km/h] (106[r.p.m]) in actual use becomes 30[Nm]. The motor torque was calculated with 5[Nm] by the design value until the previous year. These conditions fulfill the requirement of planning.

Table.1: Motor characteristic

Motor (EC 40)	
Rotational speed / Torque	9.9 [r.p.m/mN·m]
Torque constant	19 [mN·m/A]
Rotational speed constant	500 [r.p.m/V]
Gear (GP 42 C)	
Reduction ratio	53 : 1

ER clutch

The ER clutch is made by ER Tech Ltd.(Fig.5).

The disk type clutch (Fig.6) is used for the system. Two kinds of fluid (the dispersed ER fluid and the homogeneous ER fluid) are prepared and comparative study are made.



Fig.5: ER clutch

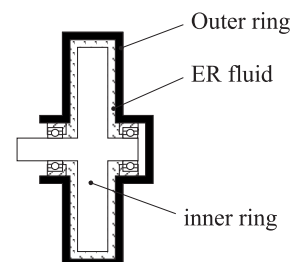


Fig.6: section of clutch

Self-propelled examination

The figure shown below is an example of the data obtained by the prototype. The example is the reciprocation to make the tire by one rotation with motor rotational speed of 28[r.p.m].

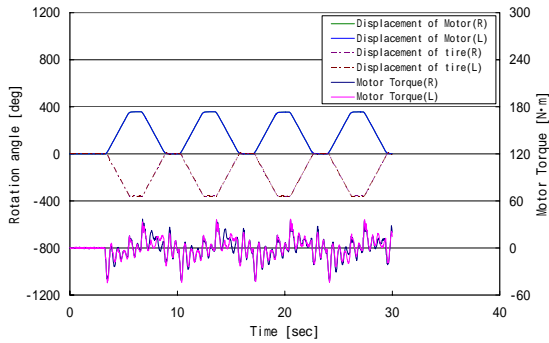


Fig.7: Example of the data

The content of the examination in the future is to change the voltage of the ER clutch, and to measure actual traction. Moreover, this prototype has the problem such as being not able to get over the bump immediately before the bump. The corrective strategy is examined about other problems including this thing.

UNIT EXPERIMENT OF ER CLUTCH

In the ER fluid, it is divided roughly into two kinds, the dispersed ER fluid and the homogeneous ER fluid. Each of fluid has different behavior when the electric field is impressed. This time, a basic characteristics of both fluid were evaluated in order to install them to the ER clutch for the walking support machine. By the way, it experimented on the impressed voltage by the specification of the device by 1.5kV max.

Experimental apparatus

The construction of the experimental device is shown in Fig.8. In the actual experiment, the rotational speed and the torque of each impressed voltage were measured, when the rotation was added with the clutch output side (tire side) fixed.

Torque characteristic of ER clutch

The transmission torque was measured when a constant voltage was applied to the ER clutch and the motor was rotated at a constant speed.

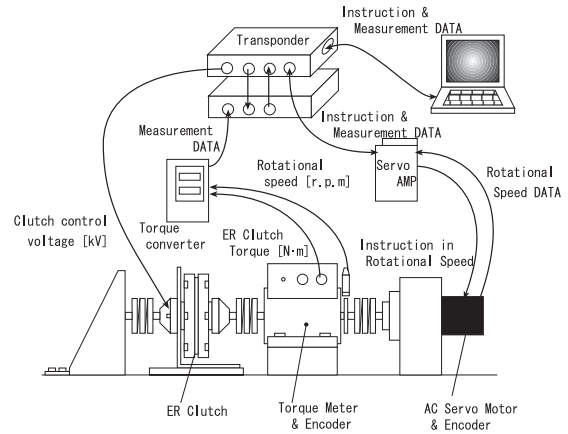
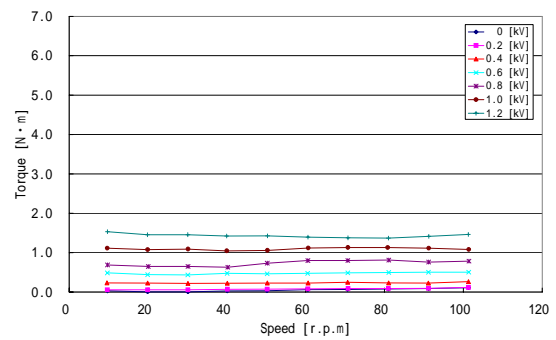
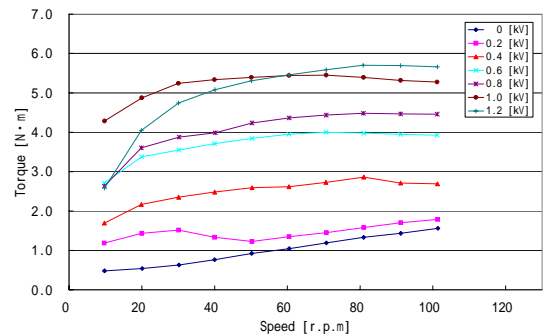


Fig.8: Experimental device



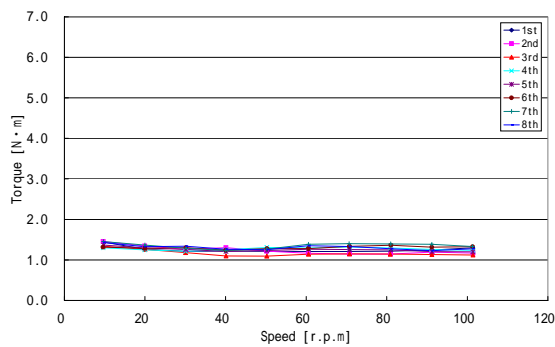
(a): Dispersed ER fluid



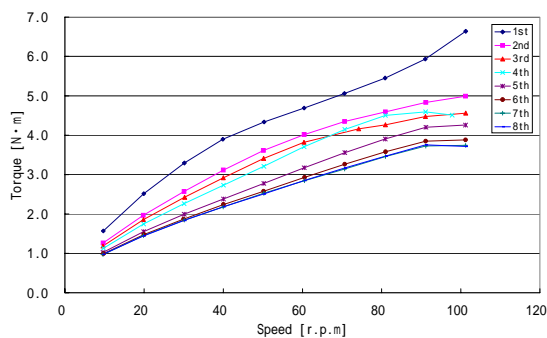
(b): Homogeneous ER fluid

Fig.9: Rotational speed - Torque

As it is well known, the fluid of homogeneous ER fluid obtained the result that the transmission of Torque is higher than the other. However, the decrease in the ER effect by the rise of temperature was observed in the fluid of homogeneous ER fluid. Then, change of each ER fluid's characteristics through time was confirmed. The impressed voltage to ER fluid is set to 1.0[kV], the rotational speed of the motor is given as a step input for 10[sec] at each iteration, and this sequence was done for three times. Input rotational speed is changed from 10 to 100[r.p.m], and this sequence was repeated. The experimental result is shown in Fig.10.



(a): Dispersed ER fluid



(b): Homogeneous ER fluid

Fig.10: Change of ER fluid's characteristics

As a result of the experiment, stable torque was observed in a dispersed ER fluid. However, a decrease of the ER effect was confirmed in the homogeneous ER fluid until the seventh times. About 30 minutes had passed, ER effect becomes stable.

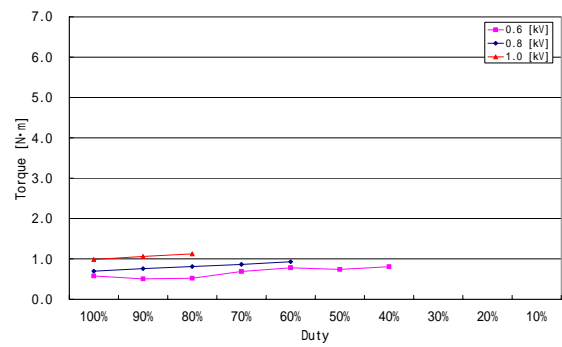
PWM drive experiment

Generally, it is assumed that the ER fluid has a long life if it is driven in PWM method. We will evaluate the ER effect when ER fluid is driven in PWM method and Duty ratio is changed. A impressed voltage with Duty ratio was set to 0.6, 0.8, and 1.0kV.

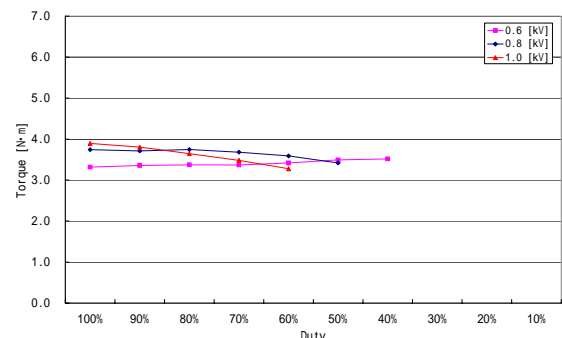
As a result, the increase of the transmission power in the dispersed ER fluid was observed when Duty ratio is decreased. But it is decreases in the homogeneous fluid. However, it is necessary to reconfirm in different operating condition, because if the homogeneous fluid is continuously driven, the ER effect is reduced.

About the design of the ER clutch

Existing device is evaluated in this paper. And, problems such as the insulating and torque shortage were found. The ER equipment is divided roughly into the clutch and



(a): Dispersed ER fluid



(b): Homogeneous ER fluid

Fig.11: PWM drive Torque

the brake type. Moreover, the structure is divided into the disk type and the cylinder type. The redesign and the further examination are planned for the sub-optimal combination of the elements for practical use.

SUMMARY

We had developed the experimental prototype. And the characteristic of Dispersed ER fluid and Homogeneous ER fluid, which is used for the transmission device, was evaluated. The control that can draw out the ER effect in the maximum method is examined. To that end, it is necessary to get experimental data in various conditions, and to confirm the characteristic. Moreover, a suitable device for this equipment is designed in the present stage, and we would like to have the chance of the report again.

REFERENCES

- [1] K.Koyama, A.Inoue, "Development of Electro Rheological Fluid", CMC,pp.82-90,140-151,1994.
- [2] A.Inoue, U.Ryu, "Expected Materials for the Future", NTS Inc. Vol.2 No.8,pp27-34,2002.

Dynamic Shear Flow of Electro-Rheological Fluids Between Two Rotating Parallel Disks

Masami Nakano*, Kiyotaka Yamashita*, Shinya Koizumi* and Ryosuke Keta*

* Department of Mechanical Systems Engineering, Faculty of Engineering
Yamagata University
4-3-16 Jonan, Yonezawa, Yamagata 992-8510, Japan
(E-mail: nakano@mnaka.yz.yamagata-u.ac.jp)

ABSTRACT

The transient response of induced shear stress and the related flow behavior of two types of the ER fluids containing particles have been investigated when they have been under the simultaneous stimulus of an constant DC or AC electric field and shear using a parallel rotary disk rheometer. For only one type of the ER fluid containing sulfonated polymer particles, as the electric field strength increases, the particles in the ER fluid form lamellar formations in the direction of shear, which may be responsible for the ER activity more than the strength of the chains. And, as the gap of parallel disks decreases down to about 0.1 mm, the particles gather around the outer edge of the disk to form a thick ring of the aggregation of the particles, which may be responsible for the increase of the shear stress. In this way, it would be expressed that the shear stress should change consistently with the morphology of the formations. In this work, the effects of shearing time, electric field strength, DC or AC, gap height between disk electrodes and types of ER fluid on the shear stress and the flow morphology are investigated.

KEY WORDS

Key words : Non-Newtonian Fluid, Electro-Rheological Fluid , Steady Shear Flow Mode, Dynamic Flow Behavior, Flow Morphology

NOMENCLATURE

- E : Applied electric field strength of a parallel rotary disk rheometer ($=V/h$). In the case of AC electric field, E represents the amplitude of an applied AC electric field strength.
- h : The gap height between two disk electrodes of the rotary rheometer.
- $\dot{\gamma}$: The shear rate of the ER fluid flow defined at the outer edge of the disk.
- τ : Induced shear stress
- t : Shearing time

INTRODUCTION

Electrorheological (ER) fluids consisting of micron-sized polarizable particles dispersed in a dielectric liquid exhibit intriguing properties of yielding solids under the application of an electric field, which are associated with the alignment of the particles into a fibrous structure in the direction of the field due to electrostatic forces. The ER suspensions behave like a Bingham fluid having yield stress, which can be rapidly changed in reversible manner by applied electric fields [1]. So, ER fluids are known as a class of intelligent materials. These intelligent properties are anticipated

some applications of industrial devices such as dampers, valves, clutches, brakes, and so on. One of the problems presented by these fluids is hysteresis in flow-curves [2,3], which makes the precise control of the ER mechanical devices very difficult.

In this study, the transient response of induced shear stress and the related flow behavior of two types of the ER fluids containing particles have been investigated experimentally when they have been under the simultaneous stimulus of an constant DC or AC electric field and shear using a parallel rotary disk rheometer. The effects of shearing time, electric field strength, DC or AC, gap height between disk electrodes and types of ER fluid on the shear stress and the pattern formulation of the particles are investigated. This study is very important for the practical use of ER fluids in clutches and brakes.

EXPERIMENTAL APPARATUS AND MEASUREMENT SYSTEM

Two types of ER fluids were studied. One of them (TX-ER6 [4], 20 Vol%) is composed of numerous sulfonated polymer particles of average diameter of 5 μm suspended into silicone oil. Another one (FKER-V5, 35 Vol%) is composed of the composite type of organic and inorganic particles (average diameter 15 μm) dispersed into silicone oil.

As shown in Fig.1, the electrorheological properties of these fluids are evaluated by means of a rotary parallel disk rheometer (HAKKE, RheoStress RS150), in which an upper disk of 20 mm diameter rotates and a lower disk is fixed. A transparent glass disk electrode coated with ITO film of 38mm diameter replaces the lower disk, in order to enable to visualize the flow behavior from a bottom side. The gap between two parallel disks is set 0.1 , 0.2 , 0.3 , 0.4 , 0.5 and 0.7mm. An electric field is applied between two disk electrodes through a high voltage amplifier.

In the experiments, the shear rate $\dot{\gamma}$ defined at the outer edge of the disk is set a constant value of 100 s^{-1} , and the transient response of the induced shear stress and the pattern formulation of the particles are measured as a function of the gap height h and the DC and AC electric field strengths E .

TRANSIENT RESPONSE OF SHEAR STRESS AND FLOW PATTERNS

(a) TX-ER6 ER Fluid under DC Electric Field

Figure 2 shows the transient responses of the shear stress τ measured for the case of TX-ER6 ER fluid under the simultaneous stimulus of DC electric field and shear ($h=0.2 \text{ mm}$, $\dot{\gamma}=100 \text{ s}^{-1}$). The shear stress is

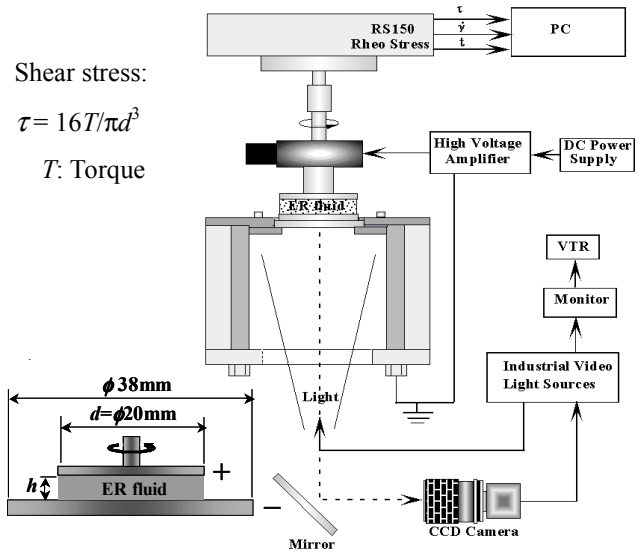


Fig.1 Experimental apparatus and measurement system using a rotary parallel disk rheometer

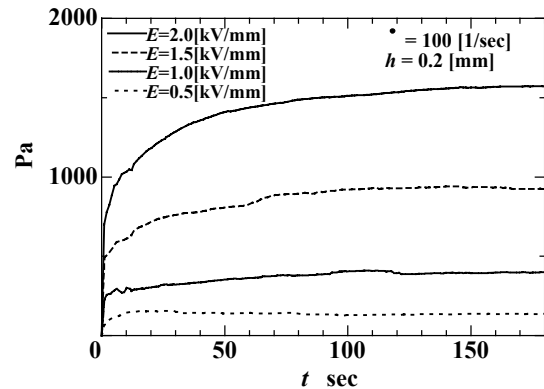


Fig.2 Time history of induced shear stress after simultaneous stimulus of constant shear and DC electric field (TX-ER6, $h=0.2 \text{ mm}$, $\dot{\gamma}=100 \text{ s}^{-1}$)

suddenly increased just after the experiment is started and then is gradually increasing to approach a certain maximum value for every applied electric field strengths E . As the electric field strength is increased, this trend becomes remarkable and the maximum shear stress is increased due to the strengthened binding force acting between particles in the ER fluid. The maximum shear stress is increased in proportion to the square of the electric field strength.

As seen in Fig. 3 where the dark rings are composed of particles, the time variation of the shear stress can be explained by the evolution of the flow patterns with time. In the presence of an electric field, the particles align into a fibrous structure in the direction of the field due to electrostatic forces. When the ER fluid is sheared at a constant shear rate, at first the particles are uniformly dispersed between the disks, and then the

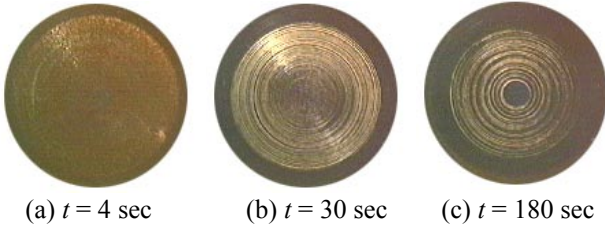


Fig. 3 Structure evolution of ER fluid shear flow with time ($E=2.0$ kV/mm, $h=0.2$ mm, $\dot{\gamma}=100$ s⁻¹, DC)



Fig.4 Changes of ER fluid shear flow patterns with electric field strength ($t=150$ sec, $h=0.2$ mm, DC)

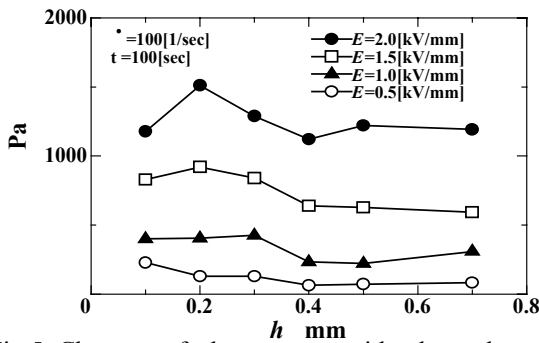


Fig.5 Changes of shear stress with electrode gap in terms of applied electric field strength ($t=100$ sec, DC)

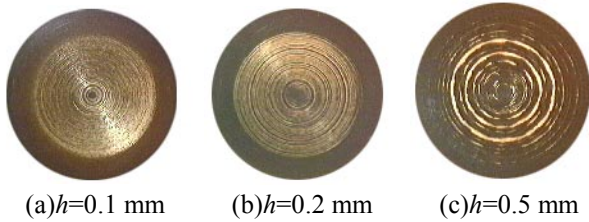


Fig.6 Changes of ER fluid shear flow patterns with electrode gap ($E=2.0$ kV/mm, $t=100$ sec, DC)

particles are moved to the outer edge of the rotating disk, resulting in the lamellae formation having many thin rings inside the disk and a thick dark ring around the perimeter of the disk. The thickness of the dark ring is increased with time, indicating the particle gathering to the perimeter of the disk. As the results, the torque acting on the disk is increased and the induced shear stress is also increased. Thus, the morphology of the particle formations is closely related to the induced shear stress.

Figure 4 shows the effect of the electric field strength on the flow pattern of the ER fluid. As the electric field

strength is increased, the thick dark ring around the perimeter of the disk becomes thicker.

Figure 5 shows the effects of gap of the electrodes on the shear stress ($t=100$ sec). For the relatively narrow gap h of 0.3mm or less, the induced shear stress is a little larger than for the gap of 0.4 mm or more. In the case of the gap of 0.4 mm or more, the shear stress takes an almost constant value determined by the applied electric field strength E , independent of the gap. The effects of the gap h on the flow pattern are shown in Fig. 6. For the relatively large gap h of 0.5mm, the dark ring of the particles on the perimeter of the disk is not observed obviously and the lamellar rings of the particles are formed. The thick dark ring of the particles, which would cause the increase of the shear stress, is obviously observed in the case of relatively narrow gaps of 0.1 and 0.2 mm.

(b) TX-ER6 ER Fluid under AC Electric Field

Figure 7 shows the transient response of the induced shear stress τ measured for the case of TX-ER6 ER fluid in the presence of AC 10 Hz electric field ($h=0.2$ mm, $\dot{\gamma}=100$ s⁻¹). The shear stress increases with increasing the electric field strength E due to the strengthened binding force acting between particles in the ER fluid, as well as the case of DC electric field. But the induced shear stress has an intense fluctuating

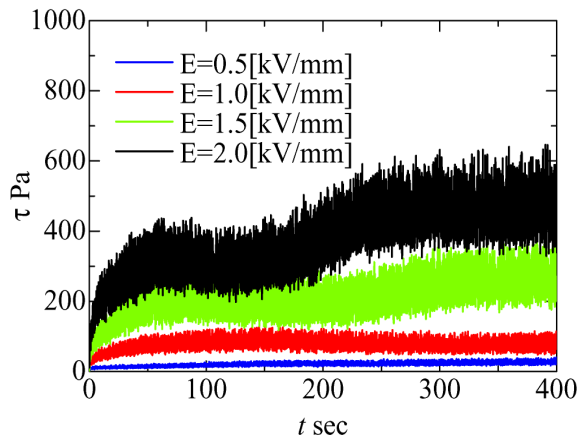


Fig.7 Time history of induced shear stress after simultaneous stimulus of constant shear and AC 10 Hz electric field ($h=0.2$ mm, $\dot{\gamma}=100$ s⁻¹)

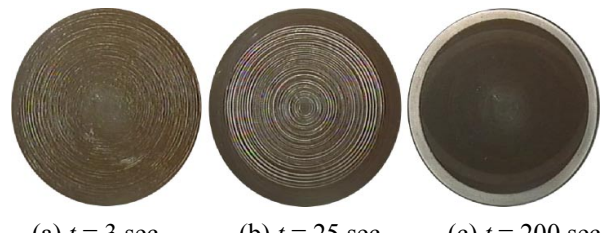


Fig. 8 Structure evolution of ER fluid shear flow with time ($E=2.0$ kV/mm, $h=0.2$ mm, $\dot{\gamma}=100$ s⁻¹, AC10Hz)

component. The formation and destructions of fibrous structures of the particles might be caused alternately because of the applied AC electric field. The induced shear stress is smaller than that for the DC electric field case.

Figure 8 shows the transient response of the flow pattern of the ER fluid between the electrodes (AC 10Hz, $E=2.0$ kV/mm). As seen in Fig.8(a), (b), many thin rings inside the disk and a thick dark ring on the perimeter of the disk are observed at relatively early time, as well as the DC electric field case. The thick dark ring spreads inside with time, and finally a stable flow pattern is formed, consisting of one uniform circular structure of the particles inside the disk and a thin transparent ring of silicone oil on the perimeter of the disk, as observed in Fig.8(c).

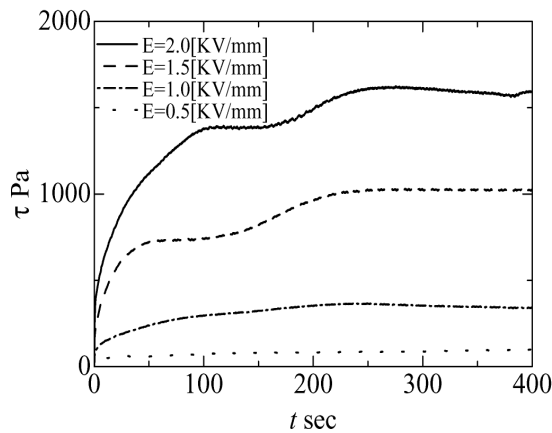


Fig.9 Time history of shear stress after simultaneous stimulus of constant shear and AC 50 Hz electric field ($h=0.2$ mm, $\dot{\gamma}=100$ s⁻¹)



(a) $t = 3$ sec (b) $t = 25$ sec (c) $t = 200$ sec

Fig. 10 Structure evolution of ER fluid shear flow with time ($E=2.0$ kV/mm, $h=0.2$ mm, $\dot{\gamma}=100$ s⁻¹, AC50Hz)



(a) $E=0.5$ kV/mm (b) $E=1.0$ kV/mm (c) $E=2.0$ kV/mm
Fig. 11 Changes of ER fluid shear flow patterns with electric field strength ($t=300$ sec, $h=0.2$ mm, AC50Hz)

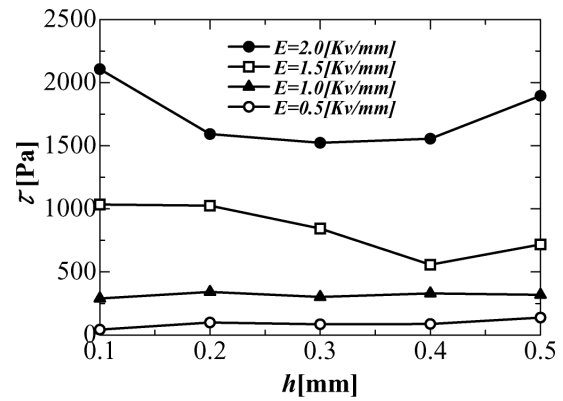


Fig.12 Changes of shear stress with electrode gap in terms of applied electric field strength ($t=400$ sec, AC 50Hz)



(a) $h=0.1$ mm (b) $h=0.3$ mm (c) $h=0.5$ mm

Fig.13 Changes of ER fluid shear flow patterns with electrode gap ($E=2.0$ kV/mm, $t=400$ sec, AC50Hz)

The transient responses of the induced shear stress τ measured in the presence of AC 50 Hz electric field ($h=0.2$ mm, $\dot{\gamma}=100$ s⁻¹) are shown in Fig. 9. As the electric field strength increases, the shear stress increases in the same way as the DC electric field case. At relatively high electric field, the shear stress gradually increases with time and then settles at a constant value after a sufficiently long time. In this case, the intense fluctuations of the shear stress under AC 10Hz electric field are not observed because the formations and destructions of the fibrous structures of the particles might be caused alternately according to the AC frequency. The levels of the shear stress are greater than that for AC 10 Hz electric field case, and are almost the same levels as for the DC electric field case. The flow pattern evolution of ER fluid shear flow with time under AC 50Hz electric field strength is almost the same as the AC 10Hz electric field case, as seen in Fig.10. Figure 11 shows the effect of the electric field strength on the flow pattern of the ER fluid. The thick dark ring of the particles on the perimeter of the disk spreads inside to become thicker as the electric field strength increases, and at $E=2.0$ kV/mm the uniform circular structure of the particles is formed. So, it can be concluded that the dark ring on the perimeter of the disk spreads inside the disk to form the uniform circular structure in an earlier stage of shear as the electric field strength increases.

Figure 12 shows the effects of gap of the electrodes on the shear stress ($t=400\text{sec}$) for the case of AC 50 Hz electric field. It is obviously accepted that the induced shear stress do not significantly depend on the gap height, but for $E=2.0$ kV/mm the shear stress clearly increases at the relatively narrow gap of $h=0.1$ mm. It is found from Fig.13 that this increase of shear stress at $h=0.1$ mm might be due to the uniform circular structure of the particles spreading all over the disk, while at $h=0.3\text{mm}$ and 0.5 mm the thin transparent ring of silicone oil appears on the perimeter of the disk as observed in Fig.13 (b), (c).

(c) FKER-V5 ER Fluid under DC Electric Field

Figure 14 shows the transient responses of the shear stress τ of the FKER-V5 ER fluid under DC electric field ($h=0.2$ mm, $\dot{\gamma}=100$ s⁻¹). The shear stress is suddenly increased just after the experiment is started and then maintains an almost constant value determined by the applied electric field strength, unlike the TX-ER6 ER fluid. That is, the shear stress of the FKER-V5 ER fluid under DC electric field does not exhibit any significant variation with time to keep a constant value. And unlike TX-ER6 ER fluid, the shear stress increases nearly in proportion to the electric field strengths ranging from 1.0 to 4.0 kV/mm, and is almost half as large as for TX-ER6 ER fluid.

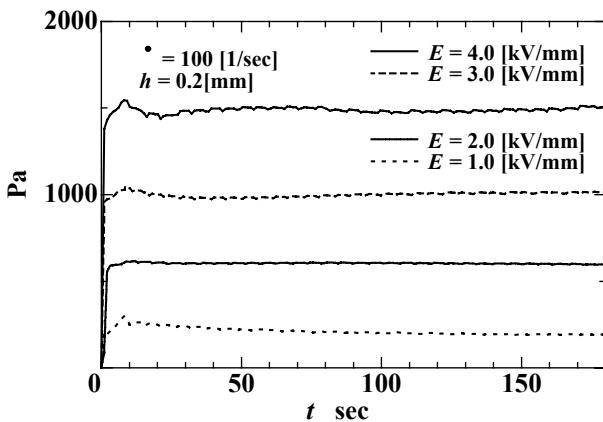


Fig.14 Time history of induced shear stress after simultaneous stimulus of constant shear and DC electric field (FKER-V5, $h=0.2$ mm, $\dot{\gamma}=100$ s⁻¹)

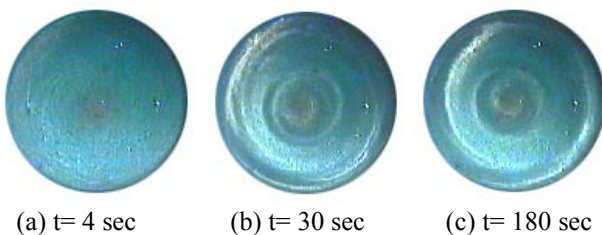


Fig.15 Structure evolution of ER fluid shear flow with time ($E=4.0$ kV/mm, $h=0.2$ mm, $\dot{\gamma}=100$ s⁻¹, DC)

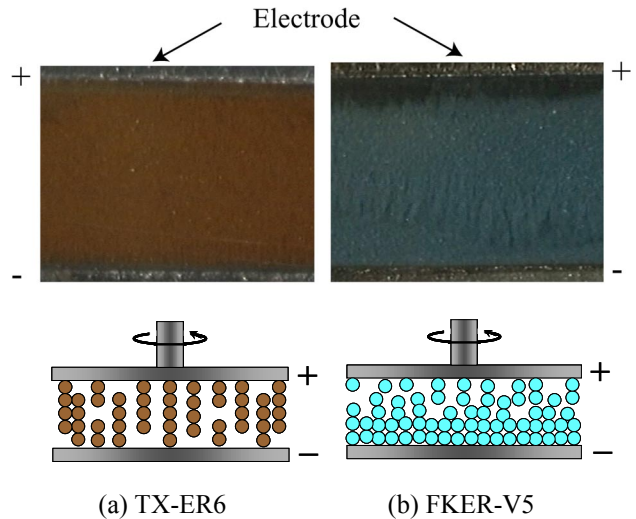


Fig. 16 Side-view of particles formation between two plane electrodes under electric field ($h=2.0$ mm, $E=1.0$ kV/mm), and schematic image of particles formation between two rotating disks

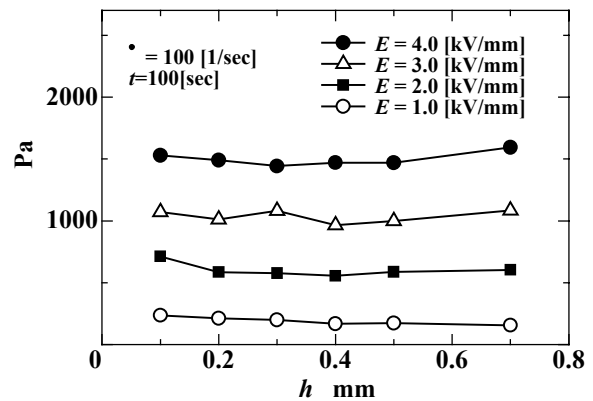


Fig.17 Changes of shear stress with electrode gap in terms of applied electric field strength ($t=100$ sec, DC)

As observed in Fig.15, the thick dark ring and the lamellar many rings of the particles, which appear in the case of TX-ER6 ER fluid, have never been observed. As shown in Fig. 16(b), in the case of FKER-V5, almost all particles could be observed to adhere to the GND electrode due to the electric charging of the particles under the DC electric field by the side-view visualization of particles behavior between two electrodes. Because of this, the particles are difficult to move easily to form the lamellar rings. While in the case of TX-ER6 ER fluid, because the chains of particles adhere to either of the electrodes as shown in Fig.16 (a), the particles might be easily moved to form the lamellar formations in the direction of shear.

The effects of the gap height h on the shear stress at $t=100\text{sec}$ are shown in Figure 17. It can be concluded that the induced shear stress of the FKER-V5 ER fluid does not depend on the gap height h .

(d) FKER-V5 ER Fluid under AC Electric Field

Figure 18 shows the transient response of the shear stress τ measured for the case of FKER-V5 ER fluid under the simultaneous stimulus of AC 50 Hz electric field and shear ($h=0.2$ mm, $E=1.0, 2.0, 3.0, 4.0$ kV/mm, $\dot{\gamma}=100$ s⁻¹). The shear stress is suddenly increased just after the experiment is started and then is gradually increased to approach a certain maximum value, unlike the DC electric field. As the electric field strength increases, the shear stress also increases in the same manner as the DC electric field case. Figure 19 shows the flow pattern evolution of the ER fluid shear flow between the electrodes ($E=4.0$ kV/mm). Unlike the DC electric field case of Fig.15, very fine lamellar rings are formed all over the disk, but this flow pattern does not significantly change with time. When applied AC electric field, the polarity of the upper disk electrode changes alternately to be positive and negative as the lower electrode is grounded, so that the electric charged particles may easily move to upper or lower electrode according to the polarity of the upper electrode due to electrostatic forces, resulting in the formation of the very fine lamellar rings of the particles.

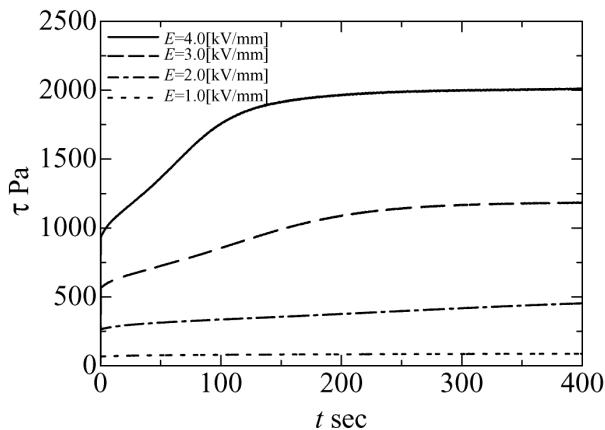
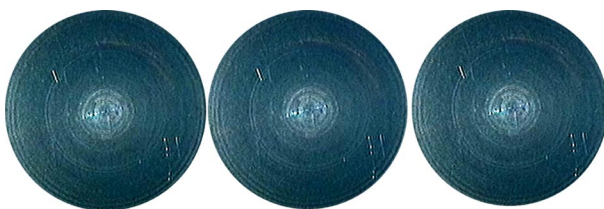


Fig.18 Time history of induced shear stress after simultaneous stimulus of constant shear and AC 50 Hz electric field (FKER-V5, $h=0.2$ mm, $\dot{\gamma}=100$ s⁻¹)



(a) $t = 3$ sec (b) $t = 25$ sec (c) $t = 200$ sec

Fig. 19 Structure evolution of ER fluid shear flow with time ($E=2.0$ kV/mm, $h=0.2$ mm, $\dot{\gamma}=100$ s⁻¹, AC50Hz)

CONCLUDING REMERKS

We have experimentally studied the transient response of induced shear stress and the related dynamic flow behavior of two types of the ER fluids containing particles under the simultaneous stimulus of the constant DC or AC electric field and shear using a parallel rotary disk rheometer.

The ER fluid (TX-ER6) of numerously sulfonated polymer particles shows the remarkable time variations of the induced shear stress which increases gradually to saturate with time at relatively high electric field strength. It can be explained that the increase of the shear stress with time is due to the flow structure evolution to the lamellar formation of the particles in the direction of shear and the dense thick ring formation on the perimeter of the disk. Especially, as the electrode gap h decreases less than about 0.3 mm and the electric field strength E increases, the formation of the outer thick ring becomes remarkable and the thickness is increased with time, resulting in the increase of the shear stress. In the AC electric field of low frequency 10 Hz, the induced shear stress has an intense fluctuating component and shows a smaller value.

In the case of the ER fluid (FKER-V5) of organic and inorganic composite particles, we can not observed a big change in the flow structure because all of the dispersed particles adhere to one of the electrodes under DC electric field, so that the shear stress doesn't change with time and takes a stable value determined by the applied electric field strength. However, the induced shear stress is relatively low, about half of that for TX-ER6. While under AC electric field, the shear stress increases gradually with time in spite of almost no change of the flow structure.

ACKNOWLEDGEMENT

We would like to thank Mr. S. Yamamura for his assistance in the experiments.

REFERENCES

- (1) M.Nakano , T.Yonekawa , Trans. of the Japan Society of Mechanical Engineers , **61**-581 , (1995)B, 166-172, in Japanese.
- (2) R. Aizawa, M. Nakano, et al., Int. J. of Modern Physics B, Vol. 15, Nos.6&7, (2001-3) 1070-1077.
- (3) M. Nakano, K. Tsuge, T. Nagata, Proc. of 1st Int. Symp. on Advanced Fluid Information (AFI-2001), Sendai Japan, (2001-10) 498-501.
- (4) Y. Asako, et al., Progress in Electrorheology, Havelka, K.O. and Filisko, F.E. eds., Plenum Press, (1995).

Semi-active and Active Control of an ERF Embedded in Pneumatic Vibration Isolator

Ming-Chang Shih, Teng-Yen Wang, Ping-Chang Chen

Department of Mechanical Engineering, National Cheng-Kung University
No.1, Ta-Hsueh Road, Tainan 701, Taiwan
(E-mail:mshih@mail.ncku.edu.tw)

ABSTRACT

In the paper, the Electrorheological fluid(ERF) is embedded in the pneumatic vibration isolator and three kinds of control systems are designed, which experimental results are also compared. The first kind of the control system is the semi-active control system, which is designed for ERF controllable damper. The second kind of the control system is the active control system, which is designed for the air servo position control of the platform of the pneumatic vibration isolator. The third kind of vibration isolator control systems is the combination of the active air servo control system and the ERF controllable damper. The experimental results are shown and compared to those of the passive pneumatic vibration isolators, the transmissibility of a vibration source to the isolation platform can be reduced by the first control system. Using the second kind of the control system, the transmissibility of the system is less than that of the first kind of the control system. Using the third control system, the transmissibility becomes the least of these control systems.

KEY WORDS

ER fluid, Active control, Semi-active control

NOMENCLATURE

d	Gap thickness
v_0	Piston velocity
A_d	Cross-sectional are of annulus
A_p	Piston area of the isolator
A_{pe}	Piston head area of ERF damper
C_r	flow restriction constant
C_m	Equivalent viscous damping
V_t, V_b	Volume of the top and bottom chamber
P_t, P_b	Pressure of the top and bottom chamber
L	Length of inner electrode
n	Polytropic exponent
μ	Viscosity of ER fluid

1. INTRODUCTION

Vibration isolation systems are essential in ensuring a higher productivity, an improvement in quality, and an enhanced safety. Vibration isolators are commonly applied during the performance of optical experiments, during semiconductor manufacturing, and in high precision measurement instrumentation. Vibrations are generated by a wide variety of sources, including passing traffic, elevators, human activity, and nearby motorized equipment. Hence, vibration isolators are designed to isolate delicate equipment from environmental vibrations. Vibration isolation systems can be categorized as either active or passive, depending on whether or not external

power is required. Passive vibration isolation systems provide a simple yet reliable means of protecting a mechanical system from a vibration environment. However, these elements have inherent performance limitations which cannot be overcome. By contrast, vibration isolation systems comprised of the actuators can provide a significantly enhanced vibration isolation performance [1]. For achieving the reduction of the transmissibility, the active system is added to the pneumatic vibration isolator. Fowler [2] added an active damping system in parallel with the pneumatic isolation. Eric [3] developed a product that incorporates piezoelectric actuators to minimize the motion of the payload.

The ER fluid is a substance, which changes its rheological characteristics according to the strength of the applied electric field. This fluid has been widely applied in a variety of mechanical engineering applications, including vehicle suspensions, rotation machinery, railway vehicles, hydraulic systems, and damping-controlled dampers [4]-[7]. Conventionally, the term “ER fluid” refers to the particle-type ER fluids which exhibit Bingham characteristics [8]. Jin and Zhang [9] presented a friction-type ER damper, and applied it to dissipate the vibratory energy of robots. Kenaley and Cutkosky [10] employed ER fluid to control the stiffness of a robotic finger. In addition to particle-type ER fluids, macromolecular liquid crystals have been used to develop a homogeneous-type ER fluid which exhibits Newtonian fluid characteristics. Takesue [11] et al. utilized this particular form of ER fluid in a viscous damping arrangement for the precise positioning control of robot arms. The results of their study confirmed the effectiveness of this arrangement in improving both the precision of the positioning and the stability of the arm.

In the study, a pneumatic vibration isolator which is embedded with the ER damper is designed and controlled. A semi-active control system, an active control system, and a hybrid control system are designed for the pneumatic vibration isolator embedded with ERF damper. The first control system is designed for the damping controllable damper. The second control system is designed for the air servo control of the pneumatic vibration isolator. The third control system is the air servo control and the ER damper control.

The remainder of this paper is organized as follows. Section 2 introduces the design of the pneumatic vibration isolator embedded with the ERF Damper. Section 3 presents the layout of the current experimental system, while Section 4 develops the design of the controllers and presents the experimental results. Finally, Section 5 presents conclusions.

2. DESIGN OF PNEUMATIC VIBRATION ISOLATOR EMBEDDED WITH ERF DAMPER

The scheme of the pneumatic vibration isolator embedded with the ERF damper is usually shown in figure 1. It has two chambers and flow restrictors between the top chamber and bottom chamber. The ERF damper is located between the platform and the top chamber.

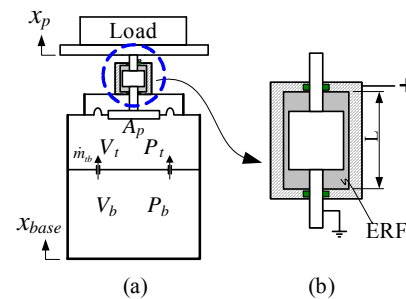


Figure 1 Scheme of the designed isolator

An Electro-rheological fluid is a substance, which can change its rheological characteristics according to the strength of an applied electric field. The ER fluids are classified as particle-type ER fluids and homogeneous ER fluids. ER fluids of particle-type are colloidal fluids comprising solvents with dispersed particles. In the absence of an electric field, the ER fluid exhibits Newtonian fluid characteristics. However, when an electric field is applied, the fluid demonstrates the characteristics of a Bingham fluid. The other is homogeneous ER fluids developed by using low-molecule liquid crystals or macromolecular liquid crystals. For homogeneous ER fluids, the shear stress is basically proportional to the shear rate, and that its slope, i.e. its viscosity, is governed by the strength of the applied electric field. The ER fluid used in this study is a liquid crystalline polymer, a sort of homogeneous ER fluids, because the fluid has the characteristics of no sedimentation and no particle-crushing. The characteristic of the fluid is shown in Figure 2.

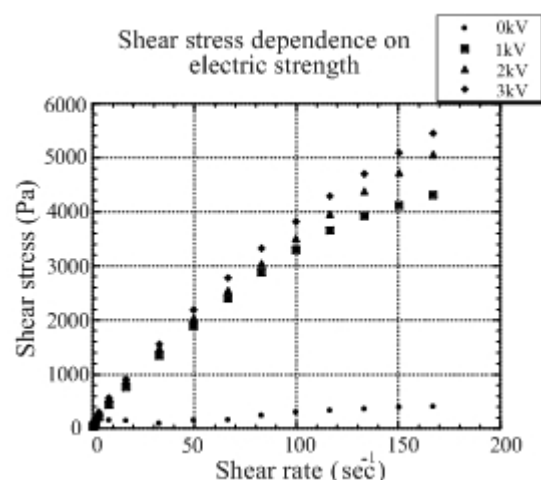


Figure 2 Characteristics of homogeneous ER fluid

Three ER vibration control modes exist, namely flow mode, shear mode, and squeeze mode. In the study, the mixed damper is composed of the flow mode and shear mode and shown in figure 1(b). The damper has the inner electrode attached to the piston head, and so it moves with the piston head. In the damper, rate-dependent damping force results from the pressure drop in the electrode gap as well as direct shear of the fluid in the gap due to the piston head motion. The mixed mode damper is considered as the approximate parallel plate analysis. The 1D axisymmetric analysis is given in [12], and the expression for the force is written as :

$$F = \frac{12\mu A_{pe}^2 L}{A_d d^2} \left(1 + \frac{A_d}{2A_p}\right) v_0 = C_m v_0 \quad (1)$$

The mathematical models of the pneumatic vibration isolator are the same as those of a servo-pneumatic cylinder and the nonlinear models of a servo-pneumatic cylinder first proposed by Shearer [13]. These models include the enthalpy equations for the pneumatic chambers, an equation for the flow through the restrictor, and a displacement equation for the piston under load. The linear model of the pneumatic vibration isolator can be derived from the nonlinear model. Harris and Crede [14] were the first researchers to propose a linear model of the pneumatic vibration isolator. However, DeBra [15] has also developed a linear model of the pneumatic vibration isolator.

The mathematical model of the pneumatic vibration isolator embedded with the ERF damper comprises thermodynamic equations for the upper and lower chambers, a displacement equation for the piston under load, the air flows through the restrictor between the upper and lower chambers and the damping force of the ER damper. Air compressibility characteristics cause the associated mathematical models to be nonlinear, which significantly complicates the system analysis process. However, the Taylor series expansion can be used to linearize the model. After linearization, the transfer function of the pneumatic vibration isolation embedded with the ER fluid can be written as:

$$G_{PE}(s) = \frac{X_p(s)}{X_{base}(s)} = \frac{c_m s^2 / m_p + [\omega_n^2 + c_m / m_p (1 + \alpha)]s + a\omega_n^2}{s^3 + [a(1 + \alpha) + c_m / m_p]s^2 + [\omega_n^2 + ac_m / m_p (1 + \alpha)]s + a\omega_n^2} \quad (2)$$

Where $a = nP_0 C_r / V_b$, $\omega_n^2 = nP_0 A_p^2 / m_p V_{t0}$, $\alpha = V_b / V_{t0}$

In equation (2), C_m is the damping coefficient of ERF damper and has the influence on the transmissibility of the pneumatic vibration isolator embedded with the ERF damper. When the ERF damper is not embedded in the pneumatic vibration isolator, hence, the damping

coefficient of ERF damper is zero, and the transfer function of the pneumatic vibration isolator can be written as:

$$G_P(s) = \frac{x_p(s)}{x_{base}(s)} = \frac{\omega_n^2 s + a\omega_n^2}{s^3 + a(1 + \alpha)s^2 + \omega_n^2 s + a\omega_n^2} \quad (3)$$

The simulation result of the pneumatic vibration isolator embedded with and without the ERF damper is shown in figure 3. It is shown that the transmissibility of the system could be reduced with the increased electric field near the nature frequency.

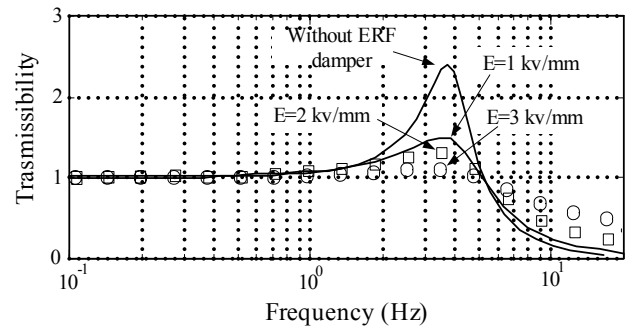


Figure 3 Simulation of the pneumatic vibration isolator embedded with the ERF damper at different electric field

3. LAYOUT OF EXPERIMENTAL EQUIPMENT

Figure 4 shows the experimental arrangement employed to measure the transmissibility of the system. The pneumatic vibration isolator embedded with the ERF damper is located on a flat base connected to a hydraulic servo-cylinder, which serves as a small vibration source. The chambers of the pneumatic vibration isolator are pressurized with air and support a load. Position sensors are attached to the load and to the base of the pneumatic vibration isolator. The ER power supply generates the electric field on the ERF damper and the pneumatic servo valve regulates the air flows in/out the upper chamber. For the passive system, the displacements of the load and the base are measured by the two position sensors, which then transmit the displacement signals to the computer. For the semi-active control system, the electric field is applied to the ERF damper embedded in the pneumatic vibration isolator. For the active control system, the computer acts as a controller and sends the control signals to the pneumatic servo valve to regulate the air flows in/out the upper chamber in order to reduce vibration. For the hybrid control system, the air servo control and the applied electric field act on the isolator.

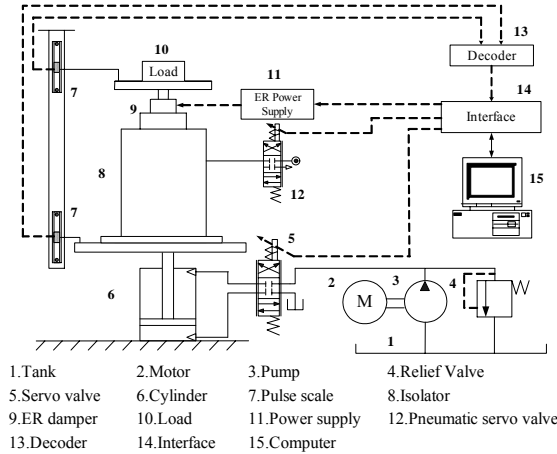


Figure 4 Layout of the experimental equipment

4. CONTROLLER DESIGN AND EXPERIMENTAL RESULTS

4-1 Open-loop control of ERF damper

Figure 5 shows the block diagram of the electric field applied to the pneumatic vibration isolator embedded with the ERF damper. From equation (1), the damping force of the ERF damper increases with the increased applied electric field. The experimental results of the pneumatic vibration isolator embedded with ERF damper are shown in Figure 6. It is observed that the transmissibility near the natural frequency decreases as the strength of the applied electric field increases, but the transmissibility is not improved when the frequencies are lower and higher than the nature frequency. So the semi-active control for the ERF damper is used to improve the performance.

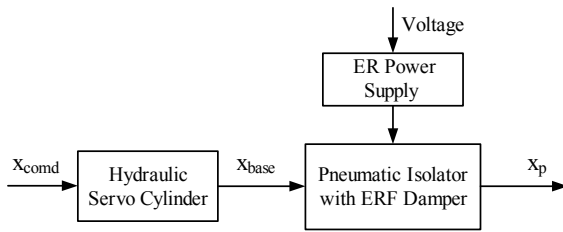


Figure 5 Block diagram of the pneumatic vibration isolator with open-loop controlled ERF damper

4-2 Semi-active control

The block diagram of the semi-active control is shown in figure 7. The input command, r , is the reference displacement of the load supported by the pneumatic vibration isolator, while the output, x_p , is the current displacement of the platform of the pneumatic vibration isolator. The vibrations to the pneumatic vibration isolator is x_{base} . In this case, the reference displacement is set to zero. The error is written as:

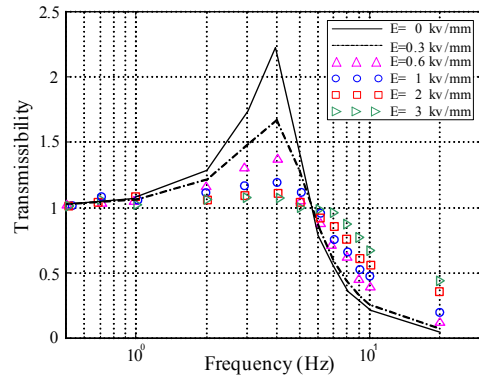


Figure 6 Transmissibility of different preset electric field

$$e = r - x_p = -x_p \quad (4)$$

The transmissibility is defined as:

$$T = \frac{x_p}{x_{base}} = \frac{-e}{x_{base}} \quad (5)$$

From equation (5), the switch condition of the electric field can be given as:

$$\begin{cases} T \leq 1, E = 0 \\ T > 1, E \neq 0 \end{cases} \quad (6)$$

When the transmissibility is smaller than 1 or equal to 1 ($T \leq 1$), the electric field is not applied to the ER damper. When the transmissibility is larger than 1, the electric field acts on the ER damper.

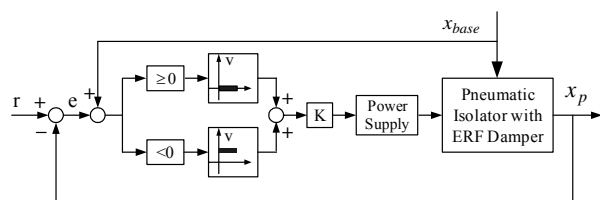


Figure 7 Block diagram of semi-active control system

4-3 Active Control

An active vibration isolation system is designed which employs an active controller to regulate the operation of a pneumatic servo valve. The active control system regulates the flow of air into, and out of, the upper chamber of the pneumatic vibration isolator such that the load is protected from vibration. Figure 8 presents a block diagram of the developed active control system. The fuzzy control can be described as follows.

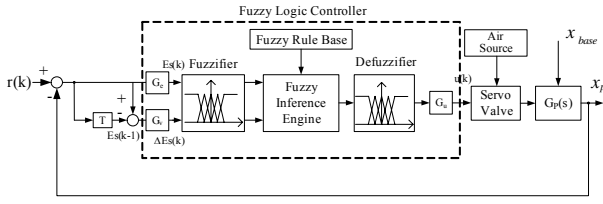


Figure 8 Block diagram of active control system

The fuzzy controller comprises four basic elements, namely a fuzzifier, a fuzzy inference engine, a defuzzifier, and a fuzzy rule base [16],[17]. E_s and ΔE_s represent the input signals to the fuzzy logic controller, and u represents the output of the fuzzy controller. The input command and the plant output are crisp values but non-fuzzy variables, and must therefore be fuzzified by the fuzzifier, which performs a mapping from the crisp points to the corresponding fuzzy set. A fuzzy set is denoted by a linguistic term such as “positive error” or “negative error”, and is characterized by a membership function. The fuzzifier of the fuzzy logic control system is a nonsingleton (triangular) fuzzifier. The fuzzy rule base of the fuzzy controller comprises a set of IF-THEN rules, which are typically expressed in the form of a fuzzy conditional statement, i.e.

$$R_i: \text{IF } E_s \text{ is } A_i \text{ AND } \Delta E_s \text{ is } B_i, \text{ THEN } u \text{ is } C_i$$

where A_i , B_i and C_i are fuzzy sets characterized by membership functions $\mu_{A_i}(E_s)$, $\mu_{B_i}(\Delta E_s)$ and $\mu_{C_i}(u)$ respectively.

If there are n fuzzy sets for each of the variables E_s , ΔE_s and u , then the total number of fuzzy rules will be given by n^2 . This fuzzy rule set can be combined into a single rule by means of the following operator: $R = R_1 \cup R_2 \cup \dots \cup R_{n^2}$.

To compute the subsequent output u , the present study adopts a max-min inference method as the fuzzy inference engine, i.e.

$$\mu_G(u) = \max \{ \min \{ \mu_{A_i}(E_s), \mu_{B_i}(\Delta E_s), \mu_{R_i}(E_s, \Delta E_s, u) \} \} \quad (7)$$

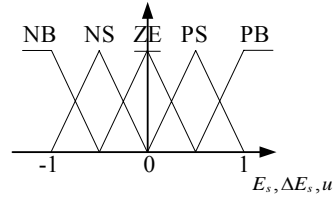
Applying the max-min inference technique yields a fuzzy output value. Hence, it is necessary to employ a defuzzifier to transform this fuzzy quantity into the corresponding crisp value. This study adopts the center-of-gravity method as the defuzzifier function, i.e.

$$u = \frac{\sum_{i=1}^{n^2} u_i \cdot \mu_G(u_i)}{\sum_{i=1}^{n^2} \mu_G(u_i)} \quad (8)$$

Equation (8) yields a crisp output command from the fuzzy logic controller. If the output command is positive, air is flowed into the upper chamber of the pneumatic vibration isolator. Conversely, if the output command is negative, air is discharged from the chamber.

The present study employs the fuzzy sets ‘zero (ZE)’,

‘positive big (PB)’, ‘positive small (PS)’, ‘negative big (NB)’ and ‘negative small (NS)’. Figure 9 depicts the triangular membership functions for each fuzzy set. It is observed that these functions are symmetric with respect to the vertical axis as a result of the symmetric nature of the operating of the servo valves. Table 1 displays the fuzzy control decision table adopted in the current study.



$\frac{E_s}{\Delta E_s}$	NB	NS	ZE	PS	PB
NB	NB	NB	NS	NS	ZE
NS	NB	NS	NS	ZE	PS
ZE	NS	NS	ZE	PS	PS
PS	NS	ZE	PS	PS	PB
PB	ZE	PS	PS	PB	PB

Figure 9 Membership function

Table 1 Fuzzy rule

4-4 Hybrid control

The hybrid control system includes the air servo control and the damping control of the pneumatic vibration isolator embedded in the ER damper. When the transmissibility is larger than 1, the electric field is applied to the ER damper to reduce the transmissibility, and the air servo control controls the flow of air into, and out of, the upper chamber to reduce the transmissibility. When the transmissibility is smaller than 1, only the air servo control acts on the pneumatic vibration isolator embedded in the ER damper. The block diagram of the hybrid control system is presented in figure 10.

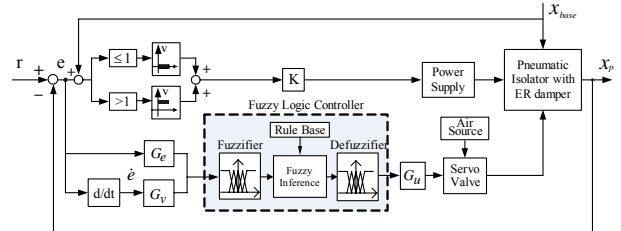


Figure 10 Block diagram of hybrid control system

4-5 Experimental results

The system supply pressure is taken to be 5 bar, while the sampling time is specified to be 20ms. Figure 11 shows the experimental results of the transmissibility of the pneumatic vibration isolation systems. It can be seen that compared with the passive system, the transmissibility is reduced near its natural frequency by using the semi-active control. Using the active control, the transmissibility is smaller than 1 at the frequency lower than nature frequency. Using the hybrid control system, the transmissibility of the vibration source to the payload is improved more effectively.

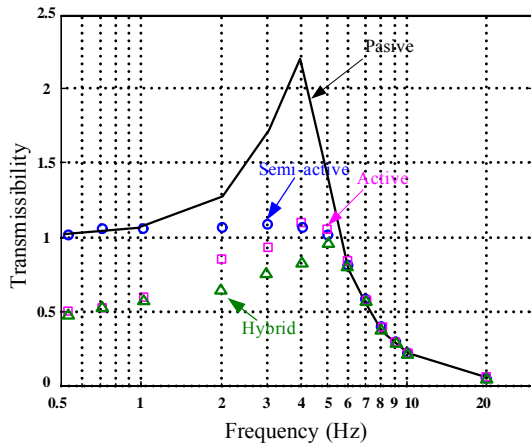


Figure 11 Transmissibility of different control systems of pneumatic vibration isolator embedded with ERF damper

5. CONCLUSION

This paper has presented the design of pneumatic vibration isolator embedded in the ER damper and the control systems. The experimental results were carried out and came to the following conclusions:

- (1) Compare with the case of passive vibration isolator, when using the semi-active control system, the transmissibility is improved near the nature frequency.
- (2) Using the active pneumatic control system, the transmissibility is smaller than that of the semi-active control system, when the frequency is lower than the nature frequency.
- (3) Using the hybrid control system, the performance of the vibration source to the payload is better than the semi-active control system and the active control system.

ACKNOWLEDGMENT

This research is supported by Nation Science Council (NSC, Taiwan) project "91-2212-E-006-070".

REFERENCES

- [1] Su, H., Ralhrja, S. and Sankar, T. S., Vibration isolation characteristics of an active electromagnetic force generator and the influence of generator dynamics, Transactions of the American Society of Mechanical Engineers, Journal of vibration and acoustics, 1990, **112**, pp.8-15.
- [2] Fowler, Leslie, Buchner, Stephen, Ryaboy and Vyacheslav, Self-contained active damping system for pneumatic isolation tables, Proceedings of SPIE - The International Society for Optical Engineering, 2000, **3991**, pp.261-272.
- [3] Anderson, E. H. and Houghton, B., ELITE-3 active vibration isolation workstation, Proceedings of SPIE

- The International Society for Optical Engineering, 2001, **4332**, pp.183-196.
- [4] Winslow, W.M., Induced fibrillation of suspensions J. Appl. Phys., 1949, **20**, pp.1137-1140.
- [5] Wang, K.W., Kim, Y.S. and Shea, D.B., Structural vibration control via electrorheological-fluid-based actuators with adaptive viscous and frictional damping, J. Sound Vib., 1994, **177**, pp.227-237.
- [6] Nguyen, Q.D. and Boger, D.V., Measuring the flow properties of yield stress fluids, Ann. Rev. Fluid Mech., 1992, **24**, pp.47-88.
- [7] Powell, J., An application of nonlinear phenomenological model to the oscillatory behavior of ER materials, J. Rheol., 1995, **39**, pp.1075-1094.
- [8] Uejima, H., Dielectric mechanism and rheological properties of electro-fluids, Japan J. Appl. Phys., 1972, **11**, pp.319-326.
- [9] Li, J., Jin D., and Zhang X., An electrorheological fluid damper for robots, in Proc. 1995 IEEE Int. Conf. Robotics and Automation, 1995, **3**, pp. 2631-2636.
- [10] Kenaley, G.L. and Cutkosky, M.R., Electrorheological fluid-based robotic fingers with tactile sensing, In Proc. IEEE Int. Conf. Robotics and Automation, 1989, pp. 132-136.
- [11] Takesue, N., Zhang, G., Furusho, J. and Sakaguchi, M., Precise position control of robot arms using a homogeneous ER fluid, In Proc. IEEE Int. Conf. Robotics and Automation, 1998, **3**, pp. 2470-2475.
- [12] Kamath, G. M., Hurt, M. K. and Werely, N. M. Analysis and testing of Bingham plastic behavior in semi-active electrorheological fluid dampers, Smart mater. Struct., 1996, **5-5**, pp. 576-590.
- [13] Shearer, J.L., Study of pneumatic processes in continuous control of motion with compressed air, Transactions of ASME, 1956, **78**, pp.233-242.
- [14] Harris, C.M. and Crede, C.E. (1961), Shock and Vibration Handbook, McGraw-Hill, New York.
- [15] Debra, D.B., Vibration isolation of precision machine tools and instruments, CIRPAnnals, 1992, **41-2**, pp.711-718
- [16] Zadeh, L. A., Fuzzy sets, Information and Control, 1965, **8**, pp.338-353.
- [17] Lee, C.C., Fuzzy logic in control systems: fuzzy controller part I, IEEE Trans. SMC, 1990, **20-2**, pp.419~435.

Realistic Filter Performance Evaluation -Cyclic Stabilization Test-

Takemi NAMBA*and Kazuyasu IZAWA**

* Scientific and Laboratory Services Division, Aeropower Company
Nihon Pall LTD
46, Kasuminosato, Ami-machi, inashiki-gun, Ibaraki, 300-0315 Japan
(E-mail: Takemi_namba@pall.com)
** Aeropower Company
Nihon Pall LTD
6-8-1 Nishishinjyuku, Shinjyuku-ku, Tokyo, 163-6017 Japan

ABSTRACT

The Multi-pass filter test is the most common method to evaluate the performance of hydraulic filters. The test is conducted at a constant flow rate at constant temperature and very high dirt ingress in order to evaluate filter performance at accelerated test condition. This standard test does not represent operating condition of the modern hydraulic control systems. In order to precisely represent filter performance in the field in the laboratory, the Cyclic Stabilization Test (CST) has been developed. The CST can reliably measure the ability of the filter to control contamination in an even lower ingress environment. It also simulates cyclic flow condition to measure filter performance. In this paper, the CST is proposed as a more effective method for filter performance evaluation method.

KEY WORDS

Hydraulic fluid, Cyclic flow, Stability, Filter performance, Cyclic Stabilization Test

INTRODUCTION

Solid particulate contamination in hydraulic fluid causes component wear, valve sticking, fluid life shortage, resulting in shorter component and fluid life, lower system reliability, lower efficiency, lower stability. Hydraulic filters are designed to control hydraulic fluid cleanliness to accomplish reliable system operation and longer system lives.

Modern hydraulic control systems are required to be operated with higher pressure, and very sophisticated control systems as well as higher reliability and higher energy efficiency. These systems need cleaner hydraulic fluids. Filters for these systems are usually exposed to flow surges,

repetitive cyclic flow, vibration, and cyclical thermal conditions.

IMPORTANCE OF CLEAN FLUID ON RELIABILITY AND LONG COMPONENT LIVES

A significant part of the DTI research studied the effects of solid particulate contamination on working systems and also quantified the relationship between the fluid cleanliness level and the reliability level experienced by those systems. The relationship between cleanliness levels, as represented by the ISO 4406 coding system [1], and the mean time between failures is presented in Figure 1.

Figure 1 clearly shows a direct relationship and demonstrates that high levels of reliability and long component lives can only be achieved by operating with clean hydraulic fluids. The report stated that, generally, very clean hydraulic fluid was achieved by the use of 'fine' filters (3 or 6 μm) but its cleanliness level that the filter achieved was dependent on its rating and how it performed in the system concerned. The report cited instances where nominally "identical" filters gave significantly higher ISO cleanliness levels when the duty cycle of the system was more severe. Hence, the need to select filters on a system-to-system basis with consideration of a number of factors was emphasized.

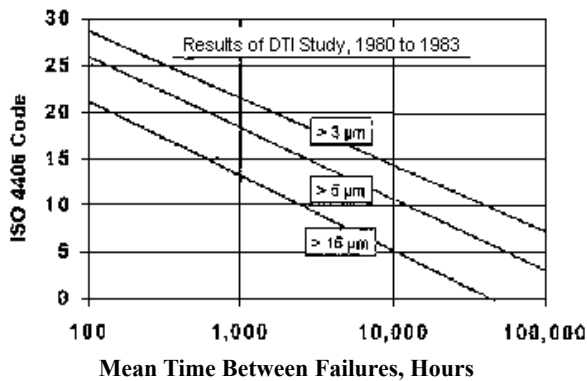


Figure 1 Effect of cleanliness level on the reliability of hydraulic systems

CURRENT FILTER TESTING METHOD

The filtration performance characteristics of hydraulic filters are determined by the ISO 16889 Multi-pass test [2]. The Multi-pass filter test is conducted at a constant flow rate of contaminant at constant temperature. The contaminant is dispersed in the reservoir and circulated to challenge the filter. Contaminant that isn't removed is returned back to the reservoir where it mixes with the incoming contaminant and is re-offered for further chances to capture. The test circuit is shown in Figure 2.

LIMITATIONS OF MULITI-PASS TEST METHOD

Although the Multi-pass test is a much better than previous nominal method, there are many deficiencies in the test that reflect actual condition.

- One of the primary defect of the Multi-pass test is the steady state condition under which test is conducted.
- Contamination concentrations are 1,000 to 10,000

times higher than actual in order to evaluate filter performance at accelerated test condition.

- Test element is not exposed to cold startup condition or vibration which can be expected in actual applications.

These operating conditions that differ in actual service from the controlled laboratory test, tend to reduce the performance of the filter element in actual service.

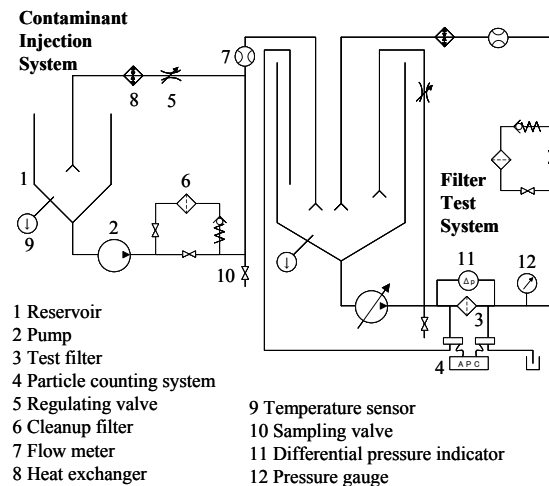


Figure 2 Multi-pass filter test schematic

NEED FOR REALISTIC TESTING CONDITIONS

Unfortunately, filter selection and comparisons are usually made primarily on the basis of the filtration ratio and contaminant holding capacity obtained from a single Multi-pass test. However, there are many other parameters vital to maintaining filter element integrity and desired performance in actual operation. These include the strength and stability of the filtration medium, the dominant mechanism of particle captures, and the filter's ability to withstand flow and pressure surges, as well as those conditions induced by cold start-ups. Using Multi-pass performance as the sole filter specification is inadequate as often weaknesses or deficiencies in performance are overlooked or not exposed because of limitations in the scope of testing. Furthermore, the effect of dynamic operating conditions on filter performance has yet to be addressed by an ISO standard.

IMPACT OF OPERATING CONDITION ON MULTI-PASS PERFORMANCE

Impact of Unsteady Flow

A survey of hydraulic equipment manufacturers revealed that nearly all filter installations are subjected to some type of variable (cyclic) flow [3]. And many studies also have been conducted relative to impact of unsteady flow on filter performance. Generally, the results indicate that the filtration (Beta) ratio was found to decrease as a function of increasing cycle rate [4].

Impact of Reduced or No Contaminant Ingression

As we mentioned already, the contaminant ingress rate during the ISO 16889 Multi-pass test are 1,000 to 10,000 times higher than the average ingress in actual service. This high ingress rate tends to overshadow performance degradation and particle unloading. When clean-up tests are conducted on a previously contaminated system with no ingress, the performance of filter, measured in terms of efficiency, generally degrades as the system becomes cleaner. In fact, the system contamination level stabilized at some measurable level and does not go to zero. This is one of the primary flaws in the interpretation of the basic Multi-pass test, where the filtration ratio is assumed to be roughly constant in any ingress rates. In reality, when the system contamination level stabilizes, the Beta ratio approaches a value of one and the upstream level is roughly equal to the downstream level. For a system clean-up test with constant flow, the stabilization level is related to the quality of the filter and the degree of particle unloading [1].

THE CYCLIC STABILIZATION TEST

In order to address the deficiencies in the Multi-pass test, Pall Corporation has developed the Cyclic Stabilization Test (CST), which provides a more realistic measurement of filter performance. This laboratory test examines a number of areas of operation: steady state performance, cyclic flow performance, and the effects of contaminant loading on the retention and unloading characteristics of the filter.

The test stand utilized is basically the same as a standard Multi-pass test, except an electrically controlled valve is installed to allow the test flow to be cycled from zero to full flow. The cycle rate chosen for the test was 0.1Hz. Although the test could be conducted with any cyclic condition, the rate chosen was based on a survey [3].

CST Result for Filter "A"

During the test procedure, clean up and stabilized particle count levels at the upstream and downstream

of a test filter are measured for both steady and cyclic flow condition at different stages of the filter's life. The result of particle count levels in each stage are shown as "stabilized clean" during steady flow and "stabilized clean", "stabilized 2.5% ΔP " and "stabilized 80% ΔP " during cyclic flow in Fig. 3 and Fig. 4.

A great deal of information can be gathered from a CST. This includes:

- Measurement of the initial steady flow filtration ratio.
- Measurement of the initial cyclic flow filtration ratio.
- Initial clean-up and stabilization measurement (with the filter in a clean condition) – both with steady and cyclic flow.
- A measurement of cyclic flow filtration ratio throughout the remainder of the test.
- Clean-up and stabilization measurement as the filter is loaded.
- Clean-up and stabilization measurement at 80% of terminal pressure drop (with the filter in a nearly completely loaded condition).
- A measurement of retained dirt capacity under cyclic flow conditions.

Figure 3 shows the upstream particle counts greater than 5 $\mu\text{m(c)}$ obtained while conducting a CST on a test filter "A". At each step the initial particle concentration is very similar, but cleanup is reduced with the introductions of cyclic flow, and further reduced as the filter becomes more plugged.

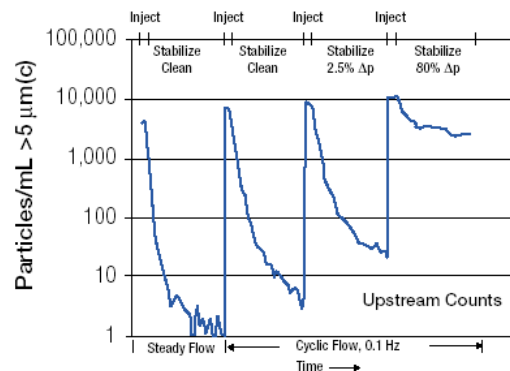


Figure 3 CST result – upstream particle counts >5 $\mu\text{m(c)}$

The stabilized contamination level at 2.5% pressure drop, Δp , is 11 times that of the steady flow value. At 80% pressure drop, Δp , the stabilized contamination level is 1,200 times that of the new filter steady flow value. These increases are indicative of the inability of the filter to retain

contaminant under these conditions.

Figure 4 shows downstream contamination data for the same test filter "A". Hence, stabilized counts increase substantially during flow cycling and filter loading. The data represents a final Beta ratio at 5 $\mu\text{m(c)}$ of 1.8 compared to the initial steady state Beta ratio of 310.

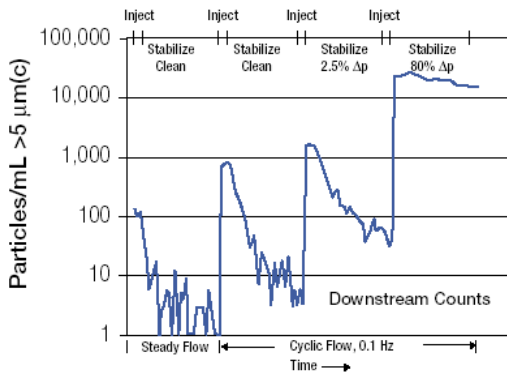


Figure 4 CST result – downstream particle counts > 5 $\mu\text{m(c)}$

CST Result for Various Filters

The CST provides a much clearer picture of a filter's performance throughout its life in a fluid system.

In order to demonstrate the ability of the CST to discriminate among similarly rated filters, tests were conducted on filters from several manufacturers. Figure 5 shows the 5 $\mu\text{m(c)}$ downstream particle counts for these filters. These test demonstrate that although the filters provide good control of particles >5 $\mu\text{m(c)}$ when new or with steady flow, their ability to control particles changes substantially when they become loaded and are under cyclic conditions. For example, Filter "B", which was one of the best performers under steady flow, exhibited the worst particle control under cyclic and loaded conditions.

When comparing filter performance, one should focus on the stabilization data at 80% of terminal pressure drop. This is where the greatest performance drop-off occurs, and the point in the filter's life where any hydraulic system can be most at risk.

REPEATABILITY AND REPRODUCIBILITY

Repeatability tests were performed at both Pall Corporation and an independent laboratory using various sets of identical filters. Stabilized 80% Δp downstream particle counts at 4, 6, and 14 $\mu\text{m(c)}$ taken, and an ISO 4406 code was provided for each filter. Tables 1 and 2 present the data from these tests.

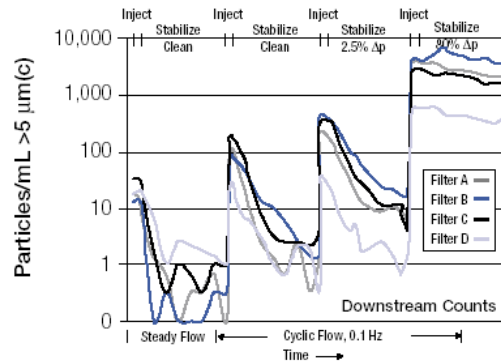


Figure 5 Downstream CST results from four "3 μm " filters

Table 1 shows the results of test on four different sets of filters: A, B, C and D. Two filters of each type were tested in Lab 1. The data in Table 1 shows excellent repeatability of the stabilization results, with nearly all data for a given filter agreeing within one ISO 4406 code. Table 2 shows excellent repeatability I Lab 2 for filter groups E, F, and G. The only exception is in the 14 $\mu\text{m(c)}$ ISO code, where there is more variability. This is because accuracy is lower due to particle counting statistics.

Table 1. Repeatability Data from Lab 1

Filter	4 $\mu\text{m(c)}$	6 $\mu\text{m(c)}$	14 $\mu\text{m(c)}$	ISO4406 (particles/mL)
A1	78	2.4	0.09	13/8/4
A2	69	2.7	0.07	13/9/3
B1	166	6.5	0.07	15/10/3
B2	149	4.7	0.10	14/09/4
C1	395	34	0.15	16/12/4
C2	447	42	0.12	16/13/4
D1	932	363	0.27	17/16/5
D2	1061	402	0.39	17/16/6

Table 2. Repeatability Data from Lab 2

Filter	4 $\mu\text{m(c)}$	6 $\mu\text{m(c)}$	14 $\mu\text{m(c)}$	ISO4406 Average of 2 or more tests (particles/mL)
E1	399	20	0.0	16/12/0
E2	410	23	0.5	16/12/6
F1	229	38	0.0	15/12/0
F2	187	29	0.0	15/12/0
G1	76	1	0.0	13/7/0
G2	96	4	0.0	14/9/0

The sets of E, F, and G filters were also used to verify reproducibility between Lab 1 and Lab 2. For each set, two filters were tested in Lab 1, and two identical filters were tested in Lab 2. Stabilized 80% Δp downstream counts at 4, 6, and 14 $\mu\text{m(c)}$ were taken, and an ISO 4406 code was provided for each filter. Table 3 supplies the data from these tests.

- Filters", Paper No. P-74-38, 8th Annual Fluid Research conference, 1974, pp.38-1 to 38-5
4. Rao, H.P, "CYCLIC MULTI-PASS TEST WITH VIBRATION AND OTHER TEST VARIABLES", 5th International Filtration Conference, 2002, pp.65-69.

Table 3. Repeatability Data from Labs 1 and 2

Filter	4 $\mu\text{m(c)}$	6 $\mu\text{m(c)}$	14 $\mu\text{m(c)}$	ISO4406
Average of 2 or more tests (particles/mL)				
E-Lab1	480	57	0.00	16/13/0
E-Lab2	404	21	0.25	16/12/5
F-Lab1	82	2	0.00	14/8/0
F-Lab2	208	5	0.00	15/9/0
G-Lab1	115	4	0.08	14/9/3
G-Lab2	86	2	0.00	14/8/0

These results demonstrate that the CST procedure is quite reproducible. This is especially true when one considers that the test equipment in both labs was different, as were the operators.

CONCLUSIONS

Conditions such as varying flow, cold starts, shock, and vibration can potentially reduce the effectiveness of a filter in an operating system. This may cause the filter to release previously held contaminant, and consequently make it less effective at removing the critically sized particles.

The data from an ISO Multi-pass test is often used by procurement agencies as the key performance factor in the process of selecting filters, and sometimes as the sole criterion. This test has the potential to exaggerate a filter's capabilities. The CST examines the effects of cyclic flow conditions and contamination loading on the capture and retention characteristics of the filter. The result is an improved filter performance reporting method that provides a much more realistic measure of how a filter performs in actual service.

REFERENCES

1. Bench, L.E., "A Realistic Approach To Measuring Filter Performance", IFPE 2000, 2000.
2. ISO 16889, "Hydraulic fluid power – Filters-Multi-pass method for evaluating filtration performance of a filter element", 1999.
3. Bench, L.E., "A Cyclic Flow Test For Fluid Power

NOTES ON CONTAMINATION CONTROL

Eizo URATA*

* Department of Mechanical Engineering, Faculty of Engineering
Kanagawa University
3-27-1 Rokkakubashi, Kanagawa-ku, Yokohama, 221-8686 Japan
(E-mail: urata@mech.kanagawa-u.ac.jp)

ABSTRACT

Contamination control is a technology to keep working fluids clean. Using a hydraulic filter is the commonest means of keeping the working fluid clean. The contamination level of a fluid exiting a filter increases with the operating time of the filter. The pressure loss across a filter element increases when the element retains contaminants. To describe these variations with operating time, this paper proposes: (1) a filter clogging model with an effective opening area; (2) a pressure-loss model related to the effective opening area; (3) a filtration model concerned with the effective opening area and the mean lodging time of particles; (4) a quasi-single-pass test method for evaluating the filtration performance of a filter. The paper also shows a system of equations describing contamination levels in fluid power systems and discusses the relevant industrial standards which are presently widely used.

KEYWORDS

Contamination control, Element clogging, Filtration, Single-pass test

NOMENCLATURE

a_0 : projection area of a representative particle

$a(x)$: projection area of a particle of size x

K_f : form factor in pressure-loss coefficient

L : length in Reynolds number

M : number of representative particles retained in an element

$n_{d,x}$: number of particles greater than x in unit volume of fluid exiting filter

$n_{u,x}$: number of particles greater than x in unit volume of fluid entering filter

n_d : number of representative particles in unit volume of fluid exiting filter

n_c : number of representative particles in unit volume of

fluid at a certain point in a system

n_u : number of representative particles in unit volume of fluid entering filter

S : effective opening area

S_0 : initial value of effective opening area

S_F : area of representative surface = front surface area

Q : flow rate through filter element

R : ingress rate of particulate contaminants

R_e : Reynolds number of flow in filter medium

T : mean lodging time of particles

t : time

U_e : fluid velocity in element opening area = Q/S

V_R : fluid volume in reservoir

V_s : fluid volume in system except reservoir

β : beta-value = n_d/n_d

Δp : pressure loss across filter element
 Δp_0 : initial value of Δp
 v : fluid kinematic viscosity
 ρ : fluid density
 ζ : pressure-loss coefficient

1. INTRODUCTION

The purpose of contamination control is to keep working fluids clean. Keeping working fluids clean, we can extend the life of hydraulic components and reduce failures of fluid power systems. Thus, contamination control is a basic technology supporting the reliable operation of fluid power systems.

Although there are many kinds of contamination, this paper is only concerned with particulate contamination. The number of particles in a unit volume of working fluid determines the particulate contamination level.

A hydraulic filter is the commonest means of rejecting contaminants from fluid and to keep the working fluid clean. There are two important filter performance characteristics: the first is the ability to reduce contaminants in fluid; the second is the capacity to retain contaminants. The first characteristic should be estimated by the contamination level of the fluid at the exit of a filter. The second characteristic is estimated by the amount of contaminants retained in a filter element at the end of its service life.

The service life of a filter element ends when the contamination level of filtered fluid reaches an unacceptable limit, or the pressure loss across the element reaches an unacceptable limit. Usually, the contamination level of the downstream fluid of an element increases with operating time; when it reaches the maximum allowable upper limit the element life ends. Throughout operation of a filter, contaminants are accumulated in the filter element. The accumulated contaminants induce additional fluid resistance that results in a rise of pressure difference across the filter element. When the pressure difference exceeds the limit of strength of the element, deformation or breakage will result if the filter has not been equipped with a safety valve. Thus, there is an allowable limit for the pressure difference that determines the element life. The pressure difference across a filter element is influenced by operational parameters, for example, flow rate, fluid temperature, and other fluid properties.

The phrase "contamination control" was introduced into fluid power technology in the 1960s, by E.C. Fitch, Jr.[1]. Most of the technical development in this area was stimulated by him and his co-workers. Before their work, little attention had been paid to filtration or phenomena related to fluid contamination. Since then, much experimental study of contaminants measurement, filter element performance, and the influence of contaminants on hydraulic elements has been made in many countries

[2],[3]. However, the theoretical work in this subject is limited.

In this paper, the author tries to improve the filtration model of a former report [4], and intends to build a consistent set of mathematical models for contamination control. Section 2 describes a time-dependent change of filter medium, and introduces the idea of "effective opening area". Section 3 describes relations between the effective opening area and pressure loss due to filter elements. Section 4 shows a relation between the effective opening area and the filtration process. Section 5 proposes a single-pass test to identify filter characteristics. Section 6 explains the role of filters in hydraulic systems. Sections 7 and 8 give the discussion and conclusion, respectively.

2. A MATHEMATICAL MODEL FOR CLOGGING OF MEDIUM

Particles in the fluid flow arrive at the element randomly in time and space. Some of the particles lodge on the element. The points where the particles lodge are not restricted to the front surface of the element, but are distributed in a three-dimensional space of the medium. The lodging particles decrease the free space for fluid and moving particles. This phenomenon is called clogging. As a result of particle lodging, the filtration ability and pressure loss of a filter change with time.

Since the void in the medium is distributed randomly, its average along the depth is equal to a distribution of holes on a plane surface. Therefore, we can take a plane surface as representative of a layer of medium with finite thickness. We call this surface a representative surface.

Particles have various shapes and sizes. Measurement and definition of particle size are still being studied [5]. Therefore, this paper does not deal with the matter of particles size distribution. Instead, to simplify mathematical expressions, we assume single-sized particles. The projection area of one of the particles is a representative projection area.

Now, consider a continuous steady flow of fluid in which particles are randomly distributed. Some of the particles pass through the holes on the representative surface and the other particles are captured on the surface. Figure 1 illustrates the representative surface and the arriving particles. We count the number of particles before and after passing through the holes during an infinitesimally short time. In the inflow, the counted number is $n_u Q dt$; in the outflow, the counted number is $n_d Q dt$.

The idea of opening area is not restricted to a particular type of element, for example, a surface-type element or a depth-type element. Our mathematical model for the filter element is a surface having this effective opening area. If the element is a simple sieve, then the effective opening area is equal to the geometric opening area. For a depth-type filter, the effective opening area is equal to front surface times void ratio.

In an infinitesimal interval, the number of particles added to our representative surface is $Q(n_u - n_d)dt$. As shown in Fig. 1, some particles arrive at the points already blocked: others arrive at the opening area. The latter particles newly block some portion of the opening area. Points of arrival on the representative surface do not depend on whether the points are already blocked or not yet blocked. Therefore, the probability of blocking by an arriving particle is proportional to the effective opening area. Consequently, the decrease of the opening area due to arriving particles is

$$dS = -\frac{S}{S_E} a_0 Q(n_u - n_d)dt$$

or, equivalently

$$\frac{dS}{dt} = -\frac{S a_0 Q}{S_E} (n_u - n_d). \quad (1)$$

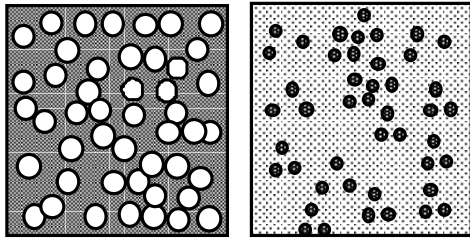
Actual particulate contaminants have a particle size distribution. For a continuous distribution, we have

$$\frac{dS}{dt} = -\frac{S}{S_E} \left[\int_0^\infty Qa(x) \left(-\frac{\partial n_{u,x}}{\partial x} + \frac{\partial n_{d,x}}{\partial x} \right) dx \right]. \quad (2)$$

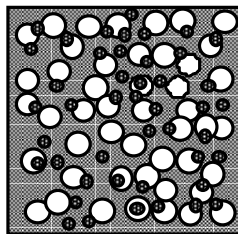
This equation shows that the effective opening area decreases with time. The change depends on the particle size distribution function upstream and downstream of the filter element. Its velocity of change is proportional to itself.

When the integral in Eq. (2) changes little over time, an approximate expression for S becomes

$$S \approx S_0 \exp \left\{ -\frac{t}{S_E} \left[\int_0^\infty Qa(x) \left(-\frac{\partial n_{u,x}}{\partial x} + \frac{\partial n_{d,x}}{\partial x} \right) dx \right] \right\} \quad (3)$$



Randomly placed holes Randomly placed particles



Overlap of holes and particles

Fig. 1: Effective opening area

This suggests its change with respect to time is approximately exponential.

3. PRESSURE LOSS IN AN ELEMENT

For most commercially available hydraulic filters, the pressure loss by a filter element is proportional to the flow rate when the element is new. After the element has retained many contaminants, the relation between pressure loss and flow rate changes from the initial linear relation: usually still linear but with a different gradient. Particles packed in the void in the filter medium reduce the free space where fluid and particles can move towards the pressure gradient. Thus, the retained particles increase the resistance against motion of the fluid. The pressure loss by the effective opening area is expressed by

$$\Delta p = \zeta \frac{\rho U_E^2}{2} = \zeta \frac{\rho}{2} \frac{Q^2}{S^2}. \quad (4)$$

Regardless of the type of restriction, ζ is a function of Reynolds number:

$$R_e = QL / \nu S. \quad (5)$$

The dimensionless coefficient ζ is inversely proportional to Reynolds number by laminar flow. By turbulent flow, ζ becomes a complicated function of Reynolds number.

To determine Reynolds number, we must define a representative velocity and a representative length. There will be no question of taking Q/S as the representative velocity. However, there is no common consent about the representative length for flow in porous media [6]. Therefore, we avoid determining the representative length here. Instead, we restrict our consideration to the flow in which the pressure loss is proportional to the flow rate through the element.

Under this restriction, we can write

$$\zeta = \frac{K_l}{R_e} = \frac{K_l \nu S}{QL}. \quad (6)$$

Thus, a typical mathematical model for pressure loss by the filter element takes the following form:

$$\Delta p = \frac{K_l}{L} \frac{\rho Q \nu}{2} \frac{1}{S}. \quad (7)$$

The constant, K_l/L , should be determined by suitable experiments.

Equation (7) shows that the effective opening area determines the pressure loss of the filter element. It will be interesting to compare Eqs. (3) and (7). When the difference between upstream and downstream contamination levels is almost constant, the differential pressure across the filter element grows as an exponential function of time. In this condition, the logarithmic plot of measured pressures against time on the linear scale lie on a straight line.

As seen from Eq. (5), the Reynolds number of the flow increases when the opening area decreases. If the flow

regime changes from laminar to turbulent, the gradient of ζ against R_e will also change. Then the assumed relation (6) is no longer valid and the pressure-time curve in logarithmic scale deviates from the straight line.

4. FILTRATION MODEL FOR MEDIUM

We begin our consideration with an isolated filter element illustrated in Fig. 2. Fluid carries particles to the upstream side of the filter element and takes away some particles to the downstream side. This situation is expressed by

$$\frac{dM}{dt} = Qn_u - Qn_d. \quad (8)$$

We call this relation “the law of conservation of particle numbers”.

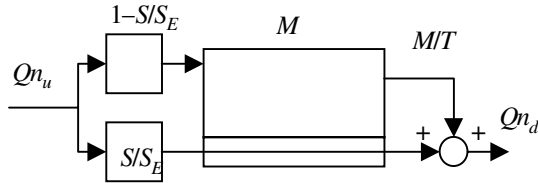


Fig. 2: Filtration model

Some of the particles arriving at the element are captured by the element while the remaining ones carry on with the fluid. Particles once captured can separate, or desorb, from the element at a later point in time. Therefore, the particles downstream of the element are a mixture of those that have passed through the element and those that have desorbed from the element. For captured particles, we introduce mean stay time, T . In other words, the number of particles leaving the element in an infinitesimal time dt is $(M/T)dt$. Then, the number of particles exiting from the element is expressed by

$$Qn_d = \frac{S}{S_E} Qn_u + \frac{M}{T}. \quad (9)$$

The forces acting on the retained particles increase with flow velocity. Eddies in the flow agitate local vibration of the element medium. Therefore, the rate of release of particles will increase with unsteady flow. When the flow in the medium becomes turbulent, it will also increase the release of particles. This indicates that T decreases with unsteady flow and with a turbulent flow regime.

A better filter has a large value of T with very small value of S/S_E . Finding the characteristics of S_E and T , we can express the filtration ability of hydraulic filters.

5. EVALUATION OF FILTRATION PARAMETERS: QUASI-SINGLE-PASS TEST

Filtration characteristics are expressed using the

parameters and variables shown in Eq. (9). Evaluation of M is easy since it is obtained by direct integral of the right-hand side of Eq. (8). Evaluation of S based on Eq. (2) is not easy and may induce a large numerical error. Fortunately, we have a simple relation between S and Δp from Eq. (7):

$$S \cdot \Delta p = \text{const} = S_0 \cdot \Delta p_0. \quad (10)$$

When we use this relation, Eq. (9) is rewritten as

$$Qn_d = \frac{\Delta p_0}{\Delta p} \frac{S_0}{S_E} Qn_u + \frac{1}{T} \int_0^t Q(n_u - n_d) dt \quad (11)$$

The filtration parameters $\Delta p_0(S_0/S_E)$ and T can be evaluated using observed values of variables, Q , Δp , n_u and n_d . The unknown parameters are supposed to depend on operating variables such as upstream contamination level and flow velocity, and also on the particle size and the state of the element itself. For measurement of these parameters, therefore, we should design a test facility that can control the flow velocity and upstream contamination level. The multi-pass test facility is inconvenient for determining the parameters [4] because it induces variation of the upstream contamination level.

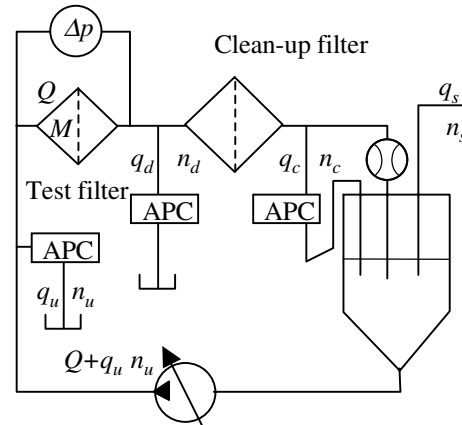


Fig. 3: Quasi-single-pass test

For this test, it is essential to put the upstream level under our control independent of system variables. One possible method is to use a single-pass test. However, we need a tremendous amount of fluid to perform a real single-pass test.

If we remove the essential part of contaminants in the fluid downstream of the testing filter, then the fluid can be used again as a clean fluid. Adding new contaminants to the fluid and supplying it to the upstream of the filter, we can satisfy the condition of the single-pass test. The idea is illustrated in Fig. 3. We call it a quasi-single-pass test.

We carry out the test and parameter identification with the following procedure [7].

Slurry of a predetermined concentration of contaminants is supplied to the reservoir with constant flow rate. The pump supplies fluid flow to the test filter. Flow from the filter is filtered by the clean-up filter and returns to the reservoir. The contamination level of the fluid at the upstream side of the test filter is kept constant because the fluid returning to the reservoir is sufficiently clean. The contamination level in the downstream of the clean-up filter is monitored to confirm its cleanness level. The test is stopped when the pressure difference Δp reaches a limiting value, or when the downstream contamination level exceeds a limiting value. Carrying out this experiment, we obtain the data for u_s , u_d , Δp and u_c at suitable running times. Using thus obtained data, we can evaluate the parameters shown in Eq. (11), namely, p_0 , S_0/S_E and T , with the aid of a suitable parameter identification technique, for example, the least-squares method.

We can use this test rig as long as the fluid downstream of the clean-up filter is satisfactorily clean. A basic question about the quasi-single-pass test is whether it is possible to reject essential part of the contaminants downstream of the filter. The author carried out a few experiments into this and got a positive result [7].

6. FILTRATION IN A FLUID POWER SYSTEM

In this section, we will briefly review the effects of filters in hydraulic circuits. Some contaminants are generated in the system through wear, surface layer separation, and other physical or chemical processes. Some contaminants exit from the fluid through sedimentation or by sticking to the internal walls of system components. The remains are included in the system fluid, and are expressed by one input variable, R . Particles in the system escape to outside when fluid leaks from the system. Usually, the leakage is small; hence, it does not have a serious influence on the contamination level of the system fluid. The function of a filter is to retain these contaminants and keep the contamination level below a specified level.

The contamination level of fluid in a hydraulic system varies from place to place in the system; and the inserting position of the filter influences the level. The filter position in a system can be classified as off-line or on-line. An off-line filter system is illustrated in Fig. 4. The law of conservation of particle numbers applied to the system, the reservoir, and the filter are as follows:

$$V_s \frac{dn_s}{dt} = Q_s (n_u - n_s) + R \quad (12)$$

$$V_R \frac{dn_u}{dt} = -Q_s (n_u - n_s) + Q(n_d - n_u) \quad (13)$$

$$\frac{dM}{dt} = Q(n_u - n_d). \quad (14)$$

There are four unknown variables, n_u , n_d , n_s and M in the above three equations. Therefore, we need additional equations that express the characteristics of the filter:

$$n_d = \frac{S}{S_E} n_u + \frac{M}{QT} \quad (15)$$

$$\frac{dS}{dt} = -\frac{Sa_0 Q}{S_E} (n_u - n_d). \quad (16)$$

Now the number of unknowns and the number of equations are the same. Hence, solving these equations, we can predict the contamination level of the system.

If we have the parameters expressing the filter performance, namely, Δp_0 , S_0/S_E , and T , we can predict the contamination level of the system. It must be noted that the so-called beta, n_u/n_d , depends on the system parameters and configuration. In other words, it is not a parameter given by the filter, but a system variable.

An on-line filter system is shown in Fig. 5. For this system, we can write five equations as before, while there are six unknowns. We can find another necessary equation considering system configuration; for example, if the sub-system 2 is a reservoir with fluid volume V_2 , then the required equation is $n_2 = n_s$.

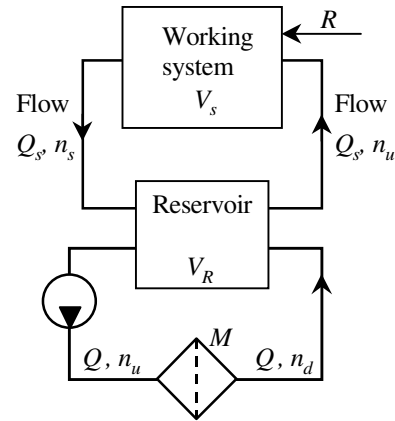


Fig. 4: Off-line filter system

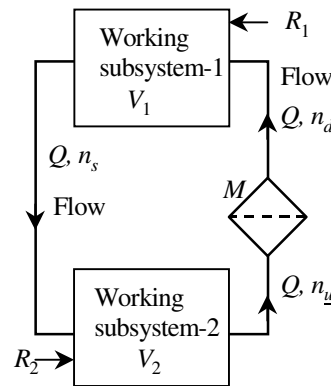


Fig. 5: On-line filter system

7. DISCUSSION

In the 1960s, Fitch, E. C. Jr. proposed the following filtration model:

$$n_u = \beta n_d, \text{ (Fitch model).} \quad (17)$$

He assumed β (beta-ratio, beta-value, or beta) to be a characteristic constant of the element. The Fitch model and its assumption formed the basis for evaluating the performance of hydraulic filters performance of hydraulic filters. National and international standards [8,9], and the catalogues of filter manufacturers use beta-value as the constant that characterises a filter element. In ISO 4572-1981(E), beta-values measured at four different operating instants are required to be within 10% of their mean value. The inevitable change of beta-value with operating time was regarded as a measuring error.

The concept of a constant beta contradicts our experience. First, many observations have revealed that the beta is a function of time. Second, the beta depends on flow velocity. Third, if we put a used filter into a fluid power system filled with clean fluid, then we observe that the fluid becomes contaminated by dirt contained in the element. In the last case, the beta becomes less than unity and a better filter shows a smaller beta. Thus the initial idea about beta led to confusion.

Hong and Fitch revised the filtration model to include separating particles and assumed a model [10,11] different from Eq. (17). Their revised model resulted in time-dependent values of beta and they proposed a new filter rating which they call beta prime.

The revised ISO standard (ISO16889) for the multi-pass test, however, took different direction [12]. The new definition of beta by ISO16889 is the ratio of time mean of the particle numbers at element upstream and time mean of the particle numbers at element downstream. The new beta obtained is independent of time variation of filtration characteristic. However, filter users need to know the time variation of fluid contamination level when they are running their hydraulic systems.

To respond to the needs of filter users, determination of the parameters shown in this paper and applying them to the analysis described in Section 6 will be necessary. However, when a filter is exposed to flow pulsation, or frequent switching of flow, it might show less ability to retain contaminants than the analysis. This will occur when the filter is used as an in-line filter as shown in Fig. 5.

It was frequently pointed out that a filter in an unsteady flow shows a lower beta relative to that obtained by steady flow [13, 14]. Although filtration performance under unsteady flow is an important subject, we did not deal with it in this paper. For that, we must develop a more sophisticated mathematical model.

8. CONCLUDING REMARKS

To estimate hydraulic filter performance characteristics, the author proposed:

1. A filter-clogging model with effective opening area
2. A pressure-loss model related to the effective opening area
3. A filtration model concerning the effective opening area and mean lodging time of particles
4. A quasi-single-pass test method to evaluate filtration performance of a filter.
5. A system of equations that describes contamination levels in hydraulic systems.

REFERENCES

1. Bensch, L.E.; E.C.Fitch and R.K. Tessmann, Contamination control for the fluid power industry, Pacific Scientific Co., 1978.
2. Mager, M., Untersuchung der Feststoffpartikelkontaminationen in hydraulischen Systemen, Dissertation RWTH Aachen, 1992.
3. Stecki, J., Total contamination control, Fluid Power Net, 1999.
4. Urata, E., Evaluation of filtration performance of a filter element, PTMC 2002, pp.291-304, (Bath, 2002).
5. Allen, T., Particle size measurement, Vol.2, 5th Ed., Chapman & Hall, 1997.
6. Purchas, D. B. and Sutherland, K., Handbook of Filter Media, 2nd Ed., Elsevier, 2002.
7. Yonaga, M, Suzuki, K. and Urata, E., Method for evaluating filtration performance of a filter for hydraulic systems, JSME Kyuushuu Branch 58th Conf Proceedings, pp.375-376, (Fukuoka, 2005-3). [in Japanese].
8. ANSI B93.31-1973, "Multi-Pass Method for Evaluating the Filtration Performance of a Fine Hydraulic Fluid Power Filter Element," American National Standards Institute, 1973.
9. ISO 4752 "Hydraulic fluid power Filters Multi-pass method for evaluating filtration performance", 1986.
10. Hong, I. T., The beta prime-a new advanced filtration theory, Proc. of IMech Conference, "Contamination Control in Hydraulic Systems", pp.83-88, (Bath, 1984).
11. Hong, I. T. and Fitch, E.C., An Innovative Technique in Filter Rating, SAE Paper 851590, 1985.
12. ISO 16889:1999(E) "The multi-pass test method for evaluating filtration performance of filter elements", 1999.
13. Pierce, F. D., Filter Performance with Cyclic Flow, SAE paper No.8601736, April 8-10, 1986.
14. Bensch, L.E. and Needelman, W.M., The Influence of Surge Flow on Filter Performance, SAE Earthmoving Industry Conference, SAE Paper No.860737, April 8-10, 1986.

INVESTIGATION INTO PRESSURE DISTRIBUTION OF SPOOL VALVE WITH NOTCHES

Xin FU*, Hong JI** , Shohei RYU***

* The State Key Lab of Fluid Power Transmission and Control
Zhejiang University, 310027, Hangzhou, China
(E-mail: xfu@zju.edu.cn)

** School of fluid power & control engineering
Lanzhou University of Technology, 730050, Lanzhou, China
(E-mail: jihong@lut.cn)

***Technical Research Laboratory
Hitachi Construction Machinery Co. Ltd, Tsuchiura, Ibaraki, Japan
(E-mail: Liu99@Hitachi-kenki.co.jp)

ABSTRACT

A novel test apparatus used to measure the pressure distribution of spool valve with notches has been designed, thus the mechanism of the noise differences related to the different notches can be investigated. Some small holes used to detecting pressure were arranged on a sleeve that can be shifted and rotated in preset locations. Several ways are introduced to minimize the internal leakage, which include the hydraulic force used to close the gaps between the sleeve and valve body, the large distance between the small holes and a high requirement of small clearances between the body, the spool and the sleeve. The effect of this test apparatus on the flow field inside the valve is limited to the minimum to improve the accuracy of the method proposed. The experimental results of pressure distribution are agreed well with the CFD results as a whole, particularly in diverging flow direction in notch (called 'FLOW-OUT'). In converging flow (call 'FLOW-IN'), the correspondence between the experiment and CFD results is not good as the former due to the numerical errors in CFD. The CFD and experimental results of two typical notches, the sloping notch (V-notch) and the notch with a passage of same cross-section areas (U-notch), was presented in this paper. As a result, it is revealed that the U-notch has a two-stage orifice characteristic that can be helpful to suppress the cavitation noise.

KEY WORDS

Notch, Spool valve, Pressure distribution measurement, CFD, Cavitation noise

INTRODUCTION

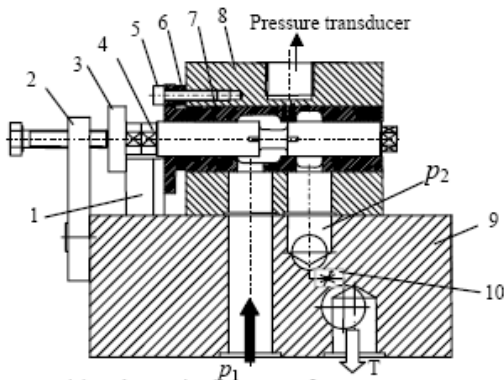
The notches in spool valve are one of main configurations of orifice in fluid power systems. It is widely used in spool valves to throttle flow. The notch with different geometry has different noise level in practical applications. However, there has been few

works concerning the noise characteristics on the notch. Shigeru Oshima (1994-2003) used a unique half cut model of poppet valve, had studied the pressure distribution and cavitation in a poppet valve in detail. Hisanori (1994) reported the noise measurement and numerical simulation of a relief valve. These works show that the flow passage and the orifice geometry

have a great effect on the valve noise. It is necessary to understand exactly the relationship between the geometry of a notch and the noise. Though the CFD approach has popularly adopted to investigate the flow in hydraulic components, papers including the pressure distribution obtained by CFD and experiment are still lack.

In this paper, for the purpose of understanding the effects of the geometry of notch on the noise characteristic in spool valve, a method and a test apparatus to measure the pressure distribution and to detect noise is proposed. The pressure distribution results of two typical notches obtained by experiment and CFD was presented.

EXPERIMENTAL APPARATUS



(a) Schematic diagram of test apparatus



(b) Picture of the test apparatus

Fig.1 The test apparatus

- 1. Gauge blocks for spool location, 2.Screw,
- 3.Measurement plate, 4.Spool, 5.Screw for sleeve location,
- 6.Gauge block for sleeve location, 7.sleeve,
- 8.valve body, 9.Manifold, 10. Backpressure valve

The apparatus to measure the pressure distribution are shown in figure 1 - figure 3. Four notches with the same size and configuration are symmetrically placed on each spool. In figure 2, the nineteen small holes are placed on the sleeve, five of which are used to measure the wall pressure distribution between high-pressure regions and return pressure area, the others are placed on both sides of the sleeve to detect the return chamber pressure. In order to stop the leakage among the holes, the small holes are arranged in three rows with the distance between the adjacent holes fixed at 4 mm. Several ways have been introduced in the test apparatus to stop leakage, which include the hydraulic force used to close the gaps between the sleeve and valve body (see the figure 1a), a high requirement of small clearances ($5 \mu\text{m}$ in radial) among the body, the spool and the sleeve.

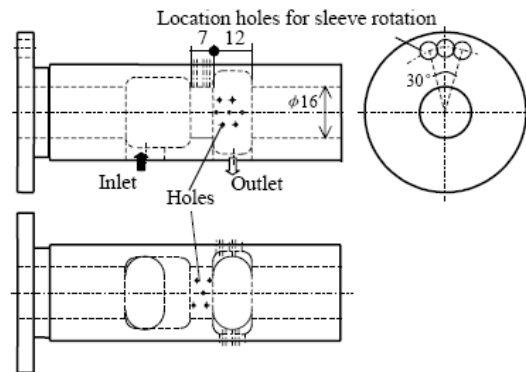


Fig.2 diagram of sleeve

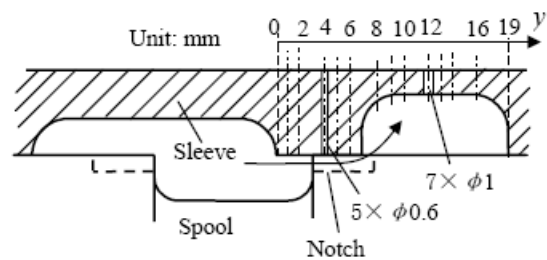


Fig.3 Holes location in axial direction for measuring pressure distribution

The sleeve is movable and rotatable which makes it able to connect each small hole with the pressure transducer. Holes to be selected to connect the transducer are determined by the thickness of the gauge blocks for sleeve location and the selection of location holes for sleeve rotation. The thickness of gauge blocks for the spool location determines the valve opening. When a point in the low-pressure area is detected, the transducer with a narrow range is selected to improve measurement accuracy. In figure 3, it is shown the holes location in spool axial direction,

the distance between two adjacent holes is 1 mm or 2 mm.

Sound noise was measured using a noise spectrum analyzer with the microphone 90 mm away from the test valve body.

TYPICAL NOTCHS

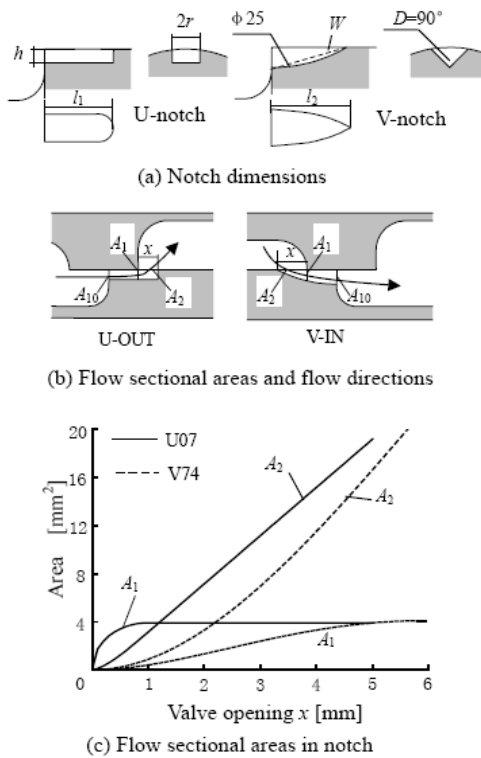


Fig. 4 notch configuration and flow areas

The flow areas and main dimensions of two types of typical notches are shown in figure 4. The two types of notches are named as U-shape and V-shape notch (simply called U and V), the numbers followed the U or V indicating the different size notches in the paper, the followed letters IN or OUT to indicate the flow direction in the notch passage in this paper. U-notch and V-notch have typical difference in flow areas and profiles. The profile of U-notch has a passage of same cross-section area, its length being the function of the opening x . while the feature of the V-notch profile is slope along the flow direction. The actual orifice area of V-notch is determined by the flow area A_1 because of the valve of A_2 being larger than the A_1 in all range of opening. The orifice location of the U-notch is not fixed in one position. When the opening is equal to a certain value (for example, 1.2 mm in fig.4c), the flow areas A_1 and A_2 of U-notch is equal, thus the two-stage orifice is formed in U-notch. When the opening is less than the certain value (1.2 mm), the actual orifice area of U-notch is determined by A_2 . On

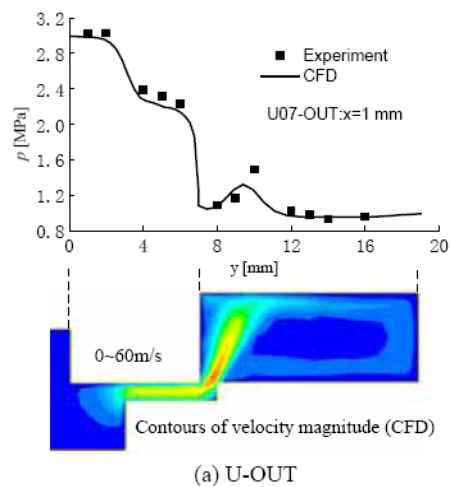
the other hand, when the opening is larger than this certain value, the actual orifice area is determined by A_1 . This change of the orifice location is called the shift of orifice location in this paper.

RESULTS OF PRESSURE DISTRIBUTION

Figure 5-figure 6 show the pressure distribution of the sleeve internal surface in FLOW-OUT state and in FLOW-IN on the two typical notches described in the previous section. The results in figure 5 and figure 6 are obtained with the inlet pressure fixed at 3.0 MPa and the pressure in valve chamber at 0.98 MPa. In that condition, no cavitation occurs in the valve and the state of flow in the valve can be thought single-phase flow. Both the experimental result and the CFD result are showed in these figures with the experimental result showed in scattered dots and the CFD result in continued solid lines. The CFD results are obtained on FLUENT software adopted RNG k- ϵ turbulence model. The oil density ρ is 889 kg/m³, the kinetic viscosity is 4×10^{-5} m²/s.

Case of FLOW-OUT

Figure 5 shows the pressure distribution measured along the sleeve surface at one opening in FLOW-OUT. It is known from the figure that the CFD result agrees with the experimental result very well. The pressure drop steeply at the position of $y=7$ mm. Since the pressure within the notch remains considerable value, there is no cavitation occurrence in this restriction part. On the other hand, since the pressure reduction due to the flow contraction close to the valve chamber is remarkable, the minimum pressure appears at the corner between the notch and the valve chamber (around $y=8$ mm). Cavitations tend to occur at this low-pressure area in FLOW-OUT.



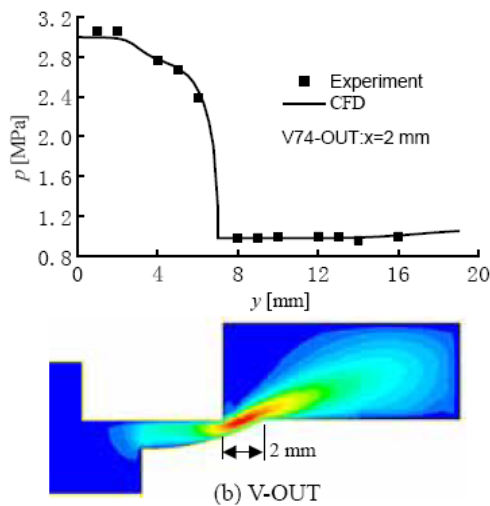


Fig.5 pressure distribution in FLOW-OUT

Figure 5a shows the pressure distribution in the opening $x=1$ mm of U07 model. The pressure difference drops on two positions ($y=3$ mm, $y=7$ mm) and the pressure within the notch decrease slowly because of the resistance in the notch passage with a length of same sectional area, which can be understood in Figure 4. It is revealed that the U-NOTCH has a characteristic of two-stage orifice. The curve of pressure distribution in the return chamber has one peak at the position of $y=10$ mm due to the impact of the high-speed flow stream to the surface of the valve chamber. As the valve opening increases, the pressure peak tends to occur in the rear of the valve chamber due to the smaller flow spray angle, and the pressure value in peak decreases due to the momentum loss caused by the longer distance between the point of spray and the valve chamber surface along the flow stream.

As to the notch of V74, the pressure in the notch drops gently when the valve opening is small. The pressure mainly drops to the return pressure steeply in the fixed position of $y=7$ mm. Compared with the U-NOTCH, the pressure in the wall of the return chamber almost keeps constant, and increases only in the rear of the chamber for the flow spray angle under different openings is small and changes little.

Case of FLOW-IN

Figure 6 shows the pressure distribution measured along the sleeve wall in FLOW-IN state. Since no small holes for detecting the pressure are arranged within the region between $y=0$ mm and $y=1$ mm for the difficulty of small machining, the experimental results do not show the pressure distribution in this region. However, the pressure distribution in this region can be conceived from the CFD result. Because the flow

detaches from the sleeve wall at the entrance corner, the pressure drops deeply within the region between 0 mm and 0.3 mm. After passing the detaching area, the flow is decelerated and reattaches to the sleeve wall, thus the pressure regains and approaches the pressure value near to the return chamber of the valve.

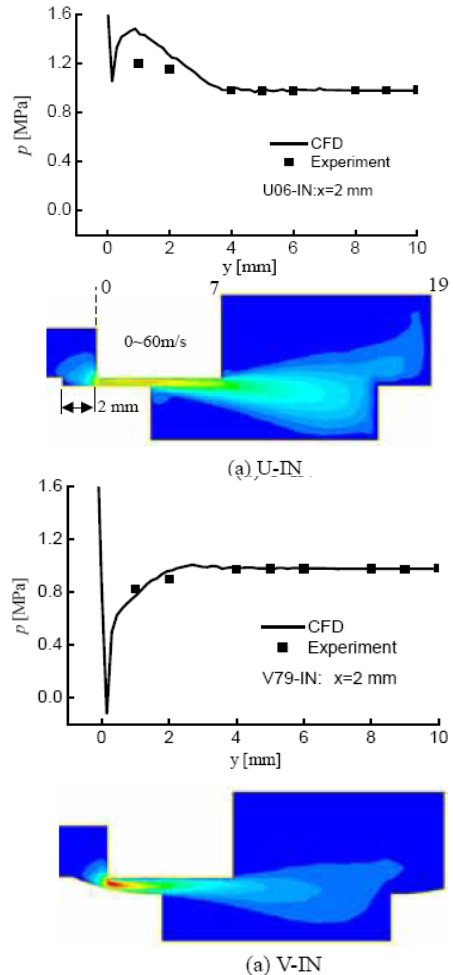


Fig.6 pressure distribution in FLOW-IN

Compared the pressure distribution of U-notch with that of V-notch, the pressure at the restriction of U06 regains more quickly and more easily than that in V79. As to the notch of U06, when the valve opening is 2 mm, there exists a length of 3 mm flow passage with same sectional area behind the notch orifice to resist the flow from the notch orifice again. Thus a higher pressure at the position of $y=1$ mm than the pressure of the next position occurs. Two factors, the flow rate from the orifice ahead and the length of passage mainly determine the resistance of the same sectional passage. In turbulence flow state, the resistance (or pressure drop) is proportional to the square of flow rate and the length of passage.

SOUND NOISE LEVELS

Figure 7 shows the change of the sound noise level with the increase of pressure in the return chamber at the inlet pressure fixed at 5 MPa and oil temperature kept in the range between 46C° and 50C°. Since the environmental noise level is comparatively low (65dB) and steady in the test environment, the measurement results of noise showed in the figures contains the environmental noise. The flow rate of the U07 and V75 in an opening of 2 mm is 15 l/min and 12.5 l/min at the return pressure p_2 0.2 MPa.

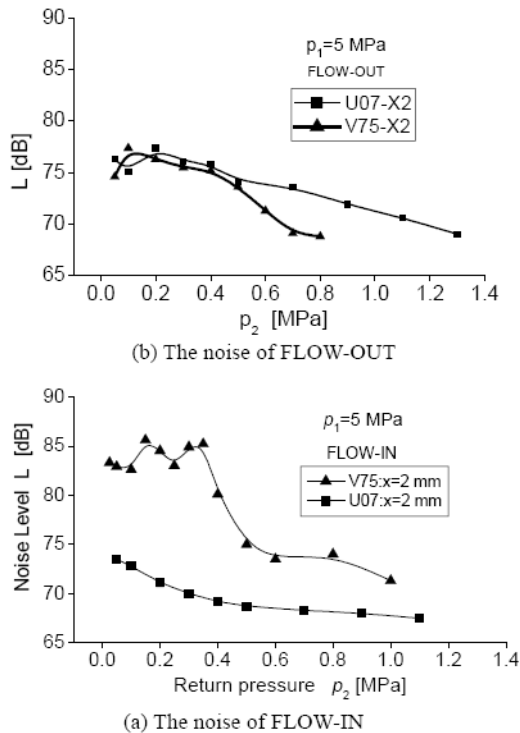


Fig.7 the noise level difference

In FLOW-IN shown in figure 7a, the noise characteristics between the U-notch and V-notch are remarkable difference. Compared with the V75-notch, the noise level of the U07 is much lower. When the return pressure p_2 is less than 0.4 MPa, the noise level of V75 reaches 85 dB, whereas the noise level of U07 is less than 75 dB. When the return pressure is gradually increasing, the noise level of V75 decreases steeply. The noise of U07 decreases steadily. Compared with V75, the noise of U07 drops more slowly with the increase of return pressure.

The noise level In FLOW-OUT is shown in figure 7b, there is not marked difference between the noise levels of two notches. Their noise characteristics are similar and there is no high squeal noise as FLOW-IN state. When the return pressure increase beyond 0.5 MPa,

the noise level of V75 is lower than that of U07 due to the flow rate of the former being lower.

CONCLUSIONS

The pressure distribution of spool valve with notches was investigated by a novel apparatus. The experimental results agree with that of CFD as a whole. Particularly, in flow direction of FLOW-OUT, the correspondence between experiment and CFD is very good. The pattern of pressure distribution in typical notches can be concluded. In FLOW-OUT state, the pressure within notches has a high value to restrain the occurrence of cavitations, and the area of low pressure lies in the return chamber due to the flow contraction. In FLOW-IN, the pressure distribution has remarked difference between the typical notches. The pressure of U-notch regains quickly, and the pressure of V-notch has a slow and long process to regain the pressure value of the return chamber.

The noise characteristics in FLOW-OUT are similar. The noise of FLOW-OUT is low and no squeal noise occurs. There exists a critical return pressure where the maximum noise level appears. When the return pressure exceeds the critical return pressure, the noise level decreases gradually with the increase of the return pressure because the location of the flow stream contraction lies near to the return chamber. As the return pressure rises, it enhances directly the pressure of the flow contraction. The occurrence of cavitations is restrained and the noise level drops down.

There are remarkable differences in noise between U-IN and V-IN. The differences are almost due to the difference of the pressure distribution determined by the notch configurations. The squeal noise appears at middle openings in V notch.

ACKNOWLEDGMENTS

The authors are grateful to the National Natural Science Foundation of China for the financial support.

REFERENCES

1. Shigeru Oshima, Tsuneo Ichikawa. Cavitation phenomena and performance of oil hydraulic poppet valve. Bulletin of JSME, 1985, 28(244): 2264-2271.
2. Shigeru Oshima, Timo Ieino, Matti Linjama, etc. Effect of cavitation in water hydraulic poppet valves. International journal of fluid power, 2001, 2(3):5-13.
3. Hisanori UENO, Noise measurement and numerical simulation of oil flow in pressure control valves, JSME International Journal, series b, V.37, N.2, 1994.
4. Frank R., Siegfried H., Basic investigation of characteristics of flow and noise for oil-hydraulic valves, Proceedings of the 8th SICFP'03, May 7-9, 2003, Tampere, Finland, 565~575.

ENERGY-EFFICIENT MOTION CONTROL OF A DIGITAL HYDRAULIC JOINT ACTUATOR

Matti LINJAMA and Matti VILENIUS

Institute of Hydraulics and Automation
Tampere University of Technology
P.O.Box 589, FIN-33101 Tampere, Finland
(E-mail: matti.linjama@tut.fi)

ABSTRACT

This paper studies the energy efficiency of a heavily loaded cylinder drive. Pulse code modulation is used to control all four flow path independently with parallel connected on/off valves. A valve manifold with 4×5 two-way screw-in cartridge valves is used and the dimensions of the test system are such that actuator size, load force, effective inertia and natural frequency are at the same level as in joint actuators of typical medium size mobile machines. A cost function based control solution is used for online minimization of power losses. Power losses are compared with traditional proportional load-sensing system.

KEY WORDS

Digital hydraulics, pulse code modulation, energy efficiency

INTRODUCTION

The main reason for the use of hydraulic actuators is high power to weight ratio. This is why typical applications are in high-power systems, e.g. mobile machines. Unfortunately, the total efficiency of typical hydraulically actuated machines is very low, even below 5 percent [1]. This yields of excess fuel consumption, emissions and economical losses.

The reduction of power losses has been under active research for decades. The most commonly applied approach is Load Sensing, in which the pump flow is matched according to flow demand of all actuators and the pump pressure is matched according to the highest

load pressure. This is only a partial solution because high losses still occur when pressure demands of actuators are not at the same level. More sophisticated solutions are the use of hydraulic transformers [2] or pump-controlled actuators [3]. These are relatively expensive solutions and are not widely used yet. The separate meter-in and separate meter-out (SMISMO) control approach has also been studied quite a lot [4–6]. It gives freedom to control independently velocity and pressure level of the actuator, which can be utilized in energy saving by minimizing pressure losses. Mattila [4] used hydraulic circuit of Fig. 1 (a) to implement a SMISMO controlled cylinder. Energy saving up to 50 percent was demonstrated with overrunning loads. Jansson and Palmberg [5] used four two-way proportional valves as shown in Fig. 1 (b).

Different control strategies were discussed including differential circuit. Liu and Yao [6] added one extra valve to control cross port flow as shown in Fig. 1 (c). This valve was used to minimize pump flow with overrunning loads. Basic problems of SMISMO approach are the need for several high-quality proportional/servo valves as well as complexity of control systems. Typically, a model based controller with closed-loop pressure and flow/velocity controllers are used. Successful pressure control requires high-bandwidth valves and good dynamic model of the system.

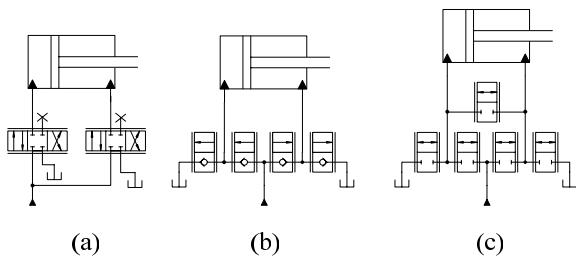


Figure 1. Different SMISMO systems found in literature.

This paper studies so-called digital hydraulic SMISMO system [7]. The basic idea is that each flow path is controlled by a parallel-connected on/off valve series – so called digital flow control unit (DFCU), see Fig. 2. The flow capacities of on/off valves are set according to binary sequence, which is known as pulse code modulation (PCM) approach [8]. The approach gives 2^N discrete opening values for each DFCU where N is the number of parallel connected valves. Some benefits of digital hydraulic control approach are that low-cost on/off valves can be used and that the system is fault-tolerant [7, 9].

Although PCM control is an old idea, it has seldom been applied in hydraulic systems. Virvalo [10] used the PCM method to control the velocity of an oil hydraulic cylinder. One DFCU with four valves was installed in the outflow path of the cylinder in order to synchronize piston velocity with trolley conveyor. Similar meter-out control with one DFCU was used by Liu et al. [11], who controlled the position of the joint actuator of a spraying robot. Tanaka [12] implemented a high-speed DFCU for small flow rates. He addressed also the inherent pressure surge problem of PCM control.

The author's research group has studied SMISMO PCM control systems, such as shown in Fig. 2 [7, 9, 13-15]. The aim is to combine good properties of SMISMO control and robust on/off technology. The hydraulic circuit of Fig. 2 is flexible and allows simultaneous control of velocity and pressure level, for example. One difficulty is that the system has 2^{4N} different states and the control system must somehow select the best opening

combination of valves for each situation. This problem was addressed in [13, 14] where a cost function based control approach was developed. The controller utilized the steady-state model of the system, and did not hence require any dynamic model of the system. The aim of this paper is to show that power losses can also be included in this general framework and that high-quality and energy efficient motion control is possible with slow-response on/off valves without any active pressure control.

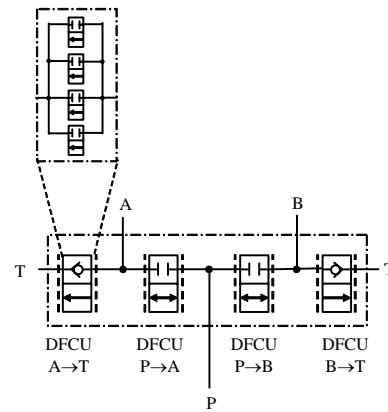


Figure 2. Digital hydraulic SMISMO valve system.

TEST SYSTEM AND SIMULATION MODEL

The system studied is the same as in [14] and its hydraulic circuit diagram is shown in Figure 3. The system mimics the dynamics of the joint actuator of a typical medium sized mobile machine boom. The design as well as static and dynamic characteristics of the system are presented in [15].

The results of this paper are based on simulations and the simulation model includes rigid body dynamics of the boom, standard models for cylinders and oil volumes together with following assumptions:

- On/off valves are modeled as 30 ms delay plus first order dynamics (time constant 2 ms, maximum rate 200 1/s)
- On/off valves of DFCUs P→A and P→B allow flow in both directions
- Flow capacities of on/off valves are the same as in [14], i.e. the largest valve 19 l/min @ $\Delta p = 0.5$ MPa and the others approximately according to binary series
- Pump is modeled as variable supply pressure source with first order dynamics (time constant 50 ms)
- Hose dynamics are neglected but the effect of hoses on the effective bulk modulus is included

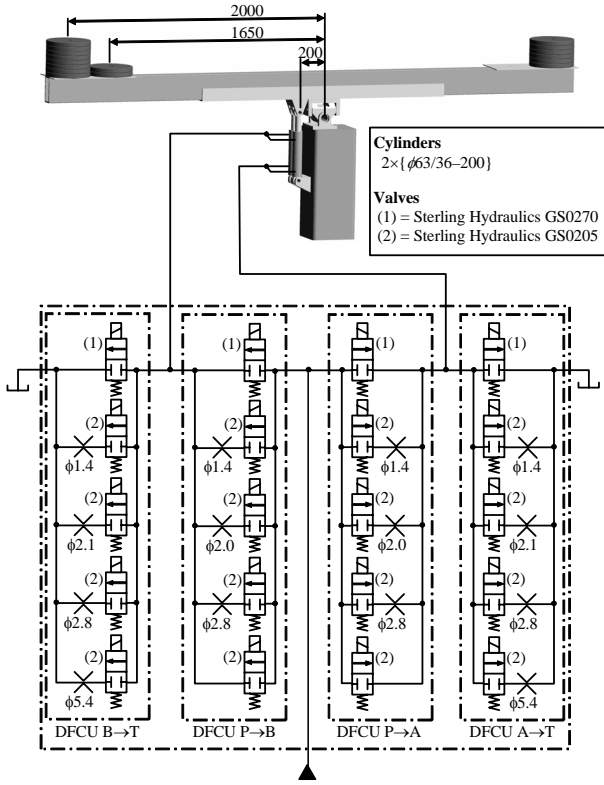


Figure 3. Hydraulic circuit diagram of test system.

Figure 4 compares simulated and measured responses. It is seen that the simulation model predicts accurately the dynamic response of the system and that the system dynamics is dominated by a 4 Hz natural frequency.

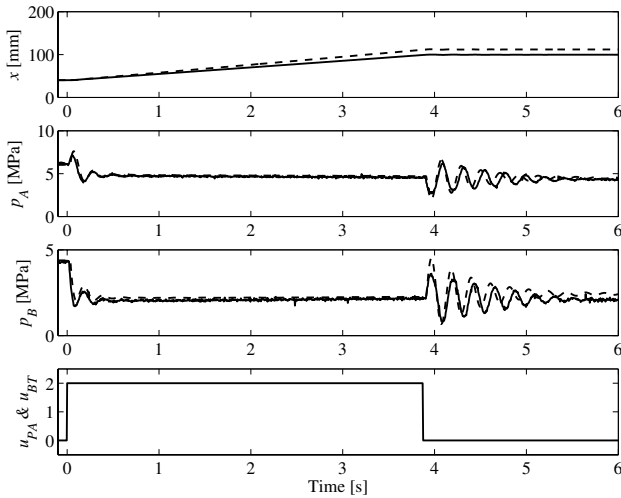


Figure 4. Simulated (---) and measured (—) response when second smallest valves are opened and closed. The load masses are 200+100 kg at piston side and 100+0 kg at the other end.

CONTROL PRINCIPLE

The control principle is similar to predictive control approach: the future response of the system is calculated via a model and valve controls are selected by minimizing a cost function. The steady-state model of the system is used:

$$\begin{aligned} Q_{N,PA}(u_{PA})\sqrt{p_P - p_A} - Q_{N,AT}(u_{AT})\sqrt{p_A - p_T} &= A_A v \\ Q_{N,PB}(u_{PB})\sqrt{p_P - p_B} - Q_{N,BT}(u_{BT})\sqrt{p_B - p_T} &= -A_B v \end{aligned} \quad (1)$$

$$F = A_A p_A - A_B p_B$$

where $\sqrt{\bullet}$ is a shortcut for signed square root $\text{sgn}(\bullet)\sqrt{|\bullet|}$, and $Q_{N,PA}$, $Q_{N,AT}$, $Q_{N,PB}$ and $Q_{N,BT}$ are flow coefficients of DFCUs P→A, A→T, P→B and B→T, respectively (see Fig. 3). Each flow coefficient depends on the state u of the DFCU and has therefore 2^5 different values. The steady-state velocity and pressures can be solved from Eq. 1, if the load force F as well as supply and tank pressure of the system are known. The system has $2^{20} \approx 10^6$ different states, which makes the real-time calculation of all combinations impossible. Therefore, the reduced search space is defined by analyzing flow balance of both chambers separately (see [14] for details). The steady-state velocity and pressures are then solved from Eq. 1 for all elements of the reduced search space by using Newton-Raphson iterations. Finally, the cost-function values are calculated for each steady-state solution and the best opening combination is selected. This process is repeated at each sampling instant. It is important to note that the approach allows control of all four flow paths simultaneously. The inputs of the controller are target velocity and pressures, measured or estimated supply and tank pressures, and measured or estimated load force.

MINIMIZATION OF POWER LOSSES

The hydraulic input power of the system is

$$P_{in} = Q_P p_P \quad (2)$$

where Q_P is flow rate into the valve system and p_P is pressure at the P-port. Following rules and assumptions are used in the development of the control strategy:

- The lowest allowed target pressure is 2 MPa in order to avoid cavitation
- Pressure differential over active DFCUs should be at least 2 MPa for sufficient controllability
- Tank pressure p_T is zero

Four cases are studied: large restricting load and large overrunning load at both directions.

Restricting load force

The control strategy for restricting load is straightforward. The target pressure for the meter-out side is 2 MPa, and the target pressure of meter in-side is calculated according to load force and meter-out pressure. Let us consider the extending movement with restricting load force. Pressure references can be calculated as follows:

$$\begin{aligned} p_{B,ref} &= 2 \text{ MPa} \\ p_{A,ref} &= (p_{B,ref} A_B + F) / A_A \\ p_{P,ref} &= p_{A,ref} + 2 \text{ MPa} \end{aligned} \quad (3)$$

where it has been assumed that the load force is so big that $p_{A,ref}$ is bigger than 2 MPa. The power losses can be minimized by minimizing flows P→B and A→T. As the results of [13] show, these ‘short-circuiting’ flows are needed only at lower velocities for improving controllability. The suggested cost function for extending movement with restricting load is

$$\begin{aligned} J &= (v_{ref} - v)^2 + K_1 \left\{ (p_{A,ref} - p_A)^2 + (p_{B,ref} - p_B)^2 \right\} + \dots \\ &K_2 \left[\left\{ Q_{N,PB} (p_P - p_B)^{3/2} \right\}^2 + \left\{ Q_{N,AT} (p_A - p_T)^{3/2} \right\}^2 \right] \end{aligned} \quad (4)$$

The cost function has three quadratic terms, one for velocity error, one for pressure errors and one for power losses in DFCUs P→B and A→T. Tuning parameters K_1 and K_2 can be used to find good trade-off between velocity/pressure tracking and power losses. Velocity and pressures in Eq. 4 are not measured but calculated from steady state model of Eq. 1. The retracting movement with restricting load can be handled similarly.

Overrunning load force

For overrunning load force, the meter-out pressure must be so big that the minimum pressure requirement is met at the meter-in side. For extending motion, pressure references can be calculated as follows:

$$\begin{aligned} p_{A,ref} &= 2 \text{ MPa} \\ p_{B,ref} &= (p_{A,ref} A_A - F) / A_B \\ p_{P,ref} &= p_{A,ref} + 2 \text{ MPa} \end{aligned} \quad (5)$$

Again a large load force is assumed, which yields the condition $p_{B,ref} > p_{P,ref}$. In this case, power losses can be minimized by allowing flow B→P and minimizing flows A→T and B→T, i.e. differential circuit. Small flow from pump is needed to compensate for piston rod area. Energy saving is significant especially if high supply pressure must be used because of demands of other actuators. The cost function for this situation is

$$\begin{aligned} J &= (v_{ref} - v)^2 + K_1 \left\{ (p_{A,ref} - p_A)^2 + (p_{B,ref} - p_B)^2 \right\} + \dots \\ &K_2 \left[\left\{ Q_{N,BT} (p_B - p_T)^{3/2} \right\}^2 + \left\{ Q_{N,AT} (p_A - p_T)^{3/2} \right\}^2 \right] \end{aligned} \quad (6)$$

The retracting motion can be handled similarly, but the meter-out flow is bigger than meter-in flow. The excess flow can be drained to tank via DFCU A→T or it can be utilized in other actuators. Therefore, the retracting motion with large overrunning load requires no pump flow and power losses are zero.

SIMULATION RESULTS

Implementation of Controller

The controller is implemented according to block diagram of Figure 5. Trajectory generator generates the fifth order polynomial position reference x_{ref} and corresponding velocity reference v_{ref} . Position feedback and velocity feedforward are used to generate the closed-loop velocity reference v_{ref2} . The load force estimate F is calculated from the chamber pressures by using a second order low-pass filter. Pressure references are calculated by using Eqs 3 and 5, and finally the optimisation procedure is used to find minimum of the cost function (Eqs 4 and 6) and corresponding optimal control. The details of the optimisation procedure are given in [13, 14].

The block diagram shows that required measurements are chamber pressures, supply (and possibly tank) pressure and piston position. However, chamber pressures are used only for estimation of load force and not for active pressure control. The numerical values of main parameters are given in Table 1.

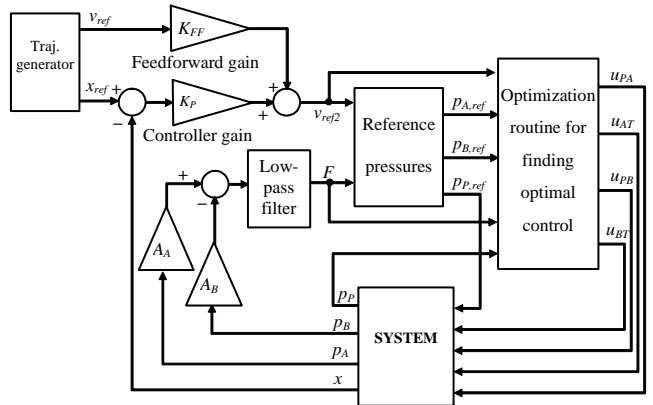


Figure 5. Block diagram of the control system.

Table 1. Main parameters of the control system.

Sampling time [ms]	40
Controller gain K_P [1/s]	2.5
Feedforward gain K_{FF} [-]	0.8
Weight for pressure error K_1	7×10^{-19}
Weight for power losses K_2	1×10^{-11}
Break frequency of low-pass filter [rad/s]	15

Simulated response with digital hydraulic valve

Figure 6 presents the simulated response when the load masses at boom tips are 200+200 kg at cylinder side and 0+0 kg at the other side. The load force is thus strongly restricting for extending movement and strongly overrunning for retracting movement. Figure shows that the system works as designed: inflow-outflow control is used in extending movement and differential circuit in retracting movement. The input power is even negative in retracting movement. The total work is 4710 J if negative power is considered and 5190 J if negative power is neglected.

It can be seen in Fig. 6 that the position and velocity tracking is good and similar to experimental results in [14]. Slight cavitation exists in large retracting movement and it could be prevented by adopting the anti-cavitation scheme presented in [15].

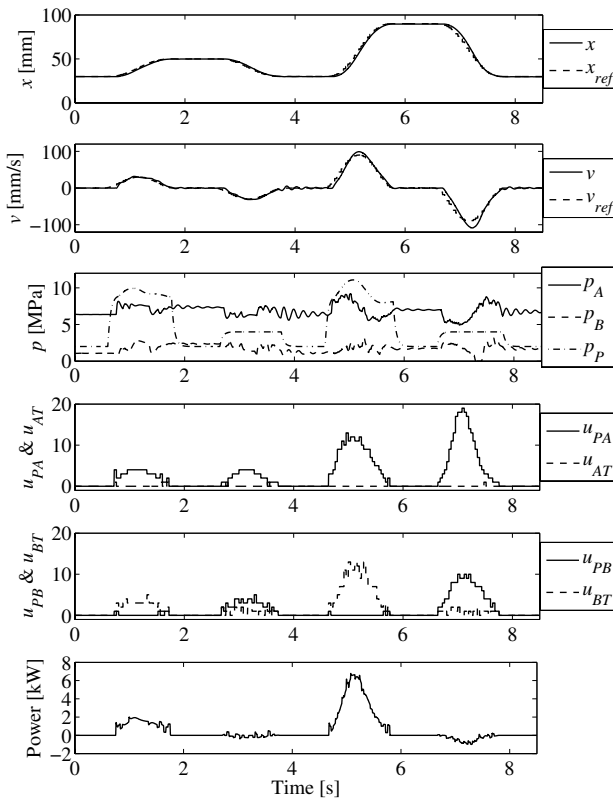


Figure 6. Simulated response with digital hydraulic valve system.

Simulated response with proportional valve

In order to compare power losses to traditional valve solution, the simulation of Fig. 6 is repeated with a proportional valve. The valve has matched flow areas, no hysteresis or non-linearity and first order dynamics with 30 ms time constant. The valve does not have pressure compensator. In the extending movement, the pump pressure is adjusted to be 1 MPa higher than p_A . In the retracting movement the pump pressure is adjusted 6 MPa higher than p_B in order to avoid cavitation. Similar P-controller plus feedforward is used as a closed-loop controller. Figure 7 shows the simulated response. It is seen that the tracking performance is similar to digital hydraulic system but power losses are higher. The total work is 7340 J, which is 56 percent more than in digital hydraulic solution.

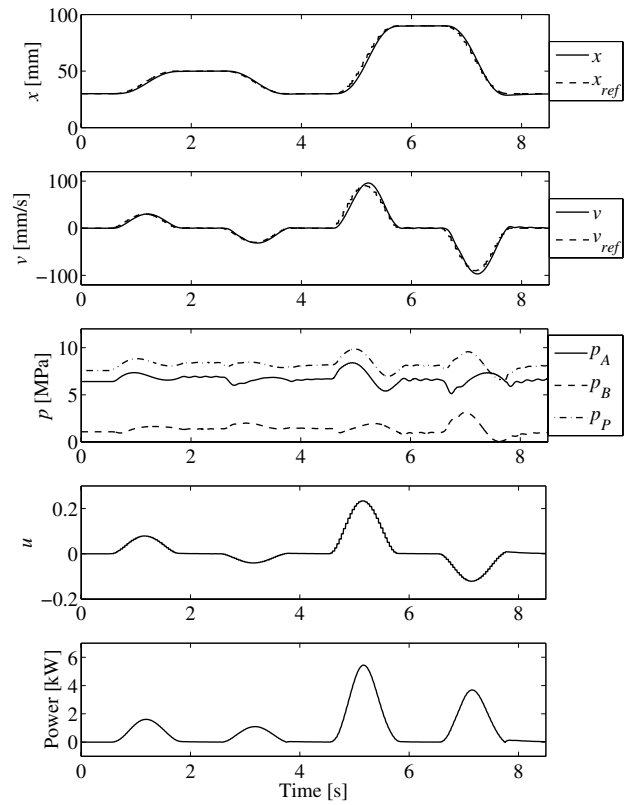


Figure 7. Simulated response with proportional valve.

SUMMARY

The main result of this paper is that energy efficient motion control is possible with rather slow-response on/off valves. The digital hydraulic valve system allows independent control of all flow paths, which is big advantage when compared to traditional valves where flow paths are mechanically linked together. In this paper, the flexibility of the valve system was utilized by using differential connection when lowering load. This

resulted in 36 percent reduction in power losses when compared to traditional valve. The energy saving control was implemented by including power loss terms in the cost function. In this approach, there is no need for active pressure control or accurate dynamic model as in other SMISMO solutions.

The results of this paper are based on simulations and the next step of the research is experimental validation. It can be expected that the real system has more pressure peaks because real valves have variation in delays. The bumpless transfer between different control modes is also an important research topic because the load force may change its sign during the motion in real machines.

ACKNOWLEDGEMENT

The research was supported by the Academy of Finland (Grant n:o 80411).

REFERENCES

1. Virvalo T. & Vilenius, M. 2000. The Influence of Pumps and Valves on the Efficiency of a Hydraulic Boom. **In:** Garbacik, A. & Stecki, J. (eds.) *Developments in Fluid Power Control of Machinery and Manipulators*, pp. 183–208 (Fluid Power Net Publication, Cracow, 2000).
2. Vael, G., Achten, P. & Potma, J. 2003. Cylinder Control with the Floating Cup Hydraulic Transformer. *The Eighth Scandinavian International Conference on Fluid Power*, Tampere, Finland, pp. 175–190.
3. Grabbel, J. & Ivantysynova, M. 2001. Control Strategies for Joint Integrated Servo Actuators in Mobile Machinery. *The Seventh Scandinavian International Conference on Fluid Power*, Linköping, Sweden, pp. 281–296 (Vol. 2).
4. Mattila, J. 2000. *On Energy Efficient Motion Control of Hydraulic Manipulators*. Dissertation, Tampere University of Technology, Publications 312, Tampere.
5. Jansson, A. & Palmberg, J.-O. 1990. Separate Controls of Meter-in and Meter-out Orifices in Mobile Hydraulic Systems. *International Off-Highway & Power Plant Congress and Exposition*, Milwaukee, WI, USA.
6. Liu, S. & Yao, B. 2002. Energy-Saving Control of Single-Rod Hydraulic Cylinders with Programmable Valves and Improved Working Mode Selection. *The 49th National Conference on Fluid Power*, Las Vegas, Nevada, USA, pp. 81–91.
7. Linjama, M., Laamanen, A. and Vilenius, M. 2003. Is it time for Digital Hydraulics? *The Eight Scandinavian International Conference on Fluid Power*, Tampere, Finland, pp. 347–366.
8. Bower, J. 1961. *Digital Fluid Control System*, US Patent n:o 2999482.
9. Siivonen, L., Linjama, M. & Vilenius, M. 2005. Analysis of Fault Tolerance of Digital Hydraulic Valve System. To be published in the *Bath Workshop on Power Transmission and Motion Control*, PTMC 2005, Bath, UK.
10. Virvalo, T. 1978. Cylinder Speed Synchronization. *Hydraulics & Pneumatics*. Dec 1978, pp. 55–57.
11. Liu, R., Wang, X., Tao, G. and Ding, F. 2001. Theoretical and Experimental Study on Hydraulic Servo Position Control System with Generalization Pulse Code Modulation Control. **In:** Lu, Y., Chen, Y. & Xu, L. (Eds.) *Proceedings of the Fifth International Conference on Fluid Power Transmission and Control (ICFP'2001)*, pp. 176–179 (International Academic Publishers, Beijing, China).
12. Tanaka, H. 1988. Electro-hydraulic PCM control. *Journal of Fluid Control*, Vol. 18, No 1, pp. 34-46.
13. Linjama, M. & Vilenius, M. 2005. Improved Digital Hydraulic Tracking Control of Water Hydraulic Cylinder Drive. *International Journal of Fluid Power*, Vol. 6, No 1, pp. 29–39.
14. Linjama, M. & Vilenius, M. 2005. Digital Hydraulic Tracking Control of Mobile Machine Joint Actuator Mockup. *The Ninth Scandinavian International Conference on Fluid Power*, Linköping, Sweden, 16 p.
15. Linjama, M. & Vilenius, M. 2004. Digital Hydraulic Control of a Mobile Machine Joint Actuator Mockup. *Bath Workshop on Power Transmission and Motion Control*, PTMC 2004, Bath, UK, pp. 145–158.

ENERGY SAVING SYSTEM FOR HYDRAULIC EXCAVATOR (SIMULATION OF POWER ASSISTANT SYSTEM WITH ACCUMULATOR)

Hironao YAMADA*, Shuji SHIOZAKI**, Hiroshi MATSUYAMA** and Takayoshi MUTO***

* Department of Human and Information Systems
Gifu University

Yanagido 1-1, Gifu 501-1193 Japan
(E-mail: yamada@cc.gifu-u.ac.jp)

** YANMAR Co., Ltd.,

1600-4, Umegahara, Maihara, Sakata, Shiga, 521-8511 Japan

*** Gifu Research and Development Foundation,

4-179-1 Sue-cho, Kakamigahara, Gifu, 509-0108 Japan

ABSTRACT

In this study we investigate development of energy saving system for hydraulic excavator. In the system an accumulator stores power when energy exceeds and assists necessary power which is required by the actuators. As a first step of the study, simulation program of the system is developed. By using the simulation program it is expected that the static and dynamic performance is easily grasped. And it will contribute to the rationalization of the system design. In this paper, the validity of the energy saving system is evaluated.

KEY WORDS

Key words, Energy saving , Hydraulic excavator, Simulation, Accumulator

NOMENCLATURE

C_d : Flow coefficient	P_g : Pressure in accumulator [Pa]
C_p, C_v : Constant-pressure molar heat and constant-volume molar heat [j/mol-k]	P_{PR} : Minimum gas pressure [Pa]
d_a : Diameter of pipeline [m]	p_{wr} : Work performed by pump [kW]
d_{pr} : Displacement volume per revolution [m ³]	q_1, q_2 : Flow rate at pipe inlet and outlet [m ³ /s]
$G(x)$: Transfer function of a rack system	q_{ag} : Flow rate into an accumulator [m ³ /s]
j : Moment of inertia around a crankshaft [kg-m ²]	r_1 : Pump revolution [rpm]
k_{pr1} : Proportional gain	r_2 : Target pump revolution [rpm]
k_{ir1} : Integral gain	Δr : Difference between the target revolution and actual revolution [rpm]
k_p : Pump efficiency [%]	s : Laplace operator
K : Bulk modulus [Pa]	t_q : Motor torque [kgf-m]
p_1, p_2 : Inlet pressure and outlet pressure for each element [Pa]	t_l : Load [kgf-m]
	t_e : Engine torque [kgf-m]
	u : Control input into a rack system

v_G : Accumulator capacity	[m ³]
v_{AC} : Maximum gas volume	[m ³]
v_{LQ} : Liquid volume in accumulator	[m ³]
x_r : Target rack position	[m]
x_{ra} : Actual rack position	[m]
ρ : mass density of fluid	[kg/m ³]

INTRODUCTION

In recent years, environmental consciousness has risen in various fields and “energy saving” for hydraulic equipment (construction machinery) has become an important keyword [1]. In the present hydraulic driving system, the constant capacity pump is driven with a constant velocity by the engine, and the hydraulic pressure and flow rate are regulated by the control valve in order to supply necessary power for the actuator. In such system, rate of fuel consumption increases under the condition such as too much load on the actuator or small load while idling, because engine runs at constant rotational speed and it makes combustion efficiency low. Thus, it is considered that energy saving may be attained by storing excess energy by using an energy storage device, such as an accumulator, and utilize the stored energy when it is needed. This study was to prepare a basic simulation program of an actual equipment system as a preliminary step to conduct comparative verification experiments for the energy saving of a small-sized hydraulic shovel using the method mentioned above.

Once the simulation program is prepared, it would be easy to understand the dynamic characteristics of the actual equipment system. Even if the parameters and structures of the equipment system are changed, the change of the performance and behavior may be easily understood and the program would be a very effective means to promote the rationalization and efficiency of the system design [2].

In view of the above background, this study intended to prepare the simulation program of a power assist system for the purpose of energy storage and recovery using an accumulator and verify the effectiveness of the power assist system using the analysis result.

SYSTEM CONSTRUCTION

The power assist system is a type of system to store and recover energy using an accumulator as if it were a storage battery. It is a system to store energy into an accumulator during equipment idling periods and utilize the stored energy during loaded periods for energy saving purpose. Fig. 1 shows the schematic diagram of

the power assist system.

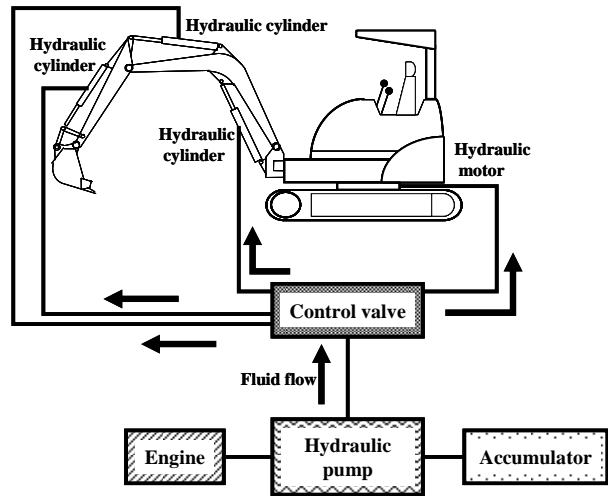


Fig. 1 Schematic diagram of the power assist system

The power assist system consists of an engine, accumulator, hydraulic pump /motor unit. The sensor of the power assist system measures the pump load and accumulator pressure then the computer begins to calculate a control input and gives it to the hydraulic pump/motor unit. By this signal, the system, as shown in Fig. 2, makes the hydraulic pump/motor unit operate as a hydraulic pump during no-load idling periods in order to pump hydraulic fluid into the accumulator to store it. When load is applied to the system, the system recovers the energy of the hydraulic fluid stored in the accumulator to drive the hydraulic pump/motor unit as a motor in order to assist the engine. The engine can maintain a constant and most efficient load and revolution with this method and, as result, fuel efficiency can be improved.

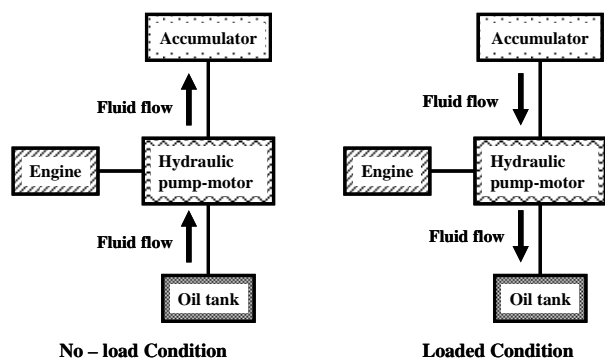


Fig. 2 Operating procedures of power assist system

An actual equipment system to verify the effectiveness of the power assist system is assumed to consist of an engine, two hydraulic pump/motor units, pipelines, an accumulator and a control system as its main elements.

The schematic outline of the hydraulic circuit diagram is shown in Fig. 3. The two hydraulic pump/motor units are connected directly to the crankshaft. The hydraulic pump/motor unit 2 that is connected to the accumulator compresses the accumulator and assists to drive the engine. The hydraulic pump/motor unit 1 functions as a variable-displacement pump and it may be considered as a load-producing device because it produces a load torque. It is considered that the unit 1 can produce almost the same workload of an actual working condition by changing the discharge amount. The controller determines the control input into the hydraulic pump/motor unit 2 from the load torque and accumulator pressure that are detected by the sensor.

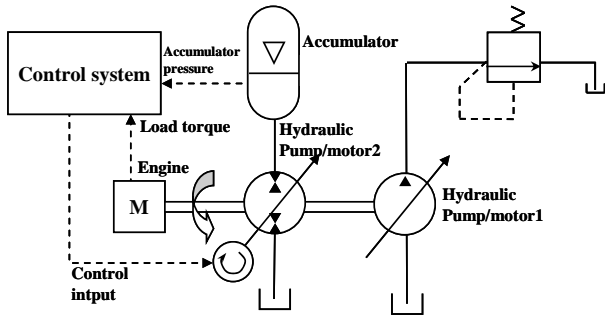


Fig. 3 Hydraulic circuit diagram of the power assist system

MATHEMATICAL MODEL FOR SIMULATION

This section explains the mathematical model of the accumulator, hydraulic pump/motor units and engine that are the main constituting elements of the power assist system. Fig. 4 shows the schematic model of the accumulator.

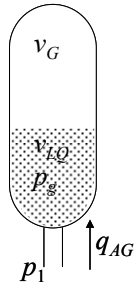


Fig. 4 Accumulator model for simulation

This element is composed of a bladder-type gas compression-method accumulator. The inflow into the accumulator should be obtained next. As an orifice is installed at the connection point of the pipe and the accumulator, the following equation can be made by assuming the orifice flow as being a laminar flow:

$$q_{AG} = \frac{\pi d_a^3 C_d^2}{2 \mu R_{ET}} (p_1 - p_g) \quad (1)$$

The following equation can be derived:

$$p_1 = p_g + \frac{2 \mu R_{ET}}{\pi d_a^3 C_d^2} q_{AG} \quad (2)$$

p_g , the hydraulic fluid pressure in the accumulator can be obtained as follows:

$$p_G v_G^\gamma = \text{constant} = p_{PR} v_{AC}^\gamma \quad (3)$$

where, γ is the ratio of the specific heat of gas c_p to c_v as follow:

$$\gamma = c_p / c_v$$

Thus, the pressure of the hydraulic fluid in the accumulator can be obtained as follow:

$$\dot{p}_g = \frac{K}{\rho} \left[\frac{\rho (q_1 - q_2)}{v_{LQ}} \right] / \left[1 + \frac{K}{\rho} \cdot \frac{\rho v_G}{\gamma p_g v_{LQ}} \right] \quad (4)$$

The volume of the hydraulic fluid, v_{LQ} , and the volume of gas, v_g , in the accumulator can be given by the following equations:

$$v_{LQ} = v_{AC} - v_g \quad (5)$$

$$v_g = v_{AC} \left(\frac{p_{pr}}{p_g} \right)^{\frac{1}{\gamma}} \quad (6)$$

Fig. 5 shows the schematic diagram of a variable displacement type axial piston pump/motor unit. The pump is made of the main elements of a swash plate, pistons, cylinders, a cylinder block and a valve plate. The inlet and outlet ports are separated by the valve plate.

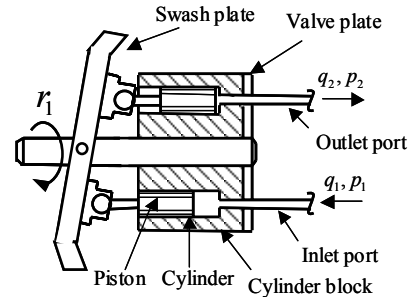


Fig. 5 Model of an axial piston pump for simulation

The outlet discharge of the hydraulic pump shown in the figure can be expressed by the following equation:

$$q_2 = d_{pr} \times r_1 \quad (7)$$

The work, p_{wr} , performed by the pump can be expressed by the following equation:

$$p_{wr} = \frac{q_2 \times (p_2 - p_1)}{k_p} \quad (8)$$

The relationship between the torque t_q that occurs when the pump/motor unit is used as a motor can be expressed as follow:

$$t_q = \frac{P_{wr}}{2\pi r_1} \quad (9)$$

Fig. 6 shows the schematic view of the engine element. This element consists of an electronic governor and an engine. The engine should be a simple one to produce torque by revolution and injected fuel without taking into consideration the combustion.

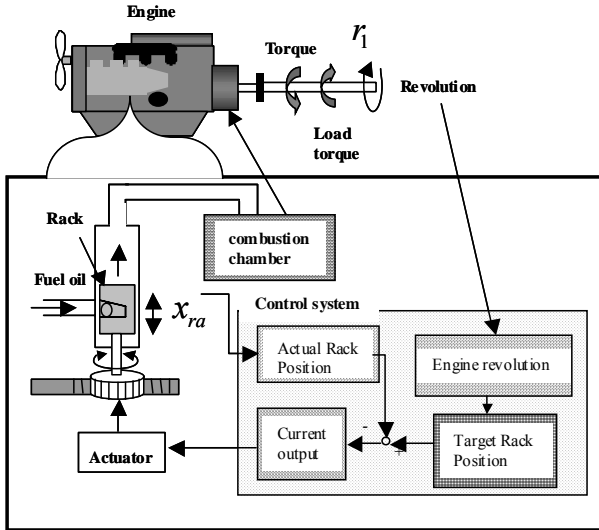


Fig. 6 Engine element model for simulation

The electronic governor is a device to detect engine revolution by the revolution sensor, calculates the target rack position that attains the target revolution of the engine and controls the rack position by the actuator. The simulation process is shown in Fig. 7.

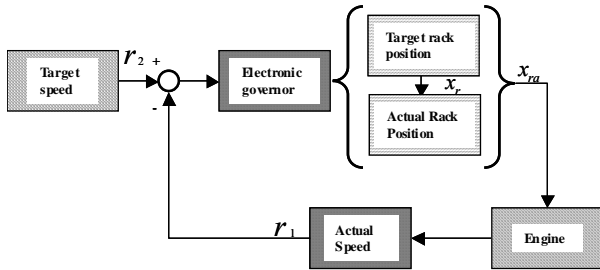


Fig. 7 Simulation process of engine model

The difference Δr between the target revolution r_2 and the actual revolution r_1 can be expressed by the following equation:

$$r_2 - r_1 = \Delta r \quad (10)$$

The target rack position x_r should be obtained at first. This is equivalent to the control system of the electronic governor and determines the target rack position x_r based on the control function.

$$x_r = g(\Delta r) \quad (11)$$

Input u to the rack system is to be obtained next. This is equivalent to the electric output of the control system and determines the input u by PI control. Thus, Input u can be obtained from x_r and x_{ra} by the following equation:

$$u = k_{pr1}(x_r - x_{ra}) + k_{ir1} \int (x_r - x_{ra}) dt \quad (12)$$

The transfer function $G_{(r)}$ of the actuator from the input u of the rack system to x_{ra} can be derived from the system identification as follow:

$$G_{(r)} = \frac{0.0073}{0.04s + 1} \quad (13)$$

The engine torque t_e can be obtained by the following equation:

$$t_e = f(x_{ra}, r_1) \quad (14)$$

The function $f_{(x,r)}$ is based on Fig.8. This was obtained as a result of tests conducted by changing the revolution r_1 and the rack position x_{ra} of the actual equipment system. The abscissa indicates the engine speed and the ordinate indicates the torque. The shaded area indicates the rack position. If the rack position is at a constant position, the torque becomes greater when the revolution decreases. On the other hand, the torque becomes smaller when the revolution increases. Thus, the torque can be obtained from the engine revolution and rack position in Fig. 8.

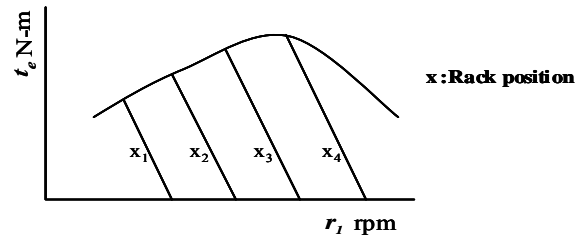


Fig. 8 Torque map

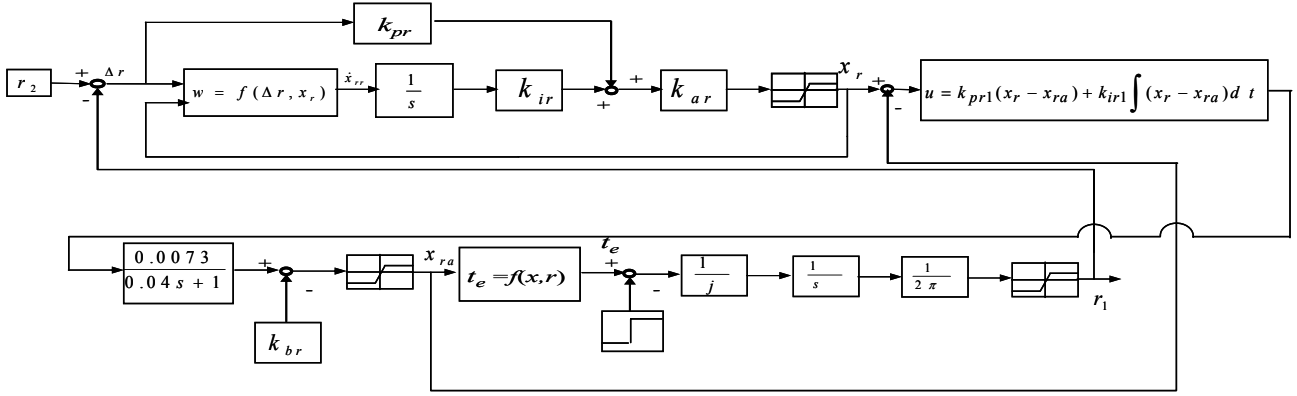


Fig. 9 Block diagram of engine

The equation of motion at the rotating shaft of the engine can be expressed by the following equation:

$$2\pi J \dot{r}_1 = t_e - t_l \quad (15)$$

Based on the above equation, the block diagram becomes as shown in Fig. 9. The controller element changes the discharge amount per one turn of the hydraulic pump/motor unit and alternates the pump/motor operation. Input into the controller is the accumulator pressure and engine load torque values. The block diagram of the controller is shown in Fig. 10.

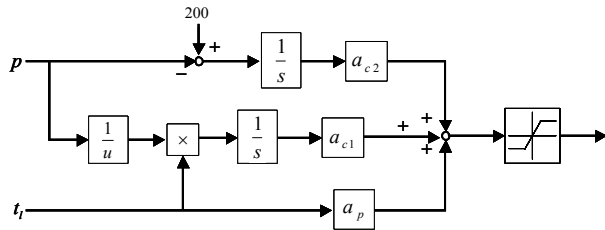


Fig. 10 Block diagram of controller

Based on the block diagram, the mathematical simulation of the power assist system can be made.

SIMULATION RESULTS

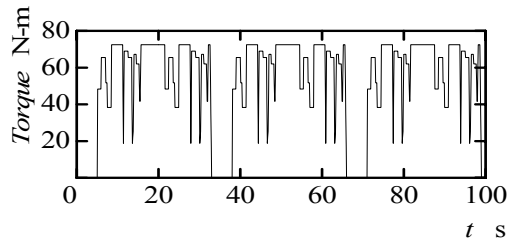
This section delineates the verification of the effectiveness of the power assist system by the simulation conducted based on the mathematical model described in the previous section. The simulation results of the two-types of load patterns (load-torque waveforms) are shown in Figs. 11 and 12 respectively. The given load torque waveforms are shown in the graphs (a), the torque of the hydraulic pump/motor unit in the graphs (b), the accumulator pressures in the graphs (c) and the engine speeds in the graphs (d) in both figures respectively. The fine lines in graphs (d) show the simulation results without power assist. The given load-torque waveforms were determined based

on data obtained through actual equipment operation.

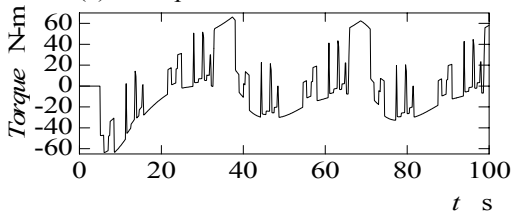
When looking into the results shown in Fig. 11 and paying attention to the torque of the hydraulic pump/motor unit shown in Fig. 11 (b), the graph indicates that the hydraulic pump/motor was functioning as a hydraulic motor under zero-load condition. It can be seen from the accumulator pressure shown in Fig. 11 (c) that the accumulator was pressurized during the zero-load periods. However, zero load is occurred between 0 to 5 second and at the period the accumulator pressure is constant. The reason is that the pressure in the accumulator is set at the maximum at the initial condition. When comparing the engine speed shown in the graph (d) of Fig. 11, it is clear that the engine speed greatly deviated in the simulation without power assisting. But, the deviation of the engine speed became smaller in the simulation when power assist was used. As for the relationship between the engine speed and fuel consumption, the smaller the deviation of engine speed, the more efficiently it is possible to operate the engine by maintaining a better engine speed. Thus, it is considered that the power assist system may be able to attain energy saving.

When looking into the simulation results using a different load torque pattern shown in Fig. 12 and paying attention to the torque of the hydraulic pump/motor unit in graph (b) and the accumulator pressure in graph (c), it can be seen that the hydraulic pump/motor unit was functioning as a hydraulic motor and pressurizing the accumulator when the load became zero as the same as the case shown in Fig. 11. The accumulator pressurization was made not only during zero-load periods but also during a time when the load was small. Even there were no zero-load periods shown in Fig. 12 (a), the accumulator pressure did not drastically drop.

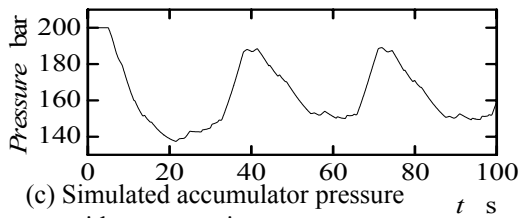
As for the engine speed shown in Fig. 12 (d), when the power assist system was used the deviation of the engine speed was small as the same as the case shown in Fig. 11. Thus, it is considered that energy saving was attained. As described above, the effectiveness of the power assist system was verified by this study.



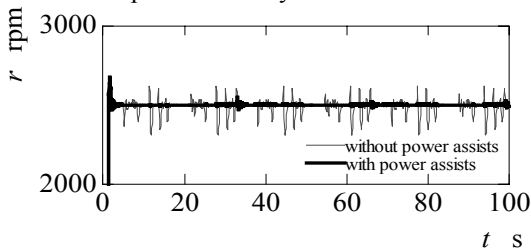
(a) Load pattern used for simulation



(b) Simulated torque of hydraulic pump/motor unit with power assist system



(c) Simulated accumulator pressure with power assist system



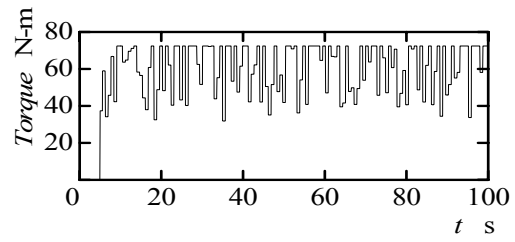
(d) Engine speed comparison

Fig. 11 Simulation result (load-pattern a)

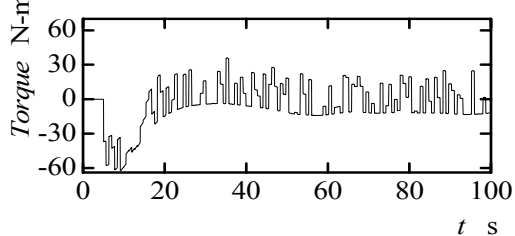
CONCLUSION

In this study, a mathematical model of a power assist system was made for the purpose to prepare a simulation program of the power assist system to store and recover energy using an accumulator. Based on the mathematical model, the simulation of the dynamic characteristics of the power assist system was conducted. From the simulation analysis results, the effectiveness of the power assist system was verified.

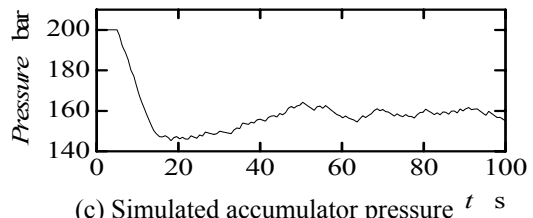
As a future work we would like to build an actual experimental facility and would like to discuss how much the proposed system could save energy.



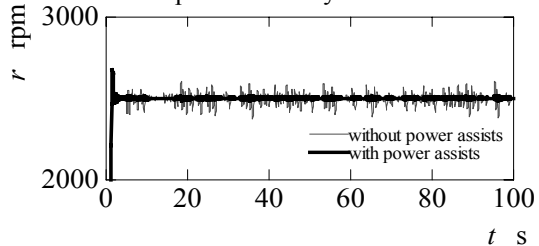
(a) Load pattern used for simulation



(b) Simulated torque of hydraulic pump/motor unit with power assist system



(c) Simulated accumulator pressure with power assist system



(d) Engine speed comparison

Fig. 12 Simulation result (load-pattern b)

ACKNOWLEDGEMENTS

The authors would like to express their deep appreciation to Dr. M., Tahmeen and Mr. D., Mishima of Gifu University for their extensive cooperation in performing the experiments.

REFERENCES

1. Hirano, K. and Ohba, K., A recent Saved Energy Type of Hydraulic System, Journal of the Japan Hydraulics and Pneumatics Society, 2001, **32-4**, pp.225-230 (in Japanese).
2. Tahmeen, M., Yamada, H., Kato, H., Maehata, K. and Muto, T., A Study on Simulation of Hydraulic Construction Machine, Proceeding of SICE Annual Conference, 2003, Japan, MPII-6-3, pp.363-368.

A Study on Bilateral Telecontrol of Networked Robot with Variable Time-delay

XIU Zhen*, KITAGAWA Ato*, and WU Pingdong**

* Department of Mechanical and Control Engineering
Tokyo Institute of Technology
2-12-1 O-okayama, Mekuro-ku, Tokyo, 152-8552 Japan
(E-mail: xiuzhen@cm.ctrl.titech.ac.jp)

** Mechatronics Center
Beijing Institute of Technology
Zhongguancun South Street-5, Haidian, Beijing, 100081 China

ABSTRACT

With the great advancement of Internet, the bilateral telecontrol system will enable operator to accomplish complicated tasks with haptic information all over the world. The paper emphasizes on the main problem of such system, that is variable time-delay which brought by the Internet will cause the telecontrol system to be unstable. Firstly, after the discussion about the master-slave operation and the effect of Internet to it, one kind of control architecture based on compensator, which can ensure the stability of system with constant time-delay, is proposed. Secondly, the uncertainty characteristic of the time-delay is described under TCP and UDP separately, and the problems of the two protocols in telecontrol system are presented, and also the corresponding solution is given out. Thirdly, in order to solve those uncertainty problems, using the idea of sliding mode control, the telecontrol architecture with switching compensator is investigated.

KEY WORDS

Bilateral Telecontrol, Networked Robot, Internet, Time-delay, Master-slave

NOMENCLATURE

$G_s(s)$: The whole system of slave side
 $G_M(s)$: The whole system of master side
 $G_1(s)$: The compensator for forward path
 $G_2(s)$: The compensator for feedback path
 $F_1(s)$: The time-delay of forward path
 $F_2(s)$: The time-delay of feedback path
FWP/FWO: Forward Processor (TCP)/Observer (UDP)
FBP/PBO: Feedback Processor (TCP)/Observer (UDP)
 $Z_0 / Z_e / Z_{vp}$: Impedance of master/object/pseudo-operator

INTRODUCTION

Telecontrol requires different transmission media to separate the controller and remote system. And now Internet which is the largest network with open and world-wide characteristics has provided a convenient way to develop the telecontrol system. For a few years, the improvement of Internet-based telecontrol system's performance has been studied [1]. And recently the research on the combination of Internet and master-slave system is carried on with the cooperation between Kitagawa lab in Tokyo Institute of Technology,

Japan and Mechatronics Center in Beijing Institute of Technology, China. Master-slave bilateral control can create a sense of “telepresence”, which would enable a human being to accomplish the complicated operation task with the haptic information. However the bilateral control system is greatly sensitive to the time-delay and with the variable time-delay caused by Internet the system will go to be unstable, this is the biggest problem of the telecontrol system.

For the significant aspects, many researchers have focused their attentions on the related works. Anderson and Spong proposed a control law for Master-slave system with any non-varying time-delay based on passivity and scattering theory for the first time [2]. Then Gunter Niemeyer of MIT developed this law into wave-variable and introduced Internet into the system [3], and also Munir.S and Wayne J.Book of Georgia Institute of Technology, Yasuyoshi YOKOKOHI and Teruhiro TSUJIOKA of Kyoto University in Japan have done some jobs on the wave-based subject [4-5]. Imad Elhajj and Xi Ning of Michigan State University carried their researches based on Event-Based Control [6]. Wave-based method makes a set of theory for teleoperation, but it will generate the problem of wave reflection which is a little difficult to deal with.

This paper proposed one kind of compensator-based telecontrol architecture, which will make the system into stability under the variable time-delay.

MASTER-SLAVE OPERATION METHODS

Indirect Operation and Direct Operation

In the research, a new method different from the traditional method has been developed, which considers the operator into the system [7]. Here, the traditional method was named as indirect operation, and the new method was named as direct operation.

From basic operating method for the object, indirect operation means that operator operates the object by a tool, such as robot, and when it comes to master-slave system, master robot matches to slave robot, the

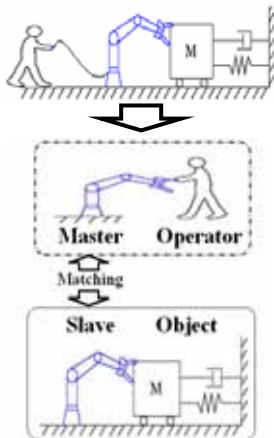


Fig.1 Indirect Operation

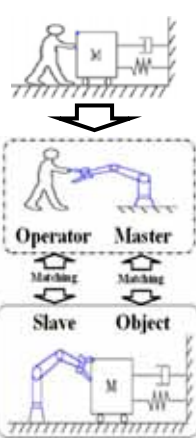


Fig.2 Direct Operation

operator operating the master feels like operating the slave. Figure 1 shows its conceptual sketch. Oppositely, direct operation method means that the operator operates the object directly, and when it comes to master-slave system, master robot matches to the object and slave robot matches to operator, the operator operating master feels like operating the object directly. Figure 2 shows its conceptual sketch.

F-F and M-F

Master-slave operation can be classified into four basic types according to the types of information exchanged between the master and slave. Here only the force-feedback system will be discussed, which includes Force-Force Transmission type (F-F) and Motion-Force Transmission type (M-F). Figure 3 shows the F-F type operation, in which force is transmitted to slave and force of object is feedback to master. Figure 4 shows M-F type, in which motion signal (velocity) is transmitted to slave and force of object is feedback to master. They are both based on the direct operation method.

Comparing the F-F and M-F type, it can be seen that their control structures are radically different. F-F type is a parallel system and M-F type is a feedback system, although they both have force feedback. Therefore the effects of Internet are different and they should have different resolutions. This paper focuses on the study of M-F type based on direct operation method.

TELECONTROL ARCHETECTURE FOR M-F

Effect of Time-delay

The original intention of the TCP/IP-based Internet emphasizes on the sharing of data resources but not the real-time transmission of data and the experiments

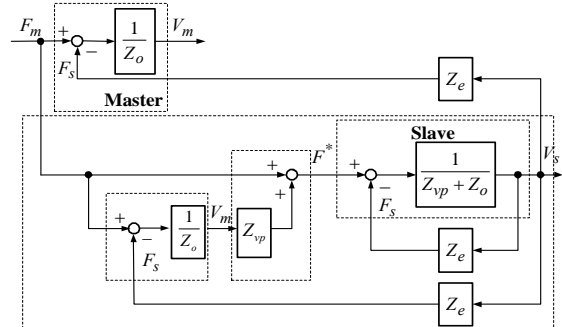


Fig.3 Force-Force Transmission Type (F-F)

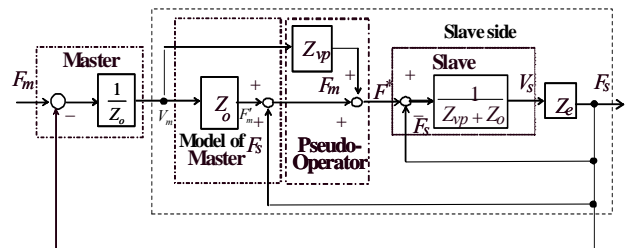


Fig.4 Motion-Force Transmission Type (M-F)

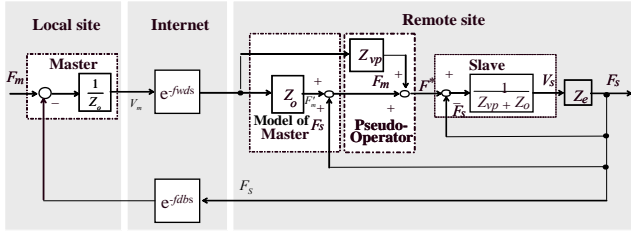


Fig.5 Introducing Internet into System

prove that there is certain network time-delay in the process of data transmission through Internet. So when introducing Internet into master-slave system, the time-delay caused by Internet will exist in the forward and feedback path, shown in Fig.5. This will worsen the performance of control system, and even cause it to be unstable. Figure 6 presents the simulation result. Sine wave signals with frequency of 1rad/s and amplitude of 100N was used as input operation force, the object was modeled as a spring, and the time-delay in forward and feedback path are both 100ms. From the result it can be seen that the force of slave can not follow the operation force and as the time goes on, the system turned to be unstable.

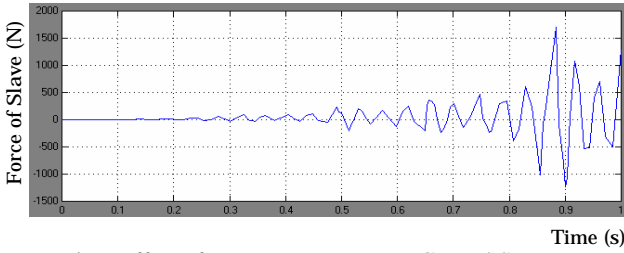


Fig.6 Effect of Internet to M-F Type Control System

Principle of Compensator

For the convenience of discussion, in this paper G_M is used to represent the whole system of master side and G_S is used to represent the whole system of slave side. The main idea of designing the compensator is to design the forward compensator $G_1(s)$ and feedback compensator $G_2(s)$ separately according to the characteristic of time-delay which exists in both forward and feedback path. The main principle of $G_1(s)$ is to estimate the dynamic model of the system and to parallel estimator with the system to compensate for the time-delay of system, to ensure the system to act ahead by trying to send the delayed control signal into system as early as possible, so the effect of time-delay in forward path can be eliminated. And the main principle of $G_2(s)$ is to remove the delay section in the equation which is appended for the effect of time-delay in the feedback path, that will ensure that the response of the telecontrol system is equal to the original system. According to the above principle, the forward compensator $G_1(s)$ and feedback compensator $G_2(s)$

are designed, which are shown in Eq.(1) and Eq.(2) separately, $F_1(s)$ and $F_2(s)$ represent the time-delay section in the forward and feedback path separately.

$$G_1(s) = F_2(s) \cdot (1 - F_1(s)) \cdot G_S(s) \quad (1)$$

$$G_2(s) = \frac{1}{1 + G_M(s) \cdot G_S(s) \cdot (1 - F_2(s))} \quad (2)$$

And the working principle of the whole compensator is shown in Fig.7, by the compensation of $G_1(s)$ and $G_2(s)$, the transformation function of the close loop is shown in Eq. (3).

$$G(s) = \frac{G_M(s) \cdot G_S(s)}{1 + G_M(s) \cdot G_S(s)} \cdot F_1(s) \quad (3)$$

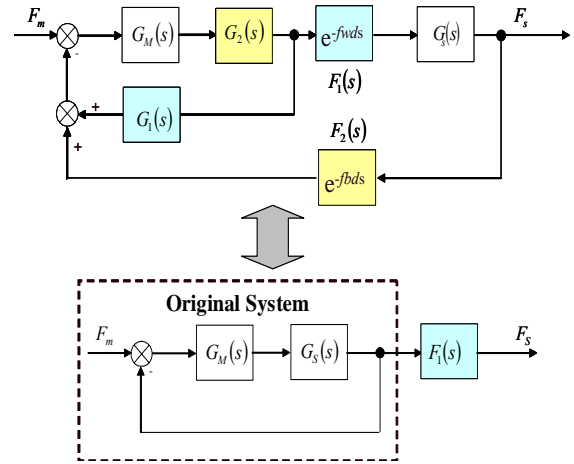


Fig.7 Principle of Compensator

From the above equation, it can be seen that lag has been eliminated which will worsen the performance of telecontrol system and the telecontrol system with compensator is equal to the original system linking with a delay section which can be seen clearly from Fig.7. However, from the Eq.(1) and Eq.(2) it can be seen that there are network time-delay sections in both of the two compensators. When the time-delay is constant and can be modeled in the compensator, the system will be stable by the principle above, but unfortunately, according to our experiment the time-delay caused by Internet may vary during the data transmission and also have many other problems, which will be discussed in the following.

TIME-DELAY CHARACTERISTIC

Figure 8 shows the time-delay of TCP and UDP data grams and its influence to signal transmission. In the experiment, sine wave signals were transferred through Internet from Beijing, China to Tokyo, Japan by data grams with the sending period of 10ms. Every point in the figures stands by a data gram. The bottom figures of both Fig.8(a) and Fig.8(b) show the time delay of TCP and UDP data grams separately over a period of 10s.

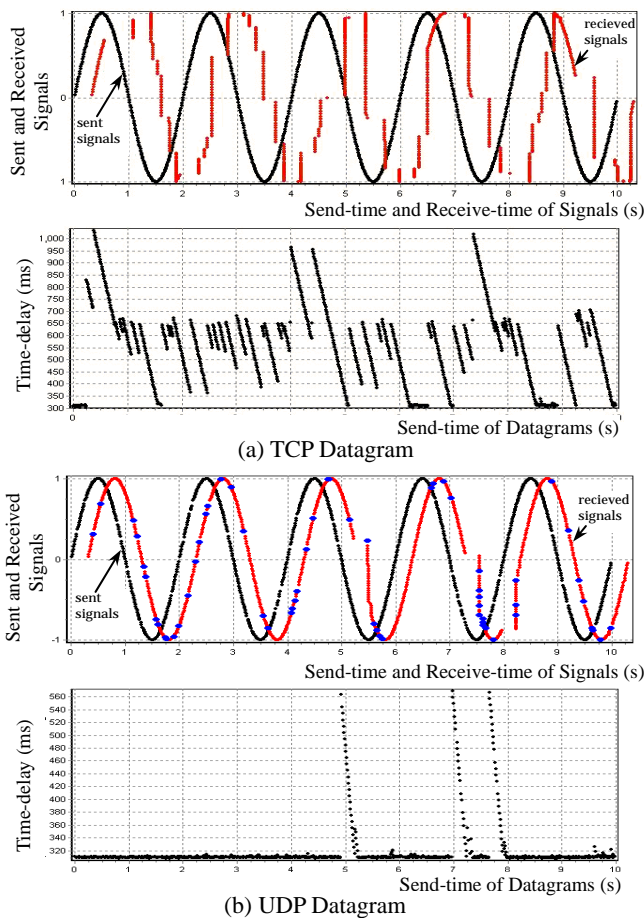


Fig. 8: Time-delay of TCP and UDP Datagrams on Internet and its Influence to Signal Transmission

The top figures of both Fig.8(a) and Fig.8(b) show the sent and received signals of sine wave. And the bigger points in the top figure of Fig.8(b) denote the lost data grams.

From the figures, it can be seen that the time-delay of Internet under both TCP and UDP have the uncertainty characteristic which is a term used to illuminate that network time-delay may vary according to events occurring all along the transmission lines, and furthermore the time-delay do not comply with any statistic standard curve according to the analyzing with tools of SPSS for windows. The uncertainty characteristic of time-delay will bring blank-sampling and more-sampling, which will bring bad effect to the control sampling system.

Also the difference between TCP and UDP can be seen clearly from the figure. TCP which is connection-based can guarantee the transmission of every datagram but will bring larger time-delay and more serious time-delay uncertainty which may ruin the shape of the sine wave, and UDP which is not connection-based has shorter time-delay and can preserve the shape of the sine wave better but can not guarantee the transmission of every datagram.

Both TCP and UDP can be used in the telecontrol

system in case that signal distortion problem of TCP and signal losing problem of UDP can be solved well. Therefore, Sampled-information Processor for TCP and Sampled-information Observer for UDP in both forward and feedback path have been used in the system.

The Processor for TCP has been introduced in the previous works [1], and the following will present the principle of Sampled-information Observer for UDP.

Sampled-information Observer for UDP

It is true that UDP data grams can be lost or duplicated, or will arrive out of order, the bigger points in Fig.8(b) show the lost or out-of-order data grams. This problem will worsen the performance of control system. So Observer for UDP was introduced into the system.

The basic idea of Observer for UDP is to make sure that the datagram sending period is smaller than the sampling period in the receiving site. And the sending period should be limited by the load capacity of the network, the sampling period should be satisfied with the Shannon theorem. Figure 9 shows an example, in which sampling period is double of sending period. So averagely, two data grams can be received in one sampling period if no datagram is lost. In case that one datagram is lost, signal in another datagram can be used as the sampled-information. Otherwise the latest information will be used as the sampled-information.

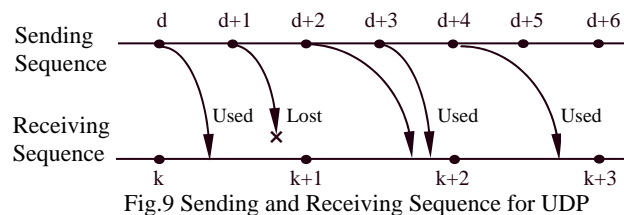


Figure 10 shows one experiment example for the signal transmission under the same network situation as Fig.8(b) using the observer, in which sending period is 5ms and sampling period is 10ms. From the figure it can be seen that the lost control information was reduced, but there is also two bigger points which means two sequential data grams were both lost at that time.

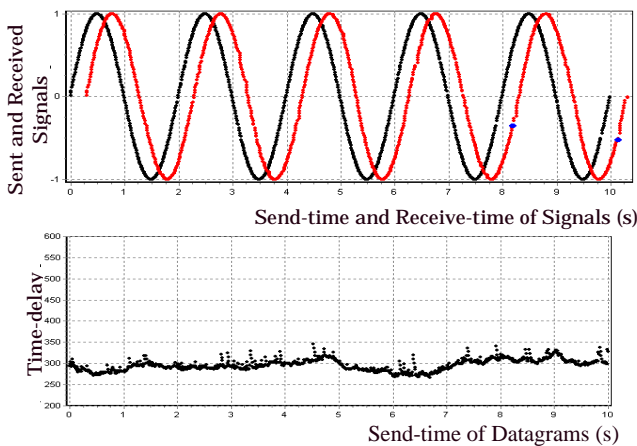


Fig.10 Signal Transmission using Observer for UDP

Accordingly the previous sampled-information can be used to minimize its negative effect to the system. Besides, the time-delay uncertainty will also exist under UDP which is just better than that under TCP. So the situation of blank-sampling and more-sampling will still happen, therefore the same strategy as used under TCP should be used to solve those problems. Although the Processor for TCP and Observer for UDP can lessen the adverse effect of the uncertainty time-delay and data losing caused by network, the stability of system can not be ensured substantially, the compensator presented in the last section must be advanced, which will be discussed in the following.

TELECONTROL ARCHITECTURE WITH SWITCHING COMPENSATOR

By transforming the compensators given by Eq.(1) and Eq.(2) into block diagram, putting them into Fig.7 and making a simplification, eventually the system can be transformed into the block diagram shown in Fig.11, and also the processor or observer discussed in last section are included in the system.

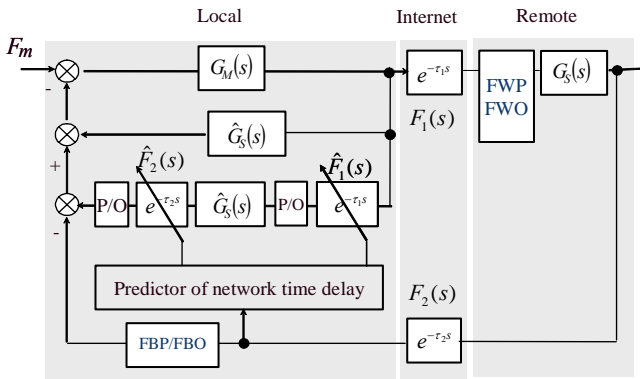


Fig.11: Telecontrol System with Time-delay

The control architecture discussed above is model-based, and the models of time-delay and remote system are used in the compensators, so the uncertainty of those two parts will have adverse effect to the system's stability, in another word, the system's robust. Because the problem of time-asynchronization between the local and remote computer system, the half loop time-delay is so difficult to get, and also because the time-delay is so irregular, the prediction of the time-delay which was tried with structure shown in Fig.11 has been proved to be a hard task to realize.

Sliding mode control which is an important robust control approach provides an effective way to the problem of maintaining stability and consistent performance in the face of modeling imprecision. Using the idea of sliding mode control, this section investigates one kind of switching compensator to deal with the problem of model uncertainty. The telecontrol architecture with switching compensator is shown in Fig.12.

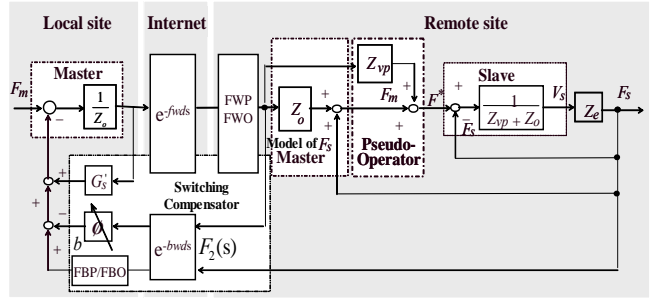


Fig.12 TeleControl Architecture with Switching Compensator

The structure of variable adjustor Φ in the controller will be dynamically switched according to different situations of the received feedback signal to let the whole system satisfy the principle discussed above. Actually, the model of the slave system in the sliding mode architecture and the master system in the local site would compose a close loop which will equal to the original system, so using the variable adjustor Φ to build a virtual loop to reduce the negative affectation caused by the delayed feedback signal can ensure the stability of the whole system.

And also it can be seen that the input signal of variable adjustor Φ is the control signal passing through forward and feedback path, so the compensator will include the real Internet time-delay sections of both forward and feedback path, and the modeling of this two parts are not needed in the local compensator, that is to say, the forecast for the time-delay of Internet is not necessary, this will make the compensation more accurate and effective. As a result, the adjustor Φ only needs to switch to different constructions every sampled-period by the three different sampling situations of the local site, which are blank-sampling period, single-sampling period and multi-sampling period.

And the basic idea to design the variable adjustor Φ is to let it satisfy Eq.(4) at any situation to the best of its ability.

$$\phi \times F_2(s) = \text{FBP}(s) \times F_2(s) \times G_s(s) \quad (4)$$

Because $\text{FBP}(s)$ will have different structure at different sampling situation, in order to be satisfied, the variable adjustor Φ will switched among three structures according to the different sampling situation which can be decided by the comparing between the received-time information of the corresponding datagram and its above datagram every sampling period.

Considering the local sampling period of No. i , the adjustor Φ can designed as the following.

In case of single-sampling situation, Φ can be designed as Eq.(5):

$$\hat{x}(i) = \hat{A}\hat{x}(i-1) + \hat{B}u(i-1) \quad (5)$$

$$b(i) = \hat{y}(i) = \hat{C}\hat{x}(i)$$

In case of blank-sampling situation, Φ can be designed as Eq.(6):

$$b(i) = b(i-1) \quad (6)$$

In case of multi-sampling situation, Φ can be designed as Eq.(7):

$$x'(i) = \hat{A}^m \hat{x}(i-m) + \sum_{k=0}^{m-1} [\hat{A}^{m-1-k} \hat{B} u(i-m+k)] \quad (7)$$

$$b(i) = \hat{y}(i) = \hat{C} \hat{x}(i)$$

Where $b(i)$ is the output of variable adjustor Φ which can be seen from Fig.12, and \hat{A} , \hat{B} , \hat{C} are the state equation parameter matrixes of the remote system model.

SIMULATION RESULT

In order to prove the validity of the compensator discussed above, the simulation system was done based on the architecture shown in Fig.12, in which sine wave signals with frequency of 1rad/sec and amplitude of 100N were used as input operation force, the object was modeled as a spring, which are the same conditions as those in the simulation shown in Fig.6. And the time-delay in the forward and feedback path are shown in Fig.13, which are time-delay measured under UDP protocol from Beijing, China to Tokyo, Japan. Figure 14 shows the simulation result, from which it can be seen that the system has turned to be stable and force of the slave can follow force of the master with a certain lag and some disturbances. And here the lag is caused by the time-delay and the disturbances are caused by the blank-sampling and multi-sampling which are generated by the uncertainty characteristic of time-delay. And it should be pointed out that in the simulation the master and the slave knew nothing about the time-delay.

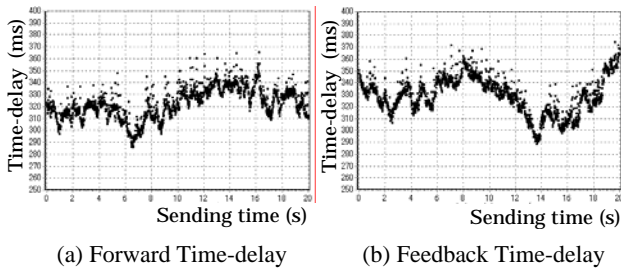


Fig.13 Network Environment in the Simulation

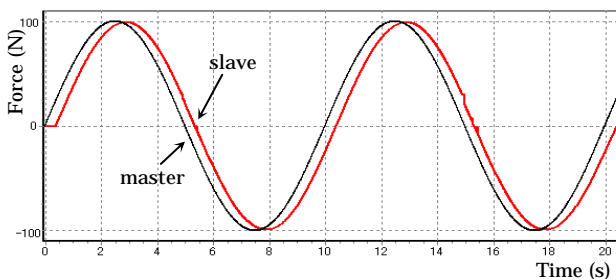


Fig.14 Simulation Result of the Telecontrol System

CONCLUSION AND FUTURE WORKS

This paper presented the research on bilateral telecontrol of networked robot with variable time-delay. And Internet was used as the communication media for its convenience. Firstly, one kind of control architecture was brought out according to the corresponding master-slave operation method to solve the unstable problem caused by time-delay existing in forward and feedback path. Secondly the uncertainty characteristic of time-delay was presented with the comparing between the different situations under TCP and UDP protocols, and their problems were discussed. The paper has focused on the UDP, which is not aimed to show that UDP is better than TCP when used in telecontrol system. Both TCP and UDP have their strongpoints and their problems in telecontrol system. The proposed sampled-information observer for UDP can reduce the losing control signals under UDP. And after that the telecontrol architecture with switching compensator which can maintain the system's stability in face of the uncertainty time-delay is investigated. And this will be a good approach to solve the problem of uncertainty of the object in the near future; also the application robot is planned to be developed.

REFERENCES

1. Jie Huang, Ping-dong Wu, Zhen Xiu, Compensator in Internet based telecontrol system. IEEE the Second International Conference on Machine Learning and Cybernetics. VOL .11, pp. 818-823, 2003.
2. Anderson, Spong, Bilateral control of teleoperators with time delay. Proceedings of the 27th Conference on decision and Control, Austin, Texas, 1988.
3. Gunter Niemeyer, Towards Force-Reflecting Teleoperation Over the Internet. Proceedings of the 1998 IEEE International Conference on Robotics and Automation, Leuven, Belgium, 1998.
4. Munir.S, Wayne J.Book, Internet-based teleoperation using wave variables with prediction. IEEE/ASME TRANSACTIONS ON MECHATRONICS, VOL. 7, pp.124-133, JUNE 2002.
5. Yasuyoshi YOKOKOHI, Teruhiro TSUJIOKA, Bilateral Control with Time-Varying Delay including Communication Blackout. Proceedings of the 10th Symp. On Haptic Interfaces for Virtual Envir. & Teleoperator Sys. (HAPTICS'02), 2002.
6. Imad Elhadj, Xi Ning, Real-time control of Internet based teleoperation with force reflection. Proceeding of the 2000 IEEE International Conference on Robotics & Automation, San Francisco, CA. 2000.
7. Canghai LIU and Ato KITAGAWA, Impedance Control of Hydraulic Master-Slave Robot. 2nd FPN International Scientific Forum on Developments in Fluid Power Control of Machinery and Manipulators, pp.113-116, 2000.

FAULT DIAGNOSIS OF ELECTROHYDRAULIC SYSTEMS

Oscar VILLALOBOS*, Colin BURVILL* and Jacek STECKI**

* Department of Mechanical and Manufacturing Engineering, Faculty of Engineering
The University of Melbourne
Grattan Street, Parkville, 3010 Australia
(E-mail: colb@unimelb.edu.au)

** Maintenance Technology Institute, Monash University, Australia
(E-mail: jstecki@fluid.power.net)

ABSTRACT

Reliability is essential for electro-hydraulic systems due to the high energy densities associated with their operation. A failure can have catastrophic results, for example, if a contamination failure of hydraulic fluid at high pressure occurs. A novel approach for fault diagnosis of hydraulic systems has been proposed, using genetic algorithms as the parameter optimization method, and model based simulation. Performance tracking of critical parameters within the hydraulic system assesses subtle state changes and attempts to identify failure modes associated with these state changes. The proposed approach, which requires analysis of each component of the hydraulic system under normal operation and with specific, induced failure modes, has been successfully applied to a hydraulic system incorporating a servovalve and linear actuator. The results of this study provide a basis for future studies of more complex hydraulic components and systems.

KEY WORDS

electro-hydraulic systems, fault diagnosis, modeling, performance tracking, genetic algorithms

INTRODUCTION

Mechanical systems in general can be expected to develop faults if operated for any length of time. These faults need to be detected and identified, preferably at an early stage before they become compounded. There would be clear advantages if an automated system were used to monitor the performance of a complex mechanical system, providing early warning fault conditions. A monitoring system would need to recognize faults in specific components in particular those that are central to the best and safe operation of the mechanical system.

This paper reports on the performance of fault diagnosis tasks by applying model-based and optimization techniques, which aims to detect potential and on-going

failures in electro-hydraulic systems, by looking at small changes at the state of the hydraulic system that could be associated with typical or expected failure modes. Reliability is essential for electro-hydraulic systems due to the high energy densities associated with their operation. A failure can have catastrophic results, for example, if a containment failure of hydraulic fluid at high pressure occurs.

A novel approach for fault diagnosis of hydraulic systems has been proposed, using Genetic Algorithms (GA) techniques as part of the optimization method used, and parametric model-based simulation. Performance tracking of critical state parameters within the hydraulic system assesses subtle state changes and attempts to identify failure modes associated with these state changes. The proposed approach requires the

analysis of each component of the hydraulic system under normal operation and with specific, induced failure modes. A detailed study has been completed on one sub-system: a servovalve and linear actuator configuration. This study provides a template for future studies of other hydraulic components.

While GA toolbox used was developed by [1] and MatLab/Simulink used as the simulation software, the combination of GA and a parametric simulation model is an innovative contribution to the field of fault diagnosis in hydraulic systems.

Experimental results show that the developed diagnosis algorithm can detect and classify small changes in state parameters of the hydraulic system due to controlled and induced failures [2]. However, when sudden step changes are induced to the hydraulic system, the developed diagnosis algorithm has only been able to detect the abnormal behavior of the hydraulic system.

An advantage of the developed technique is the reusability of the knowledge introduced in the monitoring system. This benefit provides a good flexibility of the software that could be fitted into other application, in which the basic engineering rules may only be changed.

HEALTH MONITORING OF MECHANICAL SYSTEMS

Health monitoring systems perform two basic tasks: diagnosis and prognosis of failures. Fault diagnosis assesses the state of a mechanical system and performs an automated diagnosis to evaluate potential failures. Fault diagnosis may be subdivided into fault detection and fault classification stages, where the former triggers the latter by detecting possible failures in the system. After detection, the monitoring system classifies the fault into its most probable failure mode. Features of the classification algorithm usually are part of the monitoring system's requirements and can be addressed towards the end user. Some examples of this final classification: Clogged filter / Critical failure, "*stop the machine*"; Electronic controller failure / Abnormal system event, "*call service personnel*"; Pressure sensor communications lost / System abuse, "*change mode of operation*".

Fault prognosis is concerned with the estimation of potential future failures and the associated implication to the mechanical system, for example [3, 4; 5]. For example, prognosis aims to enhance maintenance planning and scheduling of expected failures [6].

EXPERIMENT SETUP AND TEST RIGS

This section outlines the test rig development. When setting up the experiment, it was necessary to accommodate possible variables that, if overlooked, may adversely impact upon the results. The number of

uncertainties is minimized in the experimental test rig by eliminating erroneous inputs that may affect the desired output, maximizing the certainty of experimental repeatability.

An accumulator was used at the inlet pressure port of the servovalve. It was found that a sudden change in spool speed direction, associated with the change of movement of the actuator, causes high ripples that the input line cannot compensate. This ripple caused undesired pressure spikes in the resulting outputs. The pressure at the inlet pressure port rises sharply when the actuator starts changing direction.

Pressure transducers were used in both chambers of the linear actuator. The analog signal from the pressure transducers is proportional to the measured pressure, and a conversion chart was generated to determine pressure from the analog voltage value. The actuator drive command signal was acquired from the test rig. This signal drives the servo-valve's torque motor.

FAILURE MODES CONSIDERED

The scope of the completed study focused on functional failures, which occur when one or more of the target functions are lost. In addition, degradation failures are sought in this work, which are difficult to detect and if so, the standard procedure involves manual troubleshooting that is time consuming and sometimes low in accuracy of its results.

Clogged filter: This failure mode considers a clogged filter in the servovalve's pilot line. In order to reassemble the blockage condition, a restrictive nozzle (orifice) was used to throttle the oil flow going to spool end chambers. An adapter was manufactured to hold the orifice in position and replace the original filter. The new orifice does not filter pilot oil, but decreases pilot pressure to values that can be adjusted by changing the size of the orifice.

The original filter adapter was machined and modified to hold the new orifice adapter. Pilot pressure was measured at both spool end chambers using custom manufactured end plates, with integrated pressure ports, installed on both sides of the valve body.

Pressure gauges on an existing hydraulic test rig were used to measure the reduced pilot pressure. Pressure gauges measured pilot pressures at both sides of the spool, and supply pressure.

The function of the flapper-nozzle valve is to create an unbalanced pressure differential between both chambers at spool ends. The spool moves from one side to the other within the bushing according to this pressure differential. Merritt [7] argues that the optimal pilot pressure for flapper-nozzle servovalves occurs at a value of half of the supply pressure. This optimal value gives the maximum pressure sensitivity and is considered as a design criterion. Two thirds of supply pressure is the nominal design value for pilot pressure in

two stage servovalves. Experimental results in this work produced a pilot pressure between half and two thirds of supply pressure.

Broken feedback wire: The ball at the end of the feedback wire was removed to reproduce this type of failure. The backlash between the broken end of the feedback wire and the hole in the spool increases dramatically with this failure mode. Two torque motors were used in these tests (i.e. one with a normal feedback wire and the other with a broken feedback wire).

Sticky spool: Guillon and Griffiths [8] analyzed valve sticking in a generic spool. They argue that the most common method to reduce spool sticking on the bushing is to groove the spool in order to reduce pressure that creates unbalanced radial forces, which may push the spool against the bushing. The unbalanced pressure may induce high forces between the spool and bushing creating large amounts of heat.

Another cause of valve sticking is the presence of contaminants such as lacquers that would produce a physical contact between the spool and the bushing. This failure mode increases the friction between the latter elements by the addition of foreign material. Given that this study focused on failure modes induced by oil contamination, the second failure mode for spool sticking was selected.

In order to reassemble the increased spool-sticking force, two grooves were machined at both side ends in the spool. Pairs of rings were then fitted onto each spool end: one o-ring and one friction ring. The o-rings provide the spring effect that pushes the friction ring against the bushing.

SIMULATION MODEL

The development of a theoretical model for the hydraulic arrangement (figure 1) implemented theory developed by other researchers, in particular, [9, 10, 11, 12, 13], and the authors, to generate the appropriate simulation equations.

The simulation includes input signals that come from the test rig, such as fluid pressure, valve drive and piston position. Initial position conditions are recorded at the particular sampling data file that is being assessed for failures, such as initial pressures and positions. The two active components under investigation are the servovalve and associated actuator.

Hydraulic model development. The servovalve simulation “block” design is a third order equation model that contains two additional blocks that correspond to each of the servovalve’s stages. The actuator simulation design incorporates the position transducer, which is a Linear Variable Differential Transformer (LVDT) that is located inside the cylinder rod, and three cylinder chambers. Including additional sub-systems, such as line pressure drop and hose

expansion, increases the accuracy in the simulation output plot. The implication of these sub-systems in the simulation was assessed.

Servovalve simulation design. A third order model, used for the servovalve design, located in the armature-flapper valve block. The model structure was developed with a “tune-up” phase using specifications from the manufacturer.

The armature-flapper valve model tune-up procedure included: *Frequency response tune-up:* Preliminary sensitivity trials showed that hydraulic gain parameter has the most significant influence in model design performance); and, *Step response tune-up:* A 50mA step signal was used as the input signal to the proposed simulation design. The chosen hydraulic gain most precisely models both frequency response and step response specifications of the chosen servovalve in the experimental test rig.

Additional simulation blocks were incorporated in the simulation design to include potential non-linearities caused by failures in the servovalve: *Saturation block:* Limits the maximum electrical current that can be applied to the torque motor; *Threshold block:* Models the minimum pressure required to overcome the coulomb friction between the spool and the bushing from rest; *Supply and Return pressure compensation block;* *Filter and orifices restriction block.*

Spool flow dynamics model. A novel representation of the pressure-flow fluid in the spool was developed, incorporating the overlap and leakage flow at null, which was assessed in the overall diagnosis algorithm.

Actuator simulation design: The simulation is first adjusted to match published specifications from the manufacturer. Adjustments are associated with frequency and step response. Geometric and functional parameters associated with actuator function were measured and grouped as either model or state parameters, 7 and 6 parameters, respectively.

System issues (adjunct components): The simulation accommodates the effect of the compressibility of oil at each of chambers; describes the relationship between flows and pressures in chambers; applies Newton’s second law to the piston to define its dynamic behavior; and, models the non-linear performance of the hoses associated with the test rig (pressure drop and expansion). Hydraulic flow resistance is caused by irregularities on the internal hose walls and capillarity, which are converted into a temperature increase in the fluid and is often associated with power losses [7]. Loss coefficient values for hydraulic fittings, manifolds, lines and valves were used [14].

MODEL PARAMETERIZATION

The simulation model developed contained 41 model parameters. A two dimensional array was used to

represent parameter information: nominal parameter values that best describes a fault-free condition of the servovalve-actuator hydraulic system; the minimum and maximum boundary values of the associated parameter (the useful operational range within the simulation); whether the parameter will be considered in the optimization algorithm or not (*0* not included, *1* included); and, a description of the parameter and its associated units. The parameters are grouped in the array in accordance with the simulation block to which they correspond: Group 1: First stage of the servovalve; Group 2: Second stage of servovalve; Group 3: Linear actuator model; and, Group 4: Adjunct components. Sources for quantitative data associated with the parameters: measured from the existing laboratory equipment; test rig experiments; data from [7, 14, 15] and manufacturer specifications; calculations using the servovalve's specification; and, comparing simulation data recorded from the test rig with simulation outcomes.

FAULT DIAGNOSIS ALGORITHM

The diagnosis algorithm contains both automated and manual features to process sample data from the test rig, and using the simulation model, to assess their similarities, which are expressed in terms of the simulation error. An increased simulation error corresponds to a reduced similarity. The algorithm aims to detect subtle changes in the sampled data coming from the test rig by performing a continuous on-line evaluation of the simulation error and attempts to classify the detected failure by optimizing model parameters that best match faulty data. Two types of data are used by the diagnosis algorithm: *sample data* acquired from the test rig by the data acquisition hardware; and, *simulation data* calculated by the simulation model. Genetic Algorithms (GA) were found to be the most appropriate optimization method to find the new set of model parameters that would reduce the simulation error below the required threshold. The following paragraphs outline features of the fault diagnosis algorithm.

Objective function: Reflects relevant, targeted functions of the hydraulic system, sub-systems or components and assesses their associated performance.

Filtering: A low pass analog filter was used between the test rig and the data acquisition hardware. Another two filters were used in the diagnosis system to process the sampled data acquired from the test rig: the moving average filter to smooth sample data coming from the test rig; and, a conventional notch digital filter design was used to remove 50Hz noise digitally.

Parameter tune up: The diagnosis algorithm has a self-tuning feature that takes sampled data that is free of failures, to tune-up nominal model parameters. The algorithm evaluates the effectiveness of each parameter

in the sampled data string, by changing its value to the minimum and then to its maximum.

Fault detection threshold determination: A small value of threshold error would trigger the diagnosis system too early and may introduce false alarms.

Simulation step time: Preliminary analyses were carried out with a fixed simulation step time of 1e-5 seconds, which was found to provide enough resolution to identify all significant features within the input data.

Parameter finding approach: GA methods are used when multiple model parameters are being optimized simultaneously. An advantage of GA is that a group of model parameters can be divided in sub-groups, whereas each group can include a different Failure Mode Identifier (FMI) to initiate the model.

Model parameter selection criteria: There are always redundant model parameters (attributes), that must be set to their constant nominal value (i.e. discarded) before the model parameters are incorporated in the GA loop. Otherwise they would provide redundant solutions to the optimization process, and hence, there is no unique arrangement of model parameters that satisfy the optimization routine.

Null adjustment: There are some state variables in hydraulic systems that do not produce a system failure when they are not working at their nominal operational condition (i.e. out of calibration). It was experimentally found that a state variable associated with this event is an uncalibrated servovalve null.

ANALYSIS OF DIAGNOSIS ALGORITHM PERFORMANCE

Two types of experiments were performed using the diagnosis algorithm: *type-1* using the diagnosis algorithm alone (three sets of experiments – these experiments analyse the performance of the features included in the diagnosis algorithm prior to the analysis of real data from the test rig); and, *type-2* using actual sampled data from the test rig in the diagnosis algorithm (three sets of experiments). A total of 35 trials of the type-1 experiments were performed, and a total of 116 trials of the type-2 were completed using the data from the test rig.

Self diagnosis analysis: Experiments sought to determine the performance of: parameter tune-up; automated model parameter selection; and, self diagnosis simulation. The diagnosis algorithm was not able to determine any combination of simulation parameters that reduced the simulation error below the threshold, although parameters 1 (i.e. valve filter blockage ratio: positive speed) and 2 (valve filter blockage ratio: negative speed) are able to represent a high clogged condition of the servovalve filter. A summary of some of the conclusions reached following these experiments: **1.** Only small variations in model parameters values can lead to a successful classification

of failures. Large changes in the sample data caused by failures in the hydraulic system may lead to erratic solutions associated with different combinations of model parameters. **2.** A population of 50 GA “individuals” provides classification results similar to 100 individuals. Simulation cycle times are dramatically reduced by using the 50 individual population size. **3.** Low classification performance in some model parameters results in the number of model parameters that can be used simultaneously being reduced considerably.

Experimental analysis: Clogged filter A clogged filter fault has an associated condition where the pilot pressure at the servovalve is reduced. A series of different pilot pressure values were manually measured in test rig. A pilot pressure greater than 50% of supply pressure was found in all the experiments using a fault free servovalve. When the restrictive orifice was used to replicate a clogged filter condition, the pilot pressure dropped significantly. Simulation results obtained for this failure mode are in accordance with observations and show that the diagnosis algorithm can successfully recognize the introduced clogged filter condition in the servovalve.

Experimental analysis: Broken feedback wire There are two failure modes found in the experiments that can develop when the feedback wire is broken: *increased backlash* (i.e. the feedback wire is still located in the spool hole, but the backlash between the feedback wire and spool hole is high due to the absence of the feedback ball) and *loss of feedback* (i.e. occurs when the feedback wire is too short and cannot reach the spool hole). When the drive command signal is disabled, the final null position is affected by the force from the feedback wire pressing against the spool. This results in an erratic null position when the servovalve is at idle, that may exceed normal operational limits. In addition, spool position feedback is lost and the valve acts as a proportional valve, only.

The servovalve was observed to behave differently during experimental trials, depending on which sub-failure mode is in effect. Pilot pressure considerably increased when the loss of feedback failure mode occurred, reflected as an increased hydraulic gain. Simulation model parameters associated with this failure mode are: hydraulic amplifier gain (parameter 6); valve glitch (parameter 9); and, servovalve null (parameter 41). The variation in the three model parameters can be matched with the induced failure modes, because when there are no failures introduced in the test rig, the diagnosis algorithm selects the nominal model parameter values (i.e. no failure condition) as a result of the classification. When the model parameters 6, 9 and 41 are compared against their nominal values in this set of experiments, broken feedback wire

sub-failure modes can be qualitatively identified.

Experimental analysis: Sticky spool This failure mode is caused by the blockage of spool travel by contaminants between the spool and the bushing. The maximum unbalanced force for the servovalve under investigation can be calculated [7].

The sticky spool failure mode was introduced through the use of o-rings located at both ends of the spool. The o-ring specifications used, and the squeeze factor on each o-ring between spool and bushing, were used to calculate the radial diameter variation in the o-rings after being mounted. The o-rings modified the servovalve’s performance, but performance remained within acceptable specification limits.

O-ring influenced servovalve performance results were introduced into the diagnosis algorithm. The increase in the sliding friction force introduced by the o-rings produced a close correlation between the simulation output and the actual hydraulic test rig output, even though no failure was apparent. As the experimental servovalve was not available for testing to destruction, more significant friction inducing components could not be introduced to a modified spool. This will be the subject of future study.

Sticky spools are a significant problem in hydraulic systems, but the underlined cause is not well understood [8].

CONCLUSIONS

This paper describes research that demonstrates that model-based simulation and optimization techniques can be used to diagnose failures in electro-hydraulic systems. The research identifies new opportunities to further develop automated tasks that can dramatically increase the availability and reliability of electro-hydraulic systems. The following specific tasks has been completed: development of a simulation model that replicates in detail the electro-hydraulic system used in the test rig; validation of the simulation model with real sampled data; parameterization of the simulation model with real sampled data: creation of model parameters; development of the diagnosis algorithm to optimize model parameters and match real sampled data; and, analysis of the diagnosis algorithm performance. The diagnosis algorithm facilitates the analysis of subtle changes in the state parameters of electro-hydraulic systems. The simulation experiments have shown successful results when diagnosing some subtle failure modes (i.e. clogged filter and broken feedback wire) introduced in the servovalve, but not in other experiments associated with almost imperceptible failure modes (i.e. sticky spool). However, the simulation of the servovalve performance close matches observed servovalve behavior.

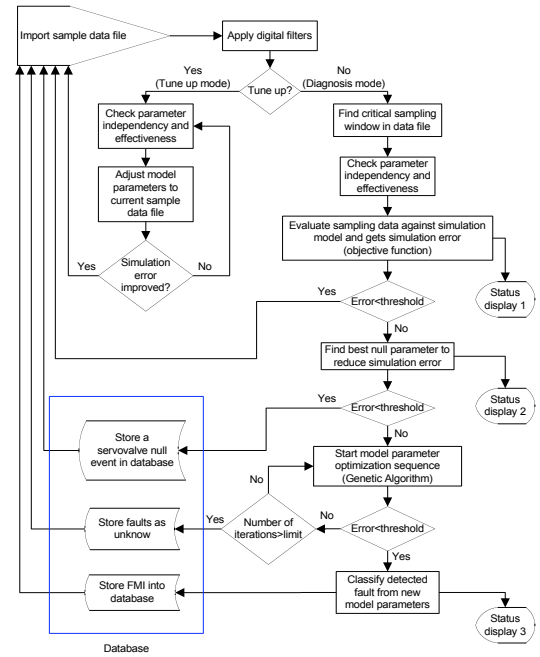
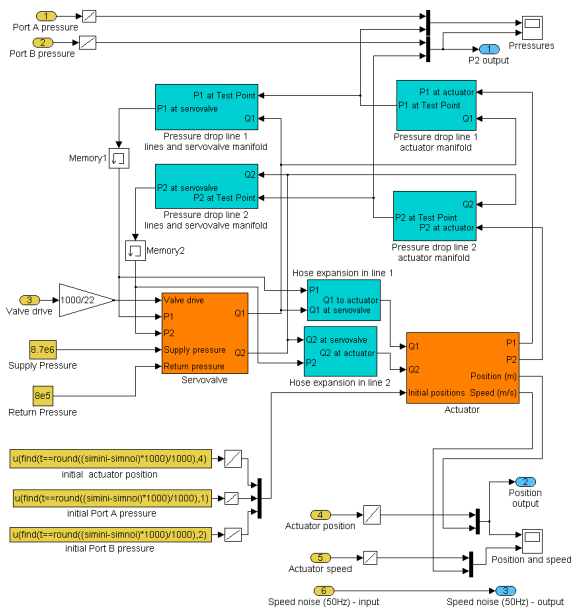


Figure 1. Left: Simulation Model layout (yellow blocks = inputs, blue = outputs, orange = two active components under investigation, i.e. servovalve and linear actuator), and green = adjunct components
 Right: Fault diagnosis and tune-up flow diagram.

REFERENCES

1. Chipperfield A., Fleming P., Pohlheim H., Fonseca C. "Genetic Algorithm Toolbox, for use with MatLab – User's Guide" Version 1.2 (1994), Department of Automatic Control and Systems Engineering, The University of Sheffield.
2. Villalobos, O. "Fault Diagnosis of electro-hydraulics systems", Master of Engineering Science thesis, The University of Melbourne, 2003
3. Engel, S.J., Gilmartin, B.J., Bongort, K., Hess, A. "Prognostics, the real issues involved with predicting life remaining" IEEE Aerospace Conference Proceedings, Vol 6 (2000), pp 457–469
4. Smith, G., Schroeder, J.B., Navarro, S., Haldeman, D. "Development of a prognostics and health management capability for the Joint Strike Fighter" AUTOTESTCON '97, IEEE Autotestcon Proceedings, Sep 22-25 (1997), pp 676–682.
5. Byington, C.S., Roemer, M.J., Galie, T. "Prognostic enhancements to diagnostic systems for improved condition-based maintenance" IEEE Aerospace Conference Proceedings, Vol 6 (2002), pp 6-2815 - 6-2824.
6. Angeli, C., Chatzinikolson, A. "Prediction and diagnosis of faults in hydraulic systems" Proc ImechE, Vol 216, Part B, J Engineering Manufacture (2002), pp293-297.
7. Merritt, H. E. "Hydraulic Control Systems" John Wiley & Sons, New York, NY, 1967.
8. Guillon, M., Griffiths, R. T. "Hydraulic Servo Systems, Analysis and Design" Butterworth & Co. Ltd, 1969.
9. Book, R., Goering, C. E. "Load Sensing Hydraulic System Simulation" Applied Engineering in Agriculture, 1997 American Society of Agricultural Engineers, Vol 13(1), pp 17-25.
10. Edge KA, Brett PN & Leahy JC. "Digital computer simulation as an aid in improving the performance of positive displacement pumps" Proc.I.Mech.E. Vol. 198, No.14 (1984), pp. 267-274.
11. Eryilmaz, B., Wilson, B.H. "Modeling of hydraulic servovalves with internal leakage" Proceedings of the ASME Dynamic Systems and Control Division, Nov 2000.
12. Hsue, C.Y, Hullender, D.A "Modal approximations for the fluid dynamics of hydraulic and pneumatic transmission lines". Fluid transmission line dynamics, ASME, H00278 (1983), pp. 51-77.
13. Pollmeier, K, Burrows, CR & Edge, KA. "Mapping of large scale fluid power system simulations on a distributed memory parallel computer using genetic algorithms" 1996 ASME International Mechanical Engineering Congress and Exposition, Atlanta, Georgia, USA, November 17-22, 1996.
14. Stecki, J. S., Garbacik, A. "Design and Steady-state Analysis of Hydraulic Control Systems" Fluid Power Net, Melbourne, Australia, 2002.
15. Thayer, W. J. "Transfer Functions for Moog Servovalves" Technical Bulletin 103, Moog Inc, Controls Division, East Aurora, NY, 1965.

ADVANCES IN AUTOMOTIVE HYDRAULIC HYBRID DRIVES

Jacek Stecki and Paul Matheson

Department of Mechanical Engineering, Monash University, Melbourne, Australia.
E-mail stecki@eng.monash.edu.au

ABSTRACT

The consumption of fossil fuels is one of the largest problems facing humankind. One of the heaviest users of our non-renewable resources is the automotive industry, in particular, the heavy road transport sector. Tightening worldwide legislation aims to place restrictions on the heavy transport industry to reduce its use of fossil fuels and reduce the levels of pollution being released to the atmosphere. Although several different alternatives to the conventional Internal Combustion Engine (ICE) have been investigated, none have as yet become a competitive source of energy. Alternative research into development of hybrid-drive vehicles was specifically concerned with electric hybrids especially for passenger vehicles. Currently there is a resurgence of interest in the Hydraulic-type Hybrid Vehicle (HHV) in application to commercial and to a lesser degree to large passenger vehicles. This paper gives an overview of hydraulic hybrid technology.

KEYWORDS

Hydraulic hybrid, pumps, motor, hydrostatic drive

INTRODUCTION

Hybrid vehicles are not a new concept; Justus B. Entz built the first petrol-electric hybrid vehicle in 1897 [1]. At the time of its development the electric system was mainly included to assist the acceleration of the internal combustion engine (ICE). Shortly after this prototype was built the capabilities of subsequent ICE's improved and removed the necessity to include the electric motor. Interest in hybrid vehicles resurged in the 1970's following the oil crisis and was driven by perceived advantages of hybrid drives [2]. Several different types of hybrid have been considered in the past and are still undergoing extensive research. The development of Electric Hybrids Vehicles (HEV's) which use a motor/generator and battery packs, resulted in commercial availability of such vehicles [3]. Mechanical

Hybrid Vehicles (MHV's), which use flywheels to store energy were less successful in commercialization, although a number of such vehicles were tried [4]. Hydraulic Hybrid Vehicles (HHVs), which use hydro-pneumatic accumulators to store kinetic energy captured during braking and return energy to driveline during vehicle acceleration, reemerged only over the last few years as viable technology, especially in applications to larger vehicles. The development of Hydraulic Hybrid Vehicle (HHV) is the main topic of this paper.

HYDRAULIC HYBRID CONFIGURATIONS

A generic model of a power flow in a powertrain has three internal power paths, Figure 1. In general, there is a power flow between three basic components: the engine ICE (the primary source of power), the wheel W

(transfer of motive power to the wheels) and the storage ESU (a generic device able to store and release energy). The energy storing capability the ESU block can be implemented in several ways, the most common being electrical, mechanical, and hydraulic. Using combinations of different paths we may derive three basic powertrain schemes.

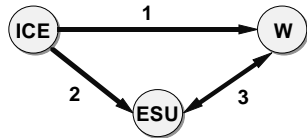


Figure 1 Generic power flow model

In Scheme 1, there is no ESU and the first possible energy converter between ICE and W (path 1) is the standard closed circuit hydrostatic transmission with a variable pump connected to a fixed or variable motor (with proper additional subsystems for boosting, limiting pressure and fluid replacement) and possibly complemented by a mechanical gearbox, Figure 2. In principle, a similar solution is offered by the so called hydromechanical units where the power follows two paths, one through shafts and gears, and the other through a hydrostatic transmission.

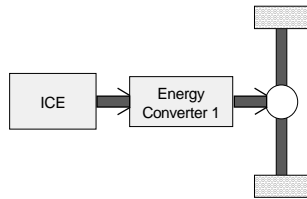


Figure 2 Conventional driveline layout (Scheme 1)

In Scheme 2 (serial - paths 2 and 3) the energy converter is a closed circuit hydrostatic transmission with a variable pump connected to a reversible motor (i.e. motor displacement can go from zero to maximum in both directions) and an accumulator in a high pressure line. The transmission, which is also known as secondary controlled transmission, has the usual additional subsystems and can be complemented by a mechanical gearbox. The primary feature of the transmission is its ability to recover a certain percentage of the braking energy of the vehicle. This scheme offers a looser link between the speed of engine and wheels thus making possible to have more efficient engine operation. In principle, a similar solution could be implemented using a hydromechanical unit. Figure 3 shows the driveline layout for the series hybrid vehicle. Energy converter 1 represents a pump in a hydraulic circuit whereas energy converter 2 represents a hydraulic motor. With the series hybrid, the ICE is effectively uncoupled from the road, i.e., the operation of the engine is independent of the vehicle operation. The vehicle is capable of regenerative

braking to recharge the storage device, or by using the ICE, either during driving or when the vehicle is stationary.

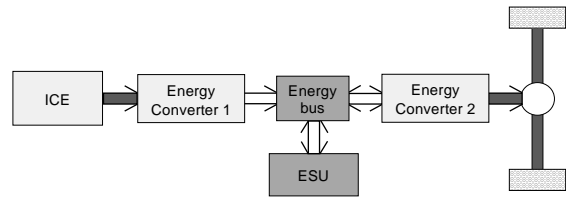


Figure 3 Serial driveline layout (Scheme 2)

In Scheme 3 (parallel – path 1 and path 3) a conventional mechanical transmission is inserted between the engine and the wheel block (path 1), while a hydrostatic reversible unit is inserted between the wheels and the storage block ESU, i.e. the accumulator (path 3). The driveline layout for the parallel hybrid (power assist, launch assist or add-on) is shown in fig. 4. Both the ICE and regenerative system are able to add torque to the driveline at the same time, however the ICE speed is determined by the vehicle speed and the selected transmission ratio. The storage unit is recharged via regenerative braking, and depending on the position of the regenerative system and the clutch, can be recharged by the ICE whilst vehicle is stationary. The operating condition for this scheme is generally the same as in Scheme 2, but it is clear that unlike the series hybrid, parallel hybrid vehicles can still be driven following the failure of the regenerative sub-system.

Schemes 2 and 3 can be combined in a form of power split hybrid drive which uses a planetary gear set (CVT) to combine both the parallel and series configurations. This driveline configuration has the advantage of being able to operate the ICE at speeds independent of the vehicle, or even turn it off during periods of low demand. There is no gear shifting in this configuration, and the regenerative system is able to add or take power from the driveline depending on the demand.

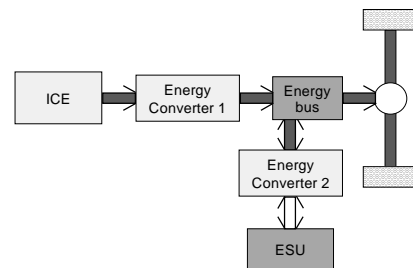


Figure 4 Parallel driveline layout (Scheme 3)

HYDRAULIC HYBRID VEHICLES (HHV)

This section of the paper briefly discusses past and current work in the field of HHVs.

Laboratory simulations

One of the earliest investigations into the hydraulic hybrid system for energy recovery was performed by Searl Dunn and Wojciechowski [5, 6]. From this initial research, using flywheel-accumulator apparatus, they concluded that well over 50% of the normally wasted kinetic energy during braking could be captured by the hydraulic system. Similar experiments were performed by Pourmovahed *et al* [7, 8] and by Maeda [9]. Although experimental results of these experiments differed, the above experiments provided some indicators regarding energy recovery of hydraulic systems.

Computer simulations

Simulation software packages for vehicle powertrain modeling are usually *forward facing* in which simulations begin with a driver model, which determines the vehicle input (accelerator and brake pedal displacements) through feedback control of the current vehicle speed. A *backward-facing* automotive simulation, e.g. the ADVISOR (ADvanced VehIcle SimulatOR) developed by the National Renewable Energy Laboratory (NREL) in the United States, begins the tire/road interface [10]. Calculation is made to find vehicle acceleration required to meet the given duty cycle over the time step. This acceleration is then used to calculate a wheel force and speed requirement, which works its way *backward* up the driveline towards the engine. All simulation models discussed below are *forward facing* unless stated otherwise.

A methodology for modeling of vehicles was proposed by Rubin *et al* [11], with further elaboration and discussions by Munns [12]. Elder and Otis [13] developed a computer model of the series type hydraulic hybrid vehicle. Their work covered several vehicle types, such as buses and delivery vans, but focused primarily on the urban passenger car. The study shows that the hydraulic hybrid powertrain is a feasible concept and that considerable gains are to be made in fuel economy and emissions reduction.

In a study by Wu *et al.* [14], a small passenger car was the subject of a computer-based investigation aimed to find the optimum operating parameters for a series hybrid driveline with fixed component sizes. Since in series hybrids the ICE can be operated at speeds independent of the vehicle speed, it was the goal of the researchers to find the optimum engine speed for a list of different control parameter combinations. It was concluded that for the 3000 lb passenger car a fuel economy of 60 mpg was attainable with a serial hydraulic hybrid system.

Tollefson [15] evaluated the parallel hydraulic hybrid vehicle system. Model of the system was based on the baseline vehicle used by Wu *et al.* [14] and used the same control concept. The difference between the two studies was in the driveline layout, and selection of driving cycles used for the study. This investigation

looked at the effectiveness of the hybrid system in two urban cycles (FUDDS and NYCC) and one highway cycle (FHC). It was concluded that fuel economy of 65 mpg was attainable for urban driving situations, but little benefit was obtained for the open highway driving due to the lack of opportunity for regenerative braking.

Heggie and Sandri [16] considered the series driveline arrangement with an additional *mechanical-bypass* feature. The results of this work showed, that the fuel economy of the hybrid vehicle could be increased by an additional 17% to 22% by inclusion of driveline de-clutching during periods of constant velocity.

Studies by Buchwald *et al* at the Denmark Technical University [17] were focused on two hybrid parallel buses (one equipped with an automatic transmission and the second bus equipped with a manual transmission) and a small delivery van, which was used as a mini prototype vehicle for model validation. The overall conclusion of this research was that a fuel saving of 25 to 30% is possible with the hybrid hydraulic system. The experimental and simulated results were within 2% of each other.

Kapellen *et. al.* [18] conducted a computer-based research focused on refuse collection trucks and compared four different powertrain configurations, two using accumulator energy storage and two using flywheels. Four different hybrid configurations were run over a simulated garbage truck cycle to measure the potential fuel gains over an estimated baseline fuel use showed that hybrid powertrains could significantly improve fuel economy under urban driving conditions from around 63% to 128%.

A novel hybrid concept, which utilized both hydraulic and electric technologies for a hybrid bus, was investigated by Chicurel and Lara [19]. The main idea behind the system was to reduce peak currents in the battery pack during hard braking by redirecting power to the hydraulic system. An estimate for the round-trip efficiency of the system was made at 60%.

An extensive simulation work on the hybrid military truck was carried out by Stecki and Matheson at Monash University [20, 21, 22]. The work involved development of vehicle models for the purpose of parametric design studies, drive cycle performance analysis, control strategy development and fuel consumption estimates. Models of the system components were developed in the Matlab/Simulink environment, and then implemented the ADVISOR [10]. Additionally *forward facing* models of the vehicle were developed using Vissim [23] and verified against *backward facing* model by Kikker [24].

Control strategy

The control strategy used by Wu *et al.* [14] was based on a *space allocation* concept, that for a given vehicle velocity a certain amount of the accumulator volume must be reserved for regenerative braking, and the remainder must be used for power decoupling.

Buchwald *et al.* [17] considered three different control strategies: an *on-off* strategy, a *best efficiency* strategy, and a *constant ICE torque* strategy, each with their associated advantages and disadvantages.

Kapellen *et al.* [18] in investigation of different hybrid configurations of the garbage truck used an *on-off* control strategy, which enabled the engine to be turned off when the energy stored was at a high enough level.

System controlling Braking Energy Storage and Regeneration System (BER System) developed by Mitsubishi for installation onto Japanese city buses, Nakazawa [25], was realized via a look-up table type arrangement, where the load distribution between the ICE and the hydraulic system was determined by the accelerator pedal stroke. During vehicle cruising, when torque demand is low, the entire load is taken-up by the diesel engine. At stages when the torque demand is high, i.e. during acceleration or passing maneuvers, torque is sourced from both the engine and the hydraulic system. Hugosson [26] dealing with the Cumulo Hydrostatic Drive (CHD), a series type hydraulic hybrid bus developed in the early 1990's, focused on the control strategies employed for the secondary hydraulic unit, a variable displacement pump/motor that delivers torque to the output shaft. The primary unit was run from the ICE and was used to maintain system pressure in the accumulator to varying levels depending on the vehicle speed, in order to keep enough energy for regenerative braking.

Prototype vehicles

A passenger car prototype was developed by Shiber [27]. The vehicle used a powertrain in the power split configuration, combining a CVT with a hydraulic accumulator to store braking energy. This prototype vehicle completed nine ECE driving cycles and doubled the fuel economy in comparison with a vehicle without the hybrid system. One of the earliest hydraulic hybrid projects was undertaken by MAN Maschinenfabrik Augsburg-Nuernberg Ag. in Berlin, Germany [28]. MAN has had vast experience in hybrid bus prototype development, having worked on both flywheel hybrid projects (Gyrobuss I and II) and hydraulic hybrids. A cost-benefit analysis of the MAN prototype hydraulic hybrid buses showed that the most likely payback period for savings on fuel and maintenance versus capital investment costs will be approximately 2.75 years for inner city operation, with a worst case being 4.9 years, and a best case of 1.6 years.

Mitsubishi Motors Japan in 1987 developed the Braking Energy Storage and Regeneration System (BER System), for installation onto Japanese city buses [25]. The BER system, which utilized the power assist (parallel) driveline layout, was installed onto a standard city bus with a downsized engine from 165 kW to 125 kW. The BER and standard buses were tested on a chassis dynamometer according to the M15 Japanese

driving cycle, and a fuel saving of 30% was recorded. It should be noted that Mitsubishi hybrid buses are in production since 1996.

Hugosson (26) presented a collective report on the status of hydraulic hybrid development at the Cumulo Division of Volvo Flygmotor. The development of Cumulo Brake Energy Drive (CBED), a parallel type hydraulic hybrid, began in 1983 and by 1985 several prototypes were in operation around Stockholm. An average reduction in fuel consumption was recorded at 16% to 25% for normal operation.

The parallel hydraulic hybrid system on a 9700 kg city bus developed in the Mechanical Engineering Division of the Canadian NRC [29] showed during fuel economy trials on 30 mph constant speed cycle, with 5 stops per mile found a 19% improvement from the baseline vehicle. NRC in a three-way project with a Canadian trucking company FIBA Canning Inc. and Volvo Flygmotor installed the CHD system on a city bus and a refuse truck for fuel economy testing [30]. According to FIBA Canning a reduction in energy consumption utilizing BTU measurement of at least 50% and reduction in lubricants use by at least 90%. Similar finding for the hybrid garbage truck were reported.

A Hydraulic Power Assist (HPA) SUV (recreational vehicle), a parallel hybrid, was developed by Ford Motor Company [31] in cooperation with Environmental Protection Agency of USA. Results of dynamometer tests produced a 23.6% saving in fuel consumption over the EPA Federal Test Procedure driving cycle. Environmental Protection Agency (EPA) of USA subsequently produced a comprehensive report on studies of hybrid drives comparing economics of running hybrid and equivalent conventional vehicles and concluded that there are sound economic and environmental reasons for application of hybrid hydraulic technology [32].

The Vehicle Research Institute, Technical University of Lodz, Poland, developed a prototype hybrid drive for a bus. Tests showed that 10-12% saving in fuel and almost 50% lowering of toxicity of exhaust gases is achievable. The system is Scheme 2 hybrid [33, 34].



Figure 5 Hybrid FMTV during fuel trials

Permo-Drive Technologies Ltd, an Australian-based

research and development company, focused its research on the development of a hydraulic parallel hybrid system for use on heavy vehicles, [35, 36]. In the development of hybrid technology, Permo-Drive and DANA Corporation have teamed up with the US military to develop a prototype US Army FMTV HHV tactical vehicle shown in Figure 5.

HYDRAULIC HYBRIDS – THE ISSUES

Some major issues in the development of hybrid technology are:

- Safety – accidents involving hybrid vehicles with high-pressure energy stored in accumulators may present major hazards. Thus further advances in accumulator technology, hydraulic fuses (shutting accumulators when major leakage is developed) and leak proof fittings and valves are required.
- Weight – hydraulic accumulators and components are heavy. This is not a major issue with heavy vehicles but even in heavy vehicles the hydraulic system may be 5-10% of total weight of the vehicle. Development of low weight accumulators using composite material should reduce the weight of systems.
- Optimization of automotive powertrains usually aims to identify the best overall size of driveline components that maximize vehicle fuel economy, performance, and driveability within certain constraints. However it appears that two major factors influencing the fuel economy are the drive cycle and control strategy.
- Control strategy will be of paramount importance to the acceptance of hydraulic hybrids. Decisions related to charging and discharging functions, algorithms relating level of charging with position of swash plate, etc. will have to be considered.
- Driveability of the hydraulic hybrid vehicle. As accumulator charging/recharging is a matter of second rather than minutes, the control system must assure that in the event of exhausting of hydraulic energy the driver must not notice any difference in driveability of the vehicle.
- Availability of pump/motors. Direct hybrid drive, like in Permo-drive system, requires units with a very large speed (equal to shaft speed) and torque capabilities. As such units are not currently commercially available the transfer boxes (like in Cumulo system) and disconnect features allowing disconnect of the pump/motor units are currently used.
- Design of energy storing systems – e.g. utilization of charge bottles. Conventional accumulators are only using approx. 50% of the volume to accommodate fluid between minimum and maximum pressure.

- Defining performance of a particular vehicle, such as fuel economy, acceleration performance and gradeability, over a given drive cycle which can be used as the objective function in the optimization process. Constraints imposed on the optimization are established by the industry, such as the Partnership for the Next Generation of Vehicles (PNGV), a joint effort between the US government and major car manufacturers in the US.
- In the case of hybrid vehicles, it is important to identify the target sizes for the energy conversion and storage devices so that the additional weight penalty is not too great, yet the system has enough capacity to successfully assist vehicle propulsion and capture the maximum energy possible during braking.

CONCLUSION

Current resurgence of interest in the Hydraulic-type Hybrid Vehicle (HHV) resulted in application of this technology to commercial and to lesser degree to large passenger vehicles. This paper provided overview of technology and discussed some design and safety issues, which are important to its success.

ACKNOWLEDGEMENTS

Authors greatly appreciate assistance of Dr. Luca Zarotti, Imamoter, Italy in preparation of this paper

REFERENCES

1. Wakefield, E.H., History of the Electric Automobile. Hybrid Electric Vehicles. Society of Automotive Engineers Inc., 1998.
2. Pourmovahed, A., Vehicle propulsion systems with hydraulic energy storage: a literature survey. *Int. J. of Vehicle Design*, 12(4):378-403, 1991.
3. King, R.D., Haefner, K.B., Salasoo, L. and Koegl, R.A., Hybrid electric transit bus pollutes less, conserves fuel. *Spectrum*, 1EEE, 32(7):26-31, 1995.
4. Scott, D. and Yamaguchi, J., Regenerative braking for buses gives big fuel savings. *Automotive Engineering*, SAE, 92(10):95-99, 1984.
5. Searl Dunn, H. and Wojciechowski, P.H., High-pressure hydraulic hybrid with regenerative braking. In *Seventh Intersociety Energy Conversion Engineering Conference Proceedings*, pages 989-995, San Diego, California, 1972.
6. Wojciechowski, P.H. and Searl Dunn, H., Energy regeneration and conversion efficiency in a hydraulic hybrid propulsion system. *High Speed Ground Transportation Journal*, 9(1):383-392, 1975.
7. Pourmovahed, A., Beachley, N. H. and Fronczak, F. J., Modelling of a hydraulic energy regeneration system - part i: Analytical treatment. *ASME Journal*

- of Dynamic Systems, Measurement, and Control, 144:155-159, 1992.
8. Pourmovahed, A., Beachley, N. H. and Fronczak, F. J., Modelling of a hydraulic energy regeneration system - part ii: Experimental program. ASME Journal of Dynamic Systems, Measurement, and Control, 144:160-165, 1992.
 9. Maeda, T., Energy saving system of an automobile using hydraulic accumulators. In International Conference on Fluid and Thermal Energy Conversion, pages 221 - 226, Indonesia, 1994.
 10. Markel, T., Brooker, A., Hendricks, T. *et al*, Advisor: a systems analysis tool for advanced vehicle modelling. Journal of Power Sources, 10(2002):255-266, 2002.
 11. Rubin, Z.J., Munns, S.A. and Moskwa, J.J., The development of vehicular powertrain system modelling methodologies: Philosophy and implementation. SAE Paper 971089, 1997.
 12. Munns, S.A., Computer Simulation of Powertrain Components with Methodologies for Generalized System Modeling. M.s. thesis, University of Wisconsin-Madison, 1996.
 13. Elder, F.T. and Otis, D.R., Simulation of a hydraulic hybrid vehicle powertrain. ASME 73-ICT-50, 1973.
 14. Wu, P., Luo, N., Fronczak, F.J. and Beachley, N.H., Fuel economy and operating characteristics of a hydropneumatic energy storage automobile. SAE Paper 851678, 1985.
 15. Tollefson, S., Beachley, N.H. and Fronczak, F.J., Studies of an accumulator energy-storage automobile design with a single pump/motor unit. SAE Paper 851677, 1985.
 16. Heggie, W.S. and Sandri, R., An energy-saving hydro-pneumatic power plant for the automobile. ASME 79-WAIDSC-15, 1979.
 17. Buchwald, P., Christensen, G., Larsen, H. *et al*, Improvement of city bus fuel economy using a hydraulic hybrid propulsion system - a theoretical and experimental study. SAE Paper 790305, 1979.
 18. Kapellen, D.R. , Jarnzadeh, F. , Frank, A.A., and Wang, S., Analysis of energy-storage concepts for refuse collection trucks. SAE Paper 840056, 1984.
 19. Chicurel, R. and Lara, P., Control of a hybrid propulsion system for a city bus. Instrumentation and Development, 3(6):3-7, 1995.
 20. Matheson, P.L. and Stecki, J.S., Modeling and Simulation of a Fuzzy Logic Controller for a Hydraulic-Hybrid Powertrain for use in Heavy Commercial Vehicles. SAE Paper Number 2003-01-3275. 2003 SAE Powertrain and Fluid Systems Conference, Pittsburgh, Pennsylvania, USA, October 2003.
 21. Matheson, P.L. and Stecki, J.S., Development and Simulation of a Hybrid-Hydraulic Powertrain for use in Commercial Heavy Vehicles. SAE Paper Number 2003-01-3370. 2003 SAE Truck and Bus Expo, Fort Worth, Texas, USA, November 2003.
 22. Matheson, P.L. and Stecki, J.S., Optimisation of a Hybrid Diesel-Hydraulic Automotive Powertrain using ADVISOR, Matlab and Simulink. Proc. 1st International Conference on Computational Methods in Fluid Power Systems. Melbourne, Australia, Fluid Power Net Publications, ISBN 0-9578574-1-1, pp 165-174, November 2003
 23. Visual Solutions, Inc., "Vissim User Guide", Version 4.5, 2000.
 24. Kikker, A., A Comparative Studies of Approaches to Simulation of a Vehicle Powertrain, A report for the Dept. of Aircraft Systems, Technical University of Hamburg-Harburg, 66 pp, 2004.
 25. N. Nakazawa, Y. Kono, E. Takao, and N. Takeda. Development of a braking energy regeneration system for city buses. SAE Paper 872265, 1987.
 26. C. Hugosson. Cumulo hydrostatic drive - a vehicle drive with secondary control. In Third Scandianvian International Conference on Fluid Power, Sweden, 1992.
 27. Shiber, S., Automotive energy management system. In National Conference on Fluid Power, pages 141-147, 1979.
 28. Martini, S., The M.A.N hydrobus: A drive concept with hydrostatic brake energy recovery. In International Symposium on Advanced and Hybrid Vehicles., 1984.
 29. Davies, A.S., The reduction of city bus exhaust emissions by means of a regenerative powertrain. SAE Paper 890267, 1989.
 30. FIBA Canning Inc. FIBA Canning home page, Feb 2004. Web: www.fibacanning.com/default.htm.
 31. Kepner, R.P., Hydraulic power assist - a demonstration of hydraulic hybrid vehicle regenerative braking in a road vehicle application. SAE Paper 2002-01-3128, 2002.
 32. Progress Report on Clean and Efficient Automotive Technologies, EPA420-R-04-002, United States Environmental Protection Agency, 2004.
 33. Pawelski, Z., Modeling and Design of Hydrobus. Technical University of Lodz, , 2000.
 34. Pawelski, Z., Hydraulic hybrid bus. Technical University of Lodz, Monografia No. 890, 1996 (*in Polish*).
 35. Stecki, J. S. Conrad, F. Matheson, P. L. and Rush, A. ,Development of a Hydraulic Drive for a Novel Hybrid Diesel-Hydraulic System for Large Commercial Vehicles. Fifth JFPS International Symposium on Fluid Power, Nara, Japan, 2002.
 36. Matheson, P.L. and Stecki, J.S., Development of Hybrid Diesel-Hydraulic System for Large Commercial Vehicles. The Eighth Scandinavian International Conference on Fluid Power, SICFP'03. Tampere, Finland, May 2003.

Information Management for Failure Analysis of Fluid Power Systems

Takehisa KOHDA* and Koji YAMAMOTO**

* Department of Aeronautics and Astronautics
Kyoto University
Kyoto, 606-8501 Japan

(E-mail: kohda@kuaero.kyoto-u.ac.jp)

** Research & Development Center

TADANO Ltd.

2217-13, Hayashi-Cho, Takamatsu, 761-0301 Japan

(E-mail: yamamotok@tadano.co.jp)

ABSTRACT

As fluid power systems improve their performance, the demand for their safety and reliability increases and so the failure analysis plays an important role. In the product lifecycle, the failure analysis is performed before and after the launch of the product. The former is a kind of conventional risk analysis to prevent system failure in the design process, while the latter identifies the cause of a customer's complaint; why the product cannot work as the customer expects. This paper considers an information management for the latter, which is divided into two processes: one is to answer the customer's complaint, and the other is to improve the product quality. Based on its objective, a different kind of information flow must be organized. Since fluid power systems work in various operating conditions, the clear specification of environmental factors is essential. An illustrative example shows a simplified treatment process of a customer's complaint.

KEY WORDS

Information flow, Task structure, Customer complaints, Organization

INTRODUCTION

As fluid power systems advance their performance, the demand for their safety and reliability also increases; a kind of risk assessment and management [1] becomes required through the lifecycle of fluid power systems. In the first step toward this goal, the failure analysis plays an important role in identifying problems latent in the subject system. Considering the product lifecycle, two types of failure analyses are identified: before and after the launch of the product. Before the launch, the failure analysis is performed as a part of conventional risk analysis to identify all possible causes of system failure

to be considered in the design stage. Information necessary for the analysis can be collected and stored inside the organization or company. The object is to minimize the risk caused after the launch of a product. On the other hand, the failure analysis after the launch is mainly performed to identify the cause of a customer complaint; why the product cannot work as the customer expects. The main object is to maximize the customer satisfaction. Compared with the consumer products, the fluid power systems such as cranes are used under various conditions, which make it difficult to identify the cause of a system failure. It is necessary to obtain appropriate information from the customer such

as the condition where the accident occurs or the product fails to meet its requirement. Further, for the identification of possible root causes and the planning of their countermeasures, the cooperation of design, manufacturing, and maintenance parts is as essential as in the failure analysis at the design stage. Since the good cooperation depends on the good communication among members, the management of information flow in the organization is important.

The construction and evaluation of the information flow for the production system is extensively studied in [2-7]. As the quality of information flow depends on the quality of its contents, MIR (maturity of information reliability) concept is proposed for evaluation of information quality [2]. Using MIR, several case studies have been performed (for example, see [3-5]). Further, a guideline is proposed for building field feedback information flows using MIR revised with consideration of the span-of-control affecting the decision [6]. In [7], IDEF0 approach is modified to analyze a manufacturing enterprise.

This paper considers an information management for the failure analysis after the launch of the product. To communicate appropriate information with the relevant parts and store the analysis results for the future reference in its design, manufacture, and maintenance, the overall task structure of the failure analysis is to be identified in analyzing information flow. For each task, necessary information flow is obtained as requirement to achieve its object. Comparing the information requirement with its current condition for each task, problems such as the loss of information flow can be identified. An illustrative example shows a simplified treatment process of a customer's complaint.

FAILURE ANALYSIS OF CUSTOMERS' COMPLAINTS

For the improvement of the product quality, the feedback from customers is very important. Usually, the feedback takes a form of complaint about the product like "this machine did not work as expected or specified in the catalog", but this kind of superficial information is not valuable not only for the product improvement, but also for determination of an appropriate customer treatment. The root cause of the complaint must be identified so that an appropriate measure can be taken. For this purpose, the collection of the right information from the customer is essential.

Classification of Customers' Complaints

From the viewpoint of customer satisfaction, the treatment of a customer complaint should be quick. This quick response requires that the cause of the complaint must be classified as the customer's fault or the company's fault as soon as possible. When complaints of the same type occur frequently, the answer to the complaint is easy. But, when an unexpected event

occurs in the product, the failure analysis is necessary to investigate its cause. From the viewpoint of the readiness of response, the following customers' complaints can be answered easily and quickly:

1) Complaints on items listed in the manuals or checklist

The treatment of the complaint is determined based on what item is wrong and its warranty.

2) Complaints with similar cases in the past

The treatment is to follow the past case similar to the present one.

The response of the complaint in either case is (1) a gratuitous or onerous repair/replacement, or (2) an instruction on how to use the product appropriately. Although these quick responses may be satisfactory for the customer, the company or organization obtains no gain from customers' information. The valuable knowledge for the improvement can be obtained from unfamiliar cases such as unexpected result of the product with/without following the user manual. The failure analysis can give the valuable information on the product quality and the customer usage. This process can be considered as a kind of learning process from failure cases to obtain their root causes.

Requirements for Failure Analysis

For the failure analysis to be effective for the improvement of product quality, the following points must be considered:

1) The information on the field use of the product (especially, customer complaints) should be considered from the viewpoints of not only product warranty, but also design improvement.

2) Loss of information on accident and customer complaints as time passes yields the reoccurrence of the past accident and the reduction of the opportunities of the technology transfer from a veteran to a freshman. To prevent this kind of problem, the transfer and retention of safety knowledge are essential.

3) For the share of common information and exact informational transfer in an organization, it is necessary to investigate what knowledge should be stored from users' viewpoint and how to coordinate the information flow in an organization.

Considering these points, the information flow must be designed for the root-cause analysis of customers' complaints.

Overview of Treatment Process

A conventional organization in the product industry has the following divisions for the treatment of customers' complaints as shown in Figure 1, where an arrow indicates a communication flow.

1) Service Division (SD): A customer always contacts with SD about his complaint.

2) Sales Division (SaD): SaD informs a customer on the current state of his treatment.

3) Quality Assurance Division (QAD): QAD performs the main role in the root cause analysis of the customer

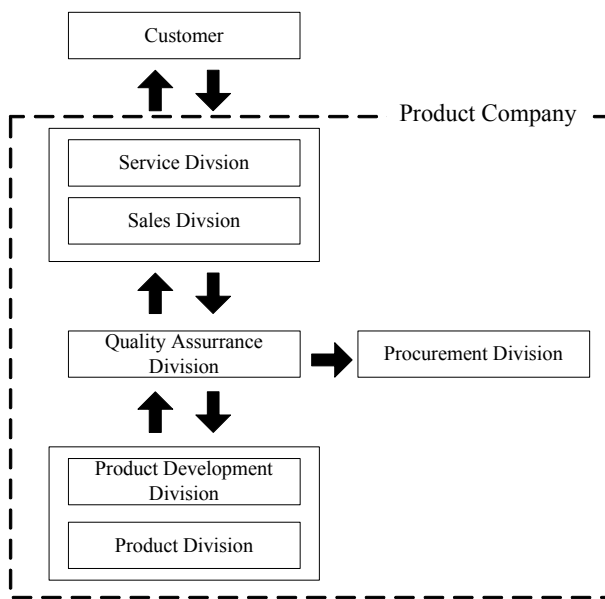


Figure 1 Organizational Structure

complaint.

4) Product Development Division (PDD): PDD is further divided into three subdivisions: design, experiment, and control. They deal with the research and development of the product.

5) Product Division (PD): PD deals with production engineering.

6) Procurement Division (PrD): PrD contacts with the suppliers.

At the first step, a customer submits his complaint to SD, which tries to answer it based on its experience. If SD cannot, SD asks QAD to deal with the root cause analysis of his complaints in cooperation with PDD, PD and PrD. Finally, the customer gets the answer from SD.

Detailed Failure Analysis

The situations where the detailed failure analysis is necessary are classified into the following four cases:

Case 1: SD and SaD cannot deal with a customer's complaint.

Case 2: The product is broken, but its cause (failure) cannot be identified.

Case 3: A component has a lot of customers' complaints, which implies a quality problem.

Case 4: A lot of cases with onerous repair occur, which implies that the revision of customer treatment may be necessary.

The common feature among these cases is that the root cause of the complaint or failure cannot be identified and an appropriate measure should be taken immediately. The main object in cases 1 & 4 is to establish a new decision criterion about the treatment, while the object in cases 2 & 3 is to improve the product quality by understanding the abnormal phenomena.

TREATMENT PROCESS OF CUSTOMERS' COMPLAINTS

To perform the detailed failure analysis to obtain the root cause of a customer's complaint, a wide range of information on the use of a product is necessary. For example, how the product was used? Under what condition was the product? What was the product quality? Different parts of the organization must cooperate with one another to collect the information. For this purpose, a good communication is necessary so that the right person can get the right information. Since the object or output of a task can specify necessary information, the task structure or procedure for failure analysis of customers' complaints must be understood first to design a good communication.

Task Analysis

To identify the task structure present in the organization, the overall task is analyzed as follows:

Step 1: For each task component composing the subject task, identify its input information or material, its performer, and its output information or product. If additional requirements or conditions are necessary to perform the task component, they must be attached to it.

Step 2: Based on the information obtained at step 1, the overall task structure can be easily obtained by connecting input and output with the same content.

The task structure shows the relation between task components as well as the flow of information and material among task components. When some information is utilized, it is an output from some task component and inputs to other task components. Thus, unnecessary or useless information can be identified as one being no input to task components.

Even if all the information is utilized, the overall task structure is not necessarily complete. This structure may have missing information. To complete the information structure, the following step must be supplemented.

Step 3: For each task component to achieve its task objective or output, examine whether any additional information or material is necessary. If necessary, supplement it.

Since an identified task corresponds to an information source, how to obtain necessary information can be determined easily. For the future reference to improve the design or the manufacture, additional information can be supplemented to the information management system based on how the information is used in the design, manufacture and maintenance of the subject system.

Task Structure of Treatment Process

Using the task analysis in the previous section, the treatment process of a customer complaint can be summarized as follows:

(0) The customer makes a complaint against SD.

(1) Can SD make the judgment based on the manual and the stored knowledge?

- Yes: SD replies to the customer. [End]
 No: SD asks QAD for the judgment. Go to (2).
 (2) QAD performs the investigation & analysis with additional information from the customer through SD. Can QAD decide using the database of past analysis records?
 Yes: QAD makes a report to SD. [End]
 No: QAD asks PDD for Investigation and analysis of uncertain items in the database. Go to (3)
 (3) With the answer from PDD and additional information from the customer, can QAD decide whether the problem is due to a design error or a customer problem?
 No: QAD requests Quality Measure Meeting (QMM) consisting of QAD, PDD, PrD (Production Div), SD, and SaD to solve the problem.
 Yes: Due to a customer problem:
 QAD makes a report with onerous result to SD. [End]
 Due to a design error:
 (a) If the cause is known, the appropriate measure is verified by QAD and Experiment of PD. [End]
 (b) If a cause is unknown, QAD request QMM. Go to (4)-(b).
 (4) QMM discusses countermeasures for the problem with the additional from the customer and decides whether the problem is due to a design error or a customer problem?
 (a) Due to a customer problem:
 QMM makes a report with onerous result to SD. [End]
 (b) Due to a design error:
 QMM determines an appropriate measure, and asks QAD and Experiment of PD for its verification and validation. Go to (5)
 (5). PDD and PrD take the measures for quality (such as design revision and improvement of production process) to prevent the recurrence of the same problem, and planning for the next production. Verification and validation are also required for the measures. Go to (6)
 (6) PDV and PrD make the final report to QAD. Go to (7)
 (7) QAD reports the final result to SD and SrD reports to the customer. [End]

Here, [End] indicates that the problem is solved or the process finishes.

Evaluation of Treatment Process

Although the business process is developed according to ISO9000, the information flow seems not necessarily effective as general comments in [2]. Since the task process is sequential as well as hierarchical, the information exchange among different divisions is restricted so that the response to the customer cannot be quick. Since QAD plays the central role in transferring information as well as analyzing the cause of a customer

complaint, the failure analysis fails if QAD does not work appropriately. Further, the current object of QMM seems ambiguous because the duties of each member in QMM seem to be decided in advance by QAD. The role of QMM seems to be to confirm and transfer the statement. For the improvement of both product quality and information flow, QMM on customers' complaints should be held regularly instead of the initiative of QAD so that all the divisions related to the product quality can share and understand the feedback from the customers as well as the background information on the objective of their own role and duties. This will also facilitate the interactions between the customer and SD in obtaining the appropriate information. Since the task analysis result shown above focuses on the treatment process of a customer's complaint, the information flow should be also considered from the viewpoint of the retention of valuable information for future reference.

ILLUSTRATIVE EXAMPLE

This chapter discusses the first part of the treatment process of customers' complaints in detail, which determines whether the problem is due to a design error or a customer problem. Compared with conventional failure analysis, this part considered as a kind of diagnosis decision based on the observational data. The second part which identifies the root cause of a customer complaint corresponds to a conventional failure analysis.

Task Description

Consider a system failure "The arm of a hydraulic crane fell down by itself". Figure 2 shows the schematic diagram of the crane related to this example. A customer calls up SD about this accident. SD inquire the customer about the overall condition. The first concrete information is:

(C1) There was an oil leak from the holding side of the derrick cylinder.

Then, the process of question & answer continues between the customer and SD according to the task analysis shown in Task Structure.

The parts related to the system failure are (P1) hose, (P2) joint at the holding side, (P3) holding valve, and (P4) cylinder. The failure analysis in this step is to identify the failed part and examine its condition. The failed conditions to be considered for each part can be summarized as below.

(P1) Hose:

1. The hose at holding side of the derrick cylinder was cut.
2. The hose at the holding side of the derrick cylinder was burst.
3. The hose at the holding side of the derrick cylinder was torn loose.
4. The joint of hose at holding side of the derrick cylinder loosened.

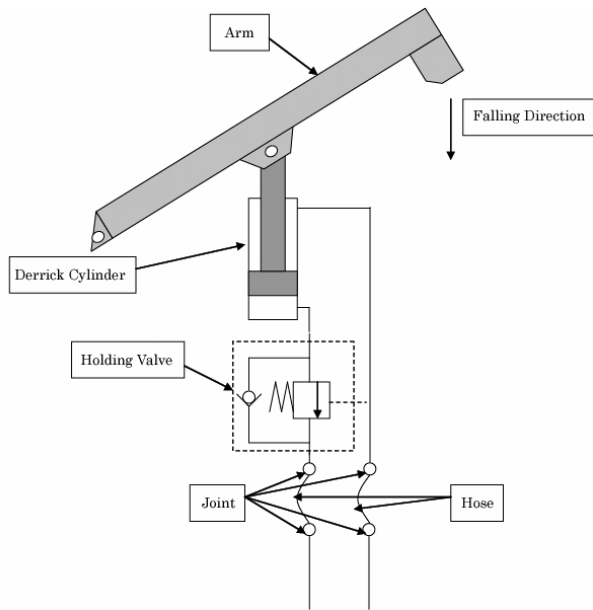


Figure 2. Schematic Diagram of Crane

(P2) Joint:

1. The joint at the holding side of the derrick cylinder loosened.
2. The joint at the holding side of the derrick cylinder was damaged.

(P3) Holding Valve:

1. Attachment bolt of valve of the derrick cylinder was loosened.
2. The seal of the valve of the derrick cylinder was lost.
3. The seal of the valve of the derrick cylinder was damaged.
4. The valve armor of the derrick cylinder was damaged.

(P4) Cylinder:

1. The cylinder of the derrick cylinder had a crack in an externally damaged part.
2. The cylinder of the derrick cylinder had a crack in a welding part.
3. The seal at the cylinder of the derrick cylinder was damaged.

Depending on the customer's information on the failed part, SD must determine whether the failure is due to the customer's fault or design fault. For this purpose, SD performs a field check to confirm the customer's information and collects additional information from the customer.

If the failed condition is different from the above list, SD asks QAD for their help to identify how the system failure occurred.

Onerous Service vs. Gratuitous Service

After the failed part and its condition are identified, the problem is to determine whether the customer has to pay the repair cost or not. For this purpose, the additional information must be checked as follows:

(P1)-1:

Is the externally caused damage is expected?

If no, onerous service. Otherwise, gratuitous one.

(P1)-2, 3, & 4:

Is the damage caused in its normal use?

With excessive load, beyond the temperature boundary, over the service life: onerous service.

With hose joints loosened: depending on the warranty period.

(P2)-1 & 2:

Is the damage caused in its normal use?

With excessive load: onerous service.

With joints loosened: depending on the warranty period.

(P3)-1:

Depending on the warranty period.

(P3)-2 & 3:

Decomposition examination of the valve is necessary.

With excessive load: onerous service.

Attachment error of the seal, or manufacturing error of the valve: gratuitous service.

(P3)-4: Onerous service.

(P4)-1: Onerous service.

(P4)-2:

With excessive load: onerous service.

Over the service life: depending on the warranty period.

(P4)-3:

Decomposition examination of cylinder is necessary.

With excessive load: onerous service.

Over the service life: depending on the warranty period.

Even if the situation does not fit any case in the above, the detailed examination must be performed by QAD. This corresponds to the start of the second stage or the conventional failure analysis procedure.

CONCLUSIONS

This paper considers the failure analysis to identify the root cause of a customer complaint. Compared with the failure analysis in the design process, the detailed information on the failure is uncertain. Thus, the cooperation among different divisions in a company is essential to collect the right information, which requires their good communication. Based on the task structure of treatment of a customer complaint, the communication or information flow can be evaluated. Task analysis of a simplified process in the illustrative example points out the redundant information flow structure. One is to satisfy the customer satisfaction, and the other is to improve the product quality for the prevention. Since this paper focuses only on the task structure or information flow structure, the evaluation of consistency of required information with provided information must be checked. Thus, the evaluation of contents and quality of information as well as the effective use of documentations obtained from the

analysis is our next step toward the design of information management for the failure analysis of a customer complaint.

REFERENCES

1. Kumamoto, H., and Henley, E. J., Probabilistic Risk Assessment and Management for Engineers and Scientists, IEEE Press, 1996.
2. Sander, P. C. and Brombacher, A. C., MIR: The Use of Reliability Information Flows as a Maturity Index for Quality Management, Qual. Reliab. Engng. Int., 1999, 15, pp. 439-447.
3. Brombacher, A. C., Maturity Index on Reliability: Covering Non-Technical Aspects of IEC61508 Reliability Certification, Reliability Engineering and Systems Safety, 1999, 66, pp. 109-120.
4. Petkova, V. T., Sander, P. C., and Brombacher, A. C., The Role of the Service Centre in Improvement Processes, Qual. Reliab., Engng. Int., 1999, 15, 431-437.
5. Berden, T. P. J., Brombacher, A. C., and Sander, P.C., The Building Block of Product Quality: An Overview of Some Basic Concepts and Principles, Int. J. Production Economics, 2000, 67, pp. 3-15.
6. Petkova, V. T., Yuan, L., Ion, R. A., and Sander P. C., Designing Reliability Information Flows, Reliability Engineering and Systems Safety, 2005, 88, 147-155.
7. Kim S., and Jang K., Designing Performance Analysis and IDEF0 for Enterprise Modelling in BPR, Int. J. Production Economics, 2002, 76, pp. 121-131.

DEVELOPMENT OF AN INTELLIGENT PNEUMATIC-PIEZOELECTRIC HYBRID SERVO POSITIONING SYSTEM WITH HIGH RESPONSE, LARGE STROKE AND NANOMETER ACCURACY

Mao-Hsiung CHIANG^{*}, Chung-Chieh CHEN, Chin-Chuan HUANG and Jun-Yih CHEN

^{*}Institute of Automation and Control,
National Taiwan University of Science and Technology,
Taipei 106, Taiwan.
(E-mail: mhchiang@mail.ntust.edu.tw)

ABSTRACT

This investigation aims to develop an intelligent hybrid pneumatic-piezoelectric servo positioning system with high response, large stroke and nanometer precision. The rodless pneumatic cylinder serves to position in coarse stroke and the piezoelectric (PZT) actuator compensates fine stroke. Thus, the overall control systems become a dual-input single-output (DISO). Although the rodless pneumatic cylinder has relative higher friction force, it has the advantage of mechanism for multi-axes development. In order to develop an intelligent controller, self-organizing fuzzy sliding mode control theory (SOFSMC) is proposed here for the DISO system. SOFSMC is based on fuzzy sliding mode control (FSMC) combining with self-organizing strategy. Thus, SOFSMC has simple fuzzy rule base and on-line self-organizing ability. Besides, in order to reduce the coupling effects of the DISO system, a decoupling controller is developed. The experimental results clarify that the servo pneumatic-piezoelectric control system can achieve excellent positioning response and accuracy of 20 nm with high response for maximum stroke of 250 mm and multi-step positioning.

KEY WORDS

pneumatic-piezoelectric, positioning control, large stroke and nanometer accuracy and self-organizing fuzzy sliding mode control.

INTRODUCTION

Pneumatic servo positioning control systems have the advantages of high response, easy maintenances and cleanliness. However, the non-linearity of pneumatic systems, such as friction force, restricts the positioning accuracy. Research about the field of pneumatic servo

control has been developed since 1954. Control algorithms, such as PID control, state space control and adaptive control of pneumatic servo control system were developed via higher speed microcomputers in 1980s. However, the robustness and the control accuracy of pneumatic cylinders in the past research are still unsatisfactory due to the high non-linearity and the

compressibility of compressed air, so that till now pneumatic servo control is still not widely used. Some research [7,8] paid attentions to the influence of non-linearity on pneumatic servo control systems, such as stick-slip effect. The stick-slip effect, which results mainly from friction force of pneumatic cylinders, makes pneumatic cylinders unable to keep steady motion in low velocity conditions. Therefore, the non-linear problems complicate pneumatic servo control so that modern control strategies are essential. Self-tuning adaptive control was used in the position control of pneumatic servo cylinders for adapting control parameters on-line such that the positioning accuracy of 5 μm in no loading conditions was achieved [5]. The additional velocity feedback is inserted in the position control for compensating the influence of friction force. [15].

Because the characteristics of the servo pneumatic driving seriously restricts the positioning accuracy, it can be improved by means of combining with other actuators. Piezoelectric actuators are developed in recent years and already applied in many different fields. One of the application examples is the hard disk reader control system [9]. The piezoelectric actuator works as the second stage positioning combined with an electric motor that operates as the first stage positioning for improving the positioning accuracy of the hard disk driving. The overall system is a dual input single output (DISO) control system. So, the PQ-method was introduced to simply the DISO control system into a single-input single-output (SISO) system, but mathematical models of the two subsystems are necessary for this method. Besides, the piezoelectric actuator, which generates high frequency impact force by open loop control, is combined with the servo pneumatic driving system in order to reduce the friction force effects. The total stroke and the positioning accuracy can reach 2 mm and 1 μm [4]. The research group of Chiang [3,16] has engaged in pneumatic-piezoelectric servo positioning control since 2000 and has some results [3,16]. The pneumatic cylinder with double rod is combined with piezoelectric actuator can achieve 180mm stroke and 0.1 μm that is the minimum resolution of the linear scale used in this paper. From Reference [3,16], the possibility of the nanometer accuracy of the pneumatic-piezoelectric for large stroke could be expected.

This study aims to develop an intelligent hybrid pneumatic-piezoelectric actuator for high response, large stroke of 250 mm and high precision of 20nm positioning control, which includes a pneumatic servo cylinder and a piezoelectric actuator. The servo pneumatic cylinder serves to coarse positioning with high speed and large stroke; the piezoelectric actuator positions in precision range for compensating the influence of friction force and for achieving large stroke, high response and high positioning accuracy at the same

time. The overall control systems have complex dual-input single-output (DISO), and coupling interaction exists between the two subsystems. Therefore, a new control strategy of decoupling self-organizing fuzzy sliding mode control (DSOFSMC) is developed in this investigation. Self-organizing fuzzy sliding mode control (SOFSMC) is used for designing the two positioning controller and a decoupling compensator for on-line weighting the two subsystems according to control error and error rate.

TEST RIG LAYOUT

The new high precision pneumatic-piezoelectric hybrid positioning control system developed in this paper contains a pneumatic servo system and a piezoelectric servo system, as shown in Fig. 1. Table 1 specifies the main components.

Table 1 Specification of the test rig

Components	Specifications
Rodless cylinder	Diameter 25mm Stroke 317mm
PZT actuator	Stroke 90 μm Freq. 15kHz Voltage 0~150 V
PZT amplifier	Input: 0~5V Gain: 30
ADDA card	12bit D/A D/I, D/O
Servo valve	5/3, input: 0~10v
Linear scale	Range: 450mm Accuracy 20nm
Counter card	3x 24-bits counters 1.0MHz Input Rate
Compressor	5HP, 0.38KW

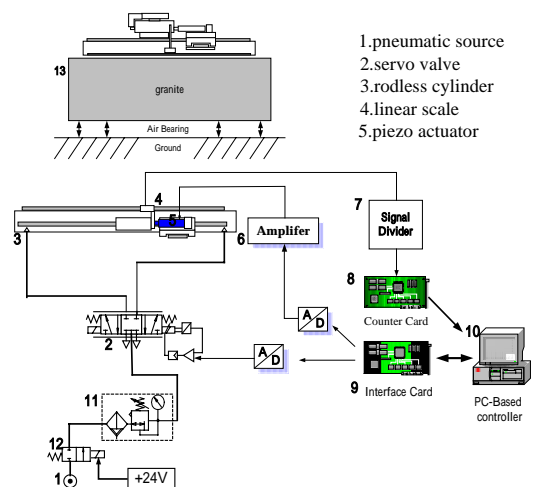


Figure 1 Test rig of pneumatic-piezoelectric hybrid positioning system

The pneumatic servo system mainly consists of a pneumatic source, a servo valve and a double acting rodless cylinder. In order to improve the positioning accuracy of the pneumatic cylinder, a piezoelectric actuator with a stroke of 90 μm is mounted on the pneumatic cylinder via an adaptor. Hence, the pneumatic cylinder and the piezoelectric actuator drive the loading mass simultaneously. In addition, a linear encoder with the resolution of 20nm is necessary for measuring the overall position, which is the sum displacement of the pneumatic cylinder and the piezoelectric actuator. The measuring signals of the linear encoder are fed back to the control computer via a decoder and a digital I/O converter. The control signals of the pneumatic servo valve and the piezoelectric actuator are given from the control PC with the sampling time of 1 ms via D/A converters and enlarged by a servo amplifier and a piezoelectric amplifier respectively.

Therefore, the overall control systems have dual-input single-output, which is shown in Fig. 2 to illustrate the complex block diagram of the overall control system. The servo pneumatic cylinder serves to coarse positioning with high speed and large stroke and the piezoelectric actuator positions in fine stroke for compensating the influence of friction force. The position control of the two control systems, namely pneumatic servo system and piezoelectric servo system, performs at the same time. Therefore, the integrated overall system can achieve large stroke, high response and high positioning accuracy simultaneously.

DECOUPLING SELF-ORGANIZING FUZZY SLIDING MODE CONTROL

In this study, decoupling self-organizing fuzzy sliding mode control (DSOFSMC) is developed for solving the DISO control problem, decreasing the fuzzy rule numbers and on-line self-organizing the fuzzy rules. DSOFSMC contains, self-organizing fuzzy sliding

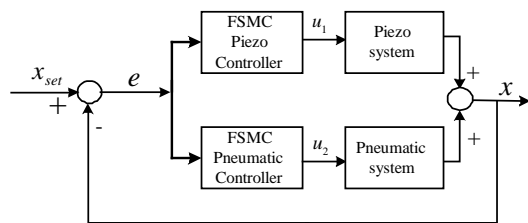


Figure 2 Block diagram of decoupling dual-input single-output (DISO) system for pneumatic-piezoelectric hybrid positioning control system

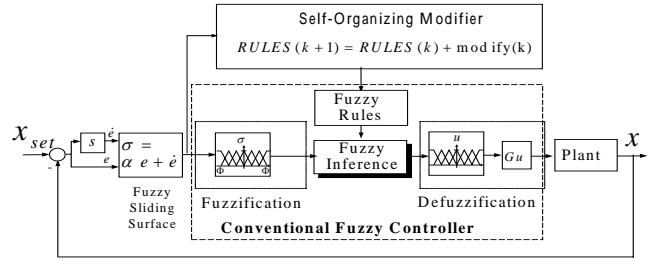


Figure 3 Self-organizing fuzzy sliding mode control

mode control (SOFSMC) and decoupling controller. Figure 3 schematically depicts the control block diagram of the SOFSMC.

Self-organizing fuzzy sliding mode control

Consider the state vector of a second order system as

$$\mathbf{x} = [x, \dot{x}]^T \quad (1)$$

The tracking error of the state vector is defined as

$$\mathbf{e} = \mathbf{x}_d - \mathbf{x} = [e, \dot{e}]^T = [x_d - x, \dot{x}_d - \dot{x}]^T \quad (2)$$

where x_d and \dot{x}_d indicate the desired output and the desired output change rate. The fuzzy sliding surface is described as

$$\sigma = (\dot{e} + \alpha \cdot e) = \text{ZERO} \quad (3)$$

where α is a positive constant. The fuzzy sliding surface $\sigma = \text{ZERO}$ is a straight line with slope α in the phase plane, as shown in Fig. 3(a). The sliding surface can be divided into 7 sections by the membership function set of $M(\tilde{\sigma}) = \{NB, NM, NS, ZR, PS, PM, PB\}$. The membership function set for the control input u is defined as $M(\tilde{u}) = \{NB, NM, NS, ZR, PS, PM, PB\}$. Therefore, the fuzzy sliding mode control can reduce the fuzzy rules into 7 rules via the fuzzy sliding surface σ , shown in Fig. 3. The Mamdani method is used in the fuzzy inference and the centroid method is used for defuzzification.

The self-organizing modifier of the SOFSMC is designed by self-organizing fuzzy control theory for on-line adapting the fuzzy rules according to the variations of working points and external disturbance. The detailed derivation of the self-organizing modifier is shown in [17].

the i^{th} rule can be modified by the modifying value Δu through an exciting intensity w_i

$$\begin{aligned} u_i(nT + T) &= u_i(nT) + w_i \cdot \Delta u \\ &= u_i(nT) + w_i \frac{\gamma_s}{M_s} \sigma(nT) \quad , \quad i = 1, \dots, 7 \quad (4) \end{aligned}$$

where the exciting intensity w_i is the grade of

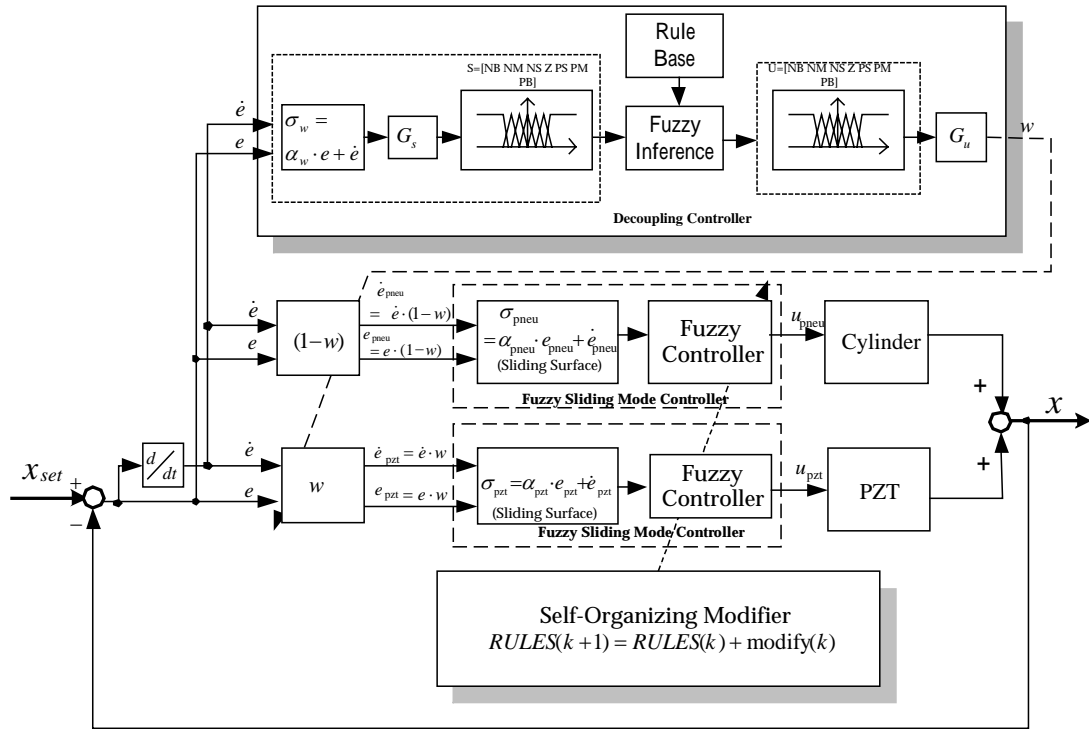


Figure 4 Decoupling self-organizing fuzzy sliding-mode control

membership. According to the normalized fuzzy sliding surface $\tilde{\sigma}$, two rules, the i^{th} and $(i+1)^{\text{th}}$ rules, are excited and modified at the same time. Therefore, the fuzzy rules of the SOFSMC can be described as

$$\text{RULES}_i(nT + T) = \text{RULES}_i(nT) + w_i \frac{\gamma_s}{M_s} \sigma(nT) \quad (5)$$

Decoupling controller

In order to solve the structure coupling interference, the decoupling controller designed by SOFSMC is merged. The output of the decoupling controller can be considered as weighting functions for the two subsystems in the DISO system.

Controller design for DISO using DSOFSMC

Figure 4 shows the control strategies to solve the DISO system using DSOFSMC. The overall systems contain the pneumatic controller, the piezoelectric controller and the decoupling controller that are designed using SOFSMC.

EXPERIMENTAL RESULTS

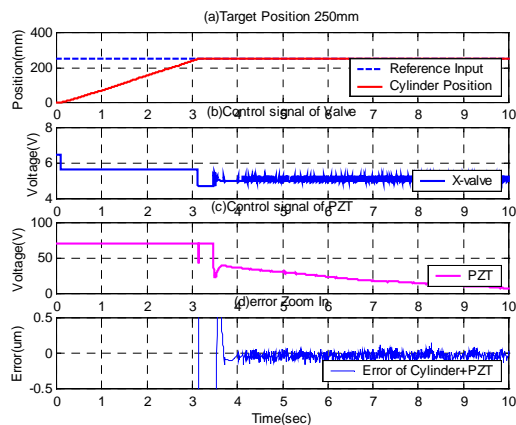
Figure 5 shows the test results of the positioning control with 250 mm stroke in the pneumatic-piezoelectric positioning system using SOFSMC and DSOFSMC respectively. Figures 5A describes the control

performance of SOFSMC and Figs.5B show that of DSOFSMC. The step response of the positioning control, control input of pneumatic system, control input of piezoelectric system and the error zooming are shown respectively. The steady state error of the SOFSMC can reach about $0.1\mu\text{m}$ with high frequency vibrations. Through the compensation of the decoupling controller, the steady state error of the DSOFSMC is smooth and he settling time ($e < 0.5\mu\text{m}$) is 3.695 sec and the steady state error can reach 20nm, as shown in Fig.5B(c). The rising time in the test rig is limited by the transformation speed of the counter card. If the counter card with higher speed and support of real-time demand is used, the rising time can be improved significantly.

CONCLUSIONS

A novel large stroke and high precision pneumatic-piezoelectric hybrid positioning control system is well developed and verified experimentally in this study, which contains a pneumatic servo cylinder serving for high speed, large stroke positioning and a piezoelectric actuator positioning in fine stroke. The two controllers work in parallel and the two position outputs are added in cascade. Such complex dual-input single-output systems are solved by the DSOFSMC both for the pneumatic cylinder positioning control system and the piezoelectric positioning control system as well as the decoupling controller. The DSOFSMC developed in this paper incorporates fuzzy sliding mode

SOFSMC (5A)



DSOFSMC (5B)

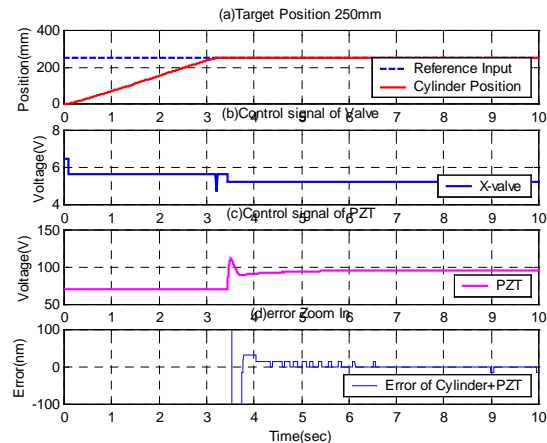


Figure 5 Experimental comparison of pneumatic-piezoelectric positioning control with SOFSMC and DSOFSMC
(a) step response of 250 mm, (b) pneumatic control input, (c) PZT control input, (d) error zoom.

control, self-organizing modifier and decoupling controller. The test results show that the developed pneumatic-piezoelectric positioning control system can achieve 20nm accuracy for 250 mm with high response.

REFERENCES

- [1] Murrenhoff H. Grundlagen der Fluidtechnik, Teil 2: Pneumatik (in German). Lecture notes of RWTH Aachen, Germany, 1999.
- [2] Murrenhoff, H., Czinki, A., Jansen R, Hantke, P., Neuere Entwicklungen in der Pneumatik (in German). The 2nd International Fluid Power Conference (2. IFK), (Aachen, Germany), Mar. 2000; 2: 355-378.
- [3] Chiang, M.H., CHEN C.C., Chow, D.N., High precision pneumatic-piezoelectric hybrid positioning control using adaptive discrete variable structure control, *Mechatronics* 15, 2005, pp.523-545.
- [4] Liu Y.T. and Higuchi T. Precision positioning device utilizing impact force of combined piezo-pneumatic actuator, *IEEE/ASME Transactions on Mechatronics*, 2001, 6(4): 467-473.
- [5] Shih MC, Huang YF. Pneumatic servo cylinder position control using a self-tuning controller. *JSME Int. J., Series C*, 1992; 35(2): 247-254.
- [6] Wang YT, Chang MK. Experimental implementation of decoupling self-organizing fuzzy control to a TITO pneumatic position control system. *JSME Int. J., Series C*, 1999; 42(1): 85-92.
- [7] Fujita T, Tokashiki R, Kagawa T. Stick-slip motion in pneumatic cylinders driven by meter-out circuit. *Proc. of the 4th JHPS International Symposium on Fluid Power. (Tokyo), 1999: 131-136.*
- [8] Kazama T, Fujiwara M. Experiment on frictional characteristics of pneumatic cylinders. *Proc. of the 4th JHPS International Symposium on Fluid Power. (Tokyo), 1999: 453-458.*
- [9] Evans, R.B., Griesbach JS, Messner WC. Piezoelectric microactuator for dual stage control. *IEEE Trans. on Magnetics*, 1999; 35(2): 977-982.
- [10] Li CJ, Beigi HSM, Li S and Liang J. Non-linear piezo-actuator control by learning self-tuning regulator, *ASME, Journal of Dynamic, Systems, Measurement, and Control*, 1993; 115, 720-723.
- [11] Han JM, Adriaens TA, Willem L de K, and Banning R. Modelling piezoelectric actuators, *IEEE/ASME Transactions on Mechatronics*, 2000, 5(4), 331-341.
- [12] Eschmann, R., *Modellbildung und Simulation pneumatischer Zylinderantriebe (in German)*, Dissertation of RWTH Aachen, Germany, 1994.
- [13] Schillings, K., *Servopneumatische Antriebssysteme und Handhabungsgeräte (in German)*, Dissertation of RWTH Aachen, Germany, 2000.
- [14] Kollar, I., *Frequency domain system identification toolbox –for use with MATLAB*, The Math Works Ltd., 1995.
- [15] Shih M.C, Pai, K.R., Development of the pneumatic servo control system. *Proc. of the 5th JFPS International Symposium on Fluid Power, (Nara, Japan), 2002: 11-22.*

- [16] Chiang, M.H., Chang, Y.S., Intelligenter hybrider Pneumatik-Piezo-Aktuator zur Lageregelung mit großem Hub und hoher Genauigkeit, Ölhydraulik und Pneumatik Nr. 6/2003, 2003.
- [17] Chiang, M.H., Chien Y.W., Parallel control of velocity control and energy-saving control on a hydraulic valve controlled system using self-organizing fuzzy sliding mode control, JSME International Journal, Series C, Vol.46, No.1, pp.224-231, 2003.

DESIGN AND FABRICATION OF MICRO FLUID POWER SYSTEM BY STEREOLITHOGRAPHY

Yutaka TANAKA*, Naoki TAKEMURA**, Seiya ISHIKURA**, Gaku MINORIKAWA***

* Department of Art & Technology, Faculty of Engineering
**Graduate school of Engineering
*** Department of Mechanical Eng., Faculty of Engineering
Hosei University
3-7-2 Kajinocho, Koganeishi, Tokyo, 184-8584 Japan
(E-mail: y_tanaka@k.hosei.ac.jp)

ABSTRACT

Neither high accumulation nor densification on micro mechatronics are so advanced comparing with semiconductor devices. Our research aims at the establishment of design and fabrication to perform miniaturization, high accumulation and high densification by integrating mechano-micro elements. In difficult assembly of these elements, a stereolithography method is used to form the entire micro fluid power systems in all-in-one design including actuators, pumps and valves. In this paper, prototype models based on a bourdon type and diaphragm type of micro fluid power devices are fabricated and experimentally investigated. Some problems regarding design and fabrication of micro fluid power systems are discussed.

KEY WORDS

Actuator, Bourdon tube, Diaphragm, ECF, Stereolithography

NOMENCLATURE

a, b : transverse section length diameter, short diameter
 E : modulus of elasticity of material
 g : acceleration gravity
 h : wall thickness of bourdon tube
 P_a : internal pressure of tube
 P_p : output pressure of pump
 R : curved radius of bourdon tube
 ΔR : change in curved radius
 S : displacement of tube tips
 λ : a^2/Rh
 θ : arc angle of bourdon tube

INTRODUCTION

In 1989 gear trains and motors on a wafer have been firstly reported by using the semiconductor micro fabrication technology in U.S.A [1]. Semiconductor processing technology applied to these fabrications has touched off since the latter half of 1980's, and the research specialized in microscopic environment has begun to be paid to attention rapidly all over the world. The research on the micro nanotechnology has been carried out as seeds in a wide range of fields such as information and communication technology, mobile machine, manufacturing and inspection, and medicine and biotechnology. Moreover, it is the most important

technical issue to develop new concept of devices with the best use of characteristics on not only a miniaturization of conventional products but also emphasis of future in microscopic environment.

Recently there are many micro integrated elements such as micro mirrors and acceleration sensors applied to the semiconductor manufacturing process for the practical use [2],[3]. These elements are made on the flat surface of the silicon wafer with fine fabrication and high integration. Therefore, application of these elements has been limited within the practical use of sensors with the control of electronic and optical signals.

On the other hand, neither accumulation nor the integration of various elements in micro mechatronics devices are so advanced comparing with the semiconductor devices. The mechatronics device has functions of sensors, actuators and mechanism, and signal processing. It is difficult for the micro mechatronics device to manufacture and assemble complete parts under microscopic world. Under the microscopic world, adsorption, friction, viscosity and abrasion originated on the surface phenomenon have much influence on the performance, energy efficiency, durability and reliability of the micro mechatronics device.

The component with mechanical moving parts is not suitable for the structure of micro mechatronics system because of large power consumption. Moreover, it is difficult for the micro mechatronics system to assemble many parts in three dimensional configuration. Therefore, it is preferable to produce it with a complete part where the mechanism is simple and the parts size few as much as possible.

Various actuation principles, for example piezoelectric, electrostatic and thermal expansion have already been reported for the micro actuation system [4]. However, fluid power actuation system has a great potential to realize large output power density comparing to the conventional actuation system under the microscopic environment [5]. In conventional fluid power actuation system, however, there are many mechanical parts in the system, for example valves for actuator control and pumps for power source.

Our research aims at the establishment of design and fabrication to perform miniaturization, high accumulation and high densification by integrating mechano-micro elements. In difficult assembly of these elements, a stereolithography method is used to fabricate a three dimensional structure of the entire micro fluid power systems in all-in-one design.

CONCEPT OF MICRO FLUID POWER SYSTEM

Our final goal is to develop a new micro fluid power system fabricated by the stereolithography. The device consists of four modules, a signal and sensor module, a

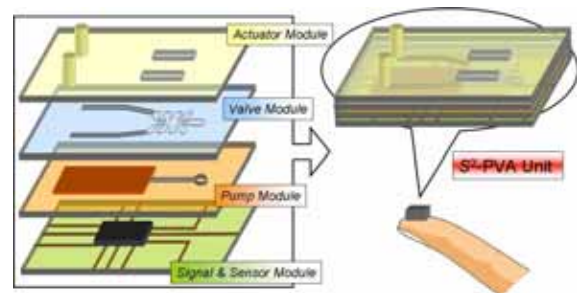


Figure 1 Concept of micro fluid power system

pump module, a valve module, and an actuator module. We call this device the S^2 -PVA unit. Figure 1 shows a concept of the S^2 -PVA unit with accumulating, integrating, miniaturizing and high performance on one single-chip. This is all-in-one design and fabrication unit consisting of the actuator, the valve, the pump and the sensor modules and functions.

In this paper we report a trial manufactured and an experimental investigated pumping and actuation devices for the actuator module and the pump module by the production technique of the stereolithography.

FABRICATION BY STEREO LITHOGRAPHY

In the micro processing and micro fabrication, it is difficult to assemble parts on the three dimensional (3D) structure. Prof. Ikuta has pointed out that an optical prototyping has advantage of production for micromachining [6]. Conventional micromachining has made only a two dimensional structure. However, a three-dimensional micro processing becomes possible by using the optical prototyping. Moreover, the optical prototyping method has the potential of processing one time as the internal configuration also included a complex solid model.

In this study, the 3D optical rapid prototyping method, stereolithography, is used to manufacture the each module for the micro fluid power system. Figure 2 shows the optical prototyping process based on a 3D CAD data. The forming process irradiates the ultraviolet laser ($Nd:YVO_4$) to optical thermosetting property of the liquid based on the 3D CAD data, and cures the resin. The 3D shape of prototyping objects can be made by accumulating layers of a certain constant thickness [7]. The stereolithography (3D Systems Co. Viper si2 SLA) used in our research has the accumulating pitch of 50 microns or less. The material property of the resin after curing greatly influences the performance of the fabricated object when the forming thing is used as actuator using the material deformation. The material property after hardening of the resin (the Accura SI 10 Material) used in our experiments are tabulated in Table 1.

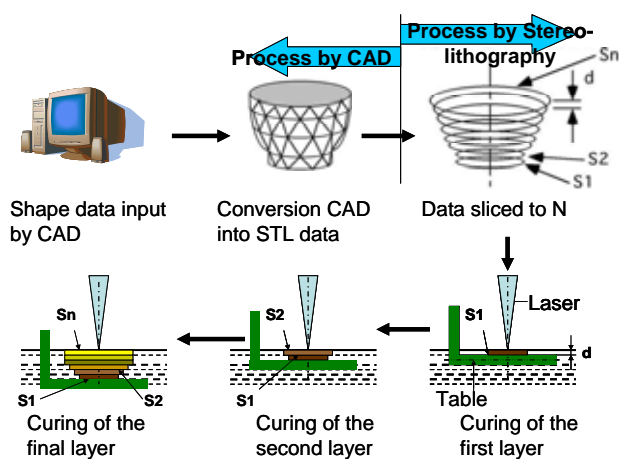


Figure 2 Process of stereolithography

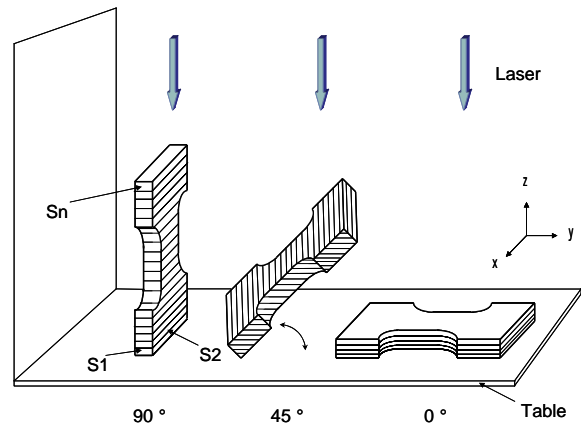


Figure 3 Layer models for fabricated angle

The material property of the resin is measured at final curing after irradiating ultraviolet rays during 90 minutes.

The stereolithography is a new layering technique to fabricate three-dimensional structure of the solid model. A fabricated angle is the important design factor for the stereolithography to fabricate the layered object. Figure 3 shows the fabricated angle of the layered models. Three types of the layered model as shown in Fig.3 are experimentally investigated to consider the fabricated angle of the layer in the stereolithography. The fabricated angle ψ is defined with the respect to the x-y plane on the table (horizontal flat surface). The fabricated angles are selected for experiments in the case of $\psi=0^\circ, 45^\circ$ and 90° , respectively.

Table1 Properties of material

	Accura SI 10 Material
Tensile Strength	62 - 63 [MPa]
Elongation at Break	3.1 - 5 [%]
Tensile Modulus	3048 - 3255 [MPa]
Flexural Strength	89 - 97 [MPa]
Flexural Modulus	2827 - 3102 [MPa]
Impact Strength (Notched Izod)	18.7 - 27.7 [J/m]
Glass Transition, Tg	61.7[°C] (143.1[°F])
Hardness, Shore D	86

ACTUATOR MODULE

In this section two types of actuator for the actuator module of the micro fluid power system are described. It has already been shown that the output power density rises as for the fluid actuator under the microscopic environment [5]. Some fluid motors and the elastic deformations using the fluid power have been reported [8], [9]. These actuators have a simple structure and no mechanically operating parts, so that the friction does not influence on the performance of the actuators. Also the power density (power/weight ratio) rises when decreasing dimensions under the microscopic environment. In this paper, we propose bourdon tube type and diaphragm type actuators using the elastic deformation with the fluid power.

Bourdon tube actuator

Figure 4 shows the geometry of the bourdon tube actuator. Dimensions of the actuator are tabulated in Table 2. The bourdon tube actuator has a high weight torque ratio and small coefficient of friction because of structurally no sliding surface [10], [11]. The bourdon tube actuator is fabricated by the stereolithography to accumulate a number of the layer. The each layer has a thickness of $50 \mu\text{m}$ that is the minimum fabricated layer. A tip of the bourdon tube deforms in response to the applied pressure in the tube. The displacement of the tip S is given by the following Eq.(1).

$$S = \sqrt{2(1 - \cos \theta) - 2\theta \sin \theta + \theta^2} \cdot \Delta R \quad (1)$$

where θ is the arc angle of the bourdon tube, ΔR is the change of the bourdon tube curved radius. And the change of the bourdon tube curved radius ΔR is written as follows.

$$\Delta R = \frac{a^3}{h^3} \frac{K_2}{1 + \lambda^2 K_1} \left(\frac{P_a R}{E} \right) \quad (2)$$

where P_a is the internal pressure in the bourdon tube, R is the radius of the bourdon tube, E is the Young's modulus, h is the wall thickness of the bourdon tube, a is the length of the long axis in the oval across the transverse section, respectively. Coefficients $\lambda (= a^2/Rh)$, K_1 and K_2 are determined by the shape of the cross-section of the bourdon tube and the length ratio. In this study K_1 and K_2 is given as 0.11 and 0.90, respectively. Moreover, the aspect ratio $\nu (=b/a)$ is given as 0.43 across the oval section [12].

Table 2 Dimension of bourdon tube

$\nu(=b/a)$	a [mm]	b [mm]	h [mm]	R [mm]	θ [rad]
0.43	5.25	2.25	0.5	10	4.712

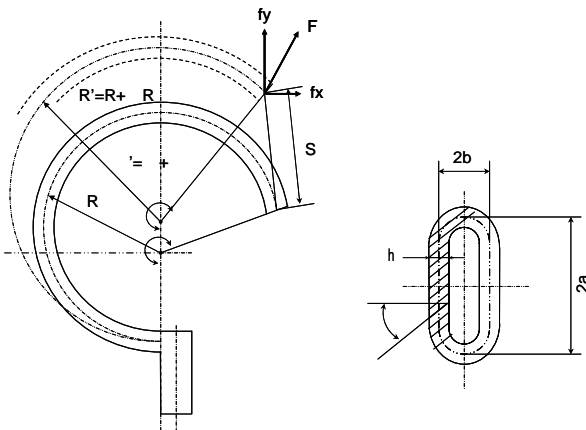


Figure 4 Bourdon tube

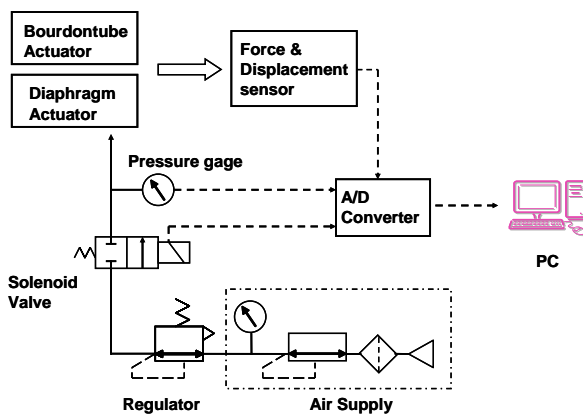


Figure 5 System configurations for experiments

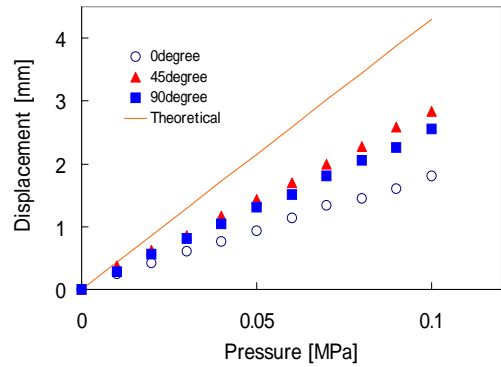


Figure 6 Static characteristics of bourdon tube

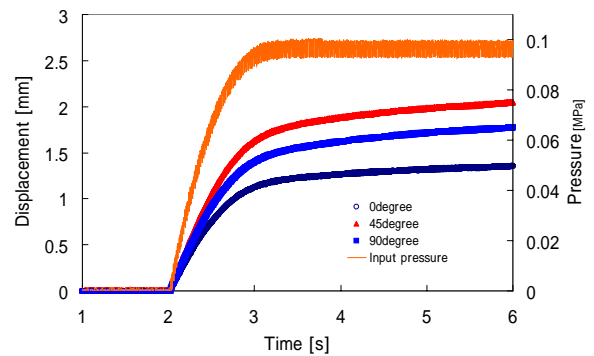


Figure 7 Dynamic characteristic of bourdon tube

Figure 5 shows the system configuration chart used by the fundamental experiment for the characteristics of the actuator. The compressed air is used for the power source in the experiment.

Figure 6 shows the experimental result of the static characteristic of the output displacement of three kinds of bourdon tube actuators with the different fabricated angle. The output displacement is proportional to the supplied pressure. The output displacement nearly depends on the fabricated angle ψ . There is no hysteresis property between the supplied pressure and the displacement.

The change of the theoretical displacement calculated from Eq. (1) and Eq. (2) is also plotted in Fig.6. For example the bourdon tube actuator with the fabricated angle $\psi=45^\circ$ has the displacement of 2.84mm under the supplied pressure condition of 0.1 MPa. The experimental value is below 2/3 comparing to the value calculated from Eq. (1). Uniformed materials are assumed to derive the theoretical value by Eq. (1). The structure of the bourdon actuator fabricated by the stereolithography is, however, layered and aeolotropic. Therefore, the fabricated angle influences elastic deformation of the actuator and it causes smaller values compared with the theoretical ones.

The step signal is applied to the solenoid valve as an evaluation of the dynamic characteristics of the actuator. Figure 7 shows the experimental results for the step response of the actuator. The steady state values in the fabricated angles $\psi=45^\circ$ and 90° are larger than that in the angle $\psi=0^\circ$. Thus there are found that the fabricated angle ψ greatly influence on the response of the actuator. The bourdon tube actuator is easily fabricated by the stereolithography. The output displacement of the actuator and dynamic characteristics are significantly influenced by the direction of the fabricated layer structure. The fabricated angle is one of the important factors to design and fabricate the actuator by the stereolithography.

Diaphragm actuator

Figure 8 shows geometry of the fabricated diaphragm actuator by stereolithography. The whole film for the diaphragm is made by the curing resin. The shape of the diaphragm is a circle with a diameter of 5mm and the film thickness of 0.1mm. The surface film of diaphragm is fabricated under the condition of only $\psi=90^\circ$ for the fabricated layer angle. The film of the diaphragm has a very thin membrane so that the fabrication has resulted in failure in the case of the fabricated angle $\psi=0^\circ$ and 45° . The output displacement and the dynamic characteristic are measured by using the pneumatic system shown in Fig.4 as well as the experiment for the bourdon tube actuator.

Figure 9 shows the experimental results for the static characteristic of the diaphragm actuator. There is a large nonlinear and hysteresis characteristic between the output displacement and supplied pressure to the diaphragm. The internal stress stays in when the resin is cured under the ultraviolet. Figure 10 shows the step response for the diaphragm actuator.

The diaphragm actuator is easily fabricated rather than the bourdon tube actuator. But the performance of the actuator depends on the film of the diaphragm. In this time, the prototype of diaphragm actuator is fabricated as all-in-one design by using the stereolithography. But the stereolithography method using this study could not fabricate thin film.

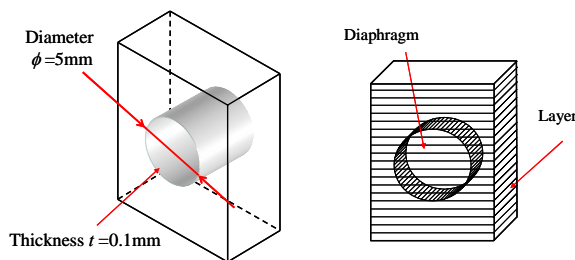


Figure 8 Diaphragm actuator

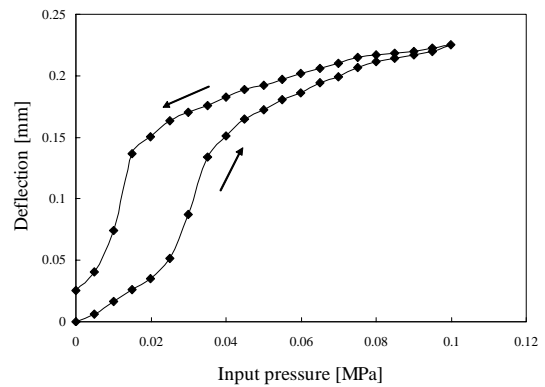


Figure 9 Static characteristics of diaphragm actuator

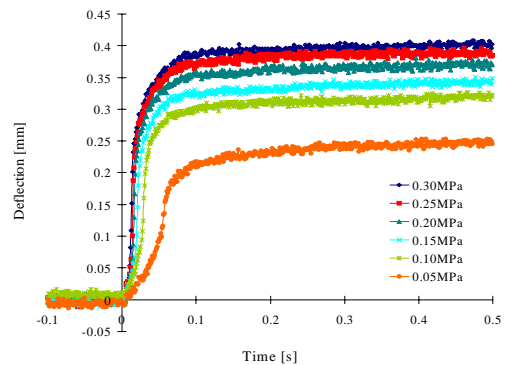


Figure 10 Dynamic characteristics of diaphragm actuator

PUMP MODULE

In this section we consider about the pump module. Functional fluid ECF (Electro-Conjugate Fluid) is used to be pumping function for the pump module. The ECF occurs the jet flow that is impressed high electrical voltage of direct from a positive electrode to a negative electrode inserted into the fluid [8].

Figure 10 shows structure of the multistage ECF pump module made for trial purposes in this study. A number of electrodes are installed in a pipe with an inner diameter of 2 mm. These electrodes have a spacing of 0.4mm and a diameter of 0.1mm. The coupled electrodes are displayed to the series in 5mm spacing for the type of the multistage amplification. Dibutyl decanedioate (DBD) type ECF is used for experiments. The electrical voltage is applied to each couple of electrode from 0kV to 5kV. The output pressure (P_p) of the actuator is measured by manometer type of pressure sensor.

Figure 12 shows the experimental result of the output pressure using multistage ECF pump. The output pressures have changes of quadratic curve with a little hysteresis according to the applied voltage. Moreover, it

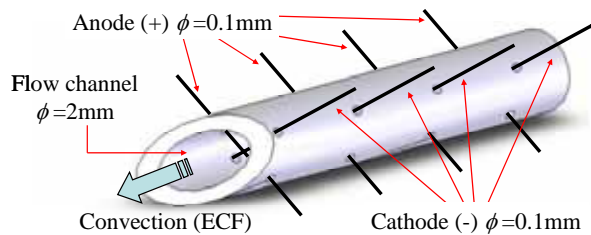


Figure 11 Multistage ECF pump

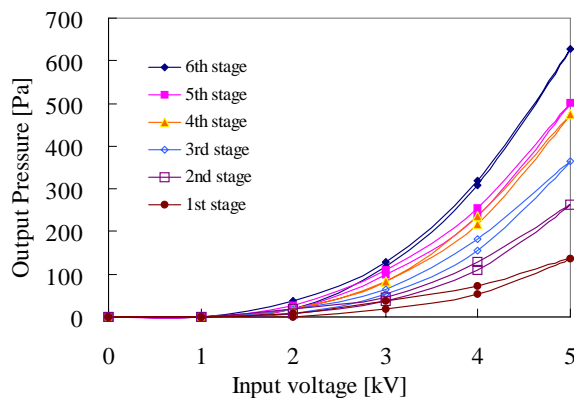


Figure 12 Output pressure for multistage ECF pump

appears to obtain an enough output pressure by increasing number of the electrodes.

It is possible to use the multistage structure of ECF pump as the pump module. The fluid power source using the ECF can be embedded in the main body of the micro systems and can be effective as driving source of the micro actuator. For example these fabricated parts such as actuators and pumps are able to contribute on one single-chip, it may realize to the simplification of the assembly process.

CONCLUSION

The bourdon tube actuator and the diaphragm actuator are fabricated for trial purposes by using the stereolithography. It is experimentally verified that these actuators have performed by using the fluid power. Moreover the multistage ECF pump is a powerful source to supply necessary power to the actuator for the micro fluid power system. The stereolithography method to fabricate the actuator is the unique technique to integrate and miniaturize some complex parts under the microscopic environment. It is suitable principle for the micro actuator to deform elastically materials without mechanical moving parts. It is clearly pointed out for our

experiments that the fabricated angle for the stereolithography is the most important factor to design and fabricate the actuators. It is clarified for all-in-one design unit consisting of the actuators and the pump module to use the stereolithography for fabrication.

Acknowledgement

This study has been supported in part by Grant-in-Aid for Scientific Research in Priority Areas "next-generation actuators leading break-through" of the ministry of Education, Culture, Sports, Science and Technology of Japan.

REFERENCES

1. L.S.Fan, Y.C.Tai and R.S.Muller, IC-Processed electrostatic micro motor, *Sensor&Actuators*, 1989, 20, pp.41-48.
2. K.D.Wise and K.Najafi, *Science* 1991, 254, pp.1335-1342.
3. J.M.Bustillo, et al., *Proceedings of the IEEE* 86, 1998, pp.1552-1574.
4. Park, J.-H., Yoshida, K. and Yokota, S., Resonantly Driven Piezoelectric Micro Pump-Fabrication of a Micro pump Having High Power density, *Mechatronics*, Vol.9, No.7, 1999, pp687-702.
5. K.Yoshida and S.Yokota, Study on High-power Micro Actuator Using Fluid Power, *Proc. of 6th FLOMEKO*, Seoul, 1993, pp.120-130.
6. K.Ikuta, K.Hirowatari, Real Three Dimensional Micro Fabrication Using Stereo Lithography and Metal Molding, *Proc. of International Workshop on Micro Electromechanical Systems(MEMS'93)*, 1993 pp.42-47.
7. Jey Won, Kathryn De Laurentis, Constantinos Mavroidis, *Rapid Prototyping of Robotic Systems*, *Proceedings of the 2000 IEEE, International Conference on Robotics & Automation*, 2000 pp.3077-3082.
8. S.Yokota, Y.Kondoh, A.Sadamoto, Y.Otubo, K.Edamura, A Micro Motor Using Electroconjugate Fluids (Proposition of Stator Electrode-Type (SE-type) Micro ECF motors), *JSME International Journal*, Vol.44, Ser.C, No.3, 2001, pp.756-762.
9. H. F. Schulte Jr., *The Characteristics of the McKibben Artificial Muscle*, *The Application of External Power in Prosthetics and Orthotics*, pp.94-115.
10. Alfred Wolf, Tuisa Okla, *An Elementary Theory of Bourdon Gauge*, *Journal of Applied Mechanics*, Vol.13, No3, 1946, pp209-210.
11. Y.Fujiwara, Y.Saito, K.Hattori : Study of a Pneumatic Robot Utilizing a BTA (Bourdon Tube Actuator), *3rd JHPS International Symposium*, 1996, pp.127-132.
12. Flow measurement *JSME handbook*.4, 1991, pp.7-10, (in Japanese)

A PIEZOELECTRIC MICROPUMP USING FLUID INERTIA IN PIPE AND ITS APPLICATION

Kazuhiro YOSHIDA^{*1}, Yeon-Oh JUNG^{*2}, Takeshi SETO^{*3}, Kunihiko TAKAGI^{*3},
Jung-Ho PARK^{*1} and Shinichi YOKOTA^{*1}

*1 Precision and Intelligence Laboratory, Tokyo Institute of Technology
R2-42, 4259 Nagatsuta-cho, Midori-ku, Yokohama-shi, Kanagawa-ken, 226-8503 Japan
(E-mail: yoshida@pi.titech.ac.jp)

*2 Graduate School, Tokyo Institute of Technology

*3 Corporate Research & Development Div., Seiko Epson Corporation
3-3-5 Owa, Suwa-shi, Nagano-ken, 392-8502 Japan

ABSTRACT

For millimeter-sized fluid-driven micromachines performing power-needed tasks, we proposed a novel micropump using fluid inertia in an outlet pipe. The paper describes the pump structure for higher output power and an application of the micropump to a micro fluid power system. First, a simple nonlinear mathematical model with lumped parameters was proposed and the validity was confirmed comparing the simulation and experimental results. Second, based on the simulations varying the sizes of the outlet pipe and the diaphragm, the pump structure for higher output power was obtained and the validity was verified through experiments. Finally, as an application of the micropump, a position control microsystem was fabricated using the micropump, a microvalve using magneto-rheological fluid valve-body, and a bellows microactuator. The characteristics were experimentally clarified and the validity was confirmed.

KEY WORDS

Micromachine, Micropump, Modeling, Actuator, Magneto-rheological fluid (MRF)

INTRODUCTION

For millimeter-sized micromachines performing power-needed tasks such as micro maintenance systems for 10mm diameter pipelines in industrial plants, microfactories, and so on [1][2], we proposed and have been developing micromachines using fluid power with high power density [2]-[6].

To realize micromachines using fluid power, high output power micropumps are indispensable. However previous micropumps for μ TAS (Micro Total Analysis Systems) developed to transport small amount of liquids or gases precisely [7] can not produce high power.

We proposed and have been developing high output power piezoelectric micropumps using resonance drive [3] and the one using fluid inertia in pipe [6]. Especially,

the latter micropump has been experimentally clarified to produce higher power. However, the optimal structure has not been clarified yet.

To increase the output power in small size, the paper investigates the pump structure. A nonlinear mathematical model with lumped parameters is proposed and the validity is confirmed comparing the experimental and simulation results. Then, based on simulations using the mathematical model, the pump structure for higher output power is obtained. The validity of the pump structure is verified through experiments. Finally, as an application of the micropump, a position control microsystem is fabricated using the micropump, a microvalve using magneto-rheological fluid (MRF) valve-body, and a bellows microactuator and the characteristics are experimentally investigated.

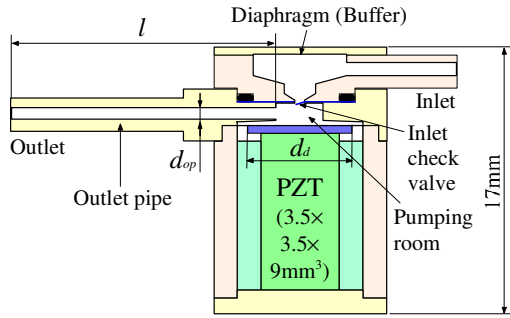


Figure 1 Schematic of micropump using fluid inertia in pipe

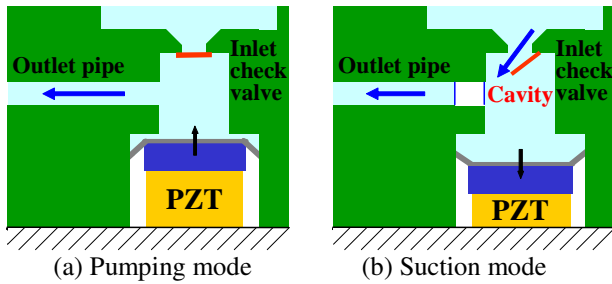


Figure 2 Working principle of the proposed micropump

PIEZOELECTRIC MICROPUMP USING FLUID INETIA IN PIPE [6]

Figure 1 shows the schematic of the piezoelectric micropump using fluid inertia in pipe. The micropump consists of a reciprocating pumping room driven by a multilayered PZT actuator, an inlet check valve, and an outlet pipe with small diameter. An accumulator, which is a flexible silicone tube for outflow in this study, is attached to the outlet and the outlet pressure is constant. In the room above the inlet check valve, a plastic diaphragm is installed as a buffer. The working fluid is degassed water.

In a pumping mode shown in Fig. 2(a), the PZT actuator contracts the pumping room, the inner pressure increases, the inlet check valve closes, and the working fluid flows out through the outlet pipe at a high flow velocity. In the subsequent suction mode shown in Fig. 2(b), the PZT actuator expands the pumping room, the inner pressure decreases, and the working fluid flows in through the opened inlet check valve. At the same time, in the outlet pipe, the flow is going to maintain due to fluid inertia in the outlet pipe with a column separation. Thus, the micropump flows out the working fluid in not only pumping but also suction modes and realizes an output flow rate higher than the value estimated with the displacement. Through experiments, we clarified the pumping room pressure modes and realized an output fluid power of 0.21W with 2.3cm³ in volume.

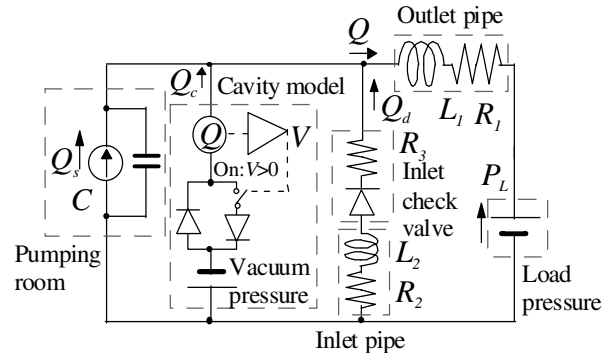
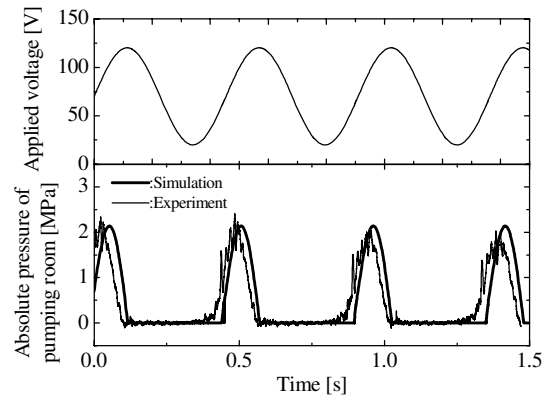
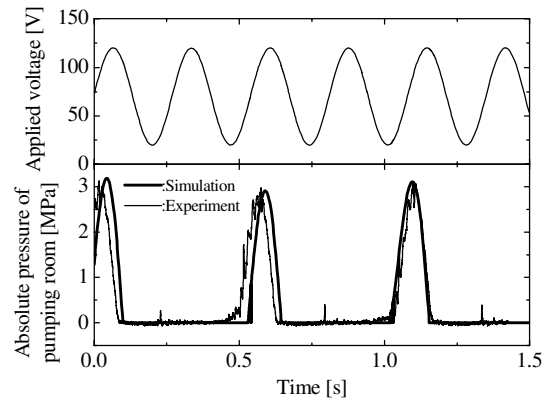


Figure 3 Proposed mathematical model of the micropump



(a) With driving frequency 2.2kHz and load pressure 0.29MPa



(b) With driving frequency 3.7kHz and load pressure 0.32MPa

Figure 4 Experimental and simulation results of pumping room pressure

MATHEMATICAL MODEL OF THE MICROPUMP

Proposition of Nonlinear Mathematical Model with Lumped Parameters

To investigate the pump structure to increase the output power in small size, a simple nonlinear mathematical model with lumped parameters is proposed as shown in

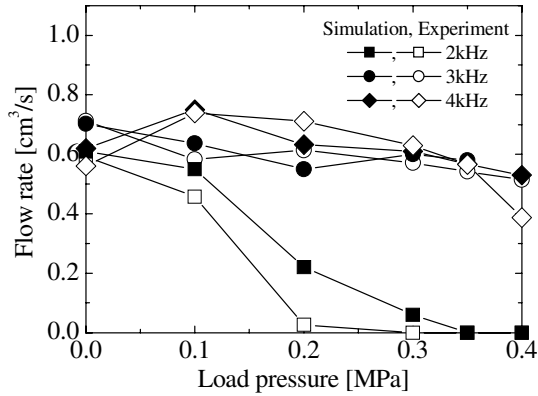


Figure 5 Experimental and simulation results of load characteristics

Fig. 3. Part models are a serial connection of a diode and a resistor R_3 for the inlet check valve, a serial connection of an inductor L and a resistor R for the pipes, a parallel connection of an ac current source and a capacitor C for the reciprocating pumping room. For the column separation, a cavity model is developed. In a suction mode, when the absolute pressure of the pumping room is going to be negative, the cavity model holds the pressure to be 0 supplying fluid from a virtual tank. In the subsequent pumping mode, the cavity model holds the pumping room pressure to be 0 until the inflow in the previous suction mode flows back to the virtual tank. The cavity model is expressed with lumped parameters as shown in Fig. 3.

The resistances are calculated assuming laminar flow, and the inductances are 1.3 times of the calculated value based on basic experiments. The capacitance is obtained considering bulk modulus of the working fluid and elasticity of the PZT actuator.

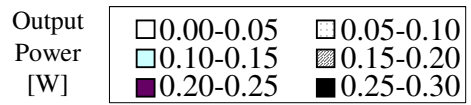
Verification of the Proposed Mathematical Model

Figure 4 exemplifies the simulation and experimental results of the absolute pressure of pumping room. The simulations were performed using MATLAB®. The pulse frequency of the pumping room pressure is the same as the one of the driving frequency in Fig. 4(a), on the other hand, the pulse frequency of the pumping room pressure is twice as large as the one of the driving frequency in Fig. 4(b). The modes are the feature of the micropump and the former is called “1st mode” and the latter “2nd mode”. The peak value and phase of the pumping room pressure coincide with the experimental results for both modes. The average flow rates shown in Fig. 5 also indicate the agreements. The validity of the simple mathematical model was confirmed.

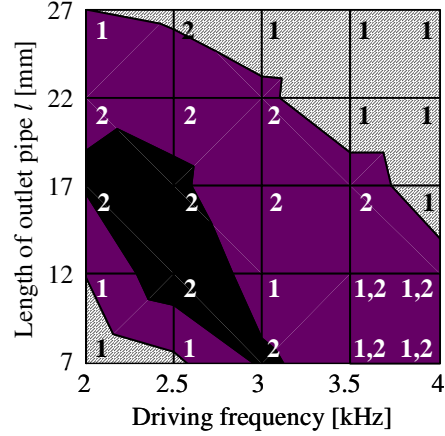
PUMP STRUCTURE FOR HIGHER OUTPUT POWER

Investigations Based on Simulations

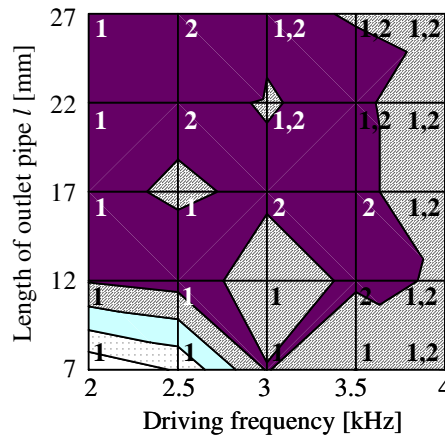
To investigate the pump structure for higher output power, simulations were performed with different



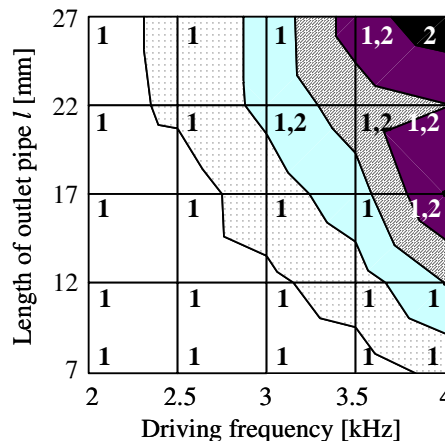
1: 1st mode, 1,2: 1st and 2nd mode, 2: 2nd mode



(a) Diameter of outlet pipe $d_{op}=0.5\text{mm}$



(b) Diameter of outlet pipe $d_{op}=0.75\text{mm}$



(c) Diameter of outlet pipe $d_{op}=1\text{mm}$

Figure 6 Simulated output power with different sizes of outlet pipe and driving frequencies

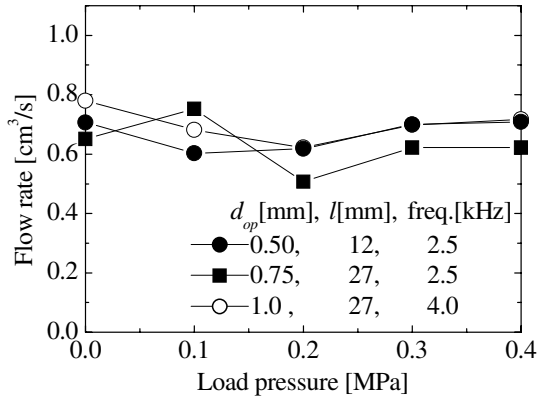


Figure 7 Simulated load characteristics with different sizes of outlet pipe and driving frequencies

Table 1 Simulated output power with different diaphragm diameters

Diaphragm diameter d_d [mm]	3.0			6.3			9.0		
Outlet pipe diameter d_{op} [mm]	0.50	0.75	1.0	0.50	0.75	1.0	0.50	0.75	1.0
Outlet pipe length l [mm]	12	22	27	12	22	27	12	12	22
Driving frequency [kHz]	4.0	4.0	4.0	2.5	2.8	4.0	3.0	2.5	2.5
Output power [W]	0.12	0.14	0.13	0.28	0.29	0.29	0.21	0.25	0.22

diameters d_{op} and lengths l of the outlet pipe shown in Fig. 1 with the established mathematical model. The diaphragm diameter d_d was 6.3mm, diameters d_{op} were 0.50, 0.75, and 1.0mm, and lengths l were 7, 12, 17, 22, and 27mm. The driving frequencies 2~4kHz and the load pressure 0~0.40MPa are in allowable range for the inlet check valve.

Figure 6 shows the maximum output power at each diameter d_{op} and length l of the outlet pipe and driving frequency. Based on the results, it is found that with large inductance with small diameter d_{op} and large length l , the output power is maximized at low driving frequency, and that the 2nd mode produces higher power.

Figure 7 shows the selected results of the load characteristics. As a result, with diameter d_{op} =0.5mm and length l =12mm of the outlet pipe, driving frequency 2.5kHz, and load pressure 0.40MPa, output flow rate of 0.71cm³/s is obtained, which is 35% higher than the previous experimental value.

Next, the effect with different diaphragm diameter d_d was simulated using the same PZT actuator. The maximum output powers obtained varying diameter d_{op} and length l of the outlet pipe and driving frequency are shown in Table 1. It is found that the diaphragm diameter d_d =6.3mm generates the maximum output power.

Experimental Verifications

Based on the simulation results, micropumps were fabricated as shown in Fig. 8 with diaphragm diameter d_d =6.3mm, diameters d_{op} =0.50, 0.75, and 1.0mm and

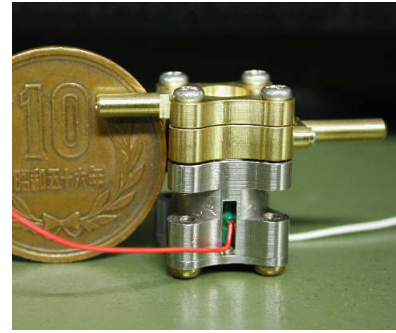


Figure 8 Photocopy of the fabricated micropump

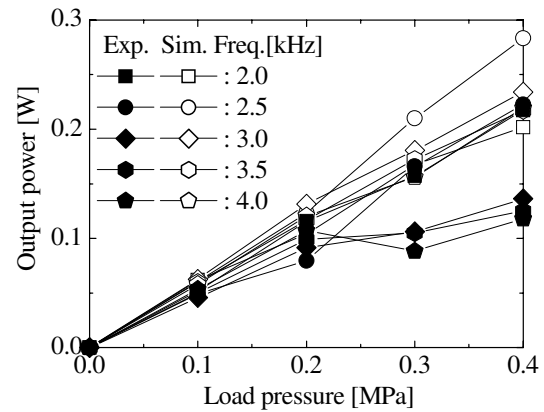


Figure 9 Comparisons of experimental and simulation results

length l =12, 17, and 22mm of the outlet pipe. The PZT actuator (PSt150/3.5×3.5/7, Pizeomechanik Co.) produces the maximum displacement of 4.6μm (applied voltage 100V) and offset 60V and amplitude 100V_{p-p} were applied. As the load, a variable restriction was installed and the outlet pressure was measured by a semiconductor type pressure transducer (pressure range: 1MPa). The flow rate was measured based on the time to flow out 10g mass.

Figure 9 exemplifies the results. It is ascertained that the maximum output power is obtained with diameter d_{op} =0.5mm and length l =12mm of the outlet pipe, driving frequency 2.5kHz, and load pressure 0.40MPa, which coincide with the simulated results. However, due to variation of capacitance C in reassemble, the maximum output power is 0.22W, which is only 5% higher than the previous value.

APPLICATION TO POSITION CONTROL MICROSYSTEM

Fabricated Microvalve Using MRF Valve-Body [5]

To control fluid power irrespective of machining errors, we proposed a microvalve using MRF valve-body as shown in Fig. 10. MRF has micrometer-sized magnetic particles dispersed in an oily fluid and is pulled by magnetic field. An MRF column is supported in the

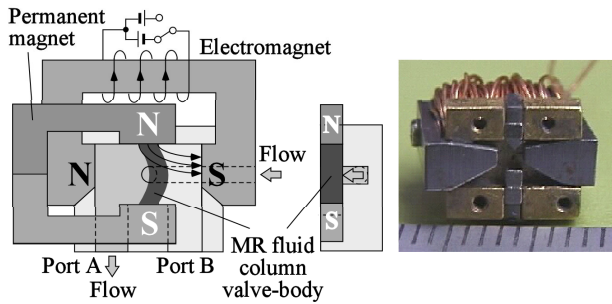


Figure 10 Fabricated microvalve using MRF valve-body

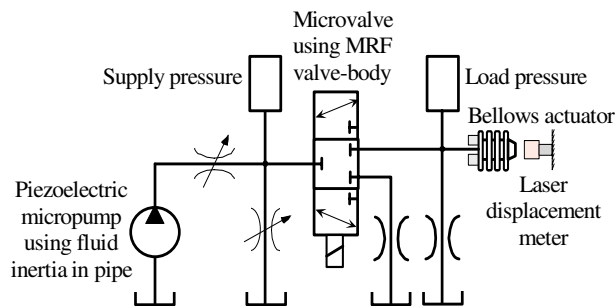


Figure 11 Hydraulic circuit of fabricated position control microsystem

flow channel by a permanent magnet and shuts off the working fluid flow as a valve-body. The MRF column is deformed by perpendicularly applied magnetic field using an electromagnet. With increasing the deformation, the working fluid flow increases. Thus, the valve opening is controlled by the current applied to the electromagnet. The microvalve features simple structure, shut off capability due to the adaptable liquid valve-body irrespective of the larger machining errors, energy saving due to the shut off capability, wide selection of the working fluid that should only be independent from magnetic field and the MRF, and so on. The fabricated microvalve has 10mm×10mm×7mm in size and can control water flow rate from 0 to 30mm³/s at supply pressure 35kPa.

Fabricated Position Control Microsystem

Utilizing the piezoelectric micropump using fluid inertia in pipe, the microvalve using MRF valve-body, and a bellows microactuator, a position control microsystem was fabricated as shown in Fig. 11. The restrictions at downstream ports of the microvalve have differential pressure 35kPa for flow rate 30mm³/s. The bellows microactuator has 3.2mm in outer diameter, 3.1mm in length, and 0.40kN/m in spring constant. With large circulation flow, the variation of supply pressure to the microvalve was small. The working fluid was degassed water. Current was applied to the microvalve with a voice coil motor driver (maximum current: ±3A) with dither. Supply pressure and load pressure were measured with semiconductor type pressure transducers (pressure range: 0.1MPa). Output displacement was measured with a laser

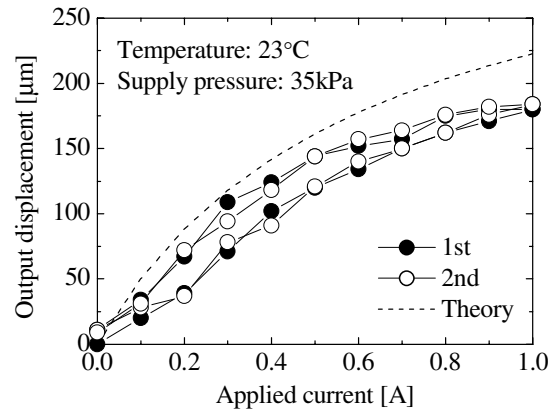


Figure 12 Measured static characteristics of the position control microsystem with open loop control

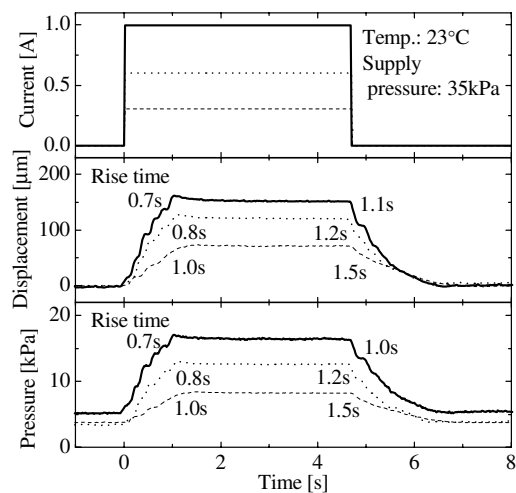


Figure 13 Measured step responses of the position control microsystem with open loop control.

displacement meter (resolution: 0.2μm). The measured values were fetched by a personal computer through A/D converter with sampling frequency 200Hz.

The basic characteristics with open loop control were measured. Figure 12 shows the measured static characteristics. The origin of displacement is the position without current. It is found that the displacement can be controlled up to 180μm with high reproducibility, though there are some hystereses due to friction between the MRF valve-body and valve seat, and that the displacement begins to saturate at current 0.6A. The dotted line in Fig. 12 is theoretically calculated results based on the measured resistance of the microvalve without load. Good agreement is confirmed with some errors due to variation of the MRF valve-body width.

Figure 13 shows the measured step responses. It is found that higher response is obtained with larger current amplitudes for both step up and down. The reason is thought that with high current amplitude, the MRF valve-body approaches to the electromagnetic pole and driving force increases. Also it is found that the

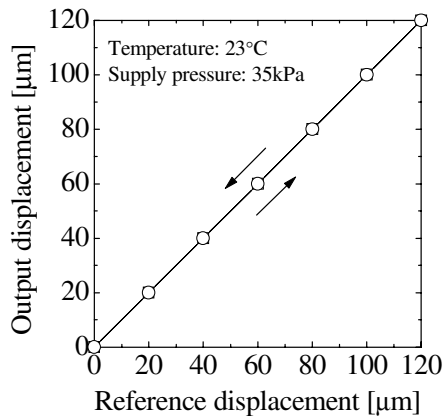


Figure 14 Measured static characteristics of the position control microsystem with PI control

step up response is higher than that of step down. The reason is thought that the force to bend the MRF valve-body by the electromagnet is higher than that by the permanent magnet to recover the shape. There are some stepwise waveforms, which are due to friction between the MRF valve-body and valve seat.

Characteristics of the Position Control Microsystem

A PI control system was constructed by software written in language C. The Proportional gain $0.07\text{A}/\mu\text{m}$ and integral gain $0.03\text{A}/(\mu\text{m}\cdot\text{s})$ were determined based on measured step responses for $10\mu\text{m}$ amplitude. To prevent the MRF valve-body separation, the applied current amplitude was restricted up to 0.6A .

Figure 14 shows the measured static characteristics. High reproducibility was confirmed up to $120\mu\text{m}$.

Figure 15 shows the measured step responses with 0.1Hz square wave. Comparing to open loop system in Fig. 13, rise times decrease and the rise time for step up becomes equal to the value for step down. The reason the rise time for step down is the same as the open loop system is thought that current saturation continues long time. Also, for high step amplitude, the settling time becomes large because current saturation continues long time and wind up occurs highly. The dead time is thought to be due to friction between the MRF valve-body and the valve seat.

CONCLUSIONS

To realize a high output power piezoelectric micropump using fluid inertia in pipe, the pump structure and the application were investigated. The main results are as follows:

- (1) A simple nonlinear mathematical model with lumped parameters was proposed and confirmed comparing the simulation and experimental results.

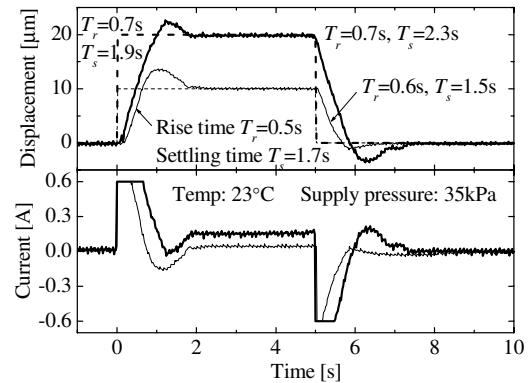


Figure 15 Measured step responses of the position control microsystem with PI control

- (2) The pump structure for higher output power was obtained based on simulations using the mathematical model.
- (3) The validity of the obtained pump structure was confirmed based on experiments.
- (4) The microvalve was applied to a position control microsystem. The characteristics were experimentally clarified and the validity was confirmed.

A part of the research was supported by Grant-in-Aid for Scientific Research in Priority Areas, No.16078205 of the Ministry of Education, Culture, Sports, Science and Technology of Japan.

REFERENCES

1. Takeda, M., Applications of MEMS to Industrial Inspection, Proc. MEMS 2001, 2001, pp.182-191.
2. Yoshida, K. and Yokota, S., Study on High-Power Micro-Actuator Using Fluid Power, Proc. FLOMEKO'93, 1993, pp.122-130.
3. Park, J.-H., Yoshida, K. and Yokota, S., Resonantly Driven Piezoelectric Micropump - Fabrication of a Micropump Having High Power Density -, *Mechatronics*, 1999, **9**-7, pp.687-702.
4. Park, J.-H., Yoshida, K. and Yokota, S., Micro Fluid Control System for Micromachines, Proc. FLUCOME 2000, 2000, CD-ROM.
5. Yoshida, K., Jung, Y.-O., and Yokota, S., A Microvalve Using MR Fluid Valve-Body, Proc. ICMT 2002, 2002, pp.423-428.
6. Seto, T., Takagi, K., Yoshida, K., Park, J.-H., Yokota, S., Development of High-Power Micropump Using Inertia Effect of Fluid for Small-Sized Fluid Actuators, *J. of Robotics and Mechatronics*, 2003, **15**-2, pp.128-133.
7. Reyes, D. R., Iossifidis, D., Aruoux, P. A., Manz, A., *Micro Total Analysis Systems, Anal. Chem.*, 2002, **74**, pp.2623-2628.

DEVELOPMENT OF MICROVALVE MECHANISM USING FLUIDICS

Yutaka Tanaka*, Sadahisa Yamada**, Naoto Nakamura**, Gaku Minorikawa***

* Department of Art and Technology, Faculty of Engineering

**Graduate School of Engineering

*** Department of Mechanical Engineering, Faculty of Engineering

Hosei University

3-7-2 Kajinocho, Koganeishi, Tokyo, 184-8584 Japan

(E-mail: y_tanaka@k.hosei.ac.jp)

ABSTRACT

In the field of MEMS technology, the high accumulation and high density for making semiconductor devices are rapidly advanced. On the other hand, neither high accumulation nor densification on micro mechatronics are so advanced comparing with semiconductor devices. In our laboratory, it pays attention to microfluidic systems which can control fluids without mechanical moving parts. In this paper, design and fabrication of microfluidic devices with small, light and integration are discussed. A prototype models based on fluidics is fabricated and experimentally investigated. A view point of future application for the micro fluidic devices is also reported.

KEY WORDS

Down Scaling, Fluidics, Laminar Proportional Amplifier, Microvalve, Vent Port

INTRODUCTION

A micromachine and a micro mechatronic device is a general term for devices and integrated systems including parts of 1mm or less. It has a high potential key technology to realize a miniaturization, low power consumption, high density and high integration in many fields such as medical, information and communication, biotechnology and aerospace industry. Recently, according to advance of semiconductor technology, story of the micromachine is not a dream because of development of micro processing and fabrication technologies. Research and development for the micromachine has been widely and actively carried out all over the world for the important technology in the next generation. As a result, a variety of new processing

methods and devices for micromachines have been proposed and developed, and begun to walk steadily on the road of practical use.

Especially, according to advance in the biotechnology field the micro fluid control devices such as Micro/Miniaturized Total Analysis Systems (μ -TAS) [1][2], DNA chips and microchips based on capillary electrophoresis become one of the main device in the micromachine. In the medical industry field, the micromachine has been just beginning to be applied a drug delivery system. The drug delivery system (DDS) is a method of surely making the medicine arrive to the treatment part in the inside of a human body without a surgical operation with a present surgical knife [3]. It is possible to make the load reduced to the patient dramatically. Therefore, it is necessary to develop the

micro mechatro devices that combines the micro fluid control devices such as micro actuators, micro sensors, micro valves and micro pumps.

Under an environment marked by the micro size, adsorption, friction, viscosity and abrasion occurring in the surface phenomenon have a large influence on the performance, energy efficiency, durability and reliability of the micromachines. In the micromachine or the micro mechatro device, the micro valve is the most important functional device for the part of the DDS or the unit of the μ -TAS.

It is not suitable for the structure of the valve with mechanical moving parts because of large power consumption. Moreover, it is difficult for the micromachine to assemble many parts in three dimensional structures. Therefore, it is preferable to produce it with complete parts where the mechanism is simple and the parts size is small as much as possible. In our laboratory, it pays attention to microfluidic systems controlled fluid flow without mechanical moving parts. In this paper, design and fabrication of microfluidic devices with small, light and integration are discussed. A prototype models based on fluidics is fabricated and experimentally investigated. A view point of future application for the micro fluidic devices is also reported.

LAMINAR PROPORTIONAL AMPLIFIER

The fluidics is a unique device without mechanical moving parts to control and switch the flow rate and the pressure. The fluidics is the technology of using the internal flow characteristics between walls, i.e., collision of jet flow, generation and settling of turbulence flow, preservation of momentum flow, attachment and separation of jet flow, and resistance or change in relation between the flow rate and the differential pressure. The flow characteristic of the fluidics depends on the shape of the geometry of the flow channel [4][5]. The fluidics has the advantage of easy miniaturization, high reliability and environmental compatibility. Additionally, the method of putting the film and the valve moved by the flow is effectively used according to the condition.

In this research, a laminar proportional amplifier (LPA) in the fluidics is used for control valves. The LPA is the typical analogue element in the fluidics. Figure1 shows the flow channel geometry and the three dimensional structure of the LPA [6]. The LPA consists of supply ports, control ports, output ports and vent ports symmetrically. The important dimension depends on a main nozzle width b_s , a control nozzle width b_c , an output nozzle width b_o and a splitter distance X_{sp} . The dimension of the each part is based on the main nozzle width, and the aspect ratio is selected by one or less to operate because flow range is within a laminar flow of air. Both sides of the plate (Plate2) with the flow

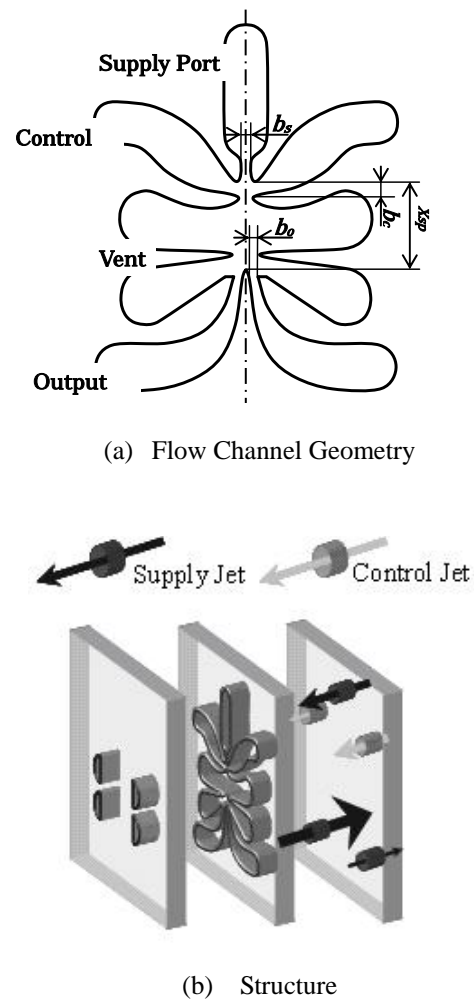


Figure 1 Laminar Proportional Amplifier

channel geometry are sealed up in two plates (Plate1 and Plate3). A main jet emerging from the supply port interacts with flows from the control ports. As a result, a right and left output port receives an inclining main jet flow, and the output differential pressure is proportional to the control difference pressure. The vent port has the role of preventing the influence of flow from output sides to input sides.

The LPA has the principle of similitude on the dimension of the flow channel geometry. The multistage LPA is also easily realized to amplify the output signal. It suggests that the operating performance of the LPA may be improved by means of being miniaturized, aligned, arrayed and multistage.

EXPERIMENTS

In this study the standard models of the LPA are designed by the previous model based on [7] and fabricated through a stereolithography method. The

stereolithography can fabricate a complex solid model including internal shape in the process of one time and easily reproduce a new shape of form with changing 3D CAD data [8][9]. When we produce the micromachines, it is necessary to reduce the number of parts and assembly process as much as possible. In this respect, the stereolithography is one of most effective method because of manufacturing micro-parts on the whole form. The fabricated LPA consists of three parts of plates; a vent cover (Plate1), a plate with the flow channel geometry (Plate2) and a plate with supply and control ports (Plate3). The final structure of the developed prototype LPA is shown in Figure 2. In the final designing, the Plate 2 are assembled and united with the Plate 3 to reduced number of parts for the fluidics device.

In this paper the standard model of the prototype LPA is called Model_S. The Model_S has the height X_h of flow channel geometry of 12.065mm, the width X_w of 8.89mm, the supply nozzle width of 0.38mm and the thickness of 0.5mm. In the principle of the LPA the shape of the vent ports is one of the important design factor to perform better. The influence for the cover plate and the shape of the vent port for the LPA has not been reported before. We also investigate to effect on the shape of the vent ports on the cover plate fabricated two kinds of vent covers; the semicircular type and circular type of the vent ports.

The Reynolds number Re is defined by the following expression as the thickness of the representative length,

$$Re = \frac{\sqrt{\rho}}{\mu} h \sqrt{2P_s} \quad (1)$$

where h is the thickness of the element, P_s is the supply pressure at the supply port, ρ is the density of the fluid and the μ is the viscous coefficient of the fluid. When the supply pressure is kept at a constant value, the Reynolds number is dependent on the thickness of the elements, and it isn't involved the width of the supply nozzle b_s . In case of using fluids as air, ρ is 1.024kg/m³ and μ is 1.808×10⁻⁵ Pa s. If the supply pressure P_s is kept at 1kPa, the Reynolds number is calculated as 1357 and the air flow at the point of the supply nozzle becomes laminar flow.

Figure 3 shows a system configuration for experimental apparatus. The supply pressure P_s , the control pressures P_{c1} and P_{c2} , the output pressures P_{o1} and P_{o2} are measured with pressure gauges and stored in a microcomputer through an A/D converter, respectively. Amount of minute pressure at the supply and control ports are kept at the constant value by the upstream side of the speed controllers. The static characteristics between pressure difference ΔP_c ($=P_{c1}-P_{c2}$) and ΔP_o ($=P_{o1}-P_{o2}$) are calculated and analyzed.

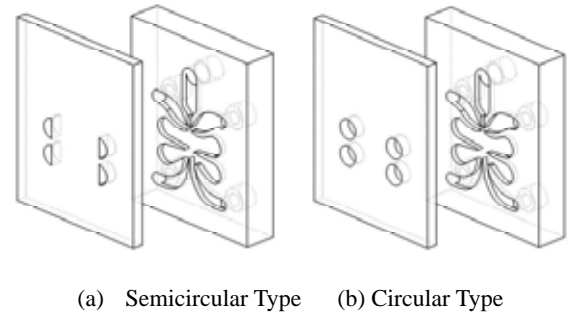


Figure 2 Structure of Prototype LPA

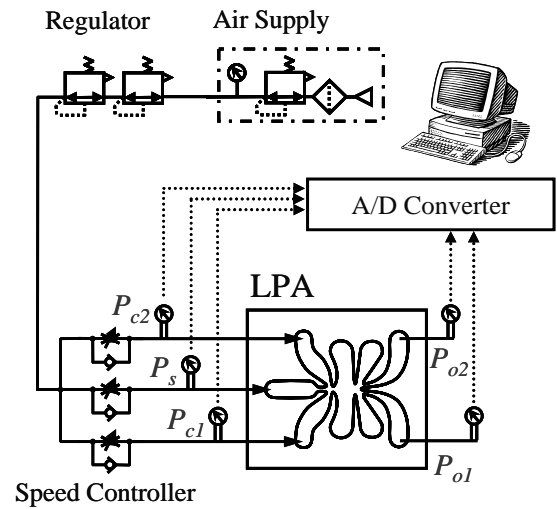


Figure 3 System Configuration of Experimental Apparatus

STATIC CHARACTERISTICS OF LPA

Standard Type of the LPA

On the first stage of our experiments, the static characteristics for the standard models with circular and semicircular types of the vent ports are clarified under the supply pressure P_s of 1kPa. Figure 4 shows the static characteristics between the differential control pressure ΔP_c and the differential output pressure ΔP_o . The ΔP_o is nearly proportional to the ΔP_c in the range of near the origin. The linear characteristics of the pressure gradient are linearized and defined as the pressure gain G_p . However, ΔP_o is saturated as increasing ΔP_c , so the range width between the two saturation points on ΔP_c is defined as a linear range L_p . Moreover, the ratio of P_{o1} to P_s under ΔP_c having zero is defined as the pressure recovery ratio R_p . The width of the linear range L_p is dependent on the shape of the vent cover. Table 1 indicates that G_p for the semicircular type is six times comparing to the amount of circular type. The pressure recovery ratio R_p for the semicircular type is 3% larger than the amount of circular type. These results suggest that the output pressure strongly depends on the shape

of the vent ports for the LPA.

Next, all pressure data are normalized by the supply pressure in order to verify the static characteristic of the LPA with change of the supply pressure. Figure 5 shows the normalized static characteristics between $\Delta P_c/P_s$ and $\Delta P_o/P_s$ under the standard model with the semicircular type of vent ports. The linear range L_p becomes larger as decreasing the supply pressure. The pressure gain G_p and the pressure recovery ratio R_p become large with increasing the supply pressure as shown in Table 2. Especially, the pressure gain under P_s of 1kPa becomes two times comparing to the pressure gain under P_s of 500Pa.

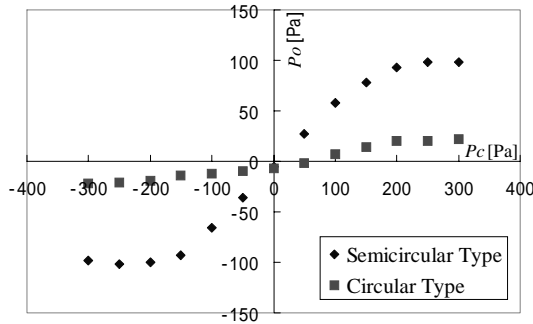


Figure 4 Static Characteristic of Standard Models under Supply Pressure of 1kPa

Table 1 Pressure Gain and Pressure Recovery Ratio with Change of Vent Port

	Semicircular Type	Circular Type
$G_p[-]$	0.6	0.1
$R_p[\%]$	9.2	6.1

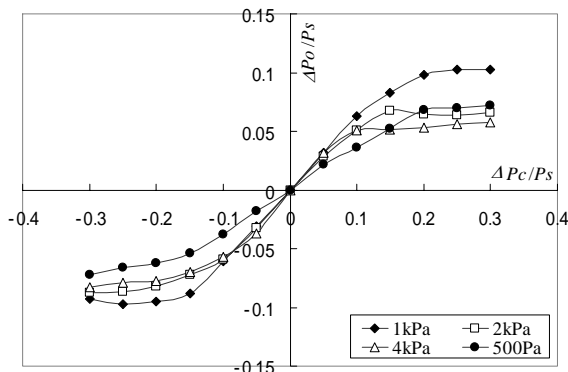


Figure 5 Static Characteristics under Change of Supply Pressure

Table 2 Pressure Gains and Pressure Recovery Ratio under Change of Supply Pressure

P_s	500[Pa]	1[kPa]	2[kPa]	4[kPa]
$G_p[-]$	0.3	0.6	0.6	0.6
$R_p[\%]$	8.9	9.2	9.8	9.9

Table 3 Dimensions of Prototype LPA

	Model_S (standard model)	Model_8	Model_5
$b_s[\text{mm}]$	0.38	0.304	0.19
$b_c[\text{mm}]$	0.38	0.304	0.19
$b_o[\text{mm}]$	0.513	0.410	0.257
$X_{sp}[\text{mm}]$	3.0	2.4	1.5
$h[\text{mm}]$	0.5	0.4	0.25
$X_h[\text{mm}]$	12.065	9.652	6.033
$X_w[\text{mm}]$	8.89	7.11	4.45

Down scaling of the LPA

In this research, the fluidics is applied to the micro valve. However, there are few reports on the characteristic of the miniaturized LPA since it is difficult to fabricate one. In this section, the influence on scaling of the LPA is experimentally investigated and evaluated the effectiveness of the fluidics. The dimensions of the prototype LPA are tabulated in Table 3. Two different type of the LPA (Model_8 and Model_5) for scaling of the geometry are used to investigate the effect of downscaling comparing to the standard model (Model_S). The downscaling model Model_8 is 0.8 times the Model_5 is 0.5 times as large as the size of the standard model Model_S.

On the second stage of our experiments, the supply pressure is kept at the constant value of 1 kPa and the semicircle type of the vent port is chosen to investigate the static characteristics of the LPA. As shown in Figure 6, the Model_S and the Model_8 are operated normally, but the Model_5 has unstable to operate. It seems the oscillation phenomenon appears since it is too much the supply pressure to generate the flow from the vent to the output side. So we test on the situations of decreasing the supply pressure and changing the vent cover.

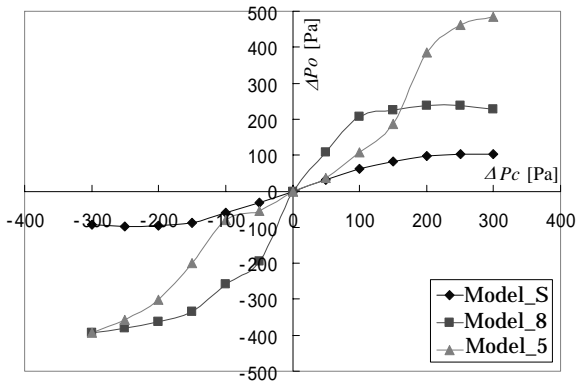


Figure 6 Static Characteristics with Semicircular Type of Semicircle under Supply Pressure of 1kPa

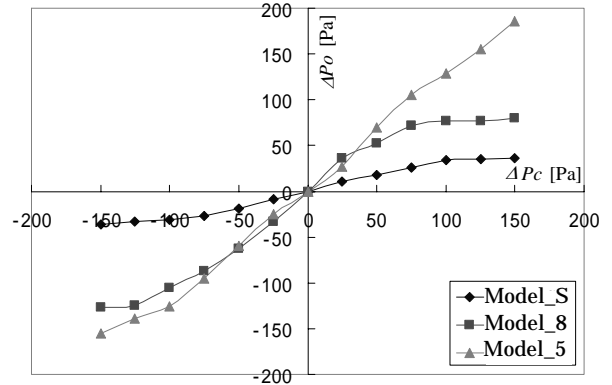


Figure 7 Static Characteristics with Semicircular Type of Semicircle under Supply Pressure of 500Pa

Table 4 Pressure Gain and Pressure Recovery Ratio With Semicircular Type of Vent Port (Supply pressure:1kPa)

	Model_S	Model_8	Model_5
G_p [-]	0.6	2.4	-
R_p [%]	9.2	17.4	-

Table 5 Pressure Gain and Pressure Recovery Ratio With Semicircular Type of Vent Port (Supply pressure:500Pa)

	Model_S	Model_8	Model_5
G_p [-]	0.3	1.0	1.2
R_p [%]	8.9%	14.1%	17.7%

Figure 7 shows the experimental result under the supply pressure of 500Pa. The oscillatory phenomenon of the pressure in the Model_5 disappeared for decreasing the supply pressure, and L_p becomes larger by miniaturization of devices. The pressure gain and the pressure recovery ratio in using the LPA with circular type of the vent port under the supply pressure of 500Pa and 1kPa are tabulated in Table 4 and Table 5, respectively. G_p and R_p become larger by downsizing of the fluidics and increasing of the supply pressure. Especially, the pressure gain G_p strongly comes under the influence of the value of the supply pressure.

Figure 8 shows the static characteristics for the LPA with circular type of the vent ports under the supply pressure of 1kPa. The oscillatory phenomenon of the pressure doesn't appear as well as the case of decreasing pressure. The pressure gain and the pressure recovery ratio are tabulated in Table 6. The Model_5 has the pressure gain G_p of 3.3 and the pressure recovery ratio R_p of 0.27. These results indicate the highest value in our experiments. Down scaling of the LPA becomes high performance to operate with under high pressure conditions.

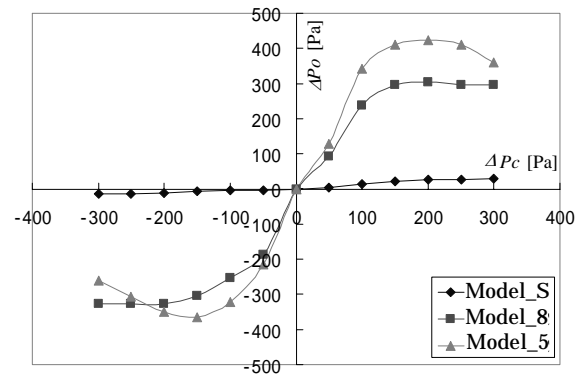


Figure 8 Static Characteristics with Circular Type of Vent Port under Supply Pressure of 1kPa

Table 6 Pressure Gain and Pressure Recovery Ratio With Circular Type of Vent Port (Supply pressure:1kPa)

	Model_S	Model_8	Model_5
G_p [-]	0.1	2.5	3.3
R_p [%]	6.1[%]	18.1[%]	27[%]

CONCLUSIONS

In our research project it has aimed at the development of the micro valve. In this paper the effectiveness of the micro valve using the fluidics has been experimentally investigated. The fluidics is a suitable structure for fabrication under the microscopic environment because of easy uniting and accumulating for multistage devices. The LPA has the principle of similitude on the dimension of the flow channel geometry. It has been confirmed that the normal operation of the LPA has been improved by miniaturization. Moreover the linear range of operation for the LPA between the control pressure and the output pressure has been extended and the pressure recovery ratio and the pressure gain have become larger when the size of the LPA is down scaling. The shape of the vent port greatly affects the range of operation. Therefore the fluidic devices are suitable for using as the micro valve in micro fluid power systems.

The traditional type of the LPA has been fabricated by machining of metals. In our study the LPA is fabricated by the stereolithography for all-in-one design. By use of the stereolithography the edge surface of the flow channel is rough comparing to the traditional machining of metals such as electric discharge machines. In the future work, we develop the micro power fluidics valve that has a smaller size and control ability of high-power with the fine fabrication of minute channel through the microfabrication technology. The integrated multistage LPA is suitable to realize control valves for micro mechatronics under the microscopic world.

ACKNOWLEDGEMENTS

The authors wish to thank Prof. Oyama, O. of Meiji University and Dr. Yoshimitsu, T. of Kanagawa Institute of Technology for their offer of the standard model concerning the fluidics and their valuable suggestion with our experiments. This study has been supported in part by Grant-in-Aid (#17040023) for Scientific Research in Priority Areas "Next-generation actuators leading break-through" of the ministry of Education, Culture, Sports, Science and Technology of Japan.

REFERENCES

1. A.Manz, et al.,Sensors and Actuators B1, 1990, pp.244-248,
2. M.A.Burns,et al.,Science 282,pp.484-487,1998
3. J.T.Santini Jr.,et al.,Nature 397,pp.335-338,1999
4. J.M.Kirshner.editor, Fluid Amplifiers, McGraw Hill Book Company, 1966
5. J.M.Kishner, Introduction to Fluidics, Fluidics Quaterly,vol.1,number.2, 1968, pp. 93
6. James w. Joyce, Design Guide for Fluidic Laminar Proportional Amplifiers and Laminar Jet Angular Rate Sensors, Harry Diamond Laboratories,

HDL-SR-84-6, 1984

7. Toshihiro Yoshimitsu, Osamu Oyama and Keijiro Yamamoto, Characteristic of Opto-fluidic Control System, Proceeding of the Fourth JHPS International Symposium on Fluid Power Tokyo'99, 1999, pp.431-436
8. K.Ikuta, K.Hirowatari, Real Three Dimensional Micro Fabrication Using Stereo Lithography and Metal Molding, Proc. of International Workshop on Micro Electromechanical Systems(MEMS'93), 1993, pp.42-47
9. Jey Won, Kathryn De Laurentis, Constantinos Mavroidis, Rapid Prototyping of Robotic Systems, Proceedings of the 2000 IEEE, International Conference on Robotics & Automation, 2000, pp.3077-3082

OPTIMISATION OF THE LIFT CHARACTERISTICS OF AN AXIAL PISTON PUMP GROOVED SLIPPER.

Josep M. BERGADA* and John WATTON**

* Fluid Mechanics Department ETSEIT
Universitat Politècnica de Catalunya
Colon 11 Terrassa 08222, Spain.
(E-mail: bergada@mf.upc.edu)

** Cardiff School of Engineering, Cardiff University
Queen's Buildings, The Parade PO Box 925 Cardiff CF24 0YF Wales UK.
(E-mail: wattonj@cardiff.ac.uk)

ABSTRACT

Grooves effects on slippers are understood from a qualitative point of view and analytically for slippers without grooves. This study addresses the effect of groove dimensions and position via expanding the equations of flow, pressure distribution and force developed for any number of lands. A unique advantage of having explicit equations is that they may then be used to design slippers in order to have maximum lift, via optimizing the groove length, depth and position. This cannot be achieved at present using previous knowledge apart from many simulation runs using a numerical simulation package.

KEY WORDS

axial piston slipper, effect of lands, direct solution

NOMENCLATURE

h_i slipper general height (m)
 n number of flat plates, including the grooves
 P_i general pressure (N / m^2).
 Q_i generalized flow (m^3 / s)
 r_i slipper general radius (m)
 μ fluid dynamic viscosity. ($kg / m s$)

INTRODUCTION

In the majority of cases the effect of the different pressure balancing grooves cut on pistons and slippers has been neglected. Although the groove effect on the flow and the pressure distribution is not expected to give a radically different pattern from the single-land case, the extension developed in this paper is a step

forward towards a better understanding of the effect. A mathematical approach was presented by Bergada and Watton [1,2] for a single grooved slipper and Fisher [3] studied the case of a flat slipper with single land on a rotating plate. Böinghoff, [4] studied theoretically the static and dynamic forces and torques acting on a single piston. Hooke [5] showed that a degree of non-flatness was essential to ensure the successful operation of the slipper, and the non-flatness must have a convex profile. He later [6] studied more carefully the couples created by the slipper ball. Iboshi and Yamaguchi [7,8], working with a single land slipper, determined the flow and the main moments acting on the slipper. Hooke [9] also studied more carefully the effect of non-flatness and the inlet orifice on the performance of the slipper. In [10,11] Hooke focused on the lubrication of overclamped slippers and considered the three different tilting

couples acting on slipper, finding that the tilting couple due to friction at the slipper running face is much smaller than the ones created at the piston-cylinder, piston-slipper interfaces, and the centrifugal term. Takahashi et al [12] studied the unsteady laminar incompressible flow between two parallel disks with the fluid source at the centre of the disks. Li et al [13] studied the lubrication of composite slippers on water based fluids. Koc et al [14] focused their work on checking whether underclamped flat slippers could operate successfully or whether a convex surface was required. They took into account the work done by Kobayashi et al [15] on the measurements of the ball friction. They concluded that polishing of the running face of the slipper to a slightly convex form, appeared to be essential for successful operation under all conditions. Harris et al [16], created a mathematical dynamic model for slipper-pads, in which lift and tilt could be predicted, the model was able to handle the effect of the possible contact with the swash plate. Koc and Hooke[17,18] studied more carefully the effects of orifice size, finding that the underclamped slippers and slippers with larger orifice sizes run with relatively larger central clearances and tilt more than those of overclamped slippers with no orifice. Ivantysynova [19] developed a package called CASPAR which uses the bi-dimensional equation of lubrication and the energy equation in differential form. It was shown how transient cylinder pressure could be computed by knowing the leakage characteristics of the piston chamber. In addition, the dynamic clearance and tilt of the slipper was studied over one revolution of the pump and a single land slipper plate was used in the theoretical and experimental analysis.

ANALYSIS

Although a large amount of work has been done in order to better understand slipper behaviour, very little work has focused on flow characteristics for slippers with two or more lands, and no attempt to explain mathematically the two land slipper behaviour has been found. The main piston and slipper assembly used in this study is shown in figure 1, and is one of nine pistons from a pump having a maximum volumetric displacement is 0,031 dm³/rev.

It will be seen that the slipper design uses two full lands and the approach selected seems to be the personal design philosophy of the particular pump manufacturer. Considering previous work [1,2] together with the assumptions of laminar flow, no slipper tilt, steady state conditions, rotation effects are negligible, the flow is radial, the pressure drop is dominated by the radial flow, then the solution of Reynolds gives equation 1.

Such a generic equation can be used for a slipper with any number of lands, bearing in mind that the equation presented here does not regard the slipper pocket as one of the lands.

$$Q = \frac{\pi}{6\mu} \frac{P_{inlet} - P_{outlet}}{\sum_{i=1}^n \frac{1}{h_i^3} \ln \frac{r_{(i+1)}}{r_i}} \quad (1)$$

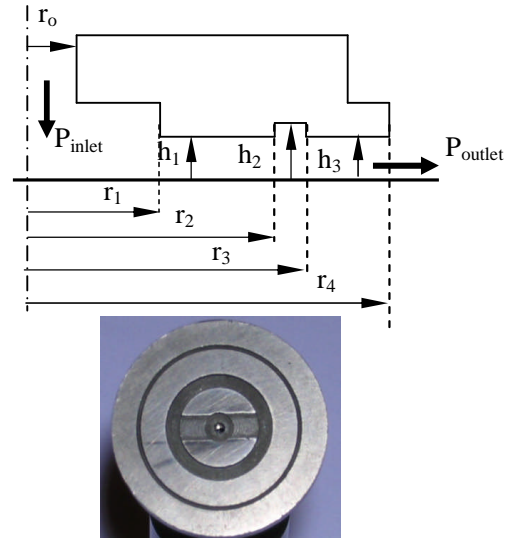


Figure 1. Slipper studied (Courtesy Oilgear Towler UK)

The dominant hydrostatic force will be given as the addition of the slipper pocket force plus the force due to the integration of the pressure distribution along the slipper two lands and groove. The force balance for the single-groove slipper design under study will be:

$$F_{lift} = P_{inlet} \pi (r_4^2 - r_o^2) - C\pi r_4^2 \left(\frac{1}{h_1^3} \ln \left(\frac{r_2}{r_1} \right) + \frac{1}{h_2^3} \ln \left(\frac{r_3}{r_2} \right) + \frac{1}{h_3^3} \ln \left(\frac{r_4}{r_3} \right) \right) \quad (2)$$

$$+ C\pi \left(\frac{r_2^2 - r_1^2}{2h_1^3} + \frac{r_3^2 - r_2^2}{2h_2^3} + \frac{r_4^2 - r_3^2}{2h_3^3} \right) \quad (3)$$

$$C = \frac{P_{inlet} - P_{outlet}}{\frac{1}{h_1^3} \ln \left(\frac{r_2}{r_1} \right) + \frac{1}{h_2^3} \ln \left(\frac{r_3}{r_2} \right) + \frac{1}{h_3^3} \ln \left(\frac{r_4}{r_3} \right)}$$

In this study the slipper is assumed to be parallel to the swash plate, hence $h_1 = h_3$.

MODIFYING GROOVE GEOMETRY AND POSITION.

Data for the two slippers evaluated is shown in Table 1. Figure 2 shows the typical pressure distribution along the entire slipper face for a 0.4 mm width groove, when the groove is located near the inner radius or near the

outer radius. It was noticed that for groove depths of 0.4 mm, pressure is maintained constant along the groove length and for depths of few microns there is a considerable pressure differential between groove borders. It must be pointed out that the pressure distribution curve for an inner groove with 15 microns depth falls below the curve at 0.4 mm depth, while the opposite happens for the outer groove. Integrating the pressure distribution shows that the grooves located at an inner radius will produce higher lift than when located in any other position.

Table 1. Dimensions of the two slippers considered

	Slipper 1 (1 groove)	Slipper 2 (1 groove)
r_0 (mm)	0.5	0.4
r_1 (mm)	5	7.7
r_2 (mm)	7.43	11.175
r_3 (mm)	7.83	11.725
r_4 (mm)	10.26	15.2
Pocket depth (mm)	$h_1 + 0.6$	$h_1 + 0.55$
Groove depth (mm)	$h_1 + 0.4$	$h_1 + 0.4$

Calculations in Table 2 show the leakage flow percentage increase compared with the single land slipper, when modifying groove depth and length, while maintaining the slipper clearance at 10 microns. Different groove positions such as groove centred,

groove located at the centre of the inner land and groove located at the centre of the outer land are also evaluated. Notice that leakage increases with groove length and depth, on the other hand leakage increases much faster when the groove is located at the inner land. Due to its linearity, the leakage percentage increase is independent of the inlet pressure.

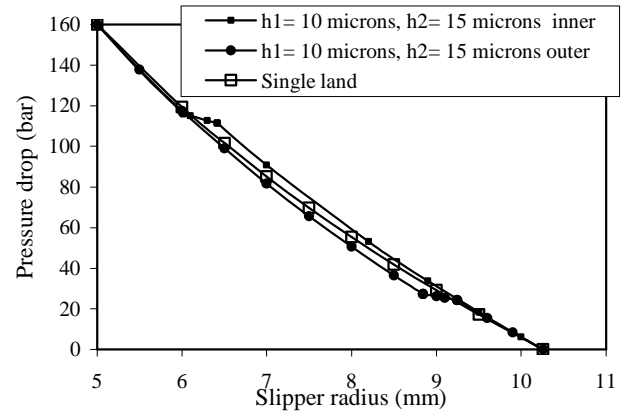


Figure 2 Pressure distribution for different groove positions, groove length 0.4 mm, inlet pressure 160 bar (slipper 1)

Table 2 Leakage increase for different designs (slipper 1)

Groove depth Groove length	Leakage increase %	Groove depth Groove length	Leakage increase %	Groove depth Groove position	Leakage increase %
$h_2 = 0.4$ mm length = 0.8mm	16.6	$h_2 = 15$ microns length = 0.8mm	11.1	$h_2 = 0.4$ mm Inner	9.8
$h_2 = 0.4$ mm length = 0.4mm	7.9	$h_2 = 15$ microns length = 0.4mm	5.4	$h_2 = 0.4$ mm Central	7.9
$h_2 = 0.4$ mm length = 0.2mm	3.8	$h_2 = 15$ microns length = 0.2mm	2.7	$h_2 = 0.4$ mm Outer	6.6

Table 3 Lift force % change for different slot positions and depths (slipper 1).

Slot position	Groove length= 0.4 mm Slipper single land force =1746N@100bar					
	$h_1 = 2.54$ microns		$h_1 = 10$ microns		$h_1 = 20$ microns	
	h_2 microns	Force %	h_2 microns	Force %	h_2 microns	Force %
Inner	5	2.60	15	2.10	25	1.50
	400	3.00	400	3.00	400	3.00
Centred	5	-0.28	15	-0.23	25	-0.16
	400	-0.33	400	-0.33	400	-0.33
Outer	5	-2.60	15	-2.10	25	-1.40
	400	-3.06	400	-3.06	400	-3.06

In Table 3 the lift force has been evaluated when a groove of 0.4 mm length is located at a inner, centre and outer radius. It can be concluded that for an inner slot, lift force decreases as the gap slipper plate increases, and the force increases as the groove depth does. On the other hand when the groove is located at the outer radius the force will increase when increasing the slipper clearance, and it will decrease as the groove depth increases. It is clear that a groove located at an inner land will produce lift forces higher than for a single land slipper. From the equations presented, and based on (slipper 1) is shown that the effect of groove depth on pressure change across the groove is negligible for depths beyond 0.1 mm and absolutely beyond 0.3 mm.

A more comprehensive comparison of the effect of groove position and width on the lift force and leakage flow rate, for the same geometrical conditions, may be seen from the 3D plots shown as figure 3.

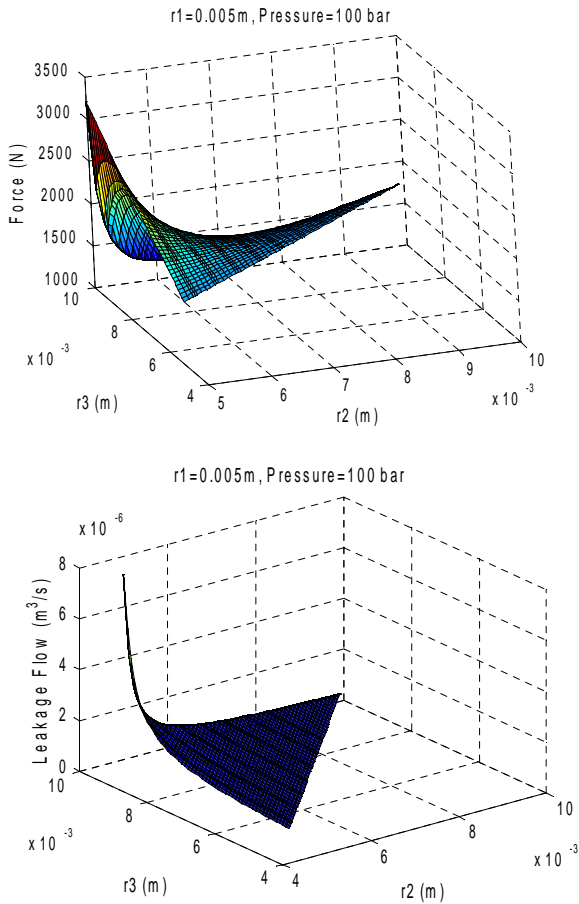


Figure 3. Variation of the force over the slipper face, and the leakage flow rate. Inlet pressure 100 bar (slipper 1).

The hydrostatic force provided at the piston side is

1678N@100bar piston pressure which has to be ostensibly balanced by the slipper hydrostatic lift by design. For no groove the hydrostatic lift would be 1746N@100bar piston pressure and the slipper would be underclamped. When operating with grooved slippers, it would be useful to know the groove dimensions to obtain maximum lift. This is now possible analytically for the first time using the previously set of equations. Since several parameters such as groove length, depth and position affect the lift force, some conditions must be established:

- dimensions r_1 and r_4 will be maintained constant.
- Given inner land outside radius, r_2 , it is possible to find the value of r_3 to obtain maximum lift.
- this value can be obtained from the derivative of the total lift force, equation (2), versus r_3 , and equating the resulting equation to zero. This process leads to the equation:

$$0 = r_3 \left[\frac{1}{h_1^3} \ln \left(\frac{r_2}{r_1} \right) + \frac{1}{h_2^3} \ln \left(\frac{r_3}{r_2} \right) + \frac{1}{h_3^3} \ln \left(\frac{r_4}{r_3} \right) \right] - \left(\frac{1}{r_3} \right) \left[\frac{1}{h_1^3} \frac{r_2^2 - r_1^2}{2} + \frac{1}{h_2^3} \frac{r_3^2 - r_2^2}{2} + \frac{1}{h_3^3} \frac{r_4^2 - r_3^2}{2} \right] \quad (4)$$

When substituting the values of r_1 , r_2 , r_4 , h_1 , h_2 , and h_3 in equation (4), the optimum external groove radius r_3 to obtain maximum lift can be found.

Figure 4 shows the optimum groove external radius r_3 to obtain maximum lift for a given internal radius r_2 , and for a set of inner land inside radius r_1 and the two different slippers. Notice that for a given slipper, the smaller the radius r_2 the bigger r_3 can be, and this will lead to bigger lift forces. The evaluation of slipper leakage for different inlet radius r_1 , a set of inner groove radius r_2 and for each case the optimum outer groove radius r_3 shows that the leakage increases as r_2 decreases.

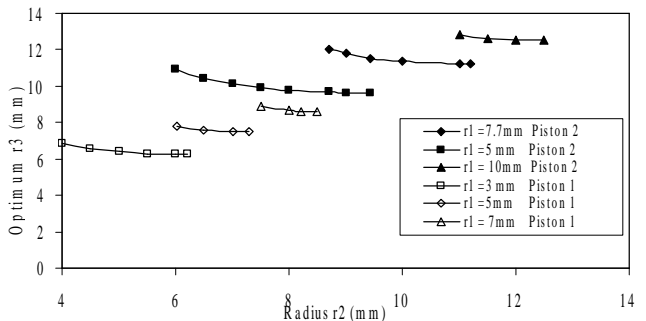


Figure 4 Optimum r_3 versus r_2 for a set of inner land inside radius, both slippers.

CONCLUSIONS

- Considering the boundary conditions for a multi-land slipper, it has been shown that a completely generalised solution for flow rate and radial pressure distribution can be obtained.
- It has been shown that the hydrostatic lift force can vary with groove placement and design and a localised optimum position exists.
- Lift in any single land slipper can be increased when creating a groove at an inner radius of the slipper land and maximum lift can be obtained when groove length is design according to equation (4).
- Grooves located at the slipper centre or towards the outer radius create lifts lower than a single land slipper, and therefore should be avoided unless necessary for stability.
- To maintain pressure constant along the slipper groove, it has been found thanks to the equations presented that a depth higher than 0.3 mm is needed for the groove and about fifty times the slipper clearance (about 0.5→ 0.6 mm) for the pocket.

REFERENCES

1. Bergada JM and Watton J. A direct leakage flow rate calculation method for axial pump grooved pistons and slippers, and its evaluation for a 5/95 fluid application. 5th JFPS international symposium on fluid power, Nara Japan, 2002, 259-264
2. Bergada JM and Watton J. Axial piston pump slipper balance with multiple lands. ASME International Mechanical Engineering Congress and exposition. IMECE 2002, New Orleans, 2002, paper 39338.
3. Fisher MJ. A theoretical determination of some characteristics of a tilted hydrostatic slipper bearing. BHRA. Report RR 728, April 1962.
4. Böinghoff O. Untersuchen zum Reibungsverhalten der Gleitschuhe in Schrägscheiben-Axialkolbenmaschinen, VDI-Forschungsheft 584. VDI-Verlag, 1997, 1-46.
5. Hooke CJ and Kakoullis YP. The lubrication of slippers on axial piston pumps. 5th International Fluid Power Symposium September 1978, B2-(13-26) Durham, England.
6. Hooke CJ and Kakoullis YP. The effects of centrifugal load and ball friction on the lubrication of slippers in axial piston pumps. 6th International Fluid Power Symposium, England, 1981, 179-191.
7. Iboshi N and Yamaguchi A. Characteristics of a slipper bearing for swash plate type axial piston pumps and motors, theoretical analysis. Bulletin of the JSME, Vol 25, No 210, December 1982, 1921-1930
8. Iboshi N and Yamaguchi A. Characteristics of a slipper bearing for swash plate type axial piston pumps and motors, experiment. Bulletin of the JSME, Vol 26, No 219, September 1983, 1583-1589.
9. Hooke CJ and Kakoullis YP. The effects of non flatness on the performance of slippers in axial piston pumps. Proc IMechE, December 1983, Vol. 197 C, 239-247.
10. Hooke CJ and Li KY. The lubrication of overclamped slippers in axial piston pumps centrally loaded behaviour. Proc IMechE, 1988, Vol 202, No C4, 287-293.
11. Hooke C.J., Li K.Y. The lubrication of slippers in axial piston pumps and motors. The effect of tilting couples. Proc IMechE, 1989, Vol 203, part C, 343-350.
12. Takahashi K and Ishizawa S. Viscous flow between parallel disks with time varying gap width and central fluid source. JHPS International Symposium on Fluid Power, Tokyo, March 1989, 407-414.
13. Li KY and Hooke CJ. A note on the lubrication of composite slippers in water based axial piston pumps and motors. Wear, 147 1991, 431-437.
14. Koc E, Hooke CJ, Li KY. Slipper balance in axial piston pumps and motors. Trans ASME, Journal of Tribology, Vol 114, October 1992, 766-772.
15. Kobayashi S, Hirose M, Hatsue J, Ikeya M. Friction characteristics of a ball joint in the swashplate type axial piston motor. Proc Eighth International Symposium on Fluid Power, Birmingham, England, 1988. J2- 565-592
16. Harris RM, Edge KA, Tilley DG. Predicting the behaviour of slipper pads in swashplate-type axial piston pumps. ASME Winter Annual Meeting. New Orleans, November 28-December 3, 1993, 1-9.
17. Koc E and Hooke CJ. Investigation into the effects of orifice size, offset and oveclamp ratio on the lubrication of slipper bearings. Tribology International, Vol. 29, No 4, 1996, 299-305.
18. Koc E and Hooke CJ. Considerations in the design of partially hydrostatic slipper bearings. Tribology International, Vol 30, No. 11, 1997, 815-823.
19. Wiecezorek U and Ivantysynova M. CASPAR-A computer aided design tool for axial piston machines. Proc Power Transmission Motion and Control International Workshop, PTMC2000, Bath, UK, 2000, 113-126.

A NUMERICAL MODEL FOR THE SIMULATION OF EXTERNAL GEAR PUMPS

Paolo CASOLI, Andrea VACCA and Germano FRANZONI

Dipartimento di Ingegneria Industriale
Università degli Studi di Parma
Parco Area delle Scienze 181/A, 43100 Parma, Italy
(E-mail: paolo.casoli@unipr.it)

ABSTRACT

External gear pumps are the most widely employed source of power in hydraulic applications, allowing good performance and low manufacturing costs. The present paper reports the description of a numerical model for the simulation of these kind of machines, developed by the authors. The model has been implemented using the software AMESim[®], introducing new in-house C++ models, with the main aim of an accurate prediction of the pressure ripple at the delivery port and the calculation the flow rate time course through the pump. In fact the reduction of flow pulsations is one of the crucial targets in the development of these machines.

The fluid dynamic model of the pump is based on a finite volumes framework: each chamber presents uniform fluid properties and is connected with the adjoining ones by variable orifices. The pump is described by the interaction between a fluid dynamic model, that predicts the instantaneous pressures and the flow rates between the chambers, with a geometrical sub-model for the evaluation of the actual values of the variable volumes (defined by teeth, housing, and side wear plates) and the throat areas, as functions of the shaft angular position.

This paper reports a deep description of the fluid dynamic model and a comparison between its numerical results and data available from experiments, showing how a correct evaluation of the flow when the chambers expand (and oil is pushed from the supply tank) or decrease (and oil is ejected into the outlet port) allows a good prediction of the pump characteristics.

The results reported in the paper show how the model can be a powerful tool for design and development of external gear pumps, e.g. it easily allows the prediction of the maximum and minimum pressure reached inside the teeth space volumes, giving important information to prevent cavitation and damages as well as to reduce the pump noise. Moreover the simulation environment easily allows the evaluation of the pump behaviour when it works in a given hydraulic system.

KEY WORDS

External gear pump, simulation, flow ripple, pressure ripple

NOMENCLATURE

n : shaft speed
 p : pressure
 p_m : pump maximum constant pressure
 t : time
 V : volume
 \dot{V} : volume flow rate
 ρ : fluid density
 \mathcal{G} : angular position
 ω : angular velocity

Subscripts

in : entering
 out : leaving

1,2 : driver gear (1) and driven gear (2)
 i,j : indexes of tooth space volume

Abbreviations

CV: control volume

INTRODUCTION

Fixed displacement pumps remain the most widely used sources of power in hydraulic applications, despite many present researches oriented to the evolution and cost reduction of variable displacement machines. In this perspective external gear pumps still have the role of prime actor. These machines combine the manufacturing simplicity, leading to reduced costs, with good efficiencies;

moreover their application area is extremely wide [1,2] spacing from the low pressure (such as the case of charge or lubricating pumps) to the medium-high pressure applications, including open loop and closed loop circuits. Notwithstanding gear pumps are relatively simple to manufacture, their operation involves a lot of complex phenomena of both mechanical and fluid nature; for this reason these pumps have been captivating the interest of many researchers for more than five decades. The first important studies pertain to Wilson [3] and Castellani [4]; in the late eighties Nervegna and Mancó proposed a simulation model for external gear pumps [5] and some studies about the experimental evaluation of the pressure transients [6] in the machine. After this time, several papers [7-10] concerned the analysis of the inter-teeth pressure, of the leakages, of the pressure and the force distribution on the gear side faces. Other researches analyzed the performance of the pump bearings and the fluid borne noise generated at the suction port [11,12], while in [13] the effects of changing teeth geometry on pump flow ripple is described.

Nowadays at the Industrial Engineering Dept. of the University of Parma the authors are developing a simulation model for external gear pumps in cooperation with Casappa S.p.A., an important Italian fluid power industry. The present paper refers to the first step of the research, presenting the basic model structure and the first significant results that have been reached.

For the model implementation the authors have chosen the simulation software AMESim[®]. Some new in-house modules have been created using AMESet[®], writing sections of code in C++ language. These have been added to a new user-defined library that is used to build up the complete model of the pump. The model is lumped parameter based; the chosen framework has the purpose of evaluating the flow and pressure course at the suction and delivery port and also in each tooth space volume and the leakages within the pump. The geometrical calculations were performed with CAD/CAE based tools provided by the manufacturer. These tools, not described in the paper, interact with the developed AMESim[®] model for the evaluation of all the pump geometrical characteristics (namely the flow areas between the volumes and the instantaneous volume entity) as a function of the position of the gears, accounting for the real shape of teeth and the geometry of the balancing bearing blocks.

In order to verify and calibrate the model, experimental test were performed on a stock pump using a rig specific for pump characterization.

NUMERICAL MODEL DESCRIPTION

The lumped parameter framework

According to the chosen approach, the pump is subdivided in a number of control volumes in which fluid properties are assumed uniform and only time dependent. As reported in fig. 1a, the model considers a control volume (CV) for each tooth space volume of both gears. Under the hypothesis of same number of teeth on the driver and driven gears, fig. 1a highlights how, as the shaft rotates, the generic tooth space volume $V_{1,i}$ of driver gear always meshes with the corresponding $V_{2,i}$ of the driven gear. The

solution adopted to describe the fluid dynamics of two conjugated teeth space volumes $V_{1,i}$ and $V_{2,i}$ is similar to the one presented in [7,10], although the method developed in the mentioned work is suitable only for the prediction of the inter teeth volumes pressure transient, while in this work the model is conceived to characterize the whole pump operating. Following each tooth space volume as a separated CV during the whole rotation of the gear, the model differs also from the scheme proposed in [5], which analyzes the pump using an eulerian approach for the CVs. Fig. 1b shows the definition of CVs for the inlet and the delivery volumes of the pump.

The model takes into account the connections between every tooth space volume with its surroundings, and the changing of net volume in the meshing zone. Eq. (1) gives the pressure course inside a generic CV as a function of fluid properties, the geometric volume variation and the net mass transfer with the adjacent CVs.

$$\frac{dp_{CV}}{dt} = \frac{1}{V_{CV}} \frac{dp}{d\rho} \left[\sum \dot{m}_{in,CV} - \sum \dot{m}_{out,CV} - \rho_{CV} \frac{dV_{CV}}{d\theta} \omega \right] \quad (1)$$

The flow areas connecting each tooth space volume with its surroundings and the actual values of volumes are considered depending on the shaft angular position.

Fig. 2 summarizes the framework on which the model is based. During a shaft rotation teeth go into mesh and the actual value of each CV changes; besides, with the gear rotation, it can be connected to several other chambers by means of variable orifices, whose areas follow a precise trend.

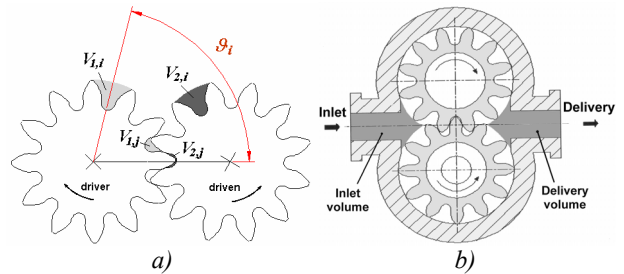


Figure 1 – Control volumes assumed in the model: teeth space volumes (a); inlet and delivery volumes (b)

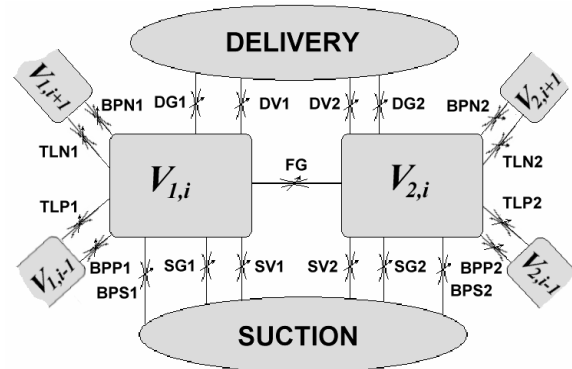


Figure 2 – Basic scheme of connections between the CVs of corresponding teeth space volumes

Referring to fig. 2, abbreviations have been adopted to identify the different flow areas:

- FG represents the connection between the two corresponding teeth space volumes when they are meshing (fig. 3a);
- DV1 (or DV2) is the connection between $V_{1,i}$ (or $V_{2,i}$) and the delivery volume through the gear whole depth (fig. 3a);
- SV1 (or SV2) is the connection at the opposite side, to the suction volume (fig. 3a);
- DG1 (or DG2) represents the connection between V_1 (or V_2) and delivery port through the bearing blocks recesses (fig. 3b). Fig. 4 shows also how the possible presence of side grooves (commonly used to compensate axial forces) can be considered by the DG1 (or DG2) orifices (DG1' and DG2' indicate the backflow grooves, if they are present);
- SG1 (or SG2) is the analogous connection with the suction port (fig. 3b);
- TLP1 and TLN1 (or TLP2 and TLN2) pertain to the leakages between adjacent teeth space volumes, due to the clearances between teeth tip and pump casing, as shown in fig. 5a (TLN refers to the next tooth space volume, while TLP to the previous one);
- BPP1 and BPS1 (or BPP2 and BPS2) refers to leakages through the lateral clearances between gear side faces and bearing blocks internal surfaces, as shown in fig. 5b (BPP: flow between the volume and the previous one, BPN: flow with the next volume);
- BPS1 (or BPS2) indicates the leakage flow between the tooth space volume $V_{1,i}$ and the drain line (fig. 5b), which, in the analyzed case, returns to the suction line.

A correct evaluation of the effect of orifices displayed in figs. 3 and 4 is necessary to analyse a solution widely used for the reduction of the pressure peak due to the compression of the inter teeth trapped volume between two adjacent contact points. This solution consists in a proper design of recesses [4,5], that makes the trapped volume never isolate from inlet and delivery (e.g. fig. 6). As shown in fig. 6, SG2 comes up before the closure of DG1. In this way pressure peaks – or excessive pressure drops – are avoided, but there is a flow that comes back from delivery to the inlet port. For this reason it is important to obtain a proper design of recesses inducing a tiny loss of flow while the inter teeth pressure does not rise too much.

As explained above, every connection between each control volume is accounted as equivalent orifice, whose area is described as a function of the angular position \mathcal{G}_i of the tooth space volume $V_{1,i}$ (see fig. 1a). In particular, that function is null outside a defined interval (for example for each $V_{1,i}$ and $V_{2,i}$ FG is greater than zero only in the meshing zone). Consequently, a correct implementation of the model strictly depends on the accurate evaluation of these geometrical functions.

Flow rates between adjacent volumes are evaluated considering the incompressible steady-state turbulent flow equation for orifices; according to the solution implemented in AMESim[®] standard models (described in [14-16]); the influence of the efflux dynamics on the correlation between \dot{V} and Δp is described by a discharge coefficient that depends on Reynold's number.

Leakage flows (represented in fig. 2 by BPN, BPP, BPS,

TLN, TLP), are approximated by the modified Poiseuille equation, for fully developed laminar conditions, accounting of relative motion of boundary surfaces [14].

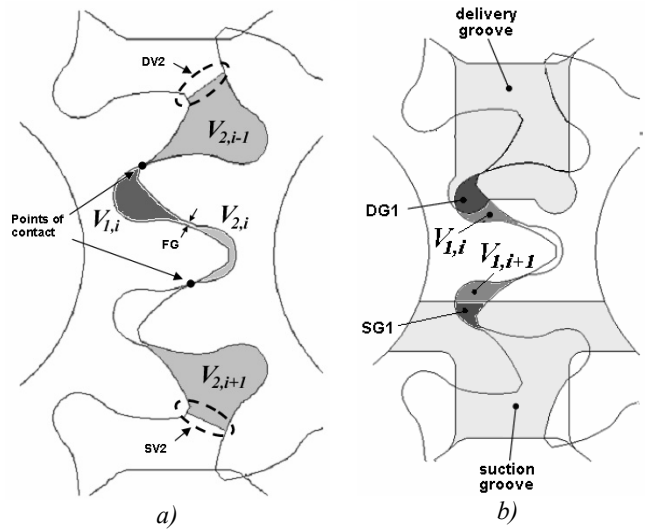


Figure 3 – a) connection between V_2 and delivery (DV2), suction (SV2) and V_1 (FG). b) connection between V_1 and suction (SG1) and delivery (DG1) through the recesses in the bearing blocks

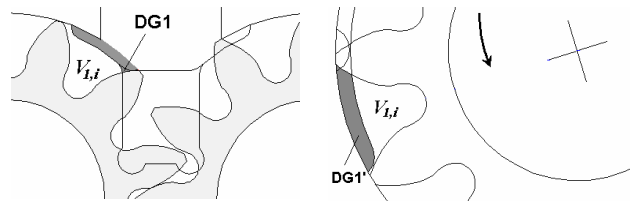


Figure 4 – Particular connections represented by DG1 due to the delivery groove and to the backflow grooves (DG1')

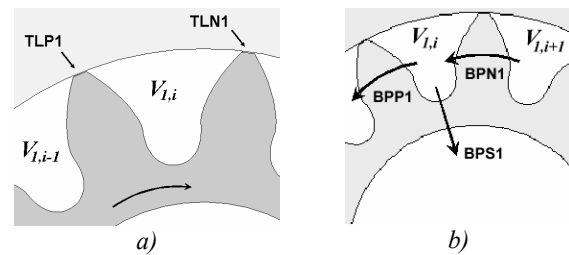


Figure 5 – Evaluation of leakages: between adjacent teeth space volumes (a) and in the clearances bounded by gears lateral sides and bearing blocks internal surfaces (b)

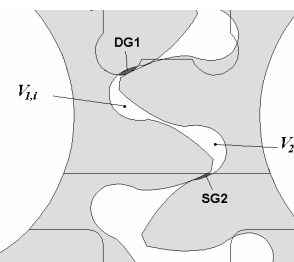


Figure 6 – Inter-teeth trapped volume between two adjacent contact points in the meshing zone

Model implementation

In fig. 7 the AMESim[®] diagram of the entire pump is presented. A major advantage of the generated pump simulation model lies in its suitability as a core element (supercomponent) inside the AMESim[®] simulation environment: it is therefore possible to study the behaviour of the machine in several circuit dispositions appraising the pump-circuit interaction. The majority of sub-models have been developed in-house, in C language, through the AMESet facilities [16]. The simulation model follows the framework of fig. 2, it can be easily adapted to different external gear pump geometries. The model has been conceived in order to allow the user to describe the pump by a number of parameters easy to define. Main pump features (e.g. number of teeth per gears, throat areas of inlet and delivery ports, etc.) and pump operating conditions are declared at the beginning of each simulation. The most important sub-models in the sketch of fig. 7 are indicated with the label “Multi Ch”. In the sketch of the model, the upper “Multi Ch” model refers to driver gear (fig. 1), while the lower pertains to the driven gear. The C-routine of such model implements the scheme displayed in the figure: the “Multi Ch” icon represents an array of hydraulic chambers (CVs) whose behaviour is governed by eq. (1). The course of the volume of each chamber and its first derivative come from an external ASCII file, while mass flow rates exchanged with the connected volumes are evaluated with external orifices models (only the leakage flows TLN_i and TLP_i are implemented into the sub-model itself). All these orifices are modelled with a in-house “Multi Orifice” component (fig. 7), in which a number of

variable orifices equal to the number of teeth of each gear is implemented in a C language subroutine. The variable chambers located at the bottom left and bottom right of the model (fig. 7) compensate the discrepancies of volume that would come from the chosen volume framework. In fact, when two teeth start meshing, there is a portion of volume that instantaneously passes from the tooth to the delivery (or suction) volume, as represented in fig. 8.

A prerequisite of the described model, in order to achieve a good prediction of flow as a function of pump operating conditions, is the knowledge of all necessary geometrical data, namely the variable volumes of teeth space and the throat areas of variable orifices, as a function of gear position. In the literature (e.g. [5,8]) it is possible to find simplified analytic expressions of teeth space volumes as a function of gear angular position, however the real trend and the throat areas of all orifices are strongly dependent on design of gear and recesses in the bearings plates. In this work, with the aim of comparing simulation results with available experimental data, a deep analysis of pump geometry for a particular stock pump was carried out. In particular, the evaluation of all needed geometrical data was performed through CAD/CAE tools, starting from the drawings.

RESULTS

The model results have been verified through the comparison with some available experimental data. In fact test campaigns were carried out on a stock pump whose main features are summarized in tab. 1. Details concerning the test rig utilized are reported in [17].

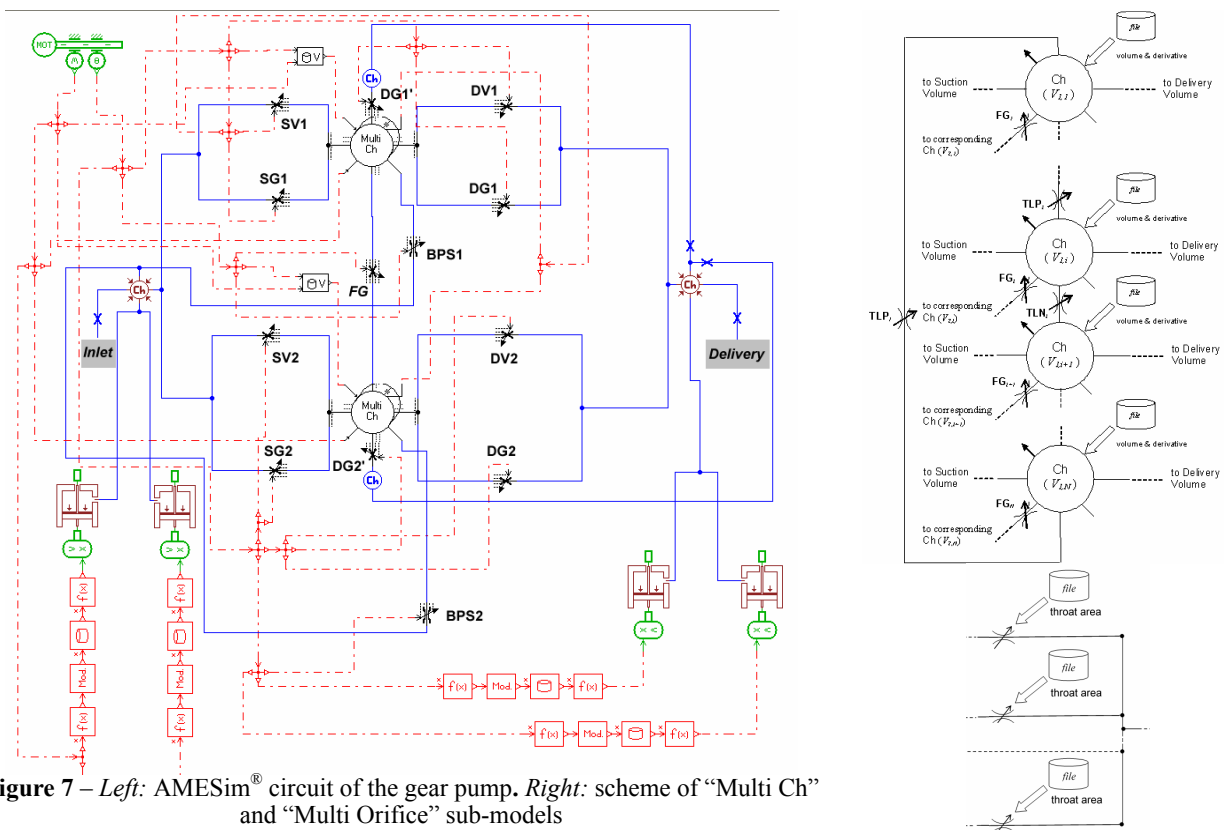


Figure 7 – Left: AMESim[®] circuit of the gear pump. Right: scheme of “Multi Ch” and “Multi Orifice” sub-models

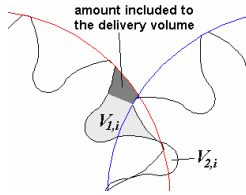
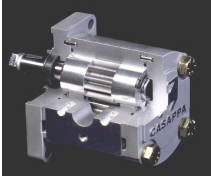


Figure 8 – Portion of volume assigned to delivery



pump name	PLP20.11.2 standard	
displacement	[cm ³ /r]	11.23
maximum speed	[r/min]	3500
minimum speed	[r/min]	600
number of teeth per gear		12

Table 1 – Main features of the pump

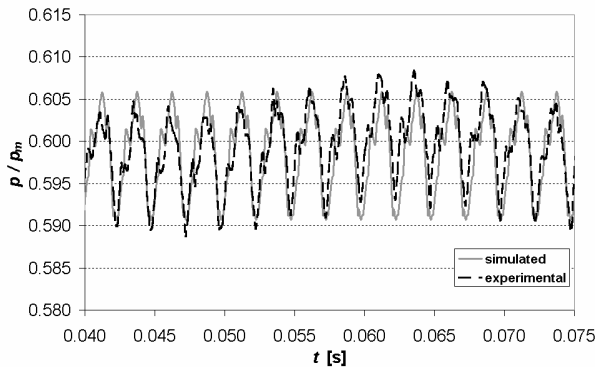


Figure 9 – Delivery pressure ($n = 2000$ r/min)

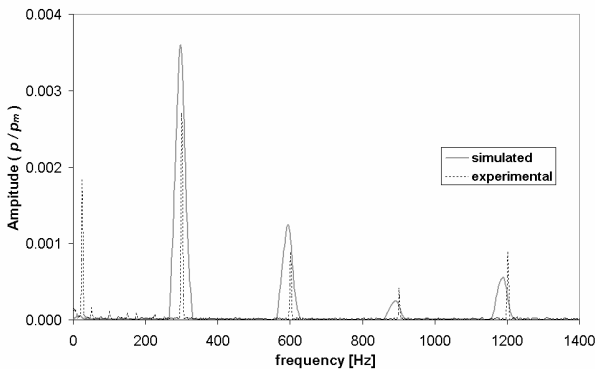


Figure 10 – FFT courses ($n = 1500$ r/min, $p/p_m \approx 0.8$)

The pressure measured at pump delivery, for a constant pump speed, and the measured pump flow rate were later compared with the numerical data, obtained simulating the whole test circuit used for pump characterization. In particular the delivery pipeline downstream of the pump was modelled through a distributed line models that account for wave propagation and frequency dependent friction phenomena, according to the standard models provided by the software [16].

Calibration parameters required by the code, namely all the discharge coefficients, were first assumed from the data reported in [7,18] for similar conditions, later they were slightly adjusted to better match with test data. The model has been validated through the comparison between predicted and measured pressure at the delivery port for

several working conditions (e. g. fig. 9). These simulations were performed assuming the pump operating with the nominal geometrical parameters, neglecting the deformation of pump structure with pressure and the initial period of adjustment. From fig. 9, the 12 teeth of each gear are noticeable observing the 12 pressure peaks during a shaft revolution (about 0.03 s at 2000 r/min), corresponding to 12 couples of teeth going into mesh. For all the considered cases the pressure ripple characteristic of this pump is well reproduced in detail by the simulation code. As displayed also in the representation of fig. 10, the experimental course highlights a low frequency trend – not observable in the calculated data – with a period equal to the time required for an entire gear revolution. Other peaks in the spectrum are well predicted, taking into account the approximation imposed by the windows method used for the FFT calculation to avoid leakage. The reason of this discrepancy could be the eccentricity of gears caused by the dimensional tolerances.

One of the most important results provided by the simulations is the trend of pressure inside a tooth space volume (fig. 11). The figure shows both pressure and tooth space volume versus gear angular position. From the figure it is possible to observe how the volume decreases when the tooth goes into mesh, with the typically parabolic trend (similar to those reported in [5,10]). The figure is very useful for understanding the working concept of the pump: starting from the condition of tooth volume outside the meshing zone (for ϑ approximately greater than 30°), it is possible to notice how the pressure begins to increase as effect of the aforementioned leakage flows (fig. 5) when the pump casing starts covering the tooth tip. The pressure suddenly reaches the delivery pressure when the backflow groove (DG1' see fig. 3) starts working (for $\vartheta \approx 150^\circ$, point B of fig. 11). The described increase follows an initial smooth increment (from point A), caused by the leakage from the adjacent tooth space volume in which pressure has already reached the delivery value. After point B, the pressure inside V_i follows the same trend as the delivery one, until the tooth reaches again the meshing zone. In fact in this period V_i is connected with the delivery through DG1' and DG1, or DV1 (figs. 3 and 4). Fig. 11 points out the effect of the shape of the backflow groove adopted in the analyzed pump (whose geometry is confidential): it realizes a further connection between the tooth space volumes in the zone marked with the letter C. The final peak marked with D corresponds to the minimum value of tooth space volume, reached in the meshing zone. As previously described, the maximum pressure value directly affects noise and fluctuations at pump delivery, so that its prediction is fundamental for the evaluation of pump performance. It is also important, in order to verify the design of the recesses and avoid any conditions of trapped volume isolated from inlet or delivery, the prediction of the minimum pressure value related to the quick increase of volume V_i (zone E). In this case the model is useful to predict any possible onset of cavitation.

Figure 12 shows the calculated flow rate at the delivery port. This result permits the estimation of important parameters as the flow ripple and the volumetric efficiency. In particular, the course of \dot{V} in fig. 12 gives a time average value of flow rate of about 15.4 l/min; this results

is consistent with the measured volumetric efficiency of this pump, even if the model deals with the leakages in a simple manner.

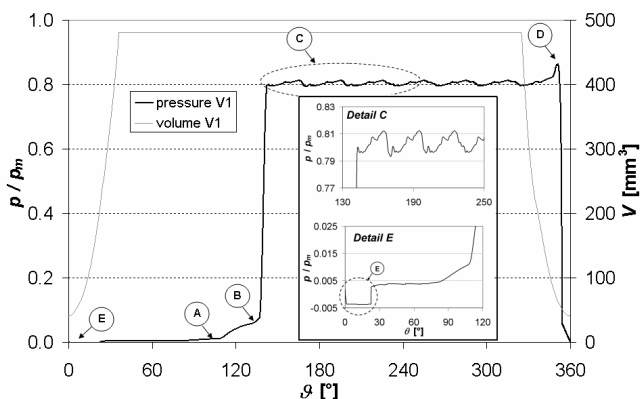


Figure 11 - Simulated pressure inside a tooth space volume V_1 ($n = 1500$ r/min, delivery pressure = 200 bar)

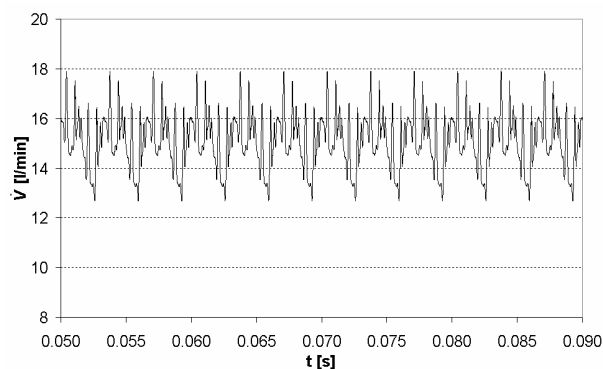


Figure 12 – Predicted mass flow rate at pump delivery ($n = 1500$ r/min, $p = 200$ bar)

CONCLUSION

This paper describes a numerical model for the simulation of external gear pumps. The model, implemented in AMESim[®] environment, is based on a lumped parameter framework and it stands out for its ease of use and simulation swiftness. The model has been developed and validated using as reference a commercial pump produced by Casappa S.p.A. Results provided by the model permit to analyze the pump operation deeply, showing the trend of some parameters which are difficult to measure (e.g. the inter-teeth pressure transient) and giving plenty of useful information to understand the influence of the main design parameters (e.g. the design of the recesses on the bearing blocks). Despite the model requires an accurate definition of all the pump geometrical features (as functions of the gear position) it easily allows the characterization of the fluid dynamics of the whole pump, with a wide versatility of simulation. Future works will take advantage of the approach adopted for the definition of the control volumes in the model for prediction of dissymmetric geometrical conditions (for example due to possible damage of some teeth, or to consider the actual eccentricity of gears while pump is operating).

ACKNOWLEDGEMENTS

The authors are grateful to Prof. G.L. Berta for his precious suggestions and help and to M. Guidetti (Casappa S.p.A.) for test and experimental data.

REFERENCES

- [1] Ivantysyn J., Ivantysynova M., 2003, *Hydrostatic Pumps and Motors*, Tech Books Int., New Delhi, India
- [2] Esposito A., 2000, *Fluid Power with Applications*, Prentice Hall Int. Inc.
- [3] Wilson W. E., 1948, *Performance Criteria for Positive Displacement Pumps and fluid Motors*, Proc. of ASME semi-annual meeting, June 1948.
- [4] Castellani G., 1967, *Pompe ad Ingranaggi a Denti Dritti*, Progetto delle Dentature, Giornata Mondiale della Fluidodinamica, FLUID'67, Oct. 13-14, MI, Italy.
- [5] Mancò S., Nervegna N., 1989, *Simulation of an External Gear Pump and Experimental Verification*, JHPS International Symposium on Fluid Power, Tokyo, Japan.
- [6] Mancò S., Nervegna N., 1993, *Pressure Transient in an External Gear Hydraulic Pump*, Second JHPS International Symposium on Fluid Power, Tokyo, Japan.
- [7] Eaton M., Edge K., 2001, *Modelling and Simulation of Pressures within the Mesching Teeth of Gear Pumps*, Int. Conf. on Recent Advantages in Aerospace Actuation Systems and Components, June 13-15, 2001, Toulouse, France.
- [8] Bonacini C., Borghi M., 1990, *Calcolo delle Pressioni nei Vani fra i Denti di una Macchina Oleodinamica ad Ingranaggi Esterni*, Oleodinamica-Pneumatica, Nov. 1990, Tecniche Nuove.
- [9] Paltrinieri F., Borghi M., Milani M., 2004, *Studying the Flow Field Inside Lateral Clearances of External Gear Pumps*, 3rd FPNI-PhD Symposium on Fluid Power, Spain, June 2004.
- [10] Zardin B., Paltrinieri F., Borghi M., Milani M., 2004, *About the Prediction of Pressure Variation in the Inter-Teeth Volumes of External Gear Pumps*, 3rd FPNI-PhD Symposium on Fluid Power, Spain, June 2004.
- [11] Poy Ferrer M., Codina E., 2002, *Suction Capability of Gear Pumps*, 2nd Int. FPNI PhD Symposium, Italy, July 2002.
- [12] Gutes M., Gamez Monter P.J., Castilla R., Codina E., 2000, *Journal Bearing Performance in Gear Pumps*, 1st Int. FPNI-PhD Symposium, Germany, Sept. 2000.
- [13] Manring N. D., Kasaragadda S., 2003, *The Theoretical Flow Ripple of an External Gear Pump*, ASME Journal of Dynamic Systems, Measurement, and Control. Vol. 125.
- [14] Blackburn J. F., Reethof G., Shearer J. L., 1966, *Fluid Power Control*. USA: MIT Press.
- [15] McCloy D., Martin H. R., 1980, *Control of Fluid Power*. UK: John Wiley & Sons.
- [16] IMAGINE S.A., 2004, *AMESim[®] and AMESet[®] version 4.2 User manual*, Roanne, France, September 2004.
- [17] Casoli P., Vacca A., Franzoni G., 2003, *A Numerical Model for Simulation of "Load Sensing" Spool Valves*, The 18th Int. Conf. on Hydraulics and Pneumatics, Prague, Czech Republic, September 2003.
- [18] Idel'cik E., 1986, *Memento del Pertes de Charge, Coefficients de Pertes de Charge Singulières et de Pertes de Charge par Frottement*, Edition Eyrolles.

WAVELET APPROACH FOR PERFORMANCE MONITORING AND DIAGNOSIS OF A HYDRAULIC PUMP

Yingjie GAO^{*}, Xiangdong KONG^{*}, Qin ZHANG^{**}

^{*} Department of Mechatronic Engineering, ,
Yanshan University
Qinhuangdao, Hebei, 066004 China
(E-mail: yjgao@ysu.edu.cn)

^{**} Department of Agricultural and Biological Engineering
University of Illinois at Urbana-Champaign
Urbana, IL 61801, USA

ABSTRACT

Hydraulic pump performance monitoring methods that can detect failures by using the outlet pressure signals of the pump are investigated. Two faults diagnosis methods, namely conventional spectral analysis method based on FFT and wavelet based multi-resolution analysis method, are introduced and their efficiency and reliability are discussed. The performance of both diagnoses methods were evaluated based on simulation results and experimental results. Validation results obtained from using both methods in analyzing the same sets of data indicated that the wavelet transform based fault diagnosis method showed a more sensitive and robust detecting results for all three tested pump faults than that obtained from a spectrum analyses approach.

KEY WORDS

Wavelet based MRA, FFT spectrum analysis, fault diagnosis, hydraulic pump

INTRODUCTION

The purpose of performance monitoring and fault diagnostics are to detect and distinguish faults occurring in machinery, in order to provide a significant improvement in plant economy, reduce operational and maintenance costs, and improve the level of operation safety. Hydraulic systems have been used in a wide variety of applications ranging from precision control on machine tools to task implementation on construction equipment and aircraft because of its advantages, i.e., the high force to weight ratio, forces

can be rapidly generated and transmitted over considerable distances with very little loss, etc. A hydraulic pump is a key component in a hydraulic system, and its performance will affect the reliability of any hydraulic systems. Therefore, a sensitive and accurate faults detection and identification method for hydraulic pump performance monitoring and diagnosis has great interest to the industry.

For hydraulic pump/motor performance monitoring, potential signals which can be employed include oil chemical properties, temperature signal, vibration of the shell, flow rate and pressure signals. Efforts have been made to implement on-line monitoring and fault

detection techniques using easily monitored operating parameters. Jardine *et al.* [1] used a proportional hazards modeling statistical approach to optimize a mine haul truck wheel motor condition monitoring program by analyzing oil test results. Although oil analysis has proven a good tool for timing oil changes and even fault detections, it has two drawbacks: 1) the difficulty of obtaining a representative of oil sample and 2) the temporal requirements for sampling, testing, and evaluating results. Flow data is a hydraulic pump operation parameter that is a good indicator of pump failure; however, flow data is not cheaply and reliably obtained during typical operation and is not applicable to variable displacement pump either in real applications. As temperature signals are associated with the working environment, they are not fit to detect the malfunction of pump. Therefore, reliable means of analyzing more readily sensed signals is more desirable. Because of high noise levels in the pump pulsation pressure signal, many existing health diagnosis methods, such as limit checking, spectrum analysis, and logic reasoning, cannot effectively perform a reliable on-line health diagnosis for hydraulic pumps [2]. Many different diagnostic tools have been used for health diagnosis purposes and system performance monitoring. An and Sepehri [3] demonstrated a scheme in which an extended Kalman Filter is used to estimate the state of a hydraulic actuator system. By comparing with the corresponding measured states, the residuals between the actual state of system and the estimator could be used to determine if there any defects occur. Wolfman, *et al.* [4] proposed a multi-model approach for fault detection and diagnosis of a centrifugal pump. The whole process was decomposed into three sub-models pump, pipes, and mechanical subsystem. Individual neural-fuzzy sub-model was associated with each component to generate relative normal state. Evaluation residuals then were designed to implement the fault detection process. The superior of this method is the capability of supervision of nonlinear system and consequently the accuracy of the diagnosis may be improved. Parametric models have been developed and tested for on-line diagnostics of hydraulic pumps [5][6]. Although sound and proven theoretical approaches to on-line hydraulic pump health diagnosis, these methods are dependent on the accuracy of the parametric model chosen [7]. Since many factors can influence pump performance, parametric models are difficult to perfect. The complexities of interrelating pump operating parameters are not easily modeled. Using methods that are not sensitive to slight changes of pump operating features would allow more applicable and reliable pump health diagnostics. Fourier transforms decompose a signal into its frequency content. From this decomposition, a power spectrum can be calculated to determine which

frequencies are most prevalent in the signal. Similarly, wavelet analysis, a waveform signal analysis method performed by breaking up an evaluating signal into shifted and scaled versions of a standard wavelet, can identify feature signals in multiple decomposed band window of the original signal [8]. Where the FFT decomposes a signal into scaled versions of a sine wave, wavelet analysis can decompose a signal into both scaled and shifted versions of almost any waveform preserving the time parameter of the signal. Both methods are sensitive to changing of the evaluating signals in interested frequency bands. Therefore, these two methods are promising hydraulic pump fault detection techniques as each method allows for the pump system to create a characteristic pattern for the pump being monitored on a specific machine. This flexibility will eliminate errors often encountered by model-based techniques.

In this paper, outlet pressure data of the pump is selected as the signal to evaluate because most hydraulic systems already have pressure gauges incorporated into the system for monitoring during operation. The presence of this signal in most hydraulic systems makes it a prime candidate to use in an on-line hydraulic pump health monitoring system. The pressure signals were analyzed using two methods, Fourier transforms and wavelet packet analysis, in order to achieve high accuracy and reliability for pump performance monitoring.

FUNDAMENTAL OF METHODOLOGY

FOURIER TRANSFORMS – Fourier transforms decompose a signal into its frequency content by comparing various scales of a sine wave to the signal. The result is a frequency versus amplitude relationship. Here, the discrete Fourier transform in Eq. (1) is calculated using the Fast Fourier transform (FFT) algorithm.

$$F_n = \sum_{k=0}^{N-1} f_k e^{-j(2\pi)nk/N} \quad (1)$$

From the Fourier transform of the pressure signal, the power spectra was calculated and used to determine which frequencies are most prevalent in the signal.

WAVELET AND WAVELET PACKET ANALYSIS - Wavelet analysis is a waveform signal analysis method performed by breaking up an evaluating signal into shifted and scaled versions of a standard wavelet. However, there are two important differences between wavelet analysis and Fourier transforms. Where the FFT decomposes a signal into scaled versions of a sine wave, wavelet analysis can decompose a signal into scaled and shifted versions of almost any waveform. Waveforms can be selected to closely match the shape of the signal

being analyzed. Selecting a waveform to be similar to a normal signal provides more sensitivity to detecting changes [8]. Secondly, wavelet analysis retains the time dimension of the data. The chosen wavelet is compared to local sections of the signal through translation of the wavelet along the signal at different dilations or scales of the mother wavelet. Wavelet coefficients are preserving the time parameter of the signal. This distinguishing feature of wavelet analysis allows the time of a specific event to be identified. For this research, the discrete wavelet transformation (DWT) is used. The DWT uses the power-of-two logarithmic scaling of both the dilation and translation steps, known as a dyadic grid arrangement. The discrete wavelet transform of a signal using a mother wavelet $\psi_{m,n}(t)$ using the dyadic grid is shown in Eq. (2).

$$W_{m,n}(f) = 2^{-m/2} \int dt f(t) \psi(2^{-m}t - n) \quad (2)$$

Where, m, n range over Z (integer space). For a special choice of $\psi(t)$, the discrete wavelets can constitute an orthonormal basis, and a signal $f(t)$ can be represented by the sum of its smooth approximation (low-pass) and its detail description (band-pass), which is given by

$$\begin{aligned} f(t) &= \sum_{n=-\infty}^{\infty} \langle f, \varphi_{m_0,n}(t) \rangle \varphi_{m_0,n}(t) \\ &+ \sum_{m=-\infty}^{m_0} \sum_{n=-\infty}^{\infty} \langle f, \psi_{m,n}(t) \rangle \psi_{m,n}(t) \quad (3) \\ &= P_{m_0} f(t) + \sum_{m=-\infty}^{m_0} D_m f(t) \end{aligned}$$

Where, the first term $P_{m_0} f(t)$ is the coarser approximation of $f(t)$ in scale m_0 , and the second term $D_m f(t)$ leads to the differences among each dilation. $\varphi(t)$ is the so called ‘scaling function’ [9]. Consequently, there is $P_{m_0-1} f(t) = P_{m_0} f(t) + D_{m_0} f(t)$. Which implies that: if a signal is fine-scale approximated at $P_{m_0} f(t) = f_0$, then it can be decomposed into $f_0 = P_{m_0+1} f(t) + D_{m_0+1} f(t) = f_1 + d_1$, where f_1 is the next coarser approximation of f_0 , and d_1 is what is lost in the transition from scale m_0 to m_1 . Using the same approach, the i th level decomposition of the original signal f_i can be further decomposed into $f_i = f_{i+1} + d_{i+1}$, $i = 1, 2, \dots$. The approximation of f_0 in the i th level can be represented with the approximation coefficient vector with the scaling function, whilst the detail of f_0 is represented with the

detail coefficient vector and the scaled mother wavelet as shown in Eq. (4).

$$\begin{aligned} f_0 &= \sum_{n=-\infty}^{\infty} \langle f, \varphi_{0,n}(t) \rangle \varphi_{0,n}(t) = \sum_{n=-\infty}^{\infty} a_{0,n} \varphi_{0,n}(t) \\ f_i &= \sum_{n=-\infty}^{\infty} \langle f, \varphi_{i,n}(t) \rangle \varphi_{i,n}(t) = \sum_{n=-\infty}^{\infty} a_{i,n} \varphi_{i,n}(t) \quad (4) \\ d_i &= \sum_{n=-\infty}^{\infty} \langle f, \psi_{i,n}(t) \rangle \psi_{i,n}(t) = \sum_{n=-\infty}^{\infty} da_{i,n} \psi_{i,n}(t) \end{aligned}$$

In harmonic analysis, such a decomposition procedure is referred to as a ‘two-channel’ sub-band filtering scheme. The incoming sequence is convolved with two different filters, one low-pass and one high-pass. The two resulting sequences are then sub-sampled. Based on this scheme, a set of examining signals is decomposed using a low-pass filter and a high-pass filter, which results in two sets of sub-band signals. The sub-bands signals are then reassembled to perform wavelet analysis. Schematically, the scheme of a three-level decomposition wavelet analysis to reassemble the original signal and the sub-band by each sub-sampled signal can be represented as shown in Figure 1.

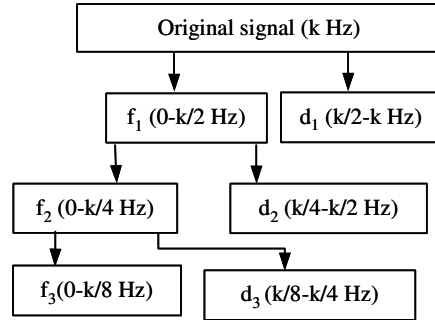


Figure 1 A three level wavelets decomposition scheme

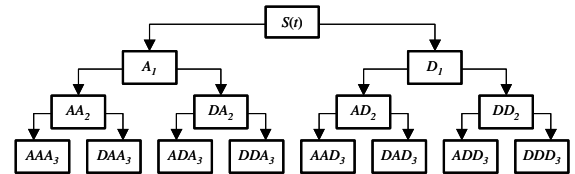


Figure 2 Wavelet packet decomposition

Unlike wavelet analysis, in which only the

approximation of the signal is further decomposed and the number of details depends on the level of decomposition, wavelet packet analysis decomposes both approximations and details of a signal. Hence, wavelet packet analysis is capable of identifying feature signals in multiple decomposed band windows of the original signal. Figure 2 illustrates the decomposition of a signal using wavelet packet analysis with three level decomposition.

From wavelet analysis of the pressure signal, the wavelet coefficients corresponding to interested sub-band are calculated and used to determine if defects of the monitored pump occur.

FAULT DETECTION AND DIAGNOSIS RESULTS

SIGNAL SELECTING - The common faults of an axial piston pump include swash plate wear, control (or valve) plate wear, loose of the ball-socket joints, bearing failure, and fatigue failure of the central return spring. Those faults will be reflected in the pump discharge pressure and are normally buried in the pressure pulsating signals. Furthermore, other fault scenarios, such as cavitation, hydraulic blocking, pipe resonance and leakage, will also be reflected in the discharge pressure signals. Thus, the pressure signal covers sufficient information and takes little effectives of the background noise signals because of its property of 'inner measurement'. When compared with the vibration signal, the pressure signal is considered more suitable for the analysis and detection of faults of the axial pump. This paper considers two kinds of common faults of the axial piston pump, namely control plate wear and loose ball-socket joints. For validating the proposed method, simulations and analysis based on a theoretical model are carried out prior to completing the experiment itself.

SIMULATION ANALYSIS - A simulation model of piston pump was developed for this investigation in previous work [10]. For a pump with seven pistons, where the rotational speed is n (rpm), then the rational flow pulsation frequency is $\omega_1 = 14\pi n/60$ (rad/s), the disturbance frequency due to piston ball-socket excitation is $\omega_2 = 2\pi n/60$ (rad/s), and the disturbance frequency due to swash plate excitation (ω_3) depends on the worn condition of the swash plate. Under normal operating conditions, the pump speed (n) was set at 1470 rpm, and the swash plate was worn within the high-pressure area. This resulted in the following parameters for the model: $\omega_1 = 1077.57$ (rad/s) = 171.5 (Hz), and $\omega_2 = \omega_3 = 153.94$ (rad/s) = 24.5 (Hz).

In this case, ω_1 is the highest frequency, and ω_2, ω_3 are each $\omega_1/7$. Therefore, the proper critical frequency should be around ω_2 . the simulation signals of the normal condition and two malfunction scenarios are shown in Figure 3.

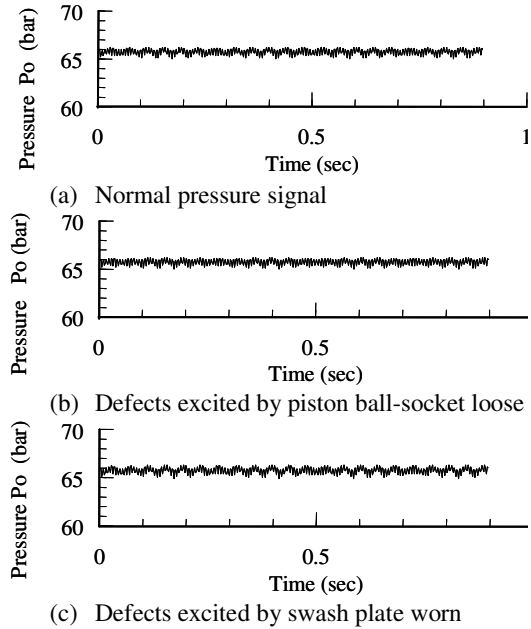


Figure 3 Simulation results based on the pump pulsation model

Figure 4 shows the Fourier transform result for the simulation results. From these plots, the feature frequencies are identified to be 25 Hz, 158 Hz, and 185 Hz. Where frequencies of 158 and 185 Hz figure out the normal pulsation frequencies of outlet pressure of the pump, the frequency 25 Hz features malfunction of pump. The power spectrum changes most between pumps at the 25 Hz regions. Therefore, the power of the signal was summed for a 30 Hz window around this key frequency in order to create a feature parameter to judging the performance of the monitored pump.

By applying Fourier transform, the summation of the spectra power of each fault signal from 10 Hz to 40 Hz is compared with the one of the normal signal to form a relative residual. Similarly, applying a three level wavelet packet transform to the original pressure signals, eight wavelet coefficients can be obtained for each signal. The square root of the summation of square coefficient vector to each wavelet coefficient is calculated to construct a wavelet feature parameter. Then the fault wavelet feature parameters are compared with the normal feature parameters to determine the residuals of wavelet analysis. This process can be described as the following equation:

$$FR = \left| \frac{\sum fP - \sum nP}{\sum nP} \right| \quad (5)$$

$$WR_i = \left| \frac{\sqrt{\sum fc_{3,i}^2} - \sqrt{\sum nc_{3,i}^2}}{\sqrt{\sum nc_{3,i}^2}} \right|$$

where, FR is the Fourier residual, fP , nP the fault and normal power of signal. WR is the residual of the wavelet analysis, fc , nc the fault and normal wavelet coefficients. The results are shown in Table 1.

When looking round the simulation results shown in Table 1, it can be seen that the Fourier residuals and the wavelet residuals within 23 to 46 Hz are sensitive to the change of pump performance. If the obtained residual value exceed relative threshold value for a health pump, it can conclude that the corresponding pump is faulty. This result can be used to design an on-line pump performance monitoring and diagnosis algorithm.

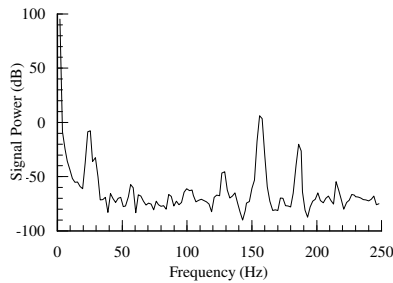
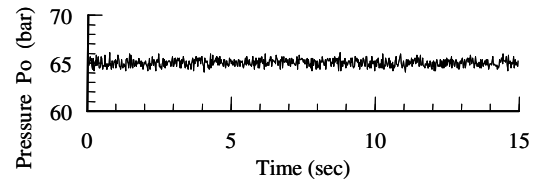


Figure 4 Spectra analysis of the pressure signal

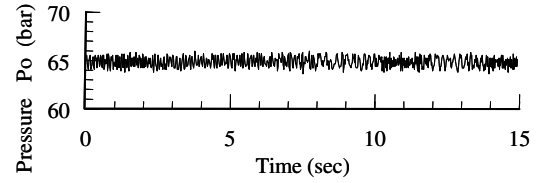
EXPERIMENTAL VALIDATION - The validation test of the proposed fault diagnosis methods are conducted on a laboratory scale hydraulic system test-rig. The test-rig consists of an electro-hydraulic servo valve, two testing pumps (a normal pump and a defected pump), and other auxiliary devices and sensors. The pumps used in this test are 10 ml/rev fixed displacement axial piston pumps. Both pumps were operated at 1,470 rpm. The system pressure was 6.5×10^6 Pa set by a relief valve. The pressure sensors are installed on the discharge port of the pumps for collecting the pressure signals. When one pump was being tested, the other pump was shut off to avoid any possible inference to the discharge pressure of the testing pump. The obtained pressure signal was analyzed on-line using a MATLAB program developed for this research based on the method discussed earlier in this article.

Figure 5 shows the pump discharge pressure obtained from the normal pump, a defective pump with loose ball-socket, and a defective pump with a worn swash plate. The residuals obtained are shown in Table 2.

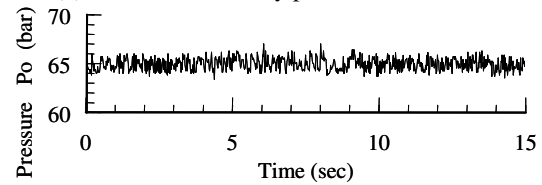
Comparing the results showed in Figure 5, the raw



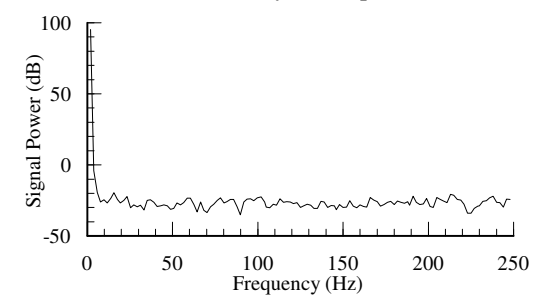
(a) Normal pressure signal



(b) Defects excited by piston ball-socket loose



(c) Defects excited by swash plate worn



(d) Spectra power of the pressure signal

Figure 5 Test pressure signals

signals, the discharge pressures, showed little difference between the normal pump and the defected pumps. This indicates that the surface data (for the pump outlet pressure), was not able to provide sufficient information to support pump health diagnosis. After applying wavelet decomposition on the raw pressure signals from three pumps, wavelet residuals from both defected pumps (within 23 to 46 Hz and 69 to 93 Hz) resulted in wilder variations than that of the normal pump. Both the theoretical analysis and experimental tests showed that the 3rd level wavelet decomposition could extract the feature signals from pump discharge pressure signal for diagnosing the piston pump health conditions. More importantly, the patterns of the coefficient changes were different for different types of pump defects. This fact verified that the wavelet analysis method can improve the capability of diagnosing the health conditions of the piston pumps by decomposing the original pulsation

Table 1 Simulation results: Fourier residuals and wavelet residuals

	Spectra analysis <i>FR</i>	Wavelet packet analysis WR								
		Sub-band (Hz)	0-23	23-46	46-69	69-93	93-116	116-139	139-162	162-185
f_{normal}	0	f_{normal}	0	0	0	0	0	0	0	0
f_{fault1}	3.6	f_{fault1}	0	0.263	0.004	0.021	0.085	0.036	0.003	0.0027
f_{fault2}	15.07	f_{fault2}	0	0.938	0.004	0.039	0.079	0.043	0.003	0.0017

Table 2 Test results: Fourier residuals and wavelet residuals

	Spectra analysis <i>FR</i>	Wavelet packet analysis WR								
		Sub-band (Hz)	0-23	23-46	46-69	69-93	93-116	116-139	139-162	162-185
f_{normal}	0	f_{normal}	0	0	0	0	0	0	0	0
f_{fault1}	0.089	f_{fault1}	0.003	0.668	0.707	0.883	0.201	0.178	0.470	0.368
f_{fault2}	2.738	f_{fault2}	0.002	0.949	0.309	0.553	0.871	0.439	0.212	0.322

pressure signals, and that the patterns and the amplitudes of wavelet coefficients obtained from different decomposed signal windows are relevant to the types of pump defects.

CONCLUSIONS

The use of discharge pressure provided the direct information for the diagnosis of the health of system signals. This can improve the diagnostic accuracy by overcoming the limitations caused by noise and disturbances acting on the indirectly measured signals. The following concluding remarks follow from the results obtained from theoretical analysis and experimental testing.

- The decomposition of the original pressure signals resulted in sub-band informative signals. Reassembling these sub-bands signals and comparing them with a standard wavelet resulted in distinguishable changes between wavelet coefficients from normal and defective pumps.
- The differences in the patterns and amplitudes of the resulting wavelet coefficients within different band windows provided distinguishable features to identify the types of pump defects.
- The validation tests proved that the wavelet analysis could be implemented on-line to support real-time health diagnosis without affecting the normal operation of the pump.

REFERENCES

1. Jardine, A. K. S., Banjevic, D., Wiseman, M., Buck, S., and Joseph, T., Optimizing a Mine Haul Truck Wheel Motors' Condition Monitoring Program: Use of Proportional Hazards Modeling, *Journal of Quality Maintenance Engineering*, 2001, 7-4, pp.286-301.
2. Gerlter, J., Costin, M., Fang, X., Kowalczyk, Z., Kunwer, M., and Monajemy, R., Model-based

- Diagnosis for Automotive Engines –Algorithm Development and Testing on a Production Vehicle, *IEEE Transactions on Control System Technology*, 1995, 3-1, pp.61-68.
3. An, L. and Sepehri, N., Hydraulic Actuator Circuit Fault Detection Using Extended Kalman Filter, *Proceedings of the American Control Conference Denver, Colorado, 2003, June 4-6*, pp.4261-4266.
4. Wolfram, A., Fussel, D., Brune, T., and Isermann, R., Component-Based Multi-Model Approach For Fault Detection And Diagnosis Of A Centrifugal Pump, *Proceedings of The American Control Conference, Arlington, 2001, June 25-27*, pp. 4443-4448.
5. Skormin, V. A., and Apone, J., On-line Diagnostics of a Variable Displacement Pump of a Flight Actuation System, *Proceedings of the IEEE 1995 National Aerospace and Electronics Conference, Dayton, NY, 1995, V1*, pp.503-510.
6. Liu, S., and Hung J.C., "On-line Diagnostics of a Variable Displacement Pump of a Flight Actuation System," *Proceedings of I ECON 91, Institute of Electrical and Electronics Engineers, 1991*, pp.2145-2150.
7. Hancock, K. M. and Zhang, Q., Maintenance and Fault Diagnosis Tools For Hydraulic Pumps, *Proceedings of the 50th National Conference on Fluid Power, Las Vegas, Nevada, 2005, March 16-18*, pp.361-369.
8. Addison, P.S., *Discrete Wavelet Transform, Illustrated Wavelet Transform Handbook: Introductory Theory and Applications in Science, Engineering, Medicine, and Finance*, Institute of Physics, London, 2002, pp.65-143.
9. Daubechies I., *Ten Lectures on Wavelets*, Capital City Press, Montpelier, Vermont, USA, 1992.
10. Gao, Y., Zhang, Q. and Kong, X., Waveletbased Pressure Analysis for Hydraulic Pump Diagnosis, *Transactions of the American Society of Agricultural Engineers, ASAE, 2003, 46-4*, pp.969-976.

A New Type of Low Speed High Torque Hydraulic Motor with Continuously Variable Displacement

Li Yong, Shi Guanglin, Chen Zhaoneng

Research Institute of Mechatronics, Shanghai Jiaotong University,
1954 Huashan Road, Shanghai, 200030, P. R. China
(E-mail: sjtuliyong@sjtu.edu.cn)

ABSTRACT

A new type of camshaft connecting-rod low speed high torque (LSHT) hydraulic motor providing continuously variable displacement is presented in this paper. On the base of traditional LSHT hydraulic motor with dual displacement, a continuously variable displacement mechanism, which is composed of a hydraulic control valve with mechanical-positional feedback to camshaft, is designed for the traditional LSHT hydraulic motor. So the cam ring on camshaft of the traditional LSHT hydraulic motor can stop at any position between minimum and maximum eccentricity, according to an input fluid pressure signal or an input electric control signal, and can stay anywhere stabilized through self-adjusting. The new type of continuously variable displacement mechanism is simple, stable and easy to be made. Firstly, the structure and principle of the continuously variable displacement mechanism is introduced in this paper. Secondly, the mathematic model is set up.

KEY WORDS

low speed high torque hydraulic motor, camshaft connecting-shaft type, continuously variable displacement, mechanical-positional feedback

NOMENCLATURE

A_1 : cross section area of the small varying displacement piston

A_2 : cross section area of the large varying displacement piston

A_c : cross section area of the valve collar

B_c : viscous damping coefficient

C_d : flow coefficient

e : eccentricity

F : loading force acting on the cam ring

k_1 : spring coefficient of the restoring spring

k_2 : spring coefficient of the one in the small varying displacement piston chamber

K : eccentric rate

m : mass of the cam ring and two varying displacement pistons

P : hydraulic force of the intake port fluid acting on one radial piston

p_0 : draining pressure, $p_0 \approx 0$, here
 p_1 : pressure in the small varying displacement piston chamber
 p_2 : pressure in the large varying displacement piston chamber
 p_c : control pressure
 p_s : supply pressure
 Q_1 : flow into the small varying displacement piston chamber
 Q_2 : flow into the large varying displacement piston chamber
 V_{01} : initial volume of the small varying displacement piston chamber
 V_{02} : initial volume of the large varying displacement piston chamber
 V_1 : instantaneous volume of the small varying displacement piston chamber
 V_2 : instantaneous volume of the large varying displacement piston chamber
 w : area gradient
 x : valve collar displacement
 x_0 : pre-compression distance of the restoring spring
 x_s : displacement of spool from a initial position
 y : displacement of the cam ring
 y_0 : pre-compression distance of the spring in the small varying displacement piston chamber
 β : structure angle, $\frac{\pi}{5}$, here
 β_e : fluid bulk modulus
 ρ : fluid density
 φ_1 : geometric rotating angle of the cam ring from the axis of a piston chamber in the motor

INTRODUCTION

Camshaft connecting-rod type low speed high torque hydraulic motors are widely used in many industrial fields. They are typically of fixed or single displacement. If the camshaft connecting-rod type low speed high torque hydraulic motors work in two discrete positions through the fluid pressure control in the two varying displacement piston chambers on the camshaft, the working mode is of dual placement. Unlike axial piston pumps or motors, there is still no mechanical structure or circuit that could accomplish the task of continuously varying displacement in radial piston

pump or motor yet. People just added hydraulic and electronic valves or circuits to fixed or dual placement motors to continuously control the angular velocity of the camshaft^[1]. Thus camshaft connecting-rod type motors could work in a status of constant power output to improve overall efficiency.

Based on the traditional LSHT hydraulic motor with dual displacement, a continuously variable displacement mechanism is designed for the traditional LSHT hydraulic motor in this paper. The patented mechanism is mainly composed of a hydraulic control valve with mechanical-positional feedback to camshaft. So the cam ring on camshaft can stop at any position between minimum and maximum eccentricity, according to an input fluid pressure signal or an input electric control signal, and can stay anywhere stabilized through self-adjusting. Firstly, the structure and principle of the continuously variable displacement mechanism is introduced in this paper. Secondly, the mathematic model is set up.

MECHANISM AND PRINCIPLE

Mechanical structure

A typical radial piston camshaft connecting-rod LSHT hydraulic motor with dual displacement is shown in Fig.1. Two fluid channels connect two varying displacement piston chambers on the camshaft respectively. If one channel is supplied with high pressure oil from the intake port of the motor or from an isolated power unit, the corresponding varying displacement piston chamber is full of high pressure oil

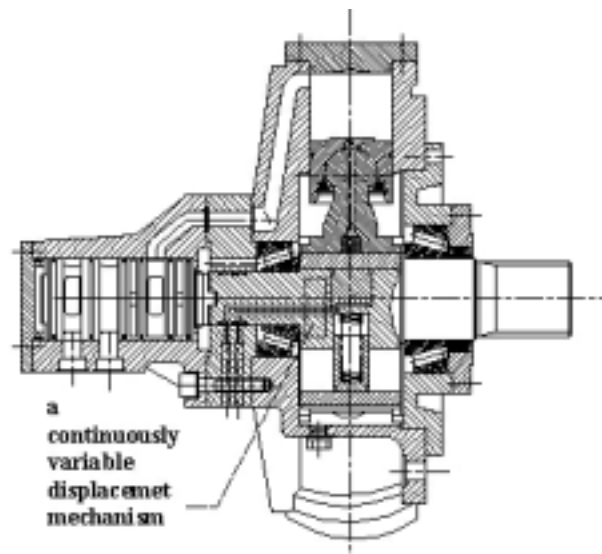


Figure 1 Schematic diagram of a radial piston LSHT hydraulic motor with dual displacement

and the corresponding large or small varying displacement piston will push the cam ring on the camshaft to a limited position. Thus, the motor works at its maxi or mini eccentric position and has its maxi or mini fluid discharging volume. As shown in Fig.1, when the small varying displacement piston pushes out, the motor is at its maxi eccentric position. While the large piston pushing out, it is vice versa.

As shown in Fig.1, the author improves the camshaft connecting-rod LSHT hydraulic motor with dual displacement by adding a spool valve structure to the camshaft and cam ring to realize the continuously displacement function. Fig.2 is a schematic diagram of the continuously variable displacement mechanism. As shown in Fig.2, component 1 is a valve collar that has five pairs of round or quadrate orifices on it. Component 2 is a 3-land valve spool and has a long draining orifice to prevent dead cavity. Component 3 is a restoring spring acting on the open side of the valve collar and precision tempered. Component 4 is a screw-worm structure making the valve spool and component 5, the cam ring, hard-connected to send out a mechanical-positional feedback signal. Component 6-9 is the small varying displacement piston, the restoring spring in the small varying displacement piston chamber, the camshaft and the large varying displacement piston respectively. Component 6, 7 and 9 are unchanged compared with the typical radial piston camshaft connecting-rod LSHT hydraulic motor with dual displacement.

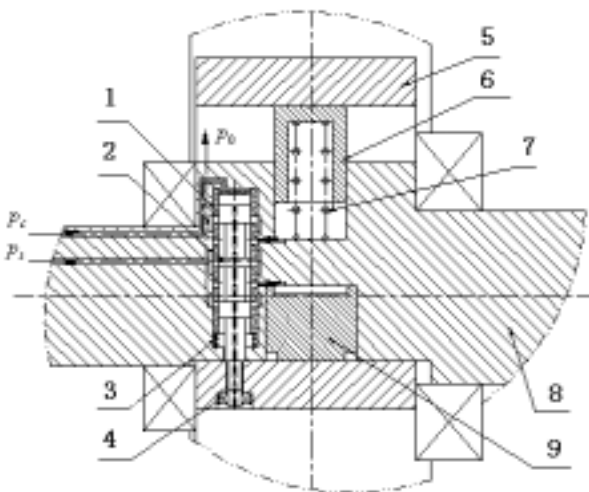


Figure 2 Schematic diagram of a continuously variable displacement mechanism

Fig.3 is a schematic diagram of the working principle of a continuously variable displacement mechanism. Seen from Fig.2 and Fig.3, there is a machined valve house in the camshaft. There are 5 grooves in the valve house named as e1-e5. e1 and e5

connect the draining channel, the fluid pressure is p_0 , the pressure in the motor main-body house which can be assumed to be 0. e2 connects the small varying displacement piston chamber and e4 connects the large one. e3 connects the supply channel which fluid pressure is p_s . The supply fluid comes from the intake port of the motor or an isolated power unit. The top of the valve house connects the control channel which fluid pressure is p_c . The control fluid which pressure signal p_c is determined by a hydraulic circuit or adjusted by an electric control circuit, acts on the close side of the valve collar, moving the valve collar against the restoring spring. The five pairs of orifices on the valve collar are named as w1-w5, mapping e1-e5. The fit between the valve house, the valve collar and the valve spool is close-tolerance, forming five cavities named as z1-z5.

Fluid in cavity z2 and z5 drains into the motor main-body house through the orifice on the spool and clearance between spool and the open side of the valve house.

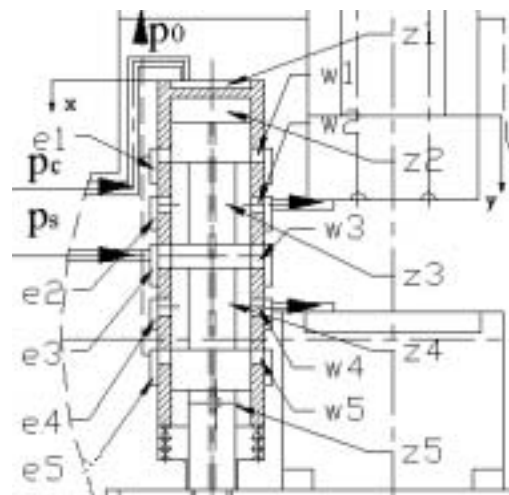


Figure 3 Schematic diagram of the working principle of a continuously variable displacement mechanism

Principle

Seen from Fig.3, the motor works at its maxi eccentric position and has its maxi fluid discharging volume. The working principle is explained through 4 cases: case 1-case2 on how to reduce or improve the eccentric rate, case 3-case4 on returning to its stable working status from a smaller or larger discharging volume.

Case 1

If a smaller discharging volume is needed, the

control fluid with an adjusted pressure signal p_c enters cavity z1 and pushes the valve collar down overcoming resistance of the restoring spring until the force formed by p_c equals the one formed by the restoring spring. Then the valve collar stops at a new balance position. Assuming the friction between the valve collar and the spool could be neglected, movement of the spool is independent from the valve collar. When the collar shifts down, the orifices w3 on the valve collar open, supply fluid which pressure is p_s enters the large varying displacement piston chamber through the access of groove e3, orifices w3, cavity z4, orifices w4 and groove e4, pushes large varying displacement piston out. Thus the cam ring goes down and the eccentricity decreases. The spool moves together with the cam ring because of the mechanical linkage between them. When the cam ring and the spool move to the place where the valve collar is, orifices w3 is closed and the access is shut down. Motor is at its new eccentric position. This is a typical mechanical-positional negative feedback. When the supply fluid which pressure is p_s enters the large varying displacement piston chamber, the fluid in the small varying displacement piston chamber drains into the motor main-body house through the access of groove e2, orifices w2, cavity z3, orifices w1 and groove e1. The two accesses open up and shut off at the same time. Because the control fluid pressure signal p_c could be adjusted continuously, the eccentricity could also change continuously. The function of continuously variable displacement is realized.

Case 2

When the motor works at a middle eccentricity and a larger discharging volume is needed, the pressure signal p_c comes down, the restoring spring pushes the valve collar up overcoming resistance of the control fluid until the force formed by p_c equals the one formed by the restoring spring. Then the valve collar stops at a new balance position. When the collar shifts up, the orifices w3 open, supply fluid which pressure is p_s enters the small varying displacement piston chamber through the access of groove e3, orifices w3, cavity z3, orifices w2 and groove e2, pushes small varying displacement piston out. Thus the cam ring goes up and the eccentricity increases. When the cam ring and the spool move to the place where the valve collar is, orifices w3 is closed and the access is shut down. Motor is at its new eccentric position. At the same time, the fluid in the large varying displacement piston chamber drains into the motor main-body house through the access of groove e4, orifices w4, cavity z4, orifices

w5 and groove e5. The eccentricity could change continuously.

When p_c equals 0, the motor has a maxi fluid discharging volume. When the restoring spring is compressed to the bottom, the motor has a mini fluid discharging volume. Theoretically, the eccentricity could decrease to 0.

Case 3

While the spool valve structure working at a stable position, all the fluid accesses are blocked. If the eccentricity decreases because of load impact or leakage, the spool shifts down because of the mechanical linkage with the cam ring. The fluid accesses are the same as case 2. Supply fluid enters the small varying displacement piston chamber and the eccentricity increases again until the fluid accesses are blocked. The motor returns to its stable status.

Case 4

If the eccentricity increases because of load impact or leakage, the spool shifts up. The fluid accesses are the same as case 1. Supply fluid enters the large varying displacement piston chamber and the eccentricity decreases again until the fluid accesses are blocked. The motor returns to its stable status.

MATHEMATICAL MODEL

The movement law of the cam ring and the spool valve structure on the camshaft is a composite linear and rotating motion. The rotating speed of LPHT motors is always quite low and the system pressure is usually rather high. So the effect of rotating motion on linear motion could be neglected.

The character of the spool valve structure is the same as that of a 4-way spool valve. It is had better zero-lapped. The character of the spool valve structure and two varying displacement piston chambers is the same as that of a valve-controlled hydraulic cylinder except that the two varying displacement piston chambers are unsymmetrical.

Assuming there is no leakage and supply fluid enters the small varying displacement piston chamber, the flow equations of the spool valve structure are given by

$$Q_1 = C_d w x_v \sqrt{\frac{2}{\rho} (p_s - p_1)} \quad (1)$$

$$Q_2 = C_d w x_v \sqrt{\frac{2}{\rho} p_2} \quad (2)$$

The flow equations of the two varying displacement piston chambers are given by

$$Q_1 = \frac{dV_1}{dt} + \frac{V_1}{\beta_e} \frac{dp_1}{dt} \quad (3)$$

$$Q_2 = \frac{dV_2}{dt} + \frac{V_2}{\beta_e} \frac{dp_2}{dt} \quad (4)$$

where V_1 and V_2 are given by

$$V_1 = V_{01} + A_1 x_v \quad (5)$$

$$V_2 = V_{02} - A_2 x_v \quad (6)$$

The force balance equation of the valve collar and the restoring spring is expressed as

$$A_c p_c = k_1(x_0 + x) \quad (7)$$

The force balance equation of the system is expressed as

$$A_1 p_1 - A_2 p_2 = m \frac{d^2 y}{dt^2} + B_c \frac{dy}{dt} - k_2(y_0 - y) + F \quad (8)$$

When the camshaft rotates the force F changes from time to time. The varying law^[2] is determined by structures of LSHT motors:

While $0 \leq \varphi_1 \leq \beta$

$$F = P \left[\frac{\sin\left(\frac{\beta}{2} - \varphi_1\right)}{2 \sin \frac{\beta}{2}} + \frac{K \cos(2\varphi_1 - \beta)}{2 \cos \beta} - \sum \frac{K}{2} \right] \quad (9)$$

While $\beta \leq \varphi_1 \leq 2\beta$

$$F = P \left[\frac{\sin\left(\frac{3\beta}{2} - \varphi_1\right)}{2 \sin \frac{\beta}{2}} - \frac{K \cos(2\varphi_1 - 3\beta)}{2 \cos \beta} - \sum \frac{K}{2} \right] \quad (10)$$

When supply fluid enters the large varying displacement piston chamber, the force balance equation of the system is expressed as

$$A_2 p_2 - A_1 p_1 = m \frac{d^2 y}{dt^2} + B_c \frac{dy}{dt} + k_2(y_0 + y) + F \quad (11)$$

where

$$y = x \pm x_v \quad (12)$$

When the spool valve structure works at a stable position, $y = x$.

Getting y by solving equation (8) or (11), the relationship between control pressure and eccentricity (seen from Fig. 4):

$$e = e_{\max} - y \quad (13)$$

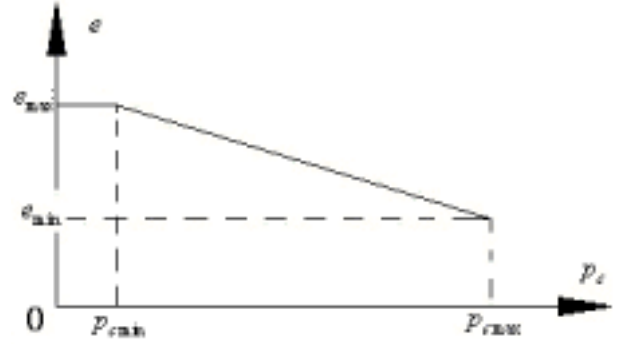


Figure 4 relationship between p_c and e

CONCLUSIONS

By adding a spool valve structure to a traditional radial piston crankshaft connecting-rod LSHT hydraulic motor with dual displacement, the task of continuously varying displacement is realized. Through mechanical-positional feedback and self-adjusting of the continuously variable displacement mechanism, the cam ring on camshaft of the traditional LSHT hydraulic motor can stop at any position between minimum and maximum eccentricity. The new type of continuously variable displacement mechanism is simple, stable and easy to be realized.

The character of the spool valve structure is the same as that of a 4-way spool valve. The character of the spool valve structure and two varying displacement piston chambers is the same as that of a valve-controlled hydraulic cylinder. These characters are very typical and there have been many literatures about them.

REFERENCES

- [1] David, F. Creffield and Allen, J. Carlson, Electro-hydraulic Displacement Controls for Low Speed High Torque Radial Piston Hydraulic Motors, Proceedings of the 40th national conference on fluid power, 1984, pp.113-117
- [2] Chen Zhuoru, The Theory, Calculation and Design of Low Speed High Torque Hydraulic Motor, Peking, Publishing house of mechanism industry, 1989, pp.151-237

SHAPE STABILIZER USING AN ARTICULATION-TYPE PASSIVE ELEMENT

Takashi MITSUDA* and Norichika MATSUO**

* Department of Human and Computer Intelligence

** Graduate School of Science and Engineering

Ritsumeikan University
1-1-1 NojiHigashi, Kusatsu, Shiga, 525-8577 Japan
(E-mail: mitsuda@ci.ritsumei.ac.jp)

ABSTRACT

An articulation-type passive element is a planate bag containing articulating thin plates. It can be freely contracted and bent to fit an arbitrary rounded surface. Evacuation of the internal air renders the bag rigid so that it maintains whatever shape it has been given. The stiffness of the articulation-type passive element is proportional to the reduction in internal pressure below atmospheric pressure. Experimental results show that the stiffness is higher and more stable than that of other passive elements that function by vacuum pressure. As an application of the new passive element, we developed an orthopedic cast that is easy to remove or change in shape. The passive element is also applicable to wearable force displays. Passive elements fixed on an operator provide a sensation of reaction force by constraining his or her motion. The new passive element is suitable for wearable mechanisms, by virtue of being lightweight, soft, and safe.

KEY WORDS

Wearable robot, Passive element, Medical and Welfare Equipment

INTRODUCTION

Wearable robots for assisting human motion must be lightweight so as not to impose a burden on the wearer. They also must be soft so as not to obstruct various motions made by the wearer. Lastly, they must be safe so as not to injure the wearer when they are broken. In view of these requirements, conventional robots composed of electric motors and metal frames seem

unsuitable. Since pneumatic actuators such as rubber actuators are soft and lightweight as compared with electric motors, wearable robots employing pneumatic actuators have been developed [1-5]. However, these robots also involve a risk of exerting excessive force when they are broken. We have developed some wearable robots that employ passive elements. For example, fixing knee joints by passive elements lightens the load of lower limbs for supporting body weight [6]. Adding resistance to hand motion by passive elements

fixed on the hand provides the wearer with a sensation of touching an object or of moving water with viscosity [7]. These wearable robots work as inherently passive systems that never exert excessive force in the event they malfunction. In this paper, we examine a novel passive element called an articulation-type passive element. It can be freely contracted and bent to fit an arbitrary rounded surface. Evacuation of the internal air renders the element rigid so that it maintains whatever shape it has been given. We have developed several types of passive elements that function by vacuum pressure [8]. The new passive element has higher and more stable stiffness than do other, previously developed passive elements. The structure and mechanical properties of the element will be described in this paper.

Structure of the articulation-type passive element

Figure 1 depicts the structure of the articulation-type passive element. A planate bag contains articulating thin plates, which are bound by wires through rectangular holes formed in the plates. Each plate can rotate about the rectangular hole and slide. By combining the rotation and sliding, the element can be contracted and bent as shown in Figure 2. As shown in Fig. 3, the element also forms a curved surface by rotation and the sliding of the plates. The bag containing the articulated thin plates is made of a vinyl film, which is easily bent but cannot be lengthened. The thin plates are made of plastic. When the inside air is evacuated, atmospheric pressure compresses the thin plates, and the plates motions are locked into an arbitrary shape by friction. Stiffness can be adjusted by varying the internal pressure.

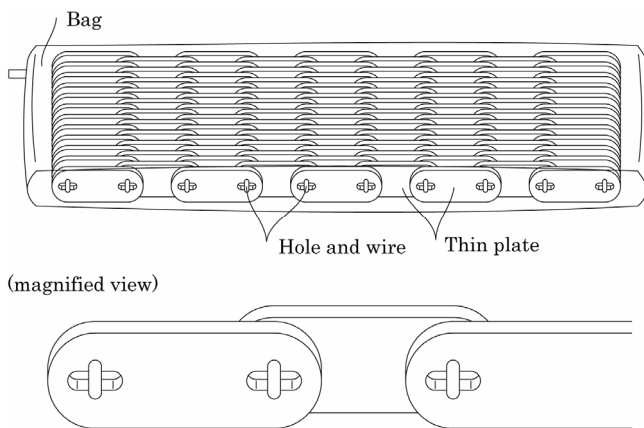


Figure 1 Structure of the articulation-type passive element.

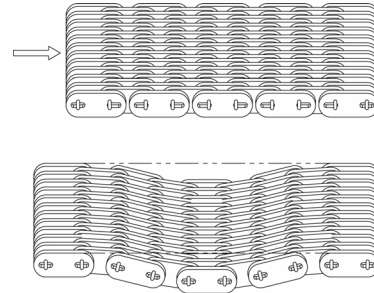


Figure 2 Contraction and bending.

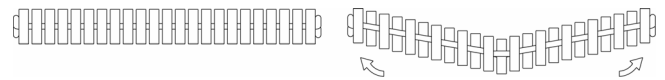


Figure 3 Bending along the connection wires.

Mechanical properties of the articulation-type passive element

Factors of stiffness

The stiffness of the articulation-type passive element is produced by the friction of the stacked plates and the elasticity of the covering film. The constraint torque exerted by the friction force on the plates can be expressed by

$$T = -\frac{1}{2} n \mu P \pi r^3 \quad (1)$$

where

T Constraint torque

n Number of stacked plates

μ Friction coefficient

P Gauge pressure

r Radius of the contact circle area on the plates.

The stiffness produced by the covering film is affected by the elasticity, the friction between the covering film and the plates, and the size of the covering film.

Experimental setup

In order to examine mechanical properties, we measured the stiffness of articulation-type passive elements. All articulation-type passive elements measured in the following experiments were composed of Polyester plates. Figure 4(a) depicts the size of a plate. The thickness of the plate is 0.188[mm]. Ten plates were articulated in series, and 50 to 150 plates were stacked and bound by plastic wires. One edge of the articulation-type passive element was fixed, and the adjacent plate was pushed to rotate around the hole on the fixed plate. The reaction force and the displacement were measured during this operation. Stiffness is affected by the distance of neighboring plates, because

the distance correlates with the contact area on the plates. The distance was set to the maximum in the following experiments. Therefore, the stiffness measured in the following experiments is expected to be minimum. The distance between the point of pushing and the axis of rotation was 13[mm].

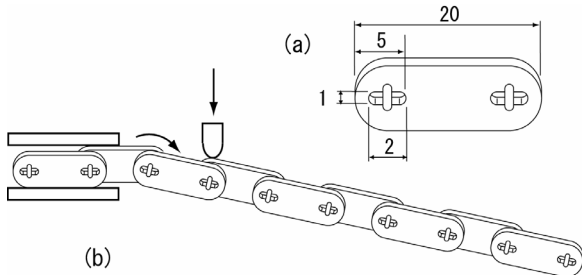


Figure 4 (a) Size of a plate (b) Experimental setup.

Effect of inside air pressure

Figure 5 shows the stiffness of an articulation-type passive element at various inside air pressures. The covering film of the passive element was urethane having a thickness of 0.2[mm]. Fifteen articulated plates were stacked and bound by wires. Therefore, the passive element consists of 150 plates. Figure 6 shows the relation between reaction force at various translations and internal air pressure. Stiffness was proportional to the reduction in internal pressure below atmospheric pressure. However, stiffness at 0[kPa] is almost zero. This characteristic indicates that the stiffness of the articulation-type passive element can be controlled by the internal air pressure.

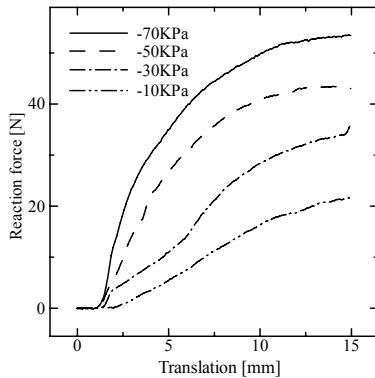


Figure 5 Stiffness at various internal air pressures.

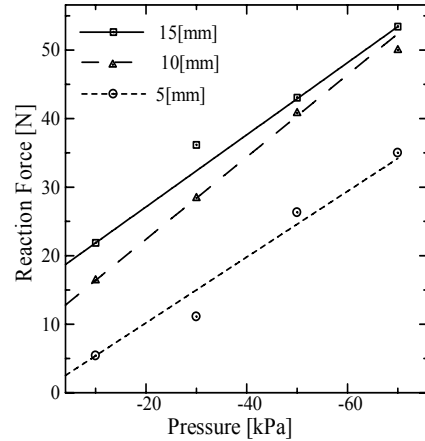


Figure 6 Relation between stiffness and internal air pressure.

Effect of number of stacked plates

Figure 7 shows stiffness of the articulation-type passive elements, consisting of 50, 100, and 150 stacked plates, at -70[kPa]. The width of the passive element was 10, 20 or 30[mm]. The covering film was urethane having a thickness of 0.2[mm]. Figure 8 shows the relation between the number of stacked plates and stiffness of the passive element. Stiffness is proportional to the number of stacked plates; this relation coincides with the theoretical expression of constrained torque shown in Eq.(1). However, the effect of the number of stacked plates should be examined in isolation from the effect of the covering film, since the covering films of these passive elements differ in thickness. The analysis will be described in the following section.

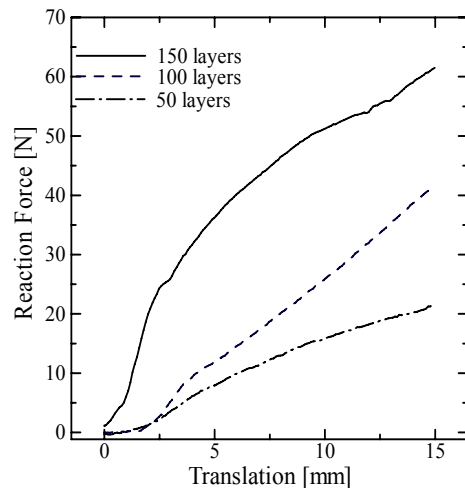


Figure 7 Stiffness of the passive elements, consisting of various numbers of stacked plates.

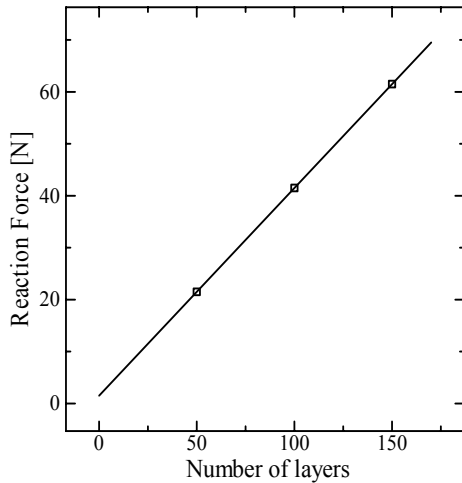


Figure 8 Relation between number of stacked plates and stiffness.

Effect of the covering film

Figure 9 shows stiffness of passive elements composed of various covering films. The materials of the covering films are urethane (thickness 0.2[mm]), rubber (thickness 0.3[mm]), cloth-coated vinyl (thickness 0.2[mm]), and vinyl (thickness 0.1, 0.2, 0.3[mm]). Figure 10 shows elongation stiffness of these covering films. The measured covering films have a width of 10[mm] and a length of 50[mm]. These figures indicate that stiffness of the passive elements correlates with the elongation stiffness of the covering films.

To dissociate the effect of covering film and the brake torque of stacked plates in stiffness of the passive element, we used two methods to estimate the stiffness produced by the covering film. The first method estimates stiffness from the elasticity of the covering film. The elongated length is estimated geometrically, under the assumption that the covering film does not slip on the thin plates. The second method estimates stiffness from observation of stiffness at various internal air pressures (Figure 11). Since the linear relations between stiffness and internal air pressure have their intercepts at 0[kPa], we assume that these intercepts represent stiffness produced by the covering film. Note that actual stiffness at 0[kPa] is almost zero. Figure 12 compares values of stiffness estimated by the two methods. Over the entire range depicted, the two estimates are almost identical. Figure 13 shows the breakdown of stiffness of the passive elements. The estimated brake torque was derived by subtracting the stiffness produced by the covering film from total stiffness of the passive elements. Estimated brake torque was almost identical, with the exception of the elements covered by thick vinyl sheets.

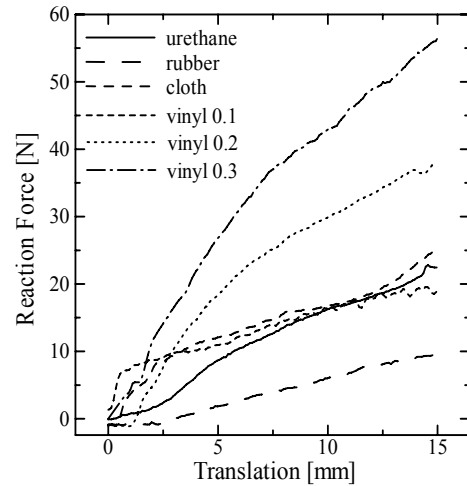


Figure 9 Effect of the covering film.

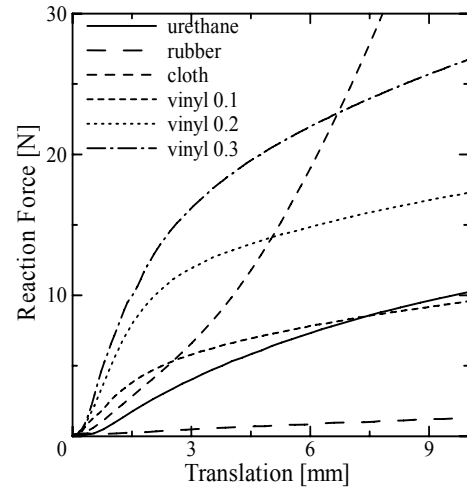


Figure 10 Elongation stiffness of covering films.

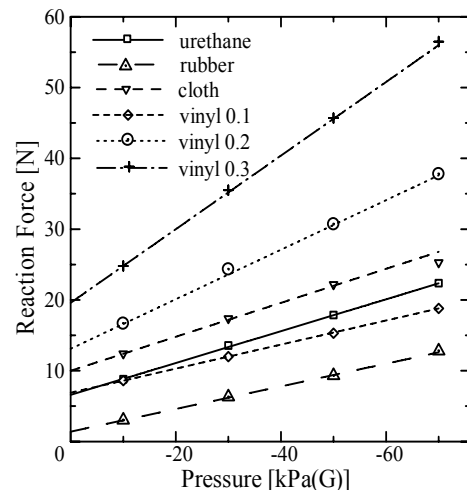


Figure 11 Relation between stiffness and internal air pressure.

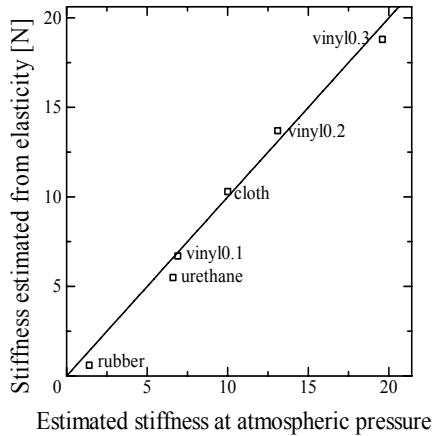


Figure 12 Stiffness values estimated by two methods.

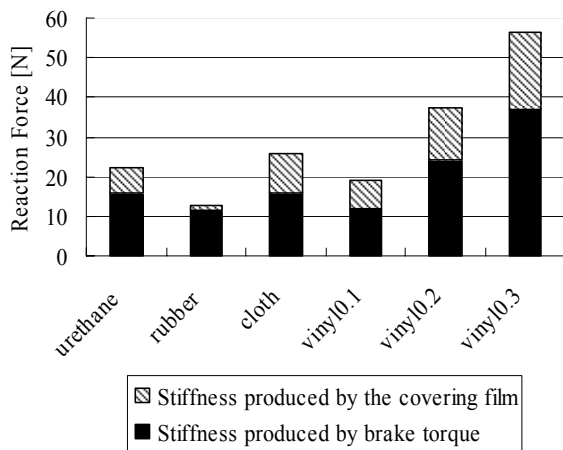


Figure 13 Breakdown of stiffness.

Reusable cast composed of articulation passive elements

Structure of the reusable cast

We developed a reusable orthopedic cast as an application of the articulation-type passive element. Conventional casts are made rigid by chemical reaction with water. Once it becomes solid, a conventional cast can be removed only by cutting with a grinder. The cutting process is unpleasant for patients. The cast developed from the articulation-type passive element is made rigid by evacuating the inside air. It is reusable, and shape and stiffness can be adjusted by the internal air pressure.

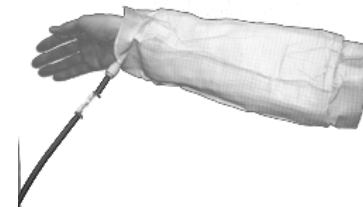


Figure 14 Reusable cast composed of articulation-type mechanical constraint.

Figure 14 shows a reusable cast developed from articulation-type passive elements. Twenty plates are articulated in a circular pattern, and 1,400 sets of such circularly-arranged plates are stacked and bound by wires. The cast is composed of 28,000 thin plates in total. Total weight is 566[g]. Maximum diameter is 85[mm], and overall length is 220[mm]. The diameter is adjustable, owing to the translational freedom of each articulation. The wrist portion of the cast shown in Figure 14 is contracted for fitting the surface to the skin. Minimum diameter is 60[mm].

Reusable cast composed of particle mechanical constraints

Particle mechanical constraint is another passive element, which we developed previously. It is a bag containing beads. It can be changed in shape, and evacuation of the inside air renders the bag rigid so that it maintains whatever shape it has been given. We also developed a reusable cast using the particle mechanical constraint, in order to compare stiffness with that of the cast composed of the articulation-type passive element. Figure 15 depicts the structure. The torus-shape cloth tubes containing beads are connected to form a cylinder. The cylinder is enveloped by a cloth-coated vinyl sheet. Stiffness of the particle mechanical constraint correlates with the material of beads. We developed two reusable casts using Styrofoam beads and nylon shots. The diameter and length are the same as those of the cast developed from the articulation-type passive element. Both casts have a thickness of 10[mm]. The weights of these casts were 312[g] and 70[g], respectively.

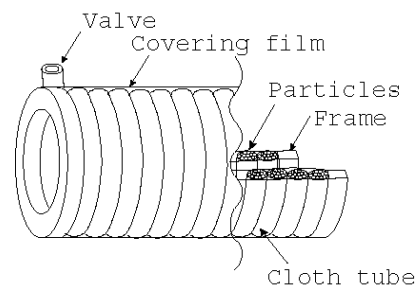


Figure 15 Reusable cast composed of particle mechanical constraint.

Evaluation of stiffness

We examined stiffness of the casts developed from the various passive elements described above. We also examined the stiffness of a conventional, commercially available cast. Figure 16 shows the relation between reaction force and compression ratio when a testing machine compressed the center of the casts by a circular plate. The outer diameter of the plate was 200[mm]. The cast developed from the articulation-type passive element had greater stiffness than that developed from particle mechanical constraints. It also had a greater stiffness than the conventional cast below 300[N]. However the stiffness of the articulation-type passive element gradually declined with increasing reaction force, because the stiffness is exerted mainly by friction force. The necessary stiffness of orthopedic casts is not clear because there are many types of use. The stiffness of the articulation-type passive element is not enough to guard an arm from accidental collision, though the stiffness is enough to fix an arm.

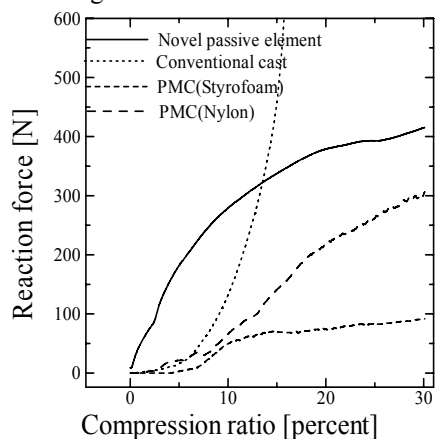


Fig. 16 Stiffness of four different casts.

Conclusion

This paper describes a novel passive element that can be freely contracted and bent to fit an arbitrary rounded surface. A reusable cast developed from this passive element shows higher stiffness than a reusable cast developed from particle mechanical constraints. The cast also shows higher stiffness at small compression force than a commercially available cast. Reduction in thickness and weight is a problem to be solved for practical use. The problem correlates with the stiffness of the passive element. We are investigating better materials for the plates and the covering film in order to increase stiffness of the passive element. This passive element is applicable also for haptic displays and wearable robots for assisting human motion. Development of such applications is the subject of our future studies.

Acknowledgments

This study was completed with the assistance of the 2004 Industrial Technology Research Grant Program of the New Energy and Industrial Technology Development Organization (NEDO).

REFERENCES

1. Kobayashi, H., Hiramatsu, K., Development of Muscle Suit for Upper Limb, Proc. of the 2004 IEEE Int. Conf. on Robotics and Automation, pp.2480-2485.
2. Sasaki, D., Noritsugu, T., Takaiwa, M., Development of Active Support Splint Driven by Pneumatic Soft Actuator, Journal of Robotics and Mechatronics, 2004, **16-5**, pp.497-503.
3. Kawamura, S., Hayakawa, Y., Tamai, M., Shimizu, T., A design of motion-support robots for human arms using hexahedron rubber actuators, Proc. of the 1997 IEEE/RSJ Int. Conf. On Intelligent Robot and Systems, **3**, pp.1520-1526.
4. Belforte, G., Gastaldi, L., Sorli, M., Pneumatic active gait orthosis, Mechatronics, 2001, **11-3**, pp.301-323.
5. Yamamoto, K., Hyodo, K., Ishii, M., Matsuo, T., Development of Power Assisting Suit for Assisting Nurse Labor, JSME Int. J. Series C1, **45-3**, pp.703-711, 2002
6. Mitsuda, T., Wakabayashi, M., Kawamura, S., Development of a wearable chair using pneumatic passive elements, Journal of Robotics and Mechatronics, 2004, **16-3**, pp.256-263.
7. Mitsuda, T., Kuge, S., Wakabayashi, M., Kawamura, S., Wearable force display using a Particle Mechanical Constraint, Presence, 2002, **11-6**, pp.569-577.
8. Kawamura, S., Yamamoto, T., Ishida, D., Ogata, T., Nakayama, T., Tabata, O., Sugiyama, S., Development of Passive Elements with Variable Mechanical Impedance for Wearable Robots, Prof. of Int. Conf. On Robotics and Automation, 2002, pp.248-253.

Development of Master-Slave Manipulator Using Pneumatic Cylinders

Kenji Kawashima*, Kotaro Tadano**, Supawat APIRAK**
and Toshiharu KAGAWA*

* Precision and Intelligence Laboratory

** Graduated school student

Tokyo Institute of Technology

4259 Nagatsuta, Midori-ku, Yokohama, 226-8503 Japan

(E-mail: kkawashi@pi.titech.ac.jp)

ABSTRACT

Recently, development of instruments for minimally invasive surgery has been considerably required. This surgical procedure, as compared with traditional open surgery, enables the incision smaller, and this result in less patient pain and shorter duration of hospital stays. However, it requires increased skill on the part of the surgeon. To solve this problem, robotic manipulators using electric actuators that have multi-DOFs at the tip of them have been reported as alternative to conventional instruments. These systems, however, has the problem that force sensing is difficult. In this paper, we propose a master-slave manipulator using pneumatic cylinders as actuators that can be useful for laparoscopic surgery. This system can provide force feedback to the surgeon from the differential pressure of the cylinders. We designed a bilateral dynamic control system using neural network for acquisition of the inverse dynamics. The obtained inverse dynamics is used for feedforward and estimation of the external force. Experimental results showed that the developed system successfully display the contact force.

KEY WORDS

Pneumatics, Bilateral Control, Forceps, Neural Network

INTRODUCTION

Minimally invasive laparoscopic surgery has been widely performed in recent years. This surgical procedure enables a smaller incision as compared with traditional open surgery. This result in less patient pain and shorter duration of hospital stays. However, it requires increased skill on the part of the surgeon. This is because surgical instruments in laparoscopic surgery are restricted to the degrees of freedom (DOFs) motion due to trocars. As a result, surgeons have to handle the

instruments at the opposite end to the abdominal cavity with respect to the trocar point. This prevents surgeons operating intuitively.

To solve the above problems, robotic manipulators, which have multi-DOFs at their tip, have been reported as alternative to conventional instruments [1]. These manipulators can be divided into two approaches with regard to the operating method. One is the manipulator where some DOFs are added to the tip of the conventional forceps [2][3]. A system of this type is comparatively small, and it is easy to introduce into

surgery. However, the problem that the operation is not intuitive still remains. The other is a master-slave type in which the operating portion for the surgeon is separated as master from the forceps [4]. In this type, a surgeon is able to teleoperate the forceps at the master side, as if one handles the forceps at the slave side in the abdominal cavity. Therefore, this master-slave type is useful from the view of intuitiveness. This system, however, has the problem that the sense of force is lost. Some studies have been made on the force display in the master-slave surgery system [5][6], in which the force sensor, that is almost strain gauge, is attached into the tip of forceps manipulator. However, the sensor at the end of manipulator makes sterilizing and downsizing difficult.

In this research, we propose a master-slave system with multi-DOF forceps manipulators that is able to provide a force display to surgeons without a force sensor. This is to realize a bilateral control without force sensors that is quite different from the conventional methods [7]. To achieve this, pneumatic cylinders are used as the actuator, because they are effective for a haptic device due to the facility in measurement and control of their driving force, and enable the estimation of the external force from the driving force and the impedance.

DEVELOPED MANIPULATOR

Structure of the Manipulator

Fig.1 shows the developed forceps manipulator that has 7-DOFs. It has 4-DOFs at the tip, a roll, two bending joints and a holder, and 3-DOFs at the upper part, which is parallel mechanism with three cylinders. The size of the manipulator is about 800mm in height and 300mm in width. It is quite compact compared with daVinci and Zeus that are commercial systems. Moreover, the developed system can provide a force display using pneumatic cylinders not electric motors as the actuators. Fig.2 shows the tip part of the manipulator. The diameter of the manipulator is 10mm that is useful for laparoscope surgery. The power for two bending joints at the tip of the manipulator is transmitted by a wire rope as shown in Fig. 3. The cylinder made by Airpel was used because it uses a precision fit graphite piston which slides freely - without lubrication - inside a pyrex glass cylinder. Therefore, the friction force is negligible small. The sizes of the cylinder used at the lower and upper part are 9.3mm and 14.9mm in diameter, 3.2mm and 5.0mm in the piston rod diameter and 25mm 75mm for the full stroke. The driving force of the cylinder F_{dr} is given as

$$F_{dr} = A\Delta P \quad (1)$$

where A and ΔP indicate the pressurized area and the differential pressure in the cylinder.

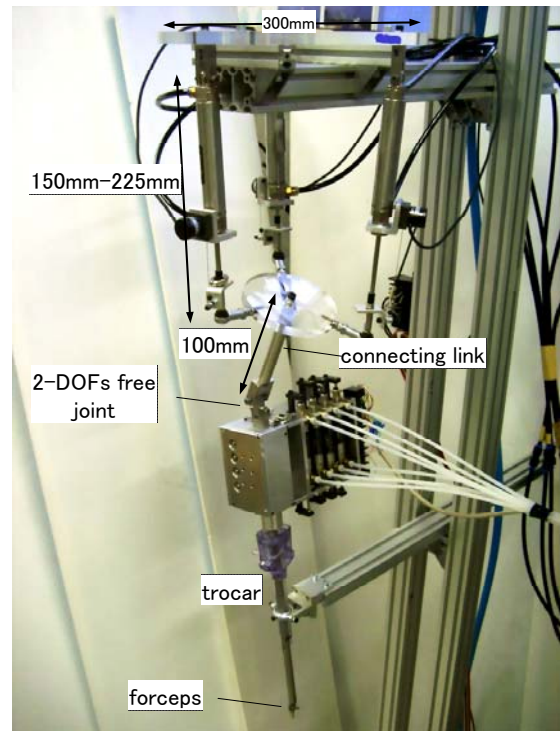


Fig.1 Developed manipulator

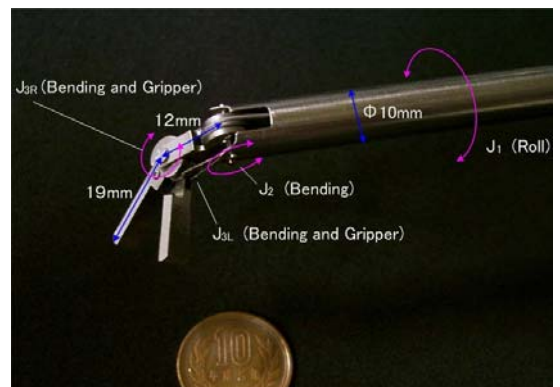


Fig.2 Tip photo of the developed manipulator

The supply pressure was set at 500kPa and a pressure sensor having a resolution of 20Pa was used. Since the pressurized area is 60mm², the maximum driving force at the tip becomes 30N which is considered to be enough for driving the manipulator.

The cylinder was controlled by a five ports servo valve made by FESTO. The servo valve receives the voltage signal and controls the flow rate to the cylinder. Pressures in the cylinder are measured with semiconductor type sensors and are used to control the driving force. Position is measured by an encoder having a resolution of 1000Pulse/Rev. We have confirmed in the preliminary experiment that the position error of the cylinder is not more than 0.1mm using a PID controller. Also, we have confirmed that the force control could be achieved with 0.05N accuracy.

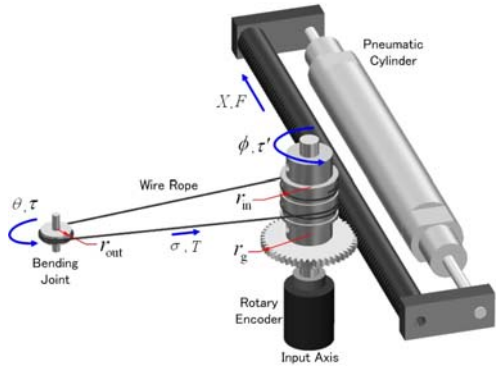


Fig.3 Mechanism for power transmission

At the tip, the displacement of the wire rope l shown in Fig.3 is proportional to that of the cylinder X .

$$l = r_{in}\phi = \frac{r_{in}}{r_g} X \quad (2)$$

where ϕ is the rotation angle of the pinion gear and the pulley, r_g is the pitch circle radius of the pinion and r_{in} is the radius of the pulley. Then, the angle of bending θ is given as

$$\theta = \frac{l}{r_{out}} = \frac{r_{in}}{r_{out}r_g} X = \frac{X}{R} \quad (3)$$

where r_{out} is the radius of the small pulley at the bending joint. Thus, the angle of bending θ is linear to the displacement of corresponding cylinder. We designed that the wire rope for driving the bending joint J_3 passed through the center of the joint J_2 to prevent interference between the joints. Additionally, the relationship between the torque τ for bending and the driving force of the pneumatic cylinder F is also linear and is given by

$$\tau = RF \quad (4).$$

Where R is an equivalent value to reduction ratio. To improve the resolution of the rotation angle at the tip of the manipulator, R should be small. However, in contrast, to improve the force sensitivity R should be large. In this prototype manipulator, we adopted 8 [mm] as R ($r_{in} = 6.5\text{mm}$, $r_g = 13\text{mm}$, $r_{out} = 4\text{mm}$) to reasonably satisfy both of these conditions. As a result, the resolution of the bending angle is considered to be 0.7degree. The weight of the tip part is 20N.

At the upper side, 3-DOFs are realized with parallel mechanism as shown in Fig.4. The maximum angle of

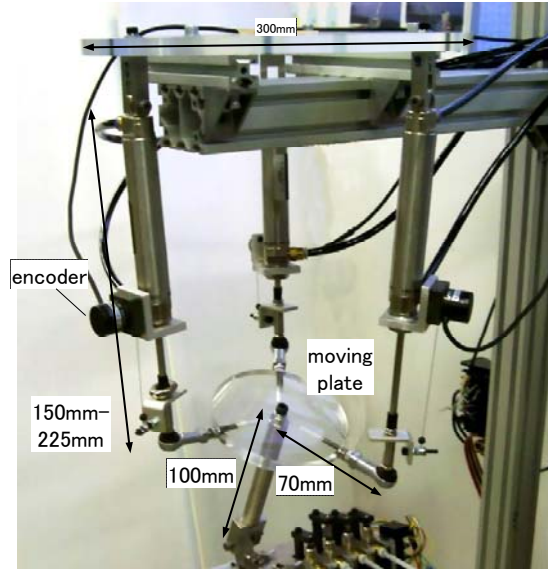


Fig.4 Upper part of the developed manipulator

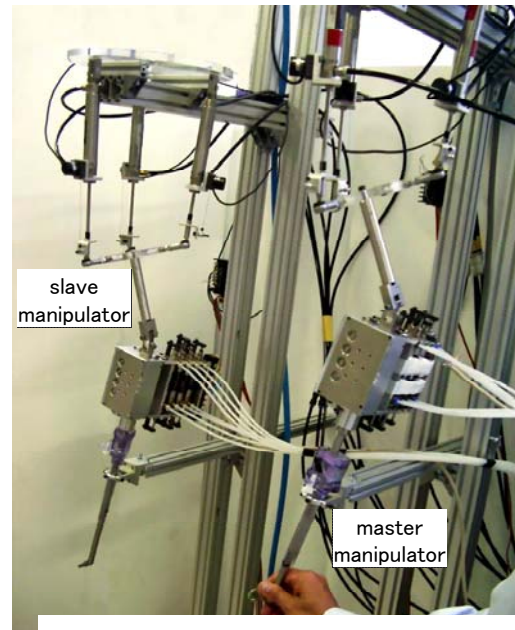


Fig.5 Developed Master-slave system

the moving plate is 30 degrees. The maximum force with the three cylinders is 90N, which is enough to hold the tip part. The tip and upper part were connected with a free joint. The length of the connecting link determines the moving angle at the tip of the manipulator. Therefore, it was designed as 100mm, which realizes the moving range of a circle whose diameter is about 120mm. The manipulator whose structure is the same as that of the slave side is used as the master side for simplification of control as shown in Fig5. Measured position and pressure signals are sent to a computer for control, and the computed voltage signals are provided to the servo valves.

BILATERAL CONTROL

Proposed control method

In this section, we describe the proposed method of bilateral control without force sensors in the master-slave system. Although a bilateral control method called symmetric position servo type needs no sensing of force, the performance is influenced by the dynamics of the manipulator. Therefore, the dynamic control using the impedance and the external force that are estimated by neural network as the driving force of the cylinders has been implemented.

The ideal response of the master-slave system is that both the position and force response in the master and slave side are identical with each other [7]. Consider a teleoperation system with two 7-DOF master and slave manipulator, whose dynamics described as

$$F_{dr}^s = Z^s(X^s, \dot{X}^s, \ddot{X}^s) + F_{en} \quad (5)$$

$$F_{dr}^m = Z^m(X^m, \dot{X}^m, \ddot{X}^m) - F_{op} \quad (6)$$

where F_{dr} , F_{op} , F_{en} , Z and X are translational vectors of the driving force of the pneumatic cylinders, the force exerted by an operator on the master side, the force applied on the environment, the impedance function of the manipulator and the displacement of the cylinder respectively, and subscript s and m denote slave and master side. The conditions of ideal response in this system can be written as

$$X^s = X^m \quad (7)$$

$$F_{op} = F_{en} \quad (8).$$

To satisfy Eq.(8), the driving forces of cylinders should be

$$F_{dr}^s = Z^s(X^s, \dot{X}^s, \ddot{X}^s) + F_{op} \quad (9)$$

$$F_{dr}^m = Z^m(X^m, \dot{X}^m, \ddot{X}^m) - F_{en} \quad (10).$$

There are, however, disturbances due to the uncertainty of impedances, external forces and so on. Therefore, position and velocity feedback has been added to restrain them as follows:

$$F_{dr}^s = K_p^s(X^m - X^s) + K_d^s(\dot{X}^m - \dot{X}^s) + Z^s(X^s, \dot{X}^s, \ddot{X}^s) + F_{op} \quad (11)$$

$$F_{dr}^m = K_p^m(X^s - X^m) + K_d^m(\dot{X}^s - \dot{X}^m) + Z^m(X^m, \dot{X}^m, \ddot{X}^m) - F_{en} \quad (12)$$

where K_p and K_d are gain vectors. Substituting Eq.(11) and (12) to Eq.(5) and (6) yields

$$K_p^s e + K_d^s \dot{e} + F_{op} - F_{en} = 0 \quad (13)$$

$$-K_p^m e - K_d^m \dot{e} - F_{en} + F_{op} = 0 \quad (14)$$

where

$$e \equiv X^m - X^s \quad (15).$$

Combining Eq.(13) and (14) yields the error equation:

$$(K_p^s + K_p^m)e + (K_d^s + K_d^m)\dot{e} = 0 \quad (16).$$

Hence, e converges asymptotically to zero with appropriate gains, and then from Eq.(13) or (14), Eq. (8) is also satisfied. This means that the ideal response is realized. In practical control, the position, velocity and acceleration of the other side were used as the input of the impedance function as shown in Eq.(17) and (18) to improve the speed of response.

$$F_{dr}^s = K_p^s(X^m - X^s) + K_d^s(\dot{X}^m - \dot{X}^s) + Z^s(X^m, \dot{X}^m, \ddot{X}^m) + F_{op} \quad (17)$$

$$F_{dr}^m = K_p^m(X^s - X^m) + K_d^m(\dot{X}^s - \dot{X}^m) + Z^m(X^s, \dot{X}^s, \ddot{X}^s) - F_{en} \quad (18).$$

Here $Z^s(X^m, \dot{X}^m, \ddot{X}^m)$ and $Z^m(X^s, \dot{X}^s, \ddot{X}^s)$ behave as a feedforward controller having inverse dynamics. The controller symmetrically sends the values of displacement and external force to one another. This symmetrical system is able to change the roles of master and that of the slave side.

Acquisition of inverse dynamics using a neural network

To implement Eq.(17) and (18), it turns out that the impedance function and the external force must be given in addition to the position. Here, it should be noticed that the driving force of pneumatic cylinder can be obtained from the differential pressure as shown in Eq.(1). Therefore, if the values of the impedance are given, the external force F_{ext} is given by

$$F_{ext} = F_{dr} - Z(X, \dot{X}, \ddot{X}) \quad (19)$$

where F_{ext} denotes the vector of external force to the cylinder, which is F_{en} at the slave side and $-F_{op}$ at the master side. We can estimate the external force from Eq.(19) using a disturbance observer. Therefore, it is significant to obtain the impedance of the manipulator which is equivalent to the inverse dynamics problem. Thus, acquisition of the inverse dynamics enables both estimation of the external force and feedforward control.

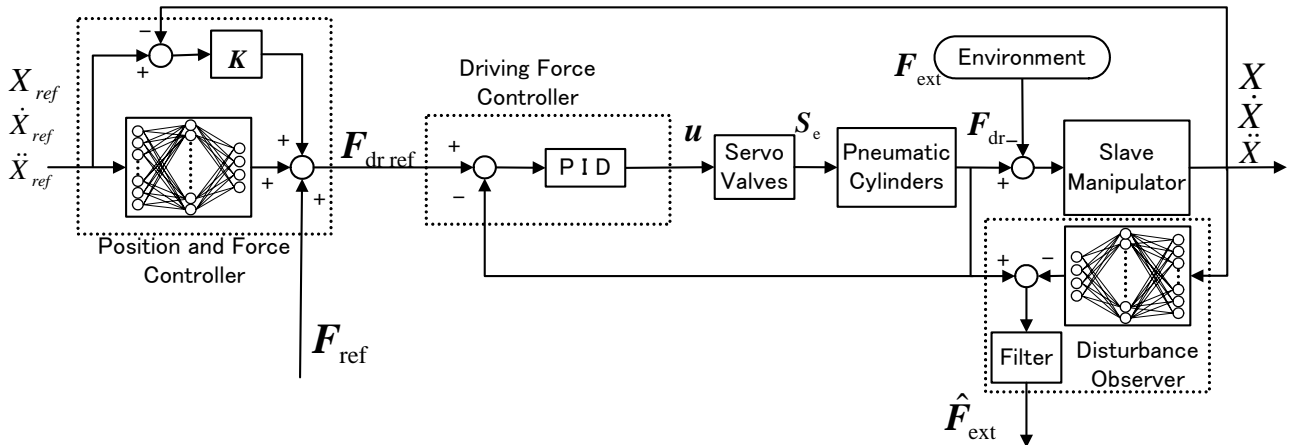


Fig.6 Block diagram of the designed bilateral control

Generally, the dynamics of a multi-DOF manipulator depends on its attitude, mainly because of the influences of inertia and gravity varies with the position. The tip of the forceps manipulator is small and light so that their effects are negligible. In the prototype manipulator, there is, however, the dependence of dynamics due to the position. This is because of the variation in friction caused by the wire rope. This friction characteristic seems to have strong nonlinearity and is very difficult to model mathematically. Although friction model in a single pneumatic cylinder has been reported [8], the model is unable to represent the dependence on the position.

For the reason mentioned above, a neural network is used to obtain the inverse dynamics of the manipulator. We used a three-layered neural network in which there are twenty-one inputs (displacements, velocities and acceleration of each joint) and seven outputs of impedance. The network is trained offline with back-propagation using the data collected through a closed-loop experiment in which the manipulator is assigned random position trajectories and no external load. In no-load motion, the driving force corresponds to the impedance from Eq.(19). After the training is finished, the network can be used as a feedforward controller and disturbance observer. The detail of the master or slave controller is represented as Fig. 6. The controllers are the same at the master and slave side. The controller has a major loop for position and a minor loop for differential pressure which realize the desired driving force. The neural network is incorporated as feedforward and disturbance observer. The measured position and estimated external force are provided to the other side as an input.

EXPERIMENTAL RESULTS

Examination of Force Estimation

Some experiments were undertaken to verify the precision of the force estimation by the disturbance observer. We placed a single axis load cell that is a force sensor as an object on the slave side. To compare the external forces estimated by Eq.(19) with the output of the force sensor, we transformed them into Cartesian coordinate system at the tip of the manipulator using a Jacobian matrix.

Fig.7 shows the experimental results. It is clear from the results that the estimated force is slightly larger than the output of the load cell especially at the maximum value. This is because the force at the tip of the manipulator was not entirely transmitted to the cylinders due to mechanical flexure and the friction caused by the load. This could be improved by modifying the structure of the manipulator. However, the estimated value corresponded well with the output of the load cell on the whole.

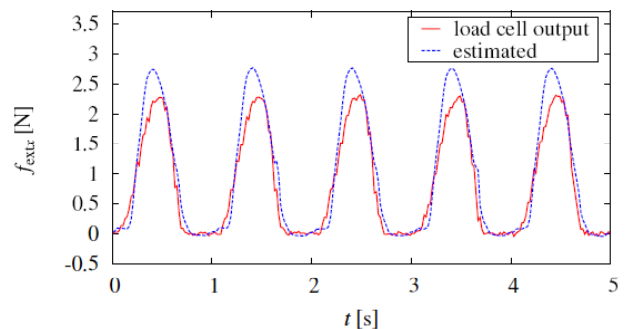


Fig.7 Experimental results of force sensing

Bilateral Control Experiment

The performance of the master-slave system was examined with the proposed bilateral control by use of the estimated inverse dynamics and external force. The neural networks in the master and slave side were previously trained with the data in the no-load motion. The slave manipulator was brought into contact with an object by the operator handling the master manipulator. The experimental results at joint J_1 and J_{3L} at the tip are shown in Fig.8 and Fig.9.

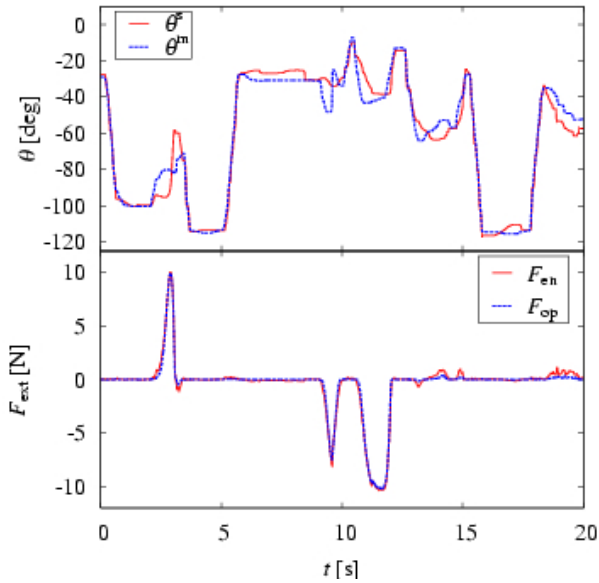


Fig.8 Experimental results of bilateral control at J_1

The upper graphs indicate the position of the cylinder.

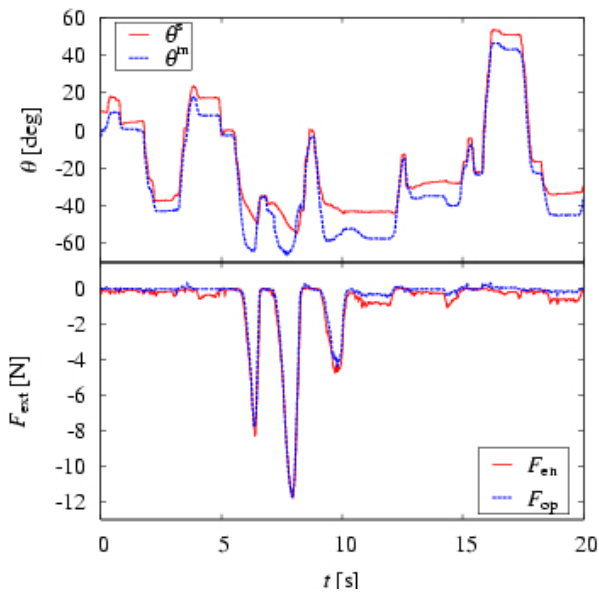


Fig.9 Experimental results of bilateral control at J_{3L}

The lower graphs show the external forces at the master and slave side. While there are some disagreement in the position, which is caused by the mechanical flexure and friction under load and also by the convergence speed of the controller, it can be seen that the force exerted by the operator on the master side and the force applied on the environment correspond well. The effectiveness of the proposed bilateral control method was therefore demonstrated.

CONCLUSIONS

In this paper, a manipulator has been developed which has 7-DOFs actuated by pneumatic cylinders. A master-slave system has been established with the manipulator for laparoscopic surgery. Neural networks were applied to the controller for acquisition of the inverse dynamics and the external force without using force sensors. The experimental results indicated that the operator felt the force at the slave side to a satisfactory extent.

REFERENCES

1. Garth H. Ballantyne, Jacques Marescaux, and Pier Cristoforo Giulianotti, editors. Primer of Robotic & Telerobotic Surgery. LIPPINCOTT WILLIAMS & WILKINS, 2004
2. H. Yamashita, D. Kim, N. Hata, T. Dohi Multi-Slider Linkage Mechanism for Endoscopic Forceps Manipulator Conference on Intelligent Robots and System, 2003, pp2577-2582
3. N. Matsuhira, et al Development of a functional model for a masterslave combined manipulator for laparoscopic surgery Advanced Robotics, 2003, 17-6, pp523-539
4. K. Ikuta, M. Kawai, K. Fukuda and T. Hasegawa Hyper Finger for Remote Minimally Invasive Surgery in Deep Area Robotics society of Japan, CD-ROM, 2003
5. Carsten Preusche, Tobias Ortmaier, Gerd Hirzinger Teleoperation concepts in minimal invasive surgery Control Engineering Practice, 2002, 10, pp1245-1250
6. M. Tavakoli, R.V. Patel and M. Moallem A Force Reflective Master-Slave System for Minimally Invasive Surgery, IROS 2003, pp3077-3082
7. Y. Yokokohji and T. Yoshikawa, Bilateral Control of Master-Slave Manipulators for Ideal Kinesthetic Coupling, IEEE Trans Robot Automat, 1994, 10-5, pp605-620
8. Luis R. TOKASHIKI, Toshinori FUJITA, Toshiharu KAGAWA, Stick-Slip Motion in Pneumatic Cylinders Driven by Meter-out Circuit, journal of the Japan Hydraulics and Pneumatics Society, 1999, 30-4, pp110-117

Development of Pneumatically Assisted Walking System

Takayoshi FUJITA*, Osamu OYAMA*, Toshihiro YOSHIMITSU**

* Graduate School of Science and Technology

Meiji University

(E-mail: ce55258@isc.meiji.ac.jp)

1-1-1, Higashimita Tama-ku, Kawasaki-shi, Kanagawa, 214-8571 JAPAN

** Welfare systems Engineering

Kanagawa institute of Technology

1030, Shimoogino, Atsugi-shi, Kanagawa, 243-0292 JAPAN

ABSTRACT

We have developed a human walking assist system for the people who have handicap or are injured. A pair of orthosis which actuated by pneumatic liner actuators and shoes having a weight sensor makes up this system. The reason why we decide to use pneumatic actuators is that the pneumatic characteristic caused by air pressure is soft for human and also fits for environment. This assist system supports the lift of legs and stretch of knees when the human walks on ground or stairs. The supportable angles of knee are enough large and this system can be widely used.

We will evaluate the usefulness of this system by the factor of human power reducing for walk and his impression for use.

KEY WORDS

Force measuring sensor, Floor reaction force, Assist torque, Frictional torque, and Knee joint orthosis

NOMENCLATURE

α	: Angle [deg]
β	: Angle [deg]
γ	: Angle of knee joint [deg]
θ	: $180 - \gamma$ [deg]
P_S	: Supply pressure [kPa]
T_A	: Assist torque [Nm]
T_B	: Frictional torque [Nm]
T_S	: Synthetic torque [Nm]
L_S	: Thrust of actuator [N]

1. INTRODUCTION

Walking is one of the most important functions to support our life. However, a decrease in walking ability by getting old or injury makes the inconvenience in various scenes. In the result researched yet, we have developed assisted walking system using pneumatic actuator. But this system didn't satisfy the support walking for daily life in both the mental and functional point in use. And the biggest subject in a present system is an improvement of the force sensor and outfit.

In this report, we develop the outfit and sensor system

which can be co-used by various people.

2. Structure of system

2.1 Outline of system

Fig.1 shows how to control the pneumatically assisted walking system. We detect the floor reaction force by the sensors on the sole. The signals are amplified with the amplifier, and taken into CPU through an A/D converter. CPU identifies the three categories of walking mode by analyzing input signals. There are “climbing the stairs”, “descending the stairs”, and “walking flat ground” modes. CPU outputs the operate signals to the servo valves through a D/A converter when the joint of the knee starts to expand. Compressed air is supplied from servo valves to the air actuator. We think that this system can assist walking by expanding the joint of the knee.

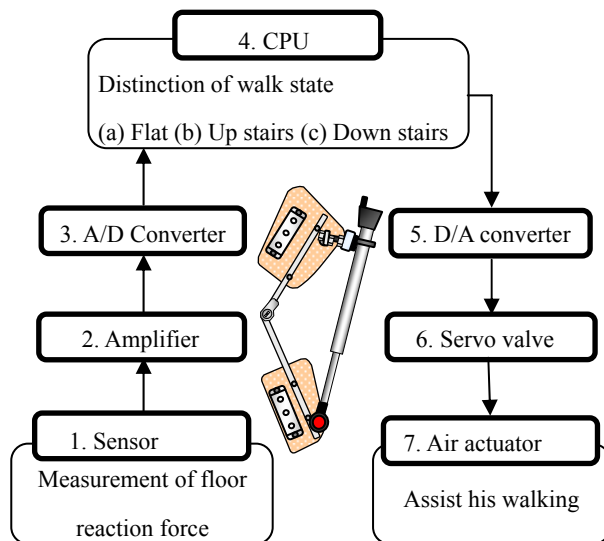


Fig.1 The assist walking system

2.2 Program to distinguish the assist timing

In this system, the signal wave which measured by the sensor are used to identify the mode of walking styles. We use a characteristic of the signal wave form of floor reaction force to identify the walking mode. In case of climbing the stairs, we observe that the peaks of floor reaction force at heel and thenar appear the same time. In case of descending the stairs, the floor reaction force of heel rises first, and then the reaction force of the thenar rises later. The last case of walking flat ground, we observe that the floor reaction force rises first at the contact of foot, and then the reaction force of the heel rises later, and the magnitude of the floor reaction force at thenar is larger than that of the heel.

We discern the walking mode using these features and decide the proper assist timing when the air is supplied to actuator, which fits for each walking modes.

3. Using the knee joint orthosis with many people

3.1 Purpose of using the only one orthosis with many people

In the past, we made the orthosis adapting tester's own leg size and shape. But it was difficult to make many orthosis because of problems of both the time and cost. So if we needed a lot of walking test, the testers had to use other people's orthosis which were not fit for him. Therefore, smoothly walking assistance couldn't have been done.

To solve these problems, we make universal orthosis which can be used by many people and has light weight.

3.2 common orthosis

Fig.2 shows outline of orthosis we made.

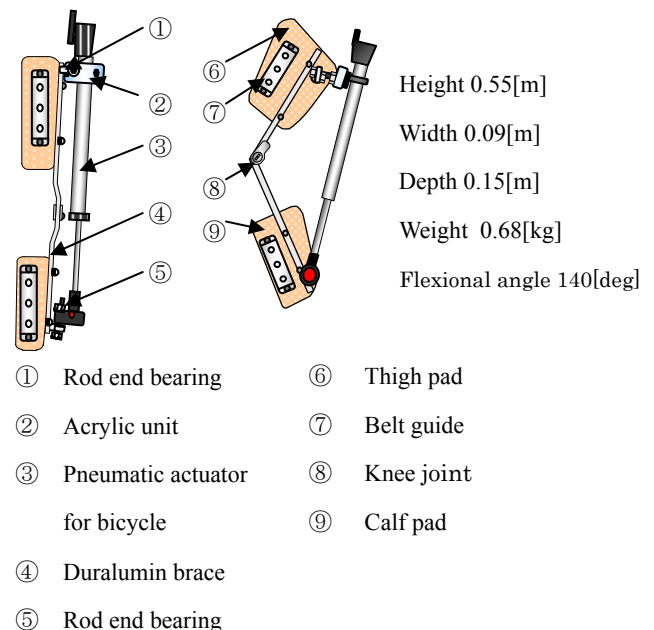


Fig.2 Knee orthosis for common use

We used the housing shaped by processing as the “low temperature degree sheet plastic”. The sponges with skid net were put in the pad. The purposes of these are to improve the feeling for wearing the orthosis. To fit the orthosis for the various people, we adopted supporter through the belt guide which made by “neo plain rubber stretch nylon”. The pneumatic linear actuator used in this orthosis has 0.025[m] inside diameter, 0.200[m] stroke length, and is yielded 5.0 [kgf/cm²] supply air pressure. The maximum bending angle of orthosis has increased from previous 90[deg] to 110[deg], so the range of operation has extended. We used portable air pump for bicycle as the actuator and the weight of actuator becomes light as former pneumatic industrial actuator. Fig.3 shows uniting part of orthosis and actuator.

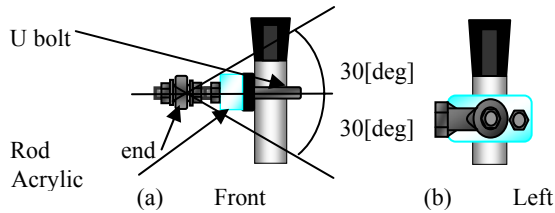


Fig.3 Knee orthosis – Actuator Unit

4. Theoretical characteristic of common knee joint orthosis

By generating the assist torque by the compressed air, the orthosis expands. We have analyzed the assist torque theoretically.

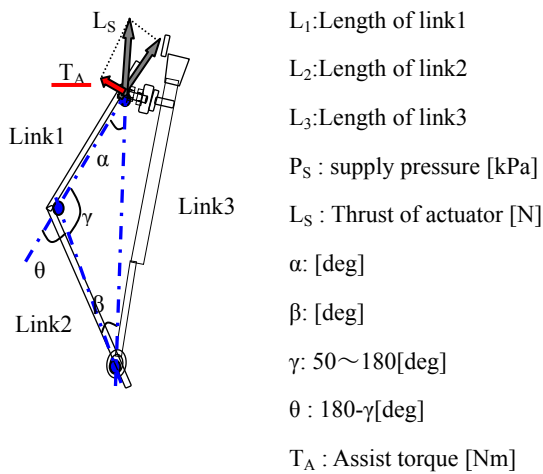


Fig.4 Link model for assist torque

4.1 Theoretical value of assist torque

Fig.4 shows link model of knee joint orthosis. We deduce the theoretical assist torque T_A shown Fig.4 adopting sine and cosine theory.

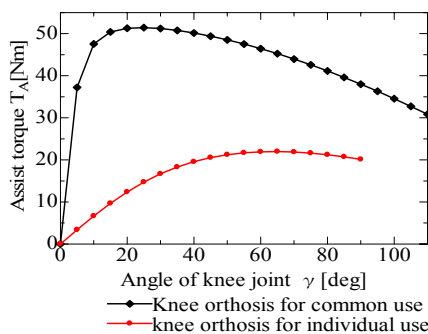


Fig.5 Theoretical value of assist torque

Fig.5 shows the value of T_A . The T_A dotted large mark shows common use type which newly developed and line dotted small shows the previous one.

Comparing developed result and previous individual one, it is shown that the maximum assist torque differs large. The maximum of theoretical value of common use is 52[Nm] (Angle of knee joint is 25[deg]) while its value of individual use is 22[Nm] (Angle of knee joint is 65[deg]). We think user of newer orthosis can get stronger assist feeling because the mainly desired portion for assist angle of knee joint for assist is 20~30[deg] where is three times bigger than individual one as assist torque in this angle. We will execute much lower pressure compressed air so it will be possible to be reduced motive power.

4.2 Theoretical value of frictional torque

The difference of frictional torque by the change of actuator is compared. We calculate torque in order to know the frictional characteristic of actuator and frictional loss torque when the actuator expands and contracts. We use link model of assist torque to calculate it. The calculated frictional torque is defined as T_B in Fig.6..

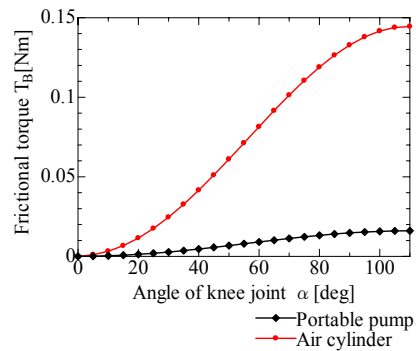


Fig.6 Theoretical value of frictional torque

According to the increasing the angle, the differences grow large as frictional torque. A former actuator has nine times bigger frictional torque than that of portable pump for bicycle. So we could reduce the frictional torque about 11% using portable pump.

4.3 Total theoretical torque of knee joint orthosis

By subtracting frictional torque T_B from theoretical value T_A of assist torque is shown as the theoretical value of synthetic torque T_s . Fig.7 shows the comparison of theoretical value of assist torque and the synthetic torque in common knee joint orthosis. And Fig.8 shows the comparison of knee joint orthosis for common use using the portable pump and knee joint orthosis for individual use using the pneumatic cylinder.

Fig.7 shows that the influence of frictional torque is rather small because it has been much smaller than the assist torque (Frictional torque is about 0.4 percent of assist torque). Influence of frictional torque in use of pneumatic cylinder is about 5 percent loss of assist torque. The losing torque from friction of actuator is small and is shown Fig.8, and the assist torque of knee

joint orthosis decides the synthetic torque. So knee joint orthosis is important to decide the value of assist torque for walking assistance. It is thought theoretically that knee joint orthosis for common use is more useful than knee joint orthosis for individual use in the view point of assist torque.

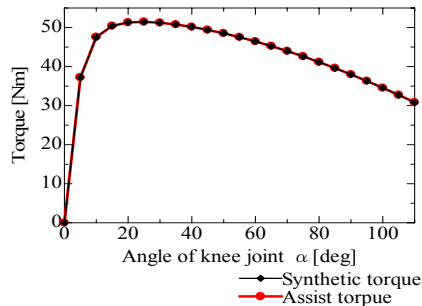


Fig.7 Synthetic torque and Theoretical value of assist

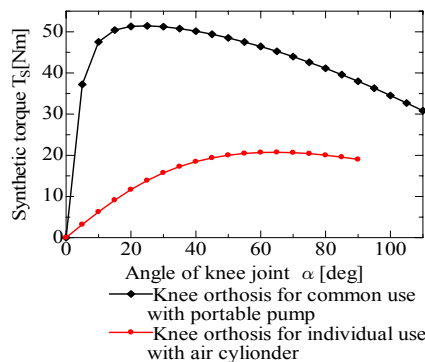


Fig.8 Theoretical value of Synthetic torque

5. Evaluation for knee joint orthosis

We have experimented to evaluate the feeling of knee joint orthosis for common use. And we examine the utility of knee joint orthosis with theoretical characteristic.

5.1 How to evaluate the knee joint orthosis

To evaluate the utility of knee joint orthosis for common use, we have scored it by tester's subjectivity. We judge its performance by follow methods.

- ① The testers wear orthosis.
- ② The testers operate as follows. (1) Climbing the stairs, (2) descending the stairs, and (3) walking ground.
- ③ The testers scored eight terms (A~H) by ten point full marks what they feel.

The testers walk in free speed, because we want to examine in the usual walk. The standards for admission are different by each tester. So we have done standardization and scored objectively. The orthosis which testers worn are knee joint orthosises for common use and for individually use respectively. Eight

evaluation terms is shown respectively below.

- A. Assist feeling for walking ground
- B. Assist feeling for climbing the stairs
- C. Assist feeling for descending the stairs
- D. Assist timing for walking in the plain
- E. Assist timing for climbing the stairs
- F. Assist timing for descending the stairs
- G. Fitness
- H. Weight of orthosis

5.2 The results of evaluation.

The standardization result of objective estimation in knee joint orthosis after standardization is shown in Fig.9.

It can be shown that the knee joint orthosis for individual use gives good impression for tester because the size and shape fit him.

Fig.10 shows standardization result of tester's subjective evaluation of knee joint orthosis for individual use.

Knee joint orthosis for individual use has high evaluation score. But term of evaluation for orthosis wearing fitness has received low evaluation score.

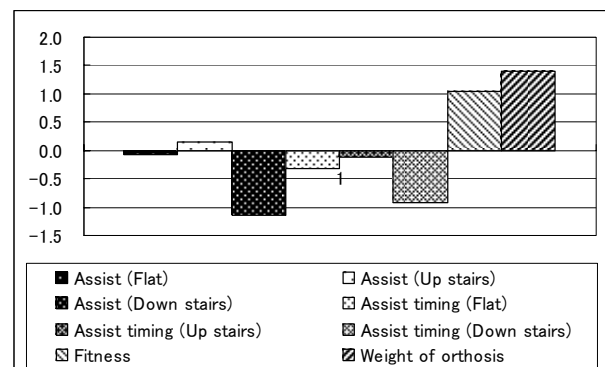


Fig.9 Tester's standardization evaluation of knee orthosis for common use

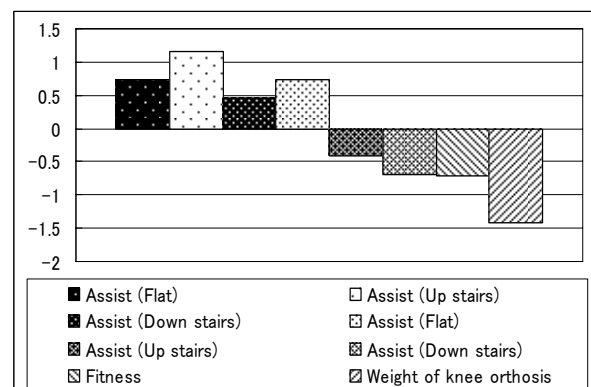


Fig.10 Tester's standardization evaluation of knee orthosis for individual use

5.3 Examination of the evaluation result

The knee joint orthosis for common use has high evaluation score of term as shown in Fig.9. Because, using new material of orthosis pad, the flexibility was improved, and covering the part of contact between foot and orthosis by elastic supporter enables the appropriate fixation. The weight of the knee joint orthosis for common use was 0.68[kg] while the weight of orthosis for individual was 1.5[kg] and the light weight of former gives good score.

The knee joint orthosis for individual use gives low evaluation score of term shown as Fig.10. Because the tester award high score to term of assist feeling rather than the term of its fitness feeling. The knee joint orthosis for individual use have satisfied the assist power, while the improvement is needed in the structure and shape in itself. The term of orthosis weight get low score because the heel part of this orthosis has additional weight in order to increase the fitness feeling and unexpectedly the tester feels reaction force when he raises the foot.

Finally, the evaluation of knee joint orthosis for common use is compared with evaluation score of knee joint orthosis for individual use. The knee joint orthosis for individually use is more suitable and get high score as fitness than that for common use. Because, knee joint orthosis for individual use was made for the specific user, it is natural. As the theoretical value of assist torque, the knee joint for common use is more large value than the individual use. So we expected that the common use yields the large assist torque. Actually, the experiment shows that knee joint orthosis for individual use get high score in this point. In a word, the influence of pad shape is larger than that of link length for assist torque. Therefore the knee joint orthosis for common use can be shared with many people but we need more examination about shape of pad or supply pressure to obtain larger assist torque.

6. Replacing the sensor system

6.1 Purpose of replacing the sensor

The next important device for this study is sensor to measure the floor reaction force. We have used small compression type load cell. Because it has good resolution and linearly to analyze the walking. But the load cell doesn't have proper shape for measuring the reaction force, so we decide to use newer sensor.

To use the current study, the sensor is placed by another type which is easy to match to foot shape.

6.2 Seat sensor

The newer force measuring sensor has structure of putting polymer into dielectric materials and we call the sensor as "seat sensor". The measurement principle is resistance changes if the load applies to the sensor, the load can be easily measured using the change of voltage

change occurred in the resistance. As one of the most important characteristic, the sensor is very thin with 0.4[mm]. Tester can stick sensor on their sock of own shoes, so we don't have to change the shoes. And we can measure floor reaction force effectually. In addition, the sensor is high sensitivity i.e., the resolution of 10 grams and a delay time is very small because the signal transmission speed is fast. Fig.11 the shows force measuring sensor.

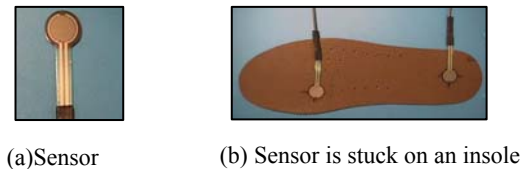


Fig.11 Force measuring sensor

6.3 Experiment to evaluate the utility of sensor

We experimented to examine whether the seat sensor can be used in this system instead of load cell. The evaluation method is shown below.

- ① We stick the seat sensor on heel and thenar.
- ② The testers operate as follows. (1) Climbing the stairs, (2) descending the stairs, and (3) walking ground.
- ③ We measure the floor reaction force and analyze the characteristic of usefulness the seat sensor to evaluate.

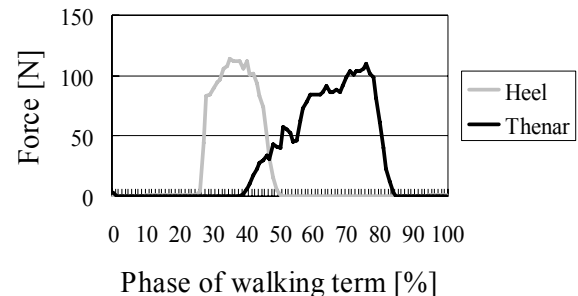


Fig.12 Floor reaction force (Flat course)

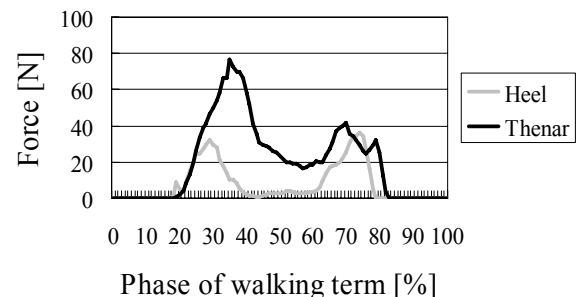


Fig.13 Floor reaction force (Up stairs course)

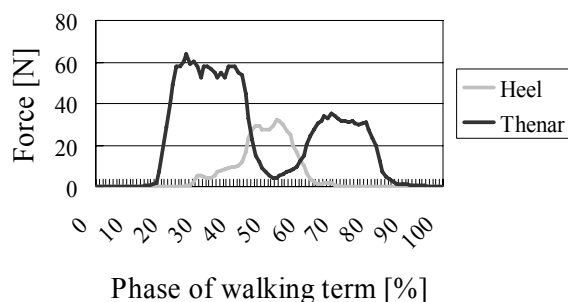


Fig.14 Floor reaction force (Down stairs course)

force measured by the seat sensor when tester walks the ground. Fig.13 shows that in the climbing of stairs, and Fig.14 shows in descending of stairs. By comparing the result of these experiments and the same one of load cell which we measured before, the characteristic of the wave shapes of output signal is very similar. In walking ground, the heel was loaded first, and the toe was loaded later. In climbing the stairs, the heel and the toe were loaded at once. And two peaks of the load change of heel and toe existed. At the end in descending the stairs, the toe was loaded first, and the heel was loaded later. And the load of the toe was bigger than the load of the heel.

6.4 Consideration of evaluation experiment in the force measuring sensor

The new force measuring sensor and the load cell has similar characteristic as detecting the signal wave of force reaction form from experiment.

The load cell detects only vertical load because of its transformation principle, so the structure of attachment influenced the accuracy of measurement. Moreover it was difficult for light weight person to measure the reaction force by using the load cell because the floor reaction force was relatively small in this case. And several time lags occur. The seat sensor solved these problems. Because the force measuring sensor has high sensitivity so this system will be able to assist walking for the light weight person more exactly. So the new force measuring sensor can use to identify the walking more instead of the load cell.

7. Conclusion

In this report, we could find the way of using the only one orthosis with many people. More high sensitive output of measuring system can be realized by using new seat sensor, so it will be possible to identify the state of walking more exactly.

As a problem in the future, to increase the number of tester and to improve program for assist will be important to certain better evaluation for assist feeling. And the parts for the signal such as D/A, CPU, and A/D will be able to miniaturized. So, this system will be able

to use in the large field.

REFERENCES

1. Understandable social welfare, F. Yamagata and T. Okada, MINERVA Publishing Co., Ltd. , 2004 pp.24-27, pp.144-147
2. National statistic center <http://www.statgo.jp/index.htm>
3. Kyoyo-Hin Foundation <http://www.kyoyohin.org>
4. Applied Research Institute <http://www.ari.co.jp>
5. Iwate University Faculty of Engineering <http://www.wel.iwate-u.ac.jp/fukushi>

Development of Tendon-Driven Assistance Manipulator System by Air Pressure Control

Takahiro TAKEUCHI*, Osamu OYAMA* and Toshihiro YOSHIMITSU**

* Mechanical Engineering Major, Science and Engineering Research Course
Graduate School of Meiji University
1-1-1 Higashimita, Tama-ku, Kawasaki-shi, Kanagawa, 214-8571 Japan
(E-mail: ce55236@isc.meiji.ac.jp)

** Welfare system Engineering
Kanagawa institute of Technology
1030, Shimoogino, Atsugi-shi, Kanagawa, 243-0292 Japan

ABSTRACT

At the close of the 20th century, in Japan, the reduction of incidence of the care worker in an aging society is becoming pressing need. Then, we aim at the development of the robot arm for care which is flexible and united with the motion of man.

In this subject, we suggest to develop the “Tendon-Driven 2-Link Manipulator Driven by Pneumatic Cylinder” as the care lift for assisting the rising and sitting of elderly people, disabled people or wheelchair users.

The tendon-driven manipulator system developed in this subject makes use of the pneumatic cylinder as an actuator. A pneumatic actuator is characterized by enabling the flexible action by the compressibility of the air. By means of the flexible action caused by the compressibility of the air, the welfare system making use of a pneumatic actuator can be expected to the “Human-Friendly Assist”.

KEY WORDS

Key words: Tendon Drive, Air Pressure Control, Pneumatic Actuator, Welfare Equipment

NOMENCLATURE

θ_1 : Angle of Link 1
 θ_2 : Angle of Link 2
P1 : Supply Pressure to Cylinder 1
P2 : Supply Pressure to Cylinder 2
P3 : Supply Pressure to Cylinder 3
 M_d : Mass of Load
 L_d : Point of Load from Joint 2

INTRODUCTION

It tries to face a worldwide aged society in Japan now. And there is a necessity of immediate development of the welfare nursing equipment according to such a social background. Moreover, there is a feature in the air pressure system that is a safe, gentle assistance of the patient by flexible equipment operation. Then, it pays attention in this thesis to the development of the tendon drive manipulator system using the pneumatic cylinder

as the welfare nursing equipment. In this report, we propose the development of the nursing lift that aims to support the senior people, handicapped person or the wheelchair user's independence changing ships.

OUTLINE OF SYSTEM

Tendon-Driven Manipulator System

Figure 1 shows the outline chart of the tendon drive manipulator system that is developed. The manipulator part is lightened in the weight by locating the pneumatic cylinder apart from the manipulator by transmitting a forth with the tendon which is made by steed wire^[1], and making the structure of an acrylic material, and the danger on the accidental collision to the patient has been reduced.

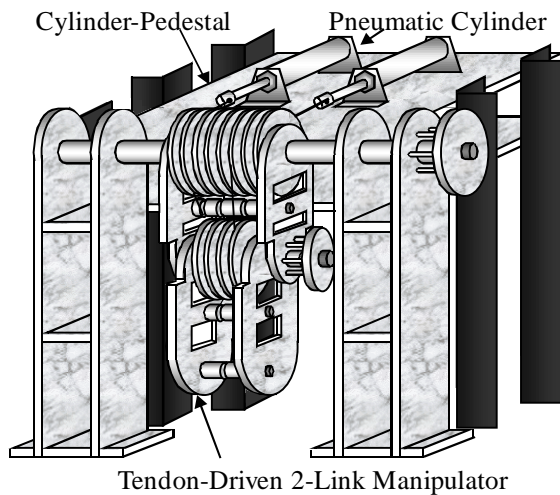


Figure 1 Diagrammatic Illustration of Tendon-Driven 2-Link Manipulator and Cylinder-Pedestal

The manipulator part is composed of two links, six belt pulleys, and four tendons as shown in figure 2. The pneumatic cylinders and each links are connected through the tendon and the belt pulley. This manipulator is a mechanism that drives the vertical plane by giving the tension of the tendon generated by the thrust of the pneumatic cylinder to each link as driving torque.

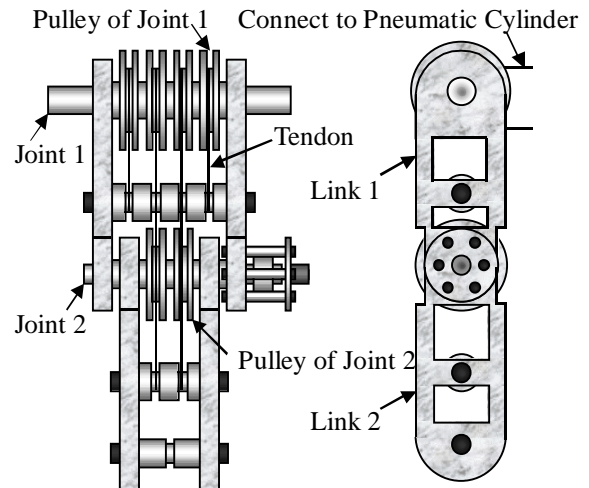


Figure 2 Diagrammatic Illustration of Tendon-Driven 2-Link Manipulator

Tendon-Driven Mechanism

Figure 3 shows the outline chart of the tendon transportation of the tendon drive manipulator system.

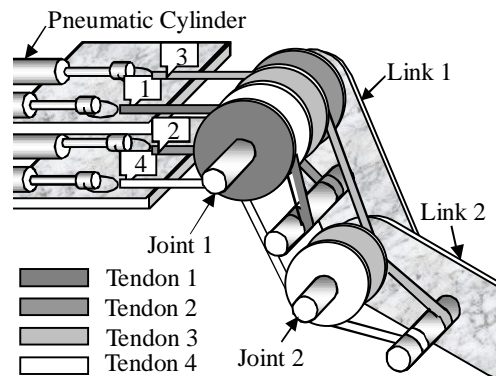


Figure 3 Diagrammatic Illustration of Tendon-Driven Mechanism with 2 D.O.F. and 4 Tendons

Tendon 1 drives Link 1 for above direction, and Tendon 2 drives Link 1 below. And, Tendon 3 drives Link 1 and Link 2 at the same time for above direction, and Tendon 4 is a mechanism that drives Link 1 and Link 2 below at the same time. The pneumatic cylinder which gives the tension to Tendon i shown in figure 3 is defined as Cylinder i .

ELECTROPNEUMATIC SERVO SYSTEM

Figure 4 shows the outline chart of the electropneumatic servo system to control the tendon drive manipulator system.

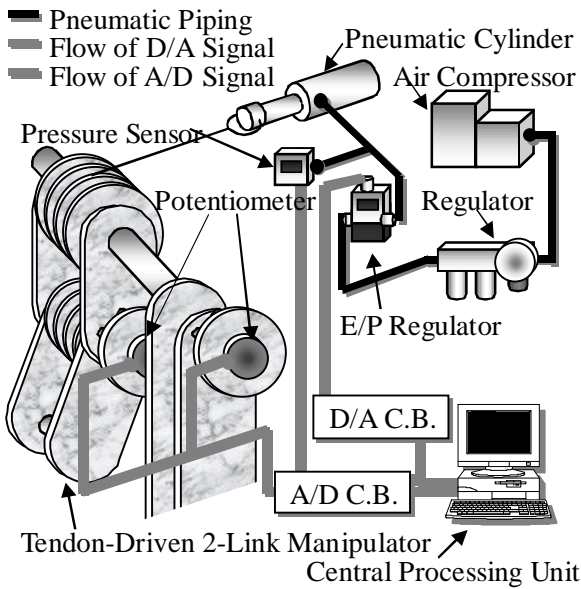


Figure 4 Diagrammatic Illustration of Electro pneumatic Servo System

Four pneumatic cylinders, four electropneumatic regulators, and four pressure sensors are set up in this subject. Each cylinder is a stroke 150 [mm], and is 40 [mm] in the inside diameter, and the compressed air of 0.5 [Mpa] is supplied and used in the maximum. Only the pressure of rod side is controlled, and the pressure is measured with the pressure sensor. The head side of cylinder is always assumed to be the atmospheric pressure liberating. The link angle is measured by the potentiometer.

REAL TIME SYSTEM

In this case, the real time system of the measurement and the control is constructed by using RTLinux^[2] that is the real-time Operating System.

RTLinux adopted for the electropneumatic servo system in order to assure the real time response, is a kind of a hard real-time Operating System. The Linux process in the program and the relation of the RTLinux module are simply shown in figure 5.

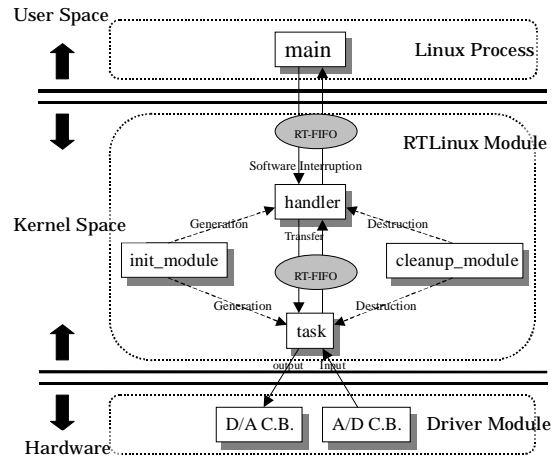


Figure 5 Conceptual Diagram of Real Time System

DEVELOPMENT OF NURSING LIFT

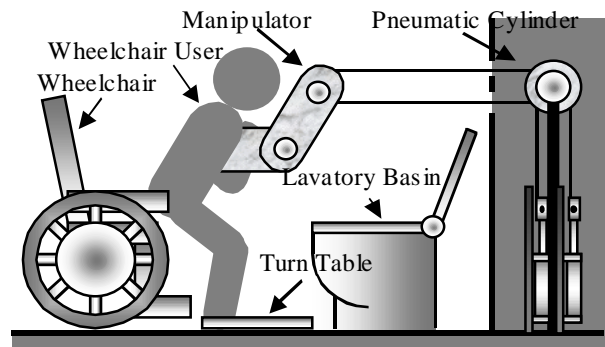


Figure 6 Diagrammatic Illustration of Suggested Care Lift

In this study, the development for the idea of practical use as the nursing lift shown in figure 6 is proposed. The principle of the motion of the lift is to keep the slant of the arm supporting a user to be horizontal in any cases, in order to avoid the slip of user along the arm. Link angle θ_1 and θ_2 measured in this report are defined as shown in figure 7.

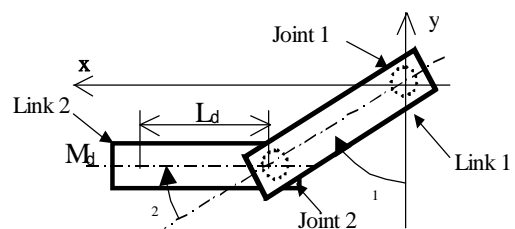


Figure 7 Defining Angle of Link View case with Measuring by Potentiometer

The manipulator must drive satisfying $\theta_1 + \theta_2 = 90^\circ$, $0 < \theta_1 < 90^\circ$, $0 < \theta_2 < 90^\circ$ so that Link 2 may always become the horizontal in this nursing lift. The reason to drive the manipulator is that it is an ideal to operate the same arm in case of the case for the person to nurse in this manner.

When the person nurses, the forearm is made the horizontal and it does. Therefore, link 2 corresponding to person's forearm is always made to become to the horizontal.

STATIC CHARACTERISTIC EXPERIMENT

The state geostationary at the link angle of the manipulator is examined. The result when the load is not built is shown in figure 8 and the result when the load is built is shown in figure 9. P1, P2, and P3 of explanatory notes show the supply pressure to Cylinder 1, Cylinder 2, and Cylinder 3 and L1 and L2 show the link angle of Link 1 and link 2.

The supply pressure to each pneumatic cylinder to each link angle is calculated in this experiment, when the pressure is supplied to each pneumatic cylinder actually, and each link angle is measured.

Each cylinder and each link name relation are as shown in the above-mentioned.

Because the angle is attached in a positive direction from the origin with pressure not supplied to Cylinder 1, Link 1 has returned the starting point the angle of Link 1 by supplying pressure to Cylinder 2.

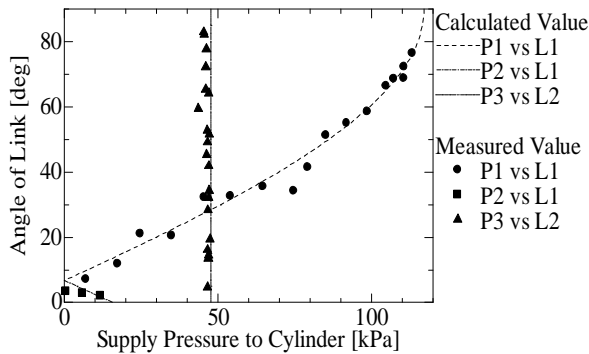


Figure 8 Static Characteristics of Manipulator case with Angle of Link vs. Supply Pressure to Cylinder (No Load)

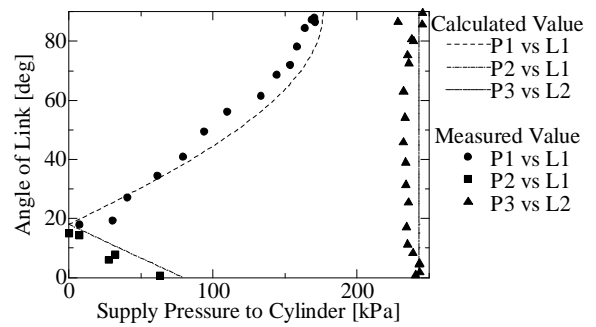


Figure 9 Static Characteristics of Manipulator case with Angle of Link vs. Supply Pressure to Cylinder (Load Point : $L_d = 0.22$ [m], Load Mass : $M_d = 3.0$ [kg])

An excellent result without a big error margin when there was no load as showing in Figure 8 was obtained. It reaches the angle of the target when applying load as shown in Figure 9 by the supply pressure whose link angle of Link 2 is smaller than the theory as the supply pressure to Cylinder 3. It seems as the cause of the error in this experiment is that the weight actually used as a load was not complete ideal mass and so has distributed mass and then it does not load at the constant portion at manipulator.

However, it was confirmed that the theoretical equation of the manipulator was almost effective to deduce the torque against the load by this experiment.

DYNAMIC CHARACTERISTIC EXPERIMENT

Figure 10 shows the result of dynamic characteristic experiment with PID feedback control. This is a control result for adjusting the angle of the link of targets of Link 1 to 60° , and adjusting the angle of the link of targets of Link 2 to 30° to make the arm being horizontal.

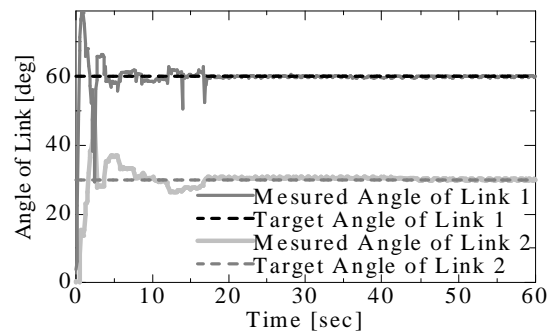


Figure 10 Dynamic Characteristics of Tendon-Driven 2-Link Manipulator case with Angle of Link vs. Time : Dynamic Characteristics ($\theta_{ta1} : 60$ [deg], $\theta_{ta2} : 30$ [deg])

When the angle of the link of targets of Link 1 is set to be 60° and the angle of the link of targets of Link 2 is set to be 30° as shown in Figure10, each link settled to the target link angle and an excellent result was obtained.

However, there is the problem such as setting to a link angle different from the target link angle takes long respond time. And the overshoot was seen, the range of deflection reaches at 30° as Link 1 and 45° as Link 2. The improvement may be expected by adjusting the parameters of the PID feedback control.

CONCLUSION

By using the real time system named RTLinux, the demanded posture of the manipulator could be proven in the achievement of both the static and dynamic controls of the tendon drive manipulator as a nursing lift system that uses the pneumatic cylinder as an actuator.

To put it to practical use as a nursing lift, establishing the stability of system and deriving the dynamic equation of the manipulator that considers the patient's operation is necessary, and these are problems in the next future.

REFERENCES

1. Souichi Satou, Research on tendon control drive robot that uses air pressure actuator, master degree claim thesis, Meiji University graduate school reason engineering research course, 1998.
2. Matt Sherer / FSMLabs Technical Staff, RTLinux textbook, CQ publisher, 2003.

Development of a haptic glove to use a master-slave rehabilitation robot hand system

Takashi KOMEDA*, Shinichi UCHINO* , Yoshiyuki TAKAHASHI, Mario ELASYEH**, Yukio KAWAKAMI, Hiroyuki KOYAMA* and Shin-ichiro YAMAMOTO*

* School of Systems Engineering
Shibaura Institute of Technology
Fukasaku 307, Minuma-ku, Saitama, 337-8570, Japan
(E-mail: komeda@se.shibaura-it.ac.jp)
** Department of Machine Design
Royal Institute of Technology
S100-44, Stockholm, Sweden

ABSTRACT

We have developed a haptic glove system to use rehabilitation field, e.g. rehabilitation robotics system. This glove has angle sensors to detect each finger position and small balloons inside of the glove to present a force to the user who wear the glove by pressurized air. This glove makes it possible to give angle information of each finger to slave hand system, and also to present the force which is detected the slave hand to the glove user. To control this force feedback system, we use PWM control method to show the quantity of the force. Force affecting the user is updated by a frequency of 10Hz and has several steps resolution. Total weight of this glove with haptic feedback capabilities is less than 200 grams. We tried to use this glove as a master-slave hand system, we could feel the slave hand force though haptic glove like a real force.

KEY WORDS

Haptic device, Force feedback, Robot hand, PWM control

INTRODUCTION

It is exhausting, both physically and emotionally, to assist physically handicapped persons in 24 hours. As an one of solution to solve this problem, an assistive mobile system called AMOS (Assistive MOBILE robot System) has been developed to help alleviate this burden [1]. The purpose of AMOS is to pick up and transport daily use objects, placing them in a designated indoor location semi-autonomously. The target objects

identified by AMOS are items used on a daily basis, and they have different sizes and shapes. However, it is difficult to recognize a target object, to measure its location using image processing in real-time and to manipulate using robotic hand automatically. Therefore, we are developing and propose a user interface system which allows the user to intervene in the robotic hand control. Almost users of this robot system may not have knowledge about computer and robot, it is required simple and easy user interface. We are trying to develop



Figure 1 Assistive Mobile Robot System

a master-slave robotic hand system. The user wears the master glove and tries to grasp the target object, the slave hand moves simultaneously with the master. The robot hand as a slave is guided to the target object using image processing. The user can select the object and decide how to grasp it by her/him with force feedback.

The aim of this research is to provide a simple user interface for handling the target object, which has different sizes and shapes. In this paper, we describe the master glove system and its force feedback experiments using pressurized air.

Master Slave Hand System

The image of the master slave hand system shows in Fig.2. This system is composed of a haptic glove on master side (master hand), and a robot hand with finger component on slave side (slave hand). Slave hand follows master hand, and grasps the target object by user put on master hand. The force when the slave hand holds the object can be fed back to the master hand and the master hand expresses the sense of force that corresponds to the force of the holding to the user by swelling the balloon inside the glove.

Haptic glove is composed of glove, flex sensors, balloons, air valves and a micro controller. It goes for the micro controller to data processing of the finger angle with the flex sensor, and control of the valve for expansion and shrinkage the balloons to present the force. These data are sending to personal computer by CAN (Controller Area Network). The position sensors are attached on the thumb, index and middle finger. They can measure the angle of each finger of the user.

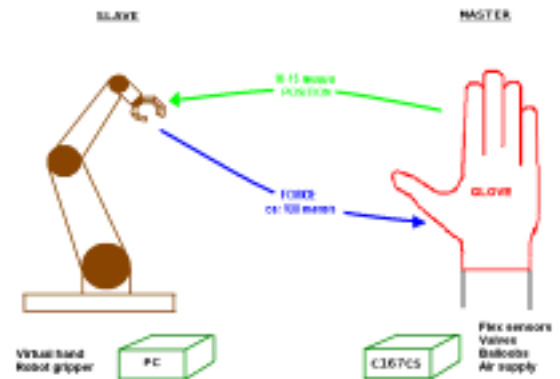


Fig.2 Image of Master Slave Hand

The force when slave hand grasps a target object, it is possible to express it as a sense of force by swelling the balloon which was installed in the thumb, the index finger, the long finger and push to each abdomen by compressed air (Fig. 3).

Fig.4 shows external view of the slave glove and the allocation of the sensors. The position sensor is attached on the surface of the glove. It is a flexible material and the resistance is changed due to the angle of the sensor.

Intake and exhaust pneumatic valves (Fest co., high speed switching valve) are controlled by the micro controller using regulated inner pressure of the balloons. Then, the user can feel the grasping force as he/she handles the object directly. The micro controller (SIEMENS Infeion Co., C167) communicates with slave finger controller (PC) sending position data of the master finger and receive the force data to display on the slave finger using CAN interface.[2]



Figure 3. Balloons allocation



Figure 4 External view and sensor allocation

Experiments of force feedback

Main objectives of these experiments are to determine the balloons state during intake and exhaust of air. Particularly significant for this system is the ability of the master glove to provide sufficient force feedback. Another important objective is to conclude the reaction time or response time of the balloons inflations and deflations. They are essential in order to estimate the total delay time obtained when inflating and deflating a balloon. We decided to use PWM control to preset force with several steps resolution, because it is easy to change the level of force by computer to change duty ratio. [3]

Outline of Experimental apparatus is shown in Figure 5. A pressure gage sensor is used to determine maximum inflation response time of one balloon, affected only by the pressure inside the balloon. It was attached to one balloon outlet and at the other outlet a coupling connecting pressure-supply and exhaust.

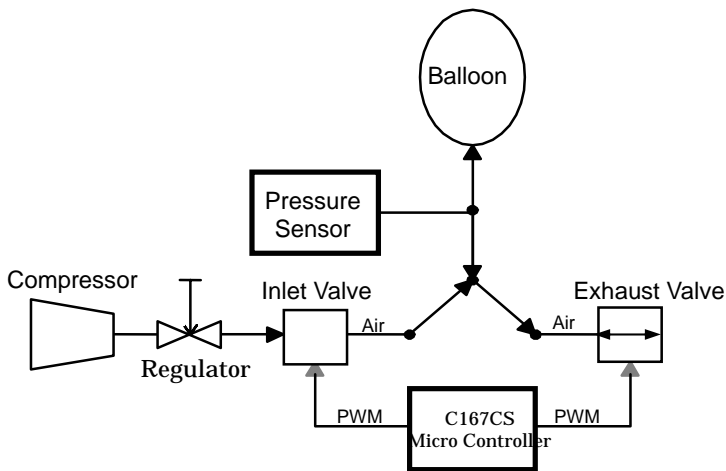


Figure 5. Experimental setup

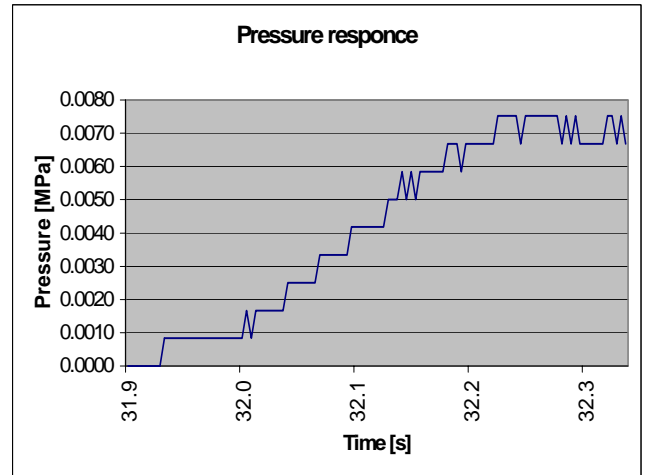


Figure 6 Pressure change at 100% duty

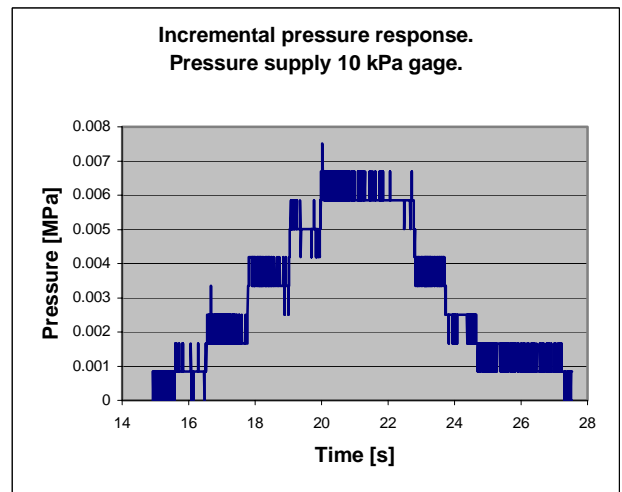


Figure 7 Pressure according to the duty ratio

The micro controller on the master side controls both the suction valve and the exhaust valve. In the program, either the suction valve or the exhaust valve can be operated simultaneously. Air in the balloon is discharged into an atmospheric inside by the exhaust valve's pressure in the balloon increasing when the supply pressure from the compressor connects with the suction valve.

Exhaust of the air pressure to the balloon was assumed to do the opening and shutting time of the valve by the PWM method. To fill the demanded PWM cycle, the supply pressure was calculated using following equation. [2]

$$P_u = \frac{V_b \cdot d_{AIR}}{S_{em} \cdot T_{ON} \cdot \sqrt{\frac{k}{R \cdot \theta_a} \left(\frac{2}{k+1}\right)^{\frac{k+1}{k-1}}}} \dots \dots \dots (1)$$

Here,

- V_b : Estimated volume a balloon
- d_{air} : Density of air
- k : Isentropic constant of air (=1.4)
- R : Gas constant
- S_{em} : Valve orifice area

Figure 6 shows one example of the experiment result of recording a pressure increase when supplying it from pressure value 0 to the maximum by 100% with the duty of PWM. It rises to about 7kPa though it doesn't reach 10kPa though 250ms passes. It is thought that time was required from no rise of pressure immediately after the supply to the swelling of the balloon.

Secondly, when change duty ratio of PWM, we experimented whether the difference of pressure was able to expressed. Six states were set by setting the state of pressure to six stages including the state not pressured, we increased the duty ratio each 20% from 0%. Result is shown in Figure 7. We confirmed internal pressure had changed according to the duty. Therefore, it is possible to present the level of force using these balloons and PWM control. A smooth result was not obtained in Fig.7, the reason is only the resolution of the pressure sensor was not enough.

From these results, we checked whether the sense of force is able to recognize by human. It is interview experiments and number of subjects is six. There are two processes to present the force. One is swelling process, it means to give force stronger than previous status (Ex1). The other one is shrinking process, to give force weaker (Ex2). It is different process, but, if system present same duty ratio of PWM, it must be feel same force. Fig.8 shows correct answer rate of each subject. Highest score is over 80%, it is not 100%. Then, it is difficult to present the force precisely using this method. Especially, shrinking process is lower than swelling process and the lowest correct answer rate is 0 %. The human sense of force is not so correct and it is better to present the force using the swelling process even there is an individual variation.

Conclusion

The master glove system with haptic force feedback has been developed. The master glove can sense finger angle and provide virtual haptic force on each finger using inside balloons and PWM control. We confirmed that the system can present the different force level using this method. However, it was difficult to be feel the different level of force to human. We will try to change PWM frequency and present method to aim 100% correct answer rate, and to improve for practical use.

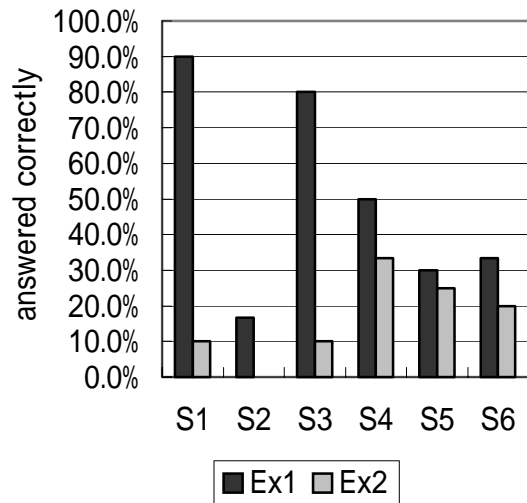


Figure 8 Correct answer rate

References

1. Y. Takahashi, T. Komeda and H. Koyama, "Development of the Assistive Mobile Robot System: AMOS - To Aid in the Daily Life for Physically Handicapped", *Advanced Robotics*, Vol.18, No.5, pp.473-496, 2004
2. Mario Elsayeh "Development of haptic glove and interacting virtual graphic user interface", Master of Science Thesis Stockholm (2003)
3. Yukio Kawakami et.al. "Pulse-Width-Modulation control of a pneumatic actuator", 4th International Conference on Control, Automation, Robotics and Vision (1996)

RELATIONSHIP BETWEEN OSCILLATION FREQUENCY AND GEOMETRY OF OSCILLATING LPA FLOW SENSOR

Hisaki SHIMIZU*, Fujio HIROKI** and Keijiro YAMAMOTO***

* Department of Intelligent Systems Engineering
Ichinoseki National College of Technology
Takanashi ,Hagisyo, Ichinoseki, Iwate, 021-8511 Japan
(E-mail shimiz6@ichinoseki.ac.jp)

**Department of Mechanical Systems Engineering, Faculty of Engineering
Kogakuin University
2665 Nakanochō, Hachioji, Tokyo, 192-0015 Japan

***Department of Welfare Systems Engineering, Faculty of Engineering
Kanagawa Institute of Technology
1030 Shimoogino, Atsugi, Kanagawa, 243-0292 Japan

ABSTRACT

The oscillating LPA(Laminar Proportional Amplifier) flow sensor having bilateral feedback loops is available for the measurement of small volume flow. Pattern of LPA and feedback loops were sculpted on a flat plane. The relationship between the oscillating frequency and the geometry of the oscillating LPA flow sensors were measured. As the result of experiments, it was appeared that the oscillating frequency of the oscillating LPA flow sensor closely connected with the geometry and the sizes of the sensor, and the signal transport time through the feedback loop was about a half of the acoustic time delay, and it was proved that the signal transport time on the supply jet from the supply nozzle to the splitter were occupied about 60% of the oscillating frequency. It was demonstrated that the range ability of the oscillating LPA flow sensor could be extended by arranging the pattern of LPA and feedback loops in the same plane.

KEY WORDS

Laminar proportional amplifier, flow sensor, feedback oscillator, frequency, geometry

1. INTRODUCTION

The oscillating LPA flow sensor utilizing Laminar Proportional Amplifier (LPA) is available for the measurement of the small volume flow. In previous papers^{1), 2), 3)}, we clarified that the oscillating frequency of the oscillating LPA flow sensor closely connected with the geometry and the sizes of the pattern of LPA and that of feedback channels. In this study, we investigate the oscillation mechanism of the feedback oscillator utilizing LPA.

2. GEOMETRY OF THE OSCILLATING LPA FLOW SENSOR

Figure 1 shows a schematic diagram of feedback oscillator utilizing a LPA which consists of LPA and bilateral feedback loops. This oscillator is available for the measurement of the small volume flow, because LPA is operated efficiently under the condition of low Reynolds number, i.e., laminar flow.

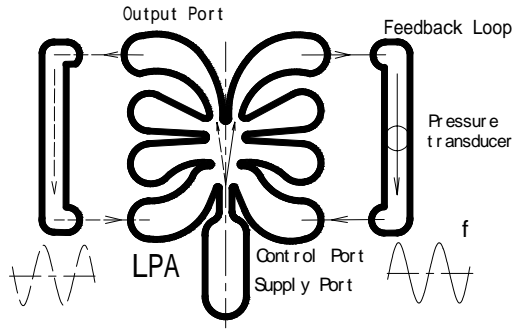


Figure 1 Geometry of LPA flow sensor

The jet goes out through one of the output ports, by feeding back a part of the jet flow, periodic oscillation of the jet between the feedback loops can be achieved. The oscillating pressure signals at the output ports were measured by using condenser type microphones. The oscillation frequency was measured by using FFT analyzer.

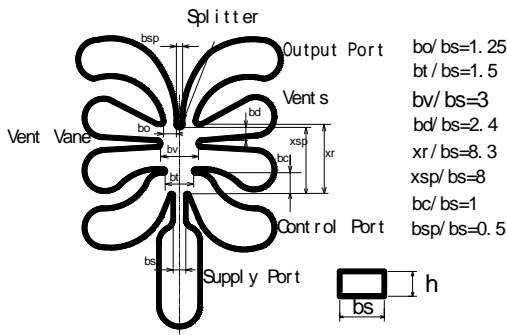


Figure 2 Geometry of LPA

Figure 2 shows a schematic diagram and major dimensions of LPA normalized by supply nozzle width. The material of the flow sensors is thin stainless steel. They were manufactured by an electric discharge machine. The flow sensors were sandwiched by two covering plates made of brass. In this study, air was used as a working fluid.

We manufactured two type flow sensors. Figure 3 shows the geometry of the flow sensor (1), which consists of LPA and bilateral feedback loops of round tubes(sections of a oblique line in the figure).

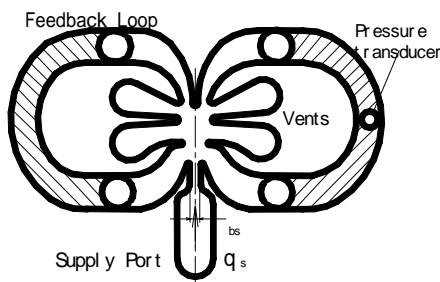


Figure 3 Geometry of flow sensor (1)

Figure 4 shows geometry of oscillating flow sensor (2) which arranged the ports of LPA and feedback loops in same plane.

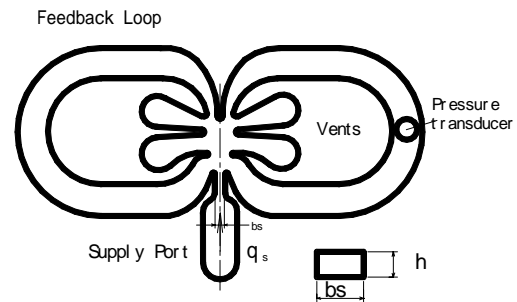


Figure 4 Geometry of oscillating flow sensor (2)

3. FREQUENCY - FLOW RELATIONSHIP

Figure 5 shows comparison of the frequency-flow ($f-q_s$) characteristics of sensor (1) and sensor (2). The height and width of the supply nozzle of the sensor (1) and sensor (2) were 0.75mm and 0.8mm, respectively.

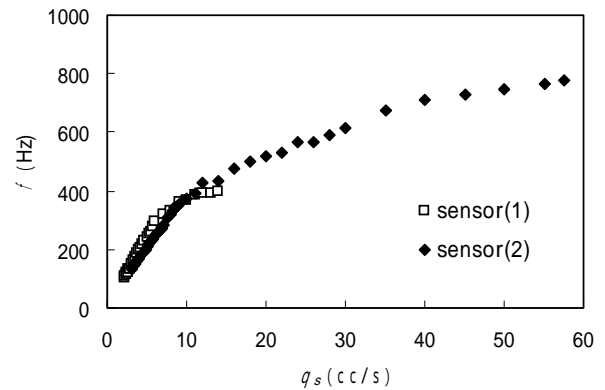


Figure 5 $f-q_s$ Characteristics of sensor (1) and sensor (2)

In the case of sensor (1), sizes of the round feedback loop are the diameter $D=4\text{mm}$ and the length $L=172\text{mm}$. In the case of sensor (2), sizes of the rectangular feedback loop are width $b_f=2.4\text{mm}$, depth $h_f=0.8\text{mm}$ and the length $L=48\text{mm}$. The frequency increases proportionally to the volumetric flow rate of supply jet within low flow range up to the breaking point. In the case of sensor (1), there are the lower limit of flow rate for the oscillation at 2.2cc/s and the upper limit of flow for the oscillation at 15cc/s , and the breaking point is 8cc/s .

In the case of sensor (2), there are the lower limit of flow for the oscillation at 3cc/s and the upper limit of flow for the oscillation at 60cc/s , and the breaking point is 12cc/s . In the case of sensor (2), the thin feedback loops has a highly inhibitory action against the flow turbulent. This results show that the structure arranging the pattern of LPA and feedback loops in the same plane have the

effect to expand oscillating flow range.

4. MEASUREMENTS OF PRESSURE TRANSMISSION AND PROPAGATION PERIOD

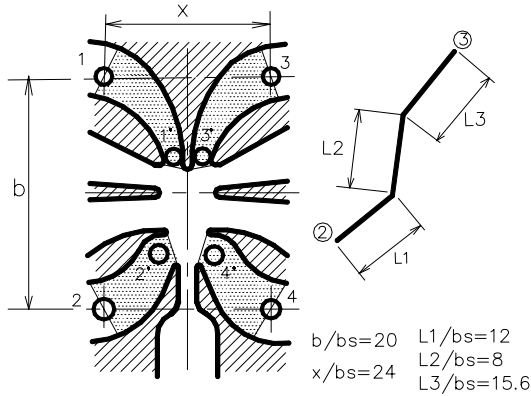


Figure 6 Points of measurement

To clarify the relationship between the oscillation frequency and the geometry of the sensor, pressure signal transport times between specific points were measured. Points of measurement are shown in figure 6. Figure 7 shows the conjectural propagation lengths.

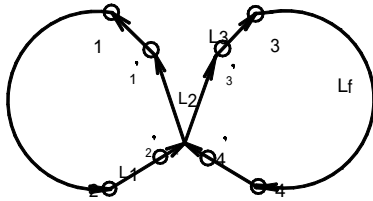


Figure 7 Conjectural propagation lengths

Oscillation frequency f can be appeared as follows,

$$f = 1 / total \quad \dots\dots\dots (1)$$

$$total = t_{12} + t_{23} + t_{34} + t_{41} \quad \dots\dots\dots (2)$$

$$t_{23} = t_{2'2'} + t_{2'3'} + t_{3'3} \quad \dots\dots\dots (3)$$

$$t_{41} = t_{4'4'} + t_{4'1'} + t_{1'1} \quad \dots\dots\dots (4)$$

where $total$ is the period i.e. total time required for pressure signal propagates one round, t_{12} is the signal transport time from point 1 to point 2 of the left-hand feedback loop, t_{23} is the signal transport time from point 2 to point 3, t_{34} is the signal transport time from point 3 to point 4 of the right-hand feedback loop, t_{41} is the signal transport time from point 4 to point 1, $t_{2'2'}$ is the signal transport time from point 2 to point 2' of the left-hand input nozzle, $t_{2'3'}$ is the signal transport time from point 2' to point 3', $t_{3'3}$ is the signal transport time from point 3' to point 3 of the right-hand output duct, $t_{4'4'}$ is the signal transport time from point 4 to point 4' of the right-hand input nozzle, $t_{4'1'}$ is the signal transport time from point 4' to point 1' and $t_{1'1}$ is the signal transport

time from point 1' to point 1 of the left-hand output duct.

5. RESULTS AND DISCUSSION

5.1 FEEDBACK LOOP

The relationships between the signal transport time in the feedback loops for various lengths of the sensor (1), and volume flow rates are shown in Figure 8. The values on the ordinates are the mean value of t_{12} and t_{34} .

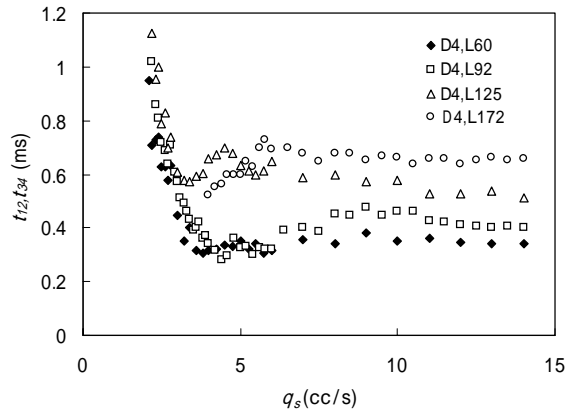


Figure 8 t_{12} , t_{34} versus q_s of sensor (1)

In case of the sensor (1), it was appeared that the signal transport times t_{12} , t_{34} decrease as flow increase in the small flow region under 3~4cc/s, on the other hand, they does not change in the region of flow above 3~4cc/s and they increase with the lengths of the feedback loop. Figure 9 shows the signal transport velocity, U_f versus volume flow, q_s . The value of U_f is calculated by the signal transport time in the both feedback loops and the length of them.

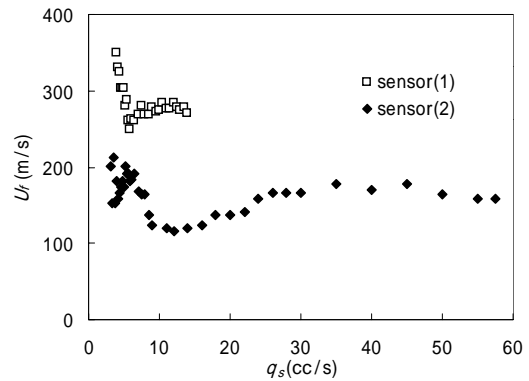


Figure 9 U_f versus q_s

In the case of the sensor (1), the signal transport velocity is nearly equal to the speed of sound in the small flow region. But in the sensor (2), the signal transport velocity is about half value of the speed of sound due to the effects of thin rectangular feedback loops.

5.2 INPUT NOZZLE

Figure 10 shows the signal transport time the both input nozzles, t_{22} , t_{44} versus volume flow rates, q_s . In both sensors, the signal transport times t_{22} , t_{44} decrease as flow increases in small flow region under 5cc/s, but they does not change in the region of flow above 6cc/s.

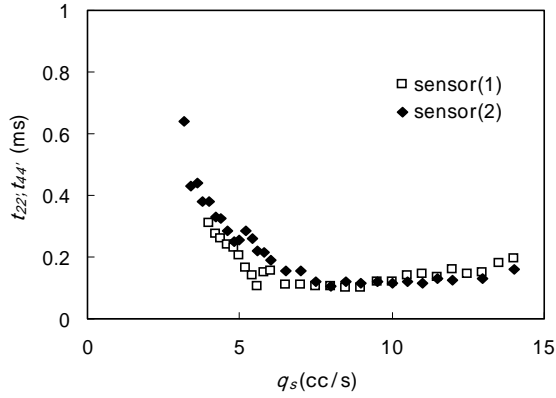


Figure 10 t_{22} , t_{44} versus q_s

Figure 11 shows the signal transport velocity in the both input nozzles, U_1 versus volume flow, q_s . The value of U_1 is calculated by the signal transport time in the both input nozzles and the length of them. Since the length of the input nozzles was short, the signal transport velocity in the input nozzles is smaller than that of the feedback loops.

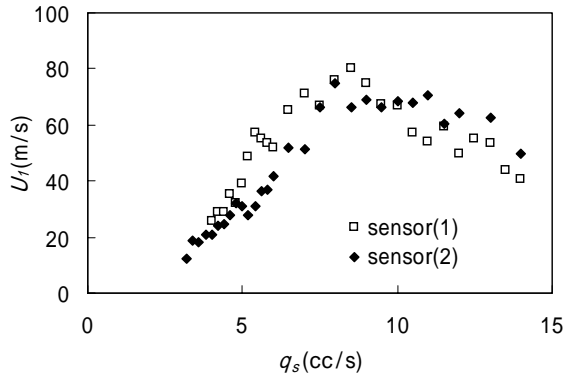


Figure 11 U_1 versus q_s

5.3 SUPPLY JET

Figure 12 shows the signal transport time of the supply jet, $t_{2'3'}$, $t_{4'1'}$ versus volume flow rates, q_s . In previous paper⁴⁾, the signal transport time through the supply jet, t_j was appeared as follows,

$$t_j = x_{sp} / 0.5U_s \cdot \dots \cdot (5)$$

where x_{sp} is the distance between supply nozzle and splitter and U_s is the signal transport velocity through the supply jet. In both sensors, the signal transport time

through the supply jet, $t_{2'3'}$, $t_{4'1'}$ are nearly equal to t_j . The signal transport time through the supply jet occupy the most of the oscillation period.

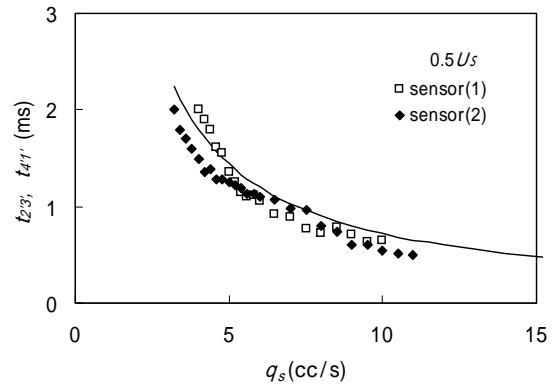


Figure 12 $t_{2'3'}$, $t_{4'1'}$ versus q_s

5.4 OUTPUT DUCT

Figure 13 shows the signal transport velocity in the both output ports, U_3 versus volume flow, q_s . The value of U_3 is calculated by the signal transport time in the both output ducts and the length of them. This signal transport velocity is smaller than the signal transport velocity in the feedback loops. The signal transport velocity increase proportionally with the volume flow within small flow region under 4~5cc/s.

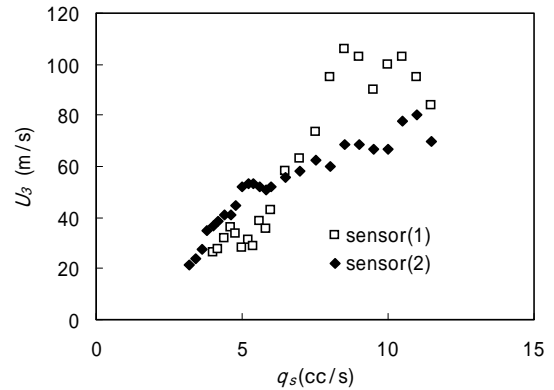


Figure 13 U_3 versus q_s

5.5 RELATIVE SIGNAL TRANSPORT TIMES

Figure 14 shows the ratio of the signal transport time, $t/total$ versus volume flow, q_s of the sensor (2). t_j is the mean of t_{12} and t_{34} , t_1 is the mean of t_{22} and t_{44} , t_2 is the mean of $t_{2'3'}$ and $t_{4'1'}$ and t_3 is the mean of $t_{1'1}$ and $t_{3'3}$. The signal transport time through the supply jet, t_2 occupy about 50% of the oscillation period under the flow of 8cc/s. The signal transport time in the feedback loops, t_f increase gradually as flow increase. t_1 and t_3 occupy about 15% of the oscillation period. Therefore, the oscillating frequency is affected considerably by the signal transport time through the supply jet. t_2 of the

sensor (1) showed similar tendency.

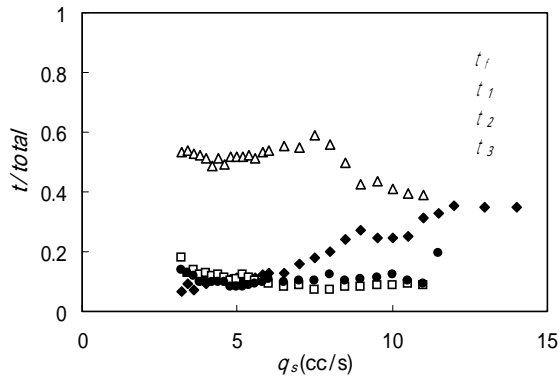


Figure 14 $t / total$ versus q_s

6. CONCLUSION

The relationship between the oscillating frequency and the geometry of the oscillating LPA flow sensor were studied. Following conclusions were obtained.

- 1) The signal transport time through the feedback loops were affected considerably by the geometry of the feedback loop. The structure which arranged the ports of LPA and feedback loops in the same plane have the advantage in expanding working range.
- 2) The signal transport velocities in the input nozzle and in the output nozzle were smaller than that of the feedback loop.
- 3) The signal transport time from the supply nozzle to the splitter occupied about 60% of the oscillation period.

REFERENCES

1. Hisaki SHIMIZU and Keijiro YAMAMOTO: Characteristics of The Jet Deflection of Laminar Proportion Amplifiers, Papers of the 18th Sensing Forum, Soc. Instrum. & Control Eng., Japan, 2001. pp.95-98.
2. Hisaki SHIMIZU and Keijiro YAMAMOTO: Study of Oscillating LPA Flow Sensor (Characteristics of The Jet Deflection), Papers of the 19th Sensing Forum, Soc. Instrum. & Control Eng., Japan, 2002. pp.361-364.
3. Hisaki SHIMIZU, Masahiro CHIBA, Fujio HIROKI and Keijiro YAMAMOTO: Comparison of the Characteristics of Oscillating LPA Flow Sensor, Papers of the 20th Sensing Forum, Soc. Instrum. & Control Eng., Japan, 2003. pp.105-108.
4. George Mon : A fluidic Volumetric-Flow, Mass Flow Density and Viscosity Meter, The Journal of Fluid Control, 1987. pp.7-18.

THE INVESTIGATION OF FLOW FIELD IN SWIRLER

TANG Rong-ming, WANG Xue-fang, XU Hong-qing and ZHANG Zhan-feng

SMC-Tsinghua University Pneumatic Technology Centre
Tsinghua University Beijing, 100084 P.R.China
(E-mail: tangrm@mail.tsinghua.edu.cn)

ABSTRACT

In this paper the flow field in swirler is measured by five-hole probe, hotwire and LDV (Laser Doppler Velocimetry) . These results would be much the same .It can provide some ideas for design of swirler.

KEY WORDS

swirler, five-hole probe, hotwire, LDV, vortex

NOMENCLATURE

NOMENCLATURE

γ	specific weight of liquid
h_2	height of liquid
ρ	density of air
V_∞	velocity of air
K_2'	coefficient of total pressure
λ	wavelength of laser
f_d	Doppler frequency
k	cross angle of dual-beam
K_1	yaw-factor
K_2	pitch-factor

example, dedusting, increasing the stability of blast chamber, measuring of flowrate, burnishing treatment of tiny drill way, and non-touch sucking disk of delivery system. Its structure is simple, manufacture with low cost, operating with little loss, so it is paid more attention to .The inner flow field appears different feature with the difference of structure. Investigation of flow field in swirler is helpful for design various swirler with different purpose.

In this paper the experimental investigation for the inner flowfield of a cylinder swirler was done. Using five-hole probe, hotwire and LDV to measure velocities, total pressure, static pressure of the inner flow field, we can get much the same results. This can provide supports for the design and improvement of swirler.

1 EXPERIMENTAL MODEL AND MEASURING METHOD

As described by figure 1, air flows in from two sides tangentially and forms vortex. Flowrate is controlled by upstream valve; therefore the flowrates of two sides are the same. Air is discharged from outlet. Because the

INTRODUCTION

Swirler is widely used in industrial manufacturing. For

flowfield of swirler is complicated, three methods of measurement were used.

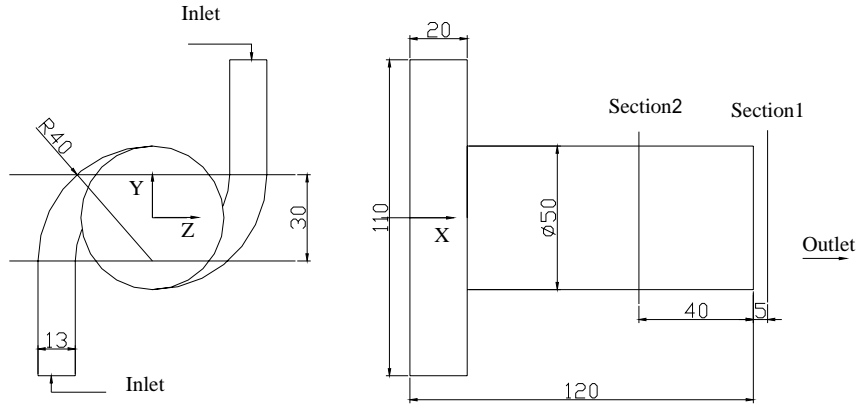


Figure 1 The model of swirler

1.1 Measurements with five-hole probe

The theory of measurement with five-hole probe is based on flow over a sphere.

Velocity component can be calculated by the following equations:

$$\begin{cases} U_x = V_\infty \sin \beta \\ U_y = V_\infty \sin \alpha \cos \beta \\ U_z = V_\infty \cos \alpha \cos \beta \end{cases}$$

Where

V_∞ is the velocity of the coming flow .

U_x, U_y and U_z are axial, radial and tangential velocity respectively.

In addition static pressure is:

$$P = \gamma h_2 - \frac{1}{2} K_2' \rho V_\infty^2$$

Total pressure is

$$P_0 = \gamma h_2 + \frac{1}{2} (1 - K_2') \rho V_\infty^2$$

1.2 Measurement the inner flow field of swirler with hotwire.

The basic theory of hotwire is to measure the heat loss of the hotwire with flow over it.

Heat loss is related with fluid temperature ,velocity , pressure, density and thermotics feature of fluid and hotwire's temperature and geometry .If only one

parameter is changed , heat loss can be explained as directly measurement varied parameter.. Usually this parameter is velocity or temperature of fluid. If more than one parameter is changed, we must use compensation technique to remove the affect of other variance.

When the turbulence of flow is very low, using single probe we can consider only average velocity is affecting heat loss of the hotwire. At a certain point, we measure three effective cooling velocities respectively when hotwire is set on three planes; horizontal, vertical and oblique plane at the angle to horizontal plane. Therefore we have three equations about cooling velocity and the average velocity of axial direction, radial direction and tangential direction.

$$\begin{cases} U_{1eff}^2 = U_x^2 + K_1^2 U_y^2 + K_2^2 U_x^2 \\ U_{2eff}^2 = U_x^2 + K_2^2 U_y^2 + K_1^2 U_x^2 \\ U_{3eff}^2 = U_x^2 + K_1^2 (U_y \sin \theta - U_x \cos \theta)^2 + \\ K_2^2 (U_y \cos \theta + U_x \sin \theta)^2 \end{cases}$$

U_x, U_y and U_z are average velocity along axial direction, radial direction and tangential direction respectively.

1.3. Measurement by LDV

The basic theory of LDV is that the difference of frequency between incoming ray and scattered ray of moving particle is direct ratio with the moving velocity of particle. This is;

$$V = \frac{\lambda}{2 \sin \frac{k}{2}} f_d$$

Essentially, LDV measures the velocity of particles. We use home-made particle producer to seeding oil drop with micron size into the air flow. In swirling flow field, particles are forced with centrifugal force, so the number of particles in the center of the model is few. Hence the data rate will be reduced. In order to get good signal to noise ratio and data rate, the frequency range should be compressed and laser power would be increased. So the experimental results will be much better

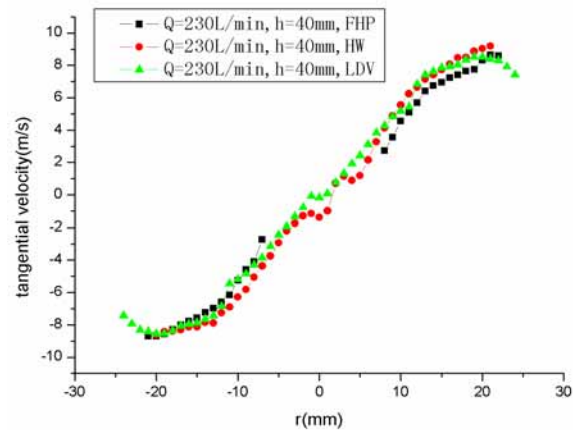
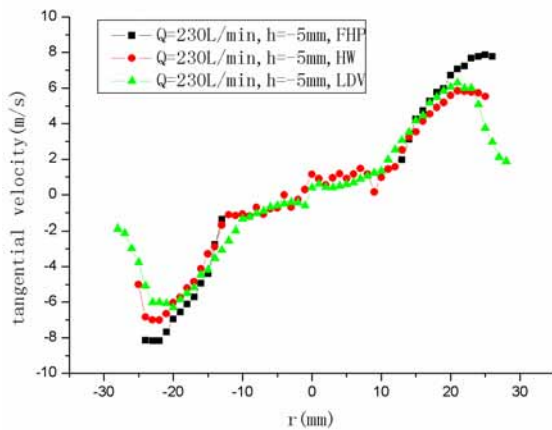
2 EXPERIMENTAL RESULTS

Experimental condition: The flowrate at inlet was $Q=220,350, 470$ L/min respectively; at outlet the pressure was atmosphere pressure

$$P_0 = 0.1MPa$$

The distribution of tangential velocity in swirler is shown in figure.2. From the above figures it can be found that the tangential velocity in the center of the swirler is about zero., and along the radial direction from center to outside it becomes bigger and bigger .There is a point having maximum tangential velocity. From the point with maximum tangential velocity, to wall, the tangential velocity reduces gradually. It can be used the maximum tangential velocity as boundary to divide the flowfield of the swirler into forced vortex region and free vortex region. The forced vortex region is the dominant.

The axial and radial velocity distribution in swirler is shown in figure 3. The distribution of radial velocity in swirler can also be divided into two parts; in external



region the direction of flow is outward while in the center region the direction of flow is inward. Radial

Velocity compared with other two components is smaller. The radial velocity is almost only 1/10 of the tangential velocity.

The distribution of pressure is shown in figure 4. With different flowrates, the intersection of positive and negative pressure for static pressure and total pressure in swirler is almost the same position. It means that negative pressure area doesn't change with the increase of flowrate, However magnitude of negative pressure and positive pressure changes with flowrate.

Negative pressure area in the center of the swirler occupies about 2/3 of the transverse section .Due to the existence of the negative pressure area in the outlet of the swirler the reverse flow occurs. Correspondingly there is negative value of axial velocity.

In addition, local tangential turbulence intensity measured by LDV is:

$$T_\omega = \frac{\sqrt{\omega'^2}}{\omega}$$

where

ω is local mean velocity;

ω' is tangential fluctuation velocity

The experimental results are shown as figure 5:

Local Turbulence intensity is very high in the central region of swirler, while turbulence intensity is relative low in the outer region.

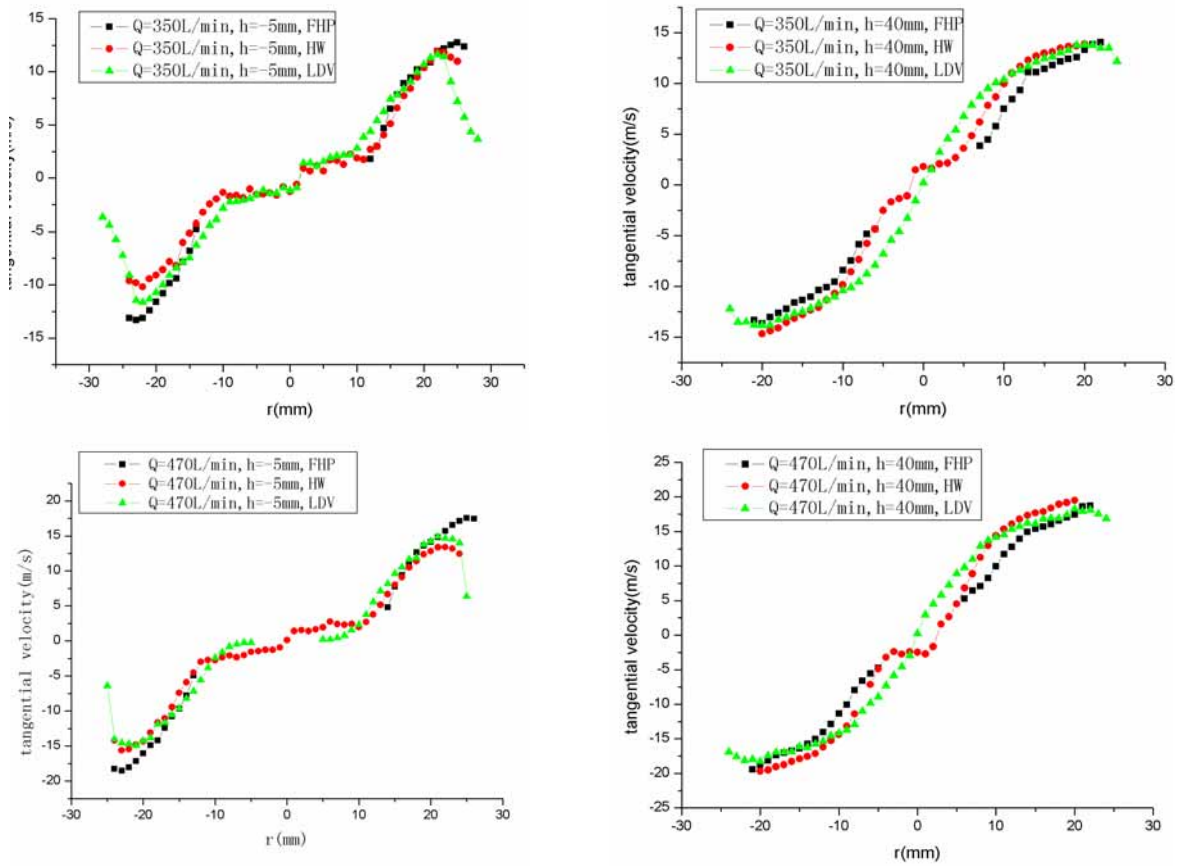


Figure 2 The distribution of tangential velocity

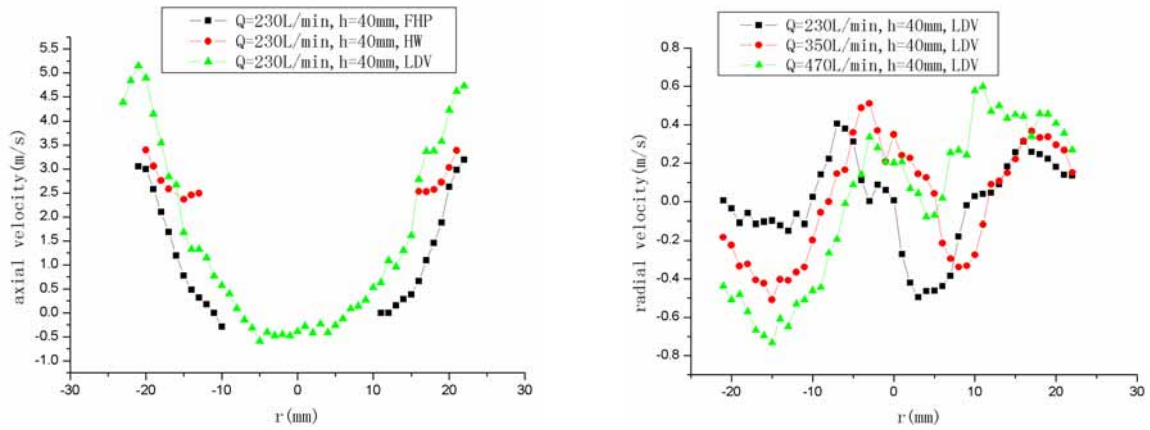


Figure 3 The distribution of axial and radial velocity

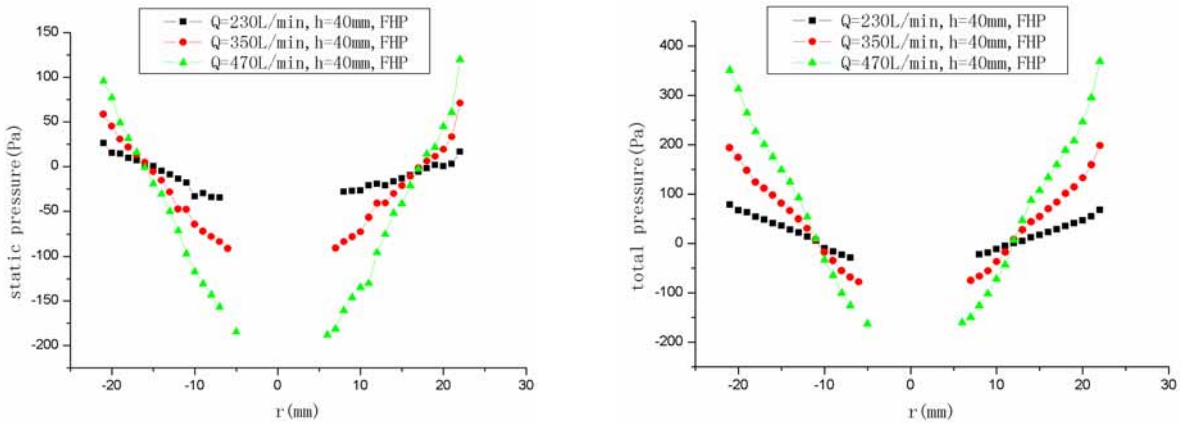


Figure 4 The distribution of pressure

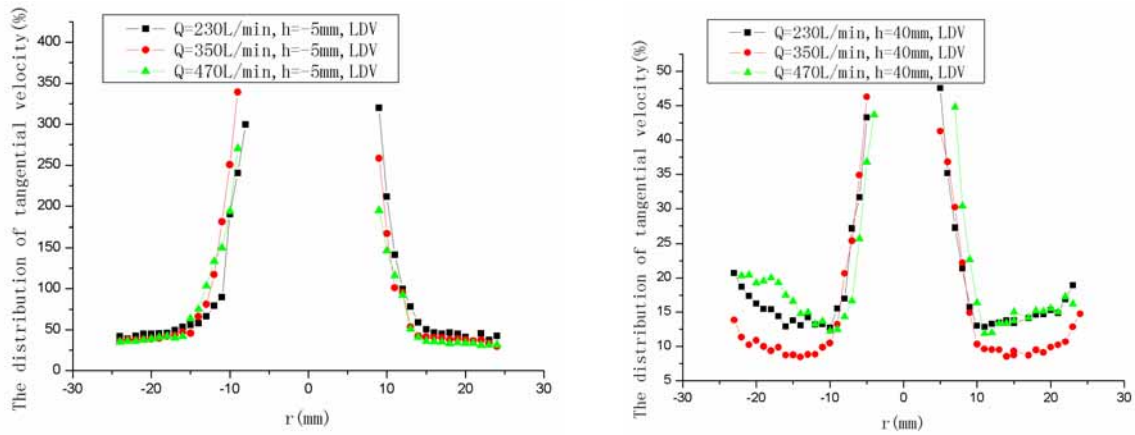


Figure 5 The distribution of tangential velocity

3 NUMERICAL SIMULATIONS

Differential equations of flow field for swirler (mass conservation equation and momentum conservation equation) are

$$\frac{\partial \rho}{\partial t} + \frac{\partial}{\partial x_i} (\rho u_i) = 0$$

and

$$\frac{\partial (\rho u_i)}{\partial t} + \frac{\partial}{\partial x_j} (\rho u_i u_j) = -\frac{\partial p}{\partial x_i} + \frac{\partial \tau_{ij}}{\partial x_j} + \rho g_i$$

Where: p is static pressure; τ_{ij} is stress tensor and g_i is body force of gravity.

Using RNGK- ε turbulence model to calculate, RNGK- ε is a kind of empirical mode.

Figure 6 shows the comparison between experimental and numerical simulation results of tangential velocity.

The numerical simulations show good agreement with experimental data

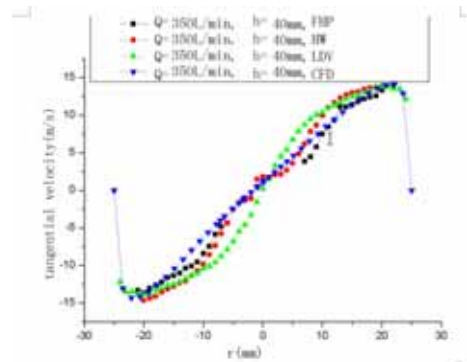


Figure 6 The distribution of tangential velocity

The results of experiment about the static and total pressure measurement and the numerical simulation are

shown in the figure 7.

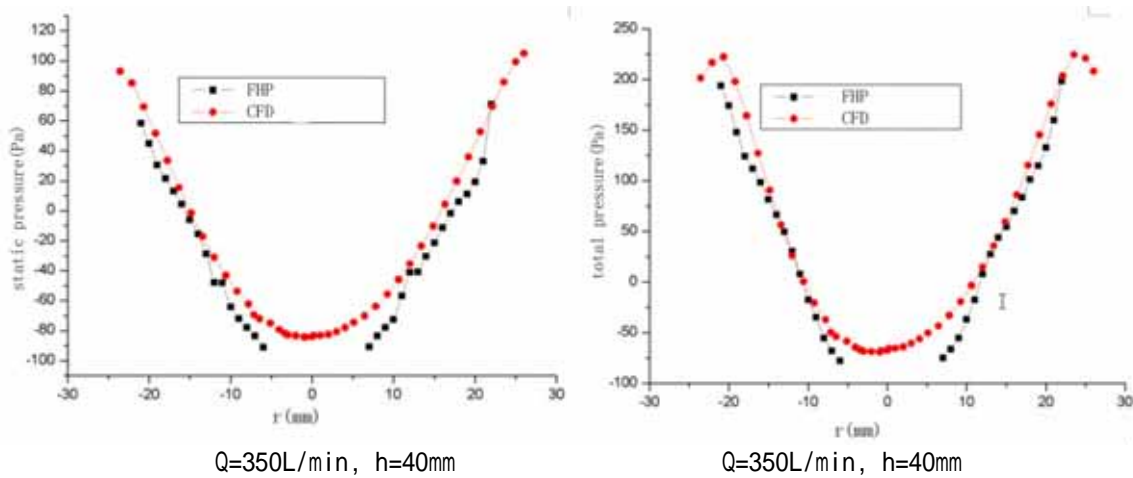


Figure 7 The distribution of pressure

The result of numerical simulation indicates that the experimental data get from five-hole probe are almost the same with numerical simulation. From the above two results there are both negative pressure region in the center part and positive pressure in outer part. The experimental results and numerical simulation can provide us reliable basis for the design of swirler.

4 CONCLUSIONS

1、 We can measure distribution of total and static pressure with five-hole probe . But it can interfere flow field seriously. The velocity is low and turbulence intensity is high in the center part, therefore, the error of measurement is bigger here. Measurement with hotwire has many merits, such as high frequency response, little interference to flow field, and easily collecting data and doing statistical processing with computer. But when the measured value is near to zero, measuring error is very big. LDV is a kind of non-contact measurement technique. It can measure velocity with a wide range. It can measure reverse flow and it has a relatively high spatial resolution and a quick dynamic response .But its measurement is limited by the seeding particles.

2、 The tangential velocity in the swirler is dominant The axial velocity is smaller. The radial velocity is the least. .

3、 The results of measurement indicates that there are two kinds of flow pattern in the swirler There are forced vortex in the center region and free vortex in the outer part. . From experiment, It can be found that the region of forced vortex is dominant .The region of free vortex is relatively small.

4、 There is the phenomenon of reverse flow around the outlet of the swirler.. There are negative pressure region both in total pressure and static pressure. And the range of negative pressure area is almost the same with

variation of flowrate. The negative value in the central part increases with the increase of flowrate.

REFERENCES

1. Furio Cascetta, Field test of swirlmeter for gas flow measurement, *Flow Measurement and Instrumentation*, 1999, 10, pp183~188
2. Heinrichs. Kay, Flow measurement by a new push-pull swirlmeter. *Sensor and Actuators, Physical*, 1991, 27-3, pp 809-813

A NEW MASS FLOW-RATE MODEL OF GAS THROUGH ORIFICE-TYPE RESTRICTORS IN AEROSTATIC BEARINGS

Jyh-Chyang RENN and Jia-Feng YANG

Department of Mechanical Engineering,
National Yunlin University of Science and Technology
Douliu, Yunlin, Taiwan 640, R.O.C.
(E-mail:rennyc@yuntech.edu.tw)

ABSTRACT

This paper proposes a new mathematical model to describe the mass flow-rate characteristics of gas through orifice-type restrictors in aerostatic bearings. In the conventional design of gas-lubricated aerostatic bearings, the mass flow-rate of gas through an orifice-type restrictor is generally derived from a well-known mathematical model, which is originally developed to describe the mass flow-rate property of gas through an ideal nozzle. In this paper, however, a series of CFD-simulations and experiments according to ISO 6358 are carried out and the results show that the mass flow-rate characteristics through an orifice-type restrictor are different from those through an ideal nozzle. Consequently, the conventional model to determine the mass flow-rate of gas through orifice-type restrictors in aerostatic bearings may have to be modified and updated to the proposed new model for more precise design and modeling of the gas-lubricated aerostatic bearings.

KEY WORDS

Mass Flow-rate, CFD, Aerostatic Bearing, Orifice, Restrictor

NOMENCLATURE

A	: area of the restrictor	P_1	: absolute pressure at inlet
b	: critical pressure ratio	P_2	: absolute pressure at outlet
C	: the sonic conductance	R	: gas constant
C_0	: orifice discharge coefficient	T_1	: absolute temperature at inlet
g	: acceleration due to gravity	T_2	: absolute temperature at outlet
k	: specific heat ratio of gas	ρ_2	: density of gas at outlet
\dot{m}	: mass flow-rate	Ψ	: coefficient of flow through orifice
		ϕ	: test restrictor's diameter

INTRODUCTION

Aerostatic bearings have been widely used for measuring instruments, machine tools, dental drills, jet engines and computer peripheral devices because of their substantially low friction loss and heat generation. Like other fluid lubricated bearings, aerostatic bearings serve two purposes. One is to support an external load and the other is to lubricate a pair of surface. Nowadays, the aerostatic bearings are commonly used in the field of precision engineering. Figure 1 shows the schematic sectional view of an aerostatic bearing with an orifice-type restrictor. The gas from an external source is fed into the clearance space through flow restrictors which are often orifice-type feed holes in one of the bearing surface, and escapes continuously to the atmosphere from the outside edges of the bearing. However, the mass flow-rate of the gas through such an orifice throat is generally derived from a well-known mathematical model, which is originally developed to describe the mass flow-rate of gas through an ideal nozzle. It is reasonable to doubt if there is any difference between the property of mass flow-rate of gas through an orifice and that through a nozzle.

To simplify the analysis, we propose a new model and assume initially that the mass flow-rate property through an orifice is similar to that through an ideal nozzle. Thus, the formulas of the latter to calculate the mass flow-rate are preserved. The basic idea of this paper is trying to tune the parameters used in the formulas such that the formulas for the ideal nozzle may also be applied to the case of the orifice. Figure 2 indicates such a mass flow-rate property through an ideal nozzle, in which the constant maximal mass flow-rate of the ideal gas is noticeable. Later in this paper, it will be shown that this maximal value depends on a parameter C , which is generally called the sonic conductance. Besides, if the ratio of the outlet pressure to the inlet pressure is small, meaning that the pressure drop across the nozzle is quite large, the gas-flow through the nozzle becomes a jet with high velocity. The acoustic velocity, however, physically limits this velocity through the nozzle. This is precisely the reason why the constant maximal flow-rate exists in the flow property shown in Fig. 2.

The parameter b , called the critical pressure ratio, is defined as the intersection of the straight flow-rate of the so-called choked flow and the elliptic flow-rate curve of subsonic flow. For an ideal nozzle with a fixed cross-sectional area, the parameters C and b are constants because the former depends chiefly on the cross-sectional area and the latter is proved analytically to be a constant value of 0.5283. Similarly, for a fixed orifice, it is also reasonable to assume that both the parameters C and b are constants. The remaining question is how to derive the best-fit values for

parameters C and b . In this paper, therefore, the CFD simulations as well as a series of experiments according to ISO 6358 are introduced to determine the best values for the two parameters.

Surveying some previous reports [1-3, 4, 6], it is found that the model to calculate the mass flow-rate of gas through orifice-type restrictors copies without exception the conventional model originally developed for ideal nozzles. One interesting paper presented by the author dealt with the experimental approach to build a new mass flow-rate model for gas through orifice-type restrictors [7]. However, the dimension of the test restrictor is too large as compared with that of an actual orifice-type restrictor installed in industrial aerostatic bearings.

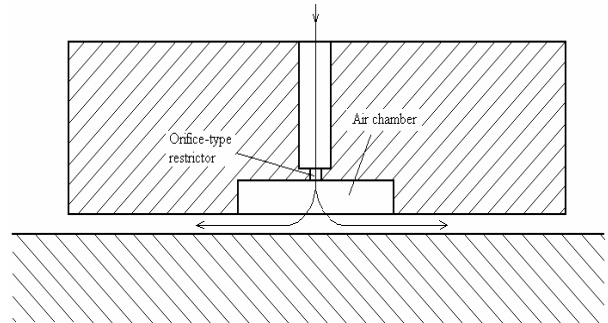


Figure 1 Orifice-type restrictor in aerostatic bearings

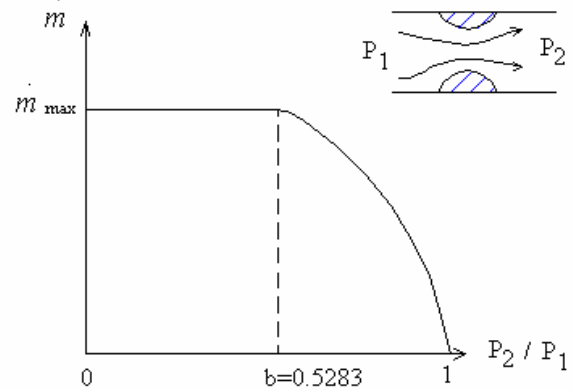


Figure 2 The mass flow-rate property through an ideal nozzle

MODEL OF THE MASS FLOW-RATE CHARACTERISTICS THROUGH AN IDEAL NOZZLE

The mass flow-rate of gas through a restrictor can be described by the generalized formulas [5, 7].

$$\dot{m} = C\rho_0 P_1 \sqrt{\frac{T_0}{T_1}} \quad \text{for } \frac{P_2}{P_1} \leq b, \quad (1)$$

and

$$\dot{m} = C\rho_0 P_1 \sqrt{\frac{T_0}{T_1}} \sqrt{1 - \left(\frac{P_2/P_1 - b}{1-b} \right)^2} \quad \text{for } \frac{P_2}{P_1} > b \quad (2)$$

Where \dot{m} : mass flow-rate

C : the sonic conductance,

b : critical pressure ratio,

P_1 : absolute pressure at inlet,

P_2 : absolute pressure at outlet,

T_1 : temperature at inlet,

T_0 : outlet temperature under standard reference conditions (293.15K),

ρ_0 : density under standard reference conditions (1.189 kg/m³).

If the restrictor is an ideal nozzle, the critical pressure ratio is given by

$$b = \left(\frac{2}{k+1} \right)^{\frac{k}{k-1}}, \quad (3)$$

where k denotes the specific heat ratio of the gas.

On the other hand, similar equations, which are commonly used in the modeling of the mass flow-rate of gas through an orifice-type restrictor in aerostatic bearings, are summarized as [1, 2, 3, 4, 6]

$$\dot{m} = AC_0 \Psi \frac{P_1}{g\sqrt{RT_1}}, \quad (4)$$

$$\Psi = \sqrt{2g \frac{k}{k-1} \left(\frac{2}{k+1} \right)^{\frac{2}{k-1}}} \quad \text{for } \frac{P_2}{P_1} \leq \left(\frac{2}{k+1} \right)^{\frac{k}{k-1}}, \quad (5)$$

$$\Psi = \sqrt{2g \frac{k}{k-1} \left\{ \left(\frac{P_2}{P_1} \right)^{\frac{2}{k}} - \left(\frac{P_2}{P_1} \right)^{\frac{k+1}{k}} \right\}} \quad \text{for } \frac{P_2}{P_1} > \left(\frac{2}{k+1} \right)^{\frac{k}{k-1}}, \quad (6)$$

where A : area of the restrictor,

C_0 : orifice discharge coefficient,

R : gas constant,

Ψ : coefficient of flow through orifice,

g : acceleration due to gravity.

The Eq. (5) and Eq. (6) represent the sonic and subsonic flow conditions respectively. The orifice discharge

coefficient, C_0 , is basically a contraction coefficient. Generally, it is derived experimentally.

Comparing Eq. (1) with Eqs. (4)-(5), the sonic conductance can be rewritten as

$$C = \frac{AC_0}{g\rho_0} \sqrt{\frac{2gk}{(k-1)RT_0} \left(\frac{2}{k+1} \right)^{\frac{2}{k-1}}}. \quad (7)$$

Hence, the sonic conductance depends chiefly on the area of the restrictor. Obviously, the set of Eqs. (1)-(3) is nearly equivalent to the set of Eqs. (4)-(6) if the temperature from inlet to outlet keeps unchanged. One minor difference, however, is the functions used to describe the subsonic mass flow-rate property. One is the simplified Eq. (2) and the other is the original Eq. (6). The maximal deviation, however, is only 3% [5].

For ideal gas, $k = 1.4$. According to Eq. (3), the value of critical pressure ratio is found to be 0.5283. However, we propose that the value of b may not equal 0.5283 for other types of restrictor. Consequently, the conventional model described by Eqs. (4)-(6) to calculate the mass flow-rate of gas through an orifice-type restrictor may have to be modified because such a model is originally developed only for the nozzle-type restrictor.

In this paper, the Eqs. (1), (2) and (7) are recommended for the analysis of the mass flow-rate properties through orifice-type restrictors in aerostatic bearings because they are much easier for the numerical calculation. In the following, both the values of the parameters C and b are determined by simulation as well as experimental approach.

CFD-SIMULATION OF THE ORIFICE-TYPE RESTRICTOR

In this paper, the commercial software package CFD-RC is utilized as a tool to analyze the properties of mass flow-rate through orifice-type restrictors. The test probe with a built-in orifice-type restrictor is shown in Fig. 3. Moreover, four different diameters ($\phi = 0.1$ mm, 0.1445mm, 0.182 mm and 0.25 mm) of the test restrictor are chosen for the simulation. Figure 4 indicates the schematic geometry of the test restrictor with diameter $\phi = 0.1$ mm.

In the development of the mass flow-rate equations for nozzles, it is generally accepted that nozzles of different cross-sectional areas possess the same mass flow-rate properties described by Eqs. (1)-(3) or Eqs. (4)-(6). In addition, the critical pressure ratio given by Eq. (3) is a constant ($b=0.5283$) for nozzles of different cross-sectional areas and the sonic conductance given by Eq. (7) is proportional to the cross-sectional area of the nozzle. Similarly, it is proposed in this study that orifices of the same structure but of different cross-sectional

areas should have the same air flow properties described by the parameters C and b . Moreover, the value of b should be a constant for orifices of different cross-sectional areas and the value of C should be proportional to the cross-sectional area of the orifice.

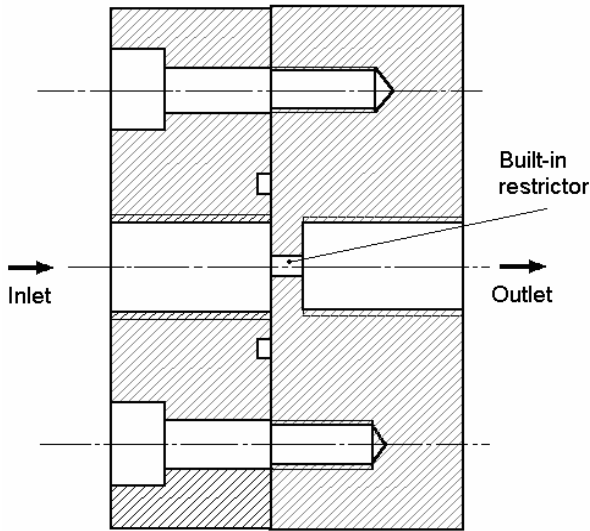


Figure 3 Test probe with built-in test restrictor

In the following, the CFD simulation is employed to numerically determine the mass flow-rate of gas through the test restrictor. Since the gas-flow in the test restrictor is axis-symmetric, a two-dimensional Cartesian coordinate model of the flow field is established for the quantitative analysis of the mass flow-rate through the test restrictor ($\phi = 0.1$ mm) as shown in Fig. 5.

The initial and boundary conditions for the CFD-simulation are:

- (1) The input velocity of the gas-flow is set to be 36 m/s. Different setting of input velocity influences only the speed of convergence of the numerical calculation. It, however, does not affect the accuracy of numerical analysis.
- (2) The gas flow is compressible.
- (3) The gas density is assumed to be $1.189 \text{ Kg}/\text{m}^3$ at room temperature.
- (4) The dynamic viscosity of the gas is set to be $1.789 \times 10^{-5} \text{ N} \cdot \text{s}/\text{m}^2$ at room temperature.
- (5) The room temperature is set to be 20°C or 293°K .
- (6) The reference acoustic velocity of gas is assumed to be 340 m/s.
- (7) The boundaries of the flow field are considered as the wall, which means that no gas-flow across the boundaries is allowed.

- (8) No heat transfer and chemical reaction exists in the flow field.
- (9) The outlet conditions are set to be atmospheric pressure and room temperature.

After CFD simulations, the velocity vector diagram of the test restrictor is found and shown in Fig. 6. From this velocity vector diagram and the corresponding numerical velocity data at the outlet, the average mass flow-rate of the gas can be derived. Other relevant simulation results together with the experimental data are discussed in the following section.

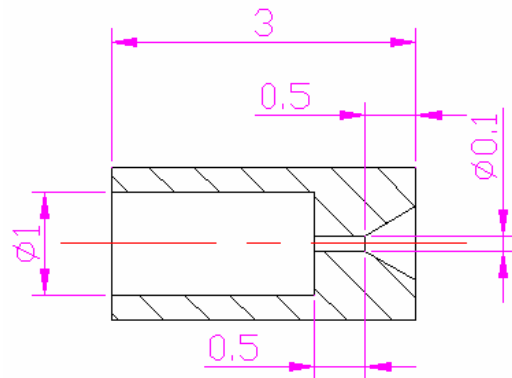


Figure 4 Geometry of the restrictor ($\phi = 0.1$ mm)

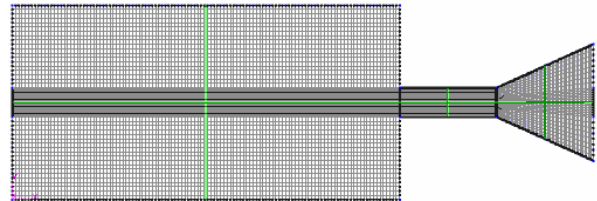


Figure 5 Two-dimensional Cartesian coordinate model of the flow field ($\phi = 0.1$ mm)

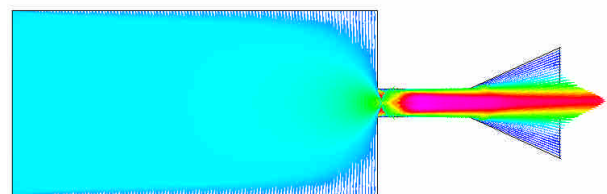


Figure 6 The velocity vector diagram ($\phi = 0.1$ mm)

EXPERIMENTAL RESULTS AND DISCUSSION

Figure 7 shows the schema of test bench for the orifice-type test restrictor according to ISO 6358. The most

important device is the mass flow meter, which serves to measure the mass flow-rate of gas through the test restrictor. At the inlet to the test restrictor, a pressure regulator is employed to vary the supply pressure. Moreover, two pressure sensors are utilized in this test bench. One is installed at the inlet and the other at the outlet. The measured pressure signals are used to calculate the pressure ratio of the outlet pressure to the inlet pressure. All the measured data are sampled and stored in the PC by using a data-acquisition software.

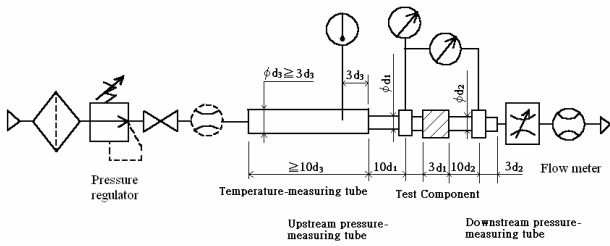


Figure 7 Test bench for the orifice-type restrictor according to ISO 6358

In this study, the method of exhaust-to-atmosphere is utilized. The outlet pressure, P_2 , is basically the atmospheric pressure plus the negligible pressure drop across the mass flow meter (the flow control valve is kept fully open). Hence it is approximately a constant. To vary the pressure ratio P_2/P_1 , only the inlet pressure, P_1 , is adjusted by using the pressure regulator. In a real aerostatic bearing, however, the inlet pressure is kept constant and the outlet pressure is variable according to different external loads. Obviously, these two conditions are basically equivalent since only the pressure ratio P_2/P_1 is employed in the calculations of the mass flow-rate through the orifice-type restrictor. Besides, the outlet pressure for the orifice-type restrictor in an aerostatic bearing is defined as the pressure in the air-chamber at the outlet as shown in Fig. 1.

Figure 8 shows the simulation curves as well as experimental results of the mass flow-rate of gas through test restrictors with different diameters. Obviously, every curve shown in Fig. 8 can be divided into two parts. At higher supply pressure, the curve is more like a straight line. On the contrary, at lower supply pressure, the curve can be described by an elliptical function. The intersection of these two parts is exactly the critical pressure ratio. Figure 9 indicates the values of the critical pressure ratio as a function of the test restrictor's diameter. It is observed that the critical pressure ratio for an orifice-type restrictor is approximately a constant value of 0.36.

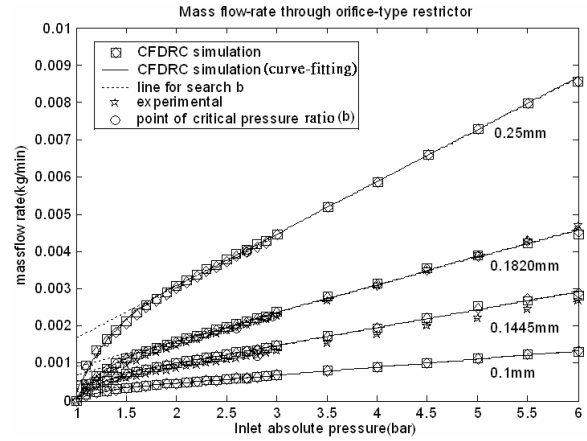


Figure 8 Simulation and experimental results of the mass flow-rate as a function of different diameters

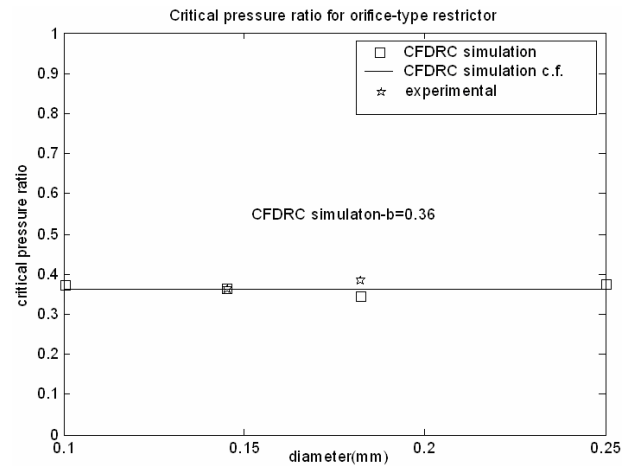


Figure 9 Critical pressure ratio as a function of different diameters

Figure 10 shows the graphical relation between the sonic conductance and the pressure ratio for different test restrictor's diameters. It is observed that only two experimental curves corresponding to test restrictors of diameters 0.1445 mm and 0.182 mm are shown in Fig. 10. This is chiefly because the test restrictors of diameters 0.1 mm and 0.25 mm are not available. It is further noticeable that every curve in Fig. 10 is quite similar to the curve of mass flow-rate through an ideal nozzle shown in Fig. 2 except the value of the critical pressure ratio. This proves one of our previous assumptions that the mass flow-rate property through an orifice is similar to that through an ideal nozzle. Figure 10 further illustrates the sonic conductance is approximately proportional to the square of the test restrictor's diameter. Such a proportional relation proves the second assumption that the sonic

conductance depends chiefly on the cross-sectional area of the orifice-type restrictor.

Finally, the orifice discharge coefficient C_0 can be determined from Eq. (7) and Fig. 10. After some calculations, C_0 is found to be 0.83, which agrees very well with the general assumption used in the conventional model.

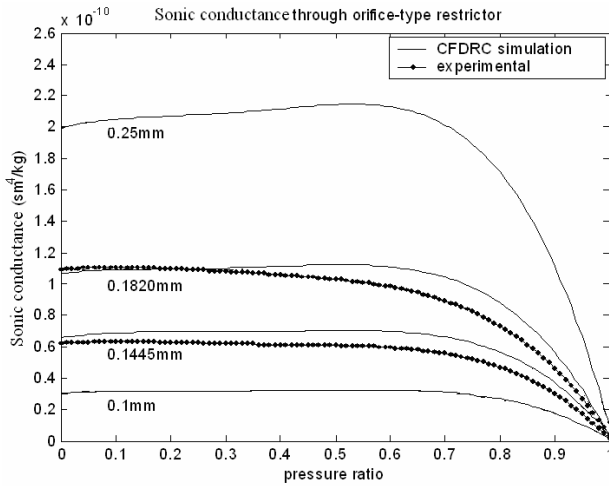


Figure 10 Sonic conductance as a function of pressure ratio for different test restrictor's diameters

CONCLUSION

In this paper, we have proposed a new model for the calculation of the mass flow-rate of gas through orifice-type restrictors in the aerostatic bearings. Four conclusions may be drawn from this research.

- (1) The experimental results agree very well with the results of CFD simulation.
- (2) The simulation and experimental results have both shown that the major difference between the conventional and the new proposed model is the value of the critical pressure ratio. In details, for an orifice-type restrictor of which the length is larger than the diameter, the recommended value for the critical pressure ratio is in the range $0.35 < b < 0.4$ instead of 0.5283.
- (3) The orifice discharge coefficient shown in Eq. (7) is found experimentally to be 0.83. Hence, the recommended value for the orifice discharge coefficient is in the range $0.8 < C_0 < 0.85$. This value is applicable only to the orifice-type restrictor of which the length is larger than the diameter.
- (4) The proposed new model, which is described by Eqs. (1), (2) and (7), is recommended for the determination of the mass flow-rate of gas through an orifice-type restrictor in aerostatic bearings.

ACKNOWLEDGMENT

The financial supports of the *National Science Council* under grant number NSC-92-2212-E-224-005 is greatly appreciated.

REFERENCES

1. Powell J.W., Design of aerostatic bearing, Machinery Publishing Co. Ltd., 1970.
2. Kogure K, Kaneko R, Ohtani K., "A study on characteristics of surface restriction compensated gas bearing with T-shaped grooves," Bulletin, JSME 1982, Vol. 25, No. 210, pp. 2039-2045.
3. Nakamura T. and Yoshimoto S., "Static tilt characteristics of aerostatic rectangular double-compound restrictors," Tribology International 1996, Vol. 29, No. 2, pp. 145-152.
4. Lin G., Tojiro A. and Ichiro I., "A computer simulation method for dynamic and stability analysis of air bearing," Wear 1998, Vol. 126, pp. 307-319.
5. Murrenhoff H., Grundlagen der Fluidtechnik, Teil 2 : Pneumatik, Umdruck zur Vorlesung, 1. Auflage, RWTH Aachen, Germany, 1999.
6. Chen M.F. and Lin Y.T., "Static behaviour and dynamic stability analysis of grooved rectangular aerostatic thrust bearings by modified resistance network method," Tribology International 2002, Vol. 35, p. 329-338.
7. Renn J.C. and Hsiao C.H., "Experimental and CFD study on the mass flow-rate characteristics of gas through orifice-type restrictor in aerostatic bearings," Tribology International 2004, Vol. 37, pp. 309-315.

A NEW MEASUREMENT METHOD OF THE FLOW-RATE CHARACTERISTICS OF THE REGULATOR

Guang-zheng PENG Xi-yan CHAI Wei FAN

SMC-BIT Pneumatics Center, Department of Automatic Control,
Beijing Institute of Technology, Beijing 100081, China
(E-mail: smcpeng@bit.edu.cn)

ABSTRACT

A new measurement method of the flow-rate characteristics of a regulator was proposed in this paper. Through charging a chamber connecting with the outlet of the regulator and measuring the pressure response in the chamber with a pressure sensor, the flow-rate characteristics curve was obtained from these sampled data. The process needs only one charge, so it brings high efficiency, good precision and less air consumption. The new method was studied through numerous simulations and experiments at different pressures. Results obtained from experiments and simulations were compared to find in good accordance, which verified the feasibility of the new measurement method.

KEY WORDS

Regulator, Flow-rate characteristics, Simulation, Measurement

NOMENCLATURE

B : viscous frictional coefficient, Ns/m
 C_d : coefficient of the flow rate, $C_d = 0.7$
 G : mass flow rate, kg/s
 K : spring coefficient of adjusting spring, N/m
 K_f : spring coefficient of restoring spring, N/m
 m : mass of the valve core, kg
 p_0 : absolute pressure of environment, MPa
 p_2 : outlet pressure of the regulator, MPa
 p_s : absolute pressure of air source, MPa
 R : gas constant, $R = 287 \text{ N}\cdot\text{m}/(\text{kg}\cdot\text{K})$
 r : ratio of specific heats, $r = 1.4$

S : effective area of elastic-membrane, m^2
 T : temperature of environment, K
 V : cubage of the chamber, m^3
 W : air mass in chamber, kg
 x : displacement of the adjusting spring, m
 x_f : displacement of the valve core, m

INTRODUCTION

As well known, regulator is used in almost every pneumatic system. The function of the regulator is to maintain the working pressure of the system at a value

which is set in advance and keep the outlet pressure constant while the flow rate changes. So it is very important to know the flow-rate characteristics of the regulator in order to optimize the design of a pneumatic system. The flow-rate characteristics is defined as the relationship of air flow capacity passing through the regulator and the differential pressure of the input pressure and outlet pressure[1]. The traditional measurement method[2] of the flow-rate characteristics of the regulator was showed in Figure 1. The working pressure of the system was set in advance. When the solenoid valve received an electrical signal, compressed air from the air source flow through the regulator. The pressure gauges $P1$, $P2$ were used to record the input pressure and outlet pressure of the regulator, respectively, and the flow meter was used to measure the gas flow rate. One point in the flow rate characteristics curve was obtained at a set throttle uncork. By changing the uncork of the throttle, a curve was obtained from a group of points. It was apparent that this method was of low efficiency and needed large air consumption. In order to resolve these problems, a new measurement method of the flow-rate characteristics of a regulator was proposed in this paper.

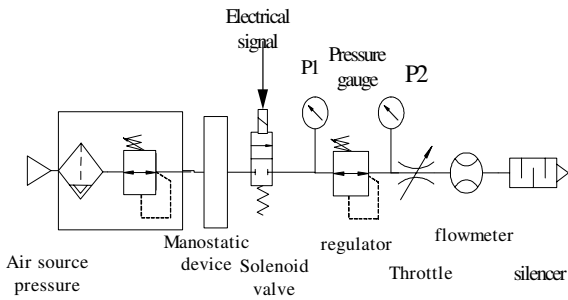


Fig.1 Experimental Device Of The Conventional Method

The principle of the new measurement method was introduced and dynamic model of the regulator was established and simulated with Simulink[3]. Meanwhile, experimental research on the conventional measurement was carried out and LabVIEW was used to acquire data in the experiment. The simulation results and experimental results were compared in order to verify the feasibility of the new measurement method.

1. Principle of the new measurement method

The principle of the new method was shown in Figure 2. The system of the measurement was composed of a solenoid valve, a regulator to be measured, a chamber, a pressure sensor, a data acquisition card and a PC. When the solenoid valve received a signal from the PC, compressed air from the air source flow through the regulator to charge the chamber. The pressure response

in the chamber was measured by the pressure sensor and the data acquisition card. And then a flow-rate characteristics curve was gained by analyzing the acquired pressure signals. It should be pointed out that only the quasi-equilibrium section of the regulator response in the course of charging was used to analyze its static characteristics in the new measurement method.

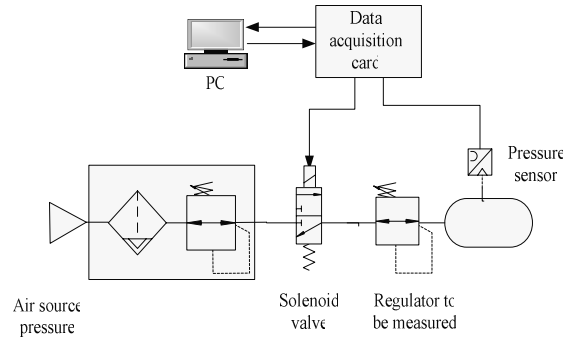


Fig.2 Principle Of The New Measurement Method

Assuming the pressure of air source and the cubage of the chamber were constant. The measurement principle of the new method could be explained using the equation of the energy and ideal-gas state equation. The state equation for compressed air in a chamber was written as Eq. (1).

$$PV = WRT \quad (1)$$

The following equation was derived by totally differentiating Eq. (1):

$$V \frac{dP}{dt} = GRT + WR \frac{dT}{dt} \quad (2)$$

If the state of compressed air in the chamber during charge or discharge remained isothermal, the following equation could be obtained from Eq. (2).

$$G = \frac{V}{RT} \frac{dP}{dt} \quad (3)$$

It was clear from Eq. (3) that if the cubage of the chamber V and the temperature of environment T were known, the mass flow rate G was proportional to the differentiated value of the pressure P in the chamber. Because the flow rate was continuous, the mass flow rate through the regulator was equal to which flew into the chamber. Assuming the outlet pressure was the same as the pressure in the chamber. So the curve of the flow rate characteristics of the regulator could be acquired from these data.

2. Simulation of the new measurement method

SIMULINK was used to verify the theoretical validity of the new measurement method by simulating the regulator and comparing the simulated curve with the traditional experimental curve. The simplified model of the direct-type regulator which was used to establish the mathematical model was shown in Figure 3.

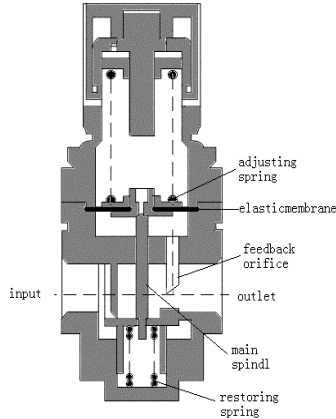


Fig.3 Simplified Model Of The Direct-type Regulator

2.1 Theoretical formulae used in simulation

When establishing the mathematical model[4][5] of the system, the following assumptions were made:

- 1 Compressed air accorded with the ideal-gas state equation, and the air leakage because of ill sealing was neglected.
- 1 The pressure and the temperature in the same chamber were even.
- 1 The outlet pressure of the regulator was equal to the pressure in the chamber. Air source, atmospheric pressure and environmental temperature kept stable.
- 1 The temperature of compressed air was isothermal in the chamber.

In the simulations, the mass flow rate G in the chamber was calculated with Eq. (3) and that through the regulator could be calculated with the following equation:

$$G = c_d S P_s \sqrt{\frac{2}{RT}} \phi \left(\frac{P_2}{P_s} \right)$$

$$\phi \left(\frac{P_2}{P_s} \right) = \begin{cases} \sqrt{\frac{r}{r-1} \left[\left(\frac{P_2}{P_s} \right)^{\frac{2}{r}} - \left(\frac{P_2}{P_s} \right)^{\frac{r+1}{r}} \right]} & 0.528 \leq \left(\frac{P_2}{P_s} \right) < 1 \\ \left(\frac{2}{r+1} \right)^{\frac{1}{r-1}} \sqrt{\frac{r}{r+1}} & 0 < \left(\frac{P_2}{P_s} \right) < 0.528 \end{cases} \quad (4)$$

The force equilibrium equations were as follows:
For charging:

$$K(x_v - x) - P_2 S - K_1 x - B \dot{x} = m \ddot{x} \quad (5)$$

For discharging:

$$P_2 S - K x_v - K x_1 - B \dot{x}_1 = m \ddot{x}_1 \quad (6)$$

According to the Eq. (3), Eq. (4), Eq. (5), Eq. (6), the emulator of the regulator was shown in Fig 4.

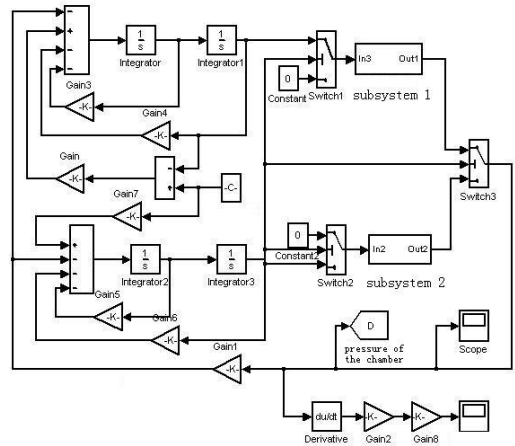


Fig.4 Emulator Of The Regulator

2.2 Results of simulation

2.2.1 The impact of the chamber cubage V

In the simulations, the pressure of air source and the outlet pressure were set 0.7MPa and 0.3MPa, and the chamber cubage V was 0.01 liter, 0.1 liter, 1 liter, 10 liter and 100 liter, respectively. Figure 5 showed the simulation results of the new measurement method of the flow-rate characteristics of the regulator. The five lines in the figure represented different chamber cubage. A conclusion was drawn from the figure: if the chamber cubage V was too small, there was no quasi-equilibrium process; if the chamber cubage V was too big, the pressure response became too slow. So it was very important to choose an appropriate cubage.

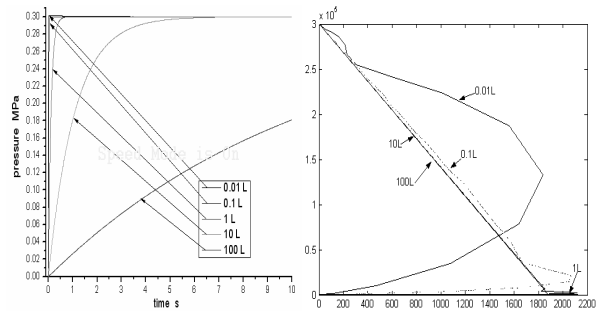


Fig.5 Simulated Curve Of The New Method

2.2.2 Comparison of the simulated curve and the traditional experimental curve

As shown in Figure 1, the air source pressure and the outlet pressure of the regulator were set to 0.5MPa and 0.2MPa, respectively. Only the quasi-equilibrium phase in the simulated curve was analyzed in the research. As shown in Figure 6, the simulated curve agreed well with the experimental curve, which proved the feasibility of the new method.

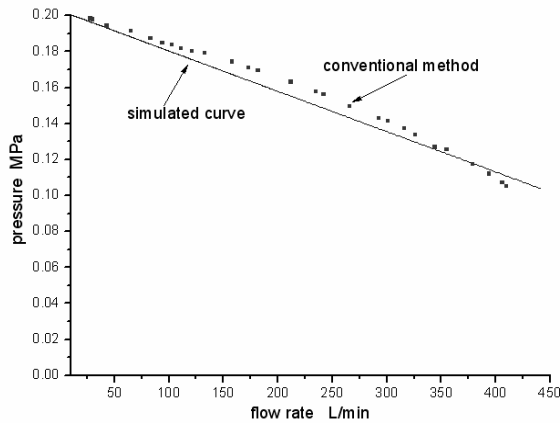


Fig.6 Comparison Of The Simulated Curve And The Experimental Curve

3. Experiment of the new measurement method

As shown in Figure 2, the air source pressure and the outlet pressure of the regulator were set 0.5MPa and 0.2MPa respectively to keep consistent with the conventional measurement method. The pressure signals in the chamber, which were sampled by the pressure sensor and the data acquisition card, were dealt with by ORIGIN, so the pressure-time curve and flow rate-time curve were shown in Figure 7 and the flow-rate characteristics curve of the new method was shown in Figure 8.

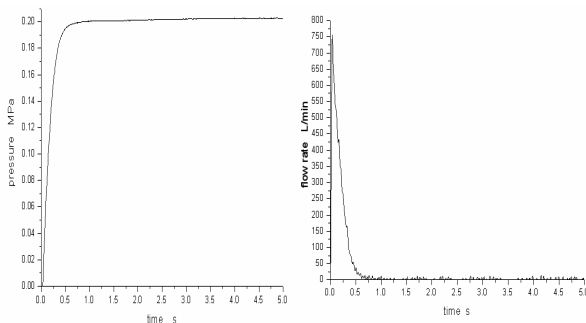


Fig.7 The Pressure-time And Flow Rate-time Figure

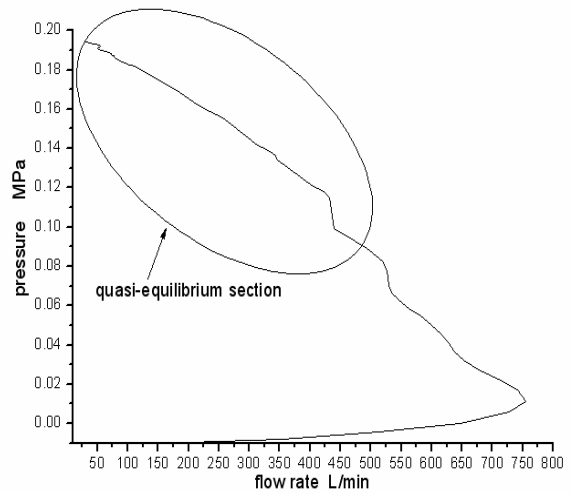


Fig.8 Flow-rate Characteristics Curve Of The New Method

Figure 9 showed the comparison result of the new measurement method and the conventional method. From this figure, it was clear that the curve gained by new method was similar to the curve obtained from the conventional method. Because the temperature was changing while charged the chamber, which was unchangeable during the simulation, there were some differences between two curves.

The result verified the feasibility of the new measurement method of the flow-rate characteristics of the regulator.

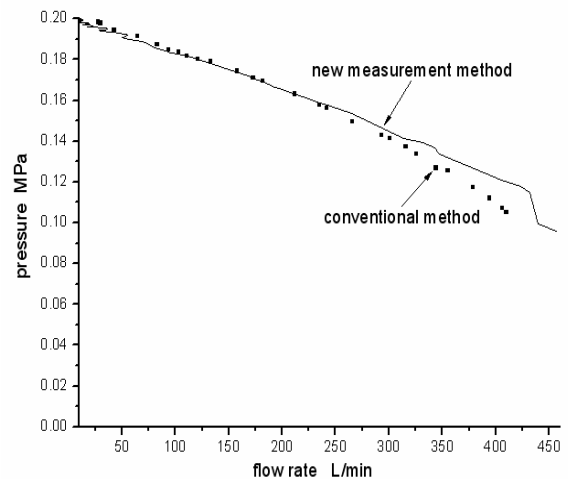


Fig.9 Comparison Result Of The New Method And The Conventional Method

4. Conclusion

This paper proposed a new measurement method of the flow-rate characteristics of a regulator. The basic

principle of the new method was detailed. Then, simulations and the conventional method experiments were performed. The curves obtained from the conventional method and the new method were in good accordance, which verified the feasibility of the new method.

The new measurement method has some advantages such as high efficiency, good precision and less air consumption. So it will be possible to become a standard measurement method of the flow-rate characteristics of the regulator in future.

REFERENCES

1. SMC (China) Co. Ltd., The Practical Pneumatic Technique of the Present-day, Publishing House of Mechanical Industry, Beijing, 1998 pp.134-140.
2. Sanville.F.E. A new method of specifying the flow capacity of pneumatic fluid power valves. Fluid power symposium,BHRA, 1971.
3. Wang, M. R., Modeling and Dynamic Simulation with Simulink 4, Publishing House of Electronics Industry, Beijing,2002,pp.15-50
4. Dasgupta, K and Karmakar, R., Modeling and Dynamics of Single-stage Pressure Relief Valve with Directional Damping, Simulation Modeling Practice and Theory, 2002,**10** ,pp. 51–67.
5. Dasgupta, K. and Karmakar, R., Dynamic Analysis of Pilot Operated Pressure Relief Valve, Simulation Modeling Practice and Theory, 2002,**10** , pp.35–49.

CHARACTERIZATION AND MODELING OF A PROPORTIONAL VALVE FOR CONTROL SYNTHESIS

Osama. OLABY, Xavier. BRUN, Sylvie. SESMAT, Tanneguy. REDARCE and Eric. BIDEAUX

Laboratoire d'Automatique Industrielle - <http://www-lai.insa-lyon.fr> –

LAI, Bât St Exupéry, 25 Av Jean Capelle INSA de Lyon,

69621 Villeurbanne Cedex, FRANCE

(E-mail: osama.olaby@insa-lyon.fr)

ABSTRACT

This paper presents a global characterization and an analytical model of the static flow stage of an electro-pneumatic proportional valve FESTO MPYE-5-M5-010-B. This study is useful for linear or nonlinear control synthesis in our application for medical robotics. Firstly, the experimental measurements are carried out using 3D graphs where a set of curves gives the output mass flow rate as a function of the electrical input of the electronic stage for different values of the output pressure. The exhaust and supply pressures, during these tests, are assumed to be constant. Moreover, 2D classical curves given by some constructors can be reconstructed, such as mass flow gain, pressure gain and mass flow characterization. Secondly, an approximation of the mass flow stage characteristics of this five-way proportional valve by a polynomial function is described. The model elaborated enables a good reproduction of the pressure gain and the global mass flow characterization curves to be obtained.

KEY WORDS

Pneumatic proportional valve, Experimental characterization, Modeling.

I. INTRODUCTION

Pneumatic systems are increasingly present in a number of industrial manufacturing procedures, handling, medical, armament and robotics, etc.

The use of proportional distributors in pneumatic systems has a practical design and simple use, especially to carry out the synthesis of the linear and nonlinear control laws in feedback control, for example position feedback control or force feedback control tracking according to desired trajectories [1]. Moreover, the proportional valve is a power modulator that does not consume much energy [2],[3]. A servo-distributor is known as proportional when it provides a mass flow rate in bi-directional operating mode which is a function of

the input voltage of the electronic stage of the proportional valve.

FESTO MPYE-5-M5-010B is a proportional valve, 5/3-way function, with a maximum flow rate of about 140 Nl/mn* at a supply pressure of 7 bar abs**. This mass flow rate is suitable for developing a medical robot (BirthSIM) [4],[5].

BirthSIM is a childbirth simulator developed in collaboration between INSA Lyon (Institut National des Sciences Appliquées) and HCL (Hospices Civils de Lyon) [6]. BirthSIM is a dynamic functional simulator, which takes into account the movement of a baby

*1 Nl/mn = 0.0215 g/s

**Thereafter, all the pressure values expressed in bar, will be in absolute bar.

through its mother's pelvis. In fact this type of simulator will help to teach, in a realistic way, and in complete safety the medical techniques of childbirth in the midwife schools and the Faculty of Medicine. It has been developed to enable obstetricians to learn how to perform the procedure for the first time. The operative part of BirthSIM contains a pneumatic actuator which produces the movement of the head of the newborn and supplies a programmable resistance to the force of traction. The actuator will enable BirthSIM to imitate contractions and the mother's pushing action. This actuator is a linear cylinder, double-acting and single rod which supports the head of the newborn. This cylinder can position the newborn, and more particularly its head, on a horizontal axis. Two FESTO MPYE-5-M5-010B proportional valves control this pneumatic cylinder. In order to carry out the automatic piloting of the electro-pneumatic system, it is necessary to know the mathematical model of the power modulator.

Servo-distributor manufacturers do not provide sufficient characteristics to obtain a model of the flow rate stage of the pneumatic components in their documentation [7]. No precise characteristics are provided by FESTO. This is why the global static characteristics (port P) of the proportional valve, were established. Moreover, experimental measurements carried out can give a precise knowledge of the mass flow rate delivered by the flow stage of this proportional valve and then a simulation model can be deduced. These measurements form a table, having as inputs the output pressure and the electrical input of the electronic stage integrated into the proportional distributor and giving the output mass flow rate. The procedures followed to carry out the global characterization of the FESTO proportional valve confirm the possibility of applying a protocol carried out previously for a servo-distributor of the Asco JOUCOMATIC company [7],[8], to other fluid power components. Servotronic Asco JOUCOMATIC is a three-way electro-pneumatic servovalve, its maximum flow rate is about of 1400 NI/mn. This flow rate value is much larger than that of the FESTO MPYE-5-M5-010B proportional valve.

This article is organized as follows: In section II, the FESTO proportional valve is briefly described. In section III, experimental results of a global characterization of this type of pneumatic component is provided. Section IV presents a mathematical model of the static flow rate stage. The results obtained with this model are compared with the experimental results and two types of errors are then discussed.

II. USAGE OF THE PROPORTIONAL VALVE

The MPYE-5-M5-010B proportional valve is a 5/3-way function distributor. It is thus composed of five ports N, P, S, E and E with three configurations for the air flow (Figure 1). The five ways present an S orifice of compressed air (it is numbered orifice (1) by the manufacturer), two working orifices for P(4), N(2) and

two for the exhaust E(3 and 5). For a voltage of 5 V, when the spool is in mid-position, the flow rate of the distributor is theoretically null. If the input control is varied from 5 V to 0 V, the compressed air exits from port (1) towards port (2) and the exhaust goes from port (4) towards port (5). By varying the voltage of 5 V to 10 V, the compressed air exits from port (1) towards port (4) and the exhaust goes from port (2) towards port (3).

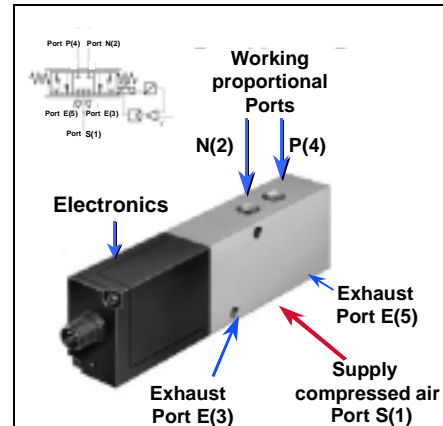


Figure 1. Photograph and schema of a FESTO MPYE-5-M5-010B proportional valve

III. EXPERIMENTAL CHARACTERIZATION RESULTS

The characterization suggested for the FESTO proportional valve is a global static characterization for constant exhaust and supply pressures.

- Global since the output mass flow rate is given as a function of both the electrical proportional valve input and of the output pressure, the supply and exhaust ports being as in normal working conditions which means that none of them is shut.
- Static, because for each variation in the electrical input control or in the output working pressure, the measurement readings (pressure and flow rate) are taken when the flow rate is in established mode.

Figure 2 shows the testing device used for measuring the desired characteristics of the port P(4) when the port N(2) is shut. The experimental procedure consists of recording the output flow rate for each variation of the input voltage and of the working pressure P_p . It is necessary to vary one of these two independent values and to keep the other constant.

It can be seen from Figure 2 that, for this purpose, the output pressure P_p and the supply pressure ($P_s=7$ bar) are kept constant by using two pressure regulators.

Considering the nonlinear character of this type of component (Figure 4), it was necessary to make more voltage measurements between 4 V and 6 V. These values correspond too to the significant part of the pressure gain characteristic at null mass flow rate (Figure 11).

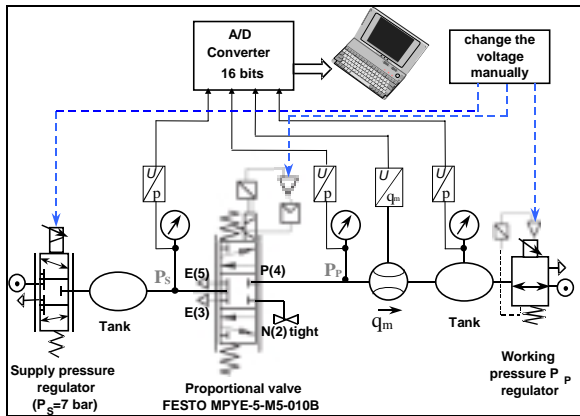


Figure 2. Testing device

Figure 3 shows (after having carried out a linear interpolation of the measurement points) the three-dimensional evolution of the mass flow rate as a function of valve-input control and its working pressure. In fact, if this characteristic is projected on two planes (U, q_m) and (P_p, q_m) the network of mass flow gain (Figure 4) and the network of mass flow rate characterization (Figure 5) can be obtained respectively.

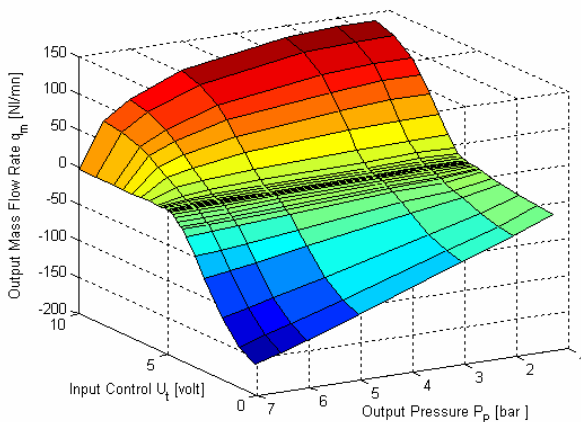


Figure 3. 3D-global static characteristics

Figure 4 shows the evolution of the output proportional valve mass flow rate q_m as a function of electrical input U , for eight different values of the output pressure P_p , distributed from 1.25 to 7 bar. In this figure is shown:

- The non-linearity of the curves for values near the supply and exhaust pressures, for values of input control near the 5V value.
- The eight curves are monotonous.
- A phenomenon of saturation is noticed for the values of input control higher than 8 V and lower than 2V.

The set given in Figure 5 shows the output mass flow rate as a function of the output pressure for 26 different values of the input voltage control from 0.153V to 10V.

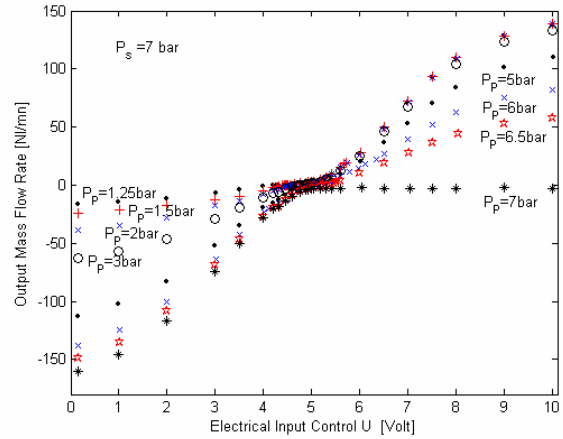


Figure 4. Set of mass flow rate curves as a function of proportional valve input

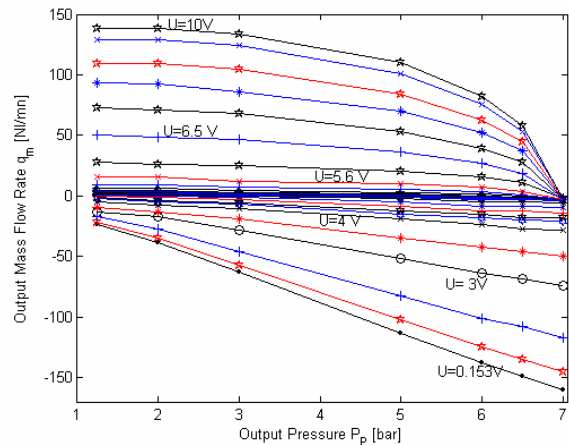


Figure 5. Set of mass flow rate curves as function of proportional valve output pressure

This network clearly shows the classical behavior of the servo-distributor orifices related either to a supply process or to an exhaust process for large absolute values of the valve proportional input control.

Each of the two sets of curves (Figure 4 and 5) determines simply the variation of mass flow rate against both an output pressure P_p and an input control. This constitutes useful information about the power modulator under study which is not directly available on the manufacturer documentation. This information enables a simulation model of the static flow stage in the form of an easily programmable 3D-table to be used for any simulation. By interpolation between the points, it

gives the real global mass flow rate at the output port whatever are the output pressure and the input control.

IV. ANALYTICAL CONTROL MODEL

The synthesis of certain control laws requires the knowledge of a flow stage model in a mathematical form [2]. The modeling of a servodistributor enables the mass flow rate at its output as a function of the output working pressure, and of the electrical input control to be determined. For the control objective, it is tried to reproduce the static behavior of the FESTO distributor proportional valve, via a mathematical expression.

A method had been proposed, using a mathematical expression of the mass flow rate evolution law, depending on the global characteristics of the servo-distributor JOUCOMATIC SERVOTRONIC [8]. This control model for the FESTO proportional valve is validated by carrying out a translation of the valve-input control U to new values of control U_i varying around 0V: ($U_i = 5.0412 - U$). The value equal to 5.0412V (deduced from the measurements) corresponds to the intersection point of the pressure gain characterization orifice P and orifice N thus to the same pressure on both output ports. The mathematical expression affine in the control input is :

$$q_m(U_i, P_p) = \varphi(P_p) + \psi(P_p, \text{sgn}(U_i)) \times U_i \quad (1)$$

- $q_m(U_i, P_p)$ illustrates a mass flow rate (Nl/mn) that is a function of the working pressure P_p and an input control voltage U_i .
- $\varphi(P_p)$ is a polynomial function whose evolution corresponds to the mass flow rate leakage (Nl/mn) from the orifice P. It is identical for all input control values U_i (Figure 6.)

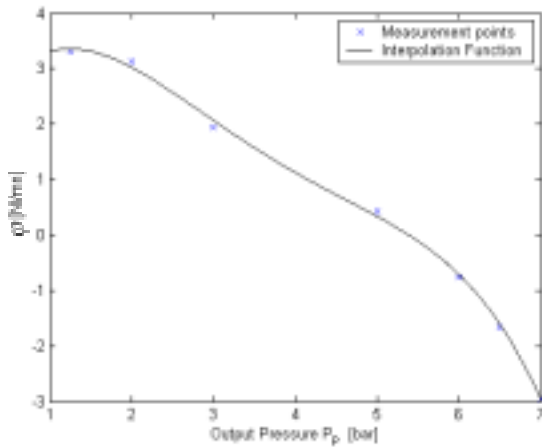


Figure 6. Approximation of mass flow rate measured for $U_i = 0$: Function $\varphi(p)$

- $\psi(P_p, \text{sgn}(U_i))$ is a polynomial function of the input control sign (Figure 7) because it is different for the inlet ($U_i > 0$) and for the exhaust ($U_i < 0$).

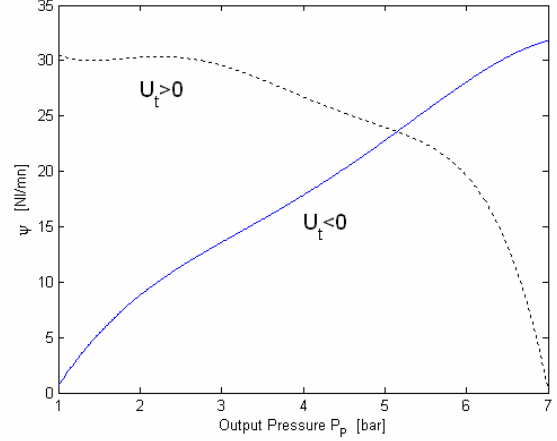


Figure 7. Approximation of the $\psi(P_p, \text{sgn}(U_i))$ function.

The form of the mass flow rate shown in Figure 5. justifies the approximation by two different ψ functions, one defined for positive values of U_i and the other for negative values. The nonlinear shape of the global characteristics of the mass flow rate, as a function of the output pressure and the input control, justifies the choice of the polynomial function of the form (1). The minimal degrees of the polynomials $\varphi(P_p)$, $\psi(P_p, U_i < 0)$ and $\psi(P_p, U_i > 0)$ to have the smallest absolute estimated error, equal to 4, 4 and 5 respectively.

IV.1. CONTROL MODEL VALIDATION

In this paragraph, a comparison of the characteristics resulting from the approximations with those resulting from the experimental measurements of the FESTO proportional valve (section III) is presented.

Figure 8 shows the evolution of the mass flow rate as a function of the electrical input control and the working pressure according to equation (1). This two-dimensional evolution has a shape rather near that of the static global two-dimensional characteristic of the FESTO MPYE-5-M5-010B proportional valve, as illustrated in Figure 3.

In fact it can be observed in Figures 9 and 10 that the mass flow rate reconstituted from the equation (1), gives good results comparatively to the measurements except for:

- the negative values of the input control U_i with output pressures P_p equal to 6, 6.5 and 7 bar.
- the positive values of input control U_i with a working pressure P_p near to that of the atmospheric pressure (1.25 bar and 1.5 bar).

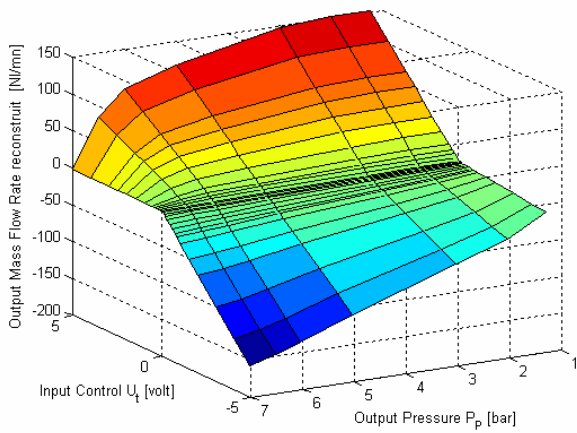


Figure 8. Global static characteristics reconstituted from the equation (1)

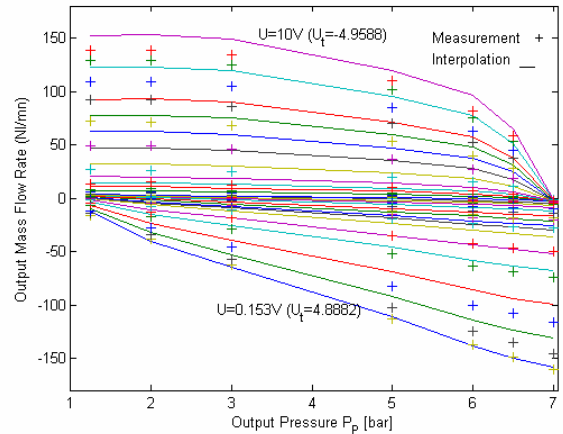


Figure 10. Comparison: experimental and reconstituted set of mass flow rate curves as a function of output pressure

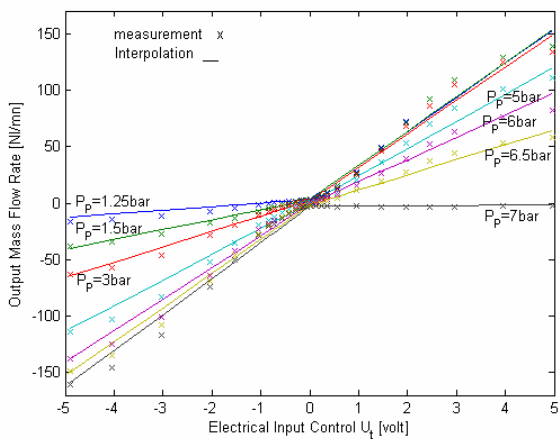


Figure 9. Comparison: Experimental and reconstituted set of mass flow rate curves as a function of valve input

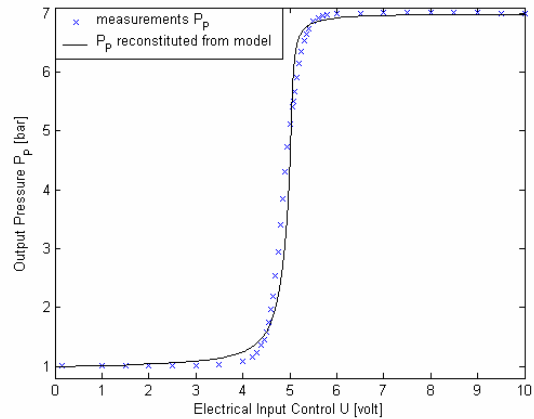


Figure 11. Comparison: Experimental and reconstituted pressure gain curve

These errors are not troublesome for the uses under consideration, because the pressure domains correspond to extreme values close to the supply or exhaust pressures which will not be examined very much.

An other way to validate the obtained approximation is to compare the pressure gain characteristic P_p at null mass flow rate reconstituted from equation (1) with the measured characteristic. It can be observed in Figure 11 that the approximation gives good results compared to the measurements. In fact the slope of the pressure gain reconstituted is larger than that measured in the experiments. In this interval the displacement of the valve spool causes the opening of one of the working orifices P or N and the closing of the other.

IV.2. MODELING ERROR

Two criteria are presented to validate the control model. On one hand, an absolute error of mass flow rate is obtained that is low on all the application fields of the FESTO proportional valve. On the other hand, a relative error of the mass flow rate for the greatest opening zone of a passage of fluid estimated for this component is obtained.

The absolute errors of the mass flow rate generated by the control model given by the equation (1) are weak (between -15 Nl/mn and +15 Nl/mn) as shown in Figure 12. They are maximal at the edges of the pressure field P_p .

The relative errors of mass flow rates generated by the approximations for the values of electrical input control

U_t outside the interval $[-1, +1]$, are between -10% and +15% (Figure 13)

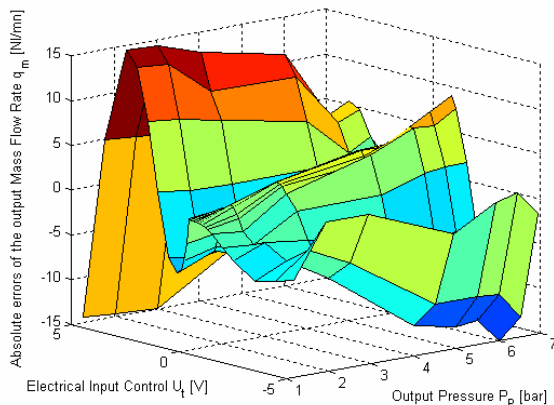


Figure 12. Mass flow rate absolute errors

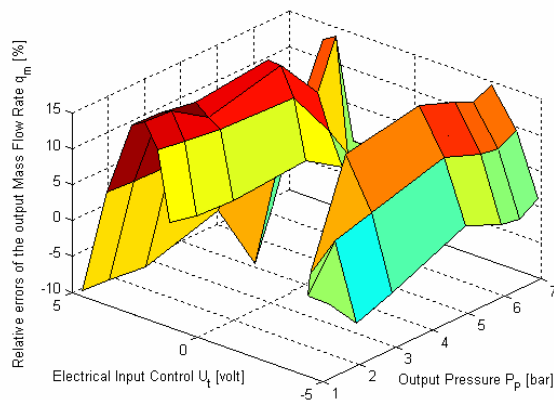


Figure 13. Mass flow rate relative errors

These approximations knowledge will be useful to synthesize nonlinear robust control law [9].

V. CONCLUSION

In this paper an analytical model of a MPYE-5-M5-010B proportional 5/3-way valve from the FESTO company has been presented. The mathematical model has been obtained after realizing a global characterization of the static flow stage of this servo flow control valve. The experimental measurements carried out for a characterization in three-dimensions (mass flow rate, output pressure and electrical input control), can be used as a simulation model. The characteristics presented in Figure 3 can consider FESTO servo-pneumatic valve is suitable to carry out the functions of the childbirth simulator BirthSIM.

The analytical model of the FESTO proportional valve

was validated by reconstituting the global two-dimensional characterizations and the pressure gain curve at null mass flow rate. The good results obtained show that the characterization and modeling protocol of a servo-distributor carried out previously [7] can be used for another pneumatic modulators. The weak errors of the mass flow rate enabled the control model to be validated. A control synthesis would enable the simulator BirthSIM to be automated. In fact the generation of input trajectories for our system is an important problem to resolve in order to translate the medical conditions into an automation problem. Later it will be necessary to synthesize robust controls which will enable to take into account the known errors of the flow stage model. This will enable to minimize tracking errors in a highly non-linear field.

REFERENCES

- [1] KAASA, G. -O., CHAPPLE, P. -J., LIE, B., *Modeling of an electro-pneumatic cylinder actuator for nonlinear and adaptive control, with application to clutch actuation in heavy-duty trucks*, In the 3rd International Ph.D. Symposium on Fluid Power, Terrassa, Spain, 30th June- 2nd July, 2004, p 255-273.
- [2] BRUN, X., BELGHARBI, M., SESMAT, S., THOMASSET, D., SCAVARDA, S., *Control of an electropneumatic actuator, comparison between some linear and nonlinear control laws*, Journal of Systems and Control Engineering, 1999, Vol. 213, N°15, p 387-406.
- [3] FERNANDEZ-JIMENEZ, A., PEREZ GARCIA, J., *Compressible bench flow adaptations to the experimental characterization of pneumatic components. Application to the determination of flow-rate characteristics of a MPYE-5-3/8-010-B proportional valve*, In the 3rd International Ph.D. Symposium on Fluid Power, Terrassa, Spain, 30th June- 2nd July, 2004, p 139-148.
- [4] SILVEIRA R., DUPUIS O., PHAM M.T., DITTMAR A., REDARCE T., BETEMPS M. *Design of a Mechanical birth simulator*. World Congress on Men's Health Medicine - WCMHM'04. 5-8/04/2004, Paris, France, 2004.
- [5] SILVEIRA R., DUPUIS O., PHAM M.T., REDARCE T., BETEMPS M. *A new mechanical birth simulator*. IEEE/RSJ International Conference on Intelligent Robots and Systems - IROS'04, 28/09-2/11 2004, Sendai, Japan, 2004, pp 3948-3953.
- [6] DUPUIS, O., DITTMAR, A., DELHOMME, G., REDARCE, T., BETEMPS, M., SILVEIRA, R., *Simulateur fonctionnel et anatomique d'accouchement*. French patent number: 0309569, August 01, 2003.
- [7] SESMAT, S., SCAVARDA, S. *Static characteristics of a three-way servovalve*, In: 12th Aachen Conference on Fluid Power Technology, Aachen, Allemagne, March 12-13, 1996, p 643-652.
- [8] BELGHARBI, M., THOMASSET, D., SCAVARDA, S., SESMAT, S., *Analytical model of the flow stage of a pneumatic servo-distributor for simulation and nonlinear control*, in the Sixth Scandinavian International Conference on Fluid Power, SICFP'99, Tampere, Finland, May 26-28, 1999, p 847-860.
- [9] SMAOUI, M., BRUN, X., THOMASSET, D., *A combined first and second order sliding mode approach for position and pressure control of an electropneumatic system*, American Control Conference, ACC'05, Portland, Oregon, USA, June 8-10, 2005

THE DESIGN OF A THREE WAY PNEUMATIC VALVE

Terenziano RAPARELLI*, Pierluigi BEOMONTE ZOBEL**, Francesco DURANTE** and Gianpaolo GAGNOLATO

* Dipartimento di Meccanica, Politecnico di Torino
Corso Duca degli Abruzzi 24, Torino, Italy
terenziano.raparelli@polito.it
** DIMEG, Università di L'Aquila
67040 Roio Poggio, L'Aquila, Italy

ABSTRACT

The paper presents the design and the construction of the power part of a three-way pneumatic valve that uses a pilot stage developed by Belforte et al., based on a compact turbulent amplifier that uses the laminar-turbulent transition of fluidic jets. The valve can be used to drive a power stage of pneumatic circuits. It has a low energy consumption to switch. The pilot stage uses an acoustic signal generated by a piezoelectric device to brake the laminar flow. The power part of the valve has been designed to obtain an high conductance and a good dynamic performance. The design of the power valve, by a mathematical model using concentrated parameters, is presented. The prototype was constructed and tested. The results of the experimental test are also reported and discussed.

KEY WORDS

Pneumatics, valve design

NOMENCLATURE

p_0 : *recovered pressure*
 p_s : *supply pressure*
 p_c : *control pressure*
 C_i : *conductance*
 R_i : *resistance*
 G_i : *flow-rate*
 D_1 : *control diaphragm*
 D_2 : *power diaphragm*
 V : *voltage*
 Q_N : *normal flow-rate*

INTRODUCTION

The paper presents the design and the construction of a three-way pneumatic valve that uses a pilot stage

developed by Belforte et al. [1,2], based on a compact turbulent amplifier that uses the laminar-turbulent transition of fluidic jets. The valve can be used to drive a power stage of pneumatic circuits. It has a low energy consumption to switch. The pilot stage uses an acoustic signal generated by a piezoelectric device to brake the laminar flow. The supply pressures at the pilot stage is about 2000 Pa, the maximum pressure recovered at the receiving nozzle is about 1200 Pa. The supply pressure at the power section is fixed at 3 bar. The power part of the valve has been designed to obtain an high conductance and a good dynamic performance. The operating principle of the low pressure/high pressure interface is based on a flapper nozzle sensor. The classical architecture of the flapper nozzle in a valve is formed by a circular hole, where supply air comes, that faces to the flapper [3]. The idea was to use an annular shape of the hole that supplies air and a circular shape

inside it bonded to the exterior. In this way the air flux flows to the exterior by two surfaces and it is possible to reduce the displacement of the flapper. The design of the power valve is also presented. The prototype was constructed and tested. Finally the results of the experimental test are reported and discussed.

THE PILOT STAGE

The pilot stage of the valve was developed and constructed by Belforte et al. [1,2]. It is based on a compact turbulent amplifier and it uses the laminar-turbulent transition of fluidic jets. Between the emitting and the receiving nozzles there is a diffuser, to improve the amplifier performance, and an open chamber. The open chamber is open to the environment and the control signal is located in it.

The control signal is obtained by an acoustic signal generated by a commercial low power piezoelectric element (power supply = 1 V, max frequency = 17100 Hz, max acoustic amplitude = 94.5 dB). It emits a sound disturbance capable of producing jet transition. In fact the fluidic jet shows a high sensitivity to acoustic signal whose frequency is close to the natural frequencies of the jet. Some experimental tests were carried out on the pilot stage to define the optimal values of the supply pressure, voltage and frequency of the piezoelectric element. The distance between the jet and the piezoelectric element is 1.2 mm to minimize the energy consumption.

The characteristic geometrical dimensions of rectangular nozzles are as follows.

- Emitting nozzle-Receiving nozzle distance = 14 mm
- Emitting nozzle section = 0.5 mm x 0.4 mm
- Receiving nozzle section = 0.5 mm x 0.4 mm
- Diffuser inlet section = 0.8 mm x 0.6 mm
- Diffuser outlet section = 1.5 mm x 0.6 mm
- Emitting nozzle-Diffuser nozzle distance = 6 mm

Figure 1 shows the final result of these tests as characteristic diagram of the pilot stage: the output pressure versus the supply pressure.

The maximum pressure recovered at the receiving nozzle is about 1500 Pa. The presence of the piezoelectric element reduces the maximum pressure recovered to about 1200 Pa, because of the partial occlusion of the exhaust section.

A numerical model of the air flux in the pilot stage was created to verify the behavior of the numerical calculation of compressible flow in a spatial geometry. The numerical model was defined by a Computational Fluid Dynamic (CFD) software package, FLUENT code, in which the Finite Volume Method is used to solve the numerical equations of the air flux in a spatial geometry.

The results of the numerical simulation were compared with the experimental ones as pressure drop at the receiving nozzle in steady flow conditions. A good agree was obtained between numerical simulation and experimental tests.

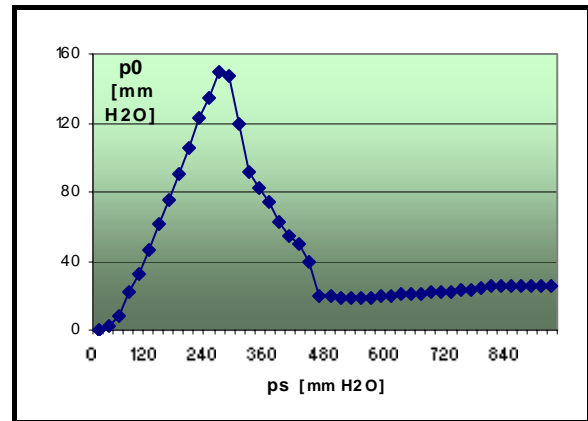


Figure 1. Output pressure p_0 vs. supply pressure p_s for the pilot stage

THE POWER SECTION

The three-way normally closed valve was designed using the operating principle of a flapper nozzle sensor. The supply pressure was fixed at 3 bar at this stage. The Fig. 2 shows a simplified drawing of the valve useful to understand the working principle of the valve, where p_c is the control signal arriving from the pilot stage. The upper part of the drawing shows the control diaphragm D_1 , where the control signal p_c acts, that is a pneumatic amplifier. Under this diaphragm the power part of the valve is observable.

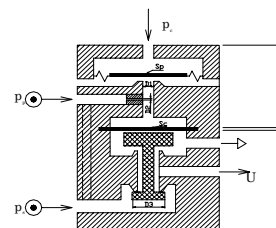


Figure 2. Simplified drawing of the power section of the valve

In the absence of the control signal p_c the supply air p_s , which reaches the volume between the power diaphragm D_2 and the control diaphragm D_1 , via the d_2 diameter resistance and the d_1 diameter nozzle, flows to the exterior by a discharge port located below the diaphragm D_1 . When the control signal p_c is applied, the control diaphragm D_1 closes the d_1 diameter nozzle and the pressure p_p rises stretching the power diaphragm D_2 and, moving, consequently, the flapper, leading to the switching of the valve.

The control diaphragm D_1 used was designed with the the pilot stage by Belforte et al. [2], while a design was made by the authors for the power diaphragm D_2 . The design has considered two materials: silicone and natural latex. With silicone, different materials was used as internal structural part: cotton (thickness 0.75 and 1 mm), viscous synthetic tissue (t. 0.75 mm) and tulle (t. 0.75 mm). No structural part was used for natural latex. A technological set up was implemented to construct these diaphragms. Liquid silicone was degassed using a vacuum pump to prevent the presence of inclusions of air in the final diaphragms. Both silicone and latex based diaphragms were manufactured using an alluminium forming shape (Figure 3) and a slow flow-rate of iniecton was adopted to avoid air inclusion in the texture of internal structural part.

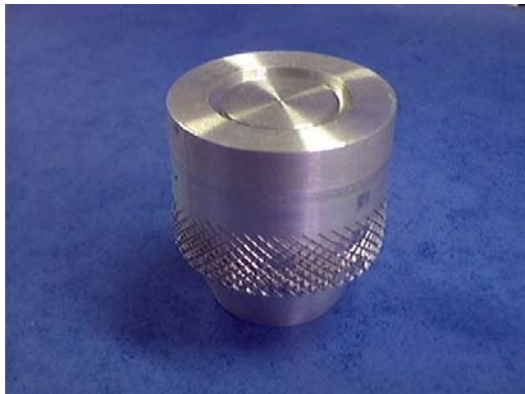


Figure 3. Diaphragm D_2 forming shape

All these diaphragms were tested at a pressure of 3 bar, measuring the displacement of the central point. Finally all of them were tested in the prototype of the valve. The Figure 4 shows the silicone-based diaphragm with internal cotton texture.

A theoretical scheme was used to define the focal sections of the valve, in order to ensure and to verify the static functionality of the system and to have also a valid tool to gain sensibility in realizing unforeseen behaviour of the valve. A concentrated parameters model was adopted. The approximation of concentrated parameters can reasonable be accepted because the ratio of conduit length against its diameter is not too large. Moreover the distance covered by a generic sonic



Figure 4. The silicone-based diaphragm

pressure signal, for the duration of transitory of the valve switch, is much more larger than the same conduit. It can be noticed that neither capacitive nor inductive quantities are included in the scheme but it can be easily proved that these ones are not essential in steady-state conditions.

Boundary conditions for inlet pressure and outlet pressure are known, while some dimensions of internal restrictions were fixed to solve the above equivalent scheme.

The Fig. 5 shows the equivalent scheme of the power section of the valve

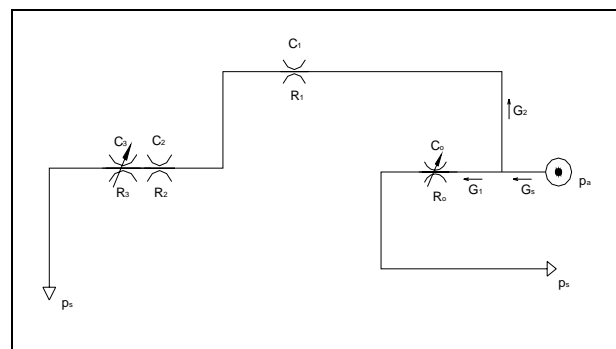


Figure 5. The equivalent scheme of the power section

Resistances R_0 and R_3 are represented as variable quantities, infact they are respectively associated to the power flapper nozzle and to the control flapper nozzle: their resistances can assume value ∞ (infinite), when the nozzle is closed by the flapper, or R_i . R_1 is the resistance of the restriction in the cylindric element, shown in Figure 6.a, below the power diaphragm D_2 .

Solving the equivalent scheme, by using (1), (2), and (3) all the conductances of the pneumatic system are determinated:

$$R = \frac{\Delta p}{G} \quad (1)$$

$$C = \frac{1}{R} \quad (2)$$

$$G_1 + G_2 = G_s \quad (3)$$

$$C_1 = 3.33 \cdot 10^{-12} \text{ m}^3/(\text{s Pa})$$

$$C_2 = 3.43 \cdot 10^{-11} \text{ m}^3/(\text{s Pa})$$

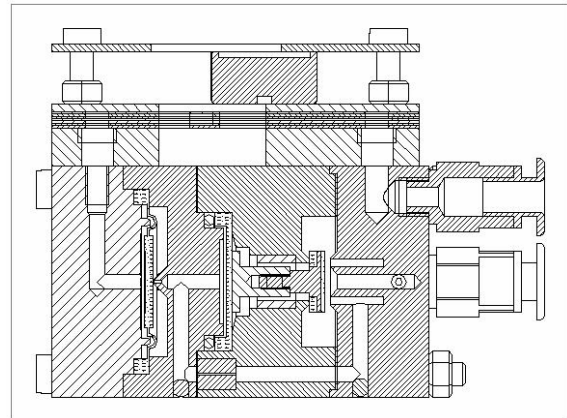
$$C_3 = 3.53 \cdot 10^{-10} \text{ m}^3/(\text{s Pa})$$

About the flapper nozzle the goal was to obtain a high conductance and a good dynamic performance. The classical architecture of the flapper nozzle in a valve is formed by a circular hole, where supply air comes, that faces to the flapper. The idea was to use an annular shape of the hole that supplies air and a circular shape inside it bonded to the exterior. In this way the air flux flows to the exterior by two surfaces and it is possible to reduce the displacement of the flapper growing the dynamic performance of the valve.

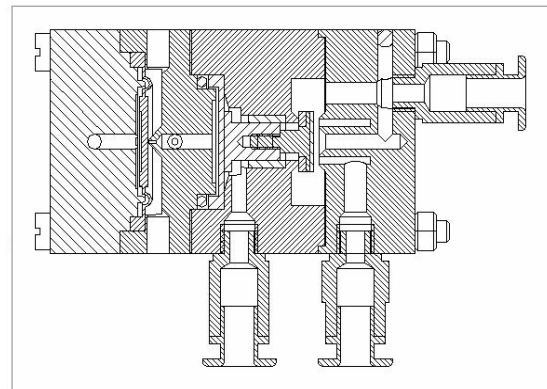
The Fig. 6 shows two sectional views of the designed valve, while in the Fig. 7 is shown the prototype manufactured.

In the upper part of the Fig. 6 a) the pilot stage is located. The connections on the right side are for the pressure supply of the pilot stage, in the upper part, and for the exhaust of the power stage, in the lower part. From left to right in the Fig. 6 a) is possible to see four parts that represent the power section of the valve. The first part shows the air connection between the pilot stage and the power section of the valve. It is linked to the second part by the control diaphragm D_1 . Continuing on the right side it is possible to see the power diaphragm D_2 , between the second and the third part of the valve, that moves the spool, that's means the flapper, to close the nozzle. In the fourth part it is possible to see the annular shape volume, connected to the air supplier in the bottom of Fig. 6 b) on the right, and the central hole that, together with the volume of the flapper, is connected to the exhaust port, on the right in the same figure. The material used for the power part of the valve is aluminium.

The Fig. 7 shows a photo of the prototype, where the pilot stage is on the top of the valve, while the power section is the lower part. In this figure you can see the fittings for air connection, and the electrical wires to command the piezoelectric element. Two of the 4 fittings are to be connected to the air supplier, 3 bar for the pilot and 3 to 8 bar for the power section. While the 2 fittings remained are the exhaust ports.



a)



b)

Figure 6. Sectional views of the valve: vertical section a) and horizontal section b)

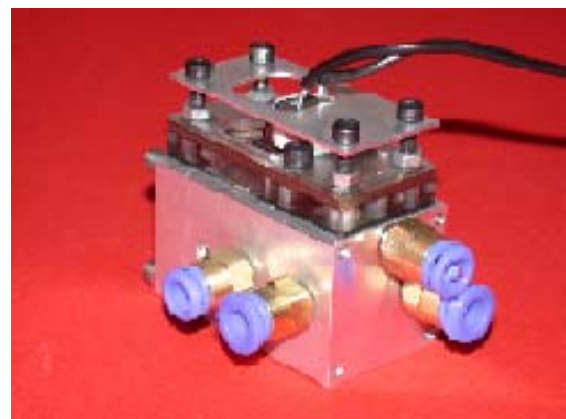


Figure 7. Photo of the valve's prototype

THE EXPERIMENTAL TESTS

Following the design and the manufacturing of the prototype of the 3/2 pneumatic valve, an experimental activity was defined to validate the design by calculating the main characteristic curves of the valve: the flow diagram inside the valve and the diagram of the step response test.

The flow diagram, shown in Fig. 8, was calculated following the international standard ISO 6358 [5] for three pressure values P_s before the valve: 3, 4 and 5 absolute bar. Also the valve's characteristic coefficients were calculated: C, conductance, and b, critical pressure ratio, Table 1.

For the step response test the international standard ISO12238 was followed [6]. In this case the valve was tested measuring the electric signal of the pressure transducer outside the valve versus time, so that the time delay of the valve can be calculated. A data acquisition board was used to acquire the signal both from the pressure transducer and from the signal generator used to send the command signal to the piezoelectric element. The electrical command signal for the piezo has an amplitude of 1 V and a frequency of 16.4 kHz in a square wave shape. The tests were carried out for the 5 different power diaphragm D_2 previously described. The results are shown in the Fig. 9 and the diaphragm in silicone with 1 mm of cotton has the shortest response time: 19 ms. This result confirms that the most rigid diaphragm gives the best dynamic performance at the valve. At this step no experimental tests are carried out on the fatigue life of the valve.

Table 1 Characteristic coefficients of the valve

P_s [bar]	C [dm ³ /(s bar)]	b
3	0.64	0.27
4	0.60	0.29
5	0.56	0.30

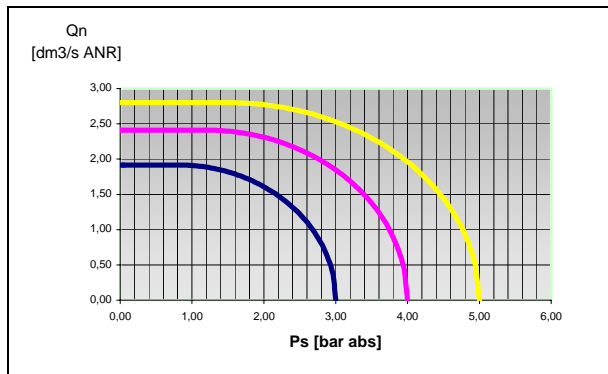


Figure 8. Flow diagram of the valve

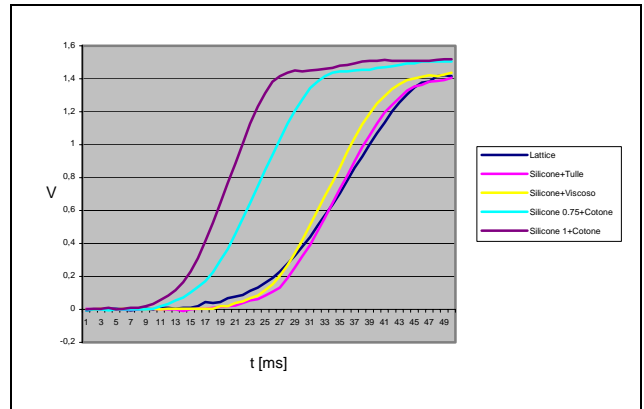


Figure 9. Step response tests for the different power diaphragms D_2

CONCLUSIONS

This paper presents the design and the construction of the power part of a 3/2 pneumatic valve that uses a low power pilot stage, based on laminar-turbulent transition of a fluidic jet. The valve can be used to drive a power stage of pneumatic circuits. The pilot stage uses an acoustic signal generated by a piezoelectric device to brake the laminar flow. The design of the power valve is presented. The prototype was constructed and tested. The results of the experimental tests has shown an interesting behaviour of the valve and confirm the design choices. Future work includes fatigue tests on the diaphragms D_1 and D_2 and on the complete valve.

REFERENCES

- Belforte, G., Eula, G., Ferraresi, C., Viktorov, V. and Visconte, C. 2000. Optimization of a laminar-turbulent amplifier for electro-pneumatic interface. Flucom 2000, Sherbrooke, Quebec.
- Belforte, G., Eula, G., Ferraresi, C., Viktorov, V. and Visconte, C. 2002. Integration of an electro-fluidic pilot stage in pneumatic valves. 3rd International Fluid Power Conference, Aachen.
- Belforte, G., Manuello Bertetto, A., Raparelli, T. 1995. Back pressure sensor for very high precision measurement. ISMCR '95, Smolenice Castle, Slovakia.
- Murrenhoff, H. 2002. Trends in valve development. 3rd International Fluid Power Conference, Aachen.
- International Standard ISO 6358 Pneumatic Fluid Power. Component using compressible fluids. Determination of flow-rate characteristics, 1989.
- International Standard ISO 12238 Pneumatic Fluid Power. Directional control valves. Measurement of shifting time, 2001.

Development of direct drive type pneumatic servo valve

Dong Soo Kim*, Won Hee Lee* and Beong Oh Choi*

* IT Machinery Research Center, Korea Institute of Machinery & Materials
171 Jang-Dong, Yuseong-Gu, Daejeon, Korea
(E-mail: kds671@kimm.re.kr)

ABSTRACT

In this study, firstly, we have modeled a system consisting of various electro-mechanical and mechanical subsystems. The appropriateness of the model has been verified by simulation. The simulation model resolves the motion of spool, the winding current and the magnetic force. Also, we have calculated the displacement and velocity of the spool, flux contour line, b vector, flux density, flux linkage and back EMF etc. Secondly, a program for analysis the flow in the spool was developed, and a study was conducted on the flow rate of the nozzle depending upon the pressure ratio between the upstream pressure and the downstream pressure, when the valve is fully open in the spool and the flow force depending upon a displacement of the spool in the valve. Further, the performance of pneumatic servo valve has been verified through an overall performance test on the developed product.

KEY WORDS

Servo Valve, Fluid Power, Servo Solenoid, Spool Commutation Mechanism, PWM

NOMENCLATURE

B_r : Residual magnetic flux density [T]
 B_g : Magnetic flux density at operating point
of permanent magnet [T]
 μ_r : Specific permeability of magnet
 P_d : Thickness of magnet [mm]
 g : Pore length [mm]
 n : Number of windings of coil
 P_H : Pressure at valve inlet [N/m^2]
 P_L : Pressure at valve outlet [N/m^2]
 \dot{m} : Mass flow rate of air passing through valve [kg/s]
 b : Critical pressure ratio
 R : Gas constant [N m/kg K]
 T_H : Temperature at valve inlet [$^{\circ}C$]
 A_e : Effective sectional area of valve [m^2]
 k : Specific heat ratio of air

1. INTRODUCTION

A pneumatic actuator provides a power of which the level stands between the power level of an electric actuator and a hydraulic actuator, and it is steadily used in the industry. The pneumatic servo system has a competitive power in the price aspect and its maintenance is simple. Also, its work environment is clean and its reliability is high. So, it has been applied to a manipulator and further recent new fields, such as a bio-machine, and the like. In these systems, a servo valve is a very important element to control the power [1]. In this study, a pneumatic servo valve was designed, and each simulation was conducted on any variation in the flow rate depending upon the magnetic force of the solenoid and the displacement of the spool. And ferromagnetic permanent magnet was used as a material for the plunger of the servo valve. Thereby, a low power consumption-type coil was designed, and a

modeling for the coil design was conducted by using the magnetic circuit. Also, the feasibility of the modeling was verified by using a commercial magnetic field analysis program. The designed and fabrication of spool and sleeve, position sensor, servo controller and the dynamic characteristic verified by the experiment.

2. DESIGN OF SERVO SOLENOID

2.1 Configuration and design specifications

A configuration of the servo valve developed in this study is as shown in Fig. 1. An actuating system of the servo valve comprises a solenoid having coil wound on a plastic bobbin, a yoke for preventing any leakage flux and a mover using a permanent magnet. As the permanent magnet used for the mover, a neodymium-series magnet (NdFe35) which is recently widely applied to various fields was used [2]. And, the permanent magnet was fixed to the right side and the left side, and a pure iron washer was made to cling to both sides to which the permanent magnet was to be fixed. In order to enhance the magnetic force, the washer was designed so that its outer diameter might be thicker than its inner diameter and further so that it might be built in the aluminum spool [3][4].

And, as a precision valve for controlling flow rate, this valve is basically operated with a 5/3 way structure, and the operating signal is in the range of 0~10 [V]. Specification of the servo valve to be developed is as shown in Table 1.

2.2 Design and modeling

Such modeling as shown in Fig. 2 was conducted for analysis of the solenoid of the servo valve. F_T [N/m], a total force acting between the solenoid and the permanent magnet is as shown in the following Eq. (1).

$$F_T = F_L + F_R \quad (1)$$

$$F_L = \ln B_g i, \quad F_R = \ln B_g i \times (-1) \quad (2)$$

Where, F_L and F_R are force acting on the right-hand coil and the left-hand coil respectively, which are as shown in Eq. (2). And the coil resistance and the number of windings are the same between both coils, and only the coil winding direction is opposite to each other. Where, l is an axial effective length of the coil, and i is the current flowing on the coil. And the voltage equation at the current coil of the solenoid is as shown in Eq. (3).

$$e = Ri + L \frac{di}{dt} + k_s \frac{dx}{dt} \quad (3)$$

Item	Specification	
Operating voltage	24 [V]	
Control voltage	0~10 [V]	
Current consumption	mid-position	0.05 [A]
	maximum	1.5 [A]
Turns per coil	260 [N]	
Diameter of coil	0.18 [mm]	
Resistance of coil	20 [Ω]	
Permanent Magnet	Series	NdFe35
	Residual flux density	1.23 [T]
	Size of magnet	O.D.: ϕ 15, I.D.: ϕ 4, Width: 6 [mm]
Stroke	\pm 1.3 [mm]	
Air gap	0.7 [mm]	
Supply pressure	6 [bar]	
Standart nominal flow rate	700 [l/min]	
Connections	1/8 [inch]	
Effective diameter	6 [mm]	
Diameter of spool	11 [mm]	

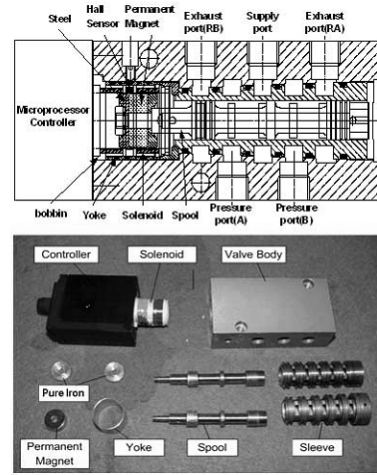


Fig. 1 The Developed of Servo valve

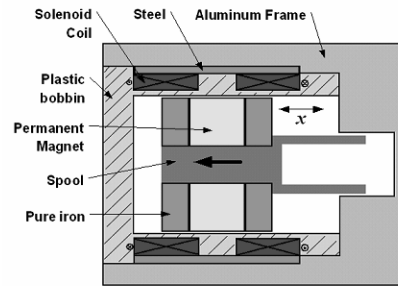


Fig. 2 Model of the servo valve (solenoid part)

In the above equation, the third term of the right-hand is a electromotive force caused by the motion of the permanent magnet, and the mechanical equation of motion is as shown in Eq. (4).

$$M \frac{d^2 x}{dt^2} = k_g i - Cd \frac{dx}{dt} \quad (4)$$

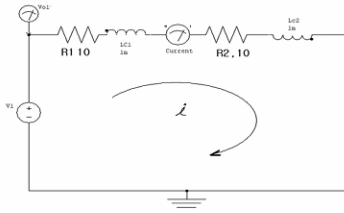


Fig. 3 Scheme of the solenoid circuit

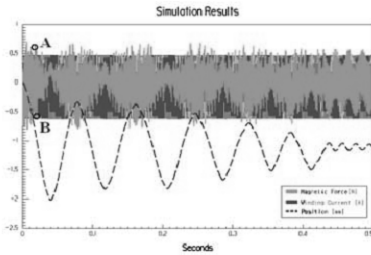


Fig. 4 Scheme of the solenoid circuit

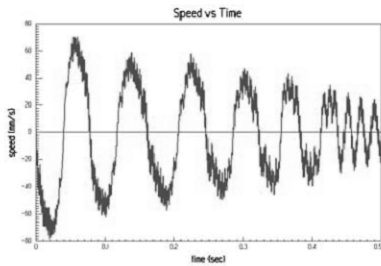


Fig. 5 Speed of spool

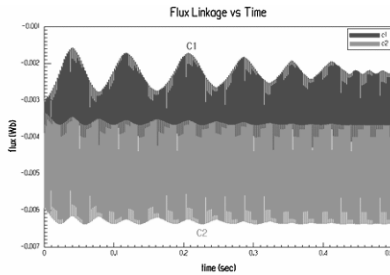


Fig. 6 Flux linkage of solenoid coil (C1, C2)

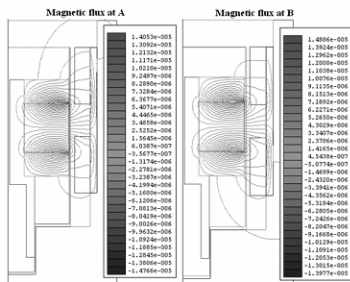


Fig. 7 Flux density diagram in A, B point of Fig. 4

The pore flux density caused by the permanent magnet, the mover at the solenoid of the servo valve is as shown in Eq. (5).

$$B_g = k \times \frac{B_r}{1 + \frac{\mu r}{P_d / g}} \quad (5)$$

2.3 Simulation

A simulation was conducted on the solenoid of the designed servo valve, and the internal electric circuit of the solenoid is as shown in Fig. 3. R1 and R2, the coil resistance are 10Ω respectively. And the supply voltage was applied at +/-12[V] by square wave with 35 kHz. Offset voltage was 1 volt. Also time step for simulation was 0.001 second, total time of simulation was 0.5 second. Therefore, simulation results are as shown in from Fig. 4 to Fig. 8. Fig. 4 is magnetic force, winding current, and position of spool and Fig. 5 is speed of spool. Maximum magnetic force is 0.8[N], winding current at normal state is 500[mA], and maximum velocity of spool is 80[mm/s]. And Fig. 6 is a flux linkage of solenoid coil. Lastly, Fig. 7 is a flux density diagram (A, B) when the magnetic force is positive and negative.

3. CHARECTERISTIC ANALYSIS OF SPOOL COMMUTATION MECHANISM

3.1 Analysis of flow rate in spool

Fig. 8 shows model of a spool and a sleeve. For analysis the flow in the spool of the pneumatic servo valve, the valve was considered as a general compressible nozzle flow, and the energy equation of the compressible fluid is as follows:

$$u_1 + \frac{P_1}{\rho_1} + \frac{V_1^2}{2} + gz_1 = u_2 + \frac{P_2}{\rho_2} + \frac{V_2^2}{2} + gz_2 - q + w \quad (6)$$

If any potential energy of the nozzle is ignored and any inflow of heat and work is not made from outside, defined as an ideal gas, the following equation is satisfied;

$$P = \rho RT, \quad k = \frac{C_p}{C_v}, \quad R = C_p - C_v \quad (7)$$

If the above ideal gas equation and the above isentropic equality are applied to the energy equation, the result is as follows;

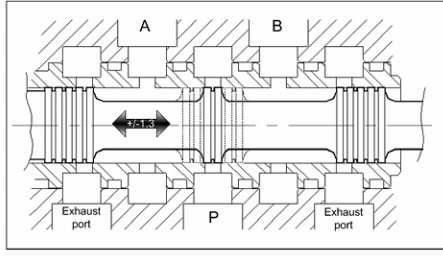


Figure 8. Model of servo valve (spool and sleeve parts)

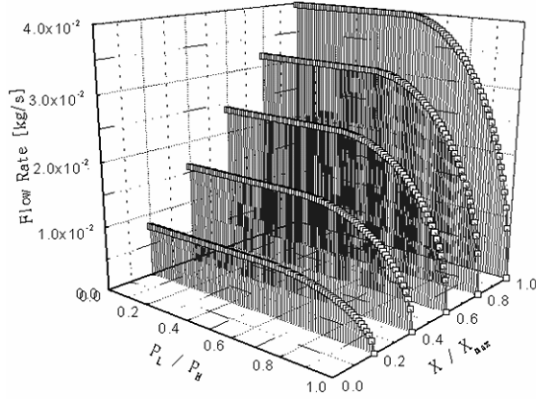


Fig. 9 Relations of flow rate to pressure ratio and full opened ratio.

$$V_2^2 = \left(\frac{2k}{k-1} \right) \frac{P_1}{\rho_1} \left[1 - \left(\frac{P_2}{P_1} \right)^{k-1/k} \right] \quad (8)$$

Where, if $z = p_2/p_1$ is defined, the mass flow rate passing through the nozzle is as shown in Eq. (9).

$$\begin{aligned} \dot{m} &= \frac{P_1}{RT_1} \sqrt{\left(\frac{2k}{k-1} \right)} (RT) \left(z^{2/k} - z^{k+1/k} \right) \\ &= \frac{A_{12} P_1}{\sqrt{T_1}} \sqrt{\left(\frac{2k}{k-1} \right) \frac{1}{R} \left(z^{2/k} - z^{k+1/k} \right)} \end{aligned} \quad (9)$$

And, at a given nozzle area, a maximum mass flow rate depending upon a total pressure and a temperature exists, wherein, the value of the pressure ratio (z) is referred to as the critical pressure ratio. This is a relational equation of the mass flow rate of the compressible air passing through the valve nozzle, applying Anderson's experimental method, and the critical pressure ratio of the valve is shown as follows;

$$\dot{m} = \dot{m}_c f(z) \quad (11)$$

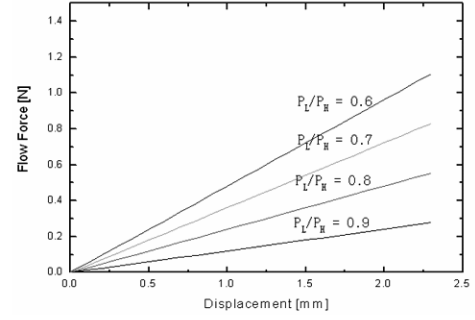


Fig. 10 Relation of flow force to displacement at various pressure ratios

$$f(z) = \begin{cases} 1 / \sqrt{\left(1 - \left(\frac{z-b}{1-b} \right)^2 \right)} & z \leq b \\ & z > b \end{cases} \quad (12)$$

$$z = \frac{P_L}{P_H}$$

$$\dot{m}_c = \left(\left(\frac{2}{k+1} \right)^{\frac{k+1}{k-1}} \cdot \frac{k}{R} \right)^{1/2} \cdot A_v \frac{P_H}{\sqrt{T_H}} \quad (13)$$

Fig. 9 shows the flow rate of the nozzle depending upon the opening ratio of the valve in the spool and the pressure ratio between the upstream pressure and the downstream pressure [5].

3.2 Flow Force on Spool

Bernoulli's equation is applied under the assumption of the compressible and non-viscous flow, the jet velocity (U) at vena contractor (The point at which the flow area reaches its minimum is called Vena Contractor) of the nozzle is as follows;

$$U = \sqrt{(2\Delta P) / \rho} \quad (14)$$

$$F_{AB} = F_{fz} - F_{h1} = QU \rho \cos \theta \quad (15)$$

The net axial force, F_{AB} is as shown in Eq. (14). In the above equation, if C_v (discharge coefficient) of the nozzle flow is applied, the result is as shown in Eq. (15). If the flow force against the axial length is shown under the following condition, it is as shown in Fig. 10.

$$\begin{aligned} F_{AB} &= SC_v \omega z \Delta P \cos \theta \\ &= \rho \frac{Q^2}{\omega z C_v} \cos \theta \end{aligned} \quad (15)$$

Where,

$$C_v = \frac{Q}{\omega z \sqrt{(2\Delta p) / \rho}}$$

ω = Peripheral width of nozzle
 x = Axial length of nozzle
 z = Diagonal length of nozzle
 $(\sqrt{x^2 + C_v^2})$

4. DESIGN OF MICROPROCESSOR CONTROLLER

As described in Fig. 11, this system is an apparatus to enable an amount of the fluid flowing in the pneumatic cylinder to be controlled linearly in proportion to the magnitude of the reference signal to be inputted from outside. Wherein, it is necessary to build up a closed loop system that can detect a difference between the reference signal and the actual response of the control system and further control by such difference value consecutively in order to control the flow rate so that it may be in conformity with the reference signal inputted from outside.

4.1 Detection of a position

Any adjustment of the flow rate of the pneumatic servo valve is made by controlling a position of the spool located in the valve. A hall sensor was used for detecting a position of the spool, and Fig. 12 is a schematic view of the position detection system

4.2 Control method

The opening amount of the pneumatic servo valve is determined by the electromagnetic force acting between the solenoid coil and the plunger. The electromagnetic force on the solenoid is in proportion

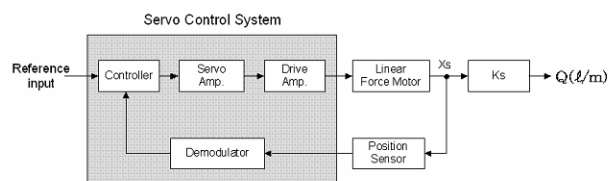


Fig. 11 Scheme of control block

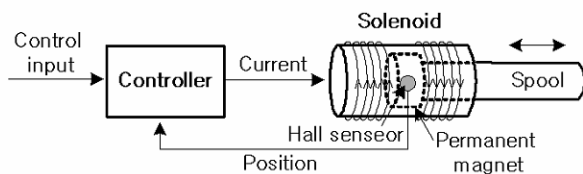


Fig. 12 Scheme of position detection system

to the current applied to the coil and the number of windings. Wherein, as the number of windings and the coil resistance are fixed, the current amount can be controlled by the input voltage. Therefore, in this study, the PWM (pulse width modulation) method was used as a method for controlling any voltage. The offset voltage variation method was used as a method for controlling the voltage against the control input, and the PWM control method of high frequency was used for controlling any displacement of the spool caused by pneumatics or other disturbance rapidly and precisely [6][7].

5. PERFORMANCE TEST

5.1 Design of performance tester

In this study, in order to develop the technology for evaluating the overall performance and reliability of the pneumatic servo valve, the following tester was directly designed and manufactured, and Fig. 13 show the developed overall performance tester. First, the performance tester as shown in Fig. 13(left) was designed and manufactured so that the performance test might be conducted on the servo valve by using a low-friction high-speed cylinder. Then, an air filter, a flow rate sensor, a pressure sensor, a temperature sensor, a displacement sensor and a velocity sensor were fixed to it, and for a dynamic characteristic test on the servo valve, a length of the pipe connecting between the valve and the actuator was designed so that it might be the shortest.

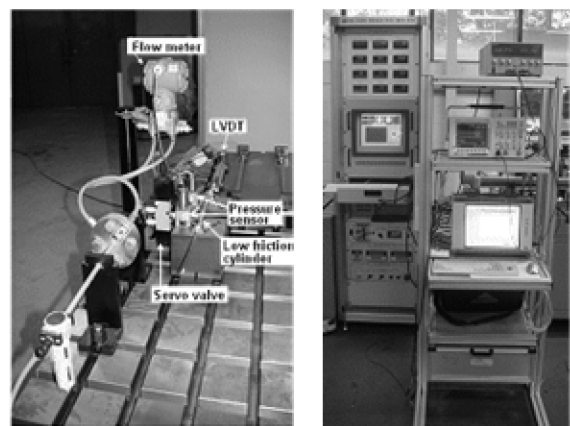


Fig. 13 Pneumatic servo valve performance tester

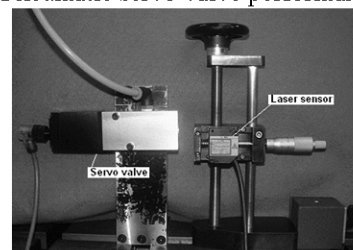


Fig. 14 Dynamic characteristic tester

And the controller for conducting the performance test comprises an indicator and a PC system for control enabling data from each sensor to be converted and real-time processed. The PC system for control is driven by the software dedicated to the dynamic characteristic test on the servo valve as developed in this study, having a function generating function, a noise filtering function and various signals processing function including real-time FFT. Also, as an interface device between sensors and the PC system for control, the NI-DAQ board having a signal conditioner built instrument for measuring each displacement of the therein was used, and thereby, the reliability of the experimental data was enhanced. Fig. 14 shows a spool of the servo valve directly by using a laser displacement sensor. In the case of the pneumatic servo valve, unlike a hydraulic servo valve, when a displacement of the cylinder is measured by using a general cylinder, the dynamic characteristic of the servo valve cannot be exactly measured due to compressibility of the working fluid. Therefore, in this study, a method for measuring the spool's displacement directly was used in order to avoid such problem.

5.2 Flow rate and pressure test

This test is the maximum outward flow rate test on the servo valve, and in order to test an outward flow rate depending upon the supply pressure, the supply pressure is first set. Then, the outward flow rate depending upon a change in the spool's position is measured by applying the control input to the servo valve at 0~10 [V].

As a result of conducting such tests, it could be identified that the outward flow rate of the servo valve met 700[l/min], the target value for development, and further that the pressure also met 0~10 bar, the target value for development.

As a result of conducting the flow rate test and the pressure test on the 1st pilot model, it was identified that the blind zone of the neutral point was great. When designing the 2nd pilot model, in order to reduce such blind zone, the range of the neutral point regime of the spool was reduced so that the blind zone could be reduced in the 2nd pilot model.

5.3 Dynamic characteristic test

A test to identify dynamic characteristics of the developed pneumatic servo valve was conducted in several ways, but there was a difficulty resulting from the time delay problem caused by the basic compressibility of air. In this study, in order to solve the time delay problem, a displacement of the servo valve spool was directly measured by using a laser sensor, and thereby the problem could be solved. As experimental conditions, the supply pressure was 6 bar, the flow rate was 700ℓ/min and a sine wave was used for a control input. Also, an experiment was conducted

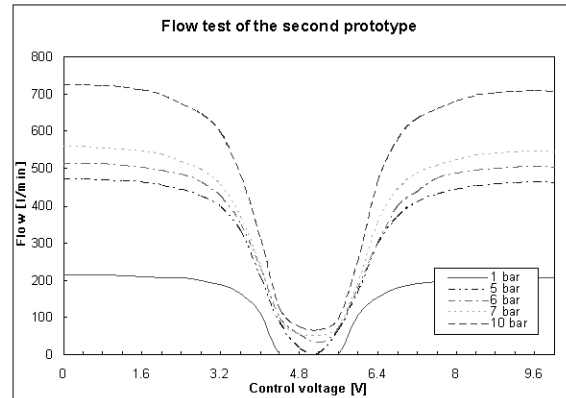


Fig. 15 Results of flow rate test on 2nd pilot model

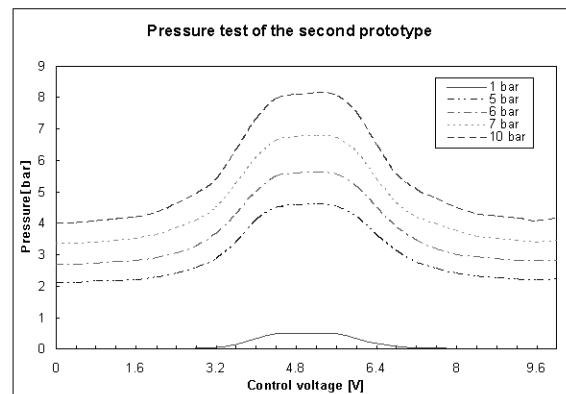


Fig. 16 Results of pressure test on 2nd pilot model

on a gain and a phase delay when the sine wave input signal was used as the 80% input of the experimental rated input signal of the valve and the frequency was varied in the range of 1Hz~100Hz. And, as a result of conducting the dynamic characteristic test by respective frequencies, the gain and the phase delay were shown in the frequency response graph as shown in Fig. 17.

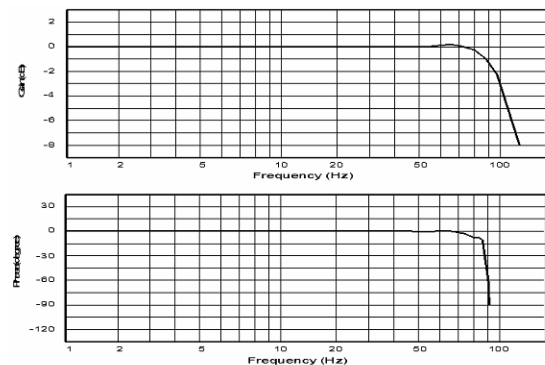


Fig. 17 Frequency response for gain and phase

6. CONCLUSION

In this study, the pneumatic servo valve was developed, and the study results could be summarized as follows;

1. A servo solenoid was designed, and its electromagnetic field was interpreted and the system's transient response was identified by using a commercial analysis program.
2. A program for analysis the flow in the spool was developed, and a study was conducted on the flow rate of the nozzle depending upon the pressure ratio between the upstream pressure and the downstream pressure, when the valve is fully opened in the spool and the flow force depending upon a displacement of the spool in the valve.
3. A PWM analogue controller was designed and manufactured in order to actuate the servo solenoid and further control a position of the spool by using a hall sensor.
4. In order to solve the time delay problem in dynamic characteristic test, a displacement of the servo valve spool was directly measured by using a laser sensor, and thereby the problem could be solved.

ACKNOWLEDGEMENTS

This study has been performed under the support program for the project for "development of direct drive type pneumatic servo valve of a 100Hz" or lower sponsored by Ministry of Commerce, Industry and Energy. We thank all concerned persons for such support.

REFERENCES

1. S. H. Choi, A Study on analysis and design of a poppet type electro pneumatic servo valve," KAIST, 2000.
2. Yoon Seok-Gil, "Rare Earth Material for Permanent Magnet and Application thereof," UUP, 1999.
3. W.J. Duffin, "Electricity and magnetism," McGraw-Hill, p162-193, 1990.
4. John D. Kraus, "Electromagnetic," McGraw-Hill, Third edition, 1984.
5. Anderson, "The Analysis and Design of Pneumatic System," 1967.
6. N. Ye, S. Scavarda, M. Betemps and A. Jutard, "Models of a pneumatic PWM solenoid valve for engineering applications," Transactions of the ASME, Vol. 114, p680-688, 1992.
7. K. Ichiryu, H. Tamura, and S. Kogarashi, "Development of linear motor servo valve," Fluid Power, Third JHPS, p391-396, 1996.

Computation analysis and optimal design of a high speed response and low power micro valve

Dong Soo Kim*, Sang Woon Park*, Hyun Sub Kim* and Jae Sub Yoo*

* IT Machinery Research Center, Korea Institute of Machinery & Materials
171 Jang-Dong, Yuseong-Gu, Daejeon, Korea
(E-mail: kds671@kimm.re.kr)

ABSTRACT

This study was conducted to analyze the special quality of a very low power consumption type of pneumatic on-off micro valve, and to numerically investigate its flow characteristic depending upon a change in stroke. As a result, it was identified that an enough electromagnetic force (2.4N) acted on the solenoid so that the poppet of the micro valve might run a stroke (0.3 mm) at the high response speed (5ms), and that the yoke caused no magnetic force to be emitted. It was identified that the dynamic pressure acting on the poppet wall was little reduced when the poppet stroke was 0.4 mm or less, but that as it got to be beyond 0.4 mm, it was remarkably reduced and when it was 0.8 mm, it went down to 40%.

KEY WORDS

Micro valve, Poppet, Solenoid, Plunger, Stationary core

NOMENCLATURE

F : magnetic force
 B_g : magnetic flux density
 S : section area of a plunger
 m : number of coil layers
 N : number of coil turns
 h : coil height
 μ_0 : magnetic permeability
 ρ : flow resistivity
 ξ : space factor
 d : coil diameter
 λ : coil height

1. INTRODUCTION

A remarkable development in computer and control technologies enables users to control a micro valve precisely, and so it is widely applied to various fields such as semiconductor chip mounter, production line of electronic products, automatic feeding line of bearing, injection molding machine, fatigue and vibration tester, and so on. It has been recently highlighted as a key technology in development of a technology-intensive process in the semiconductor industry and the like.

The micro valve has an excellent high-speed and repetitive operability, and makes a pressure act on a dynamic area of the poppet uniformly and shows the high responsiveness irrespective of a change in the pressure applied to the port.

The purpose of this study is to design and analyze a very low power consumption type of pneumatic on-off micro valve which has the characteristics of high

responsiveness and very low power consumption. Thereby, this study is to verify its performance. We analyzed a magnetic field of the solenoid and a flow of the poppet by using commercial software (Maxwell and Fluent). As a result, we could verify the performance of the designed micro valve. We plan to ensure optimum design data through future experiments

2. DESIGN OF MICRO VALVE

2.1 Composition and Operation Principle of Micro Valve

Fig. 1 shows the schematic diagram of the micro valve. The micro valve comprises a poppet valve, a plunger, a stationary core and a spring for controlling the direction of compressed air, and an O-ring and a gasket for intercepting any leakage, and others.

The operation principle of the micro valve is as follows: When the solenoid is electrified, a magnetic force forces the poppet valve to move forward, and thereby, the compressed air flows into a pressure port through a supply port. When the solenoid is not electrified, a spring force forces the poppet valve to move back and thereby, a supply port gets to be closed and the compressed air is exhausted out of an exhaust port. Thereby, it reciprocates at a high speed.

2.2 Design Specifications of Micro Valve

Table 1 shows the design specifications and specifications for performance of the micro valve. Specifications for performance are 24VDC in supply power and 3 mm in diameter.

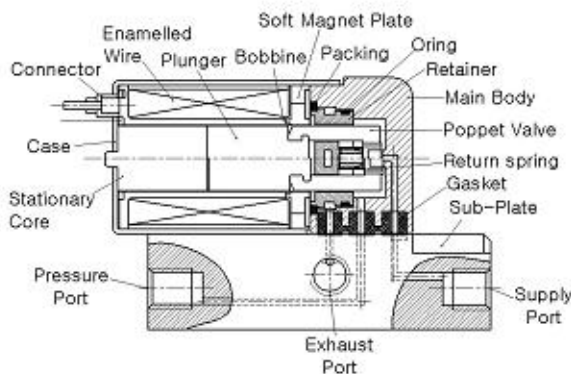


Fig. 1. Schematic Diagram of Micro Valve

Table 1. Design Specifications

Item	Value	Unit
Supply Pressure	3	bar
Supply Voltage	24	V
Electric Power	0.3	W
Port	3	mm
Stroke	0.3	mm
Coil Turn Number	6,200	turn
Coil Diameter	0.04	mm
Coil Resistance	1.5	kΩ
Effective Area	0.19	mm ²
Flow coefficient	0.01	-
Response Time	10	ms
Temperature Rise Value	50	°C
Magnetic Force	2.4	N
Spring Constant	0.015	N/mm

Design specifications are 0.3W, responsiveness of 10ms or less, compactness of 7 mm in thickness, and low noise of 40dB or below. It is, therefore, characteristically used for the medical purpose.

3. ANALYSIS OF MAGNETIC FIELD OF ON-OFF SOLENOID

3.1 Design Theory of Solenoid

The key technologies of the micro valve as designed and manufactured are classified into the solenoid technology and the poppet technology. In the case of the solenoid technology, analysis of the magnetic field is important. The magnetic force (F) generated by the solenoid is represented by Equation (1).⁴⁾

$$F = \frac{B_r^2 S}{2\mu_0} = \frac{10^7}{8\pi} B_r^2 S \quad [N] \quad (1)$$

Where in, B_r is the magnetic flux density brought about by a permanent magnet and μ_0 is the magnetic permeability. If S, a section area of the plunger is obtained from Equation (1), it is induced by Equation (2):

$$S = \frac{8\pi \times 10^7 \cdot F}{B_r^2} \quad [m^2] \quad (2)$$

The radius of the plunger is represented by $r_1 = \sqrt{(2\mu_0 F) / \pi B_p^2}$ and the magneto motive force (U) is induced by Equation (3).

$$U = NI = \frac{B l_v}{\mu_0} + \sum H l_i \quad [A] \quad (3)$$

Then, h and T, which determine a coil space, are determined by Equation (4) as represented by θ_v and which are values by θ_f which the temperature is increased.

$$\begin{aligned} \theta_v &= (I^2 R) / (2\lambda l_\pi h) \quad [^\circ C] \\ \theta_f &= (q\rho / 2\lambda\xi T) \cdot (NI / h)^2 \quad [^\circ C] \end{aligned} \quad (4)$$

Wherein, θ_v is the value by which the final temperature is increased, and θ_f is the value by which a continuous specific temperature is increased, and T is the coil width (h / β).

If h (coil height) is obtained from Equation (4), it is induced by Equation (5):

$$h = \sqrt[3]{\frac{q\beta\rho U^2}{2\lambda\xi\theta_f}} \quad (5)$$

Wherein, q is the rated time, ρ is the flow resistivity, λ is the heat dissipation coefficient of the coil, and ξ is the space factor of winding

Then, the inner diameter/outer diameter (r_1', r_2') of the coil should be determined. The inner diameter (r_1') is determined by the outer diameter of the plunger + the coil polarity + the bobbin thickness. From $r_2' + r_1' + T$ and $V = IR$, the voltage expression, Equation (6) is induced:

$$V = \frac{4\rho(r_1' + r_2')NI}{d^2} \quad [V] \quad (6)$$

Therefore, the coil diameter (d) can be obtained as in Equation (7).

$$d = \sqrt[3]{4\rho(r_1' + r_2') \frac{NI}{V}} \quad [mm] \quad (7)$$

Accordingly, the number of coil layers is determined by $m = T / d$, and the number of windings is determined by $N = ((h / d) - 1)m$.

For an increase in temperature, the exciting current (I_a) should be obtained in the first place. The mean length (l_π) and full length (l_f) of the coil are as in Equation (8).

$$l_\pi = \pi(2r_1 + T), \quad l_f = M_\pi \quad (8)$$

Coil resistance (20°C) = $l_f \times$ resistance coefficient,
Coil resistance (100°C) = $1.314 \times R_c$; Exciting current (I_a) = V / R_{th} ; and magneto motive force (U) = NI_b . Therefore, an increase in the temperature is determined by θ_f .

3.2 Solenoid Modeling and Result of Analysis thereof

In order to analyze the solenoid part of the micro valve, the solenoid is modeled as shown in Fig. 2. The analysis results including the response characteristic of the micro valve depending upon the solenoid are shown in Figs. 2~ 5.

As can be known from Figs. 2~ 9, it can be known that an enough electromagnetic force (2.4N) is working so that a displacement (0.3 mm) in which the micro valve moves may take place. They show characteristics of the high-speed position responsiveness and the speed responsiveness.

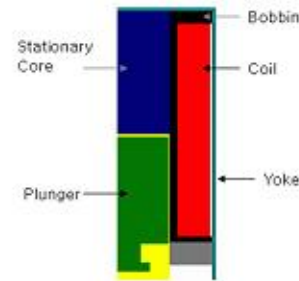


Fig. 2 Modeling of Solenoid

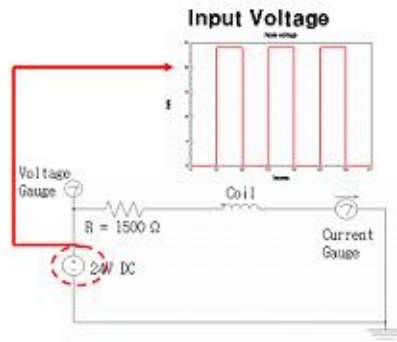


Fig. 3 Schematic Diagram of Solenoid Circuits

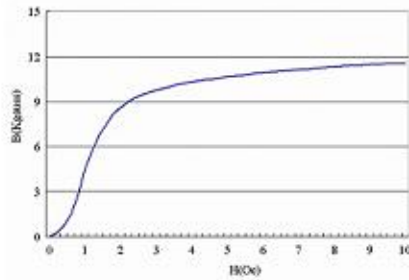


Fig. 4 B-H Curve of Material

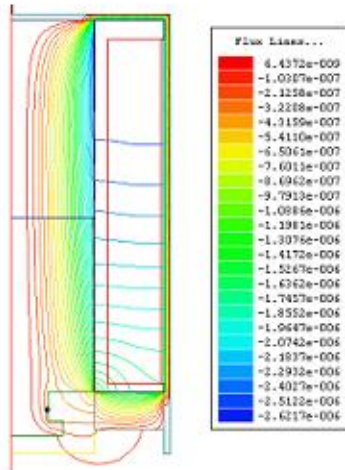


Fig. 5 Flux Contour of Solenoid

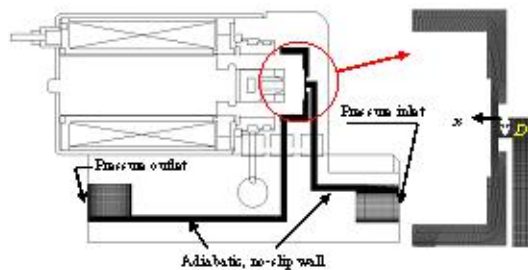


Fig. 6 Schematic diagram and grid system used in numerical computation

4. NUMERICAL ANALYSIS OF THE FLOW FIELD OF THE POPPET

4.1 Calculation Area and Boundary Conditions

In order to grasp the flow field characteristic in the micro valve, the flow field of the poppet was analyzed by changing the pressure ratio between upstream and downstream in the flow field and the poppet stroke. Fig. 6 shows the calculation area and the grid system used in numerical computation. Air (the ratio of specific heat is 1.4) was used as an operating fluid in numerical computation. Pressure inlet conditions were applied to the inlet boundary, pressure output conditions were applied to the outlet boundary, and adiabatic no-slip conditions were applied to the wall. The upstream supply pressure (P_0) was fixed at 0.3MPa and the outlet pressure (P_b) was set at the atmospheric pressure. Then the flow field of the poppet was numerically analyzed by changing the dimensionless length to 0.2, 0.4, 0.6 and 0.8 in 4 phases with respect to the maximum stroke of the poppet. The range of the poppet stroke displacement is $0 \leq x \leq 0.438$.

The alignment grid system was used in numerical computation and it generated about 40,000 node points. Also, in order to simulate properly development of boundary layers by viscosity on the wall and the flow field in the minimum area, grids were concentrated on the wall and the minimum sectional area.

4.2 Dominant Equation

In numerical computation, compressive Navier-Stokes equations as follows were used. In order to simulate properly the effect of turbulence on the flow field in the micro valve, a standard $k-\varepsilon$ turbulent model was used, which was an eddy viscosity model using the Boussinesq hypothesis¹²⁾.

$$\frac{\partial \rho}{\partial t} + \frac{\partial (\rho u_i)}{\partial x_i} \quad (9)$$

$$\frac{\partial}{\partial t} (\rho u_i) + \frac{\partial}{\partial x_j} (\rho u_i u_j) = \frac{\partial}{\partial x_j} \mu \left(\frac{\partial u_i}{\partial x_j} + \frac{\partial u_j}{\partial x_i} \right) - \frac{\partial}{\partial x_i} \left(\frac{2}{3} \mu \frac{\partial u_i}{\partial x_i} \right) - \frac{\partial p}{\partial x_i} + \frac{\partial}{\partial x_j} (-\rho \overline{u_i u_j}) \quad (10)$$

Equations (9), (10), and (11) were made to be discrete by FVM (finite volume method). The upwind scheme was applied to the space term and the 4-phase Runge-Kutta method was applied to the time term. For convergence determination of a solution, a residual difference in each state quantity was set at 10^{-4} . We investigated the change of the mass flow at the inlet

and outlet of the flow field and then the condition in which the sum of the mass flow was 0.3% or less was set as the convergence condition.¹⁾

$$\frac{\partial}{\partial x}(\rho E) + \frac{\partial}{\partial x_i}(\rho u_i H) = \frac{\partial}{\partial x_i} \left[\left(x + \frac{\mu_i}{Pr_i} \frac{\partial T}{\partial x_i} + u_i (\tau_{ij})_{eff} \right) \right] \quad (11)$$

4.3 Result and Review of Numerical Analysis

Fig. 7 shows the velocity vector and the Mach number at the point in which the poppet strokes against the maximum displacement of the poppet is 0.2. At the point that the sectional area gets to be minimum as the poppet approaches to the flow outlet, fluid passes through the flow channel with it being accelerated at the supersonic speed. Also, it can be identified that the flow is separated in the lower end of the poppet so that a vortex flow is formed.

Fig. 8 shows the dynamic pressure distribution along the poppet wall. The horizontal axis indicates the position along the poppet wall in a red dotted line to the upper-left part of the graph and the longitudinal axis indicates the dynamic pressure which represents the supply pressure at the dimensionless length.^{2,3)} A high distribution of the dynamic pressure is shown in the center of the poppet wall due to the effect of the air as emitted out of a narrow pipeline in the inlet, and it tends to be rapidly reduced beyond the minimum sectional area. Considering the change of dynamic pressure depending upon the poppet stroke, the dynamic pressure is little reduced and a similar value is maintained until x/D gets to be 0.4, while it is rapidly reduced after x/D gets to be 0.6. It can be, therefore, known that when x/D gets to be far, upto 0.8, only 40% of a peak of the dynamic pressure at the initial position acts on the poppet wall.

Fig. 9 shows the velocity vector inside the flow field as obtained by three-dimensional analysis. The incoming fluid from the inlet gets to be accelerated through a narrow pipeline so that as a flow thereof is formed around the poppet, it gets to be spouted to the outlet of the flow field. It can be known that the flow rate is accelerated again as the fluid gets out of the lower end of the poppet and goes down through a pipe of which the sectional area is narrow.

Fig. 10 shows the turbulence intensity inside the flow field. The expected result of the turbulence intensity and the distribution thereof inside the flow field can be identified in it. Also, it can be known that the closer the flow goes to the outlet, the greater the turbulence intensity increases, and particularly that a strong turbulence intensity is shown in the point where the flow is turned.

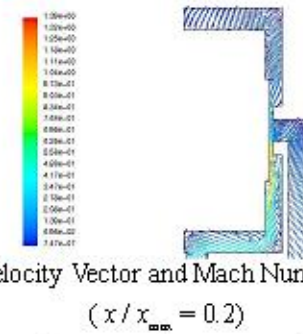


Fig. 7 Velocity Vector and Mach Number (color)
($x/x_{max} = 0.2$)

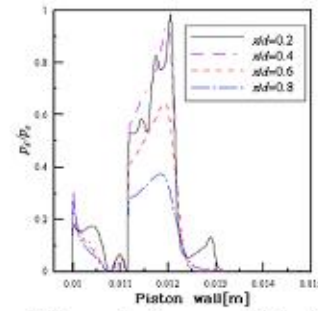


Fig. 8 Dynamic Pressure Distribution along the Poppet

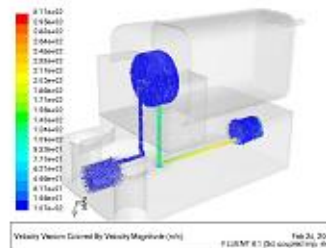


Fig. 9 Valve Interior Flow Chapter Velocity Vector

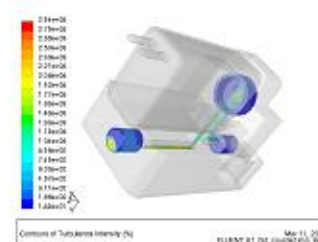


Fig. 10 Turbulence Intensity of Flow Field



Fig. 11 Micro Valve Parts

5. TEST ON MICRO VALVE

Fig. 11 shows components of the micro valve and Fig. 12 shows a performance test device for the micro valve. In order to measure the flow capacity of the developed micro valve, it was tested by opening it with the

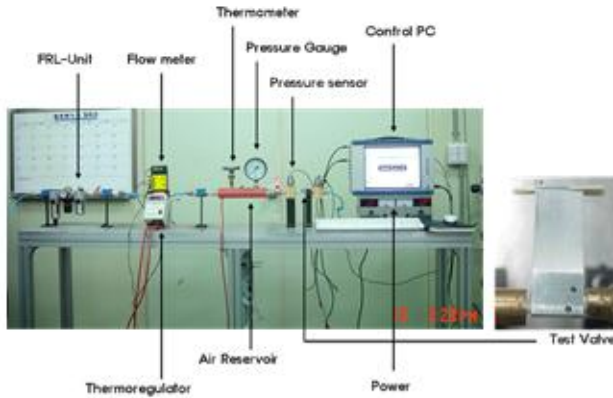


Fig. 12 Performance Test Device

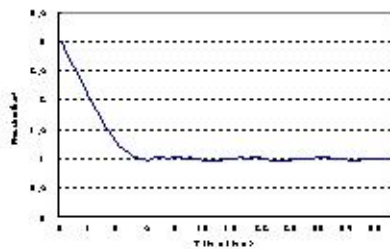


Fig. 13 Flow Coefficient Test

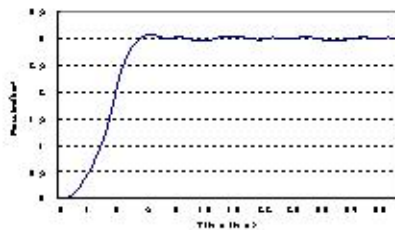


Fig. 14 Response Test

operating pressure set at 3 kg/cm^2 until the operating pressure gets to be 1 kg/cm^2 . The result is shown in Fig.13. Also, in order to measure the response characteristic of the micro valve, it was tested by applying voltage to the valve so that it may be on from off until the operating pressure gets to be 3 kg/cm^2 from 0 kg/cm^2 . The result is shown in Fig. 14. As can be known from the test results, it was identified that the flow capacity coefficient (C_v) of the developed micro valve was 0.01 and the dynamic response time was 5msec (at 3bar).

6. CONCLUSION

In this study, the performance of the micro valve was evaluated through analysis of the characteristics of the very low power consumption type of pneumatic on-off micro valve and test thereof, and thereby, the following results were obtained;

1. It was identified that an enough electromagnetic

force (2.4N) acted on the solenoid so that the poppet of the micro valve might run a stroke (0.3 mm) at the high response speed (5ms), and that the yoke caused no magnetic force to be emitted.

2. The characteristics inside the flow field depending upon a change of the poppet stroke were numerically analyzed. As a result, the velocity vector field and the pressure field inside the micro valve were properly simulated. Also, it was identified that the dynamic pressure acting on the poppet wall was little reduced when the poppet stroke was 0.4 mm or less, but that as it got to be beyond 0.4 mm, it was remarkably reduced and when it was 0.8 mm, it went down to 40%. This means that the flow capacity coefficient indicating the effective sectional area of the micro valve is 0.01.

3. The micro valve was manufactured and further tested in order to verify its performance by using a performance test device. The test results showed the winding current (16mA), the electric power (0.3W), the flow capacity coefficient (0.01), the effective area (0.19 mm^2), and response time(5ms). The performance test and the analysis thereof demonstrated that the optimum design of the micro valve was feasible.

ACKNOWLEDGEMENTS

This study was performed under the program of "Development of a Very Low Power Consumption Type of Micro Valve" sponsored by the Ministry of Commerce, Industry and Energy. We thank all persons concerned from the bottom of our heart.

REFERENCE

1. B. W. Andersen, "The Analysis and Design of Pneumatic Systems", John Wiley & Son Inc., pp. 48~61, 1967.
2. W. L. Green, "The Poppet Valve-Flow Force Compensation," Proceedings of Fluid Power International conference, pp. S1-S6, 1970.
3. K. Kakano, H. Watanabe and G. Mao-ving, "Experimental Study for the Compensation of Axial Flow Force in a Spool Valve", Journal of the Japan Fluid Power System Society, Vol. 18, No. 6, pp. 475~482, 2000.
4. 中田 高儀, "有限尿素法による 交直電磁石の設計と應用", 森北出版株式会社, pp. 63~90, 1991.

STUDY ON IMPROVEMENT OF THE SUCTION VALVE OF A COMPRESSOR FOR AN AUTOMOTIVE AIR-CONDITIONER

Taizo SATO*, Tetsuhiro TSUKIJI**, Yoshihito MATSUMURA* and Eitaro KOYABU**

* FACE Center, R & D Division, SANDEN CORPORATION, Japan
20 Kotobuki-cho, Isesaki-shi, Gunma, 372-8502 Japan
(E-mail: satou_taizou@sanden.co.jp)

** Department of Mechanical Engineering,
Sophia University, Japan
7-1 Kioi-cho, Chiyoda-ku, Tokyo, 102-8554 Japan

ABSTRACT

The simplified test model of the commercial reciprocating compressor for an automotive air-conditioner is used to measure the displacement of the suction valves using a strain gauge and to investigate the velocity distributions of the discharge flow from the valves using the particle image velocimetry system. This paper is focused on the effects of shape of the suction valve on the vibration-reduction. The size of the suction valve hole and the width of the tip of the suction valve are changed as main parameters of the valve shape. First, the size of the conventional valve hole and the width of the tip of the conventional valve are changed and seven new valves are manufactured to reduce the vibration of the valve. Next, the influence of the natural frequency on the vibration-reduction is investigated using one shape of the new valves by changing the material and the thickness of the valve. Finally, the reason of the vibration-reduction for one shape of the new valves is discussed from the results of the flow analysis around the valve. The vibration-reduction for one of the new valve is confirmed by measurement of the displacement of the valve in the reciprocating compressor.

KEY WORDS

Key words, Flow Visualization, PIV, Vibration, Suction Valve, Compressor, Automotive Air-conditioner

INTRODUCTION

The noise is usually caused from the evaporator for an automotive air-conditioner because the evaporator resonates with the pressure-pulsation in the commercial reciprocating compressor. Therefore the decrease of the pressure-pulsation is one of the important problems in the reciprocating compressor for the automotive air-conditioner. Tsukiji et al. [1] found through the

previous studies that the vibration of the suction valve affects the pressure-pulsation. Sato et al. [2,3] conducted the flow visualization of the discharge flow from the suction valve using the commercial compressor, which is improved to observe inside it under the actual condition. Chung et al. [4] and Myung et al. [5] investigated only the flow analysis around the suction valve using PIV system with the test facility for the flow visualization. On the other hand, Ishii et al. [6] and En et al. [7] performed only the measurement of the vibration using

the strain gauge for the suction valve. Despite the above-mentioned studies, it is not done about the reduction of valve vibration.

This paper is focused on the effects of shape of the suction valve on the vibration-reduction. The size of the suction valve hole and the width of the tip of the suction valve are changed as main parameters of the valve shape. First, this paper describes the relevant fundamental studies employing a cylinder with one suction valve on the valve plate as a test model instead of the reciprocating compressor for the automotive air-conditioner. The test model was designed to measure the displacement of the suction valve and to visualize the discharge flow from the suction valve inside the cylinder. The valve vibrations of the conventional valve and the improved valve were measured using a strain gauge. On the other hand the measurement of the velocity distributions was performed to analyze the flow field around the suction valve using the PIV(Particle image velocimetry) system. Next, the size of the conventional valve hole and the width of the tip of the conventional valve are changed and seven new valves are manufactured to reduce the vibration of the valve. Consequently, it is found that one shape of the new valves is the most effective for the vibration reduction. Next, the influence of the natural frequency on the vibration-reduction is investigated using one shape of the new valves by changing the material and the thickness of the valve. Finally, the reason of the vibration-reduction for one of the new valves is discussed from the results of the flow analysis around the valve. The vibration reduction for one of the new valves is confirmed by measurement of the displacement of the valve in the reciprocating compressor for the automotive air-conditioner.

TEST APPARATUS

Experimental set up

The schematic layout of the test model designed in this study is shown in Fig.1. An air as a working fluid is compressed using the air compressor and the inlet pressure is kept constant to reduce the pressure from the compressor with the pressure-reducing valve. The solenoid valve is used to stop or flow the air. The pressure difference between the upstream and the downstream parts of the suction valve is set with the differential pressure sensor. Moreover, the inlet pressure and the differential one are measured by the pressure transducer.

The test model is shown in Fig.2. In the figure, the right-hand side of the figure is the upstream direction, and left-hand side is the downstream direction. The valve plate, the suction valve and the cylinder are arranged in the test model. A commercial reciprocating compressor for an automotive air conditioner has usually seven cylinders. However one cylinder was used to simplify the

experimental device in our experiments. The cylinder made of acrylic resin was designed to visualize the flow around the valve inside the cylinder. The diameters of the suction port and the cylinder, and the depth of the valve stopper are same as a commercial reciprocating compressor for an automotive air-conditioner. The diameter of the suction port is 9 mm in order to make the same influence of the suction port on the vibration of the suction valve and the flow around the valve. In our experiments the air is used instead of refrigerant to visualize the flow clearly in the valve.

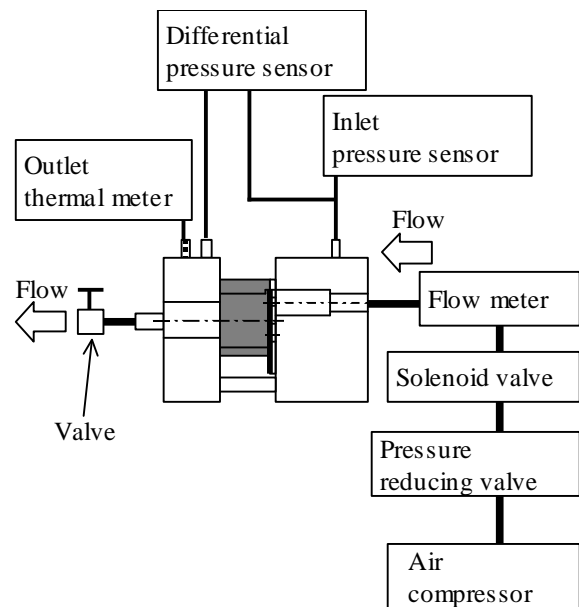


Figure 1 Experimental apparatus

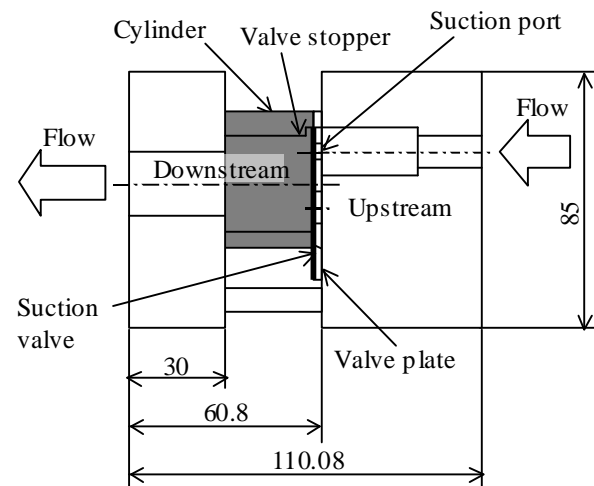


Figure 2 Test model

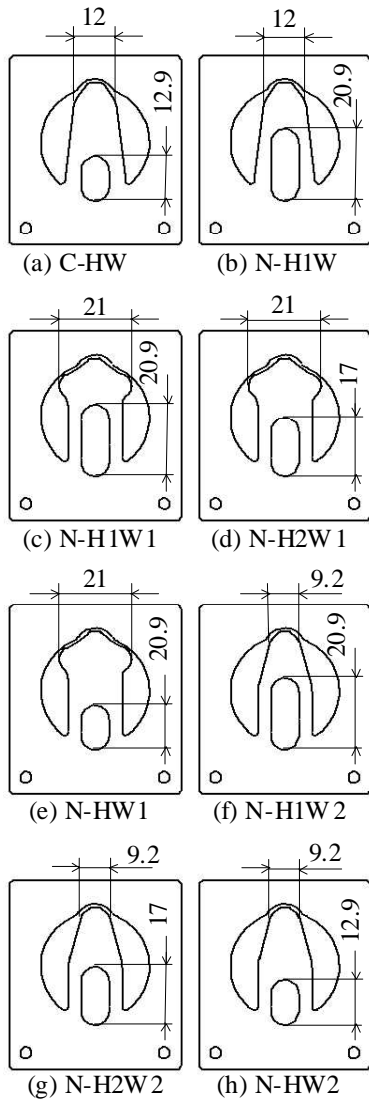


Figure 3 Suction valves

Figure 3 (a) shows a conventional valve of the type C-HW. Moreover, seven kinds of the improvement valves are shown in Figures 3 (b) ~ (h). The size of valve hole and the width at the tip of a valve for the improved valves are changed to compare with the conventional valve C-HW. In this experiment, seven kinds of valves were manufactured as the first stage of our study.

Measurements of the displacement of the suction valves

The strain gauge is pasted on the part of the valve, which is expected to be deformed largely with quick drying glue. As shown in Figure 4, the output signals from the strain gauge are amplified through the bridge box and the voltage amplifier and are recorded to the data recorder. The relation between the valve displacements measured using a laser sensor and the output voltages using a strain gauge is obtained.

Flow visualization using PIV (Particle Image Velocimetry) system

The PIV system is used to visualize the flow field around the suction valve and to obtain the velocity distributions for the conventional valve C-HW and the improved valve without the vibration. The light sheet using the double-pulsed YAG laser is used as a light source. The positions of the laser light sheets are shown in Figure 4. The laser light sheets are placed on the sections perpendicular to the valve plate including the axes A-A of a suction port. The tracer particles DEHS are introduced in the tube between the mass flow meter and the test model, as shown in Figure 1. DEHS is a liquid and becomes the mist phase using the pressurized tank. The mist of the DEHS is introduced into the experimental circuit.

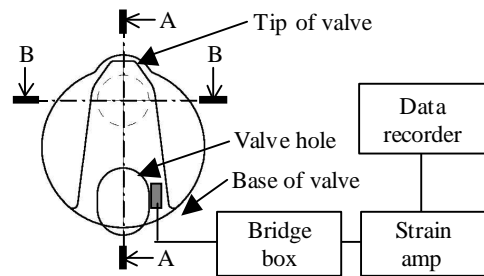


Figure 4 Position of strain gauge and Laser sheet

Test condition

The upstream pressure is kept constant at 0.2MPaG in the present experiments because the suction pressure of the reciprocating compressor for an automotive air conditioner is also about 0.2MPaG. The mass flow rate is changed from 3.0kg/h to 10.5kg/h in our experiments.

RESULTS

Displacement of the suction valve

Figure 5 shows the displacement for the conventional valve C-HW and new valve N-H2W1 for 3.0kg/h of the mass flow rate as one of the typical example. Time is shown in the horizontal axis and the displacement of a suction valve is shown in the vertical axis.

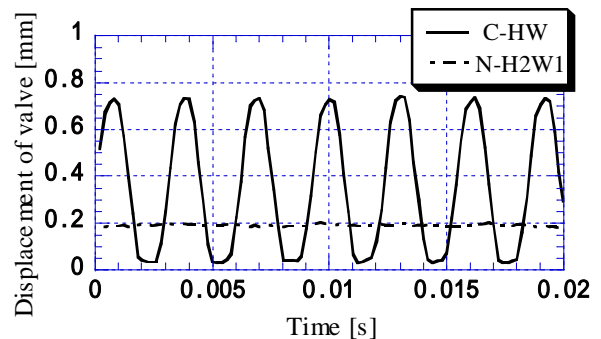


Figure 5 Valve vibration (Flow rate=3.0kg/h)

Figure 6 shows the amplitude and the frequency of the seven suction valves, respectively. The flow rate is

shown in a horizontal axis and the amplitude of a suction valve is shown in a vertical axis. As shown in Figure 6, the amplitude of the new valve N-H2W1 was 0.01mm or less. Therefore, there is almost no vibration for the new valve N-H2W1. Furthermore, the valves (C-HW,N-H1W,N-H1W2,N-H2W2,N-HW2) vibrated for 3.0 kg/h of the low flow rate. Therefore the experiments were not conducted for other parameters of the flow rate except it. For new valves, the frequency of the valves N-H1W1 and N-HW1 is about 200Hz and is about 320~340Hz except it.

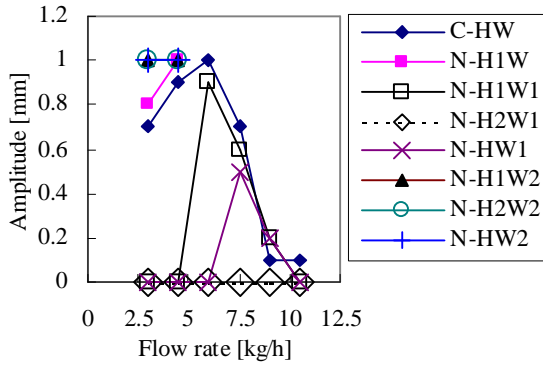


Figure 6 Amplitude of the suction valves

The natural frequency f_n Hz and mass m g of the valves used in our experiments are shown in Table 1.

Table 1 Characteristics of the suction valves

	f_n [Hz]	m [g]
C-HW	216	0.87
N-H1W	205	0.72
N-H1W1	167	0.83
N-H2W1	165	0.91
N-HW1	165	0.99
N-H1W2	199	0.66
N-H2W2	193	0.74
N-HW2	201	0.81

The natural frequencies are about 165Hz or 200Hz. The frequencies of the valves during the vibration in the experiment are 200Hz. The natural frequencies of each new valves N-H1W1, N-H2W1 and N-HW1 are almost 165Hz. But we have found that some these valves vibrate and the other do not vibrate.

Next, we changed the natural frequency of the vibration-reduced new valve N-H2W1 with 165Hz of the natural frequency by changing its material and thickness keeping its shape, in order to investigate the influence of natural frequency. The natural frequency f_n Hz and the mass m g of seven kinds of valves manufactured are

shown in Table 2.

Table 2 Characteristics of the suction valves (N-H2W1 Type)

	f_n [Hz]	m [g]
PK0.2	113	0.61
PK0.3	165	0.91
PK0.4	223	1.0
G0.2	119	0.61
G0.3	177	0.91
G0.4	230	1.0
PK-200	200	1.06

Furthermore, it was found from the previous experimental results that the valve tends to vibrate for 200Hz of the natural frequency. We made the valve PK-200 with 200Hz of the natural frequency by changing the thickness of the valve N-H2W1. On the same experimental conditions shown in Figure 6, the mass flow rate was changed between 3.0 and 10.5 kg/h. As for the experimental results, the oscillating amplitude was about 0.3mm only for 9.0 kg/h of the valve G0.3, and frequency was about 200Hz. But the other valve's amplitudes were 0.01mm or less almost without the vibration. Therefore, in the mass flow range of this experiment, the valves were without the vibration and it turns out that there is less influence of the natural frequency. It is effective to enlarge width of tip of a valve, and it turns out that the optimal size for the valve hole also exists. It is because the size of the valve hole changes the influence of the flow on the valve. Even if we change the material's quality and thickness, keeping the valve shape of the valve N-H2W1, it turns out that the vibration of the valve can be suppressed mostly. From the above results, the important factors for designing the suction valve are both the shape of the suction valve and the size of valve hole. Then, we paid attention to the valve PK-200 of the same shape of the valve N-H2W1. The pressure drop is investigated using the pressure drops ΔP_{PK-200} of the valve PK-200 divides by the pressure drops ΔP_{C-HW} of the conventional valve C-HW. The results are shown in Figure 7.

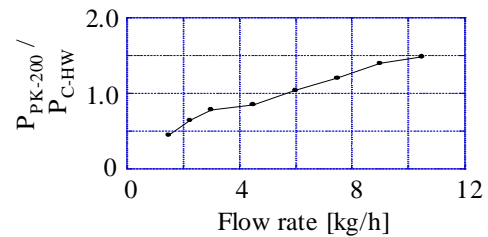
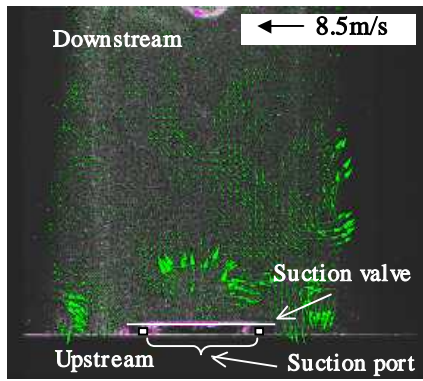


Figure 7 Pressure loss of the valve PK-200

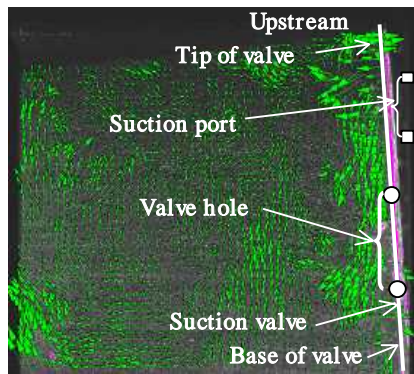
The pressure drop of the valve PK-200 in low mass flow rate is smaller than the pressure drop for the valve C-HW. If the mass flow rate increases to 6.0kg/h or more, the pressure drop of the valve PK-200 is higher than the pressure drop of the conventional valve. Therefore, it turns out that the effect of the shape of the valve N-H2W1 without vibration is effective in the range of the low mass flow rate.

Velocity distributions around the valve

Figure 8 shows the velocity distributions obtained using the PIV technique for the valve C-HW when the flow rate is 3.51kg/h. The displacement of the valves changes between 0mm and 0.8mm during the vibration as mentioned in the section ‘Displacement of the suction valve’. In the image shown in Figure 8 the displacement of the valve is almost 0.4mm and it is increasing.



(a) section A-A



(b) section B-B

Figure 8 Visualized results of conventional valve (Flow rate=3.51kg/h)

Figure 8(a) shows the velocity distributions in the section A-A and Figure 8(b) shows those in the section B-B. The magnitudes of instantaneous velocity vector obtained are from 4m/s to 7m/s. In the Figure 8(a) the direction of the downstream velocity vectors from the suction port is the same direction of the movement of the valve because the valve is opening and going up. From the Figure 8(b) it is

found that the fluid flows from the suction port along the surface of the suction valve to the bottom of the valve and the flow structure is random and turbulent in the downstream region from the suction valve. The velocity vectors are obtained at the several times and the flow structures observed in the section B-B are almost same. In this experimental range, the valve N-H2W1 did not almost vibrate as mentioned in the section ‘Displacement of the suction valve’. Figure 9 shows the velocity distributions of downstream direction for the valve N-H2W1 obtained using the PIV technique.

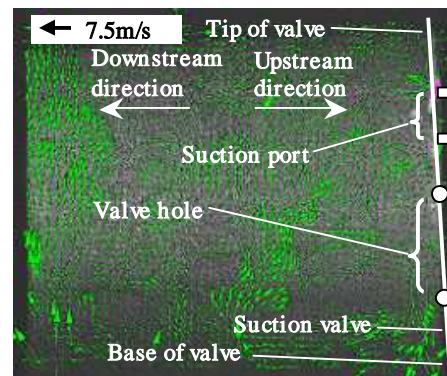


Fig.9 Visualized results of new valve (top:using PIV technique, bottom:sketched figure, Flow rate=3.0kg/h)

The bottom figure of Figure 9 is the sketched figure in the section A-A. From the figure 9 the vortex exists in the downstream region of the new valve without the vibration. It was confirmed that the design to generate the steady large vortex near the suction valve is useful to prevent the vibration of the valve. The generating of the two-dimensional flow in the width direction near the center of the valve N-H2W1 is useful to exist the vortex and the vortex has the influence on the vibration reduction.

Displacement of the suction valve in the reciprocating compressor for the automotive air-conditioner

From the results using the test model, it is found that the shape of the valve N-H1 has most effective to reduce the

vibration. To investigate the effect of the vibration-reduction for the valve N-H2W1 the valve is set in the reciprocating compressor for the automotive air-conditioner and the displacements of the suction valves are measured using the strain gauge. The results are shown in Figure 10.

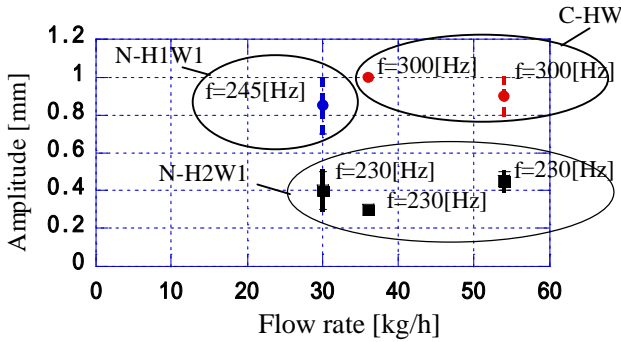


Figure 10 Amplitude and frequency of the valve in reciprocating compressor

In order to compare it, the valves C-HW and N-H1W1 were also investigated. The mass flow rate for the circuit of refrigerate is shown in a horizontal axis and the amplitude of the vibration is shown in a vertical axis. The frequency f Hz was also shown in the left or right-hand side of each data. Although the valve N-H2W1 vibrates compared with the results using the simplified test model, the vibration was reduced compared with the valves C-HW and N-H1W1. It is confirmed that the shape of the valve N-H2W1 is the most effective for the vibration-reduction.

CONCLUSIONS

To perform the vibration-reduction of the suction valve of the reciprocating compressor for the automotive air-conditioner, the simplified test model is designed to improve the conventional valve. Detailed study is conducted by measurement of the displacement for the valves using the strain gauge. And the velocity distributions around the suction valves without vibration are measured using PIV technique. Furthermore, the new valve is set in the reciprocating compressor for the automotive air-conditioner and the displacement of the suction valves is measured using the strain gauge. It is confirmed that the shape of the valve N-H2W1 is the most effective for the vibration-reduction.

Summary of this paper is itemized as follows;

1. The generating of the two-dimensional flow in the width direction near the center of the valve N-H2W1 is useful to obtain the two-dimensional vortex flow and the vortex has the influence on the vibration reduction of the valve. Moreover, the optimal size for the valve hole exists.
2. Even when the natural frequencies of the valves are

the same, we have found that the valves vibrate or do not vibrate according to the shape of the valve. Therefore, it was found that the vibration was affected by the three-dimensional flow.

3. The new valve with the optimal shape obtained to reduce the vibration using this simplified test model showed good result for the case of the compressor of the commercial system.
4. The pressure loss for the new valve N-H2W1 without the vibration was compared to the conventional valve C-HW with the vibration. The pressure loss of the new valve is small in the range of low mass flow rate. When the mass flow rate increases, the pressure loss of the conventional valve is less than that of the new valve .

ACKNOWLEDGMENTS

The authors are greatly thankful to Prof. K. Nagai of Gunma University and H. Suzuki of Sanden Corporation, for their contribution to the present study.

REFERENCES

1. Tsukiji, T., Hashimoto, K., and Sato, T., Numerical simulation of pressure-pulsation for an automotive air-conditioner, Proceeding of the 34th Japanese Joint Conference on Air-conditioning and Refrigeration, 2000, pp.61-64.
2. Sato, T., Hashimoto, K., and Tsukiji, T., The visualization around the suction valve in a reciprocating compressor for an automotive conditioner, Proceeding of the 35th Japanese Joint Conference on Air-conditioning and Refrigeration, 2001, pp.113-116.
3. Sato, T., and Tsukiji, T., Flow analysis around the suction valve and the vibration characteristics of the valve in a compressor for automotive air-conditioner, Japan Society of Refrigeration and Air Conditioning Engineers , 2001, 19, pp.163-171.
4. Chung, M. K. et al., A study on the flow in a discharge system of the reciprocating compressor using computational simulation and PIV, Proceeding of the 15th International compressor engineering conference, 2000, 1, pp.377-382.
5. Myung, H. J., and Lee, I. S., Investigation of the discharge flow of a reciprocating compressor using PIV, Proceeding of the 15th International compressor engineering conference, 2000, 1, pp.391-396.
6. Ishii, N. et al., Flow-induced vibration of reed valve in refrigerant compressors, The Japan Society of Mechanical Engineers (Series B), 1991, 57 , pp.1828-1833.
7. En, n, K. et al., Motion analysis of reed valve for micro-compressor, Hokkaido branch of the Japan Society of Mechanical Engineers , 1998, pp.55-56.

Development of Continuous Unsteady Flow Generator for Gases

Tatsuya FUNAKI*, Shunpei YAMAZAKI**, Kenji KAWASHIMA* and Toshiharu KAGAWA*

* Precision and Intelligence Laboratory, Tokyo Institute of Technology
R2-45, 4259 Nagatsuta Midori-ku, Yokohama City, Kanagawa Prefecture, 226-8503, Japan
(E-mail: funaki@pi.titech.ac.jp)

** Graduated School Student, Tokyo Institute of Technology
R2-45, 4259 Nagatsuta, Midori-ku, Yokohama City, Kanagawa Prefecture, 226-8503, Japan

ABSTRACT

Recently, unsteady flow rate measurement of gases is very important in the various industrial fields. However, there is no way to calibrate and to examine the unsteady flow rate of gases experimentally. As a result, there is no test bench for the unsteady flow rate measurement of gases.

In this paper, we developed a new type of unsteady flow generator for gases. Especially, we realized to generate the unsteady flow of gases continuously. Then, we verified experimentally the generated unsteady flow rate using a laminar flow meter that has quick response up to 50[Hz]. Moreover, we investigated the heat transfer in the generator. As a result, we confirmed that this generator could generate the oscillatory flow up to the frequency of 30[Hz], and the target flow continuously for 30 minutes. The generator is effective for the verification of the various unsteady phenomena of gases experimentally.

KEY WORDS

Flow measurement, Unsteady flow, Generator, Isothermal chamber, Heat transfer

NOMENCLATURE

a : Amplitude ratio of flow rate ($=Q_{amp}/Q_{ave}$)	[-]	G : Mass flow rate	[kg/s]
b : Critical pressure ratio	[-]	K_G : Gain of flow rate	[kg/(s · mm ²)]
C_p : Specific heat at constant pressure	[kJ/kg · K]	K_p : Proportional gain of pressure	[-]
C_v : Specific heat at constant volume	[kJ/kg · K]	K_{dp} : Proportional gain of pressure differentiate	[-]
f : Frequency	[Hz]	k : Coefficient of flow rate converter	[m ³ /kg]
f_d : Time constant	[s]	P : Pressure	[Pa]
h : Heat transfer coefficient	[W/(m ² · K)]	P_a : Atmospheric pressure	[Pa]
		P_{ref} : Target of pressure	[Pa]
		\dot{P} : Differentiated value of pressure	[Pa/s]

Q : Volumetric flow rate at standard condition	[m ³ /s]
Q_{amp} : Amplitude flow rate of oscillatory flow	[m ³ /s]
Q_{ave} : Average flow rate of oscillatory flow	[m ³ /s]
Q_{ref} : Reference of Generated oscillatory flow	[m ³ /s]
q : Heat transfer rate	[W]
R : Gas constant number	[J/(kg · K)]
S_e : Effective area	[m ²]
t : Time	[s]
T_p : Integral action time of pressure	[-]
T_{dp} : Integral action time of pressure differentiate	[-]
u : Input voltage to the servo valve	[V]
V : Volume of the chamber	[m ³]
W : Mass of air in the chamber	[kg]
κ : Specific heat ratio	[-]
θ : Temperature of gas	[K]
θ_a : Room temperature	[K]
ρ : Density of air	[kg/m ³]

Subscripts

c : chamber
 e : control volume
 in : inlet
 out : outlet
 s : supply

INTRODUCTION

Recently, unsteady flow rate measurement of gases is very important in the various industrial fields. Especially, it has been increased the importance to control the gas flow rate for the fuel cell and the semiconductor fabrication equipment, to control the expired and inspired gas for the medical treatment, and to measure the pulsated flow of the pump. However, there is no way to calibrate and to examine the unsteady flow rate of gases experimentally. As a result, there is no test bench for the unsteady flow rate measurement of gases.

In this paper, we developed a new type of unsteady flow generator for gases using an isothermal chamber and two spool type servo valves. Especially, we realized to generate the unsteady flow of gases continuously for 30 minutes. Then, we verified experimentally the generated unsteady flow rate using a laminar flow meter that has quick response up to 50[Hz] [3]. Moreover, we

investigated the heat transfer in the generator. As a result, it could be seen that there is no influence of the temperature change in the chamber. And it is shown that the generator is effective for the verification of the various unsteady phenomena of gases experimentally.

CONTINUOUS UNSTEADY FLOW GENERATOR

Principle

The unsteady flow generator in the former research [2] has the limitation of the generating time. In this research, we realized to generate the unsteady flow continuously. We adopted the method that the charging and the discharging in the isothermal chamber are synchronal. Here, the state equation for compressible fluids in a chamber can be written as

$$PV = WR\theta \quad (1)$$

The following equation can be derived by differentiating Eq.(1), if the chamber volume is constant.

$$V \frac{dP_c}{dt} = (G_{in} - G_{out})R\theta + WR \frac{d\theta}{dt} \quad (2)$$

If the state of air in the chamber during charge or discharge remains isothermal, the volumetric flow rate can be obtained from Eq.(2).

$$Q_{out} = kG_{out} = Q_{in} - k \frac{V}{R\theta_a} \frac{dP_c}{dt} \quad (3)$$

As the condition is isothermal, the average temperature in the chamber is equal to the room temperature. It is clear from Eq.(3) that if the volume of the chamber V and the room temperature θ_a are known, the instantaneous volumetric flow rate can be obtained from the pressure

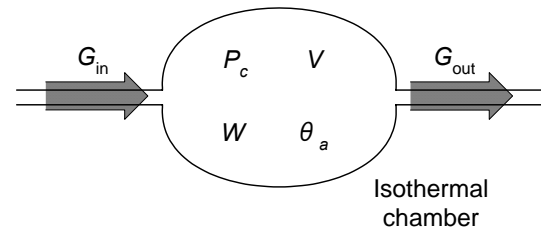


Fig.1 Schematic diagram of mass flow rate while charging and discharging from an isothermal chamber

response and the inlet volumetric flow rate. The flow rate through a pneumatic valve is represented in the following two formulas [4]. The case of choked flow is given by,

$$Q = 11.1 S_e P_s \sqrt{\frac{273}{\theta_a}} \quad (4)$$

The case of non-choked flow is given by,

$$Q = 11.1 S_e P_c \sqrt{\frac{273}{\theta_a}} \sqrt{1 - \left(\frac{P_a/P_c - b}{1 - b} \right)^2} \quad (5)$$

where b is the critical pressure ratio. In the choked flow, the pressure response equations in the chamber, which can be derived from Eqs.(2), (3) and (4), are provided below when we assume the supply pressure is P_s and downstream pressure is the pressure in the chamber.

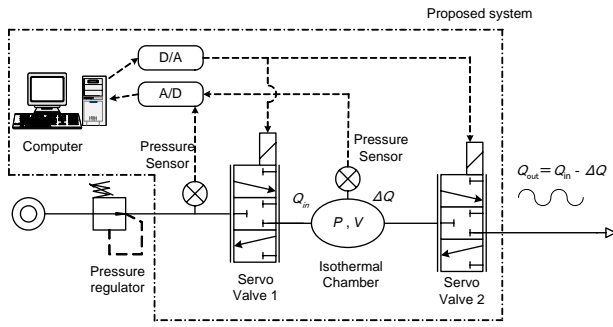


Fig.2 Apparatus of a continuous flow generator

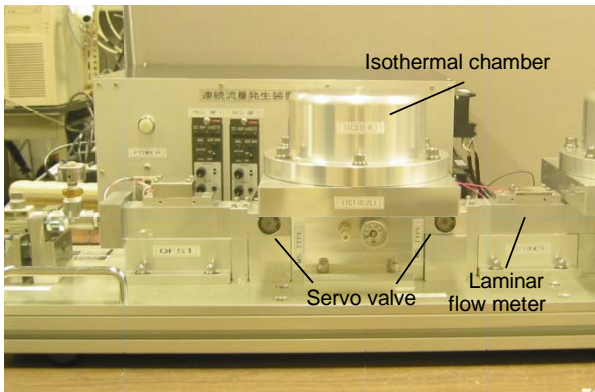


Fig.3 Photograph of a continuous flow generator

In the case of non-choked flow, the critical pressure ratio b and the uncertainty of the pressure and the temperature in the chamber are important factors in this generator.

Generally, the unsteady flow can be generated using the servo valve with choked flow. However, there is a problem of changing the temperature in the chamber. Therefore, the former research [2] has been reported that the measured sinusoidal flow rate has error on the gain and the phase. In this paper, we controlled the inlet mass flow rate using a servo valve. And the generated unsteady flow rate using this system is controlled using a servo valve at the downstream side.

Apparatus

The developed continuous flow generator is shown in Fig.2 and the photograph of it is shown in Fig.3. The apparatus consists of an isothermal chamber, two spool type servo valves, two pressure sensors, an AD converter, a DA converter and a personal computer. The servo valve has a dynamic response of about 100[Hz]. The pressure sensor was a semiconductor type with a resolution of 50[Pa]. The servo valve 1 controls the charged flow rate to the isothermal chamber, and the servo valve 2 controls the generated unsteady flow from the chamber. The AD converter is used to obtain the supply pressure, the pressure in the chamber and the measured flow rate using the laminar flow meter. The internal volume of the isothermal chamber is $2.0 \times 10^{-4} [\text{m}^3]$.

Control method

We controlled the absolute pressure in the isothermal chamber to be the choked flow at the servo valve 1 and the non-choked flow at the servo valve 2. The supply pressure was set up at 600[kPa] and the pressure in the isothermal chamber was about 180[kPa]. Therefore, the pressure ratio is about 0.3. We confirmed that the choked condition is realized at the servo valve 1, because the critical pressure ratio of this valve was about 0.35. The manipulated value by the servo valve 1 is the average value of the generated flow rate. Fig.4 shows the block diagram of the continuous flow generator. At first, we calculated the reference flow rate using Eq.(3). The control signal to the servo valve is estimated as $G/(K_G S_e)$. This value is given as a feed-forward element to the system. And two PI controllers were adopted for the

SPECIFICATION

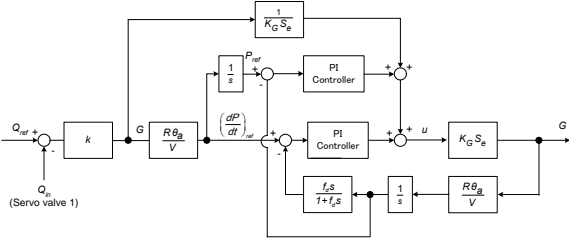


Fig.4 Block diagram of a continuous flow generator

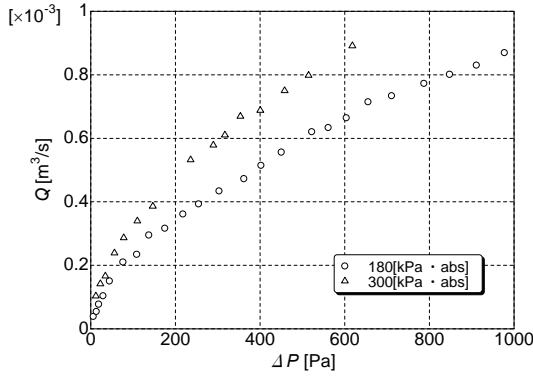


Fig.5 Pressure loss through the isothermal chamber

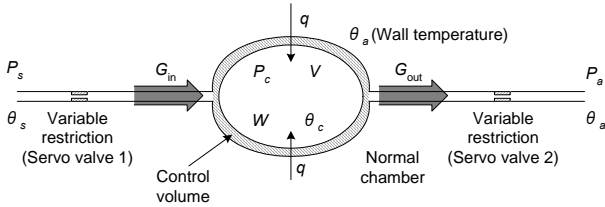


Fig.6 Control volume in the chamber

pressure control in the isothermal chamber. Therefore, this flow generator can generate the unsteady flow rate continuously, calculating the pressure change in the isothermal chamber and the charged flow rate through the servo valve 1. And the input voltage of servo valve 2 can be written as follows.

$$u = K_p \left(1 + \frac{1}{T_p S} \right) (P_{ref} - P_c) + K_{dp} \left(1 + \frac{1}{T_{dp} S} \right) (\dot{P}_{ref} - \dot{P}_c) + \frac{G}{K_G S_e} \quad (6)$$

Pressure distribution

In this system, the isothermal chamber that was set up in the line was a resistant component. We measured the pressure loss of the chamber, when the flow rate is constant. Fig.5 shows the experimental results of the pressure loss through the isothermal chamber. The symbol “○” is the results when the pressure in the chamber was 180[kPa] and the symbol “△” is that of 300[kPa]. From this figure, if the generated volumetric flow rate is about 8.0×10^{-4} [m³/s], the pressure loss through the isothermal chamber is about 800[Pa]. As a result, the measured error of the pressure in the chamber has a maximum of 0.44[%]. Therefore, the pressure loss through the chamber was very small, and there was no influence in pressure measurement of the chamber. In addition, the pressure in the isothermal chamber was measured at the both side of cylindrical chamber and confirmed that the pressure distribution in the chamber was negligible small, when the unsteady flow was generated.

Temperature change

In this generator, it is very important to know the influence of changes in air temperature on the accuracy of it. However, it is very difficult to measure temperature change of air in the chamber rapidly. Therefore, we confirmed the temperature change in the normal chamber and the isothermal chamber theoretically while generating the sinusoidal flow, considering the energy change of air in the chamber.

Fig.6 shows the RC circuit of the continuous unsteady flow generator. The state equation for compressible fluids in the chamber is given by as follows using the spatial average density of air.

$$P_c = \rho_c R \theta_c \quad (7)$$

Pressure change ratio in the chamber is,

$$\frac{dP_c}{dt} = \rho_c R \frac{d\theta_a}{dt} + \frac{R\theta_a}{V} G \quad (8)$$

As Eq.(8), the pressure change in the chamber is obtained from the mass flow rate and the average air temperature change in the chamber. Considering the energy change of air in the chamber, energy equation is expressed as

follows.

$$\frac{d}{dt} \int_V C_V \rho_c \theta_a dV = G C_V \theta_e + \frac{P_c}{\rho_e} G + q \quad (9)$$

where θ_e and ρ_e are temperature and density of air across the control volume respectively.

In the case of $G < 0$, discharging air temperature across the control volume is equal to spatial average temperature in the chamber. And based on the Newton's law of cooling the heat transfer rate q is written as,

$$q = h S_h (\theta_a - \theta_c) \quad (10)$$

Finally, while discharging from the chamber, the spatial average temperature change can be obtained as follows.

$$C_V W \frac{d\theta_c}{dt} = G_{out} R \theta_c + h S_h (\theta_a - \theta_c) \quad (11)$$

In the case of $G > 0$, the air temperature across the control volume θ_e is thought to be different from former case. Through the restriction, the air temperature approaches to the atmospheric temperature, the energy equation (9) can be transformed as,

$$\frac{d}{dt} \int_V C_V \rho_c \theta_a dV = G_{in} C_V \theta_a + \frac{P_c}{\rho_{ca}} G_{in} + q \quad (12)$$

Using the Eq.(7) and Eq.(10), the spatial average temperature change in the chamber can be written as,

$$C_V W \frac{d\theta_c}{dt} = G_{in} C_V (\theta_a - \theta_c) + R \theta_a G_{in} + h S_h (\theta_a - \theta_c) \quad (13)$$

Comparing the Eq.(13) with Eq.(11) which is discharged case, Eq.(13) has additional term.

Based on the above mentioned, the pressure changes in the chamber while charging and discharging can be obtained as follows.

$$\frac{dP_c}{dt} = \frac{\kappa - 1}{V} h S_h (\theta_a - \theta_c) + \frac{1}{V} \{ G_{in} (\kappa - 1) C_p \theta_a - \kappa G_{out} R \theta_c \} \quad (14)$$

And the spatial temperature change in the chamber can be written as follows from Eq.(11) and Eq.(13).

$$C_V W \frac{d\theta_c}{dt} = G_{in} (C_p \theta_a - C_V \theta_c) - G_{out} R \theta_c + q \quad (15)$$

Here, we considered the case that the oscillatory flow is set at $5.0 \times 10^{-4} + 2.5 \times 10^{-4} \sin(2\pi f t)$ [m³/s] and h is 20[W/(m²·k)], S_h of the normal chamber is 199.25[cm²], S_h of the isothermal chamber is 7155[cm²]. Fig.7 shows the simulation results of the pressure and the temperature

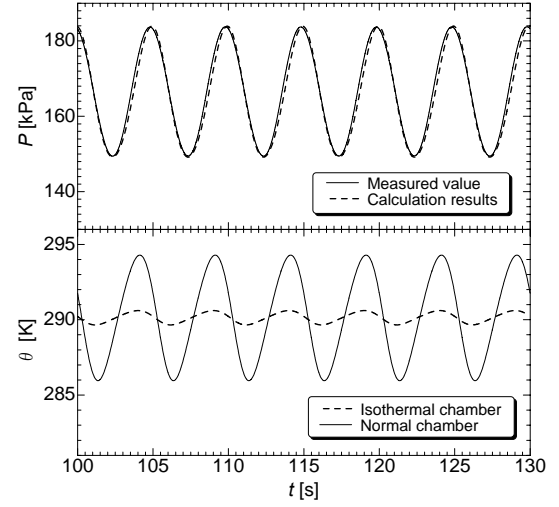


Fig.7 Pressure and temperature change in the isothermal chamber when the oscillatory flow was generated

changes in the normal chamber and the isothermal chamber. As a result, the magnitude of the temperature changes is about 8[K] using the normal chamber. On the other hand, the magnitude of it is about 1.5[K] using the isothermal chamber. Therefore, it could be confirmed that there is no influence of the temperature changes in the chamber.

Uncertainty

The error for the pressure sensor is 0.5[%]. The error due to the change in the pressure of the chamber is a maximum of 2[%]. The temperature measurement error is a maximum of 2[K]. The error of the chamber volume measurement error is 1[%]. The error of the inlet volumetric flow rate is a maximum of 3[%]. As a result, the generated flow rate has a maximum of 5.1[%]. Therefore, this generator has sufficient accuracy for the practical use.

EXPERIMENTAL RESULTS

Fig.8 shows the experimental results when the generated flow rate was set at $5.0 \times 10^{-4} + 2.5 \times 10^{-4} \sin(2\pi f t)$ [m³/s] and the frequency 0.1[Hz]. From the figure, the target flow rate and the generated flow rate show good agreement. Also, the measured flow rate using the laminar flow meter and the generated flow rate show

good agreement. And we generated the flow for 30 minutes continuously and confirmed its effectiveness. Fig.9 shows the experimental results at the frequency of 1[Hz]. Fig.10 shows the experimental results at the frequency of 30[Hz]. From these results, it could be confirmed that the target flow rate and the generated flow rate show good agreement. On the other hand, it can be

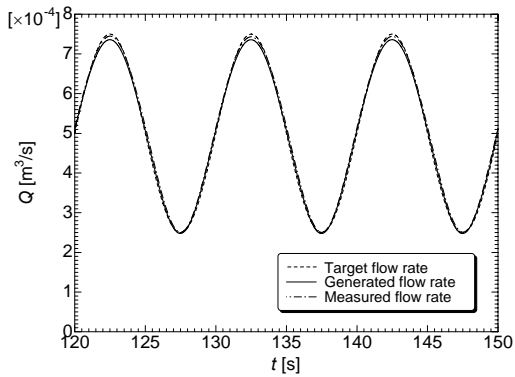


Fig.8 Generated oscillatory flow at 0.1[Hz]

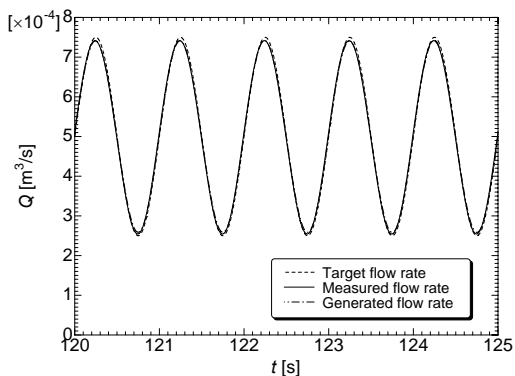


Fig.9 Generated oscillatory flow at 1[Hz]

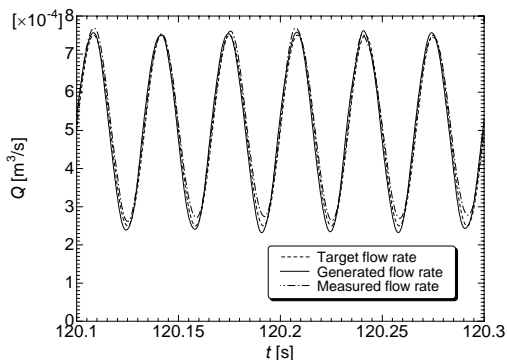


Fig.10 Generated oscillatory flow at 30[Hz]

seen that there is a difference between the generated flow rate and the measured flow rate using the laminar flow meter, when the frequency is 30[Hz]. This is because of the characteristics of the laminar flow meter [3].

CONCLUSIONS

In this research, a continuous flow generator for gases was developed. Then, the performance of the generator was evaluated experimentally using a laminar flow. As a result, we confirmed that this generator could generate the oscillatory flow up to the frequency of 30[Hz]. Moreover, the uncertainty due to temperature change in the chamber was investigated theoretically. Finally, we confirmed that the generator could generate the target flow continuously for 30 minutes.

ACKNOWLEDGMENTS

The authors are grateful to the Tokyo Meter Corporation for their support.

REFERENCES

1. R.W.Miller, Flow measurement engineering handbook, 3rd ed., McGraw-Hill, New York, 1996.
2. Kenji Kawashima, Toshiharu Kagawa, Unsteady flow generator for gases using an isothermal chamber, Measurement, Vol.33, pp.333-340, 2003.
3. Tatsuya Funaki, Kenji Kawashima, Toshiharu Kagawa, Characteristics Analysis of Laminar flow meter for gases with high speed response, SICE, Vol.40, No.10, pp.1008-1013, 2004. (In Japanese)
4. ISO6358, Pneumatic Fluid Power-Components Using Compressible Fluids Determination of Flow-rate Characteristics, 1989.
5. JIS B 8390, Pneumatic Fluid Power Components Using Compressible Fluids Determination of Flow-rate Characteristics, 2000 (In Japanese)
6. Toshiharu Kagawa, Masashi SHIMIZU, Heat transfer effect on the dynamics of pneumatic RC circuit, 2nd International Symposium on Fluid Control, Measurement, Mechanics and Flow visualization, pp.498-502, 1988.

Design and Implementation of Lab. Simulator for Vehicle Control

Jeongdai Jo*, Dong-Soo Kim*, Kwang-Young Kim*, and Hyung-Eui Kim**

* Division of Intelligence & Precision Machine Research, IT Machinery Research Center
Korea Institute of Machinery & Materials(KIMM)
#171, Jang-dong, Yuseong-gu, Daejeon, 305-343, Korea
(E-mail: micro@kimm.re.kr)

** Division of System Engineering Research, Mechanical Systems Reliability Research Center
Korea Institute of Machinery & Materials(KIMM)
#171, Jang-dong, Yuseong-gu, Daejeon, 305-343, Korea

ABSTRACT

The Lab. simulator for conducting a performance test and a reliability test on a vehicle and components has been designed and embodied. In order to control non-linear of a vehicle, a fuzzy control algorithm, a running mode tracking algorithm and a vehicle speed control algorithm were applied to the actuator control. The vehicle controller functions were implemented; setup of the actuator, position control, the gear shift control depending upon the vehicle RPM, the serial interface function for data communication and control with the servo controller, and transmitting and receiving data. The servo controller performed the function to drive the actuator by controlling the pneumatic servo valve, and measured data information such as a position, a velocity and an acceleration as obtained through operation by means of the second differentiator and controlled a position precisely. An experimental apparatus was consisted of a dynamometer and a vehicle, and the performance and durability of the controller was verified. The Lab. simulator was mounted onto the vehicle, and the position control test and a LAP mode tracking test were conducted. It was found that the response characteristic, the tracking capability and precision of the position control were so excellent.

KEY WORDS

Lab. simulator, Vehicle controller, Servo controller, LAP mode tracking test

NOMENCLATURE

u : Output Feedback Control Input
 K_p : Position Control Gain
 K_v : Speed Control Gain
 K_a : Acceleration Control Gain
 x_d : Object Position Input
 x : Position Output of Actuator Load Mass

\dot{x} : Speed Output of Actuator Load Mass
 \ddot{x} : Acceleration Output of Actuator Load Mass
 e : Position Error

INTRODUCTION

The Technologies used in a vehicle control simulator can be categorized into a servo actuator control technology, a fractional technology of the computer

interface technology, a vehicle control technology and a vehicle-related test system technology pertaining to the system integration technology[1]. The Lab. simulator (comprising a vehicle controller and a servo controller) for conducting a performance test and a reliability test on a vehicle and components has been designed and embodied. In order to control non-linear characteristics of a vehicle, a fuzzy control algorithm, a running mode tracking algorithm and a vehicle speed control algorithm were applied to it[2]. The Lab. simulator comprised a vehicle controller having functions for controlling, obtaining data, receiving vehicle information and processing control signals, a servo controller for controlling an actuator and processing data, a second differentiator for producing a position, a velocity and an acceleration and a serial interface converter[3].

An experimental apparatus was consisted of a chassis dynamometer and a vehicle of 1500cc displacement, and the performance and durability of the controller was verified. The Lab. simulator was mounted onto the vehicle, and a basic control characteristic test and a LAP mode tracking test were conducted[4]. As a result, it was found that the response characteristic, the tracking capability and precision of the position control were so excellent that it would be possible to use it as a vehicle controller. It is thought that the Lab. simulator for controlling a vehicle will be greatly applicable to the whole industry related to vehicle technology as well as the auto pilot system, including development and test of a test system to which it is applied, particularly, the mileage accumulator test, the exhaust gas measurement test, the fuel consumption test, the environment test, the noise measurement test and so on.

DESIGN OF LAB. SIMULATOR

Design of Control Algorithm

The Lab. simulator was designed by means of the fuzzy control algorithm for the vehicle controller, the position and load control algorithm for the servo controller and the interface software. The vehicle controller was designed so that it could be received a vehicle speed from the running mode and the control software, produce a displacement of the actuator according to the situation and further transmit it to the servo controller. The servo controller controlled a position and a load of the actuator, and it was designed so that it could be received an instruction value from the actuator of the vehicle control system and control feedback. Such designed servo control algorithm enables feedback of a position and a velocity and an acceleration as obtained by differentiating it. In order to implement fast response, high precise position control, tracking control performance, the position and load control algorithm, the speed control algorithm and the tracking control algorithm were applied to the actuator control.

The structure of the servo control algorithm is as shown in Figure 1, and the control input for consist of the controller is as in Eq. (1).

$$u = K_p \cdot e - K_v \cdot \dot{x} - K_a \cdot \ddot{x} \quad (1)$$

Wherein,

$$u = [u_1 \ u_2 \ u_3 \ u_4 \ u_5]$$

$$u = [K_{p1} \ K_{p2} \ K_{p3} \ K_{p4} \ K_{p5}]$$

$$u = [K_{v1} \ K_{v2} \ K_{v3} \ K_{v4} \ K_{v5}]$$

$$u = [K_{a1} \ K_{a2} \ K_{a3} \ K_{a4} \ K_{a5}]$$

$$u = [x_{d1} \ x_{d2} \ x_{d3} \ x_{d4} \ x_{d5}]$$

$$u = [x_1 \ x_2 \ x_3 \ x_4 \ x_5]$$

$$e := x_d - x = [e_1 \ e_2 \ e_3 \ e_4 \ e_5]$$

$$\dot{x} = [\dot{x}_1 \ \dot{x}_2 \ \dot{x}_3 \ \dot{x}_4 \ \dot{x}_5]$$

$$\ddot{x} = [\ddot{x}_1 \ \ddot{x}_2 \ \ddot{x}_3 \ \ddot{x}_4 \ \ddot{x}_5]$$

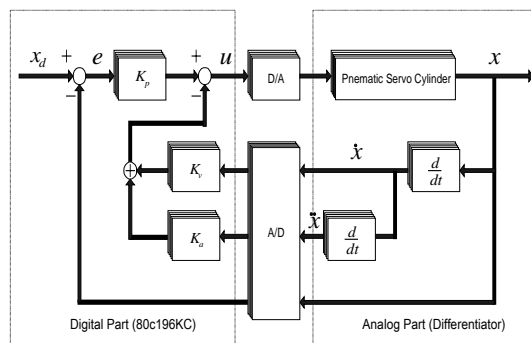


Figure 1 Block diagram of servo control algorithm

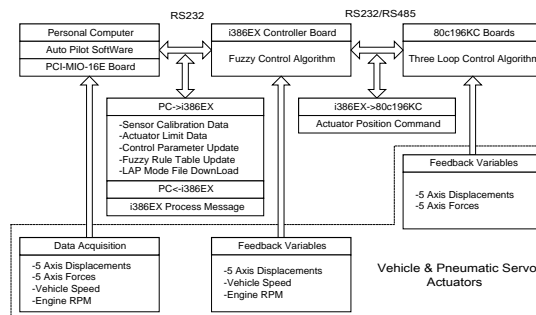


Figure 2 Control block diagram for implementation of the software

The vehicle control software for the Lab. simulator was designed so that it could be had the following functions: manipulation and renewal of system parameters, revision of controller information, real-time system monitoring, download of the running mode file, and saving and output of experimental results. It was designed in consideration of convenience and flexibility for the use so that if any vehicle information is changed, the controller information might be revised only by manipulating control parameters. Figure 2 is a control block diagram for implementation of the software.

Design of Controller

The vehicle controller was designed by means of the i386EX CPU board, and the servo controller was designed by means of the 80C196 CPU board[5][6]. Figure 3 shows a data linkage diagram of the vehicle control system comprising the vehicle controller, the servo controller, the actuator and the sensor. Through the vehicle controller, the following functions were implemented; setup of the actuator, position control, the gear shift control depending upon the vehicle RPM, the serial interface function for data communication and control with the servo controller, and transmitting and receiving data. The servo controller performed the function to drive the actuator by controlling the pneumatic servo valve, and measured data information such as a position, a velocity and an acceleration as obtained through operation by means of the second differentiator and controlled a position precisely.

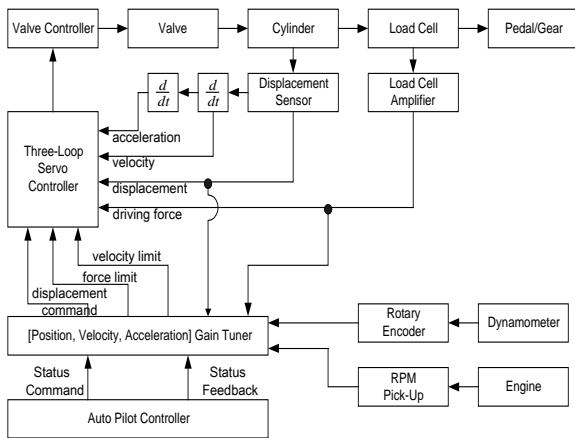


Figure 3 data linkage diagram of the vehicle control system

The serial interface converter(RS232/RS485) performed the bidirectional communication function to transmit an instruction on position and selection of the actuator from the vehicle controller to the servo controller and transmit the actuator status depending upon a position value to the vehicle controller[7]. The second differentiator, which was an analog circuit using an

operational amplifier, produced a position, a velocity and an acceleration in consideration of driving characteristics of the actuator and performed the function to enhance the control performance by reducing a load to process data in place of the numerical operational function of the servo controller. Figure 4 is an image of the Lab. simulator comprising the vehicle controller of i386EX board and the servo controller of 80C196 board.



Figure 4 Image of the vehicle controller and the servo controller

EXPERIMENTS AND RESULTS

An experiment was conducted to verify the performance and the position control characteristic of the Lab. simulator for controlling a vehicle, which comprised the vehicle controller, the servo controller, the actuator and the sensor as shown in Figure 5.

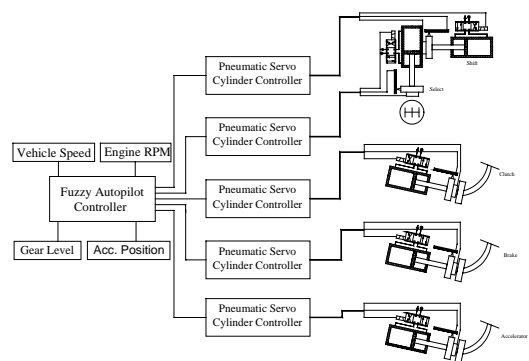


Figure 5 Schematic of Lab. simulator apparatus

The Lab. simulator was applied to the vehicle control system and then a position control experiment was conducted. Since the gear shift actuator requires the point-to-point position control, a step response experiment was conducted as illustrated in Figure 6. And, since the acceleration pedal actuator and the clutch

pedal actuator had to tracking in process of time, each tracking control experiment in response to each input of the 0.25 Hz and 1Hz of the ramp wave and the sine wave was conducted as illustrated in Figure 7 and Figure 8. The Lab. simulator satisfied the target specification that any error of its performance and position control precision should be within ± 1 mm, and its excellent tracking capability was verified.

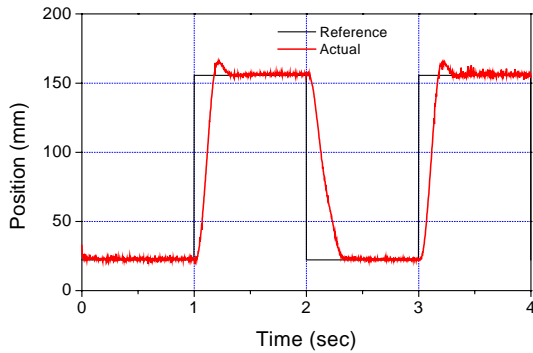
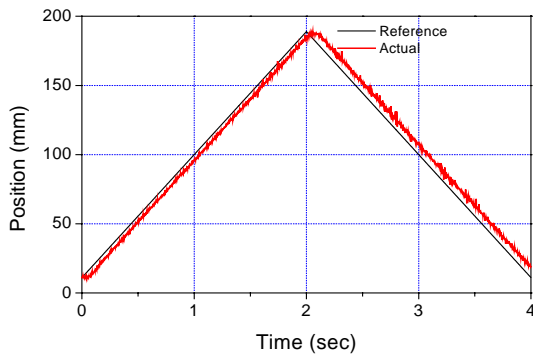
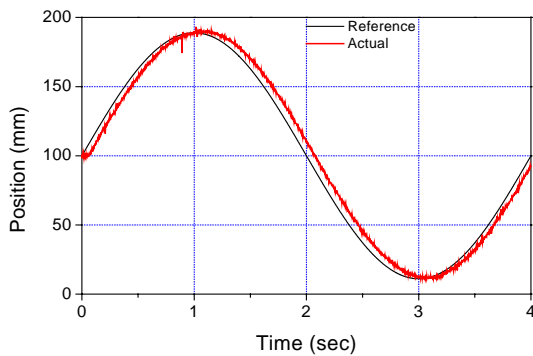


Figure 6 Result of step response test

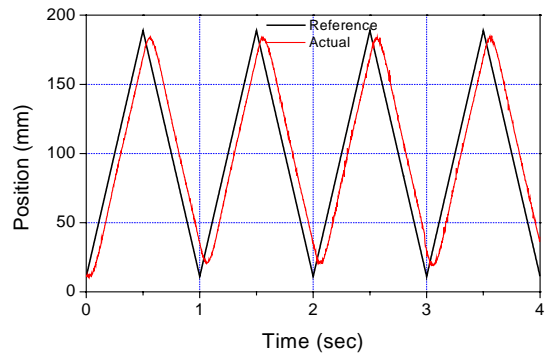


(a) Tracking test of ramp wave signal

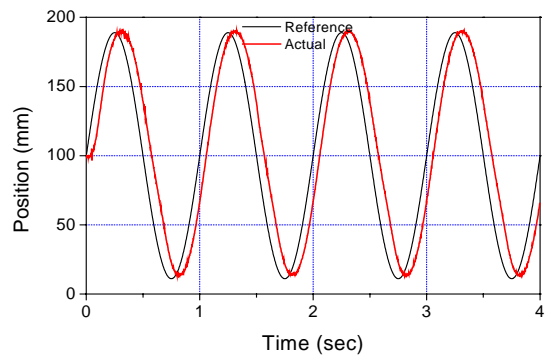


(b) Tracking test of sine wave signal

Figure 7 Results of tracking test at input of 0.25Hz



(a) Tracking test of ramp wave signal



(b) Tracking test to sine wave signal

Figure 8 Results of tracking test at input of 1Hz

The vehicle control test was conducted in the running mode, and each result of the tracking control test as conducted in the JPN1015 LAP mode and the CVS test mode was described in Figure 9 and Figure 10. In the JPN1015 LAP mode, the said test was repeatedly and periodically conducted 10 times every 200 seconds, while in the CVS test mode, it was repeatedly and periodically conducted 10 times every 900 seconds. As a result of conducting the test, it could be verified that it was excellent in the tracking performance, durability and stability.

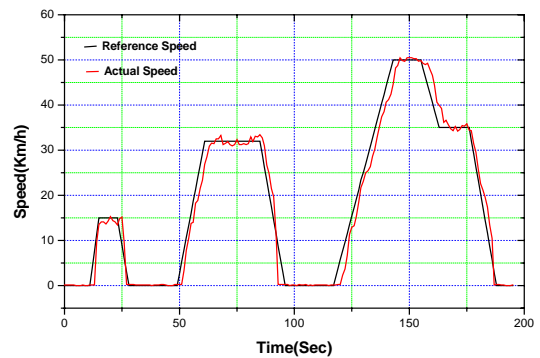


Figure 9 Result of tracking test at JPN1015 LAP mode

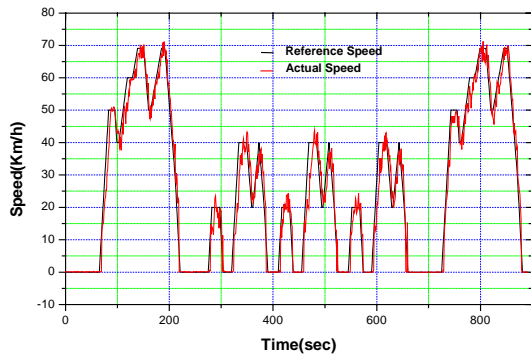


Figure 10 Result of tracking test at CVS test mode

CONCLUSIONS

The Lab. simulator comprising the vehicle controller and the servo controller was designed and embodied, and it was installed in an actual vehicle. Then, its performance and control characteristic experiment was conducted. The results of such experiment could be summarized as follows:

- 1) The step response experiment, the triangular wave and sine wave experiment and the LAP mode tracking test were conducted by using the Lab. simulator which was designed and embodied as above described, and as a result, its tracking capability and position control precision satisfied the target specification. And, it was verified that it was applicable to the vehicle test.
- 2) The vehicle controller and the servo controller were applied to the vehicle control system, and then a test was conducted. As a result, its repeatability, precision, control characteristic and stability were excellent.
- 3) It is thought that the Lab. simulator for controlling a vehicle will be greatly applicable to the whole industry related to vehicle technology as well as the auto pilot system, including development and test of a test system to which it is applied, particularly, the mileage accumulator test, the exhaust gas measurement test, the fuel consumption test, the environment test, the noise measurement test and so on.

REFERENCES

1. Hyung-Eui Kim et al, Develop Report of Auto Pilot Lab. Simulation, MOICE, 2000.
2. Jeongdai Jo et al, The Design of Lab. Simulator, *Proc of KSAE 2002*, pp445-449.
3. Auto Pilot Operation Manual, ATOMAX, 1992.
4. Lap Mode Test Sheet, EPA, 1996.
5. Intel 386EX Embedded Microprocessor User's Manual, Intel, 1996.
6. 8XC196Kx Microcontroller Family User's Manual, Intel, 1990.
7. In-Uk Kong et al, Intel 80386EX Microrobot Design, Ohm Inc., 1998.

A NEW METHOD TO PREDICT THE OCCURRENCE OF STICK-SLIP IN PNEUMATIC CYLINDERS

Bai-hai ZHANG, Yan-feng MA, Hai-feng CHENG and Guang-zheng PENG

SMC-BIT Pneumatics Center, Department of Automatic Control,
School of Information Science and Technology,
Beijing Institute of Technology
Beijing 100081, China
(E-mail: smczhang@bit.edu.cn)

ABSTRACT

Pneumatic cylinders can not usually retain steady motion when a low speed is required because of the stick-slip effect. Stick-slip is a kind of motion in which the piston stops its motion intermittently because of the friction force. In this paper a neural network (NN) classifier is set up as a new method to predict the occurrence of stick-slip by different dynamic working parameters.

The classifier is made of an NN, and the training samples come from the simulation. It classifies different working conditions into two groups: stick-slip will occur and stick-slip won't occur, without concerning the process and the model. The NN is based on a back-propagation (BP) neural network. The input variables may be single variables of the dynamic working parameters or the combinations of them and the output variables are the two groups.

KEY WORDS

Pneumatic cylinder, Stick-slip, Neural network, Continuous genetic algorithm, Classifier

INTRODUCTION

Pneumatic cylinders play a key role in pneumatic systems. They transform the energy of compressed air into mechanical energy. The steady motion of pneumatic cylinders directly affect whether the driving system works regularly, therefore it is necessary to estimate the occurrence of stick-slip in pneumatic cylinders.

The structure of the pneumatic system is illustrated in Figure 1. It is a meter out circuit. The system is composed of the following parts: air source, a directional control valve, one meter-out speed control valve, a pneumatic cylinder and load mass. In this paper, we just consider the push out process of the cylinder.

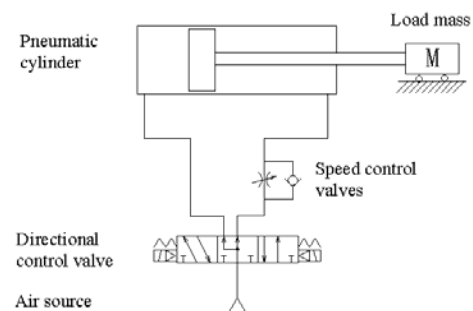


Figure 1 Pneumatic driving system by meter out circuit

We use 20-sim and bond graph as the modeling and simulation tool in our work [1,2].

The criterion of the occurrence of stick-slip in the pneumatic cylinder is whether the piston velocity reaches 0. Since the stick-slip motion has a correlation with many potential pneumatic conditions such as friction forces, air source pressure, lubrication condition, temperature, system stiffness, it is difficult to build a comprehensive fundamental stick-slip model. A black box model, NN is used to classify whether stick-slip motion will occur or not under certain working parameter settings. With this method, input and output variables can be related without any knowledge or assumptions about the mathematical representation. Many experiments and simulations on pneumatic cylinders have been done before and are found in good accordance, so that simulation can make an excellent data set for use with NN as training samples.

Of the many possible NNs, BP is one of the most commonly used NN architectures for classification. In this study, BP is used to classify whether the stick-slip motion will occur or not. The performance of the BP network is affected by the architecture and parameter settings of the network [3]. Users must therefore determine the required numbers of optimal layers, neurons in the hidden layers, weights of the NN and bias of the neurons. However, there has been no clearly defined theory for calculating the ideal parameter settings, and even slight parameters' changes can cause major variations in the behaviors of almost all networks [4]. In this study, in order to optimize the architecture of NN, continuous genetic algorithm is employed to determine the weights and bias.

1. NN INCORPORATING GENETIC ALGORITHMS IN STICK-SLIP PREDICTION

The architecture of NN has considerable influence on their performance. For multi-layered BP, the first thing is to decide the number of layers. The architecture of three or four layers is commonly used. There is also a two-layered architecture whose input layer is connected with the output layer directly. This architecture is used only when the input model is similar to the output model. Otherwise if the input model is different from the output model, hidden layers should be added between them to transmit the information which can make the nonlinear classification problem in the input space be transformed into linear classification in the hidden space. The more hidden layers are in the NN the more effect on the information transmission. However it is not the more hidden layers the better NN. There are two reasons. The first reason is that as the increasing of the number of hidden layers it brings increasing computation of the error's back propagation, and the

training time increases sharp. The second reason is that as the increasing of the number of hidden layers local minimal error increases. It is easy to be lost in the local minimal value during the training process.

Based on the above analysis a three-layered architecture with one input layer, one hidden layer and one output layer is chosen in this study. The number of neurons in the input layer, hidden layer and output layer are set at 4, 3(4, 5, 6, 7), and 1, respectively [5]. These numbers of neurons in the hidden layer n_h is set by Eq. 1.

$$n_h = \text{sqrt}(n_i + n_o) + n \quad (1)$$

n_i is the number of neurons in the input layer; n_o is the number of neurons in the output layer; n is an integer and its range is 0~7. The architecture of the NN is shown in Figure 2.

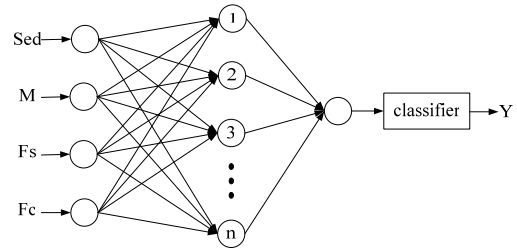


Figure 2 Architecture of the neural network

In the input layer, each neuron corresponds to a working parameter. In the hidden layer and the output layer each neuron's output is calculated using Eq. (2).

$$net = x_1\omega_1 + x_2\omega_2 + \dots + x_n\omega_n + bias_i \quad (2)$$

Usually a neuron's output is modified by the transfer function. The sigmoid function as shown in Eq. (3) is used for this transfer function.

$$f(net) = \frac{1.0}{1.0 + e^{-net}} \quad (3)$$

Here x_i is the value of the input variable, ω_i is the connection weight between the input and hidden neurons and between the hidden and output neurons, $bias_i$ is bias term for the hidden and output neurons, respectively.

In Fig.1, a classifier is used to classify the output of the NN into two types:

$$Y = f(x) = \begin{cases} 1 & x \geq 0.5 \\ 0 & x < 0.5 \end{cases} \quad (4)$$

Here $Y=1$ means the stick-slip motion will occur, otherwise won't occur, x represents the output of the

output layer.

2. OPTIMIZING NN'S PARAMETERS BY USING GENETIC ALGORITHMS

A continuous genetic algorithm application process for optimizing the parameters (the weights and the biases) of NN is used. This will avoid being lost in the local minimal value during the searching process. The continuous GA has the advantage of requiring less storage than the binary GA because a single floating-point number represents the variable instead of N bits binary number. The continuous GA is also inherently faster than the binary GA, because the chromosomes do not have to be decoded prior to the evaluation of the cost function [6].

The momentum of the chromosomes has a lower bound of 0 and an upper bound of 1. The number of chromosomes (population size) and the number of generations are set to 100 respectively. Every chromosome in a generation evolves into new chromosomes for 100 generations unless the break condition is satisfied.

The flow chart of the NN classifier can be expressed in Figure 3.

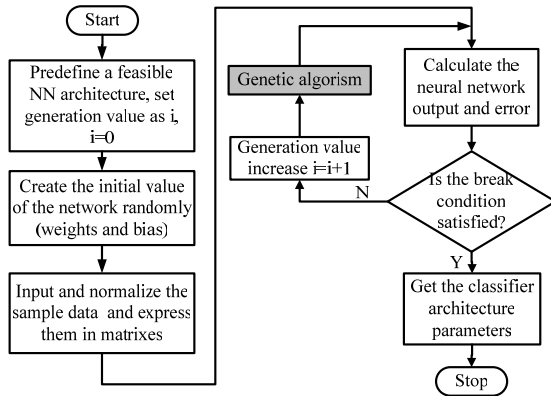


Figure 3 The flow chart of the NN classifier

It is reasonable to express a continuous variable by a float-point number, so the m chromosomes with n vectors can be expressed as a matrix named A with m rows and n columns. a_{ij} is the j^{th} variables of the i^{th} chromosome.

The basic algorithms in continuous variables GA can be expressed as follows:

2.1. CROSS-OVER

Choose the k^{th} and the l^{th} chromosomes in the m chromosomes group stochastically. The cross-over is realized through Eq. (5) and Eq. (6):

a_{kj} is variable of the k^{th} chromosomes

$$\xrightarrow{\text{Chiasma}} a'_{kj} = a_{kj}(1 - \beta_j) + \beta_j a_{lj} \quad (j = 1 \sim n) \quad (5)$$

a_{lj} is variable of the l^{th} chromosomes

$$\xrightarrow{\text{Chiasma}} a'_{lj} = a_{lj}(1 - \beta_j) + \beta_j a_{kj} \quad (j = 1 \sim n) \quad (6)$$

Here $0 < \beta_j < 1$ is the cross-over parameter, and a'_{kj} and a'_{lj} present the new values after cross-over. Since cross-over is the information exchange of the chromosomes, the sum of the variables in the cross-over chromosomes keeps the same value as shown in Eq. (7):

$$a_{kj} + a_{lj} = a'_{kj} + a'_{lj} \quad (j = 1 \sim n) \quad (7)$$

Different from the scattered variables' cross-over, the continuous variables' cross-over exchange every variable in the chromosome. It is similar to the n section exchange in binary variables' cross-over which will enrich the exchange information.

2.2. MUTATION

Choose m variables in the chromosome group, and choose $0 < \xi, \eta < 1$ stochastically, operate the mutation according to Eq. (8):

$$\begin{cases} a''_{ij} = a_{ij} - (a_{ij} - \underline{a}_j)\eta & 0 < \xi \leq 0.5 \\ a''_{ij} = a_{ij} + (a_{ij} - \bar{a}_j)\eta & 0.5 < \xi < 1 \end{cases} \quad (8)$$

Here \underline{a}_j and \bar{a}_j is the lower limit and the upper limit of the j^{th} variable, a''_{ij} is the new value after mutation. The mutation variables get increased when $0 < \xi \leq 0.5$ and decreased when $0.5 < \xi < 1$. And the extent is controlled by η .

Generalize the continuous GA's step as follows:

- 1) Build the initial chromosome group as mother generation, named as array A . The row number is m , which will affect the searching result. In this study, m is set to 100.
- 2) Extend the chromosome group to 2 times. m variables are chosen from the $2m$ variables to do cross-over stochastically. n variables are chosen to do mutation stochastically. n is 1% of the whole variables.
- 3) Connect the original array and the new array after mutation, which is 3 times extension of the original array. Calculate the NN output and error.

Choose the variables corresponding to the m least errors as the new mother generation.

- 4) Finish propagates. There are 3 conditions to break the evolutionary cycle. Firstly, when the error gets 0 the cycle will break. Secondly, if it has reached 100 generations the cycle will break. Thirdly, if the NN output error hasn't improved for more than 10 generations, the cycle will break and return the optimal value. Otherwise return to step 2.

The continuous variables genetic algorithm shown in the Figure 3 is expressed in Figure 4.

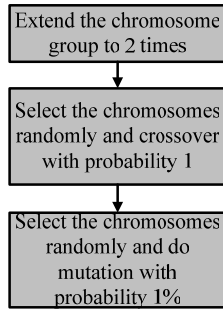


Figure 4 The continuous variables genetic algorithm

3. SAMPLE PREPARATION

Stick-slip is a kind of motion in which a body stops its motion momentarily or definitively because of the action of friction force. The friction force depends on a number of factors, such as lubrication condition, the velocity of pneumatic cylinders and the load mass. In order to derive how the parameters affect the stick-slip, the model of a pneumatic system by meter out circuit is built by using bond graph method. Simulations are carried out with different working parameters such as the friction characteristics, the effective area of the outlet speed control valve and load mass [1]. The training samples used in the NN come from the simulations of the stick-slip in pneumatic system. Simulations are carried out by running multiple simulations with parameter sweep.

Through the simulations under different working parameters, stick-slip will occur or not. It can be seen that the different working parameters such as friction characteristics, the effective area of the outlet speed control valve and load mass have some nonlinear relations with stick-slip occurrence in pneumatic cylinders. The working parameters or their combinations can be set as the input parameters of input layer of the NN. Whether the stick-slip will occur is set as the output of output layer of the NN. To realized this, a new variable Y is set as the output to express the state of stick-slip. If the stick-slip occurs, $Y=1$; otherwise, $Y=0$. In this study, four input variables: the effective area of

the outlet speed control valve Sed , load mass M , the maximum static friction force F_s and coulomb friction force F_c are set as the input of NN, so that there are totally four neurons in the input layer. If more working parameters or their combinations are expected, the neurons in the input layer should be increased, and the neurons in the hidden layer should also be changed accordingly.

100 training samples are used to train the NN. 40 test samples are used to test the training result. They both come from the simulation of stick-slip. Table 1 shows part of the samples of the parameters extracted from the simulation results.

Table 1 Extracted parameters

	$Sed(m^2)$	$M(kg)$	$F_s(N)$	$F_c(N)$	Y
1	1.0e-8	8	18	13	0
2	1.0e-8	20	28	7	1
3	1.5e-8	12	24	16	0
4	2.0e-8	20	36	10	1
5	4.0e-8	40	36	10	0

Parameters dimension in the first column of table 1 Sed is much smaller than the others. The weights and the biases of the network are extracted from a generation's array of stochastic numbers whose elements are uniformly distributed in the interval (0, 1). Then the effect brought by Sed will be much less than the other parameters, which will decrease the precision of the output or lead to the float of the optimize value. Hence the samples should be preprocessed by normalizing the inputs and outputs so that they have means of 0 and standard deviations of 1 before training.

4. TRAINING RESULT

The training process for the NN classifier to predict the occurrence of the stick-slip is carried out when the number of neurons in hidden layer is 3, 4, 5, 6 and 7 respectively. The result shows that when there are 3 neurons in the hidden layer optimal result can be found with the least time. The optimal architecture of NN is build by one hidden layer with 3 neurons. The NN's parameters which are trained by the optimal architecture are used to test the 40 test samples. Figure 5 shows the test result of the NN classifier.

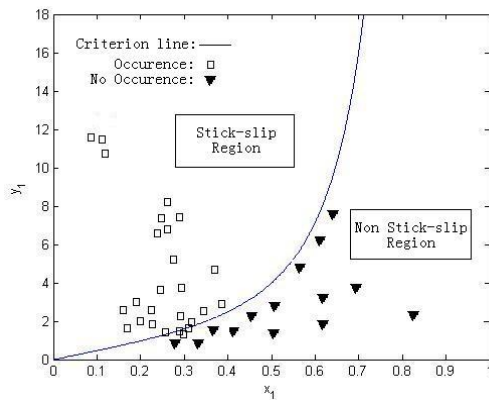


Figure 5 The result of the classifier

In Figure 5, x_1 axis and y_1 axis represents two dimensionless values calculated through the model of pneumatic system, which is presented in reference [7]. The curve in Figure 5 is the criterion curve which separates the whole area into stick-slip region and non stick-slip region. Test samples are marked in Figure 5. It shows that most test samples located in the right region. The error rate of the classifier is less than 4%.

CONCLUSION

A classifier made of the NN based on continuous GA is realized to predict the occurrence of stick-slip in a pneumatic cylinder. Continuous GA ensures the precision of the classifier. To complete the training process, simulations are carried out with different working parameters to acquire the training and test samples. The prediction results of the classifier are in agreement with former analytical solution. The error rate of the classifier is acceptable.

REFERENCES

1. Zhang, B.H. and Cheng, H. F., Bond Graph Modeling and Simulation of Stick-slip Characteristics of a Pneumatic System, The Sixth International Conference on Fluid Power Transmission and Control, 2005, pp.569-572.
2. Controllab Products B.V. Getting Started with 20-sim 3.4, Controllab Products B. V., Enschede, 2003
3. Kim, G.H., Yoon, J.E., An S.H., Cho, H.H. and Kang, K. I., Neural Network Model in Cooperating a Genetic Algorithm in Estimating Construction Costs, Building and Environment, 2004, **39**, pp.1333-1340.
4. Finnie, G.R., Witting, G.E. and Desharnais, J.M., A Comparison of Software Effort Estimation Techniques: Using Function Points with Neural Networks, Case-based Reasoning and Regression Models, Systems and Software, 1997, **39-3**, pp.281-289.
5. Cui, R., Hong, B. ,On Constructing a Hidden Layer for Three-layered Feed forward Neural Networks ,Computer Research and Development, 2004, **41-4**.
6. Haupt, R., Haupt, S. Practical Genetic Algorithms 2nd Edition, John Wiley & Sons, Inc., New Jersey, 2004, pp.51-64.
7. Tokashi, L.R., Fujita, T., Kagawa, T. and Ikegami, T., Stick-slip Motion in Pneumatic Cylinders Driven by Meter Out Circuit, Transactions of the Japan Hydraulics & Pneumatics Society, 1999, **30-4**, pp.22~29.

CHARACTERISTICS OF THE COMPRESSIBLE FLOW BETWEEN TWO PARALLEL DISKS

Hiroyuki SATO*, Koji TAKAHASHI**, Keigo OHTANI***, Shigeru IKEO****

*Development Department, Technical Center, SMC Corporation
4-2-2, Kinunodai, Yawara-mura, Tsukuba-gun, Ibaraki 300-2493, Japan
(E-mail: hiroyuki_sato@smcjpn.co.jp)

**Professor Emeritus, Sophia University

4-23-9 Hiyoshicho, Kokubunji, Tokyo 185-0032, Japan

***Data Processing Department, Suzuki Motor Corporation

1300 Takatsukacho, Hamamatsu-shi, Shizuoka 432-8611, Japan

****Professor, Department of Mechanical Engineering, Sophia University
7-1 Kioicho, Chiyoda-ku, Tokyo 102-8554, Japan

ABSTRACT

Compressible flows between two parallel disks are frequently encountered in fluid power components such as pneumatic statistical bearings, pneumatic nozzle-flapper valves and pneumatic valves. Such flows are difficult to solve theoretically because both viscous and compressible effects exist. In the present study, a theory is developed to predict the flow characteristics, assuming that the flow is one dimensional and steady. Experiments are performed, and their results agree fairly well with theoretical results.

KEY WORDS

Viscous compressible flow, Flow characteristics, Critical pressure ratio, choked flow rate

NOMENCLATURE

A : flow sectional area= $2\pi rh$
 b : critical pressure ratio
 c_p : specific heat at constant pressure
 d_i : valve seat hole diameter= $2r_i$
 f : friction factor= 0.0026
 h : gap clearance
 k : specific heat ratio= 1.40
 LL : lap length (see Figure 1)
 M : Mach number
 p : absolute pressure
 R : gas constant= 287 J/(kg.K)
 r : radial coordinate
 T_0 : stagnation temperature, constant for an adiabatic flow
 T : absolute temperature
 V : mean velocity at a section
 w : mass flow rate
: fluid density

Subscript

e : outer edge of the gap
 i : inner edge of the gap
 0 : upstream condition
 $*$: condition at the choked flow

INTRODUCTION

Flows between two parallel disks are frequently seen in fluid power components such as statistical bearings, nozzle-flapper valves and seat valves. Although many theoretical papers [1] have been published for incompressible flows, those related to compressible flows are not so many, because for such flows both viscous and compressible effects should be taken into consideration.

Mori [2] analyzed an unstable phenomenon named whirl which occurs in a gas bearing. Ogami [3]

analyzed a one-dimensional viscous compressible flow by numerical method. Kamiyama and Yamamoto [4] numerically investigated a compressible flow in aerostatic journal bearing. Kobayashi [5] investigated the stability of gas-lubricated journal bearings experimentally and numerically.

In the present study, the authors assumed the flow between two parallel disks to be one-dimensional and steady and developed a theory to solve the flow. Experiments were performed, and the comparison between theoretical and experimental results showed that the theory can predict the flow characteristics.

THEORY

The flow between two disks as shown in Figure 1 is to be analyzed [6].

The equation of state for an ideal fluid is

$$p = \rho RT \quad (1)$$

Mach number is

$$M^2 = V^2 / (kRT) \quad (2)$$

The energy equation for adiabatic flow is

$$c_p T + \frac{V^2}{2} = c_p T_0 \quad (3)$$

The continuity equation is

$$w = A\rho V = 2\pi rh\rho V \quad (4)$$

Applying the equation of motion for steady flow in the radial direction, we have

$$VdV = -\frac{dp}{\rho} - \frac{\tau}{\rho} \frac{dA_w}{A} \quad (5)$$

where τ is the wall shear stress and dA_w is the wetted area on which τ is exerted.

Provided that the friction losses between two disks are similar to those in a circular tube, friction factor f is defined by

$$f = \frac{\tau}{\rho V^2 / 2} \quad (6)$$

Differentiating Eqs.(1), (2), (3) and (4), and combining these equations, Eqs.(5) and (6), we finally obtain the following:

$$\frac{dp}{p} + \frac{dr}{r} = -\frac{1 + (k-1)M^2}{2\left(1 + \frac{k-1}{2}M^2\right)} \frac{dM^2}{M^2} \quad (7)$$

and

$$\frac{1 - M^2}{M^2 \left(1 + \frac{k-1}{2}M^2\right)} dM^2 = 2 \left(\frac{fkM^2}{h} - \frac{1}{r} \right) dr \quad (8)$$

Generally speaking, Eq.(8) may be difficult to be solved. Friction factor f , however, has normally a small value and the effect of M^2 in the first term in the parenthesis on the right-hand side will be small. Accordingly, assuming that M^2 is constant,

$$M^2 \approx M_{av}^2 = (M_i^2 + M_e^2) / 2 = \text{const} \quad (9)$$

Then, Eq.(8) can be integrated from r_i to r_e to obtain the following:

$$\frac{r_e}{r_i} \frac{G(M_i)}{G(M_e)} = \alpha \quad (10)$$

where

$$G(M) = \frac{1}{M} \left(1 + \frac{k-1}{2} M^2 \right)^{\frac{k+1}{2(k-1)}} \quad (11)$$

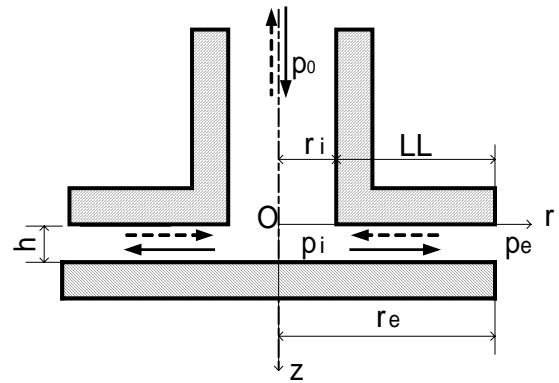


Figure 1 Flow between two parallel disks

and

$$\alpha = \exp \left[\frac{fkM_{av}^2 (r_e - r_i)}{h} \right] \approx 1 + \frac{fkM_{av}^2 (r_e - r_i)}{h} \quad (12)$$

Outward flow

Integrating Eq.(7), we get

$$\frac{p_e}{p_i} = \frac{r_i}{r_e} \frac{M_i}{M_e} \sqrt{\frac{1 + \frac{k-1}{2} M_i^2}{1 + \frac{k-1}{2} M_e^2}} = \frac{r_i}{r_e} \frac{H(M_i)}{H(M_e)} \quad (13)$$

where

$$H(M) = M \sqrt{1 + \frac{k-1}{2} M^2} \quad (14)$$

In an outward flow, pressure p_e at the outer edge divided by stagnation pressure p_0 upstream is usually taken as pressure ratio for outward flow.

The following formula holds for isentropic change:

$$\frac{p_0}{p_i} = \left(\frac{\rho_0}{\rho_i} \right)^k = \left(\frac{T_0}{T_i} \right)^{\frac{k}{k-1}} \quad (15)$$

Combining Eqs.(2), (3) and (15) we have

$$p_i = \frac{p_0}{\left(1 + \frac{k-1}{2} M_i^2 \right)^{\frac{k}{k-1}}} \quad (16)$$

By substituting p_i in Eq.(16) into Eq.(13) and using Eq.(10), the pressure ratio p_e/p_i is obtained as follows:

$$\begin{aligned} \frac{p_e}{p_0} &= \frac{r_i}{r_e} \frac{1}{G(M_i)H(M_e)} = \frac{1}{\alpha G(M_e)H(M_e)} \\ &= \frac{1}{\alpha \left(1 + \frac{k-1}{2} M_e^2 \right)^{\frac{k}{k-1}}} \end{aligned} \quad (17)$$

When substituting any Mach number M_i at the inner edge and Mach number M_e obtained from Eq.(10) into Eq.(17), the pressure ratio p_e/p_0 corresponding to M_i can be calculated.

Next, mass flow rate w is to be obtained. Substituting Eqs.(1), (2), (16) and (15) into Eq.(4) we get

$$\begin{aligned} w(M_i) &= 2\pi r_i h \sqrt{\frac{k}{R}} \frac{p_0}{\sqrt{T_0}} \frac{M_i}{\left(1 + \frac{k-1}{2} M_i^2 \right)^{\frac{k+1}{2(k-1)}}} \\ &= 2\pi r_i h \sqrt{\frac{k}{R}} \frac{p_0}{\sqrt{T_0}} \frac{1}{G(M_i)} \end{aligned} \quad (18)$$

Choked flow rate w^* is

$$w^* = 2\pi r_i h \sqrt{\frac{k}{R}} \frac{p_0}{\sqrt{T_0}} \frac{1}{G(1)} \quad (18')$$

When Mach number M_i at the inner end is unity, Eq.(10) is rearranged as

$$\alpha(1, r_e)G(M_{ec}) - \frac{r_e}{r_i} G(1) = 0 \quad (19)$$

where M_{ec} is the Mach number at the outer end corresponding to $M_i=1$.

Substituting the value of M_{ec} into Eq.(17), critical pressure ratio b is expressed as

$$b = \frac{1}{\alpha \left(1 + \frac{k-1}{2} M_{ec}^2 \right)^{\frac{k}{k-1}}} \quad (20)$$

Inward flow

Consider an inward flow in which the flow is reversed. In this case subscript e denotes upstream conditions, and subscript i downstream ones in Figure 1. Since most equations derived for an outward flow can be applied as well, we will describe here only those equations which need modification. It should be noted that velocity V is negative, so that shear stress and friction factor f are negative. Consequently in Eq. (10) should be replaced by $1/$

$$\frac{r_i}{r_e} \frac{G(M_e)}{G(M_i)} = \alpha \quad (21)$$

Giving any value of M_e into Eq.(21), we can get M_i . Equation (16) is modified as follows:

$$p_e = \frac{p_0}{\left(1 + \frac{k-1}{2} M_e^2 \right)^{\frac{k}{k-1}}} \quad (22)$$

In an inward flow, pressure p_i at the inner edge divided by stagnation pressure p_0 upstream is usually taken as pressure ratio for inward flow, which is expressed by

$$\frac{p_i}{p_0} = \frac{r_e}{r_i} \frac{1}{G(M_e)H(M_i)} \quad (23)$$

Substitution of Eq.(21) into Eq.(23) yields

$$\frac{p_i}{p_0} = \frac{1}{\alpha \left(1 + \frac{k-1}{2} M_i^2 \right)^{\frac{k}{k-1}}} \quad (24)$$

When substituting any Mach number M_e at the outer edge and Mach number M_i obtained from Eq.(21) into Eq.(17), the pressure ratio p_i/p_0 corresponding to M_e can be calculated.

Using Eq.(21) mass flow w is expressed by

$$w = 2\pi r_e h \sqrt{\frac{k}{R}} \frac{p_0}{\sqrt{T_0}} \frac{1}{\alpha G(M_i)} \quad (25)$$

Choked flow rate w^* is

$$w^* = 2\pi r_e h \sqrt{\frac{k}{R}} \frac{p_0}{\sqrt{T_0}} \frac{1}{G(1)} \frac{1}{\alpha(M_e, r_i)} \quad (25')$$

When Mach number M_i at the inner end is unity, Eq.(21) is rearranged as

$$\frac{G(M_{ec})}{\alpha} - \frac{r_e}{r_i} G(1) = 0 \quad (26)$$

where M_{ec} is the Mach number at the outer end corresponding to $M_i=1$. Substituting the value of M_{ec} into Eq.(24), critical pressure ratio b is expressed as

$$b = \frac{1}{\alpha} \left(\frac{2}{k+1} \right)^{\frac{k}{k-1}} \quad (27)$$

When there is no friction loss, b becomes unity, and $b=0.528$, which coincides with the value for the isentropic flow in a convergent nozzle.

EXPERIMENT

Figure 2 shows the test valve used. In an outward flow compressed air was fed from port A, and in an inward flow from port B.

The supply pressure of air was kept 500 kPa abs, and air temperature was 290 K during experiments. The downstream pressure (p_e for an outward flow and p_i for an inward flow) was adjusted with a throttle valve placed downstream of the test valve.

In Figure 1, actual dimensions are as follows:

Outer radius $r_e=10$ mm,

Valve seat hole diameter $d_i=5$ and 10 mm,

Lap length $LL=1, 3$ and 5 mm.

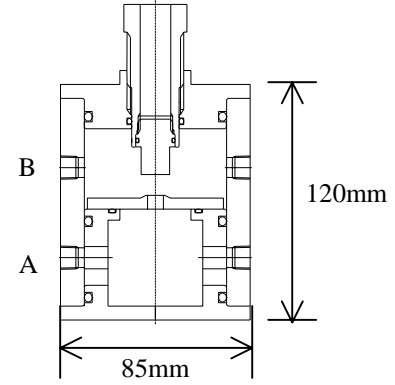
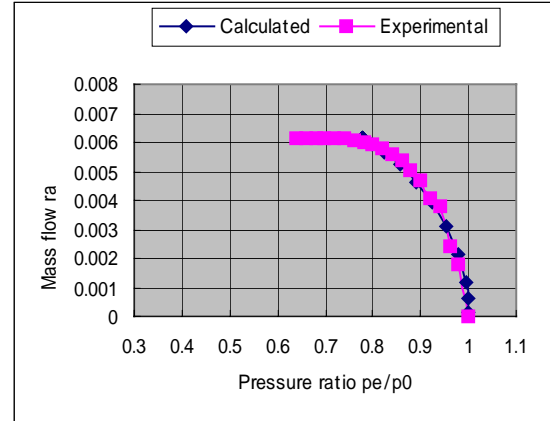


Figure 2 Test valve

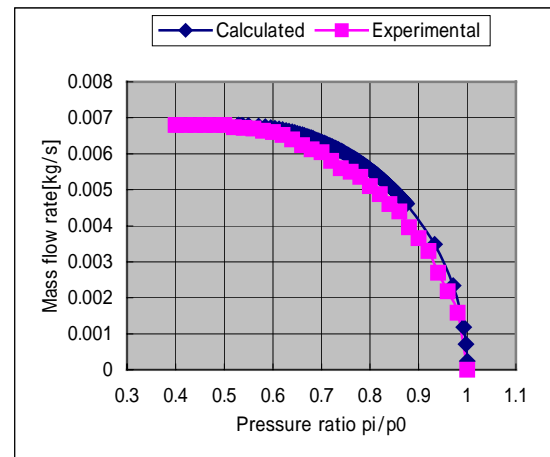
RESULTS

Flow characteristic

Figure 3(a) shows an example of the comparison of the calculated results with the experimental ones for an



(a) Outward flow



(b) Inward flow

Figure 3 Comparison between theory and experiment, $d_i=10$ mm, $LL=5$ mm

outward flow with some modification in lap length explained later, and Figure 3(b) for an inward flow.

The calculated results agree well with the experimental ones for inward flows. The values of critical pressure ratio are close to 0.528, the value of critical pressure ratio for isentropic flow in a convergent nozzle.

In an outward flow, however, calculated results did not agree well with experimental ones. And the calculated results deviate from the experimental ones as approaching choke flow. It can be deduced that flow separation might occur at the inner end. It would be necessary to estimate the lap length smaller than the real size. In Figure 3(a), LL was set to 0.9 mm instead of 5 mm in calculation, the difference in LL is considered to be the flow separation. After this modification, calculated results agree fairly well with experimental ones, as shown in Figure 3(a).

Figure 4 shows that for the same gap width choked flow rate w^* for an outward flow is less than that for an inward flow.

As can be seen from Figures 5(a) and 5(b), critical pressure ratios for outward flows are greater than those for inward flows.

Effect of viscosity

Throughout the experiment, gap width h was between 0.1 and 0.3 mm. For such widths, α in Eq. (12) is approximately unity, and the viscous effect of air can be neglected. For smaller gap width, however, it would be necessary to take into consideration the effect of friction.

Effect of lap length

Figure 5(a) shows the experimental results of the effect of lap length on critical pressure ratio for outward flows, and Figure 5(b) for inward flows. In theory, the lap length only affects friction, which is very small in the range of experiment, the results for inward flows are reasonable.

In outward flows, however, critical pressure ratio increases with an increase in lap length.

Critical pressure ratio vs. mass flow rate

Figures 6 show the relations between critical pressure ratio b and choked mass flow rate w^* . According to the theory, as can be seen from Eqs.(20) and (27), values of critical pressure ratio are independent of choked flow rate in frictionless flows ($\alpha=1$).

In experiment, choked mass flow rate w^* gives little effect on b for both outward and inward flows as shown in Figures 6, and the theory agrees to the experimental results in the range of the experiment. More experiments with larger flow rates would be necessary, however, to confirm the validity of the theory.

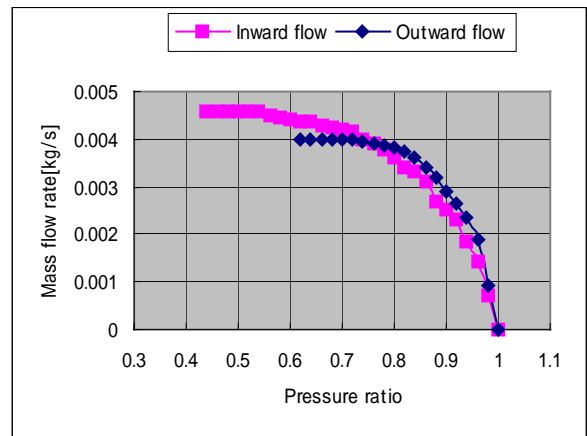
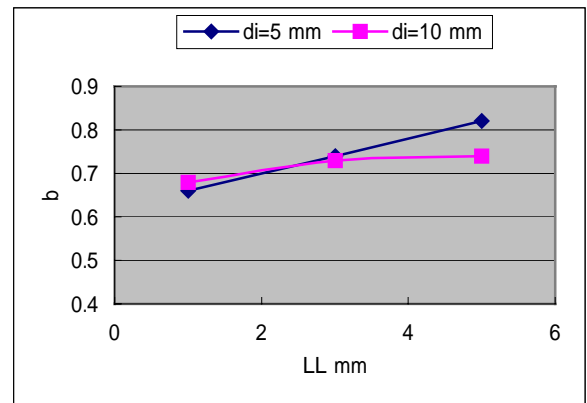
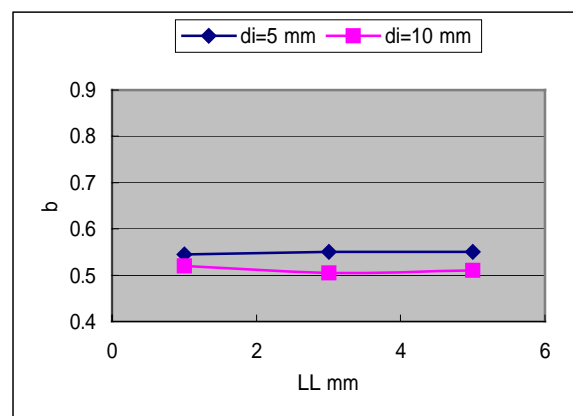


Figure 4 Comparison between outward and inward flows, $d_i=5$ mm, $h=0.22$ mm

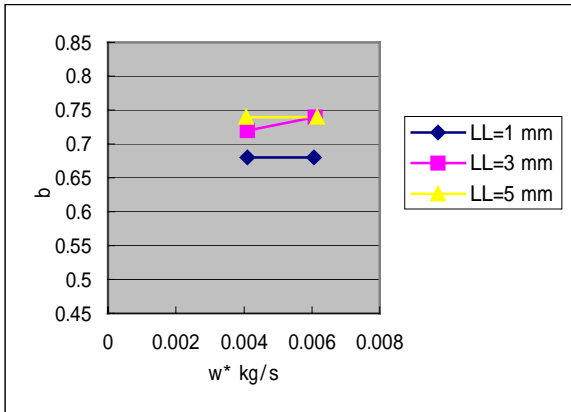


(a) Outward flow

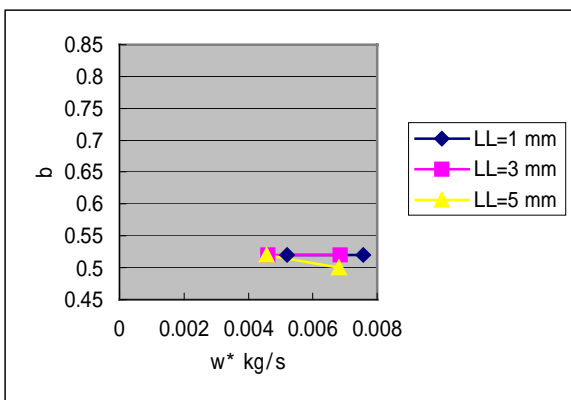


(b) Inward flow

Figure 5 Effect of lap length



(a) Outward flow



(b) Inward flow

Figure 6 Relation between critical pressure ratio and choked mass flow rate, $d_i=10$ mm

CONCLUDING REMARKS

A theory is developed for flow characteristics between two parallel disks, and its validity is confirmed by the comparison with experimental results. In regard to outward flows, however, some discordance between theory and experiment is observed.

Consequently, the following conclusions are drawn:

- 1) In inward flows, flow characteristics can be predicted from the theory. The value of critical ratio is close to that of convergent nozzle flow;
- 2) In outward flows, some modification is necessary to apply the theory to flow characteristics, i.e., the lap length in lap length should be taken smaller than real size.

This is considered to result from the separation at the inner edge of the gap;

- 3) For the same gap width, the choked flow rate for outward flows is less than that for inward flows;
- 4) Critical pressure ratio for outward flows is generally larger than that for inward flows;

5) Friction losses through the gap little affect the values of w^* and b in the range of this study, i.e., gap widths larger than 0.1 mm. If the gap width were more reduced, however, the frictional effect would appear;

6) In outward flows, an increase in lap length increases critical pressure ratio, while in inward flows lap length little affects the value.

ACKNOWLEDGMENT

The authors would like to express their deepest appreciation to Messrs. N. Oneyama, H. Zhang and M. Senoo, Technical Center of SMC Corporation, for their kind help and advice in conducting this study.

REFERENCES

1. e.g., Ishizawa, S., Watanabe, T. and Takahashi, K., Unsteady Viscous Flow between Parallel Disks with a Time-Varying Gap Width and a Central Fluid Source, *Trans. ASME, J. Fluid Eng.* Vol.109, (1987), p.394
2. Mori, A., On the Whirl Instability in Gas-Bearings (In Japanese), *Lubrication*, Vol.20, No.7, (1975), p.481
3. Ogami et al, Numerical Simulation of One-Dimensional Viscous Compressible Fluid Motion Using particle method (In Japanese), *Trans. JSME*, Vol.62, No.604, (1996), p.4084
4. Kamiyama, T. and Yamamoto, M., Numerical Investigation of Compressible Flow within Aerostatic Journal Bearing (In Japanese), *Trans. JSME, Ser. B*, Vol.65, No.629, (1999), p.144
5. Kobayashi, T., Stability of Axially-Grooved Self-Acting Gas-Lubricated Journal Bearings (In Japanese), *Trans. JSME, Ser. C*, Vol.65, No.629, (1999), p.330
6. e.g., Shapiro, A. H.: *The Dynamics and Thermodynamics of Compressible Fluid Flow*, Vol. 1, (1953), Ronald Press, p. 80